Proceedings of the Sixth International Workshop on

The Physics of Compressible Turbulent Mixing

Institut Universitaire des Systèmes Thermiques Industriels
Marseille 18-21 June 1997, France

Georges Jourdan & Lazhar Houas

IUSTI/CNRS, Université de Provence, Technopôle de Château-Gombert
5, rue Enrico Fermi, 13453 Marseille cedex 13, France

Printed in France, 1997
by Imprimerie Caractère
26, rue Saint Bruno, 13004 Marseille

Preface

The sixth International Workshop on the Physics of Compressible Turbulent Mixing was held from 18 to 21 June, 1997, in Marseille Institut Universitaire des Systèmes Thermiques Industriels building of the University of Provence.

The first Workshop was held in Princeton (NJ, USA) in 1988, soon followed by the second in Pleasanton (CA, USA) in 1989. From this time these conferences repeated every two years: Royaumont (France, 1991), Cambridge (UK, 1993) and Stony Brook (NY USA, 1995), and the name International Workshop on the Physics of Compressible Turbulent Mixing was adopted from 1991.

The main topics of these workshops deal with the problems of hydrodynamic instabilities of different density fluid interfaces submitted to constant or varying acceleration, called Rayleigh-Taylor instability, and shock wave impulsive type of acceleration, called Richtmyer-Meshkov instability, at all stages, that is from the development of the initial small perturbation to the turbulent mixing.

The total number of participants who registered was 113 from 9 countries: Russia (35), USA (30), France (29), Israel (8), UK (5), Switzerland (2), Spain (2), Japan (1) and China (1). During the workshop, 47 oral presentations have been given (in plenary sessions), and 58 posters have been exposed and discussed. Both were selectioned from the 140 abstract submissions which the Review Committee had received, and among them 96 are published in the present proceedings. Papers are classified in alphabetical order, according to the author's names. Their rapid edition has been possible because we have decided to give greater place to the quickness instead of the perfection.

The scientific committee meeting was held on the Thursday June 19th, 1997. The place and chairman of the next workshop was determined by vote. The Seventh International Workshop on the Physics of Compressible Turbulent Mixing will be held in Russia and will be chaired by Dr. E.E. Meshkov of the Institute of Experimental Physics of the Sarov Russian Federal Nuclear Centre.

First of all, I would like to express my friendly thanks to my colleague Georges Jourdan for doing so much in organizing the Workshop and preparing the proceedings.

My sincere gratitude goes to Mrs. Colette Chauvin and Mr. Francis Caccinttolo, Director of the Research Technology Energy Department and Vice-President of the Conseil Général des Bouches-du-Rhône, respectively, for contributing financial support essential to the operation of the Workshop.

I would like to specially thank the Conseil Général des Bouches-du-Rhône, and its President, Mr. Lucien Weygand, and the Commissariat à l'Energie Atomique / Direction des Applications Militaires, and its Director, Mr. Jacques Bouchard, for their rapid decision to support the organization of the 6^{th} International Workshop on the Physics of Compressible Turbulent Mixing, financially.

I wish to thank all the members of the Local Committee, for their help in the organization of the Workshop, and Mrs. M. Houas, Miss H. Pelorson, Mr. A. Canova and Mr. M. Crousillat

for their arrangement and management of the social events and programmes.

I gratefully acknowledge Mr. Patrick Gaune, Dean of the School Engineering of the Institut Universitaire des Systèmes Thermiques Industriels, in helping to the on-site organization of the Workshop.

Finally, I would like to express my gratefulness to both the 6^{th} International Workshop on the Physics of Compressible Turbulent Mixing participants and companions, who came all the way from abroad and inside of France, and who contributed to make of this workshop a scientific and social success.
Thanks to all of you.

September 1997 Lazhar Houas

The 6th IWPCTM - Committees and Supporting Organizations

Host Organization

Institut Universitaire des Systèmes Thermiques Industriels,
UMR Centre National de la Recherche Scientifique,
Université de Provence, Marseille, France

Scientific Committee

D.C. Besnard (France)
G. Ben-Dor (Israel)
A.C. Buckingham (USA)
S.B. Dalziel (UK)
J. Glimm (USA)
B.T. Goodwin (USA)
J.F. Haas (France)
P.A. Holstein (France)
L. Houas (France)
J.W. Jacobs (USA)
Y.A. Kucherenko (Russia)
M. Lesieur (France)
P.F. Linden (UK)
E.E. Meshkov (Russia)
T.A. Peyser (USA)
Y. Pomeau (France)
J.M. Redondo (Spain)
B.A. Remington (USA)
G. Rodriguez (France)
V.C. Rupert (USA)
D.H. Sharp (USA)
B. Sturtevant (USA)
D.L. Youngs (UK)
S.G. Zaytsev (Russia)

Paper Selection Committee

B. Porterie (Responsible)
D.C. Besnard
M. Billiotte
Y. Burtschell
E. Daniel
J.F. Haas
L. Houas
G. Jourdan
M. Larini
J.C. Loraud
R. Saurel
D. Zeitoun

Organizing Committee

L. Houas (Chairman)
G. Jourdan (Local Committee)
D.C. Besnard
M. Billiotte
Y. Burtschell
A. Canova
M. Crousillat (MCO Boreale)
E. Daniel
S. Fausti (MCO Boreale)
F. Giroud
J.F. Haas
M. Houas
M. Larini
N. Latil (MCO Boreale)
J.C. Loraud
F. Nicolas
H. Pelorson
B. Porterie
R. Saurel
E. Valerio
D. Zeitoun

Chairman Session

D.C. Besnard (France)
G. Ben-Dor (Israel)
S.B. Dalziel (UK)
J.P. Dussauge (France)
B.T. Goodwin (USA)
J.F. Haas (France)
P.A. Holstein (France)
J.W. Jacobs (USA)
M. Lesieur (France)
E.E. Meshkov (Russia)
D. Shvarts (Israel)

Financial Support Organizations

We gratefully acknowledge the following organizations for their financial support of the accomplishment of the 6^{th} International Workshop on the Physics of Compressible Turbulent Mixing.

Conseil Général des Bouches-du-Rhône,
Commissariat à l'Energie Atomique / Direction des Applications Militaires,
Centre National de la Recherche Scientifique,
Ministère des Affaires Etrangères,
Université de Provence,
European Research Community On Flow Turbulence And Combustion,
Association Universitaire de Mécanique.

Contents

Investigation of Richtmyer-Meshkov Instability Induced by the Incident and the Reflected Shock Waves

A.N. Aleshin, E.V. Lazareva, E.I. Chebotareva, S.V. Sergeev and S.G. Zaytsev
Krzhizhanovsky Power Engineering Institute (ENIN)
Leninsky pr. 19, Moscow, 117071 Russia

Abstract: We performed a set of experimental studies on shock-induced excitation of hydrodynamic instability on the interface between two gases (Richtmyer-Meshkov instability) under various initial conditions.

1. Introduction

Experiments were performed in a shock tube of square cross-section (72×72 mm^2). Mach number of the incident shock wave ranged within 2.5-4.5. Initial interface was modeled by a thin polymeric film, 1.5-3 μm for 2D perturbations and about 0.5 μm for 3D initial perturbations. As working gases, the inert gases He, Ar, Kr, and Xe were used at initial pressure 380 torr.

The experimental studies of Richtmyer-Meshkov instability (RMI) included the following problems.

1. Investigation of RMI evolution at the shock passage through 2D initial interface from light gas to heavy one. Initial perturbation was sinusoidal and harmonic: a_0 is the initial amplitude of perturbation measured from peak to peak of sinusoid; k is the wave number of initial perturbation, $k = 2\pi/\lambda$, where λ is the wavelength of initial perturbation. The curvature of initial perturbation a_0k was varied from 0.4 to 7.8. Parameter a_0k was changed by changing the amplitude and the wave number of initial perturbation. The wavelength of initial perturbation λ was chosen from the following set: 8, 12, 24, 36, and 72 mm, initial perturbation amplitude a_0 was chosen from the following set: 5, 10, 20, and 30 mm. Atwood number At_0 (before the arrival of the shock) varied from 0.22 (Kr-Xe) to 0.94 (He-Xe).

2. Investigation of RMI evolution at the shock passage through 2D initial interface from heavy gas to light one. For this series, the shape and parameters of initial perturbations were the same as for the previous one.

3. Investigation of RMI evolution for the case when the interface disturbed by the incident shock undergoes the attack of the shock waves reflected from the end wall of the shock tube. The main attention was focused on the problem of "memory" of the previous shock passages through the growing perturbation.

4. Investigation of RMI evolution at the shock passage through 3D initial interface from light gas to heavy one. The experiments were performed for two cases, He-Xe and Ar-Xe. The initial perturbations were generated by deformation of a thin film with a small excess of pressure (about 1 torr) on the side of the heavy gas. The value of parameter a_0k was about 1. Here $k = \sqrt{{k_z}^2 + {k_y}^2}$, where $k_z = 2\pi/\lambda_z$ and $k_y = 2\pi/\lambda_y$, λ_y and λ_z are the periodicities of perturbation lengthwise the axes.

5. Investigation of RMI evolution for non-harmonic 2D initial interfaces. Here, the initial

More information - Email: sgz@mazilin.msk.ru

perturbations resulted from superposition of several sinusoidal perturbations with different wavelengths and amplitudes.

2. Regimes of RMI evolution

The performed investigations allowed us to distinguish three regimes of RMI evolution according to a_0k, At_0, and Mach number of the incident shock M_{e1a}. The diagram in Fig. 1 shows the

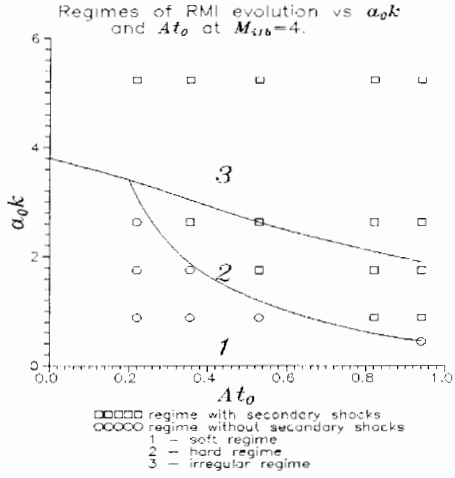

Figure 1. The definition of regimes of RMI evolution.

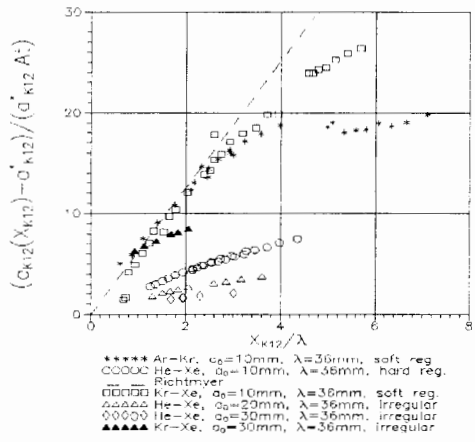

Figure 2. Amplitude of K_{12} vs distance passed.

areas of realization for different regimes of RMI evolution according to a_0k, At_0, and a given Mach number of the refracted shock wave M_{i1b} for the shock passage from light gas to heavy one. We distinguish "soft", "hard", and "irregular" regimes. Each of them is characterized by certain peculiarities of both the refraction of the incident shock on initial interface and the generation of high pressure regions responsible for the growth and distortion of the shape of initial perturbation.

For "soft" and "hard" regimes, refraction of the incident shock wave on the interface proceeds through generation of regular gas-dynamic configurations at the point of interaction [1, 2, 3]. In this case, the pressure at the point of interaction is practically independent on the angle of interaction of the interface with the incident shock wave. For these regimes, just after the end of refraction, two distorted shock waves are generated. The interface is localized within the space between these waves, where the pressure is practically constant. The regimes differ by the mechanism of generation of the high pressure regions. The "hard" regime is characterized by generation of the secondary shock waves propagating across the flow and characteristic breakpoints observed on the refracted and reflected shock waves, while for the "soft" regime, no gas-dynamic discontinuities are observed except the interface. The generation of the secondary shock waves slows down the growth of pressure and results in relative decrease (e.g., with respect to the Richtmyer relation) in perturbation growth rate on the interface (Fig. 2).

As a rule, the "soft" regime is observed for small Atwood numbers, small Mach numbers of the incident shock, and low curvatures of the interface. No gas-dynamic discontinuities or

breakpoints on the shock waves are observed. The unloading and diffusion of these regions are promoted by compression waves. The growth of perturbation amplitude at the initial stage of RMI evolution is in agreement with the Richtmyer relation (Fig. 2). The growth of perturbation amplitude is symmetrical up to $a \leq 0.4\lambda$. For a larger amplitude, the rate of penetration of light gas into the heavy one decreases, and this is accompanied by distortion of perturbation shape and formation of a "spike-bubble" structure. When the amplitude reaches the value of $(0.7 \div 1.0)\lambda$, a vortex mushroom structure forms on the tip of spike, thus decreasing the spike rate.

The "hard" regime is usually observed for Atwood numbers $At_0 \geq 0.5$ and/or large Mach numbers, what results in significant difference in times of generation of secondary shock waves and as the consequence, in the discoordinated in time formation of the high pressure regions. This results in distortion of the interfaces, i.e., in formation of the "spike-bubble"system just after the end of refraction. A breakpoint present on the front of the refracted shock wave indicates to the triple configuration and is an attribute of "hard" regime. Mushroom structures form on the tip of jet in the same way as for the "soft" regime. For $a = (1.5 \div 2.0)\lambda$, the mushroom structures interact with each other, thus forming the turbulent zone.

The "irregular" regime has several important specific features as compared to the two first ones. "Irregular" regime is observed for $a_0/\lambda > 0.5$ and characterized by formation of vortex (mushroom) structures on the heavy gas jet during the refraction of the incident shock wave on initial interface. The heavily distorted refracted shock wave quickly generates the secondary shock waves, thus making the non-uniformity of pressure on the interface even more pronounced. Around the tip of jet, a compact high pressure region is formed, the unloading of which results in formation of mushroom vortex structure. This process occurs already during the refraction of the incident shock wave, and not with the evolutionary development of interface, as it was for the "soft" and "hard" regimes.

The different ways of formation of mushroom structures for "soft", "hard", and "irregular" regimes result, correspondingly, in different evolutions of the turbulent layers formed by these structures, and in qualitatively different effects of initial parameters on the growth of perturbation on the interface. Figures 3 and 4 show the plots of the depth of penetration of one gas into the other against the distance passed by the interface, X_{K12}, and the Atwood number after the interaction, At, for $a_0 = 10$ mm and $\lambda = 72$ and 36 mm, respectively. As seen, for the "irregular" regime ($\lambda = 12$ mm, Fig. 4), the depth of penetration is a non-monotone function of At, in contrast to that for the "soft" and "hard" regimes (Fig. 3).

The transition of RMI regimes from "soft" to "hard" and further to "irregular", results in relative deceleration of perturbation growth on the interface (Fig. 2).

The regimes of similar types are observed for RMI evolution at the shock passage from heavy gas to light one. Figure 5 shows the growth of perturbation amplitude plotted against the distance passed by the interface, for the shock passage from xenon to argon. The increase in a_0 from 5 mm to 10 mm results in two-fold increase of perturbation growth rate, while the increase in a_0 from 10 mm to 30 mm increases the perturbation growth rate approximately 1.5-fold. Comparison of the experimental data for the growth perturbation amplitude with those calculated by the formula suggested by Meyer and Blewett [4] has shown that at a_0 =5 mm and $\lambda = 36$ mm for Xe-Kr, Xe-Ar, and Kr-Ar, the calculated values are about two-fold overestimated.

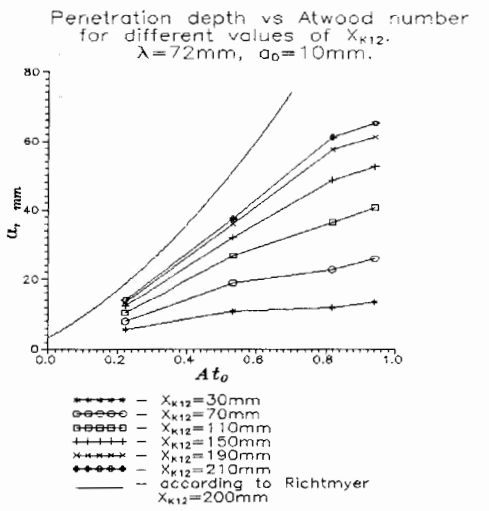

Figure 3.

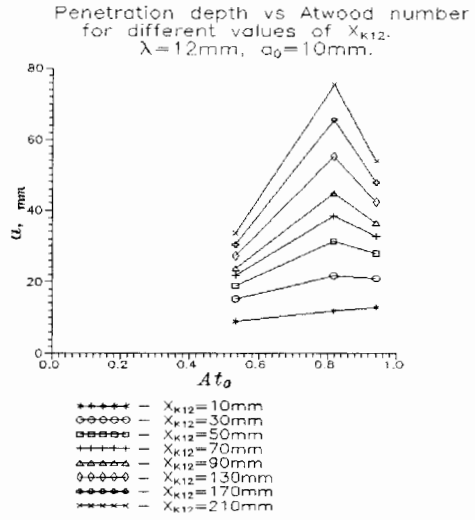

Figure 4.

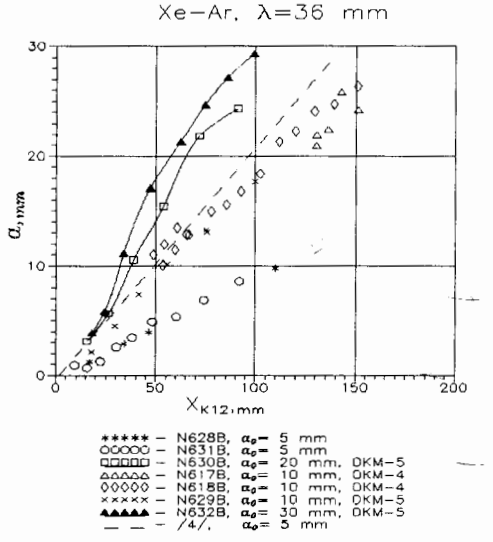

Figure 5. Perturbation growth rate versus the distance passed, for Xe-Ar at different a_0.

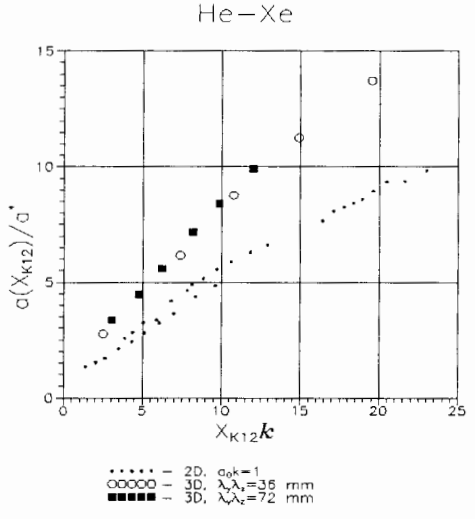

Figure 6. Amplitude of K_{12} versus the distance passed, for He-Xe at 2D and 3D initial perturbations.

3. Main experimental results

Investigation of multiple shock passage through a growing perturbation on the interface has shown that the main factor affecting the growth of perturbation amplitude is the regime of RMI realized at each of the successive shock-interface interactions. For the case when each of the steps occurred under the "soft" regime, comparison of the experimental data with the

formula suggested in [5] showed that the perturbation growth rate at a given step is not just a sum of the rates at the preceding steps. Thus, we suppose that it is necessary to introduce in the formula a coefficient of "memory" G dependent on Atwood number. According to our data, the coefficients of "memory" G are 0.2 for Xe-Kr and 0.5 for Kr-Ar.

Our investigations of 3D initial perturbation for $a_0 k \sim 1$ have shown that for Ar-Xe, the "soft" regime is realized, and the perturbation growth rate corresponds to that obtained by the Richtmyer relation. For He-Xe, at the same initial conditions, the "hard" regime is realized, and the perturbation growth rate is lower than that obtained by the Richtmyer relation. However, the growth rate for 3D perturbations was higher than that for 2D perturbations, under similar initial conditions (Fig. 6). Our experimental data demonstrated a higher stability of 3D perturbations; the 3D perturbations do not form the turbulent layer at least for $ak <\sim 20$ for He-Xe, and for $ak <\sim 10$ for Ar-Xe (a is the current amplitude of perturbation).

We performed a series of experiments to study the influence of non-harmonic initial 2D perturbation of interface on RMI evolution. Figure 7 gives the shapes of initial interfaces and the corresponding most typical Tőpler pictures of the RMI evolution for two cases, Ar-Xe and He-Xe. We have found that the growth rate of single perturbation (Fig. 7) differs from that of the corresponding harmonic perturbation when the distance between the centers of adjacent perturbations exceeds 4λ.

Acknowledgement. This work was supported by International Science and Technology Center, project No. 029-94, by the University of California, contract C 50050015-35, and by Russian Foundation for Fundamental Investigations, project No. 96-01-01295.

References

[1] Aleshin AN, Zaytsev SG, Lazareva EV, and Demchenko VV, Interaction of shock with undulate interface, Izv. Ross. Akad. Nauk, Ser. Mekh. Zhid. i Gaza, 5, 168-174, (1992).

[2] Aleshin A, Zaytsev S, and Lazareva E, Experimental and numerical studies on Richtmyer-Meshkov instability, Rus. J. Comp. Mech., 1, 2, 33-50, (1993).

[3] Henderson LF, The refraction of a plane shock wave at a gas interface, J. Fluid Mech., XXVI, 3, 607-637, (1966).

[4] Meyer KA and Blewett PJ, Numerical investigation of stability of shock-accelerated interface between two fluids, Phys. Fluids, XV, 5, 753, (1972).

[5] Brouillette M and Sturtevant B, Proc. of 17th International Symposium on Shock Waves and Shock Tubes, 284-89, (1989).

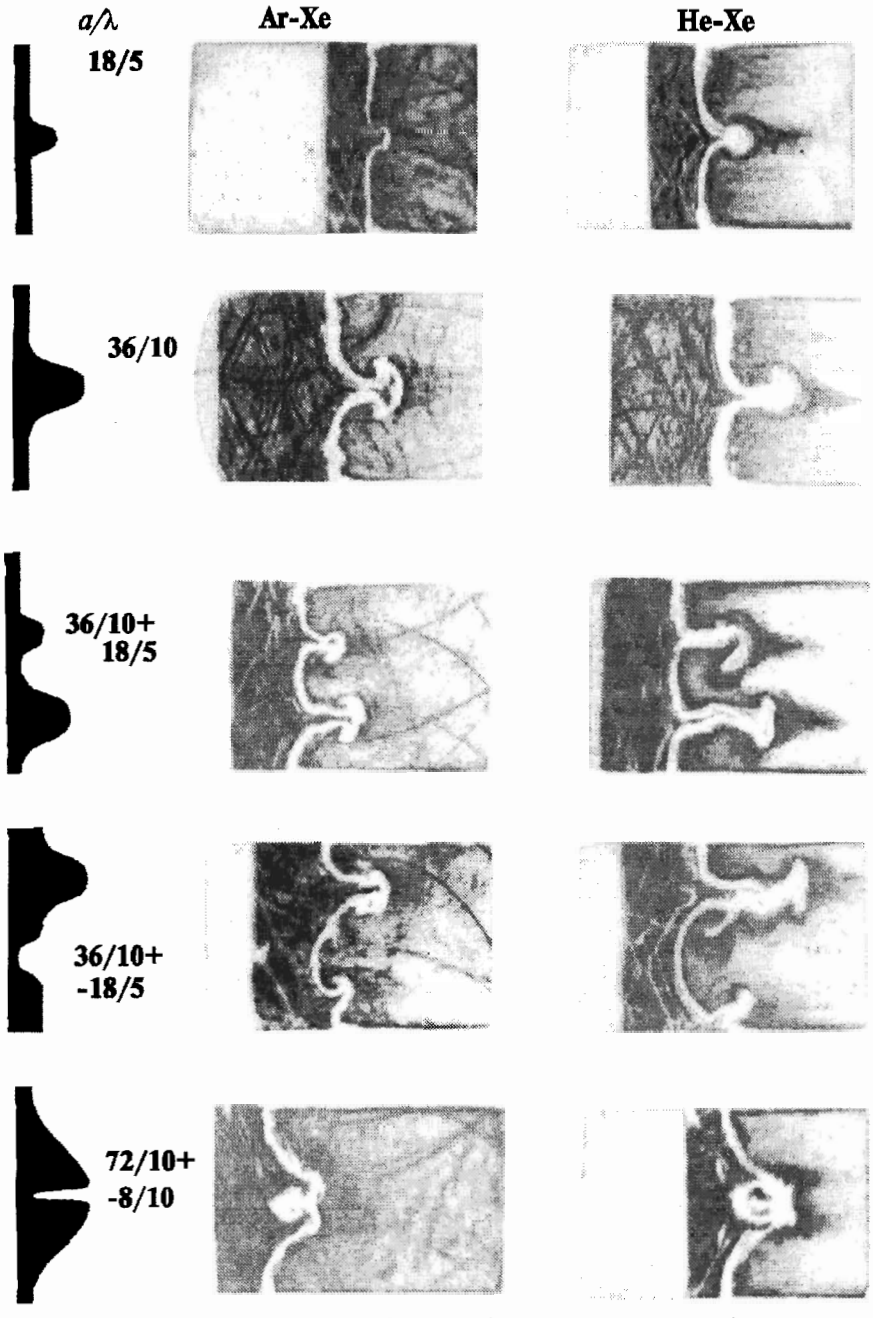

Figure 7. The used shapes of initial perturbation and most typical pictures of RMI evolution.

The Effect of Spectral Radiation Transport on Turbulent Mixing of the Laser Accelerated Target

V.A. Andronov, S.A. Bel'kov, G.V. Dolgoleva, L.S. Mkhitarian, V.V. Nikiforov and A.N. Razin
Russian Federal Nuclear Centre - Institute of Experimental Physics
Prospect Mira 37, 607190, Sarov, Nizhny Novgorod Region, Russia

Abstract: The influense of the X-ray spectral effects on the development of turbulent mixing zone in the multi layer target, accelerated by the power laser beam, was considered. The Nikiforov's model of the turbulent mixing was extended to the case of the nonequlibrium radiative plasma flows. This approximation was realized to the 1D radiative gas dynamic code SNDTUR.

1. Introduction

At volumetric compressions of the order of 10^4 (which are only worth mentioning while talking of laser thermonuclear targets ignition) development of perturbations of large wave-length disturbing DT-fuel compression spherical symmetry leads to maximum fuel density (ρR) and maximum temperature decrease. Development of mixing zone between the fuel and compressing shell , in its turn, leads to fuel volume growth and effective increase of fuel-to-shell thermal flux. As a result energy required for ignition increases and its value can not be estimated without detailed study of the processes of instability growth and mixing. Thus, they are the key processes in the problem of laser target ignition. However, the processes are so complicated that in spite of relatively long history of studies in this area, no complete and quantitatively clear picture of instability growth and mixing has been obtained yet.

A number of questions connected to turbulent mixing zone growth has been studied for a long time in experiments on gas guns and shock tubes [1, 2]. Analysis of these experiments has lead to the development of numerical techniques allowing for qualitative simulation of mixing zone growth and satisfactorily describing flows over a wide range of parameters [3, 4]. However, application of lasers for target shell acceleration brings forward new phenomena which can not be studied in ordinary experiments.

Thus, in laser experiments instabilities develop in nonequilibrium, highly spatially nonuniform, and nonstationary plasma. On the one hand, it leads to formation of well pronounced ablation front. Material mass flow from ablation front significantly changes instability increments for different wave lengths as compared to their classical values. On the other hand, hot laser corona is a source of hard X- rays, which heats different target layers nonuniformly (in accordance with its spectral paths) and changes dynamics of its acceleration and expansion.

A question arises in connection with it, to what extent may the experiments with gases under ordinary conditions and numerical techniques based on them serve as a ground for laser shell acceleration experiments description.

Experiments on instability and mixing study for laser-accelerated multilayer flat targets simulating complex spherical shells acceleration were carried out at different laboratories on

More information - Email: belkov@otd13.vniief.ru

powerful laser installations such as OCTAL (France) [5], ISKRA-4 (Russia) [6]. Analysis and description of these experimental results are of great interest to the whole problem of laser thermonuclear fusion.

The model of turbulent mixing was generalized by the authors to the case of non-equilibrium, non-stationary multicomponent plasma. 1D radiation gas dynamics code SNDTUR developed on its basis was used for analysis of the above mentioned laser experiments. The presented report shows the results of numerical investigation of the effects connected to X-ray spectral transport and their impact on multilayer target dynamics and turbulent zone mixing.

2. 1D model of mixing in multilayer laser targets - SNDTUR code

At acceleration of complex shells (for example, light ablator on heavy material shell) instability may occur at the interface which is not limited by heat conduction. Its increment will be defined in case of quasistationary acceleration (at least, during linear stage) by the expression : $\gamma_R = \sqrt{gk} \cdot \eta$, where $\eta = \frac{\rho_h - \rho_l}{\rho_h + \rho_l}$ is Atwood number. In this case short-wave accelerations should grow, most probably, and instability develops quickly into turbulent mixing zone.

All the phenomenological models agree that mixing zone width is linear with deceleration path length $L = \int_0^t dt' \int_0^{t'} g dt''$, i.e. $H = \alpha \eta L$. The parameter α is usually close to 2/3 in case of Raleigh-Taylor instability. In case of Richtmyer-Meshkov instability deceleration path length is $L = \Delta u \cdot t$ where Δu is the velocity jump conveyed to the interface by the shock wave. The parameter α in this case depends on initial mixing zone width (or roughness), vanishing with it.

In general case turbulent mixing zone development has a more complicated nature, and the objective of phenomenological models is to describe as broad a range of flows as possible in the frames of unified approach. The approach developed by V.V.Nikiforov [4] is thought to be the best in this respect allowing to observe various plasma component concentration evolution on the interface of different density layers. The model was generalized to the case of non-equilibrium plasma by introducing in equations of different turbulent quantities the generation term of turbulent pulsations A in the following form:

$$
\begin{aligned}
A &= A_S + (A_T - A_S)(1 - Y(\varphi)),\ Y(\varphi) = \left(1 - e^{-\varphi}\right) \cdot \varphi^{-1},\ \varphi = \frac{Q(\kappa_e + \kappa_\gamma)}{\rho c_P \sqrt{e^3 e_{\|}}} \\
A_S &= \frac{\frac{\partial}{\partial r}(P_e + P_i)}{\rho(\lambda_{1e} + \rho\lambda_{1i}) + \frac{T_e \lambda_{2e}^2}{\rho c_{V_e}} + + \frac{T_i \lambda_{2i}^2}{\rho c_{V_i}}} - \frac{1}{\rho}\frac{\partial \rho}{\partial r},\ A_T = \frac{\frac{\partial}{\partial r}(P_e + P_i) - \lambda_{2e}\frac{\partial T_e}{\partial r} - \lambda_{2i}\frac{\partial T_i}{\partial r}}{\rho(\lambda_{1e} + \rho\lambda_{1i})} \\
\kappa_\gamma &= 4\frac{S_\gamma U_\gamma}{T_\gamma \frac{\partial U_\gamma}{\partial r}},\ S_\gamma = \int_0^\infty S_\nu d\nu,\ U_\gamma = \int_0^\infty U_\nu d\nu \equiv \frac{4\sigma T_\gamma^4}{c} \\
\lambda_{1e,i} &= \left(\frac{\partial P_{e,i}}{\partial \rho}\right)_{T_{e,i}},\ \lambda_{2e,i} = \left(\frac{\partial P_{e,i}}{\partial T_{e,i}}\right)_\rho
\end{aligned}
$$

where $e = e_{\|} + 2e_\perp$ and $e_{\|}$, $e_\perp$ are half mean squared of the longitudinal and transversal velocity turbulent pulsations, Q is a rate of turbulent pulsations dissipation, κ_e is a coefficient of the electron heat conductivity, $c_{V_{e,i}}$, $c_{P_{e,i}}$ are the electron and ion heat capacities under constant density and pressure accordantly, S_ν, U_ν are spectral radiation flux and energy density, σ is a Stephen-Boltzmann constant, c speed of light, ρ, $T_{e,i}$, $P_{e,i}$ are density, electron and ion temperature and pressure of plasma.

Than it was implemented in 1D radiation gas dynamics code SNDTUR providing simulation of flow and heat transport in multicomponent non-equilibrium emitting plasma with account of turbulent mixing of different materials layers. Gas dynamics is calculated using Lagrangian approach [7], while radiation transport - using multigroup quasidiffusion approach [8]. Plasma ionization degree and level population of ions are described in average ion approximation. Electron state energies of multicharge ions are calculated with account of nucleus charge Z_0 screening according to hydrogen-like ion model. Plasma spectral characteristics (emissivity and absorption coefficients) are calculated in the same approximation [9]. Free-free, free-bound and bound-bound transitions of plasma electrons are taken into account.

Laser energy release power is calculated in approximation of geometric optics with account of inverse bremsstrahlung absorption of laser beam falling on plasma layer at a given angle ϑ. Heat conduction, electron-ion relaxation and viscosity coefficients are nonlinear functions of temperature, density and mean ion charge and are calculated using known formulas.

3. Calculation of laser-accelerated multilayer targets

SNDTUR code was used to study the effect of spectral X-ray transport on the turbulent mixing in laser-accelerated multilayer targets. Computations setting-up is shown in Fig.1. Typical for mixing study experiments [5, 6] three-layer target consisting of silicon, aluminum and gold layers was taken as an example. Silicon surface was irradiated by laser pulse of neodymium laser third harmonics (wave length λ=0.35 μm). Laser pulse time profile is also shown in Fig.1. Target

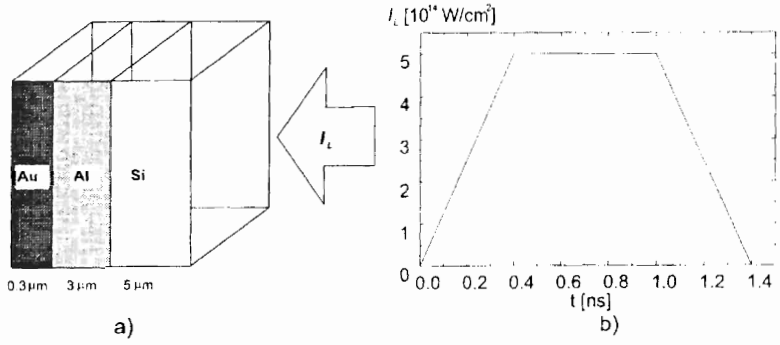

Figure 1. Computations setting-up: a) target geometry (ρ_{Au} = 16.5 g/cm^3, ρ_{Al} = 2.25 g/cm^3, ρ_{Si} = 1.85 g/cm^3), b) laser radiation intensity as a function of time.

density profile has strong influence on evolution of turbulent mixing zone at Al-Au interface. This density profile is determined not only by entropy value behind the front of the shock wave going out of ablation zone and laser target acceleration value, but also by the target heating-up with laser corona X-radiation. Therefore, account of X-ray generation in laser corona and its spectral transport play the important role in turbulence development calculations.

Two series of calculations were carried out to study the effect of spectral transport. Radiation transport was calculated in approximation of spectral diffusion in the first series. Spectral interval in quantum energy range from 0 to 5 keV was divided into 50 equal spectral groups.

The so called three-temperature approximation was used in the second series, the spectrum

considered to be of Planck-type, corresponding to a certain temperature T_γ, and mean Planck's L_{Pl} and Rosseland's L_{Ross} paths [10] used instead of spectral radiation coefficients in radiation diffusion equation. In this case source power and radiation flux are calculated according to:

$$J_\gamma = \frac{4\sigma T_e^4}{L_{Pl}},\ S_\gamma = -\frac{cL_{Ross}}{3}\nabla U_\gamma$$

and mean free paths calculated in each Lagrangian point using spectral absorption coefficient known at each moment.

First, target acceleration dynamics calculation was conducted without turbulent mixing for both series. Based on this calculation the moment t_{mix} of acceleration stabilization after the shock wave passing through Au-Al interface was determined. Maximum density jump between light and heavy layers $\delta = \rho_{Au}/\rho_{Al}$ as well as turbulent density pulsation $R_0 = 0.01\,(\delta - 1)^2/\delta$ initial value were determined for the same moment. Thus determined values were used as initial conditions in equations describing turbulent values evolution, which were included at the moment t_{mix} in calculations with account of turbulent mixing.

Fig. 2 shows Au-Al interface acceleration in calculations of the given target acceleration dynamics in the corresponding series without account of turbulent mixing. It is seen that the

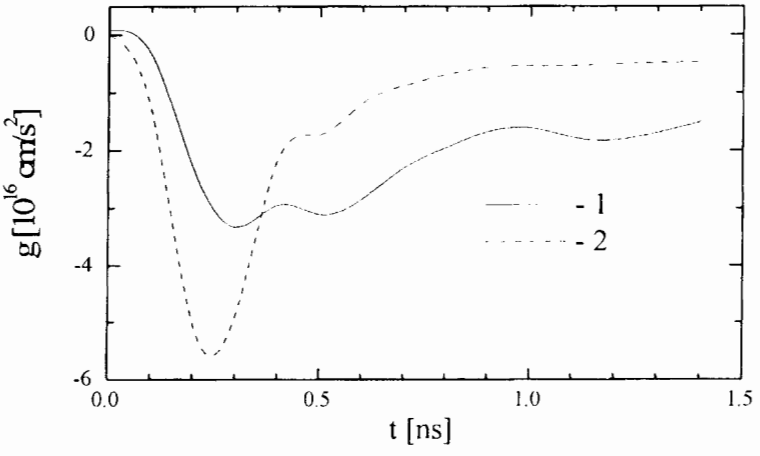

Figure 2. Au-Al interface acceleration as a function of time in spectral (1) and one-group (2) calculations without account of turbulent mixing.

target motion dynamics in the vicinity of the layers interface, where turbulent mixing zone is expected to develop, differs significantly in spectral (1) and three-temperature (2) calculations. Thus, on the one hand, preliminary heating-up by hard X-ray generated in laser corona prevents the target from strong compression after shock wave propagation in spectral calculation, as compared to three- temperature calculation (see Fig.3). On the other hand, radiation thermal wave velocity is significantly higher in the second series, which leads to higher target accelerations at the initial acceleration stage (Fig.2) and quicker layers release at the end (Fig.3). Such strong

dynamics difference leads to completely different picture of turbulent mixing zone evolution in calculations with and without spectral transport. Fig. 4 shows gold and aluminum mass concentrations distributions for the moment t=1.0 ns in corresponding series. It is seen that in three-temperature calculation gold and aluminum are completely mixed by this time, while in spectral calculation thin non-mixed layer is still left. Thus, the conducted computations show

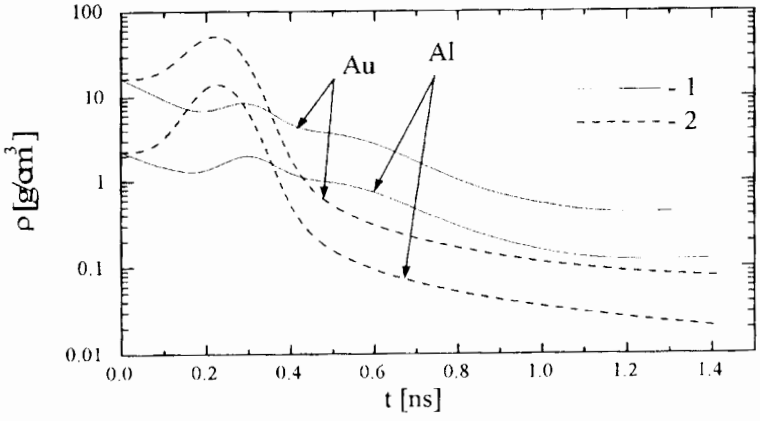

Figure 3. Au and Al density as a function of time in the vicinity of the layers interface in spectral (1) and one-group (2) calculations without account of turbulent mixing.

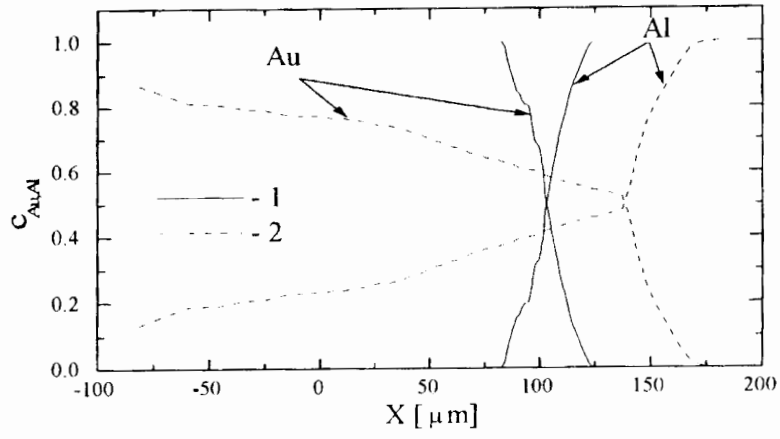

Figure 4. Au and Al mass concentration distributions in turbulent mixing zone in spectral (1) and one- group (2) calculations.

that X-ray generation and spectral transport from laser corona into plasma plays the important role in turbulent mixing calculations and should be taken into account while interpreting experimental data on hydrodynamic instability and mixing study in laser-accelerated multilayer flat and spherical targets. The code package SNDTUR developed by the authors provides the conduction of investigations of such kind and can serve for simulation and optimization of laser thermonuclear synthesis targets both for existing and future laser installations.

Acknowledgement. In closing two authors (S.A.Bel'kov, G.V. Dolgoleva) express their thanks to the Russian Fund of Fundamental Investigations (project 96-01-00046) for this work support.

References

[1] Kucherenko YA, Shibarshov LI *et al.*, Experimental study of the gravitational turbulent mixing self-similar mode, Proc. of 3d International Workshop on the Physics of Compressible Turbulent Mixing, Abbey of Royaumont (France), June 17-19, p.427, (1991).

[2] Andronov VA, Meshkov EE *et al.*, Experimental study and numerical simulation of turbulent mixing in one-dimensional flows, DAN SSSR, 264, p.76, (1982).

[3] Handbook of Turbulence Fundamentals and Applications, Edited by Frost W and Moulden TH, Vol. 1, Plenum Press, New York and London, (1977).

[4] Nikiforov VV, Calculation of Gravitational Turbulent Mixing in Non-Automodel Flows, Proc. of 4th International Workshop on the Physics of Compressible Turbulent Mixing, Cambridge (England), March 29 - April 1, p.478, (1993).

[5] Holstein PA, Galmiche D *et al.*, Hydrodynamic instabilities and mixing in laser accelerated targets, Report at the International Workshop on Hydrodynamic Instabilities, November, Arzamas-16, (1994).

[6] Andronov VA, Bel'kov SA *et al.*, Investigation of Turbulent Mixing on the Iskra-4 Laser Facility, 24th European Conference on Laser Interaction with Matter, Book of Abstracts, Madrid (Spain), June 3-7, (1996).

[7] Dolgoleva GV, Two-temperature emitting gas flow calculation technique, Voprosy atomnoi nauki i tekhniki, Ser.: Methods and codes for numerical solution of mathematical physics problems, 2 (13), p.29, (1983).

[8] Antonenko EM, Dolgoleva GV, Krupina SN, The code (SND) for 1D laser thermonuclear synthesis problems computation, Voprosy atomnoi nauki i tekhniki, Ser.: Mathematical simulation of physical processes, 2, p.3, (1993).

[9] Bel'kov SA, Dolgoleva GV, Mean ion model for calculation of ionization kinetics, level excitation populations and spectral radiation transport coefficients in SNDP code, Voprosy atomnoi nauki i tekhniki, Ser.: Mathematical simulation of physical processes, 1, p.59, (1992).

[10] Zel'dovich YB, Raizer YP, Shock waves and high temperature plasma physics, Nauka Publishers, Moscow, p.134, (1966).

Turbulent Mixing Investigation of Thin Layers of Materials with Different Densities under Laser Acceleration of Plane Multilayered Targets on the ISKRA-4 Facility

V.A. Andronov, S.A. Bel'kov, A.V. Bessarab, I.N. Voronich, S.G. Garanin, A.A. Gorbunov, V.N. Derkach, G.V. Dolgoleva, A.I. Zaretski, V.M. Izgorodin, B.N. Ilyushechkin, G.A. Kirillov, G.G. Kochemasov, A.V. Kryukov, Y.V. Kuratov, V.I. Lazarchuk, V.A. Lebedev, N.V. Maslov, E.I. Mitrofanov, V.M. Murugov, L.S. Mkhitarian, G.V. Okutin, S.I. Petrov, A.V. Pinegin, N.N. Rukavishnikov, A.N. Razin, A.V. Ryadov, A.V. Senik, N.A. Suslov, S.A. Sukharev, V.A. Tokarev and V.A. Shchennikov
Russian Federal Nuclear Centre - Institute of Experimental Physics
Prospect Mira 37, 607190, Sarov, Nizhny Novgorod Region, Russia

Abstract: We presented the results of experiments on turbulent mixing of Al and Au thin layers at laser acceleration of Si-Al-Au trilayer plane targets. Interpretation of the experimental results was performed with the help of the 1D radiative gas dynamic code SNDTUR in wich the Nikiforov's model of the turbulent mixing was used.

1. Introduction

Turbulent mixing of thermonuclear fuel with the material of the shell imploding is a serious problem in the ICF program because it appreciably increases the laser radiation (LR) energy needed for ignition.

By now, there are several physico-mathematical models of the mixing process which have been experimentally verified on shock tubes [1]. However, the laser acceleration process of the shell possesses a number of peculiar features, which do not allow to use the existing models for the case of laser fusion targets without experimental verification. In this connection of interest are specially designed experiments with the laser acceleration of shells or their plane analogs. First mixing experiments with layers of various density materials have been conducted on plane targets by A. Raven *et al.*[2] and P. Holstein *et al.*[3].

2. Experimental conditions and methodics

We have conducted experiments on mixing thin layers of Al and Au using acceleration of Si-Al-Au trilayer plane targets. The first series of these experiments has been reported in work [4]. The experimental procedure is close to that suggested in works [2, 3] and its scheme shown in Fig.1(a).

The target is irradiated on the Si side by a power laser pulse with the wavelength λ=0.66 μm, duration $\tau_p \approx$(0.8- 1.2) ns, and intensity $I_p \approx (0.5\text{-}1)\cdot 10^{14}$ W/cm^2. The Si layer thickness is selected such that during the time τ_p the heat wave would not reach the Al layer, and the Al and Au layers are accelerated in a "cold" state (if their heating by the plasma corona X-ray radiation and a shock wave is insignificant). During the target acceleration, the Rayleigh-Taylor

More information - Email: bessarab@vniief.ru

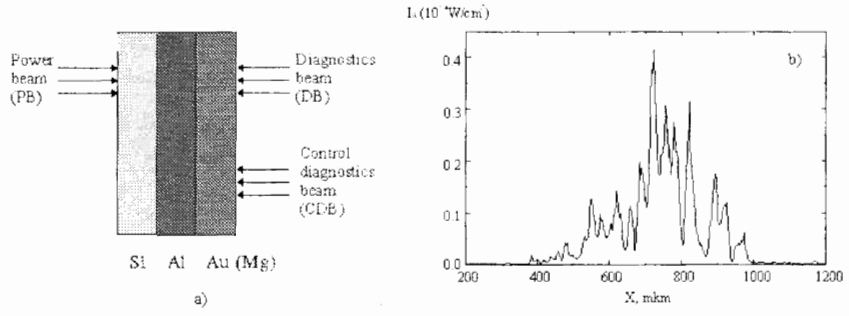

Figure 1. Scheme of the mixing experiments (a), and diagnostic intensity distribution (b).

instability at the interface of Al-Au is causing their turbulent mixing.Heating of the obtained mixture by an additional(diagnostic) laser beam of an appropriate intensity leads to formation of a plasma consisting of Au and Al ions. Appearance of the line X-ray emission of Al is a signature of mixing. Its registration is realized in the following way. The diagnostic beam with the pulse duration $\tau_d \approx$(0.3-0.5) ns and intensity $I_d \approx 10^{13}$ W/cm^2 coaxially with the power beam is delivered to the rear side of target. The delay of the diagnostic pulse relative to the power pulse should be long enough for the mixing process to evolve. In our experiments this delay is Δt$\sim$0.86 ns.

To smooth large-scale nonuniformities in the laser beam intensity distributions, random phase plates were used. But small-scale nonuniformities like "hot" spots in the diagnostic beam can influence the time of Al line X-ray emission. This effect could be established by using another(control) beam, which was directed to the rear side of target and positioned 4 mm away from the diagnostic beam (spots of both beams were simultaneously viewed by the diagnostic equipment). The delay of control beam relative to the power beam was $\sim$1.6 ns. The character of distributions and the values of intensities in the diagnostic and control spots were supposed identical. So, if the Al line emission from the diagnostic spot was prior to the corresponding X-ray pulse from the control spot (or the latter was absent) this could be considered as indication of mixing.

In our experiments the roughness of Al and Au layers did not exceed 0.05 μm, and that of Si was not more than 0.1- 0.3 μm. The thickness of Si and Al layers was 4.7$\pm$0.3 μm and 20.3 μm correspondingly, the Au layer thickness varied within 0.15-0.4 μm. In some experiments gold was replaced by 0.4-0.8 μm thick magnium.

Dimensions of the irradiation spots and the character of LR intensity distributions in them were estimated with the help of X-ray pinhole cameras and by direct filming. The X-ray diagnostic complex provides the registration of: - the time-integrated spectra of the X-ray line emission of plasma within 0.04-0.25 keV and 1.4-2.5 keV with the help of a diffraction grating spectrograph and a KAP crystal spectrograph; - line X-ray emission He$_\alpha$Al (hν $\sim$1.6 keV) and Mg1-3 (hν $\sim$1.7 keV) at the background of Au M band X-ray radiation with the time resolution of 40 ps; - continuous X-ray spectrum of plasma in the range of 1- 5 keV with the time resolution of 50 ps.

Fig.1(b) shows the intensity distribution in the diagnostic beam. One can see that it is far from

being uniform. A similar picture is also observed for other beams. One can also see rather numerous "hot" microspots on the X-ray pinhole images.
The power beam pulse duration p was within 0.83-1.1 ns, and the spot size from 500 to 700 μm. The diagnostic and control beams pulse duration was within 0.3-0.5 ns and the corresponding spot sizes were 400-600 μm.
Primary interpretation of the experimental results was performed with the help of the one-dimensional program SNDTUR [5]. In calculations the following processes were taken into account: gasdynamics, electron (with account of thermal flux limitation) and ion thermal conductions, nonequilibrium spectral diffusion of X-ray radiation, ionization kinetics of a multicharge, multispecies plasma in the approximation of the average ion model, turbulent mixing. In calculations of LR absorption only inverse bremsstrahlung mechanism was taken into account. Because the program SNDTUR is one-dimensional, the intensity distributions across the beams were supposed to be uniform.

3. Experimental results and calculation analysis

Fig.2 presents the time-resolved registration results of He_αAl (λ=0.776 nm) emission and Au continuous spectrum near this line for the experiment with intensifies of power and diagnostic pulses: $I_p \approx 8{\cdot}10^{13}$ W/cm^2 and $I_d \approx 4.4{\cdot}10^{13}$ W/cm^2 for 0.25 μm thick Au layer. Time delay between He_αAl line and Au continuum emission is absent. The form of Al emission pulse approximately follows the form of Au X-ray pulse from the diagnostic spot. At the same time

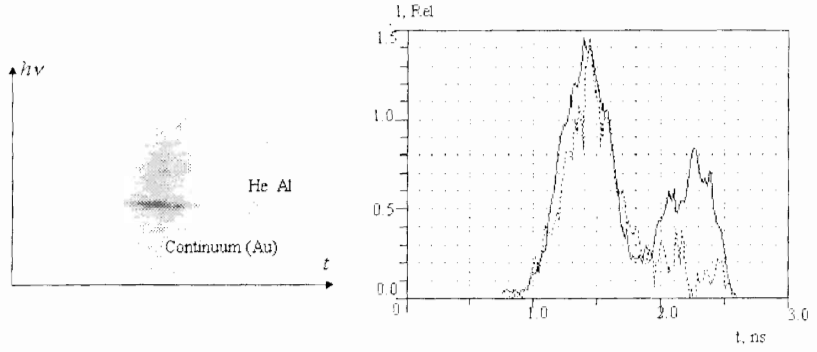

Figure 2. Time dependences of He_αAl (1) line and continuous X-ray of Au (2) for Si-Al-Au target.

aluminium emission from the control spot has not been registered. We may say that the mixing is take place.
For the conditions of this experiment the calculated delay between the emission pulses of Au continuum and Al line is 0.23 ns, but in the experiment it was absent.
To ascertain the reasons of discrepancy between the calculation and the experiment the specially designed experiments have been carried out, in which gold has been replaced by magnium. In this case the densities of Al and Mg are practically equal and there are no conditions for evolution of instabilities and Al line emission, in principle, should appear only after the heat wave initiated by the diagnostic beam reaches the interface of Al-Mg. Experimental time depen-

dences of $He_{\alpha}Al$ and Mg1-3 emissions for the experiment with $I_d \approx 10^{13}$ W/cm^2 and magnesium thickness of 0.8 μm are shown in Fig.3. The experimental delay between X-ray pulses of Mg and Al was 0.3 ns and the calculated 0.68 ns. Very likely, the only reason for this discrepancy

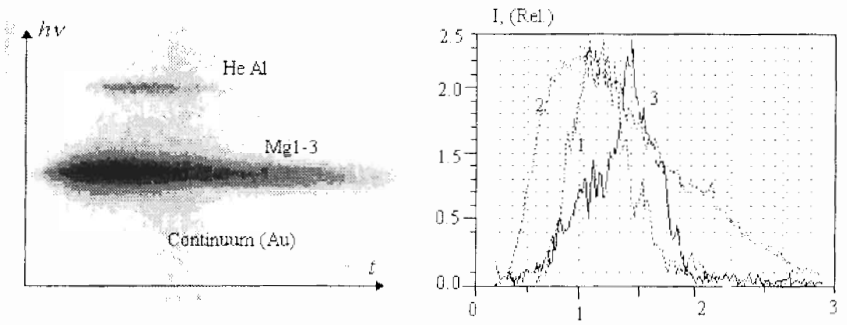

Figure 3. Time dependences of $He_{\alpha}Al$ (1), Mg1-3 (2) line emission and continuous X-ray of Au (3) for Si-Al-Mg target.

between the calculation and experiment in this case is in that nonuniformities of LR intensity distribution across the diagnostic beam, i.e. the presence of "hot" microspots in it, are not taken into account.

For a rather rough estimate of the nonuniformities effect we have used a sector approximation, i.e. we have performed one-dimensional calculations with various values of Id, putting together the contributions of various regions of the diagnostic spot to the emission of Mg and Al. To determine the spectrum of Id values, we have used the results of postprocessing the laser spot experimental densitogram. The obtained in this manner results are shown in Fig.4(a). The

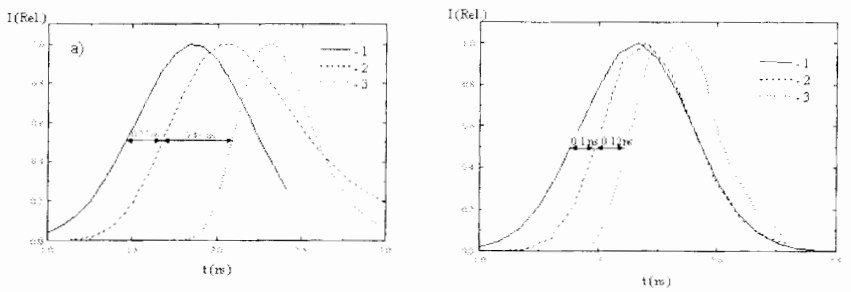

Figure 4. Calculation results for experiments with consideration of "hot" spot in the diagnostic beam: a) LR pulse (1), Mg1-3 (2) and $He_{\alpha}Al$ (3) line emission for Si-Al-Mg target; b) LR pulse (1), continuous X-ray Au (2) and $He_{\alpha}Al$ line (3) emissions for Si-Al-Au target.

delay of Al emission relative to Mg is seen to decrease down to 0.4 ns. The Mg emission is mainly determined by the average diagnostic beam intensity, and the Al line emission by the intensity in "hot" microregions.

The results of a similar approach (but with turbulent mixing taken into account) for the Si-Al-Au target are shown in Fig.4(b). As seen in the figure, the delay between the emission pulses of Au and He_{α}Al has decreased to 0.1 ns.

Several explanations can be given for remaining discrepancy between the calculation and experiment. One of them is the effect of "imprinting" [6] of the existing in the experiment nonuniformities in the LR intensity distribution across the power beam, which can lead to evolution of instabilities at the ablation front and jet formation. The described in work [6] experiments have shown that this effect does not allow the material to move uniformly under laser acceleration.

4. Conclusion

The experiments performed and their analysis show that, while studying the process of turbulent mixing of materials with different densities on laser acceleration, it is very important to have a high degree of uniformity in the power and diagnostic beams.

References

[1] Andronov VA, Meshkov EE, Nikiforov VV *et al.*, DAN SSSR, 264, 76,(1982)

[2] Raven A, Azechi H, Yamanaka T and Yamanaka C, Phys. Rev. Let., 47, 1049, (1981).

[3] Holstein PA, Meyer B, Rostaing M *et al.*, Cr. Acad. Sci, Paris, 307, 211, (1988).

[4] Andronov VA, Bel,kov SA, Bessarab AV *et al.*, Report at the 24th ECLIM, Madrid (Spain), June 3-7, (1996).

[5] Andronov VA, Kozlov VI, Nikiforov VV *et al.*, VANT, series: Mathematical Modelling of Physical Processes, issue 2, p. 59, (1994).

[6] Desselberger M, Jones MW, Edwards J *et al.*, Phys. Rev. Let., 74, 15, 2961, (1995).

Numerical Analysis of Nonlinear Rayleigh-Taylor Instability

N.N. Anuchina, N.S. Es'kov, A.V. Polionov, O.S. Ilyutina, O.M. Kozyrev and V.I. Volkov
Russian Federal Nuclear Center, All-Russian Scientific Research Institute of Technical Physics, Snezhinsk, Russia

Abstract: The results are presented obtained in two-dimensional numerical study of nonlinear phase of Rayleigh-Taylor instability evolution which was performed with the MAH-3 code. The criteria are proposed for determining the transition to self-similar turbulence in computational experiments. Three phases of nonlinear mixing were found: "relic chaos", "formation of classical energy spectrum" and "spectrum degradation".

1. Introduction

Under gravitation instability small sinusoidal perturbations of the interface between non-viscous incompressible fluids grow exponentially with time. When amplitude of perturbation becomes comparable with its wave length, nonlinear phase of the phenomenon begins.
With time the flow becomes self-similar in character that manifests itself in a proportion between typical sizes of flow structures and width of mixing zone.
In [1] a square law was proposed for describing the extension of a turbulent mixing zone after achieving self-similar phase. Numerous experimental and numerical studies of turbulent mixing [2 – 7] are devoted to the square law verification. The experiments conducted by Y.A. Kucherenko, K.I. Read and D.L. Youngs for the substances with various density differences demonstrated that the depth of "bubble" penetration was determined by the dependence $L_1 = \alpha \cdot A \cdot g \cdot t^2$, where A is Atwood's number and the constant $\alpha \approx 0.06$.
Usually sufficient conditions for accepting flow as self-similar turbulent, are realization of square law for mixing zone extension and spatial-temporal similarity of the density profiles. However, to qualify turbulent mixing as self-similar it is necessary to consider the internal features of the flow based on spectral presentation of hydrodynamic fields. This means that except determination of spatial-temporal similarity of flow functionals the practical verification is in need if there exists an inertial interval of wave numbers k for which the Kolmogorov-Obukhov law for the turbulence kinetic energy distribution $E(k) \approx k^{-5/3}$ [8, 9] is valid.
A criterion can be formulated for determining self-similar turbulent phase of flow:
a) presence of self-similar inertial mechanism for transferring energy of velocity field pulsing at intermediate range of wave numbers;
b) spatial-temporal similarity of a representative enough set of flow functionals.
The work presents the results obtained in $2D$ numerical simulation of gravitation instability with the procedure implemented in the MAH-3 code. The numerical technique of the code is based on the work [10].

More information - Email: nto1@nine.ch70.chel.su

2. Calculation set-up

On the plane (x, z) bounded by rigid walls from four sides there are two layers of non-viscous, non-heat-conducting, incompressible substances of different density in gravitation field. Gravity acceleration $\vec{g}$ acts along negative $z-$ direction from heavy substance to light one.
$H = 25$, $W = 15$ are dimensions of the system, $z_0 = 12.5$ is the initial position of the interface, $g = -0.03435$, $\rho_1 = 1.0$, $\rho_2 = 2.9$ - are densities of the lower and upper layers respectively. The initial data presented were taken from [7].
Fluid incompressibility was simulated by prescribing the isothermal equation of state $p_i = C_i^2 \cdot \rho_i$, $i = 1, 2$ with large enough values of C_i^2 . A small-scale random perturbation was given at the interface.
Two potential approximations of convection flows were used for pulse: first-order-accuracy approximation using "up-wind" differences (scheme 1) and Lax-Wendroff second-order-accuracy approximation (scheme 2). The runs proceeded are presented in the table: The runs Ss and

Run	Initial Amplitude	Cell Size	Scheme
$Ss1$, $Ss2$	0.01	$\Delta x = \Delta z = 0.25$	scheme 1, scheme 2
$Vv1$, $Vv2$	0.01	$\Delta x = \Delta z = 0.25$	scheme 1, scheme 2
$Gg1$, $Gg2$	0.05	$\Delta x = \Delta z = 0.25$	scheme 1, scheme 2
$Dd1$, $Dd2$	0.01	$\Delta x = \Delta z = 0.125$	scheme 1, scheme 2

Table 1.

Vv are for two different generations of initial random perturbations. Gg is the same as Ss, except amplitude that is 5 times greater, Dd is the same as Ss, but with the mesh twice refined along each direction.

3. Results processing

Let $\vec{u} = (u, w)$ be a velocity vector with the components u, w along $x-$ and $z-$ axis. The transition to exact spectral expansion of the discrete velocity field follows the formulas:

$$u_{ij} = \sum_{n=0}^{N_2} \sum_{m=0}^{N_1} \tilde{u}_{mn} \sin \frac{\pi \cdot n}{W} x_{ij} \cos \frac{\pi \cdot n}{H} z_{ij}, w_{ij} = \sum_{n=0}^{N_2} \sum_{m=0}^{N_1} \tilde{w}_{mn} \cos \frac{\pi \cdot n}{W} x_{ij} \sin \frac{\pi \cdot n}{H} z_{ij},$$

$i = 0, \ldots, N_1; \quad j = 0, \ldots, N_2.$
Here N_1, N_2 are numbers of the mesh nodes along $x-$ and $z-$ directions, respectively, (i, j) is node index.
Velocity field correlation:

$$B_{\vec{u}}(\xi, \zeta) = \frac{1}{2W2H} \int_{-H}^{H} \int_{-W}^{W} \vec{u}(x, z) \cdot \vec{u}(x + \xi, z + \zeta) dx dz\text{-velocity field correlation,}$$

$$b_{\vec{u}}(r) = \frac{1}{2\pi} \int_0^{2\pi} B_{\vec{u}}(r \cos \phi, r \sin \phi) d\phi\text{-velocity field correlation averaged over angle,}$$

$$\beta = \frac{b_{\vec{u}}(r)}{b_{\vec{u}}(0)}\text{-correlation function averages over angle.}$$

ℓ is Taylor's scale equal to the length of a segment intercepted on the abscissae-axis by a parabola which is second-order tangent to the correlation function graph in its top.
Spectrum (spectral function) of specific turbulent kinetic energy.
Let $q_{\max}$ is maximum value of wave vector modulus. The region $(0, q_{\max})$ is subdivided uniformly into N intervals, $q_p, p = 1, \ldots, N$ is the p -th interval, Δq - the length of each interval. Let $E(q_p)$ is partial sum of the series terms for $E = 0.5 b_{\vec{u}}(0)$, which correspond to the wave vectors getting into the p -th interval by modulus. $\kappa(\nu_p) = E(q_p)/(\ell \cdot E \cdot \Delta q)$ is dimensionless density of specific turbulent kinetic energy, $\nu_p = \ell \cdot q_p$.
The depth of light-to-heavy penetration.
The depth L_1 of light-to-heavy penetration depending on $A \cdot gt^2$ was estimated. As the above boundary of mixing zone the value of z was taken, for which volume concentration of light substance averaged over x - direction was equal to 5%.

4. Results

Fifteen frames in Fig.1 arranged from the left to the right and from top to bottom in ascending order of dimensionless time $\tau = \sqrt{Ag/W} \cdot t$ show the dynamics of specific turbulent kinetic energy spectrum for the run $Dd1$.
For the method selected for obtaining dimensionless quantities, Taylor's scale is unit of length. Therefore, on the plots in Fig.1 unit should separate perturbations containing the most portion of energy and those ones associated with most portion of dissipation. Inertial interval should be located between the frequency corresponding to maximum energy and unit if energy range and dissipation range do not overlap each other significantly [11]. In terms of spectrum, flow pattern can be described as follows:
- "relic chaos" - in spectrum for energy range and dissipation interval there are perturbations of almost the same energy scale, inertia and dissipation have not yet finished selecting perturbations with respect to frequency from initial uniform spectrum;
- "formation of classical energy spectrum" - spectrum graph gets the shape of asymmetric "cap" with maximum at $\nu \leq 0.5$, dissipation range is already without energy fluctuations comparable with those for hydrodynamic scale.
- "spectrum degradation" - spectrum graph becomes delta-shaped, almost all energy is concentrated within a small interval of frequencies corresponding to hydrodynamic scale.
In Fig.1 one might consider that the frames with $\tau = 0.80 \div 1.07$ are referred to the first phase, with $\tau = 1.20 \div 1.60$ are to the second one, and with $\tau = 1.20 \div 1.60$ - to the third one.
For the second and third phases the slope L_1 was determined. The slopes are 0.054 and 0.039 respectively and differ by a factor of 1.4.
In Fig.2 spectra of specific turbulent kinetic energy are plotted in log scale for $\tau = 1.20, 1.34, 1.47$ compared with straight line that fits the "five thirds" law. While processing calculated results, it was accepted that frequencies from energy maximum to unit correspond to "inertial interval". On the whole one can assume that self-similarity takes place on "inertial interval". Profiles on this interval agree better compared with other, and if we consider only two first moments of time, the agreement is rather sufficient. Therefore, one can take that $\alpha = 0.054$ conforms better than $\alpha = 0.039$ to the value of proportion ratio in square law. Mean slope determined by "inertial interval" and by averaging over three moments of time equals to -2.17 that differs by 30% from theoretical value of $-5/3$. It can be supposed that this difference in slope and noticeable noncoincidence of profiles for frequencies greater that unit are due to the fact that the energy and dissipation ranges overlap essentially.
The assumption is proved by calculation of just the same problem performed with scheme 2

possessing significantly less dissipative properties.
Fig.3 shows the dynamics of specific turbulent kinetic energy spectrum versus τ . Unlike the calculation with scheme 1 the phase of "classical energy spectrum" generation was more distinct with respect to both duration and visual coincidence of profiles. The times within $\tau = 1.20 \div 2.00$ can be referred to it. By four computing points of the second phase corresponding to $\tau = 1.47 \div 1.87$, the slope $\alpha = 0.059$ was obtained.
Fig.4 demonstrates in log scale spectra of specific turbulent kinetic energy for $\tau = 1.60, 1.74, 1.87$ compared with the "five thirds" law. It might be considered that within "inertial interval" and dissipation range self-similarity takes place. Determination of mean slope by "inertial interval" and by averaging over three moments of time gives the value of -1.77, which agrees with theoretical value to within 6%.
The rest runs were proceeded for a number of points twice less along each of directions. Therefore, because of larger than in runs *Dd* overlapping of the energy and dissipation ranges, the phase of "classical energy spectrum" is almost absent here. For final step of calculations, the slope L_1 was determined. The slope values are $\alpha = 0.029 \div 0.046$.

5. Conclusions

Analysis taken for dynamics of specific turbulent kinetic energy spectrum demonstrated that there were three phases of turbulent mixing: "relic chaos", "classical energy spectrum", and "spectrum degradation".
In computation the energy and dissipation ranges can overlap each other significantly due to small number of cells and redundant dissipation of difference scheme. This results in absence of the phase in which classical spectrum of turbulent kinetic energy generates and exists.
Determination of the slope α at final steps of computing without energy spectrum control might give the information not related to self-similar turbulence. Slope estimating for the time interval corresponding to a certain degree to presence of inertial interval gave the value of $\alpha \approx 0.059$, which almost coincided with the experimental one.

References

[1] Anuchina NN, Kucherenko YA, Neuvazhaev VE *et al.*, Fluid and Gas Mechanics, 6, (1978).
[2] Anuchina NN, Ogibina VN, VANT, 2/10/, (1982).
[3] Kucherenko YA, Tomashev GT, Shibarshov LI, VANT, 1, (1988).
[4] Read KI, Physica 12D, (1984).
[5] Youngs DL, Physica 12D, (1984) and 37D, (1989).
[6] Youngs DL, Phys. Fluids A, 3, 5, (1991).
[7] Youngs DL, The Third Zababakhin Scientific Talks, Kyshtym, January 14-17, (1992).
[8] Obukhov AM, Proc. of the USSR Academy of Science, 32, 1, (1941).
[9] Kolmogorov AN, Proc. of the USSR Academy of Science, 30, 4, (1941).
[10] Anuchina NN, Volkov VI, Es'kov NS, Presentation at Russian/U.S. Weapons Laboratories introductory technical exchange in computational and computer science, Livermore, (1992).
[11] Monin AS, Yaglom AM, Statistical Hydromechanics, Part 2, Moscow, "Nauka", (1967).

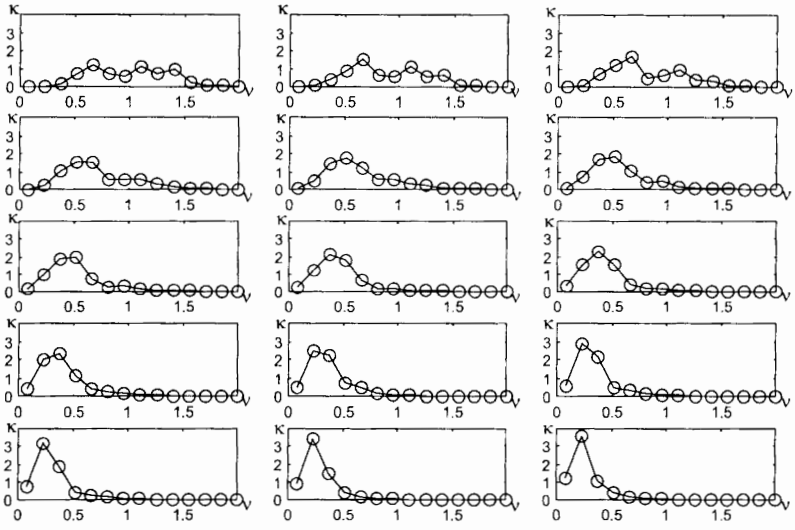

Figure 1. Dynamics of turbulent kinetic energy spectrum (run *Dd*1, τ =0.80, 0.93, 1.07, 1.20, 1.34, 1.47, 1.60, 1.74, 1.87, 2.00, 2.14, 2.27, 2.40, 2.54, 2.67).

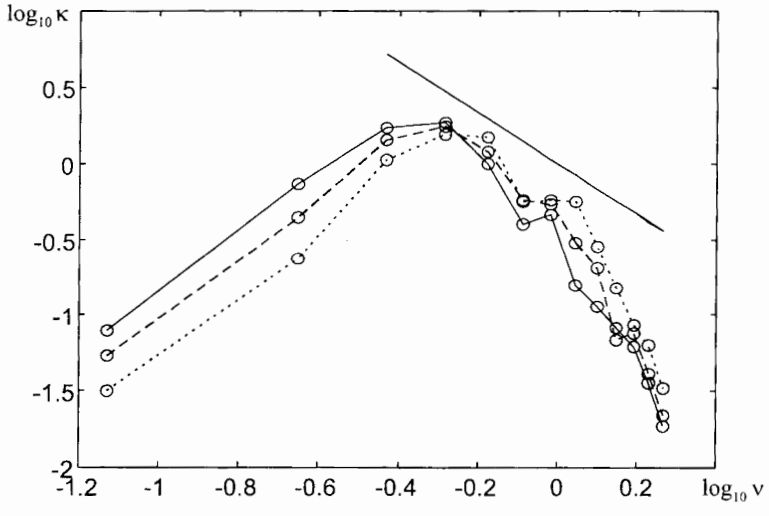

Figure 2. Spectrum of turbulent kinetic energy compare with the "five thirds" law (run *Dd*1, dotted line - τ = 1.2, dashed line - τ =1.34, solid line - τ =1.47).

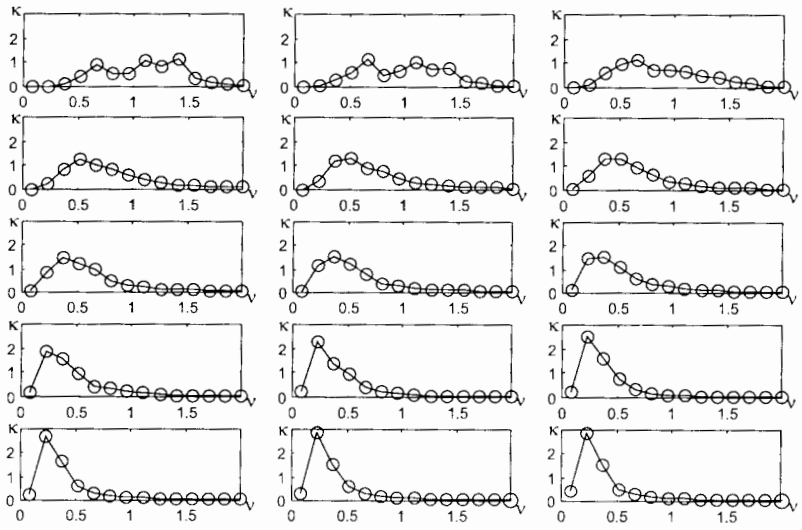

Figure 3. Dynamics of turbulent kinetic energy spectrum (run *Dd*2, τ =0.80, 0.93, 1.07, 1.20, 1.34, 1.47, 1.60, 1.74, 1.87, 2.00, 2.14, 2.27, 2.40, 2.54, 2.67).

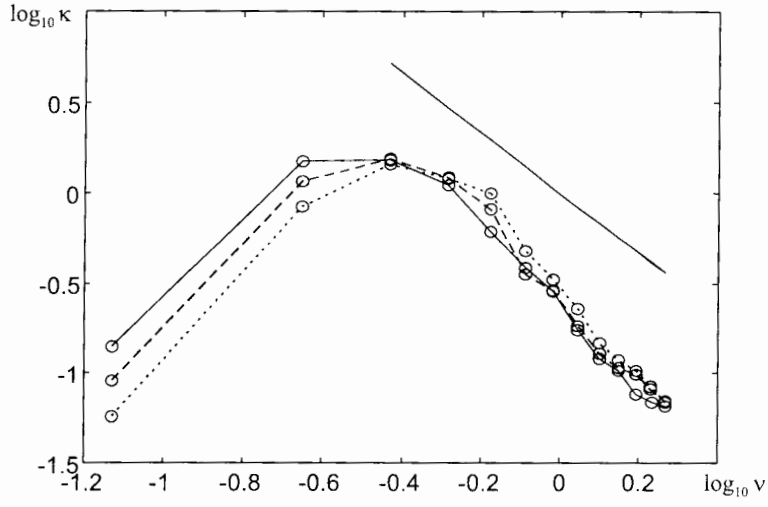

Figure 4. Spectrum of turbulent kinetic energy compare with the "five thirds" law (run *Dd*1, dotted line - τ =1.60, dashed line - τ =1.74, solid line - τ =1.87).

Three-Dimensional Numerical Simulation of Rayleigh-Taylor Instability by MAH-3 Code

N.N. Anuchina, V.A. Gordeichuk, N.S. Es'kov, O.S. Ilyutina, O.M. Kozyrev and V.I. Volkov
Russian Federal Nuclear Center, All-Russian Scientific Research Institute of Technical Physics, Snezhinsk, Russia

Abstract: The presentation offers the results obtained by direct numerical simulation of gravitation mixing evolution by the MAH-3 code.
The discrete model MAH-3 implements identical kinetic energy dissipation for both $2D$ and $3D$ computing. The laws governing the increase of light-to-heavy penetration depth are compared for the cases of two and three spatial variables and for two different mechanisms of kinetic energy dissipation.

1. Introduction

When a substance of density ρ_2 is above a substance of density $\rho_1 < \rho_2$ in gravitation field with acceleration $\vec{g}$, directed from heavy substance to light one, their interface is subject to gravitation instability.
Numerous experimental and computational studies of turbulent mixing [1 – 7] are devoted to square-law verification and quantitative estimation of $f(\rho_2/\rho_1)$. Experiments performed by Y.A. Kucherenko, K.I. Read and D.L. Youngs for substances of different density proved that depth of "bubble" penetration was defined by the function $L_1 = \alpha \cdot A \cdot g \cdot t^2$, where $A = (\rho_2 - \rho_1)/(\rho_2 + \rho_1)$ is Atwood's number and $\alpha \approx 0.06$. $2D$ numerical simulation gives $\alpha \approx 0.04 \div 0.05$. $3D$ runs [6] resulted in likewise value.
The work presents the results of 3D numerical simulation of gravitation instability obtained by code MAH-3.

2. Numerical technique and its capabilities

Code MAH-3 computes nonstationary $3D$ gas dynamic problems. Computational region is represented by a set of physical domains. Each of the domains is a topological parallelepiped. Domain boundaries can be the interfaces or external boundaries of a system: free boundaries, rigid walls, boundaries with prescribed pressure.
The code implements a numerical technique which is a generalized $2D$ MAH technique [8]. The technique is based on dividing the computational algorithm onto Lagrangian and Eulerian phases.
Lagrangian phase can be simulated with both explicit and implicit schemes. Algorithm for solving implicit difference equations is the Jacobi Jacobi-Newton iterative process.
Eulerian difference scheme is explicit and it uses locally adaptive algorithms for generating Eulerian moving mesh. The meshes are consistent at interfaces, however, they are generated independently for each physical domain. Interfaces between domains are calculated without accounting for slipping.
Each of the cells is the image of threelinear mapping of a cube into three-dimensional physical

More information - Email: nto1@nine.ch70.chel.su

space when the cube vertices become cell vertices.
Difference equations for each of the phases are approximations of the conservation laws written for curvilinear hexahedron, i.e. the scheme is divergent relatively mass, pulse, and total energy.
On the basis of multicomponent one-velocity model a capability was implemented which enabled description of strongly deformed interfaces. In this case the interface does not coincide with the coordinate surface and it can arbitrarily intersect Eulerian mesh, mixed cells containing different substances being created.
Transition to interface description with the use of mixed cells takes place at the moment when strong deformations begin and it becomes impossible to follow the interface as a coordinate surface of the mesh. To calculate mixed cells at Lagrangian phase, the conditions of thermodynamic equilibrium and continuity of component velocity vector are used.
At Eulerian phase difference approximations of convection terms in the equations of continuity and energy exploit the "donor-cell" principle. Convection flows in the vicinity of mixed cells are calculated with the account for flow direction and substance composition in the cells. Two potential approximations of convection flows were implemented for pulse:

- first-order-accuracy approximation using "up-wind" differences (scheme 1);
- Lax-Wendroff second-order-accuracy approximation (scheme 2).

3. Calculation set-up

In the space region (x, y, z) bounded by rigid walls from six sides there are two layers of non-viscous, non-heat-conducting, incompressible substances of different density in gravitation field. Gravity acceleration $\vec{g}$ acts along negative z -direction from heavy substance to light one.
$W_x = W_y = 15$, $H_z = 25$ are dimensions of the system, $z_0 = 12.5$ is the initial position of the interface, $g = -0.03435$, $\rho_1 = 1.0$, $\rho = 2.9$ are densities of the lower and upper layers espectively. The initial data presented were taken from [7].
Fluid incompressibility was simulated by prescribing the isothermal equation of state $p = c^2\rho$ with rather large value c^2, $c_1^2 = 10^2$, $c_2^2 = c_1^2 \cdot \rho_1/\rho_2$.
At initial time the density and pressure distributions correspond to hydrostatic equilibrium. A small-scale random perturbation with the amplitude $a_0 = 0.01$ was given at the interface. Initial perturbation contained the whole spectrum of harmonics which was defined by the difference mesh resolution.
$2D$ calculations were proceeded for number of points equal to $60 \times 2 \times 100$, $3D$ ones - for $60 \times 60 \times 100$ points. Four runs were performed differing in generation of random perturbations: two $3D$ runs that followed schemes 1 and 2 and two $3D$ ones also with schemes 1 and 2.

4. Results processing

- Kinetic energy dissipation.
  The temporal dependence of the difference between potential and kinetic energies gives the integral characteristic of energy dissipation:
  $p = (P - P_0)\Delta P_{\max}$ is dimensionless potential energy, P, P_0 - current and initial potential energies respectively, $k = K/\Delta P_{\max}$ is dimensionless kinetic energy, K - current kinetic energy, $\Delta P_{\max} = gH_z^2 W_x W_y(\rho_2 - \rho_1)/4$ is maximum possible change of potential energy, $\tau = \sqrt{Ag/W_x} \cdot t$ is dimensionless time. This presentation of dissipation is proposed in [6].
- Depth of light-to-heavy penetration.
  The depth L_1 of light-to-heavy penetration depending on $S = A \cdot g \cdot t^2$ was estimated. As

the above boundary of mixing zone the value of z was taken, for which volume concentration of light substance averaged over $x-$ and $y-$ direction was equal to 5%.

5. Calculated results

The runs proceeded till the depth of light-to-heavy penetration achieved about $25 \div 30\%$ of the system width.

Figs. 1, 2 depict comparative plots of potential and kinetic energies in $2D$ and $3D$ simulations for schemes 1 and 2 respectively. By the time of calculation ending kinetic energy dissipation was significant and made up 62% in $3D$ case and 61% in $2D$ one. Scheme 2 possesses much less dissipative features. Here energy unbalance was 12% and 8%. It should be noted that in $2D$ simulation by scheme 2 the unbalance of 8% was obtained for far less energy range than that of 61% by scheme 2. For the calculations presented, energy unbalance dynamics is almost the same in $2D-$ and in $3D-$simulation. Therefore, the difference between $2D-$ and $3D-$simulation might be associated with different dynamics of potential energy. By the moment of calculation ending this difference makes up about 25% for scheme 1 and 40% for scheme 2.

Fig. 3 demonstrates penetration of light substance into heavy one as a function of Agt^2 for all the four runs. In all calculations light-to-heavy penetration is almost identical at the beginning and later it is greater in $3D$ case. At the final step of calculations slopes of the curves obtained was determined. In the figure a straight line with corresponding slope is drawn for each of them. Slope values are 0.034 for the run $2D$, scheme 1; 0.035 for the run $2D$, scheme 2; 0.050 for the run $3D$, scheme 1 and 0.050 for the run $3D$, scheme 2.

A significant difference between dissipation features of schemes 1 and 2 almost did not influence the slope. The slope in $3D$ simulation was obtained to be 30% greater than that of $2D$ simulation.

6. Conclusions

Presented model for direct numerical simulation of gravitation turbulent mixing implements dissipation mechanism identically for $2D$ case and for $3D$ one.

The difference between slopes of $2D$- and $3D$-simulation might be associated with different dynamics of potential energy. The difference of $25 \div 40\%$ in dynamics is in agreement with the difference of 30% in slopes.

In $3D$ simulation the experimental value $\alpha^b \approx 0.06$ was not achieved. It might be assumed that because of insufficient large value of Reynolds's number degenerate energy spectrum is realized at final step of calculations and large-scale perturbations mostly contribute to mixing.

References

[1] Anuchina NN, Kucherenko YA, Neuvazhaev VE *et al.*, Fluid and Gas Mechanics, 6, (1978).
[2] Anuchina NN, Ogibina VN, VANT, 2/10/, (1982).
[3] Kucherenko YA, Tomashev GT, Shibarshov LI, VANT, 1, (1988).
[4] Read KI, Physica 12D, (1984).
[5] Youngs DL, Physica 12D, (1984) and Physica 37D, (1989).
[6] Youngs DL, Phys. Fluids A, 3, 5, (1991).
[7] Youngs DL, The Third Zababakhin Scientific Talks, Kyshtym, January 14-17, (1992).
[8] Anuchina NN, Volkov VI, Es'kov NS, Presentation at Russian/U.S. Weapons Laboratories introductory technical exchange in computational and computer science, Livermore, (1992).

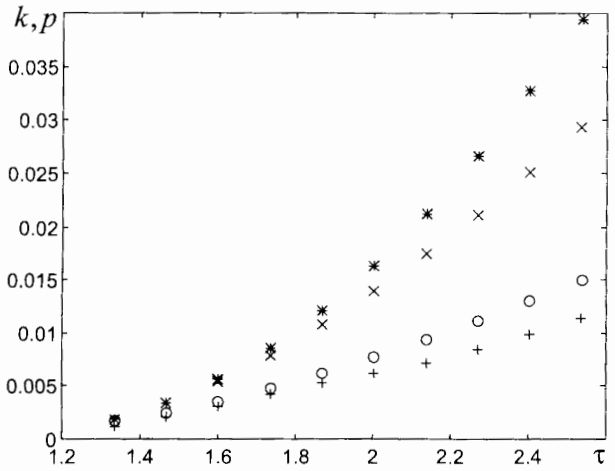

Figure 1. Temporal dynamics of potential and kinetic energies for scheme 1 ($* \rightarrow p$, $\circ \rightarrow k$ in 3D run; $\times \rightarrow p$, $+ \rightarrow k$ in 2D run).

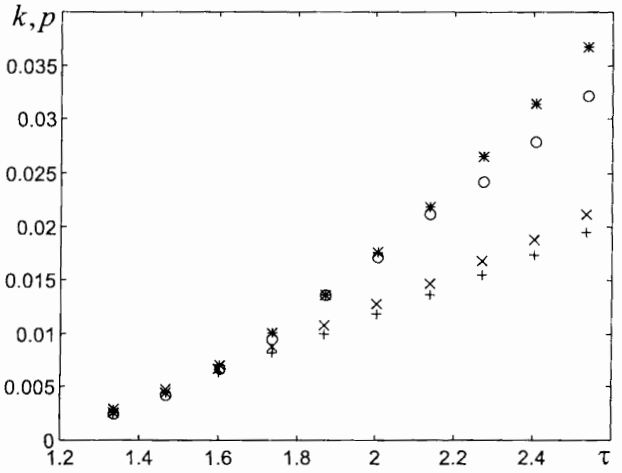

Figure 2. Temporal dynamics of potential and kinetic energies for scheme 2 ($* \rightarrow p$, $\circ \rightarrow k$ in 3D run; $\times \rightarrow p$, $+ \rightarrow k$ in 2D run).

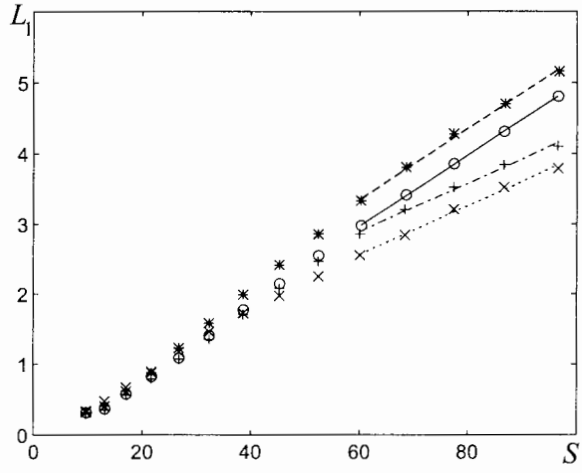

Figure 3. Light-to-heavy penetration vs. S ($\times \rightarrow$ scheme 2, $+ \rightarrow$ scheme 1 in 2D runs; $\circ \rightarrow$ scheme 1, $* \rightarrow$ scheme 2 in 3D run).

Numerical Simulation of Three-Dimensional Gravitational Instability Using Unstructured Marker's Grid on an Interface

N.N. Anuchina, V.A. Gordeichuk, N.S. Es'kov, O.S. Ilyutina, O.M. Kozyrev and V.I. Volkov
Russian Federal Nuclear Center, All-Russian Scientific Research Institute of Technical Physics, Snezhinsk, Russia

Abstract: Results are presented of direct numerical simulation of evolution of non-linear stage of Rayleigh-Taylor instability by a code MAH-3 using unstructured grid of markers at the interface.
Description of contact surface using markers is based on ideas implemented in the code MAH [1] computing non-stationary gas-dynamic flows with two spatial variables.
Evolution of elementary perturbations at the interface are compared for the cases of two and three spatial dimensions.

1. The Numerical method

The code MAH-3 is intended for computing non-stationary spatially $3D$ problems of gas dynamics and implements numerical technique generalizing $2D$ method MAH [1].

- The difference scheme of the method is based on computation algorithm splitting into Lagrangian and Eulerian stages.
- Computing of Lagrangian stage can be performed using explicit and implicit schemes. Algorithm for solving implicit difference equations involves Jacobi-Newton iteration process selecting iteration parameter from condition of maximum reduction of error per iteration.
- Difference scheme of Eulerian stage is explicit using local adaptive algorithms for reconstructing Eulerian mesh.
- Contact boundaries are described as coordinate surfaces of mesh of numerical integration region or using unstructured grid of markers and mixed cells.
- For detailed study of evolution of unstable interface the following computation technique is used:

* at linear stage of perturbation development the contact boundary is described as Lagrangian coordinate surface of the mesh;
* in the beginning of non-linear stage transition is implemented to description of contact surface using mixed cells and unstructured grid of markers not related to the mesh of numerical integration domain;
* appropriate grid at the contact surface is sustained by removing markers, adding new ones and applying algorithms of grid reconfiguration.

More information - Email: nto1@nine.ch70.chel.su

2. Statement of calculations

A problem is considered of evolution of cosine perturbations at the interface of two layers of incompressible, non-viscous, non-heat-conducting liquid of different density when gravitational acceleration is oriented from heavy to the light one.
In Cartesian coordinate system (x, y, z) the planen $z = z_0$ is a interface of the layers, ρ_1, ρ_2 ($\rho_1 < \rho_2$) is liquid density in lower and upper half spaces, respectively, gravitational acceleration g is oriented in negative direction of axis z, the system is in the state of hydrostatic equilibrium.
A regular perturbation is introduced into position of the interface at initial time moment: $z = z_0 + a_0 cos(n_x x) cos(n_y y)$, where a_0 is initial amplitude of perturbation, $n_x = 2\pi/\lambda_y$, are components of wave vector $\vec{n}$, λ_x, λ_y is perturbation wave length along directions x and y, respectively.
The problem was solved in parallelepiped $\Pi = [0, \lambda_x/2] \times [0, \lambda_y/2] \times [0, H]$, setting conditions of flow absence at its faces. To rule out influence of rigid horizontal walls on flow functionals of our interest the parallelepiped height H was taken sufficiently large.
$2D$ perturbation corresponds to value $n_y = 0, \lambda_y = \infty$. In this case the parallelepiped dimension along axis was taken much more than λ_x. Analysis of linearized differential problem shows that increment of exponential increase of perturbation amplitude is given by the following expression: $\omega = \sqrt{Ag \mid \vec{n} \mid}$, here $A = (\rho_2 - \rho_1)/(\rho_2 + \rho_1)$ is Atwood's number.
At the linear stage the regular $2D$ and $3D$ perturbations meeting the same value of wave vector modulus increase in the same way. Therefore, in order to compare results of computing the problems in $2D$ and $3D$ configurations initial perturbations were used with the same value of wave vector modulus: $\lambda_x = \lambda$ in $2D$ calculations, $\lambda_x = \lambda_y = \sqrt{2}\lambda$ in $3D$ calculations. In all calculations $a_0 = 0,\ 1,\ \lambda = 20,\ g = 100$. The calculations were performed for density jump at contact boundary $\delta = \rho_2/\rho_1 = 10$. $2D$ calculations were performed with the number of points $20 \times 2 \times 80$, $3D$ - $20 \times 20 \times 80$. Incompressibility of liquids was simulated by setting isothermal equation of state $p_i = C_i^2 \cdot \rho_i,\ i = 1, 2$ with sufficiently large value of C_i^2, $C_1^2 = 10^6$, $C_2^2 = C_1^2/\delta$

3. Processing of computation test results

In the calculations dimensionless velocity of bubble was determined
$v^+ = \sqrt{\mid \vec{n} \mid /2\pi g} \cdot w^+$, where w^+ is vertical component of rate of light liquids penetration into the heavy one.
At linear stage of perturbations growth when the interface was described as Lagrangian coordinate surface, w^+ was velocity in contact surface node corresponding to maximum value of z.
At the stage of computing the problem with mixed cells and markers the bubble velocity was determined by two techniques:

- z value was determined for which bulk concentration of light liquid averaged over directions x and y made up 5%, tabular for this z value of w^+ was determined by linear interpolation using mesh nodes;

- as velocity of marker of contact surface with maximum value of z .

As it is shown in numerous studies, e.g. in [2 – 6], the principal distinctive feature of non-linear stage of regular perturbations evolution is that rate of bubble penetration from light liquid into a heavy one reaches constant value.

4. Computation results

Dynamics of perturbation evolution at contact boundary for $3D$ calculation is given in Fig. 1. Six stills are presented on the same scale which are related to non-linear stage of perturbation evolution. At the end of non-linear stage the initial regular perturbation transferred into distinct bubble surrounded by narrow jets and adjacent jet sheet.

Difference in growth of amplitude of $2D$ and $3D$ perturbations is displayed at non-linear stage. $3D$ perturbations grow faster than $2D$. This difference is most vivid in the bubble growth rate. In Figs. 2 and 3 one can see plots of velocity of bubble $v^+ = \sqrt{\mid \vec{n} \mid /2\pi g} \cdot w^+$ versus dimensionless time it $\xi = \sqrt{Ag \mid \vec{n} \mid} \cdot t/\sqrt{\pi}$ of $2D$ and $3D$ perturbations for the two techniques of obtaining w^+.

At non-linear stage at $\xi \approx 2.0 \div 2.5$ a quasi-stationary mode of light liquid penetration into heavy one is formed.

In the calculations the light liquid velocity reaches constant $v_c^+ \approx 0.27$ for $2D$ perturbations, and this value practically does not depend on the technique of results processing. For $2D$ perturbations in computations by B. Daly [5] $v_c^+ \approx 0.21$, by code MECh [6] - $v_c^+ \approx 0.29$.

For Atwood number close to unity from analytic solution of problem of plane bubble levitation in channel [7] the velocity of light liquid penetration into the heavy one is estimated as $v_c^+ = 0.23 \pm 0.01$, that is in agreement with all the given results of numerical computations.

For $3D$ perturbations $v_c^+ \approx 0.53$ in case of the first results processing technique and $v_c^+ \approx 0.41$ in case of the second.

Difference between the results obtained can be explained by a large velocity gradient in the vicinity of the bubble boundary that leads to significant velocity variations at low variations in determination of interface position. This circumstance appeared to be very significant in $3D$ case.

In [8] for v_c^+ in case of cylindrical tubes they give the value 0.32.

5. Conclusion

Perturbation growth rate in $3D$ case is greater than in $2D$. Correct processing of calculation results is a separate complex problem. Determination of the bubble velocity through preliminary determination of its interface proceeding from the concentration field is considered as less successful solution compared to direct use of velocity distribution over the interface described by unstructured grid of markers. If we take this as an assumption, then constant value of bubble growth rate obtained in the calculations is about 1.5 times higher for $3D$ perturbations as compared with $2D$ perturbations equivalent in modulus of wave vector.

References

[1] Anuchina NN, Volkov VI, Es'kov NS, Report at Russian/U.S. Weapons Laboratories introductory technical exchange in computational and computer science, Livermore, (1992).

[2] Lewis DJ, Proc. Roy. Soc. London Ser. A, 202, 81-96, (1950).

[3] Fermi E, Collection Book by Enrico Fermi , Scientific proceedings, 128, 2, M., "Nauka", (1972).

[4] Fermi E, Von Neumann J, Collection Book by Enrico Fermi , Scientific proceedings, 129, 2, M., "Nauka", (1972).

[5] Daly BT, Phys. of Fluids, 10, 2, (1967).

[6] Anuchina NN, Ogibina VN, VANT, 2/8, (1981).

[7] Birkhoff G, Hydrodynamics, M., IL, (1963).

[8] Birkhoff G, Zarantonello E, Jets, Tracks, and Caverns, M., "Mir", (1964).

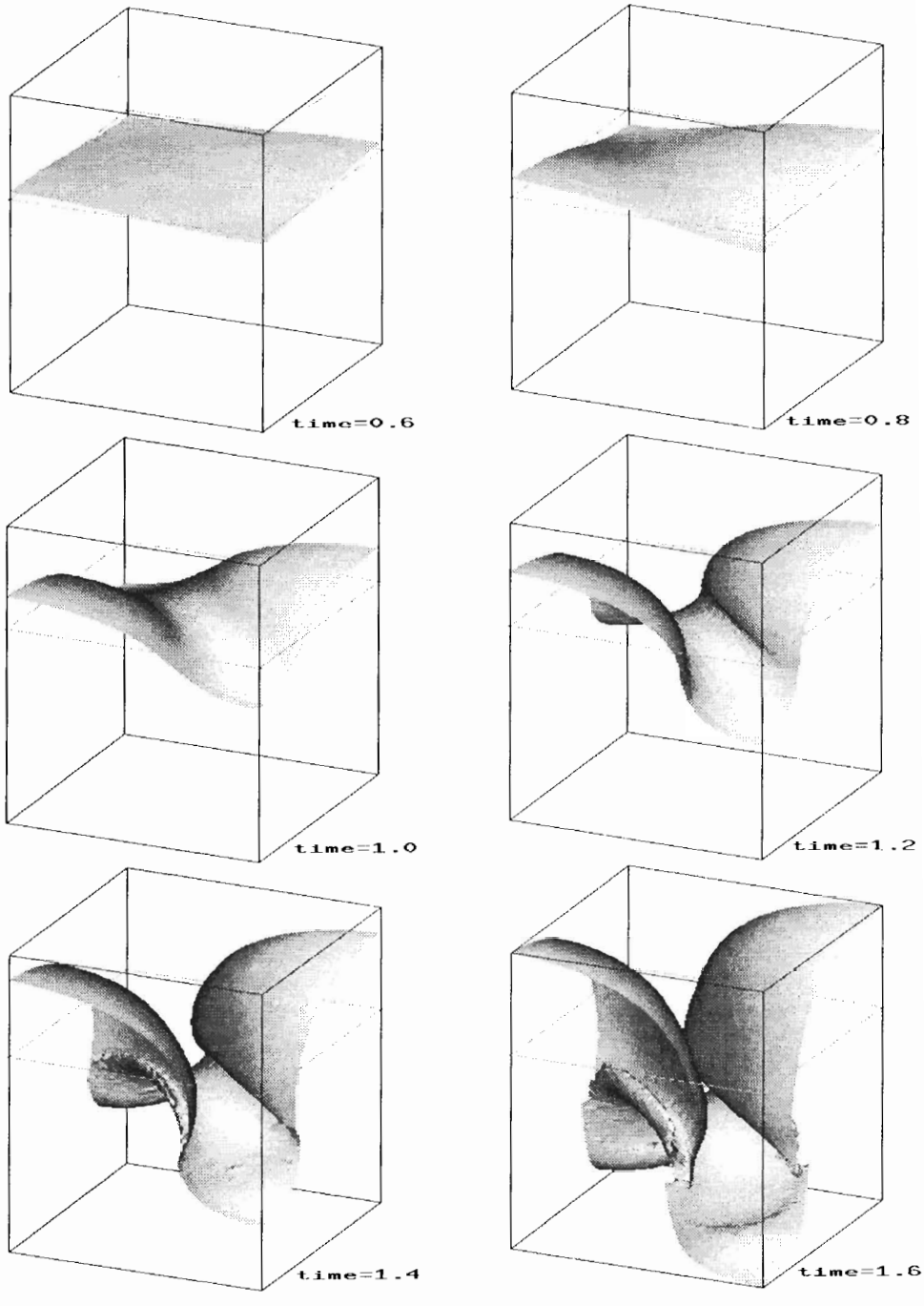

Figure 1. Dynamics of perturbations growth at interface.

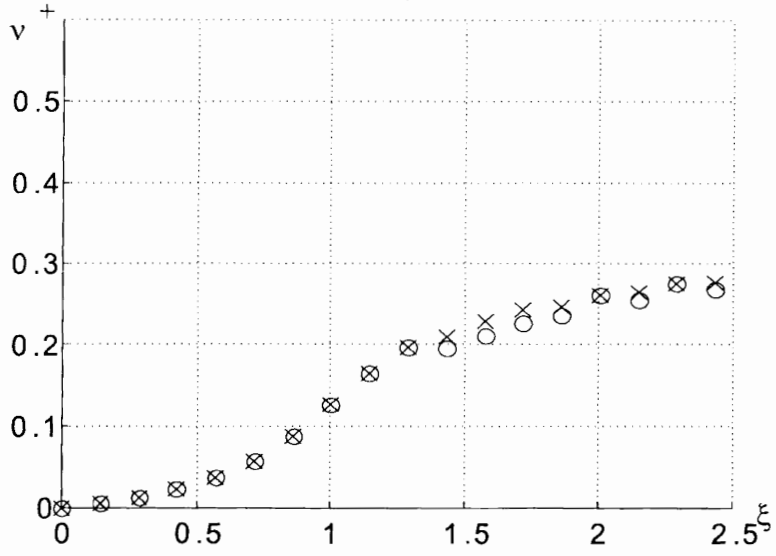

Figure 2. Velocity of light liquid penetration into the heavy one for $2D$ perturbations ($\circ \rightarrow 1^{st}$, $\times \rightarrow 2^{nd}$ techniques of results processing).

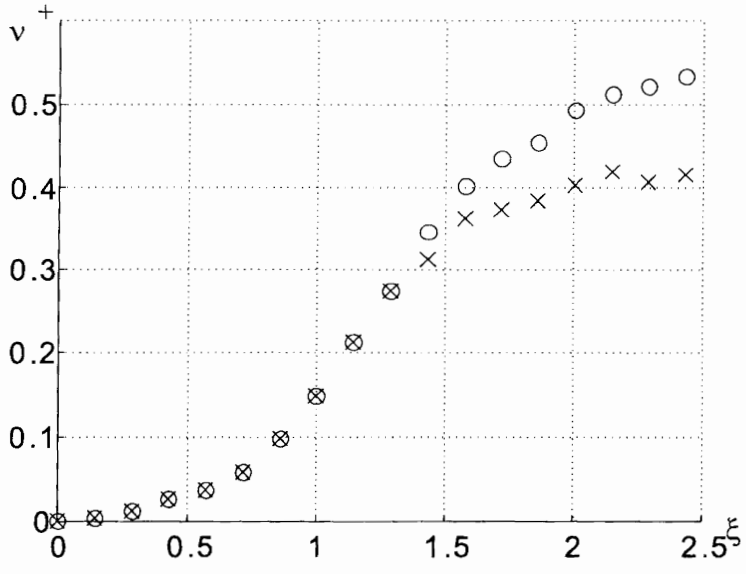

Figure 3. Velocity of light liquid penetration into the heavy one for $3D$ perturbations ($\circ \rightarrow 1^{st}$, $\times \rightarrow 2^{nd}$ techniques of results processing).

Numerical Study of Gravitational Mixing in Systems Consisting of Layers of Finite Width and Different Density

N.N. Anuchina and V.I. Volkov
Russian Federal Nuclear Center, All-Russian Scientific Research Institute of Technical Physics, Snezhinsk, Russia

1. Introduction

- Rayleigh-Taylor instability is known to form area of turbulent mixing of substances (TMA) in a number of problems where layers of substances with different densities are considered.
- Of great practical value is study of TMA evolution after interaction with other layer boundaries, in particular, with gravitationally stable ones.
- Theoretical and experimental research into this problem was presented in publications [2, 3].
- This paper presents the results of direct numerical simulation showing how one of the fronts of TMA formed in the case of gravitationally unstable interface interacts with a rigid wall and how this interaction affects further development of TMA.
- Interaction is considered of TMA fronts consisting of "spikes" of heavy substance and "bubbles" of light one with a rigid wall. Layer width of the substances was varied. Influence of the Atwood number was estimated.
- Simulation was performed in compliance with technique and program complex "MA" [1].

2. Statement of calculations

- Two plane layers of incompressible non-viscous non-heat-conducting fluids of different densities were considered in the field of constant acceleration g (Fig. 1). Two series of calculations with the following characteristics were performed:
  1. $X_{INT} = 12.5$, $X_L = 2.5, 5.5, 7.7, 11.5$, $X_U = 25$;
  2. $X_{INT} = 25$, $X_L = 0$, $X_U = 26, 29.8, 32, 35$.
- In the first series of calculations initial width d_L of light layer was varied, and in the second series - d_H - width of a heavy layer, d_L and d_H being equal to 1, 4.8, 7, 10.
- At the initial moment of time $t = 0$ fluids were in hydrostatic equilibrium. Small-scale random perturbation was defined at the interface between substances ($x = X_{INT}$) .
- Calculations used $W = 15$, $g = 35g_0$ where g_0 is Earth's free fall acceleration, $X_{INT} = 12.5$, $\rho_H = 2.9$, *10*, $\rho_L = 1$. All outer boundaries were rigid walls.

More information - Email: nto1@nine.ch70.chel.su

- Equations of state were $P_\alpha = C_\alpha^2 \cdot \rho_\alpha,\ \alpha = H,\ L,\ C_L^2 = 900$.

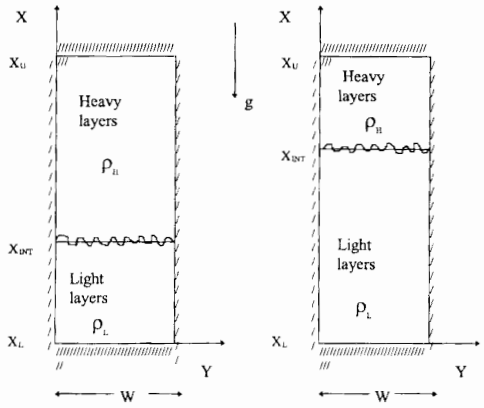

Figure 1. Statement of calculations.

3. Main calculation results

- Interface between fluids is gravitationally unstable.
- Area of turbulent mixing of substances is formed rather rapidly.
- Heavy fluid penetrates into a light one in the form of "spikes", and light fluid penetrates into the heavy one in the form of "bubbles".
- Width of the mixing area L soon begins to grow quadratically in time $L \approx 0.14 \cdot A \cdot g \cdot t^2$, that agrees with experimental results (see Figs. 2, 3).
- In the first series of calculations, where light fluid layer is thin, "spikes" of the heavy fluid interact with the rigid wall. In the area d_L of width heterogeneous mixture of fluids is formed (see Fig. 4).
- In the second series of calculations light fluid "bubbles" penetrate into the heavy fluid layer and interact with the upper rigid boundary of the light layer. Gradually density approaches some mean for the system value. Mixture of substances close to homogeneous is formed in the area of thin layer (see Fig. 5).
- Influence of the rigid wall manifests itself earlier in the case of thin light layer for the same values of d_H and d_L .
- In both series of calculations motion of TMA front decelerates gradually changing from quadratic to linear dependence in time (see Fig. 6, 7), being
$L(t) = b \cdot \sqrt{\frac{\rho_H - \rho_L}{\rho_H}} \sqrt{gd} \cdot t$ - [2], $L(t) = b \cdot \sqrt{\frac{\rho_H - \rho_L}{\rho_L}} \sqrt{gd} \cdot t$ - [3] for thin light and heavy substance, respectively.

- Growth becomes linear in time with some delay depending on d (see Figs. 4, 5).
- All calculations give the same value for b_L and b_H equal to ≈ 0.2 .
- Numerical results obtained are in good agreement with experimental ones and with asymptotic dependencies for L obtained from semiempirical models. Calculated values of b_L and b_H are lower than experimental ones: $b_L = b_H \approx 0.2, 0.38$ [4], respectively.

References

[1] Anuchina NN, Volkov VI, Es'kov NS, Numerical Modeling of Multi-Dimensional Flows with Large Deformations, Report at Russian/U.S. Weapons Laboratories introductory technical exchange in computational and computer science, Livermore, (1992).

[2] Belen'ky SZ, Fradkin ES, Theory of Turbulent Mixing, Proc. of Physics Institute of USSR SA, 29, 207, (1965).

[3] Neuvazhaev VE, Yakovlev VG, Calculation of Gravitational Turbulent Mixing Using $k\epsilon$-Model, VANT Series: Theoretical and Applied Physics, 1, 28-36, (1988).

[4] Kucherenko YA, Balabin SI, Pylaev AP, Experimental study of asymptotic stage of gravitational turbulent mixing of thin liquid layers of different densities, Proc. of the 4th International Workshop on the Physics of Compressible Turbulent Mixing, Cambridge, England, (1993).

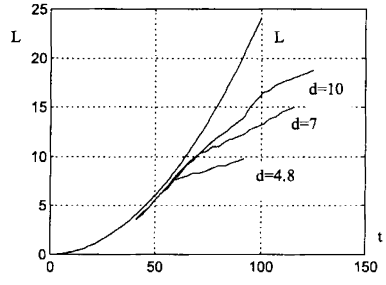

Figure 2. Dependencies L(t) and for different values of initial width d of a light layer.

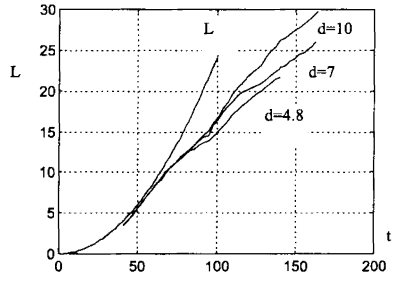

Figure 3. Dependencies $L(t)$ and for different values of initial width d of a heavy layer.

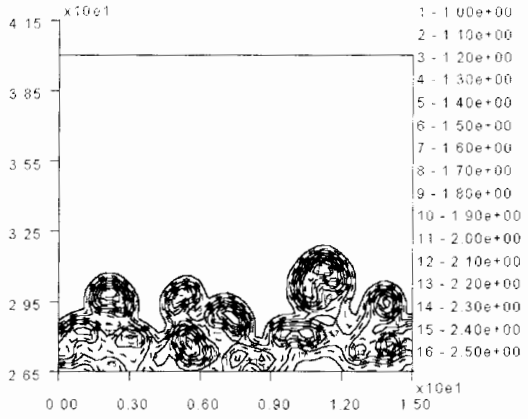

Figure 4. Density isolines $n = 2.9,\ t = 28,\ 60,\ d = 1.0.$

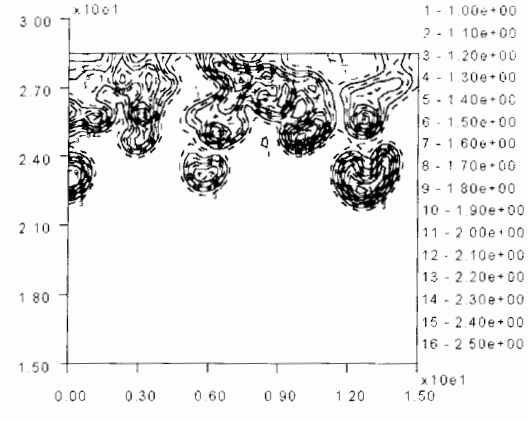

Figure 5. Density isolines $n = 2.9,\ t = 28,\ 60,\ d = 1.0.$

Numerical Study of Behaviour of Gravitational Turbulent Mixing Area for Different Modes of Acceleration Application

N.N. Anuchina and V.I. Volkov
Russian Federal Nuclear Center, All-Russian Scientific Research Institute
of Technical Physics, Snezhinsk, Russia

1. Introduction

Results of direct numerical simulation are presented for the case of two spatial variables. Results were obtained using code MAX[4].
What is under study is the following:
- evolution of mixing area (MA) and process of partial separation after instantaneous change of acceleration direction;
- evolution of MA by inertia after instantaneous acceleration cut-off;
- effect of the Atwood number on MA behavior as well as of new acceleration and moment of acceleration change both at the phase of instability evolution and at the phase of attenuation.

2. Statement of the problem

$W = 15,\ H = 25,\ X_{INT} = 12.5,\ \rho_h = 2.9,\ 10,\ 100,\ \rho_1 = 1$ (see Fig. 1).
Substances are non-viscous, non-heat-conductive, close to incompressible.
At $t = 0$
- system is in hydrostatic equilibrium in the gravity field with free-fall acceleration;
- small random perturbation is defined at the interface between the substances.

3. Acceleration variation in time

$\vec{g}_0 = 35\ \vec{g}_E,\ 200\ \vec{g}_E,\ \vec{g}_E$ - Earth's gravity acceleration;
$\vec{g}_1 = -k\ \vec{g}_0,\ k = 0,\ 0.5,\ 1,\ 3,\ 45;\ \vec{g}_2 = l\ \vec{g}_0,\ l = 0, 1$ (see Fig. 2).

4. Main results

1. Under the effect of permanent acceleration $\vec{g}_0$ (see Fig. 3) - substance mixing area (MA) is formed;
- L MA width, L_h depth of penetration of heavy substance into a light one and L_1 light-to-heavy penetration depth grow proportionally to $g_0 \cdot t^2$;
- with increasing Atwood number ($A = (n-1)/(n+1),\ n = \rho_h/\rho_1$) growth rates $L,\ L_h,\ L_1$ increase as well as asymmetry of MA evolution;
- results obtained agree with experimental data [3].
2. Instantaneous change of acceleration direction at the moment $t = t_1$ at the phase of gravitational mixing evolution alters the behavior of mixing area for $t > t_1$ (see Figs. 4, 5)
- during some time L MA width continues to grow according to the same law as at $t < t_1$. Then retardation starts and, having achieved some maximum, L begins to decrease, at first, rapidly,

More information - Email: nto1@nine.ch70.chel.su

then slowly, gradually reaching practically constant value;
- partial separation of substances occurs;
- mixing becomes more and more homogeneous;
- qualitatively the process is the same for different A, t, and new acceleration magnitude;
- the inertial part of MA growth, and maximal value of L are less, the greater is the magnitude of new acceleration and both grow with increasing A.

3. Repeated change of acceleration sign at the moment $t = t_2$ leads to the growth of mixing area. Enlargement of structures in MA occurs (see Figs. 6, 7).

4. After instantaneous acceleration cut-off at the moment $t = t_1$ at the phase of instability evolution (see Fig. 8)
- width $L(t)$ at first grows in the same manner as at $t < t_1$ then retards and reaches dependence [5] $L = L_1 \cdot (1 + \frac{2}{m} \cdot \frac{t-t_1}{t_1})^m$ (1)
($L_1 = L(t_1)$) $m = 0.34$ for $n = 2.9; m = 0.4$ for $n = 10$;
- mixture of substances becomes more homogeneous;
- depth L_l of light-to-heavy penetration varies proportionally to $\sim t^\alpha$, where α depends on A : $\alpha \approx 0.5$ for $n = 2.9, \alpha \approx 0.25$ for $n = 10$.

5. Acceleration cut-off at the moment $t = t_2$ at the phase of MA attenuation leads to growth of $L(t)$ with subsequent reaching of dependence (1) with $m = 0.27$ for $n = 2.9$ (see Fig. 9).

5. Conclusion

Qualitatively results obtained are in good agreement with experimental data and inferences of the theory. Acceleration direction being changed, calculations show partial separation of substances in the mixing area, experiments show full separation.

References

[1] Taylor GI, The instability of liquid surfaces when accelerated in a direction perpendicular to their planes. 1, Proc. Roy. Soc. A, 201, 192, (1950).
[2] Youngs DL, Physica, D12, 19, (1984).
[3] Youngs DL, Physica, D37, 270-287, (1989).
[4] Anuchina NN, Volkov VI, Es'kov NS, Numerical Modeling of Multi-Dimensional Flows with large deformations, Report at Russian/U.S. Weapons Laboratories introductory technical exchange in computational and computer science, Livermore, (1992).
[5] Belen'ky SZ, Fradkin ES, Theory of Turbulent Mixing, Proc. of Physics Institute of AS of USSR, 29, 207, (1965).
[6] Kucherenko YA, Balabin SI, Pylaev AP, Behavior of Gravitational Turbulent Mixing Layer under Conditions Leading to Separation, RAS Reports, 334, 4, (1994).
[7] Polionov AV, Yakovlev VG, Description of Mixture Separation by Means of HKE-model, Report at 4th International Workshop on The Physics of Compressible Turbulent Mixing, England, (1993).

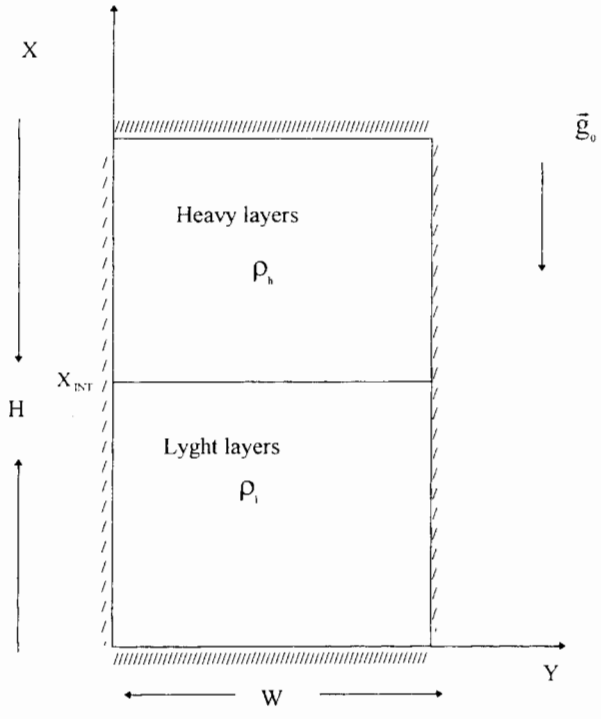

Figure 1. Statement of the problem.

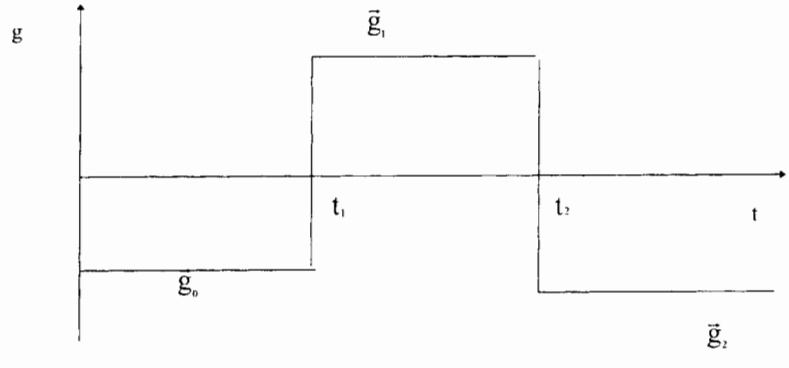

Figure 2. Modes of applied acceleration in calculations.

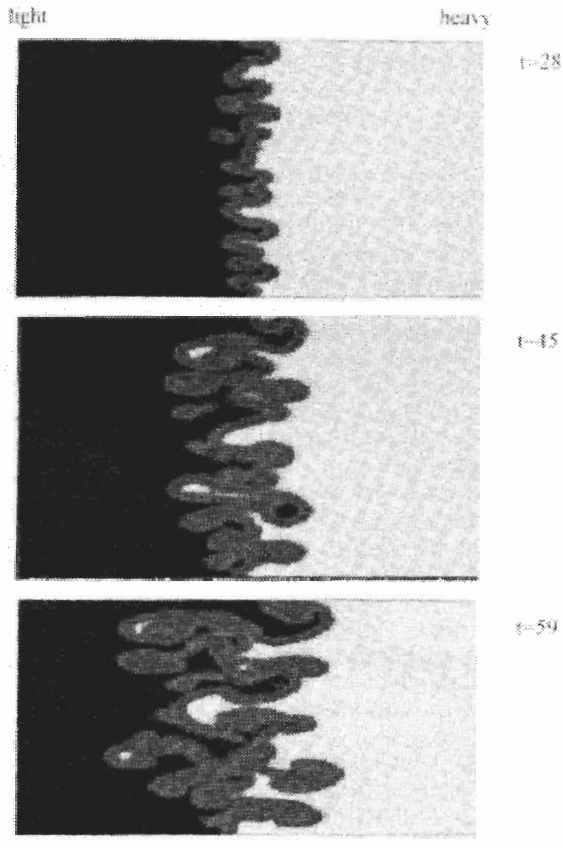

Figure 3. Density field for $n = 2.9$.

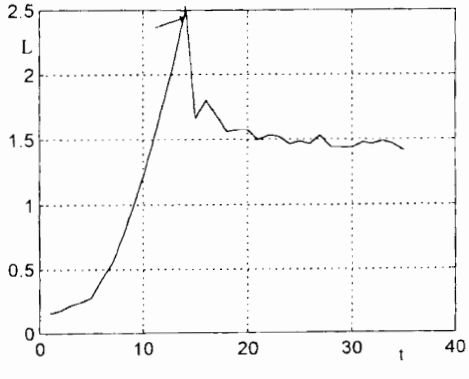

Figure 4. Dependence of mixing area width L on t (for $t > 14$ $g_1 = -45\ g_0$, $g_0 = 200\ g_E$) for $n = 3$.

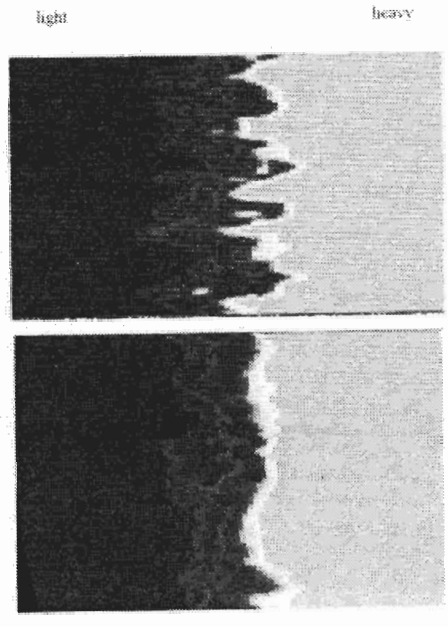

Figure 5. Density field for $n = 2.9$ at $t > 40$ $g_1 = -3$ g_0.

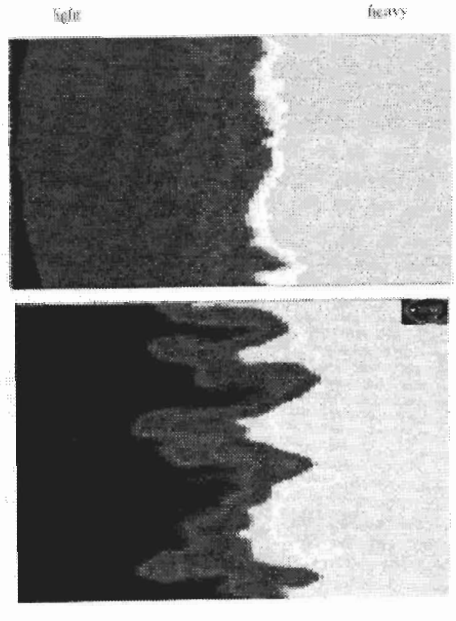

Figure 6. Density field for $n = 2.9$ at $t > 112$ $g_2 = -g_0$.

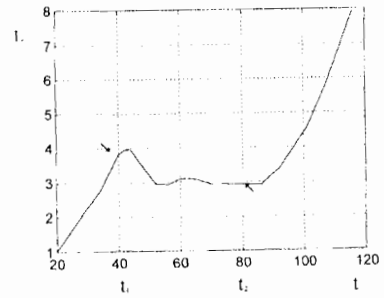

Figure 7. L versus t (at $t > 40$ $g_1 = -3\ g_0$, $t > 80$ $g_2 = g_0$) for $n = 2.9$.

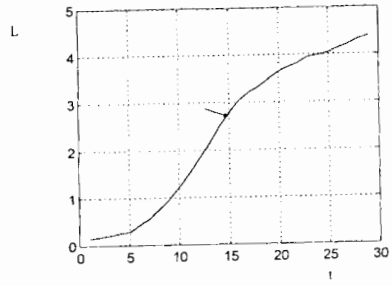

Figure 8. Dependence of mixing area width L on t (for $t > 14$ $g_1 = 0$, $g_0 = 200\ g_E$) for $n = 3$.

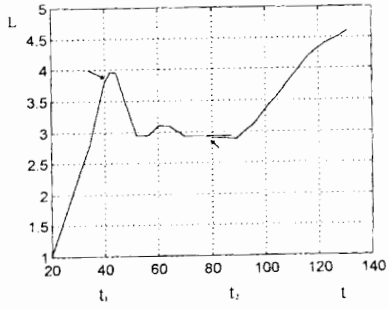

Figure 9. L versus t (for $t > 40$ $g_1 = -3\ g_0$, $t > 80$ $g_2 = 0$) for $n = 2.9$.

Initial Imprinting and Rayleigh-Taylor Instability Experiments on the GEKKO Laser

H. Azechi[1], M. Nakai[1], K. Shigemori[1], N. Miyanaga[1], H. Shiraga[1], H. Nishimura[1], H. Takabe[1], A. Nishiguchi[2], M. Honda[1], R. Ishizaki[1], K. Nishihara[1] and K. Mima[1]
[1]Institute of Laser Engineering, Osaka University, Suita, Osaka 565, Japan
[2]Osaka Institute of Technology, Omiya, Asahi-ku, Osaka 535, Japan

Abstract: A series of experiments has been conducted on the GEKKO XII laser facility to measure initial imprinting of nonuniformity in 0.53-μm laser irradiation on planar plastic foils. The imprint amplitude is reasonably represented by an imprint model based on the equation-of-motion with the pressure perturbation smoothed by the cloudy-day effect.

1. Introduction

Hydrodynamic instabilities, such as the Rayleigh-Taylor (RT) instability [1], play a critical role in inertial confinement fusion (ICF) as they finally cause fuel-pusher mixing that potentially quenches thermonuclear ignition. In direct-drive ICF implosions, where laser light directly irradiates the target, nonuniformity in laser irradiation is imprinted on the target surface as a perturbation which becomes a seed of the RT instability. The first strategy to reduce the imprint is to smooth the laser irradiation by quickly moving the nonuniform laser pattern. The relation between the time-dependent irradiation nonuniformity and the resultant imprinted amplitude is therefore the key issue to be studied. In this report we propose an imprint model based on the equation-of-motion. This model will be tested on our imprint experiments using well controlled nonuniformity: static single-mode, dynamic single-mode, and natural multi-mode.

2. Imprint model

The imprinting is modelled as a small perturbation from unperturbed hydrodynamics predicted by a one-dimensional hydrodynamic simulation. From the equation of motion, the time derivative of the momentum perturbation per unit surface $\delta(mv)$ imposed on the target should be equal to the pressure perturbation at the ablation front. The pressure perturbation normalized by the unperturbed pressure $\delta P/P_0$ may be reduced from the irradiation nonuniformity $\delta I/I_0$ by the cloudy-day effect. Then we may obtain

$$\frac{d\delta(mv)}{dt} = \delta P = \frac{2}{3}\frac{\delta I}{I_0} P_0 \frac{\int_{-\infty}^{z_{a0}} S_{abs}(z) e^{-k|z-z_{a0}|} dz}{\int_{-\infty}^{z_{a0}} S_{abs}(z) dz} \tag{1}$$

where the factor of 2/3 is from the relation of $P \propto I^{2/3}$, $S_{abs}(z)$ is the absorbed laser power per unit length, the exponential factor stands for the thermal smoothing from a point of the laser absorption at z to the ablation surface at z_{a0} (the subscript 0 denotes the unperturbed quantities), and $z = -\infty$ corresponds to a position far from the target towards the laser. Some notations are indicated in Fig. 1. The imposed momentum perturbation may be decomposed of the one carried by the fluid moving along the axial direction (z-axis in Fig. 1) and the other which is lost due to the lateral fluid motion from the strongly to the weakly pushed region: $\delta(mv) = \delta(mv)_{axial} + \delta(mv)_{lateral}$. If we assume that the density is spatially uniform

More information - Email: azechi@ile.osaka-u.ac.jp

behind the shock, $\delta\rho_s = 0$, and the velocity perturbation decreases exponentially with z as $v_z(z) = v_{a0} + \delta v_a \cdot e^{-k(z-z_a)}$ (δv_a is the velocity perturbation at the ablation front), we obtain the first order term of $\delta\,(mv)_{axial}$ as

$$\begin{aligned}\delta\,(mv)_{axial} &= \int_{z_a}^{z_s} \rho_s v_z dz - \int_{z_{a0}}^{z_{s0}} \rho_{s0} v_{a0} dz \\ &\approx \rho_{s0} v_{a0}(\delta z_s - \delta z_a) + \rho_{s0}\delta v_a \frac{1 - e^{-k(z_{s0}-z_{a0})}}{k} \end{aligned} \quad (2)$$

where z_s is the position of the shock front, and ρ_s and v_a are the density and fluid velocity behind the shock respectively. The time derivative of the lateral loss of the momentum perturbation is given by

$$\frac{d\delta\,(mv)_{lateral}}{dt} = \int_{z_a}^{z_s} (\partial\rho_s v_y v_z/\partial y) dz \approx -\rho_{s0} v_{a0} \int_{z_{a0}}^{z_{s0}} (\partial v_z/\partial z) dz \quad (3)$$

where in the second equality we have assumed the incompressibility, ignored the second and higher order terms, and replaced the mass loss $\rho_{s0}\partial v_y/\partial y$ along the y direction with $-\rho_{s0}\partial v_z/\partial z$ using the incompressibility, div $\mathbf{v} = 0$. Substituting Eqs. (2) and (3) into Eq. (1) and noting that the perturbed shock velocity $d(\delta z_s)/dt \equiv \delta v_s$ divided by the unperturbed shock velocity v_{s0} may be approximated by $\delta v_s/v_{s0} \approx (\delta v_a/v_{a0})\exp[-k(z_{s0} - z_{a0})]$, we get a differential equation for $\delta v_a(t)$:

$$[(1 - e^{-k\Delta vt})/k] \cdot d[\delta v_a(t)]/dt + 2\Delta v e^{-k\Delta vt} \cdot \delta v_a(t) = \delta P(t)/\rho_{s0} \quad (4)$$

where $\Delta v \equiv v_{s0} - v_{a0}$. The quantities ρ_{s0}, v_{a0}, and v_{s0} can be calculated with a one-dimensional (1D) hydrodynamic simulation code, such as ILESTA-1D [2] and $\delta P(t)$ is calculated from the right-hand-side of Eq. (1) using the simulated values. Solving numerically this differential equation with the initial condition at the time of the onset of the foot pulse, $\delta v_a(t = -1.8$ ns$) = 0$, gives the velocity perturbation at the ablation front $\delta v_a(t)$. The imprint amplitude may be simply obtained from $\delta z_a(t) = \int \delta v_a(t')dt'$. Similarly, the shock front perturbation amplitude δz_s is calculated from the velocity perturbation of the ablation front as $\delta z_s(t) = \int \delta v_s(t')dt' = \int [\delta v_a(t')/v_{a0}]\ v_{s0}\exp(-k\Delta vt')\ dt'$. The areal-mass perturbation may be obtained (see Fig. 1) as $\delta(\rho\ell) = |\rho_s(\delta z_a - \delta z_s) + \rho_0\delta z_s|$, where ρ_0 is the initial target density.

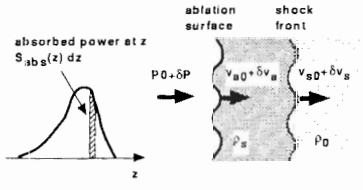

Figure 1. Schematic representation of imprint process.

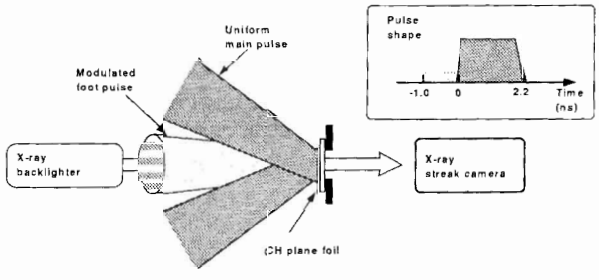

Figure 2. Experimental set up.

This model predicts imprint amplitude for the following three cases:

$$\delta I(t) = \begin{cases} \delta I_m & \text{static single-mode} \\ \delta I_m \cdot e^{i(\omega t + ky)} & \text{dynamic single-mode} \\ \delta I_m \cdot e^{i\cdot\varphi(t)} & \text{partially coherent light} \end{cases} \quad (5)$$

where δI_m is the instantaneous amplitude of the irradiation nonuniformity. The phase $\phi(t)$ randomly changes from 0 to 2π in each coherence time t_c of the partially coherent light (PCL) [3] used for the optical smoothing.

3. Experimental set up

The experiments were conducted on the GEKKO XII laser facility [4]. The experimental set up is shown in Fig. 2 and is described in more detail elsewhere [5]. The targets were first irradiated by the foot laser pulse with imposed spatial nonuniformity, then the imprinted perturbation is amplified by the RT instability driven by the uniform laser irradiation. Separate measurements of the RT growth at the same experimental condition but with an initially perturbed target irradiated with an unmodulated laser determine the equivalent imprint amplitude which would give the same amplitude after the RT growth as that for the imprint case [6].

The target material was polystyrene (PS, C_8H_8, ρ_0 = 1.06 g/cc) or 2,2,2-poly-trifluoroethyl-methacrylate (PTFMA, $C_6H_7F_3O_2$, ρ_0 = 1.18 g/cc). The PTFMA has about two times more sensitive to the areal-mass perturbation than the PS, when the areal-mass perturbations are measured with the x-ray backlighting described below. The drive laser beam in most experiments was frequency-doubled (λ_L=527 nm) PCL with a coherence time of t_c = 3.6 ps (bandwidth of 0.26 nm). For further smoothing, random phase plates (RPP's) [7] with 2 mm square segments were also implemented in front of the $f/3.15$ focusing lenses. The time-integrated focal pattern had a nearly flat shape with a 600 μm diameter in full width at half maximum (FWHM) and a 2% root-mean-square (rms) fluctuation from the smooth envelope. The PCL pulse had a nearly flat-top temporal shape with a 1.8 or 2.2-ns long. In the dynamic imprint experiments, we used nearly Gaussian shaped coherent laser with a 0.8-ns FWHM.

The growth of the areal-mass perturbation was observed with the face-on x-ray backlighting using a Cu target as an x-ray source. The range of the backlighter emission spectra was 1.15-1.3 keV, when combined with the CuI photocathode response and a 10-μm Mg foil as an x-ray filter. In most experiments, we used a 10×50-μm^2 slit as an x-ray imager for the face-on backlighting with the height direction being parallel to the perturbation ridge. The x rays transmitted through the target were imaged on an x-ray streak camera with a temporal resolution of about 90 ps.

Throughout the present study, we define the time zero (t = 0) at the time of the first half maximum of the main drive. We also define the perturbation amplitude as a half of the peak-to-valley amplitude. More specific information on the experimental setup will be given in the description of each experiment.

4. Static imprint

The beam nonuniformity was imposed by implementing a grid mask in front of the focusing lens. The beam divergence of the PCL naturally softens the spatial perturbation, generating near sinusoidal shape with $\delta I_m/I_0 \approx 40\%$. The insertion of the RPP further increases the beam divergence, reducing the modulation amplitude to be $\delta I_m/I_0 \approx 10\%$. Figure 3 shows the beam pattern on the target plane and the corresponding streaked x-ray backlighting image ($\delta I_m/I_0 \approx 40\%$). The Fourier analysis of the beam pattern (not shown here) shows that the amplitude of the harmonic components is less than 10% of that of the fundamental mode. The drive laser pulse irradiated the 16-μm-thick PS target at an intensity of 3.5×10^{12} W/cm^2 at the foot and 7×10^{13} W/cm^2 at the main pulse. Figure 3 also show the areal mass perturbation

divided by the irradiation nonuniformity. The data for the 40% and 10% modulation are in good agreement with each other, indicating that the imprint process is in linear regime with respect to $\delta I_m/I_0$. The result of the model calculation described above agrees reasonably well with the experimental data, as shown in Fig. 3. The experimental data were also compared with the results of the two-dimensional (2D) simulation IZANAMI [8]. The simulation result is in reasonably good agreement with the experimental results at around the first shock breakout at $t = -0.5$ ns.

To illustrate how equivalent initial surface perturbations are deduced, we superimpose the curve of the areal-mass perturbation $\delta(\rho\ell) = \delta(\rho\ell)_0 G(t)$, where $\delta(\rho\ell)_0$ is the equivalent initial areal-mass perturbation to be determined and $G(t)$ is the measured growth factor [9] (defined as the measured areal-mass perturbation divided by the initial one). The deduced equivalent perturbation is 1.6 μm g/cc (after some corrections [5]).

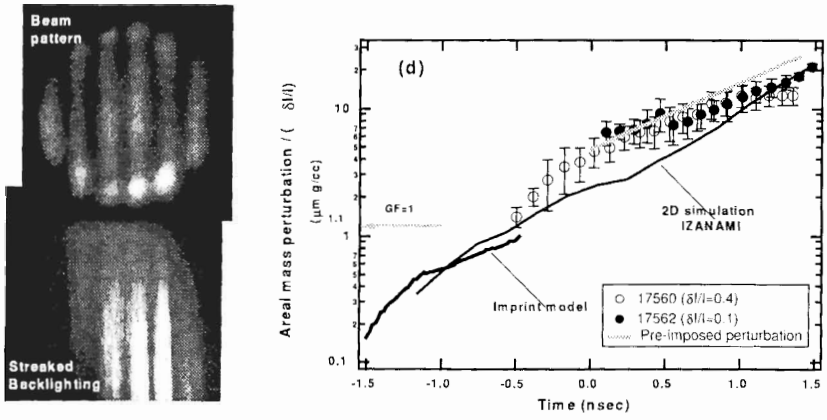

Figure 3. Static single-mode experiment.

5. Dynamic imprint

The imprint model is also tested for the experiment where the nonuniformity is temporally changed. The nonuniformity was constructed by Young's interference but with two different laser wavelengths, as shown in Fig. 4 (a). The laser beams each transmitted through a rectangular aperture construct interference fringes at the target plane. Due to the dual wavelength the interference fringes move in a direction perpendicular to the fringe ridge. The time t_{smooth} required to move one interference fringe (one perturbation wavelength) is given by $t_{smooth} = (\lambda_L/c)(\lambda_L/\Delta\lambda_L)$, where $\Delta\lambda_L$ is the difference of the two laser wavelengths, c is the speed of light. Figure 4(b) clearly show the moving interference fringe on the target plane recorded by a streak camera. The interference fringe is nearly averaged out in the time integrated image, as shown in Fig. 4 (c). However there still is a low-contrast structure in the time integrated image. This may be attributed to the defect of the optics used in the observation or to the static interference due to the imperfect separation of the different collar component. If the latter is the source of the structure, the residual static nonuniformity is estimated to be about 10%.

The target was a flat PTFMA foil with a 9-μm thickness. The laser pulse consisted of a

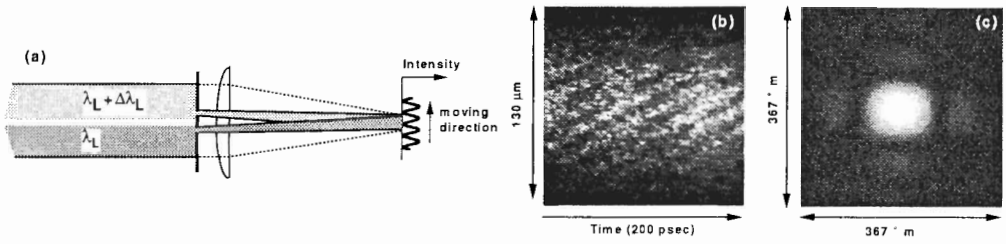

Figure 4. (a) Setup of Yorng's interferometer with two different laser wavelengths, constructing moving interference fringe. (b) A streak record of the focal pattern on the target plane. Tilted lines are the moving fringe. (c) A time-integrated focal pattern.

foot pulse with imposed nonuniformity at an intensity of 1×10^{13} W/cm^2 followed by a main pulse at an intensity of 7×10^{13} W/cm^2. The pulse width of each foot and main pulse was about 0.8 ns, and the time difference was 0.6 ns. We show, in Fig. 5 (a) and (b), the face-on backlighting images for the dynamic nonuniformity and the static nonuniformity, respectively. The conditions of the imposed nonuniformity are a perturbation wavelength of 16 μm, an instantaneous nonuniformity of $\delta I_m/I_0$ =100% and the smoothing time of t_{smooth} = 47 ps for $\Delta\lambda_L$ = 0.0198 nm at λ_L = 527 nm. Those for the static nonuniformity are a perturbation wavelength of 20 μm, and an imposed nonuniformity of $\delta I_m/I_0 \approx 20\%$. Figure 5 (c) shows the equivalent initial perturbation divided by the instantaneous nonuniformity as a function of the frequency of the moving nonuniformity. It is seen that the imprint amplitude is significantly reduced in the dynamic nonuniformity compared with the static nonuniformity.

We made a calculation using the imprint model described in the preceding section. The resultant equivalent initial surface amplitudes are plotted in Fig. 5 (c). It is seen that the imprint model reasonably well predicts the dynamic imprint as well. The underprediction of the imprint for the dynamic imprint case may be explained by the residual static interference that increases the imprint amplitude.

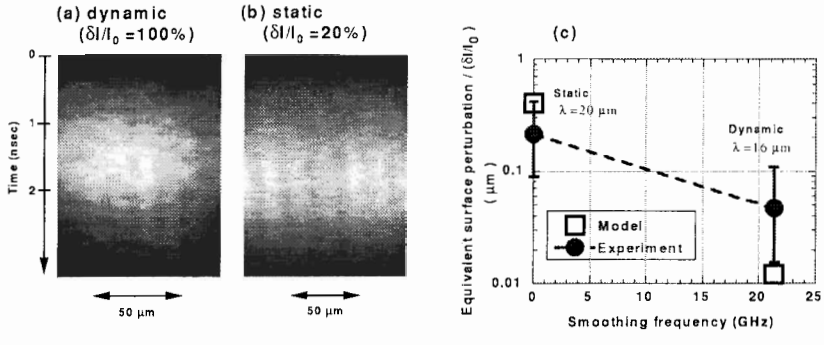

Figure 5. A face-on backlighting image of the dynamic imprint. (b) That of the static imprint. (c) Deduced areal-mass perturbation divided by the instantaneous nonuniformity vs smoothing frequency.

6. Natural multi-mode

The imprint model has been tested for the imprinting due solely to the PCL beam without imposed nonuniformity. The targets were PTFMA foils with 9-μm thickness. The equivalent initial surface perturbations were deduced from the measured areal-mass perturbation at late time. The Fourier component of the instantaneous nonuniformity $\delta I_m(k)/I_0$ is calculated from the corresponding Fourier component of the measured time integrated nonuniformity $< \delta I_m(k) > /I_0$ using the confirmed scaling $< \delta I_m(k) > /I_m(k)$ = (coherent time / pulse width)$^{1/2}$. The calculated imprint amplitudes are in agreement with the experimentally determined value. The detail of these experiments are described elsewhere [10].

7. Summary

In summary, we have proposed a reasonably simple imprint model, in that the pressure perturbation smoothed by the cloudy-day effect causes time derivative of the momentum perturbation per unit area. This imprint model has been tested on our imprint experiments using a variety of nonuniformity: static single-mode, dynamic single-mode, and natural multi-mode. The imprint amplitudes observed in these three cases are reasonably well explained by the imprint model.

Acknowledgement. We would like to acknowledge the dedicated technical supports by the staffs at the GEKKO XII facility for the laser operation organized by Dr. H. Fujita and Mr. S. Urushihara, the target fabrication by Dr. T. Norimatsu and Dr. M. Takagi, and the plasma diagnostics by Mr. O. Maekawa, Ms. K. Shimada, and Mr. M. Saito.

References

[1] Chandrasekhar S, Hydrodynamic and Hydromagnetic Stability, Oxford Univ. Press, London, Chap. 10, (1968).
[2] Takabe H *et al.*, Phys. Fluids, 10, 2884, (1988).
[3] Nakano H *et al.*, J. Appl. Phys.,73, 2122, (1993); Miyanaga N *et al.*, Proc. 15th Int. Conf. Plasma Phys. Controlled Nucl. Fusion Research, Seville, 1994, 3, 153, (IAEA, Vienna, 1996).
[4] Yamanaka C *et al.*, IEEE J. Quantum Electron., QE-17, 1639, (1981); Recent progress of the GEKKO XII system is described in Nakatsuka M *et al.*, Proc. 12th International Conference on Laser Interaction and Related Plasma Phenomena, Osaka, eds. S. Nakai and G. H. Miley (AIP, New York, 1996), 2, 963, (1995).
[5] Azechi H *et al.*, Phys. Plasmas, to be published.
[6] Glendinning SG *et al.*, Phys. Rev. E, 54, 4473, (1996).
[7] Kato Y *et al.*, Phys. Rev. Lett., 21, 1321.
[8] Nishiguchi A and Yabe T, Comput. Phys., 52, 390, (1983).
[9] Shigemori K *et al.*, Phys. Rev. Lett., 78, 250, (1997).
[10] Kawasaki *et al.*, Annual Progress Report, Institute of Laser Engineering, Osaka University, 139, (1996).

Analytical and Numerical Studies of Rayleigh-Taylor Instability of a Thin Liquid Layer

S.M. Bakhrakh and G.P. Simonov
Russian Federal Nuclear Centre - Institute of Experimental Physics
Prospect Mira 37, 607190, Sarov, Nizhny Novgorod Region, Russia

Abstract: On the basis of Lagrangian representation for equation of thin liquid layer dynamics analytic solutions of Rayleigh- Tailor instability problem at the stage non-linear in the observer's space are found. Evolution of various perturbation types both in the layer shape and in layer velocity components is considered. It is shown that there are both exponentially growing and limited oscillating solutions. The results of the theoretic considerations are substantiated with numerical calculations which employ the complete system of the law of conservation.

1. Introduction

The program in studying the non-linear phase of Rayleigh-Taylor instability in thin - wall systems results from the use of Lagrangian approach. The thin layer equations, when written in Lagrangian co-ordinates are found to be linear in partial cases. This provides an effective capability for their analysis in order to describe the non-linear (as viewed from the observer space) evolution phase of perturbations [1].

The analysis from [1] does not exhaust the entire variety of situations that may occur in the problem of perturbation evolution of a thin accelerated layer. The complete research is possible only by considering all roots of the dispersion equation including those yielding stable solutions. It is essential to estimate the feasibility for the use of resulting dependencies in more general situations.

2. Analytical studies

The planar motion of the thin liquid plate is described by the equations [1].

$$\frac{\partial^2 x}{\partial t^2} = -a\frac{\partial y}{\partial \xi}, \quad \frac{\partial^2 y}{\partial t^2} = a\frac{\partial x}{\partial \xi} - g \tag{1}$$

Here x,y - are cartesian coordinates of the observer space, t is the time, ξ - is Lagrangian coordinate of the particle represented by its initial coordinate x_0, $a = p/\rho_0$, $a > 0$, where ρ_0 – is the density, h_0 - is the initial layer thickness, p - is the external pressure applied from below, g - is the mass acceleration with the direction opposite to y.

Assume further that $a = g$. Initially the thin layer is positioned at y=0 where initial perturbations are superposed.

Further motion of the layer particles is described by equations (1) that result from the mass and momentum conservation laws for the layer components. They can be easily supplemented by the mass conservation law for the layer particles $hds = h_0 d\xi$=const, relating the current length ds.

More information - Email: smb@otd08.vniief.ru

Consider the case where a =const. The system (1) is a linear fourth order system with fixed coefficients. It is convenient to introduce the new variable x_1=x-ξ.Then the basic system in x_1, y variables will take the form:

$$\frac{\partial^2 x_1}{\partial t^2} = -a\frac{\partial y}{\partial \xi}, \quad \frac{\partial^2 y}{\partial t^2} = a\frac{\partial x_1}{\partial \xi} \ . \tag{2}$$

The system (2) reflects the adopted physical model where the external pressure produces the acceleration normal to the current deforming layer surface: the pressure is independent on the motion of the layer particles.

Consider the nonzero solution of system (2) of the form:

$$x_1 = C_1 e^{\omega t} cosk\xi, y = C_2 e^{\omega t} sink\xi \tag{3}$$

where c_1, c_2 = const. The solution (3) exists if the discriminant equal zero:

$$\omega^4 - (ak)^2 = 0 \tag{4}$$

Here $k = 2\pi/\lambda$ is the wave number, λ is the wavelength.

The dispersion equation (4) has four roots: two real $\omega_{1,2} = \pm\sqrt{ka}$ and two imaginary $\omega_{3,4} = \pm\sqrt{-ka}$ that are matched by four fundamental solution of system (2).

Consider the partial solution of system (2):

$$x_1 = (-A_0 ch(t\sqrt{ka}) + A_1 cos(t\sqrt{ka}))cosk\xi; \; y = (A_0 ch(t\sqrt{ka}) + A_1 cos(t\sqrt{ka}))sink\xi \tag{5}$$

that is the superposition of exponentially growing and oscillatory solutions.

Introduce the dimensionless parameter:

$$r_1 = (-A_0 + A_1)/(A_0 + A_1) \tag{6}$$

Then the solution (5) will take the form:

$$\begin{aligned} x_1 &= \left(\frac{r_1 - 1}{2} ch\left(t\sqrt{ka}\right) + \frac{1 + r_1}{2}\cos\left(t\sqrt{ka}\right)\right) A\cos k\xi; \\ y &= \left(\frac{1 - r_1}{2} ch\left(t\sqrt{ka}\right) + \frac{1 + r_1}{2}\cos\left(t\sqrt{ka}\right)\right) A\sin k\xi, where \quad A = A_0 + A_1. \end{aligned} \tag{7}$$

This corresponds to setting the layer shape on the form of a plane curve:

$$x = \xi + r_1 A\cos k\xi, \quad y = A\sin k\xi \tag{8}$$

the perturbations of the median layer surface shape of the form (8) lead to corresponding perturbations of the mass density distribution on the observer space and the thickness of Lagrangian particles composing the layer. Depending on the r_1 parameter the resulting thickness changes will contribute to the growth of initial perturbations of the median layer line or counteract them.

Consider the evolution of initial perturbations depending on the dimensionless parameter r_1, critical for this problem.

The following cases are possible:

1. Let r_1=-1, then the system (6) will define initially specified cycloid with the cusps directed downward, i.e. more sharp cusps are downward and less sharp cusps are upward. For the lower vertices $ds_0 < d\xi$ after the perturbations are specified and the layer thickness increases, while this decreases near upper verities. The initial mass flow in this case contributes to the further growth of the layer shape perturbation. The amplitude of cycloid perturbations is $y \sim A\ ch\left(t\sqrt{ka}\right)$ for great t. This case was discussed in [1]. However it does not exhaust the spectrum of the layer behaviour types.

2. r_1=0, then the initial perturbation represents a sinusoid; $x=\xi$, $y=A\sin k\xi$. In accordance with formulas (7), $y \sim A/2\ \mathrm{ch}\left(t\sqrt{ka}\right)$ for large t. Thus the sinusoidal perturbations grow 2 times slower than cycloid perturbations. The increment is the same and the exponent factor is 2 times lower. This is qualitatively explained by the actual lack of initial changes in the layer thickness for the sinusoidal shape perturbations.

3. r_1=1. And $x = \xi + A\cos k\xi$, $y = A\sin k\xi$. This curve represents a cycloid with the "cusps" directed upward. Unlike the case r_1=1, here the mass income is observed near the upper vertices while the lower vertices demonstrate the mass outcome. Thus the perturbations of the median layer line shape and related thickness perturbations are in the "counter-phase". It follows from (7) that for this initial perturbation the layer particles periodically oscillate around y=0 with the frequency $\omega = \sqrt{ka}$. Note that the sinusoid is a half sum of corresponding cycloids with the cusps upward and downward. Therefore the sinusoidal perturbations grow 2 times slower than the perturbations of the cycloid shape with the cusp downward.

4. $r_1 < -1$. For the sake of brevity, the generalisation of sinusoid (8) will be referred to as hypercycloid. If $r_1 < -1$, then one obtains a "sharpened" cycloid with the cusp downward. Then the hypercycloid shape perturbation grows faster than that of cycloid.

5. $r_1 > 1$. The initial layer shape is a hypercycloid with the cusps upward. In this case the initial perturbations turn over and exponentially grow backward.

Consider another possible extension of the system (2) of the form:

$$x_1 = (-B_0 sh(t\sqrt{ka}) + B_1 sin(t\sqrt{ka}))\cos k\xi;\ y = (B_0 sh(t\sqrt{ka}) + B_1 sin(t\sqrt{ka}))\sin k\xi \qquad (9)$$

that corresponds to the specified initial velocities:

$$Vx(0) = \sqrt{ka}(-B_0 + B_1)\cos k\xi;\ Vy(0) = \sqrt{ka}(B_0 + B_1)\sin k\xi \qquad (10)$$

and zero initial shifts. Denote:

$$r_2 = -(B_0 + B_1)\ /\ (B_0 + B_1) \qquad (11)$$

where r_2 is the basic dimensionless coefficient determining the evolution pattern in this case. Relation (9) takes the form:

$$\begin{aligned} x_1 &= \left(\frac{r_2 - 1}{2} sh\left(t\sqrt{ka}\right) + \frac{1 + r_2}{2}\sin\left(t\sqrt{ka}\right)\right)\frac{B}{\sqrt{ka}}\cos k\xi \qquad (12) \\ y &= \left(\frac{1 - r_2}{2} sh\left(t\sqrt{ka}\right) + \frac{1 + r_2}{2}\sin\left(t\sqrt{ka}\right)\right)\frac{B}{\sqrt{ka}}\sin k\xi,\ where\ B = B_0 + B_1 \end{aligned}$$

Similarly, we have: for r_2=-1, the system (12) determines the solution growing with large t as: $y \sim \mathrm{Bsh}\left(t\sqrt{ka}\right)/\sqrt{ka}$.

For r_2=0, the sinusoidal perturbations are initially specified only for the vertical velocity. For large t, the perturbation amplitude is $y \sim \mathrm{Bsh}\left(t\sqrt{ka}\right)/2\sqrt{ka}$.

For r_2=1, the specified initial perturbations determine the limited oscillation. This is explained by that the initial velocity Vx is specified "out of phase" relative to Vy and results in the mass outcome from lower vertices and mass income to upper vertices which prohibits the perturbation amplitude growth.

For $r_2 > 1$, the initial perturbation "turns over" and further grows exponentially backward.

If initial perturbations are specified for the shape and velocity, then we can introduce an additional dimensionless parameter r_3, describing the relative weight of velocity perturbations relative to the shape perturbations:

$$r_3 = \frac{B}{\sqrt{ka}}/A \tag{13}$$

The pattern of initial perturbations and further evolution are determined by three parameters, r_1, r_2, r_3. For example, the stability condition for the solution is now determined by the relation 1-r_1+(1-r_2)r_3=0.

The parameter r_3 also greatly contributes to the perturbation evolution. For example, if r_1=1 and r_2=1, the solution is stable. Instead, if r_1=1 and r_2=-1, the solution is stable provided r_3

Consider the case of pulsed acceleration (Richtmyer-Meshkov instability of a thin layer). Suppose that for t=0 the initially equal-thickness layer perturbed as a hypercycloid is influenced from "below" by a shock pressure pulse constant in space. The layer elements immediately take the finite velocities with the values determined by the normal angle relation to the element.

Denote $V = J/h_0$, $V > 0$, where J is the applied shock pulse. We can show that the general solution in the case of pulsed acceleration is:

$$x = \xi + (r_1 - kVt)A\cos k\xi;\ y = (1 - Vr_1kt)A\sin k\xi + Vt \tag{14}$$

Then for the perturbation "cusp" with $\sin k\xi$ =-1, one obtains:

$$\frac{dy}{dt} = Vr_1kA + V \tag{15}$$

Here if r_1=1 (cycloid with downward cusps), the perturbation grows linearly in time as given by (15). If r_1=0 (sinusoid), y perturbation does not grow. Thus various evolution patterns are possible depending on initial data that do not greatly differ. Note that we have considered the simplest case where a=const. For example, if the acceleration depends on time and $a = a(t)$, this may introduce new important patterns into the layer behaviour. Thus if the acceleration sign is changed during the motion, the "stable" cycloid converts to the "unstable" state and vice versa. Possibly this explains the fact that during the acceleration-deceleration process of the plate in experiment [2] the perturbations occurring under acceleration, grow during the deceleration at early times very slowly or do not grow at all.

3. Numerical studies

Numerical results are given below for comparison with analytical studies. The computations used the ROB codes [3] intended for non-linear interaction between thin strong shells with solid media and KGD codes [4] for 2-D gas dynamics in Lagrangian variables.

The first series of computations were run in thin layer approximation with ROB codes.

For computations, we specified the density ρ=7.8, layer thickness h=0.1, mass acceleration $a = g$=0.01. The external pressure was determined from the equilibrium condition for the unperturbed plate $p=\rho hg$. We took k=1, the amplitude of the perturbation normal to the plate was A=- 0.01. The perturbation value Ax was varied in the computations; it was determined by setting the basic dimensionless parameter r_1. 36 cells were taken for the wavelength. The initial perturbation of the layer shape was specified as hypercycloid as given by (8). After the geometry perturbation had been specified, the thickness a was recompiled in each cell from the conservation of the layer elements masses.

The computations were run with r_1= -1; 0; 1. The time variations of the amplitude are given in Fig. 1. The numerical results almost cannot be distinguished from analytical data. In this series, the thickness of the perturbed layer elements at initial time was determined from the mass conservation of Lagrangian particles. The same assumption was used to study the problem in [1]. However in general case layer elements can be specified independently.

The next computations of the layer dynamics when the consideration of the equal-mass shell behaviour is replaced by a similar while slightly different physically meaningful problem. At initial time, the perturbed layer is specified $h = h_0$=const (with t=0). Further, with $t > 0$, the thickness $h = h(\xi)$ is recalculated in each cell from the particle mass conservation law. These assumptions were used to compute the cycloids with upward and downward cusps and the sinusoid (r_1= - 1,1,0). In these conditions, the perturbation growth pattern is nearly the same irrespective of the shapes. The growth rate of any perturbation (considered) equals the growth rate of the sinusoidal perturbation with the same wave number k. As was mentioned above, it is 2 times less than that of cycloid perturbation of the equal-mass shell.

The next series of computations used 2-D gasdynamic Lagrangian code. Initially, the velocity perturbations were specified as given by (10,11). It is easier to specify the velocity perturbations as compared to coordinate perturbations since it is not necessary to monitor the mass conservation in Lagrangian cells after the perturbations are specified: this requirement is met automatically.

It was assumed that B=0.01, a=1, ρ=7.8, h=0.1, k=1. The external pressure $p = ha$ was specified at the domain boundary. The pressure p=0 was applied to the other boundary. The gasdynamic equation of state was chosen in Mie-Gruneisen form with the parameters ρ=7.8, c_0=4.6, n=3, Γ=2.54.

Five computations were run where the coefficient r_2 was varied: r_2=-1, 0, 1, -2, 2.

The time dependence of the vertical velocity Vy is given in Fig. 2. At the completion time t=5, the amplitude of the initial velocity in the computations increased by about 70 times with r_2= -1. However in the case r_2=1 it remained nearly unchanged without decreasing or increasing. Thus we may observe that the computational "noise" in 2-D gas dynamics do not "oscillate" the stable solutions without decreasing the amplitude. For r_2=0, the growth rate is 2 times lower and for r_2=-2 this is 1.5 time higher as compared to r_2=-1 as must be in accordance with the analytical solution. Thus the analytical solutions for a thin layer agree well with the numerical solutions both in shell approximation and with numerical solutions of the full system of equations for compressible fluid hydrodynamics.

This analysis is important for the considerations of Rayleigh - Taylor instability relative to the thin layer and half-space of compressible fluid. Fig. 3 shows the time dependencies of the am-

plitude growth for the perturbations of the half-space interface. The initial perturbations were applied to the initial velocities; these perturbations were determined by r_2 and exponentially decreased with the distance from the interface. The time dependence pattern for the amplitude "spikes" is qualitatively the same as for the thin layer case when the initial velocity profile was varied.

Acknowledgement. The research described in this publication was made possible in part by Grand NM4000 from International Science Foundation and Grand NM 96-01-00043a from the Russian Fund of Fundamental Investigations.

References

[1] Ott E, Non-linear evolution of Rayleigh-Taylor instability of a thin layer, Phys.Rev.Lett., 29, 1429, (1972).

[2] Ivanov AG, Novitsky EZ, Ogorodnikov VA, Pinchuk S, Plate acceleration to hypersonic speeds. Instability under airdriven deceleration, PMTF, N2, 90-94, (1982).

[3] Bakhrakh SM, Pevnitsky AV, Simonov GP, Soloviev VP, Dynamics of thin-wall chambers surrounded by fluid under pulsed acceleration, VANT. Ser.: Met. I Progr. chisl. resh. zad. mat. fiz., N1(15); 37-40, (1984).

[4] Bakhrakh SM, Spiridonov VF, Ladagin VK, Generation of a conservative scheme for 2-D time-dependent gas dynamics, Proc. of the 4th All-Union Workshop on numerical methods in viscous fluid mechanics, Novosibirsk, 51-63, (1978).

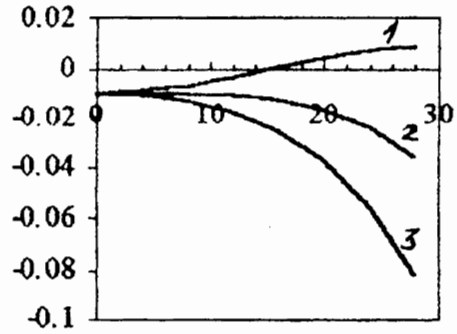

Figure 1. $1 - r_1 = 1, 2 - r_1 = 0, 3 - r_1 = -1$

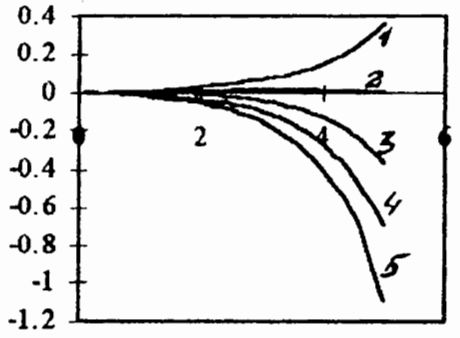

Figure 2. $1 - r_2 = 2, 2 - r_2 = 1, 3 - r_2 = 0, 4 - r_2 = -1, 5 - r_2 = -2$

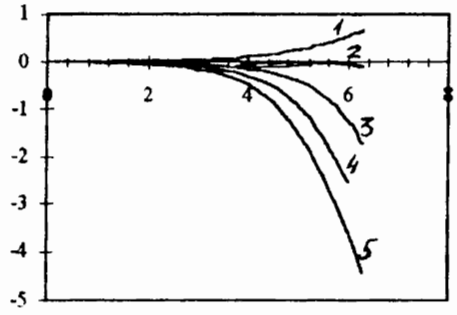

Figure 3. $1 - r_2 = 2, 2 - r_2 = 1, 3 - r_2 = 0, 4 - r_2 = -1, 5 - r_2 = -2$

Rayleigh-Taylor Instability of a Thin Liquid Layer Provided 3D

S.M. Bakhrakh and G.P. Simonov
Russian Federal Nuclear Centre - Institute of Experimental Physics
Prospect Mira 37, 607190, Sarov, Nizhny Novgorod Region, Russia

Using the Lagrangian representation for equations of motion of accelerated thin-wall systems and incompressible fluid enabled to obtain a number of new analytical solutions for the nonlinear stage of the Rayleigh-Taylor instability (RTI) [1, 2, 3, 4, 5]. For a thin liquid layer the equations of motions are maximally simplified which allows to conduct their approximate analytical study in three dimensions, find the solution dependence on the dimensionless parameters responsible for the initial data. At the same time, they contain the basic PTI features which also manifest themselves to a certain extent in more complex cases of a finite-thickness layer and perfect compressible fluid semispace.

The equations of motion of an accelerated thin liquid layer provided 3D perturbations can be represented as [3]:

$$\begin{aligned} \frac{\partial^2 x}{\partial t^2} &= -a\left(\frac{\partial y}{\partial \eta}\frac{\partial z}{\partial \xi} - \frac{\partial z}{\partial \eta}\frac{\partial y}{\partial \xi}\right), \frac{\partial^2 y}{\partial t^2} = a\left(\frac{\partial x}{\partial \eta}\frac{\partial z}{\partial \xi} - \frac{\partial z}{\partial \eta}\frac{\partial x}{\partial \xi}\right) \\ \frac{\partial^2 z}{\partial t^2} &= -a\left(\frac{\partial x}{\partial \eta}\frac{\partial y}{\partial \xi} - \frac{\partial x}{\partial \xi}\frac{\partial y}{\partial \eta}\right) - g, \quad a = p/\rho h_0. \end{aligned} \tag{1}$$

Here x,y,z are Cartesian coordinates of the observer's space, t - is time, ξ, η– are Lagrangian coordinates of layer particles for which their initial coordinates x_0, y_0 - are taken, ρ – is density, h_0– is initial layer thickness, p -is external pressure applied from "below", g -is mass acceleration whose direction is opposite to the axis OZ. At the initial time the equithick layer occupies the position z=0 the initial perturbations are superimposed on. Equation system (1) results from the laws of conservation of layer particle mass and momentum.

The liquid-layer approximation is used to determine element shifts only of the middle layer surface. This enables to reduce the spatial dimensionality of the problem. If the shifts of the middle layer surface Lagrangian elements are determined, this leads to a change in the surface density of mass σ relative to its initial value σ_0 according to [3]:

$$\sigma = \sigma_0 \left| \frac{d\vec{r}}{d\xi} \times \frac{d\vec{r}}{d\eta} \right|^{-1}$$

In its sense $\sigma = \rho h$ where ρ - current layer element density, h - thickness. When one assumes $\rho = \rho_0$, this relation allows to determine the current layer particle thickness h.

Let $a = g$=const. Assume the shifts A relative to the equilibrium position and their derivatives small ($\partial A/\partial \xi, \partial A/\partial \eta << 1$) to obtain upon linearization the following equation system in variables (ξ, η):

$$\frac{\partial^2 x_1}{\partial t^2} = -a\frac{\partial z}{\partial \xi}, \frac{\partial^2 y_1}{\partial t^2} = -a\frac{\partial z}{\partial \eta}, \frac{\partial^2 z}{\partial t^2} = a\left(\frac{\partial x_1}{\partial \xi} + \frac{\partial y_1}{\partial \eta}\right), \; x_1 = x - \xi, \; y_1 = y - \eta \tag{2}$$

More information - Email: smb@otd08.vniief.ru

Consider the solution to system (2) of the form:

$$\begin{aligned} x_1(\xi,\eta,t) &= A_1(t)\cos k\xi\cos n\eta,\ y_1(\xi,\eta,t) = A_2(t)\sin k\xi\sin n\eta, \\ z(\xi,\eta,t) &= A_3(t)\sin k\xi\cos n\eta\ , \end{aligned} \tag{3}$$

where k,n - wave numbers of the harmonic perturbations in the directions of the axes OX and OY, k=$2\pi/\lambda_1$, n=$2\pi/\lambda_2$, λ_1, λ_2 - relevant wavelengths. For the functions $A_i(t)$ we have the system of ordinary differential equations:

$$\frac{d^2A_1}{dt^2} = -akA_3,\ \frac{d^2A_2}{dt^2} = anA_3,\ \frac{d^2A_3}{dt^2} = -akA_1 + anA_2\ ,$$

hence,

$$\frac{d^4A_3(t)}{dt^4} = a^2\left(k^2+n^2\right)A_3(t)\,.$$

A similar relation has been obtained for 3D perturbations of the incompressible fluid semispace [5]. In three dimensions the dispersion equation proves, like in two dimensions [1], the fourth-order equation:

$$\omega^4 = a^2\left(k^2+n^2\right) = a^2k^2\left(1+m^2\right),\ m = n/k\,.$$

The solutions to principal linearized system (2) are highly diversified depending on setting the initial shifts, are determined by several dimensionless parameters. One can show that the initial layer shifts (and the changes in the layer particle thickness caused by them):

$$\begin{aligned} x(0) &= \xi + r_1A\cos k\xi\cos n\eta, \quad y(0) = \eta - r_1mA\sin k\xi\sin n\eta\,, \\ z(0) &= A\sin k\xi\cos n\eta \end{aligned} \tag{4}$$

and zero initial velocities are correspondent with the solution to system (2):

$$\begin{aligned} x &= \xi + 0.5\left[-P_1ch(\omega t) + P_2\cos(\omega t)\right]A\left(m^2+1\right)^{-0.5}\cos k\xi\cos n\eta, \\ y &= \eta + 0.5\left[P_1ch(\omega t) - P_2\cos(\omega t)\right]Am\left(m^2+1\right)^{-0.5}\sin k\xi\sin n\eta\,, \\ z &= 0.5\left[P_1ch(\omega t) + P_2\cos(\omega t)\right]A\sin k\xi\cos n\eta, \quad \textit{where} \end{aligned} \tag{5}$$

$$P_1 = 1 - r_1\left(m^2+1\right)^{0.5}\ , \quad P_2 = 1 + r_1\left(m^2+1\right)^{0.5}\ .$$

The general view of the perturbed layer surface by time t=4 at $n = m$=1, r_1=-1, a=1, A=0.01 is given in Fig.1. Narrow and sharp spikes moving down are interspersed with broad gentle bubbles moving upward.

Solution (5) is valid only for initial times, like for two dimensions [1].

The parameters r_1 and A determine the initial perturbation shape and amplitude. At $n = m$=0 in the section with the plane xz we have the curve x=$\xi + r_1A\cos k\xi$, $z = A\sin k\xi$, which will be referred to as hypercycloid. The hypercycloid is asymmetric about the "top" and "bottom" which considerably influences the perturbation evolution. At $r_1 < 0$ the lower vertices are sharper, while the upper are more gentle, at $r_1 > 0$ it is quite the reverse. If r_1=0, the perturbed layer shape is sinusoidal.

One can show that when there is no layer shape perturbations the initial velocities:

$$V_x(0) = r_2B\cos k\xi\cos n\eta,\ V_y(0) = -r_2mB\sin k\xi\sin n\eta,\ V_z(0) = B\sin k\xi\cos n\eta \tag{6}$$

are correspondent with the solution similar to formulas (5) where ch(ωt), cos (ωt) , r_1, A should be replaced with sh(ωt), sin(ωt), r_2, B/ω, respectively.

These solutions include both exponentially growing solutions and those limited in amplitude along the axis OZ. The limited solutions take place at zero coefficient of ch(ωt) or sh(ωt) in the third equation of relevant systems. Then $r_1\sqrt{m^2+1}$=1. At m=1 ($k = n$) r_1=$1/\sqrt{2}$. Note that for 2D perturbations when $m = n$=0 the limited solutions take place at r_1=1, while the solutions corresponding to r_1 =$1/\sqrt{2}$ are exponentially growing. In this case introduction of perturbations along the second direction stabilizes the total perturbation. The ratio q of 3D and 2D perturbation growth increments depends on the wave number ratio: q=$\sqrt[4]{1+m^2}$. At $k = n$ the growth increment of 3D perturbations is 1.2 times as high as that of 2D. If $r_1\sqrt{m^2+1} > 1$, the initial perturbation changes its phase with time.

Also, solutions are obtained corresponding to setting initial perturbations both in shape (4) and initial velocities (6) of the layer. The evolution of such perturbations is determined, alongside r_1, r_2, with the dimensionless parameter $r_3 = B/(A\omega)$.

The exponential growth of the perturbation amplitude can be promoted with two factors leading to the fact that the counterpressure retarding the perturbation growth proves ineffective. These are the fluid particle displacement tangential to the interface (fluid particle onflow into the regions of streams moving downward and outflow from the bubbles moving upward) and pressure field variation due to the interface strain. For various initial conditions these two factors can both add up and attenuate each other. The latter takes place, for example, for 2D perturbations at r_1=1 when the perturbed layer at the initial time has the shape of a cycloid with its cusps upward. The shape perturbations (close to sinusoidal) prove therewith compensated with the particle thickness perturbations acting in the counterphase. The limited oscillatory solutions are also possible at setting initial perturbations in velocities.

At the acceleration sign change during motion the "unstable" cycloid transfers to the "stable" and vice versa. This may account for the fact that in the experiments [6] the plate perturbations arising at the stage of the plate acceleration by explosion products grow very slowly, if any, at the stage of plate deceleration by air.

Dwell on the case of pulsed acceleration (the Richtmyer-Meshkov instability). For initial data (4) the solution in this case takes the form:

$$\begin{aligned} x &= \xi + (r_1 - kVt)\, A\cos k\xi\cos n\eta,\ y = \eta - (r_1 m + nVt)\, A\sin k\xi\sin n\eta, \\ z &= (1 - r_1 kVt - r_1 mnVt)\, A\sin k\xi\cos n\eta + Vt, \end{aligned} \tag{7}$$

where $V = J/\rho h_0$, J is the value of shock momentum per unit area. The perturbation amplitude growth rate along the axis OZ, $A_3(t)$, at the perturbation point at sin $k\xi$=-1, cos $n\eta$=1 equals $\frac{dA_3}{dt} = AVr_1k\,(1+m^2)$.

At $r_1 \neq 0$ the perturbation amplitude grows linearly, at r_1=0 it is constant. (7) results in the difference in the perturbation dynamics at the sign change of r_1 (position of the cusps relative to the acceleration direction either at the top or at the bottom). The effect of such an asymmetry on the semispace interface perturbation evolution was noted in experiments [7].

If the value $a = p/\rho h_0$ has, in its turn, small perturbations caused by perturbations in external pressure, initial thickness, then this introduces further essential peculiarities to the layer dynamics. Let $a = a_0 + \Delta a$, where a_0=const, Δa is a small value. Then governing linearized

system (2) takes the form:

$$\frac{\partial^2 x_1}{\partial\, t^2} = -a_0 \frac{\partial\, z}{\partial\, \xi}, \quad \frac{\partial^2 y_1}{\partial\, t^2} = -a_0 \frac{\partial\, z}{\partial\, \eta}, \quad \frac{\partial^2 z}{\partial\, t^2} = a_0 \left(\frac{\partial\, x_1}{\partial\, \xi} + \frac{\partial\, y_1}{\partial\, \eta} \right) + \Delta a \tag{8}$$

Here the small source Δa appears in the right-hand side of the second equation.

Set the acceleration perturbations $\Delta a = a_0 r_m \sin k\xi \cos n\eta$, where r_m - is a dimensionless coefficient, perturbations (4) in the layer shape and zero initial velocities of layer particles. Then one can obtain solutions to system (8) similar to (5). In particular,

$$z = 0.5\left[(AP_1 + r_m P)\, ch\, \omega t + (AP_2 - r_m P)\, \cos\, \omega t\right] \sin k\xi \cos n\eta, \text{ where } P = k^{-1}\left(m^2+1\right)^{-0.5}.$$

The sinusoidal perturbations of the layer shape (r_1=0) at the acceleration (layer thickness) perturbation at r_m=$Ak^{-1}\left(m^2+1\right)^{-0.5}$ grow two times as fast than for the equithick layer.

The above analytical solutions to linearized system (2) are in a good agreement for small initial perturbations with numerical computations of the layer dynamics in a most complete formulation of the 3D Lagrangian gas dynamics of perfect compressible fluid. The difference scheme used extends to three dimensions the approach presented in [8] where fluid particle coordinates at t=0 are taken for the Lagrangian coordinates. Computations of thin-layer 2D perturbation non-linear evolution were conducted as test computations for the numerical technique, the computed dependences practically coincide with the analytical results.

Fig.2 presents the analytical and computed time dependences of the 3D perturbation amplitude on the computational grid 4x32x32 for $n = k$=1 at setting initial perturbations in velocities (r_2=-1) (curves 1 and 2, respectively). $a = 1$, initial layer thickness h_0=0.1 were assumed. In the computations the equation of state of material was taken in the form

$$p = c^2(\rho - \rho_0), \tag{9}$$

where p - pressure, ρ - density, c=10.0, ρ_0=7.8. The computed results in terms of 3D gas dynamics confirm that at $n = k$=1 the limited perturbation at equithick layer RTI is that with r_2=$1/\sqrt{2}$ (Fig.3). The computed time dependency of the exponential growth of the perturbation amplitude for r_2=-1 for initial times practically coincides with the analytical. The numerical dependencies of the perturbation amplitude growth on time for 2D (k=1, n=0, r_2=-1) and 3D perturbations ($n = k$=1, r_2=-1) are presented in Fig.4, they coincide with relevant analytical data.

Computations were also conducted in a more simplified setting-up, like this was done in [3], with direct approximation of non-linear system (1), rather than complete gas dynamics equation system. Their results also confirm the analytical relations obtained.

Thus, the effect of initial data on the thin layer perturbation growth rate is quite considerable. Even provided the perturbation growth increment does not change at varying initial data, this effect can manifest itself through a substantial variation in the pre-exponential factor. The layer shape perturbation growth rate can be reduced by setting appropriate thickness perturbations compensating them.

The above considerations for a liquid layer are also important for a more complex problem of thick layer interface RTI and perfect compressible fluid semispace. Limited and phase-changing perturbations are also possible here, while the above dimensionless parameters characterizing initial data are also important in these cases. This is validated by the results of 3D computations

conducted in the perfect compressible fluid approximation for a thick layer of h=5 thickness comparable with the perturbation wavelength.

This computed data is presented in Fig.5. The computations were conducted on the computational grid 25*17*17. At the initial time the condition of static equilibrium of layer elements was given in terms of the model of compressible fluid with the equation of state of form (9) at c=4.6, ρ_0=7.8. The initial velocity perturbations at k=1, m=1 were given exponentially decreasing with depth, like for incompressible fluid [5].

In terms of the perfect compressible fluid model it is possible to study the velocity perturbation evolution atan arbitrary r_2. According to the computations, the perturbations with r_2=1 grow exponentially, the perturbations with r_2=1 change their phase and then grow exponentially,the perturbations with $r_2=1/\sqrt{2}$ do not practically grow during the computation (Fig.5).

At initial times the growth rate modulus of the bubbles floating up is close to the velocity modulus of spikes directed downward, like for the thin layer. However, at later times the bubble growth rate becomes lower than the spike velocity.

Thus, quite different paths of perturbation evolution are possible for a thick layer of compressible perfect fluid. They are described with the fourth-order dispersion equation. However, as the computations conducted show, the solutions are less diverse when setting initial perturbations in the interface shape (without any change in initial fluid densities). All perturbations grow exponentially, the growth rate is slightly dependent on the parameter r_1. Here one can follow certain analogs with the above-discussed case of setting thin layer thickness perturbations.

The work was carried out under support of Russian Fundamental Research Foundation, Project 96-01-00043.

References

[1] Ott E, Nonlinear evolution of Rayleigh-Taylor instability of a thin layer, Pys. Rev. Lett, 29, 21, 1429,(1972).

[2] Nizovtsev PN, Rayevsky VA, Approximate analytical solutions of the problem of Rayleigh-Taylor instability in strong media, VANT. Ser.Teor. Prikl. Fizika, 3, 11-17, (1991).

[3] Manheimer W, Colombant D, Ott E, Three-dimensional, nonlinear evolution off the Rayleigh-Taylor instability of a thin layer, Phys. Fluids, 27, 8, 2164-2175, (1984).

[4] Gasilov VA, Goloviznin VM *et al.*, On numerical simulation of Rayleigh-Taylor instability in incompressible fluid, Preprint USSR Academy of Sciences IPM, Moscow, 70, (1979).

[5] Volkova RA, Kruglyakova LV *et al.*, On simulation of Rayleigh-Taylor instability in incompressible fluid in 3D formulation, Preprint USSR Academy of Sciences IPM, Moscow, 86, (1985).

[6] Ivanov AG, Novitsky EZ, Ogorodnikov VA, Pinchuk SY, Plate acceleration up to supersonic velocities. Instability at deceleration against air, PMTF, 2, 90-94, (1982).

[7] Aleshin AN, Zaitsev SG *et al.*, Experimental study of Richtmyer-Meshkov instability at contact discontinuity with 3D perturbations, MZhG, 6, 111-117, (1995).

[8] Samarsky AA, Popov YP, Difference methods for solving gas dynamics problems. 3d edition with a supplement, Moscow, Nauka Publishers, (1992).

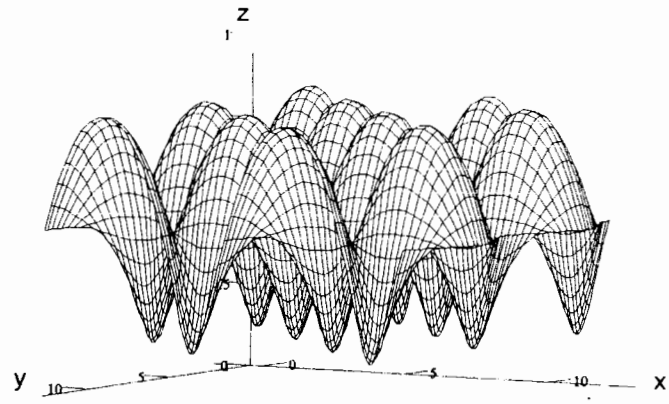

Figure 1. Perturbed layer surface.

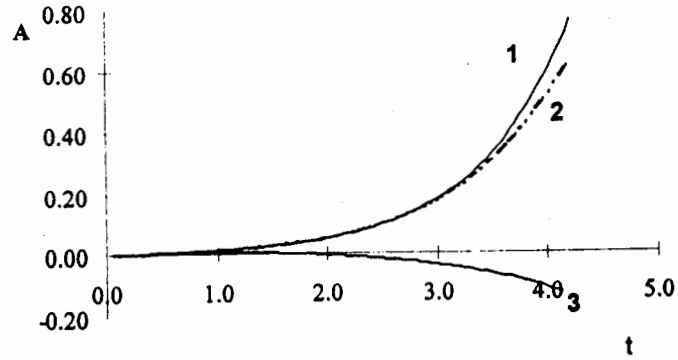

Figure 2. Perturbation amplitude vs time.$1 - r_2 = -1.0$, analyt.,$2 - r_2 = -1.0$, comput., $3 - r_2 = 1.0$, analyt.

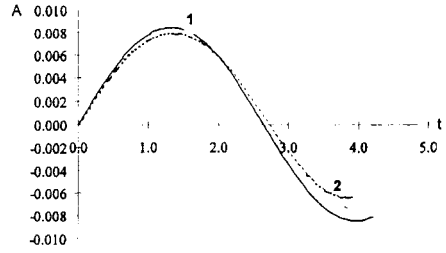

Figure 3. Limited solution, $r_2 = 1/\sqrt{2}$. 1 - analyt., 2 - comput.

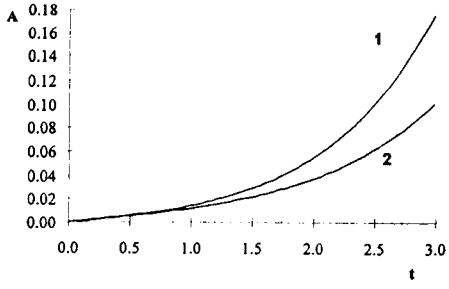

Figure 4. Comparison of 2D and 3D layer perturbation growth rates.

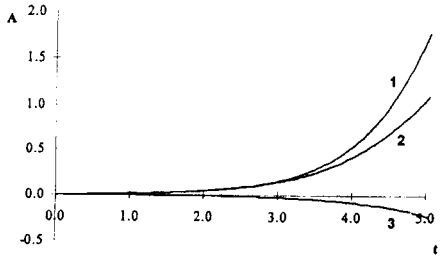

Figure 5. Perturbation evolution for a thick layer, 1 - r_2=-1, streams; 2 - r_2=-1, bubbles; 3 -r_2=1, streams.

Laser Interferometric Tomography Study of the TMZ Structure at the Boundaries of a 3D Propane Jet in Air

V.P. Bashurin, V.V. Bashurov, Y.D. Bogunenko, G.A. Bondarenko, F.A. Pletenev and V.A. Starodubtsev
Russian Federal Nuclear Centre - Institute of Experimental Physics
Prospect Mira 37, 607190, Sarov, Nizhny Novgorod Region, Russia

Abstract: Laser interferometric topography was used to study experimentally the three dimensional density distribution pattern of chemically non-reactive gases in the TM-zone. Based on this technique, the ex-periment results in the mixture density distribution integrated along the light path. Generally, TM zone has not any kind of symmetry. Therefore, the problem of reconstructing three-dimensional density distributions (TDD) of gases can be solved by providing sufficiently many TM zone integral projections (or aspects). It is technically difficult and expensive to achieve this large number of aspects ($N > 10$). Therefore, it is essential that a reconstruction method must be selected to allow the solution of the problem with the least possible number of aspects. Given that experimental data are incomplete, the reconstruction methods had done well that are based on the concept of maximum data entropy. Information a priori about the solution to be sought for an isobaric gas mixture is that it's each constituent has invariable density. Thus, a data entropy functional can be defined which is similar to Fermi gas in statistical physics. An algorithm has been suggested for reconstruction as a modified maximum-bounded entropy method [6], and computer simulation has been done for the TDD reconstruction procedure recording [2]. This makes reasonable good reconstruction achievable even with as few aspects as $N = 4$. Experiments on study of TM of a propane jet in air using 4-aspects laser interferometer were provided and reconstruction of propane concentration distribution was conducted. Received results allow to determine the TM zone spectral characteristics.

1. Introduction

The study of turbulent mixing involves model experiments to understand the main conformities of this process including those on hydrodynamic systems [11]. The important problem in the experimental investigation of instabilities' evolution and turbulent mixing is not only to form the desired turbulent motion of media (gas-gas, gas-fluid, fluid-fluid), but also to obtain quantitative data on the tur-bulent mixing zone (TMZ) structure and parameters. For the study of TMZ flows physical properties, it is preferable to use methods that do not introduce additional perturbation into the instability evolution zone. For this purpose it is desirable to use radiation to which the medium of interest is sufficiently transparent, and visible light sources are commonly used in cases of gaseous or liquid media. Experimental study re-sults in obtaining the distribution of a certain flow physical characteristic integrated along the light path. Using different experimental methods one can obtain shadow images, record phase shifts of probing light wave propagating through the TMZ with the interferential method or evaluate parameters from the prob-ing radiation absorption data. The integral distributions of flow characteristics themselves allow to obtain certain quantitative information about the TMZ

More information - Email: otd03_2305@spd.vniief.ru

structure, but local 3D-distributions (3DD) are more informative. It is possi-ble to reconstruct 3DD if we could obtain integral distributions from several directions of view (aspects). Such problems often appear in physics and medicine and are solved using the so called "reconstructive tomography" methods [9, 12, 10]. To extract the needed physical values from experimental data usually it is necessary to provide some mathematical procedures with them. At this point of view tomography is a kind of such procedures but much more complicated. Although the mathematical basics of tomography appeared about 80 years ago [13] the use of reconstructive tomography became possible with the progress in computer technology. Numerous algorithms for 3DD reconstruction were developed for the practical purposes. Some of them provide high accuracy at minimal number of aspects ($\leq 5 \div 10$) [5]. It means that it is possible to get 3DD data using several "identical" measurements without sophisticated experimental techniques. In this paper we show the possibility of using few aspects laser interferometric tomography to reconstruct 3D density distributions of two gases in TMZ.

2. Optical interferometry in the problem of turbulent mixing of gases

Choosing the method of measurements, we should be guided by those physical quantities that we want to receive as a result of reconstruction. If we are interested in obtaining the mixed gases density distribution, the most attractive as it seems to us may be the method of optical interferometry. The fact is that the gases' refraction indices slightly differ from unity $n - 1 < 10^{-3}$, therefore it is possible to neglect the deflection of a light beam at a characteristic length of $L \sim 10$ cm in the first approximation, and so the procedure of reconstruction may be appreciably simplified. Besides that the refraction indices of gases and liquids are proportional to density. So the integrals from density along the light paths are directly ob-tained from measurements. It means that we have to deal with reconstruction of a positive defined value that also simplifies this procedure. At last, the interference pattern does not depend on light absorption in a gas, as the absorption influences only the contrast of a forming picture. Automatic formation of coordi-nate lines in interference pattern may also be noted as a positive factor that simplifies spatial orientation. The optical interferometry method to analyze the material composition (density) (e. g. [4]) relies upon the following:

1) the phase of the light wave ϕ while passing through the volume to be studied with the length L along the light path varies by $\frac{2\pi}{\lambda}\int_L n\ dx$, where λ is the light radiation wavelength and n is the material refraction index along L,

2) when one material is replaced by another the light wave phase (after passing through the volume) shifts by $\Delta\phi = \frac{2\pi}{\lambda}\int_L \Delta n\ dx$, where Δn is the refraction index difference between two materials in question.

3) shifts are recorded in the interferential image occurring with the addition of the light wave passing through the medium whose properties may be changed and the non-perturbed light wave passing through the medium whose properties are constant (note that both waves must be coherent).

Interferometers are commonly used to study gas flows. In the paper [1], Mach-Zehnder interferometer was used to find the gas density distributions. In the works [15, 16] the density profile was determined in experiments on Rayleigh-Taylor instabilities, the flows mixing process was visualized and the boundary velocity for Richtmyer-Meshkov instability was evaluated.

3. Algebraic image reconstruction technique

In the experimental study of the turbulent mixing zone (TMZ) of heavy and light gases the fringe phase shift would be dependent on the integrals of gas density distribution along the

laser beam. Tilt variations of the light beam propagating through the object of interest in any plane may pro-vide a sufficient number of aspects to allow an attempt to reconstruct 3-D spatial gas density distributions of both gases with the desired accuracy. If only limited number of aspects can be obtained experimentally and the object symmetry is previously unknown, the primary consideration is what would be the smallest amount of experimental information to reconstruct the object image with the required accuracy. It is this situation we have to deal with when using optical interferometry, because some technical reasons make it almost impossible to obtain simultaneous interference patterns at the angle $0 \leq \theta \leq \pi$ with 10 or more aspects. Reconstruction of the 3DD of unknown function can be often reduced to reconstruction of a set of plane sections. Three-dimensional distribution then would be obtained by arranging two-dimensional ones. Hereinafter we shall follow the image reconstruction technique based on the ideas stated in [7, 3, 8, 6]. Basically, the reconstruction concept as suggested in these papers is the following:
Reconstruction problem is finding m values of the desired function at the spatial mesh $m \times m$. At the same time, what is only known is $m \times p$ data obtained experimentally, and often $p << m$. Thus, there is an indeterminate set of equations to calculate the values of the function to be reconstructed. In other words, the problem may have a great number of solutions, so that some additional conditions must be set to select the desired one. These conditions (criteria) should allow the selection of the most probable solution that incorporates the least amount of additional information not included in the experimental data. The suggestion [7, 3, 8] was that some norm must have the maximum at this solution and such a norm be in the form of non-equilibrium gas entropy. As a rule, there are no rigorous reasons to use concrete expressions for entropy functional but good results justify this approach. In this paper we discuss the image reconstruction technique that is consistently based on the minimization of the amount of information contained in the solution. This approach allows to find the solution with maximal information entropy. Let us use for reconstruction a mesh of $m \times m$ cells of the same size. Let us also assume that the a priori information available to us is the knowledge that each cell contains two gases with different but constant densities $\rho_1 > \rho_2$. These densities are constant across any section taken for reconstruction, and this is due to the fact that usually there is enough time for pressure and temperature relaxation. Let us split each cell into G parts (subcells) so small that only one gas may exist in each of them. In other words, subcell's size is smaller than the minimal size of nonuniformities in the TMZ. Let the number of subcells containing heavier gas be N_H, and that for lighter gas - N_L, and $N_H + N_L = G$. These numbers of heavy-gas and light-gas subcells may be corresponded with the number of possible ways to achieve them (statistical weight of "state" having the numbers N_H and N_L). As is known, this statistical weight is [5]:

$$\Gamma = \frac{G!}{N_H! N_L!} \tag{1}$$

Based on the classic definition of the amount of information entropy I [14] contained in the set of G symbols with N_H of one kind and N_L of the other, we can put down

$$I = -G\, k \sum_{l=1}^{2} (n_l \, \mathbf{Ln} \, \mathrm{n_l}) \tag{2}$$

where k is the normalization constant and $n_l = \frac{N_l}{G}$ - the frequency of occurrence for a symbol with index l ($l = 1$ corresponds to the heavier gas and $l = 2$ - to the lighter one). Since we have $n_2 = 1 - n_1 (N_2 = G - N_1)$, the mesh cell may have the value of information entropy in

the "message" that heavier gas fraction is n, expressed as follows:

$$I = -G\,k\,(n\ \mathbf{Ln}\ \mathrm{n} + (1-\mathrm{n})\ \mathbf{Ln}\ (1-\mathrm{n})) \tag{3}$$

If n_{ij} is the heavier gas fraction in the cell with indices $i,\ j$ $(i = 1:m,\ j = 1:m)$ at the reconstruction mesh, then, due to entropy additivity for statistically independent subsystems, total entropy of the entire distribution of the lighter and heavier gases is:

$$I = -G\,k\,\sum_{i=1}^{m}\sum_{j=1}^{m}[n_{ij}\ \mathbf{Ln}\ \mathrm{n_{ij}} + (1-\mathrm{n_{ij}})\ \mathbf{Ln}\ (1-\mathrm{n_{ij}})] \tag{4}$$

The resulting relationship coincides to within the constant normalization factor with the entropy equation for non-equilibrium Fermi-gas. Equation (4) for information entropy is a functional on the distribution of n_{ij} at the discrete mesh $m \times m$. The value of I will be maximal at some solution n_{ij} if the functional I has zero variation. Experimental data serve as "external restrictions" and should be taken into account by Lagrangian factors. Let consider these restrictions in more detail and look at interference patterns for p aspects. As was already mentioned above, the fringe shift or light signal phase is proportional to within the constant to

$$\Delta\phi = c_1 \int_{l_{k1}\theta} n_1\ dl + c_2 \int_{l_{k2}\theta} n_2\ dl = c_2\ l_{k2}\theta + (c_1 - c_2)\ \int_{l_{k1}\theta} n_1\ dl \tag{5}$$

where $n_1 = 1 - n_2$ and n_2 are the heavier and lighter gases concentrations, correspondingly. Integration is made over the length of the light beam that crosses the given section at the angle of θ, and k_1 is the in-terference line number. To incorporate this information into the reconstruction problem it would be suit-able to have the experimental data preprocessed. A fringe pattern taken at a certain aspect angle defines phase shifts across the section as a function of the spatial coordinate normal to the laser beam direction. This function may be determined at as many points as the number of fringes crossing the given section. When we use the mesh $m \times m$ with m much smaller than the number of lines in the experiment, we can find integrals of n over any band with the size of about the cell one in any section by adding together the lines shifts within this band (see Figure 1). The accuracy of these integral calculations over the fringe depends on interference lines density, so the number of fringes across the cell size must be adjusted to needed accuracy. Let us consider that for each projection at the angle θ we know from the fringe pattern m integrals of n_1 over the band of the number $k = 1:m$:

$$R_{k\theta} = \sum_{i,\ j=1,\ m} n_{ij}\ S_{ijk\theta} \tag{6}$$

where $S_{ijk\theta}$ is the partial area of the cell with number $i,\ j$, which is common with the band $k,\ \theta$. Thus, the reconstruction problem goes to find maximum entropy (4) with restrictions (6). To provide experiments on TMZ study for gas flows a 4-aspect experimental system with Mach-Zehnder interferometer as the basic unit was assembled. Figure 2 shows the experimental arrangement. The $YAG:Nd^{3+}$ laser radiation 1 (the second harmonic with the wavelength of $\sim 0.5\mu$m, pulse duration of $\sim$ 15 ns after DKDP-crystal 2) passes through telescope 3 (increasing the light beam diameter up to 50 mm), crosses the investigated volume 27 and goes to the films $32 \div 35$ directed by the system of rotation $4 \div 15$ and semi-transparent $16 \div 26$ mirrors. The laser radiation crosses the investigated volume from 4 directions in the same plane. Angles between nearby directions are equal to $\pi/4$ radians. A propane jet outcomes to air from an round nozzle with the cutoff diameter of about 7.2 mm and passes through the

volume 27 normally to the plane of Figure 2. The Δn value (the difference in refraction indexes between jet substance and air) used with further interferograms processing was obtained in specific experiments by measuring the fringe shift N near the nozzle cutoff. To increase the accuracy of Δn determination (which is achieved by increasing the shift N), measurements were carried out using round nozzle with 7.2 mm diameter. The propane jet velocity was measured by the differential laser Doppler anemometer (see Figure 3). He-Ne laser radiation was scattered by particles of smoke added into the jet. The smoke was obtained by burning some dose of gun powder in propane. The anemometer sensitivity vector was directed along the jet and equal to 4.8 m/s $\times$ MHz. The measured propane jet velocity was about 10 m/s. For these experimental conditions, the Reynolds number was $Re \sim 10^3$. The 3-D concentration distributions reconstruction procedure is as follows:

1. Vectorization of interferograms in order to obtain equal-phase isolines of the light signal. This vectorization was provided at local interference fringe intensity minima using gradient methods with fil-tering procedures. The vectorized interferograms are shown in Figure 4.
2. Creation of 2-D integral distributions (for all aspects of view) of additional phase shifts (due to propane only) along the light paths.
3. Reconstruction of propane concentration distributions in the set of 2-D sections parallel to all laser beams axes' plane.
4. Creation of 3-D array of propane concentrations from the set of 2-D arrays.
5. Calculation of 3-D propane concentrations' iso-surfaces and their visualization by personal computer.
6. Some results are presented at Figures 5-6.

Reconstruction procedure was found to be insensitive to experimental data errors and additional perturbations due to errors in interferogram scanning. Figures 5-6 show fast (at a distance of about the nozzle dimension) flow turbulization consistent with high Reynolds number $Re \sim 10^3$. Three-D spatial distributions of gasdynamics values of the turbulent mixing zone were used to obtain the corresponding propene concentration spectrum shown on the Figure 7. For comparison on this Figure the Kholmogorov spectrum of homogeneous isotropic turbulence is presented .It is obvious that density pulsations spectral intensity decreases faster with wave number grows in experiment than in theory. It means that homogeneous isotropic turbulence is not achieved in real experiment. This fact must be taken in to account when experimental data are used to test the numerical codes designed for predictions of turbulent transfer in complicated flows.

4. Conclusions

In this paper we showed possible applications of optical diagnostics to experimental study of gas-gas turbulent mixing. It is shown that 3D spatial concentration distributions of materials in TMZ may be extracted from experimental data obtained with the help of interferometry techniques. Laser interferometric topography was used to study experimentally the three-dimensional density distribution pattern of chemically non-reactive gases in the TM-zone. Three-D spatial distributions of gasdynamics values of the turbulent mixing zone were used to obtain the corresponding propane concentration spectrum. It was shown that homogeneous isotropic turbulence may be not achieved in real experiment. This fact must be taken in to account when experimental data are used to test the numerical codes de-signed for predictions of turbulent transfer in complicated flows.

Acknowledgement. This work was supported by ISTC, Project 029.

References

[1] Althaus W, Simberg W, Kraus E, Vortex formation in the wake of a flat plate for subsonic and supersonic freestream Mach numbers, Proc. of the International Workshop on the Physics of Compressible Turbulent Mixing, Princeton, New Jersey, October 24-27, 127-136, (1988).

[2] Bashurin VP, Bogunenko YD, Bondarenko GA, Pletenev FA, Starodubtsev VA, Quantitative measurement feasibility for 3D-distributions of hydrodynamic quantities in the turbulent mixing zone of two gases, Proc. of the 5th International Workshop on the Physics of Compressible Turbulent Mixing, Stony Brook, New York, July (1995).

[3] Bellman SH, Bender R, Gordon R, Rowe JE, ART in science being a defense of algebraic reconstruction techniques for three-dimensional electron microscopy, J. Theor. Biol., 32, 205-216, (1971).

[4] Born M, Wolf E, Principles of Optics (Pergamon Press), (1968).

[5] Brillouin L, Science and Information Theory (Academic Press, New York), (1956).

[6] Frieden RB, Zoltani CK, Maximum bounded entropy: application to tomographic reconstruction, Applied Optics, 24, 23, 3993-3999, (1985).

[7] Gordon R, Bender R, Herman GT, Algebraic reconstruction techniques (ART) for three-dimensional electron microscopy and X-ray photography, J. Theor. Biol., 29, 471-481, (1970).

[8] Gordon R, Herman GT, Johnson SA, Image reconstruction from projections, Sci. Am., 233, 4, 56-68, (1975).

[9] Herman GT, Image Reconstruction from Projections: Implementations and Applications (Springer-Verlag, Berlin & New York), (1979).

[10] Herman GT, Image Reconstruction from Projections (Academic Press, New York), (1980).

[11] Meshkov EE, Instability of Shock-Accelerated Interface Between two Gases, Izv. AN SSSR, MZhG, 5, 151-158, (in Russian), (1969); Fluid Dynamics, 4, 101 (1969, translated), NASA Tech. Trans. F-13, 074, (1970).

[12] Mueller RK, Kaveh M, Wade G, Reconstructive Tomography and Applications to Ultrasonics, Proc. IEEE, 67, 4, 146-169, (1979).

[13] Radon J, Uber die Bestimmung von Functionen durch ihre Integralwerte langs gewisser Mannigfaltigkeiten (On the determination of functions from their integrals along certain manifolds), Berichte Saechsische Akademie der Wissenschaften, 69, 262-277, (1917).

[14] Shannon CE, A mathematical theory of communication, Bell Syst. Tech. J., 27, 379-423, 623-656, (1948).

[15] Zaytsev SG, Chebotareva EI and Titov SN, The study of Rayleigh-Taylor instability in continuous interface, Proc. of the 4th International Workshop on the Physics of Compressible Turbulent Mixing, 29 March - 1 April 1993, Cambridge, England, 178-187, Ed. by P.Linden, D.Youngs & S.Dalziel, Pr. by Cambridge Univ. Press, Cambridge, England, (1993).

[16] Zaytsev SG, Chebotareva EI and Titov SN, The initiation and the development of Richtmyer-Meshkov instability in continuous interface, Proc. of the 4th International Workshop on the Physics of Compressible Turbulent Mixing, 29 March - 1 April 1993, Cambridge, England, 297-305, Ed. by P.Linden, D.Youngs & S.Dalziel. Pr. by Cambridge Univ. Press, Cambridge, England, (1993).

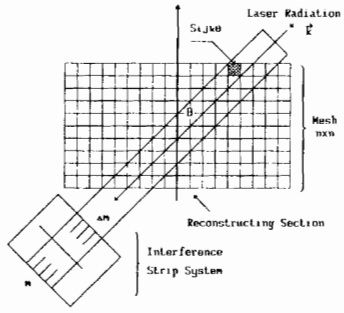

Figure 1. The experimental data preprocessing scheme.

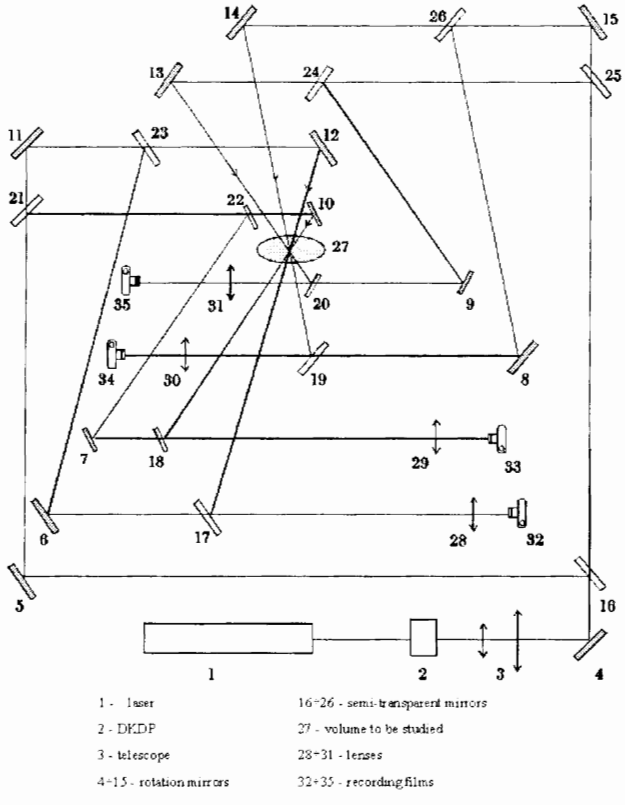

Figure 2. Optical scheme of 4-aspects experimental system.

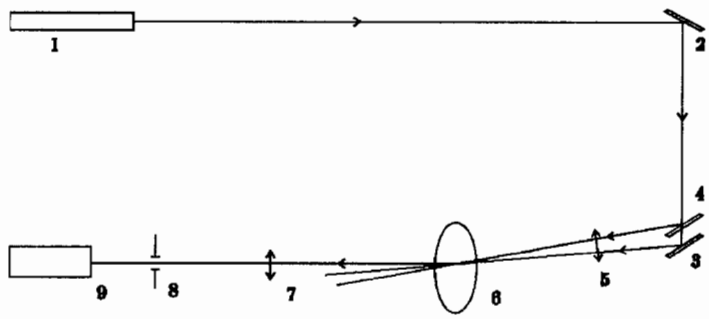

1. Laser LG-79, 8mW.
2,3. Mirrors, 100%.
4. Mirror, 50%.
5. Lens, f=300 mm.
6. Volume to be studied
7. Objective, f=300 mm.
8. Diaphragm.
9. Photomultiplier FEU-79.

Figure 3. Schematic of laser Doppler anemometer.

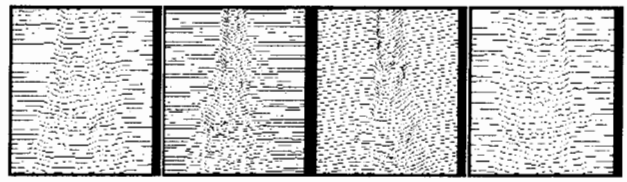

Figure 4. Interference fringe after vectorization procedure.

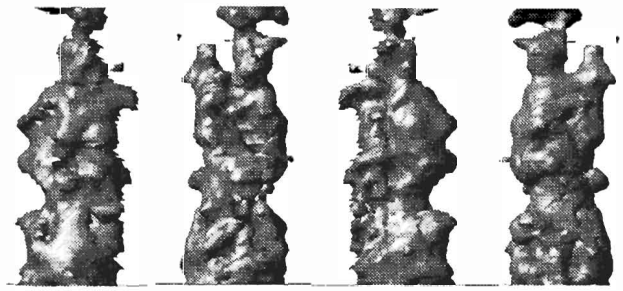

Figure 5. Propane molecules iso-concentration C=0.7 surface.

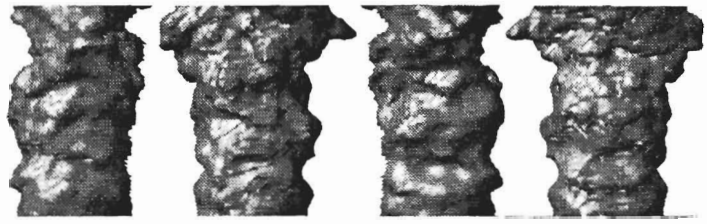

Figure 6. Propane molecules iso-concentration C=0.5 surface.

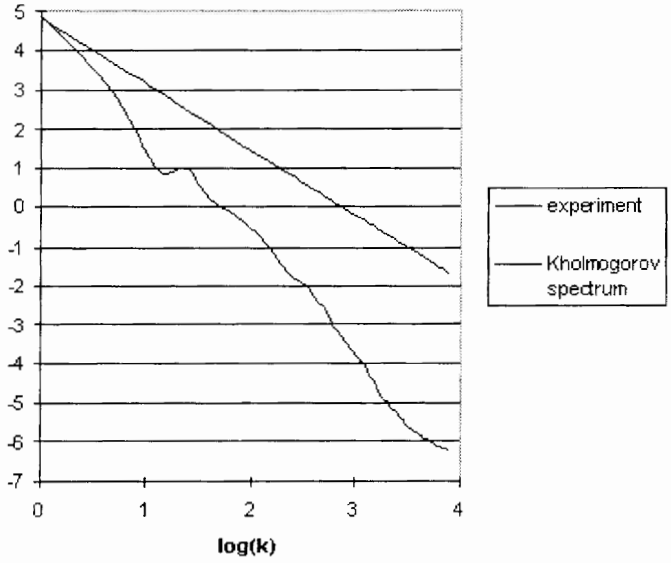

Figure 7. Propane concentration spectrum.

To the Possibility of Using Laser Interferometric Tomography in the Investigation of TMZ Structure at the Gas-Gas Interface in 2D and 3D Flows

V.P. Bashurin, V.V. Bashurov, Y.D. Bogunenko, G.A. Bondarenko, F.A. Pletenev and V.A. Starodubtsev
Russian Federal Nuclear Centre - Institute of Experimental Physics
Prospect Mira 37, 607190, Sarov, Nizhny Novgorod Region, Russia

1. Introduction

In 1995 E. Meshkov suggested new method of creating unstable gas-gas interface in experimental studying of one-dimensional hydrodynamic flows. This method lies upon using gas explosive mixture (GEM) and inert gas separated by thin film [1]. In this case some imperfections of classical shock tube experiments arrangement (the influence of finite film mass and rupture power) are avoided. Thin film evaporation occurs due to shock (detonation) wave passes through the interface. Experiments with plain flows using shock tube were fulfilled [2].

Also in 1995 the possibility of using laser interferometric tomography (LIT) to study experimentally 3D patterns of density distribution of chemically non-reacting gases in turbulent mixing zone (TMZ) was examined [3]. At this conference the results of interferometric measurements and reconstruction of 3D density distributions for the case of subsonic shear flow (the outflow of propane jet to air) are presented [4]. Four aspects of view were used, and the main details of TMZ structure with the scale of about several percent of object linear dimensions were reconstructed. The correlation function of density pulsation spectrum was obtained. Thus, it was shown that 3D distributions of substances concentrations in TMZ can be found using interferometric methods which allow to measure integral along the light trajectory in the volume to be studied wave-front disturbances, which are associated with media partial concentrations changes in TMZ.

In the present work we made an attempt to use the LIT method to study spatial concentrations distributions of gas media with shock waves. Although our finite goal is to apply LIT method to study structures of flows which are generated using suggested by E. Meshkov new method of their generation, at the first stage we restricted ourselves to gasdynamic modeling of one of considered in [1] variants of their creation. It is the pulsed energy extraction in the gas with constant initial density which is bounded by to parallel planes. The arising flow has axial symmetry but due to turbulent growth become three-dimensional. Therefore the experimental technique and algebraic method of reconstruction similar to described in [4] were used to define spatial density distribution.

2. Using of optical interferometers in medium density distribution study with compressibility accounting

Choosing the method of measurements, we should be guided by those physical quantities that we want to receive as a result of reconstruction. If we are interested in obtaining the compressible

More information - Email: bogunenko@vniief.ru

gas density distribution, the most attractive as it seems to us may be the method of optical interferometry. The fact is that the gases refraction indexes slightly differ from unity ($n - 1 < 10^{-3}$), therefore it is possible to neglect the deflection of a light beam at a characteristic length of $L = 10$ *cm* in the first approximation, and so the procedure of reconstruction may be appreciably simplified. Besides that the refraction indexes of gases and liquids are proportional to density. So the integrals from density along the light paths are directly obtained from measurements. It means that we have to deal with reconstruction of a positive defined value that also simplifies this procedure. At last, the interference pattern does not depend on light absorption in a gas, as the absorption influences only the contrast of a forming picture.

The optical interferometry method to analyze the medium density (e. g. [5]) relies upon the following:

1) the phase of the light wave φ while passing through the volume to be studied with the length L along the light path varies by $\frac{2\pi}{\lambda}\int\limits_L ndx$, where λ is the light radiation wavelength and is n the medium refraction index along L,

2) if density varies along the light trajectory the wave phase (after passing through the volume) shifts by $\Delta\varphi = \frac{2\pi}{\lambda}\int\limits_L \Delta n dx$, where Δn is the refraction index difference between medium in gasdynamic flow and initial non-disturbed state,

3) $\Delta\varphi$ shifts are recorded in the interferential image occurring with the addition of the light wave passing through the medium whose properties may be changed and the non-perturbed light wave passing through the medium whose properties are constant (note that both waves must be coherent).

3. Algebraic image reconstruction technique

Reconstruction of the 3DD of unknown function can be often reduced to reconstruction of a set of plane sections. Three-dimensional distribution then would be obtained by arranging two-dimensional ones. Hereinafter we shall follow the image reconstruction technique based on the ideas stated in [6, 7, 8, 9]. Basically, the reconstruction concept as suggested in these papers is the following:

Reconstruction problem is finding m values of the desired function at the spatial mesh mxm. At the same time, what is only known is mxp data obtained experimentally, and often $p \ll m$. Thus, there is an indeterminate set of equations to calculate the values of the function to be reconstructed. In other words, the problem may have a great number of solutions, so that some additional conditions must be set to select the desired one. These conditions (criteria) should allow the selection of the most probable solution that incorporates the least amount of additional information not included in the experimental data. The suggestion [6, 7, 8] was that some norm must have *the maximum* at this solution and such a norm be in the form of non-equilibrium gas entropy. As a rule, there are no rigorous reasons to use concrete expressions for entropy functional but good results justify this approach. In this paper we discuss the image reconstruction technique that is consistently based on the minimization of the amount of information contained in the solution. This approach allows to find the solution with maximal information entropy.

Let us use for reconstruction a mesh of mxm cells of the same size. We shall model gas concentration in the cell as a set of elements with maximal density partially occupying cell volume. Let us split each cell into G parts (subcells) so small that only gas with such maximal

density may exist or be absent in each of them. In other words, the size of subcell size is smaller than the minimal size of nonuniformities in the volume to be studied. Let the number of subcells containing gas with maximal density be N_H, and that for empty ones - N_L, and $N_H + N_L = G$. These numbers of filled and empty subcells may be corresponded with the number of possible ways to achieve them (statistical weight of state having the

$$\Gamma = \frac{G!}{N_L! N_H!}.$$

Based on the classic definition of the amount of information entropy I [11] contained in the set of G symbols with N_H of one kind and N_L of the other, we can put down

$$I = -Gk \sum_{n=1}^{2} n_l \ln n_l.$$

where k is the normalization constant and $n_l = \frac{N_l}{G}$ - the frequency of occurrence for a symbol with index l ($l = 1$ corresponds to the gas and $l = 2$ - to its absence).

Since we have $n_2 - n_1$ ($N_2 = G - N_1$), the mesh cell may have the value of information entropy in the message that gas concentration is n_1 which is expressed as follows:

$$I = -G\ k\ (n_1 \ln n_1 + (1 - n_1) \ln(1 - n_1)).$$

If n_{ij} is gas fraction in the cell with indexes i, j ($i = 1 : m,\ j = 1 : m$)at the reconstruction mesh, then, due to entropy additivity for statistically independent subsystems, total entropy of the entire gas concentration distribution is:

$$I = -Gk \sum_{n=0}^{\infty} [n_{ij} \ln n_{ij} + (1 - n_{ij}) \ln (1 - n_{ij})]. \tag{1}$$

Equation (1) for information entropy is a functional on the distribution of n_{ij} at the discrete mesh mxm. The value of I will be maximal at some solution n_{ij} if the functional I has zero variation. Experimental data serve as external restrictions and should be taken into account by Lagrangian factors. Let consider these restrictions in more details and look at interference patterns for aspects. As was already mentioned above, the fringe shift or light signal phase is proportional to within the constant to

$$\Delta\varphi = c \int_{l_{k_1}\theta} n_1 dl,$$

where n_1 is the concentration, and integration is made over the length of the light beam that crosses the given section at the angle of θ, and k_1 is the interference line number. To incorporate this information into the reconstruction problem it would be suitable to have the experimental data preprocessed. A fringe pattern taken at a certain aspect angle defines phase shifts across the section as a function of the spatial coordinate normal to the laser beam direction. This function may be determined at as many points as the number of fringes crossing the given

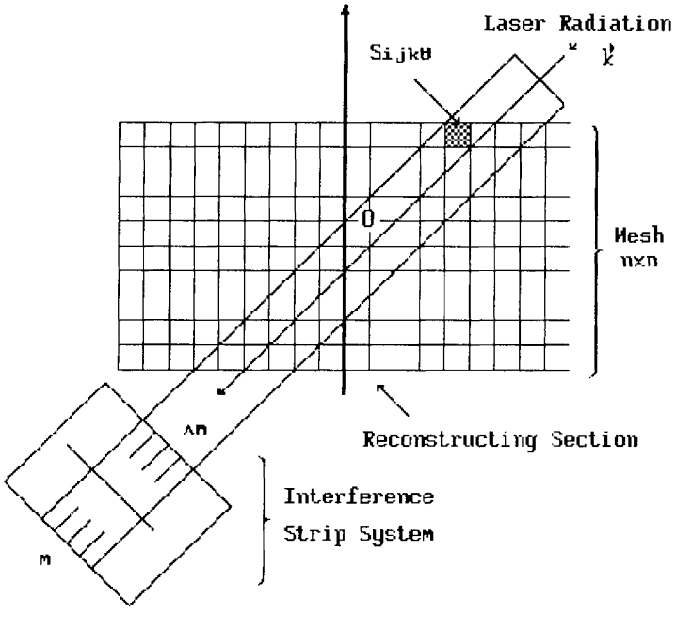

Figure 1. The experimental data preprocessing scheme.

section. When we use the mesh mxm with m much smaller than the number of lines in the experiment, we can find integrals of n over any band with the size of about the cell one in any section by adding together the lines shifts within this band (see Figure 1). The accuracy of these integral calculations over the fringe depends on interference lines density, so the number of fringes across the cell size must be adjusted to needed accuracy.

Let us consider that for each projection at the angle θ we know from the fringe pattern m integrals of over the band of the number $k = 1 : m$:

$$R_{k\theta} = \sum_{i,j=1,m} n_{ij} S_{ijk\theta}, \tag{2}$$

where $S_{ijk\theta}$ is the partial area of the cell with number i, j, which is common with the band k, θ. Thus, the reconstruction problem goes to find maximum entropy (1) with restrictions (2).

A 4-aspect experimental system with Mach-Zehnder interferometer as the basic unit was assembled to provide measurements. Figure 2 shows the experimental arrangement. The YAG:Nd^{3+} laser radiation 1 (the second harmonic with the wavelength of 0.5 μm, pulse duration of 15 ns after DKDP-crystal 2 passes through telescope 3 (increasing the light beam diameter up to 50 mm), crosses the investigated volume 27 and goes to the films directed by the system of rotation and semi-transparent mirrors. The laser radiation crosses the investigated volume from 4 directions in the same plane. Angles between nearby directions are equal to $\pi/4$ radians. The experimental device consisted of two parallel planes placed with a distance of about 15

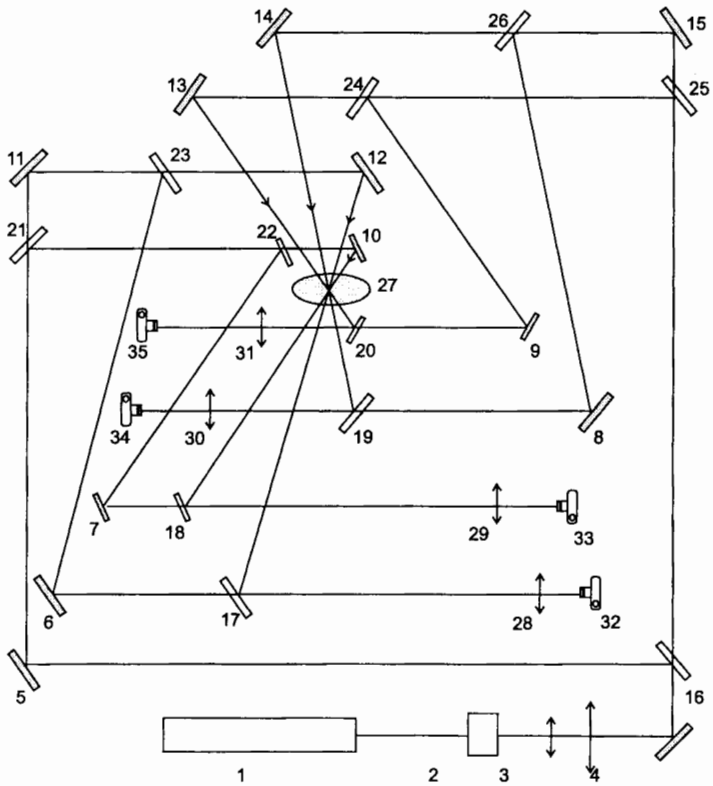

Figure 2. Optical scheme of 4-aspects experimental system.

mm between each other. A pulsed (t=40 nS) electric discharge was initiated in the air at the system center using thin wires. The energy transferred to the air was (2 J. Interferometrical measurements were provided at the time moment of 60 (s after discharge ignition.

The 3-D concentration distributions reconstruction procedure was as follows:

1. Vectorization of interferograms in order to obtain equal-phase isolines of the light signal. This vectorization was provided at local interference fringe intensity maxima and minima using gradient methods with filtering procedures. The vectorized interferograms are shown at Figure 3. 2. Creation of 2-D integral distributions (for all aspects of view) of additional phase shifts (due to air density disturbances) along the light paths.

3. Reconstruction of the set of 2-D sections parallel to all laser beams axes' plane.

4. Construction of 3-D array of air concentration from the set of 2-D arrays.

5. Calculation of 3-D iso-surfaces of air concentrations and their visualization.

Calculated iso-surfaces of different (relative to normal air) concentrations are shown at Figure 4. As expected the air between experimental plates is rarefied. The provided experiments allow to rely on LIT method in experimental study of compressible gases turbulent flows.

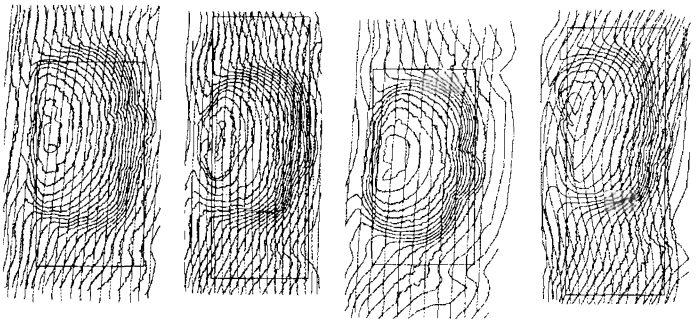

Figure 3. Interference fringe after vectorization procedure.

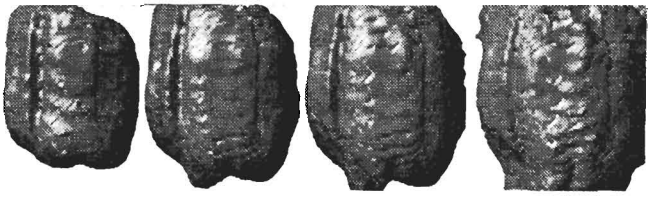

Figure 4. Air iso-concentrations surfaces (C/Cair = 0.01, 0.1, 0.2, 0.5).

Acknowledgement. This work was supported by the ISTC, Project 029.

References

[1] Meshkov EE, One approach to the experimental study of hydrodynamic instabilities: creration of a gas-gas interface using the dynamic technique. In: The Proc. of the 5th International Workshop on Compressible Turbulent Mixing. Stony Brook, New York, USA, 18-21 July 1995, 237-242. Editors R. Young, J. Glimm & B. Boston. World Scientific Publishing Co. Pte. Ltd., Singapore, (1996).

[2] Dudin VI, Gubkov EV, Meshkov EE, Nikitin AA, Stadnic AL, Statsenko VP, Tilkunov VA, Vlasov YA, Yanilkin YV, Zhmailo VA, The Perturbations and Turbulent Mixing Evolution at the Plane Gas-Gas Interface in Shock-Tube Experiments with GEM as a Driver. The 6th International Workshop on Compressible Turbulent Mixing. Marseille, France, 18-21 June, (1997).

[3] Bashurin VP, Bogunenko YD, Bondarenko GA, FA Pletenev, Starodubtsev VA, Quantitative measurement feasibility for 3D-distributions of hydrodynamic quantities in the turbulent mixing zone of two gages. In: The Proc. of the 5th International Workshop on Compressible Turbulent Mixing. Stony Brook, New York, USA, 18-21 July 1995, 124-134, Editors R. Young, J. Glimm & B. Boston. World Scientific Publishing Co. Pte. Ltd., Singapore, (1996).

[4] Bashurin VP, Bashurov VV, Bogunenko YD, Bondarenko GA, Pletenev FA, Starodubtsev VA, Using of Laser Interferometric Tomography in the Investigation of TMZ Structure at the Gas-Gas Interface in 2D Flow. The 6th International Workshop on Compressible Turbulent Mixing, Marseiile, France, 18-21 June, (1997).

[5] Born M, Wolf E, Principles of Optics (Pergamon Press), (1968).

[6] Gordon R, Bender R, Herman GT, Algebraic reconstruction techniques (ART) for three-

dimensional electron microscopy and X-ray photography, J. Theor. Biol., 29, 471-481, (1970).

[7] Bellman SH, Bender R, Gordon R, Rowe JE, ART in science being a defense of algebraic reconstruction techniques for three-dimensional electron microscopy, J. Theor. Biol., 32, 205-216, (1971).

[8] Gordon R, Herman GT, Johnson SA, Image reconstruction from projections, Sci. Am., 233, 4, 56-68, (1975).

[9] Roy Frieden B, Csaba Zoltani K, Maximum bounded entropy: application to tomographic reconstruction, Applied Optics, 24, 23, 3993-3999, (1985).

[10] Brillouin L, Science and Information Theory (Academic Press, New York), (1956).

[11] Shannon CE, A mathematical theory of communication, Bell Syst. Tech. J., 27, 379-423, 623-656, (1948).

The Evolution of the Rayleigh-Taylor Instability Under Influence of the Richtmyer-Meshkov Stage

S.A. Bel'kov[1], L.S. Mkhitarian[1], O.A. Vinokurov[1], G.G. Kochemasov[1], S.V. Bondarenko[1], D. Wilson[2] and N.M. Hoffman[2]
[1]Russian Federal Nuclear Center - Institute of Experimental Physics
Prospect Mira 37, 607190, Sarov, Nizhni Novgorod Reg., Russia
[2]Los Alamos National Laboratory, P.O. Box 990, Mail-Stop P274, Los-Alamos, USA

Abstract: We performed two groups of computations. For one group, the initial perturbations were set at the ablation front after stable density profile has been formed (problem (a)). In the other group the perturbations initially focus on the rear side of the target (problem (b)). Linear stage growth rates determined in our calculations are different in these two problems. We have found, that the reason for these differencies is in Richtmyer-Meshkov instability, which influences the perturbation evolution in both problems in a different way. When studying two modes interaction we have found that for both problems infinitely thin shell approximation (E.Ott) is in a good agreement with our 2D computations.

1. Problem setup

The calculations were carried out for the evolution of perturbations in a plane target with the initial density ρ_0=2 g/cm^3. The laser flux on the target was set to be fixed and had the value I_L=10^{15} W/cm^2, laser wave-length was λ=0.35 μm. The computations used MIMOZA code [1, 2]. Two ways were considered for the specification of initial perturbations:

a) Perturbations at the ablation front

A 1D problem was solved till the time when stable density profile was formed in the target. In our case this occurred at t=0.06 ns. Then the mesh nodes displaced at value having the form [3]:

$$\xi_x = A_0 \cdot \frac{\cos(ky)}{\cosh[k(x - x_{\max})]},\ \xi_y = A_0 \cdot \frac{\sin(ky)\sinh[k(x - x_{\max})]}{\cosh^2[k(x - x_{\max})]} \qquad (1)$$

with the x axis directed toward the laser beam (longitudinal direction); the y axis lying in the target plane (transversal direction); $x_{\max}$ - the coordinate of the point in which density is maximum at t=0.06 ns, k=2π/Λ - the perturbation wave number.

b) Perturbations at the rear side of the target

From the very beginning of the calculations the perturbations were introduced by setting the displacement of mesh nodes expressed by (1) with $x_{\max}$=0, which corresponds to the coordinate of the rear side of the target.

2. Linear stage Rayleigh-Taylor instability growth rates

To determine the increment we tracked the computations of the perturbation amplitude A at the interface between the nonevaporated target and laser corona. The interface is taken as the

More information - Email: leo_706@spd.vniief.ru

surface where $\nabla\rho$ is maximum. The major amount of computations was run on the grid with 40 cells per perturbation wavelength and 120 cells per the plate depth uniformly spaced.

For long wave perturbations ($\Lambda \geq 1.5$ μm) applied to rear side the growth-rates obtained from 2D computations are actually the same as those for the instability in the case of perturbations applied to the ablation front. For the wave length Λ=1 μm, perturbation increments applied to the rear side are considerably lower than those for Λ=1.1 and 0.9 μm in problem (a) and no perturbation growth was observed for Λ=0.5 μm in problem (b).

Generally the perturbation instability problem for the ablation front can be characterized by three dimensionless parameters: $\frac{\Gamma}{\sqrt{gk}}$, $k\Delta$, $\frac{\sqrt{gk}m_f g\Delta}{\rho_f c_s^2} = \frac{\sqrt{gk}\Delta}{c_s}$. The first characterizes the ratio of the problem increment Γ to the classical one, the second represents the ratio of the shell thickness Δ to the wave length and the third is the ratio of the gravitational energy flow at the target surface to the heat flow in laser corona (m - shell mass, ρ_f - characteristic density at the ablation front, c_s - sound speed in the laser corona). Therefore this dimensionless increment must be the function of two remaining parameters. Takabe [4] gives this function in the following form:

$$\frac{\Gamma}{\sqrt{gk}} = a - b\frac{\sqrt{gk}\Delta}{c_s}, \tag{2}$$

where $a< 1$, $b> 0$ are some constants.

However it is clear that for $k\Delta \to 0$ we must have an increment matching the classical one, i.e. a must be a function k such that $a(k\Delta \to 0)\to 1$. For large wavelengths the longitudinal velocity in the nonvaporized part is actually the same through the target thickness, however for large $k\Delta$ the longitudinal velocity decreases with the growth of the distance from the ablation front. If this decrease is assumed to follow the same law as for incompressible fluid ($\sim \exp(-kx)$), then the following expression can be obtained for $a(k\Delta)$:

$$a(k\Delta) = \sqrt{\frac{1-\exp(-k\Delta)}{k\Delta}}. \tag{3}$$

Then the expression for the increment will take the form:

$$\frac{\Gamma}{\sqrt{gk}} = \sqrt{\frac{1-\exp(-k\Delta)}{k\Delta}} - b\frac{\sqrt{gk}\Delta}{c_s}. \tag{4}$$

The Figure 1 shows the curves (4) with b=1 and our computational results together with those from [3]. The analysis shows that the major difference in the perturbations growth rate pattern in problems (a) and (b) is due to the fact that in problem (b) Richtmyer-Meshkov instability is important. In fact for perturbations in problem (a) the initial material velocity is zero and the ablation front perturbation results in the vortex behind the front where the velocity progressively grows. This vortex is responsible for the mass flow along the target and increase in the front perturbation amplitude. In problem (b), when the shock wave arrives to the rear side of the target, the perturbations generate both transversal and longitudinal velocities thus transversal velocity component is initially nonzero:

$$V_0^y \approx c_s A_0 k \approx A_0 k\sqrt{\gamma\frac{P_0}{\rho_0}} \approx A_0 k\sqrt{\gamma\frac{mg}{\rho_0}}.$$

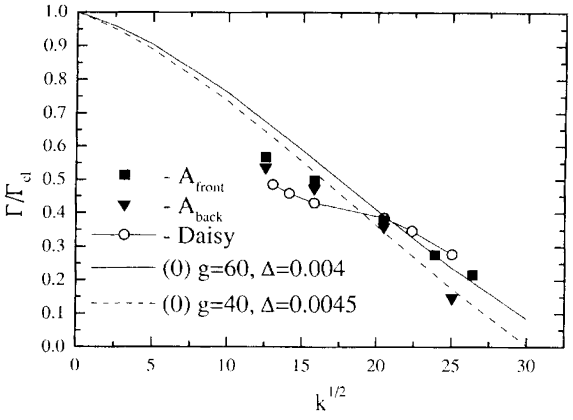

Figure 1. Normalized increment of the instability for the perturbations applied to the ablation front and rear side of the target.

The perturbations are transferred to the ablation front (in the phase opposite to that of problem (a)) and evolve in the Raleigh-Taylor instability mode.

Comparison of the 2D distributions of transversal velocity of vortices (see Figure 2 and pay attention to scale difference) shows that for the problem (b) with perturbation wavelength Δ=1 μm the vortex velocity at t=0.08 ns is order of $V_0^y \approx (0.1 \div 0.2) \cdot 10^7$ cm/s which is almost one order of magnitude higher than the vortex velocity in problem (a) at same moment for the shorter perturbation wave length Λ=0.9 μm. Moreover we saw that the distributions of transversal velocity are deformed due to vortex decay into smaller size vortices. And for the problem (b) this shapes distortion is more significant. The nonzero initial vortex velocity leads

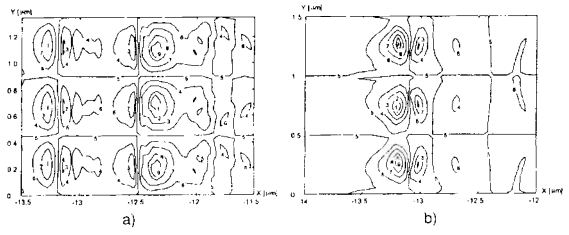

Figure 2. 2D distribution of the transversal component of velocity behind ablation front at target rear side at time t=0.08 ns in calculation for problem (a) (V_{max}=1.95·10^5 cm/s) with perturbation wavelength Λ=0.9 μm and for problem (b) (V_{max}=1.36·10^6 cm/s) with perturbation wavelength Λ=1.0 μm.. Contour levels are (-0.9, -0.75, -0.5, -0.25, 0, 0.25, 0.5, 0.75, 0.9)V_{max}.

to the formation of two smaller vortices very soon i.e. to the generation of the second harmonics. Thus in problem (b) the energy is transported from the first to the second harmonics from the very beginning, that decreases the effective increments of the interface amplitudes. Since the intensity of the second harmonic generation is proportional to $\sim k \left(V_y^0\right)^2$ (the term $(V\nabla)V$

in Eulerian equation), it is obvious that the shorter the perturbation wave length is, the more important is the role the second harmonic. We believe this factor just provides the above mentioned difference in the behavior of the increments in problems (a) and (b).

3. Nonlinear interaction of modes

To study the interaction of modes we chose the perturbation with the wavelengths Λ=10 μm and Λ=2 μm. The wave numbers k of these perturbations are on different sides from k^* for which the maximum increments are achieved. This is convenient in terms of consistency between the growth rates of perturbation for selected modes to make them move synchronously through the linear and nonlinear stages. According to (1), for Λ=10 μm ($k\Delta \approx 3$) the perturbations applied to the rear side decrease towards the ablation front much more slowly than for Λ=2 μm ($k\Delta \approx 15$). Therefore the mass involved in the motion in the transversal direction differs greatly for these two cases.

So one can expect that when the perturbation is transferred by the rarefaction wave to the ablation front, the transversal perturbation velocity will be much higher for Λ=10 μm than for Λ=2 μm. The transversal velocity of the perturbation at the ablation front is just responsible for the behavior of higher harmonics in problems (a) and (b) for Λ=10 μm. The same circumstance should lead to the difference in the evolution pattern of perturbations in two mode problem. We will illustrate our considerations as follows.

For the infinitely thin plate, the perturbations containing two modes with nonzero transversal velocity have, according to [5], the form:

$$x(\xi,t) = \frac{A_1}{2}(\cosh\Gamma_1 t + \cos\Gamma_1 t)\cos k\xi + \frac{A_5}{2}(\cosh\Gamma_5 t + \cos\Gamma_5 t)\cos 5k\xi + \frac{\beta_1}{2}(\sinh\Gamma_1 t - \sin\Gamma_1 t)\cos k\xi + \frac{\beta_5}{2}(\sinh\Gamma_5 t - \sin\Gamma_5 t)\cos 5k\xi \quad (5)$$

$$y(\xi,t) = \xi - \frac{A_1}{2}(\cosh\Gamma_1 t - \cos\Gamma_1 t)\sin k\xi - \frac{A_5}{2}(\cosh\Gamma_5 t - \cos\Gamma_5 t)\sin 5k\xi - \frac{\beta_1}{2}(\sinh\Gamma_1 t + \sin\Gamma_1 t)\sin k\xi - \frac{\beta_5}{2}(\sinh\Gamma_5 t + \sin\Gamma_5 t)\sin 5k\xi \quad (6)$$

where A_1 and A_5 are the initial perturbation amplitudes for the modes with Λ=10 μm and Λ=2 μm, respectively and β_1=V_1/Γ_1, β_5=V_5/Γ_5 where V_1 and V_5 are the transversal velocities of respective modes.

To study the interaction of modes, we choose the initial amplitude of the first harmonic, with somewhat lower increment, to be greater and of the other sign as compared with the initial amplitude of the fifth harmonic: $A_1 k \approx 0.13$ and $5kA_5 \approx -0.1$. Thus the fifth harmonic evolving from the perturbation with the wavelength Λ=10 μm will be on one hand in the counter phase relative to the initial perturbation with Λ=2 μm and on the other hand their amplitudes in the linear stage will be comparable. This would allow to avoid too early jet formation in the short wave mode and to track the modes interaction for a longer time. In problem (a) the transversal velocity of perturbation does not exist. Fig. 3 (left side) presents the shape of plate given by formulas (5), (6) at $\Gamma_1 t$=2.2 when (5), (6) are still single-valued (do not form a loop). In problem (b) we can evaluate the value of V_1 as follows. When the shock wave arrives to the rear side of the target, the maximum value of the transversal velocity is $V_0 = \frac{2}{\gamma-1} c \cdot Ak$ where $c = D\frac{\sqrt{2\gamma(\gamma-1)}}{\gamma+1}$ is the sound speed behind the shock wave moving with the velocity D.

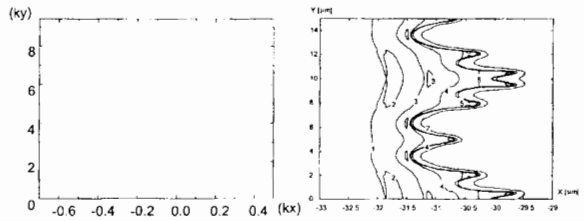

Figure 3. Surface shape (left) of the infinitely thin plate in the case where no transversal velocity exists in the initial perturbations representing the sum of the first and fifth harmonics, and the one (right) obtained from 2D computation. Contour levels are (0.1, 0.25, 0.5, 0.75, 0.9)$\rho_{\max}$.

In our problem $D \approx 10^7$ cm/s. So that $V_0 \approx 1.7 \cdot 10^6$ cm/s with $\gamma=5/3$. The values $V_{1,5}$ from $\beta_{1,5}$ are in fact determined by the average mass velocity along the plate which is related to V_0 by $\overline{V} = \frac{1}{\Delta}\int_0^{\Delta} V_0 \exp(-kx)\,dx = \frac{V_0}{k\Delta}(1-\exp(-k\Delta))$. Here k is the wave number of the corresponding mode and Δ is the plate thickness. Thus we obtain the following estimate: $V_1=6 \cdot 10^5$ cm/s for $\Lambda=10$ μm and $V_5=1.2 \cdot 10^5 << V_1$ for $\Lambda=2$ μm. Fig. 4 (left side) presents the plate shape given to moment of the loss of single-valued pattern. By comparing Figs. 3 and

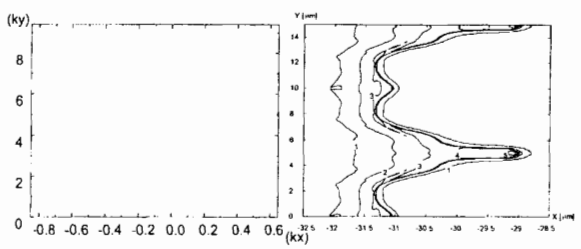

Figure 4. Surface shape (left) of the infinitely thin plate when the initial transversal velocities $V_1=6 \cdot 10^5$ cm/s and $V_2=0$ representing the sum of the first and fifth harmonics, and the one (right) obtained from 2D computation. Contour levels are (0.1, 0.25, 0.5, 0.75, 0.9)$\rho_{\max}$.

4 one can see easily the qualitative difference in the evolution of two mode perturbations for problems (a) and (b).

We computed the evolution of two mode perturbations with the initial amplitudes of the modes mentioned above (kA_1=0.13 for $\Lambda=10$ μm, $5kA_5$=-0.1 for $\Lambda=2$ μm) using MIMOZA code. It is important to note that the computations were run with Lagrangian code without mesh reconfiguration till the target burn- through corresponding to the completion of computations.

Figures 3-4 (right sides) show 2-D density distributions for problems (a) and (b). It is seen that in the nonlinear phase the plate shapes in problems (a) and (b) greatly differ while the difference pattern qualitatively agrees for the infinitely thin plate shown in the same Figures on the left sides. This confirms our statement that the source of difference is Richtmyer-Meshkov stage generating the perturbation with the nonzero transversal velocity in problem (b).

4. Conclusion

1. We considered the evolution of perturbations of the ablation front and found that our computational instability grows rates agree well with the existing theoretical estimations.

2. The perturbations applied to the rear side of the target for relatively large wave lengths ($\Delta/\Lambda \ll 1$) behave similarly to the perturbations at the ablation front. For $\Delta/\Lambda \geq 1$ the shorter the wave length is, the faster is the decrease of the amplitudes growth rate at the interface (and of mass flows) as compared to the perturbations at the ablation front. The reason of such discrepancy is that when the shock wave goes to rear side of the target the Richtmyer-Meshkov instability in problem (b) induce the transversal component of velocity. The amplitude of this component is rather large so convective nonlinearity generates the second harmonic vortices and the increment becomes smaller.

3. The computations were run for the evolution of two-mode perturbations with the wave lengths Λ=10 μm and Λ=2 μm. The MIMOZA code allows to track the interaction of modes in the deep nonlinear phase. It is indicated that the interaction of two modes qualitatively differs for perturbations applied to the ablation front and to the rear side of target. It was demonstrated that the main source of this difference is Richtmyer-Meshkov instability generating transversal velocity perturbations when the shock wave arrives to the rear side of the plate.

References

[1] Sofronov ID, Afanasieva EA, Vinokurov OA *et al.*, MIMOZA code for 2-D and 3-D applications in gasdynamics, In: Development of algorithm and computations in computational physics, Moscow, Keldysh Institute, 277, (1989).

[2] Sofronov ID, Afanasieva EA, Vinokurov OA *et al.*, MIMOZA code for 2D and 3D computations of the fluid mechanic problems at ELBRUS-2, Voprosy atomnoy nauki i tehniki, ser: Matamaticheskoe modelirovanie fizicheskih processov, vyp. 2, 3, (1990).

[3] Verdon CP, McCrory RL and Morse RL, Nonliner effects of multifrequency hydrodinamic instabilities on ablatively accelerated thin shells, Phys. Fluids, 25, 1653, (1982).

[4] Takabe H, Mima K, Montier L and Morse RL, Self-consistent growth rate of the Rayleigh-Taylor instability in an ablatively accelerating plasma, Phys. Fluids, 28, 3676, (1985).

[5] Ott E, Nonlinear evolution of the Rayleigh-Taylor instability of a thin layer, Phys. Rev. Lett., 29, 1429, (1972).

2D and 3D Comparative Study of the Richtmyer-Meshkov Instability Development

O.M. Belotserkovskii[1], V.V. Demchenko[2] and A.M. Oparin[1]
[1]The Institute for Computer-Aided Design, Russian Academy of Sciences
Vtoraya Brestskaya st., 19/18, Moscow, 123056, Russia
[2]Moscow Institute of Physics and Technology, Institutsky lane 9
Dolgoprudny, Moscow Region, 141700, Russia

Abstract: We submit the comparative study results of the Richtmyer-Meshkov instability development for the two-dimensional plane, axially symmetrical and three- dimensional cases of the initial contact surface perturbation for coordinated wave lengths and amplitudes. The reasons for the various rates of growth of the perturbation are analyzed.

1. Introduction

As numerous experimental and theoretical investigations [1 - 6] show, an increase in the spatial dimension of phenomena - the transition from two-dimensional to three-dimensional flows - is accompanied by the appearance of new physical effects, which are either absent or manifest themselves in a degree insufficient for observation in the lower - dimension problems. Among the hydrodynamic instabilities, the three-dimensional flows formed when developing the Richtmyer-Meshkov instability are the least known because, for their numerical simulation, it is necessary to have not only a large-volume difference grid, but also a higher-quality algorithms for considering violent discontinuities, in particular, the shock waves and their interactions, which complicate substantially their experimental diagnostic investigations. In numerical simulation of the Rayleigh-Taylor and Kelvin-Helmholtz instabilities [5 - 7], it was established that, for identical initial amplitudes of perturbations and wavelengths, the rate of growth of the perturbations is higher in the three-dimensional case as compared with the two-dimensional one, while the process of formation of mushroom-shaped structures proceeds slower. The similar results for the Richtmyer-Meshkov instability were obtained in experiments [8]. In this connection, there arise two category of questions associated, first, with studying physical mechanisms that lead to the observable phenomena, and, second, with establishing the relationship of the growth rates for a perturbation amplitude and a number of geometrical and physical quantities: an amplitude and a length of the perturbation, its shape, the Mach and Atwood numbers, thermodynamical properties of substances, etc. that calls for systematical investigations (both theoretical and experimental).

2. 2D and 3D numerical simulation

In this study, we present the results of comparison calculations on the development of the Richtmyer-Meshkov instability for the two-dimensional cartesian case [9] with the corresponding axially symmetrical cylindrical and three-dimensional variants. As an example, we choose the passage of a shock wave from helium to xenon medium at an initial pressure of 0.5 *atm* on the contact boundary and the Mach number of 2.5. The shape of the interface between two media before the beginning of their interaction with the shock wave for the two-dimensional

More information - Email: vdem@cnm.op.mipt.ru

plane and three-dimensional formulations of the problem are presented in Fig. 1 In the two-

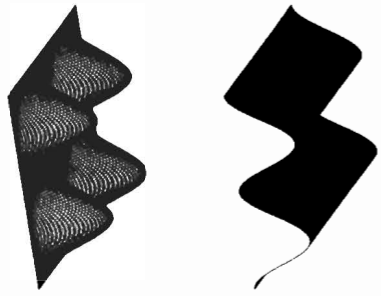

Figure 1. Fragment of the contact surface at an initial instant of time for the two-dimensional plane and three-dimensional formulation of the problem.

dimensional plane case, an initial contact boundary was perturbed by a sinusoidal wave with an 1 *cm* amplitude and a 0.8 *cm* wavelength. In the axially symmetrical variant, the calculated region represents a round-section cylinder, in which the interface between two gases was inside and had a longitudinal axially symmetrical sinusoidal shape with an 1cm amplitude and a $0.8\ \sqrt{2}$ cm diameter. On the lateral boundary of the cylinder, we set the impenetrability conditions. In the three-dimensional case, the entire plane contact boundary was divided into identical $0.8\ \sqrt{2}$ cm squares, in which the circles were inscribed. That part of the surface that occurred inside the inscribed circle was perturbed by the similar way as in the axially symmetrical variant with an 1 *cm* amplitude, whereas the remaining part retained the plane shape. The shock wave began to interact with the contact boundary from the side of the maximum of the perturbation amplitude. The passage of the shock wave through the interface between two gases will be termed further as the shock-wave refraction on the contact boundary. In the plane case for the earlier-set initial conditions, an irregular refraction with generation

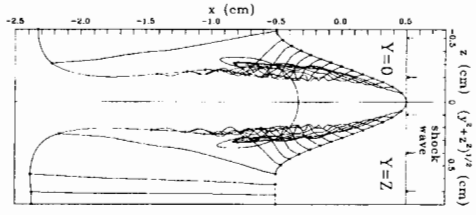

Figure 2. Calculated trajectories for a number of points at the interface since an instant of time $T = 0$ to $T = 20$ *mks* for the three-dimensional formulation of the problem.

of the transmitted and reflected shock waves take place on the larger part of the interface. This fact manifests itself in a curvilinear shape of the reflected shock wave and in the presence of the Mach wave in the vicinity of the refraction point (the point on the contact boundary, where the transmitted,reflected, and incident shock waves intersect). The character of the refraction defines the shape and position of the reflected and transmitted shock waves, the special features of the flow near the contact boundary, and, in the following, the time and the

intensity of generated secondary shock waves, the formation of local regions of elevated and lowered pressures, the positive and negative vorticities, etc. [9]. A substantial distinction of the axially symmetrical and three-dimensional variants from the plane one is the presence of additional flows beyond the fronts of transmitted and reflected shock waves caused by larger spatial dimension of the problem. The interaction between flows beyond the transmitted shock wave in the symmetry axis leads to the appearance of the elevated-pressure regions. As a result, maximum pressures in these regions turn out to be several times higher than those for the two-dimensional plane variant. As time elapses, this results in more intense penetration of

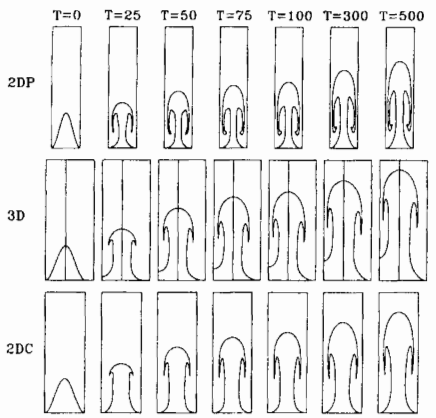

Figure 3. Calculated interface at various instants of time (in mks for three formulation of the problems under comparison: two-dimensional plane, two-dimensional axially symmetrical, and three-dimensional). In the last case, the projections are shown onto the planes $y = 0$ and $y = z$, as in Fig. 2 The scale of axes is given in cm.

a heavy-weight substance into the light-weight one beyond the front of the generated secondary shock wave. As the front of this secondary shock wave goes into the boundary with the light-weight gas, the process of formation of the mushroom-shaped structure is accelerated, although this fact does not lead to an accelerating growth of the mushroom heads as in the plane case. The transformation of the initial sinusoidally perturbed contact boundary into the mushroom-shaped one proceeds as a result of the existence of the basic local vortex structure arising in the process of the refraction [9]. The trajectories of the points of the interface between two media, which are realized in the process of developing the Richtmyer-Meshkov instability in the three-dimensional case and clarify the dynamics of the deformation of the surface, are presented in Fig. 2 The oscillating character of the behavior of a number of trajectories is associated with a multiple passage of the secondary shock waves through this region. The distinction between the three-dimensional and axially symmetrical variants consists in the accelerated motion of the plane part of the perturbation base in the direction of propagation of the incident shock wave and in the lag of neighboring axially symmetrical perturbations in the contact region. The dynamics of modification of the contact boundary for all three cases is shown in Fig. 3 In the calculations, we used the 1131×75 and 800×75 grids for the corresponding two-dimensional variants and $800 \times 75 \times 75$ grid for the three-dimensional variant. As a perturbation amplitude used below, we took a distance between the contact-boundary points that penetrated most deep

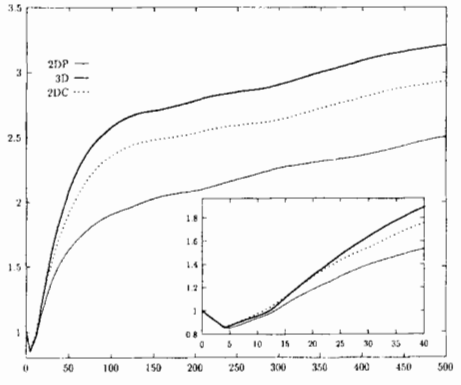

Figure 4. Change in perturbation amplitude with time for three variants under investigation.

into each of the gases under consideration. A change in the perturbation amplitude with time for three variants studied is presented in Fig. 4 For these variants of the initial formulation of the problem, the leading growth of the perturbation amplitude is observed in the axially symmetrical and three-dimensional cases as compared to the plane two-dimensional variant since completion of the refraction of the shock wave and to completion of the calculations. In the first $15 - 20$ mks, we observe a more accelerated growth of the amplitude in the axially symmetrical cylindrical case as compared with the three-dimensional case. In later instants of time, the situation is changed to the opposite, whereas the amplitude of the three-dimensional perturbation exceeds the cylindrical one.

Acknowledgement. This work is supported by ISTC (grant N° 029-94), RFBR (grant N° 94-01-01390)

References

[1] Youngs DL, Phys.Fluids A, 3, 5, 1312-1320, (1991).
[2] Town RP, Bell AR, Phys.Rev.Lett., 67, 14, 1863-1866, (1991).
[3] Glimm J, Li XL, Menikoff R *et al.*, Phys.Fluids A, 2, 11, 2046-2054, (1990).
[4] Remington BA, Haan SW *et al.*, Phys.Fluids B, 4, 4, 967-978, (1992).
[5] Ofer D, Shvarts D *et al.*, Phys.Fluids B, 4, 3549, (1992).
[6] Read KI, Physica D12, 45-58, (1984).
[7] Yabe T, Hoshino H *et al.*, Phys.Rev A, 44, 4, 2756-2758, (1991).
[8] Zaytsev S, Aleshin A, Lazareva E *et al.*, Proc. 4th Int. Workshop on Physics of Compressible Turbulent Mixing, Cambridge, 291-296, (1993).
[9] Belotserkovskii OM, Demchenko VV, Oparin AM, Dokl. Akad. Nauk, 334, 5, 581-583, (1994).

How the Film May Control the Gas-Gas Turbulent Mixing Development in Shock Tube Experiments

M.V. Bliznetsov, Y.A. Vlasov, V.I. Dudin, E.E. Meshkov, A.A. Nikulin, V.A. Til'kunov, A.I. Tolshmyakov and S.A. Kholkin
Russian Federal Nuclear Center - Institute of Experimental Physics
Prospect Mira 37, 607190, Sarov, Nizhni Novgorod Reg., Russia

1. Shock-tube turbulent mixing (TM) experiments [1, 2, 3, 4] have the interface of interest defined using thin ($\sim 0.5\ \mu m$) polymer films. Researchers use to make these films by themselves. The authors are aware of the two such film types: type L (used by VNIIEF experiments [1, 4]) and type X (used in experiments by CALTECH (US) and CEU-M (France) [3]). Comparative mechanical studies [5] of these films have shown L-type film to have 3-5 times lower stress limit than the X-type, and this may result in significant difference in the TM grown pattern for experiments using different film types. Described below are shock tube experiments in the setup as [1] using L and X film with shadowgraph and laser sheet [4] being visualization techniques for TM zone. The experimental data clearly show the qualitative and quantitative difference in TM growth behavior between the two cases and also support the TM zone measurements as described in [1]. A technique is described for a density-varied film; this approach may provide normal TM grown even for X film.

2. The experiments were performed in a shock tube using the setup as described in [1]. The shock tube of $120 \times 40\ mm^2$ cross-section with transparent side walls had the downflow part of its channel made up of mated sections and was stopped at the end with a plug (stiff wall). The end channel section was separated with a thin film, its specific mass $4{\cdot}10^{-5}\ g/cm^2$, thereby making a confinement to be filled with helium. The remaining channel space contained air at at the atmospheric pressure. The flow pattern in the test section was visualized in two ways:

- using IAB-451 shadowgraphy device in optical conjunction with VKF13 camera;
- here, consecutive photos could be obtained at different times (as in [1, 6]);
- using laser sheet technique, whereby each experiment had one photo taken at a specified time (as in [4]).

The latter case is where the air-filled section adjoining the interface in question was also separated to add into it a little cigarette smoke which is a laser scatterer. The initial smoke density was selected to make both the scattered radiation absorption and secondary scattering insignificant. The amount of smoke was measured from experiment to experiment and keeping approximately unvaried. The backlighter used was a pulsed solid-state YAG-Nd laser with the beam conversion to second harmonic by LiJO3 crystal. The laser provided the output beam at $\lambda = 532\ mm$ and $\sim 12\ mJ$ energy, and the pulse width at half maximum of $\sim 16\ ns$. Optically, cylindrical lenses were used to shape the laser beam into a thin ($\sim 1\ mm$) sheet of light $\sim 120\ mm$ wide. When produced by the lens optics, this sheet of light was directed along the shock-tube channel through the transparent stopper in the downflow section from the lighter

More information - Email: otd03_2305@spd.vniief.ru

helium gas free of any impurity, and almost unscathed it would reach the air region containing impurities. Laser beam scattering occurred in the impurity-containing gas, which was followed with a photo camera in the direction normally to the laser sheet. As long as smoke particles being very small (0.1-1 μm) should virtually follow the air flow, the special distributions of gas with impurity (air) and impurity-free gas (helium) were visualized sectionally in the image plane. Based on the upper estimate, the smoke particles can follow the air flow in fluctuations of $\geq$ 0.6 mm typical dimension [6].

3. It is shown in [5], that the film should meet the following requirements for normal *TM* zone development: (a) it must be of adequately low strength and elasticity; and (b) show large enough perturbations (represented as thickness variation). Comparatively, shadow photos from *L*-film and *X*-film *TM* experiments [5] show different patterns. However, shadowgraphy is what provides an integrated view of *TM* zone; a more evident and positive distinction between the *TM* zone patterns for the two film types can be obtained from photos taken by laser-sheet technique (Fig. 1).

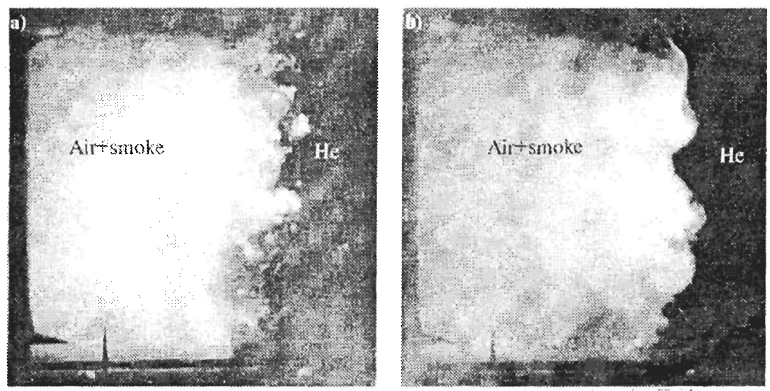

Figure 1. "Laser sheet" experimental observations: (a) *L*-film, (b) *X*-film.

Fig. 1a contains the image of *TM* zone for the experiment using *L* film (at the time 810 μs), and Fig. 1b presents a similar image for *X*-film experiment (t – 850 μs). In the former case, the film (L) is broken down into smaller pieces, and thus a standard *TM* zone is developing as observed in the experiments of [4]. In the latter, the film (X) would be torn off on the perimeter, bending, but it would move as a single piece - and no turbulent mixing zone would be developed then. There would be near the wall a strong bubble of helium to develop and move into the air.

4. There were some experiments, where X film rupture by incident shock wave was performed with *3D* perturbations specified on the gas-gas interface using a suitable technique. To this and, the gas-separating thin film was to be provided with circular thickening bosses. Their arrangement is shown in Fig. 2. The bosses had 5 mm spacing and 2.5 mm diameter, their thickness variable. The thickness in test 1 was $\delta \cong 0.2$ μs, and $\delta \cong 0.9$ μs in test 2.

Streak photos of the experiments are shown in Fig. 3. It can be seen from the streak photos, that the film in test1 (see Fig. 2a) has insufficient mass at thickened points to get broken by the incident shock wave or the subsequent one reflecting from the stiff wall. Even at later times, the film can be well seen as unbroken, and the *TMZ* develops but near the wall. What

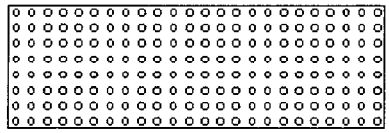

Figure 2. Tailored perturbations arranged on the film surface.

was observed by test 2 is different. The film gets broken under the incident shock wave whose passage is immediately followed by the *TMZ* starting to develop. The time-dependent *TMZ* thickness of these tests is shown in Fig. 4. *TMZ* in test 1 has a much smaller thickness, than in test 2.

However,these thickness values are yet overrated, because *TMZ* thickness measurements are significantly affected by the flow in the near-wall layer.

Away from the wall, the film is either safe or broken into fairly big pieces, that is why the *TMZ* thickness here is markedly smaller than the measured, if at all.

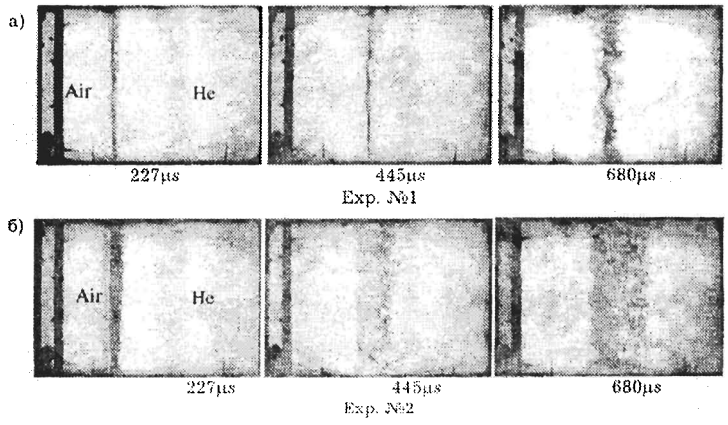

Figure 3. Streak photos of *TMZ* development with *3D* disturbances a) δ=0.2μm b) δ=0.9μm.

Thus it has been found experimentally, that the TMZ thickness in shock-tube experiments being different from researcher to researcher [1, 2, 3, 4] arises from different properties of the films used for gas separation. An approach is suggested, whereby *3D* perturbations can be made on the gas-separating film. These perturbations should result in breaking the *X*-type film by an incident shock wave and the following development of a standard TMZ across the entire channel section. The proposed approach can provide an opportunity to:

- control within certain limits the initial perturbations spectrum at the interface of interest;
- follow *3D* perturbations evolution into the later stages until initial perturbations have been "forgotten".

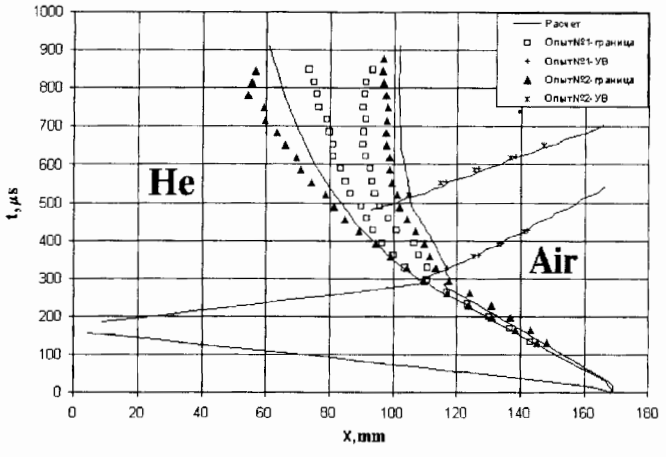

Figure 4.

Acknowledgement. The study has been performed under the ISTC Project 029.

References

[1] Andronov VA, Bakhrakh SM, Meshkov EE, Mokhov VN, Nikiforov VV, Pevnitskiy AV, Tolshmyakov AI, Turbulent Mixing at Interface Accelerated by Shocks (in Russian), JhETF, 71, 2(8), 806-811, (1976).

[2] Brouillette M and Sturtevant B, Growth Induced by Multiple Shock Waves Normally Incident on Plane Gaseous Interfaces, Physica D37, 248, (1989).

[3] Rodriguez G, Galametz I, Croso H and Haas J-F, Richtmyer-Meshkov Instability in a Vertical Shock Tube, Proc. of the 4^{th} IWPCTM, Cambridge, England, Edited by PF Linden, DL Youngs and SB Dalziel, 260, (1993).

[4] Meshkov EE, Nikiforov VV, Tolshmyakov AI, On the Turbulent Mixing Zone Strukture at a Gas-Gas Interface Accelerated by SW (in Russian), FGV, 3, 71-77, (1990).

[5] Abakumov AI, Meshkov EE, Nizovtsev PN, Nikiforov VV, Sadilov NN, Tilkunov VA, Tolshmyakov AI, Tochilin VO, Kholkin SI, Shock Tube Experiments: Film Effects on the Turbulent Mixing Zone Development, Proc. of the 5^{th} IWPCTM, Stony Brook (NY), USA, (1995).

[6] Andronov VA, Bakhrakh SM, Meshkov EE, Nikiforov VV, Pevnitskiy AV, Tolshmyakov AI, Experimental Investigation and Numerical Simulation of Turbulent Mixing in Unidimensional Flows (in Russian), DAN, 264, 1, 76-82, (1982).

Numerical Analysis of the Rayleigh-Taylor Instability at the Ablation Front

S.V. Bondarenko and G.G. Kochemasov
Russian Federal Nuclear Center - Institute of Experimental Physics
Prospect Mira 37, 607190, Sarov, Nizhni Novgorod Reg., Russia

Abstract: The linear stability of an ablating plasma is investigated as an eigenvalue problem for both flat and spherical stationary ablation flows. We use for the first time orthogonalization scheme for improving calculation accuracy. It is found that calculated growth rate is accurately expressed in the Takabe form. Calculated parameters in this dependence are close to the Takabe ones for the case of pronounced sphericity of the flow. Ablation growth rate for the flat flow is found to agree well with the analytical dependence [1] for large Froude numbers and isobaric approximation for the thermal conductivity equation.

1. Introduction

Significant progress has been achieved recently in understanding linear stage of Rayleigh- Taylor instability development in plane foils and spherical shells under laser acceleration [1, 2, 3]. Numerical methods [1] and analytical models [2, 3] were developed. The paper presents Raleigh-Taylor modes increment calculations for plane foils under laser acceleration as a development of [4]. Unlike [1] integration scheme with step-by-step orthogonalization [5, 6] is used here, which allows to increase calculation accuracy and extend plasma conditions range good for simulation.

2. Statment of the problem

Ablation flow in heat conduction wave was used in our problem as a non-perturbed flow. Such flow considered in a system of reference related to ablation front, gas dynamics flow in a certain vicinity of the ablation front (consider it wide enough) may be thought of as stationary. A class of stationary ablation flows for spherical and plane geometry was found in [4]. Rayleigh-Taylor instability growth increments were studied at ablation front in electron heat conduction wave with the coefficient $k_e = k_o T^{\frac{5}{2}}$. For instability increment calculation at large enough transversal perturbation wave numbers k it turned out necessary to "extend" non-perturbed gas dynamics flow profiles in cold region, where the flow appears to be significantly limited spatially. ρ, T,v profiles were analytically extended in this region using flow profiles in so called "isothermal atmosphere" for this purpose. Typical non-perturbed flow profiles are given in Fig. 1. Plane stationary flow perturbation in the system of reference related to ablation front for a certain gas dynamics quantity can be written in the form:

$$\phi_1\left(\vec{r},t\right) = \bar{\phi}\left(x\right)\exp(\Lambda t + iky)$$

For spherical stationary flow, correspondingly,

$$\phi\left(\vec{r},t\right) = \overline{\phi}\left(r\right)Y_{lm}\left(\theta,\varphi\right)$$

More information - Email: belkov@otd13.vniief.ru

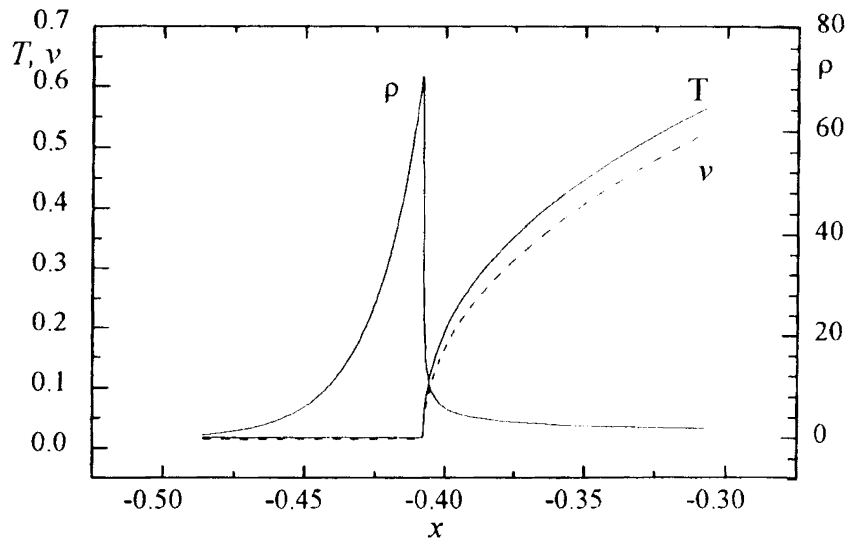

Figure 1. Dimensionless density ρ, temperature T and velocity v profiles in plane non-perturbed flow.

where Λ is instability increment value for perturbation with wave number k (or index l).

The set of equations describing gas dynamics quantities perturbations is obtained by gas dynamics equations linearization. Linearization was conducted in [1] for the case of spherical flow geometry (the set of equations is similar for plane flow).

The condition allowing to find the increment Λ value for a given k (or l) is that perturbations vanish withdrawing the ablation front. We follow the results of [4] in setting up selfconsistent perturbation problem.

The set of equations describing perturbations is a system of ordinary difference equations of the 5-th order containing non-perturbed gas dynamics quantities profiles and their derivatives along the direction of non-homogeneity as coefficients. The system was integrated numerically. The procedure of boundary conditions setting-up used here was described in [4] in sufficient detail. The condition of Λ determination for a given k (or l) is the condition (5) of sewing together integral curves meeting boundary conditions in some intermediate flow point x^* (we chose ablation front as the point x^*: $x^* = x_a$):

$$\det \left\| \begin{array}{cccc} \rho_1^{(1)}(x_a) & .. & .. & \rho_1^{(5)}(x_a) \\ v_{1x}^{(1)}(x_a) & .. & .. & v_{1x}^{(1)}(x_a) \\ v_{1y}^{(1)}(x_a) & .. & .. & v_{1y}^{(1)}(x_a) \\ Q_{1x}^{(1)}(x_a) & .. & .. & Q_{1x}^{(1)}(x_a) \\ T_1^{(1)}(x_a) & .. & .. & T_1^{(1)}(x_a) \end{array} \right\|$$

where the superscript in brackets shows the number of integral curve to which the column of gas dynamics quantities perturbation values is attributed.

3. Integration methods for the set of equations for perturbations

In the process of numerical integration of the set of equations for perturbations difficulties occur, connected to the loss of one (or more) solutions due to the existence of fast growing solutions, both in cold flow region (to the left from ablation front, see Fig. 1, i.e. at $x \leq x_a$) and in hot plasma corona region ($x \geq x_a$). The way to avoid losing one of the two solutions while numerically integrating the system in cold region is described in [1]. It implies in separating a mode, corresponding to heat conduction, which has two orders larger growth factor, and integrating the reduced system. Similar difficulties occur while integrating in hot corona region as well , at sufficiently steep profile fronts of gas dynamics quantities of non-perturbed flow near ablation front. In order not to lose all three linear independent solutions at numerical integration in this region the scheme with step-by-step orthogonalization was used. It means, Schmidt orthogonalization of three eigenvectors was conducted after each numerical integration step. Monographs [5, 6] give systematic presentation of orthogonalization methods application for numerical analysis of gas dynamics stability problems. Step-by-step orthogonalization allows not to lose all three linear independent solutions while integrating from corona hot sonic point to ablation front. It is easily seen that application of integration scheme with orthogonalization in the situation when no solution is lost leads to substitution of three columns of determinant (1) by their linear combination, which does not result in determinant zero creep.

Since non-perturbed flow profiles were also found by numerical integration of the set of equations, the values of non-perturbed quantities $\widetilde{\rho}_0, \widetilde{v}_0, \widetilde{T}_0$ and their derivatives between discrete points of non-perturbed system were determined by linear interpolation.

4. Calculation results and discussion

Typical ablation instability increment dispersion curve $\Lambda(k)$ for the case of electron heat conduction calculated for plane geometry is shown in Fig. 2. Ablation flow in this case is characterized by density ratio $\widetilde{\rho}_a = \frac{\rho_a}{\rho_s} \approx 70$ (where ρ_a is non-perturbed flow density at ablation front, ρ_s is density at hot sonic point). The figure also shows approximation of the calculated curve by the formula

$$\Lambda = \alpha\sqrt{kg} - \beta k\, v_a$$

proposed in [1] for functional representation of numerical results on instability increments in spherical flow geometry. Analytical dependencies for Rayleigh-Taylor instability increments in some simplifying assumptions were obtained for the case of plane ablation flow in a number of papers. Thus, the expression for $\Lambda(k)$ was obtained in [2] in the assumption of isobaric character of non-perturbed flow and for large values of the Froude number Fr=4.1, where $L_0 = \frac{\gamma-1}{\gamma}\frac{k_0 T_a^{\frac{5}{2}}}{A\rho_a v_a}$ – is typical length scale on ablation front in this problem (for calculation presented in Fig. 2 Fr=4.1). Analytical dependence of the form

$$\Lambda = \sqrt{A_T kg - A_T^2 k^2 v_a v_{b0}} - (1 + A_T)\, k v_a$$
$$A_T = \frac{1-\mu_0\varepsilon^{\frac{2}{5}}}{1+\mu_0\varepsilon^{\frac{2}{5}}},\ v_{b0} = \frac{v_a}{\mu_0\varepsilon^{\frac{2}{5}}}$$
$$\mu_0 = 1.031$$

was obtained for Λ. The formula for instability increment of plane ablation flow was also obtained in [3]:

$$\Lambda = \sqrt{kg\left(A - \frac{2\phi_0 - 1 + r_D}{1 + r_D}\right) + \left(\frac{1+\phi_0}{1+r_D}\right)^2} - \frac{1+\phi_0}{1+r_D} k\, v_a$$

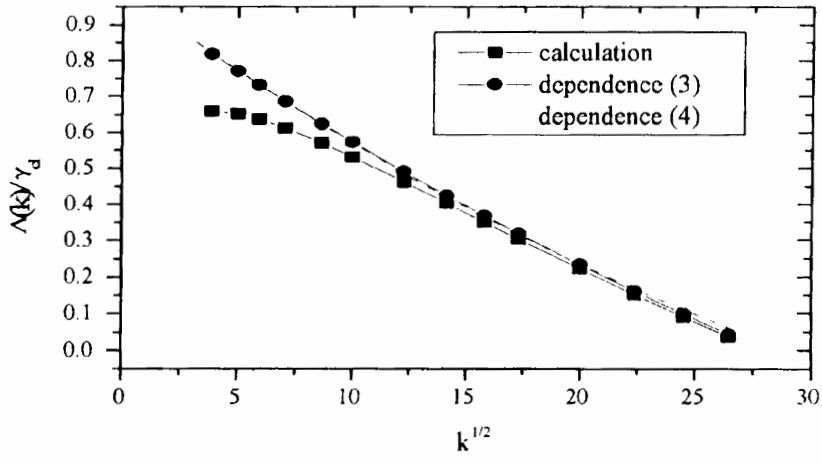

Figure 2. Raleigh-Taylor instability increments normalized to the classical increment as functions of $k^{1/2}$ for ρ_a/ρ_s=70. The dependencies (3) and (4) as well as approximation (2) with α=0.825 and β=2.11 are also shown.

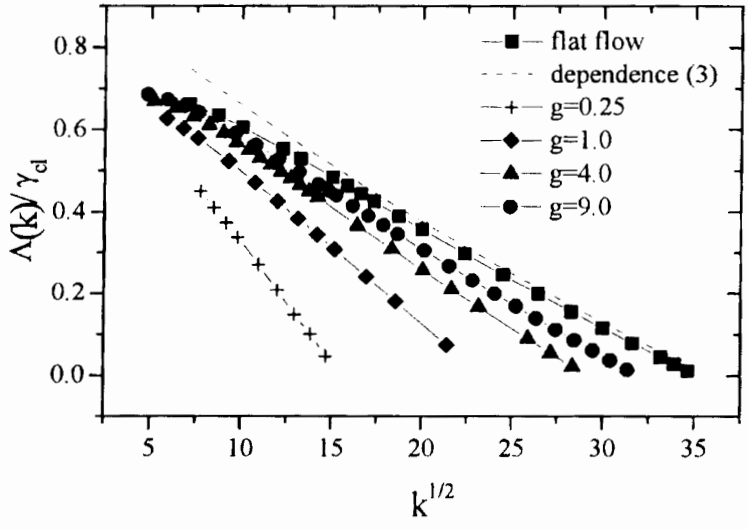

Figure 3. Calculated curves of instability increments of spherical ablation flow for different effective acceleration normalized to classical Raleigh-Taylor instability increments. Dashed lines show corresponding increment values determined by the formula (3).

where r_D is the ratio of densities on ablation front and in hot corona at the distance of $1/2k$ from ablation front, $\phi_0 = 1 + kL_a$, where $L_a = \frac{3}{5}\frac{\chi_a}{\rho_a v_a}$ is typical length scale at ablation front, $\chi_a = \frac{k_0 T_a^{\frac{5}{2}}}{C_V}$ – i is heat conduction coefficient.

Analytical dependencies (3), (4), are also shown in Fig. 2. These dependencies are normalized to classical increment and plotted as functions of $\widetilde{k}^{\frac{1}{2}}$. The quantity r_D (see formula (4)) was calculated using non-perturbed density profile (it should be noted that increment values calculated using the formula (4) depend strongly on the distance between initial integration point and ablation front while calculating r_D).

In the case of ablation flow spherical geometry one more parameter of the dimension of length is present in the equations describing non-perturbed stationary flow, namely: typical region radius (for example, sonic point radius r_s). Therefore, the dispersion curves set turns out to be two-parametric. It is convenient to use characteristic length scale of the plane problem $x_g = \frac{v_s^2}{g}$ for the purpose of numerical results comparison. Typical lengths ratio is $\frac{r_s}{x_g} = \frac{r_s g}{v_s^2}$. Let us find also, following [1], perturbation wave number for spherical problem $k = l/r_a$. At fixed density ratio in stationary spherical ablation flow the set of dispersion curves is determined by the only parameter. Dispersion curves $\Lambda(k)$ for $\widetilde{g} = 0.25, 1, 4, 9$ for fixed $\rho_a/\rho_s \approx 90$ are shown in Fig. 3. Dispersion curve for plane geometry and analytical dependence (3) for the same ρ_a/ρ_s are shown there as well. It is seen that plane ablation flow Rayleigh-Taylor instability dispersion curve is the upper limiting envelope of the set of spherical dispersion curves for $\widetilde{g} \gg 1$ for fixed ρ_a/ρ_s. Coefficients α and β for approximation of spherical and plane numerical solutions by functional dependency of the form (2) for the given ratio ρ_a/ρ_s , presented in Table 1, also demonstrate the existence of the mentioned limiting envelope.

References

[1] Takabe H, Montierth L and Morse RL, Self-consistent eigenvalue analysis of Rayleigh-Taylor instabilityin an ablating plasma, Phys. Fluids, 26, 8, (1983). Takabe H and Mima K, Self-consistent growth rate of the Rayleigh-Taylor instability in an ablatively accelerating plasma, Fhys. Fluids, 28, 12, (1985).

[2] Goncharov VN, Betti RL, McCrory RL, Sorotokin P and Verdon CP, Self-consistent analysis of ablation fronts with large Froude numbers, Phys. Plasmas, 3, 1402, (1996).

[3] Atzeni S, Ciampi ML, Piriz AR *et al.*, Inertial fusion target studies: heavy-ion target design and fast ignitor physics, Montreal, Canada, 7-11 October, 1996.

[4] Montierth LM and Morse RL, Stationary flow model of ablatively imploded spherical shells, Phys. Fluids B, 2, 2, (1990).

[5] Betchov R and Kriminale V, The questions of hydrodynamical stability, Moscow, Mir Publishers, (1971).

[6] Gershuni GZ, Zhukhovitskii and Nepomnyaschii AA, Stability of convective flows, Moscow, Nauka Publishers, (1989).

Absolute Equation of State Measurements of Shocked Liquid Deuterium up to 200 GPa (2 Mbar)

K.S. Budil[1], L.B. Da Silva[1], P. Celliers[1], G.W. Collins[1], N.C. Holmes[1], T.W. Barbee Jr.[1], B.A. Hammel[1], J.D. Kilkenny[1], R.J. Wallace[1], M. Ross[1], G. Chiu[2], A. Ng[2] and R. Cauble[1]
[1]Lawrence Livermore National Laboratory
P. O. Box 808, L-473, Livermore, CA 94550, USA
[2]University of British Columbia, Vancouver, B. C., Canada

Abstract: We present results of the first measurements of density, shock speed and particle speed in compressed liquid deuterium at pressures in excess of 1 Mbar. We have performed equation of state (EOS) measurements on the principal Hugoniot of liquid deuterium from 0.2 to 2 Mbar. We employ high-resolution radiography to simultaneously measure the shock and particle speeds in the deuterium, as well as to directly measure the compression of the sample. We are also attempting to measure the color temperature of the shocked D_2. Key to this effort is the development and implementation of interferometric methods in order to carefully characterize the profile and steadiness of the shock and the level of preheat in the samples. These experiments allow us to differentiate between the accepted EOS model for D_2 and a new model which includes the effects of molecular dissociation on the EOS.

1. Introduction

Experimentally verified equations of state do not exist for many materials in the multi-Mbar regime due to the inherent difficulties of achieving such high pressures. While high intensity lasers can readily produce shocks in this pressure regime, the requirements for an accurate EOS measurement present formidable difficulties for laser experiments. Thus, there have been few laser-driven EOS experiments despite the fact that the EOS is crucial for hydrodynamic descriptions of laser experiments. Accuracy sufficient to differentiate between various EOS models is difficult to obtain for many reasons. The initial condition of the sample may be difficult to determine due to preheat, the shock may not be spatially uniform and planar or its velocity may not be steady in time.

The EOS of hydrogen and its isotopes at high pressure are extremely important to the physics of high density matter [1, 2]. The EOS in the 1-10 Mbar regime largely determines the internal structure of Jovian planets [3]. In inertial confinement fusion (ICF), the performance of deuterated capsules is critically dependent upon shock timing and efficient compression which in turn rely on the EOS [4]. While several theoretical models of the EOS of hydrogen have been proposed, [5, 6, 7, 8] outstanding questions still exist, for instance the transition from a diatomic to a monatomic fluid. Previous experiments have obtained data for hydrogen at pressures greater than 100 GPa by both dynamic shock compression and static compression in diamond anvil cells [9]. The temperatures and densities achievable via shock compression are directly applicable to ICF and the most accurate data were produced using light gas guns [10, 11]. The properties of deuterium shocked to high pressures by a high intensity laser have previously been examined, but the EOS of the material was not determined [12].

More information - Email: budil1@llnl.gov

While early impedence match measurements of the EOS of H_2 and D_2 were found to be in good agreement with a model which neglected dissociation, [10] recent experiments revealed significantly lower temperatures than predicted for pressures higher than 20 GPa [11]. A new model that incorporates the effect of dissociation of the molecular fluid was formulated [11]. It is based on the ideal mixing of molecular and monatomic metallic hydrogen states and includes a single adjustable parameter. This model predicts that deuterium is significantly more compressible in the 20-1000 GPa regime, predicting 50% density that calculated from the previous model and the D_2 table in the widely-used Sesame EOS library [13].

2. Experimental design

2.1. Shock compression of materials

Shock compression utilizeing a single shock drives a fluid to a point on the principal Hugoniot. The Hugoniot is the locus of all final states of pressure, energy and density that can be achieved behind a single shock wave passing through a material from an initial state. The shock speed U_s, particle speed U_p, the pressure P, and final density ρ are related by

$$P - P_o = \rho_o U_s U_p \tag{1}$$

and

$$\rho/\rho_o = U_s/(U_s - U_p), \tag{2}$$

where ρ_o is the initial denstiy, P_o is the initial pressure and ρ/ρ_o is the compression [14]. These relations require that two independent parameters be measured to obtain an absolute data point.

In these experiments, liquid deuterium was compressed by a laser-driven shock wave launched from an aluminum pusher. High resolution streaked radiographs of the aluminum-D_2 interface were obtained which allow direct measurement of the shock speed in the deuterium, the particle speed (Al pusher speed), and compression, which yields the density provided the initial density is well-known.

2.2. Experimental configuration

The experimental configuration is illustrated in Figure 1. Figure 1a shows the cryogenic cell

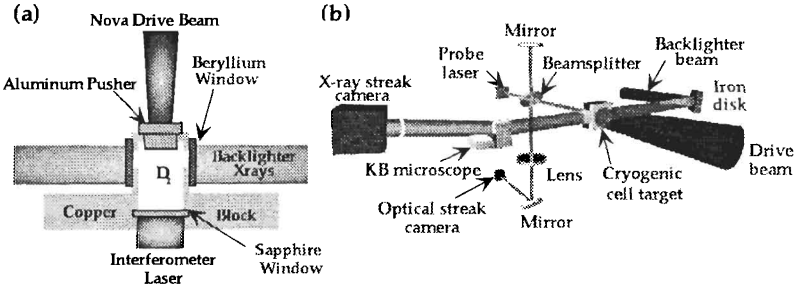

Figure 1. (a) Diagram of the cryogenic cell used in the experiment. (b) Experimental layout for the deuterium EOS measurement.

used to contain the liquid D_2. The cell was a cylinder 450 μm long by 1 mm in diameter

machined into a solid copper block. A solid aluminum pusher sealed one end of the cell. Pusher thicknesses of 100, 180 and 250 μm were used for various experiments. The side of the aluminum external to the cell was coated with 15 to 25 μm of polystyrene and a 100 nm layer of aluminum. The Al overcoat prevents direct laser shine through the plastic and the polystyrene ablator prevented direct laser ablation of the Al pusher. The low Z material minimizes x-ray emission and consequent preheating of the pusher from x rays produced in the ablator plasma. A 500 μm diameter window was drilled into each side of the cell and sealed with a 5 μm thick beryllium foil to allow the backlighter x rays to transmit through the cell.

The cell was loaded with liquid D_2 (99.98% pure containing 33% J=1 molecules) at 19.4-19.8 K (monitored to within 0.05 K) and then pressurized to a few hundred Torr. The D_2 density was determined from the saturation curve [15] and was typically 0.171 g/cm^3. The initial density ρ_o was known for each experiment with an uncertainty of less that 0.1%.

The targets were directly-driven by one beam of the Nova laser at $\lambda = 527$ μm as illustrated in Figure 1b. The laser beam irradiance profile was smoothed with a kinoform phase plate and focused onto the target in an elliptical spot with major and minor diameters of up to 900 and 600 μm respectively, depending upon the focusing. The laser pulse was 8 or 10 ns square and produced intensities in the range of 5×10^{12} to 2×10^{14} W/cm^2. A second Nova beam was focused onto an iron foil (10 ns at 6×10^{13} W/cm^2) to generate 800 eV x rays to radiograph the sample. The backlighter was placed 12 cm away from the target cell to eliminate heating of the cell and to produce a near-collimated x-ray source. The transmitted x rays were imaged by a Kirkpatrick-Baez (K-B) microscope onto a streak camera. The K-B used two tungsten/rhenium-coated 6-m-radius of curvature spherical mirrors which provided a bandpass of 750-840 eV with a 2.5 mrad collection half-angle. The resolution of the K-B microscope was found to be better than 3 μm over a 300 μm field of view and it was used at magnifications of 33$\times$ and 82$\times$. A strip 300 μm long by 5 to 30 μm wide was imaged depending upon the magnification.

2.3. Target characterization

Since the accuracy of the measurement is critically dependent upon the initial conditions of the experiment, some effort was expended to characterize the shock planarity and steadiness as well as the level of preheating experienced by the deuterium [16]. Figure 2 shows interferograms obtained with a 100 μm thick pusher overcoated with a 20 μm thick polystyrene ablator irradiated at two intensities. When the target was at $\sim 8.5 \times 10^{13}$W/cm^2, motion of the aluminum-deuterium interface is clearly observed beginning approximately 2 ns prior to shock breakout as shown in Figure 2a. A simple thermal expansion model estimates the temperature at this surface to be $\sim$ 1000 K. When the intensity was reduced to $\sim 1.5 \times 10^{13}$W/cm^2, as shown in Figure 2b, no evidence of preheating (T $<$ 400 K) is observed. The secondary curvature of the shock front is due to the "tophat", or reentrant, design of the pusher. Aluminum plasma from the sides of the tophat moves into the path of the drive beam during its 8 ns duration, effectively reducing the drive laser intensity at the outer perimeter of the aluminum, slowing down the shock considerably at the edges of the target. The shock in either case is observed to be planar and uniform to within $\pm$ 2.5 μm over the central 350 μm of the target, quite adequate for these measurements.

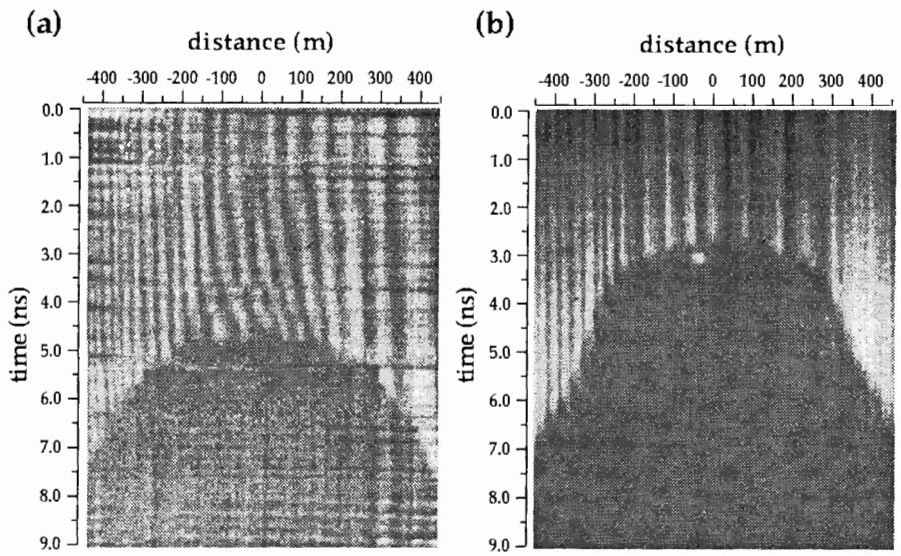

Figure 2. (a) Interferogram obtained from a target irradiated at $\sim 8.5 \times 10^{13}$W/cm^2. (b) Interferogram obtained from a target irradiated at $\sim 1.5 \times 10^{13}$W/cm^2.

3. Experimental results

Once the issue of preheat and shock planarity had been addressed, streaked radiography of the deuterium-filled cells was utilized to measure the shock speed, particle speed, and compression of the material. A representative radiograph is shown in Figure 3. Here a drive irradiance of

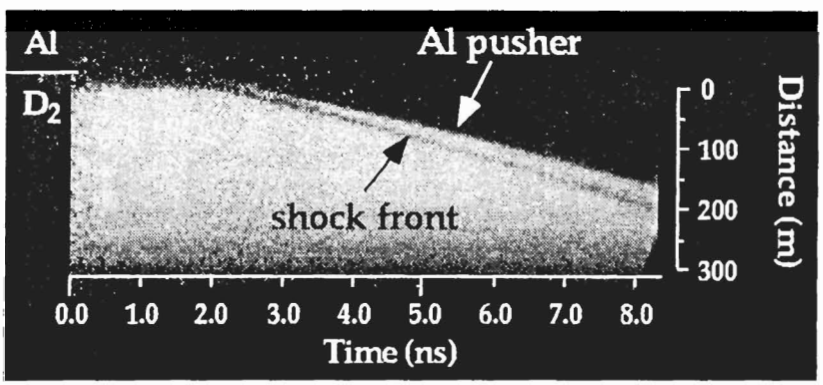

Figure 3. Streaked radiograph of the aluminum-deuterium interface used to determine the shock and particle speeds and the compression of the deuterium.

10^{14} W/cm^2 over 8 ns was used. Bright regions of the image correspond to high transmission of the backlighter x rays. At 2 ns the laser-driven shock wave crosses the aluminum-deuterium interface and the pusher begins to move at a steady speed, the particle speed. The shock front

can be seen moving through the deuterium as a dark line in the image produced by backlighter x rays being refracted by the jump in density between the shocked and unshocked deuterium, similar to the Schlieren technique for detecting density gradients. Shock reverberations in the pusher cause a second shock to be launched into the D_2 at approximately 6 ns, and the propogation of the shock front and interface are both steady until its arrival. Only data from the steady-propagation region were used in the EOS calculations.

The measured shock speeds and final densities are shown in Figure 4a. The open squares

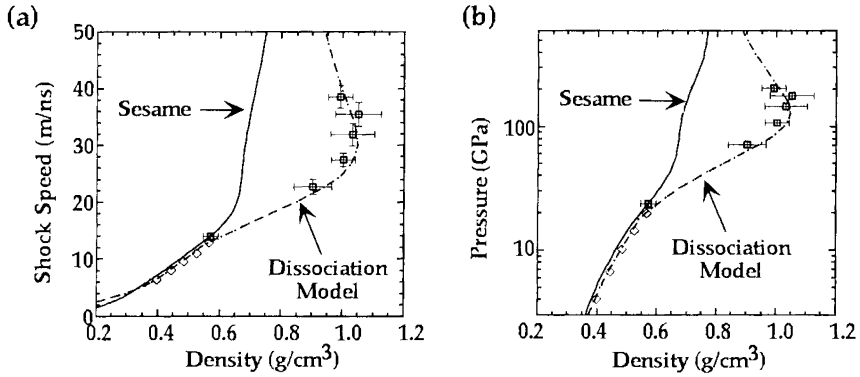

Figure 4. (a) Shock speed versus density. (b) Pressure versus density. In both plots, open diamonds represent gas gun data from Nellis *et al.* and open squares with error bars are from this measurement.

with error bars are from this measurement and the accuracy with which the slopes of the shock and interface trajectories can be measured largely determines the error bars on the data. Hugoniots calculated using the Sesame EOS table [14] and the new dissociation model [11] are shown along with data obtained from previous gas gun experiments [10]. Our data are in good agreement with the gas gun results at low compression while the higher compression data deviate significantly from the Sesame prediction. The data support the higher compression predicted by the dissociation model and we therefore conclude that molecular dissociation is indeed significant in hydrogen isotopes at compressions near 100 Gpa. Figure 4b shows pressure versus density for these measurements.

4. Conclusion

We have presented the first measurement of density, shock and particle speeds in liquid deuterium at pressures ranging from 25 to 210 Gpa. Interferometric characterization of the shock and aluminum pusher showed that the laser-driven shock wave was planar and that there was no significant preheating of the deuterium. High-resolution, time-resolved radiographs confirm that the shock is steady in time and allow for determination of absolute Hugoniot data. These data strongly indicate that a dissociative transition from a diatomic to a monatomic fluid state occurs in the deuterium and provide support for a revised equation of state model in this pressure regime.

Acknowledgement. The authors would like to thank S. Dixit for the kinoform phase plate, D. A. Young, F. J. Rogers and R. M. More for useful discussions on the theory, S. G. Glendinning for help

with image processing, T. Weiland for assistance with the interferometer laser, W. Unites, R. Jones, J. Burman, S. Letts, E. Mapoles, J. Pipes, and J. Sanchez for assembly of the cryostat and cells, J. Cox, and K. Haney for diagnostic development, J. Cardinal and D. Cocherell for diagnostic design and installation, the Nova target fabrication group, and the Nova operations technical support personnel. A. N. and G. C. acknowledge the support of the Natural Sciences and Engineering Research Council of Canada. This work was performed by the Lawrence Livermore National Laboratory under the auspices of the U. S. Department of Energy under Contract N°. W-7405-ENG-48.

References

[1] Ichimaru S, Iyetomi H and Tanaka S, Phys. Rep., 149, 91, (1987).

[2] Ashcroft NW, Phys. World, 8, 43, (1995).

[3] Smoluchowski R, Nature, 215, 691, (1967); Zharkov VN and Trubitsyn VP, in Jupiter, T. Gehrels, Ed., Univ. of Arizona press, Tucson, 135-175, (1976); Hubbard WB, Science, 214, 145, (1981); Stevenson DJ, Annu. Rev. Earth Planet Sci., 10, 257, (1982); Nellis WJ, Ross M, and Holmes NC, Science, 269, 1249, (1995).

[4] Lindl J, Phys. Plasmas, 2, 3933, (1995).

[5] Hubbard WB, Ap. J., 152, 745, (1968).

[6] Ross M, Rec FH and Young DA, J. Chem. Phys., 79, 1487, (1983).

[7] Saumon D, Chabrier G and Van Horn HM, Ap. J. Supp., 99, 713, (1995).

[8] Magro WR, Ceperley DM, Pierleoni C and Bernu B, Phys. Rev. Lett., 76, 1240, (1996).

[9] Mao HK and Hemley RJ, Rev. Mod. Phys., 66, 671, (1994).

[10] Nellis WJ, Mitchell AC, Van Theil M, Devine GJ, Trainor RJ and Brown N, J. Chem. Phys., 79, 1480, (1983).

[11] Holmes NC, Ross M and Nellis WJ, Phys. Rev. B, 52, 15835, (1995).

[12] Van Kessel CGM and Sigel R, Phys. Rev. Lett., 33, 1020, (1974); Tanaka KA *et al.*, in Shock Waves, ed. K. Takayama, Springer-Verlag, Berlin, 863, (1992).

[13] Kerley GI, Los Alamos Scientific Laboratory Report LA-4776, January, (1972).

[14] Zel'dovich YB and Raizer YP, Physics of Shock Waves and High-Temperature Hydrodynamic Phenomena, Academic Press, New York, (1966).

[15] Souers PC, Hydrogen Properties for Fusion Energy, University of California Press, Berkeley, (1986).

[16] Budil KS *et al.*, Characterization of preheat in laser-driven targets using interferometry, presented at the 38th Annual Meeting of the Division of Plasma Physics of the American Physical Society, Denver, CO, Nov. 11-15, (1996).

Nonlinear Multimode Rayleigh-Taylor Instability Experiments at Nova

K.S. Budil, B.A. Remington, S.V. Weber, T.S. Perry and T.A. Peyser
Lawrence Livermore National Laboratory
P. O. Box 808, L-473, Livermore, CA 94550, USA

Abstract: We examined the evolution of the Rayleigh-Taylor (RT) instability from an initial multimode perturbation.The RT experiments focused on the transition from the linear to nonlinear regimes for perturbation growth at an embedded, or classical, interface. The multimode experiments have attempted to observe the process of *bubble competition* wherein neighboring structures either continue to rise or are washed downstream in the flow depending upon their relative size. This competition is predicted to result in an *inverse cascade* at late times where progressively larger structures will begin to dominate the flow. Experiments to date have shown evidence of coupled modes arising, but have not yet accelerated the interface long enough to produce the several generations of coupling required for a true inverse cascade.

1. Introduction

Hydrodynamic instabilities are present in physical systems ranging from inertial confinement fusion (ICF) capsules to supernovae. In particular, the Rayleigh-Taylor (RT) instability,[1] wherein a heavy fluid is accelerated by a light fluid, can be found in a variety of situations. For ICF the imploding capsule goes through two phases of instability. Initially, the ablating outer surface of the capsule is RT unstable. Later, during the deceleration phase of the implosion, the inner fuel-pusher interface becomes unstable [2]. Astrophysicists seeking to explain the early appearance of spectral signatures from heavy elements produced at the core of an exploding star believe that large growth of RT bubbles and spikes at composition interfaces allows the heavier elements to penetrate through the outer layers of the star much earlier than would be expected just from 1D expansion plus diffusion [3].

We have performed a series of experiments to investigate the evolution of multimode perturbations at an RT-unstable, embedded interface. At an ablation front, the growth of a collection of initial modes can be described by a model proposed by Haan [4]. The growth is divided into two stages: (1) a linear regime where growth is exponential and (2) a nonlinear regime characterized by an asymptotic, constant bubble velocity. Because ablation will stabilize the shortest wavelengths and the longer-wavelength modes may not have particularly large amplitudes, this model, which neglects mode coupling, reasonably describes the evolution of a wide, smooth initial spectrum.

However, in the case of an embedded interface, isolated from the influence of ablation, short wavelength modes ($\lambda \sim 10 - 20$ μm) grow strongly [5]. For this case, where growth of longer wavelengths can be due primarily to seeding via mode coupling rather from their initial amplitudes, the development of the mixing region should lose dependence upon the initial conditions [6]. The bubble front penetration is given by

$$\eta_{\text{bubble}} = \alpha \text{Agt}^2 \tag{1}$$

More information - Email: budil1@llnl.gov

and the front evolution can be described in statistical terms from the dynamics of the individual bubbles plus two-bubble merger [6, 7]. As the coupling proceeds, longer and longer wavelength structures will begin to dominate the flow resulting in an *inverse cascade*.

1.1. Experimental configuration

In the experiments described herein, a gold cylindrical hohlraum was utilized to generate an x-ray drive to ablatively-accelerate the sample foil. The sample foils consisted of a 40 μm thick brominated polystyrene (CH(Br)) ablator backed by a 15 μm thick Ti payload. The perturbation being studied was placed at the CH(Br)-Ti interface and consisted of either two, ten or twenty cosine modes superimposed in phase. The experimental configuration is illustrated in Figure 1. An iron foil was irradiated to generate Fe He-Kα x rays at 6.7 keV to back-illuminate

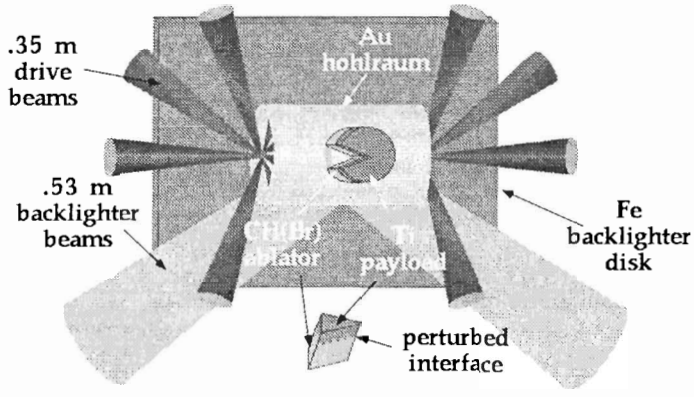

Figure 1. Experimental configuration for the classical Rayleigh-Taylor instability studies.

the target and the radiographs were recorded with a gated x-ray framing camera [8]. The radiographs were then Fourier-analyzed to determine perturbation amplitude in ln(exposure) $\propto -\delta$(OD) as a function of time, where OD represents optical depth.

2. Two mode experiments

After completion of a series of single-mode experiments [5], we began to examine the behavior of an initial spectrum of two or more modes. Initially, two readily-resolvable initial modes (λ = 10 μm, η_o = 1 μm and λ = 15 μm, η_o = 1 μm) were superimposed in phase. As the growth of the two initial modes proceeds into the nonlinear regime they begin to couple, producing "beat" modes $k_i \pm k_j$, the amplitude of which can be written at second order as

$$\eta_{k_i \pm k_j} \approx \mp \frac{1}{2}(k_i \pm k_j)\eta^L_{k_i}\eta^L_{k_j} \tag{2}$$

where $\eta^L_{k_i}$ is the spatial amplitude of the mode k_i had the growth been entirely in the linear regime [9]. Here the $k_{\lambda=10\,\mu m} - k_{\lambda=15\,\mu m} = k_{\lambda=30\,\mu m}$ beat mode is observed growing up in time. Figure 2 shows the mode amplitudes as a function of time, corrected for the instrument response (modulation transfer function or MTF) [10]. The growth of the 10 and 15 μm modes has entered the nonlinear regime, as evidenced by observation of the λ = 30 μm down-coupled mode.

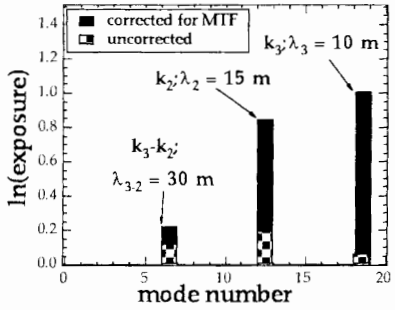

Figure 2. Fourier amplitude in units of ln(exposure) for the two initial modes ($\lambda = 10$ and 15 μm) and the coupled mode ($\lambda = 30$ μm) shown both corrected for instrument response (solid bars) and uncorrected (checkered bars) at t = 4.8 ns.

This technique was then extended to two modes both below the experimental resolution ($\lambda = 4$ μm, $\eta_o = 0.3$ μm and $\lambda = 5$ μm, $\eta_o = 0.3$ μm) [11]. This experiment was conceived as the analog of a large eddy simulation wherein short scale lengths are treated with a subgrid-scale model and larger structures are numerically simulated directly. Here the growth of the fundamental modes was inferred by observing the growth of the longer wavelength coupled mode ($\lambda = 20$ μm) as illustrated in Figure 3. A strong $\lambda = 20$ μm mode is observed growing in time

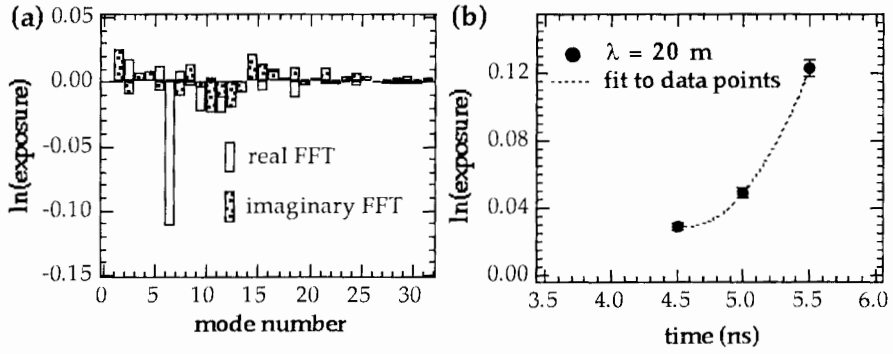

Figure 3. (a) Fourier spectrum at t = 5.5 ns. Mode 6 corresponds to $\lambda = 20$ μm. (b) Amplitude of the $\lambda = 20$ μm mode in ln(exposure) $\propto -\delta$(OD) as a function of time.

and has reached an amplitude of δln(exposure)$= -\eta$(OD) $= 0.12$ at 5.5 ns. This corresponds to a spatial amplitude of ~ 1.5 μm, assuming $\eta(\mu m) \approx [\lambda_{MFP}(\rho_o)][\eta(OD)/MTF]/(\rho/\rho_o)$, where $\lambda_{MFP} \sim 7\mu$m is the mean free path length of the backlighter x-rays in uncompressed Ti, $\rho/\rho_o \sim 1$ is the compression at 5.5 ns, and the MTF ~ 0.55 at $\lambda = 20$ μm. Preliminary calculations by D. Ofer [12] show reasonable agreement with the observations. A simple estimate of the amplitudes of the 4 and 5 μm modes can be made using Equation 2 with the observed amplitude of the $\lambda = 20$ μm mode. This indicates they have reached amplitudes of ~ 3.1 μm each corresponding to individual growth factors of 10. This is clearly deep into the nonlinear regime since $\eta/\lambda \sim 0.6$ for the 5 μm mode and ~ 0.8 for the 4 μm mode.

3. Multimode experiments

In an attempt to develop an experimental test for recent modal models [4, 7], we next imposed a multimode pattern consisting of either a "continuous spectrum" (harmonics 1-19, fundamental $\lambda = 200$ μm) or a discrete spectrum (harmonics 10-19, fundamental $\lambda = 100$ or 200 μm). Figure 4 shows the results from an experiment utilizing the 20 mode continuous spectrum target with fundamental $\lambda = 200$ μm. Growth of the initial mode spectrum is observed, but

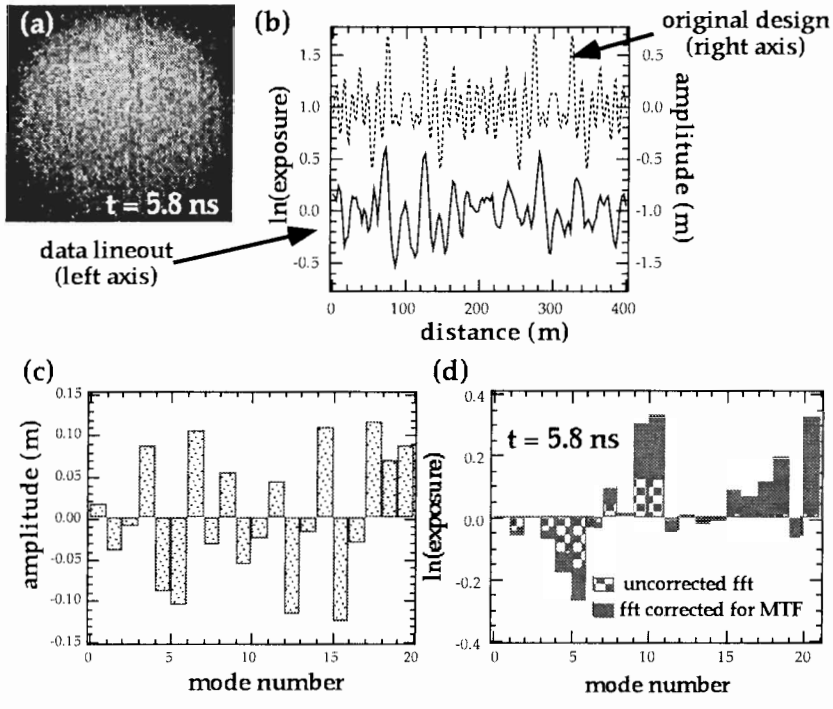

Figure 4. (a) Radiograph of the target at t = 5.8 ns and corresponding lineout. (b) The initial design of the pattern is also shown for reference. (c) Fourier spectrum for the initial multimode (20 modes, fundamental $\lambda = 200$ μm) pattern. (d) Fourier spectrum from the experimental data at t = 5.8 ns shown corrected (solid bars) and uncorrected (checkered bars) for instrument response.

the duration of the acceleration is not long enough to allow evolution well into the nonlinear regime. Additionally, the Ti layer thickness is much less than the perturbation wavelengths, which may impede the growth. The final spectrum is not yet dominated by longer wavelength structures.

4. Bubble merger experiment

In an effort to directly observe the competition between neighboring bubbles in *physical* space rather than Fourier space, as discussed by Alon *et al.* [13], we designed a target consisting of two harmonic wavelengths ($\lambda = 20$ μm, $\eta_o = 1$ μm and $\lambda = 10$ μm, $\eta_o = 1$ μm) superimposed in phase. Note the similarity of this target design and that of Sadot *et al.* for a Richtmyer-Meshkov bubble-competition experiment done on a shock tube [14]. This corresponds to an

alternating series of larger and smaller bubbles side-by-side, and the size and shape of each of the bubbles can be directly observed. For comparison, each target also had, in separate bands, the two corresponding single mode patterns. Results from this experiment are shown in Figure 5. By 4 ns the amplitude of the 10 μm mode has begun to decrease in the bubble

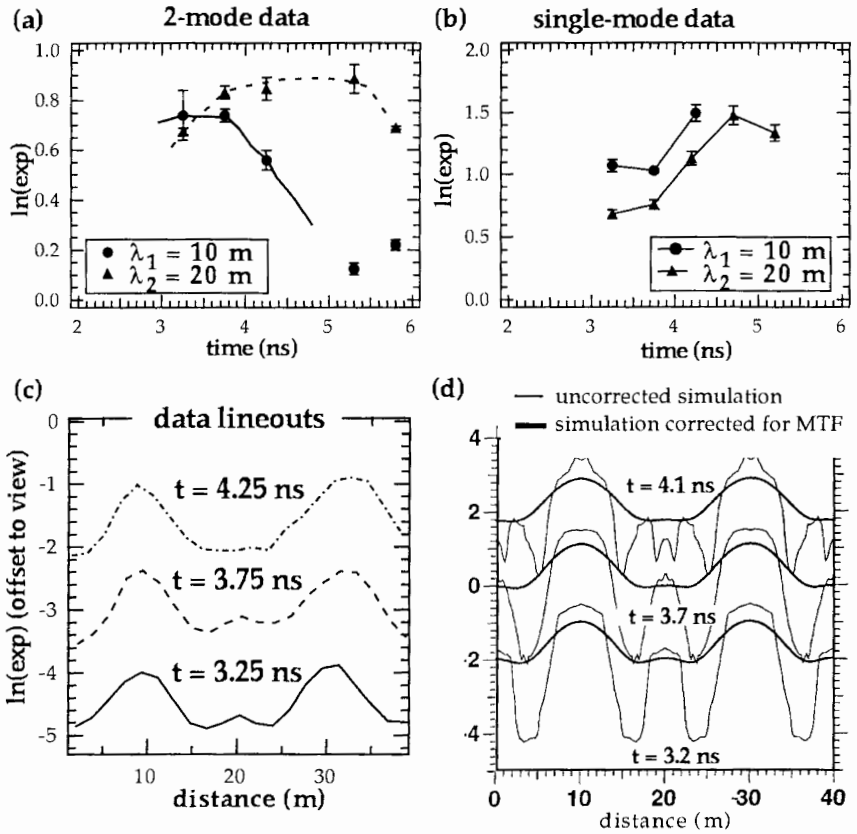

Figure 5. (a) Fourier amplitudes in ln(exposure) corrected for instrument response for the bubble merger 2-mode pattern. Solid and dashed curves are added to guide the eye. (b) Same only for the corresponding single mode patterns. Please note the suppressed origin along the time axis in plots (a) and (b). (c) Lineouts in ln(exposure) from the bubble merger pattern. (d) Same for the postprocessed LASNEX simulations.

merger pattern (Figure 5a), whereas the amplitude of the 10 μm single mode (a separate band measured on the same target) is still increasing at that time (Figure 5b). Lineouts from the data and LASNEX [15] simulations are shown in Figure 5c,d. The central, smaller bubble appears to be giving way to its larger neighbor as the experiment progresses. The LASNEX simulations (Figure 5d) before and after smearing for the instrument spatial resolution show that a rather complicated nonlinear interaction could be occuring, most of which is smoothed out by the instrument response. Note the similarity of our Figure 5 with Figures 3 and 4a of Sadot *et al.* for their Richtmyer-Meshkov bubble-competition experiment [14]. We may be

seeing the initial stages of bubble competition and merger. However, as the bubbles grow in our experiment their amplitudes begin to approach the thickness of the titanium layer, which may impede the bubble competition process.

5. Conclusion

In an attempt to develop an experimental test of the modal models developed by Haan [4] and Ofer *et al.* [7], we have investigated the evolution of an initial perturbation consisting of two, ten or twenty modes superimposed in phase at an embedded interface. Because the interface is isolated from the influence of ablation, short wavelength modes grow strongly making this target geometry particularly well suited to studying nonlinear mode coupling. The growth of two initial modes has been studied for initial wavelengths above and below the experimental resolution and the growth of coupled, or beat modes is observed. The evolution of a 20-mode continuous spectrum was also investigated. Finally, a two-mode, bubble merger experiment was conducted in order to observe directly the competition between neighboring bubbles. As time progresses, the smaller bubble was seen to be giving way to its larger neighbor.

Acknowledgement. The authors would like to thank D. Shvarts, U. Alon, and D. Ofer for many fruitful discussions and suggestions regarding this work. This work was performed by the Lawrence Livermore National Laboratory under the auspices of the U. S. Department of Energy under Contract No. W-7405-ENG-48.

References

[1] Chandrasehkar S, Hydrodynamic and Hydromagnetic Stability, Oxford University Press, London, (1968).
[2] Lindl JD and Mead WC, Phys. Rev. Lett., 34, 1273, (1975); Verdon CP *et al.*, Phys. Fluids, 25, 1653, (1982); Bodner SE, Phys. Rev. Lett., 33, 761, (1974); Lindl J, Phys. Plasmas, 2, 3933, (1995).
[3] Muller E, Fryxell B and Arnett D, Astron. Astrophys., 251, 505, (1991); Herant M and Woosley SE, Ap. J., 425, 814, (1994).
[4] Haan SW, Phys. Rev. A, 39, 5812, (1989).
[5] Budil KS *et al.*, Phys. Rev. Lett., 76, 4536, (1996).
[6] Young DL, Physica D12, 32, (1984); Haan SW, Phys. Fluids B, 3, 2349, (1991).
[7] Ofer D *et al.*, Phys. Plasmas, 3, 3073, (1996) and references therein; Layzer D, Ap. J., 122, 1, (1955).
[8] Budil KS *et al.*, Rev. Sci. Instrum., 67, 485, (1996).
[9] Remington BA *et al.*, Phys. Plasmas,f 2, 241, (1995) and references therein.
[10] Robey HF, Budil KS and Remington BA, Rev. Sci. Instrum., 68, 792, (1997).
[11] Budil KS *et al.*, Rev. Sci. Instrum., 68, 799, (1997).
[12] Ofer D, private communication.
[13] Alon U *et al.*, Phys. Rev. Lett., 74, 534, (1995).
[14] Sadot O *et al.*, these proceedings.
[15] Zimmerman GB and Kruer WL, Comments Plasma Phys. Controlled Fusion, 2, 51, (1975).

Use of the Pegasus Z-Pinch Machine to Study Inertial Instabilities in Aluminum: A Preliminary Report

E.A. Chandler[1], P. Egan[1], K. Winer[1], J. Stokes[2], R.D. Fulton[2], N.S.P. King[2], D.V. Morgan[2], A.W. Obst[2], H. Oona[2] and D.W. Oro[2]
[1]Lawrence Livermore National Laboratory
P. O. Box 808, L-473, Livermore, CA 94550, USA
[2]Los Alamos National Laboratory, Los Alamos, New Mexico 87545, USA

Abstract: We have designed a target to probe the use of the Pegasus Z-Pinch machine to image inertial instabilities that develop on cylindrically-convergent material interfaces. The Z-pinch is tailored so that the target, soft Al 1100-O, remains solid; instabilities and inertial effects are seeded by wire inclusions of different densities. We present here the first images and preliminary results from this experiment.

In materials with strength, the development of inertial instabilities is more complicated than in fluids; the application of stress leads to both elastic, or reversible, deformations, plastic deformations, and failure manifested as cracks, spall, and ejecta. The details of these processes are not well understood and remain the focus of ongoing research. In addition, in solids the regularity of the material can vary on a mesoscopic scale, and solid-liquid and solid-solid phase transitions can change the constitutive properties of the materials. These features make the application of continuum models problematic and *ad hoc*. Yet the computer simulations of inertial instabilities in solids rely on such continuum models. As a result, we would benefit from an experimental platform that can capture the dynamic processes in a macroscopic piece of metal. For this reason, we have explored using the Pegasus Z-pinch machine at the Los Alamos National Laboratory (LANL) to serve as such an experimental platform. This machine uses a pulsed magnetic field to implode a cylindrical liner on a cylindrical target; the parameters of this machine can be set so that the target remains solid. We have designed a target that probes both the dynamics of the resultant solid "flow" and also the ability of this facility to image these processes. We have used the LLNL CALE code, an adaptive Lagrangean-Eulerian hydrodynamic code that also has a full implementation of the Steinberg-Guinan strength model [1], to design the experiment. We have utilized a system of both x-ray and optical imaging diagnostics to capture this flow. We include here a preliminary view of the first data obtained.

1. The Pegasus facility and the target design

The Pegasus facility is capable of putting a peak current of 12 MA or more through a conducting cylindrical liner in a half-sine pulse lasting approximately 15 μs. The current, moving axially in the target, induces a magnetic field external to the liner that then forces the liner to move inward radially with a high degree of angular uniformity.

In our experiment, we used a liner made of soft aluminum Al 1100-O with radius 2.4 cm and thickness 0.04 cm. The outside radius of our target was at 1.5 cm. A modest current peak of 4.6 MA occurred at approximately 7.25 μs, leading to a collision of liner with target at 9.1 μs when the liner was moving at approximately 3 km/sec. The collision launched a 30 GPa shock

More information - Email: eachandler@llnl.gov or chandler2@llnl.gov

into the target.

The target was a soft (1100-O) Al cylinder with inner radius 1.0 *cm* and outer radius 1.3 *cm*, surrounded by 0.2 *cm* PMMA (lucite) and separated by vacuum from the liner (Fig. 1a). The center fill was Xe at 1 *atm*. In the Al target cylinder, several wires of different metals were embedded parallel to the axis: one wire of Ta, Cu, and stainless steel at 120° separation on a circle of 1.1 *cm* radius. Another stainless steel wire was placed 30° from the first. These wires, of different metals and therefore of different densities, melting temperatures, and constitutive properties, also had different radii to keep them within the target through the course of the experiment. In addition, a stripe of gold was plated on the inner surface of the Al target; it was placed at mid-height and extended ±60° from the Ta target, 0.1 *cm* high and 5μm thick. As shown in Fig. 1b, the target cylinder was 1.75 *cm* high and capped with PMMA caps that had a glide angle of 8° and a thickness that prevented the shock waves from reaching the Xe prematurely through the caps. The PMMA thus forms a holder for the Al sample; the PMMA holder assembly was designed and tested by Peter Adams and Joyce Guzik of LANL [2].

The embedded wires were used to follow their dynamics as they move differentially with respect to the Al due to inertial effects. Simulations with CALE predicted that the motion of the wires would also induce flow in the Al, seeding instabilities on the inner surface of Al. The second stainless steel wire was added to explore whether the wire insertion procedure affected the dynamics; different insertion procedures were used for the two stainless steel wires. The purpose of the Xe fill was to monitor the passage of the shock in the region internal to the Al sample. The Au plating was included to help image the internal radius of the Al sample; part of the motivation was exploratory as we wanted to see whether the Au would remain in place and whether it would affect the dynamics.

Aluminum was chosen as the target material for two reasons. The first is the ease of imaging; the use of Al allows us to image the density variations of the Al and the movement of the wires with x-rays. The second is that various tempers of Al have yield strengths that vary by up to an order in magnitude. In a convergent system, the strain is high and the flow is primarily plastic. In future experiments we plan to explore the effect of the yield strength, the transition point between plastic and elastic flow, on the degree of convergence, the motion of the inclusions, and the growth of instability patterns on the inner surface of the Al target.

CALE calculations show that if the Al is held at fixed density and not allowed to expand appreciably, the wires induce perturbations on the inner target surface as they move differentially outward. The features that appear on the inner surface are sensitive to the yield strength and are largest just before the shock reaches the center of the apparatus, approximately 3.5μs after the collision of the liner, when the inner surface of the liner has been decelerating and unstable for 1 μs.

The simulations showed that many short-wavelength ripples would appear on the inner surface if there were no strength (yield strength and shear modulus both set to zero); for Al 1100-O, wake-like features appeared behind the wires; for Al 6061 with high yield-strength, long-wavelength features whose length was the wire spacing dominate.

2. Imaging diagnostics

The ability to image the phenomena that occurred in this experiment was obviously crucial. As shown in Fig. 2, the diagnostics included three radial flash x-ray radiographs placed at 120° and capturing almost the full length of the target. The dynamic image obtained from each of

these radiographs can be compared to preshot static images. The timing was independent on these cameras, and was chosen so that one image was taken at 2.6 μs and two images were taken at 3.6 μs after liner impact. These sources recorded excellent images on screened film.

There were two axial flash x-ray sources; again, one was set to take an image at 2.6 μs and one at 3.6 μs after impact. These radiographic images were recorded by capturing the light produced by the x-rays in a thin (1 mm) NaI fluor with CCD cameras. Unfortunately, the first source didn't report a successful image. The second was low in x-ray flux and the image, though useful, is not optimal. Finally, there were optical cameras recording axial images. A ruby laser backlit the Xe-filled central volume. Filters allowed the images of the laser only (showing unshocked Xe region), Xe self-emission only (showing the shocked region), and both regions to be recorded. In addition, B-dots, a Faraday rotation fiber optic, and Rogowski coils were used to monitor Pegasus performance.

Unfortunately, we cannot show all the data in this limited report. A sample of the x-ray data is shown and discussed briefly. The optical data, which will not be included here, gave fine images of the shock wave which will provide us with timing and shape information to benchmark our codes.

Figure 3 a,b show the static and dynamic image taken by the axial x-ray at 3.6 μs after impact. The preliminary interpretation of the dynamic x-ray is shown in Fig 3b. The lucite, dense aluminum, spall area, wires, and shocked and unshocked Xe are shown, and they are quite unambiguous. Between the dense Al and this inner Al surface is a low-density Al area that we term "failed". We are not yet certain what the state of the Al in this region is. Also, extremely low density "wakes" appear to be formed behind the wires, and "fingers" appear at the inner edge of the dense Al. The identification of these features is less certain than for the first group, and will be analyzed further. The failed region and the fingering was unexpected.

The static and dynamic images from the radial x-ray film that points directly at the stainless steel wires are shown in Fig. 3. These images show the Ta wire on the left, two steel wires interior, and the Cu wire on the right. The dynamic image shows the degree of 3-dimensionality in the system. While the central wire is straight, radial bending of the other non-radial views is clearly visible. The Ta wire, which has highest shear modulus, shows the least bending. Also visible are vertical density lines, and the outer Al area just beyond the wires shows density variations that are suggestive of horizontal rolls. The gold plating is visible in the dynamic image, as is the high-density shocked Xe volume. Clearly, the most surprising feature of these images is the degree of 3-dimensionality.

At this point, the quality and quantity of this data is judged to be extremely promising. It will help in the benchmarking of both the 2-D CALE code and the new 3-D code Ares [3], and will play a role in the exploration of instability and flow processes in shocked solids in this geometry.

Acknowledgement. This work was performed under the auspices of the U.S. Department of Energy at Lawrence Livermore National Laboratory under Contract N° W-7405-ENG-48 and at Los Alamos National Laboratory under Contract N° W-7405-ENG-36.

References

[1] Steinberg DJ, Cochran SG and Guinan MW, J. Appl. Phys., 51, 1498, (1980).
[2] Adams P and Guzik JA, to be published.

[3] McAbee T, this volume.

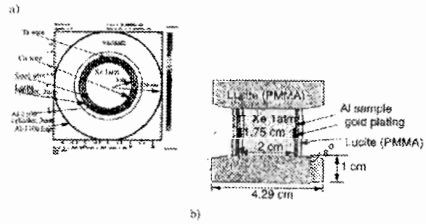

Figure 1. Horizontal and vertical view of the target. In Fig.1a, the Al liner is included; it is initially outside the assembly pictured in Fig. 1b.

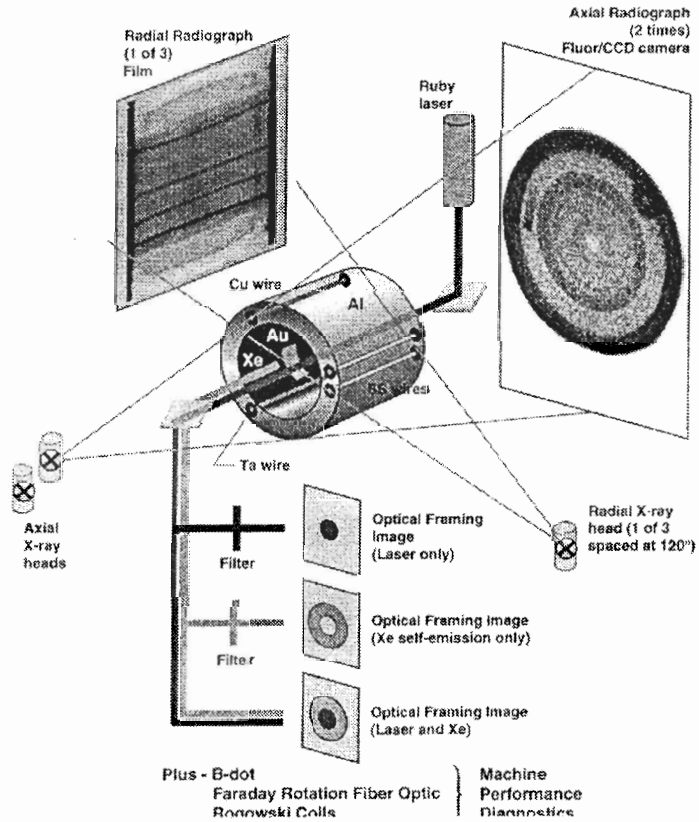

Figure 2. The diagnostics associated with the experiment, including optical and x-ray cameras.

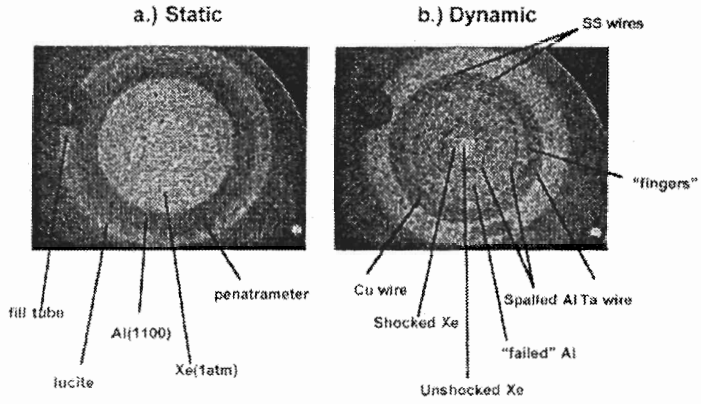

Figure 3. The static and dynamic axial x-ray image; 3b was taken 3.6 μs after liner collision and before the shock wave arrived at the center of target.

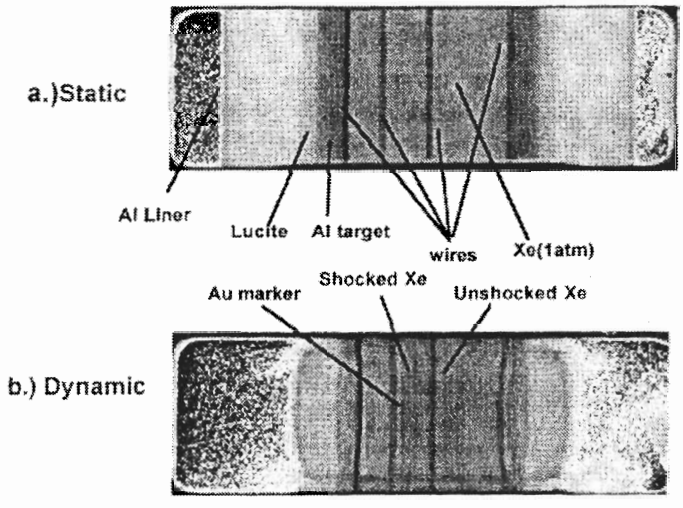

Figure 4. Static and dynamic radial flash radiographs of the target at 3 μs after liner collision. The Ta wire is at left, Cu at right. Note the bending of the wire and other 3D features.

Numerical Investigation of Convergent Rayleigh-Taylor Experiments on the Nova Laser

C. Cherfils[1], D. Galmiche[1], A. Richard[1], S.G. Glendinning[2] and B.A. Remington[2]
[1]CEA-DRIF, Centre de Limeil, 94195 Villeneuve St Georges Cedex, France
[2]LLNL, P.O. Box 808, Livermore, CA 94551, USA

Abstract: Experiments have been done on the Nova laser to investigate the effects of convergence on Rayleigh-Taylor growth. Ablatively accelerated targets were planar CH(Br) foils or hemispherical CH(Ge) capsules with identical initial 2D or 3D perturbations. Experimental results have already been presented [S.G. Glendinning *et al.*, Measurements of Rayleigh-Taylor growth in ablatively driven converging hemispherical targets at Nova, APS Plasma Physics Conference, 1996], which showed the decrease of the effective wavelength of the perturbation in the converging case, and an early onset of nonlinearity in comparison to the planar case. We will focus here on the 2D perturbation: a sinusoidal ripple of $70\mu m$ wavelength. Numerical simulations using the 2D lagrangian code FCI2 will be presented for the planar and hemispherical targets. Classical modeling of Rayleigh-Taylor growth with ablative stabilization will be compared to both numerical and experimental results.

1. Introduction

For Inertial Confinement Fusion (ICF), the Rayleigh-Taylor (RT) instability is a major constraint which has to be well controlled in order to achieve sufficient hydrodynamic efficiency to reach ignition. The main occurences of the RT instability are at the ablation front during the acceleration phase and at the pusher-fuel interface during the deceleration phase. Many experiments have measured RT growth in planar geometry, and have verified the ablative stabilization effect [1, 2, 3, 4, 5], but few experiments have examined the role of convergence [6, 7]. Radiation driven experiments have been conducted by the Lawrence Livermore National Laboratory on the Nova laser in order to study the effect of convergence on the linear and weakly nonlinear growth phase of the RT instability at the ablation front [8]. Experiments are performed in both planar and spherical geometry with face-on radiography. Corrugated spheres or planar foils are mounted on the side of a hohlraum, with axisymmetric sinusoidal perturbations facing the inside of the hohlraum. Several shots have been performed in the framework of a "Commissariat à l'Energie Atomique / US Department of Energy" collaboration. In the present paper, we report 2D hydrodynamic simulations performed at CEA/DRIF using the Lagrangian code FCI2.

2. Experimental configuration

The Nova experimental configuration, shown in Figure 1, has been described elsewhere [8]. Eight Nova beams are converted to X rays in a hohlraum, and two other beams are used to backlight the sphere or foil. The targets are CH(Br) foils or CH(Ge) capsules with a 2D single mode sinusoidal perturbation ($\lambda = 70\mu m, a_0 = 2\mu m$). The levels of bromine and germanium dopants are chosen so that the preheat shielding is similar for both geometries. Two beams are used to irradiate a rhodium disk to create an x-ray backlighting source. A gated x-ray pinhole

More information - Email: cherfils@limeil.cea.fr or galmiche@limeil.cea.fr

camera images the foil or sphere (50 ps gating time).

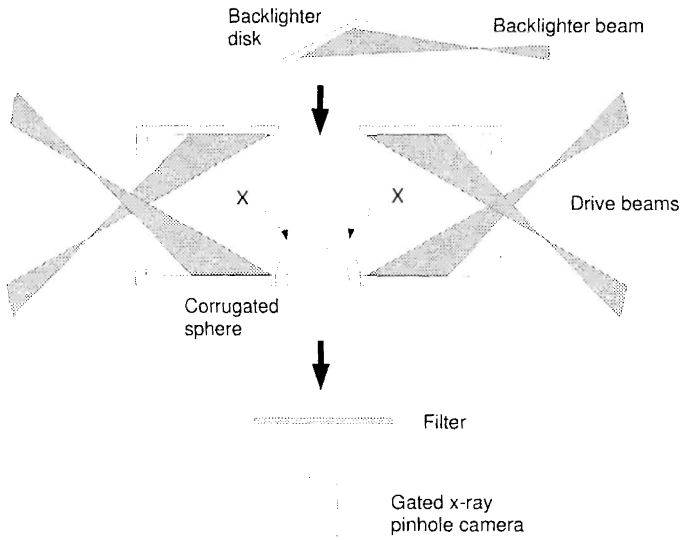

Figure 1. Schematic of the experimental geometry.

3. Simulations

Simulating the experimental x-rays radiographs was a multistep process. First, we estimated a mean radiation drive temperature using a 3D view factor code. This code, including radiative transfer but not hydrodynamics, allowed us to consider non-axisymmetric laser beams. On top of the capsule, in the angular domain $[56°, 90°]$, peak drive temperature values range between 195eV and 201 eV (Figure 2), and are quite similar to the temperature obtained with the view factor code in the planar configuration. The average drive temperature we obtained this way is in good agreement with Dante measurements [9].

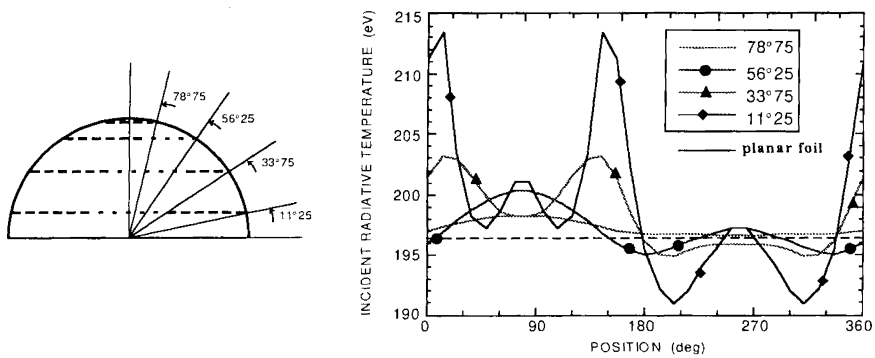

Figure 2. Peak drive temperature at the surface of the hemisphere ($t = 1.8ns$).

Then, we used the 2D radiation hydrodynamics code FCI2 to simulate the capsule implosion

or foil acceleration, and perturbation development. We checked that FCI2 correctly predicted the mean flow evolution (gross hydrodynamics) in both the planar and spherical case. For the planar configuration, FCI2 simulations are in good agreement with the foil acceleration data [9]; for the perturbed capsule, a good check is the wavelength evolution (see Figure 3). We have included an overall time shift of 250 ps to bring the gross hydrodynamics simulations into agreement with the experiments. We are currently investigating the source of this time shift.

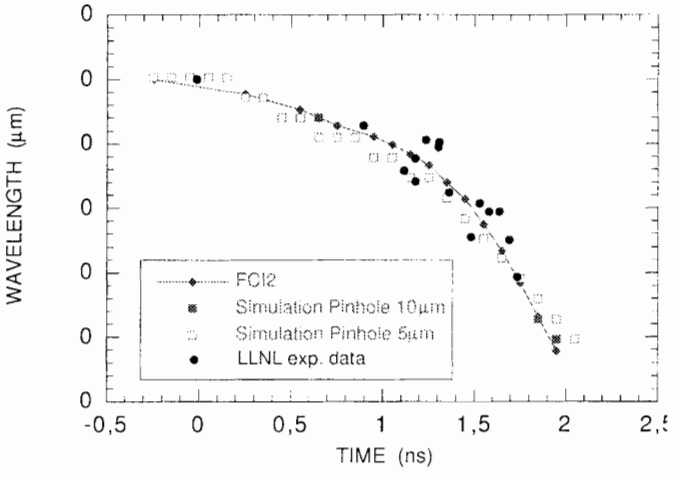

Figure 3. Time calibration between experiment and simulation is made according to wavelength evolution.

Finally, we used a post-processor code to simulate radiographs, taking into account the spatial and time resolution of the diagnostics. The predicted radiograph is then Fourier analyzed ain the same fashion as the experimental images [10].

Measured and simulated growth factors are plotted in Figure 4 for the fundamental mode and its second harmonic in the case of the spherical target. Measured ones are extracted from LLNL experimental data [8]. FCI2 curve is simulated spatial amplitude at the perturbed ablation front, whereas Simulated Pinhole results have been post processed to get optical depth amplitudes. They have been obtained from numerical runs with two distinct values for the pinhole diameter ($5\mu m$ and $10\mu m$), the experimental pinhole diameter being close to $10\mu m$. Time calibration between experiment and simulation is based on the wavelength evolution. The data and simulation have been normalized to their respective values at $t = 0.95ns$, both for the fundamental mode and second harmonic.

As, for the capsule, the predicted decompression rate during the RT phase is quite small, the relation [10] between growth factors in optical depth (GF_τ) and in spatial amplitude (GF_z)

$$GF_\tau(t) = e^{\frac{\rho-\rho_0}{\rho_0}} GF_z(t) \tag{1}$$

indicates that the optical depth amplitudes should not be too much lowered, unlike the planar case.

This behavior is confirmed for the fundamental mode, as experimental GF_τ evolves between numerical GF_τ and GF_z. Decrease of the numerical GF_τ is due to convergence effect and diagnotic resolution limit as the wavelength is diminishing (the convergence ratio is about 2);

new LLNL experimental data at latter times seem to confirm this trend, but careful analysis has to be done, especially to take into account feedthrough effects.
The experimental GF_τ for the second harmonic follows reasonably well the numerical GF_τ. The apparent saturation in the experimental evolution of the second harmonic seems to be due to the insufficient spatial resolution connected to the decrease of the associated wavelength. Recent experimental data reinforce this analysis. During the same time interval, the numerical GF_z in spatial amplitude continues to increase monotonically, i.e., the perturbation peak-to-valley amplitude continues to grow.

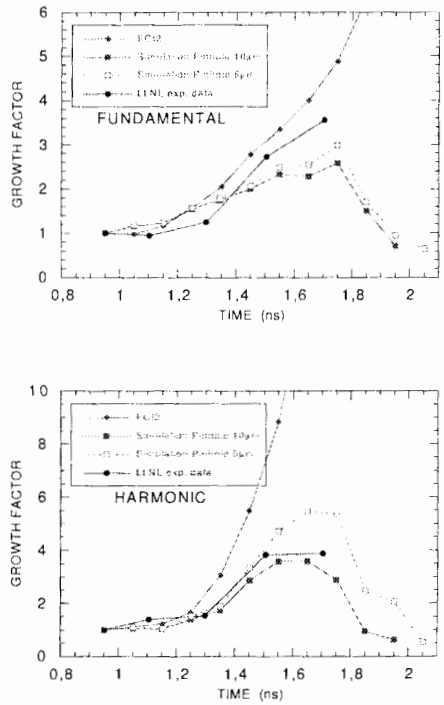

Figure 4. Comparison of FCI2 simulated growth factors in spatial amplitude and in optical depth for the capsule. Confidence limit on experimental LLNL data is about 10%.

4. Comparison to analytic theory

For conditions of nearly steady acceleration, growth rates for ablatively stabilized RT instability may be compared with the semi-empirical dispersion relation [11, 12, 13]

$$\gamma = \sqrt{\frac{kg}{1+kL}} - \beta k v_a \tag{2}$$

where $\gamma(k,t)$ is the growth rate for wave number k, g is the acceleration, L is the density gradient scale length and v_a is the ablation velocity. The adjustable parameter β is typically chosen between 1 and 4 for indirect drive targets [5, 10, 14]. Figure 5 displays the calculated $g(t)$ and $v_a(t)$ of Eq.(2) for the CH(Br) foil and the CH(Ge) capsule. We began the modeling

when shock reaches the back of the shell (or foil), which gives a starting time of 1.2ns (or 1.6 ns) - FCI2 time -.

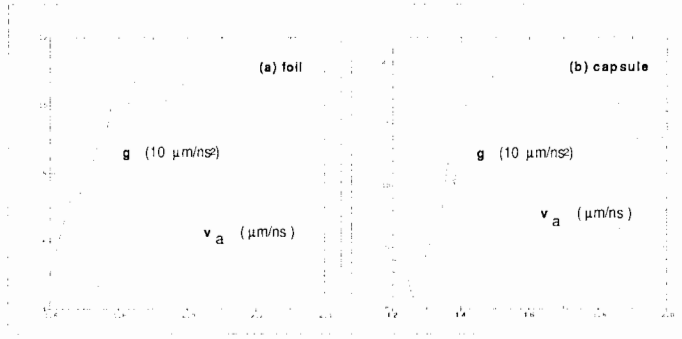

Figure 5. The calculated acceleration and ablation velocity vs time (ns) for (a) CHBr foil and (b) CHGe capsule. The density gradient scale length, $L = \frac{\rho}{D\rho}$ is about $2\mu m$ for the foil and about $1\mu m$ for the capsule.

In this section, we compare the modeling Eq.(2) to the growth rates determined directly from spatial amplitudes at the ablation surface. The best fit is obtained with $\beta = 1$ for the planar foil, or with $\beta = 3$ if we use the modified amplitude

$$a_c(t) = \frac{\rho_0}{\rho(t)} a(t) \tag{3}$$

to take into account the decompression of the foil. Simulated peak density is indeed decreasing with time from $6g/cm^3$ at 1.6ns to $3g/cm^3$ at 2.4ns.
For the spherical case, we find that for $\beta = 3$, the same formula for spatial amplitude , with the correction for decompression,is a good fit. For uncorrected Takabe formula, the best fit is for $\beta = 2.7$.
Additional fits on different wavelengths and different amplitudes are needed to make a choice among these different models. Also, the coefficient β is fairly dependent on the estimation of the ablation velocity. Nevertheless we notice that the second order correction

$$a_2(t) = -\frac{1}{2} k (a_1^{lin}(t))^2 \tag{4}$$

gives a good fit for the second harmonic in all cases.
Betti *et al.* [15] have also modelled the results of their linear stability analysis by a simple equation

$$\gamma = \alpha_{fit}\sqrt{kg} - \beta_{fit} k v_a \tag{5}$$

where α_{fit} and β_{fit} are predicted by their analytical results and are dependent on the Froude number. According to our simulations, the average Froude number is about 1 for the foil and about 1.4 for the capsule, which is outside the range of the Betti investigation ($Fr < 0.5$ or $Fr > 3$). Nevertheless, this may indicate that we can't choose exactly the same β_{fit} for the two configurations (planar vs convergent). Directly applying their complete model [16] is currently in progress.

5. Conclusion

Numerical simulations of experiments done on the Nova laser to investigate the effects of convergence on Rayleigh-Taylor growth have been presented. Simulated radiographs seem necessary for spherical targets, specially to take into account the diagnostic resolution limit. Growth factors in optical depth are strongly dependent on the instrumental spatial resolution and convergence effect. Especially for convergent geometry, saturation and decrease of the optical depth growth factor is an artifact, as spatial amplitude growth factor calculated at the ablation front continues to increase monotonically. Reasonnable agreement is found between the simulated and measured perturbations. There is little difference between planar and convergent geometry for the fundamental mode growth rate, which is about 6-8. Earlier onset of second harmonic is seen in convergent geometry, due to changing wavelength.
First comparisons with classical modeling of Rayleigh-Taylor growth with ablative stabilization have been completed, but further work is needed to investigate the effects of decompression and convergence.

Acknowledgement. The authors would like to thank P.A. Holstein, L.Hallo, S. Haan and S. Weber for suggestions, D. Kalantar for providing NOVA experimental data, R. Betti and V. Goncharov at LLE Rochester for the use of their modeling code, and R. Wallace and his highly skilled target fabrication staff. This work has been performed under the auspices of a "Commissariat à l'Energie Atomique / US Department of Energy" collaboration.

References

[1] Cole AJ *et al.*, Nature (London), 299, 329, (1982).
[2] Grun J *et al.*, Phys. Rev. Lett., 58, 2672, (1987).
[3] Desselberger M *et al.*, Phys. Rev. Lett., 65, 2997, (1990).
[4] Glendinning SG *et al.*, Phys. Rev. Lett., 69, 1201, (1992).
[5] Remington BA *et al.*, Phys. Fluids B5, 2589, (1993).
[6] Hsing WW and Hoffmann NM, Phys. Rev. Lett., 78, 20, 3876, (1997); Hsing W *et al.*, Phys. Plasmas, 4,1832, (1997).
[7] Weir S, these proceedings.
[8] Glendinning SG *et al.*, APS Plasma Physics Conference, (1996); and these proceedings.
[9] Kalantar DH, Private communication.
[10] Glendinning SG *et al.*, Phys. Rev. Lett., 78, 17, 3318, (1997).
[11] Takabe H, Montierth L and Morse RL, Phys. Fluids, 26, 2299, (1983).
[12] Takabe H. *et al.*, Phys. Fluids, 28, 3676, (1985).
[13] Lindl J, Phys. Plasmas, 2, 3933, (1995).
[14] Weber SV *et al.*, Modeling of Nova indirect drive Rayleigh-Taylor experiments, Phys. Plasmas, 1, 11, 3652, (1994).
[15] Betti R *et al.*, Phys. Plasmas, 3, 5, 2122, (1996).
[16] Goncharov VN *et al.*, Phys. Plasmas, 3, 12, 4665, (1996).

Comparison of a Spectral Turbulence Model with Experimental Data of Rayleigh-Taylor Mixing

T. Clark, F. Harlow and R. Moses
Theoretical Division, Group T-3, Theoretical Hydrodynamics, MSB216
Los Alamos National Laboratory, Los Alamos, New Mexico 87545, USA

Abstract: The effects of pressure fluctuations present a fundamental difficulty in the formulation of tractable turbulence models. In the regime of incompressible velocity fluctuations, the pressure-velocity correlations are intrinsically nonlocal and can be expressed as an integral over the flow domain wherein the integrand contains two-point velocity correlations. However, engineering transport descriptions of turbulence have traditionally modeled the pressure effects as local, differential functions rather than nonlocal integral relationships. A spectral model proposed by Steinkamp, Clark, and Harlow [1] explicitly incorporates the nonlocal nature of the pressure effects in an inhomogeneous environment. Previous comparisons of model solutions with experimental data showed reasonable agreement at intermediate to high wave numbers [2]. However, the lack of detail in previous experimental data has not allowed for a more critical evaluation of the fundamental assumptions incorporated in the model. Recent experiments at Lawrence Livermore National Laboratory (LLNL) by Dimonte *et al.* provide a richness of detail that is not present in the older data. These data are used to evaluate some of the assumptions of the spectral model of Steinkamp *et al.*, as well as single-point models such as that of Besnard, Harlow, Rauenzahn and Zemach [3]. Additionally, simulations of Rayleigh-Taylor instabilities are used to augment the experimental data to give direct insight into the effects of the fluctuating pressure correlations.

1. Introduction

Stochastic, or turbulent, Rayleigh-Taylor mixing introduces significant demands on turbulence closures. Many of the assumptions used in the development of single-point closures for fully developed constant density fluid turbulence may be tenuous at best in the circumstance of developing Rayleigh-Taylor turbulent mixing. For example, the typical approaches to modeling the fluctuating pressure-strain correlations are based on the assumption of nearly homogeneous turbulence. This assumption permits some simplification of the Poisson equation for the pressure-strain terms. However, assumptions of near-homogeneity are clearly questionable at the edge of a Rayleigh-Taylor mixing layer. Another assumption of the standard engineering closures is that the turbulence length-scales can be described by a single length-scale. Such an assumption limits a model's ability to distinguish differences in the geometric orientations of the correlations. Such assumptions have three compelling justifications. First, the resulting models have a proven history of producing useful predictions in a wide range of circumstances; second, experimental data are generally not available to ascertain the adequacy of these assumptions, and third, incorporation of such effects may introduce unwarranted complexities into the models. Nevertheless, increasing demands for physical fidelity in the stringent regime of Rayleigh-Taylor mixing warrants a detailed examination of the underlying assumptions of the closures. Recent experiments of Rayleigh-Taylor mixing conducted at LLNL [4] provide un-

More information - Email: ttc@lanl.gov

precedented detail regarding the density distributions in the mixing zone. These experiments use a linear electric motor (LEM) to accelerate a fluid test cell and laser-induced florescence in conjunction with a thin laser sheet, or "knife" for illumination. The resulting data provide an ideal opportunity to evaluate assumptions regarding the anisotropy of the length-scales associated with fluctuating density-density correlations. Unfortunately, these experiments do not yet provide information regarding fluid velocities or pressures. To provide information on the nature of the velocities and pressures in the configuration of the experimental apparatus, a series of numerical calculations were performed and analyzed to demonstrate the nature of the turbulence production due to pressure effects.

2. The spectral model

The spectral model of Steinkamp, Clark and Harlow [2] represents an attempt to extend a simple spectral flux closure for turbulence to the regime of inhomogeneous turbulence. It is an extension of earlier spectral flux models, e.g., the flux model for constant-density isotropic turbulence of Leith [5], the extension of Leith's model to anisotropic and inhomogeneous turbulence due to Besnard, Harlow, Rauenzahn and Zemach [6] and the extension of the Besnard *et al.* work to homogeneous variable density turbulence by Clark and Spitz [7]. A principal motivation of the work of the Los Alamos group was to develop a framework for modeling that is free of the heuristic and frequently *ad hoc* nature of the turbulent kinetic energy dissipation-rate equation (i.e., the ϵ-equation). The model of Steinkamp *et al.* also shares a number of features in common with a one-point closure for variable density turbulence developed by Besnard, Harlow and Rauenzahn [3], such as the the treatment of the mass-weighted-averged (Favre) triple velocity correlations. The novel aspect of the model of Steinkamp *et al.* is the treatment of the pressure-production terms in the two-point Reynolds-stress equations as a nonlocal, or integral, term. The motivation for this extension is the simple observation that the movement of fluid at the high/low-density interface of a Rayleigh-Taylor instability is communicated to the fluid at points away from the interface via the pressure acting in conjunction with the incompressibility constraint. The actual derivation of the spectral model of Steinkamp *et al.* is described in detail in [8] as well as [1]. The variables are those established by Clark and Spitz [7], including the two-point turbulence Reynolds stress,

$$R_{ij}(\mathbf{x}_1, \mathbf{x}_2, t) = \overline{\frac{1}{2}\left[\rho(\mathbf{x}_1, t) + \rho(\mathbf{x}_2, t)\right] u_i''(\mathbf{x}_1, t)\, u_j''(\mathbf{x}_2, t)}, \tag{1}$$

the two-point turbulence mass flux,

$$a_i(\mathbf{x}_1, \mathbf{x}_2, t) = \overline{\rho(\mathbf{x}_1, t)\, u_i''(\mathbf{x}_1, t)\, v'(\mathbf{x}_2, t)}, \tag{2}$$

where $v = 1/\rho$ is the specific volume of the fluid, and the two-point fluctuating density-specfic volume correlation,

$$b_i(\mathbf{x}_1, \mathbf{x}_2, t) = -\overline{\rho'(\mathbf{x}_1, t)\, v'(\mathbf{x}_2, t)}. \tag{3}$$

Following Besnard *et al.*, a change of coordinates is introduced;

$$\mathbf{x} = \frac{1}{2}(\mathbf{x}_1 + \mathbf{x}_2), \quad \mathbf{r} = (\mathbf{x}_1 - \mathbf{x}_2), \tag{4}$$

and the variables are Fourier-transformed with respect to the relative coordinate $\mathbf{r}$. At this point, the variables are complex functions of a 7-dimensional argument $(\mathbf{x}, \mathbf{k}, t)$. In summary, the angular dependence in $\mathbf{k}$ is removed by averaging over all angles in the $\mathbf{k}$-space, thus

making the variables real functions of a three-dimensional physical space coordinate, a Fourier wavenumber (rather than a wavevector) and time. Upon integration over all wavenumbers, the variables reduce to more commonly recognized single-point values such as those described by the single-point model of Besnard *et al.* [7]. The equation for the evolution of the Reynolds stress is

$$\begin{aligned}
&\frac{\partial R_{ij}(\mathbf{x},k,t)}{\partial t}+\frac{\partial R_{ij}(\mathbf{x},k,t)\tilde{U}_n(\mathbf{x},t)}{\partial x_n} \\
&+R_{in}(\mathbf{x},k,t)\frac{\partial \tilde{U}_j(\mathbf{x},t)}{\partial x_n}+R_{jn}(\mathbf{x},k,t)\frac{\partial \tilde{U}_i(\mathbf{x},t)}{\partial x_n} \\
=&\int_{-\infty}^{+\infty}\left[\left(a_i(z')\frac{\partial \overline{P}(z')}{\partial x_j}\right)+\left(a_j(z')\frac{\partial \overline{P}(z')}{\partial x_i}\right)\right]\left[\frac{\exp(-2k|z'-z|)}{\int_{-\infty}^{+\infty}\exp(-2k|z''-z|)\,dz''}\right]dz' \\
&+\frac{\partial}{\partial k}\left\{k^2\sqrt{\frac{kR_{nn}(\mathbf{x},k,t)}{\overline{\rho}(\mathbf{x},t)}}\left[-c_1R_{ij}(\mathbf{x},k,t)+c_2k\frac{\partial R_{ij}(\mathbf{x},k,t)}{\partial k}\right]\right\} \\
&+c_m\int_0^k\sqrt{\frac{kR_{nn}(\mathbf{x},k,t)}{\overline{\rho}(\mathbf{x},t)}}dk\left[\frac{1}{3}R_{nn}(\mathbf{x},k,t)-R_{ij}(\mathbf{x},k,t)\right]+c_d\frac{\partial}{\partial x_n}\left(\nu_t\frac{\partial R_{ij}(\mathbf{x},k,t)}{\partial x_n}\right),
\end{aligned} \tag{5}$$

for the turbulence mass flux is,

$$\begin{aligned}
&\frac{\partial a_i(\mathbf{x},k,t)}{\partial t}+\tilde{U}_n(\mathbf{x},t)\frac{\partial a_i(\mathbf{x},k,t)}{\partial x_n}+\frac{R_{in}(\mathbf{x},k,t)}{[\overline{\rho}(\mathbf{x},t)]^2}\frac{\partial \overline{\rho}(\mathbf{x},t)}{\partial x_n} \\
=&\frac{b(\mathbf{x},k,t)}{\overline{\rho}(\mathbf{x},t)}\frac{\partial \overline{P}(\mathbf{x},t)}{\partial x_j} \\
&-\left[c_{Rp1}k^2\sqrt{a_n(\mathbf{x},k,t)\,a_n(\mathbf{x},k,t)}+c_{Rp2}k\sqrt{\frac{kR_{nn}(\mathbf{x},k,t)}{\overline{\rho}}}\right]a_i(\mathbf{x},k,t) \\
&+\frac{\partial}{\partial k}\left\{k^2\sqrt{\frac{kR_{nn}(\mathbf{x},k,t)}{\overline{\rho}(\mathbf{x},t)}}\left[-c_1a_i(\mathbf{x},k,t)+c_2k\frac{\partial a_i(\mathbf{x},k,t)}{\partial k}\right]\right\} \\
&+c_d\frac{1}{\overline{\rho}(\mathbf{x},t)}\frac{\partial}{\partial x_n}\left(\overline{\rho}(\mathbf{x},t)\,\nu_t\frac{\partial a_i(\mathbf{x},k,t)}{\partial x_n}\right),
\end{aligned} \tag{6}$$

and for the density-specific volume correlation is,

$$\begin{aligned}
&\frac{\partial b(\mathbf{x},k,t)}{\partial t}=\left(\frac{2\overline{\rho}(\mathbf{x},t)-\rho_1-\rho_2}{\rho_1\rho_2}\right)\frac{\partial \overline{\rho}(\mathbf{x},t)\,a_n(\mathbf{x},k,t)}{\partial x_n} \\
&+c_{fb}\left[[\overline{v}(\mathbf{x},t)]^2\frac{\partial}{\partial x_n}\left(\frac{\overline{\rho}(\mathbf{x},t)}{\overline{v}(\mathbf{x},t)}\right)\right]\frac{\partial ka_n(\mathbf{x},k,t)}{\partial k} \\
&+\frac{\partial}{\partial k}\left\{k^2\sqrt{\frac{kR_{nn}(\mathbf{x},k,t)}{\overline{\rho}(\mathbf{x},t)}}\left[-c_1b(\mathbf{x},k,t)+c_2k\frac{\partial b(\mathbf{x},k,t)}{\partial k}\right]\right\} \\
&+c_d\frac{\partial}{\partial x_n}\left(\nu_t\frac{\partial b(\mathbf{x},k,t)}{\partial x_n}\right).
\end{aligned} \tag{7}$$

In this present effort, we restrict our attention to the loss of angular spectral information caused by reduction of the equations from a wavevector dependence to a wavenumber dependence, and

to general features of the nonlocality of the pressure production terms in the Navier-Stokes equations. Attempts at direct model comparisons to the LEM experiments and to numerical simulations failed to produce reasonable results. The cause of this lack of agreement has not been positively identified.

3. Density correlations in the Rayleigh-Taylor experiments

The two-point fluctuating density-density correlations computed from a single photograph from an LEM experiment are shown in Figures 1 and 2. The correlations are constructed using an averaging procedure that presumes approximate statistical homogeneity in the plane of the mixing layer (i.e., the $X-Y$ plane). Figure 1 shows the correlations at position Z as a function of a separation ΔZ around position Z. Figure 2 shows the correlations at position Z as a function of a separation ΔX around position Z. In both plots, the dark color implies a strong positive correlation and the light color is a strong negative correlation. The background gray coloration at large and small Z reflects a lack of correlation. The long range correlations in Figure 2 at large ΔX probably represent a lack of a statistically meaningful sample size at that separation distance, and should be ignored. These figures indicate that there is a significant difference in the structure of these correlation functions. The argument for neglecting this orientational dependence of the correlations must then rest on the assumption that there is no significant effect in neglecting this feature. Further research is necessary to understand the physical ramifications of the difference in the length-scales.

4. Nonlocal pressure effects in Rayleigh-Taylor mixing simulations

As part of the effort to interpret the LEM data, a series of computations were undertaken to simulate various aspects of the LEM experiments. The computations were conducted with a three-dimensional Navier-Stokes program that was first-order accurate in time and second-order accurate in space. The dimensions and material properties here taken to approximate those of the LEM. The cell size was $73mm$ x $73mm$ x $88mm$ and the fluids were decane ($\rho = 0.73gm/cm^3$) and saltwater ($\rho = 1.43gm/cm^3$). The acceleration was $1g$ (i.e., much lower than the $70g$ used in the experiment). The computational grid was 88 x 88 x 106. Sixteen individual realizations with "stochastically" perturbed interfaces were performed. The averaging methodology also exploited the inherent symmetries of the square cross-section of the box (the $X-Y$ plane). Figure 3 shows the bouyancy production $2a_z\partial\overline{P}/\partial z$ as well as the nonlocal nature of the pressure-strain production $\overline{p'(\partial u_z''/\partial z)}$, where a double prime denotes the fluctuation about the mass-weighted average velocity and a single prime denotes a fluctation about volume-weighted average. Note that at the edge of the mixing layer, the direct production due to bouyancy vanishes but the actual pressure-strain correlation is nonzero into the unmixed region.

5. Conclusion

The detailed data regarding density distributions provided by the LEM Rayleigh-Taylor experiments at LLNL have provided new information on the nature of the fluctuating density-density correlations. Further research is still necessary to understand the ramifications of the orientational dependence of these correlations observed in the experiments but neglected in the models. The simulations of Rayleigh-Taylor mixing demonstrated the motivations for incorporating the nonlocal pressure production terms in the Steinkamp *et al.* model. However, the relatively low accuracy and resolution of the runs prevents any detailed comparisons of spectra. There exists

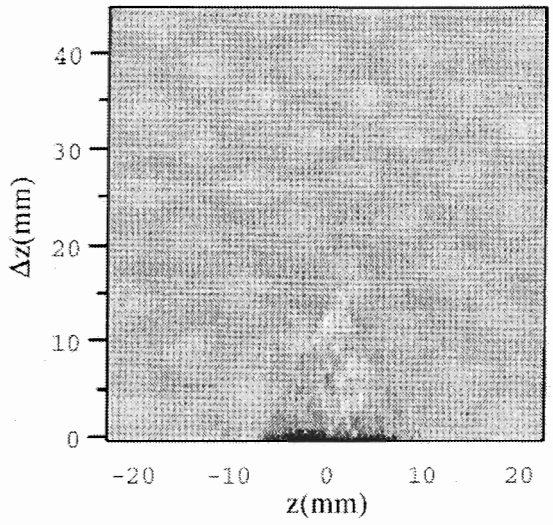

Figure 1. Intensity of two-point fluctuating density correlations $\overline{\rho'(x, z + \Delta z/2)\rho'(x, z - \Delta z/2)}$ averaged over the coordinate x. Data is from a single time from a single experiment. Black is positive, white is negative.

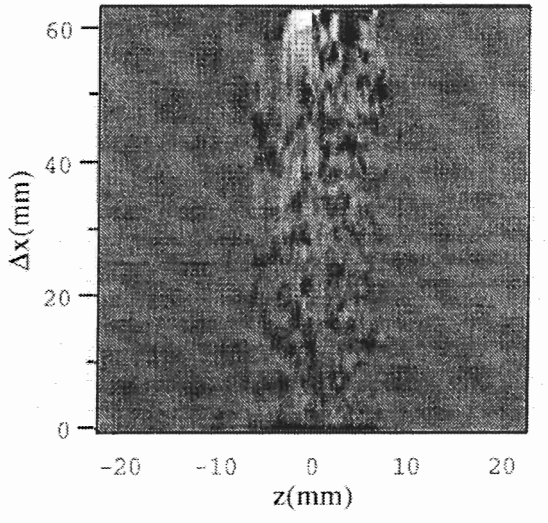

Figure 2. Intensity of two-point fluctuating density correlations $\overline{\rho'(x + \Delta x/2, z)\rho'(x - \Delta x/2, z)}$ averaged over the coordinate x. Data is from a single time from a single experiment. Black is positive, white is negative.

a significant need for experimental data regarding velocities that are of the same quality as the density distribution data of the LLNL LEM experiment. Additionally, there continues to be a

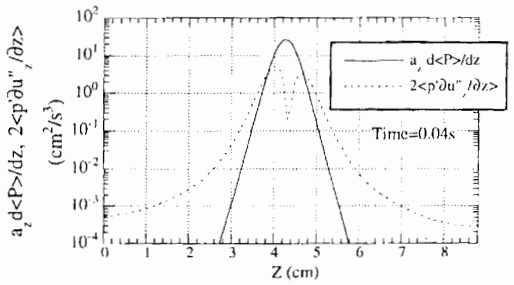

Figure 3. Plot of the pressure production due to turbulent mass flux, and the pressure strain correlation corresponding to the R_{zz} component of the Reynolds stress tensor. Note that the turbulent mass flux, a_z vanishes outside of the actual mixing layer where density fluctuations vanish.

need for robust three-dimensional higher-order computer programs that can handle the sharp discontinuitues that can exist in Rayleigh-Taylor mixing problems.

Acknowledgement. This work is supported by the United States Department of Energy through the Los Alamos National Laboratory LDRD Program.

References

[1] Steinkamp M, Clark T, and Harlow F, Two-Point Description of Two-Fluid Turbulent Mixing. Part 1: Model Formulation, Los Alamos National Laboratory Report LA-UR-96-2038, (1996).

[2] Steinkamp M, Clark T, and Harlow F, Two-Point Description of Two-Fluid Turbulent Mixing. Part 2: Numerical Solutions and Comparisons, Los Alamos National Laboratory Report LA-UR-96-2039, (1996).

[3] Besnard D, Harlow F, Rauenzahn R and Zemach C, Turbulence Transport Equations for Variable-Density Turbulence and Their Relationship to Two-Field Models, Los Alamos National Laboratory Report LA-12303-MS, (1992).

[4] Schneider M, Dimonte G and Remington B, Large and small scale structure in Rayleigh-Taylor mixing, submitted to Phys. Rev. Letters, (1997).

[5] Leith C, Diffusion approximation to inertial energy transfer in isotropic turbulence, Phys. Fluids, 10, 7, 1409-1416, (1967).

[6] Besnard D, Harlow F, Rauenzahn R and Zemach C, Spectral Transport Model of Turbulence, Los Alamos National Laboratory Report LA-11821-MS, (1990).

[7] Clark T, and Spitz P, Two-Point Correlation Equations for Variable Density Turbulence, Los Alamos National Laboratory Report LA-12671-MS, (1995).

[8] Steinkamp M, Spectral Analysis of the turbulent mixing of two fluids, Los Alamos National Laboratory Report LA-13123-T, (1996).

Three Dimensional High-Resolution Simulations of Richtmyer-Meshkov Mixing and Shock-Turbulence Interaction

R.H. Cohen[1], W.P. Dannevik[1], A.M. Dimits[1], D.E. Eliason[1], A.A. Mirin[1], D.H. Porter[2], O. Schilling[1] and P.R. Woodward[2]
[1]Lawrence Livermore National Laboratory, P.O. Box 808, Livermore CA 94550, USA
[2]Astronomy Department, University of Minnesota, Minneapolis, MN 55455, USA

Abstract: Three-dimensional high-resolution simulations are performed of the Richtmyer-Meshkov (RM) instability for a Mach 6 shock, and of the passage of a second shock from the same side through a developed RM instability. The second shock is found to rapidly smear fine structure and strongly enhance mixing. Studies of the interaction of moderately strong shocks with a pre-existing turbulent field indicate amplification of transverse vorticity and reduction of stream-wise vorticity, as well as the mechanisms for these changes.

The Richtmyer-Meshkov (RM) instability [1] is the impulsive-acceleration limit of the Rayleigh-Taylor (RT) instability, and occurs, for example, when a shock passes through an interface of two fluids of differing density. We report here preliminary results from three-dimensional high-resolution direct numerical simulations (DNS) using the piecewise-parabolic method (PPM)[2]. We study the effects of a second shock both directly and via simulations of the passage of a shock through a pre-existing turbulent field. These simulations, and our companion RT simulations, [3] represent one component (generation of benchmark DNS data sets) of a larger project to develop validated sub-grid-scale models for large-eddy compressible simulations, part of the U.S. Department of Energy's Accelerated Strategic Computing Initiative (ASCI).

Three-dimensional high-resolution hydrodynamics computations have been limited by available computer resources. While some low-resolution studies of RM instability (*e.g.*, [4]-[6]) and shock-turbulence interaction [7] have appeared, studies exceeding 10^6 computational zones are only now becoming available; see for example [8].

A recent experimental study [9] of 2-D incompressible fluids indicates dramatically the effect of subjecting developed RM turbulence through a second impulsive acceleration in the same direction as the first. The second event rapidly scrambles the bubble-and-spike structure and enhances the mixing. A natural question is, is there a comparably dramatic effect in 3D and with compressible fluids?

1. Richtmyer-Meshkov simulations

Our simulations are done with a single fluid plus a passive scalar field to monitor mix. The pre-shock gas is initialized with constant pressure and a 2x density contrast on either side of a perturbed planar interface (at stream-wise coordinate $z = 0.5$). The interface perturbation is either a product of single sinusoidal components in the horizontal (x and y) directions, or a set of 32^2 modes with a $k^2 \exp(-k^2/k_0^2)$ distribution of amplitudes and random phases and a mode width k_0 corresponding to 8 wavelengths per unit length. This gas impinges on a higher-density, higher-pressure gas to initiate a Mach 6 shock on the low-density side of the contact

More information - Email: rcohen@llnl.gov

discontinuity. Boundary conditions are periodic in x and y and continuation (zero derivative) in z. Most of the shock is absorbed at the z boundary, though a weak wave is reflected; this can be eliminated with additional computational cost. The passive scalar is initialized with two constant values (color-coded red and blue in the color plates; the light fluid is blue) on either side of the initial contact discontinuity.

Plate 1 shows the passive scalar field at $t = 3$, where time is measured in units of a nominal box length over the pre-shock sound speed in the gas on the lower-density side of the contact discontinuity. The initial surface deformation is the random-phase model with amplitude 0.02 RMS. The resolution is 256^3, the Navier-Stokes viscosity is 4×10^{-5} and the Prandtl number is 1. Our experience with Rayleigh-Taylor simulation at this viscosity and several resolutions indicates that this simulation is resolved. The largest (in z) features tend to correlate with large features in the initial perturbation, consistent with prior observations of persistence of initial conditions. Also compared to the corresponding RT visualization at comparable parameters, [3], even though the initial condition for our RM simulation is slanted more toward longer wavelengths. The growth of the RM mixing layer (measured by where the horizontal average of the passive scalar is 0.1 and 0.9) is as shown in Fig. 1a; the fit is of the form $\Delta z = c(t + t_0)^p$ with $p = 0.75$, $t_0 = 0.175$, and $c = 0.33$. That the asymptotic behavior is a power law with $p < 1$ is in agreement with the conclusions of Refs. [8], [10], and [11].

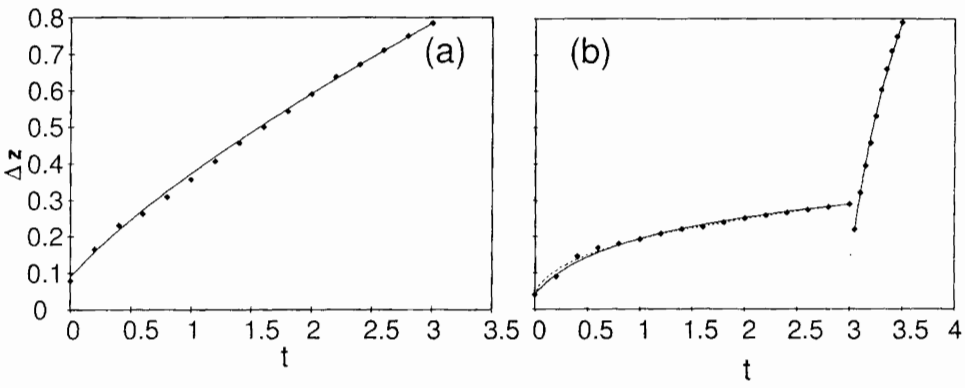

Figure 1. Mixing layer growth vs. time for (a) random-phase sum initial condition; (b) single mode initial condition with two shocks

Plate 2 shows the corresponding result for a single sine-wave perturbation with wavelength 1/2 the box width of the random-phase simulation. The resolution of $128^2 \times 288$ (not all shown) yields a resolved Navier-Stokes simulation. The development of fine-scale, non-chaotic features is evident. The growth of the mixing layer (measured by departure of the passive scalar from its initial values) is indicated by the $t < 3$ portion of Fig. 1b. The fit represented by the solid curve is asymptotically logarithmic as expected for a single bubble and spike, $\Delta z = \Delta z_0 + c_1 \ln(1 + at)$, with $c_1 = 0.010$, $\Delta z_0 = 0.04$, and $a = 3.5$. A slightly better fit is obtained by a power-law form (dotted curve), $c_p(t + t_0)^p$ with $p = 0.38$, $t_0 = 0.0165$ and $c_p = 0.19$.

Plate 3 depicts the result of passing an additional Mach 6 shock through the interface from the same (low-density) side. Even at $t = 3.1$ (not shown), there is a distinct change in character, with much of the fine structure smeared out. In the time slice shown, at $t = 3.2$, we

additionally see the beginning of an inversion in the near corner of the simulation; what had been a spike of red fluid extending into blue begins to detach while blue fluid encroaches on red around the edges of the spike. At later times ($t \sim 3.3 - 3.5$) the red spike detaches and a jet of blue penetrates (rapidly) through the former red region. The second shock significantly accelerates mixing-region growth following an initial contraction, as can be seen from the right-hand portion of Fig. 1b. Equally good (almost indistinguishable) fits of logarithmic (dotted) and power-law forms are obtained: respectively, $\Delta z_0 + c_l \ln[1 + b(t - t_0)]$ with $\Delta z_0 = 0.22$, $t_0 = 3.2$, $c_l = 0.61$, and $b = 3.5$; and $c_p(t + t_0)^p$, with $p = 0.55$, $t_0 = -3.0$, and $c_p = 0.42$ The rapid destruction of features and acceleration of mixing is reminiscent of the experimental results in Ref. [9]; though in our case, some, but not all, of the acceleration is due to the increased sound speed (factor of about 4) following the second shock.

2. Shock-turbulence interaction

We also perform simulations of the interaction of a shock with a pre-existing turbulent field. These may be viewed as providing a view of second-shock interaction on the more microscopic scale of the secondary instabilities arising in the nonlinear stages of the RM instability. A random-phase Gaussian-distributed spectrum of 8^3 modes is allowed to decay from a turbulent Mach number of 0.75 to about 0.2. Then a shock is induced by specifying inflow boundary conditions corresponding to the desired down-stream (quiescent) gas. These simulations are done with only the dissipation provided by the PPM algorithm. The resulting x vorticity field for a Mach 6 shock in a 512^3 resolution simulation is shown in Plate 4. We observe a significant amplification induced by the shock passage. The shock itself is not directly visible, but is at the right edge of the amplified region. The dark region on the left is the high-density quiescent gas introduced to generate the shock. There is considerable distortion of the shock front, but comparison with a turbulence-free run shows no measurable change in propagation speed.

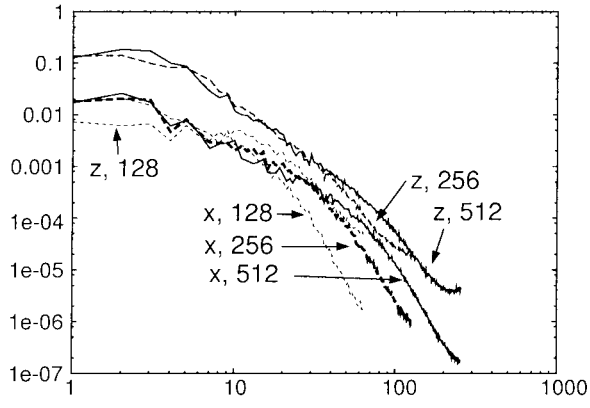

Figure 2. x and z velocity power spectra at 128^3, 256^3, and 512^3 resolution

Velocity power spectra (power per unit-thickness annulus in k_x, k_y space) are shown in Fig. 2 for several resolutions. These spectra suggest that a meaningful inertial range is present in the 256^3 and 512^3 simulations, and that the results at 256^3 and 512^3 are converged in the energy containing range and the captured portion of the inertial range. They also indicate a steepening of the v_z spectrum relative to v_x. The v_x spectrum is approximately the same

shape as that of all components in the unshocked gas (not shown), with a Kolmogorov-type $k^{-5/3}$ slope in the inertial range, but overall larger. The vorticity component ω_j spectra show a similar convergence, and a steepening of ω_x relative to ω_z.

Figure 3a shows ω_j as a function of z. Evident features are the amplification of the ω_x (and ω_y), and the smaller reduction in the ω_z, and the re-isotropization further down stream. Still further down stream, all components drop off as the quiescent gas region is entered. The amplification of ω_x, ω_y and the reduction of ω_z have a smooth variation with Mach number, as shown in Fig. 4 for a series of 256^3 simulations. The relative changes are approximately characterized by: $\Delta\omega_j/\omega_j \approx C_j\,(M-1)^{0.6}$, with $C_x \approx C_y \approx 0.38$, and $C_z \approx -0.099$.

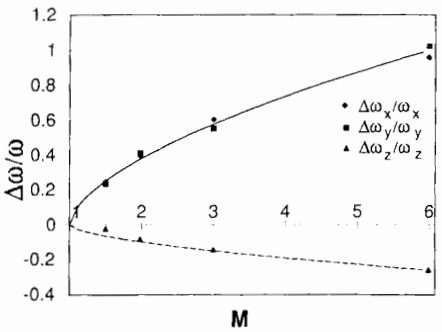

Figure 4. Relative change in vorticity vs. shock Mach number

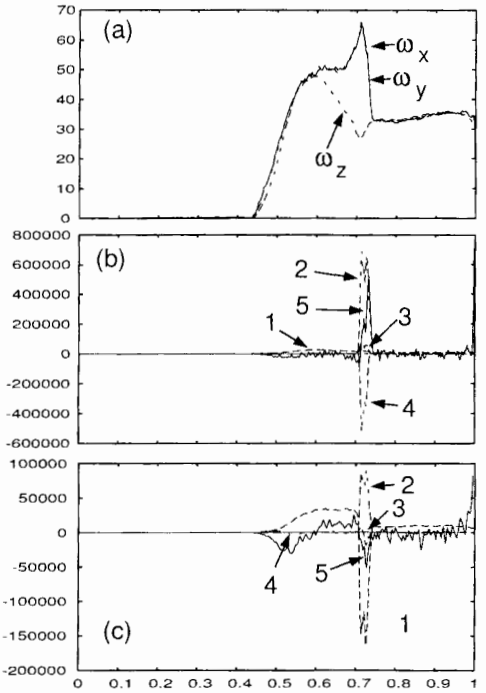

Figure 3. Vorticity component evolution: (a) r.m.s. vorticities vs. z; (b) terms in x enstrophy equation; (c) terms in z enstrophy equation

In order to identify the mechanisms responsible for the observed effects, we separately evaluate and plot each term in the equation of evolution for the horizontal averages of squares of the vorticity components ("enstrophy components"), which we write in the form:

$$\frac{\partial\left\langle\omega_j^2/2\right\rangle}{\partial t} + \langle\mathbf{v}\rangle\cdot\nabla\left\langle\omega_j^2/2\right\rangle \approx \mathbf{v}^*\cdot\nabla\left\langle\omega_j^2/2\right\rangle$$
$$= \langle\omega_i(\omega\cdot\nabla)v_i\rangle - \left\langle\omega_j^2\nabla\cdot\mathbf{v}\right\rangle + \left\langle(\omega/\rho^2)\cdot\nabla\rho\times\nabla P\right\rangle - \left\langle\mathbf{v}'\cdot\nabla\omega_j^2/2\right\rangle$$

where $\mathbf{v}^*$ is the average velocity in a reference frame in which the shock is at rest and $\mathbf{v}' = \mathbf{v} - \langle\mathbf{v}\rangle$. The terms on the right hand side are, respectively, vortex stretching, enstrophy dilatation, baroclinic production, and nonlinear advection. These terms are separately plotted along with $\mathbf{v}^*\cdot\nabla\omega_j^2$ in Fig. 3b and 3c. We observe that the increase in ω_x (and ω_y) is primarily the result of dilatation, while the decrease in ω_z and its subsequent recovery results mainly from vortex stretching. There is a significant contribution from the nonlinear advection term,

implying that conventional rapid distortion theory or linear interaction analysis, which would neglect it, would not provide an accurate answer.

3. Discussion and conclusions

In addition to reproducing familiar features of the Richtmyer-Meshkov instability, we have found smearing of fine-scale structure and rapid mixing caused by the passage of a second shock in the same direction, similar to that observed experimentally [9] for incompressible fluids, as well as detachment of spikes. We find a weaker departure from linear growth of the mixing layer for our random sum of modes than for a single mode, and for the mixing following the second shock than after the initial shock.

For the interaction of a shock with pre-existing turbulence, we find overall amplification of vorticity by the passage of a shock, as has been noted and quantified previously [7] for the case of a weak shock. However, Ref. [7] reports change in only the transverse vorticity, and finds negligible contribution from nonlinear advection and hence good agreement with a linear interaction analysis. Here we study moderately strong shocks, find that there is an opposing change in the stream-wise component ω_z, and observe that while the increase in ω_x (and ω_y) is due primarily to the compressibility term, there is an important contribution from nonlinear advection. We also find a decrease and subsequent recovery of ω_z, both resulting from vortex stretching. The overall increase in the ω^2 can be viewed as the stirring process that breaks up the fine structure when a second shock passes through a developed Richtmyer-Meshkov instability. The observed asymmetry in which vorticity components normal to the shock propagation are amplified while that in the shock propagation direction decreases implies selectivity in the *kinds* of fine-scale features broken up.

Acknowledgement. Work performed under for the U.S. Department of Energy at Lawrence Livermore National Laboratory and at University of Minnesota under Contract W7405-ENG-48. Computations performed in part on the ASCI Blue Pacific IBM SP system.

References

[1] Richtmyer RD, Comm. Pure and Applied Math, 13, 297, (1960); Meshkov EE, Isv. akad. Nauk SSR, Mekhanika Zhidkosti i Gaza, 5, 151, (1969).
[2] Woodward PR and Collela P, J. Comp. Phys. , 54, 174, (1984).
[3] Schilling O, Cohen RH, Dannevik WP *et al.*, , this volume.
[4] Cloutman LD and Wehner MF, Phys. Fluids A, 4, 1821, (1992).
[5] Demchenko VV, in Compressible Turbulent Mixing, R. Young, J. Glimm and B. Boston, eds. World Scientific, Singapore, 331, (1996).
[6] Lebo IG, Rozanov VB, Tishkin VF *et al.*, ibid, 346.
[7] Lee S, Lele S and Moin P, J. Fl. Mech, 251, 533, (1993)
[8] Youngs DL, Laser and Particle Beams, 12, 725, (1994). Ref. for persistence of i.c.'s. Ref. for development of short w.l. Linear theory reference.
[9] Jacobs JW and Sheeley JM, Phys. Fluids, 8, 405, (1996).
[10] Barenblatt GI, in Non-linear Dynamics and Turbulence, G.I. Barenblatt, G. Loos and D.D. Joseph, eds. Pitman, Boston, (1983).
[11] Neuvazhayev VY, Matematicheskoye Modelinovaniye, 3, 10, (1991).

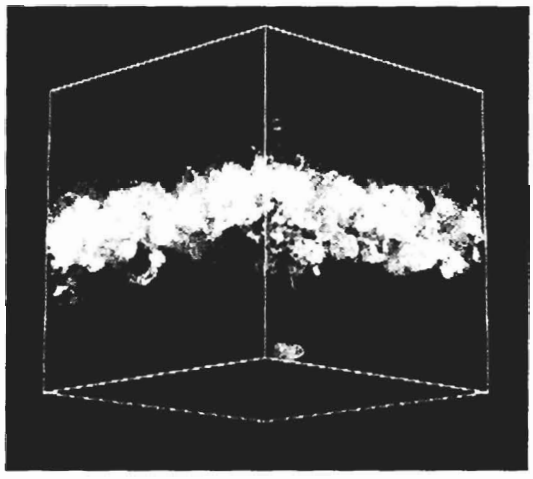

Plate 1: Passive scalar field at t=3 for random-phase sum initial condition

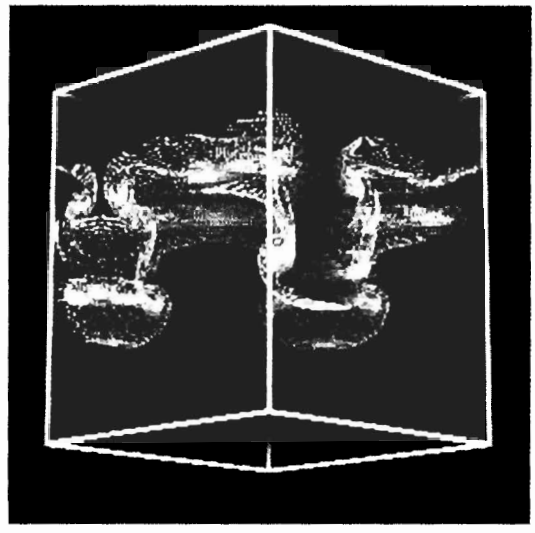

Plate 2: Passive scalar field at t=3 for single-mode initial condition, just before second shock

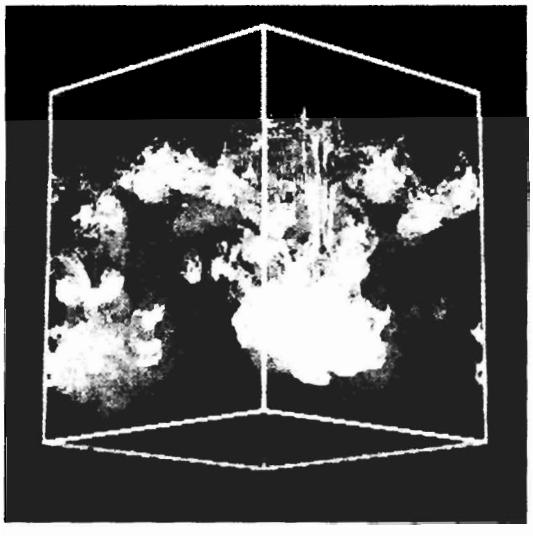

Plate 3: Passive scalar field at t=3.2 for single-mode initial condition, after second shock

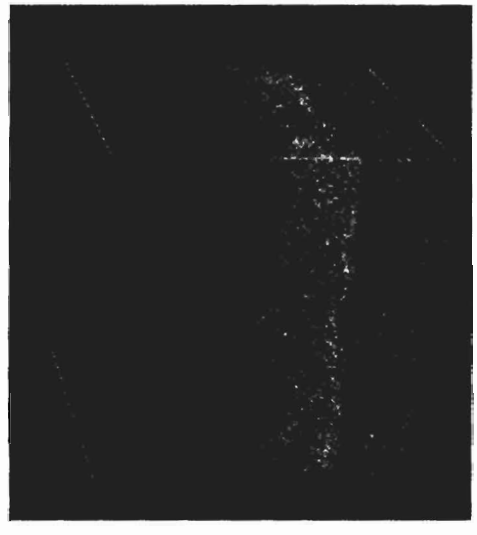

Plate 4: Magnitude of x vorticity for shock-turbulence interaction

Dispersion Relationships for Solid State Instability Growth and Sensitivity to Equation of State

J.D. Colvin, L.G. Wiley, E.A. Chandler, B.A. Remington and D.H. Kalantar
Lawrence Livermore National Laboratory
P. O. Box 808, L-482, Livermore, CA 94550, USA

Abstract: We are developing experiments on the Nova laser to investigate the effects of material strength on stabilizing the growth of the Rayleigh-Taylor (RT) instability in metal foils maintained in the solid state [1]. The first task in this effort was to create a high contrast (~50:1), laser pulse shape that would compress the metal on a very low adiabat by a factor of 1.5-2.0 and to a pressure > 3 Mbar while keeping the metal solid (at a temperature below melt temperature). The planar targets consisted of 20 microns of CH(Br) backed by 15 microns of Cu, with sinusoidal ripples at the interface, and were mounted on the wall of a hohlraum that was heated by the laser pulse. This first phase of the study successfully demonstrated material strength stabilization at high pressures, as discussed by Kalantar *et al.* [2].

In this paper we derive an approximate analytical dispersion relation for solid state instability growth. We discuss the results of 1-D calculations with the radiation-hydrodynamics code LASNEX [3] that were used in evaluating the dispersion relation for the Nova experiments, taking into account the pressure dependence of the material strength. We conclude that the perturbations on the metal foils in these experiments should remain stable at all times. We show that this result is consistent with the observation of late-time growth in the Nova experiments if the metal takes a few nanoseconds to transition to plasticity.

Solid state melt temperatures are generally a function of compression, typically increasing with increasing compression. The material pressure is dominated by the cold lattice pressure, which is a function only of compression. Hence, the treatment of equation of state (EOS) is important in characterizing the phase of the material during compression. In the LASNEX calculations we compare results for our low-adiabat compression of a Cu foil using a tabular EOS (based on a Thomas-Fermi atomic model), the analytic Quotidien EOS, [7] and a Gruneisen EOS following the formulation of Steinberg *et al.* [4]. The latter approach takes into account both the cold lattice energy and the thermal energy, but ignores the negligibly small electron thermal contribution. Measurements of melt time are shown to be an effective EOS model discriminator.

1. Derivation and analysis of dispersion relationship

We have derived an approximate analytical dispersion relation for solid state instability growth following the method of Mikaelian [1]. He starts with the general eigenvalue equation for the velocity of a perturbation on a finite-thickness fluid layer with surface tension and viscosity, and derives an exact solution numerically from det(M)=0, where M is an 8×8 matrix. He then derives an approximate solution analytically by substituting the inviscid eigenfunctions into the exact eigenvalue equation. The integrations yield a dispersion relation which is a polynomial in the growth rate γ_s. Adapting the same method to a finite-thickness solid layer with shear

More information - Email: colvin5@llnl.gov

strength G and elasto-plastic viscosity ν, we find:

$$\gamma_S^2 + 2k^2\nu\gamma_S + k \cdot tanh(kh) \cdot (kG/\rho - Aa) = 0, \quad (1)$$

where k is the wavenumber of the perturbation, h the layer thickness, ρ the layer density, A the Atwood number, and a the acceleration. The solution of this second-order equation for the growth rate is

$$\gamma_S = \nu k[(1 - (C/\nu^2 k^3))^{\frac{1}{2}} - 1], \quad (2)$$

where C=k·*tanh*(kh)·(kG/ρ - Aa).

It is easy to see that the perturbation is unstable and grows ($\gamma_S > 0$) only for $k < k_c$ or wavelength of the perturbation $\lambda > \lambda_c = 2\pi G/Aa\rho$. That is, the perturbation does not grow if the shear wave can transmit the restoring force of the lattice across the perturbation in less time $(1/k(G/\rho)^{1/2})$ than the characteristic growth time of the perturbation $(1/(kAa)^{1/2})$. Thus, the material shear strength limits the range of unstable wavelengths.

Equation (2) was evaluated for the conditions of the Nova laser experiments described by Kalantar *et al.* [2]. In those experiments we create an x-ray drive inside a cylindrical gold hohlraum using about 22 kJ of energy in eight beams of the Nova laser at Lawrence Livermore National Laboratory. We developed a temporally shaped laser pulse (ps56) that produces a temporally shaped radiation drive pulse in a hohlraum that reaches a peak radiation temperature of 97 eV at 6.5 ns. This drive pulse provides a low-adiabat compression by a factor of about 1.5 to drive a metal foil to a peak pressure of about 3 Mbar while leaving it solid. Using this pulseshape we observed that perturbations with wavelengths of 20 μm and 50 μm on 15-μm-thick Cu and Mo foils do not begin to grow until after 10 ns, more than 4 ns later than for classical fluid growth, ostensibly a demonstration of material strength stabilization.

In order to evaluate equation (2) we calculated P(t), ρ(t), T(t), and a(t) for the Nova foils using the radiation-hydrodynamics code LASNEX [3] in 1-D and the measured radiation drive of ps56. This drive pulse compresses the Mo foil to a peak density of 15.8 gm cm^{-3} and a peak pressure of 3.1 Mbar at 7.0 ns. Both the Cu and the Mo foils remain solid at all times when driven by ps56, with the melt temperature computed from the Lindemann law. The plastic ablator/foil interface, on which the perturbations have been machined, begins to move at 3.8 ns when the first shock reaches it, and the interface has moved about 20 μm in 10 ns. In evaluating equation (2) we accounted for the increase in material shear strength with pressure (strength increases as the lattice potential energy increases), according to the material strength model of Steinberg *et al.* [4]. When the pressure exceeds the yield strength, the material enters the plastic flow regime and the lattice keeps rearranging itself into a minimum energy state, i.e., the atoms "slide over" each other with a characteristic viscosity that depends on pressure P, ρ, and the strain rate $d\epsilon/dt$. The strain rate was calculated from its dependence on P, G, and the bulk modulus K, accounting for the pressure dependence of G and K. It is easy to show that, in compression, the plastic strain rate is always greater than the elastic strain rate.

The result of all these calculations is that the cutoff wavelength λ_c, which starts at a very high value when the foil first begins to accelerate, asymptotes to about 250 μm after 10 ns. Thus, the 50-μm and 20-μm perturbations of the Nova experiments should be stable at all times. At the wavelength of maximum growth, which is twice the cutoff wavelength or ~500 μm, growth is significantly suppressed in thin foils, as shown in Figure 1. This figure shows the perturbation growth at the wavelength of maximum growth as a function of time for Mo foils of thickness 15 μm and 150 μm driven by pulseshape 56. Figure 2 shows the dispersion curves for these two cases compared to the dispersion curve for classical growth.

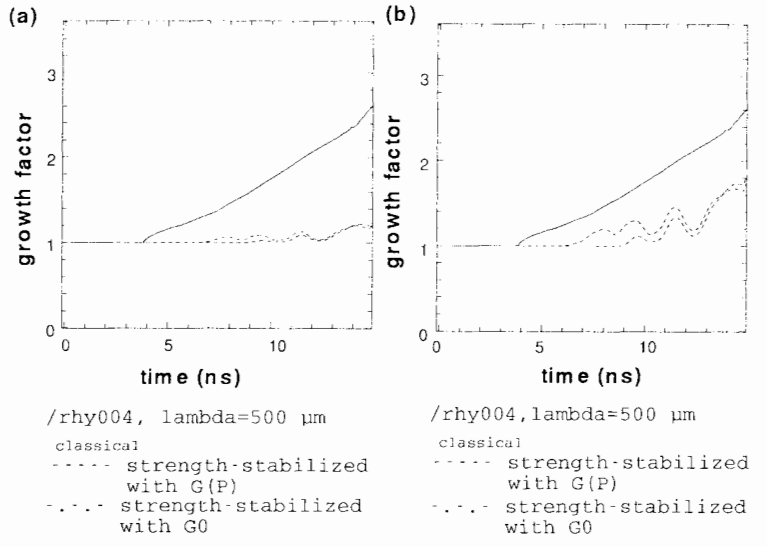

Figure 1. Growth factors of a 500-μm perturbation as a function of time on Mo foils of a) 15 μm thickness and b) 150 μm thickness driven by pulseshape 56. The dashed curve shows the growth factors calculated with accounting for the pressure dependence of the shear strength, and the dash-dot curve without. These growth factors are compared to the growth factors of the Mo foil if it were liquid (solid curve).

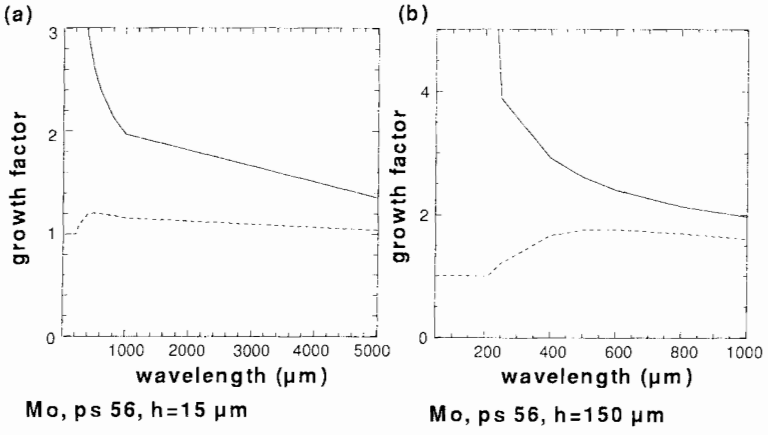

Figure 2. Dispersion curves for Mo foils of a) 15 μm thickness and b) 150 μm thickness driven by pulseshape 56. The dashed curve shows the strength-stabilized dispersion curve, and is compared to the dispersion curve of the Mo foil if it were liquid (solid curve).

2. Instability analysis and transition to plasticity

The perturbation growth of the Nova experiments has also been simulated in 2-D with LASNEX and with another radiation-hydrodynamics code, both including the Steinberg *et al.* material

strength model, and these simulations predict little difference from classical growth [5]. The codes, however, do not account for the rate dependence of the transition to plasticity. In the code simulations, wherever and whenever the stress exceeds the material strength (which at atmospheric pressure is 1.2 kbar for Cu and 16 kbar for Mo), the material is assumed to be instantaneously plastic, with a much lower shear strength G. The observed late-time growth in the experiments, therefore, is explained as the perturbation crossing an instability boundary, i.e., the material takes a few nanoseconds to transition to a plastic, when it has a much lower but non-zero shear strength, at the high strain rates of the Nova experiments (few x 10^7 s^{-1}). It is not known how the shear strength in actual metals decreases in the transition to plastic flow, so this is not accounted for in the dispersion curve analysis. In this analysis, instability growth depends only on perturbation wavelength, foil thickness, and material strength.

In recent work by Lebedev *et al.* [6] stability boundaries are derived that depend also on perturbation amplitude, but they do not derive a dispersion relation. Using their formulation, we calculate that for a 15-μm-thick Mo foil driven by ps56, the initial amplitude is larger than the threshold amplitude for instability after the shock emerges from the back of the foil, ~6.5 ns. Thus, the perturbation should become unstable after that time. Additionally, we calculate that the Cu foil melts at the interface after 10 ns if the ps56 "foot" temperature is too low, thus allowing the second shock to catch up to the first before it reaches the interface, effectively shocking the material too hard initially. The broad-band filter diode array that measures the radiation flux from which the drive temperature is inferred can determine only an upper limit to the foot temperature. Thus, the observation of late-time growth in the Nova experiments is consistent with the dispersion curve analysis (which predicts no growth), and not with the 2-D code simulations (which predict near-classical growth) if the material melts at the interface after 10 ns because the foot drive is too low, and/or if the perturbation crosses an instability boundary (transitions to plasticity) after 10 ns. The near-term focus of the experimental campaign is to measure the foot temperature by measuring the time of first shock breakout with a new "visar" technique, and to determine the state of the material by a Bragg diffraction measurement [2].

3. Sensitivity to equation of state

Melt temperatures are generally a function of compression, increasing with increasing compression. Likewise, material pressure is dominated by cold lattice pressure, which is a function only of compression. Hence, the treatment of equation of state (EOS) is important in characterizing the material state. Three different EOS models were used in the LASNEX calculations: a tabular EOS (EOP) based on a Thomas-Fermi atomic model; the analytic Quotidien EOS [7] (QEOS); and a Gruneisen EOS for which we derived the internal energies from the pressure formulation of Steinberg *et al.* [4]. The derivation of the Gruneisen EOS takes into account both the cold lattice energy and the ion thermal energy, but ignores the negligibly small electron thermal contribution. In the pressure-density regime of interest the Gruneisen EOS is softer than both EOP and QEOS. With the softer Gruneisen EOS Cu compresses to higher density and lower temperature, for the same drive pressure, than with EOP. Thus, in principle, a pulse shape can be designed to melt the metal with EOP and not with Gruneisen. We note that both Cu and Mo stay solid at all times with ps56. We have, in addition, designed another pulse shape, a higher-temperature variant of ps56 (ps 55) that melts Cu at 8.8 ns if EOP is used, but does not melt it if the Gruneisen EOS is used. This pulseshape can thus serve as an EOS model discriminator, using an experimental technique that can measure melt time. The

Bragg diffraction diagnostic technique being developed for these experiments [2] can provide these measurements.

Acknowledgement. This work was performed by the Lawrence Livermore National Laboratory under the auspices of the U. S. Department of Energy under Contract N° W-7405-ENG-48.

References

[1] Mikaelian K, Phys. Rev. E, 3676, 54, (1996).
[2] Kalantar DH, these Proceedings.
[3] Zimmerman GB and Kruer WL, Comments Plasma Phys. Controlled Fusion, 2, 51, (1975).
[4] Steinberg DG, Cochran SG and Guinan MW, J. Appl. Phys., 51, 1498, (1980).
[5] Weber SV *et al.*, these Proceedings.
[6] Lebedev AI, Nisovtsev PN and Rayevsky VA, Proceedings of the 4th International Workshop on the Physics of Compressible Turbulent Mixing, Cambridge, England, Cambridge University Press, 81, (1993).
[7] More RM, Warren KH, Young DA and Zimmerman GB, Phys. Rev. Fluids, 31, 3059, (1988).

Application of a General Purpose CFD Package to Rayleigh-Taylor Instability

S.B. Dalziel and P.F. Linden
DAMTP, University of Cambridge, Silver Street, Cambridge CB3 9EW, England

Abstract: The use of general purpose computational fluid dynamics software packages such as AEA Technology's CFX (previously known as Flow3D) is growing rapidly in a wide range of industrial problems. The predictive power of such packages for complex flows containing large density gradients remains uncertain. The techniques used may be limited by the computational power available (typically a workstation) and the need to keep the solution strategy as general as possible. to model the turbulence need to be chosen carefully and used with caution. In this paper we avoid present a comparison between preliminary simulations using TURMOIL3D, CFX, and Settle (a simple two-dimensional streamfunction-vorticity code). We attempt to simulate the flow produced in a series of laboratory experiments through the matching of the initial conditions and parameters to those found in the experiments.

1. Introduction

Numerical modelling is playing an ever increasing role in science and engineering in both research and industrial environments. The requirements of the two communities often differ. The research community is, in some sense, in search of "truth", while industry often simply want "the answer". This difference in goal, in combination with a difference in the available resource, leads to different requirements for a numerical model. In the research environment the "quality" of the end product of a numerical model is normally paramount. It should provide you with the understanding or confirmation of the underlying physics that is sought. Ease of use and an ability to model a huge range of different flow types and geometries are much less important than the accuracy. Flexibility is required at a low level so that different physical ideas can be tested for a given class of problems. In contrast industry requires the model to be "cost effective" and produce an answer which is accurate within acceptable bounds. Hardware costs may sometimes be important, but in general the personnel costs are much more significant. The software must be "easy to use" and may well be operated by non-specialists who do not fully understand the inner workings of the code. High level flexibility - so that the same code and training may be applied to a diverse range of problems - is much more important than minor variations in the physics incorporated into the model. Despite the substantial differences in the user requirements for research and industrial codes, there remains a need for general purpose industrial codes to provide an accurate representation of the fluid dynamics. In a sense their job is much harder than for a research code: they must combine accuracy with the requirements for flexibility and ease of use. In this paper compare two research codes - TURMOIL3D [1] and Settle [Dalziel, unpublished] with the general purpose CFX (from AEA Technology) using a two-dimensional Rayleigh-Taylor instability.

More information - Email: sd103@amtp.cam.ac.uk or s.dalziel@damtp.cam.ac.uk

2. Basis of codes

Table 1 summarises some of the key features for the three codes used in this study. In the case of CFX the full range of features is incredibly broad, but of little relevance to the current study. Note that both TURMOIL3D and CFX are three-dimensional codes, whereas Settle is only two-dimensional. The test problem chosen is itself two-dimensional, primarily due to hardware limitations preventing CFX from being run on a three-dimensional problem at adequate resolution, but also due in part to the inherently two-dimensional nature of Settle.

	TURMOIL3D	CFX (version 4.1)	Settle
Author	Youngs	AEA Technology	Dalziel
Model type	Research (RT & RM)	General purpose	Research (Sedimentation)
Dimensions	2D or 3D	3D	2D
Formulation	Pressure Velocity	Pressure Velocity	Streamfunction Vorticity
Dissipation	Zero (numerical only)	Laminar or Turbulent	Zero (numerical only)
Compressibility	Compressible	Compres. or Incompres.	Incompressible
Discretisation	Finite difference	Finite volume	Finite volume
Grid	Cartesian	Body fitting hexahedral	Cartesian
Scalar/velocity	Staggered	Co-located	Stagerred
Advection	Van Leer	FOU, Hybrid, Central, HUW, QUICK, CCCT, CONDIF, Min-Mod Van Leer or MSOU	FOU, SOU, MSOU Van Leer, Min-Mod, QUICK or SHARP
Momentum equation	Integral energy and equation of state giving pressure	SIMPLE; Improved Rhie Chow	Streamfunction; multigrid
Time stepping	Explicit	Implicit, iterative sol.	Explicit

Table 1. Comparison of features.

3. Problem specification

The test case is for an incompressible, inviscid, nondiffusive, miscible, Boussinesq fluid in a two-dimensional rectangular domain. The initial density field is given by:

$$\rho(x,y,t=0) = \begin{cases} \rho_1 & y > 0 \\ \frac{1}{2}(\rho_1+\rho_2) & y = 0 \\ \rho_2 & y < 0 \end{cases} \tag{1}$$

where the domain is defined as $x \in [-L/2, L/2]$ and $y \in [-H/2, H/2]$ with the aspect ratio $H/L = 1.25$. The instability growth is initiated by a divergence-free velocity field obtained from the stream function:

$$\Psi(x,y,z) = \Psi_0 U_{Barrier} L \frac{h_{Barrier}}{H} \sum_{n=1}^{N} a_n sin\frac{n\pi x}{L} \frac{sinh\frac{n\pi H}{2L}\left(1-2\frac{|z|}{H}\right)}{sinh\frac{n\pi H}{2L}} \tag{2}$$

This streamfunction is irrotational everywhere except at $y = 0$. The vorticity at this level is determined by experimental measurements [2] which specify the values of the coefficients Ψ_0 and a_n $(n = 1, 10)$.

All three codes were run at a resolution of 160 control volumes horizontally and 200 vertically. As CFX, does not have a true two-dimensional mode, simulations with CFX had a three-dimensional mesh with only two mesh points in the third direction. In addition to these two-dimensional runs, TURMOIL3D was also run for a three-dimensional problem, the three-dimensionality being triggered by the addition of high wave number noise to the initial density field at $y = 0$. Table 2 summaries the resources required for these runs.

	TURMOIL3D	CFX (version 4.1)	Settle
Resolution	200×160 $200 \times 160 \times 80$	$200 \times 160 \times 2$	200×160
Precision	Double	Double	Double
Memory requirement	32Mbyte/360Mbyte (flow solver only)	140 Mbyte (flow solver only)	3.5 Mbyte (includes interface)
Physical Mem.	16 Gbyte	160 Mbyte	64 Mbyte
Processor	Cray C98D	266 MHz alpha	266 MHz Pentium II

Table 2. Requirements for test run.

4. Comparison of codes

In this paper the comparison between the three codes will be entirely visual and based on plots of the density field as a function during the self-similar growth and subsequent overturning phases. This comparison is presented in figure 1 where a clear quantitative agreement can be seen between the two-dimensional simulations at times $\tau = 1$ and $\tau = 2$. There is also remarkably close agreement with the three-dimensional simulations in terms of the overall growth

of the mixing zone. This supports the notion that the two-dimensional velocity perturbation is controlling the growth of the instability while the three-dimensional motion is responsible primarily for the molecular mixing between upper and lower layers [3].
The differences between the two-dimensional simulations at a given time are relatively small initially, but grow with time. The lack of an exact agreement is of no surprise in this turbulent flow where any small differences are amplified by the growth of the instability. Indeed the simulations agree more closely than any two of the nominally identical experiments which were the basis for the chosen set of initial conditions.

5. Discussion

While the comparison of figure 1 shows that all three models are capable of solving this particular problem with comparable accuracy, the ease and efficiency with which they achieve this differ markedly. Moreover, some of the difficulties associated with using a general purpose package such as CFX should be highlighted. Reference back to table 2 shows that Settle places the lightest demand on computer resources such as memory. This is not surprising due to the simplicity and inherent two-dimensionality of the streamfunction-vorticity formulation. The much larger memory requirements for TURMOIL3D are acceptable given the combination of the added complexity of the compressible equations and generality of the model. However, the requirements for CFX appear excessive at first sight. The reasons, however, stem from the general purpose nature of the code and the historical use for the code to solve steady state problems. As noted in table 1, CFX uses a hexahedral body-fitted mesh. The use of such a mesh requires a substial increase in the number and size of the data structures required to manipulate it and calculate simple things like derivatives. The biggest contribution, however, probably comes from the use of an implicit scheme for the time stepping and the need to efficiently solve large systems of equations through a linearised iteration. The use of an implicit time step is a consequence of the need for CFX to similate quasi steady-state problems in a robust and efficient manner. While the stability of implicit schemes is attractive for some problems, they have fewer advantages for transient problems with large spatial gradients such as Rayleigh-Taylor instability. Indeed hidden problems may arise if the selected time step is too large. First, the iterative solution process for the implicit equations can be unstable, leading to either the code terminating due to this failure, or an incorrect solution. Second, a computation such as this containing large density gradients may suffer badly from truncation error such that a time step that converges and is stable does not produce a reasonable model of the flow. An example of this problem is illustrated in figure 2a, for the flow at $\tau = 2$, where the large time steps ($\Delta\tau = 0.04$ compared with the $\Delta\tau = 0.002$ for the CFX simulation in figure 1) cause the density gradients to be smeared out compared with the comparable density plot in figure 1b. While it is possible to achieve the required accuracy with the implicit time step, the size of the steps required are comparable with those for the explicit schemes, while the individual steps are substantially more costly. The combination of this, the overheads of the generalised grid and the lack of a true two-dimensional mode combine to slow CFX to the point where the simulations shown in figure 1 required approximately 20 hours for CFX compared with 10 minutes for Settle on machines with comparable base performance.
Another area where CFX fails to meet some of the goals itemised in the introduction is in its ease of controlling the simulation itself (the specification of the geometry and the graphics abilities are excellent, although again very taxing on computer resources). In one sense this is not really a criticism of the code, at least from the research view point, as the "problem" stems from the low level flexibility required in a research code. However, this same flexibility could

lead inexpert users to be misled by the results through inappropriate choices. For example,

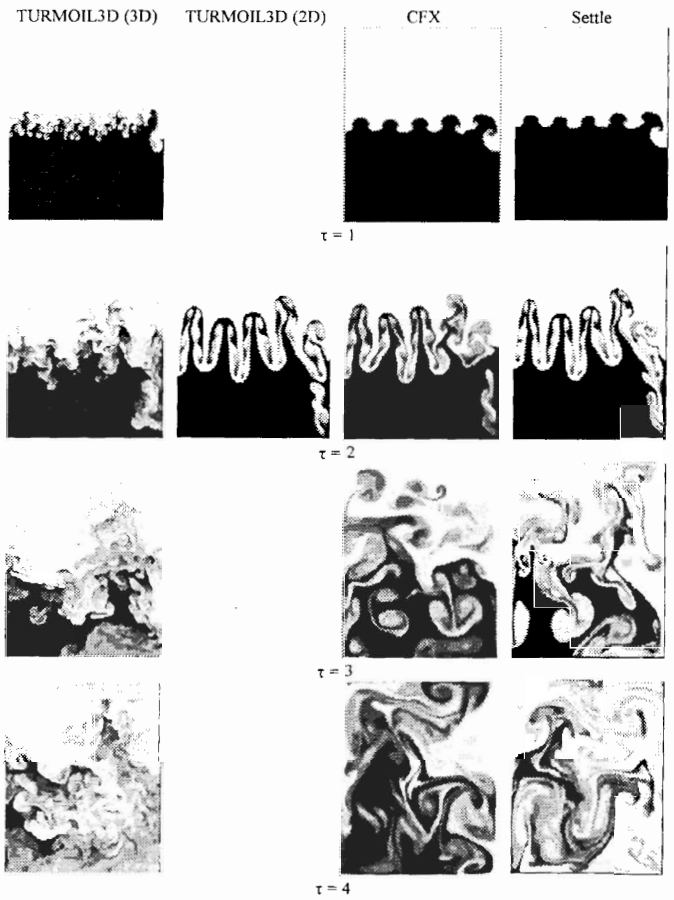

Figure 1. Comparison of simulations for the codes and times indicated. The concentration field is rendered as a greyscale image.

figure 2b (again for $\tau = 2$) shows how an inappropriate choice of a first order advection scheme can lead to an unacceptable level of numerical diffusion, yet this is the default scheme due to its robust behaviour. For many flows the numerical diffusion associated with the first order scheme is acceptable and may be considered a substitute for molecular or turbulent diffusion in the flow. However, for the large spatial gradients characteristic of Rayleigh-Taylor instability, the second and third order schemes (such as the CCCT scheme used for the CFX calculations presented in figure 1) performed much better, at least provided flux limited versions were used to prevent spurious oscillations.

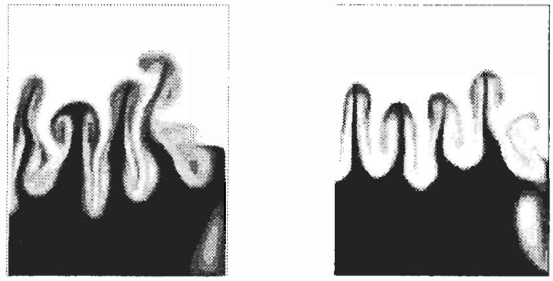

(a) (b)

Figure 2. The effect of changing the numerical control parameters. (a) Time step of $\Delta\tau = 0.04$. (b) First order upwind advection scheme.

6. Conclusions

General purpose CFD models are now able to tackle the complex physics of time-dependent, turbulent mixing but are still some way off being able to provide the performance levels achieved by specialist research codes. The (relatively) slick user interface and the ability to model complex geometries are very appealing but are the indirect cause of the poorer performance. For industrial problems, CFX would be of great value, but as a scientific tool it is limited by the excessive memory requirements, long execution times. However, as the code continues to improve and workstation performance increases, such CFD models will become of increasing value.

AEA Technology released a new version (5.1) of CFX in October 1996. This version has the advantages that it uses quadrahedral elements providing improved modelling of complex geometries and provides a more "user-friendly" interface for setting up the fluid dynamics aspects of the problem. However, at present CFX5.1 does not have the possibility of modelling inhomogeneous initial conditions, and so is of no value for mixing problems.

Acknowledgement. SBD wishes to acknowledge the financial support of Yorkshire Water plc and the Issac Newton Trust for various components of this work. Results for TURMOIL3D calculations were supplied by D.L. Youngs from AWE, Aldermaston.

References

[1] Youngs DL, Three-dimensional numerical simulation of turbulent mixing by Rayleigh-Taylor instability. Phys. Fluids A 3, 1312-1320 (1991).

[2] Dalziel SB, Linden PF and Youngs DL, Rayleigh-Taylor instability: resolving the differences between experiments and simulations, In The Proceedings of 5th International Workshop on the Physics of Compressible Turbulent Mixing, Ed. Young, Glimm & Boston; World Scientific, Singapore; 321-330 (1996).

[3] Dalziel SB, Linden PF and Youngs DL, Self-similarity and internal structure of turbulence induced by Rayleigh-Taylor instability. Submitted to J. Fluid Mech (1997).

Self-similarity and Internal Structure of Turbulence Induced by Rayleigh-Taylor Instability

S.B. Dalziel[1], P.F. Linden[1] and D.L. Youngs[2]
[1]DAMTP, University of Cambridge, Silver Street, Cambridge CB3 9EW, England
[2]Atomic Weapons Establishment, Aldermaston, Reading RG7 4PR, England

Abstract: A detailed comparison between simple experiments and three-dimensional numerical simulations of Rayleigh-Taylor instability has been undertaken. Two layers, one salt water and the other fresh, are initially separated by a rigid barrier which is removed at the start of the experiment. The aim of this work is to understand the significance of the perturbation imposed by the removal of the barrier and utilise this understanding to provide improved agreement between the experiments and numerical simulations of them. We investigate both the growth of the width of the mixing zone and the structure of the concentration field within it. Our results demonstrate that, at scales small compared with the confining geometry, the flow rapidly adopts self-similar turbulent behaviour with the influence of the barrier-induced perturbation confined to the larger length scales. Concentration power spectra and the fractal dimension of iso-concentration contours are found to be representative of fully developed turbulence and there is close agreement between the experiments and simulations.

1. Introduction

Recent work [1, 2, 3] has shown that it is necessary to model experimental initial conditions in an appropriate manner if close agreement is to be found between experimental and numerical studies. For simple laboratory experiments on Rayleigh-Taylor instability, where two layers of miscible liquid are separated initially by a barrier, the loss of memory is incomplete and the growth of the boundaries of the mixing zone is dominated by the energetic, low wavenumber components of the initial perturbation to the velocity field. This perturbation is produced by the removal of the barrier. The three- dimensionality of the resulting flow arises from higher wavenumber components with a more random configuration. For a simulation to provide close agreement for external measures of the flow, such as the width of the mixing zone, only the two-dimensional component of this initial perturbation is important. However, if the molecular mixing and other characteristics of the internal structure are to be simulated accurately, a three-dimensional perturbation must be present also.

In the case of the almost shear-free composite barrier, described initially by [4], the low wavenumber components of the initial velocity field are essentially two-dimensional and may be described in terms of a vortex sheet left behind the barrier producing an irrotational flow through the remainder of the tank. This flow field may represented as the streamfunction of the form:

$$\Psi(x,y,z) = \Psi_0 U_{Barrier} L \frac{h_{Barrier}}{H} \sum_{n=1}^{N} a_n sin \frac{n\pi x}{L} \frac{sinh \frac{n\pi H}{2L} \left(1 - 2^{\frac{|z|}{H}}\right)}{sinh \frac{n\pi H}{2L}} \qquad (1)$$

where Ψ_0 is an order one function of the Reynolds number and a_n $(n = 1, 10)$ are coefficients determined from experiments. Here x, y, z are the along, across and vertical tank coordinates with the origin in the centre of the tank of length $L = 400\ mm$, width $L/2$ and height

More information - Email: sd103@amtp.cam.ac.uk or s.dalziel@damtp.cam.ac.uk

$H = 500\ mm$. The barrier of thickness $h_{Barrier} = 2.4\ mm$ is removed at a speed $U_{Barrier}$ in the negative x direction. In the simulations presented here, we replace the higher three-dimensional wavenumber components of the initial perturbation with a random perturbation to the initial position of the interface. If the amplitude of this random perturbation is small then it may be described as a random perturbation to the density field, ρ_{Noise}, added to the density field at $z = 0$. The experiments reported here were performed using salt water and alcohol/water solutions (the alcohol was added to match refractive indices) to give an Atwood number of $A = (\rho_1 - \rho_2)/(\rho_1 + \rho_2) = 0.002$, where ρ_1 and ρ_2 are the initial densities of the upper and lower layers, respectively.

2. Growth of the mixing zone

Figure 1 summarises the initial growth of the mixing zone by presenting the concentration fields in the $x - z$ plane at $y = 0$. For the experiments (column I), only the lower half of the tank is visualised and the concentration measurements are obtained by image processing techniques from a fluorescent dye illuminated by a simple light sheet from an arc lamp. Column II shows the concentration field for a two-dimensional simulation (Settle - see [3], this volume) with the initial conditions described by (1). The full barrier simulations, performed using TURMOIL3D [5, 6, 7] with the initial conditions given by (1) and including ρ_{Noise} is in column III while idealised simulations (also computed by TURMOIL) starting with only ρ_{Noise} to initiate the flow is in column IV.

Visual comparison between the four columns in figure 1 shows a remarkable level of similarity for the width of the mixing zone between the experiments, two-dimensional simulations and barrier simulations. In contrast, the idealised simulations exhibit a substantially lower growth rate and a less coherent structure to the flow. This demonstrates clearly the dominant role of the two-dimensional low wavenumber component of the initial perturbation. The much more rapid growth down the right-hand wall is the result of the left- right asymmetry in the barrier removal process producing a vortex sheet, while the dominant wave length is believed to result from instabilities on this vortex sheet. The agreement between these flows has been quantified by [3] and measurements of the quadratic component of the temporal evolution are given in [2]. Visual comparison of the internal structure of the mixing zone again shows favourable agreement between the experiments and barrier simulations, and indeed some agreement with the idealised simulations. Before showing this agreement to be quantitative, we note that we would not expect the two-dimensional simulations to show any of the internal gradients and structure of the found in the experiments due to the absence of vortex stretching. The existence of concentrations intermediate between $C = 0$ or $C = 1$ are the result of numerical diffusion and not nonlinear, three-dimensional processes.

3. Concentration power spectra

The internal structure of the experimental and numerical flows may be analysed in a number of ways. Here we shall restrict ourselves to the concentration power spectra. We shall not present spectra for the two-dimensional simulations as these clearly lack the internal structure in which we are interested. To ensure a consistent treatment of the flows, all processing was based on images of the concentration field. In all cases the spectrum was determined for individual vertical planes in the window $x/L \in [-\frac{1}{2}, \frac{1}{2}]$ and $z/H \in [-0.1, 0]$ by calculating one-dimensional horizontal FFT after suitable windowing and padding of the data. The individual horizontal spectra within the window were then averaged. An ensemble of sixteen experiments were used with the spectra located at $y = 0$. The resulting data set was averaged over the

ensemble. For the simulations the spectra were calculated for each vertical plane across the width of the tank and these spectra then averaged. In the case of the barrier simulations

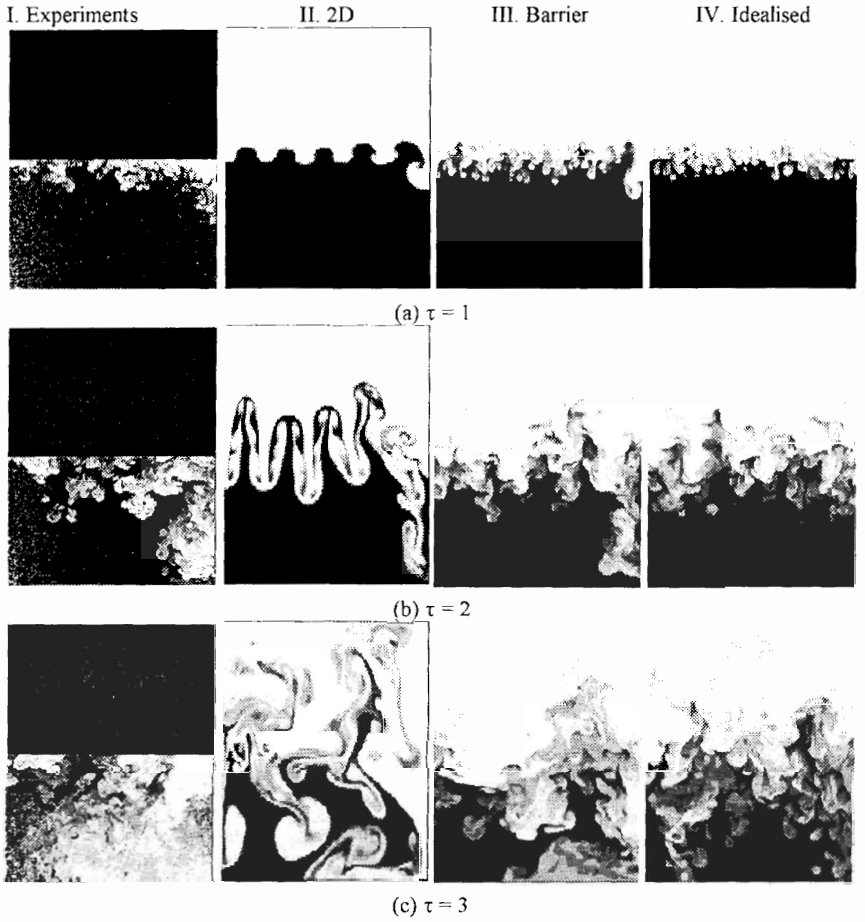

Figure 1. Comparison of concentration fields for experiments (column I), two-dimensional simulations (column II), three-dimensional "barrier" simulations (column III) and three-dimensional "idealised" simulations (column IV). The concentration fields are shown for (a) $\tau = 1$, (a) $\tau = 2$ and (c) $\tau = 3$.

an ensemble of three sets of coefficients a_n, each obtained from a different experiment where the initial conditions were measured, and the result of the cross-tank averages were averaged over the ensemble as well. Figure 2 shows typical power spectra at time $\tau = 2$ for the three flows. All show a region in wavenumber space where a power law is in reasonable agreement. The solid lines represent a least squares fit (over an appropriate sub-range of wavenumbers k) giving spectral slopes of -1.49, -1.63 and -1.79 for the experiments, barrier simulations and idealised simulations, respectively. The dot-dash lines show fits of a $k^{-5/3}$ spectrum to each of the three cases to show that the spectra are indeed close to the $k^{-5/3}$ expected during

the self-similar growth phase, and the overall power levels are similar. Note that the range of self-similarity is less for the simulations which have a much lower effective resolution than the experiments. [5] showed that the roll-off in the spectra for homogeneous, isotropic turbulence calculated with TURMOIL3D occurred at around $6\Delta x$, where Δx is the mesh size, making the smallest scales simulated approximately a factor of fifteen larger than the experiments where the pixel size was comparable with the Kolmogorov length scale. Figure 3 plots the temporal

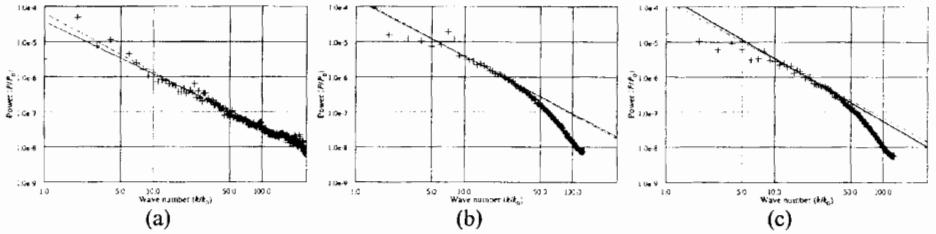

Figure 2. Concentration power spectra at $\tau = 2$ for (a) experiments, (b) barrier simulations and (c) idealised simulations.

evolution of the slope of these spectra. Of the three, the experiments reach a consistent slope fastest. This is due primarily to the existence of disturbances at all wavenumbers at the beginning of the experiments. Note that the spectral slope prior to $\tau = 0.4$ are misleading as they are contaminated by the barrier being present in the field of view. Closer examination of the individual spectra show that at early times, where a slope of around -2 is obtained using the least squares fitting procedure, the range of wavenumbers following a power law behaviour is somewhat smaller than seen in figure 2a. Indeed, a slope of $-5/3$ could reasonably be fitted over much of this range if data were restricted to a smaller range of wavenumbers. With the two simulations the initial perturbation is more confined in wavenumber space. For

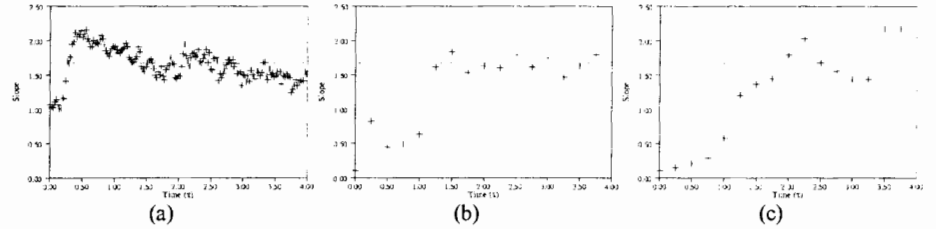

Figure 3. The time evolution of the spectral slope for (a) experiments, (b) barrier simulations and (c) idealised simulations.

the barrier simulations nonlinear interactions fill in the gap between the low wavenumber two-

dimensional barrier perturbation and the high wavenumber noise significantly more rapidly than can happen in the idealised simulations where only the high wavenumber noise component is initially present. As a result the barrier simulations achieve a spectral slope of $-5/3$ by $\tau \approx 1$ compared with closer to $\tau \approx 2$ for the idealised simulations. As with the experiments, a more direct comparison of the individual spectra shows them to be consistent with a $k^{-5/3}$ slope over a wider range of wavenumbers than is suggested by this figure. One of the conclusions we may draw from the examination and comparison on the spectral slope of the concentration power spectra is that the internal structure of the Rayleigh-Taylor instability, which is dominated by the processes occurring at higher wavenumbers, rapidly looses its memory of the initial conditions. For the experiments, the existence of a less structured initial perturbation over a broader range of wavenumber, in combination with the higher effective Reynolds number, means that the $k^{-5/3}$ spectrum characteristic of turbulent flow is attained much faster than in the simulations. In drawing a comparison between the slope of these concentration power spectra and the $k^{-5/3}$ slope of the Kolmogorov velocity power spectra we are making use of the fact that we are studying an accelerating flow where the distortion of material surfaces will be dominated by the most recent characteristics of the velocity field.

4. Fractal dimension

Another approach to characterising the internal structure is the fractal dimension of iso- concentration contours. Here we use the Kolmogorov capacity, obtained through the normal box-counting algorithm, to determine the dimension. Figure 4 shows the relationship between the number of boxes and the size of boxes required to cover a $C = 0.5$ concentration contour is well modelled by a power law for all three cases. The exponent for this power law is then the fractal dimension. The time evolution of these dimensions is plotted in figure 5 showing close

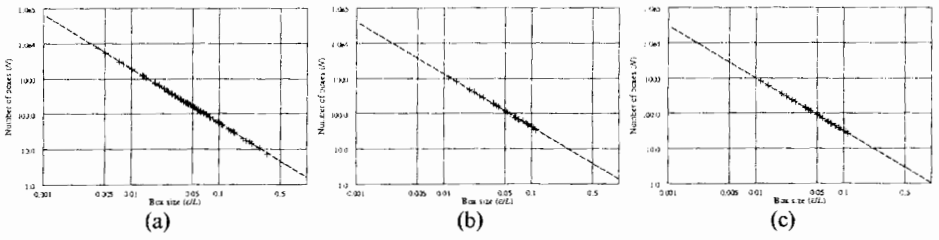

Figure 4. Power-law relationship between contour length and coverage using box-counting algorithm for (a) experiments, (b) barrier simulations and (c) idealised simulations.

agreement in all three cases for $0.7 \leq \tau \leq 2.5$. Indeed the dimension is approximately constant at $D_2 \approx 1.47$ over this period. The disparity for $\tau \leq 0.7$ is due again to the need for the simulations to fill the gaps in wavenumber space not present in the initial conditions, and for $\tau < 0.4$ the presence of the barrier in the field of view prevents the experimental dimension starting from closer to unity. At later times the increases in the experimental dimension is the result of an unmodelled three-dimensional component of the experimental initial conditions [3] and the establishment of a globally stable stratification. A relationship $s = D_2 - 3$ has been proposed [8] between the slope s of the velocity power spectrum and the fractal dimension D_2

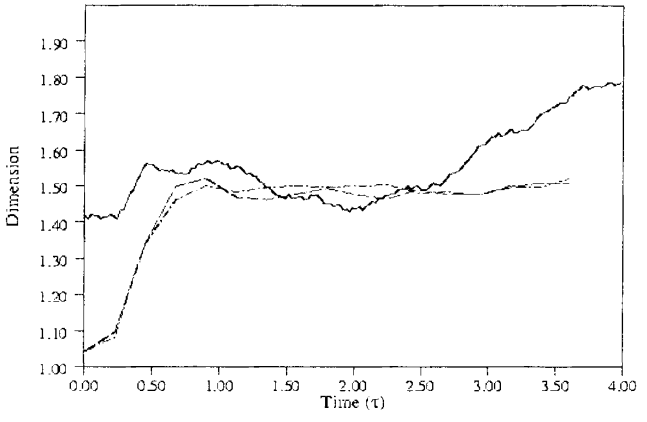

Figure 5. Time evolution of the $C = 0.5$ fractal dimension. The experimental data is shown as the solid line, the barrier simulations with the dot-dash line and the idealised simulations with the dashed line.

of the iso-concentration contour. Our results for the slope of the concentration power spectra and fractal dimension of iso-concentration contours is consistent with this.

5. Conclusions

In this paper we have shown that both the external structure of the mixing zone and the structure of the concentration field within it for a set of simple laboratory experiments may be modelled accurately if an appropriate description of experimental initial conditions is used. Two-dimensional simulations are able to model the growth of the mixing zone due to the dominance of the low wavenumber two-dimensional component of the barrier-induced perturbation. [4] has shown that the timescale for loss of memory of an initial perturbation to the velocity field (by the introduction of vorticity) may be substantially larger than the timescale for loss of memory for a perturbation to the density field where the two perturbations contain a similar energy. More recently [3] have shown that the structure is more important than the amplitude of such a velocity-field perturbation with the development of the flows presented here only weakly dependent on the amplitude of this barrier-induced perturbation. While the flow retains a memory of the low wavenumber components of these initial conditions over a period much longer than the characteristic time for the flow, the high wavenumber components soon become independent of the precise form of the initial conditions and evolve into a classical turbulent flow during the so-called self-similarity phase of the growth of the instability. Both concentration spectra and iso-concentration contour fractal dimensions are consistent with the presence of a Kolmogorov velocity spectrum. SBD wishes to acknowledge the financial support of AWE Aldermaston and the Issac Newton Trust.

References

[1] Dalziel SB, Final report: Molecular mixing in Rayleigh-Taylor instability, Report for AWE, 91 pp (1994).

[2] Dalziel SB, Linden PF & Youngs DL, Rayleigh-Taylor instability: resolving the differences between experiments and simulations, In The Proceedings of 5th International Workshop on the Physics of Compressible Turbulent Mixing, Ed. Young, Glimm & Boston; World Scientific, Singapore; 321-330 (1996).

[3] Dalziel SB, Linden PF & Youngs DL, Self-similarity and internal structure of turbulence induced by Rayleigh-Taylor instability. Submitted to J. Fluid Mech (1997).

[4] Dalziel SB, Perturbations and coherent flow in Rayleigh-Taylor instability, In 4th International Workshop on the Physics of Compressible Turbulent Mixing, ed. P.F. Linden, D.L. Youngs & S.B. Dalziel; 32-41 (1994).

[5] Youngs DL, Three-dimensional numerical simulation of turbulent mixing by Rayleigh-Taylor instability. Phys. Fluids A 3, 1312-1320 (1991).

[6] Youngs DL, Numerical simulation of mixing by Rayleigh-Taylor and Richtmyer- Meshkov instabilities. Lasers and Particle Beams 12, 725-750 (1994).

[7] Youngs DL, Direct three-dimensional numerical simulation of mixing by Rayleigh- Taylor instability. in 4th International Workshop on the Physics of Compressible Turbulent Mixing, ed. P.F. Linden, D.L. Youngs & S.B. Dalziel; 167-177 (1994).

[8] Sreenivasan KR, Fractals and multifractals in fluid turbulence, Annu. Rev. Fluid Mech. 23, 539-600 (1991).

The Perturbations and Turbulent Mixing Evolution at the Plane Gas-Gas Interface in GEM-Driven Shock-Tube Experiments

V.I. Dudin, E.V. Gubkov, E.E. Meshkov, A.A. Nikulin, A.L. Stadnik, V.P. Statsenko, V.A. Til'kunov, Y.A. Vlasov, V.V. Bashurov, E.A. Bykova, V.I. Tarasov, Y.V. Yanilkin and V.A. Zhmailo
Russian Federal Nuclear Centre - Institute of Experimental Physics
Prospect Mira 37, 607190, Sarov, Nizhny Novgorod Region, Russia

Abstract: The paper presents the results of experimental and numerical studies of turbulent mixing zone (TMZ), arising at the gas-gas interface as shock waves (SW) pass therethrough. One such gas in these experiments consisted from products of GEM-explosion (GEM-gas explosive mixture).

1. Introduction

Rayleigh-Taylor instability (R-T instability) and the corresponding turbulent mixing (TM) arise on the interface of two fluids (or two gases) different in density when acceleration is directed from lighter substance to heavier one [1, 2]. In the case of impulsive acceleration with a shock wave, the interface is found to be unstable at wave passing through from the light gas to the heavier one as well as from the heavy gas to the lighter one [3, 4]. Theoretical study of real situation, when evolution of regular $3D$ perturbations combines with TM-evolution, would require numerical calculations both expensive and uncertain. Experimental study of such flows for gas-gas interface is an extremely complicated task even for plane case. These problems are primarily associated with the problems of two gases interface realization. There is a number of methods to create such interface [4, 5, 6, 7, 8, 9, 10, 11]. In all the above cases there would be plane or cylindrical interface created. Given any initial perturbation specified, it will be two-dimensional. The only exception is shock tube experiments [12]; because in this case the initial $3D$ perturbation at the interface of two gases separated by film is set by little abundant gas pressure on the film leaning on the big-cell grid of thin and firm wire. Method [13] provides new chances for experimental study of this problem. What is allowed by this method is studying of mutual evolution of turbulent mixing and regular large-scaled $3D$ perturbations at the interface of explosive products (EP), gas explosive mixture (GEM) and inert (non-explosive) gas. A priory this scheme provides new chances for experimental study of instabilities and TM with shock tube:

- varying of disposition and time delay of initiating elements one can create required of $2D$ and $3D$ perturbations on the iterface of interest;
- high EP temperatures cause film destruction and evaporation thus avoiding its stabilizing effect upon the TM evolution;
- the explosion of GEM allows to get the flows in a wide range of a Mach number, density ratio, acceleration modes.

The experiments carried out served as the subject of theoretical analysis and calculations performed by numerical methods $TREK$ [14] ($3D$ gas-dynamics) and $EGAK$-T [15] ($1D$ and $2D$

More information - Email: otd03_2305@spd.vniief.ru

gas-dynamics with semi-empirical TM-characterization). The results of these calculations offered a deeper view of basic regularity in evolution of instability and TM in given problem and tested the methods [14, 15]. Production and results of these calculations in comparison with experiments are presented below.

2. Experimental method

The experiments were performed using a shock tube which in some respects, is substantially different from shock tubes as described in [4, 5, 6, 7, 8, 9, 10]; as follows:
1. GEM EP was used as shock wave driver instead of compressed gas;
2. The GEM of the chamber and inert (non-explosive) gas of the channel was at atmospheric pressure and was separated with a plane thin-film membrane ($\sim 0.5\ mm$) which would be evaporated due to high EP temperatures (according to estimates [16]).
3. The GEM was detonated simultaneously at different points. This would result in the occurrence of distributed detonation wave, generally, with $3D$ perturbation to be transferred to the interface between GEM EP and inert gas. The experiments described below were intended to look just at this kind of perturbation.
The shock tube with the inner channel cross-section of $8 \times 8\ cm^2$ includes two compartments: chamber 2 and channel 3 (Fig.1) separated with a thin film ($\sim 0.5\ mm$) (interface of interest). The chamber is filled with GEM ($C_2H_2 + 2.5O_2$), and the channel is filled with air; both gases are at atmospheric pressure. The channel have a plexiglass cover 7 at the end. GEM section has length of $2.05 - 2.55\ cm$, and air section - $30\ cm$.
The method to initiate GEM was that previously developed at VNIIEF [16]. The rigid wall 4 had $N = n^2$ initiating elements (IE) 5 as electric spark gaps positioned uniformly on its inside surface. Detonation firing of GEM was done through simultaneous breakdown of these gaps by a high-voltage pulse.
Imaging of the shock-tube channel flow was performed by framing visualisation.

3. Experimental results

Here are presented two types of experiments. In the first type GEM was detonated at $10 \times 10 = 100$ points.
Following the detonation wave reaching the interface of interest and its abrupt acceleration, the latter would move slowing down. When the channel gas has higher density (ρ_{IG}) than EP (ρ_{EP}), the interface will be unstable according to [3, 4] and stable according to [1, 2] (acceleration from the heavier to lighter gas). It would become unstable being reached by the shock wave reflected from the channel end according to [3, 4]. In experiments [4] an interface was accelerated by a steady shock wave and moved inertly without acceleration, so the interface was at equilibrium state from the point of instability [1, 2].
Fig.2 shows streak photography images for the experiment to study instability evolution at the GEM EP-air interface. On the start of the flow, the interface here was stable according to [1, 2]. So that small-scale perturbations of the GEM detonation front were founded to be "foot-printed" at the interface attenuate gradually with time ($t = 114\ \mu s$). The shock front in the air 3 and the interface 2 were plane-shaped practically since the onset of motion.
However, as it has been reached by the shock wave reflected from the rigid wall at the channel end, the interface would become unstable according to [3, 4] with the turbulent mixing zone growing rapidly at it ($t = 665\ \mu s$). The turbulent mixing zone was observed to have particularly high growth rate when the shock wave reflected from the left rigid wall had passed through it again ($t = 827\ \mu s$), when the interface would become unstable according to [1, 2].

The second type of experiments (test 27) was different from the above-described in that GEM detonation there was initiated in one point positioned on the chamber rigid wall.
Fig.3 shows streak photography images for this case.
The test observed the mixing zone growing together with the perturbation brought about to the interface by the detonation wave, as the shock wave reflected from the end wall of the channel was passing through the interface.
The contours of the mushroomlike stream are seen on the Fig. 3, when $t > 0.5\ \mu s$.

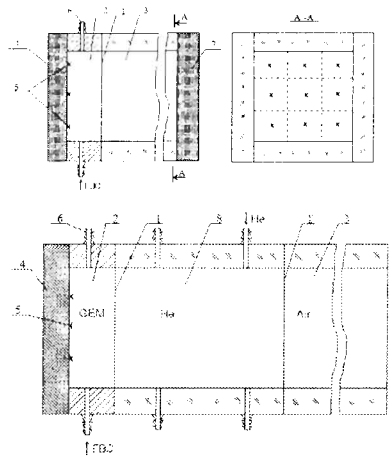

Figure 1. Schematic of the square shock tube setup: a) experiment: GEM-air-rigid wall, 1 - film to separate gases (interface), 2 - GEM chamber ($C_2H_2 + 2.5O_2$), 3 - air-filled channel (1 atm), 4 - rigid wall (textolite), 5 - spark gap, 6 - gas inlets, 7 - rigid wall; b) experiment:GEM-He-air, 1 - thin film, 8 - channel section with helium. Other notations are the same as for Fig. 1a.

4. Numerical simulation. Comparison with the experiment

The experiments observed stimulated the corresponding gas-dynamic calculations in $1D$, $2D$ and $3D$ setting.
In all calculations pointed we have choose geometry of calculation domain according to Fig.1. Detonation in region $0 < z < z_1$, occupied by GEM, was calculated with simplified (quasi-stationary) version of the method [17]. Initiation conditions were specified on the left boundary together with the detonation wave velocity D and value of specific energy release behind the front Q. These quantities were varied in calculation to get the best description of experimental $R - t$ chart of shock wave. The best values are $D = 3.1\ km/s$, $Q = 13.9\ km/s$.
State equation for explosive products (EP) was as for the perfect gas with adiabatic coefficient γ=γ_{EP}=1.19. Gases affiliated to EP considered to have equation of state as perfect gases with γ=γ_a=1.4, ρ=ρ_a=1.29×10^{-3} g/cm^3 for air. The initial density for GEM ρ_{GEM}=1.365×10^{-3} g/cm^3, the initial pressure $P_0 = 1\ atm$.
Boundary conditions on the camera walls - were as rigid wall type.

4.1. Quasi-plane experiment (initiation of detonation in 100 points)

The basic calculations, concerning to this experiment, were performed by $3D$ gas-dynamic $TREK$ code [14].
The real (for 100 points) initiation of detonation in these calculations was approximated by uniform energy release near $z = 0$ plane.
In this connection we have to set random density perturbations ($\frac{\Delta\rho}{\rho} = \pm 0.1$) in a single layer of cells near the interface $z = z_1$ before the appearance of detonation wave (DW).
The approximately uniform grid with number of points $40\times40\times150$ was used.
Fig.4 shows SW motion $Z - t$ chart in comparison with the measured in tests 29, 30. As evident, there is quite close similarity between them. The little difference while $t \geq 0.5\mu s$ is connected with delay of reflected wave in initiation compartment.
In order to get the additional qualitative information, the results of given calculations (three-dimensional arrays) were averaged upon sections, normal to the chamber axis. The obtained profiles of concentration of EP $c(z,t)$ and of total density $\rho(z,t)$ are adduced in Fig.5.
Comparison of $c(z,t)$ and $\rho(z,t)$ profiles shows that the presence of density gradients in this problem is connected not only with mixing of two different gases, but also with appearance of large difference of densities in the air when the first SW propagates there.
These gradients are positive almost always in observed flow, thus explaining different rate of turbulence evolution depending on sign and value of acceleration, that effects to this transitional layer while passing the shock wave through it.
The calculated $\rho(z,t)$ profiles are plotted also on Fig.2 There is a close similarity, as it must, between the gradients of calculated density and the blackening degree on the photo in corresponding section.
Fig.4 presents $z - t$ chart of SW and TMZ for given calculation defined by $c(z,t)$ profiles in comparison with charts, measured in experiments N^o29, 30 and calculated in $3D$ approach. It is seen that all results are close enough.
The results obtained from calculations of turbulent energy profiles $k(z,t)$ and mean-square values of density fluctuation $\sigma \equiv \frac{\langle\rho'^2\rangle}{\rho^2}$ are adduced on Fig.6 and Fig.7 correspondingly. The adduced function $k(z,t) = v_t^2(z,t)$was calculated by relation:

$$k(z,t) = \frac{\langle U_i^2\rangle - \langle U_i\rangle^2}{2}, i = x, y, z$$

On the Fig.7 there are profiles of turbulent mass flow $R_z = \frac{\langle\rho' U_z'\rangle}{\rho}$. Its maximum value appears in TZ.
Fig.6 shows the spectrum of diagonal components of Reynolds tensor [18] in the center section of TMZ- one can see approximation to Kolmogorov spectrum in region of large wave numbers. According to calculations the relation of transversal Reynolds tensor diagonal components in TZ is on average close to 1, and relation of transversal component to longitudinal one is small: about $0.2 - 0.3$. This agrees with the results obtained in [18].
We have also made $1D$ calculations with semi-empirical turbulent model [15]. Setting of this calculation is similar to the above described one for $3D$ problem. The initial values of turbulent magnitudes were set in several calculation cells at the interface between EP and affiliated air. Thus obtained data are compared on Fig.5, Fig.6 with $1D$ $c(z), \rho(z), k(z)$ profiles, resulting from $3D$ calculations.
We can see here also quite close similarity of calculations performed by two different methods. The most noticeable difference presents in the turbulent energy profiles k. The different time

delay in turbulence evolution can serve for the possible reason of such difference, that, in turn, is connected with impossibility to set similarly the initial perturbations. As a result, $k(z,t)$ and mixing in TMZ in $3D$ calculations are greater than in $1D$ case.

4.2. Quasi-two-dimensional case. One-point initiation

To analize the experimental data for this case it was performed $2D$ and $3D$ calculations (some $2D$ calculations was done using $k-\varepsilon$ model [15]).
Setting of $3D$ calculations differs from those discribed in sect.3 by two features:
- initiating energy release was set only in one point (in the center of border region when $z=0$);
- there was not performed any special generation of initial perturbations at the interface.
One of the results of this calculation - density patterns averaged along direction normal to camera axis are shown on Fig.3 in comparison with the experimental data.
As evident, this flow patterns appears to be two-dimensional. To reveal qualitative features of this flow, it is useful to keep in mind that, according to the calculation results, in given problem, as in the problem of plane initiation, the transitional density layer with $\frac{\partial \rho}{\partial z} > 0$ have been generated in the air near the interface.
Evolution of this layer before the appearance of the SW, reflected from the top pavement of the chamber ($t = 0.2\ \mu s$), looks like the pattern, observed for the non-linear stage of evolution of determined one-mode perturbation as a result of RM instability (see [16] for example): near the chamber wall the air jet ("the heavy gas") is generated, as it must, when $g > 0$ and Atwood number A > 0.
Interaction of SW, reflected from the top pavement, with the observed surface also corresponds to the predictions of RM theory: in this case parameter $gA < 0$, so amplitudes of perturbations firstly decrease, and then change their sign and continue to grow ($t = 0.6\ \mu s$). The jet of EP appears in the air at the symmetry axis.
In addition, one can see that for the moment of coming of the third shock wave to the interface, the sufficiently noticeable small-scaled perturbations have developed at this interface.
When passing of this wave through the interface region, there are realized all the conditions, necessary for intensive evolution of gravitational TM, what is observed when $t = 0.9\ \mu s$.
On the whole reasonable agreement between calculated and experimental data is seen from Fig.3.
We have performed $2D$ calculation of this case (in the axial geometry) with using k-e turbulent model . The results of this calculations are very close to ones from Fig 3.

5. Conclusions

The results presented here show that used method [13] allows to obtain new and useful information about evolution of instabilities and TM in flows with complex acceleration.
In order to get more detailed data at a later time we suppose:
- to develop methods for measuring TMZ quantitative characteristics (hydro-dynamic and turbulent values profiles);
- to perform the calculations using real state equations and detonation models.

Acknowledgement. The authors are grateful to Belova I., Bliznetsov M., Zharkova O., Senkovsky E. for help in preparing this paper. The work performed under ISTC Project 029.

References

[1] Lord Rayleigh, Proc. London Math. Soc., 14, 170, (1883).

[2] Taylor GI, The instability of liquid surfaces when accelerated in a direction perpendicular to their planes, I. Proc. Roy. Soc., A201, 192, (1950).

[3] Richtmyer RD, Taylor instability in shock acceleration of compressible fluids, Commun. Pure Appl. Math., 13, 297, (1960).

[4] Meshkov EE, Instability gas-gas interface accelerated by the shock wave, Proc. of the Academy of Sciences USSR, MZG, 5, 151-158, (1969).

[5] Jahn R, The refraction of shock waves at a gaseous interface, J.Fluid Mech., 1, 457, (1956).

[6] Benjamin R, Shock and reshock of an unstable fluid rdinterface, 3 Int. Workshop on the Phys. of Compressible Turbulent Mixing, Abbey of Royaumont, France, June 17-19, (1991).

[7] Brouilette M and Sturtevant B, Growth Induced by Multiple Shock Waves Normally Incident on Plane Gaseous Interfaces, Physics 37D, 248-263, (1989).

[8] Cavailler C, Croso H, Grandeboeuf P, Haas JF and Rodriguez G, Results from the Vaujours Vertical Shock Tube, 3 Int. Workshop on the Phys. of Compressible Turbulent Mixing, Abbey of Royaumont, France, 27-34, June 17-19, (1991).

[9] Houas L, Chemouni I, Touat A, Brun R (1991) Experimental investigation of Richtmyer-Meshkov induced turbulent mixing rdover long distances, 3 Int. Workshop on the Phys. of Compressible Turbulent Mixing, Abbey of Royaumont, France, 127-136, June 17-19, (1991).

[10] Andronov V, Zhidov I, Meshkov E, Nevmerzhitsky N, Nikiforov V, Razin A, Rogachev V, Tolshmyakov A and Yanilkin Y, Calculating-theoretical and experimental studies for gas-dynamic instabilities and turbulent mixing, An overview of papers performed in VNIIEF, Final overview for contract 0002P0004-95(008) between VNIIEF and LANL USA, N LA-12896, (1994).

[11] Jacobs JW, Klein DL, Jenkins DG and Benjamin RF, Instability Growth Patterns of a Shock-Accelerated Thin Fluid Layer, Phys. Rev. Lett., 70, 5, 583, (1993).

[12] Zaytsev S, Aleshin A, Lazareva E, Richtmyer-Meshkov instability for two- and three-dimensional interfaces. 4 Int. Workshop on the Phys. of Compressible Turbulent Mixing, Cambridge, England, 291-296, (1993).

[13] Meshkov EE, One of the opportunities of experimental study of hydro-dynamical instabilities evolution, Dynamic method for generating of the interfaces in gases, Preprint VNIIEF, 144-96, (1996).

[14] Shanin AA, Stadnik AL and Yanilkin YV, Eulerian TREK method for calculation of 3D gas-dynamic flows in multi-componental medium, VANT, ser. Math. Sim. Of Phys. Processes, 4, (1994).

[15] Yanilkin YV, Nikiforov VV, Zharova GV, Model with two equations and a method for turbulent mixing in 2D compressible flows, VANT. Ser. Mat. mod. fiz. proc. (in Russian), 1, (1995).

[16] Bashurov VV, Bondarenko YA, Gubkov EV *et al.*, Experimental and numerical evolution studies for 2D perturbation of the interface accelerated by shock waves, Preprint VNIIEF, 45-96, Sarov, (1996).

[17] Batalova MV, Bakhrakh SM, Zaguskin VL, Zubarev VN, PMTF, 3, 77, (1971).

[18] Sinkova OG, Stadnik AL, Statsenko VP, Yanilkin YV and Zhmailo VA, Direct numerical 3D simulation of gravitational turbulent mixing, these proceedings.

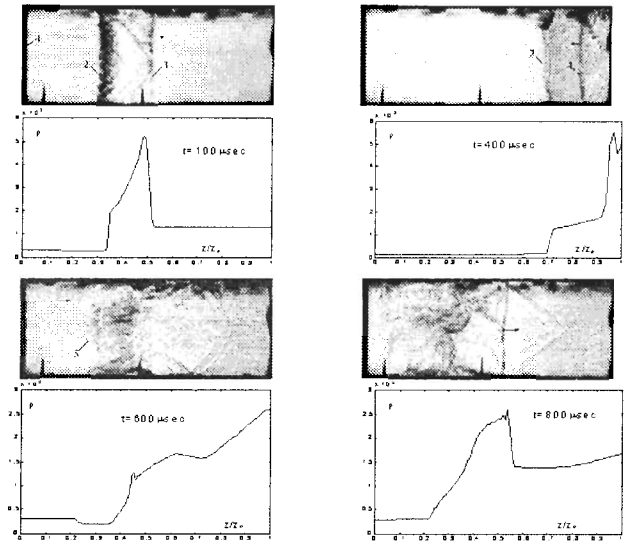

Figure 2. Instabilities growing at the *GEM EP*-air interface, 10×10=100 initiating points (test 30): 1 - *GEM*-air interface, 2 - *GEM EP*-air interface, 3 - shock wave, 4 - shock wave reflected from the channel wall end, 5 - turbulent mixing zone. Time is marked from shock wave starts to move in the air.

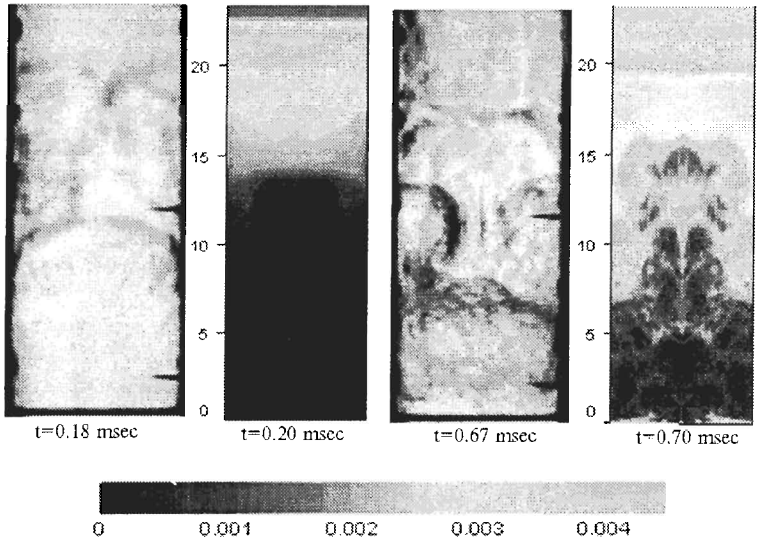

Figure 3. Shadowgraphs and corresponding *3D* calculation results, 1 point detonation case.

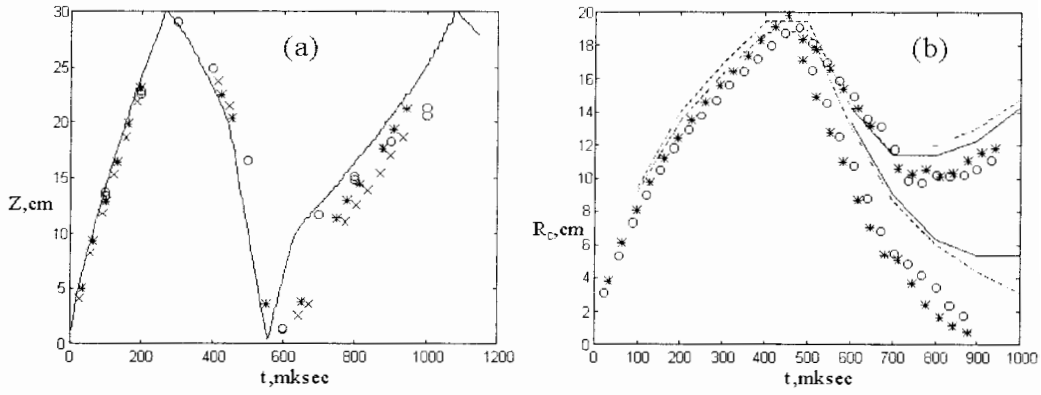

Figure 4. Calculated and measured $Z-t$ charts of shock wave (a) and TMZ (b) for experiments GEM-air: (a) $---$ $1D$ calculations, *ooo* $3D$ calculations for plane detonation case; experiments: $\times\times$ test 29, $***$ test 30, initiating in 100 points (b) $3D$ calculation for plane detonation case: $---$ on level 0.01, 0.99 C_{EP} (averaged), $---$ on level 0.05, 0.95; *ooo* test 29, $***$ test 30.

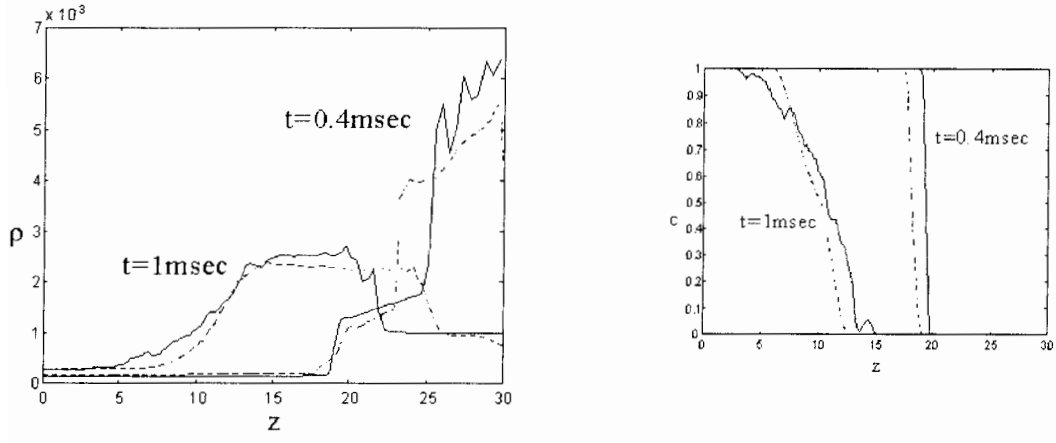

Figure 5. Density, ρ (g/cm^3), and mass concentration, c, profiles calculated for plane detonation case: $(---)$ $3D$ calculations (averaged), $(---)$ $1D$ calculations.

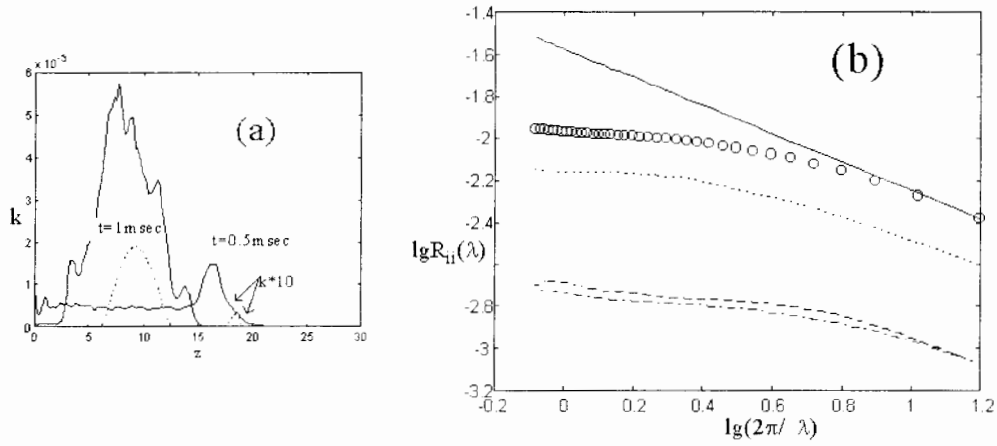

Figure 6. Turbulent energy profiles, k $(m^2/msec^2)$, and spectrum of turbulent energy $(t = 1\ msec)$ calculated for plane detonation case: (a) $(---)$ $3D$ calculations (averaged), $(---)$ $1D$ calculations; (b) *ooo* R_{ii} $\equiv 2k(\lambda)$ $(m^2/msec^2)$, $---$ R_{xx}, $---$ R_{yy}, ... R_{zz}; $---$ Kolmogorov's theory.

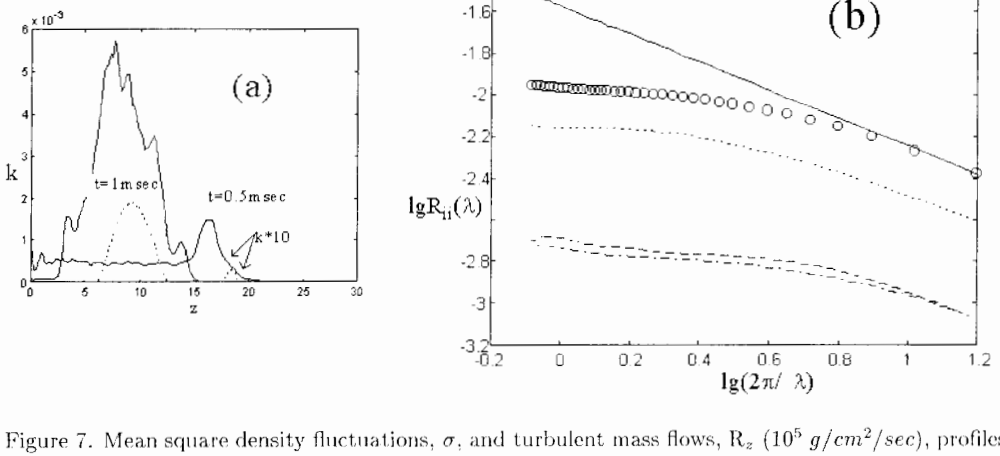

Figure 7. Mean square density fluctuations, σ, and turbulent mass flows, R_z $(10^5\ g/cm^2/sec)$, profiles in $3D$ calculation for plane detonation case: ... $t = 0.5\ msec$, $---$ $t = 1\ msec$.

Experimental Investigation of the Compressible Richtmyer-Meshkov Instability from a Broad-Spectrum, Multimode Initial Perturbation

D.R. Farley, T.A. Peyser, P.L. Miller, L.M. Logory, P.E. Stry and E.W. Burke
Lawrence Livermore National Laboratory
P. O. Box 808, L-22, Livermore, California, 94551, USA

Abstract: Experiments have been conducted using the Nova laser system to investigate the growth of the Richtmyer-Meshkov (RM) instability resuling from a strong shock wave (M $\sim$ 30) crossing a prescribed well-defined initial multimode perturbation. The perturbation was a 100 mode superposition of 1 μm amplitude sine waves with randomly generated phases between 0 and 2π. The two working fluids were fluidized brominated plastic and carbon resorcinol foam, giving a post-shock Atwood number of approximately 0.6. The present experimental results give a power-law coefficient of 0.87 $\pm$ 0.2 for the growth of the interface. This value is higher than results previously published.

1. Introduction

The Rayleigh-Taylor (RT) and Richtmyer-Meshkov (RM) hydrodynamic instabilities can occur across an interface between fluids of differing densities. The Rayleigh-Taylor instability occurs whenever a lower density fluid is supporting the lighter fluid against an imposed acceleration, whereas the Richtmyer-Meshkov instability occurs when a shock wave crosses the density interface from either direction. Simple analytical solutions are available for the linear growth of the RT and RM instabilities [1, 2, 3, 4, 5, 6]. Some experimental and numerical results are also available for single-mode and multimode initial perturbations [7, 8, 9, 10, 11]. However, further effort is needed in describing the non-linear growth of these instabilities. In particular, further quantitative analysis of the growth of multimode perturbations into the non-linear regime is required. In the present research, the growth of the compressible RM instability resulting from an initial, well-defined multimode perturbation is analyzed utilizing experimental results from the Nova laser system. As has been previously published [6], the growth of bubble and spike fronts are predicted to follow a power-law time dependence, as given by

$$\delta \sim t^{\theta} \tag{1}$$

where δ is the distance of the bubble or spike penetration into the other fluid, t is time, and θ is the power-law coefficient. According to analytical and computational results of Alon et al. [6], θ should equal approximately 0.4 for bubbles. It is believed that this value is insensitive to Atwood number [A = $(\rho_2 - \rho_1)/(\rho_2 + \rho_1)$]. For spikes, θ should vary from approximately 1 for A = 1 to 0.4 for low Atwood numbers. No analysis is made as to Mach number effects. In the present experiments, the growth of the mix region for a well-defined multimode perturbation will be analyzed to obtain θ for A = 0.6 at a high Mach number (M $\sim$ 30).

More information - Email: dfarley@llnl.gov

2. Experimental

Experiments were done using the Nova laser system. With Nova, up to ten beams can be directed to experimental packages within a vacuum chamber to conduct high energy density experiments. In the present experiments, eight beams are used to drive a strong shock wave into a miniature shock tube while two beams are used as backlighter sources. The eight drive beams are directed into opposite ends of a gold Hohlraum which has a shock tube mounted as shown in Fig. 1. The Hohlraum is a 3 mm long and 1.5 mm diameter hollow cylinder. Typically, a 1 ns square pulse of approximately 20 kJ of 0.35 μm wavelength light strikes the interior of the Hohlraum whereupon the laser energy is absorbed by the gold and emitted as x-rays. A quasi-Planckian temperature profile with a characteristic temperature of approximately 230 eV is generated within the Hohlraum which is then utilized as a source for the initiation of the ablation and shock fronts into the the target material. The initial strength of the resulting shock wave is about 85 Mbar, which decays to 35 Mbar near the density interface, and has a Mach number of approximately 30. The design of the shock tube and target were such that a strong,

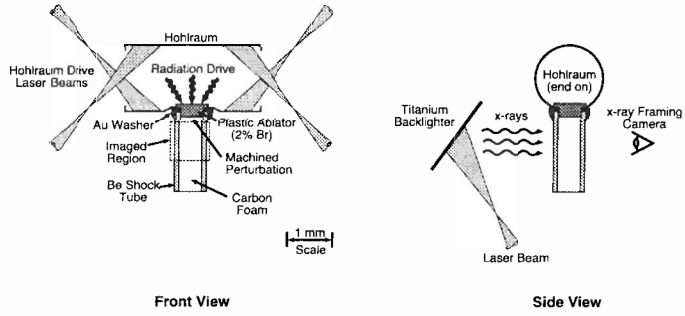

Figure 1. Experimental package mounted to a gold Hohlraum

planar shock wave would travel from heavy fluid to light and that the growth of the mix region could be seen at both early and late times. The shock tube itself is made of beryllium with an outer diameter of 700 μm and inner diameter of 500 μm and an overall length of 2200 μm. The payload within the shock tube consists of a high density ablator and low density foam. The heavy ablator material (1.22 g/cm^3) is made of polystyrene doped with 2% bromine. The bromine serves a dual purpose both as a means to increase the opacity of the plastic for imaging contrast as well as to absorb the incident x-ray energy. A tophat structure is utilized on the end of the ablator at the attachment to the Hohlraum, as shown in Fig. 1. The tophat has an outer diameter of 700 μm and a thickness of 100 μm which extends into the Hohlraum cavity. This tophat design was found to aid in shock planarity [10]. The two-dimensional multimode perturbation is machined into the end of the ablator at the density interface. The multimode perturbation is rectilinear, and is a superposition of 100 sine waves (100 modes), each wave having a 1 μm amplitude and a randomly generated phase between 0 and 2π. The wavelength of each mode varied linearly from 10 μm to 100 μm in 0.90 μm increments. The profile of the machined surface and its corresponding power spectrum is shown in Fig. 2. Shown adjacent to the ablator in Fig. 1 is a low-density carbon resorcinol foam (0.1 g/cm^3). This results in a pre-shock Atwood number of 0.85. The foam is much less opaque to x-rays than the ablator material which aids in visualizing the growth of the interface. As the shock wave crosses the perturbed interface, the interface subsequently inverts, and the shock then continues into the

foam payload. The resulting post-shock Atwood number is approximately 0.6. The growth of the interface can then be recorded using x-ray imaging.

Backlighting of the shock tube was achieved by focusing two of the Nova beams onto a titanium foil mounted approximately 4 mm from the shock tube, normal to the camera line of sight and on the opposite side of the shock tube from the imaging camera. The titanium foil is 3 to 4 mm on a side and 25 μm thick, and emits 4.7 keV x rays upon illumination by the Nova beams. These x rays then propagate through the shock tube and are differentially attenuated depending on the relative opacity of the working fluids. An x-ray framing camera is then used to record the images. These cameras are described elsewhere [12, 13]. Images are typically recorded at times between 5 to 15 ns.

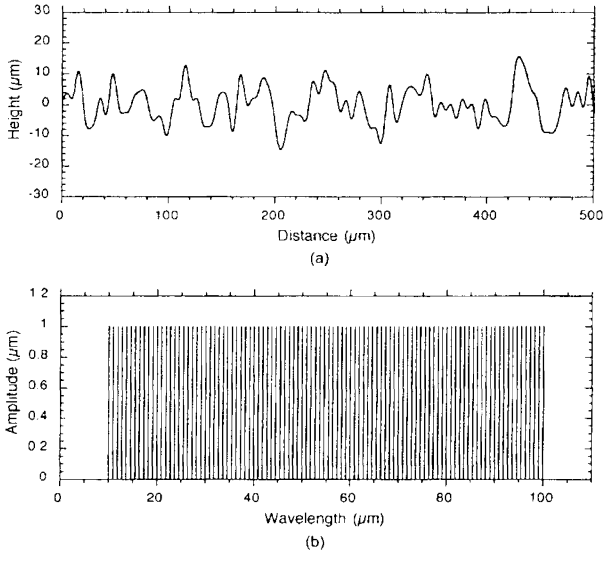

Figure 2. (a) Multimode rectilinear surface which was precision machined into the brominated plastic ablator, and (b) power spectrum of the perturbation modes

3. Results

Typical images of the experiment recorded by the x-ray framing camera are shown in Fig. 3. These images are taken at 13, 14, and 15 ns. The shock crosses the perturbation at approximately 4 ns. It can be seen from the progression of frames in Fig. 3 that there is growth of relatively large structures within the mixing region. The shocked foam behind the shock can also be seen. Bubbles penetrate into the brominated plastic ablator, but because of the higher opacity of the ablator material, it is difficult to directly observe bubble structure in this region. To quantify the width of the mixing region, a 100 μm wide vertical lineout is extracted from the x-ray framing camera images. Within this lineout is contained the unshocked foam region, the shock discontinuity, the shocked foam, the mix region, and the opaque ablator region. Because the backlighter intensity profile is typically Gaussian in shape, the transmitted intensity distribution recorded by the x-ray framing camera includes this Gaussian profile. A least-squares

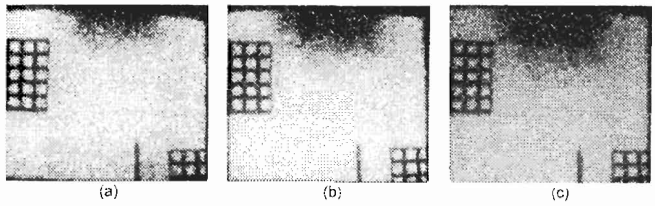

Figure 3. Framed x-ray images of the experiment depicting the opaque ablator region, the mix region, the compressed foam region and the unshocked foam at (a) 13 ns, (b) 14 ns, (c) 15 ns

Gaussian shape is fitted to the vertical lineout, and this fit is then divided out of the lineout. A typical normalized lineout is shown in Fig. 4. Identified in Fig. 4 is the foam region, the shock, the shocked foam region, the mix region, and the shocked brominated plastic region. A 5-to-95% transmission criteria across the mix region of the lineout is then used to obtain a quantitative mix width. Mix widths were obtained as outlined above at times between 5 and

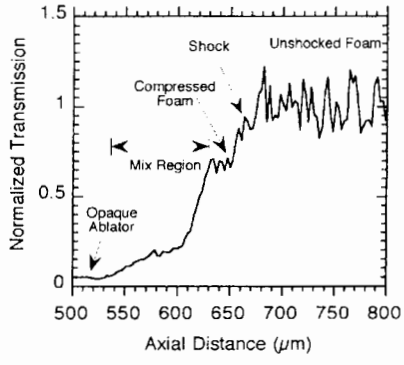

Figure 4. Normalized 100 μm-wide vertical lineout of x-ray transmission through the opaque ablator region, the mix region, the compressed foam region and the unshocked foam region

15 ns using many Nova laser shots. To compare with theoretical models, however, the effect of decompression should be removed from the mix width data. The fluids experience decompression in these experiments due to the blow-off of ablated plastic in addition to the reflected expansion wave which is generated when the shock is incident upon the density interface. Theoretical models generally do not account for such decompression effects. The two-dimensional arbitrary-Lagrange-Eulerian code called CALE was used to simulate this type of experiment. Through the use of tracers within computational simulations of the experiment using CALE, the expected decompression of the target was calculated. Experiments fielded on Nova confirmed decompression calculations [10]. This data was used to correct the experimental mix width data for decompression effects. The decompression-corrected mix width data is plotted in Fig. 5. Error bars were obtained by averaging multiple data points occurring at similar times and using their corresponding standard deviations.

To obtain the power-law coefficient θ from this data, log scales were used in plotting the

data set shown in Fig. 5. This logarithmic data is shown in Fig. 5 along with a least- squares linear fit with the late-time data occurring between 8 ns and 15 ns. As seen in Fig. 5, there is a transition to power-law behavior around 8 ns which is believed to be due to all modes having not yet reached a fully non-linear state. From this linear fit for times later than 7 ns, a power-law coefficient θ of 0.87 $\pm$ 0.2 is obtained for the two-dimensional rectilinear 100-mode initial perturbation. It should be noted, however, that this coefficient is obtained from mix width data which includes both the bubble and spike regions. However, as numerical CALE simulations have shown, at the high Mach numbers found in these experiments (M $\sim$ 30) bubble and spike structure and growth are nearly symmetric. With this assumption, the power-law coefficient presently obtained should be valid for both the bubble and spike fronts. The present coefficient

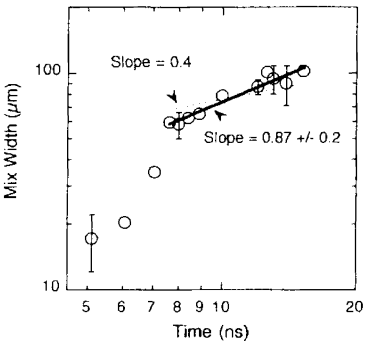

Figure 5. Experimental mix width results showing a power-law time dependence of 0.87 resulting from a strong shock crossing an initial perturbation of 100 modes

value of 0.87 is higher than 0.4 predicted by Alon et al. [6] for bubble growth, and also higher than 0.5 reported by Dimonte et al. [11]. In the work of Alon et al. [6], bubble and spike fronts were considered separately with each material having a different value for θ, depending on the Atwood number of the flow. They also were considering low Mach number flows where the spike and bubble evolution is asymmetric. There are a number of differences in the experimental configuration, target type, drive energy, and pulse shape between the present experiments and those of Dimonte which may be responsible for the discrepencies in power-law coefficients obtained. Dimonte's experiments used three-dimensional perturbations, which may result in different mode coupling effects from the present 2-D experiments. Three-dimensional perturbations were achieved in Dimonte's experiments through sandblasting or electric discharge machining of the interface. This process does roughen the surface, yet it was only possible to estimate the average wavelength of the perturbations. The considerable experimental difficulty associated with characterizing three-dimensional targets precluded quantitative knowledge of the actual surface profile. An examination of reported data from Dimonte's experiments suggests that high-amplitude, long-wavelength modes were present at the interface. These long wavelength modes may dominate the evolution of the instability.

In the present experiments, the specified rectilinear 100-mode perturbation was precision machined into the ablator interface and was closely examined for each target manufactured. From the beginning of the development of the present experiments, a well-defined mode structure of the initial condition of the perturbation was determined to be essential for the mix

results to be valuable. The reason for this is that multimode perturbations could refer to a variety of different perturbation types. In the present experiments, only the phase of each mode is random, while the amplitudes and wavelengths of the modes are specified. It is possible, in fact probable, that differing modal structures of multimode perturbations may produce different power-law coefficients. Therefore, it is important to quantify such modal structures, and to conduct experiments with differing modal structure variants in order to investigate the nature of the evolution of the multimode Richtmyer-Meshkov instability.

4. Conclusion

Experiments have been conducted using the Nova laser system to investigate the growth of the Richtmyer-Meshkov (RM) instability resulting from a strong shock wave ($M \sim 30$) crossing a prescribed well-defined initial multimode perturbation. The perturbation was a 100-mode superposition of 1 μm amplitude sine waves with randomly generated phases between 0 and 2π. The two working fluids were fluidized brominated plastic (CH + 2% Br) and carbon resorcinol foam, giving a post-shock Atwood number of approximately 0.6. The growth of the mixing region is expected to follow a power-law behavior with time. The present experimental results give a power-law coefficient of 0.87 ± 0.2. This value is higher than results previously published. The discrepency with other results may be due to 2-D versus 3-D effects, or differing experimental conditions.

Further experiments are being conducted to investigate the effect differing modal structure shapes on RM growth. From initial results, it is believed that qualitatively and quantitatively different structural growth of the mixing region can be expected from these different multimode perturbations.

Acknowledgement. The authors would like to thank the individuals who support these experiments (including taget development, fabrication and assembly, and technical support) and the Nova operations personnel.

This work was performed under the auspices of the U.S. Department of Energy by Lawrence Livermore National Laboratory under Contract N° W-7405-Eng-48.

References

[1] Taylor G, Proc. R. Soc. London, Ser. A, 201, 192, (1950).
[2] Richtmyer RD, Commun. Pure Appl. Math., XIII, 297, (1960).
[3] Meshkov E, Sov. Fluid Dyn., 4, 101, (1969).
[4] Brouillette M and Sturtevant B, Phys. Fluids, 5, 4, 916, (1993).
[5] Haan SW, Phys. Rev. A, 39, 5812, (1989).
[6] Alon U, Hecht J, Ofer D and Shvarts D, Phys. Rev. Lett., 74, 534, (1995).
[7] Remington BA, et al., Phys. Rev. Lett., 73, 545, (1994).
[8] Grove JW, et al., Phys. Rev. Lett., 71, 3473, (1993).
[9] Youngs DL, Laser Particle Beams, 12, (1994).
[10] Peyser TA, et al., Phys. Rev. Lett., 75, 2332, (1995).
[11] Dimonte G, Phys. Plasmas, currently under review, (1997).
[12] Remington BA, et al. Rev. Sci. Instrum., 63, 5083, (1992).
[13] Budil KS, et al., Rev. Sci. Instrum., 67, 485, (1996).

Parallelization of a 2D Pseudo-Spectral Dynamical Domain Decomposition Method for the Full Navier-Stokes Equations

E. Fournier and S. Gauthier
CEA/Limeil-Valenton, 94195 Villeneuve St Georges Cedex, France

Abstract: We report on preliminary results obtained with the parallel version of a 2D pseudo-spectral dynamical domain decomposition method for the full Navier-Stokes equations. Comparisons between the vectorial and the parallel versions of spectral derivation - with both Fourier and Chebyshev expansions - are presented. The efficiency versus the number of processors and the number of collocation points is also studied. Finally a Kelvin-Helmholtz instability in the subsonic domain is simulated with the vectorial and parallel versions and both simulations are compared.

1. Introduction

A multidomain pseudospectral code has been previously developed to accurately simulate unsteady subsonic viscous compressible flows, like Kelvin-Helmholtz and Rayleigh-Taylor flows [1]. First it was running on one processor of a vectorial CRAY-YMP computer. Because of the CPU time and memory limits of this kind of machine, we chose to develop a parallel version on a CRAY-T3E.
In the next section, we recall the features of the numerical method. Then we show why it is necessary to parallelize and how it is performed. We compare the times spent in the kernel of the full code of the vectorial and parallel versions. Finally we present the results obtained with the parallel version and the comparison with the results of the vectorial one on the Kelvin-Helmholtz flow.

2. Description of the numerical method

The numerical method used here is described in [1]. Let us recall its bases. It solves the 2D full Navier-Stokes equations with a pseudospectral dynamical domain decomposition method. The scheme in time is a semi-implicit third order Runge-Kutta method, in which diffusion terms are handled implicitly. For the spatial approximation, a Fourier-Chebyshev method is employed. Derivative in the homogeneous x- direction - where Fourier functions are employed - are performed with a FFT. Derivative in the inhomogeneous z-direction - where Chebyshev polynomials are used - are performed through a matrix-vector product. The domain decomposition is performed in the inhomogeneous direction, *i.e.*, in the vertical direction. In addition to this, a self-adaptative coordinate transform is applied in each subdomain and the location of the domain interfaces is dynamically calculated. In order to match density, the upstream value is used and velocity, temperature and concentration are matched owing to the influence matrix technique.

More information - Email: fournie@limeil.cea.fr, serge.gauthier@wanadoo.fr

3. Parallelization technique

3.1. Advantages of parallelism

Using a parallel version may offer a lot of advantages. As opposed to vectorial computers, which possess a small memory, available memory of parallel machines increases: for example, the maximum allocated memory for an user is 128 $\times$ 16 Mwords on a CRAY-T3E (with 128 processors), whereas only 512 Mwords can be used on a CRAY-T90 (with 24 processors and usually 24 users!). The CPU cost decreases also in parallel machines. That is the reason why for 3D calculations, one has to adapt this code to this type of computer. Since this physical domain is divided into a little number of subdomains (typically 5 to 10) in one direction, we parallelize on the subdomains which are distributed on groups of processors: instead of serial computations (subdomain after subdomain), calculations are performed simultaneously on each subdomain. Each PE is assigned for a fixed subdomain, receives data corresponding to a specific part of its and computes its own local data. Sometimes some communications between PEs are needed to match physical quantities at the domain interfaces and in special operations on matrix, like matrix transposition or when a global maximum or minimum has to be determined.

3.2. Strategy

Our strategy for the parallelization takes into account two criteria: portability and rapidity. First we tried to use PVM (Parallel Virtual Machine), which consists in a message passing library. This ensures portability, but the tests carried out have shown that the resulting code is not efficient enough. Then we added some ShMem instructions (SHared MEMory Access Library) to increase speed. Bandwith is higher with SHMEM and latency time lower, that means that a greater number of elements is passed between processors within a shorter time. This low level library is more difficult to implement correctly, because developers have to know a lot about computer architecture characteristics (memory, cache...) and to be very careful because SHMEM-put and SHMEM-get instructions modify directly memory contents of concerned processors. However, conflicts between PVM and SHMEM appeared, so they seemed to be incompatible. Finally, we chose to use only SHMEM, that should be included in a next version of MPI-2, a Message Passing Interface which could become a standard. Then we obtained efficiency, portability will be effective in the near future.

4. Tests on the code kernel

Obviously, most of time in a full typical simulation is spent in FFT computations, matrix-matrix products and matrix-vector products. To show the efficiency of the parallel version with regard to the vectorial one, we compare the times spent in a code kernel. Such a kernel is defined as a derivative in the x-direction followed by a derivative in the z-direction. The example of a calculation that is executed very often is a x-derivative (with a FFT) in one direction and a z-derivative (with a matrix-matrix product) in the other direction. This sequence becomes on a MPP machine a x-derivative (with a FFT), a local matrix transposition and then a z-derivative (with a matrix-matrix product). We applied this kind of calculation to an arbitrary function and measured the total execution time. We carried out a series of tests, by varying the number of mesh points in both directions on one hand, and the number of processors on the other hand. The figures below show the mean time ratio between CRAY-YMP and CRAY-T3D/T3E times. Each test case has been run 1000 times. The figure 1 shows the evolution of this ratio as a function of the number of processors. The figures 2, 3 and 4 represent the influence of matrix sizes on the time ratio. Such a ratio increases with the number of z-points, and at a fixed

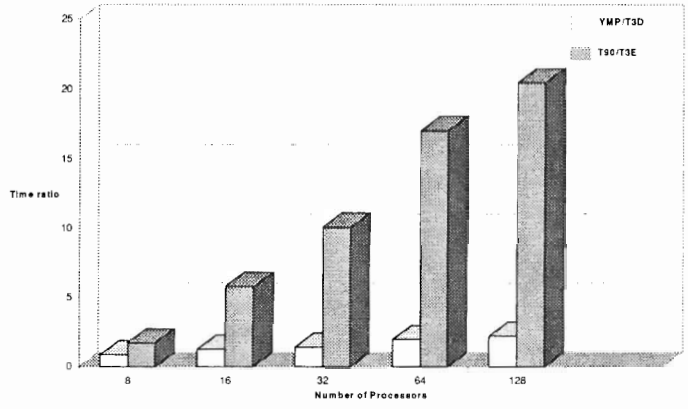

Figure 1. Ratios of CPU time YMP/T3D and T90/T3E respectively vs. the number of PEs. The number of subdomains is equal to 5. The resolution is 50 z-points in each subdomain and 128 x-points.

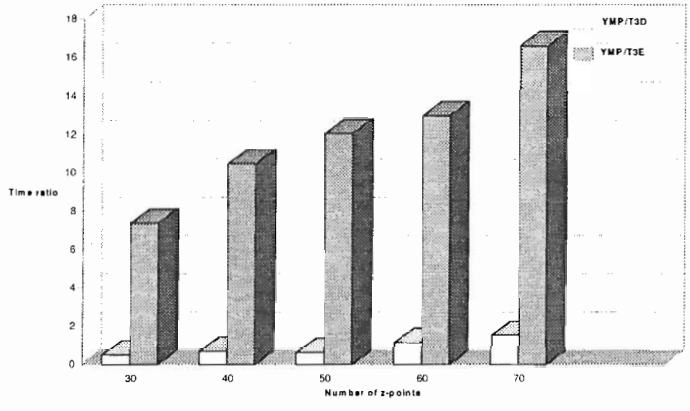

Figure 2. Ratios of CPU time YMP/T3D and T90/T3E respectively vs. the number of z-points. The number of subdomains is equal to 5. The resolution is 64 x-points.

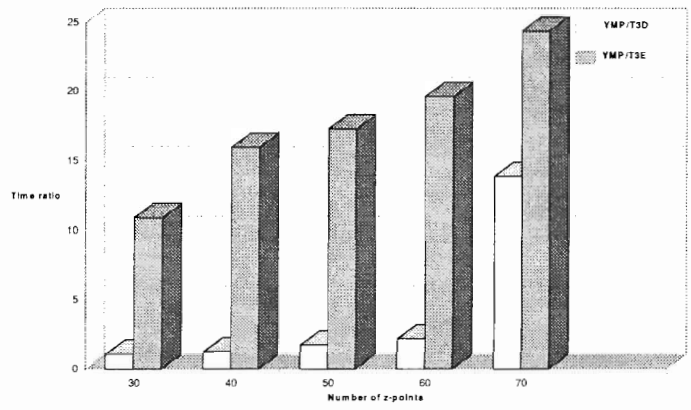

Figure 3. Ratios of CPU time YMP/T3D and T90/T3E respectively vs. the number of z-points. The number of subdomains is equal to 5. The resolution is 128 x-points.

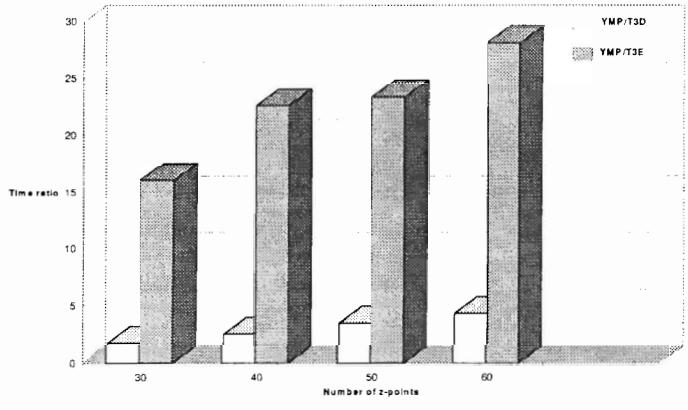

Figure 4. Ratios of CPU time YMP/T3D and T90/T3E respectively vs. the number of z-points. The number of subdomains is equal to 5. The resolution is 256 x-points.

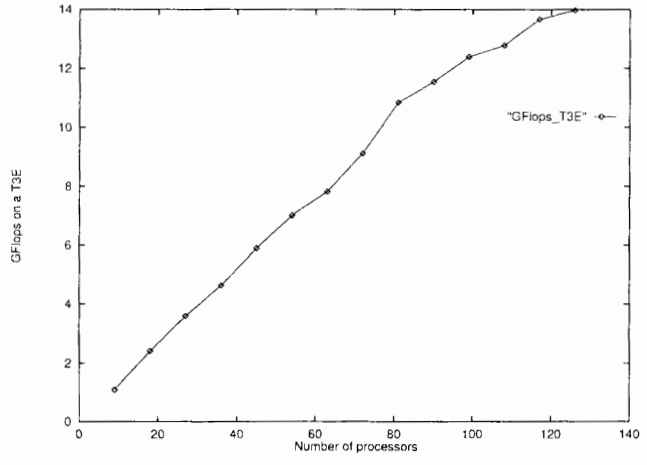

Figure 5. Performance in terms of GigaFlops on a T3E vs. the number of processors for 9 subdomains and 51 z- points in each.

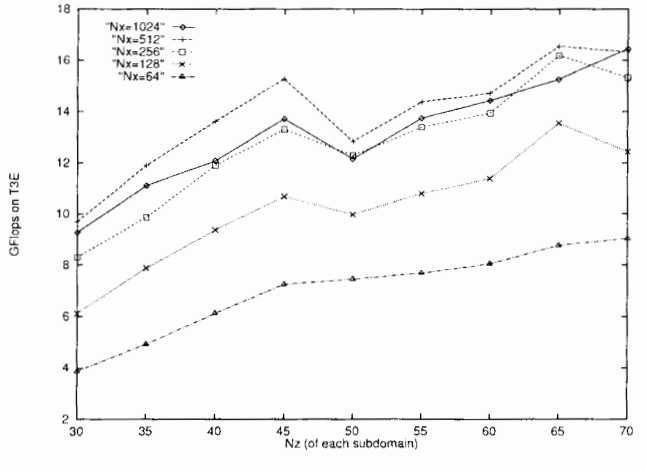

Figure 6. Performance in terms of GigaFlops on a T3E vs. the number of z-points. The number of x-points is 64, 128, 256, 512, 1024 respectively.

number of z-points, with the number of x-points. Moreover, we carried out some calculations to measure performance, in terms of GigaFlops, in each case. Such a case utilizes 9 subdomains with 51 Chebyshev points in the z-direction. Figure 5 shows the performance obtained on the CRAY-T3E versus the number of PEs. It increases almost linearly with the number of PEs up to 80 and then saturates. This saturation is probably due to the small number of columns in matrix-matrix product for such a number of PEs. In Fig. 6, the curves represent the performance, in GigaFlops, versus the number of z- points (called N_z). The various curves are obtained by varying the number of x-points (called N_x). Performances increase with N_z but do not increase regularly with N_x: a maximum is reached with $N_x = 512$, then they slightly decrease. Discrepancies between $N_x = 256$, $N_x = 512$ and $N_x = 1024$ are very small.

5. Validation of the whole code on the Kelvin-Helmholtz instability

As a first validation, we simulate the Kelvin-Helmholtz flow. The basic state of this flow, written in a non- dimensional form, is

$$u = \frac{1}{2}\tanh(2x), \quad v = 0, \quad T = 1 + \frac{\gamma - 1}{2}M^2(1 - (2u)^2), \quad P = 1, \tag{1}$$

with $0 \leq x \leq L_x$ and $-L_z \leq z \leq L_z$. Neumann boundary conditions are applied to the horizontal velocity and the temperature and Dirichlet boundary conditions to the vertical velocity. This test case is described in detail in [1]. The validation of the parallelization is based on the superposition of results of both versions (parallel and vectorial). Curves describing the vorticity evolution as a function of time have been superposed and consequently show that results are identical and validate the parallel version. In this case, 72 x-points and 3 subdomains with 51 z-points in each are used. Table 1 compares the Total Execution Time (TET) for various configurations and the CPU time used for one node and one cycle. This quantity decreases as the number of PEs increases. However, the decrease is not linear. The efficiency is increased by almost a factor 3 with the CRAY-T3E (with 52 PEs) in comparison with the vectorial machine CRAY-YMP.

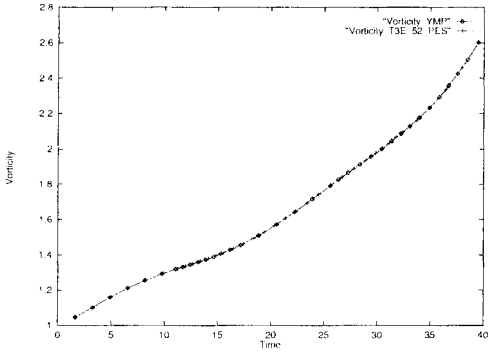

Figure 7. Evolution in time of the vorticity for the Kelvin-Helmholtz flow.

	T3E 1 PE	T3E 10 PEs	T3E 52 PEs	YMP 1 PE
Total Execution Time (in s)	$0.179\ 10^5$	$0.398\ 10^4$	$0.183\ 10^4$	$0.474\ 10^4$
Time/node/cycle (in s)	$1.53\ 10^{-3}$	$2.98\ 10^{-4}$	$1.48\ 10^{-4}$	$4.06\ 10^{-4}$

Table 1. Total Execution Time and time per node per cycle for various configurations.

6. Conclusion

We have presented preliminary results obtained with the parallel version of a 2D pseudo-spectral dynamical domain decomposition method for the full Navier-Stokes equations. This work opens the way to new perspectives : we are interested in simulations with very high resolution and nowadays only parallel methods allow to success in such attempts. In the near future the parallel version will be extended to 3D.

References

[1] Renaud F and Gauthier S, A Dynamical Pseudo-Spectral Domain Decomposition Technique: Application to Viscous Compressible Flows, J. Comput. Phys., 131, 89-108, (1997).

Hydrodynamic Instability Experiments on the Nova Laser

S.G. Glendinning[1], M.M. Marinak[1], S.W. Haan[1], D.H. Kalantar[1], K.S. Budil[1], R.J. Wallace[1], S.V. Weber[1], J.D. Colvin[1], B.A. Remington[1], C. Cherfils[2], D. Galmiche[2], A. Richard[2], W.W. Hsing[3], J. Kane[4] and D. Arnett[4]
[1]Lawrence Livermore National Laboratory, Livermore, CA 94550, USA
[2]CEA Centre d'Etudes de Limeil-Valenton, 94195 Villeneuve St Georges, Cedex, France
[3]Los Alamos National Laboratory, Los Alamos, NM, USA
[4]University of Arizona, Tucson, AZ, USA

Abstract: We have developed an ablation front RT experiment in spherically convergent geometry, to test our understanding of the effects of convergence on RT growth and saturation; and a planar multimode, ablation front, 3D experiment, to test multimode weakly nonlinear saturation and modeling. We have also developed an embedded-interface RM-RT experiment to look at the deep nonlinear mixing relevant to supernovae.

1. Introduction

The Rayleigh-Taylor (RT) instability occurs when a lower density fluid accelerates a higher density fluid, causing the interface between the two fluids to become contorted. This instability is of broad interest, because of its occurrence in astrophysics [1,2], high energy density physics [3-5], and inertial confinement fusion (ICF) [6-14]. We report here on two new ablation front RT experiments using (1) spherically converging hemispheres, and (2) planar foils with 3D multimode perturbations, and one new embedded-interface Richtmyer-Meshkov (RM) - RT experiment relevant to core collapse supernovae.

2. Spherically convergent experiments

Experiments in convergent geometry are inherently more difficult than in planar geometry. As a first step in this direction, people have done RT experiments in cylindrically convergent geometry.[14,15] We describe a spherically convergent, ablation-front RT experiment, as illustrated in Fig. 1. A standard cylindrical Au "scale-1" hohlraum is used (2.75 mm long by 1.6 mm

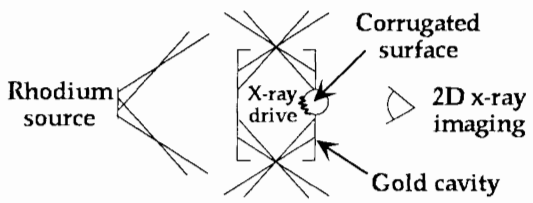

Figure 1. Experimental configuration for the convergent experiment.

diameter). The experimental sample is a standard "HEP-4" capsule [16] corresponding to a 530 μm outer diameter, $\sim$42 μm wall thickness, CH(1.3% Ge) capsule with no fill pressure. This is mounted on a hole in the wall of the hohlraum, with half the sphere interior to the hohlraum,

More information - Email: glendinning1@llnl.gov

and half exterior. The interior hemisphere has had a 70 μm wavelength, 2 μm amplitude, 2D perturbation imposed on it, using an off-line laser ablation technique [17]. Eight of the ten Nova beams enter the hohlraum in a 2.2 ns shaped ("PS26"), 6:1 contrast pulse, and convert to x-rays. This generates a 2:1 contrast, ~200 eV peak radiation temperature x-ray drive, as was used in previous "HEP-4" implosion campaigns [16]. As the interior hemisphere implodes, the ablation front perturbations grow due to the RT instability, and are diagnosed by face-on radiography, using a Rh backlighter. For comparison, identical experiments were conducted, using $\sim 50\mu$m thick planar foils of CH(2% Br) in place of the hemispheres. We used Br dopant here, because we were unable to fabricate planar CH(Ge) foils. The Br concentration was adjusted to provide the same degree of x-ray preheat shielding, based on 1D simulations.

Time sequences of raw images, taken with a fast x-ray framing camera ("FFC") run at 8x magnification with 10 μm pinholes at ~50 ps gating times, are shown in Fig. 2. The top row

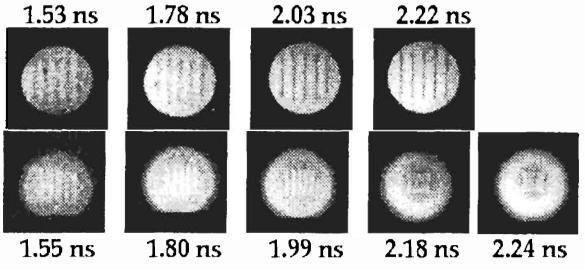

Figure 2. Raw images comparing planar (top) with spherically convergent (bottom) RT growth.

corresponds to the planar CH(Br) foil, and the bottom row to the CH(Ge) hemisphere. Shock breakout for the planar foil corresponds to about 1.6 ns, and we see the perturbation evolve rapidly into the nonlinear regime, as the foil reaches peak accelerations of about 120 μm/ns^2 at $\sim$ 2 ns. The perturbation for the hemisphere corresponded to an initial 300 x 300 μm square patch with the same 70 μm wavelength, 2 μm amplitude sinusoidal ripple imposed on it. Shock breakout here occurs at about 1.2 ns. As the hemisphere accelerates between 1.5-2.25 ns, it converges by over a factor of two, as seen by the shrinking of the perturbation patch. The 2D simulations [18] show that for convergences up to a factor of ~2, the implosion is reasonably spherical. Hence, the observed convergence translates to an acceleration history.

We show the Fourier analysis of the data in Fig. 3. Two shots are shown for each plot, distinguished by open (early-time) and closed (late-time) symbols. There are a number of similarities between the planar and spherically convergent experiments. Both experiments result in peak observed growth factors (of optical depth modulation) of 6-8, and both enter the nonlinear regime, with the appearance of the second harmonic. The appearance of the second harmonic is slightly earlier in the convergent case, suggesting somewhat earlier entry into the nonlinear regime. This is reasonable, since the perturbation wavelength is shrinking. Also, the peak rate of growth is noticeably higher in the convergent case. This may result from (1) a steeper density gradient at the ablation front, and (2) the perturbation wavelength shifting to a more unstable region of the RT dispersion curve. Finally, the roll-over immediately following the observed peak in growth factor is more extreme in the convergent case. This is at least partly an instrumental effect, because the instrument modulation transfer function (MTF) drops as the fundamental wavelength decreases [19].

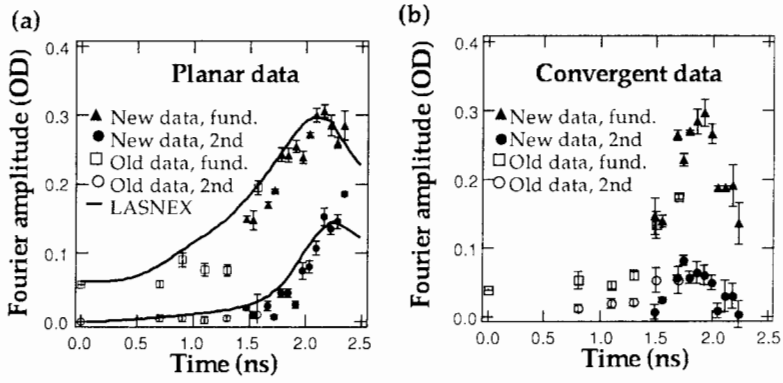

Figure 3. Fourier analysis of the data shown in Fig. 2.

The solid curves shown in Fig. 3a correspond to LASNEX [20] simulations, post processed to correspond to the experimental images. The agreement between the 2D simulation and the data is quite good, other than a slight discrepancy prior to shock breakout (t < 1.4 ns). The 2D simulations for the convergent experiments (not shown) also give reasonable agreement with the data [18].

3. 3D multimode experiment

Our most recent ablation-front planar RT experiment is to measure the 3D RT evolution of a full spectrum of well characterized initial modes. The initial pattern was carefully designed to be a square patch corresponding to the first ~10 harmonics of a cosine symmetric, 300 μm fundamental wavelength in both the x- and y-directions. In other words, the perturbation patch corresponds to a multimode cross-hatch pattern with cosine symmetry in both orthogonal directions. The designed pattern, displayed as optical depth, is shown in 4a, compared with an actual radiograph of the fabricated foil (filtered for noise and symmetrized) shown in Fig. 4b. The agreement between design and actual multimode target is striking, and represents a truly remarkable feat of precision target fabrication, utilizing laser ablation with an excimer laser [17]. The time sequences from the Nova shots are shown in Figs. 4c (simulated) and 4d (measured). The 3D simulations were done with HYDRA[13] and agree quite well with the data.

The 2D Fourier evolution is shown in Figs. 5a-d, representing the first 6 ns. The laser pulse shape in this case ("PS35") was 4.5 ns in duration with ~7:1 contrast[21]. Azimuthally averaged Fourier spectra (square root of $< \eta_k^2 >$, where the average is over the azimuthal angle) are shown in Fig. 5e. The initial Fourier spectrum is rather featureless, monotonically decreasing with mode number. As RT growth proceeds, a very distinct peak is seen in the spectrum at mode ~4, corresponding to a wavelength of ~75 μm, which is roughly where peak growth is expected, based on estimates of the indirect-drive RT dispersion curve [12,22] Furthermore, at the latest time, 6.0 ns, an observable second harmonic at mode 8 emerges, signaling entry into the nonlinear regime.

This multimode experiment represents a much more controlled and quantitative rendition of what we first attempted in 1993 [23], where the initial pattern was a random, bead-blasted

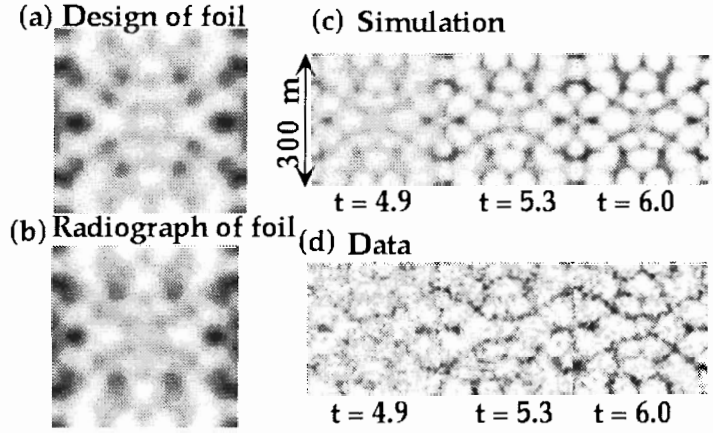

Figure 4. Initial foil for the planar 3D multimode experiments: (a) optical depth for designed foil; (b) optical depth of actual, fabricated foil; (c) simulated RT growth during the Nova shot; and (d) same, only the measured result.

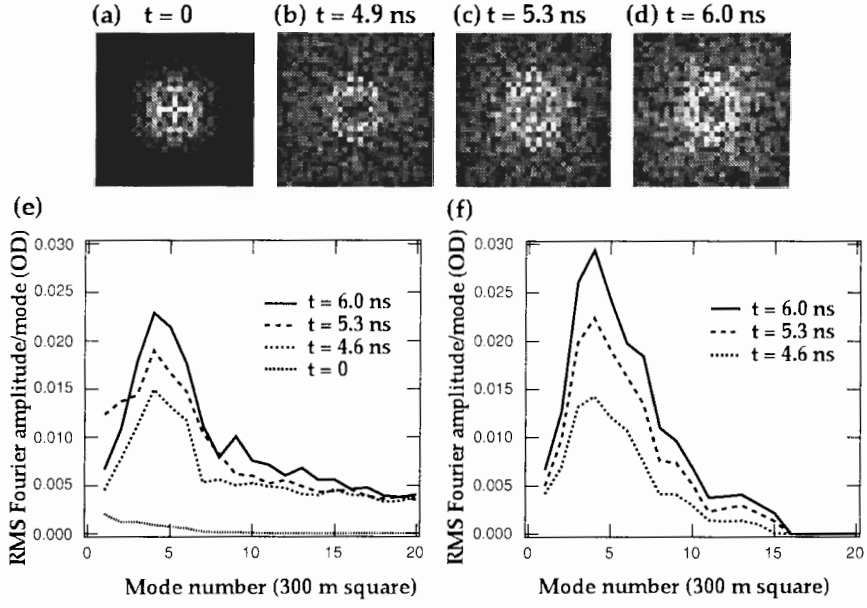

Figure 5. Fourier analysis of the RT experiment using the foil shown in Fig. 4. (a-d) images corresponding to times of 0, 4.9, 5.3, and 6.0 ns. (e) Azimuthally averaged Fourier spectra at the same times. (f) Simulated azimuthally averaged Fourier spectra at the same times.

perturbation. Surprisingly, the final result late in time after RT growth looks rather similar, with "hexagonal" bubbles developing, surrounded by spike sheets.

4. Supernova hydrodynamics experiment

When a core collapse-supernova explodes, an exceedingly strong radial shock propogates outward through the star, blowing it apart.[1] The progenitor star can be crudely thought of as a series of concentric shells of decreasing density with a dense Fe core at the center, and a low density H envelope at the outside. When the shock traverses these "interfaces", strong RM instabilities are triggered. After shock breakout, each layer gets decelerated by the next outer, lower density layer. Hence, extensive RT instability growth follows the RM phase. Core collapse supernova are virtual caldrons for deep nonlinear RM-RT mixing. [1]

We have started a supernova hydrodynamics experiment on the Nova laser designed specifically to look at deep nonlinear RM-RT mixing.[2] The initial experiment corresponded to a planar, 2-layer package: an 85 μm thick Cu ablator followed by a 500 μm thick CH_2 tamper, with a 2D, 200 μm wavelength, 20 μm amplitude sinusoidal ripple at the interface. A 10-15 Mbar shock traverses the interface, followed by a protracted deceleration and decompression phase, qualitatively similar to the situation in the supernova. We show the initial results of the observed RM-RT bubble and spike front evolution, compared with simulations using the Lab code CALE [24], and the astrophysics supernova code PROMETHEUS [1,2] in Fig. 6. These

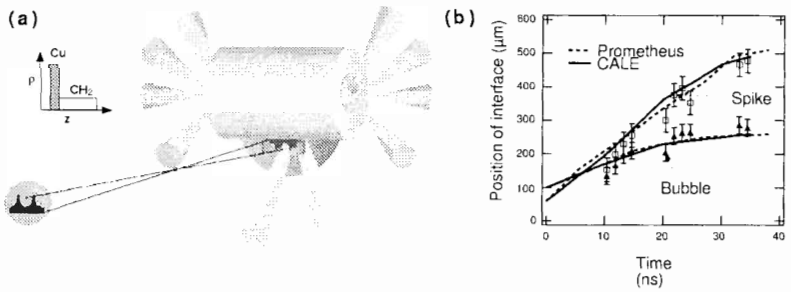

Figure 6. (a) Experimental configuration for the supernova RM-RT experiment. (b) RM-RT experiment, compared with simulations with CALE and PROMETHEUS.

initial results look very promising. We are now developing a similar experiment to compare the deep nonlinear growth of a 3D single-mode, cross-hatch ("egg-crate") ripple pattern, compared to the 2D equivalent. Predictions suggest we should observe enhanced growth in 3D[9,11,13], which has important implications for the supernova evolution.

5. Conclusion

We have developed a quantitative ablation front RT experiment in spherically convergent geometry, to test our understanding of the effects of convergence on RT growth and saturation; and a planar multimode, ablation front, 3D experiment, to test multimode weakly nonlinear saturation and modeling. We have also developed an embedded-interface RM-RT experiment to look at the deep nonlinear mixing relevant to supernovae.

Acknowledgement. Work performed under the auspices of the U.S. Department of Energy by the Lawrence Livermore National Laboratory under contract number W-7405-ENG-48. This work has been performed partially under the auspices of a Commissariat à l'Energie Atomique-U. S. Department of Energy collaboration.

References

[1] Müller E, Fryxell B and Arnett W D, Astron. Astrophys., 251, 505, (1991).
[2] Kane J *et al.*, Ap. J., 478, L75, (1997); Remington BA *et al.*, Phys. Plasma, 4, 1994, (1997).
[3] Campbell EM, Holmes NC, Libby SB, Remington BA and Teller E, Proc. of the 1995 APS Topical Conf. on Shock Compression of Condensed Matter, Seattle, WA (August 13-18, 1995); in press, Laser and Part. Beams, (1997); UCRL-JC-124258, Rev. 2, (1996).
[4] Budil KS *et al.*, Phys. Rev. Lett., 76, 4536, (1996); Rev. Sci. Instrum., 68, 799, (1997).
[5] Kalantar DH, these proceedings; Weber SV *et al.*, these proceedings; Colvin JD *et al.*, these proceedings.
[6] Kilkenny JD, Phys. Plasmas, 1, 1379, (1994).
[7] Lindl J, Phys. Plasmas, 2, 3933, (1995).
[8] Haan SW, Phys. Rev. A, 39, 5812, (1989); Phys. Fluids B, 3, 2349, (1991).
[9] Shvarts D *et al.*, Phys. Plasmas, 2, 2465, (1995); Ofer D *et al.*, Phys. Plasmas, (1996).
[10] Betti R *et al.*, Phys. Plasmas, 3, 2122, (1996); Goncharov V *et al.*, Phys. Plasmas, 3, 4665, (1996).
[11] Dahlburg JP *et al.*, Phys. Fluids B, 5, 571, (1993).
[12] Remington BA *et al.*, Phys. Plasmas, 2, 241, (1995).
[13] Marinak MM *et al.*, Phys. Rev. Lett., 75, 3677, (1995); Phys. Plasmas, 3, 2070, (1996).
[14] Hsing WW, Phys. Plasmas, 4, 1832, (1997).
[15] Weir S *et al.*, these proceedings.
[16] Landen OL *et al.*, Phys. Plasmas, 3, 2094, (1996).
[17] Wallace RJ *et al.*, ICF Quarterly Report No. UCRL-LR-105821-94-3, (1994).
[18] Cherfils C *et al.*, these proceedings.
[19] Robey HF *et al.*, Rev. Sci. Instrum., 68, 792, (1997).
[20] Zimmerman GB and Kruer WL, Comments Plasma Phys. Controlled Fusion, 11, 51, (1975).
[21] Budil KS *et al.*, these proceedings.
[22] Weber SV *et al.*, Phys. Plasmas, 1, 3652, (1994).
[23] Remington BA *et al.*, Phys. Fluids B, 5, 2589, (1993).
[24] Tipton R, author of CALE, private communication.

A General Closure Relation for Incompressible Mixing Layers Induced by Interface Instabilities

J. Glimm[1], D. Saltz[1] and D.H. Sharp[2]
[1]Department of Applied Mathematics and Statistics
University at Stony Brook, Stony Brook, NY 11794-3600, USA
[2]Theoretical Division, MS-B285
Los Alamos National Laboratory, Los Alamos, NM 87545, USA

Abstract: We describe a generalization of a recently-proposed two-phase flow model for the statistical evolution of an incompressible mixing layer. This model, which was originally developed for application to Rayleigh-Taylor mixing, predicts the distribution of volume fractions and fluid velocities across the mixing layer in terms of the trajectories of the edges. Our previous analysis of this model is extended to flows that are not self-similar.

1. Introduction

The Euler equations (with or without external forces) govern a wide variety of chaotic flows, including interface instabilities of the Rayleigh-Taylor (RT), Richtmeyer-Meshkov (RM), and Kelvin-Helmholtz (KH) types. It is natural to expect that a system of two-phase flow equations that are derived by ensemble averaging the Euler equations should likewise govern the statistical features of the same types of flows. Of course, having a complete two-phase description requires closure relations for new quantities introduced by the averaging of nonlinear terms and boundary conditions in the microscopic equations. Generally, a specific closure relation has a fairly restricted domain of validity. In Refs. [1, 2, 3], we proposed closure relations for the compressible Rayleigh-Taylor problem with constant acceleration, and devoted considerable attention to their validation. In this paper, we indicate how our original two-phase flow formulation can be extended to a broader class of interface instability problems.

2. A two-phase flow model for immiscible fluid mixing

Consider the flow of two fluids with no molecular mixing, and define the characteristic function $X_k(x,y,z,t)$ $(k=1,2)$, which returns 1 is (x,y,z) is in fluid k at time t; 0 otherwise. Let $\langle\cdot\rangle$ denote an average over an infinite ensemble of microscopic flow realizations which are "similarly prepared" in the sense described by Drew and Lahey [4]. Then $\beta_k(x,y,z,t) \equiv \langle X_k\rangle$ is the proportion of the realizations in which the fluid particle at (x,y,z) at time t belongs to material k. By convention, we call β_k the volume fraction of phase k. The single-phase average of the quantity $f(x,y,z,t)$ is $\overline{f}_k(x,y,z,t) = \langle f X_k\rangle / \beta_k$.

We assume that the statistics of the ensemble are translationally invariant in the x and y directions, and that any external acceleration or impulse is directed along the z axis. Therefore all ensemble-averaged quantities depend only on z and t. This assumption does not preclude having non-vanishing transverse components of vectors in the model, so that fluid motion in a direction tangential to the mixing layer can be described. The ensemble averaging step is important because it ties the two-phase flow equations to primitive equations that can be considered exact for the purpose of this study. A major advantage of this approach is that

More information - Email: saltz@ams.sunysb.edu

it provides a framework in which each modeling assumption can be isolated and tested by comparison to microscopic computational data.

Problems that fit into this statistical description of the ensemble include the RT, RM, and KH instabilities that arise from random perturbations of a planar fluid interface. In the RT problem, the external force is assumed to act normal to the interface, but it can be time dependent. Similarly, in the RM problem we consider only the case of a shock wave at normal incidence to the interface. Although the KH problem involves a velocity shear across the interface, there is no length scale induced by this shear in the x and y directions when the gradient of the shearing velocity is in the z direction. The assumption about translational invariance of the ensemble amounts to an implicit assumption about the mechanism for generating a KH instability, which is that the force responsible for the shear is itself translationally invariant in the x and y directions. Instabilities driven by forces oblique to the fluid interface are not included in this framework, except perhaps in a local approximation.

In this paper, we specialize to the case of incompressible fluids, and consider the general two-fluid mixing problem illustrated in Figure 1a. The two-phase flow equations are derived by ensemble averaging (i) the incompressible Euler equations within each fluid, and (ii) a kinematic equation for the material interface [4]. They are [1, 5]

$$\frac{\partial \beta_k}{\partial t} + v^* \frac{\partial \beta_k}{\partial z} = 0 \ , \tag{1}$$

$$\frac{\partial \beta_k \overline{v}_k}{\partial z} = v^* \frac{\partial \beta_k}{\partial z} \ , \tag{2}$$

$$\rho_k \frac{\partial \beta_k \overline{v}_k}{\partial t} + \rho_k \frac{\partial \beta_k \overline{v}_k \overline{v}_k}{\partial z} = -\beta_k \frac{\partial \overline{p}_k}{\partial z} + \beta_k \rho_k g(t) + (p^* - \overline{p}_k) \frac{\partial \beta_k}{\partial z} - \frac{\partial \beta_k R_k^{zz}}{\partial z} \ , \tag{3}$$

where v is the z component of velocity, p is pressure, ρ_1 (ρ_2) is the density of the light (heavy) fluid, v^* and p^* are the effective interface velocity and pressure, respectively [1], $g(t)$ is the external acceleration, and R is the Reynolds stress tensor. Equation (1) describes the conservation of volume fraction along trajectories with velocity v^*. Equation (2) is equivalent to conservation of mass in phase k combined with the microscopic incompressibility condition $\nabla \cdot \mathbf{v} = 0$ [5], and Eq. (3) represents the conservation of momentum along the z direction in phase k. In a KH instability problem, there is a non-trivial conservation law for momentum in a tangential direction (say x),

$$\rho_k \frac{\partial \beta_k \overline{u}_k}{\partial t} + \rho_k \frac{\partial \beta_k \overline{u}_k \overline{v}_k}{\partial z} + \frac{\partial \beta_k R_k^{xz}}{\partial z} = 0 \ , \tag{4}$$

where u is the x component of velocity.

So far, no approximations have been introduced in the averaged equations other than symmetry conditions and zero surface tension at interfaces, but there are now five independent equations, namely Eq. (1) for either k and Eqs. (2)-(3) for $k = 1, 2$, for the nine unknowns β_1, $\overline{v}_1$, $\overline{v}_2$, $\overline{p}_1$, $\overline{p}_2$, v^*, p^*, R_1^{zz}, and R_2^{zz}. The variable β_2 can be trivially eliminated using the identity $\beta_1 + \beta_2 = 1$. In the KH problem, there are four additional unknowns, $\overline{u}_1$, $\overline{u}_2$, R_1^{xz}, and R_2^{xz}, and two additional equations, namely Eq. (4) for $k = 1, 2$. To close the system of equations in the interior of the mixing zone, we thus need four to six more constraints among the dependent variables. Closure relations applicable to RT instability (unknowns − equations = 4) were proposed and validated in [1]; this work is summarized in [2]. Closure models applicable to RM and KH mixing are currently under study.

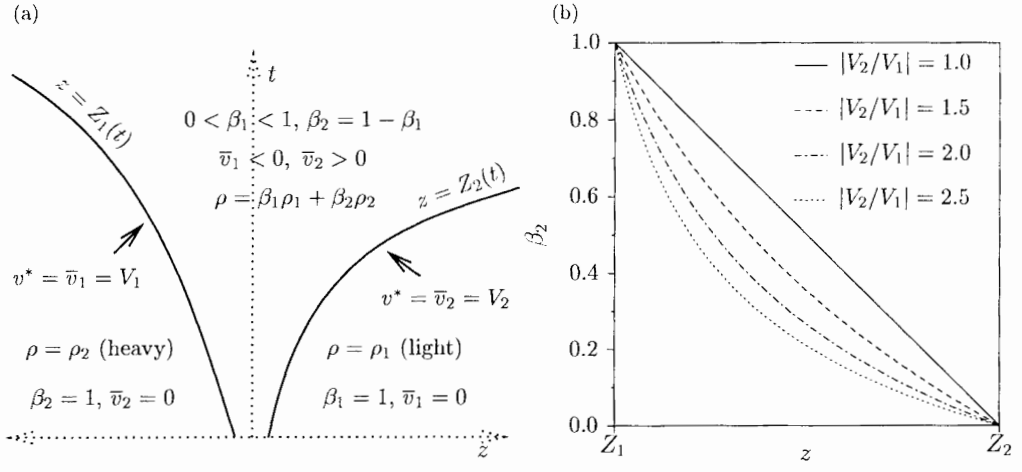

Figure 1. (a) Incompressible two-phase mixing in the (z,t) plane. The two curves are the trajectories of the mixing zone edges. The lower (upper) edge is the limit of vanishing β_1 (β_2), and it corresponds to the tip of the frontier portion of light (heavy) fluid in the pre-averaged flow. (b) The heavy fluid volume fraction β_2 along the mixing zone for different values of the mixing layer expansion ratio $|V_2/V_1|$ in the special case that this ratio is constant in time, such as in incompressible Rayleigh-Taylor mixing. The range of $|V_2/V_1|$ shown in this figure is representative of Rayleigh-Taylor experiments up to large density ratios [6].

Even when the number of equations equals the number of unknowns, a complete two-phase flow description for the entire domain still requires conditions which specify the motion of the mixing zone edges. There is much to learn about this problem, but we note that first steps toward its solution in the context of a two-phase flow model have been taken by the authors [1, 3] and by Alon *et al.* [7], who have proposed models for the edge trajectories based on buoyancy and drag forces on the leading bubble and spike tips in the microscopic flow. The positions of these tips define the mixing zone edges in the two-phase flow. Note that the growth rate of the instability enters through the boundary conditions for the mixing zone edges. We are currently studying such issues as the coupling of the momentum equations to the edge trajectories, and to what extent (if any) the growth rate is predicted by the momentum equations.

3. A new model for v^*

The model for v^* that was proposed in [1] has since been shown to be of limited applicability [5]. The problem that we wish to discuss in this paper is the form of a general closure relation for v^*, so for this purpose we assume arbitrary motions of the mixing zone edges, as shown in Figure 1a. Note that the subscript k on the edge trajectory $Z_k(t)$ labels the edge as the limit of vanishing β_k. The boundary conditions on v^* are known: $v^* = \overline{v}_k = V_k(t)$ along the trajectory $z = Z_k(t)$, for $k = 1, 2$. For intermediate positions within the mixing zone, we propose that v^* is a weighted average of $\overline{v}_1$ and $\overline{v}_2$, where the weights depend on z, t, and β_k,

$$v^* = \mu_1(z, t, \beta_1)\overline{v}_2 + \mu_2(z, t, \beta_2)\overline{v}_1 \ . \tag{5}$$

In order to satisfy the boundary conditions on v^*, we require that $\mu_k(z = Z_k(t), t, \beta_k = 0) = 0$ and $\mu_k(z = Z_{k'}(t), t, \beta_k = 1) = 1$, with $k' = 3 - k$ the complementary index to k.

The assumed absence of the single-phase pressures $\overline{p}_k$ in the v^* closure (5) decouples Eqs. (1) and (2) from the momentum equations (3) and renders them soluble in our model. As will be seen below, the explicit time dependence of the coefficients μ_k comes from the edge velocities $V_k(t)$. The z dependence is included to accommodate future extensions of this closure to compressible mixing, where there is a finite propagation speed of information from the edges to the interior of the mixing region. It is possible that simply allowing for z dependence in μ_k is insufficient to account for compressibility effects, and rather μ_k must satisfy its own evolution equation. For the present discussion of incompressible mixing, we assume that μ_k does not explicitly depend on z.

Besides the boundary conditions, there are two constraints on μ_1 and μ_2. One constraint is Galilean frame invariance. Equation (5) holds in any coordinate system moving vertically with a constant velocity if and only if

$$\mu_1(t,\beta_1) + \mu_2(t,\beta_2) = 1 \ . \tag{6}$$

The other constraint is found by solving the equations of motion as follows.

Summing Eq. (2) over k and using $\beta_1 + \beta_2 = 1$, we get $\partial(\beta_1\overline{v}_1 + \beta_2\overline{v}_2)/\partial z = 0$. We specify an inertial reference frame by requiring that $\overline{v}_1$ ($\overline{v}_2$) vanish at the upper (lower) wall of a finite but large domain. The solution to this ODE is therefore

$$\beta_1\overline{v}_1 + \beta_2\overline{v}_2 = 0 \ . \tag{7}$$

We use this equation along with the closure relation (5) to eliminate one of the velocities from Eq. (2) and obtain

$$-\frac{1}{\overline{v}_k}\frac{d\overline{v}_k}{d\beta_k} = \left[\frac{\mu_k(t,\beta_k)}{\beta_k} - \frac{\mu_{k'}(t,\beta_{k'})}{\beta_{k'}} + \frac{1}{\beta_{k'}}\right] \ . \tag{8}$$

The following analysis uses β_k and z interchangeably as independent variables. Thus there is an implicit assumption that β_k is continuous and monotonic across the mixing region.

The solution to the ODE (8) which satisfies the boundary conditions at the mixing zone edges is

$$\overline{v}_k = V_k\beta_{k'}e^{-F_k(t,\beta_k)} \ , \tag{9}$$

where

$$F_k(t,\beta_k) = \int_0^{\beta_k}\left[\frac{\mu_k(t,\phi_k)}{\phi_k} - \frac{\mu_{k'}(t,\phi_{k'})}{\phi_{k'}}\right]d\phi_k \ . \tag{10}$$

In this integration the relation $\phi_k + \phi_{k'} = 1$ holds. From Eqs. (2) and (8), we have

$$v^* = [\beta_{k'}\mu_{k'}(t,\beta_{k'}) - \beta_k\mu_k(t,\beta_k)]\frac{\overline{v}_k}{\beta_{k'}} \ . \tag{11}$$

The RHS of this expression must give the same v^* for both $k = 1$ and $k = 2$. It is easy to show [3] that this condition is satisfied if and only if

$$\left|\frac{V_2(t)}{V_1(t)}\right| = e^{-F_1(t,1)} \ , \tag{12}$$

which is the second mathematical constraint on μ_1 and μ_2. Note that if μ_1 and μ_2 are the same function, *i.e.*, $\mu_1(t,\beta_1) = \mu(t,\beta_1)$ and $\mu_2(t,\beta_2) = \mu(t,\beta_2)$, then $F_1(t,1) = 0$ and Eq. (12) implies

that the mixing zone is constrained to expand at the same rate in each direction. Thus μ_1 and μ_2 should have a similar mathematical form (reflecting the similarity between the equations of motion for each phase), but with different parameters in order to allow a time-dependent expansion ratio $|V_2(t)/V_1(t)|$.

As a specific choice of constitutive law, we propose the linear fractional form

$$\mu_k(t,\beta_k) = \frac{a_k(t)\beta_k + d_k(t)\beta_{k'}}{c_k(t)\beta_k + b_k(t)\beta_{k'}} , \tag{13}$$

for $k = 1, 2$, where the a_k, b_k, c_k, and d_k are time-dependent functions to be determined. The relations $d_k = 0$ and $c_k = a_k$ follow from the boundary conditions on μ_k. Also, μ_k is invariant under an arbitrary scaling of both numerator and denominator in Eq. (13), so we can set either a_k or b_k arbitrarily. We choose $a_k(t) = |V_k(t)|$. The remaining unknowns b_1 and b_2 are determined from the two constraints (6) and (12). The unique solution is $b_k(t) = |V_{k'}(t)|$; hence

$$\mu_k(t,\beta_k) = \frac{|V_k|\beta_k}{|V_1|\beta_1 + |V_2|\beta_2} . \tag{14}$$

Equations (9), (10), (11), and (14) give v^* as a function of t and β_k,

$$v^*(t,\beta_k) = \frac{|V_1V_2|(|V_1|\beta_1^2 - |V_2|\beta_2^2)}{(|V_1|\beta_1 + |V_2|\beta_2)^2} . \tag{15}$$

Solving the interface equation (1) by the method of characteristics, we get an implicit equation for the volume fraction profile,

$$z(\beta_k,t) = z(\beta_k,0) + \int_0^t v^*(s,\beta_k)ds , \tag{16}$$

where the integrand is provided by Eq. (15). To summarize, Eqs. (9), (10), (14), (15), and (16) give the distributions of volume fractions and velocities across the mixing layer in terms of the trajectories of the edges.

In the special case that V_2/V_1 is independent of t, then so is μ_k. If, in addition, the mixing zone expands outward (*i.e.*, $(-1)^kV_k > 0$ for all t), then there is a scale-invariant solution, where all lengths in the problem scale with the given time dependence of the edge displacements. One example is RT mixing under a constant acceleration $g > 0$, for which $Z_k(t) = (-1)^k\alpha_k Agt^2$, where α_1 and α_2 are positive constants which depend on the Atwood ratio $A = (\rho_2 - \rho_1)/(\rho_2 + \rho_1)$. The ratio $|V_2/V_1| = \alpha_2/\alpha_1$ is constant in this problem, and Eqs. (15) and (16) give the scale-invariant solution for the volume fraction profile,

$$\frac{z}{Agt^2} = \frac{\alpha_1\alpha_2(\beta_1^2\alpha_1 - \beta_2^2\alpha_2)}{(\alpha_1\beta_1 + \alpha_2\beta_2)^2} . \tag{17}$$

The scale-invariant solution for the velocities $\overline{v}_k$ follows by evaluation of Eq. (9),

$$\frac{\overline{v}_k}{2Agt} = (-1)^k\frac{\alpha_1\alpha_2\beta_{k'}}{\alpha_1\beta_1 + \alpha_2\beta_2} . \tag{18}$$

When $\alpha_2/\alpha_1 = 1$, Eq. (17) implies that the volume fraction varies linearly across the mixing zone, in agreement with experimental RT data for small A [6, 8, 9]. In fact, our model predicts

that any incompressible mixing layer has a linear, scale-invariant volume fraction profile when $|V_2/V_1| = 1$, which is typically the case in the symmetric limit ($A \to 0$). The RT experiments of Youngs give expansion ratios in the neighborhood of 2 at large A. The profiles predicted by Eqs. (15) and (16) for $|V_2/V_1|$ in this range are shown in Figure 1b. The linear fractional model for μ_k predicts an increasing amount of curvature in the profile with an increasing expansion ratio. The correct shape of the volume fraction profiles at large A, as determined from computational or experimental data, has not been adequately established. There is also uncertainty regarding the proper degree of smoothness in the profiles near the mixing zone edges. These issues are discussed in Ref. [3].

When V_2/V_1 is time dependent, as is the case in RM instability at moderate to large A [10], then the mixing zone is never dominated by a single length scale, and the solution is therefore not scale invariant. Suppose the contrary, that is, a single time-dependent length scale $\eta(t)$, for the solution to be self-similar, it is necessary that the mixing zone be stationary in a spatial cordinate system scaled by η. Thus Z_k/η must be constant for $k = 1, 2$, implying that Z_2/Z_1 is time independent, and hence so is V_2/V_1. This argument, combined with the analysis above, shows that an expanding mixing zone is self-similar if and only if V_2/V_1 is a constant.

Acknowledgement. The work of JG and DS is supported by the Applied Mathematics Subprogram of the U.S. Department of Energy, DE-FG02-90ER25084. JG is also supported by the Army Research Office, grant DAAH04-95-10414, and the National Science Foundation, grant DMS-95-00568. DHS is supported by the U.S. Department of Energy.

References

[1] Y. Chen, J. Glimm, D. H. Sharp, and Q. Zhang. A two-phase flow model of the Rayleigh-Taylor mixing zone. *Phys. Fluids* 8, 816-825 (1996).

[2] Y. Chen, J. Glimm, D. Saltz, D. H. Sharp, and Zhang Q, A two-phase flow formulation for the Rayleigh-Taylor mixing zone and its renormalization group solution, In R. Young, J. Glimm, and B. Boston, editors, Proc. of the Fifth International Workshop on Compressible Turbulent Mixing, World Scientific, Singapore, (1996).

[3] Glimm J, Saltz D and Sharp DH, Two-phase modeling of a fluid mixing layer, submitted to J. Fluid Mech.

[4] Drew DA and Lahey RT, Analytical modeling of multiphase flow, In M. C. Roco, editor, Particulate Two-Phase Flow, Butterworth-Heinemann, Stoneham, MA, (1993).

[5] Glimm J, Saltz D and Sharp DH, Renormalization group solution of two-phase flow equations for Rayleigh-Taylor mixing, Phys. Lett. A, 222, 171-176, (1996).

[6] Youngs DL, Modeling turbulent mixing by Rayleigh-Taylor instability, Physica D37, 270-287, (1989).

[7] Alon U and Shvarts D, Two-phase flow model for Rayleigh-Taylor and Richtmyer-Meshkov mixing, In R. Young, J. Glimm, and B. Boston, editors, Proc. of the Fifth International Workshop on Compressible Turbulent Mixing, World Scientific, Singapore, (1996).

[8] Snider DM and Andrews MJ, Rayleigh-Taylor and shear driven mixing with an unstable thermal stratification, Phys. Fluids, 6, 3324-3334, (1994).

[9] Schneider MB, Dimonte G and Remington B, Large and small scale structure in Rayleigh-Taylor mixing, submitted to Phys. Rev. Lett.

[10] Alon U, Hecht J, Ofer D and Shvarts D, Power laws and similarity of Rayleigh-Taylor and Richtmyer-Meshkov mixing fronts at all density ratios, Phys. Rev. Lett., 74, 534-538, (1995).

Compressibility and Density Gradients in the Modelling of the Dissipation Equation: Application to Turbulent Shear Flows

D. Guézengar[1,2], H. Guillard[1] and J.P. Dussauge[2]
[1]INRIA, BP 93, 06902 Sophia-Antipolis Cedex, France
[2]IRPHE, 12 Av. Général Leclerc, 13003 Marseille, France

Abstract: In this work, the ability of a $k-\varepsilon$ model, to calculate mixing layers with significant density gradients, is discussed. It is shown that deficiencies appear for compressible flows, even if the $k-\varepsilon$ model is coupled to compressibility corrections. A modification of the σ_ε coefficient is proposed to compute efficiently compressible mixing layers with high density variations. This new formulation for σ_ε enforces compatibility between ε-equation coefficients, density gradients and compressibility models. Moreover, subsonic and supersonic effects can be examined separately. The results are presented on mixing layer computations with density ratios between 1/7 and 7, and convective Mach number between 0 and 1.

1. Introduction

It is well known that the standard $k-\varepsilon$ model fails to predict highly compressible flows, like supersonic mixing layers. In such high speed flows, from a modelling point of view, two aspects need to be considered : a density variation and a Mach number effect. In the early '90, some models called *compressibility corrections* [11, 12] have been built to cure the second effect. Many works report the necessity to use such models to predict the correct decrease of the spreading compressible mixing layer rate, but they do not take in account the density gradients influence, which is a point on which the present paper is focused. Studies on density variation effects are still recent and are essentially on boundary layers [6, 1]. The initial idea, proposed by Huang *et al.* [6], is to account for density gradients, through coefficients σ_ε or C_{ε_1}, in order to improve the $k-\varepsilon$ model performances in the logarithmic region. The present proposal is to consider separately density gradients effects and then to couple them to Mach number effects. Mixing layers appear to be interesting test-cases because such a separation can be performed and they do not need near-wall modelling.

2. Governing equations and the $k-\varepsilon$ model

For turbulent flows, governing equations are obtained from the averaged Navier-Stokes equations. In compressible flows the velocity components (u_i) and the temperature (T) are Favre mass-weighted averaged while it is Reynolds averages for density (ρ) and pressure (p). To close this system, we need a turbulence model. In the $k-\varepsilon$ model the closure for Reynolds stresses is given by the Boussinesq assumption : $-\bar{\rho}\widetilde{u_j''u_i''} = \mu_t S_{ij} - \frac{2}{3}\rho k\delta_{ij}$.

More information - Email: Dominique.Guezengar@inria.sophia.fr or dussauge@marius.univ-mrs

3. Density gradients modelling

3.1. The ε-equation

According to Huang *et al.* [6], the ε-equation is responsible for the poor results obtained with compressible flows. The standard $k-\varepsilon$ model uses the following set of constants, which remain unchanged whatever the flow : $C_{\varepsilon 1} = 1.44$, $\sigma_\varepsilon = 1.3$, $C_{\varepsilon 2} = 1.92$ and $\sigma_k = 1.0$. C_{ε_1} was calibrated from experimental data on decay of isotropic turbulence (subsonic flows), C_{ε_2} to optimize incompressible flows computations on a flat plate, and for constant density flows, the local equilibrium condition in the wall region of a boundary layer gives the relation :

$$\frac{\sigma_\varepsilon (C_{\varepsilon 2} - C_{\varepsilon 1})}{\kappa^2} \sqrt{C_\mu} = 1 \tag{1}$$

It is easy to show that, in the density variable case, relation (1) is not verified, and density gradients have to be taken in account :

$$\frac{\sigma_\varepsilon (C_{\varepsilon 2} - C_{\varepsilon 1})}{\kappa^2} \sqrt{C_\mu} = 1 + F\left(\frac{y}{\rho}\frac{d\rho}{dy}, \frac{y^2}{\rho}\frac{d^2\rho}{dy^2}\right)$$

Huang *et al.* do this analysis in boundary layers . The same idea is used in the present work to study mixing layers with high density variations. Moreover, we do not need to neglect the diffusion term of k and we assume that ε can evolve along the flow.

3.2. Description of the density gradient correction

To derive the new formulation of σ_ε, the first step is to consider the k and ε equations :

$$\begin{cases} \rho \dfrac{Dk}{Dt} = \dfrac{\partial}{\partial y}\left(\dfrac{\mu_t}{\sigma_k}\dfrac{\partial k}{\partial y}\right) + \mathcal{P} - \rho\varepsilon_t + \overline{p'd'} \\ \rho \dfrac{D\varepsilon}{Dt} = \dfrac{\partial}{\partial y}\left(\dfrac{\mu_t}{\sigma_\varepsilon}\dfrac{\partial \varepsilon}{\partial y}\right) + C_{\varepsilon 1}\dfrac{\varepsilon}{k}\mathcal{P} - C_{\varepsilon 2}\dfrac{\varepsilon}{k}\rho\varepsilon \end{cases} \tag{2}$$

$\overline{p'd'}$ is a compressibility term (for modelling, see [9] or [13], for instance) and ε_t is the total dissipation. According to Sarkar *et al.* or Zeman, this term can be decomposed into a solenoidal part (noted ε, which verifies the above ε-equation) and a compressible part (that need to be modeled). Many models (for example [10, 12, 1]) have the general form : $\varepsilon_t = F(M_t) \times \varepsilon$, with $F(M_t) = 1 +$ function(M_t), where M_t is the turbulent Mach number : ${M_t}^2 = 2k \,/\, \gamma RT$, consequently, local equilibrium situations impose that $\mu_t = C_\mu \dfrac{\rho k^2}{\varepsilon_t}$.

To characterize mixing layers, we need some other parameters. We note with index 1 (resp. 2) the faster (resp. slower) flow, $M_c = \dfrac{\Delta U}{a_1 + a_2}$ is the convective Mach number and $s = \dfrac{\rho_2}{\rho_1}$ and $r = \dfrac{u_2}{u_1}$ are respectively the density and the velocity ratios. Now, we can introduce, in the vicinity of the inflection point, the following definitions which describe the behavior of the first and third velocity derivatives : $\dfrac{\partial u}{\partial y} = \dfrac{\Delta u}{\delta}$ and $\dfrac{\partial^3 u}{\partial y^3} = f(s, r, M_c)\dfrac{\Delta u}{\delta^3}$. δ is the mixing layer thickness. In the literature, many definitions of this quantity can be found. We choose to use the vorticity thickness. Furthermore, we use three hypothesis to obtain a new relation for σ_ε :

- the spreading rate of a mixing layer evolves according to the empirical law :
  $\delta' = \dfrac{d\delta}{dx} = \dfrac{1}{2}\delta'_{ref}\Phi(M_c) \times \dfrac{\Delta u}{U_c}$; $\delta'_{ref} = 0.15$,
- the total dissipation is proportional to the production term : $\varepsilon_t = C \times \mathcal{P}$ with $C < 1$,
- we examine the case of a self-similar mixing layer where the maximum level of k is constant along the flow : $\dfrac{\partial k_{max}}{\partial x} = 0$ and we consider the location of the maximum of the turbulent kinetic energy : $\dfrac{\partial k}{\partial y} = 0$

In a mixing layer, the point where k is maximum is also practically the point where the velocity profile is maximal : $\dfrac{\partial^2 u}{\partial y^2} = 0$. At this location it is reasonable to think that the eddy viscosity ν_t is quite a constant and by the way, it implies the cancelation of the dissipation gradient terms : $\dfrac{\partial \varepsilon}{\partial y} = 0$. Finally, according to the work of Barre *et al.* [2], we can express the eddy viscosity as a function of mixing layer parameters : $\nu_t = \dfrac{1}{2}K(s, r, M_c)\delta'_0 \Delta u \delta \Phi(M_c)$

If such hypothesis are introduces into (2), the relation which σ_ε must verify to cope with density gradients and with Mach number effects is :

$$\sigma_\varepsilon = 2F(M_t)\frac{\sigma_k\sqrt{C_\mu}\left(C^2 - C\right) + C\sigma_k\dfrac{\overline{p'd'}}{\rho k}\left(\dfrac{\partial u}{\partial y}\right)^{-1} + \dfrac{\delta'_0 F(M_t)\Phi K f}{2}}{2\sqrt{C_\mu}C_{\varepsilon 2}C^2 - \left(2\sqrt{C_\mu}C_{\varepsilon 1} + \Phi\right)F(M_t)C} \tag{3}$$

In this expression, there are only two free parameters left : C and Kf. C is the coefficient of proportionality between production and dissipation. For subsonic flows, experiments give a value of 0.7. For the studied compressible mixing layers we found that a mean value of 0.75 (in the center of mixing layers) can be retained. And $Kf = K(s, r, M_c) \times f(s, r, M_c)$ contains the influence of the density on σ_ε. According to [8], Kf is not very sensitive to the convective Mach number, as a consequence we suppose that its value does not change with M_c.

To close the problem, the following procedure has been retained :

1. incompressible cases : the calibration of the σ_ε relation determines Kf ; the correct values of Kf are tuned to predict the correct spreading rate, for flows with density gradient
2. compressible cases : the computations are made with the compressibility correction proposed by SEHK [10]: $\varepsilon_c = \alpha M_t^2$, $\alpha = 0.5 \Rightarrow F(M_t) = 1 + \alpha M_t^2$ and $\overline{p'd'} = 0$, in addition the α coefficient needs to be adapted because the model has been calibrated on a mixing layer with uniform density ($s = 1$). It will be shown that α changes for flows with variable density ($s >> 1$ or $s << 1$).

4. Numerical method

In this study, the numerical method is based on a mixed finite element / finite volume spatial approximation, and the MUSCL technique is used to obtain a second order spatial accuracy. More details can be find in [3, 5].

5. Results and discussion

5.1. Validation test-cases

To evaluate performances of the $k-\varepsilon$ model and of our modified σ_ε, we have investigated two kinds of test-cases with high density gradients : subsonic and supersonic mixing layers (convective Mach number evolves from near 0 to 1). The validation test-cases include velocity/density co-gradients and cross-gradients ($s = 1/7$, $s = 1$ and $s = 7$). Furthermore, we chose to keep the same velocity ratio (a moderate value of $r = 0.65$) for all the flows. The results were obtained on a 4840 points mesh, with an implicit scheme and a second order spatial approximation (use of limiters on turbulent variables).

5.2. Incompressible mixing layer results

The aim of this section is to evaluate the $k-\varepsilon$ model for this type of flow and to calibrate relation (3), which we have : incompressible flows ($\Rightarrow \Phi(M_c) = 1$) and no compressibility models ($\Rightarrow \overline{p'd'} = 0$ and $F(M_t) = 1$). Relation (3) is now reduced to $\sigma_\varepsilon = 1 - \frac{4}{3}Kf$. In this section, the value of the spreading rate (δ'_{0exp}) given by the semi-empirical relation (4) will be referenced by the word "*experiment*" :

$$\delta'_{0exp} = \frac{0.15}{2} \times \frac{(1-r)(1+\sqrt{s})}{(1+r\times\sqrt{s})} \tag{4}$$

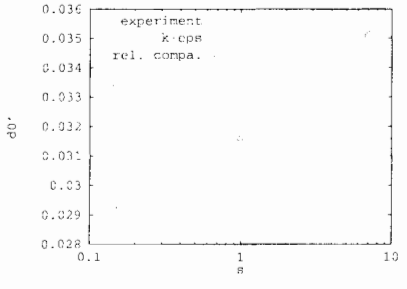

Figure 1. Comparisons of the incompressible spreading rates ($r = 0.65$)

Figure 1 shows the influence of the density ratio s on the incompressible rate. We can see that the spreading rate is well predicted by the $k-\varepsilon$ model if density is uniform. But, performances are much worse for $s \neq 1$ and we estimated that discrepancies on computed δ'_0 can reach 20 % (evaluated by $(\delta'_{0exp} - \delta'_{0computed})/\delta'_{0exp}$). Moreover, we remark that *experiment* indicates an increase of the spatial growth rate with s while $k-\varepsilon$ model results show a total opposite behavior. The values of Kf are determined to cancel the differences, and it can be seen in figure 1 that discrepancies are now negligible. In fact, the new σ_ε coefficient forces the incompressible mixing layer to reproduce the subsonic effects, consequently it controls in a coherent way the density influence. Now, values indicated in table 1 will be utilized.

5.3. Compressible mixing layer results

With the previous results, we have only considered the influence of density. Now, it has to be coupled to the Mach number effect. The value of constant α in the SEHK model had to

s	1/7	1	7
Kf	-2.5	-0.225	0.35

Table 1. Kf values versus s

be revised. It is found that a value of $\alpha = 1.66$ restores correct values of the compressible spreading rate, whatever s (see [4]). To make comparisons, we use the normalized spreading rate defined by $\delta'/\delta'_0 = \Phi(M_c)$ and the Langley curve (compilation of experimental data [7]). In the caption of tables and figures we note "*experiment*" the compressible spreading rate given by $\delta'_{exp} = \Phi(M_c) \times \delta'_{0exp}$, "*k-eps*" the results obtained by the $k-\varepsilon$ model ($\sigma_\varepsilon = 1.3$) with SEHK correction ($\alpha = 0.5$) and "*rel. compa.*" the results obtained by the new formulation of σ_ε (relation (3)) with adapted SEHK correction ($\alpha = 1.66$). Table 2 gives spreading rates obtained by the different models. About the $k-\varepsilon$ results, two points can be underlined. Firstly, even if a compressibility model is used, the discrepancy on δ' is very high and increases with the convective Mach number (to reach 70% at M_c=1), and it is mainly related to the presence of density gradients. Secondly, there is a large difference between the $s = 1/7$ and $s = 7$ cases. This trend is not supported by experimental observations. This last point is underlined in the figure 2 which gives comparisons of the computed normalized spreading rate with the experimental Langley curve. The results of the $k-\varepsilon$ model, coupled to the SEHK compressibility correction, do not reproduce the experimental decrease.

Finally, if results obtained with the proposed modification for σ_ε are examined, a very sound behavior is found : discrepancies on spreading rates remain weak for all the computed Mach numbers (see table 2) and results obtained for the two density ratios are very similar and in agreement with the Langley curve (see figure 3).

M_c	0.45	0.65	1.00
δ'_{exp}	0.0291	0.0224	0.0146
k-eps	0.0310 (+ 6.5%)	0.0287 (+ 28.1%)	0.0248 (+69.9%)
rel. compa.	0.0256 (- 12.0%)	0.0209 (- 6.7%)	0.0150 (+ 2.7%)

Table 2. s=1/7 : Comparison of the compressible expansion rates

6. Conclusion

From the present work, two main conclusions can be drawn about the performances of the $k-\varepsilon$ model in compressible mixing layers with high density variations. The standard model gives very poor predictions of spreading rates ; the deficiency increases for compressible mixing layer and we note great differences in the behavior of the $s = 1/7$ and $s = 7$ cases. To cure these problems, a modified σ_ε coefficient has been proposed that take into account density and compressibility influence. Improved results have been found in a large range of validation test-cases. By the way, we obtain reasonable differences (less than 12%) for all the computations. Finally, it has been shown that compressibility corrections, which give good results on quasi-uniform density mixing layers, have to be adapted when density is not uniform.

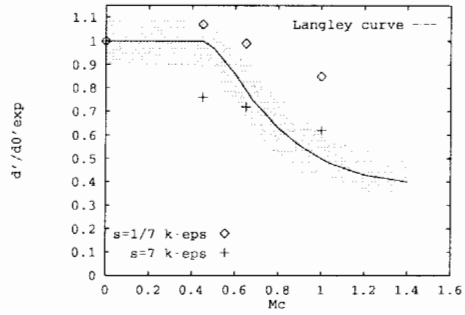

Figure 2. Compressible expansion rates results of $k-\varepsilon$ model

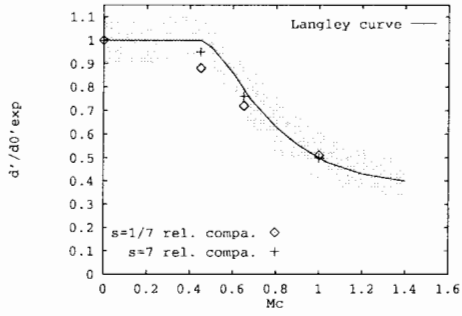

Figure 3. Compressible expansion rates results of the modified σ_ε and with $\alpha = 1.66$

References

[1] Aupoix B and Viala S, Compressible turbulent boundary layer modelling, Symposium on transitional and Compressible turbulent flows, The Westin Resort, Hilton Head Island, South Carolina, USA, (1995).
[2] Barre S, Quine C, Dussauge JP, J. Fluid Mech., 259, (1994).
[3] Fezoui L, Lanteri S, Larrouturou B, Olivier C, INRIA Report, 1033, (1989).
[4] Guézengar D, Th. Univ. de la Méditerranée, (1997).
[5] Guillard H, Mixed Element volume methods in CFD, VKI Lecture Series 95-02, (1995).
[6] Huang PG, Bradshaw P and Coakley TJ, AIAA Journal, 32, 4, 735-740, (1994).
[7] Kline SJ, Cantwell BJ, Lilley GM, Proc. of the 1980 conference on complex turbulent flows, I, 364-368, Stanford Univ., California, Sept. 3-6, (1980).
[8] Menaa M, Th. Univ. de Provence, (1997).
[9] Sarkar S, Phys. Fluids, 4, 2674-2682, (1992).
[10] Sarkar S, Erlebacher G, Hussaini MY, ICASE report, 92-6, (1992).
[11] Wilcox DC, AIAA Journal, 30, 11, 639-2646, (1992).
[12] Zeman O, Phys. Fluids, 2, 178-188, (1990).
[13] Zeman O, Phys. Fluids, 3, 951-955, (1991).

Modeling of Linear Perturbation Growth in Gas Dynamics: From Incompressible to Compressible Flows

L. Hallo[1], R.L. Morse[2], J.M. Clarisse[1], N.M. Hoffman[2] and N. Toqué[3]
[1]CEA/Limeil-Valenton, 94195 Villeneuve Saint Georges CEDEX, France
[2]Los Alamos National Laboratory, Los Alamos, New Mexico 87545, USA
[3]CEA/Bruyères-Le-Chatel, BP 12, 91680, Bruyères-Le-Chatel, France

Abstract: The present work attempts to give a unified presentation of models for predicting linear perturbation growth in converging flows. Perturbed shock waves—within the CCW approximation—as well as perturbed homogeneous compressions are considered and compared with results from a perturbation code. In addition, incompressible perturbations at interfaces in spherical systems made of uniform density fluids are treated by combining Bell's and Mikaelian's approaches.

1. Introduction

In this paper, perturbation growth in (strong) shock-driven converging flows as well as in homogeneous converging flows are addressed through: (i) simple analytical models from CCW [1, 2], characteristics theory [3], and potential flow solutions for uniform density fluids [4, 5]; (ii) numerical simulations with a perturbation code [6]. These simulations involve both incompressible and compressible perturbations, depending on the model under consideration. We focus primarily on validating models for unperturbed and perturbed flows. We first briefly present the main features of the perturbation code, PANSY. We then turn to the linear growth of perturbations at a shock-wave front within the frame of the CCW approach for stratified fluids [2]. Comparisons with numerical results from PANSY lead to discuss the validity of the self-similarity assumption and to consider the incidence of acoustic waves propagating downstream of the perturbed shock-wave front. These waves are found to follow, for intermediate wavenumbers, the dispersion relation for *acoustic-gravity waves* [7]. For incompressible perturbations, Bell's approach for treating converging flow instabilities of a uniform density fluid [4] is extended, in the spirit of Mikaelian [5], to handle stratified media. Mean flows as well as perturbations are compared with self-similar homogeneous compression solutions [8, 9] and rotational instability results obtained with PANSY.

2. The PANSY perturbation code

The numerical model/code employed here, called PANSY, calculates time development of three-dimensional modes of coupled hydrodynamic, thermodynamic, and transport phenomena, including heat flow, viscosity, fully linearized about zeroth order spherically or cylindrically symmetric compressible flows. The zeroth order solutions are calculated on a typical one-dimensional Lagrangian grid and have the form $f^j(t)$, where the f's are all of the necessary hydrodynamic and other variables, including zone radius and velocity, and where j is the radial zone index. First order quantities, of the form $f^j_{l,m}(t)\ Y_{l,m}(\theta)\ \exp[im\phi]$ for spherical or $f^j_{k,m}(t)\ \exp[i(kz+m\theta)]$ for cylindrical geometry, are calculated with difference equations which are linearly perturbed forms of the already radially discretized zeroth order equations, rather

More information - Email: hallo@limeil.cea.fr

than discretizations of the linearly perturbed continuous zeroth order equations [6]. This relatively conservative/Hamiltonian differencing doctrine produces considerably improved treatment of phenomena requiring high radial resolution, especially artificial viscosity for shocks, in contrast with earlier forms of PANSY which required higher radial resolution for the same accuracy [10].

3. Converging shock wave

Trajectories of strong converging shock waves can be modeled within self-similar hypotheses. An approximate characteristics-based ethod—*i.e.*, the CCW model—has been shown [11, 2, 3] to be in good agreement with self-similar theory, for both radius trajectory and shock wave perturbation, when the shock wave is of the accelerating type. This last hypothesis is fulfilled in converging geometries and when stratification of the unshocked medium is moderate. We compare trajectories and perturbation growth given by PANSY with those predicted by the stratified CCW model in the case of spherical shock tube problem. The purpose is here to validate the CCW model extended to converging geometries and stratified media, and to investigate the influence of acoustic modes in such a shock-induced flow on the basis of PANSY calculations.

3.1. Evaluation of shock wave trajectories

Shock wave trajectories, under the strong shock-wave assumption, have for limiting behaviours: $r \propto (t_c - t)^\alpha$ as $t \to t_c$. Comparisons of the characteristic exponents α, as given by the self-similar theory [11, 12] and the CCW model, are carried out for various density profiles of the initially unshocked medium following the dependency $\rho \propto r^{-q}$: see the table below.

	planar		cylindrical		spherical	
q	CCW	self-similar	CCW[1]	self-similar	CCW[1]	self-similar
0	1	1 [11]	0.8354	0.8353 [12] 0.8353 [11]	0.7173	0.7172 [12] 0.7174 [11]
−1/2	0.9028	0.9062 [11]	0.7665	0.8260 [12]	0.6659	0.7021 [12]
−1	0.8229	0.8319 [11]	0.7081	0.8557 [12]	0.6214	0.7039 [12]

Good agreement is found in planar geometry or for $q \approx 0$. As q decreases, increasing discrepancies are observed between exponent values given by the self-similar theory and the CCW model. Explanations for such discrepancies would require further analysis of the method presently used [12] to compute self-similar data.

3.2. Shock-wave geometric perturbation

Geometric perturbation growths for a spherical converging shock wave as predicted by the CCW model are compared with results from PANSY. For this purpose a numerical shock tube problem has been devised which attempts to comply with the strong shock-wave assumption while being suited for numerical computations. The setup consists of a perfect gas ($\gamma = 5/3$) occupying initially the two regions $0 \leq r < 0.5$ and $0.5 < r \leq 1$ with pressure and density ratios of 1 to 4, temperatures being even. In the inner region, density profiles of the form $\rho \propto (r_d/r)^q$ can be initialized through temperature gradients. For $q = 0$, the shock wave reaches the origin at about 0.225 time units. Perturbations are introduced by defining the boundary separating the two regions to be a spherical surface harmonic of order l at $t = 0$. Actual calculations have been performed in two stages. During the first stage, which corresponds to the shock wave formation

[1]CCW model extended—this communication—to non-planar [3] geometries and to stratified fluids [2]. (An error was found in the dispersion relation given in [2].)

($t \leq 0.02$), the whole shock tube is treated. For subsequent times, the computational domain reduces to the inner region with initial conditions obtained from the first stage and boundary conditions given by a perfectly spherical piston pressure law. In that way, initial perturbations are coherent with PANSY numerical dissipation while their subsequent evolutions at the shock-wave front are free from the Richtmyer-Meshkov instabilities which develop at the contact surface. Trajectories of the shock waves and perturbation radial profiles for the $l = 20$-mode are shown in Fig. 1. The radial discretization uses here 200 Lagrangian cells, the shock-wave

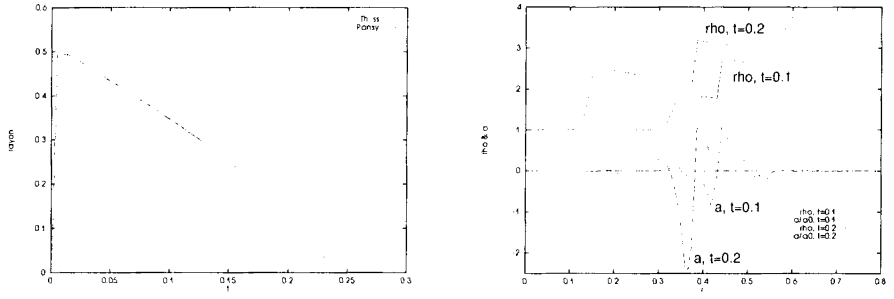

Figure 1. Front trajectory (left) and perturbation radial profiles for the $l = 20$-mode (right).

front being smeared over 5 to 6 cells. The position of the front is taken as the location of the artificial viscosity maximum. This definition may account for the trajectory discrepancies observed in Fig. 1—right. Nevertheless, the self-similar trajectory is a good approximation for this shock tube problem for times up to 0.15. Perturbation radial profiles (Fig. 1—right) show significant amplification for increasing distances downstream of the shock front. This behaviour seems to indicate that acoustic modes originated at the shock front are amplified while propagating within the shocked fluid. Perturbation growths, for the $l = 4$- and $l = 20$-modes, are displayed in Fig. 2. Agreement between PANSY and the CCW model is better for

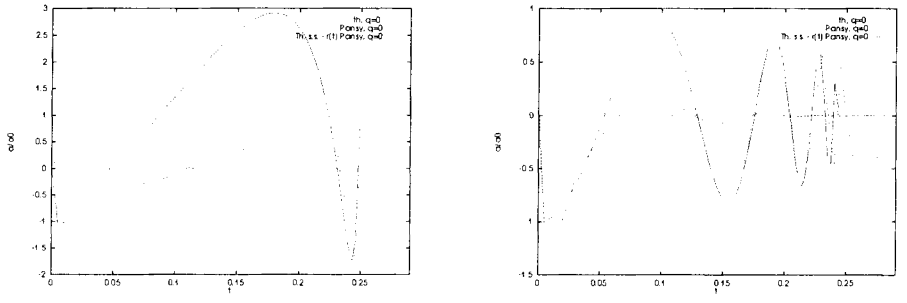

Figure 2. Growth factor vs time, PANSY and CCW model, for the $l = 4$- (left) and $l = 20$-modes (right).

$l = 20$ than for $l = 4$. In both cases PANSY results appear to be strongly damped by comparison with the CCW data. The code artificial viscosity by widening the instability front across the shock front is mainly responsible for this damping. The perfectly spherical piston boundary condition, via acoustic mode propagation, has also a limiting effect—more pronounced for small values of l—on the perturbation growth at the shock front. For larger values of l, the CCW

model predicts increasing frequencies, smaller geometric extents and larger trains of oscillations downstream of the shock front. For $l = 20$, damping dominates the results from PANSY: the perturbation is lost after only two inversions. Increasing the number of grid points improves the code resolution but results in strong unphysical oscillations. These oscillations which seem to originate from the boundary conditions hide the physical perturbations we are interested in. As a consequence, results for higher-l modes lack accuracy: a 200 grid-point calculation for $l = 100$ gives a perturbation which dies out after only half an oscillation. For stratified fluid cases, perturbation growths are given for the $l = 10$-mode and different values of the exponent q in Fig. 3. Here again, CCW model data and PANSY calculations agree in terms of phases but

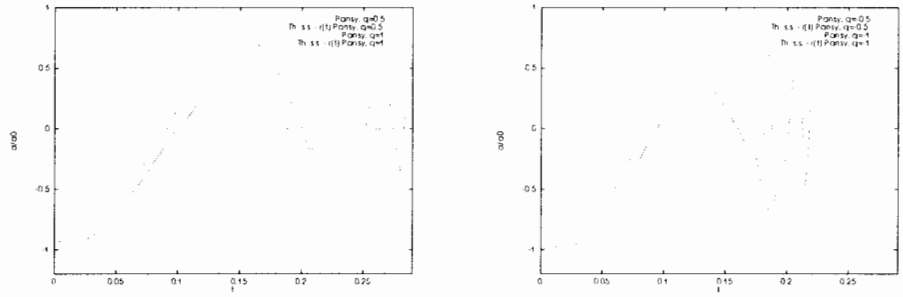

Figure 3. Growth factor vs time, PANSY and CCW model, $l = 10$-mode, for $q > 0$ (left) and $q < 0$ (right).

evidence strong damping in PANSY amplitudes. At this time, exact self-similar results for self-propagating shock waves are not available for comparison with CCW model data. Consequently we cannot state with certainty that the damping found in PANSY is entirely wrong.

3.3. Acoustic mode excitation downstream of the shock-wave front

Growth factors as functions of time presented in Fig. 2 and Fig. 3 exhibit oscillatory behaviours. These oscillations are characteristic of stability problems in a pseudo-planetary atmosphere [7]. The evolution character (growing, oscillatory...) of perturbations depends on the gradient length scale $H = \rho/(d\rho/dr)$ and on the acceleration. For intermediate wavelengths, compressibility and gravity effects may compete, so that *acoustic-gravity waves* may interact with Rayleigh-Taylor instabilities at interfaces or with other acceleration-dependent instabilities. The dispersion relation for these propagating acoustic-gravity waves is, in the absence of rotation,

$$\frac{\Gamma^2}{k^2} = \left(\frac{N^2}{\omega^2}\right)\left(1 - \frac{\omega^2}{k^2 c_s^2}\right) \tag{1}$$

where k is the wavenumber, ω the frequency, c_s the adiabatic sound speed, N^2 the Brunt-Väisälä frequency squared, Γ the Eckhart coefficient and g the acceleration[2]. Typical values of the parameters at the shock-wave front location at time $t = 0.15$ are: $g = -35.93$, $c_s = 1.296$, $\nabla\rho/\rho = 26.42$, $\Gamma = 34.61$, $N^2 = -1718$. From these values, the oscillating modes appear to be of the acoustic kind. The frequency obtained from the dispersion relation (1) with mean flow parameter values taken at $t = 0.15$ is plotted as a function of $k = l/r$ in Fig. 4. Acoustic waves, which are generated at the shock-wave front, follow the dispersion relation for acoustic-gravity

[2] $N^2 = g\left(\frac{1}{\rho}\frac{\partial\rho}{\partial r} - \frac{g}{c_s^2}\right)$ and $\Gamma = \frac{1}{2\rho}\frac{\partial\rho}{\partial r} - \frac{g}{c_s^2}$

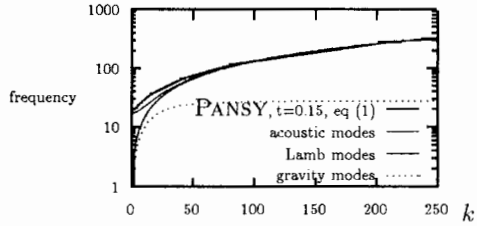

Figure 4. Frequency versus wavenumber, PANSY, acoustic and Lamb waves

waves for intermediate wavelengths thus denoting the equal importance of compressibility and gravity effects.

4. Converging uniform-density fluid flows

Another approach for tackling linear stability problems of interfaces in converging flows is that introduced by Bell [4]. Bell's original and apparently under-exploited idea was to take advantage of potential flow theory both for the unperturbed and perturbed flows while allowing for the radial compression/expansion of a fluid. Hence Bell considered the unperturbed flow to be given by a potential, ϕ, satisfying a Poisson-type equation, *i.e.*, $\Delta\phi = -\dot{\rho}/\rho$, where ρ was taken to be uniform. Bell assumed the perturbed flow to be incompressible and irrotational. Through the classical procedure of boundary condition linearization followed by harmonic function decomposition, Bell obtained a second order differential equations for the modal perturbations of a free surface bounding a single fluid of uniform density.

Here we extend Bell's perturbation treatment to the case of an arbitrary number of concentric spherical shells of uniform densities. Hence, for each modal perturbation of a set of J concentric interfaces, we obtain a second order differential equation of the form:

$$M\ddot{a} + N\dot{a} + Pa = 0, \tag{2}$$

where $a = (a^j)$, $1 \leq j \leq J$, denotes the modal geometric perturbations of the different interfaces and M, N, P are tridiagonal matrices. The coefficients of these matrices depend on the laws of motion for the unperturbed interfaces as well as on the density time evolution within each fluid shell. Arbitrary laws for compression/expansion and exact interface coupling can thus be taken into account. Moreover, by means of piecewise constant approximation of continuous density profiles, linear stability prediction in stratified compressible fluids is accessible.

Equation (2) covers the particular cases of Mikaelian's equation for incompressible shells [5], Bell's cases of a single spherical free surface [4] and Fisher's extension of Bell's spherical result to the case of two fluids. For arbitrary, yet twice differentiable radius and density laws, equation (2) is integrated numerically from initial condition data. The overall simplicity of this differential equation allows for the use of standard but highly accurate numerical integration procedures. These procedures have been successfully tested against: (i) analytical solutions for two incompressible fluids [5], (ii) irrotational perturbation solutions for the homogeneous cumulative compression of a shell [8, 9]. In the latter case, the independence of the computed solution with respect to the continuous density profile approximations is confirmed. The treatment of rotational instabilities in stratified fluids is illustrated by initializing a "Chinese hat"-profile perturbation in a spherical shell subject to the above mentioned homogeneous cumulative compression: see Fig. 5. During the first half of the implosion duration, the perturbation radial

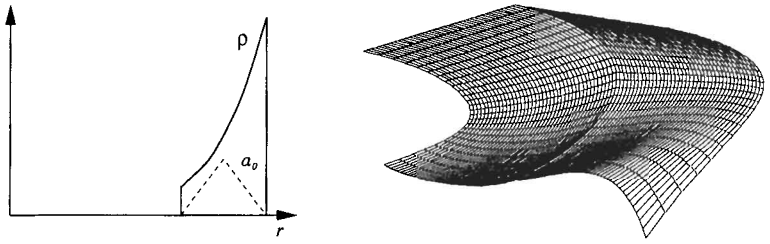

Figure 5. Initial density and perturbation profiles (left) and perturbation radial profile time-evolution (right) for the $l = 4$-mode.

profile evolves from its initial triangular shape towards the "S"-shape characteristic of the shell first rotational mode (Fig. 5—right). Later on, both inner and outer free-surface irrotational modes prevail as they are the most unstable modes.

More complex problems can be treated with the help of this multi-shell generalization of Bell's approach. In particular, demanding, yet realistic, test cases for computations of hydrodynamic instabilities—in their linear regime—with perturbation codes or fully two-/three-dimensional codes can be devised. Interface instabilities in complex systems or density-gradient originated instabilities in stratified fluids can also be studied in spherical geometry under the restriction of incompressible perturbations. Extending this approach to cylindrical and planar geometries should be equally worthy.

5. Conclusion

Linear perturbation growth of both converging shock waves in stratified fluids and interfaces in uniform-density fluid flows have been studied. For perturbed shock waves, results obtained with an extension of the CCW model and PANSY calculations reveal strong damping in PANSY amplitudes while phases agree even in the stratified cases. Incidence of acoustic-gravity waves in shock-induced flows is pointed out. Finally, incompressible perturbations in uniform-density fluid flows are handled by combining the works of Bell [4] and Mikaelian [5]. This multi-shell extension of Bell's original idea should be useful for studying realistic problems.

References

[1] Whitham GB, J. Fluid Mech., 4 (1958).
[2] Gardner JH, Book DL and Bernstein IB, J. Fluid Mech., 114, (1982).
[3] Evans A, Phys. Rev. E, 54, 5, (1996).
[4] Bell GI, Report LA-1321, Los Alamos Scientific Laboratory, (1951).
[5] Mikaelian KO, Phys. Rev. Letters, 65, 8, (1990).
[6] McCrory RL, Morse RL and Taggart K, Nuclear Sci. and Eng., 64, (1977).
[7] Scannapieco AJ, Phys. Fluids, 24, 9, (1981).
[8] Kidder RE, Nuclear Fusion, 16, 1, (1976).
[9] Book DL, Phys. Rev. Letters, 41, 22, (1978).
[10] Henderson DB, McCrory RL and Morse RL, Phys. Rev. Lett., 33, 205, (1974).
[11] Youssaf M, J. Fluid Mech., 66, 3, (1974).
[12] Toqué N, PhD Thesis, Université Paris 6, (1996).
[13] Fisher HN, Tech. Memorandum, Los Alamos National Laboratory, (1982).

Single Mode Richtmyer-Meshkov Instability: Experiment, Simulation and Theory

R.L. Holmes[1], G. Dimonte[2], B. Fryxell[3], M.L. Gittings[4], J.W. Grove[1,5], M.B. Schneider[2], D.H. Sharp[1], A. Velikovich[6], R.P. Weaver[1] and Q. Zhang[4]
[1]Los Alamos National Laboratory, Los Alamos, NM 87545, USA
[2]Lawrence Livermore National Laboratory, Livermore, CA 94551, USA
[3]Institute for Computational Science and Informatics, George Mason University
Fairfax, VA and Goddard Space Flight Center, NASA, Greenbelt, MD, USA
[4]Science Applications International Corporation, San Diego, CA, USA
[5]Department of Applied Mathematics and Statistics
University at Stony Brook, Stony Brook, NY, 11794-3600, USA
[6]Berkeley Research Associates, Alexandria, VA, 22501, USA

Abstract: Richtmyer-Meshkov instability has been the subject of considerable controversy due to the seeming disagreement between the predicted growth rates from numerical simulation, mathematical models and experiment, even in the simplest case of two-dimensional rectangular geometry. Here we attempt to resolve this disagreement by bringing together three methods of determining growth rates–experiment, simulation and theory–and applying them to the same problem under controlled conditions. We find substantial agreement between experiments, computation and mathematical models.

1. Introduction

Richtmyer-Meshkov instability (RMI) [12, 14] is generated when a shock wave refracts through the interface between two materials. Perturbations on the interface grow in size and cause the materials to mix.

Even in the simplest case of a plane shock hitting a sinusoidally perturbed interface experiments, numerical simulations and theoretical models have given conflicting values for the growth rate of the perturbations [2, 3, 4, 5, 12, 13, 14]. However, it was shown [9] that simulations can achieve good agreement with experiment as long as proper consideration is given to the effects of late-time nonlinearity in the evolution of the interface. In [11], simulations were performed for relevant experimental times that showed greatly improved agreement with experimental data while agreeing very well with previously published early time results. It was also show that at late times the perturbation growth rate decreases significantly due to nonlinear effects and the growth rates predicted by the linearized theories are too large.

We present here the results of simulations based on different codes and the results of different theories which are compared in a controlled way so that differences can be analyzed and understood. We find that experiments and simulations agree well and that the compressible nonlinear theory does a good job of predicting the time history of the perturbation growth rates.

The experimental data used is from previously published results using the Lawrence Livermore NOVA laser [6, 7]. The numerical simulations are performed using three different codes: the front tracking code FronTier, used in [9, 11], the PPM-based code PROMETHEUS [8],

More information - Email: holmes@novak.lanl.gov

and RAGE [1], an adaptive mesh code developed by Science Applications International (SAIC) for Los Alamos National Laboratory. The theoretical predictions are taken from the impulsive model of Richtmyer, the linear theory of RM instability for the case of reflected rarefaction wave formulated in [15], and a nonlinear theory for compressible fluids driven by a shock wave [16].

Ref. [10] contains a much larger study with a wide range of variations in initial amplitude and incident shock strength.

2. Comparison of experiment, simulation and theories

The experimental conditions and the justifications for the approximations used in the simulations and models are given in more detail in [10]. The configuration consists of a Mach 15.3 shock in beryllium plasma (unshocked density 1.7 g/cc) striking an interface between the beryllium and foam (density 0.12 g/cc). The pre-shock pressure of the foam is 0.1 Mbar. The beryllium and foam are modelled as perfect gases with polytropic exponents of 1.8 and 1.45, respectively. The interface between the beryllium and the foam is sinusoidally perturbed with a wavelength of 100 μm and an amplitude (zero-to-peak) of 10 μm. The simulations were run with grids fine enough that the growth rate was insensitive to further refinement. FronTier and PROMETHEUS used uniform grids with square cells of dimension 0.33 μm (300 zones per wavelength) and 0.208 μm (480 zones/wavelength), respectively, while the adaptive grid of RAGE used square cells of dimension 0.156 μm (640 zones/wavelength) at the finest level.

Figures 1(a) and (b) show perturbaton growth rates and amplitudes. We note excellent agreement among the results obtained from numerical simulations and experiment as well as good agreement with the analytical prediction of the compressible nonlinear theory. The compressible linear theory correctly predicts the growth rate of the instability at early times, but substantially overestimates the growth rate at intermediate and late times. The Impulsive Model and the compressible linear theory agree at later times.

Several interesting features of the growth rate merit discussion. First, the simulations show a very large spike in the growth rate at early times. This is due to the direct phase inversion [15] of the material interface during shock refraction, meaning that the velocity of the shocked contact is greater than that of the incident shock velocity resulting in a fully inverted interface by the time the refraction completes. The velocity spike occurs because, just prior to the end of the refraction, the shocked part of the contact has moved below the still unshocked outer edges of the interface. Thus, the lower part of the interface is separating from the upper part at a high velocity until the shock has accelerated the entire contact to approximately the same speed.

We also observe the very good agreement between the simulation results obtained with different codes. The small differences between PROMETHEUS and the other two methods are discussed below.

Included in Figure 1(a) is an experimental growth rate curve obtained by differentiating a sixth-order polynomial least-squares fit to the experimental data. Since this is a differentiated quantity and the source is rather noisy, we limit our interpretation of this curve to the observation that it reaches an early peak of 8.5 ± 1.5 μm/ns followed by a steep drop in the growth rate characteristic of the nonlinear predictions. We compare simulations and experiment further by presenting plots of density in Figure 2. While the simulations predict very similar growth rates the details of the interfaces are quite different. We note, for example, that at 1.4 ns PROMETHEUS is showing substantial grid-generated Kelvin-Helmholtz instability

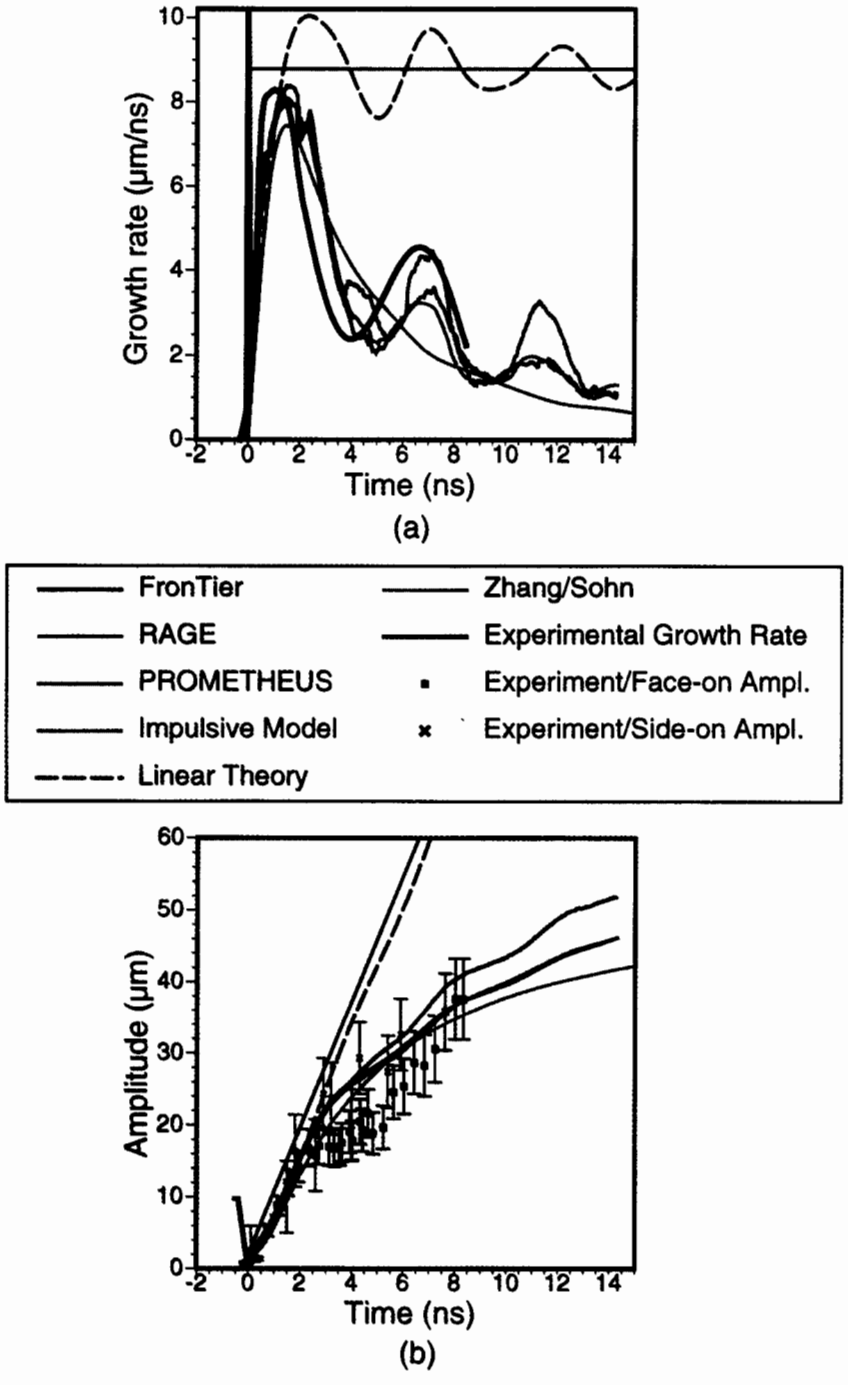

Figure 1. Experimental, simulation and theoretical perturbation growth for the Mach 15.3. $a_0 = 10\ \mu m$ case. Top figure: growth rate. Bottom figure: amplitude. Time $t = 0$ occurs when the refraction completes. The experimental growth rate curve is estimated to be accurate to within 1.5 μ/ns.

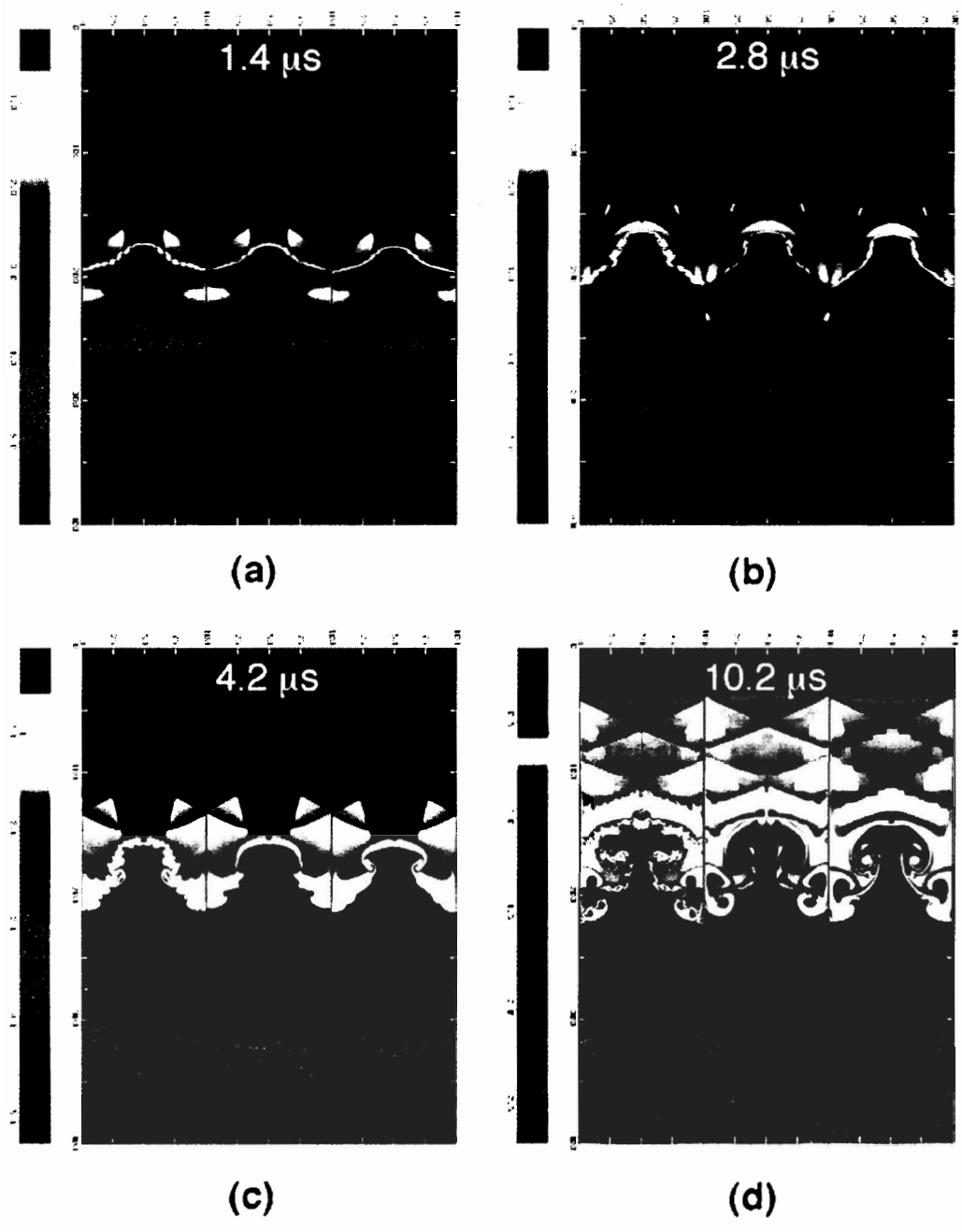

Figure 2. Density plots for the Mach 15.3, $a_0 = 10$ μm case for the three codes (PROMETHEUS, FronTier and RAGE, left-to-right). (a) t = 1.1 μs, (b) t = 2.8 μs, (c) t = 4.2 μs and (d) t = 10.2 μs.

which significantly affects the shape of the interface at later times. We believe that this is a numerical effect due, in part, to the low numerical diffusion of the PPM scheme at the interface. Kelvin-Helmholtz instability is also seen in the early time FronTier and RAGE calculations, but is much less prominent. This is for different reasons in the two codes. In FronTier the seeds of the instability are much smaller than in the other two codes since it uses a piece-wise linear curve to represent the initial conditions. In addition, the front tracking code FronTier periodically redistributes the points on the interface in order to reduce the clustering and spreading of the interface points and this will tend to suppress any very small wavelength instabilities. RAGE has somewhat more numerical diffusion at the interface than in PROMETHEUS so that the instability is washed out before it grows to significant size.

3. Conclusion

We have presented careful comparison studies of results from experiments, numerical simulations and theoretical predictions for unstable interfacial fluid mixing driven by shock waves. The numerical simulations were performed using three independent codes based on different numerical approaches. The physical parameters we used in our comparison study correspond to the NOVA experiments conducted at Lawrence Livermore National Laboratory. Good agreement is achieved among the results from three numerical methods and the simulations are in good agreement with the experimental results.

Acknowledgement. RLH, GD, MLG, JWG, DHS, MS and RPW were supported by the U.S. Department of Energy. RLH was also supported by a National Science Foundation Mathematical Sciences Postdoctoral Fellowship, while JWG received additional support from grants NSF DMS-9500568 and ARO DAA H04-95-10414. BF was supported by NASA Earth and Space Science High Performance Computing and Communications Program grant NAG5-2652. QZ was supported in part by the U.S. Department of Energy, contract DE-FG02-90ER25084, by subcontract from Oak Ridge National Laboratory (subcontract 38XSK964C) and by National Science Foundation contract NSF-DMS-9500568.

References

[1] Baltrusaitis RM, Gittings ML, Robert PW, Benjamin RF and Budzinski JM, Simulation of shock-generated instabilities, Physics of Fluids, 8, 9, (1996).

[2] Benjamin RF, Experimental observations of shock stability and shock induced turbulence, In W.P. Dannevik, A.C. Buckingham and C.E. Leith, editors, Advances in Compressible Turbulent Mixing, 341-348, National Technical Information Service, U.S. Department of Commerce, 5285 Port Royal Rd. Springfield VA 22161, (1992).

[3] Benjamin RF, Besnard D and Haas JF, Shock and reshock of an unstable interface, LANL report LA-UR 92-1185, NTIS #DE91014737, Los Alamos National Laboratory, (1993).

[4] Besnard D, Glimm J, Haas JF, Rauenzahn RM, Rupert V and Youngs D, Numerical simulation of 2D shock-tube multimaterial flow, In Proc. of Third International Workshop on The Physics of Compressible Turbulent Mixing at Royaumont France, (1991).

[5] Cloutman LD and Wehner MF, Numerical simulation of Richtmyer-Meshkov instabilities, Phys. Fluids A, 4, 1821-1830, (1992).

[6] Dimonte G, Frerking CE, Schneider M and Remington B, Richtmyer-Meshkov instability with strong radiatively driven shocks, Physics of Plasmas, 3, 2, 614-630, (1996).

[7] Dimonte G and Remington B, Richtmyer-Meshkov experiments on the nova laser at high compression, Phys. Rev. Lett., 70, 12, 1806-1809, (1993).

[8] Fryxell B, Müller E and Arnett D, Hydrodynamics and nuclear burning, Report No. 449,

Max-Planck-Institut für Astrophysik, (1989).

[9] Grove J, Holmes R, Sharp DH, Yang Y and Zhang Q, Quantitative theory of Richtmyer-Meshkov instability, Phys. Rev. Lett., 71, 21, 3473-3476, (1993).

[10] Holmes RL, Dimonte G, Fryxell B, Gittings M, Grove JW, Schneider M, Sharp DH, Velikovich A, Weaver RP and Zhang Q, Richtmyer-meshkov instability growth: Experiment, simulation and theory, Technical Report LA-UR-97-2606, Los Alamos National Laboratory, (1997).

[11] Holmes RL, Grove JW and Sharp DH, Numerical investigation of Richtmyer-Meshkov instability using front tracking, J. Fluid Mech., 301, 51-64, (1995).

[12] Meshkov EE, Instability of a shock wave accelerated interface between two gases, NASA Tech. Trans., F-13, 074, (1970).

[13] Meyer KA and Blewett PJ, Numerical investigation of the stability of a shock-accelerated interface between two fluids, Phys. Fluids, 15, 753-759, (1972).

[14] Richtmyer RD, Taylor instability in shock acceleration of compressible fluids, Comm. Pure Appl. Math., 13, 297-319, (1960).

[15] Yang Y, Zhang Q and Sharp DH, Small amplitude theory of Richtmyer-Meshkov instability, Phys. Fluids, 6, 5, 1856-1873, (1994).

[16] Zhang Q and Sohn S, An analytical nonlinear theory of Richtmyer-Meshkov instability, Phys. Lett. A, 212, 149, (1996).

Hydrodynamic Instabilities Research at VNIIEF; Past, Current and Future

R.I. Il'kaev, E.E. Meshkov and V.V. Nikiforov
Russian Federal Nuclear Centre - Institute of Experimental Physics
Prospect Mira 37, 607190, Sarov, Nizhny Novgorod Region, Russia

1. 1940 - 50 Years

1946 - founded the VNIIEF Institute

1.1. Calculation and theory

In the late '40s - early '50s, a series of unpublished studies by **S.Z. Belenky** (in part, jointly with **E.S. Fradkin**) looked analytically at many aspects of Rayleigh - Taylor instability **(Rayleigh (1883), Taylor (1950))** and turbulent mixing at unstable interface. Some findings of these studies would be reported later in ***(Belenky, Fradkin* (1965))**. **A.D. Sakharov** was involved with the stability problem of convergent spherical incompressible shell (his work summarized in **Vakhrameev (1995)**).

1.2. Experiment

On **A.D. Sakharov's** initiative in 1951, **Yu.F. Alexeev, I.G. Proskurin** and **N.F. Zelentcova** performed first, though not openly reported, experiments looking into the dynamics of a turbulent mixing zone at the liquid-liquid interface, their geometry similar to the later described by **Linden** and **Redondo (1991)** (heavier (above) and lighter (below) liquids separated by a horizontal plate pulled out initially at the experiment). Also, a technique analogous to the reported by **Lewis(1950)** was used (a liquid-containing vessel driven downwards with a higher than gravity acceleration).

2. 1960 Years

2.1. Theory

In the late '50s - early '60s, analytical solutions were developed at VNIIEF to some specific cases with the perturbations growth for shock waves and shock-accelerated interface **(R.M. Zeidel (1960, 1972)** and **Yu. Nikolaev (1965))**.

2.2. Numerical methods

The early '60s was a 1D numerical ***method MV*** developed, that would allow a linear-approximated calculation of shock-wave and interface perturbations in a broad range of applications **(G.A. Grishina (1980))**. Since the late '60s, ***2D numerical calculations*** have been developed at VNIIEF for initial perturbations growing at the unstable interface until

More information - Email: otd03_2305@spd.vniief.ru

their turbulization: **SIGMA (Batalova *et al.* (1969))** and **DMK (Sofronov, Rasskazova, Nesterenko(1985))**.

2.3. Experiment

Starting in the mid-'60s, there have been experimental research developed in shock-induced instability area ***(Richtmyer (1960))***.

VNIIEF developed later in the '60s an ***experimental technique for this instability, which employed a shock tube and thin-film gas models*** (Meshkov (1969)).

Experiments were carried out for initial perturbations growth of a shock-accelerated gas-gas interface and the associated effects (refs.: **Meshkov (1981), Meshkov (1992), Andronov *et al.* (1994)**).

3. 1970 Years

Earlier in the '70s, the shock-tube technique served the basis to start ***systematic studies into turbulent mixing at the shock-accelerated interface*** (**Andronov *et al.* (1976), Andronov *et al.* (1982), Meshkov, Nikiforov, Tolshmyakov (1990)**).

Concurrently, a technique had been developed to investigate the initial perturbations growth and turbulent mixing at the ***gas-gas interface accelerated by a convergent cylindrical shock wave*** generated by electric explosion (**Andronov *et al.* (1982), Tolshmyakov and Meshkov (1989)**).

3.1. Numerical methods

In the mid-'70s, ***semi-empirical model*** developments were started for 1D hydrodynamic flow calculations ***involving turbulent mixing***. These developments resulted in a range of methods from simple models such as k-ϵ (**Andronov *et al.* (1976)**) to well sophisticated ones (**Andronov *et al.* (1982), Nikiforov (1985), Andronov *et al.* (1994)**).

4. 1980 Years

4.1. Experiment

As suggested by **Meshkov** and **Rogachov** in the late '70s, VNIIEF started developing an ***experimental technique for unsteady hydrodynamic flows that used jellies*** (**Volchenko *et al.* (1983)**).

This technique can significantly extend experimental capabilities in RT-instability research (**Volchenko *et al.* (1989)), Zhidov *et al.* (1990), Rogachov *et al.* (1991)**). In particular, it can allow looking into RT-instability phenomena at the gas-liquid interface not only in a plane but also in a more complex geometry (e.g., cylindrical (**Meshkov *et al.* (1993,1995), Kamchibekov *et al.* (1997)** and even spherical (**Meshkov, Nevmerzhitsky and Zmushko(1997)**).

4.2. Numerical methods

In the '80s developments were continued at VNIIEF more extensively on the 2D numerical codes for initial perturbations growth at unstable interface: **DMK (Sofronov, Rasskazova, Nesterenko (1985), MIMOZA (Sofronov *et al.* (1989) and EGAK (Yanilkin et al (1993)).**

5. 1990 Years (I)

In the '90s, basic research into hydrodynamic instability problems made a substantial advance at VNIIEF as one of its ***defense-technology conversion programs***. Contributions to this development are the projects under contracts with LANL, US (1994) (**Andronov *et al.* (1994)**), CEA/DAM France (1994) (**Meshkov, Nevmerzhitsky *et al.* (1995)**, LLNL, US (1995) (**Bakhrakh *et al.* (1996)**) and the ISTC Project 029 (**Meshkov (1995), Bashurin *et al.* (1995)**).

5.1. Experiment

In the early '90s, a technique was developed ***based on compressed gas-accelerated liquid layers*** (**Meshkov and Nevmerzhitsky (1991), Nevmerzhitsky *et al.* (1993)**).

With this technique, investigations could be started into the turbulent mixing (TM) effects on basic flow dynamics and energy cumulation phenomena in laminated systems (**Zhidov *et al.* (1996)**).

A technique was suggested and then came to be developed ***which used gas models driven by gaseous explosive mixture*** (**Meshkov (1995)**).

The technique offers new opportunities for looking at hydrodynamic instabilities at the gas-gas interface with complex flows in plane, cylindrical and spherical geometries (a combination of the alternating and shock-wave accelerations; rapid Atwood number change, even to the opposite; 3D perturbation + TM).

Development was suggested and has been since successfully continuing on ***multi-beam laser interferometric tomography*** (**Bashurin *et al.* (1995)**).

This technique is what can help reconstruct the density distribution in 3D turbulent mixing zone of two gases to look into its structure.

More extensive developments have been conducted since the mid - '80s in ***research techniques for instability evolutions in solid media*** (**Lebedev *et al.* (1993), Lebedev (1996)**).

6. 1990 Years (II)

6.1. Numerical methods

In the '90s, VNIIEF made advances in the development of 2D codes for numerical calculations with the account of turbulent mixing at unstable interface: **EGAK-T** and **EGAK-V**

(Yanilkin, Nikiforov, Zharova (1994)).

In the '90s, VNIIEF embarked on development of 3D codes to calculate on initial perturbations growth at unstable interface: **TREK** package **(Stadnik, Shanin, Yanilkin (1994)).**

6.2. Prospects for future research into hydrodynamic instabilities and turbulent mixing problems (TMZ)

The problem is very complicated and offers many challenges yet to be met. In the ***basic research*** area, these challenges may be

- initial perturbations (sources of initial perturbations, their contribution to the instability and TMZ growth pattern);
- interference of initial perturbation modes at the instability transition stage;
- local perturbations;
- updated constants in phenomenological turbulent mixing theories;
- TMZ development in conjunction with large-scale perturbations
- TMZ structure
- turbulent mixing development in non-1D flows
- the various effects (strength, viscosity, surface tension) on hydrodynamic instabilities and turbulent mixing development
- turbulent mixing development with complex flow patterns (alternating accelerations, shock waves).

6.3. Applications

Research of hydrodynamic instabilities and turbulent mixing may be very important for many applications.

1. Primarily, it is ***inertial confinement fusion (ICF)***. Hydrodynamic instabilities are one of the critical bottlenecks in the implementation of fusion ignition.

2. More and more important is investigation into combustion problems, specifically in relation to:

- ***fire and explosion safety***
- ***forest fires***, fighting them by shock-wave technology.

These cases are all which need a study into the stability and turbulization of flame front being essentially a diffused interface. To simulate such cases, a complex 3D flow has to be calculated allowing for the flame front and environment turbulization.

3. Alongside the interface stabilization and mixing suppression applications, there may be a reverse case with ***enhanced mixing of two substances*** at the interface. This may, specifically, occur with disposition of nuclear reactor waste (by underground nuclear explosions).

4. There are a lot of opportunities for hydrodynamic instability research applied to ***astrophysics, oceanography and physics of atmosphere***.

6.4. Hydrodynamic Instability Research and Technology Conversion Problem

Basic science in the area of hydrodynamic instabilities and turbulent mixing is among the conversion-related programs at the Russian Nuclear Centers.

These research call for well-concerted efforts by both numerous experimentalists, theorists and mathematicians. The problem being complex and profound will need steady advance in the development and improvement of both experiments and numerical studies. Again, these research do not require too many expenses.

Hydrodynamic instabilities and turbulent mixing are the area of research likely to be attractive to junior researchers as a challenging and exciting experience for them to mature professionally and prove their competency. International interactions in this area offer another attractive opportunity for them.

About 3D Single-Mode Evolution and About Compressible Turbulence

N.A. Inogamov
Landau Institute for Theoretical Physics, 117940, Moscow, Russia

1. Single-mode 3D evolution

Let a 2D perturbation is $\eta(x, t = 0) \propto \cos kx$, $\varphi(x, z, t = 0) \propto \cos kx \exp(-k|z|)$. Then shapes of bubbles and jets are the same during a linear (symmetric) stage. Let a ratio $\mu = \rho_l/\rho_h = 0$. In a nonlinear stage the flow becomes asymmetric: wide bubbles and narrow jets.

Evolution of 3D RT and RM bubbles and jets is shown in Figs.1–3. Let an initial perturbation is $\eta(x, y, t = 0) \propto \cos kx + \cos ky$, $\varphi(x, y, z, t = 0) \propto (\cos kx + \cos ky)e^{-k|z|}$. A linear stage again is symmetric in this case. White and black circles in Fig. 1 (a) are apex points of bubbles and jets. The intersection of jets by the plane $z = 0$ is shown in Fig. 1 (b) (dashed regions). In the dashed regions $z = \eta(x, y, t) < 0$. Bubbles become wider and jets narrower in a nonlinear stage (asymmetric stage). A steady–state or asymptotic stage of 3D RTI has been considered in 1. A simulation of evolution have been performed in 2. The period of this 3D perturbation is the square $\lambda \times \lambda$, $\lambda = 2\pi/k$. Increments are the same in 2D and 3D cases.

Narrowing of jets leads to a deformation of the dashed squares shown in Fig. 1 (b). Wall

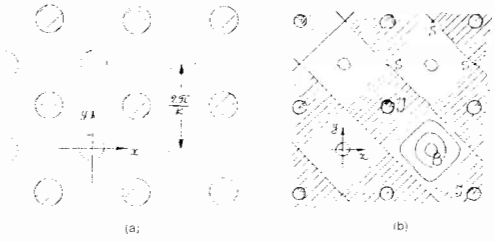

Figure 1.

type jets which separate bubbles appear. The intersection of these jets by the plane $z = 0$ is shown in Fig. 2 (a) by square dashing. The dashed region is $z = \eta(x, y, t) < 0$. The region $z = \eta(x, y, t) < 0$ taken from the symmetric stage is also shown here by the fine dashed straights. Straight walls intersect at right angles. Points of intersections are the apex points of jets.

Bubbles B and jets J were isolated at the symmetric stage. Bubbles remain isolated at the asymmetric stage. At the same time a structure of jets is changed qualitatively. Let the points S in Fig. 1 (b) are saddle points of a surface $z = \eta(x, y, t)$. The separatrixes S–S intersect at right angles at the symmetric stage. They form sides of the dashed squares in Fig. 1 (b). They are zero levels $\eta_S = \eta(x, y, t) = 0$ at the symmetric stage. The system of the positive level curves $\eta(x, y, t) = const$ are shown in Fig. 1 (b). They are closed around the apex of the bubble B.

More information - Email: nail@landau.ac.ru

The saddles drop down as the degree of asymmetry rises. They drop under the zero level – their $z-$coordinate η_S becomes negative ($\eta_S < 0$). The separatrixes are at the same level as the saddles. The angle of intersection of the separatrixes decreases. The shape of the separatrixes at an asymmetric stage is shown in Fig. 2 (b). The point J is the apex of jet. It is below the separatrix level. Let η_J is a $z-$coordinate of this apex. At a symmetric stage we have $\eta_J < 0$, $\eta_S = 0$. At an asymmetric stage we have $\eta_J < \eta_S < 0$. The level $\eta = 0$ at this stage is shown by dashed line in Fig. 2 (b). It bounds the square dashing in Fig. 2 (a). For RTI case $|\eta_S/\eta_J| \to 1$ at $t \to \infty$.

A flow started from 3D initial data presented above is a flow in the tube. The smallest tube is the three cornered tube JBS in Fig. 2 (b). We can combine square tubes BBBB or JJJJ from these tubes. In the corners of the BBBB tube are bubbles and JJJJ tube - jets. There is the bubble in the centrum of the tube JJJJ. It is isolated from other bubbles by the liquid layers moving along the walls of the square tube. Evolution in cases of RT or RM instabilities are

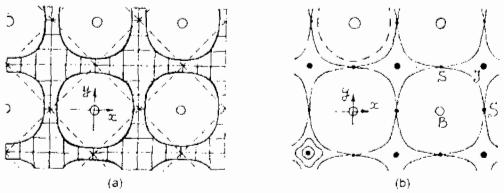

Figure 2.

shown in Fig. 3 ($\mu = 0$). The boundaries are plotted in the frame connected with the bubble apex point B. The strips between the parallel dashed straights are the walls of the smallest three-cornered tube JBS. The numbers enumerate moments $t_1 < t_2 < t_3 < t_4$, $t_4 = \infty$. The moment t_1 corresponds to the symmetric stage.

The lines of the boundary in the strips going through neighbouring apexes of the bubbles and the saddle B–S–B (a) and neighbouring apexes of the jets and the saddle J–S–J (b) in the moments 1 and 2 are shown in Figs. 3 (a) and (b). The boundary is $\Delta\eta = -(\Delta x)^2/2R_x - (\Delta y)^2/2R_y$ near the saddle S. Here $R_x > 0$ and $R_y < 0$ measure a curvature. At the asymptotic stage we have $R_x > |R_y|$. At the symmetric stage we have $R_x = |R_y| \propto 1/|\delta\eta|$. The expansions of the boundary near the apexes of bubble and jet are $\Delta\eta = -[(\Delta x)^2 + (\Delta y)^2]/2R_B$, $R_B > 0$ and $\Delta\eta = -[(\Delta x)^2 + (\Delta y)^2]/2R_J$, $R_J < 0$ respectively.

2. The case of small Atwood numbers

Let's consider 3D RMI in the case $\mu = 1 - \varepsilon$, $\varepsilon \to 0$. The simplest perturbation has a symmetry of a square lattice. There are symmetric $z = \eta(x, y, t) \approx vt(\cos kx + \cos ky)$, transitional and asymptotic stages of evolution. The solution has to be periodic. We will consider an advection of boundary near the apex point of bubble at the last stage. At this stage in this region a vorticity is small and flow is approximately potential. Velocity has to decrease when $|y|$ rises. The most important are harmonics which decrease slow at large $|y|$. They give the largest contribution into velocity field near the apex. Asymptoticaly a steady–state vortex structure and steady–state velocity field form. The potential at large distance $k|z| \gg 1$ is $\varphi = -\frac{\alpha v}{k}(\cos kx + \cos ky)\exp(-kz)$, $\alpha \sim 1$. A substitution $X = (x + y)/\sqrt{2}$, $Y = (x - y)/\sqrt{2}$ changes this potential to $\varphi = -(2\alpha v/k)\cos(kX/\sqrt{2})\cos(kY/\sqrt{2})\exp(-kz)$. This substitution

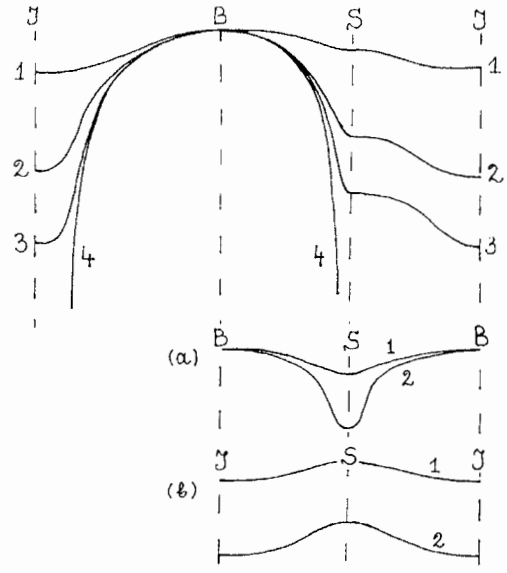

Figure 3.

conserves Laplacian $\partial^2/\partial x^2 + \partial^2/\partial y^2 + \partial^2/\partial z^2 = \partial^2/\partial X^2 + \partial^2/\partial Y^2 + \partial^2/\partial z^2$.

The boundary near the apex B is a cup. It is a round cup due to symmetry $x \leftrightarrow y$. This means that both curvatures are the same. We can use plane curves in planes $y = 0$ or $Y = 0$ to find the curvature $1/R_B$. Let's consider the plane $Y = 0$. Eqs. of an advection of a mass point in this plane are

$$dX/dt = \partial\varphi/\partial X = (1/\sqrt{2})\sin(X/\sqrt{2})\,e^{-z}, \qquad dz/dt = \partial\varphi/\partial z = \cos(X/\sqrt{2})\,e^{-z}. \tag{1}$$

Here $k = v = 1$. We have omitted insignificant factors.

Let's substitute $\xi = e^z$. Eqs. (1) are steady–state. Therefore we can write $d\xi/2\xi = d\sin(X/\sqrt{2})/\sin(X/\sqrt{2})$. The integral of this eq. is $\xi/\xi_0 = [\sin(X/\sqrt{2})/\sin(X_0/\sqrt{2})]^2$. We use this integral to eliminate ξ in the first of eqs. (1). We obtain

$$\cos(X/\sqrt{2}) - \cos(X_0/\sqrt{2}) = -t\,[\sin(X_0/\sqrt{2})]^2/2\xi_0. \tag{2}$$

after integration of it. We chose $t_0 = 0$ in (2).

Let's substitute $\cos(X/\sqrt{2})$ from (2) into the second of eqs. (1). After integration we obtain

$$\xi = \xi_0 + C_0 t - t^2\,(1 - C_0^2)/4y_0, \qquad C_0 = \cos(X_0/\sqrt{2}). \tag{3}$$

Let's eliminate X_0 from eqs. (2), (3). We find C_0 from eq. (2). The right root has a sign plus. It is $C_0 = -q + \sqrt{q^2 + 2qC + 1}$, $q = \xi_0/t$, $C = \cos(X/\sqrt{2})$. Let's substitute this root into (3). After that we obtain eq. of advection of the curve $\xi = \eta(X, t; \xi_0)$ or $z = \eta(X, t; z_0)$.

It is $\xi = K - [t^2 - (K - \xi_0)^2]/4\xi_0$, $K = \sqrt{\xi_0^2 + 2\xi_0 C\, t + t^2}$. After expansion of this eq. for small $1/t$ and X we obtain $\xi = t + tX^2/8$ or $z = \ln t + X^2/8$. ¿From this eq. we obtain that the asymptotic velocity and curvature are $v_B = 1/kt$, $R_B = 4/k$. In 2D for $\mu = 1 - 0$ we have $v_B = 1/kt$, $R_B = 3/k$.

3. 3D generalization of the Layser model

The convenient *plane* representation of the Layzer model 3, 4 has been derived in 5. Here we generalize it from 2D to 3D case. Near the apex B for a square lattice we have

$$N = \eta_0 - K\frac{X^2 + Y^2}{2}, \qquad \varphi = A\cos\frac{X}{\sqrt{2}}\cos\frac{Y}{\sqrt{2}}\exp(-z + \eta_0). \tag{4,5}$$

¿From (4), (5) we have at the curve in the plane $Y = 0$ $\varphi_t|_N = (\dot{A} + \dot{\eta}_0 A)(1 - X^2/4 + K\,X^2/2)$, $\varphi_X|_N = -AX/2$, $\varphi_z|_N = -A(1 - X^2/4 + K\,X^2/2)$, $N_t = \dot{\eta}_0 - \dot{K}X^2/2$, $N_X = -KX$.

Well known boundary conditions are $N_t = \varphi_z|_N - N_X\varphi_X|_N - N_Y\varphi_Y|_N$, $\quad \varphi_t|_N + v^2/2|_N + |g|N = 0$ in the case $\mu = 0$. ¿From them we obtain $\dot{\eta}_0 = -A$,

$$\dot{K} = A(2K - 1/2), \qquad \dot{A}(K - 1/2) = |g|K - A^2/4. \tag{6,7}$$

After eliminating of t from eqs. (6) and (7) we obtain simple *plane* differential eq.

$$AdA/dK = (A^2 - 4gK)/(1 - 2K)(4K - 1). \tag{8}$$

Eq. (8) is similar to eq. $A\frac{dA}{dK} = \frac{A^2 - gK}{(1-K)(3K-1)}$ for 2D case 5.

Eq. (8) describes 3D standing waves ($g = -1$), RT ($g = 1$) and RM ($g = 0$) instabilities. In RT case there is a singular point $A^2 = 1$, $K = 1/4$ or $v_B = \sqrt{g/k}$, $kR_B = 4$ (similar to well-known point $v_B = \sqrt{g/3k}$, $kR_B = 3$ in 2D) which attracts trajectories $A(K)$ of eq. (8).

In RM case $g = 0$ and eq. (8) can be integrated easily. A general solution of system of eqs. (6), (7) is

$$\sqrt{\frac{1-2K}{1-4K}} - 1 - \frac{\ln\frac{\sqrt{2(1-2K)}+\sqrt{1-4K}}{\sqrt{2}+1}}{\sqrt{2}} = -A_0 t, \quad \frac{A_0}{A} - 1 + \frac{\ln\left(\frac{\sqrt{2}+1}{\sqrt{2}-1}\frac{\sqrt{2}A_0 - A}{\sqrt{2}A_0 + A}\right)}{2\sqrt{2}} = -A_0 t. \tag{9,10}$$

Expressions (9), (10) give evolution of curvature ($R = 1/K$) and velocity ($v_B = -A$) of 3D RM bubble. At $t \to \infty$ eqs. (9), (10) give $v_B \to 1/kt$, $kR_B \to 4$. In 2D we have $v_B \to (2/3)/kt$, $kR_B \to 3$ 4, 5. We see that 3D square lattice bubbles $\lambda \times \lambda$ are faster (compare $1/kt$ and $(2/3)/kt$ for RMI and $\sqrt{g/k}$ and $\sqrt{g/3k}$ for RTI) and have smaller curvature than 2D bubbles with the same period λ.

4. Exact self-similar compressible mixing

A linear (spectral) consideration of power law (polytropic) density profiles $\rho(y) \propto 1/(-y)^M$, $y < 0$, $M > 0$, $\rho(y) \equiv 0$, $y > 0$ has been done in 6. These profiles approximate density distributions in ICF multilayer shells. In these shells densities of internal subshells are higher than densities of external subshells.

Compressibility introduces scale (a height of homogeneous atmosphere $h \sim c^2/g$) and therefore turbulence in compressible media usually loses its self-similarity. The only exclusion is

the polytropic case. In this case the height h is $\propto (-y)$ and therefore the problem remains its spatial invariance and hence its exact self-similarity.

Let's consider first the polytropic incompressible case with an adiabatic exponent $\gamma = \infty$. In a mixing length model 7, 8 we have eq. $\frac{\partial \rho}{\partial t} = \frac{\partial}{\partial y}\left(D_T \frac{\partial \rho}{\partial y}\right)$, which describes turbulent diffusion of density. In this eq. ρ is density averaged on x, $D_T = l_T v_T$, $l_T = \alpha g t^2$, $v_T = \sqrt{\left(l_T \frac{\partial \ln \rho}{\partial y}\right)(|g| l_T)}$, $\alpha \sim 1$, $D_T = l_T v_T$ if $\partial\rho/\partial y > 0$ and $D_T = 0$ if $\partial\rho/\partial y < 0$, $l_T(\partial \ln \rho/\partial y)$ is a relative density variation at scale l_T and $\sqrt{|g| l_T}$ is free fall velocity from a height l_T.

Let's show that diffusion eq. has a self-similar solution in the polytropic case. Previously a self-similar solution has been known only for the case of a density jump 7. Let's write $\rho(y,t) = R(\xi)/t^{2M}$, $\xi = -y/gt^2$. The function $R(\xi)$ must be so that $R(\xi) \propto 1/(\xi)^M$ at $\xi \to \infty$. This gives us a right tail at large ξ.

We substitute $\rho = R/t^{2M}$ into diffusion eq. and obtain

$$\frac{3}{2}\sqrt{\frac{\xi}{R}}\sqrt{-\xi R'}(\xi R'' + R') + \frac{\sqrt{\xi}}{2R^{3/2}} R'(-\xi R')^{3/2} - \frac{(-\xi R')^{3/2}}{2\sqrt{\xi R}} = -2MR - 2\xi R'. \qquad (11)$$

A substitution $z = -\frac{d \ln R}{d \ln \xi}$ decreases an order of eq. (11). Eq. (11) becomes

$$\frac{dz}{d\xi} = \frac{-2z^{5/2} - z^{3/2} + 4\sqrt{\xi}(M - z)}{3\xi\sqrt{z}}. \qquad (12)$$

An isocline I of zeroes $\sqrt{\xi} = -(2z^{5/2} + z^{3/2})/4(z - M)$ is shown in Fig. 4 (a). All trajectories T of eq. (12) finish in singular point M ($\xi = \infty, z = M$). Therefore they all have the right asymptotic $z \to M$ at $\xi \to \infty$. At the isocline density distributions $R(\xi)$ have maximums. One of them is marked in Figs. 4 (a, b) by point A. Trajectories under the isocline have density distributions M rising with y, see Fig. 4 (b). They are physical trajectories. We see that (i) the mixing is self-similar, the thickness of the mixed zone rises $\propto gt^2$ and (ii) the layer of high density near the boundary $y = 0$ is spreaded. We obtain the simplest compressible model valid

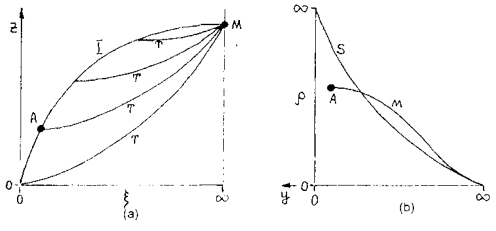

Figure 4.

for arbitrary adiabatic exponents if we change average ρ in diffusion eq. to inverse average entropy $1/s$. A hydrostatic distribution of $1/s \propto 1/(-y)^{M(\gamma-1)+1}$ is similar to a distribution of ρ. A turbulent velocity is $v_T = \sqrt{(l_T \partial \ln(1/s)/\partial y)(|g| l_T)}$. The only difference is a change of M to $M(\gamma - 1) + 1$. Therefore results concerning self-similarity of mixing and spreading of singularity of $1/s$ in $y = 0$ remain in compressible case.

Acknowledgement. This work is supported by the RBRF (Russian Basic Research Foundation) 95-02-06381-a.

References

[1] Inogamov NA, Abarzhi SI, Dynamics of fluid surface in multidimension, Physica D, 87, 339-341, (1995); Abarzhi SI, Inogamov NA, Steady-state solutions of 3D RTI..., JETP, 80, 132-143, (1995).

[2] Marinak MM, Haan SW, Tipton RE, Weber SV, Remington BA, Three-dimensional simulation..., Inertial Confinement Fusion, 5, 3, 168-178, (1995).

[3] Layzer D, On the gravitational instability..., Astrophys. J., 122, 1, (1955).

[4] Kull HJ, Nonlinear free-surface RTI, Phys. Rev. A, 33, 1957, (1986); Hecht J, Alon U, Shvarts D, Potential flow model of RT and RM bubble fronts, Phys. Fluids, 6, 4019-4030, (1994).

[5] Inogamov NA, Singular mixing in stars, Astronomy Lett., 20, 651-657, (1994); Steepening and collapse..., JETP, 80, 890-906, (1995); Many-dimensional periodicity and turbulence of RT and RM instabilities, Laser and Particle Beams, 15, 1, (1997).

[6] Inogamov NA, Reduction of increment of RTI in specially designed multilayer ICF targets, Phys. Rev. E, (1997), (to be published).

[7] Belen'kii SZ, Fradkin ES, Theory of turbulent mixing, Trudi FIAN, 29, 207-233, (1965).

[8] Neuvazhaev VE, Self–similar problems of turbulent mixing..., Prikladnaya Mekhanika i Tekhnicheskaya Fizika, 6, 82-90, (1976); Meshkov EE, Nikiforov VV, Tolshmyakov AI, About the structure of turbulent mixing layer..., 2nd International Exchange on RM and RT mixing, Pleasanton, California, October 1989, V. Rupert ed., (1990); Bonnet M, Gauthier S, A $k-\varepsilon$ model..., Phys. Fluids A, 2, 1685, (1990); Haas JF, Galametz I, Houas L, Jourdan G, Rodriguez G, Experiences en tube a chocs, Chocs, 14, 15-26, (1995); Besnard D, Melanges et turbulence, Chocs, 14, 5-14, (1995).

PLIF Flow Visualization of Single- and Multi-Mode Incompressible Richtmyer-Meshkov Instability

J.W. Jacobs and C.E. Niederhaus
Department of Aerospace and Mechanical Engineering
University of Arizona, Tucson, AZ 85721, USA

Abstract: Experiments to investigate incompressible Richtmyer-Meshkov instability have been carried out utilizing a novel experimental apparatus in which an impulsive acceleration is given to a system of two miscible liquids by bouncing it off of a fixed spring. A sinusoidal (single-mode) initial perturbation is generated by sinusoidally oscillating the container in the lateral direction. In addition, multi-mode perturbations are generated by more complex oscillation profiles. Planar laser induced fluorescence is utilized to visualize the instability, providing very clear views of the interface far into the nonlinear regime.

1. Introduction

Richtmyer-Meshkov (RM) instability is a very fundamental fluid instability which is of importance to the fields of astrophysics, inertial confinement fusion and combustion. Yet there is a scarcity of well visualized experimental results. Probably the biggest reason for this deficiency is that RM experiments are typically carried out in shock tubes [1, 2] in which the generation of a sharp well controlled interface between gases is extremely difficult. Recently, we have reported new incompressible experiments in which much clearer views of the instability are obtained by using an impulsively accelerated system of liquids [3, 4]. The use of liquids allows for the generation of very sharp, well defined interfaces. In addition, the relatively low evolution rate of this experiment significantly relaxes image acquisition requirements. The results presented here represent an extension of this earlier work in which Planar Laser Induced Fluorescence (PLIF) has been implemented to provide significantly improved visualization of the unstable interface. In addition, the initial perturbation generation system has been improved to allow for the generation of multi-mode initial interface shapes.

2. Experimental description

The experimental apparatus (figure 1) consists of a thin rectangular tank measuring 2.54 cm × 11.75 cm × 25.4 cm which is mounted to a vertical linear rail system oriented so that the tank is free to move in the vertical direction with approximately 1 m of travel. The bottom half of the tank is initially filled with a dyed salt solution ($Ca(NO_3)_2 + H_2O$) and the top half with a water/alcohol mixture yielding an Atwood number (the difference of the densities divided by their sum) of approximately 0.15. In the earlier experiments [3, 4] the rails were mounted so that they pivoted about a point at their upper end, and an initial shape was given to the fluid interface by sinusoidally oscillating the rail system in the horizontal direction to produce standing waves. In the present experiments the rails have been rigidly mounted, and the tank itself is allowed to move relative to the rails by mounting it using a set of crossed roller bearings. The tank is then oscillated using a computer controlled linear stepper motor which allows for the generation of arbitrary oscillation waveforms. The tank is released from an initial height,

More information - Email: jwjacobs@u.arizona.edu

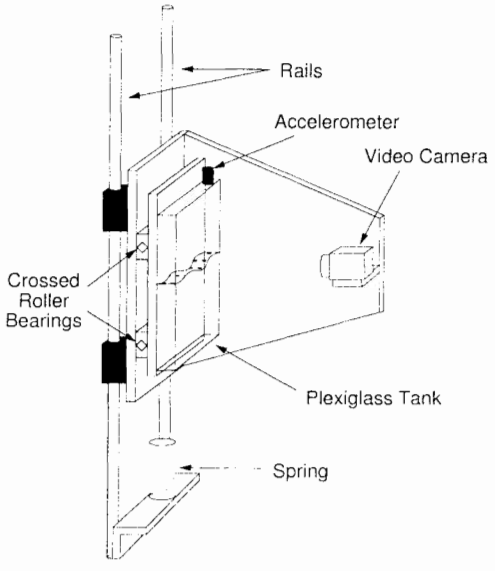

Figure 1. The experimental apparatus.

allowing it to fall and bounce off of a fixed coil spring that is mounted to the end of the translator, which generates an impulsive acceleration. After it bounces, the system travels upward and downward again before bouncing a second time. The heavy fluid is made visible by seeding it with a fluorescent dye (fluorescein) and illuminating it with a sheet of laser light (argon ion) which passes through the top of the container. The fluorescent dye is then viewed by a shuttered CCD camera which is mounted to the moving container. The video output from the camera is digitized and stored by a computer system with a frame grabber.

3. Results

Figure 2 is a sequence of PLIF images showing the evolution of the instability as viewed by the video camera. Each image is marked with a frame number (each frame increment corresponds to a 1/60 s time increment). Note that this and the following sequences are not uniformly spaced in time. Frame 0 was taken immediately before the container contacts the spring. Thus, it represents the initial interface shape. Frames 5–40 span the period of free fall between the first two bounces, while frames 41–43 were taken during and after the second bounce. The impulsive acceleration in these experiments is directed from the heavier fluid into the lighter fluid, causing the initial perturbation to invert before growing. Immediately after inversion, the instability retains a sinusoidal shape. However, with time, vortices begin to form at points midway between the crests and troughs, producing the mushroom pattern typical of the RM instability of fluids with small or moderate density differences. As time advances, these vortices grow in size as they roll the interface around their centers to form a spiral pattern. Note that, characteristic of the instability with small density differences, the interface shape retains its top-to-bottom symmetry well into the nonlinear regime. The container bounces a second time, and thus receives a second acceleration beginning at a point between frames 40 and 41. In frames 42 and 43, one can see a dramatic change in the interfacial pattern in which

the mushroom features rapidly collapse and erupt into turbulence. Close examination of these images reveals the classical patterns exhibited by Kelvin-Helmholtz instability, thus suggesting that this mechanism is the cause of the rapid transition to turbulence.

As was mentioned above, the present apparatus has the capability of generating arbitrary lateral tank motion. The single-mode perturbation utilized in the experiments described above was generated with a sinusoidal oscillation. However, the current system has the capability of generating oscillatory motion of arbitrary waveform; thus multi-mode perturbations are easily achievable. The asymmetric type of forcing utilized in these experiments limits the standing wave solutions to those with $n + \frac{1}{2}$ wavelengths within the container (where $n = 1, 2, 3, \ldots$). Thus, perturbation waveforms are limited to combinations of these modes. Figure 3 is a PLIF sequence showing the results of an experiment initiated with a combination of two modes, one with $1\frac{1}{2}$ wavelengths and one with $2\frac{1}{2}$ wavelengths. Frame 0 was taken slightly before the acceleration, and thus shows the initial interface shape consisting of the two initial modes. Because the initial amplitudes are small, the two modes evolve independently of each other early in their evolution. Furthermore, the mode with the shorter wavelength grows more rapidly. Therefore, in frame 1 the amplitude of the shorter wavelength mode has decreased to nearly zero, showing clearly the longer wavelength mode. A short time later, in frame 2, the short wavelength mode has inverted, while the longer wavelength mode has now decreased in amplitude; thus the shorter wavelength mode is clearly shown. In frames 5-40, this multi-mode instability evolves, exhibiting the formation of a more complex vortex structure than that observed in the single-mode experiments.

Figure 4 shows the results from another multi-mode experiment, in which a combination of the modes with $1\frac{1}{2}$ and $3\frac{1}{2}$ wavelengths is used. Again, frames 1 and 2 show isolated views of each mode; and again this multi-mode instability develops into a vortex pattern that is more complex than its single-mode counterpart. However, this combination of modes develops into a pattern that is much more similar to that of the single-mode instability in that it is dominated by three large vortices. Note, also, that these vortices are much further developed, i.e. there are many more coils in the final multi-mode patterns than exist in the single-mode experiments. This is a result of the fact that the multi-mode initial interface shape produces a more concentrated vorticity distribution than does the single-mode interface. Thus, the vortices form much more quickly than in the single-mode experiments.

Acknowledgement. This work was supported by the Center for Advanced Fluid Dynamics Applications at the Lawrence Livermore National Laboratory and by NASA's Microgravity Science and Applications Division.

References

[1] Meshkov EE, Instability of the interface of two gases accelerated by a shock wave, Izv. Akad. Nauk. SSSR Mekh. Zhidk. Gaza, 4, 151-157, (1969).

[2] Brouillette M and Sturtevant B, Experiments on the Richtmyer-Meshkov instability: single-scale perturbations on a continuous interface, J. Fluid Mech., 263, 271-292, (1994).

[3] Jacobs JW and Sheeley JM, Experimental Study of Incompressible Richtmyer-Meshkov Instability, Phys. Fluids, 8, 405-415, (1996).

[4] Jacobs JW, Jones MA, and Niederhaus CE, Experimental Studies of Richtmyer-Meshkov instability, Proc. 5th Intl. Workshop on Compressible Turbulent Mixing, 18-21 July 1995, Stony Brook, NY, 195-202.

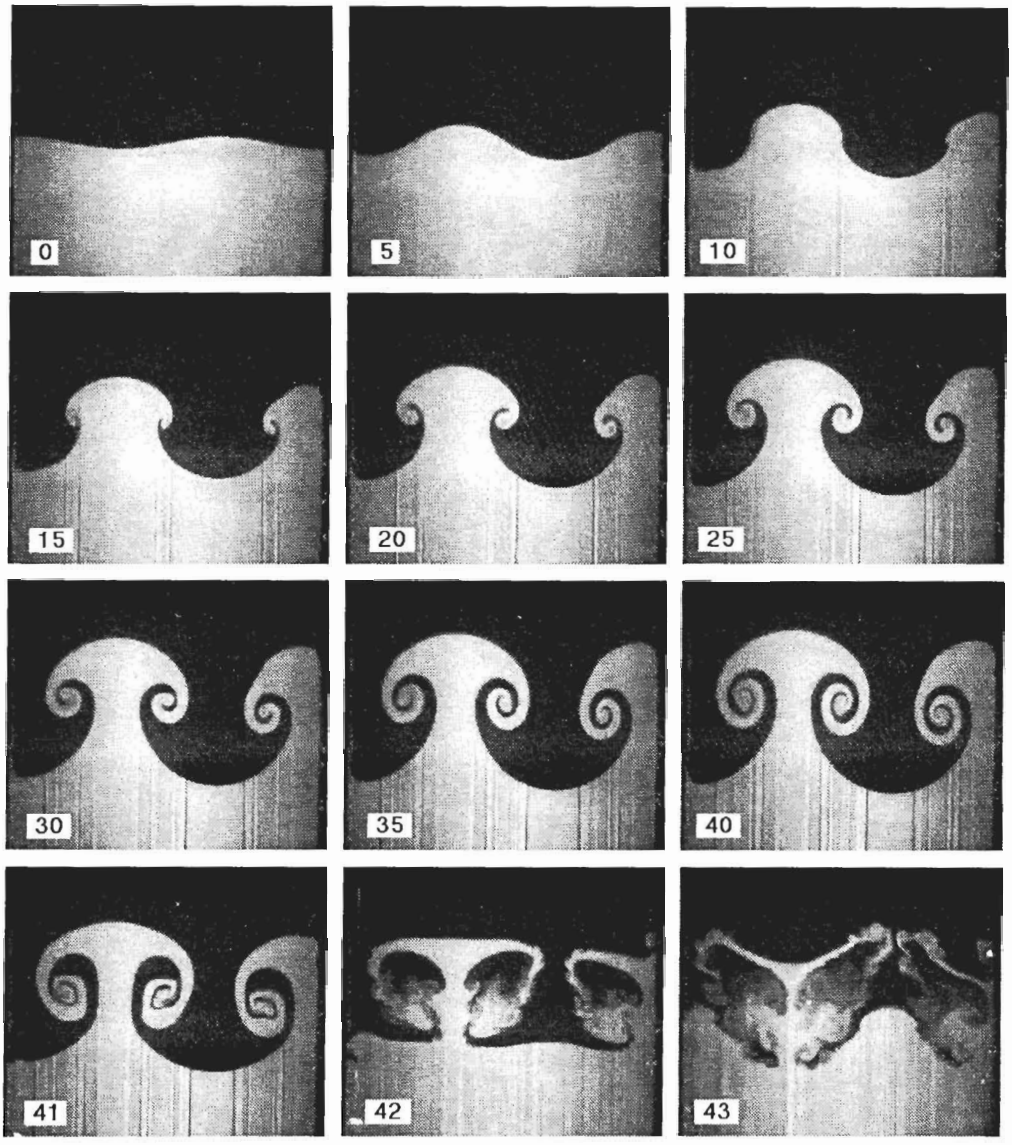

Figure 2. A sequence of PLIF images from an experiment initiated with a single-mode initial perturbation. Each image is marked with a frame number (each frame increment corresponds to a 1/60 s time increment). Note that this and the following sequences are not uniformly spaced in time.

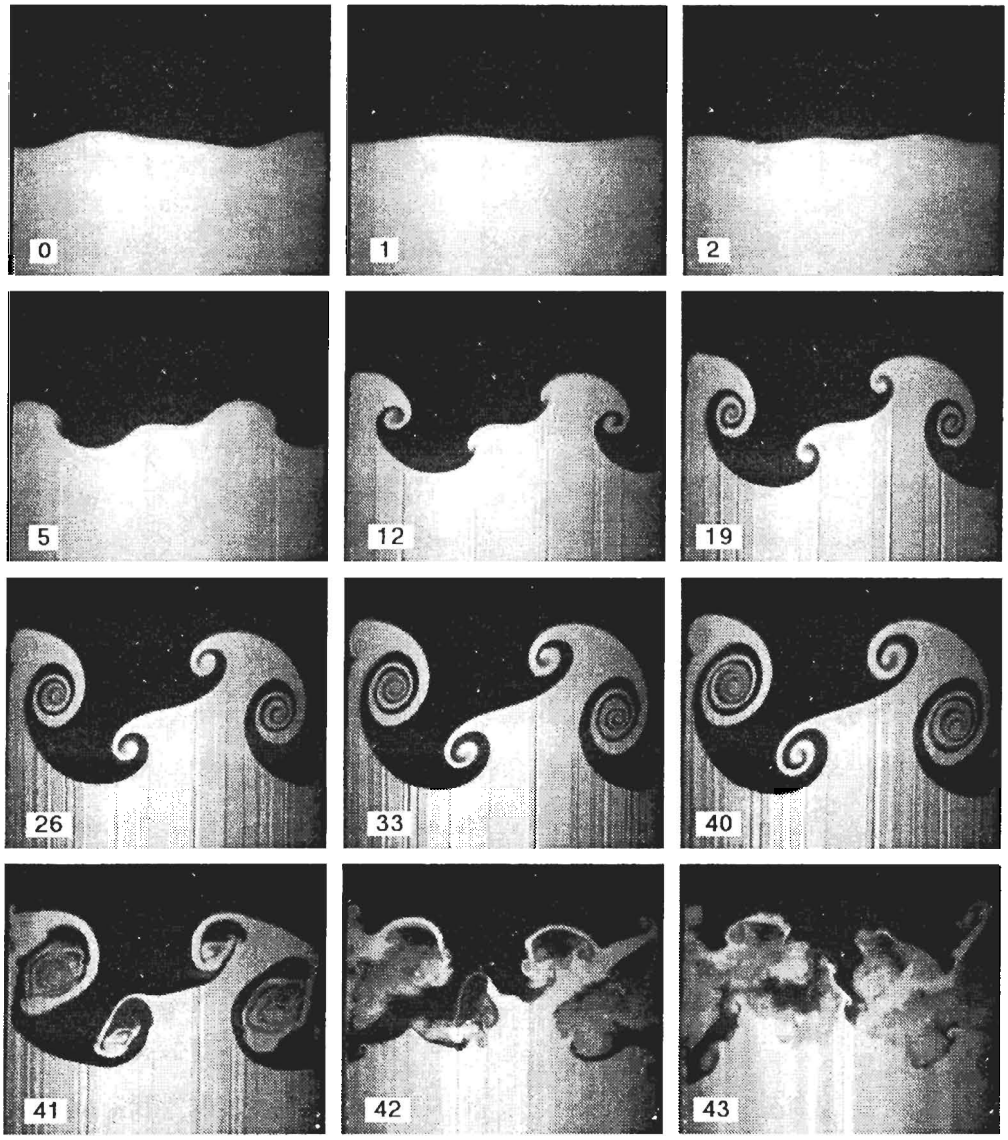

Figure 3. A sequence of PLIF images from an experiment initiated with a multi-mode initial perturbation consisting of a combination of the $1\frac{1}{2}$ wavelengths and $2\frac{1}{2}$ wavelengths modes.

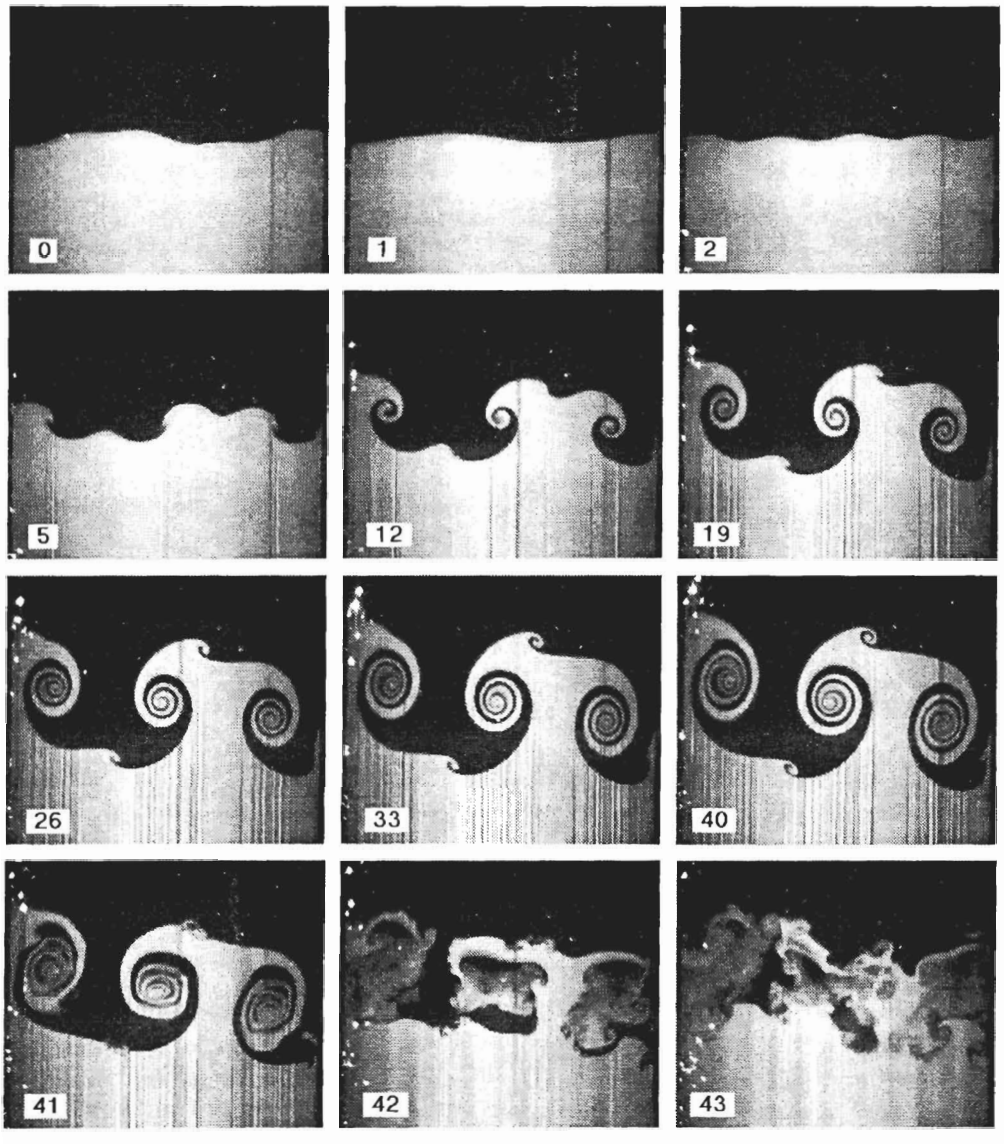

Figure 4. A sequence of PLIF images from an experiment initiated with a multi-mode initial perturbation consisting of a combination of the $1\frac{1}{2}$ wavelengths and $3\frac{1}{2}$ wavelengths modes.

On the Interest of the Using of the Hot Wire Technique as a Diagnostic Investigation for the Richtmyer-Meshkov Instability Study

G. Jourdan[1], J.F. Debièvе[2] and L. Houas[1]
[1]IUSTI, Umr 6595 CNRS, Université de Provence, Technopôle de Château-Gombert
5 rue Enrico Fermi, 13453 Marseille cedex 13, France
[2]IRPHE, Umr 6594 CNRS, Université Aix-Marseille I et II
12 avenue Général Leclerc, 13003 Marseille, France

Abstract: We present experimental investigations based on the opportunity, or not, to exploit the hot wire diagnostic technique for the study of the Richtmyer-Meshkov instability induced turbulent mixing in shock tube. This technique, in comparison with other shock tube experiment methods, presents some advantages.

1. Aims

For several decades, turbulent-flow research has relied on the anemometry to measure fluctuations owing to the turbulence. However, in applications to compressible flows, the interpretation of its response has remained a subject of study and controversy. Research anemometer instrumentation can generally be classified in two fundamental categories:

- the Laser Doppler Anemometer (LDA) [1]
- the thermal anemometer usually referred to as Hot Wire Anemometer (HWA) [2]

We can notice that such classical anemotry method are not intensively used in study of the the Richtmyer-Meshkov [3, 4] instability. We present, here, preliminary results obtained from the hot wire diagnostic technique for the study of the Richtmyer-Meshkov instability induced turbulent mixing in shock tube.

First, it is necessary to draw up an overview of the different diagnostic methods, applied to the shock induced hydrodynamic interface instability, with their characteristics, in order to better place the possibility of the using of the HWA as a diagnostic investigation for the Richtmyer-Meshkov instability study.

The fact that HWA features small measuring volumes and good frequency response invites us to use it for characterization of the passage of the shock induced turbulent mix region.

However, the crucial problem is to observe the mechanical resistance of the wire sensors in the presence of membrane particles, which initially materializes the gaseous interface, in shock tube experiments and how could we detect the mixing zone during its passage at the probed location. As the turbulent mixing zone follows the very high gradient corresponding to the shock wave passage, other problems are the limitation imposed to the shock tube working point by the electronic device of the anemometer, the temperature bandwidth and the sensitivity of the wire sensors.

More information - Email: jourdan@iusti.univ-mrs.fr or dussauge@marius.univ-mrs.fr

2. Overview of shock tube diagnostic methods

Up to this day, different types (qualitative and quantitative) of diagnostic techniques have been tested in the domain of Richtmyer-Meshkov instability induced turbulent mixing. The principal technique are:

- Visualization methods like shadowgraph or schlieren [5], that both help for the understanding of the physical phenomenon, and give the thickness of the mixing zone which is one of the most important parameter as it is correlated to the degree of generated turbulence.
- Techniques based on the light source emission, diffusion or absorption which allow the determination of quantitative physical parameters as the density, temperature, concentration, velocity ... All these techniques have the advantage to be non intrusive. But usualy both their cost is very high, and their complex set-up requires some restrictive precautions.

Each diagnostic method has its technological characteristics, financial criterion, domain of validity, optimal conditions and requires generally specific test gases. In this way, we have tried to investigate the well known HWA technique both because it is ship and simple to set-up, and also in order to prospect if it could be of some interest in our area because of its intrusive aspect.

3. The HWA system

Recently, the application of HAW has expanded greatly due to better equipment. Typical dimensions of the wire sensors are $\approx 5\ \mu m$ in diameter and $1-3\ mm$ long. Hot wire sensor must have two characteristics to make it a useful device: a high temperature coefficient of resistance and an electrical resistance such that it can be easily heated with an electrical current at pratical voltage and current levels. The most common wire materials are tungsten, platinum and platinum-iridium alloy.

In successfully using an anemometer for a specific fluid mechanics measurement the selection of a sensor is of primary importance. However, this sensor must be controlled with an electronic circuit and some basic knowledge of its function and operation is important. It supplies a controlled amount of electrical current to heat the sensor and provides frequency compensation for the sensor. The constant current type of anemometer operates by taking the voltage signal caused by wire resistance changes and compensates for the frequency lag with a non-linear amplifier. The constant temperature control system, while certainly not a recent innovation, has gained rapidly in acceptance during the last few years. It operates by utilizing a feedback controlled bridge circuit to maintain the sensor at constant temperature. In the present work, the used HWA system and the data acquisition were:

- Platinum tungsten hot wires (2.5 μm and 5 μm in diameter)
- Dantec (CTA 90 C 10) constant-temperature anemometer system (2 Disa symetric bridges)
- System calibration and performance test on known high-speed flows
- Data acquisition: Digitizing oscilloscope Tektronix TDS 400
- Data treatment: Personal Computer

4. Results from HWA in Richtmyer-Meshkov instability shock tube experiments

A study of feasibility has been realized in order to test the mechanical resistance of the wires sensors and to determine compatible working points of the IUSTI' shock tube ($8.5 \times 8.5\ cm^2$) with the hot-wire anemometer system. The aim of this preliminary work is to prove the possibility to obtain an experimental qualitative signal, correct in first approximation. Given that the hot wire responds to a combinaison of velocity, density and temperature fluctuations, the signal deconvolution seems to be not obvious. Then, for this first step study, no calibration has been made.

4.1. Mechanical resistance

Platinum tungsten hot wires ($2.5\ \mu m$ and $5\ \mu m$) have been tested. Concerning their mechanical resistance, they adequately behave for initial pressures from $0.1\ atm$ to $1\ atm$, which corresponds to shock wave Mach numbers from 1.2 to 3. In the presence of a $1.5\ \mu m$ thick mylar membrane, which materializes the initial interface between the two test gases, we have found the time life to be three to four runs. In this way, the exploitation of the hot wire technique seems to be compatible with the initial objective to study.

4.2. Shock tube working point

Several preliminary runs were undertaken in a pure gas (air, Ar, CO_2 ...) and for different shock wave Mach numbers (from 1.2 to 3) in order to determine the best initial condition compatible with the anemometer working temperature range. Indeed, in the most of cases, electronic oscillations due to the high shock wave gradient, not adapted for the hot-wire constant-temperature electronic device, perturb the HWA measurements. We concluded that the temperature behind the shock wave must not be too high so as to keep the constant temperature system. So, in order to conserve the advantages of the constant-temperature anemometer system, we have to limit the post-shock temperature. The stagnation temperature jump must not exceed $150°\ K$ behind the shock wave, which corresponds to a shock wave Mach number of about 1.5. Also, in this case, the velocity is small enough to be compatible with the bandwidth of the HWA. The most difficulty is the choice of the operating point of the feedback controlled bridge circuit.

4.3. Exploitation of the HWA

In a second test series, good hot wire response signals were obtained for an incident shock wave Mach number of about 1.4 and a air/Ar interface, materialized by a $1.5\ \mu m$ thick mylar membrane, with the atmospheric initial pressure and a constant temperature electronic system. Table 1 gives the thermodynamical parameters for the present test.

$P_i\ [Pa]$	M_{isw}	$\rho_1\ [kg/m^3]$	$\rho_2\ [kg/m^3]$
100000	1.4	1.19	1.64
A	A'	$\Delta U\ [m/s]$	$T'_{Ar}\ [K]$
0.15	-0.1	201	383

Table 1. Initial conditions and thermodynamical parameters of the air/Ar experiment.

where P_i, M_{isw}, ρ_1, ρ_2, A, A', ΔU and T'_{Ar} correspond to the initial pressure, the incident

shock wave Mach number, the initial density of the gases 1 and 2 at rest, the pre-shock Atwood number, the post-shock Atwood number, the velocity jump of the interface through the impulsive acceleration and the temperature of Ar behind the transmitted shock wave, respectively.

The air/Ar mixing zone was clearly observed (Fig. 1) and the time passages coincide with the Rankine-Hugoniot calculated (x,t) diagram (Fig. 1).

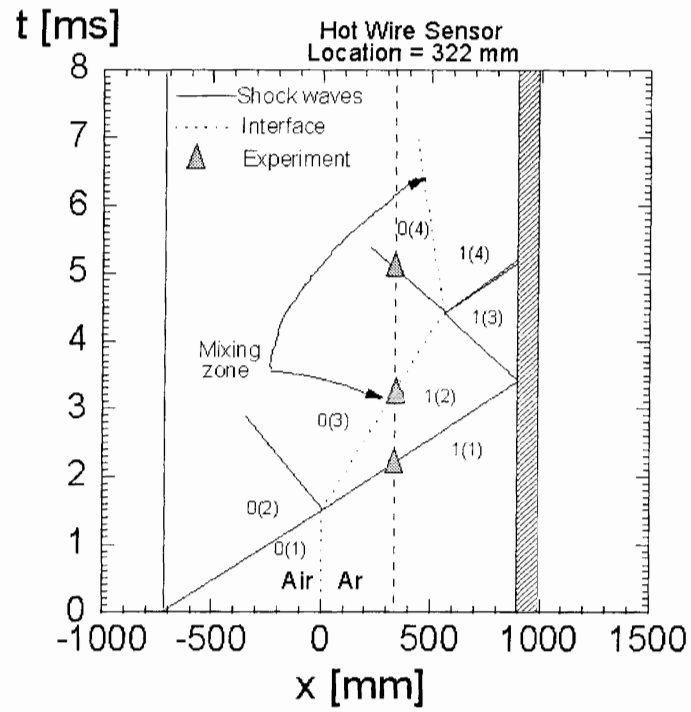

Figure 1. (x,t) diagram of the air/Ar experiment induced by a 1.4 incident shock wave Mach number.

The hot wire breaks after three or four runs, but the mixing zone thickness can easily be deduced from the experimental records. Figure 2 presents the response of the HWA in the case of a air/Ar experiment induced by a 1.4 incident shock wave Mach number. One can discern the transmitted shock wave across the initial material interface, the reflected shock wave on the shock tube end-wall and the turbulent mixing zone identified by a continuous variation of the signal.

The nature of the HWA signal, here, is mainly a function of $\rho \times u$ product, but also both of the temperature and Prandtl number. In this way, the deconvolution of the signal in order to separate each variable seems to be difficult and the real interest of this single shipper diagnostic method is essentially the turbulent mixing zone detection with its thickness estimation. It can be noted that in the present case, the mixing zone thickness is about 30 mm.

Moreover, this kind of "signature" can be exploited to characterize the structure of the interface (i.e., distinguish different mixing packets) from a suitable signal processing.

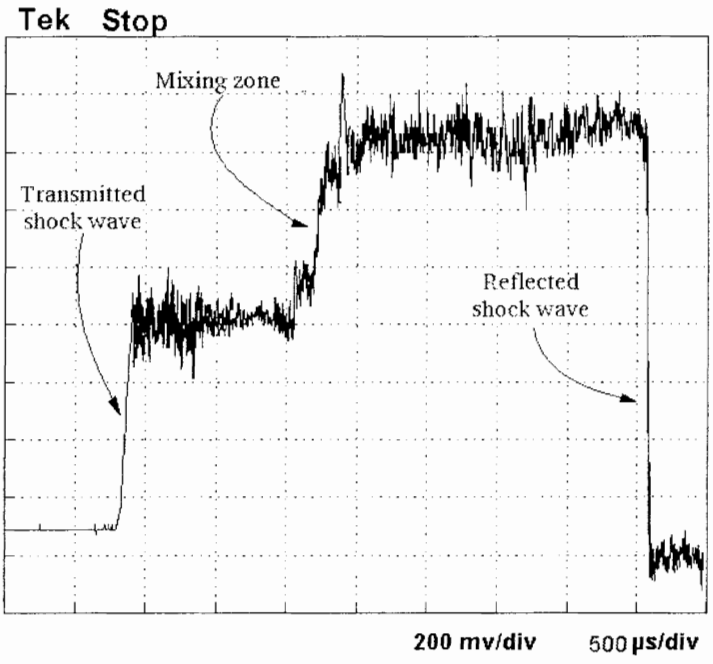

Figure 2. HWA signal for the air/Ar experiment induced by a 1.4 incident shock wave Mach number.

5. Discussion

The HWA technique has been tested to investigate the Richtmyer-Meshkov induced mixing in shock tube experiments. Results show that the time life of probes is of about three to four runs, and the passage of the mixing zone has been successfully detected.

Even if no measurement after the reshock passage is available because of the intrusive nature of the present diagnostic method itself, we believe that both its low cost and its simple setting up, added to the possibility to easily determine the thickness of the mixing zone (i.e., in first approximation, the mean velocity multiplied by the time passage), are of interest in the field of the Physics of Compressible Turbulent Mixing.

Furthermore, from HWA signal processing, it can be possible to estimate turbulent scales and coupled with the LDA method [1], one can obtain the level of turbulence from the velocity and density fluctuation profiles within the mixing zone.

References

[1] Poggi F, Thorembey MH, Rodriguez G and Haas JF, Velocity measurements in turbulent gaseous mixtures induced by Richtmyer-Meshkov instability, Proc. of the 6th International Workshop on the Physics of Compressible Turbulent Mixing, G. Jourdan & L. Houas Editors, Marseille, (1997).

[2] Dupont P and Debiève JF, Hot wire method for meaning turbulence in transonic or supersonic heated flow, Exp. in Fluids, 13, 84-90, (1992).

[3] Richtmyer RD, Taylor instability in shock acceleration of compressible fluids, Commun. Pure Applied Math., 13, 297-319, (1960).

[4] Meshkov EE, Instability of a shock wave accelerated interface between two gases, Sov. Fluid Dyn., 4, 107-108, (1969).

[5] Proceedings of the 1^{st} to 6^{th} International Workshops on the Physics of Compressible Turbulent Mixing, (1988 - 1997).

Simple Approach for the Richtmyer-Meshkov Mixing Growth Description in Shock Tube Experiments

G. Jourdan[1], L. Houas[1], J.F. Haas[2], G. Ben-Dor[3] and E.E. Meshkov[4]
[1]IUSTI, CNRS Umr 6595, Université de Provence
Technopôle de Château-Gombert, 5 rue Enrico Fermi, 13453 Marseille cedex 13, France
[2]CEA Vaujours-Moronvilliers, BP7, 77181 Courtry, France
[3]PCAES, Department of Mechanichal Engineering, Ben-Gurion
University of the Negev, Beer Sheva, Israel
[4]Institute of Experimental Physic, (VNIIEF) Sarov, 607190, Nizhni Novgorod Region, Russia

Abstract: From different experimental conditions carried out in a $8.5 \times 8.5\ cm^2$ square cross sectional shock tube using a CO_2 tridirectional laser absorption diagnostic method, a simple approach to describe the mixing zone thickness growth, with time, is proposed.

1. Introduction

Up to this day, if the influence of the product $|A\Delta U|$ is an accepted fact, two laws of the temporal thickness evolution have been already suggested. The first law is a linear evolution with time and the second is proportional to a t^{α} power law where $\alpha \leq 2/3$. However, the influence of the wall boundary layer in shock tube experiments and the presence of a membrane in horizontal shock tubes, or a diffusion zone created after the retraction of a separating plate before the shock wave passage in vertical shock tubes, did not permit such a well-defined, self-similar law of the mixing zone thickening. Here, we propose a strong assumption where the experimental conditions, as the effects of the membrane, the shock membrane interaction, the Richtmyer-Meshkov growth and the boundary layer interaction are supposed to be linearly superposable.

2. Experiments

The diagnostic method principle [1] is based on the measurement of the absorption of a CO_2 laser line by the CO_2 present in the flow (mixing zones CO_2/CO_2, CO_2/He, CO_2/Ar and CO_2/Kr). The absorption coefficient, at a determined frequency, α_ν, depends on the temperature T and the density ρ of the absorbing medium (CO_2 in the present study), i.e.,

$$\alpha_\nu = f(T, \rho) \tag{1}$$

If thermodynamic equilibrium is assumed then by a simultaneous measurement with two different wavelengths, ν_1 and ν_2, the problem reduces to the solution of the following two equations:

$$\begin{cases} \alpha_{\nu_1} = f(T, \rho_{CO_2}) \\ \alpha_{\nu_2} = f(T, \rho_{CO_2}) \end{cases} \tag{2}$$

where the unknowns T and ρ_{CO_2} are the mean temperature and density profiles of the absorbing medium (CO_2 in the present case). Note that α_{ν_1} and α_{ν_2} which are measured, are known. We have applied this spectroscopic method for thickness and volume determinations, by considering the part $10\% - 90\%$ of the resulting concentration profiles of CO_2.
Inspired by the idea of Wang [2], suggesting the additivity of the optical paths, and assuming

More information - Email: jourdan@iusti.univ-mrs.fr

the mixing zone to be multidimensional, i.e., non uniform across the test section, the test chamber cross section was conceptually divided into nine identical square sub-regions, where in each one, the mixing zone was considered to be one-dimensional [3]. Theoretically, from two

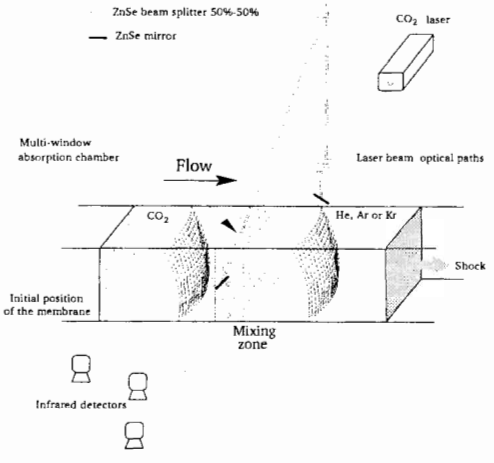

Figure 1. Experimental principle

runs for two different wavelengths, ν_1 and ν_2, one can deduce simultaneous multi-profiles $T_i(t)$, $\rho_i(t)$ and $\%(CO_2)_i(t)$, where i represents the center, the wall or the corner. However, assuming a small variation of temperature through the probed region, a single wavelength absorption experiment only is needed. When this criterium is satisfied, the technique described represents a considerable simplification over the more generally required dual wavelength experiments [4]. Three simultaneous absorption signals were deconvoluted in order to distinguish between the contributions of the center, the wall and the corner sub-regions. Of course, the different time durations of the mixing zone passage, and its velocity, which was assumed to be constant between shocks, allowed a strong estimation of its thickness in the three characteristic regions of the shock tube. However, it was shown that the present method provided more accurate thickness measurements, considering the part $10\% - 90\%$ of the resultant concentration profile within the mixing zone itself. In addition, the simultaneous use of three detectors in one run enabled us to obtain a three-dimensional visualization of the mixing zone shape and the estimation of its mean total volume:

$$V_{total} = \int\int f_{front}(x,y)dx\,dy - \int\int f_{rear}(x,y)dx\,dy \tag{3}$$

A simple approximation of the volume of the mixing zone was calculated from:

$$V_{total} = \left(\frac{a}{3}\right)^2 [L_{center} + 4\,L_{wall} + 4\,L_{corner}] \tag{4}$$

where a is the width of the square cross section ($8.5\ cm$) and L_i (i = center, wall, corner) are the thicknesses measured in the three different regions of the test section. Dividing it by the

area of the cross section, L_{vol} which is the thickness of a $1D$ mixing zone of the same volume was obtained:

$$L_{vol} = \frac{V_{total}}{S} = \frac{1}{9}\left[L_{center} + 4\,L_{wall} + 4\,L_{corner}\right] \quad (5)$$

The decision to use the total mixed volume (i.e., L_{vol}) as the measure of the Richtmyer-Meshkov growth, in the present work, is arbitrary but it seems to be a clever choice because this parameter includes the effects of all of the artifacts occuring in shock tube experiments. Indeed, we can consider that in the volume there may be beneficial cancellations (e.g., membrane effect, wall boundary layer perturbation, etc...) which yield the best overall measure of the mixing zone.

2.1. Influence of the experimental configuration for $A \approx 0$

Under ideal, i.e., membraneless conditions, in the absence of a post-shock density mismatch on the interface (Atwood number $A_0 = 0$) there should not be any instability or mixing between the two test gases. In order to understand the case $A \to 0$, experiments with the gas combination CO_2/CO_2, for the incident shock wave Mach numbers 2.4, 3.1 and 4.5 were conducted. The signature of a "mixing zone" (between two regions of CO_2 which are at different thermodynamic states) with a measurable thickness was observed on the absorption profiles, which can be attributed solely by the influence of the experimental set-up. The figure 2 represents an example

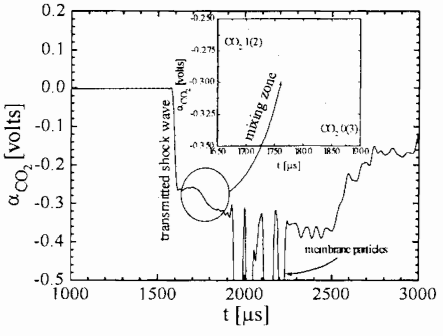

Figure 2. Example of an absorption signal obtained for the gas combination CO_2/CO_2 showing the presence of a mixing zone, where the incident shock wave Mach number in CO_2 is 3.1

of such an absorption signal, obtained in the center of the shock tube cross section, at the location $x = 55\ cm$, for a CO_2/CO_2 case with a shock wave Mach number of 3.1. About 100 μs after the passage of the transmitted shock wave, a decrease of the signal corresponding to the passage of a "mixing zone" is observed, between the states $CO_2 1(2)$ and $CO_2 0(3)$. The real origin of this phenomenon is the nature of the interaction between the incident shock wave and the second membrane. The flow near the membrane rupture point is much more complicated when the rupture is delayed and can vary greatly with increasing time delay as shown in figure 3. The consequence is that the CO_2 on both sides of the membrane is, in fact, in different thermodynamic states after the shock passage, which creates a "mixing zone" between the states $CO_2 1(2)$ and $CO_2 0(3)$, detectable by laser absorption.

Considering the three test conditions, CO_2/CO_2 for the incident shock wave Mach numbers 2.4, 3.1 and 4.5, added to the experiments CO_2/Kr with shock wave Mach numbers 2.4 and 3.1, where the post-incident-shock Atwood number was very close to zero, we have presented

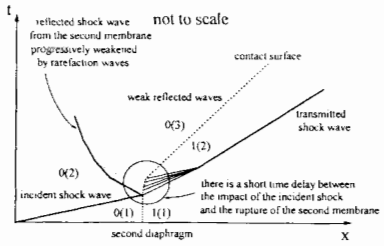

Figure 3. Schematic wave diagram of the experiment shown in figure 2 when the second membrane rupture is delayed

on figure 4 the evolution of L_{vol} and L_{center}, with time for the CO_2/Kr and CO_2/CO_2 cases, respectively. As can be seen, accounting for the mean volume of the mixing zone cancelled the

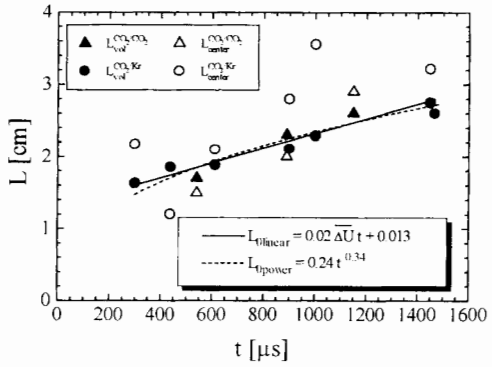

Figure 4. Evolution of the mixing zone thickness with time for experiments with $|A| \approx 0$. The L_{vol} experimental points are fitted with linear and power laws

scattered evolution observed in the centerline. Then, only L_{vol} experimental data have been considered.

3. Discussion

All the experimental data have been fitted by a linear regression as:

$$L_{0_{linear}} = a_1 t + b_1 \tag{6}$$

with $a_1 = 10.42$ and $b_1 = 0.013$, where $L_{0_{linear}}$ and t are in meter and second, respectively. In order to compare the present work with the empirical law given by Zaytsev [5]:

$$\frac{dL}{dt} = (a + b\,|A|)\,\Delta U \tag{7}$$

with $a = 0.02$ and $b = 0.07$ for the incident phase ($A < 0$), where L and ΔU are in meter and $m\ s^{-1}$, respectively, we have done the following substitutions. If $A = 0$, the previous equation

becomes:

$$\frac{dL}{dt} = a\Delta U \tag{8}$$

After integration we obtain:

$$L = a\Delta U t + const \tag{9}$$

For $A = 0$the Zaytsev empirical relation suggests the presence of a "minimum mixing" zone. Let us change the form of $L_{0_{linear}}$, with as $\overline{\Delta U}$ the arithmetic average of the different mixing zone velocity jumps with an Atwood number close to zero. For $\overline{\Delta U_{A\simeq 0}} = 510\ m\ s^{-1}$, we found:

$$L_{0_{linear}} = a_2\, \overline{\Delta U_{A\simeq 0}}\ t\ +\ b_1 \tag{10}$$

with $a_2 = 0.02$ and $b_1 = 0.013$. As can be seen, the value of a_2 is close to Zaytsev's constant a. The function L_0 corresponds to the "minimum mixing zone" thickness induced by the experimental set-up when the Atwood number is close to zero. It should be noted that different functions of L_0 are appropriate to different experimental set-ups.
Considering $L_{0_{linear}}$ as a limit function of our Richtmyer-Meshkov shock tube experiments for $A = 0$, we have fitted all the other experimental data, with Atwood number $A \neq 0$, by the function:

$$L = L_{0_{linear}} + k\,|A\Delta U|\,t \tag{11}$$

The results are shown in figure 5. Unfortunately, the non constant value of k ($\in\ [0.035; 0.095]$)

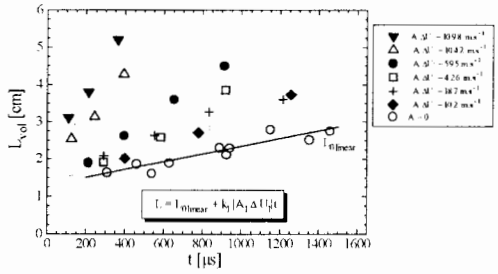

Figure 5. Evolution of the mixing zone thickness with time for different $|A\,\Delta U|$. The experimental points are fitted by $L = L_{0_{linear}} + k_1\,|A\,\Delta U|\,t$

is strongly correlated with a term, which corresponds to the loss of the mixing towards the wall of the shock tube due to the presence of the boundary layer. In sumary, the time evolution of the thickness of the mixing zone could be expressed as:

$$L = a\,\overline{\Delta U_{A\simeq 0}}\ t\ +\ b\ +\ k\,|A\Delta U|\,t\ -\ L_\delta \tag{12}$$

With this form, the first term depends on the interaction nature of the shock wave with the membrane which initially separates the two gases, but not on the Atwood number. The second term can be considered as the part of the mixing induced by the membrane particles and depending on the membrane material properties. The third term represents the growth of the mixing zone depending on all the fundamental parameters: the Atwood number, the velocity jump of the interface and the time. The fourth term L_δ, corresponds to the loss of the mixing towards the wall of the shock tube due to the presence of the boundary layer and is in

competition with the third one. For example, L_δ will be high for both high shock wave Mach number and low pressure experimental conditions, and low for both weak shock waves and high pressures.

4. Conclusion

A simultaneous three-directional laser diagnostic technique was developed for thickness and volume determinations of a gaseous mixing zone originated from the Richtmyer-Meshkov instability in a square shock tube. It was shown that, even if the initial Atwood number was equal to zero, the initial experimental shock tube configuration, and particularly the membrane, always induced a "mixing zone" between the two gases. This "membrane minimum mixing thickness" resulted from the delay in the interaction of the incident shock wave and the membrane and depended essentially on the velocity jump of the interface. A strong assumption where the experimental conditions, as the effects of the membrane, the shock membrane interaction, the Richtmyer-Meshkov growth and the boundary layer interaction are supposed to be linearly superposable, has been proposed. As the effects of the membrane, the shock membrane interaction, the Richtmyer-Meshkov growth and the boundary layer interaction were supposed to be linearly superposable, this strong assumption would probably produce results comparable only under conditions identical to the present experiments. However, it would be interesting to consider this type of approach in further works. Considering the growth time evolution of the mixing zone, and even if the present diagnostic technique enabled us to reduce the uncertainty on the part of the mixing lost towards the walls, the measurement of the mean volume, instead of the thickness of the mixing zone at the shock tube center, has not clearly favoured the hypothesis of a linear dependence on time instead of a power law.

References

[1] Fortes J, Ramdani A and Houas L, CO_2 laser absorption measurements of temperature and density in shock induced Richtmyer-Meshkov mixing zone, Phys. Rev. E, 50, 4, 3041-3049, (1994).

[2] Wang JT, Laser absorption methods for simultaneous determination of temperature and species concentration through a cross section of radiating flow, Appl. Opt., 15, 13, 768-773, (1976).

[3] Houas L, Touat A and Jourdan G, Richtmyer-Meshkov mixing zone study by a multidirectional laser absorption technique, Phys. Rev., E5-B, 52, 5344-5351, (1995).

[4] Jourdan G, Fortes J, Billiotte M and Houas L, Laser absorption density direct measurements with the limitation of temperature variation field in shock-induced gaseous mixing, Shock waves J., 7, 43-47, (1996).

[5] Zaytsev SG, Lazareva EV, Chernuka VV and Belyaev VM, Intensification of mixing at the interface between media of different densities upon the passage of a shock wave through it, Dolk. Akad. Nauk. SSSR, 283, 94-98, (1985).

Nova Experiments to Investigate Hydrodynamic Instabilities in the Solid State

D.H. Kalantar, B.A. Remington, E.A. Chandler, J.D. Colvin, D.L. Griswold, R.E. Turner, S.V. Weber and L.G. Wiley
Lawrence Livermore National Laboratory, Livermore, CA, 94550 USA

Abstract: Experiments were done to shock compress and accelerate copper foils at peak pressures of ~3 Mbar above and below the melt temperature to study the effects of material strength on hydrodynamic instabilities. An x-ray drive generated in a hohlraum target was used to generate the shock wave profiles. The growth of a preimposed perturbation at an embedded interface is diagnosed by x-ray radiography. Results obtained using a high contrast shaped laser pulse show that the growth of the modulation is delayed compared to fluid simulations, which could be due to material strength stabilization. In contrast, when a copper foil is placed above the melt temperature at >3 Mbar with a single shock, it melts upon compression and the modulation growth is consistent with fluid modeling. Experimental results from copper shocked to 3 Mbar both below and above the melt temperature are presented and compared with simulation.

1. Introduction

In a classical fluid model, when a light fluid accelerates a heavier fluid, the interface is Rayleigh-Taylor unstable. As a result, modulations at the unstable interface will grow. We show the growth is modified by material strength in the solid state.

We are conducting hydrodynamic instability experiments using the Nova laser [1] to study the effect of material strength on shock compressed metal foils. Thin Cu foils are shock compressed with an x-ray drive incident on a brominated plastic ablator to a peak pressure of about 3 Mbar. Using a high contrast (1:25) shaped laser pulse, the foils remain solid, and the material strength appears to reduce the growth of the Rayleigh-Taylor unstable preimposed mass modulation. By contrast, thin Cu foils compressed with a single strong shock melt promptly under compression, and show growth at the interface consistent with fluid modeling.

In this paper, we describe the Nova experiments and target design that allows us to shock compress Cu foils to 3 Mbar, while maintaining a solid state. We present details of the x-ray drive characterization, and results of the instability growth measurements of the shock compressed foils. Comparison with modeling shows that the measured growth is delayed relative to simulation, even when material strength is included in the simulation. This may be the result of a strain-rate dependence for the yield strength [2]. This is approximated in the numerical simulations by scaling the yield strength in the standard Steinberg-Guinan [3] model.

2. Experimental details

We create an x-ray drive inside a cylindrical gold hohlraum using eight beams of the Nova laser. The beams are focused onto the inner wall of the hohlraum through laser entrance holes, as shown in Fig. 1a. The foil package consists of a brominated plastic ablator and a Cu foil payload

More information - Email: kalantar1@llnl.gov

mounted over a hole in the side of the hohlraum. The plastic ablator is 22 μm thick CH with 3% atomic fraction bromine dopant. The payload foil is 15 μm thick. The x-ray drive ablates the brominated plastic, launching a sequence of shocks into the metal foil, compressing and accelerating it away from the hohlraum. We diagnose the growth of the unstable embedded

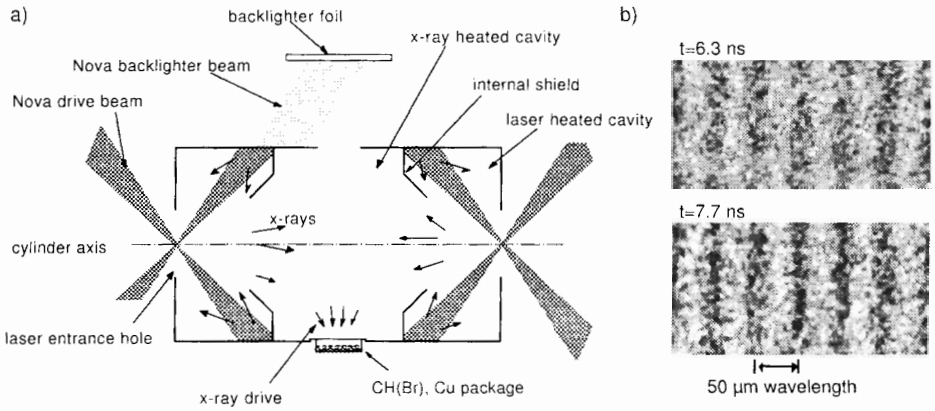

Figure 1. a) Schematic showing the internally shielded hohlraum and target geometry for x-ray backlighting. Face-on radiography is done with the backlighter as show, side-on radiography is done with the backlighter placed behind the target in this view. b) Sample face-on x-ray radiographs shown as modulation in optical depth.

interface by x-ray radiography using a large area (0.7 mm) backlighter generated with two additional Nova beams aligned to a separate backlighter foil [4]. A 2-3 ns square laser pulse shape was used for these beams, and they were delayed up to 12 ns to record a time-sequence of radiographs over several Nova shots. X-ray pinhole images such as those shown in Fig. 1b were recorded with a gated x-ray framing camera [5].

In order to shock compress the Cu foil to a peak pressure of about 3 Mbar, while maintaining it in the solid state, we use a high contrast shaped laser pulse and an internally shielded hohlraum. The laser pulse shape is designed to generate an x-ray drive temperature that launches a sequence of staged shocks into the package. The 0.51 μm laser pulse starts with a low intensity foot that delivers 0.4 TW (total for 8 beams) for 2 ns, before ramping up to a peak power of 10 TW. The overall pulse length is 6.5 ns, and the total energy delivered into the hohlraum is about 22 kJ at 0.53 μm laser wavelength. The high contrast pulse shape is shown in Fig. 2a, overlaid with the measured x-ray drive temperature, which is described in the next section below. The "scale-2" hohlraum is 3.44 mm in diameter, and 5.75 mm long, shown in Fig. 1a. The laser entrance holes are 1.2 mm in diameter, and the holes in the internal shields are 1.6 mm in diameter. The laser beams generate an x-ray radiation environment in the two laser heated cavities of the target. Re- emitted x-rays heat that pass through the holes in the internal shields heat the central (x-ray heated) cavity and launch a sequence of shocks into the package. The internal shields are positioned so that the Au M-band x-ray emission from the laser spots inside the laser heated cavities do not preheat the package. Without the internal shielding, the 2-4 keV Au M-band emission from the laser plasmas would be absorbed by the full volume of the package, potentially causing the foil to melt and decompress. With the internal shielding, the x-rays incident on the ablator are generated by re-emission from the

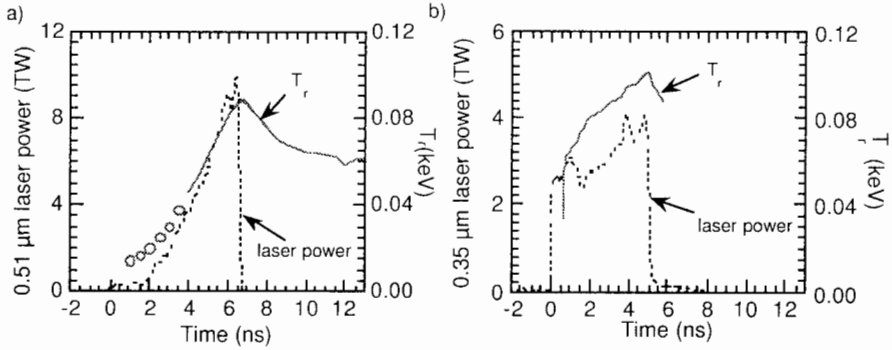

Figure 2. Laser pulse shape and x-ray drive temperature measurements for a) the low isentrope drive, and b) the square pulse drive. The open circles show measurements of x-ray drive using the absolute sensitivity of individual Dante diodes.

regions of the wall that are not directly illuminated by the laser beams. The spectrum of these x-rays is nearly Planckian without a significant M-band component.

For comparison, we also shock compress a Cu sample to ~4 Mbar with a single shock. This is well above the 2.2 Mbar Hugoniot melt point for Cu [6] implying that the Cu melts promptly. Here, we use a "scale-3" hohlraum that is 4.8 mm in diameter and 8.0 mm long without internal shielding. A 5 ns square laser pulse (Fig. 2b) is used at a power of ~4 TW at 0.35 μm laser wavelength. The x-ray drive from this target is also shown on the figure [7].

3. X-ray drive measurement

The x-ray drive inside the hohlraum was measured with the Dante [8] diagnostic, a filtered array of absolutely calibrated x-ray diodes that view the inner wall of the hohlraum through a beryllium-lined diagnostic hole. For the case of the high contrast shaped laser pulse, the lowest energy channels of the Dante (sensitive to ~50 eV photons) detected signals starting at about 1.0 ns. The absolute signal levels from 1-2 diodes were best fit to a Planckian spectrum, which started at about 15 eV and rose to 40 eV at 3 ns. Above 40 eV, enough channels recorded signals that a spectral unfold could be performed, relaxing the Planckian shape requirement. The radiation temperature rose from 40 eV at 3 ns to 90 eV at the end of the laser pulse at 6.5 ns.

For the case of the large hohlraum using a square laser pulse shape, the Dante measurement showed an x-ray drive temperature starting at about 60 eV, ramping up to about 100 eV at the end of the 5 ns laser pulse.

The measured drive temperature for each target is shown overlaid with the laser pulse shapes in Fig. 2. Note that this measured drive is the re- emission from the wall of the hohlraum. The package experiences the x-ray drive that is incident on the wall, which is related to the measured drive by the albedo of the wall [9]. We calculated the albedo correction using the LASNEX [10] computer code. We assume that the drive temperature ramps up linearly from zero to 15 eV at 1 ns, and we impose a lower limit of 0.1 for the albedo at early time.

We used 1-D LASNEX to model to the Cu as a function of time. Comparing the temperature at the embedded interface with the melt temperature calculated by the Lindemann law [3] (Fig.

3a) suggests that foil remains solid throughout the experiment with the low isentrope drive. The drive launches a sequence of shocks into the foil that start at about 0.4 Mbar, ramp up and peak at 3 Mbar. The peak material temperature from the simulations is about 0.2 eV, compared to the predicted melt temperature of ~0.5 eV. The temperature at the interface late

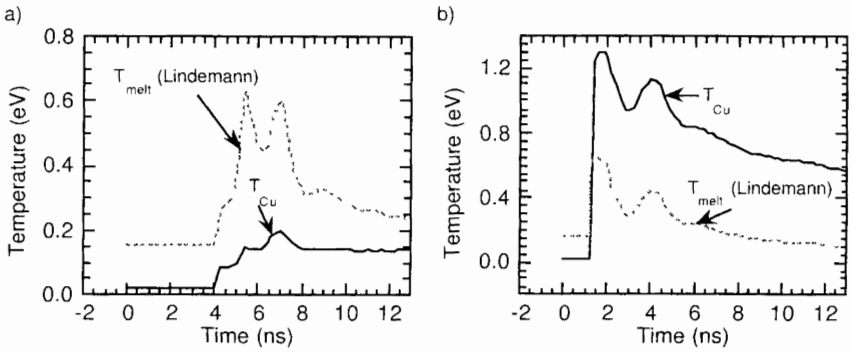

Figure 3. Temperature of the Cu at the embedded interface as a function of time for a) the low isentrope drive, and b) the square pulse drive. The Lindemann law melt curves are also shown.

in time is sensitive to the strength of the first shock. This in turn is sensitive to the actual foot temperature in the hohlraum. If the foot temperature is too low, then the second shock may overtake the first shock before it reaches the ablator/Cu interface, and the foil is shocked to a higher adiabat, which means it may melt at late time when the material temperature crosses the Lindemann melt curve.

We measured the trajectory of different thickness foils by using a side-on radiography technique in order to verify the foot and peak drive that is incident on the package in this experiment. We mounted a nominal package consisting of 22 μm ablator with a 13 μm Cu foil on the side of the hohlraum, and used a high magnification x-ray streaked imager to resolve the motion of the rear surface of the foil to characterize the peak drive. We repeated this with a 10 μm brominated plastic ablator with a 3 μm ($\pm$1) Cu foil to study the drive in the foot of the laser pulse.

The initial breakout from the thin package is sensitive to the foot drive temperature, and the overall foil acceleration is sensitive to the peak drive.

The trajectories for both thick and thin targets are shown in Fig. 4, overlaid with simulations. We reduced the albedo corrected drive in the peak by 7% to match the overall foil trajectory (Fig. 4a). This may indicate uncertainties in the opacities of the plastic ablator at such a low drive temperature, which affects the overall acceleration of the foil. The combination of the measurements with different foil thicknesses constrains the drive. For the case of the square laser pulse, the x-ray drive shocks the copper foil above the single shock melt pressure of 2.2 Mbar. This melts the foil at the interface, wherein the interface evolves as a fluid. The simulated material temperature is >1 eV, at a pressure of about 4 Mbar, as shown in Fig. 3b.

4. Instability growth experiments

Sinusoidal modulations were machined in the Cu foils with amplitudes of 1.0-2.5 μm, and wavelengths of 20-50 μm. We pressed 22 μm of CH(Br) ablator onto the modulated foils, and

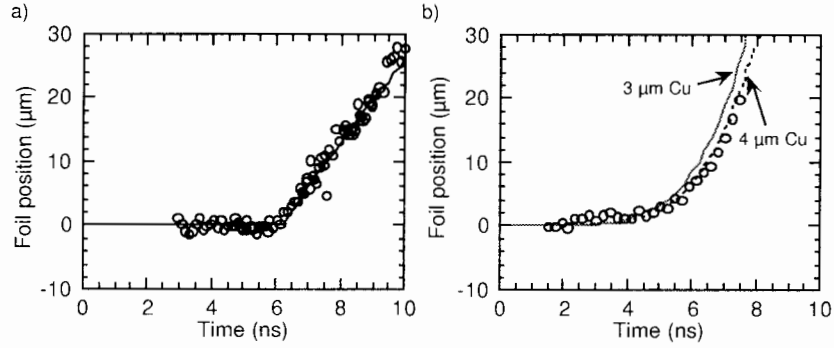

Figure 4. Side-on trajectories of a) a 22 μm CH(Br) ablator and a 13 μm Cu foil, and b) 10 μm CH(Br) ablator and a 3 μm Cu foil. Note that the uncertainty in foil thickness was about 1 μm.

then mounted them onto the side of the hohlraum. We used x-ray radiography to measure the mass modulation as a function of time with an Fe backlighter foil, which provided images of optical depth contrast to the 6.7 keV backlighter x-rays. We recorded backlit images such as those shown earlier in Fig. 1b.

Fourier analysis was used to extract the modulation amplitude at each time. We measured the initial Cu foil contrast on a separate Nova shot at the backlighter energy of 6.7 keV. The Fourier amplitude of the 50 μm wavelength modulation normalized to the initial contrast is plotted in Fig. 5a for the cases of Cu with the shaped low isentrope drive, and in Fig. 5b for the case of the single strong shock using a square laser pulse. Overlaid on Fig. 5a, we have

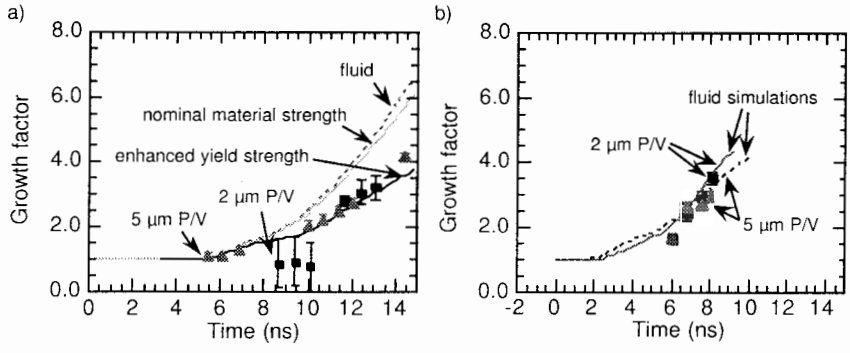

Figure 5. Instability growth factors as a function of time for a 50 μm wavelength modulation at the embedded plastic/Cu interface for the cases of a) the low isentrope drive, and b) the square pulse drive. Simulations for an initial 5 μm peak-valley are shown in Fig. 5a, and simulations for both 2 μm and 5 μm are shown in Fig. 5b.

plotted the growth of the instability due to the low isentrope shaped drive modeled for the 50 μm wavelength in three different ways: using a fluid model (LASNEX with no material strength included) including a material strength package in LASNEX as described by Steinberg *et al*, and by artificially enhancing the material yield strength by a factor of 30. The fluid simulations done for the 5 ns square laser drive are shown in Fig. 5b.

When Cu is shock compressed by the low isentrope drive, the instability growth is reduced relative to the fluid calculation. In contrast, the instability growth (with no material strength included) is in agreement with the fluid modeling when the sample is compressed with a single strong shock.

Incorporating the material strength model described by Steinberg *et al* into the LASNEX simulations results in an instability growth history that is not very different than the fluid case. Enhancing the yield strength by 30 $\times$, however, leads to a reduced growth, in better agreement with the data. Note that artificially scaling the yield strength in this way may be a crude approximation to a strain-rate dependence of the yield strength [2].

5. Summary

We have measured the growth of a Rayleigh-Taylor unstable interface to demonstrate material strength effects in a shocked metal foil. An x-ray drive was used to shock compress and accelerate Cu foils at about 3 Mbar. The reduced growth of an embedded modulated interface relative to fluid simulations may be due to material strength. Enhancing the yield strength for copper by a factor of 30 in the Steinberg-Guinan model shows a similar effect.

Acknowledgement. We acknowledge the technical support of the Nova Operations and Target Fabrication groups. G. Chandler and R. Olson of Sandia characterized the drive from a large hohlraum using the 5 ns square laser pulse. G. Glendinning provided useful discussions throughout. This work was performed under the auspices of the U.S. Department of Energy by the Lawrence Livermore National Laboratory under contract No. W-7405-ENG-48.

References

[1] Campbell EM *et al.*, Rev. Sci. Instrum., 57, 2101, (1985).
[2] Colvin JD *et al.*, these proceedings.
[3] Steinberg DJ *et al.*, J. Appl. Phys., 51, 1498, (1980). material strength
[4] Glendinning SG *et al.*, SPIE Proceedings, 2523, SPIE, Bellingham, WA, 29-39, (1995).
[5] Budil KS, *et al.*, Rev. Sci. Instrum., 67, 485, (1996).
[6] Moriarty JA, High Pressure Research, 13, 343, (1995); and in Shock Waves in Condensed Matter, Gupta, Y. M., Ed., Plenum, New York, 101, (1986).
[7] We obtained this drive courtesy of R. Olson of Sandia National Laboratory.
[8] Kornblum HN *et al.*, Rev. Sci. Instrum., 57, 2179, (1986).
[9] Lindl J, Phys. Plasmas, 2, 3933, (1995).
[10] Zimmerman GB and Kruer WL, Comm. Plasma Phys. Controlled Fusion, 11, 51, (1975).

On the Gas-Liquid Interface Shape Effects on Turbulent Mixing

M.D. Kamchibekov, E.E. Meshkov, N.V. Nevmerzhitsky and E.A. Sotskov
Russian Federal Nuclear Centre - Institute of Experimental Physics
Prospect Mira 37, 607190, Sarov, Nizhny Novgorod Region, Russia

Abstract: The paper summarizes experimental studies of turbulent mixing development at an unstable surface of the pressurized gas-driven liquid layer. The layer had been made of a jelly of water-solved gelatin, so it would behave like liquid even at smaller pressures *(~10 atm)*. The studies considered plane versus cylindrical cases. Each of the three cases in question: *(a)* cylindrical shell expansion, *(b)* plane case, *(c)* cylindrical shell convergence-show the turbulent mixing zone *(TMZ)* to have different development. The zone growth rate would be increasing from *(a)* to *(c)* case. To account for this *TMZ* behavior, a numerical model is proposed which represents in general the *TMZ* front development in a plane geometry.

1. Introduction

When a liquid-liquid interface is moving with an acceleration directed normally to it from the lighter to heavier liquid, it will show instability *(RT-instability)* [1, 2]. Given initial perturbations evolving at this interface, this would develop into a turbulent mixing zone [3]. Some experiments [4, 5, 6, 7, 8] were accomplished to look at how the *TMZ* develops at the unstable gas-liquid interface in a plane case. Given constant acceleration g, the TMZ is moving into the liquid as $h \approx aAgt^2$. Experimentally [4, 5, 6], α=0.05-0.07. From data of [7, 8], this value may vary between 0.06-0.12 due to wave processes. Jelly technique [9] is what allows flows such as this to be investigated not only for plane but also cylindrical case [10]. This technique is based on the idea that jelly of water-solved gelatin, its concentration C$\leq$ 4.4%, can be used for a liquid (cylindrical shell) model. When this model is driven by compressed gasdynamic at about 8-10 *atm* of pressure, the jelly would show behavior similar to that of incompressible liquid. Numerical studies were performed on the instability development in a plane geometry using the model [12, 13] assuming that the *TMZ* in this case will have its linear measures dependent on one and the same quantity, i.e the average wavelength $\langle\lambda\rangle$ that varies in time as $\langle\lambda\rangle \sim gt^2$ and is independent of the initial spectrum. Comparison front evolution predictions by the model [12, 13] against experimental data and numerical *TMZ* simulation for an arbitrary complex initial spectrum [12] has shown reasonable agreement.

2. Experimental techniques

The following procedure was used to accelerate plane jelly layers with compressed gasdynamic: there were two compartments one each on both sides of the jelly layer placed in a tightly sealed acceleration channel of 40x40 cm sectional area, which had been filled with equally pressurized gasdynamic (helium). The layer thickness was 28 mm, with the gasdynamic pressure being initially $P \cong$ *17 atm*. Then, the channel was dispressurized rapidly on its one end, so that the gasdynamic from under the layer would flow out to the atmosphere, and the gasdynamic

More information - Email: otd03_2305@spd.vniief.ru

pressure above the layer thus made the latter accelerate vertically downwards. As it was accelerating, the layer would have its lower interface stable, and the upper-unstable. (The experimental geometry is more detailed in [7]). Convergence of the cylindrical jelly shell was provided by pressurized helium using an experimental setup as shown in Fig.1. The shell had been placed in between two transparent plane plates supported by the setup frame. The *A*

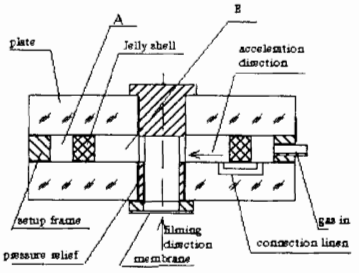

Figure 1. Schematic of experimental setup for cylindrical shell convergence

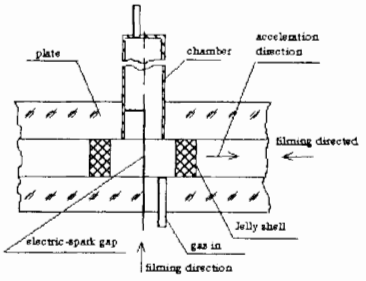

Figure 2. Schematic of experimental setup for cylindrical shell divergence

and *B* compartments of the experimental setup were filled with equally pressurized gas. When the membrane got broken, the gasdynamic from the space *B* would flow through the pressure relief line out to the atmosphere, and the gasdynamic of *A* compartment would force the shell to accelerate towards the center. So, it was the outer shell boundary showing instability. Geometrically, the shell had outer radius of $R \cong 70$ mm, inner radius of $r \cong 58$ mm, height of $b \cong 16$ mm, and initial gasdynamic pressure of $P \cong 18$ *atm.* Divergence of the cylindrical jelly shell was provided by explosion products *(EP)* pressure of the mixture C_2H_2+2.5O_2 using the experimental setup illustrated by Fig.2. Same as in the former case, the shell was placed between two transparent and plane plates tightly secured one relative to another. Both the inner shell and chamber spaces had been filled with gaseous explosive mixture (*GEM*). The mixture was detonated from the electric spark gap. The *EP* pressure made the shell accelerate expanding out to the atmosphere, with the shell other surface being thus stable and the inner unstable. Geometrically, the shell had $R \cong 39$ m, $r \cong 18$ mm, $b \cong 30$ mm, and the equilibrium *EP* pressure estimated cases all $P = 13.5$ atm. The above - mentioned cases all have plane layers and cylindrical shells made of jellies using gelatin solved in water at the concentration

of C $\cong$ 3.6%. This jelly has compression strength below 0.1 kg/cm^2 [10]. The models had small-scaling perturbations specified as tetrahedral pyramids (of the amplitude $\alpha_o \cong 0.15$ mm and wavelength $\lambda_o \cong 0.5$ mm) on their unstable surface. These perturbations growing with

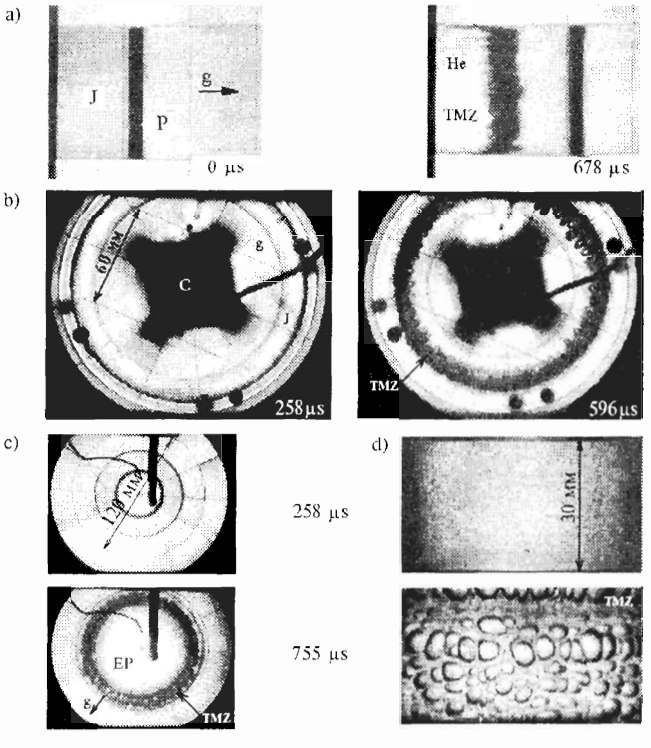

Figure 3. Turbulent mixing development at the unstable interface of *a)* plane layer, *b)* convergent cylindrical shell, *c)* diverging cylindrical shell-axially projected, *d)* diverging cylindrical shell- frontally (see Fig.2). Notation: *J* - layer (shell) of jelly; *EP* - explosion products; *He* - pressurized helium; *TMZ* - turbulent mixing zone; *P* - plywood; *C* - pressure relief; *g* - shell acceleration direction. Time since initial motion of layer (shell)

the layer (shell) acceleration resulted in the occurrence and development of *TMZ*. The model accelerations and *TMZ* evolution were visualized using high-speed filming.

3. Experimental results

Figs.3 a, b, c and d show individual filming shots from experiments for turbulent mixing growth at the unstable surface of a plane layer, and of the convergent and divergent cylindrical shells, respectively. Fig. 4 includes *h(S)* relationships for the experiments mentioned, where h is the averaged penetrating depth of the lighter (*EP*, gas) to heavier (jelly) substance, and S is the distance covered by the interface. We can see from the plotter relationships, that the rate of *TMZ* penetration into the jelly is significantly different from one main flow geometry to another for $S > 7$ mm; the highest penetration depth observed is for convergence, the lowest -

for expansion case; the rate of *TMZ* penetration into jelly is of intermediate value.

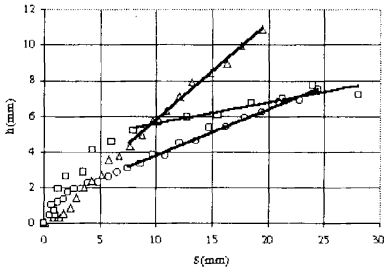

Figure 4. Lighter-into-heave r penetration depth h as a function of S, the interface - covered distance. Notations: o - plane layer, △ - cylindrical convergence, □ - cylindrical expansion

4. Numerical model

Refs. [12, 13, 14] contain studies of multimodal perturbations at the plane interface of two media under the conditions accounting for *RT* instability. A statistical model for bubble coalescence [12, 13, 14] that simulates the *TMZ* front evolution in a heavier liquid, was used to show that whatever initial perturbations spectrum would develop with time into the self-similar, thus represented by a cluster ("package") of harmonics to occur in the neighborhood of the mean wavelength $\langle\lambda\rangle$, which would grow in time. It was found possible in this case to describe the bubble front development in terms of the simple model [12, 13, 14] that incorporates the following two equations:

$$\frac{dh}{dt} = \gamma\sqrt{g\langle\lambda\rangle} \tag{1}$$

$$\frac{d\langle\lambda\rangle}{dt} = \beta\sqrt{\frac{g}{\langle\lambda\rangle}}\langle\lambda\rangle \tag{2}$$

where h is the bubble penetration into the heavier liquid (front depth); g - acceleration; γ and β - constants. Refs. [12, 13] used the constants for two-dimensional bubbles: γ =0.23 and β = 1. It follows from (1-2) that $h = \frac{\gamma}{\beta}\langle\lambda\rangle$ and

$$\frac{dh}{dt} = \sqrt{\gamma\beta hg} \tag{3}$$

For largest times and constant g, h varies as $h \to \frac{\gamma\beta}{4}gt^2$, where $\frac{\gamma\beta}{4} = 0.06$ for plane geometry and two-dimensional bubbles (γ=0.23; β=1). Let us try to extend the above under standing [12, 13, 14] of how the *TMZ* front is developing in a plane geometry to a case where the unstable interface of two media is of cylindrical shape having a considerably large radius R_0, and the harmonics responsible for perturbations growth have quite a high number. The assumption we make is that eq.(2) describing the so-called "reverse cascade" effect, i.e. the occurrence with time of yet a larger structure at the *TMZ* front, follows the case that the perturbations energy E_0 of the liquid flow ahead of the *TMZ* front is growing, i.e.

$$E_0 = \int\limits_{(z>h)} \frac{\rho\overrightarrow{u}^2}{2}dv \sim W_f S_f\langle\lambda\rangle \sim \langle\lambda\rangle^2 S_f \tag{4}$$

where: $\overrightarrow{u}$- is the velocity flow of perturbed flow;
ρ - heavier liquid density;
W_f - perturbation energy density at the front; $W_f \sim g\langle\lambda\rangle$;
S_f - front area.
As follows from (4) for plane case,

$$\frac{dE_0}{dt} = 2\beta\sqrt{g/\langle\lambda\rangle}E_0 \tag{5}$$

We would consider the following equations as basic definitions of the mixing front evolution R_f in a cylindrical geometry:
1) simulated (of scaling)

$$|R_f - R_0| \equiv h = \frac{\gamma}{\beta}\langle\lambda\rangle \tag{6}$$

2)"reverse cascade" equation for perturbations energy E_0 (5), incorporating the same γ and β constants as for plane geometry. Given relationships (4, 6) we can obtain from eq. (5)

$$\frac{d\ln h^2 S_f}{dt} = 2\sqrt{\frac{g(\gamma\beta)}{h}} \tag{7}$$

It would be suitable to include a new variable, which is the normalized front depth.

$$\tilde{h} = h\sqrt{\frac{S_f(t)}{S_f(0)}}, \tag{8}$$

Then, we obtain for $\tilde{h}$ the equation

$$\frac{d\tilde{h}}{dt} = \sqrt{\gamma\beta\tilde{h}g}\left(\frac{S_f(\tau)}{S_f(0)}\right)^{1/4} \tag{9}$$

which differs from (3) by $\left(\frac{S_f(\tau)}{S_f(0)}\right)^{1/4}$, the factor relating weakly of the system geometry.

5. Research results and discussion

Given in Fig.5 are relationships for the interface S motion with t^2 for plane and cylindrical cases, that illustrate the accelerated motion pattern. From this figure, these relationships are linear for $t^2 \geq 0{,}1$ ms^2, i.e. the case for approximately constant acceleration. To evaluate the acceleration g in these tests, the experimental data processing for $t^2 \geq 0{,}1$ ms^2, was done using least-squares technique. Given the specific relationships of *TMZ* front depth versus S as obtained in Section 2, it may be useful to consider the value $\sqrt{h}$ as dependent variable and $\tau = \sqrt{g}t$ as independent. Fig.6 shows the relationships $\sqrt{h} = f(\tau)$ for three tests in plane geometry. The experimental data were approximated by a linear function such as $\sqrt{h} = a + b \cdot \tau$, where a and b quantities were found by least-squares technique. As it has been found, $\left(\sqrt{h}\right)_{cp} = 0.75 + 0.30 \cdot \tau$, mm$^{1/2}$. From plane experiments data, $h \sim 0.09gt^2$. Fig.7 presents experimental results for cylindrical geometry as $\sqrt{\tilde{h}} = f(\tau)$, together with the linear relationships representing *TMZ* growth in plane geometry for different initial perturbations values (when $\tau = 0$), and also the linear approximation of experimental data of Fig.6 - line 1. The reduced front depth $\tilde{h}$ in cylindrical experiments as defined by (8), was to be found from

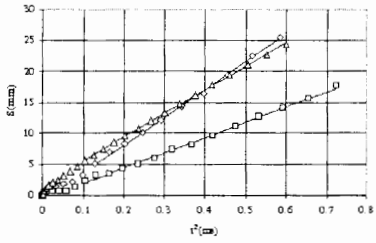

Figure 5. $S(t^2)$ relationship. Notation: $\Diamond$ - cylindrical expansion, $\Box$ - cylindrical convergence, $\triangle$ - plane geometry

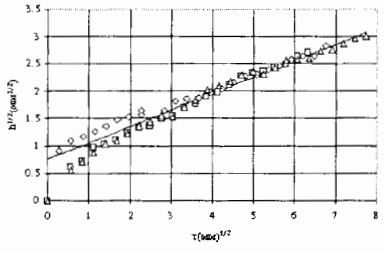

Figure 6. Plane-case relationships $\sqrt{h} = f(\tau)$. Notation: $\Diamond$, $\Box$, $\triangle$ - experimental points, - linear approximation on three tests

experimental data by the following formulae:
expansion case: $\widetilde{h} = h_{\exp}\sqrt{\frac{R(t)+h_{\exp}}{R(0)}}$; convergence: $\widetilde{h} = h_{\exp}\sqrt{\frac{R(t)-h_{\exp}}{R(0)}}$.

From the data observed in Fig.7, the slopes for relationships $\sqrt{\widetilde{h}} = f(\tau)$ obtained in cylindrical experiments, agree with plane test slopes for $\tau \geq 4$ mm$^{1/2}$ in convergence and $\tau \geq 3$ mm$^{1/2}$with expansion. Thus, one of the conclusions from the model suggested in Section 3 to account for mixing fronts in cylindrical geometry, that reduced fronts $\widetilde{h}$ are little dependent on the front area variations with time, is consistent with experimental data.

6. Conclusions

The difference in time history between *TMZ* fronts in cylindrical and plane cases is primarily attributed by the proposed model to the front vs. time variation effect which is to be accounted in the model by including the reduced quantities $\widetilde{h} = h\sqrt{S_f}$ which by themselves do not much depend on this effect. The authors are thankful to V.A.Zhmailo, V.P.Statsenko, V.E.Neuvazhayev for valuable discussion of the results, and to E.D.Senkovsky, M.V.Bliznetsov, O.L.Zharkova, Z.V.Sokolova, N.N.Chukhontseva and T.V.Korableva for their assistance in the paper preparation. The study has been performed under the ISTC Project 029.

References

[1] Rayleigh Lord, Proc.London Math. Soc., 14, 170, (1883).
[2] Taylor GI, The instability of liquid surfaces when accelerated in a direction perpendicular to their planes, I. Proc. Roy. Soc., A201, 192, (1950).

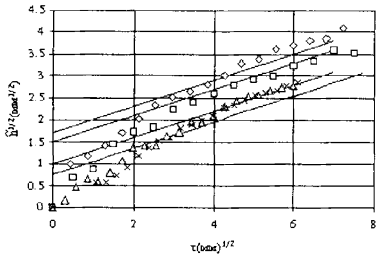

Figure 7. Cylindrical - case relationship $\sqrt{\bar{h}} = f(\tau)$. Notation: $\diamondsuit$, $\square$, - two experiments for expanding cylinder case; $\triangle$, x - experiments cylinder convergence e case; 1 - linear approximation on three plane tests (Fig.6), - plane experiments ranging in initial perturbation values (for $\tau = 0$)

[3] Belen'kii SZ, Fradkin ES, Theory of turbulent mixing, in Russian, Tr. FIAN AS USSR, 29, (1965).

[4] Read KJ, Experimental investigation of turbulent mixing by Rayleigh-Taylor instability, Physica D12, 45, (1984).

[5] Youngs DL, Three-dimensional numerical simulation of turbulent mixing by Rayleigh-Taylor instability, Phys. Fluids A, 3, 5, 1312, (1991).

[6] Kucherenko Y, Shibarshov L, Chitaikin V, Balabin S and Pylaev A, Experimental study of the gravitational turbulent mixing self-similar mode, Proc. of the 3rd IWPCTM, Abbey of Royaumont, France, June 17-19, (1991).

[7] Meshkov EE, Nevmerzhitsky NV, About turbulent mixing dynamics at unstable boundary of liquid layer, accelerated by compressed gas, Proc. of the 3rd IWPCTM, Abbey of Royaumont, France, June 17-19, (1991).

[8] Nevmerzhitsky N, Meshkov E, Ioilev A, Zhidov I, Pylaev I and Sokolov S, Wave processes effect on the dynamics of turbulent mixing at liquid layer surface accelerated by compressed gas, Proc. of the 4^{th} IWPCTM, Cambridge, England, Edited by P.F. Linden, D.L. Youngs & S.B. Dalziel, 112, (1993).

[9] Volchenko OI, Zhidov IG, Klopov BA, Meshkov EE, Popov VV, Rogachev VG and Tolshmyakov AI, Method to modelnonstationary flows of incompressible liquid, in Russian, A.C.1026154, bulletin of inventions, 24, (1983).

[10] Meshkov E, Nevmerzhitsky N, Rogachev V and Zhidov I, Turbulent Mixing Development Investigation with Converging jelly Rings, Proc. of the 4^{th} IWPCTM, Cambridge, England, Edited by P.F. Linden, D.L. Youngs & S.B. Dalziel, 578, (1993).

[11] Volchenko OI, Zhidov IG, Meshkov EE and Rogachev VG, Growth of confined perturbations on instable interface of accelerated liquid layer, in Russian, Letters to ZhTF, 15, 1, 47-50, (1989).

[12] Alon U, Hecht G, Mukatel D and Shvarts D, Phys. Rev. Lett., 18, 72, (1994).

[13] Alon U, Hecht G, Ofer D and Shvarts D, Phys. Rev. Lett., 4, 74, (1995).

[14] Shvarts D, Alon U, Ofer D, McCrory RZ and Verdon CP, Phys. Plasmas, 2, 6, (1995).

Simple Model for Description of the Geometry Influence of the Accelerated Shell for Turbulent Mixing of its Surface with Gas

M.D. Kamchibekov, B.P. Tikhomirov and V.A. Zhmailo
Russian Federal Nuclear Centre - Institute of Experimental Physics
Prospect Mira 37, 607190, Sarov, Nizhny Novgorod Region, Russia

Abstract: The report presents the approximated method for discount of influence of geometry (plane, cylindrical or spherical) to evolution of turbulent mixing zone of different gases (or liquids) near accelerated interface between them. The results of calculations by this method are compared with corresponding experimental data.

1. Introduction

There is the great number of experiments (liners, targets for ICF et al.), where instability of the interface of accelerated shell with gas surrounding arrives. Evolution of such instability at the linear stage was studied sufficiently good both for the plane geometry [1, 2] and for cylindrical and spherical geometry [3, 4]. The results of these works allow, in part, to get dependence of evolution increment for unstable mode versus the shell radius: the shell extension leads to deceleration of the instability growth, and compression - to acceleration in comparison with the plane case. Problem of non-linear stage is significantly complicated, that greatly prevents estimation of the influence of geometry to the velocity of evolution of perturbations. This paper presents one of possible ways for its solving. It is based on the using of semi-empirical approach [5]. In spite of appearance of the great number of more complicated and semi-empirical models during last years this approach (approximation of the "turbulent" diffusion) seems the most suitable for solving our problem because of its simplicity and clearness.

2. Setting of the problem. The initial equations

Let's examine the shell with thickness δR and with radius R, considering it thin ($\delta R \leq R$) and incompressible. Let's consider the motion of the shell given. There are possible two variants: either this shell boundary with the same one (but different in density), or it borders with gas. At the latter case let's consider the motion of the gas adiabatic and uniform. Depending of sign of acceleration either outer or inner border of the shell appears unstable. The evolution of density profiles near the interface, when $\gamma t \geq 1$ let's describe as "turbulent" diffusion. Let's assign: ρ_o - density of the shell observed, ρ_1 - density of gas (or the other shell). $\rho = \rho_o + \rho_1$. With the help of [5] let's write:

$$\frac{d\rho}{dt} = -div\,\vec{j} + Q\,(r,t) \qquad (1)$$

where $Q = 0$ for $\rho_1 = \text{Const}$ (uncompressed shell) $Q = -\frac{V+1}{R}\ddot{R}\rho C_1$ for gas.
Here , $C_1 = \frac{\rho_o - \rho(t,r)}{\rho_o - \rho_1(t)}$, $\vec{j_t}$ - is mass turbulent flow. In the observed one-dimensional geometry

More information - Email: otd03_2305@spd.vniief.ru

$\overrightarrow{j_t} = (j_t, 0, 0)$.
Following [5]

$$j_t = -D_t \frac{\partial \rho}{\partial r} \tag{2}$$

$$D_t = l_t V_t \tag{3}$$

where - D_t coefficient of diffusion, V_t^2 - turbulent energy, l_t - "length of the distance passed" [5]. By using V_t the balance equation for turbulent energy [5] one can obtain:

$$V_t = l_t \left(-q \frac{\partial \rho}{\partial r} \frac{1}{\rho} \right)^{1/2} K \tag{4}$$

where coefficient K is expressed via semi-empirical constants, used for deduction of (4) in the balance equation for turbulent energy ($K \sim 1$, see below). In this paper (similar to [5]) the simplest Prandtl relation is used for l_t

$$l_t = \alpha L(t) \tag{5}$$

where $L(t)$ - width of turbulent mixing zone (TMZ). The diffusion equation, obtained when inserting (2) into (1), is supplemented by corresponding initial and boundary conditions.

3. Approximated (quasi-self-similar) solving

For further investigation it is convenient to introduce the Lagrangian coordinates r_o. When using these coordinates and the assumption that within the mixing zone $r(r_o, t)/r_0 = \frac{R(t)}{R_o}$, where $R(t)$ - is current radius of the shell, we can write the equation (1) as follows:

$$\frac{d\rho}{dt} = \frac{1}{r_o^v} \frac{\partial}{\partial r_o} \left[r_o^v D(r_o, t) \frac{\partial \rho}{\partial r_o} \right] \tag{6}$$

where $D(r_o, t) = L^2(t) \mathbf{Re} \left[\frac{1}{\rho} \frac{\partial \rho}{\partial \mathbf{r_o}} \ddot{\mathbf{R}} \right]^{1/2} \left(\frac{\mathbf{R}}{\mathbf{R_o}} \right)^{5\nu/2} \mu.//$ Here $\mu = \alpha^2 K$; $v = 0, 1, 2$ - is the size of the problem. Assuming $L(t) << R(t)$, for searching for the solving (6) it is naturally to use "quasi-plane" self-similar approximation. For this purpose, let's introduce into (6) variable [5]:

$$\xi = \frac{r_o - R}{L_o(t)} \tag{7}$$

where R_o - is coordinate of unstable boundary, $L_o(t)$ - thickness of turbulent mixing zone in Lagrangian variables, that is $L_o(t) = L_o^{(0)} - L_o^{(1)}$.
Here $L_o^{(0,1)}$ - are Lagrangian TMZ boundary in the layers "0" and "1" correspondingly. Using the variable ξ, let's write the equation (6) as follows:

$$-\frac{1}{G(t)} \frac{\partial \rho}{\partial t} \Big|_{\xi = Const} + \frac{1}{x} \xi \frac{d\rho}{d\xi} + \frac{dS}{d\xi} + \frac{\varepsilon v}{1 + \xi \varepsilon} S = 0 \tag{8}$$

where

$$\chi = \dot{L}_0 / L_0 G(t), \qquad S = \left(\frac{1}{\rho} \frac{d\rho}{d\xi} \right)^{1/2} \frac{d\rho}{d\xi}, \tag{9}$$

$$\varepsilon = \frac{L_0(t)}{R_0}, \qquad G(t) = L^2(t) \left[\ddot{R} \left(\frac{R}{L_0 R_0} \right)^5 \right]^{1/2} \mu \tag{10}$$

Neglecting the members $\sim \varepsilon$ in equation (10), and $\frac{\partial \rho}{\partial t G(t)}$ we can obtain (while $\chi = Const$) the equation, similar to [5]:

$$\xi \frac{d\rho}{d\xi} + \chi \frac{dS}{d\xi} = 0 \tag{11}$$

with corresponding boundary conditions). The approximated method of this equation solving (permitting to clear its qualitative features) is described in Appendix. The result can be written as follows:

$$L(t) = L_0(t) F(t) \tag{12}$$

where

$$\sqrt{L_0(t)} = \sqrt{L_0(0)} + \sqrt{\eta} \int_0^t \sqrt{\frac{\ddot{R}(t)}{F(t)}}\, dt, \tag{13}$$

where

$$\eta = (\mu/2\chi)^2, \left(\frac{1}{2\chi}\right)^2 = 0.91 \cdot 10^3 \cdot \frac{(a^2-1)(a+1)^2}{q(a)}, \tag{14}$$

$$q(a) = (2a+1)^2 + (2a+1)(a^2-1) + \frac{2}{7}(a^2-1)^2 \tag{15}$$

Here $a = (\rho_o/\rho_1)^{1/3}$, function $F(t)$ describes the kinematic connection between L and L_0. For instance, at the case of mixing at the interface of two uncompressible liquids

$$F(t) = (R_0/R(t))^v \tag{16}$$

In doing so mixing zone width in the shell $L_0^{(0)} = L_0 \cdot \xi_0$, where ξ_0 self-similar coordinate of mixing zone in the $\ll 0 \gg$ shell

$$\xi_0 = \frac{a+2}{3(a+1)} \tag{17}$$

The corresponding coordinate in layer $\ll 1 \gg$: $\xi_1 = \xi_0 - 1$: Profiles of the functions searched for ρ and V_t^2 are determined by relations

$$\rho/\rho_1 = \left(1 + \frac{2}{3}\left(\frac{a-1}{9\chi}\right)^2 \cdot Q(\xi)\right)^{3/2} \tag{18}$$

$$V_t^2 = \eta L(t) \cdot \ddot{R} \left[\frac{2(a-1)}{9\alpha} \Pi(\xi)\right]^2 \tag{19}$$

Here $Q(\xi, a)$ and $\Pi(\xi, a)$ are algebraic functions, ξ, a (see Appendix). Comparision of the (12-19) with exact (numerical) solution of (11) shows their satisfactory agreement and allow us to use those formulas for $v \neq 0$ and $R = R(t)$ Fig.1 present the calculation results $L(t), (v = 1)$ illustrating effect of geometry. These figure adduce (for convenience) function $f(t, v) = \sqrt{\frac{L(v,t)}{L(0,t)}} - 1$ for the cases of positive acceleration (outer shell-gas border is unstable, curve 1) and of negative acceleration (inner shell-gas border is unstable, curve 2). As evident, in the dependence $L = L(v, R)$ there is same tendency, that reveals at the linear stage of instability evolution: decreasing of the radius of unstable surface leads to growth acceleration $L(t)$ and the reverse. One can see the interesting example of shell dynamics and curvature effect on the evolution: the case, when this effect leads to decreasing of $L(t)$ in spite of the border instability $L(t)$. Fig.2 shows this example. We observe here the case of the border between two incompressible shells moving at constant acceleration $g = 1$ and with initial velocity $V_0 = -1$.

4. Comparison of calculation results with experimental data

The paper [6] presents the results of experimental study of TM evolution at the unstable boundary of accelerated jelly layer. There were studied plane and cylindrical cases, and was obtained that in the plane geometry the observed front of gas bubbles $h(v=0,t)$ behaves as

$$\sqrt{h(v=0,t)} = a + b \cdot \tau \tag{20}$$

where $\tau = \sqrt{g}t$, a and b are measured constants [6] (The largest part of trajectory the shell moved with constant acceleration.) Using (13) for $v=0$, we can write

$$b = \sqrt{\eta \xi_0} \tag{21}$$

where (according 17) $\xi_0 \approx 1/3$ for $a \gg 1$. In order to determine the coefficient μ in relation $D(r_0,t)$ one can use the results of [7] of study of evolution of turbulent gravitation mixing zone (when $a = (3)^{1/3}$) by direct 3D numerical simulation. Determination χ by (15) and substitution of obtained value $\mu = \alpha^2 k$ into (14),(21) gives $b = 0.38$ instead of $b = 0.30 \pm 0.05$ in the experiment. The exceeding of calculated value b above experimental one appears to be explained by difference of jelly, used in experiments [6], and perfect liquid. Comparison of calculated and measured values $h(t,v)$ for cylindrical geometry ($v=1$) seems to be the most interesting. According to (13), in this case

$$h_1(t) = \left(\frac{R_0}{R}\right)^{1/2} \left[\sqrt{h_1(0)} + b\int_0^\tau \left(\frac{R}{R_0}\right)^{1/2} d\tau'\right]^2, (h_1 \equiv h(v=1,t)) \tag{22}$$

where b is value, obtained from the experiments with $v=0$. One can calculate functions $h_1(t)$ for divergence ($g<0$) case and convergence of the shell in gas ($g>0$) with the help of values $R_0, h_1(0)$ and g, obtained from experiments, and using the fact, that when $g \neq g(t)$ $h_1(t)$ is expressed by elementary functions. These values are shown at Fig.3 and 4 as solid curves. There are also plotted the corresponding experimental data [6] (For fig.3 $R_0 = 19mm$, $g = +90mm/ms^2$, for Fig.4 $R_0 = 70mm, g = -50mm/ms^2$ and $67mm/ms^2$). Comparison of these data with calculated ones allows to conclude that relation (13) reflects not only qualitative tendency of shell motion dynamics and curvature effect on TMZ evolution, but also gives acceptable quantitative agreement with the experiment.

5. Conclusion

The basic results of given work are the following:

- Geometry effect on TMZ evolution reduces to deceleration of its growth when shell divergence ($g>0$) and acceleration when convergence ($g<0$)
- This effect depends little on value of different density
- There is satisfactory agreement between measured and calculated values of width of gas bubble front zone of penetration into accelerated shell for plane and cylindrical geometry.

In conclusion the authors are grateful to Dr. V.P.Statsenko for useful discussions and N. Kotljarova for help in preparing this paper.

6. Appendix. Approximated solving of the equation for TM

Initial equation

$$\xi\frac{d\rho}{d\xi}+\chi\frac{d}{d\xi}\left[\frac{1}{\rho^{1/3}}\left(\frac{d\rho}{d\xi}\right)\right]^{1/3}=0 \tag{23}$$

with border conditions

$$\rho=\rho_1,\quad \frac{d\rho}{d\xi}=0\quad \xi=\xi_1\quad \rho=\rho_2,\quad \frac{d\rho}{d\xi}=0\quad \xi=\xi_2 \tag{24}$$

where $\xi_2-\xi_1=1,\chi$ - unknown parameter (it is considered that $\rho_1<\rho_2$).
Let's introduce $f^2=\frac{1}{\rho^{1/3}}\left(\frac{d\rho}{d\xi}\right)$, then from (23) follows:

$$f=-\frac{1}{3\chi}\int\limits_{\xi_1}^{\xi}\xi'\rho^{1/3}(\xi')d\xi' \tag{25}$$

Let's consider in (25) $\rho^{1/3}=\rho_1^{1/3}[1+x\delta a]$, where $x=\xi-\xi_1$, $\delta a=a-1$, $a=\left(\frac{\rho_2}{\rho_1}\right)^{1/3}$. When substitution of this expression into (25) allows (with using of (24)) to obtain explicitly $f(f=x,a)$, $\xi_{1,2}$. After that from condition

$$\int\limits_{\xi_1}^{\xi_2}f^2d\xi=\frac{3}{2}\left[(\rho_2/\rho_1)^{2/3}-1\right] \tag{26}$$

one can obtain **x** (see expression (15)), $\rho(\xi)$ and $V_t^2(\xi)$:

$$\frac{\rho(\xi)}{\rho_1}=\left[1+\frac{2}{3}\left(\frac{\delta a}{gt\chi}\right)^2Q(\xi)\right]^{3/2} \tag{27}$$

$$V_t^2/L(t)g\eta=\left[\frac{2\delta a}{ga}\Pi(\xi)\right]^2 \tag{28}$$

where

$$Q(\xi)=x^3\left[\frac{x_1^2}{3}-x\frac{x_1(x_1+1)}{2}-x^2\frac{(x_1+1)^2+2x_1}{5}-x^3\frac{x_1+1}{3}+\frac{x^4}{7}\right] \tag{29}$$

$$\Pi(x)=\frac{x(1-x)(x-x_1)}{1+x\delta a} \tag{30}$$

where

$$x_1=\frac{3\xi_1}{\delta a},\xi_1=-\frac{2a+1}{3(a+1)} \tag{31}$$

References

[1] Lord Rayleigh, Proc. London Math. Soc., 14, 170, (1883).
[2] Taylor GI, The instability of liquid surfaces when accelerated in a direction perpendicular to their planes, Proc. Roy. Soc., A201, 192, (1950).
[3] Chandrasekhar S, Hydrodinamic and Hydromagnetic Stability, Clarendon Press, Oxford, (1961).

[4] Gamaly EG, Rozanov VB, Samarsky *et al.*, Hydro-dynamic stability of spherical laser targets compression, JETP, 79, 2980, 459-470, (1980).

[5] Belen'ky SZ, Fradkin ES, Turbulent mixing theory, Proc. of FIAN after Lebedev, 29, 207-250, (1965).

[6] Kamchibekov MD, Meshkov EE, Nevmerzhitsky NV, Sotskov E, Turbulent mixing at the cylindrical gas-liquid interface, Preprint RFNC VNIIEF, 46-96, Sarov, (1996).

[7] Stadnik AL, Statsenko VP, Yanilkin YV, Zhmailo VA, Direct numerical simulation of gravitational turbulent mixing, Proc. of the 5^{th} Workshop on Compressible Turbulent Mixing, 392-401., Ed. R. Young, D. Glimm, B. Boston, (1995).

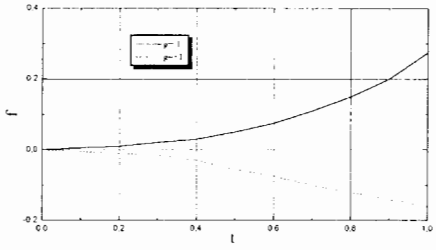

Fig.1. Time dependence of the relative ZTM width for the cylindrical shell.

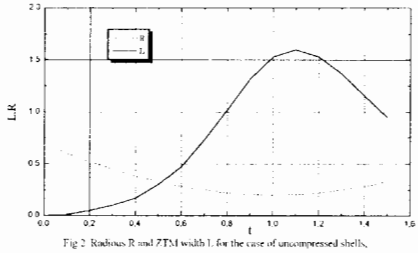

Fig.2. Radiuses R and ZTM width L for the case of uncompressed shells,

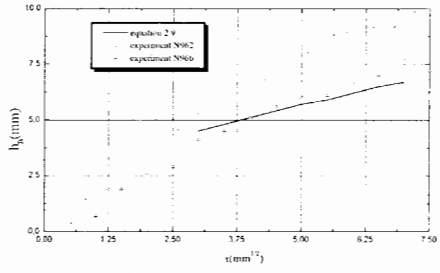

Fig.3. Width of bubble penetration zone into cylindrical shell. Expansion case.

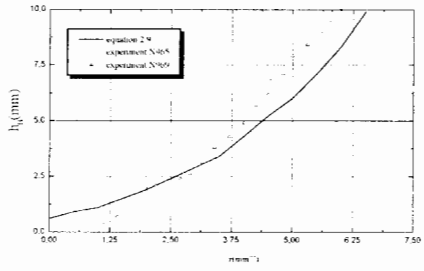

Fig.4. Width of bubble penetration zone into cylindrical shell. Squeezing case.

Study of Point Blast Wave Instability in Numerical Experiment

V.M. Ktitorov and V.Y. Meltsas
Russian Federal Nuclear Centre - Institute of Experimental Physics
Prospect Mira 37, 607190, Sarov, Nizhny Novgorod Region, Russia

Abstract: The direct calculations of blast wave in a uniform ideal gas are carried out using 2D hydrodynamic code. Small blast wave perturbation evolution is studied. The following cases are considered: a)$\gamma = 1.15, n = 16$, and b)$\gamma = 1.06, n = 64$ both cases corresponding to the blast wave being unstable. The results of computations of the linear stage of perturbation evolution agree closely with self-similar theory results. It is found that the self-similar regime of perturbation evolution is formed in a short time in which shock front radius increases two to for times. The instability of the blast wave in the considered cases is demonstrated. The results of computations of the non-linear stage of perturbation evolution show that the cumulative jet is predominantly formed in the end of a single perturbation evolution. This jet is directed outside the blast center.

1. Introduction

The problem of a search for cases of unstable evolution of expanding shock waves with non-radial perturbations growing in amplitude was formulated long ago but there was no essential progress in this field until the 1980s. The first proof of an existence of the unstable regime of perturbation evolution was published in the paper by E.Vishniac [1] where stability of point blast wave in an ideal gas with a specific heat ratio equal to unity ($\gamma = 1$) was considered. In this case the gas behind the shock front was compressed into a thin dense layer moving under influence of pressure of hot gas in the center region. The calculation of this layer motion could be done simply by application of conservation laws The solution of the point blast wave stability problem in the general case of an arbitrary $\gamma > 1$ was first published by V.Ktitorov [2] and E.Vishniac and D.Ryu [3]. There the point blast wave in a uniform gas of a constant density was considered. The calculation was made in [2] for small blast wave perturbations those being expanded in spherical harmonics. Results of these calculations were as follows:
- small perturbation evolution had an oscillating pattern,
-perturbations with sufficiently large harmonic numbers and sufficiently small values of$(\gamma - 1)$ were growing in amplitude with power dependence on time, the power exponent being a complex number,
- the discovered instability was of the Rayleigh-Taylor type.
There values were found determining the perturbation evolution: the increment of perturbation growth (or damping), and the period of oscillations. These values were calculated for a large number of sets: harmonic number n and gas specific heat ratio γ The critical value of γ determining the blast wave stability was found too [2, 3]:$\gamma_c = 1.20$. If γ were greater than this value then the blast wave would be stable with respect to perturbations of all harmonic numbers; if $\gamma < 1.20$, on the contrary, there would exist harmonics growing in amplitude. This solution was obtained owing to using in [2, 3] a self-similar approach for calculation of

More information - Email: otd64_0709@spd.vniief.ru

perturbation structure. The physical sense of this approach was in considering an asymptotic regime of perturbation evolution. This regime takes place when time of perturbation evolution is large enough to make the influence of initial conditions negligibly small. The analogy could be made between the role of this solution in describing the perturbation evolution and the role of the well-known Taylor-Sedov solution [4] in describing an evolution of spherically symmetric blasts. Later on there an experimental validation of some calculation results was found [5, 6]: In these experiments energy of laser was used to generate a spherically symmetric blast wave in ideal gas. The value of the gas specific heat ratio g was estimated as 1.15 in [5] and 1.06in [6]. In both these cases blast wave is unstable according to the results of the self-similar stability theory of [2, 3]. The instability region for the considered blast wave stability problem is shown on Fig.1 taken from [7]. The authors of laboratory experiments obtained the following results:
- They observed oscillations of front values of perturbations [5], and so they confirmed the results of self-similar theory of oscillatory pattern of small perturbation evolution.
- They observed the final turbulent stage of perturbation evolution when shock front was completely distorted [6], and so they confirmed the self-similar theory result that blast wave should be unstable in this case. The photograph of the distorted shock front from [6] is shown on Fig.2. However, it should be noted that blast wave instability study in laboratory experiments is a very complicated matter. The severe conditions should be satisfied in the experiment during all time: the pressure in shock wave should remain much greater than the external pressure, the value of γ should remain close to unity (much less than its usual valuesγ˜5/3). The above said explains an interest in 2D computer simulation of the point blast wave pattern. Numerical calculations in this case require a very refined mesh near the front. This is due to the structure of the blast wave: almost entire mass behind the front concentrates in a thin spherical layer. In the case $\gamma = 1.06$ its thickness is about 0.01of shock radius R. In these calculations another feature is represented by severe restrictions on the calculation time step. The restrictions are determined near the explosion center where the sound speed value is high. These two difficulties resulted in that blast wave instability was not previously demonstrated in computer experiments. So we set ourselves a task to do it. The following results were planned to obtain: -to demonstrate blast wave instability in the linear regime of perturbation evolution, -to study the nonlinear regime of perturbation evolution. For this purpose the point blast was numerically calculated using a 2D hydrodynamic code. This code selected the shock wave front and used the 1st order Godunov scheme (See [8]).

2. Blast wave computation

The computation geometry was as follows:
At t=0, the initial pressure was set constant in the center region, and the pressure was equal to zero beyond this region. The central region represented a slightly perturbed sphere with the radius demonstrating a small perturbation proportional to a spherical harmonic. The entire material was an ideal gas with the unit density. Then the computation of the formed blast wave was run till the increase of the shock wave radius was about $10 - 150$ times as large as its initial value. To reduce the number of cells the computations were performed not in the hole space but in a space region bounded by one or two conic surfaces. So at the computation beginning (t=0), the radius $R_0$of the central region (i.e .the region in which the blast energy was given) was slightly perturbed : $R_0 = 1 + \Delta R_0$, where ΔR_0 was proportional to the spherical harmonic Y_{n0} (i.e. to Legendre polynomial $P_n(\cos\theta)$. The following cases were considered:$\gamma = 1.15, n = 16$, and $\gamma = 1.06, n = 64$
$\gamma = \mathbf{1.15}, \mathbf{n = 16}$

Two computations were carried out in this case. The computations were done inside the space region bounded by a cone surface $\alpha = 79.9$ deg, and a plane $\alpha = 90$deg. This region was so chosen that exactly half a wavelength of 16th harmonic was enclosed by the region boundaries. The initial perturbation amplitude was as follows: $\Delta R_0 = 0.01$, and $\Delta R_0 = 0.1$. The computations lasted until shock front radius became 150. The objective of these computations was to study the linear regime of perturbation evolution.

$\gamma = \mathbf{1.06}, \mathbf{n = 64}$

Five computations were carried out in this case. The computations were done inside a region bounded by a cone surface $\alpha = 6.496$deg. This angle was so chosen that exactly one wavelength was enclosed by z-axis and the cone surface. The objective of these computations was to study the non-linear regime of perturbation evolution so the initial perturbation amplitudes were so set that the beginning of non-linear stage of perturbation evolution happened in different phases of oscillations.

3. Computation results

According to the self-similar theory all carried out computations should describe the unstable blast wave . Shock front radius perturbations DR/R should depend on R as a power function: $\Delta R_0/R_0 \tilde{} R^{\lambda}$ where λ is a complex number with a positive real part. Values of λ for γ=1.15, γ=1.06 are presented on Fig.3 for a large set of harmonic numbers n. These values were calculated using the technique of [2]. In our cases the values of $\lambda$are as follows:

γ=1.15, n=16, λ=0.320+i 4.642

γ=1.06, n=64,λ=2.518+i 9.799

$\gamma = \mathbf{1.15}, \mathbf{n = 16}$

In the case of n=16 the objective of the computations was studying the linear regime. So we correlated the computation results with the formulas of the self-similar theory:

$\Delta R/R \tilde{} R^{0.320} * cos(4.642(lnR + const))$

The comparison of the results of the self-similar theory and of computer experiments is shown on Fig.4. The computation results (solid line) and the theoretical ones (heavy line) are in a good agreement. The next result of the comparison is that the formation of the self-similar regime of perturbation evolution is finished in a short time in which shock front radius increases by two to four times. For the sake of estimation of the role of the non-linear effects one more computation was performed; the initial perturbation value ΔR_0 in this computation was 10 times greater (0.1 instead of 0.01) than in the previous one. The results of this computation (see dashed line on Fig.4) demonstrated a visible deviation from the self-similar results because of nonlinear effects.

$\gamma = \mathbf{1.06}, \mathbf{n = 64}$

In the case of $n = 64$ the objective of the computations was studying the non-linear regime. Especially we paid attention to the process of a transformation of a single perturbation to a cumulative jet. For this purpose a number of similar computations were performed; the initial perturbation values in these computations were so set that the beginning of the non-linear stage of perturbation evolution occurred in different phases of perturbation oscillations. The following suppose was used: "if phase difference in oscillations of two perturbations at the moment when the non-linear stage begins is Φ then the ratio of the initial values of these perturbation is $\Phi * Re\lambda/Im\lambda$. In our case Φ was equal to $\pi/2$ so this expression was equal to 1.497. So the initial perturbation amplitudes $\Delta R_0/\Delta R_0$ were set as follows: 0.0001, 0.00015 ,0.00022, 00034, 0.00050. This number of computations provided the set of four different values of oscillation initial phases for studying the non-linear perturbation evolution. The

results of the computations of the linear regime of perturbation evolution are shown on Fig.5. The comparison of these results(solid lines on Fig.5) with the results of the self-similar theory (heavy line on Fig.5) is shown, from this figure we notice that the results are in a reasonable agreement until ΔR_0 exceeds 0.001. The results of computations of the non-linear regime are shown on Figs. 6, 7. The shock wave profiles (patterns of equal density lines) are presented there. Ten subsequent shock wave profile patterns from the computation with $\Delta R_0/\Delta R_0 = 0.00015$ are shown on Fig.6. On this figure the shock wave radii of neighboring patterns are in ratio 1.1-1.2; the 1st pattern corresponds approximately to the beginning of the non-linear stage of perturbation evolution at R=4.5, and the 10th one corresponds to the computation stop at R=14.1 when formation of a cumulative jet is already visible. On Fig.7 the final shock front profiles for all considered initial values of perturbation amplitude are shown: (a) $\Delta R_0/\Delta R_0 = 0.0001$,(b) $\Delta R_0/\Delta R_0 = 0.00015$,(c) $\Delta R_0/\Delta R_0 = 0.00022$,(d)$\Delta R_0/\Delta R_0 = 0.00034$,(e)$\Delta R_0/\Delta R_0 = 0.00050$. The patterns of three cases (a,b,d) demonstrate the formation of cumulative jet on the cone axis directed outside the blast center; however on the figure (c) formation of singular points outside the axis is demonstrated. The demonstrated slight difference between (a) and (e) cases should be attributed to the inaccuracy of computations. Note that the predominant formation of the jets directed outside the blast center is in a good agreement with the general law of Rayleigh-Taylor instability that jets should be directed from the high density region to the low density one.

4. Conclusion

The direct calculations of blast wave in a uniform ideal gas were carried out using 2D hydrodynamic code. Small perturbations evolution of the blast was studied The following cases were considered:$\gamma = 1.15, n = 16$,and $\gamma = 1.06, n = 64$. The results of computations of the linear stage of perturbation evolution agreed closely with the self-similar theory results. It was found that the self-similar regime of perturbation evolution was formed in a short time in which shock front radius increases by two to four times. The proof of the blast wave instability in these cases was obtained by the direct computer experiment. The results of computations of the non-linear stage of perturbation evolution showed that the cumulative jet was predominantly formed in the end of a single perturbation evolution. This jet was directed outside the blast center.

References

[1] Vishniac ET, The dynamic and gravitational instabilities of spherical shocks, Astrophys.J., 274, 152, (1983).

[2] Ktitorov VM, Asymptotical development of point blast wave small perturbations, Voprosy Atomnoi Nauki i Tekhniki, Ser.Teoreticheskaya i Prikladnaya.Fizika (Atomic Science and Technique Issues, Ser. Theoretical and Applied Physics), 2, 28, (1984).

[3] Ryu D and Vishniac ET, The growth of linear perturbations of adiabatic shock waves, Astrophys.J., 313, 820, (1987).

[4] Landau LD, Lifshits EM, Fluid Mechanics, 2nd edition, Pergamon, NY, (1987).

[5] Stamper J, Manca C, *et al.*, Instabilities of Taylor-Sedov blast wave propagating through uniform gas, Phys.Rev.Let., 66, 21, 2738, (1991).

[6] Manca C, Grun J, Stamper J, *et al.*, Images of unstable Taylor-Sedov Blast Waves propagating through uniform gas, IEEE Transactions on Plasma Science, 24, 1, 35, (1995).

[7] Ktitorov VM, Stability of blast wave propagating through a gas with a power depending density, Khimicheskaya Fizika (Chemical Physics Issues), 14, 2-3, 169, (1995).

[8] Godunov SK, Finite difference method of numerical calculation of discontinuous solutions of hydrodynamic equations, Matematicheskii Sbornik, 47, 271, (1959).

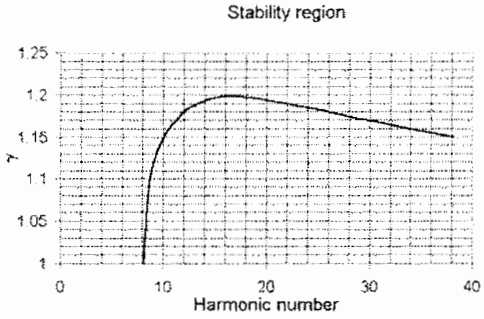

Figure 1. The boundary between the stability region and the instability one on the n-γ plane from [7]. The instability region is under the shown line.

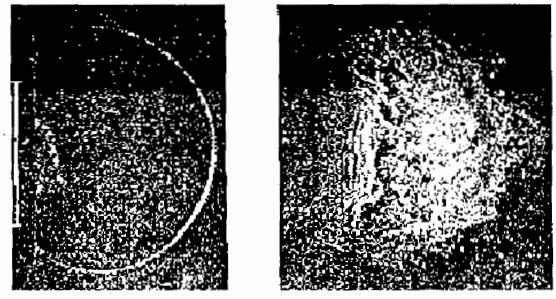

Figure 2. Presentation of dark-field shadowgraphs from [6]. The blast waves are shown in: the stable case (left) when the ideal gas is nitrogen with γ=1.3, and in the unstable case (right) when the ideal gas is xenon with γ=1.06. The vertical bar at the extreme left is a 1-cm-scale reference.

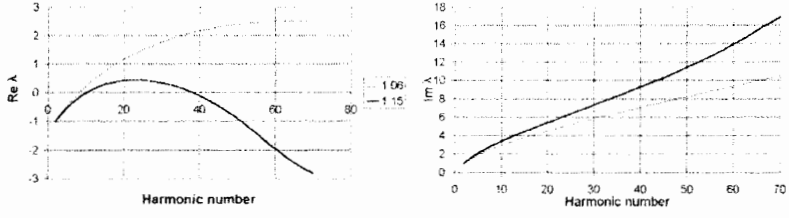

Figure 3. Values of front perturbation growth increments (Re λ), and oscillation frequencies (Im λ) for the cases: γ=1.06, γ=1.15 calculated according to the self-similar technique published in [2]

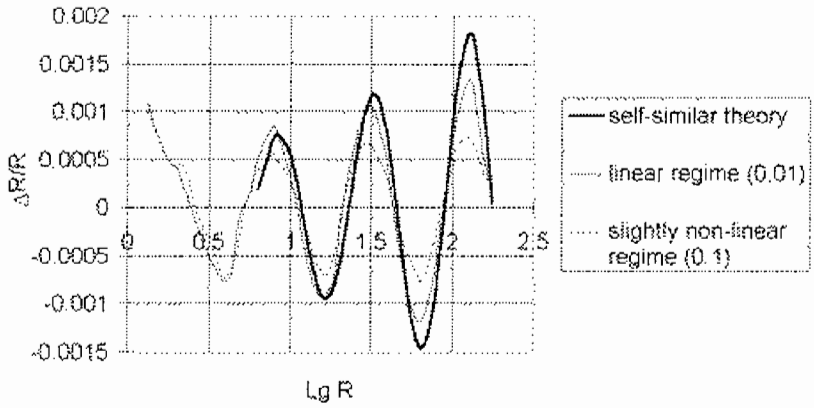

Figure 4. Shock front radius perturbations amplitude $\Delta R/R$ in the case: γ=1.15, n=16. The results of two computations are compared with the theoretical results (heavy line). Solid line corresponds to the computation with the initial perturbation amplitude $\Delta R_0/\Delta R_0$ =0.01. The dashed line corresponds to the computation with $\Delta R_0/\Delta R_0$=0.1. For the sake of convenience of comparison the ordinates of the dashed line are demagnified by 10. The demonstrated difference between solid and dashed lines on the chart should be attributed to the non-linear effects.

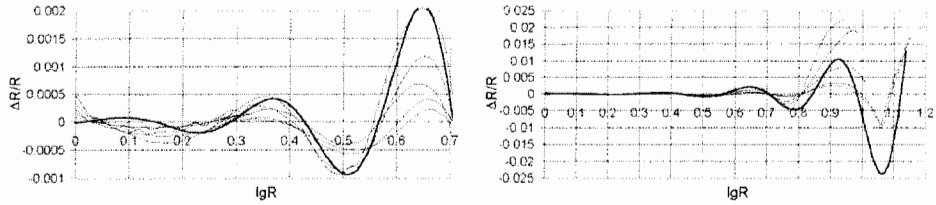

Figure 5. Axis values of shock front radius perturbations amplitude $\Delta R/R$ in the case: γ=1.06, n=64. The results of five computations are compared with the results of the self-similar theory. The heavy line corresponds to the self-similar theory. There is a reasonable agreement between the results of the self-similar theory and of the computer experiment on the linear stage (lgR<0.7). The linear regime of perturbation evolution is shown on (a). Values $\Delta R/R$ on the linear and the non-linear stage of perturbation evolution up to computation stop are shown on (b).

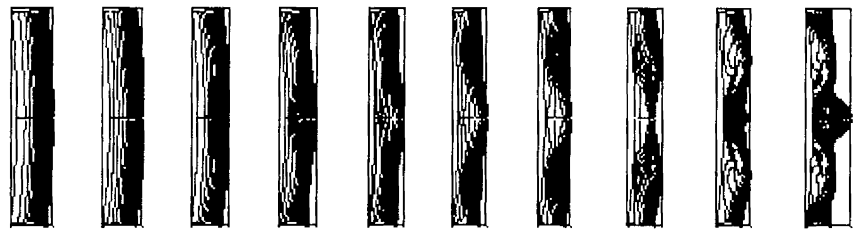

Figure 6. Shock front profile in the computation of the blast wave in the case: γ=1.06, n=64, and initial value of perturbation amplitude $\Delta R_0/\Delta R_0$=0.00015. Ten subsequent patterns of equal density lines are shown inside the cone with the edge angle being equal of 6.496degrees. Shock wave radii of neighboring patterns are in ratio 1.1 -1.2; the 1st pattern corresponds approximately to the beginning of the non-linear stage of perturbation evolution at R=4.5, and the 10th one corresponds to the computation stop at R=14.1.

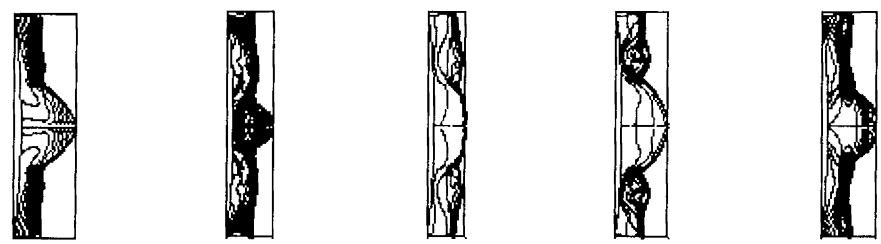

Figure 7. The final shock front profiles in the case γ=1.06, n=64 for all considered initial values of perturbation amplitude: (a) $\Delta R_0/\Delta R_0$ = 0.0001,(b) $\Delta R_0/\Delta R_0$ = 0.00015,(c) $\Delta R_0/\Delta R_0$ = 0.00022, (d)$\Delta R_0/\Delta R_0$ = 0.00034, (e)$\Delta R_0/\Delta R_0$ = 0.00050. The figures of the cases (a,b,d) demonstrate the formation of cumulative jet on the cone axis directed outside the blast center; and figure (c) demonstrates the formation of singular points near the axis. The demonstrated slight difference between (a) and (e) cases should be attributed to the inaccuracy of the computations.

Determination of Space and Time Distributions of the Average Density of Substance in the Turbulized Mixture Region at the Stage of Separation

Y.A. Kucherenko[1], , S.I. Balabin[1], R.I. Ardashova[1], O.E. Kozelkov[1], I.A. Romanov[1], R. Chéret[2], J.F. Haas[2]
[1]Russian Federal Nuclear Center - Institute of Technical Physics
456770 Chelyabinsk-70, P.O. 245, Russia
[2]CEA/DAM, BT12 F91680, Bruyères-le-Chatel, France

Abstract: By X-ray technique, at the installation EKAP, for Atwood number $A = 0,5$ the space and time distributions of the average density of substance in the turbulized mixture at the stage of separation have been determined. As a result of the Rayleigh-Taylor instability development at the contact boundary of two different density liquids during some definite time, the turbulized mixture is obtained. At some instant of time t^* the sign of acceleration was changed, at the same time, the turbulized mixture separation took place. At the stage of the separation and the inertial motion the space and time distributions of the average density of substance in the nondimensional form have been obtained.

1. Introduction

In the presence of different density regions the nonstationary motion of fluids is always unstable when the light substance accelerates the heavy one. At the contact boundary of these substances the gravitational turbulent mixing (GTM) induced by the Rayleigh-Taylor instability is developing. In this case the artificial gravitational field acceleration is directed from the heavy medium to the light one. If in the process of motion the contact boundary acceleration changes its sign, then the boundary appears to be stable gravitationally. Since this instant of time the separation process of the heavy and light substances being found in the turbulent mixing zone begins. Similar phenomena often take place in high-intensive shock and explosive processes. Thus, in the problem of laser thermonuclear fusion (LTF) the turbulent mixing and the separation take place during the compression of single-shell targets as well as targets with several shell. It is especially important to take these processes into account in the problem of the inertial thermonuclear fusion (ITF). These processes exert an influence directly on the dynamic of the targets compression. At present, it is possible to take the mixing and the separation into account in the calculation of LTF targets compression within the framework of the semiempirical theories. For the determination of the constants being available in these theories it is necessary to perform special experiments. In such experiments the mixing and the separation are investigated under definite specified conditions. Experimental study into GTM was performed in the works [1-4]. In RFNC-VNIITF such work has been carried out at the laboratory installations EKAP and SOM. For this purpose two liquids were located in the ampoule which was accelerated by means of vertical gas guns. The turbulent mixing rates have been determined for different Atwood numbers. Up to now the processes of the turbulized mixtures separation were studied insufficiently. The first experimental and theoretical investigations into the separation of the turbulized mixtures have been performed in the works [5-7].

More information - Email: Kucherenko@five.ch70.chel.su or bkv@vniitf.ch70.chel.su

The turbulized mixtures were obtained as a result of the Rayleigh-Taylor instability development at the unstable stage of motion of the contact boundary between heavy and light liquids when the artificial gravitational field acceleration was directed from the heavy liquid to the light one. The size of the mixture region L12 is growing with time according to the law [3, 4]:

$$L_{12} = 2\alpha_m AS \tag{1}$$

where α_m - nondimensional rate of mixing, A - Atwood number, $S = g_{11}t^2/2$ - parameter (for the given scheme of experiments the parameter S coincides with the contact boundary displacement in the laboratory system of coordinates during ampoule acceleration). The value of the constant am for different Atwood number: $\alpha_m \approx 0.07$. If in some instant of time $t = t^*(S = S^*)$ the sign of acceleration g1 is changed, then the system of two different density liquids appears to be stable. At the same time, as it is known from works [6,7], the size of the turbulent mixing region L_{12} attains its maximum value at some instant of time $\tau' = 0$ at the stable motion stage, after that the decrease in the size of this region begins. In this case the size L_{12} is determined by the relationship:

$$\sqrt{L_{12}(\tau')} = \sqrt{L_{12}(\tau' = 0)} - \sqrt{2A\alpha_s S} \tag{2}$$

where $S = g_{12}\tau'^2/2$ - parameter, $g_{12} = \text{Const}$ - artificial gravitational field acceleration directed from the light liquid to the heavy one. In these works the theoretical description of the separation processes of turbulized mixtures has been proposed, and the separation constant $\alpha_s \approx 0.01$ characterizing the mixture separations intensity has been experimentally determined for A = 0.27 in the range of $(S - S^*)/S^* \leq 1.5$. In the present work the subsequent experimental study into the process of the substances separation in the GTM zone has been undertaken. At the same time, the task has been set to determine the distribution of the substance average density in the turbulized region at the stable motion stage and the nondimensional rate of separation for the Atwood number value $A = 0.5$.

2. Set-up of experiments and roentgenographic measurements

According to the scheme shown in Fig. 1 experiments have been performed with respect to the determination of space and time distributions of the substance average density in the turbulized mixture region at the separation stage. At the outlet of the tube of the vertical gas gun 1, the piston 2 with the membrane 3 is mounted. The membrane is secured to the piston by the nut 4. The ampoule 6 with liquids having different densities ($\rho_2 > \rho_1$) is hung up to the piston by means of the catch 5. Into the slots on the cylindrical surface of the piston the inserts 7 are placed. The projecting parts of these inserts are introduced into the slots of the positive acceleration channel 8. The inserts and the slots formed the spline joint of the piston and the positive acceleration channel. This joint was ended with the stop formed by the face surface F of the mechanical inverter 9. The scheme of the inverter construction is given in Fig. 2. In the inverter there were two diametrically opposite slots through which the braking plates 10 were pulled out inside the channel at the cut thickness l. The plates thickness b was chosen so that to provide the necessary amplitude of the negative acceleration of the ampoule. The braking plates were compressed by means of bolts inside the ring which was secured to the body of the inverter. For performing roentgenographic measurements the rectangular slots and the trajectory gauges 11 for the X-ray tubes start-up were envisaged along the whole length of the inverter. The whole device was adjusted so that the interface between liquids was perpendicular to the direction of the Earth's gravitational field g.

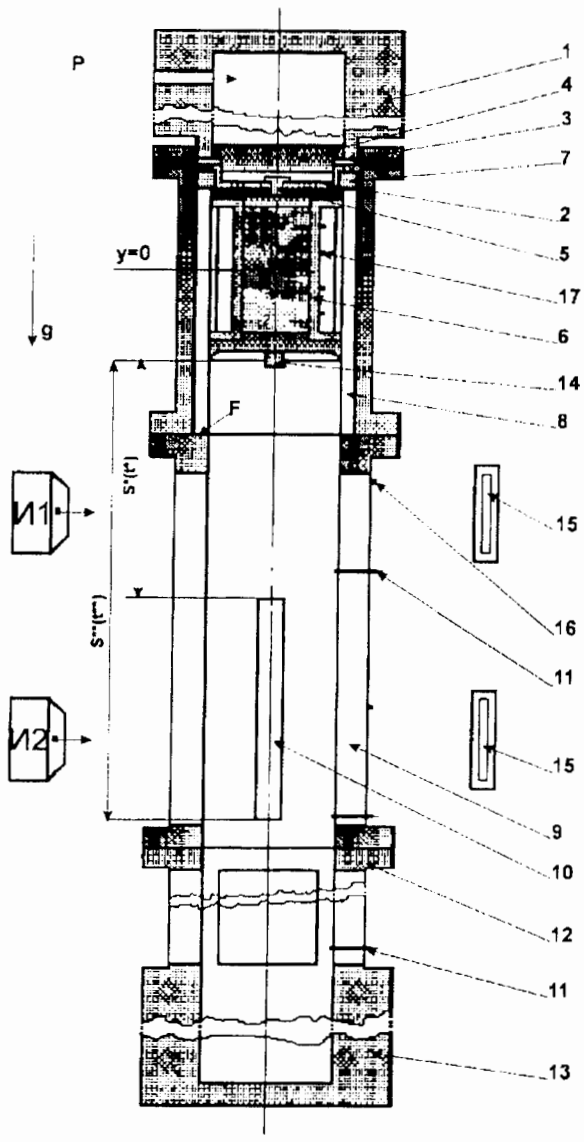

Figure 1. Scheme of the set-up of experiments.

The principle of work consists in the following. Gas is forced from the system of high pressure into the tube of the gas gun. When such pressure is reached in the tube which is equal to the pressure of cutting the membrane P_1 (instant of time $t = 0$) the membrane is cut, and the ampoule together with the piston begins to move in the positive acceleration channel with acceleration a1 in the direction of acceleration g of the Earth's gravitational field. At the same time in the system of coordinates associated with the membrane the artificial gravitational field

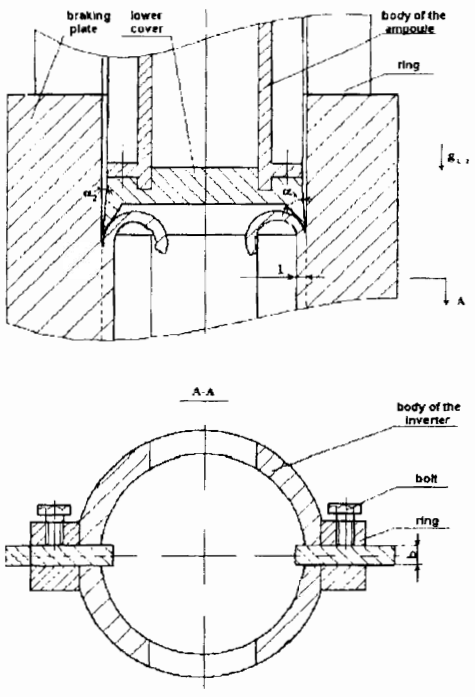

Figure 2. Scheme of the mechanical inverter.

with acceleration g_{11} directed from the heavy liquid to the light one exerts an action on the system of the different density liquids. The system is found in the gravitationally unstable state. In the region of the contact boundary the turbulent mixing is developing. At the instant of time $t = t^*(S = S^*)$ the piston inserts come in contact with the front surface F of the negative acceleration channel 9. The piston stops and cuts the gas flow from the ampoule, thereby the force accelerating the ampoule is removed. At the same instant of time the breakage of the catch takes place, and the ampoule continues to move in the negative acceleration channel. The interaction of the lower cover of the ampoule, whose lateral surface has been made in the form of the cutting edge being characterized by angles $\alpha_1 \approx 45^0$ and $\alpha_2 \approx 1^0$, with the material of the projecting braking plates creates the force stipulating the negative acceleration of the ampoule α_2. At the same time, in the system of coordinates associated with the ampoule, the artificial gravitational field g_{12} is acting on the mixing region which has been developed to this moment. The process of the mixture separation begins. The interaction of the ampoule with the braking plates is continued up to the instant of time $t = t^{**}(S = S^{**})$, then the action of forces the ampoule ceases, the ampoules moves by inertia during some time in the channel 12 and then gets into the catcher 13 where its complete stop takes place. The ampoule acceleration was registered by means of the accelerometer 14 secured to the lower cover of the ampoule. The typical oscillogram of the ampoule acceleration which has been obtained in the process of the ampoule motion at $S^* = 300$ mm is given in Fig.3. It can be seen that the positive acceleration of the ampoule up to the moment of acceleration reversal and the negative acceleration in the investigated range change insignificantly and amount to 80 - 90 % of the corresponding initial

acceleration of the ampoule. At different instants of time $t_i(S_i)$ during the ampoule motion,

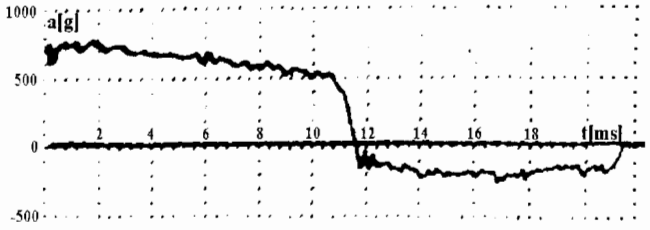

Figure 3. Characteristic oscillogram of the ampoule acceleration in experiments with $n = 3$ at $S^* = 360$ mm.

the action of trajectory gauges 11 located in a definite manner takes place. This leads to actuating the corresponding X-ray chambers I_1 and I_2. The X-ray radiation of these chambers makes possible to obtain the half-tone image of the turbulent mixing region on the immovable X-ray film 15. The distribution of the average of the substance in the mixture region and the coordinates of the mixing fronts in light and heavy liquids are determined according to these images. The mark-benches 16 located on the channel wall and the mark-benches 17 located on the ampoule are used for the determination of the distance S_i passed by the ampoule to the moment of radiography as well as for the determination of the coordinates of the mixing fronts in light and heavy liquids.

3. Determination of the space and time distributions of the average density of substance in the mixture region at the stage of separation

The determination of the space and time distributions of the average density of substance in the mixing region was carried out for the mixture of substances with the relation of densities n = 3. Initial perturbations at the contact boundary were characterized by the value $L_0 = 1$mm and $\lambda_{min} \approx 2$ mm. Two groups of experiments have been performed which have been distinguished by the different value of the distance S^* at which the reversal of the ampoule acceleration has taken place. The first group of experiments was performed at $S^* = 140$ mm, the second - at $S^* = 360$ mm. This made possible to obtain the different width of the mixing region to the moment of the acceleration reversal. In each group of experiments the following was determined experimentally: average density of substance $\rho(y)$ for four fixed values of distance S_i, average sizes $L_{2.1}$ and $L_{1.2}$ of the regions involved into the turbulent motion in light and heavy liquids at the level of nondimensional density $\delta_1 = 0.1$ and $\delta_2 = 0.9$. The average initial values of acceleration α_1 and α_2 at which the experiments have been performed are given in the table below. The measurements of the average density of substance in the mixing region were

Group of experiments	S , mm	a_1, m/s^2	a_2, m/s^2
1	140	6060	1760
2	360	6060	2450

Table 1.

performed as follows. The measuring channel was preliminary calibrated with using the known distribution of substance density. For this purpose the samples with the known distribution of density instead of the investigated system were placed into the measuring channel. At the outlet of the measuring channel the distribution of the optical density of blackening of the X - ray film $D^*(y)$ which is, unambiguously, associated with the known density distribution of the sample $\rho^*(y)$ is obtained. After this the calibration dependencies $D^*(\rho^*)$ were found. The X - ray images of the turbulent mixing region which have been obtained in experiments and have been analogous to those given in Fig.4 were treated with taking the calibration dependencies $D^*(\rho^*)$ into account. At the same time , at first the average distribution of the optical density was determined according to the mixing region image, then the distribution of the average density of substance was found. The results of the average values of $\rho(y)$ obtained in the

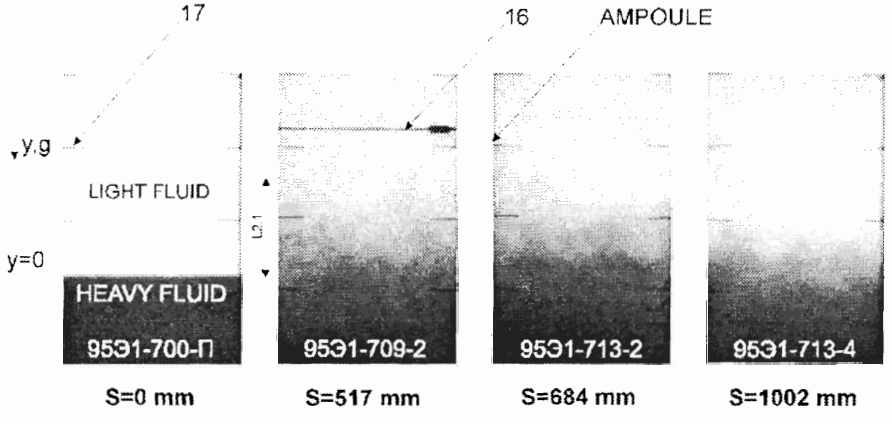

Figure 4. X-ray images of the mixing region at the stage of the acceleration sign change at $S^* = 360$ mm.

experiments for one of the chosen values of the flight path S_i at $S^* = 140$ mm are given in 5. The analogous results of the average values $\rho(y)$ at $S^* = 360$mm are presented in Fig. 6. In the same figures the average values of the coordinates of the mixing fronts in light and heavy liquids are given. Moreover, the average values of the coordinates of the mixing fronts $L_{2,1}$ and $L_{1,2}$

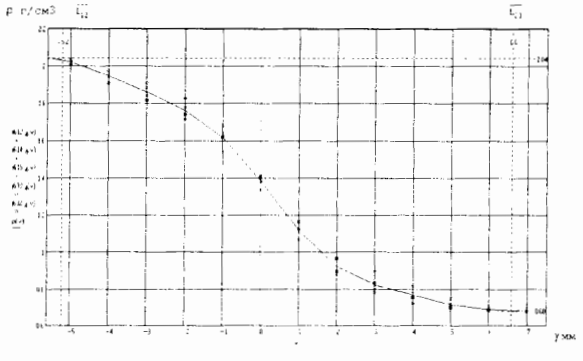

Figure 5. Averaged profile of density for $S = 790$ mm at $S^* = 140$ mm.

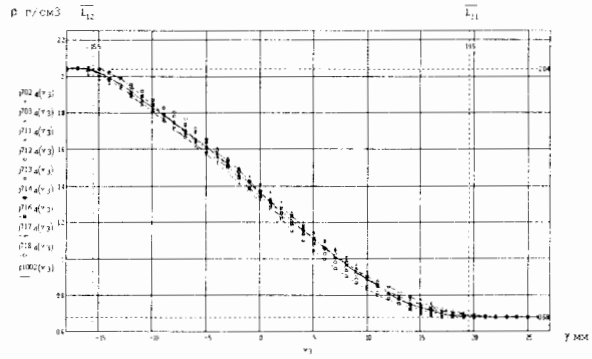

Figure 6. Averaged profile of density for $S = 1002$ mm at $S^* = 360$ mm.

are plotted on the graph of Fig.7 depending on the flight path for both groups of experiments. The dependencies $L_{2.1}(S)$ and $L_{1.2}(S)$ previously obtained for the self-similar mode of mixing [4] are also given here. It is seen that after the acceleration reversal at $S = S^*$ the mixing region size continues to grow for some time. Then, since the moment $S = S_c$ the mixing region size decreases. This is the consequence of the separation of the different-scale particles of heavy and light liquids. Distributions of density $\rho(y, s)$ obtained for both groups of experiments were

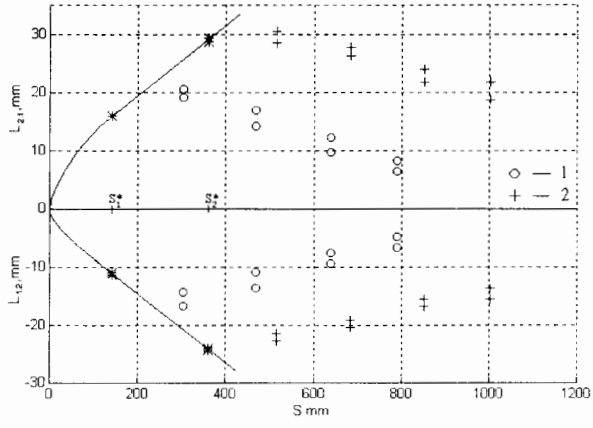

Figure 7. Dependence of coordinates $L_{2.1}$ and $L_{1.2}$ of the mixing fronts on the flight time of the ampoule at $S^* = 140$ mm (1) and $S^* = 360$ mm (2).

used for the determination of the nondimensional density $\delta(\chi)$, where $\delta = (\rho - \rho_1)/(\rho_2 - \rho_1)$ As a nondimensional coordinate the following value was chosen: $\chi = (y - y_{0.1})/(y_{0.9} - y_{0.1})$, where $y_{0.1}, y_{0.9}$ - coordinates of mixing fronts at which the nondimensional density assumes the values $\delta_1 = 0.1$ and $\delta_2 = 0.9$, respectively. In Fig.8 the experimental results are presented for both groups of experiments in the coordinates $\delta = (\chi)$. The experimental dependence obtained previously for the self-similar mode of mixing is shown by a solid line. Thus, it is seen that the space and time distributions of the substance average density $\rho(y, S)$ obtained in the process of separation for both groups of experiments can be described by a single dependence $\delta(\chi)$. At

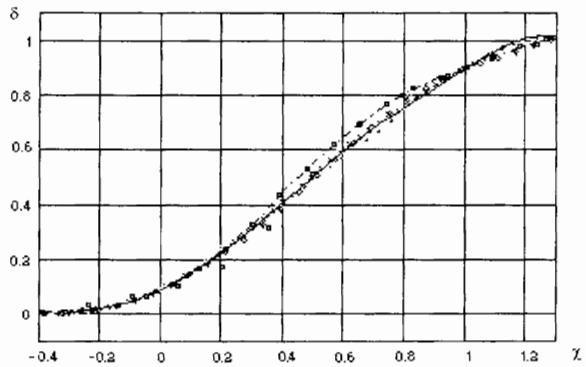

Figure 8. Dependence $\delta(\chi)$ at the stage of the acceleration sign change in experiments with $n = 3$ at $S^* = 140$ mm and $S^* = 360$ mm.

the same time, the reveled dependence $\delta(\chi)$ coincides with the self-similar one (differences are observed at the turbulent mixture zone boundaries) in the wide range of χ values.

4. Conclusion

At the installation EKAP, by the roentgenographic technique the space and time distributions of the average density of substance have been determined in the turbulized mixing region for Atwood number A = 0.5 at stage of the separation and at the stage of inertial motion. It has been set that in the nondimensional form these distributions coincide between themselves within the error of measurements. The obtained results can be used for the calibration of calculation-theoretical models and numerical codes of turbulent mixing.

Acknowledgement. This work has been performed under the financial support of the Commissariat for Atomic Energy, France.

References

[1] Anuchina NN, Kucherenko YA, Neuvazhayev VE *et al.*, Turbulent mixing at the accelerating boundary between fluids having different densities, Rus. Jour. Mechanics of fluids, Issue 1, (1978).

[2] Kucherenko YA, Tomashev GG, Shibarshev LI, Experimental investigation into gravitational turbulent mixing, Problems of Atomic Science and Engineering, Series: Theoretical & Applied Physics, Issue 1, (1988).

[3] Youngs DL, Physica D12, 19, (1984).

[4] Kucherenko YA, Shibarshev LI, Chitaikin VI, Balabin SI, Pylaev AP, Experimental investigation into the self-similar mode of the gravitational turbulent mixing. Report at the 3rd International Workshop on the Physics of Compressible Turbulent Mixing, (1991).

[5] Youngs DL, Physica D37, 270-287, (1989).

[6] Kucherenko YA, Neuvazhayev VE, Pylaev AP, Behavior of Gravitational Turbulent Mixing Region under Conditions Leading to Separation. Report at the 4th International Workshop on the Physics of Compressible Turbulent Mixing, (1993).

[7] Kucherenko YA, Neuvazhaev VE, Pylaev AP, RAS, 334, 4, 445.

Investigation into the Interaction of the Stationary Shock Wave with the Turbulized Layer

Y.A. Kucherenko[1], A.T. Linvin[1], O.E. Shestachenko[1], J.A. Piskunov[1], A.I. Baishev[1], I.B. Kotov[1], A.V. Pavlenko[1] and B.A. Remington[2]
[1]Russian Federal Nuclear Center - Institute of Technical Physics
456770 Chelyabinsk-70, P.O. 245, Russia
[2]Lawrence Livermore National Laboratory
P. O. Box 808, L-473, Livermore, CA 94550, USA

Abstract: Russian Federal Nuclear Center - VNIITF and Lawrence Livermore National Laboratory have joined their efforts for the experimental study into the interaction of stationary shock waves with a turbulized layer. In VNIITF the experiments have been run at the installation OSA. The results of experiments will be used for the calculations of the targets compression in the laser thermonuclear fusion problem. The turbulized layer has been formed at the contact boundary of two different density gases with the external initiation of the controlled separating membrane prior to the stationary shock wave arrival.

1. Introduction

The unstationary flow of liquids and gases with the availability of different density regions is unstable in most cases when we are dealing with energy cumulating. In this case, at the contact boundaries, the turbulent mixing induced by the Rayleigh-Taylor or Richtmyer-Meshkov instabilities develops. Mathematical codes being developed and semiempirical models taking into account the mixing under the compression of the targets demand for calibration by means of experiments performed specially. Experiments have been performed at the installation OSA in VNIITF. When doing so the interaction of shock waves with the turbulized layer has been realized according to the scheme shown in Fig.1. At some instant of time $t < t_1$, a flat turbulized layer, $L_0(t)$ in width, is created which consists of the mixture of two gases. Gas 1 density is ρ_1 , and gas 2 density is ρ_2. In this case the turbulized layer, as a whole, is not moving, i.e. its mass velocity $U = U_0 = 0$. At the instant of time $t > t_1$ the first shock wave D_{20} passes through the turbulized layer from gas 2 to gas 1 (see Fig.1). After the shock wave passage the tur- bulized layer size decreases up to $L(t_1)$, the layer mass velocity becomes equal to $U = U_1$. For the case of $\rho_2 > \rho_1$ the shock wave D_{11} is moving in gas 1, and the wave of unloading C_{21} is moving in gas 2. The layer size $L(t)$ begins to increase at $t > t_1$ due to the partial absorption of the shock wave energy in the layer. Then, at the installation OSA, the reflection of the wave D_{11} from the hard wall was realized at the instant of time $t_2 > t_1$. The reflected shock wave D_{12} interacts with the turbulized layer at the instant of time $t_3 > t_2$. As a result of this interaction, the passed shock wave D_{23} is moving in gas 2, and the reflected shock wave D_{13} is moving in gas 1. The layer mass velocity becomes equal to $U = U_3$ in this case (for $t > t_3$). The part of the wave D_{12} energy is again transformed into the turbulent motion. Therefore, beginning from the instant of time $t = t_3$ the growth rate of the layer width $L(t)$ again changes. At the installation OSA some reflections from the hard wall were organized so that to obtain the wave picture given in Fig. 2 (case of $\rho_2 > \rho_1$). Here x_{CB} - position of the contact boundary, x_R - position of the hard reflecting wall at $t = 0$. The trajectories of the shock waves are denoted

More information - Email: Kucherenko@five.ch70.chel.su or bkv@vniitf.ch70.chel.su

by D. The first lower index denotes gas in which the shock wave is moving. The second lower index denotes the instant of time after which the shock wave has been generated. In the odd instants of time t_1, t_3, t_5, ... shock waves interact with the contact boundary of gases. In the even instants of time t_2, t_4, t_6, ... the shock waves are reflected from a hard wall. For this reason the designations of the contact boundary trajectories have only odd indexes (U_1, U_3, U_5, ...) and also U_0 . The front of the unloading wave is moving with sound velocity relative to gas, therefore, it is designated as C_{21} (the wave in gas 2 after the instant of time t_1). In the

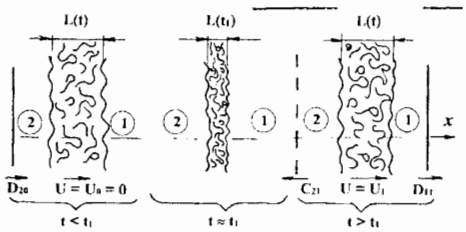

a) Interaction with first shock wave

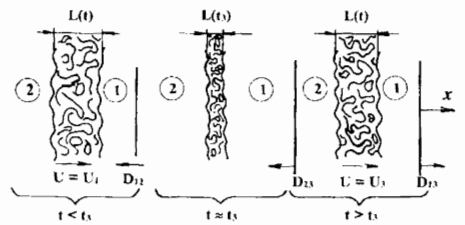

b) Interaction with second shock wave

Figure 1. Scheme of interaction of shock waves with a turbulized layer.

present work the investigation into the interaction of a turbulized layer with a stationary shock wave was carried out in a new set-up. The distinctive peculiarity of these experiments was that the separating membrane was disrupted by an external force at a specified instant of time (the characteristic scale of perturbations $\sim \lambda$). As the result, the turbulent layer having the width $L_0(t)$ has been organized (the time dependence of the layer width depends on enclosed energy during the membrane disruption). The experiments were carried out with respect to the following scheme (Fig.1 and 2):

1. By the instant of time $t = 0$ a stationary shock wave D_{20} was formed in gas 2. By the instant of time $t < t_1$ the turbulent layer, $L_0(t)$ in width, with a definite spectrum of turbulence was created. The turbulent layer forming conditions were chosen so that one can consider the layer as thin (case $L_0(t) \sim \lambda$) or thick (case $L_0(t) > \lambda$) by the instant of time $t = t_1$.
2. Beginning from the instant of time $t = t_1$ the turbulent layer behavior after passing of the incident shock wave D_{20} has been investigated.
3. Beginning from the instant of time $t = t_3$ the turbulent layer behavior after passing of the reflected shock wave D_{12} has been investigated and so on.

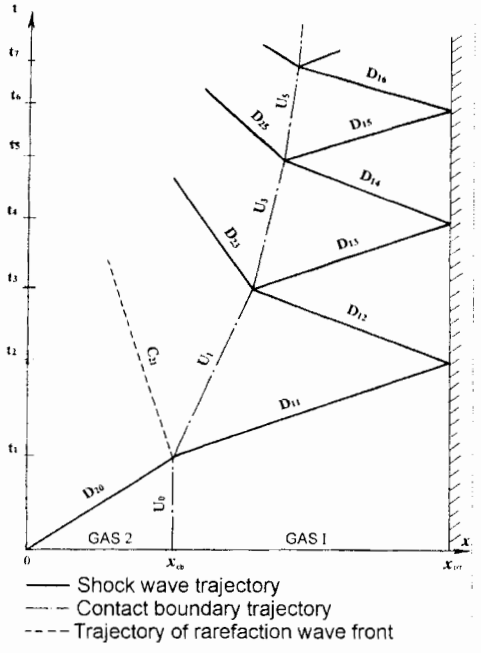

Figure 2. x-t diagram of multiple interaction of shock waves with a turbulized layer.

2. Set-up of experiments

The experiments concerned with studying the interaction of the shock wave with the turbulized layer were conducted at the installation OSA. The scheme of the measuring module of the installation OSA is shown in Fig.3. At the top there is the high pressure reservoir separated from the remaining part of the shock tube by the aluminum membrane 0.5 mm in thickness. The block of the controlled high pressure membrane provides the powerful pulse of current on the membrane that ensures its rupture at the specified instant of time. Then the transition section follows which provides the gas-dynamic conformity of the flow in the round section with the flow in the square section. The low pressure chamber is of square cross-section ($138 \times 138 mm^2$) and is filled up with inert gas with its density ρ_2. The separating membrane prevents from mixing of working gases during the preparation of the experiment. The following section of the shock tube is the measuring chamber which makes possible to perform the registration of the turbulized layer by light methods at different instants of time. It is filled up with working inert gas having its density ρ_1. In the lower part of the measuring module there is the shock wave reflector block which provides the series of the reflected shock waves. The succession of the installation work is the following. Prior to conducting the experiment the low pressure chamber and the measuring chamber are filled with different density gases. The separating membrane prevents from mixing of gases. The high pressure reservoir is filled up with nitrogen compressed up to pressure $P = 1.0 MPa$. At the specified moment t_1 the aluminum membrane opens up under the action of the powerful pulse of current, and gas begins to flow out of the high pressure reservoir. The formed shock wave is propagating along the transition section and the low pressure chamber. At instant of time t_2 the controlled separating membrane is ruptured

up to the typical scale by means of a weak electric explosion. At the same time at the contact boundary of gases the turbulized layer begins to be formed. The instant of time t_2 is chosen so that by the moment of the shock wave arrival the turbulized layer width was equal to $L_0(t_1)$. After the shock wave interaction with the turbulized layer the shock wave is propagating in gas of density ρ_1, the unloading wave (case of $\rho_2 > \rho_1$) is moving in gas ρ_2 and the turbulized layer itself moves to the side of the reflector. When the layer is found between the optic glasses of the measuring chamber the photographic record of the turbulized layer takes place. The shock wave being reflected from the reflector interacts again with the turbulized layer. In so far as the shock wave passes from the light gas into the heavy one, shock waves are propagating in both sides from the contact boundary. Then another shock wave again reflects from the reflector and interacts with the turbulized layer. At the same time the intensity of the shock waves decreases, and the contact boundary is braked. This takes place until the unloading wave being reflected from the gas reservoir flange arrives. The geometry of the experiments

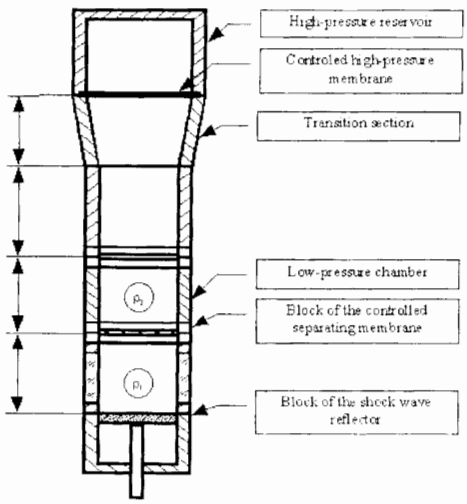

Figure 3. Scheme of installation OSA.

is shown in Fig.3. The whole measuring module of the installation OSA is subdivided into three parts. The gas reservoir, 1553 mm in length, is filled up with compressed nitrogen. The transition section and the part of the low pressure chamber are filled up with the working gas with its density ρ_2 under normal pressure (length of this part amounts to 2758 mm). The measuring chamber (between the separating membrane and the reflector) is filled up with the working gas with its density ρ_1. The chamber length is equal to 400 mm. In the given work the following working gases were used: helium (He) (density $\rho = 0.178kg/m^3$), argon (Ar) (density $\rho = 1.78kg/m^3$), SF_6 gas (density $\rho = 6.0kg/m^3$). The relations of densities n and Atwood numbers for different pairs of gases are shown in Table 1. Two series of experiments have been conducted. In each series different pairs of gases were used. Both series consisted of two groups of experiments being distinguished by different values of the turbulized layer thickness by the moment of the falling shock wave arrival. Trajectories of shock waves and trajectories of the turbulized layer boundaries were measured after passing of shock waves. In the first series of experiments $Ar - He$ pair of gases (Atwood number $A = 0.82$) was used. The falling shock

Pair of gases	Relation of densities	Atwood numbers
$Ar - He$	10.0	0.82
$SF_6 - Ar$	3.4	0.54

Table 1.

wave was formed with Mach number $M = 1.7$. In group 1.1 of experiments the turbulized layer thickness $L_0(t_1)$ amounted to 9 mm by the moment of the falling shock wave arrival. In group 1.2 of experiments $L_0(t_1) = 17mm$. In the second series of experiments $SF_6 - Ar$ pair of gases (Atwood number $A = 0.54$) was used. The falling shock wave was formed with Mach number $M = 2.0$. In group 2.1 of experiments the turbulized layer thickness $L_0(t_1)$ amounted to 9 mm by the moment of the falling shock wave arrival. In group 2.2 of experiments $L_0(t_1) = 17mm$.

3. Results of experiments and their discussion

During the electric explosion the turbulized layer whose width is changed with time is formed. For the determination of the dependence of the turbulized layer width $L_0(t)$ the special experiments without shock waves have been performed. The arithmetic mean value is assumed to be the turbulized layer width L_0 according to ten measurements of the size L_{0i}. Fig. 4 shows the characteristic photographic images of the turbulized layer for different instants of time for the pair of gases $Ar - He$. The turbulized layer is seen in photographs in the form of the wide dark band. It can be seen that the layer width is increased with time, but the layer itself is moving downwards. Near the measuring chamber walls the boundary layer is seen which lags behind the basic turbulized layer. In heavy gas (argon) the reflected shock wave which is moving upwards is well seen. Time t is counted off from the moment of the shock wave interaction with the

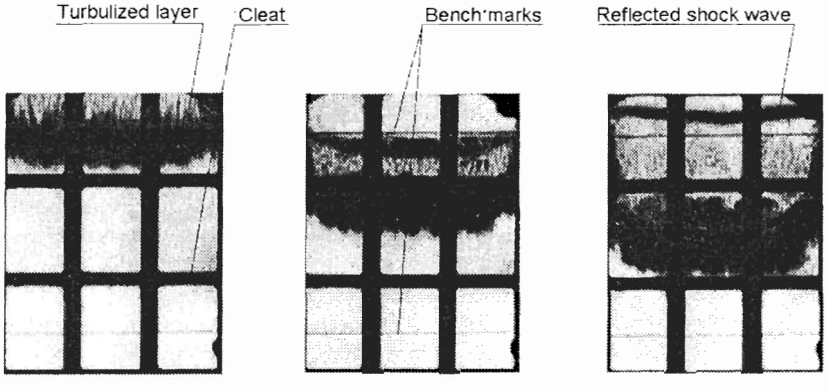

Figure 4. Typical photographic images of the mixing process of gases.

turbulized layer. For the exact determination of the image scale the bench marks are set before the measuring chamber glasses. The cleat retaining the glass is also seen in photographs. After the interaction the turbulized layer attains mass velocity approximately equal to 365 m/s and expands with average velocity approximately equal to 24 m/s. The falling shock wave reflects from the reflector and interacts again with the turbulized layer at instant of time $t > 1.65$ ms.

At the same time the average width growth rate of the layer dL/dt is increased up to 95m/s, but its mass velocity decreases up to 146 m/s. The next interaction of the reflected shock wave with the turbulized layer takes place at the instant of time $t_5 > 1.9$ ms. The width growth rate of the layer dL/dt is increased to 99 m/s but its mass velocity decreases to 79 m/s. In the experiments of the group 1.2 the controlled separating diaphragm was ruptured in 4 ms prior to the shock wave arrival. By the moment t_1 of the shock wave interaction with the turbulized layer the width amounted to $L_0 > 17$ mm. The average rate of the layer width growth and the mass velocity of the layer are given in Table 2 for different instants of time. Fig. 5 shows the

	Rate of the layer width growth, m/s	mass velocity, m/s
falling shock wave ($t \geq t_1$)	20	462
first reflected shock wave ($t \geq t_3$)	78	149
second reflected shock wave ($t \geq t_5$)	85	26

Table 2.

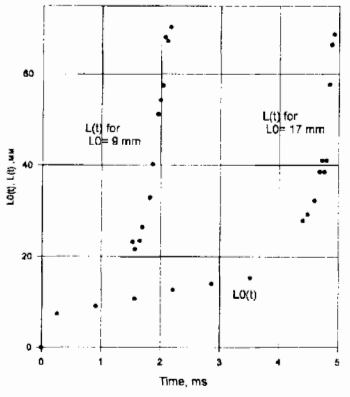

Figure 5. Dependence $L_0(t)$ and $L(t)$ for gases $Ar - He$.

summary dependencies of the turbulized layer width on time for three cases (gases $Ar - He$):
1) $L_0(t)$ - layer width when there are no shock waves. The layer width is growing due to the electric explosion energy.
2) $L(t)$ - layer width when the shock wave falls on the contact boundary in 1 ms after the separating diaphragm destruction (the turbulized layer has been increased to the size $L_0(t_1) > 9mm$ by this moment). The layer width is growing due to the energy absorbed from shock waves at the instants of time t_1, t_3, t_5.
3) $L(t)$ - layer width when the shock wave falls on the contact boundary in 4 ms after the separating diaphragm destruction (the turbulized layer has increased up to the size $L_0(t_1) > 17$ mm by this moment). The layer width is growing due to the energy absorbed from shock waves

at instants of time t_1, t_3, t_5. From the presented graphs it is possible to conclude that, after passing the shock waves through the interface, the rate of the turbulized layer expansion is sharply increased, whereas the acceleration of the layer width growth depends on the shock wave intensity. The set-up of experiments with gases SF_6 and Ar (the second series of experiments) has completely corresponded to the experiments of the first series described above (the group of experiments 2.1). By the time of the first shock wave arrival the turbulized layer width amounted to $L_0 > 9$ mm. The rate of the layer width growth and the mass velocity of the layer are shown in Table 3 for different instants of time. By the time of the first shock

	Rate of the layer width growth, m/s	mass velocity, m/s
falling shock wave ($t \geq t_1$)	21	217
reflected shock wave ($t \geq t_3$)	106	75

Table 3.

wave arrival the turbulized layer width amounts to $L_0 > 17mm$ (the group of experiments 2.2). The layer width growth rate and the mass velocity of the layer for different instants of time are shown in Table 4. Fig. 6 demonstrates the summary dependencies of the turbulized layer width on time (gases $SF_6 - Ar$).

	Rate of the layer width growth, m/s	mass velocity, m/s
falling shock wave ($t \geq t_1$)	11	225
reflected shock wave ($t \geq t_3$)	41	65

Table 4.

4. Conclusion

The investigation regarding the interaction of the stationary shock waves with the turbulized layer have been performed. The first series of experiments was conducted by using gases $Ar - He$ with Mach number of the falling shock wave $M = 1.7$. The average rate of the turbulized layer width growth $\overline{dL/dt}$ is shown in Table 5 for different initial thicknesses L_0 of the turbulized layer. The second series of experiments was conducted by using gases $SF_6 - Ar$ with Mash number of the falling shock wave $M = 2.0$. The average rate of the turbulized layer width growth $\overline{dL/dt}$ is shown in Table 6 for different initial different conditions.

Acknowledgement. This work is supported by the LLNL, Contract N° B317312.

References

[1] Neuvazhayev VE, Turbulent layer spreading, Rus. J. PMTF, 2, (1988).

[2] Neuvazhayev VE, Yakovlev VG, On mixing of the Contact Boundary Decelerated by Stationary Shock Waves, Rus. J. PMTF, 2, (1981).

[3] Zaitzev SG, Lazareva EV, Chernukha VV, Belyaev VM, Intensification of Mixing at the Different Density Media Boundary when a shock wave passes through it, Reports of USSR Acad. of Sci., 238, 1, (1985).

[4] Rozanov VB, Lebo IG, Zaitzev SG *et al.*, Experimental Investigation into Gravitational Instability and Turbulent Mixing of stratified Flows in the Field of Acceleration in Connection with ICF Problems, Preprint FIAN, 56, (1990).

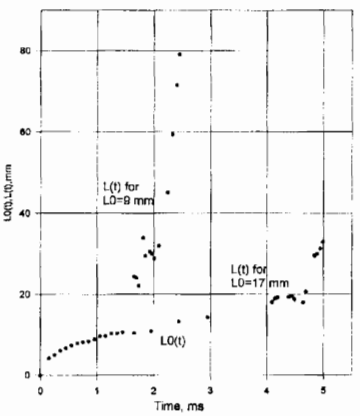

Figure 6. Dependence $L_0(t)$ and $L(t)$ for gases $SF_6 - Ar$.

	$L_0 = 9$ mm	$L_0 = 17$ mm
	$\overline{dL/dt}$	$\overline{dL/dt}$
falling shock wave ($t \geq t_1$)	24 m/s	20 m/s
first reflected shock wave ($t \geq t_3$)	95 m/s	78 m/s
second reflected shock wave ($t \geq t_5$)	99m/s	85 m/s

Table 5. Initial width of the turbulized layer.

	$L_0 = 9$ mm	$L_0 = 17$ mm
	$\overline{dL/dt}$	$\overline{dL/dt}$
falling shock wave ($t \geq t_1$)	21 m/s	11 m/s
reflected shock wave ($t \geq t_3$)	106 m/s	41 m/s

Table 6. Initial width of the turbulized layer.

Experimental Determination of the Turbulized Mixtures Separation Rate for Different Atwood Numbers

Y.A. Kucherenko[1], A.P. Pylaev[1], S.I. Balabin[1], V.D. Murzakov[1], R.I. Ardashova[1], V.N. Popov[1], O.R. Komarov[1], V.E. Savel'ev[1], O.E. Kozelkov[1], R. Chéret[2] and J.F. Haas[2]
[1]Russian Federal Nuclear Center - Institute of Technical Physics
456770 Chelyabinsk-70, P.O. 245, Russia
[2]CEA/DAM, BT12 F91680, Bruyères-le-Chatel, France

Abstract: Experimental study into the turbulized mixtures separation at the installations EKAP (X-ray technique) and SOM (light technique) has been performed. The turbulized mixtures of different density liquids were obtained as a result of the Rayleigh-Taylor instability action during the definite time. At some instant of time the sign of acceleration was changed. Since that instant of time the conditions for the separation were created. For three Atwood numbers being essentially different the nondimensional rate of separation has been determined. The asymptotic stage of separation has been investigated. The nondimensional rate of separation was shown to be independent of Atwood number.

1. Introduction

The nonstationary flow of fluids at the availability of different density regions is always unstable when the light substance accelerates the heavy one. At the contact boundary of these substances the gravitational turbulent mixing induced by the Rayleigh-Taylor instability develops. In this case the acceleration of the artificial gravitational field is directed from the heavy medium to the light one. If in the process of motion the contact boundary acceleration changes its sign, then the boundary appears to be gravitationally stable. Since this instant of time the separation process of the heavy and light substances being found in the turbulent mixing zone begins to proceed. Similar phenomena take often place in high-intensive shock and explosive processes. Thus, in the problem of laser thermonuclear fusion (ICF), the turbulent mixing and the separation take place during the compression of the targets having a single shell as well as several shells. Taking into account these processes is especially important during the compression of the special targets in the ICF problem. These processes have an influence directly on the dynamics of the targets compression.

2. Set-up of experiments

Assume that the system of two different density liquids having densities $\rho_2 > \rho_1$ appears to be in the artificial gravitational field with acceleration $g_{11} = Const$ directed from the heavy fluid to the light one (Fig.1). In consequence the turbulent mixing develops under the action of the Rayleigh-Taylor instability. The size of the mixture region L_{12} is growing with time according to the law [1, 2] $L_{12} = 2\alpha_m AS$ where α_m - nondimensional velocity of mixing, A - Atwood number, $S = g_{11}t^2/2$ - parameter (for the given scheme of experiments the parameter S coincides with the contact boundary displacement in the laboratory system of coordinates with the ampoule acceleration). For different Atwood numbers the value of the constant $\alpha_m \approx 0.07$. Assume

More information - Email: Kucherenko@five.ch70.chel.su or bkv@vniitf.ch70.chel.su

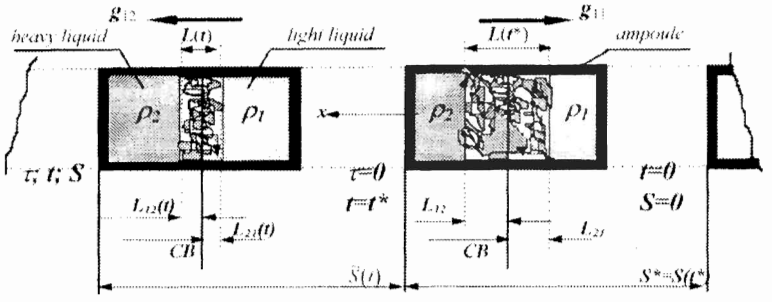

Figure 1. Scheme of the turbulized mixture separation of different density fluids; 1 - light liquid, 2 - heavy liquid, 3 - ampoule.

that at some instant of time $t = t^*$ ($S = S^*$) acceleration g_1 changes its sign (Fig.2). Since

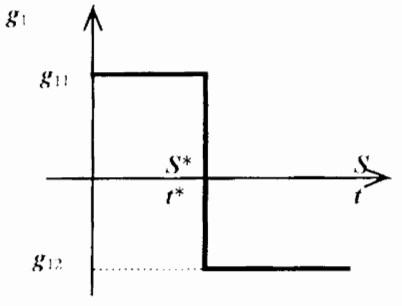

Figure 2. Mode of the acceleration.

this instant of time the system of two different density liquids becomes stable gravitationally, therefore, the conditions are created for separating the turbulized mixture. As it is known [3, 4], the size of the turbulent mixing zone L_{12} attains the maximum value at some instant of time $\tau' = 0$ at the stage of stable motion, after that the size of this region begins to decrease. At the same time the size of L_{12} is determined by the relation:

$$\sqrt{L_{12}(\tau')} = \sqrt{L_{12}(\tau' = 0)} - \sqrt{2A\alpha_s \widetilde{S}} \tag{1}$$

where $\widetilde{S} = \frac{g_{12}\tau'^2}{2}$ - parameter, $g_{12} = Const$ - acceleration of the artificial gravitational field directed from the light liquid to the heavy one. In the works [3], [4], for the value of Atwood mumber $A = 0.5$ the value of the constant $\alpha_s \approx 0.01$ has been determined in the range of $(S - S^*)/S^* \leq 1.5$. Therefore, the turbulized mixture separation rate in the given range of the parameter S is less by a factor of ~ 7 than the size growth of the mixing region at the stage of unstable motion. The task of the given investigation was to determine the constant α_s for other Atwood numbers and to investigate the asymptotic stage of separation. Experiments were performed at the installation EKAP by the X-ray technique for the densities relation of liquids $n = 3$ and $n = 6$ and at the installation SOM by the light technique for $n = 1.5$ and $n = 3$. For obtaining the density relation $n = 1.5$ two liquids, namely, benzine and aqueous solution of sodium chloride have been used, for $n = 3$ - benzine and aqueous solution of zinc chloride.

but for $n = 6$ - benzine and Klerichi liquid. The liquids being investigated are placed into the hermetically sealed ampoules which at the initial instant of time are mounted into the measuring modules of the corresponding installations. The internal working sizes of ampoules amount to $(50 \times 50 \times 140)$ mm^3 for the installation EKAP and $(54 \times 64 \times 120)$ mm^3 for the installation SOM. At the contact boundary of liquids the random initial perturbations were specified. The width of the initial perturbations zone was equal to $L_0 = (1 \mp 0.2)mm$ at the installation EKAP and $L_0 = (2.3 \mp 0.5)mm$ at the installation SOM. The ampoules had bench marks for the determination of the contact boundary position and the boundaries of liquids penetration into each other. The ampoules were set in motion by means of gas accelerators. The functional scheme of the installation EKAP is shown in Fig.3, and its description is given in [5]. At the

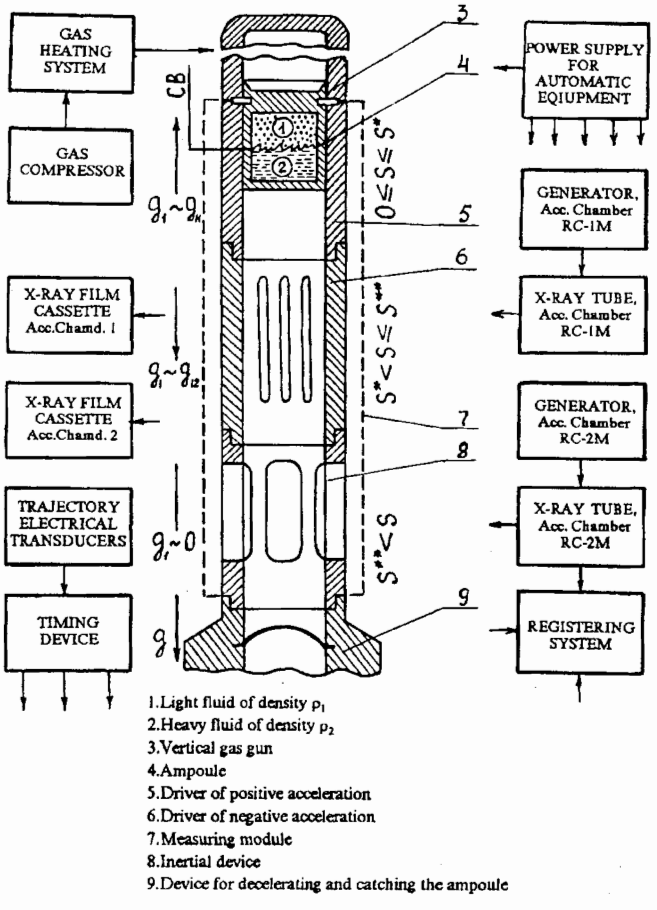

Figure 3. Functional block-diagram of the installation EKAP.

installation EKAP the negative acceleration was created through the deformation of the metal plates. In so far as at the installation SOM the asymptotic stage of separation was studied when $(S - S^*)/S^* > 10$, then, with a view to increase the path of the ampoule motion, the scheme with its return motion was used at this installation (Fig.4). The description of the scheme

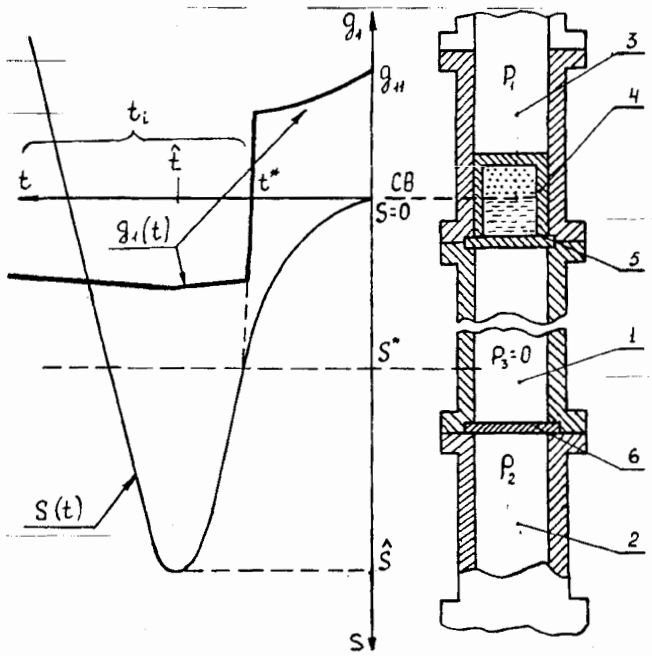

Figure 4. Physical scheme of the measuring module of the installation SOM.

operation with the return motion of the ampoule is given in [6]. During the ampoule motion in the channel of the negative acceleration the roentgenographic registration of the turbulent mixing zone was performed by means of the pulse X-ray chambers at the installation EKAP, but the optical registration - by means of the pulse sources of light at the installation SOM. The pulls X-ray chambers and the pulse sources of light were actuated by the trajectory gauges being located in the appropriate manner. The acceleration of the ampoules was registered by means of piezoceramic accelerometers. The typical oscillograms of the ampoule acceleration are presented in [5].

3. Experimental results

3.1. Experiments at the installation EKAP

In Table 1 the parameters of experiments performed at the installation EKAP are given. Each group consisted of 8 - 12 experiments. In Fig. 5 the typical X-ray images of the turbulent mixing zone which have been obtained in one of the experiments at the installation EKAP are shown. From X-ray images it is seen that the turbulent mixing zone size decreases with time. According to X-ray images the values of the penetration of one liquid into another (L_{12} and L_{21}) were determined by the method of scanning with using the calibration dependencies. The coordinate L_{12} was determined in such a way that nondimensional density $\delta = (\rho - \rho_1)/(\rho_2 - \rho_1)$ being averaged over the ampoule width was equal to $\delta_2 = 0.9$. The coordinate L_{21} was determined by the level of nondimensional density $\delta_1 = 0.1$, respectively. For the densities relation $n = 6$ only the coordinate L_{21} was determined according to X-ray images. In Fig. 6 the experimental

Group of experiments	n	S^*, mm	g_{11}/g	g_{12}/g
1	3	140	600	176
2	3	360	600	245
3	6	140	700	176
4	6	360	490	245

Table 1. Parameters of experiments at the installation EKAP

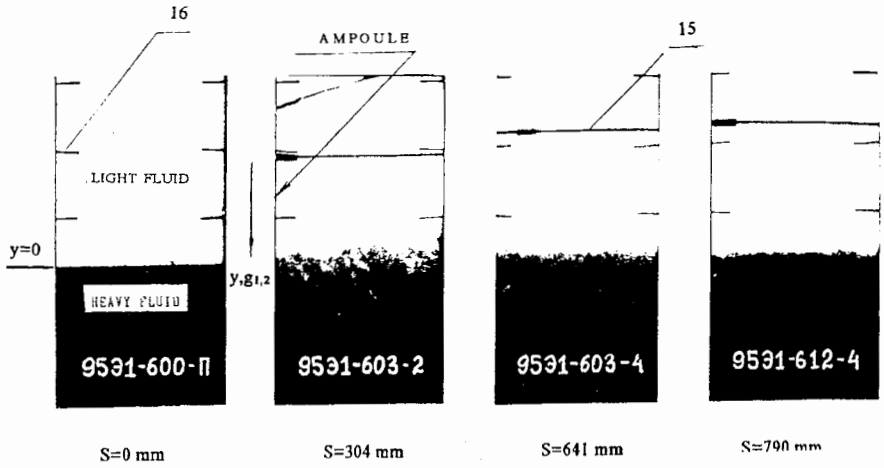

Figure 5. Typical X-ray images of the mixing zone at the stage of separation

results have been given with respect to the determination of the average values of $\sqrt{L_{12}}$ and $\sqrt{L_{21}}$ depending on $\sqrt{\widetilde{S}}$ for each group of experiments.

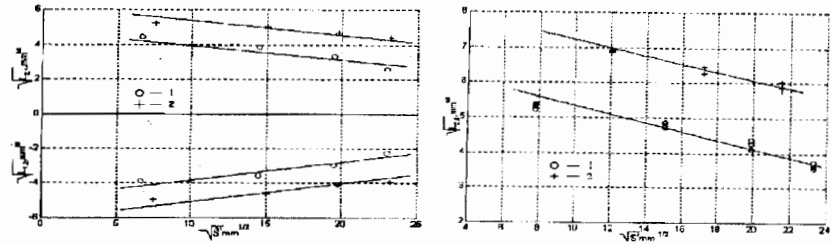

(a) (b)

Figure 6. Dependencies of $\sqrt{L_{12}}$ and $\sqrt{L_{21}}$ on $\sqrt{\widetilde{S}}$ which have been obtained at the installation EKAP a) $n = 3$, $S^* = 140$ mm (1) and $S^* = 360$ mm (2); b) $n = 6$, $S^* = 140$ mm (1) and $S^* = 360$ mm (2).

3.2. Experiments at the installation SOM

In Table 2 the parameters of experiments performed at the installation SOM are given. Each

Group of experiments	n	S^*, mm	g_{11}/g	g_{12}/g
1	1.5	360	120	110
2	1.5	360	120	230
3	1.5	136	120	110
4	1.5	136	120	230
5	3	360	200	300
6	3	360	200	200
7	3	136	200	170

Table 2. Parameters of experiments at the installation SOM

group consisted of 10 - 12 experiments. In Fig. 7 the typical photographs of the turbulent zone which have been obtained in one of the experiments are presented. From the photographs it

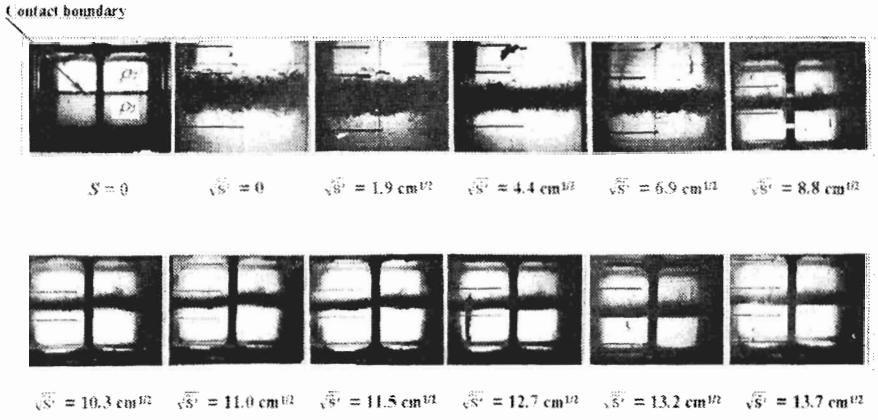

Figure 7. Characteristic photographs of the mixing zone at the separation stage.

is seen that the turbulent mixing zone size is growing with time. Experimental results with respect to the determination of average values of $\sqrt{L_{12}}$ and $\sqrt{L_{21}}$ depending on $\sqrt{S}$ for each group of experiments are given in Fig. 8.

4. Discussion of results

As it follows from the arrangement of experimental points, obtained by the X-ray technique and presented in Fig. 6 for the same values of S^* and n but for different values of g_{11}/g_{12}, the experimental points can be related to the same dependence. Therefore, the separation process

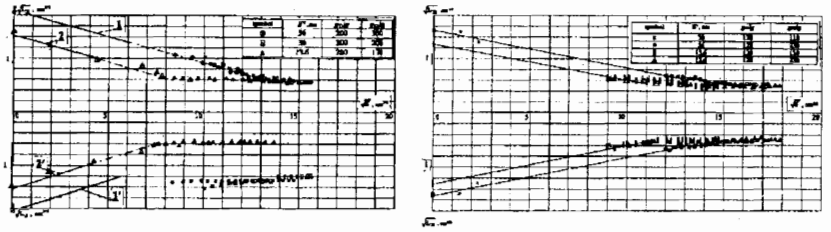

(a) (b)

Figure 8. Dependencies of $\sqrt{L_{12}}$ and $\sqrt{L_{21}}$ on $\sqrt{\tilde{S}}$ which have been obtained at the installation SOM a) $n = 3$; b) $n = 1.5$.

in the chosen coordinates does not depend on the accelerations relation g_{11}/g_{12}. Experimental points have been described by linear dependencies by the least- squares method. The slope angle of the straight lines gives possibility for the determination of the separation constant α_s in each case. This value being determined by means of the relation (1) for both values of S^* and both values of n appeared to be found within the limits of error and to be equal to $\alpha_s \approx 0.01$. It was coincident with previously determined value of α_s for $n = 3$ in [4]. It should be noted that the value of α_s appeared to be identical for the coordinates L_{12} and L_{21}. The asymptotic stage of separation was studied at the installation SOM. As it is seen from the arrangement of the experimental points in Fig. 8, they belong to the same dependencies for the same S^* and n. In Fig. 8a) the experimental dependencies, obtained for $n = 3$ at the initial stage of separation in the work [3] (1 and 1′ - for S^*=36 cm, 2 and 2′ - for S^*= 13.6 cm), are shown in solid straight lines. It is seen that the experimental points obtained at the asymptotic stage are located on the continuation of these straight lines. This means that the separation constant $\alpha_s \approx 0.01$ and it remains the same value at the asymptotic stage. The experimental points for $n = 1.5$ which have been given in Fig. 8b) had been calculated by the least-squares method. The separation constant obtained by means of the relation (2.1) has appeared to be $\alpha_s \approx 0.01$. By summarizing the results obtained at the installations SOM and EKAP, it is possible to say that the separation constant α_s for all the investigated values of Atwood number and values of S^* have the same value and remains it up to the separation cessation. At the same time α_s does not depend on the acceleration relation g_{11}/g_{12}. From Fig. 8a) it is seen that in case of $S^* = 36$ cm the separation in heavy liquid is proceeding considerably slower than for $S^* = 13.6$ cm beginning from $\sqrt{\tilde{S}} \approx 9cm^{1/2}$. At the same time the separation in light liquid is proceeding practically equally for both values of S^*. From this it follows that at the concluding stage of separation the average density of substance in the mixture being found in the heavy liquid is $\delta < 0.02$. Such a small value of density, is most likely, associated with the fact that in this region there are finely-divided particles of the light liquid which, practically, do not move in the direction of acceleration g_{12}.

5. Conclusion

At the installations EKAP and SOM the experimental study into the separation of substances from the Rayleigh-Taylor turbulent mixing zone of different density liquids for three Atwood numbers and study into the asymptotic stage of separation have been performed. Nondimensional rates of separation α_s for Atwood numbers $A = 0.2$, $A = 0.5$, $A = 0.71$, in the range of

$0 < \sqrt{\widetilde{S}} \; ; \; 13 \; cm^{1/2}$ have been determined. Being found both by roentgenographic technique and by the light one they, practically, coincide for all three values of Atwood number and for different values of the relation of the positive and negative accelerations and are equal to $\alpha_s \approx 0.01$. It has been found out that separation is continued up to the definite final size of the turbulized mixture region which exceeds the zone size of the initial perturbations of the contact boundary between fluids.

Acknowledgement. The given work has been performed under the financial support of Commissariat for Atomic Energy, France.

References

[1] Youngs DL, Physica D12, 19, (1984).

[2] Kucherenko YA, Shibarshev LI, Chitaikin VI, Balabin S and Pylaev AP, Experimental investigation into the self-similar mode of the gravitational turbulent mixing, Proc. of the 3^{rd} International Workshop on the Physics of Compressible Turbulent Mixing, Abbey of Royaumont, France, 17 - 19, (1991).

[3] Kucherenko YA, Neuvazhayev VE and Pylaev AP, Behavior of Gravitational Turbulent Mixing Region under Conditions Leading to Separation., Proc. of the 4^{th} International Workshop on the Physics of Compressible Turbulent Mixing, Cambridge, England, 70-80, (1993).

[4] Kucherenko YA, Neuvazhayev VE and Pylaev AP, RUS, 334, 4, 445, (1994).

[5] Kucherenko YA, Pylaev AP, Balabin SI, Murzakov VD, Ardashova RI, Popov VN, Savel'ev VE, Komarov OR, Kozelkov OE Tyaktev AA, Chéret R and Haas JF, Experimental investigation into the Behavior of Turbulized Mixtures at the Stage of Inertial Motion for Different Atwood Numbers, these proceedings.

[6] Kucherenko YA, Pylaev AP, Murzakov VD, Popov VN, Savel'ev V E, Komarov OR, Chéret R and Haas JF, Experimental Study into the Asymptotic Stage of the Separation of the Turbulized Mixtures in Gravitationally Stable Mode, Proc. of the 5^{th} International Workshop on Compressible Turbulent Mixing, Stony Brook, USA, 221, (1997).

Experimental Investigation into the Behavior of Inertial Motion for Different Atwood Numbers

Y.A. Kucherenko[1], A.P. Pylaev[1], S.I. Balabin[1], V.D. Murzakov[1], R.I. Ardashova[1], V.N. Popov[1], V.E. Savel'ev[1], O.R. Komarov[1], O.E. Kozelkov[1], A.A. Tyaktev[1], R. Chéret[2] and J.F. Haas[2]
[1]Russian Federal Nuclear Center - Institute of Technical Physics
456770 Chelyabinsk-70, P.O. 245, Russia
[2]CEA/DAM, BT12 F91680, Bruyères-le-Chatel, France

Abstract: The experimental study into the behavior of the turbulized mixtures at the stage of their inertial motion (with removed acceleration) has been performed. The turbulized mixtures have been obtained as a result of the Rayleigh-Taylor instability development at the contact boundary of two different density fluids during the definite time . At some instant of time t^* the sign of acceleration was changed, and conditions for the separation of the mixture were created. Then at instant of time $t^{**} \geq t^*$ acceleration was removed, and the turbulized mixture continued to move from force of inertia. In the experiments at the installations EKAP and SOM, at the stage of inertial motion, the distribution of average density in the region of the mixture and the size of the turbulized mixture region were determined.

1. Introduction

During the work of the laser thermonuclear fusion targets (LTF) the processes induced by the action of the Rayleigh-Taylor (R-T) and Rihtmyer- Meshkov (R-M) instabilities take place. As a results of the action of these instabilities on the moving contact boundaries of the different density layers, the turbulence leading to mixing of the material of these layers develops. The turbulent mixing at the boundaries of the converging shells leads to changing the laser targets work for the worse [1, 2]. The formed regions of turbulent mixing can, in their turn, be subjected to the shock waves action, to different artificial gravitational fields or can move from the force of inertia. It is important to take into account the turbulent mixing zone development during the calculation of LTF targets. The present work is devoted to the experimental investigations into the inertial properties of the R-T zone of turbulent mixing, i.e. to the investigation into the regularities of the turbulent region spreading after stopping the action of acceleration. Theoretical results being available regarding this question [3, 4] give only the asymptotic law of the turbulent layer spreading when the initial state of the system can be neglected.

2. Set-up of experiments

The task is formulated as follows. At first the system of two different density liquids with densities ρ_1 and ρ_2 ($\rho_1 < \rho_2$) is found in artificial gravitational field with accelerations g_1 directed from the heavy liquid to the light one in the frame of reference associated with the contact boundary (Fig. 1). L_0 - size of the initial perturbations zone, L_{21} and L_{12} - depth of the heavy fluid penetration into the light one, respectively, and vice versa, CB - contact boundary. The acceleration mode is shown in Fig.2. At the instant of time t^* acceleration changes its sign, at the instant of time t^{**} acceleration is removed. During the period $\Delta t = t^{**} - t^*$ the system is found in a stable state, therefore, in the turbulent mixing zone the separation of substances

More information - Email: Kucherenko@five.ch70.chel.su or bkv@vniitf.ch70.chel.su

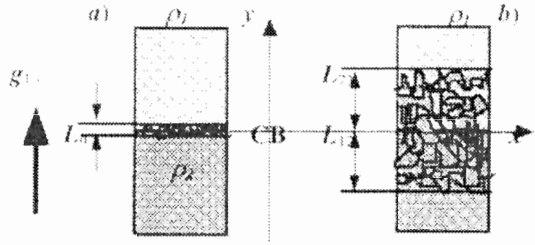

Figure 1. Schematic image of the turbulent mixing zone a) at initial instant of time $t = 0$ b) at the stage of inertial motion.

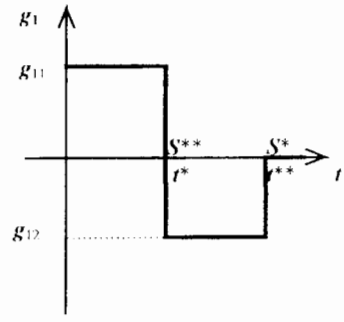

Figure 2. Mode of acceleration.

takes place. At $t > t^{**}$ the system is moving by inertia. The experiments were performed for two cases: 1) $t^{**} \neq t^*$; 2) $t^{**} = t^*$. Experiments were performed at the installation EKAP by the X-ray technique for the liquid densities relation $n = 3$ and $n = 6$ and at the installation SOM by the light technique for $n = 3$. For obtaining the densities relation $n = 3$ two liquids benzine and aqueous solution of zinc chloride have been used, but for $n = 6$ - benzine and Klerichi liquid. The functional schemes of the installations EKAP and SOM are given in Fig. 3. The investigated liquids were placed into the hermetically sealed ampoules which at the initial instant of time were located in the upper parts of the measuring modules of the corresponding installations. The internal working sizes of the ampoules amount to $(50 \times 50 \times 140) mm^3$ for the installation EKAP and $(54 \times 64 \times 120) mm^3$ for the installation SOM. At the contact boundaries of liquids the random initial perturbations were specified. The width of the initial perturbations zone $L_0 = (1 \pm 0.2)$ mm at the installation EKAP and $L_0 = (2,3 \pm 0,5)$ mm at the installation SOM. Ampoules had bench marks for the determination of the contact boundary position and the boundaries of liquids penetration into each other. The ampoules with pistons being mounted at the top of them were set in motion by means of gas accelerators. At instant of time t^* (flight distance of the ampoule S^*) the ampoule got into the channel of negative acceleration in the first case ($t^{**} \neq t^*$), and in the channel of inertial motion in the second case ($t^{**} = t^*$). At the same time, the piston was braked by a special device and the gas flow was cut off from the ampoule. At both installations negative acceleration was created due to the plastic deformation of the metal plates by the lower edge of the ampoule. For the first case ($t^{**} \neq t^*$), at the instant of time t^{**} (flight distance of the ampoule S^{**}), acceleration was removed due to the cessation

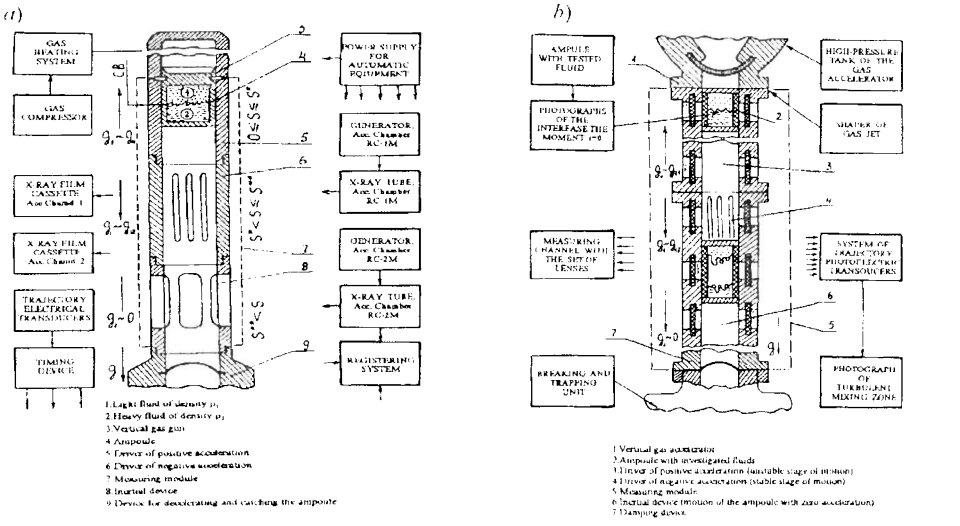

Figure 3. a)Functional scheme of the installation EKAP; b) Functional scheme of the installation SOM.

of the contact of the lower edge of the ampoule with the metal plate. For the second case ($t^{**} = t^{*}$) the channel of negative acceleration was absent. At the stage of the inertial motion of the ampoule, gas pressure above and under the ampoule was equalized by means of special controlled membranes. During the ampoule motion at the inertial section, the X-ray registration of the turbulent mixing zone was performed by the pulsed X-ray chambers at the installation EKAP and the optical registration - by pulsed sources of light at the installation SOM. The pulsed X-ray chambers and the pulsed sources of light were put into action by trajectory gauges being located in the appropriate manner. The ampoules acceleration was registered by means of piezoceramic accelerometers. In Fig.4 the typical oscillograms of the ampoules acceleration are shown which have been obtained at the installations EKAP and SOM.

3. Experimental results

3.1. Experiments at the installation EKAP

In table 1 the parameters of the experiments performed at the installation EKAP are given. Each group consisted of 8-12 experiments. Fig. 5 shows the typical X-ray images of the turbulent mixing zone which have been obtained in one of the experiments at the installation EKAP at the inertial part of the ampoule motion. From the X-ray images it is seen that the turbulent mixing zone size is growing with time. Using X-ray images for the densities relation $n = 3$, the values of the penetration of one liquid into the other one - L_{12} and L_{21} - as well as the distribution of the average density of substance in the mixing zone were determined by the scanning method with using the calibration dependencies. The coordinate L_{12} was determined in such a way that nondimensional density $\delta = (\rho - \rho_1)/(\rho_2 - \rho_1)$ being averaged over the coordinate x was equal to $\delta_2 = 0.9$. The coordinate L_{21} was determined by the level of nondimensional density $\delta_1 = 0.1$. For the densities relation $n = 6$ only the coordinate L_{21} was

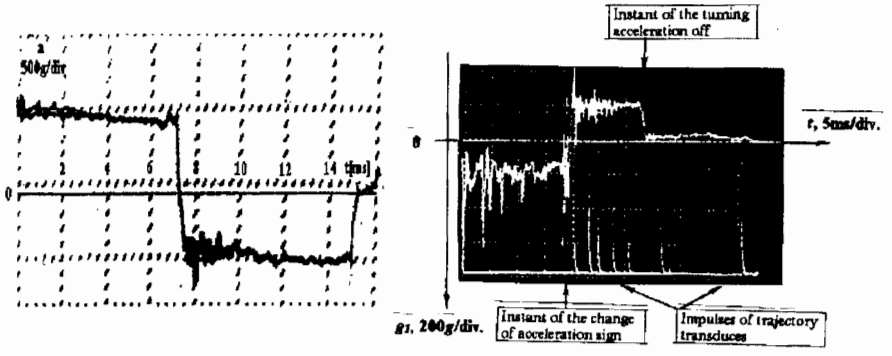

(a) (b)

Figure 4. a)Oscillogram of acceleration obtained at the installation EKAP; b)Oscillogram of acceleration obtained at the installation SOM.

Group of experiments	n	S^*, mm	S^{**}, mm	g_{11}/g	g_{12}/g
1	3	140	140	500	-
2	3	140	340	570	400
3	3	360	360	500	-
4	3	360	900	600	245
5	6	140	140	880	-
6	6	140	340	600	400

Table 1. Parameters of experiments at the installation EKAP.

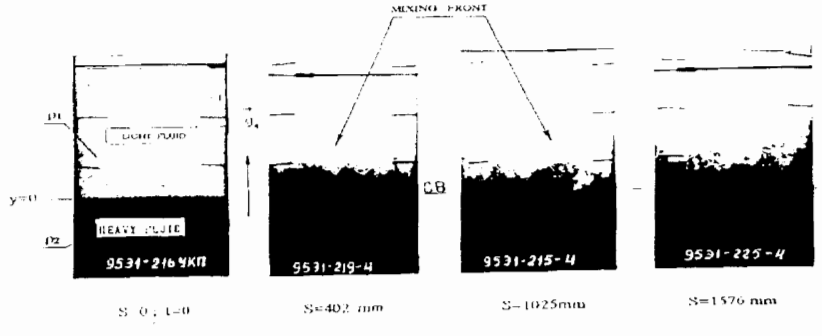

Figure 5. Characteristic X-ray images of the mixing zone.

determined according to X-ray images. The distributions of the average density of substance for $n = 3$ are given in Fig. 6 in the nondimensional coordinates $\delta(\chi)$, where the nondimensional coordinate χ is determined as $\chi = (y - y_{0.1})/(y_{0.9} - y_{0.1})$. Here $y_{0.9}$ and $y_{0.1}$ - values of the coordinates of the mixing fronts at which the nondimensional density assumes the values $\delta_2 = 0.9$ and $\delta_1 = 0.1$, respectively. In Fig. 8 the experimental results are given with respect to the

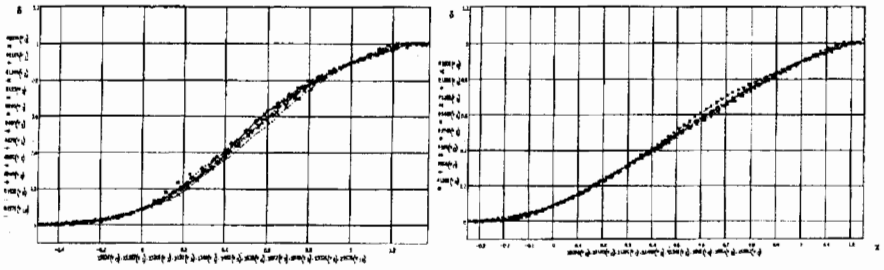

Figure 6. Dependence $\delta(\chi)$ at the inertial stage of motion for $n = 3$ a) $S^* = S^{**} = 140$ mm and $S^* = 140$ mm, $S^{**} = 340$ mm.

determination of the average values of the nondimensional coordinates L_{12}/L_{12}^{**} and L_{21}/L_{21}^{**} for each group of experiments depending on the nondimensional value of S/S^{**}.

3.2. Experiments at the installation SOM

Table 2 gives the parameters of experiments performed at the installation SOM. Each group

Group of experiments	S^*, mm	S^{**}, mm	g_{11}/g	g_{12}/g
1	136	396	200	200
2	136	396	200	100
3	136	136	200	-

Table 2. Parameters of experiments at the installation SOM.

consisted of 10 - 12 experiments. Fig. 7 shows the typical photographic images of the turbulent mixing zone which have been obtained in one of the experiments at the installation SOM at the inertial part of the ampoule motion. From the photographic images it is seen that the turbulent mixing zone size is growing with time. In Fig. 8 the experimental results are given with respect to the determination of the average values of the nondimensional coordinates L_{12}/L_{12}^{**} and L_{21}/L_{21}^{**} for each group depending on the nondimensional value of S/S^{**}.

4. Discussion of results

From comparing the dependencies given in Fig.6a and Fig.6b it is seen that they are essentially not distinguished from each other. This means that at the inertial stage of motion (when forces do not act on the system), the average density distribution of substance in the turbulent mixing zone does not depend on the kinetic energy of turbulence for the moment of acceleration removal as well as on the fact whether the separation stage of the process preceded the moment

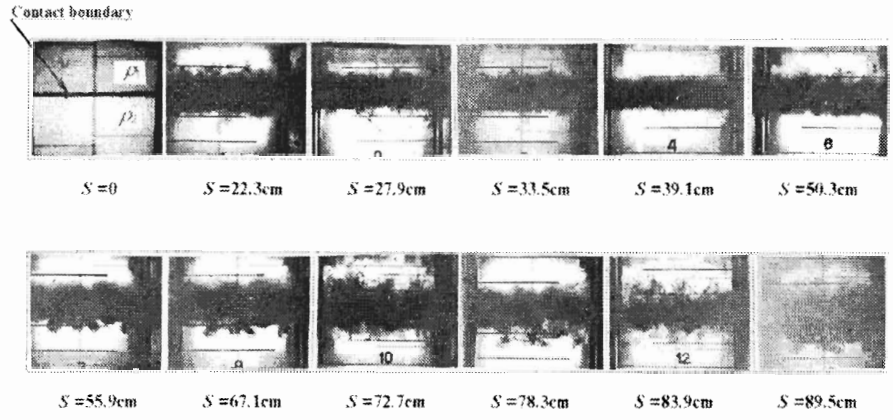

Figure 7. Characteristic photographic images of the mixing zone for $n = 3$.

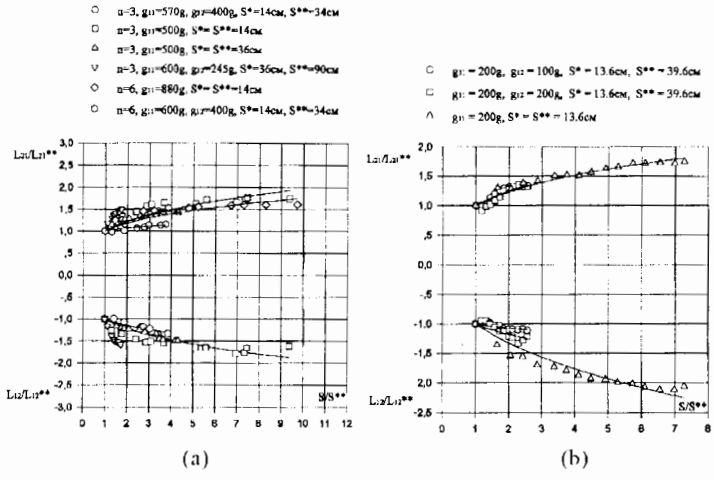

Figure 8. Experimental dependencies obtained at the installations: a) EKAP; b) SOM.

of acceleration removal. Moreover, the comparison of the distribution obtained at the inertial stage in nondimensional coordinates with the analogous distributions of the average density for the self-similar stage of the gravitational turbulent mixing [5] and for the separation stage of the process [6] makes possible to draw the conclusion that all these distributions are coincident with each other within the errors of measurements. Experimental points obtained by the X-ray technique and presented in Fig.8 *a*) as well as the experimental points obtained by the light technique and presented in Fig. 8 *b*) have been described by the method of least squares by nondimensional dependencies : $L_{12}/L_{12}^{**} = (S/S^{**})^k$, $L_{21}/L_{21}^{**} = (S/S^{**})^k$. The obtained values of k are presented in tables 3 and 4. As it is seen from the tables, in most of cases the values of k are within the limits $0.27 < k < 0.32$. In some cases the discrepancies in the values of k from the shown range are explained either by insufficient statistics or by a small range of measurements with respect to S/S^{**}.

Group of experiments	For L_{21}	For L_{12}	Group of experiments	For L_{21}	For L_{12}
1	0.29	0.28	4	0.82	0.94
2	0.30	0.20	5	0.25	-
3	0.28	0.27	6	0.10	-

Table 3. The values of k in experiments at the installation EKAP.

Group of experiments	For L_{21}	For L_{12}
1	0.32	0.10
2	0.32	0.24
3	0.30	0.31

Table 4. The values of k in experiments at the installation SOM.

5. Conclusion

As a result of the experimental investigation into the behavior of the R-T turbulized layer of two different density liquids mixture, under conditions of removed acceleration, the spatial-time distributions of the substance density in the mixture zone have been obtained and the parameters of the layer spreading with time have been determined. It has been found out that the density distribution in the nondimensional form does not depend on the kinetic energy of turbulence for the acceleration removal moment as well as on the fact whether the separation stage of the process preceded the acceleration removal moment. The parameter of spreading of the layer k is within the range of $0.27 < k < 0.32$.

Acknowledgement. The given work has been performed under the financial support of the Commissariat for Atomic Energy of France.

References

[1] Andronov VA, Bakhrah SM, Mokhov VN, Nikiforov VV, Pevnitzky AV, Turbulent Mixing Influence on Laser Targets Compression, Letters to ZhETF, 29, 1, (1979).

[2] Lykov VA, Murashkina VA, Neuvazhayev VE, Shibarshov LI, Yakovlev VG, Turbulent Mixing Influence on the Compression of shell Targets, Letters to ZhETF, 30, 6, (1979).

[3] Barenblatt GI, Spreading of Turbulent Layer, In. coll. Kochin N.E. and Development of Mechanics, Moscow, NAUKA, (1984).

[4] Neuvazhaeyev VE, Spreading of the Turbulent Layer of Mixture, PMTF, 2, (1988).

[5] Kucherenko YA, Balabin SI, Pylaev AP, Experimental study of the gravitational turbulent mixing self-similar mode, The 3^{rd} International Workshop on the Physics of Compressible Turbulent Mixing, Abbey of Royamont (France), June 17-19, (1991).

[6] Kucherenko YA, Balabin SI, Ardashova RI, Kozelkov OE, Romanov IA, Cheret R, Haas JF, Determination of space-time distributions of the average of matter in the turbulized mixture region at the stage of separation by X-ray technique, these proceedings.

Experiment and Numerical Computation on a Large-Scale Richtmyer-Meshkov Instability

G. Lacassin, F. Poggi and G. Rodriguez
Commissariat à l'Énergie Atomique, Centre d'études de Vaujours-Moronvilliers
BP 7, 77181 Courtry, France

Abstract: We report an experimental and numerical study of a Richtmyer-Meshkov instability. The initial configuration is a bulged discontinuous interface separating two gases of different densities. These initial conditions lead to the reversal of the bulged interface and to the development of large three-dimensional vortices. The inviscid 2D computation predicts the experimental shape of the wall vortices and the boundary positions of the interface with a good agreement. For the 3D computation, the lack of mesh resolution is the reason of the observed discrepancies. However, the time evolution of the instability thickness is well predicted. A spectral analysis of the perturbation provides a comparison with the impulsive theory.

1. Introduction

We first present shock tube experiments on the Richtmyer-Meshkov instability (RMI) of a bulged discontinuous interface between the couple of gases sulphur hexafluoride (SF_6)/air. The characteristic of this bulged interface is to be a large-scale initial spatial perturbation. Two- and three-dimensional simulations, performed with a Cray-YMP computer, are reported and compared to the experimental results. The RMI appears by a baroclinic phenomenon, when a plane shock wave impulsively accelerates the two gases. It leads to the initial bulge reversal, as predicted by the RMI theory in the heavy-light acceleration case for a single-wavelength sinusoidal perturbation, and develops into one bubble and several spikes, which produce large wall vortices.

2. Experiment

2.1. Initial configuration

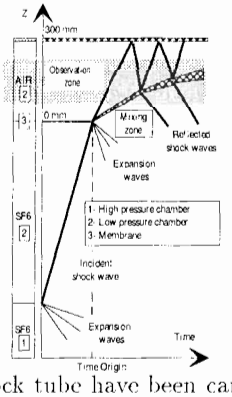

Figure 1: Schematic shock tube and (z, t) diagram.

Experiments in a vertical shock tube have been carried out with the couple of gases SF_6/air. Fig. 1 shows the schematic shock tube and a (z,t) diagram. The shock tube has a square cross

More information - Email: haas@vaujours.cea.fr

section which is separated in three parts. The first one is a high pressure chamber: it contains air which generates the incident shock wave. The two other parts are atmospheric pressure chambers which contain SF_6 and air respectively. The two gases are initially separated by a plastic membrane, 0.3 μm thick, deformed by a slight over-pressure in the heavy gas (SF_6). This bulged membrane is fragmented by the passage of an incident upward propagating shock wave. The interface between gases is then put in motion before being slowed down by several reflected shock waves from the top wall of the tube.
The initial interface is not simply visualizable. We have therefore developed an optical method using laser beams to measure at several locations the initial form of the interface. For a difference of pressure of 1.44 mbar, a bulge of amplitude η_0=6.8 mm$\pm$0.5 was obtained. Several membranes have been tested so as to verify the reproduciblity of their behaviour. We have chosen to approximate the initial form of the interface by a simple analytic law (1).

2.2. Diagnostics

Two experiments have been realized with an incident shock of Mach number M_{is}=1.44. The first test was conducted with a schlieren system coupled to a rapid (rotating drum) camera to visualize the interface. We have obtained the trajectory of the interface during about 2 ms with a time interval between successive images of about 28 μs. The second test used differential interferometry and we realized only one image per shot. These two diagnostics are sensitive to the density gradient along a chosen direction, here the vertical axis of the tube. For each test we measured the pressure with the help of a pressure gauge located 95 mm above the initial position of the interface.
could not use the rapid camera and we realized only one image per shot. In the interferometry diagnostics, every deviation of a light ray generates a change of color which can be associated to a density gradient value. The calibration is made with the help of interference bands obtained in static conditions, without any density gradient but with a little modification of the optical apparatus.

2.3. Schlieren visualizations

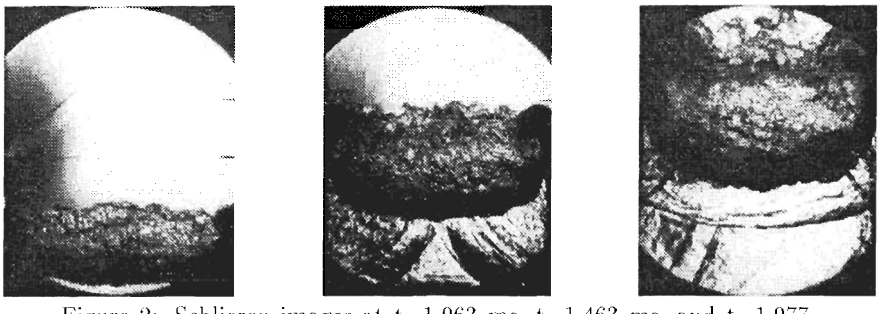

Figure 2: Schlieren images at t=1.063 ms, t=1.463 ms, and t=1.977 ms.

Fig. 2 represents schlieren images of the interface corresponding to three different times of its evolution. We can see that the initial bulge has reversed before the first reshock passage. Then, the perturbation amplitude increases during time.
The crest line of the wall vortices is visible on all the tube walls. The schlieren diagnostics integrates the inhomogeneities along the optical path.

We notice a local thickness of the interface on the schlieren images, in the lowest part of the bulge. This thickness could indicate the presence of a mixing zone between the gases. In that case, the word "interface" is not appropriate. The differential interferometry helped us to interpretate this point.

2.4. Interferometry visualization

Fig. 3 shows an interferometric image at the time of 1.442 ms. Here, only the density gradients in SF_6 (below the interface on the image), where we observe oblique shock waves, can be determined. We can establish that the membrane has really been torn in small pieces in the lowest part of the bulge. This implies the presence of a mixing zone with small structures. The positions and shape of the interface and shock waves are in agreement with that obtained, by schlieren, at a similar time. We conclude that the initial conditions are well controlled and the experiments are reproducible.

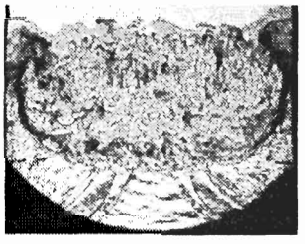

Figure 3: Interferometric image at t=1.442 ms.

3. Numerical method

Our computations have been carried out with the multi-material hydrodynamical HESIONE computer program. The solved equations are the compressible three-dimensional Euler's equations. An ideal gas equation of state is used for each gas with a constant ratio of specific heats γ. Neither the thin film nor the initial over-pressure present in the experiment have been simulated herein.

As in many compressible fluid codes, the calculation for each time-step is divided into two successive phases, a "lagrangian" phase and an advection (or rezoning) phase. The calculation is based on the second order BBC [1] explicit finite differences scheme. A front-tracking method provides an approximate interface between two fluids in a cell.

The plane incident shock wave is moving in SF_6 with the velocity W_{is}=194.2 m/s. The interface velocity jump induced by the incident shock is ΔV=127.8 m/s: this value has been calculated by solving the Hugoniot's equations. The post-shock Atwood ratio across the interface is defined as $A'_t=(\rho'_A-\rho'_S)/(\rho'_A+\rho'_S)=-0.697$, with ρ' the density of the gas just after the incident shock passage.

We use a Cartesian frame with the z-direction along the vertical axis of symmetry of the shock tube, and with x and y the cross directions. The position z=0 corresponds to the initial lower position of the material interface, and z=30 cm is the shock tube end. A typical 2D-mesh size is 140×1100 zones, with zones with constant sizes of dx=0.571 mm and dz=0.40 mm for $10<z<30$ cm. For the 3D computation, we have used only 30×30 zones to model the shock tube cross section. We have used a periodic boundary condition, and a flow through boundary condition

for the lower boundary of the computation domain.
The initial three-dimensional and two-dimensional interface shape between SF and air are defined by

$$Z_{3D}(x,y) = \eta_0 \,|\cos(\pi x/L)\cos(\pi y/L)|, \quad (1)$$

$$Z_{2D}(x) = \eta_0 \,|\cos(\pi x/L)|, \quad (2)$$

with L=8 cm the tube width and $\eta_0 = \eta(t{=}0)$ the initial (pre-shock) amplitude.

4. Results and discussion

4.1. Comparison between experiment and computation

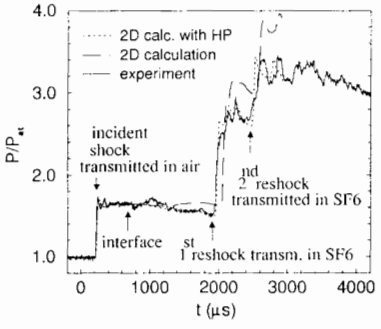

Figure 4: Wall pressure vs time at 95 mm above the initial interface.

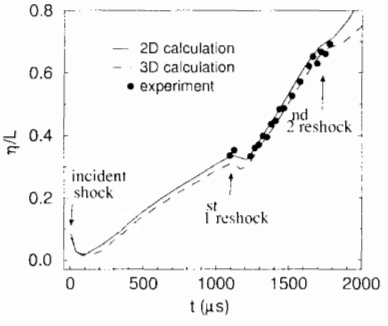

Figure 5: Perturbation amplitude $\eta(t)$ vs time.

The pressure measured with a wall-mounted gauge is shown in Fig. 4. The first abrupt increase of pressure is the passage of the incident shock transmitted in air. The interface, put in motion by the incident shock, goes past the gauge position at about 660 μs. In the middle of the first pressure plateau, the gauge records the rarefaction waves coming from the high pressure chamber. The following pressure jumps correspond to successive passages of reflected shock waves from the top tube wall. The calculation with the high pressure chamber takes into account the rarefaction waves passage: it predicts well the shape of the experimental curve.
Fig. 5 presents the amplitude of the perturbation $\eta(t)$. The thickness $\eta(t)$ is the "crest-to-trough" vertical distance at each instant t (with $\eta(0){=}\eta_0$), and can be viewed as the macroscopic interpenetration length of the two gases. Experimental data of $\eta(t)$, deducted from schlieren and interferometric visualizations of the flow, are available after the first reshock/interface interaction. We observe a very good agreement between the 2D computation and the experimental points. The 3D computation does not fit so well the experimental data before reshock. Fig. 6 shows at two different instants, the comparison of the interface shapes between the simulations and the experiments. The experimental profiles correspond to the local maximum of the vertical gradient $\partial\rho/\partial z$. We observe the complex waves system amplified by the first reshock passage at t=1463 μs. The 2D computation flow predicts the experimental boundary positions of the interface with a good agreement. membrane present in the flow. But, the shock-tube wall boundary layers lift the spikes off the walls and retard their penetration. This drag-induced retardation could explain the little differences beetween the spikes positions at t=1634 μs.
We observe a systematic position shift between the 3D computation interface and the experimental one. This tendancy is more pronounced as the instability evolves in time. We explain

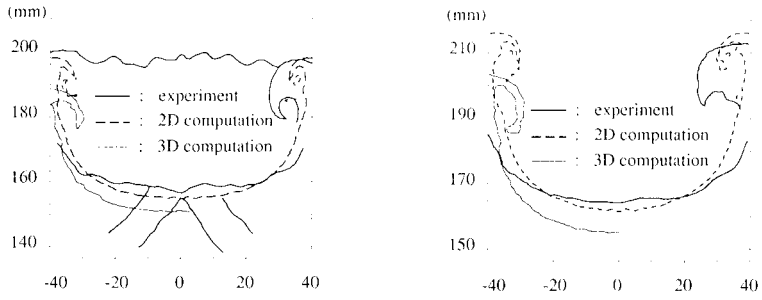

Figure 6: Interface shape at t=1463 μs and t=1634 μs.

these discrepancies by a lack of mesh resolution which does not ensure the grid convergence for the 3D computation.
At the light of these results, we conclude that the inviscid two-dimensional computation describes with a good accuracy the experiment.

4.2. Comparison between theory and computation

In this part, we are going to introduce the Richtmyer theorical approach in our case.
The predict growth rate of the amplitude, $\dot{a}_n(t)$, of an initial single-wavelength sinusoidal perturbation of index n is given by the incompressible impulsive formula initially proposed by Richtmyer [2]:

$$\dot{a}_n(t) = k_n \, \Delta V \, A'_t \, a'_n(0), \tag{3}$$

with k_n the wavenumber, A'_t and $a'_n(0)$ the post-shock Atwood ratio number and initial amplitude. The impulsive growth rate (3) is constant and is valid as long as $k_n a_n(t) \ll 1$ (linear regime).
The symmetric 2D perturbation (2) can be expanded into a Fourier serie of the following form: $Z(x,\ t{=}0) = \sum_{\substack{p=1 \\ n=2p}}^{\infty} a_n(0)\ cos(k_n\ x)$, with $a_n(0)/\eta_0 = 4(-1)^{n/2-1}/\pi(4n^2 - 1) = c_n$ and $k_n{=}2\pi n/L$. If we assume that the instability retains a sinusoidal shape just after the incident shock passage, one obtains $a'_n(0) = c_n\ \eta'_0$.
The duration of the incident shock/interface interaction is about 35 μs. In this period, we suppose the decrease rate of $\eta(t)$ is ΔV (see Fig. 5), and the compression of the initial perturbation is given by the small-amplitude relation: $\eta'^{th}_0 = \eta_0(1 - \Delta V/W_{is})$. We obtain η'^{th}_0=2.3 mm when the computation gives η'_0=2.8$\pm$0.2 mm. We are now able to apply the impulsive formula (3) at each sinusoidal mode n which composes the Fourier spectrum of the initial interface.
In order to compare the Richtmyer prediction to our computation, we have determined the computed interface shape at several instants.
We have used the density distribution [3] $\hat{Z}(x,t){=}\int \rho(x,z,t)\ dz$ which gives us a single-value function when the wall vortices evolve. Then, we calculate numerically the amplitude $a_n(t)$ of the mode n (see Fig. 7a). Fig. 7b shows that the growth rate of some chosen modes is rather well predicted by the Richtmyer model until t=500 μs. After, we suppose that the nonlinearity plays a significant role. We notice an abrupt increase of the growth rate of the short wavelengths above the n=14 mode (Fig. 7a); this is similar to an amplitude saturation phenomenon observed by Aleshin *et al.*[4].
The interface reversal induces first a decrease, then a phase inversion of all the $a_n(t)$ before a sustained growth. This phase shift changes the initial sign of the $a_n(t)$. It occurs more rapidly

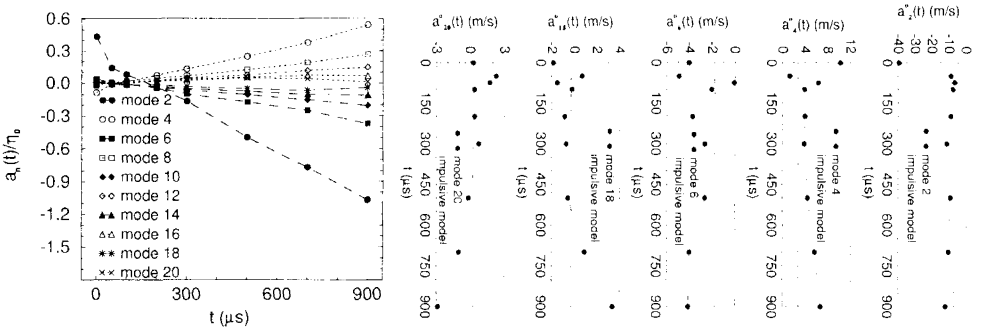

a) Amplitude $a_n(t)$ of the first ten modes from the computation.

b) Growth rate $\dot{a}_n(t)$ of five modes: comparison with the Richtmyer's equation.

Figure 7: Results from the spectral analysis of the 2D computed interface.

in time as the mode index is greater. The n=2 mode is the last mode to reverse its phase at about 150 μs, so it imposes the characteristic time of bulge reversal.
The n=2 mode is preponderant: it's the fastest mode to evolve with its large growth rate value, and it keeps a large amplitude value. The time of reversal estimed with the impulsive formula (3) applied on this unique mode gives the same time. This implies a good agreement between theory and computation.

5. Conclusion

We have presented an experimental, numerical and theoretical approach of a Richtmyer-Meshkov instability. Experimentaly, we obtain reproducible experiments by a good control of initial conditions, with a differential interferometry visualization of the instability. The comparison with the 2D computation shows encouraging agreement in respect of the outline and shape of the interface.

References

[1] Sutcliffe WG, BBC hydrodynamics, Lawrence Livermore National Laboratory Report No. UCRL-ID-17013, (1973).

[2] Richtmyer RD, Taylor instability in shock acceleration of compressible fluids, Comm. Pure Appl. Math., 13, 297, (1960).

[3] Ofer D, Sharts D, Zinamon Z and Orszag SA, Mode coupling in nonlinear Rayleigh-Taylor instability, Phys. Fluids B, 4, 3549, (1992).

[4] Aleshin AN, Gamalii EG, Zaitsev SG, Lazareva EV, Lebo IG and Rozanov VB, Nonlinear and transitional stages in the onset of the Richtmyer-Meshkov instability, Sov. Tech. Phys. Lett., 14, 466, (1988).

Shock-Induced Intensification of Turbulent Mixing

E.V. Lazareva[1], A.N. Aleshin[1], S.V. Sergeev[1], S.G. Zaytsev[1] and J.F. Haas[2]
[1]Krzhizhanovsky Power Engineering Institute (ENIN)
Leninsky pr. 19, Moscow, 117071 Russia
[2]Commissariat à l'Energie Atomique, Centre d'Etudes de Vaujours-Moronvilliers
BP7, 77181 Courtry, France

Abstract: Interaction of the shock wave with turbulized interface between two gases of different density was studied. The following problems were investigated: 1) the effect of turbulized interface on the shock that has passed through it; 2) shock-induced intensification of turbulent mixing; 3) the effect of shock strength on the intensification of mixing.

1. Design of experiment

The study was performed in a shock tube of square section 72×72 mm^2. The investigations were performed for a wide range of Atwood numbers (At) at initial pressure 0.5 atm. To solve the formulated problems, different modifications of the set-up were used. To solve the problem 2, the driven was divided by a thin membrane into two parts which were filled with two different gases A and B. We studied the interaction of the shock reflected from the end wall with the interface developed after the passage of the incident shock wave; the reflected shock wave passed from light gas into the heavy one and vice versa. To solve the problems 1 and 3, the set-up was modified. Its block diagram is given in Fig. 1. The test sections providing

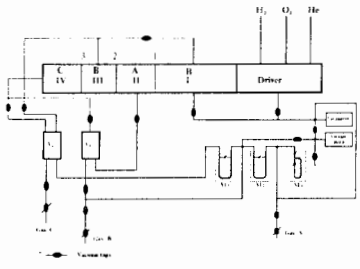

Figure 1. Block diagram of the set-up.

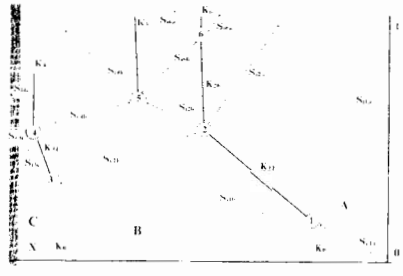

Figure 2. X,t-diagram of the process.

the division of the driven into four parts with three thin plane membranes, were constructed and mounted. The first and third membranes were 10 μm thick, the second one was 1.5-3 μm thick. The first and third parts were filled with the same gas B. This allowed us to save the expensive inert gases Ar, Kr, and Xe. The wave image observed in gases A, B and C, and the denotations used are given in Fig. 2. In this part of the study, only the strength of the reflected shock S_{e2b} interacting with the interface K_{12} was changed. The properties of K_{12} were unchanged due to the constant Mach number of the incident shock S_{i1a} which varied within

More information - Email: sgz@mazilin.msk.ru

4.7±0.5. The strength of the reflected shock S_{e2b} was varied with different combinations of gases which formed the interface to reflect the shock. The subject of the present study is the interaction of the interface K_{12} with the reflected shock S_{e2b}. As the working gases A, B, and C, inert gases were used, provided that $\rho_c > \rho_b$ and $\rho_a > \rho_b$. In this case, the reflected shock S_{e2b} passed from light gas into the heavy one.

To visualize the process, the test-section was equipped with optical glasses. The disposition of the glasses, separating membranes, and the corresponding synchronization of the process allowed us to record the moment of interaction of S_{e2b} with K_{12}. The process was recorded by Schlieren method with snapshot (Fig. 3) and streak pictures (Fig. 4). Each of the used

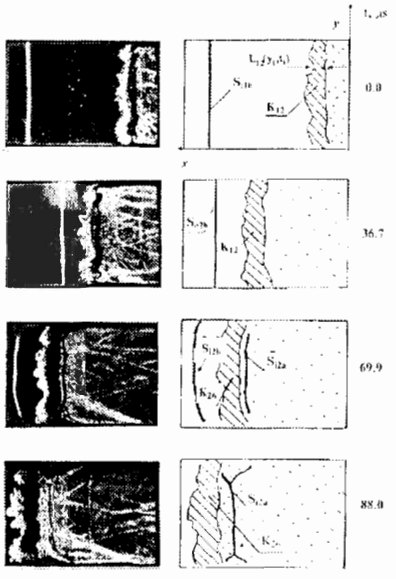

Figure 3. Snapshot recording of the process.

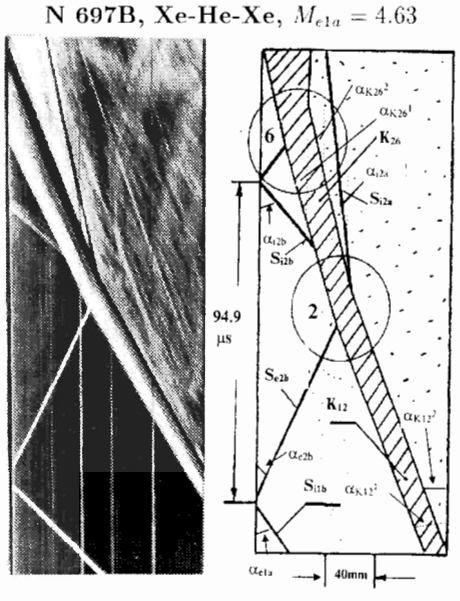

Figure 4. Continuous recording of the process. The characteristic lines are shown on the streak picture.

methods has its advantages, and they complement each other. The snapshot pictures allow us to obtain the image of the interface for several moments of time. However, the small number of frames allowed us to determine the velocities of characteristic lines with the accuracy not higher than ~20%. The streak picture allows us to record, in a given cross-section, the behavior of the whole wave image, and to measure the velocities of characteristic lines with accuracy ~ 7%. In this case, the higher accuracy is due to the continuous recording and the sharp borders of characteristic lines.

To define the construction of the set-up and experimental conditions, and to analyse our experimental data, we performed one-dimensional calculation for the wave image shown in Fig. 2. This calculation does not account for the development of turbulence in the interface between the media with different densities and the presence of membranes. All the calculated values are denoted by symbol "*".

2. Results of experiments

Figure 3 gives a series of Schlieren snapshot pictures and the denotations of recorded objects. The processing of Schlieren snapshot pictures included determination of the thicknesses of mixing zone $L_{12}(y_i, t_i)$ and $L_{26}(y_i, t_i)$ for a number of cross-sections y_i. Figure 5 shows the

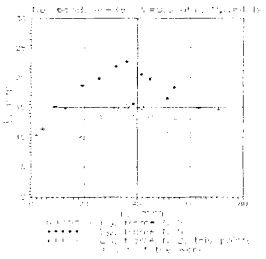

Figure 5. L_{12} and L_{26} against y.

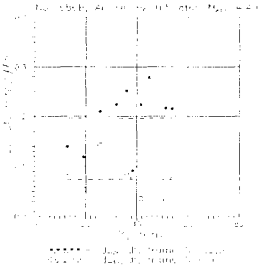

Figure 6. dL_{12}/dt and dL_{26}/dt against y.

values of $L_{12}(y_i, t_i)$ and $L_{26}(y_i, t_i)$ as functions of y for a given moment of time. To exclude the influence of wall effects, the values measured at the walls were excluded from the further analysis. As seen, L_{12} and L_{26} vary around the mean value. These variations are due to the random nature of the process. The range of variation is a characteristic of the evolution of turbulent mixing zone. The deviation of L from the mean value is 15%, and those of dL_{12}/dt and dL_{26}/dt are 60 and 30% (Fig. 6), respectively.

Figure 4 shows a Schlieren streak picture obtained by continuous recording of the process through a 0.3 mm slit parallel to the longitudinal axis of the test-section. This system of recording allows us to perform continuous recording of the wave image for a given cross-section y_i defined by the position of the slit. The obtained Schlieren streak pictures were used to determine the characteristics of wave image of the process and the velocities of all the shock waves and interface boundaries. The slopes α of all the observed shock waves and interface boundaries were measured. The tangent of this slope is the ratio of the shift of shock wave or interface to the shift of the film for a time t. The desired velocity is $v \cdot \Omega \cdot \tan\alpha$ (where Ω is the scale of recording of the process on the film; the time t is determined by the film; v is the recording rate of the process). It should be noted that just after the reflection, the shock wave S_{e2b}, under the influence of the membrane weight, moves faster than at the moment of interaction with K_{12}. Thus, the value of α at the moment of reflection of S_{e2b} is higher than that at the moment of interaction of S_{e2b} with K_{12}. Figures 7 and 8 give the plots of dL_{26}/dt and ΔU, $(dL_{26}/dt)\Delta U^{-1}$ against M_{e2b} for two At: 0.9 (Xe-He-gas C) and 0.62 (Xe-Ne-gas C); $\Delta U = U_{K_{12}} - U_{K_{26}}$; the At is given for the border of K_{12}. For these plots, the values of M_{e2b} corresponding to the moment of interaction of S_{e2b} with K_{12} were used (lines 2 and 3 in column 4 of Table 1 give two independent measurements). The relation between ΔU and Mach number was obtained by one-dimensional calculation. The calculation was performed adequately to the experiment: M_{e1a} was constant, and M_{e2b} was varied by changing the combinations of gases.

3. Discussion

We have found that within the error of experiment (7%), the shock wave S_{i1b} propagates at calculated speed. In most runs, because of the effect of membrane, the speed of the shock wave S_{e2b} at the moment of interaction with K_{12} was higher than that obtained by calculation. In

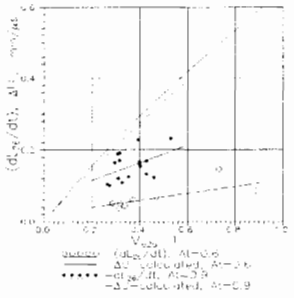

Figure 7. dL_{26}/dt and ΔU against the strength of the reflected shock wave S_{e2b}; At=0.6 and 0.9.

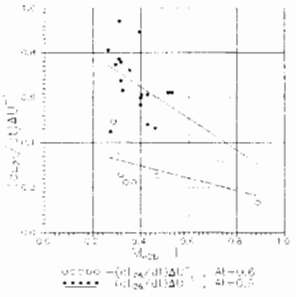

Figure 8. $dL_{26}/dt \cdot \Delta U^{-1}$ against the strength of the reflected shock wave S_{e2b}; At = 0.6 and 0.9.

all the runs, the speed of the shock wave S_{i2a} was lower than the calculated one. To compare the speeds of the shock waves S_{e2b} and S_{i2a} measured in experiment with those obtained by calculation, the following relations were used:

$$\Delta_{e2b} = 1 - \frac{U^*_{K_{12}} + {W_{e2b}}^{exp}}{U^*_{K_{12}} + {W_{e2b}}^*}; \qquad \Delta_{i2a} = 1 - \frac{U^*_{K_{12}} + {W_{i2a}}^{exp}}{U^*_{K_{12}} + {W_{i2a}}^*} \tag{1}$$

Because within the error of experiment, the shock wave S_{i1b} propagates at calculated speed, in our analysis we used the calculated values for $U^*_{K_{12}}$ in both numerator and denominator of the relations (1). When estimated by the velocities measured from the streak pictures, the error of determination of Δ_{e2b} and Δ_{i2a} is about 14%. To improve the accuracy, the processing was performed so that the accuracy depended only on the accuracy of measurement of the slopes. The following relations for the S_{i2a} (and for S_{e2b}) were obtained:

$$\frac{U^*_{K_{12}} + {W_{i2a}}^{exp}}{{W_{i1b}}^*} = \frac{U^*_{K_{12}}}{{W_{i1b}}^*} + \frac{\tan\alpha_{i2a}}{\tan\alpha_{i1b}} = \frac{2}{\gamma+1}(1 - 1/{M_{i1b}}^2) + \frac{\tan\alpha_{i2a}}{\tan\alpha_{i1b}} \tag{2}$$

With this procedure, the accuracy of determination of relations (1) was increased up to 4%. Table 1 represents the results of comparison of the experimentally measured velocities of shock waves S_{e2b} and S_{i2a} taken in the flow $i1b$ coordinate system, with the corresponding calculated values. As seen, within the error of experiment (4%), the speed of the shock wave S_{e2b} is either equal to the calculated value or exceeds it. The speed of the shock wave S_{i2a} is lower than the calculated one in all the runs except for 699B. Supposingly, its strength was affected by the interaction with the turbulent mixing zone.

Figure 9 represents the experimental data obtained in different studies, in different time, and in different shock tubes; when compared to each other, they demonstrate a significant variation. As seen from Fig. 5 and 6, as y changes, the thickness and the growth rate of interface change chaotically and vary around the mean value within 15% for L and within 30% for dL_{26}/dt. The solid line 3 in Fig. 9 represents the experimental data obtained in [2] and [7], processed by the least square method on the assumption that the function $(dL/dt)\Delta U^{-1}$ is a linear function of At. To account for the chaotic nature of the process, the confidence region is drawn (lines 2 in Fig. 9), which should include all the experimental data with probability 95%. As seen, with this approach, the agreement between the experimental data obtained by different authors is sufficiently good.

Table 1.

1	2	3	4	5	6	7	8	9	10
690B	Xe-He-Xe	4.37*	1.376* 1.316 -	0.9831	1.0289	0.3296 0.3240	0.2903	+4.45	-12.57
691B	Xe-He-Ar	4.14	1.255* 1.325 1.353	1.0006 1.0226	0.9521	0.2732	0.2506	-6.25	-9.02
692B	Xe-He-Ne	4.16	1.184* 1.263 1.310	0.9649 0.9991	0.8972	0.2578	0.2285	-9.45	-12.80
693B	Xe-He-Kr	4.68	1.359* 1.403 1.394	1.0128 1.0078	0.9989	0.3097	0.2864	-1.14	-8.14
694B	Xe-Ne-Kr	4.94	1.254* 1.338 1.317	0.8530 0.8406	0.7999	0.4760	0.4202	-5.86	-13.28
695B	Xe-Ne-Ar	5.23	1.122* 1.286 1.314	0.8235 0.8429	0.7077	0.42997	0.3612	-17.73	-19.04
696B	Xe-Ne-Xe	5.30	1.344* 1.371 1.468	0.8734 0.9376	0.8458	0.5706	0.4583	-7.06	-24.50
697B	Xe-He-Xe	4.63	1.395* 1.428 -	1.0303	1.0278	0.3387	0.2978	-0.24	-13.73
698B	Xe-He	4.40	1.574* 1.530 1.515	1.1436 1.1312	1.1746	0.3769 0.3886	0.3557	+3.17	-7.60
699B	Xe-Ne	5.23	1.939* - 1.887	1.1817	1.2228	0.7239 0.7704	0.7287	+3.36	-0.67 +5.72

1 –number of the experiment; 2 - A-B-C; 3 – M_{e1a}; 4 – M_{e2b}; 5 – $\frac{U^*_{K12}+W_{e2b}{}^{exp}}{W_{i1b}{}^*}$;
6 – $\frac{U^*_{K12}+W_{e2b}{}^*}{W_{i1b}{}^*}$; 7 – $\frac{U^*_{K12}+W_{i2a}{}^{exp}}{W_{i1b}{}^*}$; 8 – $\frac{U^*_{K12}+W_{i2a}{}^*}{W_{i1b}{}^*}$; 9 – $\Delta_{e2b}\%$; 10 – $\Delta_{i2a}\%$.

Figures 7 and 8 give the experimental plots of dL_{26}/dt, and the calculated plots of ΔU and $(dL_{26}/dt)\Delta U^{-1}$ against M_{e2b} of the wave S_{e2b}. By the experimental points, using the least square method, the lines for dL_{26}/dt and $(dL_{26}/dt)\Delta U^{-1}$, on the assumption of their linear dependence of Mach number, were drawn. The variation of experimental points with respect to the line is 30%. This variation coincides with that obtained for the processed Schlieren snapshot pictures. It is due to the random nature of the process and is a characteristic of turbulent mixing evolution. During the interaction of S_{e2b} with K_{12}, the intensification rate of turbulent mixing (L_{26}/dt) increases, and the $(dL_{26}/dt)\Delta U^{-1}$ decreases with increasing strength of S_{e2b}. This is due to the fact that when M_{e2b} increases, the ΔU grows faster than the dL_{26}/dt. Comparison of the data for two At given in Fig. 8 demonstrates that the absolute value of $(dL_{26}/dt)\Delta U^{-1}$ as a function of Mach number decreases with decreasing At.

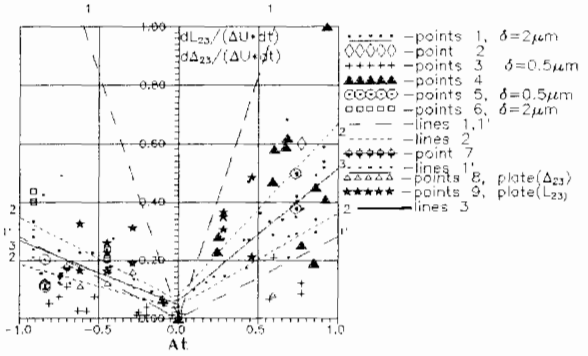

Figure 9. Intensification of turbulent mixing in K_{26} according to the Atwood number: points 1, 5, 6, 8, 9 - reports No. 01-94(CEA/DAM#3672/DIR) and No. 01-96 (CEA/DAM#3773/DIR); 2 - [1]; 3 - [4]; 4 - [3, 6]; 7 - [5]; lines 1 and 1′ - [7].

4. Conclusions

1. It has been demonstrated that the interaction of S_{i2b} with turbulized K_{12} decreases the strength of S_{i2a}. 2. When accounted for the chaotic nature of turbulent mixing, all the experimental data on the investigation of intensity of turbulent mixing obtained by different authors are in sufficiently good agreement with each other. 3. It has been shown that as the strength of the S_{e2b} increases, the rate of turbulent mixing dL_{26}/dt increases, and the value of $(dL_{26}/dt)\Delta U^{-1}$ decreases.

Acknowledgement. This work was supported by Commissariat á l'Energie Atomique, contract No. 3773, and by Russian Foundation for Fundamental Investigations, project No. 96-01-01295.

References

[1] Andronov VA, Bakhrakh SM, Meshkov EE, Mokhov VN, Nikiforov VV, Pevnizhitskii AV, and Tolshmyakov, Turbulent mixing on the interface accelerated by shock waves, Zh. Eksp. i Tekh. Fiz., 71, 2, 8, 806, (1976).

[2] Zaytsev SG, Lazareva EV, Chernukha VV, and Belyaev VM, Intensification of mixing on the interface between media of different density at the shock passage through it, Dokl. Akad. Nauk SSSR, 283, 1, 94-98, (1985).

[3] Houas L, Brun R, and Hanana M, Experimental investigation of shock-interface interaction, AIAA J., 24, 8, 1254-1255, (1986).

[4] Brouillette M and Sturtevant B, Growth induced by multiple shock waves normally incident on plane gaseous interfaces, Physica D37, 248-263, (1989).

[5] Vetter M and Sturtevant B, Experiments on the Richtmyer-Meshkov instability of an air/SF_6 interface, Shock waves, 4, 247-253, (1995).

[6] Houas L and Chemouni L, Experimental investigation of Richtmyer-Meshkov mixing in shock tube, Phys. Fluid, 8, 2, 614-627, (1996).

[7] Neuvazhaev VN, Ratio of turbulent and kinetic energies in mixed substance. Preprint, 3, Chelyabinsk-70, (1991).

Analysis of the Turbulence in Bubble Two-Phase Flows by NMR

F. Le Gall[1], J. Leblond[2] and S. Pascal-Ribot[1]
[1]CEA Cadarache /DEC/SECA/LTEA, Bat 216
13108 St Paul Lez Durance cedex, France
[2]ESPCI, Laboratoire PMMH (URA 857) and GREDIC (GdR 1027)
10 rue Vauquelin, 75231 Paris cedex 05, France

Abstract: Turbulence characterictics of an upward air-water bubbly flow in a circular pipe were investigated by experimenting a Nuclear Magnetic Resonance method (N.M.R.). This method based on the P.F.G.S.E. (Pulse Field Gradient Spin Echoe Sequence) allows the measurement of the liquid superficial velocity and of the mean velocity of the liquid entered in the measurement volume during 18 ms.
The first results of the experiment show that the increase of flow rate causes the increase of the fluctuations of velocities.

1. Introduction

Bubble flow is one of representative flow regimes in two-phase which takes place in a wide range of energy conversion devices such as nuclear steam generators. In order to analyse the safety of nuclear reactors, it is essential to improve the understanding of interactions between bubbles, liquid and tube bundle. Indeed, in the inverted U-tube bundle region, it has been noted that two- phase cross flow induced vibrations which can cause serious tube failures.
The purpose of this paper is then to try to relate two-phase turbulence to the structural characteristics of bubble flow. For that, an experimental study based on Nuclear Magnetic Resonance (N.M.R.) technique is carried out with intend to measure turbulent velocity fluctuations of an air-water bubbly flow. A new method using a modified P.F.G.S.E. sequence has been applied showing for this approach the experimental technical limits and, as a result of the way in which improvements must be brought.
After a short presentation of our experimental set-up (spin flow) the modified P.F.G.S.E. sequence designed to analyse turbulence in air-water bubbly flows is exposed followed by its mathematical interpretation. Some experimental data obtained in the Laboratoire de Physique Thermique (ESPCI Paris) are presented.

More information - Email: flegall@cea.fr

2. Experiment

2.1. Nomenclature

A_0	reference section area (m^2)		
c	constant		
$\Delta\phi$	phase difference (degree)	T	period of the sequence (s)
f_M	maximum frequency of the spectrum (Hz)	τ	time interval (s)
g_a	maximum field gradient pulse $(gauss.cm^{-1})$	V	measurement volume (m^3)
j	superficial velocity $(m.s^{-1})$	$\mathcal{V}_i$	volume occuped by the liquid which entered into the volume V between t and $t+3\tau$ (m^3)
J	flow rate (on flow meter) $(m^3.s^{-1})$		
M	magnetisation		
M_i	mass flow rate of the phase i $(kg.s^{-1})$	w	axial velocity component $m.s^{-1}$
P_3	Probability	χ	phase density function
ρ	density $(kg.m^{-3})$		
$R_{1,2}$	space fraction		

Subscripts		*Symbols*	
i	phase index $i=1$ for water	$\langle\rangle$	space-averaging operator over A_0
	$i=2$ for air	$\ll\gg$	space-averaging operator over $\mathcal{V}_1$
j	particle index	$\overline{\quad}^{3\tau}$	time- averaging operator over 3τ

2.2. Experimental apparatus

A schematic diagram of experimental facility is presented in figure 1 :

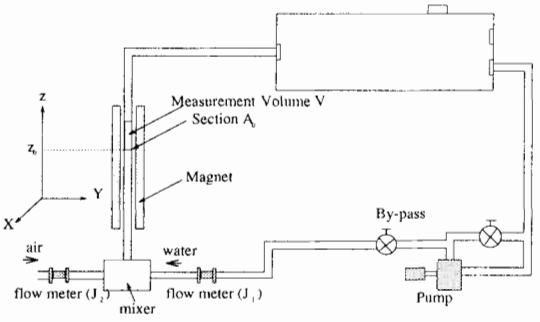

Figure 1. Experimental apparatus

The air-flow and the water flow are mixed into the mixer. Then the gaz-water bubbly flow goes up into the pipe. The N.M.R. measurements are performed in a section of the pipe 240 cm above the mixer. A grid which is situated 40 cm under the measurement volume V calibrates the size of the bubbles.

2.3. Sequence : measurements of the fluctuation of liquid flow ($i=1$)

In a attempt to analyse turbulent fluctuations, the P.F.G.S.E. sequence has been modified in a continuous and periodic sequence of frequency ability higher than 1 kHz.
At each period start, as shown in figure 2, a $\frac{\pi}{2})_X$ radio frequency pulse is applied, between two strong magnetic field gradient pulses designed to cancel all the components of the magnetisation in the volume V.

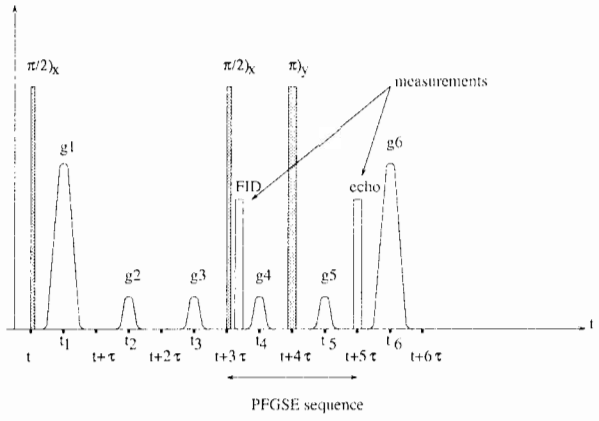

Figure 2. sequence

Between t and $t + 3\tau$, a new liquid flow goes into the volume V. This liquid takes a volume noted $\mathcal{V}_1$ which leads a new z-component of the macroscopic magnetisation.
At time $t + 3\tau$, a classical P.F.G.S.E. sequence is applied on that volume $\mathcal{V}_1$ to determine $j_1(t)$ the superficial velocity of the liquid and $\ll w_1 \gg$ the mean velocity of the liquid entered in the volume V between t and $t + 3\tau$.
Thus, at time $t + 3\tau$, the P.F.G.S.E. sequence starts with a $\frac{\pi}{2})_X$ radio frequency pulse, which is applied to rotate the z-component in the O,X,Y plan. The acquisition that follows (figure 2), allows the measurement of the magnetisation $M(t + 3\tau)$, which is proportionnal to the volume of the liquid $\mathcal{V}_1$. The following paragraphs show the mathematical expressions of these measurement.

2.3.1. Expression of the superficial velocity of the liquid : $j_1(t)$.

As mentioned earlier, the magnetisation $M(t+3\tau)$ is proportionnal to the mass flow rate $M_1(t)$ which enters the volume V through the section A_0 at t.

$$M(t + 3\tau) \propto \int_t^{t+3\tau} M_1(t)dt \quad \text{with} \quad M_1(t) = \rho_1 \int_{A_0} \chi_1(t) w_1(t) dA \tag{1}$$

On the other hand, the mean velocity of the liquid in the section A_0 is defined by:

$$\langle w_1(t) \rangle_2 = \frac{\int_{A_0} \chi_1(t) w_1(t) dA}{\int_{A_0} \chi_1(t) dA} \tag{2}$$

Leading for $M_1(t)$, the following expression :

$$M_1(t) = \rho_1 A_0 R_{1,2}(z_0, t) \langle w_1(t) \rangle_2 \tag{3}$$

Therefore,

$$\begin{aligned} M(t + 3\tau) &\propto \rho_1 A_0 3\tau \overline{R_{1,2}(z_0, t) \langle w_1(t) \rangle_2}^{3\tau} \\ &= cA_0 \overline{j_1(t)}^{3\tau} \end{aligned} \tag{4}$$

Consequently, the magnetisation $M(t+3\tau)$ provides a measurement of the superficial velocity of the liquid $j_1(t)$.

2.3.2. Expression of the mean velocity of the liquid in the volume $\mathcal{V}_1$: $\ll w_1 \gg$

With reference to figure 2, after a $\frac{\pi}{2})_X$ pulse, a magnetic field gradient pulse is applied. Its mathematical expression is the following :

$$g(u) = \frac{g_a}{2}(1 + cos(\frac{2\pi u}{\tau})) \qquad u \in [-\frac{\tau}{2}, \frac{\tau}{2}] \tag{5}$$

During τ, the magnetic field gradient pulse, noted g_4, shifts the phase of the whole microscopic magnetisations of the liquid particles j :

$$\Delta\phi_j(g_4) = \gamma \int_{-\frac{\tau}{2}}^{+\frac{\tau}{2}} g(u) z(t_4 + u) du \tag{6}$$

with the following first order limited developement for axial component :

$$z(t_4 + u) = z(t_4) + w_1(t_4).u + ... \tag{7}$$

that leads to,

$$\Delta\phi_j(g_4) = z(t_4) g_a \tau + \gamma \int_{-\frac{\tau}{2}}^{+\frac{\tau}{2}} g(u) w_1(t_4) u du + ... \tag{8}$$

At time $t + 4\tau$, a $\pi)_Y$ radio frequency pulse is applied and reverses the whole microscopic magnetisations in the O, X, Y plan.
Between $t + 4\tau$ and $t + 5\tau$, the magnetic field gradient pulse, g_5, shifts the phase of the microscopic magnetisations in the same way than g_4 did. Thus,

$$\Delta\phi_j(g_5) = z(t_5) g_a \tau + \gamma \int_{-\frac{\tau}{2}}^{+\frac{\tau}{2}} g(u) w_1(t_5) u du + ... \tag{9}$$

And at time $t + 5\tau$, the complete phase difference is :

$$\begin{aligned} \Delta\phi_j &= \Delta\phi_j(g_5) - \Delta\phi_j(g_4) \\ &= [z(t_5) - z(t_4)] g_a \tau + \gamma \int_{-\frac{\tau}{2}}^{+\frac{\tau}{2}} g(u)[w_1(t_5) - w_1(t_4)] u du + ... \end{aligned} \tag{10}$$

Suppose that $t_5 - t_4$ (figure 2), the interval between g_4 and g_5 applications, is such that $t_5 - t_4 \gg \tau_{V_1}$ which τ_{V_1} the Lagrangien correlation time of the liquid particle velocity.
Therefore,

$$(z(t_5) - z(t_4)) \approx \tau w_1(t + 4\tau) \tag{11}$$

and,

$$\Delta\phi_j = \gamma g_a \tau^2 w_1(t + 4\tau) \tag{12}$$

Magnetisation detected at $t + 5\tau$ is the summation of the different liquid particle contributions in the volume $\mathcal{V}_1$.
Thus,

$$M(t + 5\tau) = M(t + 3\tau) \ll exp(ikw_1) \gg \tag{13}$$

with $k = \gamma g_a \tau^2$ and $\ll\gg$ represents the mean over the volume $\mathcal{V}_1$.
Introduce $P_3(w_1, t)dw_1$, the probability to find some liquid particles at t time with a velocity between w_1 and $w_1 + dw_1$, into the volume $\mathcal{V}_1$.
Therefore,

$$M(t + 5\tau, k) = M(t + 3\tau) \int_{-\infty}^{+\infty} P_3(w_1, t) exp(ikw_1) dw_1 \tag{14}$$

with $\int_{-\infty}^{+\infty} P_3(w_1, t)dw_1 = 1$.
With a first order limited developement in k, we show that for k low enough, the phase difference $\Delta\phi$ between $M(t + 5\tau)$ and $M(t + 3\tau)$ is proportionnal to the mean velocity of the liquid in the volume $\mathcal{V}_1$.

$$\Delta\phi = k \ll w_1(t + 5\tau) \gg \tag{15}$$

To summarize, both data give us informations about the superficial velocity of the liquid $j_1(t)$ (equation 4) and about the mean velocity of the liquid in the volume $\mathcal{V}_1$, $\ll w_1(t) \gg$ (equation 15).

2.4. Experimental results : Power spectral densities of $\overline{j_1(t)}^{3\tau}$ and $\ll w_1(t) \gg$

The influence of gaz flow rate J_2 over the fluctuations of $\overline{j_1(t)}^{3\tau}$ and $\ll w_1(t) \gg$ is studied. The obtained spectra for $J_1 = 3.5\ m^3.h^{-1}$ are shown on the following graphics (figure 3) :

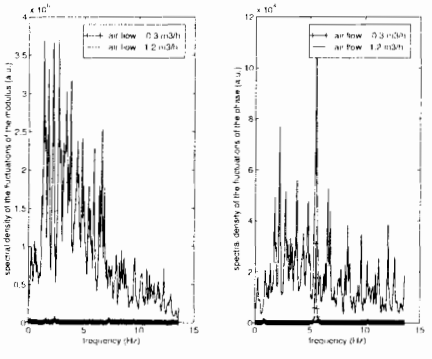

Figure 3. Experimental results for $J_1 = 3.5\ m^3/h$

These spectra obtained by a classical Fourier transformation represent the $|M(t)|$ fluctuations and the $\Delta\phi(t)$ fluctuations which are ploted versus frequency for two cases $\frac{J_2}{J_1} = 0.8$ (plots -+) and $\frac{J_2}{J_1} = 0.34$ (continuous plots).
The width of these spectra depends on the sequence length $T = 36ms$. The consequence of the Shannon Theorem is the limitation of the spectrum reading to $f_M = 14Hz$. Thus we have to keep in mind this restriction for the spectra analysis.
At low void fraction $\frac{J_2}{J_1} < 0.1$, the level of the fluctuations are insignificant. At higher void fraction, the amplitude of the fluctuations increases strongly with $\frac{J_2}{J_1}$. For $\frac{J_2}{J_1} = 0.34$, the level of the fluctuations is more important than this noted for $\frac{J_2}{J_1} = 0.8$. Moreover the low frequency fluctuations (0 to 7 Hz) are predominant.
For the spectral densities of $\Delta\phi$, a peak at $5.5Hz$ is observed. It is probably due to the pump frequency rotation or to the presence of an air pocket into the pipe.

3. Conclusion

The modified P.F.G.S.E. sequence has been tested. For all the interest of these first experimental results, a conclusion seems to be premature. Some technical improvements must be brought in order to better characterize the air-water bubbly flow.
In the same way, an experiment is being built with the aim to provide, with a high frequency pressure tranduceur, the pressure fluctuations preserving the experimental conditions given by the N.M.R. experiment. Both experiments would allow us to know more about the link between the structural characteristics of bubble flow and the power spectral densities of pressure and velocities.

References

[1] Leblond J, Benkedda Y, Javelot S and Oger L, Meas. Sci. & Techn, 5, (1994)
[2] Leblond J and Stepowsky D, Multiphase Science and Technology, 5.
[3] Javelot S, Leblond J and Baradel C, Proc. 2nd Inter. Conf. on Multiphase flow 95-Kyoto, IN2-33-38, (1995).

Rayleigh-Taylor Instability in Strong Substances: Calculated Experimental Studies of Instability in Titanium

A.I. Lebedev, P.N. Nizovtsev, V.A. Rayevsky and V.P. Soloviov
Russian Federal Nuclear Centre - Institute of Experimental Physics
Prospect Mira 37, 607190, Sarov, Nizhny Novgorod Region, Russia

Abstract: The results of calculated experimental study of Rayleigh-Taylor instability in titanium are presented. Perturbations growth at plate surface accelerated by products of chemical HE explosion is been dealt with. Perturbations growth for different initial amplitudes and wavelengths was studied. Experimentally verified are the conclusion on stability area threshold dependence from wavelength as well as from initial perturbations amplitude and substance strength.

1. Introduction

One of examples of Rayleigh-Taylor instability is perturbations growth at pressure accelerated plate surface, pressure being applied on one side [1, 2]. As a result of instability propagation a complete destruction of accelerated layer can bee finally observed. R-T instability strong media substantially differs from instabilities in liquids and gases. In the last perturbation growth is restrained by shear substance strength.
Earlier papers [3-6] comprised some peculiarities of R-T instability growth in strong media. Namely paper [6] experimentally confirmed that stability area threshold position at aluminium layer acceleration depends on wavelength and initial amplitude. These results contradicted the conclusion from papers [7-10]. Due to this, it should be of interest to verify commonness of the obtained results for other media featuring strength.
Present paper provides the results of calculated experimental study of R-T instability propagation at titanium layer acceleration. It should be noted, that titanium features higher shear strength if compared to aluminium. That is why the presented experimental results demonstrate as well stability dependence from substance strength.

2. Experimental and numerical techniques

Experiments were made using X-ray method. Experimental setup was similar to those used for papers [6, 9, 10]. Similarly to instability study in aluminium [6] we have examined various perturbation propagation modes-stable (restricted perturbation growth) and unstable (unrestricted perturbation growth resulting with destruction of plate under investigation). Note that Ti layer loading pressure value exceeded over 3 times and acceleration value exceeded over ~ 40 % that of the aluminium [6].
Titanium plates were accelerated using two-cascade loading device. Fig.1 shows the draft of experimental assembly. Periodic two-dimensional perturbations were applied to 1.5 mm thick plate surface, the plate facing HE. Perturbations were imposed by making longitudinal recesses of triangular section. Recess depth determined the initial amplitude (A_i) and periods between

More information - Email: otd03_2305@spd.vniief.ru

them determined perturbations wavelength (λ). Present-state perturbations amplitude was determined by X-ray photographs of plates under investigation.
Fig.2 shows loading pressure (P) and Ti plates shift (S) vs time (t). Numerical simulation

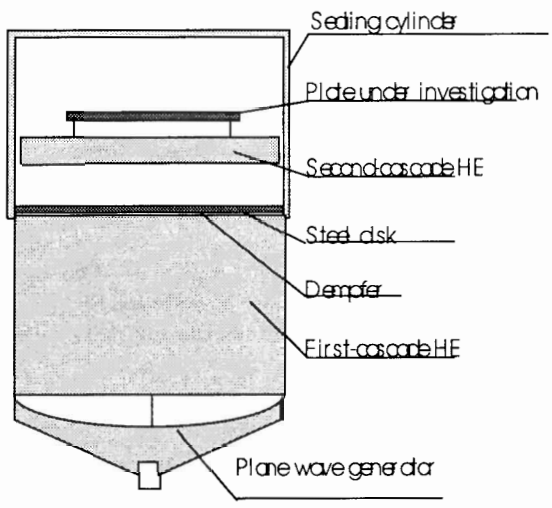

Figure 1. Draft of experimental assembly.

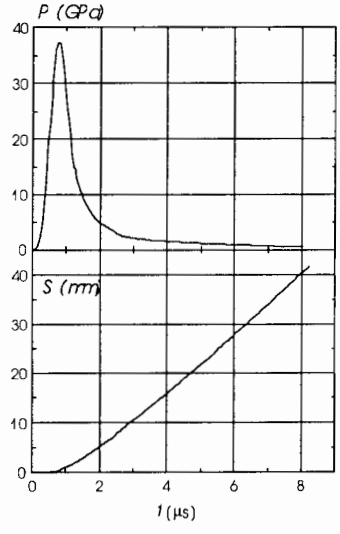

Figure 2. Titanium plate loading pressure (P) and shift (S) vs time (t).

of R-T instability was made using Lagrangian method [3] in viscous-elasto-plasttic approximation. Similarly to aluminium [6] experimental results on perturbations growth Ti plate surface could be described using viscous-elasto-plastic model featuring medium strength vs deformation velocity. Dynamic yield point ($Y_{\ddot{a}}$) and dynamic viscosity ($\mu_{\ddot{a}}$) can be, thus, presentted as follows

$$Y_{\ddot{a}} = Y_0^{Ti} * \{exp[-\alpha(E_t/E_{t.melt})^2]\} \quad (1)$$

$$\mu_{\ddot{a}} = \mu_0^{Ti} * \{exp[-\alpha(E_t/E_{t.melt})^2]\} \quad (2)$$

Where: Y_0^{Ti} =2 GPa, μ_0^{Ti}=0.75 EPa.s, A_t, $A_{t.melt}$ present-state thermal energy a nd substance thermal energy in melting point with respect to compression, a=5. The value of Y_0^{Ti} =2 GPa was selected as the medium value of dynamic yield point of annealed titanium alloy $B\grave{O}-14$ at pressure about 20, 40 GPa.

3. Results

Fig. 3, 4 comprise the results of experiments and calculation on gravitational instability development in titanium. Judging by the results it can be concluded that threshold position,

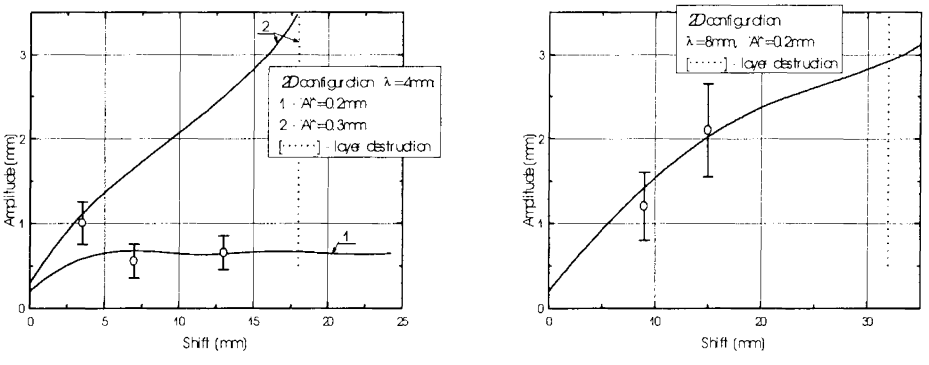

Figure 3. Titanium plate perturbations growth vs sift.

separating perturbations stability and instability areas, depends both on initial amplitude and perturbations wavelength, provided that gravitational instability growth in titanium similarly to aluminium [6]. Fig.5 shows dependence of stability area threshold for aluminium layer [6]. By comparing the results from fig.4 and fig.5 can be concluded that stability area boundary for titanium, featuring greater strength than aluminium, is located higher than that of aluminium. Note that titanium layer acceleration value exceeded over $\sim$ 40 % that for aluminium. The results are in good coordination with conclusions from papers [3-8].

4. Conclusions

Obtained results show that dependence of stability area threshold position at layer acceleration on wavelength and initial amplitude is common for media featuring strength. Experimental results presented in present paper serve as well as the basis for numerical simulation of testing and upgrading different models, describing material behaviour at high-velocity deformation.

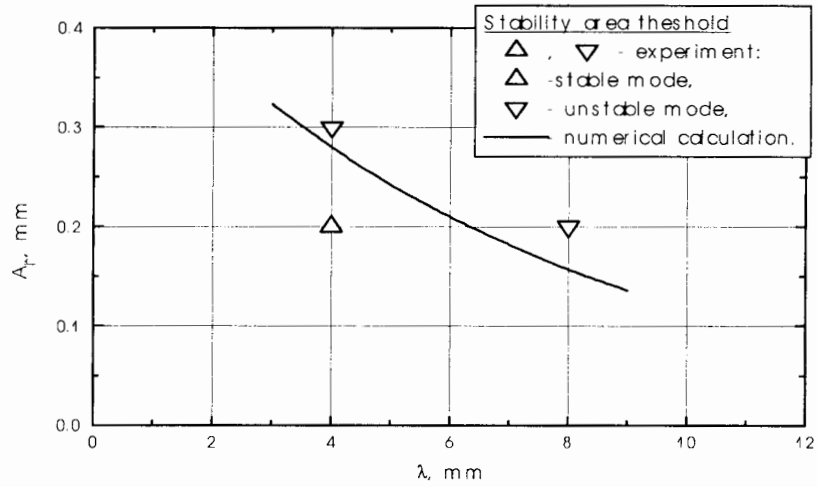

Figure 4. Position of stability area boundary for titanium at loading pressure P_{max}=37 GPa.

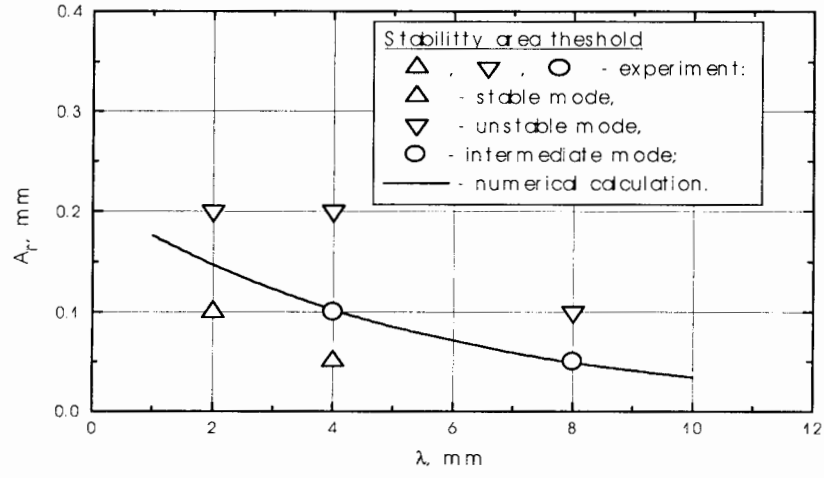

Figure 5. Position of stability area boundary for aluminium at loading pressure P_{max}=13 GPa.

References

[1] Taylor GI, The instability of liquid surfaces when accelerated in a direction perpendicular to their planes, Proc. of the Roy. Soc., 201, 1065, 192, (1950).

[2] Sharp DH, An Overview of Rayleigh-Taylor Instability, Physica 12D, 3-18, (1984).

[3] Abakumov AI, Lebedev AI, Nizovtseva IA, Nizovtsev PN, Rayevsky VA, Rayleigh-Taylor instability in elastoplastic medium. Numerical study, VANT. Ser. Teor. i Prikl. Fizika., 3, 14-19, (1990).

[4] Nizovtsev PN, Rayevsky VA, Approximate analytical solution of Rayley-Taylor instability problem in strong media, VANT. Ser. Teor. i Prikl. Fizika, 3, 11-17, (1991).

[5] Robinson AC, Swegle JW, Acceleration instability in elastic-plastic solids, 1. Numerical simulations of plate acceleration, 2. Analytical techniques, J. Appl. Phys., 66, 7, 2838-2872, (1989).

[6] Lebedev AI, Nizovtsev PN, Rayevsky VA, Soloviov VP, Rayleigh-Taylor instability in strong media, Proc. of the 5th Int. Workshop on the Physics of Compressible Turbulent Mixing, Stony Brook, (NY), USA, 18-21 July, 231-236, (1993).

[7] Miles JW, Taylor instability of a flat plate, General Atomics Rep., GAMD-7335, (1960).

[8] Drucker DC, Taylor instability of surface of an elastic-plastic plate, In: Mechanics Today., 5, (Nemat-Nasser S., ed.), Pergamon Press, 37-47, (1980).

[9] Barnes JF, Blewett PJ, McQueen RG, Meyer KA, Venable D., Taylor instability in solids, J. Appl. Phys., 45, 727-732, (1974).

[10] Barnes JF, Janney DH, London RK *et al.*, Further experimentation on Taylor instability in solids, J. Appl. Phys., 51, 4678, (1980).

Computational Modeling of the Hydrodynamic Instability Development In Shock Tube and Laser Driven Experiments

I.G. Lebo[1], V.B. Rozanov[1], V.F. Tishkin[2] and V.V. Nikishin[2]
[1]Lebedev Physical Institute, Moscow
Leninski prospect 53, 117924, Moscow, Russia
[2]The Institute of Mathematical Modeling,
Miusskaya sq.4, Moscow, 125047, Russia

Abstract: A 2D and 3D Euler codes "NUT" and "NUT-CY"(cylindrical 2D geometry), and a 2D Lagrange-Euler code "ATLANT" have been used in studying the laws of the development of the instabilities in two cases: 1) the shock waves are passing through the contact interface of two gases (the initial density of the gases is similar, and the adiabatic indices γ differ), 2) the laser acceleration of thin foils. The computer simulations have been made for concrete experiments to be held with the shock tubes at the Krzhizhanovsky Power Institute (Moscow), and those being performed with the laser facilities "MISHEN" (TRINITI, Troitsk, Moscow region, Nd-laser, the pulse energy up to 50 J, and the duration $\approx$ 2 ns) and "GARPUN" (Lebedev Phys. Inst. Moscow, KrF-laser, the energy up to 100 J and duration $\approx$ 100 ns).

1. The development of instability in the contact boundary of two gases of the same initial density

We used the "NUT" code to study the problem of the development of the instability at the contact boundary between the two gases of the same density and different adiabatic indices (γ) under the shock wave propagation. The results are given for the following two gases: CO_2 and Argon. The initial density in the gases is $\rho = 8.289 * 10^{-4}\ g/cm^3$. The adiabatic index in argon is γ =5.3, and in the CO_2, γ =1.25. The Mach number of the incident wave is equal to 3.5. The calculations have been performed in 2D (x,z coordinates) and 3D (x,y,z coordinates) geometry (the code NUT). The wave has been propagating along the OZ axis. In 2D geometry the initial perturbation of the contact boundary has the form Am(x,z) = a_0*cos(k*x) + Z_c, where k=2*π/λ, Z_c - boundary. The calculations have been made for $0 \leq x \leq 0.5*\lambda$, $0 \leq z \leq L_z$. At x=0 and x=0.5λ u=0.

In 3D geometry Am(x,y,z)=a_1*cos(k_3*x)*cos(k_3*y) + Z_c, where $k_3 = \pi/\lambda$. In 2D simulations a_0=0.5 cm, in 3D a_1 = 1 cm. We have studied the behaviour of the perturbations having the wavelengths λ = 3.6 cm, and 2.4 cm. In the first set of simulations the shock wave comes from CO_2 to Ar. In the second - from Ar to CO_2 gas. Figure 1a illustrates the dependences of the total amplitudes (the distance from the wave "peak" to the "bottom") for the cases when the shock wave comes from argon to CO_2 (the upper curve) and from CO_2 to argon. Here λ = 3.6 cm and a_0 = 0.5 cm). 2D-geometry. The "crosses" are the experimental results (Zaitsev S. et al., Krzhizhanovsky Power Institute, Moscow).

Figure 1b shows the concentration isolines in the vicinity of the contact boundary for the first and the second variants at the time moment t = 600 μs. One can see that in the first

More information - Email: lebo@neur.lpi.msk.su

case the perturbation development is slower than in the second one, and there is observed the "re-phasing" of the perturbation amplitude (see Fig.1a, left). In the discussed case, due to higher compressibility of the CO_2 (in strong shock waves the degree of the gas compressibility is proportional to $(\gamma+1)/(\gamma-1)$, its density behind the shock wavefront is higher than the argon density. The "crosses" are the experimental results. We have good agreement between numerical and experimental data. Fig. 2 shows the experimental data.

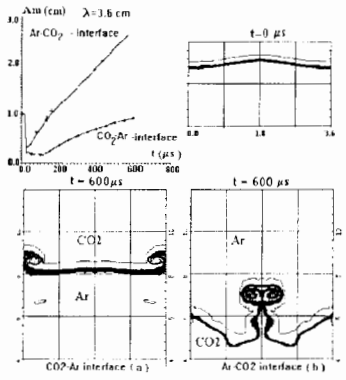

Figure 1: The amplitude growth for the cases Ar-CO_2 and CO_2-Ar interfaces and the isolines of concentration near the contact boundary for two cases.

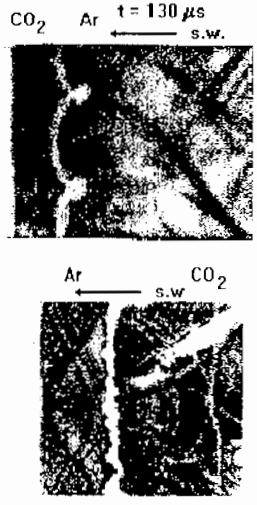

Figure 2: The Schlieren snapshot pictures for cases (1 - CO_2-Ar-interface) and (2 - Ar-CO_2-interface).

Figure 3 shows the results of the comparison of 2D and 3D calculations for the cases when λ =3.6 cm and λ =2.4 cm, and the shock wave comes from argon to CO_2 (M=3.5). Figure 3a presents the amplitude temporal dependences for the mentioned four cases. The solid lines - 3D geometry, dashed lines - 2D geometry. One can see that the growth rates of the perturbations with the same λ in 2D and 3D geometry are approximately equal at the initial stage.

The obtained result differs from the one observed for the case when the shock wave comes from the gas of the lower density into the gas of higher density at the same γ (see [1]). In that case the growth ratio of the 2D and 3D perturbations with the same wave number k, but differ wavelength would be similar This is in agreement with the Richtmyer formula $\frac{da}{dt} = k * a^* * W * A$, where a is the current amplitude of the perturbation; k, the wave number; W, the velocity of the second gas behind the shock-wave front; A, the Atwood number; a^*, the perturbation amplitude at the moment when the shock wave has passed through the contact surface. At such wavelength ratio the 2D (λ_{2D}=2.4 cm) and (λ_{3D} = 3.6 cm) perturbations will have approximately the same wave numbers. Actually, in 2D geometry $k_{2D}=2^*\pi/\lambda_{2D}$, and in 3D geometry $k_{3D} = \sqrt{(2 * \pi/\lambda_x)^2 + (2 * \pi/\lambda_y)^2}$. Hence, at $\lambda_x=\lambda_y=\lambda_{3D}$, $k_{2D} \approx k_{3D}$ at λ_{2D}=2.4 cm and λ_{3D}=3.6 cm.

We decreased the initial amplitudes up to Am^0=0.2 cm and repeated the calculations.

Fig.3b illustrates the growth of 2D and 3D perturbations (λ_{2D}=2.4 cm, λ_{3D} = 3.6 cm).

In Fig.4 are shown the isoconcentration lines in the vicinity of the contact boundary (for 3D geometry the axial cross section y=0 is given). The initial amplitudes equal 1 cm. As seen from Fig.5, the 2D perturbation is damaged faster, and at the later stage (t $\geq$ 600 μs) one can observe the turbulent mixing zone instead of a continuous boundary.

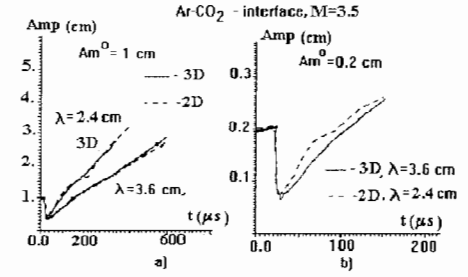

Figure 3. The amplitude growth for the cases Ar-CO_2 interface for 2D and 3D geometry. The initial amplitudes are equal Am^0=1 cm (a) and Am^0=0.2 cm (b), the wavelength λ are 2.4 and 3.6 cm.

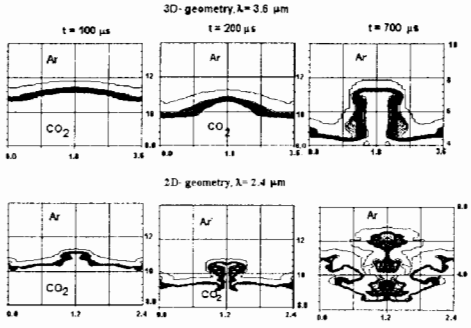

Figure 4. The isolines of concentration near the contact boundary for 3D (λ=3.6 cm), and 2D geometry (λ=2.4 cm) The initial amplitude Am^0 = 1 cm.

We observed the same results for other pair of gases: Air-Ar (γ=1.4 in Air).

2. Numerical modeling of the foil laser accelerations

We have discussed [2] a method to compensate the effect of large-scale inhomogeneity of the laser target irradiation by creating a special "relief" of the shell surface. The experiments on the acceleration of the aluminum "corrugated" foils have been made with "MISHEN" laser facility. The experiments have been performed with the focal spot of large diameter (1500-1800 μm), and, hence, with a small intensity of the laser radiation (q $\approx 2^{*}10^{12}$ W/cm^2).

The dynamics of the foils flight has been modeled with the help of code "ATLANT" (2D-geometry). The thickness of aluminum layer equals d_0 = 1.5 μm.

In the first set of calculations we have been modeling the acceleration of a plane foil without "relief" in "quasi-cylindrical" coordinates. The laser flux has been taken in the following form: $q_{las} = q_1(t) * q_2(r)$, where q_1(t) is the time-dependent term, $\int_0^\infty q_1(t)dt = E_{las}$, $q_2 = \exp(-(r/r_0)^2)/\text{Const}$, the coefficient Const is taken $\int_0^{r_{max}} q_2 r dr = 1$. The laser energy equals E_{las}=50 J, r_0= 750 μm, the laser wavelength = 1.06 μm. The laser pulse temporal shape presents a broken line with the time moments over the base t_1 = 0 ns, t_2 = 0.3 ns, t_3=2.2 ns, t_4 = 2.5 ns (see Fig.5).

Figure 5 illustrates the foil shape at the moment of time of 3 ns. Figure 6 shows the plasma density distributions of non-evaporated part of the targets along the axis at the moments t=3 and 8 ns. The results were got by using 2D "ATLANT". We compared our results with the results obtained by using 1D Lagrange-Euler code "EGAK" [3] with take into account turbulent mixing process (k-ϵ model). The much lower density of non-evaporated foil was obtained in that case.

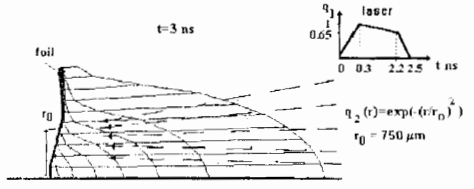

Figure 5: the form of laser pulse and the shape of plasma jet at t=3 ns.

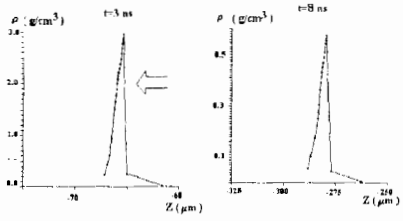

Figure 6: the plasma density distribution along 0Z-axis at the moments t=3 ns and 8 ns (the results of "ATLANT"-code simulations).

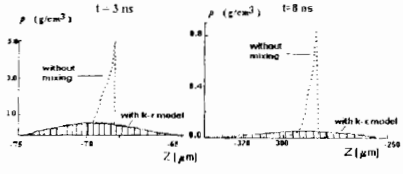

Figure 7: The plasma density distribution along 0Z-axis at the moment t= 3 and 8 ns . The results were obtained by using "EGAK" code (VNIIEF, Sarov).

We have studied the development of perturbations of foil using Lagrange code "ATLANT" and Euler code "NUT-CY" for the cases 1) "large-scale", ($d_0 \ll \lambda \leq r_0$); 2) "middle-scale" ($d_0 \leq \lambda \ll r_0$) and 3) "short-scale"($\lambda < d_0$) initial perturbations. The numerical results for the case of "large-scale" perturbations we have compared with experimental data.

Figure 8 (top) presents shadow photos of the "corrugated" foils at the rear side (a).

The numerical results are shown at the bottom of the figure. The laser flux over the cross-section is constant $q_m = 1.2 * 10^{12}\, W/cm^2$, $q_2 = 1$. The pulse temporal form is the same as in the previous simulation. Figure 8b illustrates the dependences between the distance (d_Z) and radius (r) for the time moments t=3, 8 ns (this is the case of large-scale perturbations, when $d_o \ll \lambda \leq r_0$). Here d_Z is the distance covered by the Lagrange foil cell which has the maximum density over 0Z axis. Symbols " I " illustrate the experimental data.

We made the series of calculations for middle-scale and small-scale perturbations. ($d_o \leq \lambda \ll r_0$) development in laser-driven foil. Figure 9a (right side) illustrates the dependences of non-evaporated foil thickness (D(t)) and foil velocity (V(t)) from the time (t). Figure 9b illustrates the dependences between the perturbation relative amplitude growth (Am/D) and time for the cases middle-scale (λ=20 μm, Am^0= 0.2 μm) and small-scale (λ=1.4 μm, Am^0=0.04 μm) perturbations.

One can see that the foil is not destroyed in the acceleration process in all the discussed cases. The experiments showed a sharp rear boundary of the foil and it is also indicative of absence of layer "blurring".

The "k-ϵ-model" was adopted for the experiments of another space and time scales. We expect to get new coefficients for that model from laser-driven experiments. We made also the

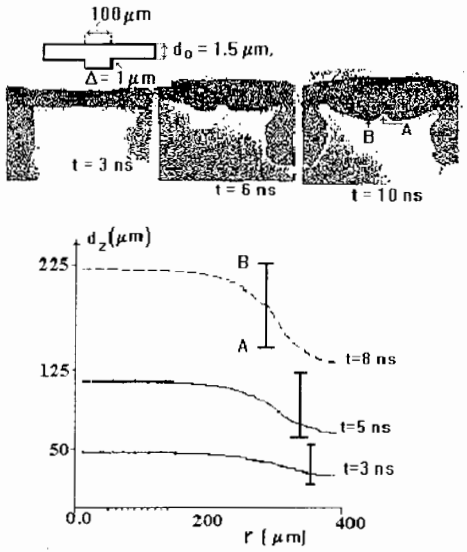

Figure 8 (top): The photographs of the accelerated foil; (bottom): the comparison of the numerical and experimental results for large-scale initial perturbations.

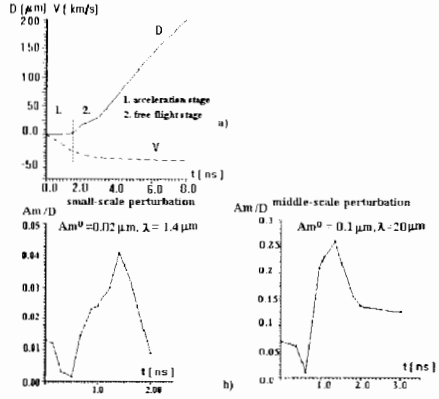

Figure 9 (top): The dependences between thickness and velocity of foil from the time; (bottom): the amplitude perturbation growth for middle-scale and small-scale perturbations.

simulations of these problems using Euler code "NUT-CY". The foil velocity was similar of one, but density was smaller in 5-6 times in that case. To our mind, the reason of this effect was the higher approximative viscosity in "NUT-CY" code simulations. We used grid (40*2000). The resources of the computer did not allow to increase grid.

Basing on the 1D numerical simulations, we have shown that with the help of a long-pulse ultraviolet laser (the laser energy, $\approx$ 50-100 J, the pulse duration is $\approx$ 100 ns) one can accelerate the foils in the cylindrical and conic channels up to the velocities 200 km/s, and create the dynamic pressure of $10^{13} - 10^{14}$ Barr in the collisions with the wall. It would allow to rich the high energy concentration in plasma and model the some interesting space-physical phenomena. Such laser with $E_{las} \simeq 0.5$ MJ would be used as the driver for hybrid fission-fusion reactor. However, the attainment of such parameters is hindered by a non-homogeneous acceleration of different parts of the foil and by the development of a hydrodynamic instability. The wavelength of KrF-laser is shorter and foil accelerated time is much longer than one of Nd-laser, as the result, the problem of the stable acceleration of foil is more difficult. In the considered case the plasma is essentially non-ideal and the process of ionization place the important role in it.

The next series of the calculations have been modeling the experiments on the burn-through time of aluminum foils of different thickness made with "GARPUN" facility. These simulations

were made by using 1D Lagrange code "DIANA" with allowance for 2T model, complicated EOS and ionization, and 2D Euler code "NUT-CY", EOS - ideal gas). The laser energy in the calculations equals 50 J, and focal radius r_0= 150 μm, $q_2 = \exp(-(r/r_0)^2)$/Const. The thickness of the layer d_0 varies in the calculations. In this case the non-evaporated foil displacement $d_Z \gg r_0$ Figure 10 illustrates the dependence of burn-through time (t_b) of foil thickness (d_0) for the cases of 1) 1D - simulations (Lagrange code "DIANA", 2) 2D "NUT-CY" code simulations; 3) experimental data (symbols "I").

It can see, that t_b in the 1D-simulations much longer. The t_b in 2D simulations is some less than in the experiments. The fact is that we don't take into account the complicated EOS and ionization effect in "NUT-CY"-code now.

Fig.11 illustrates the density distribution of non-evaporated part of the foil at the time moments t= 60 ns with and without taking account of ionization effect. These simulations were made by using 1D "DIANA"-code. The velocity of foil in the first case is lower in 1.3-1.5 times.

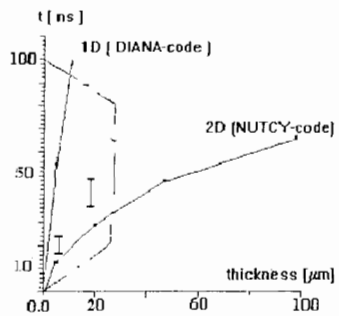

Figure 10: The dependence of burn-through time of foil thickness.

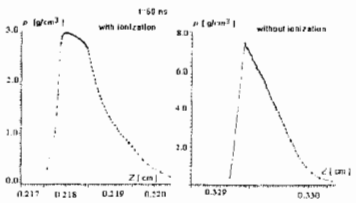

Figure 11: The density distributions of foil. The simulations were made by using "DIANA"-code with allowance for ionization (top) and without ionization (bottom).

Acknowledgement. The authors would like to thank Dr. R.Samtaney (USA) for useful discussion of the peculiarities of RMI development in the gases with the same densities. These investigations were supported by ISTC (grant N029-94).

References

[1] Lebo IG, Rozanov VB, Tishkin VF, Nikishin VV, Popov IV, Favorsky AP, Proc. of the 5th Int. Workshop on the Physics of Compressible Turbulent Mixing, Stony Brook, (NY), USA, 18-21 July, (1993).

[2] Lebo IG, Rozanov VB, Tishkin VF, Laser and Particle Beams, 12, 361-369, (1994).

[3] Bondorenko YA, Gubkov EV, Dolgoleva GV, Zharova GV, Lebo IG, Rozanov VB, Tarasov VY, Tishkin VF, Yanilkin YV, Numerical modeling of the turbulent mixing in the plane corrugated target, Preprint FIAN, 19, M., (1977).

Dynamics and Control of Vortices in Mixing Layers

M. Lesieur, P. Comte, G. Silvestrini and C. Cayssiols
Institut de Mécanique de Grenoble, Institut National Polytechnique de Grenoble
B.P. 53, 38041 Grenoble Cedex 09, France

1. Introduction

This paper will deal with Kelvin-Helmholtz instability, which is the natural instability of a thin interface of velocity (vortex sheet) in a fluid. This instability is extremely violent, and gives rise to various primary and secondary coherent vortices, whose dynamics will be studied here with the aid of large-eddy simulation techniques (LES). We will first recall these techniques, both is spectral and physical space. Then results concerning spatial incompressible mixing layers of uniform density will be given. Finally, we will discuss how to extend the LES formalism to compressible situations, and give an application for the jet.

2. Large-eddy simulation techniques

We start by considering large-eddy simulations from a spectral point of view. The formalism of spectral eddy viscosity is due to Kraichnan ([1], see also [2, 3]) in the case of a Kolmogorov subgridscale spectrum. The spectral eddy-diffusivity was introduced in [4]. We assume that Navier-Stokes is written in Fourier space (which requires periodicity in the three spatial directions). Let $\hat{u}_i(\vec{k},t)$ and $\hat{T}(\vec{k},t)$ be the spatial Fourier transforms of the velocity and scalar fields. Navier-Stokes equation (with constant density) writes

$$\frac{\partial}{\partial t}\hat{u}_i(\vec{k},t)+\nu k^2\hat{u}_i(\vec{k},t)=-ik_m\left(\delta_{ij}-\frac{k_ik_j}{k^2}\right)\int_{\vec{p}+\vec{q}=\vec{k}}\hat{u}_j(\vec{p},t)\hat{u}_m(\vec{q},t)d\vec{p}\,. \tag{1}$$

where pressure has been eliminated by projection (with the aid of the tensor $\delta_{ij}-k_ik_j/k^2$) on the plane perpendicular to $\vec{k}$, in order to respect incompressibility. For a scalar T transported by the flow, we have

$$\frac{\partial}{\partial t}\hat{T}(\vec{k},t)+\kappa k^2\hat{T}(\vec{k},t)=-ik_j\int_{\vec{p}+\vec{q}=\vec{k}}\hat{u}_j(\vec{p},t)\hat{T}(\vec{q},t)d\vec{p}\,. \tag{2}$$

We consider a low-pass filter, defined by :

$$\overline{\hat{f}}=\hat{f}\ \text{ for }\ |\vec{k}|<k_C=\pi/\Delta x,\overline{\hat{f}}=0\ \text{ for }\ |\vec{k}|>k_C\ , \tag{3}$$

where k_C is the cutoff wavenumber associated with the grid mesh Δx. Let us now define the spectral eddy viscosity and eddy diffusivity by rewriting Eqs 1 and 2 as

$$\frac{\partial}{\partial t}\hat{u}_i(\vec{k},t)+[\nu+\nu_t(k|k_C)]k^2\hat{u}_i(\vec{k},t)=-ik_m\left(\delta_{ij}-\frac{k_ik_j}{k^2}\right)\int_{\vec{p}+\vec{q}=\vec{k}\,,|\vec{p}|,|\vec{q}|<k_C}\hat{u}_j(\vec{p},t)\hat{u}_m(\vec{q},t)d\vec{p} \tag{4}$$

with

$$\nu_t(k|k_C)k^2\hat{u}_i(\vec{k},t)=ik_m\left(\delta_{ij}-\frac{k_ik_j}{k^2}\right)\int_{\vec{p}+\vec{q}=\vec{k}\,,|\vec{p}|\text{or}\,|\vec{q}|>k_C}\hat{u}_j(\vec{p},t)\hat{u}_m(\vec{q},t)d\vec{p}$$

More information - Email: Marcel.Lesieur@hmg.inpg.fr

and

$$\frac{\partial}{\partial t}\hat{T}(\vec{k},t) + [\kappa + \kappa_t(k|k_C)]k^2\hat{T}(\vec{k},t) = -ik_j \int_{\vec{p}+\vec{q}=\vec{k}\,,|\vec{p}|,|\vec{q}|<k_C} \hat{u}_j(\vec{p},t)\hat{T}(\vec{q},t)d\vec{p} \tag{5}$$

with

$$\kappa_t(k|k_C)k^2\hat{u}_i(\vec{k},t) = ik_j \int_{\vec{p}+\vec{q}=\vec{k}\,,|\vec{p}|\,or\,|\vec{q}|>k_C} \hat{u}_j(\vec{p},t)\hat{T}(\vec{q},t)d\vec{p}\ .$$

Eddy coefficients thus defined correspond to nonlinear triadic interactions such that one at least of the wavevectors $\vec{p}$ or $\vec{q}$ should be in modulus larger than k_C. They are unknown, and may be imaginary. We will assume they are real, and will determine them with the aid of the the EDQNM theory (see [3]). If one assumes first that k/k_C is small, expansions in powers of this small parameter yield for the eddy-viscosity and conductivity

$$\nu_t^\infty = \frac{1}{15}\int_{k_C}^\infty \theta_{0pp}\left[5E(p,t) + p\frac{\partial E(p,t)}{\partial p}\right]\ dp \tag{6}$$

$$\kappa_t^\infty = \frac{2}{3}\int_{k_C}^\infty \theta_{0pp}^T\ E(p,t)\ dp\ \ , \tag{7}$$

where $E(k,t)$ is the kinetic-energy spectrum, θ_{kpq} and θ_{kpq}^T times characteristic of the nonlinear damping of triple correlations in the EDQNM theory, and depending on the kinetic-energy and scalar-variance spectra. Let us start by assuming a $k^{-5/3}$ inertial range at wave numbers greater than k_C, with a Kolmogorov constant C_K. We obtain:

$$\nu_t^\infty = 0.441\ {C_K}^{-3/2}\left[\frac{E(k_C)}{k_C}\right]^{1/2} \tag{8}$$

$$\kappa_t^\infty = \frac{\nu_t^\infty}{P_r^{(t)}} \tag{9}$$

with

$$P_r^{(t)} = 0.6\quad . \tag{10}$$

If one assumes for instance $C_K = 1.4$, the constant in front of Eq. (8) will be 0.267. When k is arbitrary, the numerical evaluation of the EDQNM transfers yields

$$\nu_t(k|k_C) = K(k/k_C)\nu_t^\infty \tag{11}$$

$$\kappa_t(k|k_C) = C(k/k_C)\kappa_t^\infty\quad . \tag{12}$$

As shown by Kraichnan [1], $K(x)$ is approximately constant and equal to 1, except in the vicinity of $k/k_C = 1$ where it displays a strong overshoot (cusp-behaviour), due to the predominance of semi-local transfers across k_C. It was shown in [4] that $C(x)$ behaves qualitatively as $K(x)$ (plateau at 1 and positive cusp), and that the spectral turbulent Prandtl number $\nu_t(k|k_C)/\kappa_t(k|k_C)$ is approximately constant, and thus equal to 0.6 as given by Eq. (10). One advantage of using such a subgridscale modelling is that they are able to deal with a continuous spectrum at the cutoff, while an eddy-viscosity assumption in physical space is more or less equivalent to a a spectral-gap assumption between subgrid and resolved scales.

Now, we go back to physical space. Let us consider the EDQNM eddy viscosity (still scaling on $\sqrt{E(k_C)/k_C}$) with no cusp, and adjust the constant as proposed by [6], by balancing

in the inertial range the subgridscale flux with the kinetic energy flux ϵ in the energy spectrum evolution equation. This yields

$$\nu_t(k_C) = \frac{2}{3}\, C_K^{-3/2}\, \left[\frac{E(k_C)}{k_C}\right]^{1/2} \quad . \tag{13}$$

The problem with such an eddy-viscosity (if the energy spectrum may be computed) is that it is uniform when used in physical space. Obviously, the eddy viscosity should take into account the intermittency of turbulence, and cancel in laminar or calm regions. It was proposed by [5] to determine in the physical space the eddy viscosity with the aid of (13). $E(k_C, \vec{x})$ is now a local kinetic energy spectrum, calculated in terms of the local second-order velocity structure function of the filtered field

$$F_2(\vec{x}, \Delta x) = \left\langle \|\overline{\vec{u}}(\vec{x}, t) - \overline{\vec{u}}(\vec{x} + \vec{r}, t)\|^2 \right\rangle_{\|\vec{r}\| = \Delta x} \tag{14}$$

as if the turbulence is three-dimensionally isotropic. This yields for a Kolmogorov spectrum

$$\nu_t^{SF}(\vec{x}, \Delta x) = 0.105\; C_K^{-3/2}\; \Delta x\; [F_2(\vec{x}, \Delta x)]^{1/2} \quad . \tag{15}$$

F_2 is calculated with a local statistical average of square velocity differences between $\vec{x}$ and the six closest points surrounding $\vec{x}$ on the computational grid. In some cases, the average may be taken over four points parallel to a given plane. Notice also that if the computational grid is not regular (but still orthogonal), interpolations of (15) based upon Kolmogorov's 2/3 law have been proposed by [7].

The structure-function model (SF) works very well for decaying isotropic turbulence, where it yields a fairly good Kolmogorov spectrum [5], better than Smagorinsky's model (with $C_S = 0.2$) and Kraichnan's spectral-cusp model. But it does not work for transition in a boundary layer at low Mach (or incompressible) where, like Smagorinsky, it is too dissipative and prevents TS waves to degenerate into turbulence. To overcome the difficulty, an improved versions of the SF model has been developed, the *filtered structure-function model* (FSF). The dynamic model in physical space (see [9]) is another way of adapting the eddy viscosity to the local conditions of the flow. The FSF model was developed by Ducros and applied to a boundary layer at Mach 0.5 [8]. Here, the filtered field u_i is submitted to a high-pass filter in order to get rid of low-frequency oscillations which affect $E_{\vec{x}}(k_C)$ in the SF model. The high-pass filter is a Laplacian discretized by second-order centered finite differences and iterated three times. This model will be applied below with good results to spatially-growing incompressible mixing layers, and to a jet at Mach 1.

3. Incompressible mixing layers

We first recall results relative to a temporal mixing layer in a fluid of constant density. The flow is periodic in the streamwise and spanwise directions, and initiated by a hyperbolic-tangent velocity profile to which is superposed a small random perturbation. We take free-slip boundary conditions on the upper and lower boundaries, and use pseudo-spectral methods in the three dimensions of space. LES using most of subgrid models show the following results. If the perturbation is quasi two-dimensional, the mixing layer evolves into a set of big quasi two-dimensional vortices which both undergo pairing and stretch intense longitudinal hairpin vortices in the stagnation regions between them. Such a phenomenon has in fact been observed

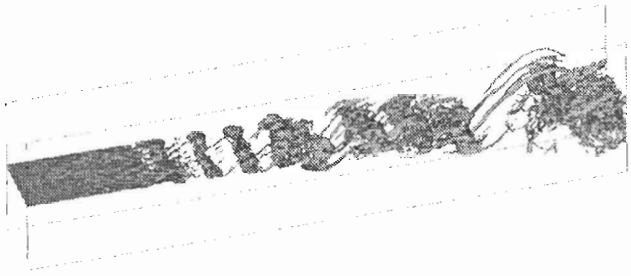

Figure 1. LES of an incompressible mixing layer forced upstream by a quasi two-dimensional random perturbation; the vorticity modulus is shown at a threshold $(2/3)\omega_i$.

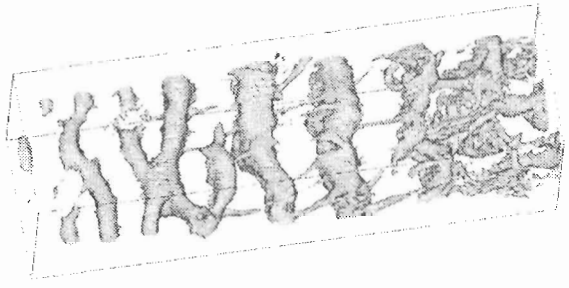

Figure 2. Same as Figure 1, but with a three-dimensional upstream white-noise forcing, low-pressure field.

experimentally for a long time (see e.g. [10, 11]). On the other hand, and if a weak three-dimensional random isotropic perturbation is superposed upon the basic shear, Comte et al. [12, 13] showed using DNS that helical pairing occurs. We have recovered the same dislocated pattern in LES of temporal mixing layers with the same forcing. We consider now LES of spatial mixing layers initiated upstream by a hyperbolic-tangent velocity profile superposed on the average flow, plus a weak random forcing regenerated at each time step. Free-slip conditions are still imposed upon the upper and lower boundaries. The outflow boundary condition are radiative. With an upstream forcing consisting in a quasi two-dimensional random perturbation, intense longitudinal hairpins stretched between quasi 2D Kelvin-Helmholtz vortices are found again (Figure 1). When the forcing is a three-dimensional random white noise, helical pairing occurs upstream, as indicated by the low-pressure maps of Figure 2. It shows that the topology of the flow may be deeply modified by tiny changes in the upstream velocity.

4. Compressible LES

We consider now the LES formalism in a compressible ideal gas. One writes first the compressible Navier-Stokes equations (flux form) for a Newtonian fluid

$$\frac{\partial U}{\partial t} + \frac{\partial F_1}{\partial x_1} + \frac{\partial F_2}{\partial x_2} + \frac{\partial F_3}{\partial x_3} = 0 \quad , \tag{16}$$

$$U = {}^T(\rho, \rho u_1, \rho u_2, \rho u_3, \rho e) \quad , \tag{17}$$

$$\rho e = \rho\ C_v\ T + \tfrac{1}{2}\rho(u_1^2 + u_2^2 + u_3^2) \tag{18}$$

$$F_i = \begin{pmatrix} \rho u_i \\ \rho u_i u_1 + p\ \delta_{i1} - 2\mu S_{i1} \\ \rho u_i u_2 + p\ \delta_{i2} - 2\mu S_{i2} \\ \rho u_i u_3 + p\ \delta_{i3} - 2\mu S_{i3} \\ (\rho e + p)u_i - 2\mu u_j S_{ij} - k\dfrac{\partial T}{\partial x_i} \end{pmatrix} \quad . \tag{19}$$

$$S_{ij} = \frac{1}{2}\left[\frac{\partial u_j}{\partial x_i} + \frac{\partial u_i}{\partial x_j} - \frac{2}{3}(\boldsymbol{\nabla}.\boldsymbol{u})\delta_{ij}\right] \tag{20}$$

where $k = \rho C_p \kappa$ is now the thermal conductivity, and κ thermal diffusivity. Sutherland empirical law is assumed for $\mu(T)$. The molecular Prandtl number $Pr = \nu/\kappa = C_p\mu(T)/k(T)$ is taken constant and equal to 0.7. The equation of state $p = R\ \rho\ T$ closes the system.

To the low-pass filter of the LES $\overline{\ }$, we associate Favre's density-weighted filter $\widetilde{\phi} = \overline{\rho\phi}/\overline{\rho}$ (see [14]). The low-pass filtered equations write

$$\frac{\partial \overline{U}}{\partial t} + \frac{\partial \overline{F}_1}{\partial x_1} + \frac{\partial \overline{F}_2}{\partial x_2} + \frac{\partial \overline{F}_3}{\partial x_3} = 0 \quad , \tag{21}$$

$$\overline{U} = {}^T(\overline{\rho}, \overline{\rho\widetilde{u_1}}, \overline{\rho\widetilde{u_2}}, \overline{\rho\widetilde{u_3}}, \overline{\rho\widetilde{e}}) \quad , \tag{22}$$

$$\overline{F_i} = \begin{pmatrix} \overline{\rho\widetilde{u_i}} \\ \overline{\rho\widetilde{u_i}\widetilde{u_1}} + \varpi\ \delta_{i1} - \tau_{i1} - \overline{2\mu S_{i1}} \\ \overline{\rho\widetilde{u_i}\widetilde{u_2}} + \varpi\ \delta_{i2} - \tau_{i2} - \overline{2\mu S_{i2}} \\ \overline{\rho\widetilde{u_i}\widetilde{u_3}} + \varpi\ \delta_{i3} - \tau_{i3} - \overline{2\mu S_{i3}} \\ (\overline{\rho}\widetilde{e} + \varpi)\widetilde{u}_i \quad - Q_i - \overline{2\mu S_{ij}u_j} - k\overline{\dfrac{\partial T}{\partial x}} \end{pmatrix} \quad . \tag{23}$$

where τ_{ij} is the deviator of the subgrid-stress tensor $\mathcal{T}_{ij} = -\overline{\rho u_i u_j} + \overline{\rho}\widetilde{u}_i\widetilde{u}_j$. We have defined a macro-temperature

$$\vartheta = \widetilde{T} - \frac{1}{2C_v\overline{\rho}}\mathcal{T}_{ll} \quad ; \quad (\mathcal{T}_{ll} = \gamma M_{\rm sgs}^2 \bar{p}\ ,\ M_{\rm sgs}^2 = \mathcal{T}_{ll}/\overline{\rho c^2}) \tag{24}$$

and a macro-pressure

$$\varpi = \bar{p} - \frac{1}{3}\mathcal{T}_{ll} = \overline{\rho} R\vartheta + \frac{3\gamma - 5}{6}\mathcal{T}_{ll} \quad . \tag{25}$$

$Q_i = -\overline{(\rho e + p)u_i} + (\overline{\rho}\widetilde{e} + \varpi)\widetilde{u}_i$ is the subgrid-heat flux. The energy relation is

$$\overline{\rho}\widetilde{e} = \overline{\rho}\ C_v\vartheta + \frac{1}{2}\overline{\rho}\ (\widetilde{u_1}^2 + \widetilde{u_2}^2 + \widetilde{u_3}^2) \quad . \tag{26}$$

These equations are exact. We write now the following approximate LES equations. The filtered equation of state is $\varpi \simeq \overline{\rho} R\vartheta$. It is valid for momoatomic gases like argon and helium (for which $\gamma \approx 5/3$), of if $(3\gamma - 5)\gamma M_{\rm sgs}^2/6 \ll 1$. For the air, this improves the condition $\gamma M_{\rm sgs}^2 \ll 1$ proposed by [15]. One takes variable-density eddy-viscosity and diffusivity models

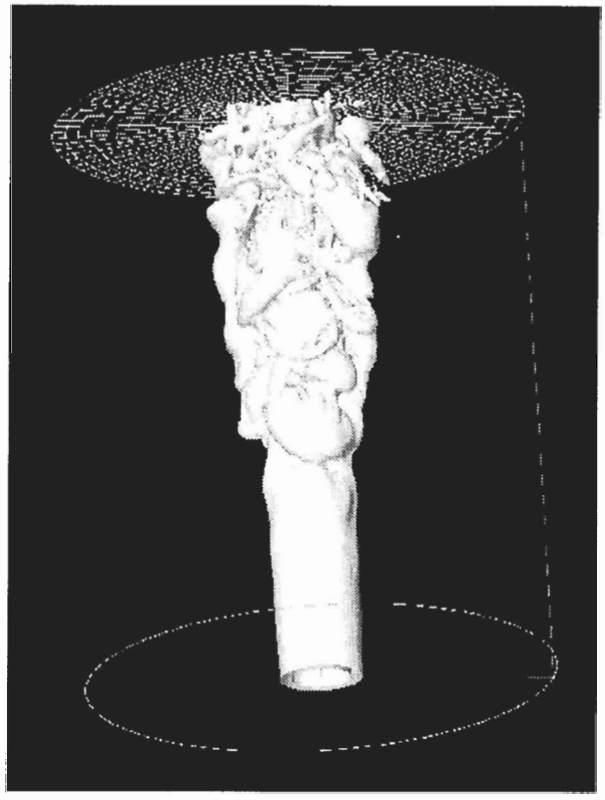

Figure 3. LES of a compressible jet at Mach 1, vorticity modulus field.

$\tau_{ij} \simeq \overline{\rho}\ 2\nu_t \widetilde{S_{ij}}$, $Q_i \simeq \overline{\rho} C_p (\nu_t / Pr_t)(\partial \vartheta / \partial x_i)$. The remaining non-computable viscous terms (of less importance at high Reynolds) are modified . The fluxes read

$$\overline{F_i} \simeq \begin{pmatrix} \overline{\rho}\widetilde{u_i} \\ \overline{\rho}\widetilde{u_i}\widetilde{u_1} + \varpi\ \delta_{i1} - 2(\bar{\mu} + \bar{\rho}\nu_t)\widetilde{S_{i1}} \\ \overline{\rho}\widetilde{u_i}\widetilde{u_2} + \varpi\ \delta_{i2} - 2(\bar{\mu} + \rho\nu_t)\widetilde{S_{i2}} \\ \overline{\rho}\widetilde{u_i}\widetilde{u_3} + \varpi\ \delta_{i3} - 2(\mu + \rho\nu_t)\widetilde{S_{i3}} \\ (\overline{\rho}\widetilde{e} + \varpi)\widetilde{u}_i \quad - 2(\bar{\mu} + \rho\nu_t)\widetilde{S_{ij}}\widetilde{u_j} - \left[k + \bar{\rho} C_p \frac{\nu_t}{Pr_t}\right] \dfrac{\partial \vartheta}{\partial x_i} \end{pmatrix} , \qquad (27)$$

$\mu(\vartheta)$ obbeys Sutherland relation. $\nu_t(\tilde{\boldsymbol{u}})$ and Pr_t correspond to the incompressible subgrid models. The resulting system is equivalent to compressible Navier-Stokes equations with the following changes:

$$u_i \to \widetilde{u_i}, \rho \to \rho, T \to \vartheta, p \to \varpi, \epsilon \to \tilde{\epsilon}, \mu \to \mu + \bar{\rho}\nu_t, k \to k + \bar{\rho} C_p \frac{\nu_t}{Pr_t} \quad .$$

We present finally an application to the LES of a round jet using the FSF model. The basic upstream velocity profile is close to a top hat, with a small three-dimensional white noise perturbation superposed upon it. Upstream, the Mach number (based on the maximal velocity)

is one, and the Reynolds number (based on the diameter of the jet) 21 000. Calculations are done in a system of cylindrical coordinates. One sees on Figure 3, representing the vorticity modulus, the growth of an alternate-pairing subharmonic mode, already observed in LES of incompressible jets (Métais, 1997, private communication). This structure is the equivalent of helical pairing for the mixing layer, and the question of its permanence at higher Mach number is an open one.

Acknowledgement. This work was sponsored by Institut Universitaire de France, CEA, CNRS, INPG and UJF.

References

[1] Kraichnan RH, Eddy viscosity in two and three dimensions, J. Atmos. Sci., 33, 1521-1536, (1976).

[2] Chollet JP and Lesieur M, Parameterization of small scales of three-dimensional isotropic turbulence utilizing spectral closures, J. Atmos. Sci., 38, 2747-2757, (1981).

[3] Lesieur M, Turbulence in fluids, third edition, Kluwer Academic Publishers, (1997).

[4] Chollet JP and Lesieur M, Modélisation sous maille des flux de quantité de mouvement et de chaleur en turbulence tridimensionnelle isotrope, La Météorologie, 29-30, 183-191, (1982).

[5] Métais O and Lesieur M, Spectral large-eddy simulations of isotropic and stably-stratified turbulence, J. Fluid Mech., 239, 157-194, (1992).

[6] Leslie DC and Quarini GL, The application of turbulence theory to the formulation of subgrid modelling procedures, J. Fluid Mech., 91, 65-91, (1979).

[7] Lesieur M and Métais O, New trends in large-eddy simulations of turbulence, Ann. Rev. Fluid Mech., 28, 45-82, (1996).

[8] Ducros F, Comte P and Lesieur M, Large-eddy simulation of transition to turbulence in a boundary-layer developing spatially over a flat plate, J. Fluid Mech., 326, 1-36, (1996).

[9] Germano M, Piomelli U, Moin P and Cabot B, A dynamic subgrid-scale eddy-viscosity model, Phys. Fluids A., 3, 1760-1765, (1991).

[10] Konrad JH, An experimental investigation of mixing in two-dimensional turbulent shear flows with applications to diffusion-limited chemical reactions, Ph.D. Thesis, California Institute of Technology, (1976).

[11] Bernal LP and Roshko A, Streamwise vortex structure in plane mixing layer, J. Fluid Mech., 170, 499-525, (1986).

[12] Comte P, Fouillet Y, Gonze MA, Lesieur M, Métais O and Normand X, Large-eddy simulations of free-shear layers, In: O. Métais and M. Lesieur (eds.), Turbulence and coherent structures, Kluwer Academic Publishers, 45-73, (1991).

[13] Comte P, Lesieur M and Lamballais E, Large and small-scale stirring of vorticity and a passive scalar in a 3D temporal mixing layer, Phys. Fluids A, 4, 2761-2778, (1992).

[14] Favre A, Equation des gaz turbulents compressibles, J. Mécanique, 4, 361-421, (1965).

[15] Erlebacher G, Hussaini MY, Speziale CG and Zang TA, J. Fluid Mech., 238, 155, (1992).

A Comparative Numerical Study of the Richtmyer-Meshkov Instability with Nonlinear Analysis Three Dimensions

X.L. Li[1] and Q. Zhang[2]
[1]Department of Mathematical Sciences
Indiana University Purdue University Indianapolis, Indianapolis, IN, 46202, USA
[2]Department of Applied Mathematics and Statistics
State University of New York at Stony Brook, Stony Brook, NY, 11794, USA

Abstract: The shock driven Richtmyer-Meshkov instability is studied numerically in three dimensions and in the nonlinear regime. The numerical solution is tested for convergence under computational mesh refinement and is compared with the predictions of a recently developed nonlinear theory based on Padé approximation and asymptotic matching. Good agreement has been found between numerical solutions and predictions of the nonlinear theory in three dimensions and for both the reflected shock and the reflected rarefaction wave cases. The numerical study is extended to the re-shock experiment in which the fluid interface interacts initially with the incident shock. Later, as the transmitted shock bounces back from the wall, the fluid interface is re-shocked.

1. Introduction

Recently, a quantitative nonlinear theory was developed for the compressible RM instability in both two and three dimensions [6, 7, 8]. This theory provides analytic predictions for the growth rate and amplitude of the RM unstable mode for both the case of reflected shock and the case of reflected rarefaction wave. It has been shown that in two dimensions the theoretical predictions are in very good agreement with the experimental data and the numerical solutions using the front tracking method. In this paper, we present a careful numerical comparison of the RM instability in three dimensions. The numerical method we use features a high resolution for both the shock front and the contact discontinuity [1]. This numerical method is based on the Total Variation Diminishing scheme and uses artificial compression (TVD/AC) to sharpen the contact discontinuity.

We also simulated of the system with re-shock in which the fluid interface is hit twice by the incident shock and the re-shock which is reflected by a wall. We report an interesting observation from our numerical study. We show that in the re-shock simulation, there exists a gradual transition for the growth rate of the fingers at the re-shocked fluid interfaces. This change depends primarily on the ratio of the wavelength of the perturbation mode to the initial distance from the fluid interface to the reflecting wall.

2. The nonlinear analytical model

The theory of Zhang and Sohn is based on a physical picture that the dominant effect of the compressibility occurs near the shock front. At an early time, the transmitted shock and reflect wave are in the vicinity of the fluid interface and the magnitude of the disturbance is small. As

More information - Email: linli@math.iupui.edu

time evolves, the magnitude of the disturbance at the fluid interface increases significantly but the transmitted shock and the reflected wave have moved away from the interface. Therefore at intermediate and late times, the effect of compressibility is reduced and the nonlinearity starts to dominate the interfacial dynamics. In another word, at early times the system is governed by the linearized Euler equations for compressible fluids, while at later times, the nonlinear equations for incompressible fluids are sufficient to describe the system.

For compressible linear system, the solution can be found in Richtmyer [4] and Yang *et al.*[5]. Approximate solutions for nonlinear, incompressible systems are constructed by Zhang and Sohn based on the method of the Padé approximation. Finally, Zhang and Sohn applied the asymptotic matching method which joins the solution for the linear, compressible system and the solution for nonlinear, incompressible system to obtain an analytical expression for the growth rate of a compressible RM unstable mode. This expression changes smoothly from the linear regime to the intermediate nonlinear regime. The matched solution for the overall growth rate, v, of the RM unstable mode is [6, 7, 8]

$$v = \frac{v_{lin}}{1 + \epsilon a_0 k^2 v_{lin} \lambda_1 t + max\{0, a_0^2 k^2 \lambda_1^2 - \lambda_2\} k^2 v_{lin}^2 t^2}, \tag{1}$$

where v_{lin} is the solution of the linear theory, which can be found from [4] for the case of reflected shock, or from [5] for cases of reflected shock and reflected rarefaction wave, a_0 is the post-shocked perturbation amplitude at the fluid interface, and k is the wave number. $\epsilon = 1$ for a system with no indirect phase inversion and $\epsilon = -1$ for a system with indirect phase inversion. Here $\lambda_1 = 1$ and $\lambda_2 = A^2 - \frac{1}{2}$ for fluids in two dimensions with $k = k_{2d}$, and

$$\lambda_1 = \frac{1}{8}(2 - 5\sqrt{2} + 4\sqrt{5} - \sqrt{10})A^2 + \frac{1}{8}(4 + 7\sqrt{2} - 6\sqrt{5} + \sqrt{10}),$$

$$\lambda_2 = \frac{1}{16}(7 + 7\sqrt{2} - 9\sqrt{5} + 3\sqrt{10})A^2 - \frac{1}{16}(4 + 7\sqrt{2} - 6\sqrt{5} + \sqrt{10})$$

for fluids in three dimensions with $k = \sqrt{2}k_x = \sqrt{2}k_y$.

3. Numerical solutions

The 3-D convergence test of the numerical solution is performed under the mesh refinement of the computational grid. The growth rate of the unstable mode is defined as the rate of change of the amplitude. The physical quantities which we present in this paper are in terms of dimensionless length kx, dimensionless velocity v/v_i and dimensionless time kv_it. Here v_i is the initial velocity behind the incident shock. Figure 1 shows the convergence test of the 3-D growth rate of the RM instability.

We conducted the numerical simulations for a system in three dimensions with a single transit shock. The numerical solutions are compared with the predictions of the linear theory, the impulsive model, and the nonlinear theory of Zhang and Sohn. Good agreement is achieved between the numerical solutions and the nonlinear solutions for both the reflected shock case and the reflected rarefaction wave case (Fig. 2). The linear theory predicts that, at early times, the growth rate reaches a constant (with some decaying oscillation around the constant). The growth rate remains constant at late times. Our numerical solution in three dimensions shows that the linear theory for the Richtmyer-Meshkov instability is only valid for a very short period of time.

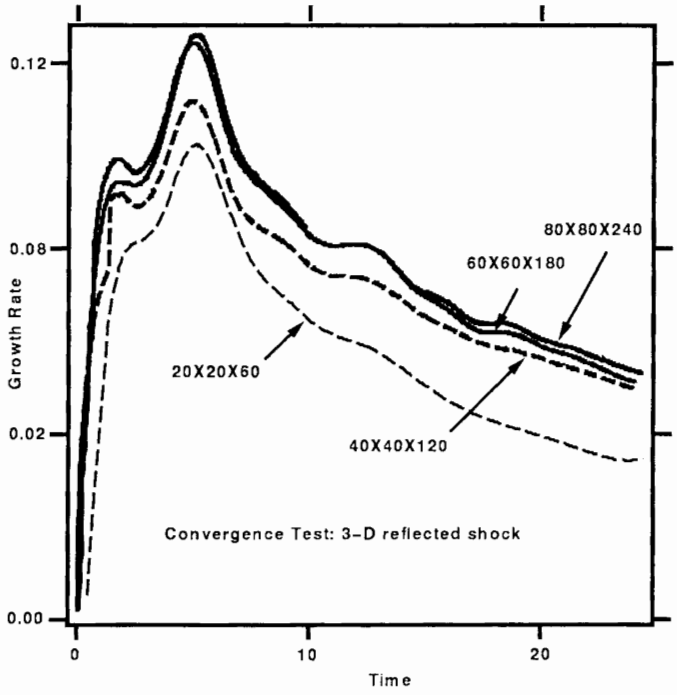

Figure 1. Convergence test of the 3-D RM growth rates with a sequence of mesh refinement: $20 \times 20 \times 60$, $40 \times 40 \times 120$, $60 \times 60 \times 180$, and $80 \times 80 \times 240$.

In the simulation of re-shock system, the fluid interface is hit twice: first due to the initial incident shock and second due the transmitted shock bouncing back from the reflecting wall at the bottom of the shock tube. The time it takes for the shock to bounce back from the wall and to arrive at the fluid interface can be estimated by the following formula

$$t = L(\frac{1}{v_{ts}} + \frac{1}{v_{bs}})\frac{v_{bs}}{v_c + v_{bs}}, \tag{2}$$

where L is distance from the mean position of the initial interface to the wall, v_c is the velocity of the fluid interface and v_{ts} and v_{bs} are the speed of the transmitted shock and its speed after bouncing back from the wall, respectively. v_c, v_{ts} and v_{bs} can be determined from the solution of the Riemann problem.

The re-shock phenomenon is very important in the problem of controlled nuclear fusion with inertial confinement (ICF). We simulated the interface motion after the first shock and the re-shock, and observed that the fluid mixing can be dramatically different with different physical parameters. We demonstrate this phenomenon by simulating two systems with different L.

In the first re-shock simulation, all sides have the dimensionless length $L = 2\pi$. The average distance from the initial fluid interface to the reflecting wall (the bottom of the computational domain) is $L = 1.4\pi$. The Mach number of the incident shock is 1.5, and the pre-shocked density ratio between two fluids across the fluid interface is $\rho_1/\rho_2 = 1/5$. The dimensionless

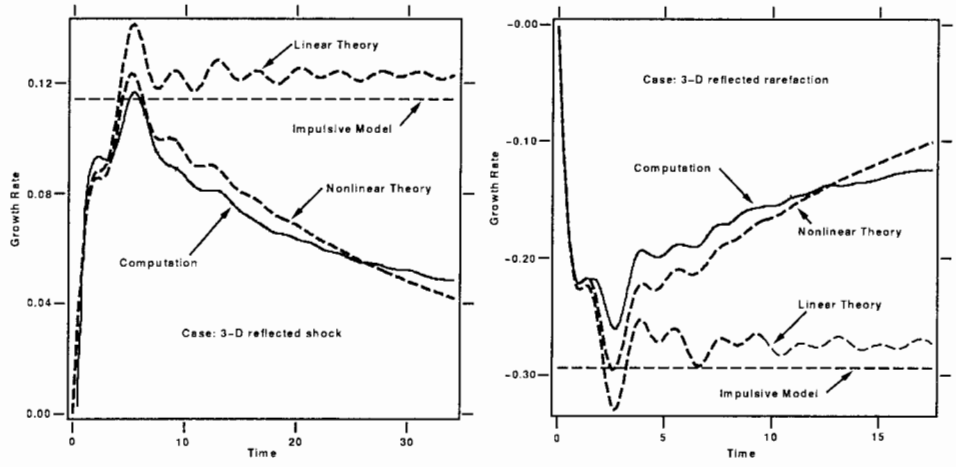

Figure 2. Comparison of 3-D growth rate from the numerical solution with the prediction of the linear theory, the impulsive model and the nonlinear theory by Zhang and Sohn. The left plot shows the growth rate in the case of reflected shock. The right plot shows the growth rate in the case of reflected rarefaction wave.

perturbation amplitudes in two horizontal directions are $k_x a_x(0-) = k_y a_y(0-) = 0.196$. The incident shock travels from the light fluid to the heavy fluid. Our numerical simulation indicates that the system has very little mixing after the re-shock.

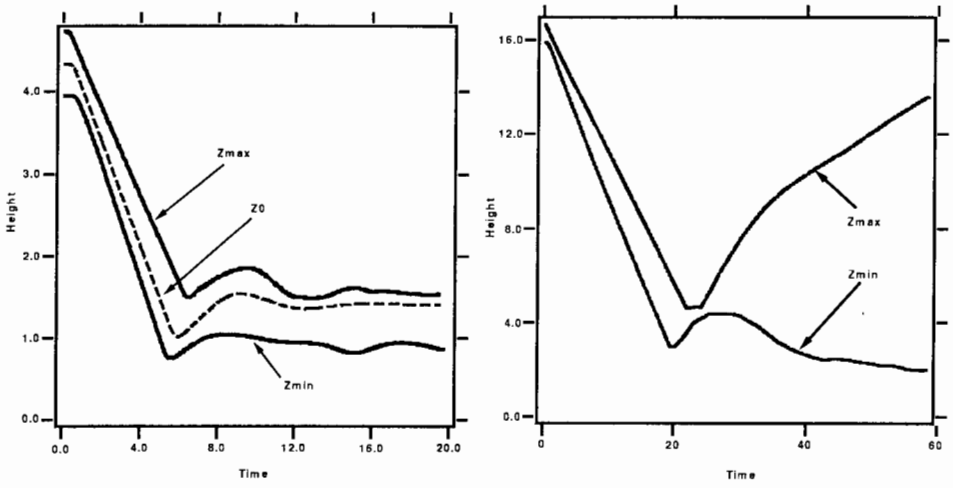

Figure 3. Maximum (z_{max}) and minimum (z_{min}) heights in the Richtmyer-Meshkov re-shock experiment. In the left case, the amplitude of the perturbed interface remains almost constant after the interaction with the re-shock. This results in a stable fluid interface. In the right case, the nterface becomes very unstable, and the amplitude ($z_{max} - z_{min}$) increases to 15 times of the initial amplitude at $t = 58.6$.

In the second re-shock simulation, the density ratio, Mach number and the perturbation amplitude at the fluid interface are all the same as the ones used in the first re-shock simulation. But in this case, we placed the initial fluid interface further away from the wall at $L = 5.17\pi$. The re-shock occurs at about $t = 22$ (the lower tips of the finger begins to turn around at about $t = 19.5$). After the re-shock, the instability develops rapidly. At the time $t = 58.6$, the amplitude of the unstable mode at the fluid interface has grown to about 15 times that in the initial perturbation. A mushroom is formed at $t = 58.6$ (Fig. 3). The comparison of the maximum and minimum heights of the fluid interface between the first and the second simulations is shown in Fig. 4.

¿From these two different re-shock simulations, we find that for a given set of density ratio and Mach number, there is a gradual transition from a stable system to an unstable system. This transition depends on the dimensionless distance from the unshocked mean fluid interface to the reflecting wall. A system with larger L is more unstable than the one with smaller L. This "freeze out" phenomenon was noted by Mikaelian in his early papers [2, 3].

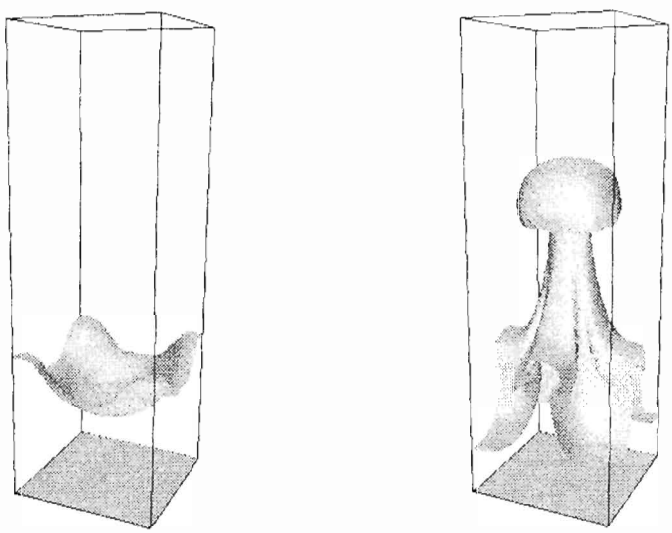

Figure 4. Evolution of fluid interface in the Richtmyer-Meshkov re-shock experiment. The fluid interface first moves downward after transition of the incident shock (left $t = 22.1$). It is then hit by the reflected shock. Since the reflected shock travels from heavy fluid to light fluid, it is the reflected rarefaction case which reverses the phase of the interface motion. A mushroom-like spike is formed at $t = 58.6$ (right).

4. Conclusion

In this presentation, We show that for fluids with the same adiabatic exponents, the TVD/AC method gives convergent numerical solutions for the growth rate of the RM instability under computational mesh refinement. The 3-D numerical solutions are in good agreement, in both

the reflected shock and the reflected rarefaction wave cases, with the predictions of a recently developed nonlinear theory of the Richtmyer-Meshkov instability. The numerical comparison shows that this nonlinear theory provides a quantitatively correct growth rate for the RM unstable interface from the linear regime to the intermediate nonlinear regime. The results of the numerical simulations of the re-shock system show that, after the second shock transition, the growth of the fingers at the fluid interface depends on the dimensionless distance between the mean position of the initial interface and the reflecting wall. As this distance decreases, the system changes gradually from an unstable one to a stable one. Such effect is important in the inertial confinement fusion.

Acknowledgement. The work of X. L. Li is supported in part by the U.S. Department of Energy grant DE-FG02-90ER25084. The work of Q. Zhang is supported in part by the U. S. Department of Energy, contract DE-FG02-90ER25084, by subcontract from Oak Ridge National Laboratory (subcontract 38XSK964C) and by National Science Foundation, contract NSF-DMS-9500568.

References

[1] Li XL, Jin BX and Glimm J, Numerical Study for the Three Dimensional Rayleigh-Taylor Instability through the TVD/AC Scheme and Parallel Computation, J. Comp. Phys, 126, 343-355, (1996).

[2] Mikaelian KO, Richtmyer-Meshkov Instabilities in Stratified Fluids, Phys. Rev. A., 31, 410, (1985).

[3] Mikaelian KO, Rayleigh-Taylor Instability and Richtmyer-Meshkov Instabilities and Mixing in Stratified Spherical Shells, Phys. Rev. A., 42, 3400, (1990).

[4] Richtmyer RD, Taylor Instability in Shock Acceleration of Compressible Fluids, Comm. Pure Appl. Math., 13, 297, (1960).

[5] Yang Y, Zhang Q and Sharp DH, Small Amplitude Theory of Richtmyer-Meshkov Instability, Phys. Fluids A, 6, 1856, (1994).

[6] Zhang Q and Sohn IS, An Analytical Nonlinear Theory of Richtmyer-Meshkov Instability, Phys. Lett. A, 212, 149, (1996).

[7] Zhang Q and Sohn IS, Padé Approximation for an Interfacial Fluid Mixing Problem, Applied Math. Lett., accepted, in press.

[8] Zhang Q and Sohn IS, Quantitative Theory of Richtmyer-Meshkov Instability in Three Dimensions, submitted to J. Fluid Mechanics.

An Experimental Study of the Richtmyer-Meshkov Instability, Including Amplitude and Wavelength Variations

L.M. Logory, P.L. Miller, T.A. Peyser, S.D. Murray, D.R. Farley, E.W. Burke and P.E. Stry
Lawrence Livermore National Laboratory
P. O. Box 808, L-22, Livermore, California, 94551, USA

Abstract: We report on results of an experimental study of the Richtmyer-Meshkov instability. The growth of the mixing region in the nonlinear regime is measured for a set of cases in which the amplitude and wavelength of the initial perturbation are varied systematically. The experiments are conducted on the Nova laser facility, and use a Nova hohlraum as a driver source to launch a high-Mach-number shock into a miniature shock tube attached to the hohlraum. The shock tube contains brominated plastic and low-density carbon foam as the two working fluids, with a micro-machined, triangular sawtooth interface between them serving as the initial perturbation. The sawtooth perturbation waveform is dominated by a single mode, and the perturbation amplitudes are chosen to expedite transition into the nonlinear phase of the instability. The shock, upon crossing the perturbation at the interface, instigates the Richtmyer-Meshkov instability. The resulting growth of the mixing region is diagnosed radiographically. Quantitative measurements of the temporal growth of the width of the mixing region are made for six different combinations of amplitude and wavelength, building upon previous results which employed a single amplitude/wavelength combination [5, 4]. Data from both experiment and supporting simulations suggest that the nonlinear growth of the mix width admits a logarithmic time dependence. The results also suggest that, properly normalized, the total mixing width grows in a nearly self-similar fashion, with a weak shape dependence.

1. Introduction

The present work addresses the behavior of shock-induced instabilities at density interfaces, in the case of very strong driving shocks and for the nonlinear, deeply nonlinear, and turbulent regimes of the instability development. Use of the Nova facility, located at Lawrence Livermore National Laboratory, provides several advantages in addressing these issues. Nova is capable of generating shocks in the Mach 30 range, in materials of densities on the order of $1\,g/cm^3$. The initial perturbations may be imposed by micro-machining the solid materials comprising the interface. These materials vaporize at the start of the experiment or upon the arrival of the shock, obviating the need for membranes or other separation strategies, yet provide us with well-defined and well-known initial conditions. By appropriate selection of the initial perturbation shape we are also able to expedite the transition to the nonlinear regime of interest.

Previous work [5] has demonstrated that a simple two-phase flow model of the instability growth agrees with the experimental data reasonably well, and that the mixing width increased logarithmically in time. Additional experiments were undertaken to test the applicability of the model, as well as provide fundamental data, by investigating the effects of initial perturbation amplitude, wavelength, and shape on the development of the resulting mixing region. Those

More information - Email: logory1@llnl.gov

additional experiments are reported on here.

2. Description of the experiment

2.1. Experiment setup

The description of these experiments has appeared previously *e.g.*, [2, 5], but is summarized again below for convenience. The experimental configuration is shown in Fig. 1. Eight beams of the Nova laser are used to heat the interior of a cylindrical gold hohlraum to 230 eV. The laser drive beams contain a total energy of 21 KJ in a 1 ns square pulse of 0.35 μm wavelength. A cylindrical shock tube made of beryllium (for low x-ray attenuation) is mounted over a hole in the hohlraum. The shock tube contains a brominated polystyrene ablator (density 1.22 g/cm^3) and a low-density carbon resorcinol foam payload (density 0.1 g/cm^3) which act as the two working fluids. A single-mode, rectilinear sawtooth profile is micro-machined into the high-density brominated polystyrene ablator which serves as the perturbation. The shock tube is glued to a gold washer for mounting stability, and the assembled package is then glued to the hohlraum. For more details about the experimental packages, see 3.

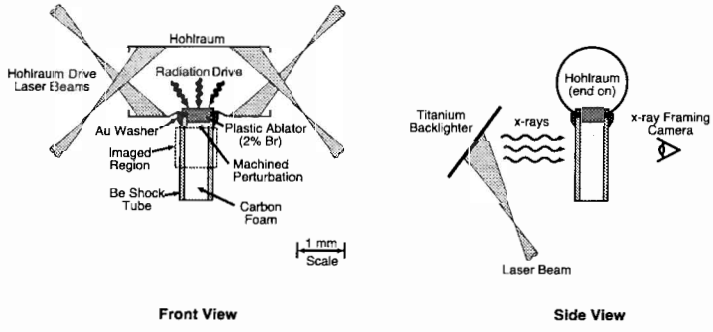

Figure 1. Experiment schematic.

2.2. Experiment sequence

The experiment sequence occurs as follows. Laser irradiation of the interior of the hohlraum produces low-energy x rays which cause a rapid ablation of the surface of the brominated polystyrene exposed to the inside of the hohlraum. The ablation launches a shock into the polystyrene which propagates down the axis of the shock tube. The instantaneous velocity imparted to the interface by the passage of the shock is about 70 μm /ns. Numerical simulations indicate that at the time the shock is incident on the interface, its Mach number is approximately 30. The passage of the incident shock heats the materials to plasma conditions, at a temperature of about 10 eV.

The presence of bromine in the polystyrene makes the material radiographically opaque relative to the low-density carbon foam payload. Perturbations consisting of parallel, isosceles, rectilinear sawtooth grooves were machined into the brominated polystyrene with a micro-lathe. When the shock traverses the interface in the high-to-low density direction, the sawtooth grooves invert, and the instability develops. Two beams of the Nova laser are used to generate x rays, by striking a metal foil, at the appropriate diagnostic time. The shock tube is backlit by the laser-generated x rays, and imaged with an 8x magnification, microchannel-plate-gated x-

ray pinhole camera [1], which provides a time-resolved x-ray radiograph of the sample. Fiducial wires provide spatial calibration and reference locations.

The x-ray camera records the image on film which is subsequently scanned and digitized for analysis. Quantitative data is obtained from a vertical lineout of the film exposure levels. The lineout averages the exposure levels over a $100\,\mu m$ wide region at the center of the image. The spatial profile of the x-ray backlighter source is normalized out of the lineout, and the x-ray transmission in the compressed carbon foam behind the shock is normalized to one. Changes in the transmission levels correspond to the uncompressed foam, shock, compressed foam, mix region, and brominated plastic. The width of the mix region is determined by applying a 5 to 95% transmission criteria to the normalized lineout as shown in Fig. 2.

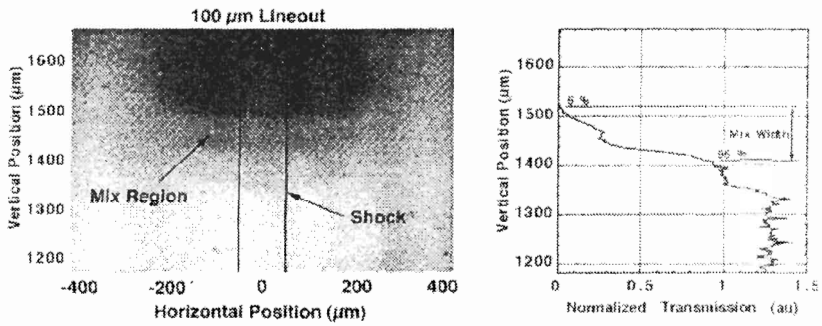

Figure 2. An experimental radiograph of the mix region approximately 8 ns after the shock has crossed the interface. Transitions in the film exposure levels are used to define the mix width.

3. Results

We have conducted a series of simulations and experiments in which the temporal evolution of the Richtmyer-Meshkov mixing region was obtained from single-mode triangular perturbations with amplitudes of 5, 10, and $20\,\mu m$, and wavelengths of 11.5, 23, and $46\,\mu m$. These values constitute an amplitude versus wavelength parameter matrix and are shown in Fig. 3. The various amplitudes and wavelengths were chosen to isolate the effects of the initial perturbation geometry and aid in comparisons. Note that perturbations of similar shape are contained within the three diagonals of the matrix.

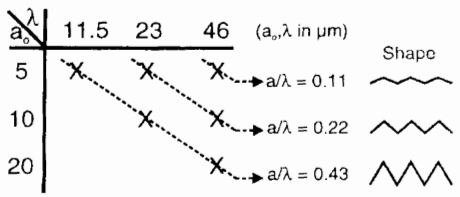

Figure 3. Initial perturbation amplitudes and wavelengths used for both simulations and experiments.

As a complement to the experimental work, simulations of the experiment have been performed using CALE, a two-dimensional arbitrary Lagrangian-Eulerian hydrodynamics code.

Simulated radiographs of the developing flowfield were obtained and analyzed in a manner identical to that described for the experimental data. The temporal growth of the mix region obtained from simulations is shown in nondimensionalized form in Fig. 4.

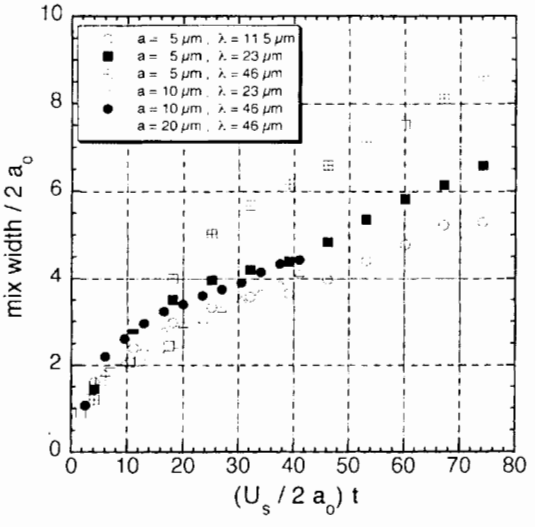

Figure 4. Nondimensionalized temporal width of the mix region obtained from simulations.

We define the characteristic length-scale of the flow as twice the initial perturbation amplitude, a_0, and the characteristic velocity as the shock velocity, U_s. A combination of these yields a nondimensional time scale, $U_s/2a_0$, which is the shock transit time across the interface. The time origin is shifted to the time of shock arrival at the first tip of the perturbations, for each of the different initial amplitudes, and then normalized by the shock transit time, yielding the nondimensional time used in Figs. 4 and 5. In contrast to the incompressible treatment of shock-induced instabilities, the compressible case introduces this natural time scale. As will be seen below, this work validates the use of the initial amplitude as the characteristic length scale. The appropriateness of selecting the shock speed as the velocity scale has not yet been fully tested.

Figure 4 shows that simulations from initial perturbations of the same shape exhibit similarity in these coordinates. The simulations also indicate a weak shape dependence, in which the mix widths obtained from smaller a_0/λ perturbations are larger, in these coordinates. The temporal growth of the mix width for similar shape perturbations are well fit by a logarithmic form (not shown here).

The temporal growth of the mix region measured in the experiment is shown in nondimensionalized form in Fig. 5. Note that data from perturbations of the same shape exhibit similarity in these coordinates. This is in agreement with the results of the simulations shown in Fig. 4. Since previous work [5] indicated that the mix width admits a logarithmic time dependence, the data for each shape was fit by a three parameter equation of the form $y = m_1 + m_2 \ln(1 + m_3 x)$. The data fits help to further discern the trends for the six different initial perturbations. We find increased mix widths as a_0/λ is decreased, in these coordinates, with the exception of

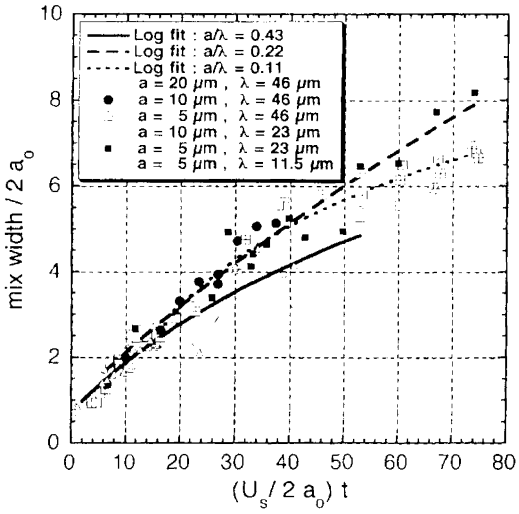

Figure 5. Nondimensionalized temporal width of the mix region obtained from experiments.

$a_0/\lambda = 0.11$, the most linear initial perturbation. For that case, the mix region extent is nearly equal to that for $a_0/\lambda = 0.22$ up to the nondimensional time of $(U_s/2a_0)t \approx 40$, after which it is less than the $a_0/\lambda = 0.22$ case. It should be noted that the $a_0/\lambda = 0.11$ case is represented by a single amplitude, and the shape is not duplicated elsewhere in the parameter matrix.

Comparing the data displayed in Fig. 5 with the simulations displayed in Fig. 4, we find that the width of the mix region for a_0/λ=0.43, for the three different initial amplitudes, is in good agreement for all times. The growth of the mix region for a_0/λ=0.22, for two different initial amplitudes, is in good agreement with simulations until approximately $(U_s/2a_0)t \approx 30$, after which the widths grow to be up to 20% larger than that indicated by simulations. Comparison of data with simulations for $a_0/\lambda = 0.11$ indicates the largest disagreement, as can be seen in the comparison of Fig. 4 and Fig. 5. At this time, we have not yet determined the reasons for the discrepancies.

4. Conclusion

We have presented results of an amplitude/wavelength study of the nonlinear Richtmyer-Meshkov growth of predominantly single-mode perturbations, for the case of strong shocks. Six combinations of three amplitudes and three wavelengths were chosen for the study. Data from initial perturbations (with the sawtooth shape) of $a_0/\lambda = 0.43$, for amplitudes of 5, 10, and 20 μm, appear self-similar when both the mixing widths and time are normalized by the initial amplitudes. Similarly, data for the shape with $a_0/\lambda = 0.22$, for amplitudes of 5 and 10 μm collapse in those coordinates. The third shape, of $a_0/\lambda = 0.11$, had only one amplitude, so collapse for that shape could not be tested.

Comparison between the data from the different shapes indicates that the three cases of $a_0/\lambda = 0.43$ grew less than the two cases of $a_0/\lambda = 0.22$, in the nondimensional coordinates. The single $a_0/\lambda = 0.11$ case had similar mix widths as the $a_0/\lambda = 0.22$ shape until about 40

shock transit times, after which it grew slightly less out to 75 shock transit times. An additional experiment, using $a_0/\lambda = 0.11$, with $a_0 = 2.5\,\mu$m and $\lambda = 23\,\mu$m, is planned to help clarify the behavior of that shape.

Acknowledgement. The authors would like to thank the individuals who support these experiments (including target development, fabrication and assembly, and technical support), the Nova operations personnel, and those involved in these experiments in the past. Their contributions to the success of this work are gratefully acknowledged.

This work was performed under the auspices of the U.S. Department of Energy by Lawrence Livermore National Laboratory under Contract No. W-7405-Eng-48.

References

[1] Budil KS, Perry TS, Bell PM, Hares JD, Miller PL, Peyser TA, Wallace R, Louis H, and Smith DE, The flexible x-ray imager, Rev. Sci. Instrum., 67, 2, 1-4, (1996).

[2] Hammel BA, Griswold D, Landon OL, Perry TS, Remington BA, Miller PL, Peyser TA, and Kilkenny JD, X-ray radiographic measurements of radiation-driven shock and interface motion in solid density material, Phys. Fluids B, 5, 7, 2259-2264, (1993).

[3] Louis H, Demiris A, Budil KS, Miller PL., Peyser TA, Stry PE, Wojtowicz DA, and Dimotakis PE, Miniature targets for high-energy density experiments on Nova, Fusion Tech., 28, 5, 1769-1882, (1995).

[4] Miller PL, Peyser TA, Stry PE, and Budil KS, Shock-hydrodynamics experiments on Nova, In: Proceedings of the 20th International Symposium on Shock Waves. Pasadena, CA, (1995).

[5] Peyser TA, Miller, PL, Stry, PE, Budil, KS, Burke, EW, Wojtowicz, DA, Griswold, DL, Hammel, BA, Phillion, DW, Measurement of radiation-driven shock-induced mixing from nonlinear initial perturbations, PRL, 75, 12, 2332-2335, (1995).

Richtmyer-Meshkov Instability in Compressible Stratified Fluids

D. Meiron and M. Meloon
Applied Mathematics 217-50, Caltech, Pasadena, CA 91125, USA

Abstract: We present the results of a study of the effect of compressibility on the interaction of shocks with stratified density layers. We extend a previous study of Pham on the use of a pressure impulse as an approximation for the interaction of a weak shock with a density-stratified layer and confirm that this approximation is valid for weak shocks. We also examine the effects of compressibility when the interaction is mediated by a strong shock. Our initial results indicate that the pressure impulse theory does break down at high Mach numbers but that the flow remains incompressible to a good approximation once the shocks have propagated away from the layer.

1. Introduction and background

The Richtmyer-Meshkov (R-M) instability [1] results from the misalignment of the pressure and density gradients when a shock passes normally through a perturbed density gradient. If the compressibility of the fluids is neglected, the R-M instability can be considered as the limit of the Rayleigh-Taylor instability when the acceleration is impulsive. Richtmyer confirmed this idea in the case where the density gradient consists of two discrete layers. The extension of this idea to density stratified layers has been considered both experimentally and theoretically by a number of authors. Saffman and Meiron [2] derived an approximation for the continuously stratified case in the spirit of the impulse approximation by assuming that the shock acts as an impulsive pressure distribution. They confirmed the result that the growth rate is reduced when the thickness of the density stratified layer is increased. In addition their approach provides an estimate of the initial vorticity deposited by the impulse as well as the kinetic energy imparted to the layer.

In this study we examine the validity of the impulsive approximation in the case where the impinging shocks are weak (with Mach number $M = 1.01$) and also in the case where the shocks are strong ($M > 2$). We find that the Saffman-Meiron impulse approximation provides reasonably accurate estimates of the vorticity deposited by a weak shock even when the amplitude of the perturbation is large. However the approximation breaks down as the shock strength is increased indicating that the impulse approximation does not adequately model the passage of the shock in this case.

1.1. The Saffman theory

Saffman and Meiron modeled the motion of a perturbed planar interface undergoing a shock-induced acceleration as one generated by the impulsive motion of the containing walls with a velocity V directed parallel to the undisturbed density gradient. The shock is modeled as a pressure impulse of the form

$$P = \bar{P}(x, y)\delta(t). \tag{1}$$

More information - Email: dim@ama.caltech.edu or mrm@ama.caltech.edu

This results in a velocity field of the form

$$u = \frac{-1}{\rho}\frac{\partial \bar{P}}{\partial x}H(t), \quad v = \frac{-1}{\rho}\frac{\partial \bar{P}}{\partial y}H(t), \tag{2}$$

where $H(t)$ is the Heaviside function, ρ is the initial density stratification, and P represents the impulsive pressure plus that pressure required to keep the flow incompressible:

$$\bar{P} = V\int_0^x \bar{\rho}dx + p'. \tag{3}$$

Using incompressibility once can derive an elliptic Poisson equation for the perturbed pressure p' and thus solve for the velocity field. The resulting flow field can then be used to compute the energy and vorticity of the flow.

1.2. Numerical experiments of Pham

Pham [3] performed numerical simulations using the incompressible Euler equations but with the mass transport equation retained:

$$\frac{\partial \rho}{\partial t} + \mathbf{u}\cdot\nabla\rho = 0, \quad \frac{\partial \mathbf{u}}{\partial t} + \mathbf{u}\cdot\nabla\mathbf{u} = -\frac{1}{\rho}\nabla P, \quad \nabla\cdot\mathbf{u} = 0. \tag{4}$$

Pham used as an initial condition a single scale density stratification of the form

$$\rho = 1 + \mathrm{At}\tanh\left[\frac{(x - a\cos ky)}{L}\right]. \tag{5}$$

Here At is the Atwood ratio, a is the amplitude, k is the wavenumber, and L is the thickness of the stratification. This initial condition can be used to examine the effect of thickness on the classical R-M growth rate. Pham's numerical results show that the velocity and vorticity fields derived from the Saffman impulse approximation provide reasonable approximations for the evolution of the flow for both single and multi-scale perturbations.

1.3. Compressible Richtmyer-Meshkov instability

The R-M instability is of course initiated via a shock wave. In order to connect with the incompressible theory one assumes that the effect of the shock is to impart a pressure impulse to the density layer. This is the foundation of the impulse model and the results above indicate how one uses it for layers with thickness. However it becomes of interest to investigate under what conditions one can assume that the shock acts as an impulse. Also of interest is to investigate the effect of compressibility on the growth rate; this is the motivation for the present paper.

2. Numerical simulation

In order to examine the role of compressibility on the estimates presented above we have carried out numerical simulations of the interaction of shocks of varying strengths impinging on density perturbations given by Eqn. 5. We have employed the AMRITA computational environment due to James Quirk [4] to perform these simulations. AMRITA provides a patch-based AMR (Adaptive Mesh Refinement) solver which can be used for any cell-centered scheme. In addition it provides tools to automate investigations. An example of its capabilities is shown in Fig. 1. Here we display a false Schlieren image of the interaction of a Mach 4 shock with a density layer of the type given by Eqn. 5. The AMR capability can be used to focus on the shock waves as well as the resulting mixing layer.

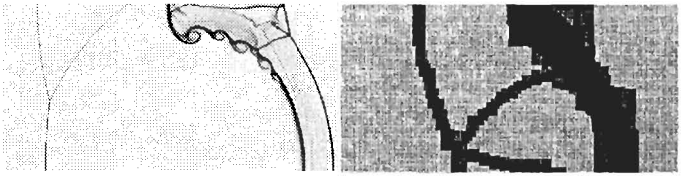

Figure 1. Left: a false Schlieren image of the interaction of a strong $M = 4$ shock with a perturbed thick interface ($L = 0.1$, At $= 0.8$, $a = 1.0$). Right: the hierarchy of grids generated by the *AMR_Sol* adaptive mesh refinement algorithm

3. Results

We have grouped the results according to the strength of the incoming shock wave. Weak shocks for the purposes of this paper have $M = 1.01$. Stronger shocks are those with $M > 2$.

3.1. Weak shocks

In the weak shock case we have examined the response of the density layer under a number of choices of parameters in Eqn. 5. We display in the figures below both the growth rate as well as the circulation. We begin by examining the low amplitude case ($a = 0.01$) with varying layer thickness. Figs. 2 and 3 show the response of a thin ($L = 0.01$) as well as a thick layer ($L = 1.0$) for a low density contrast (At $= 0.2$). Shown also for comparison are the predictions of the growth rate using the Richtmyer formula as well as predictions of the circulation using the shock polar approach of Samtaney and Zabusky[5]. This approach can only be applied when the layer is thin. In the thin layer case we see good agreement among all theories. However as the thickness is increased the Richtmyer formula over-predicts the growth rate. The Saffman approach does compute the correct growth rate in this case.

We next examine the effect of increasing the density contrast in the weak shock limit. In

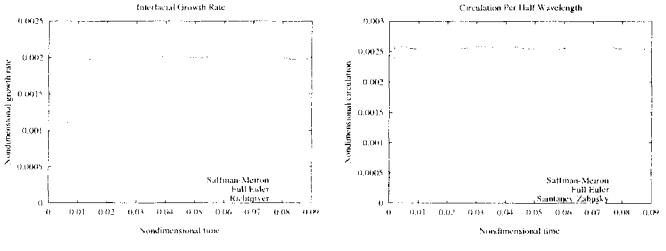

Figure 2. Results for $M = 1.01$, At $= 0.2$, $L = 0.01$, $a = 0.01$. Shown on the left is the growth rate vs. time. On the right is the circulation.

Figs. 4 and 5 it is seen that the Richtmyer formula again over-predicts the growth rate in the case of a thick layer. It is interesting to note that the Samtaney-Zabusky approximation for the circulation over-predicts the asymptotic circulation although it does capture correctly the initial circulation. The circulation is modified due to the subsequent baroclinic development of the layer in this case. In Fig. 6 we investigate the role of the amplitude. Shown in is a case in which the amplitude is large ($a = 1.0$). Surprisingly, in this weak shock limit the Saffman theory continues to provide valid estimates of both the growth rate as well as the circulation. We can conclude from this that the Saffman theory provides some improvement

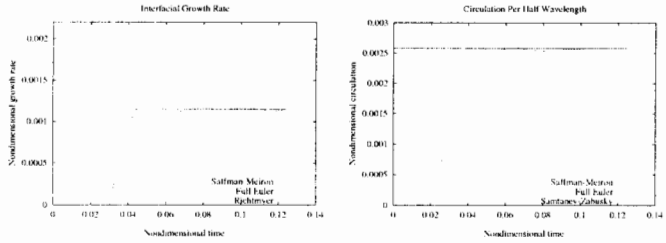

Figure 3. Results for $M = 1.01$, At $= 0.2$, $L = 1.0$, $a = 0.01$. Shown on the left is the growth rate vs. time. On the right is the circulation.

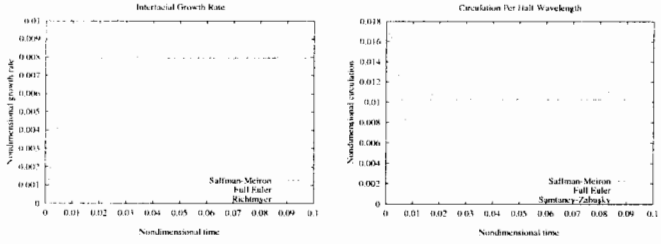

Figure 4. Results for $M = 1.01$, At $= 0.8$, $L = 0.01$, $a = 0.01$. Shown on the left is the growth rate vs. time. On the right is the circulation.

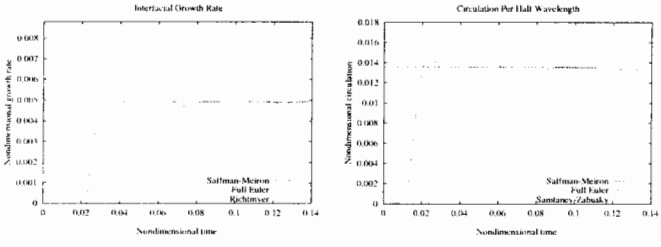

Figure 5. Results for $M = 1.01$, At $= 0.8$, $L = 1.0$, $a = 0.01$. Shown on the left is the growth rate vs. time. On the right is the circulation.

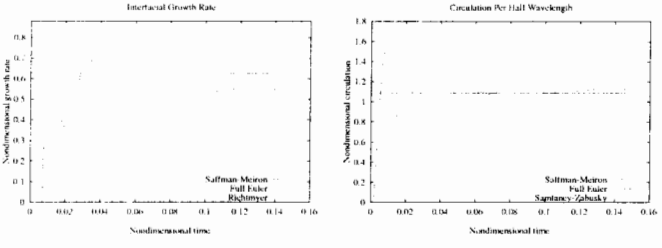

Figure 6. Results for $M = 1.01$, At $= 0.8$, $L = 0.1$, $a = 1.0$. Shown on the left is the growth rate vs. time. On the right is the circulation.

over the classical impulse model in that it can account properly for both the thickness of the layer as well as large amplitude perturbations. One drawback of this idea is that one must compute these estimates numerically by solving an elliptic equation. Our results also appear to confirm that even for large amplitude layers a shock does act as an impulse provided the shock is weak. Because the compression by such shocks is so small it is not necessary to account for post-shock compression in these cases.

3.2. Strong shocks

Shown in Figs. 7 and 8 are results for a strong $M = 4$ shock for two density contrasts. In both cases we see that none of the theories capture properly the dynamics. In the case of low density contrast the Saffman theory does capture the circulation but we believe this may be fortuitous. For larger density contrasts we again that while the growth rate is captured the circulation is not. We believe that in these cases shock refraction as well as acoustic waves propagating between the reflected and transmitted shocks are responsible for this discrepancy. In these cases we have accounted for the compression of the density gradient by the shock.

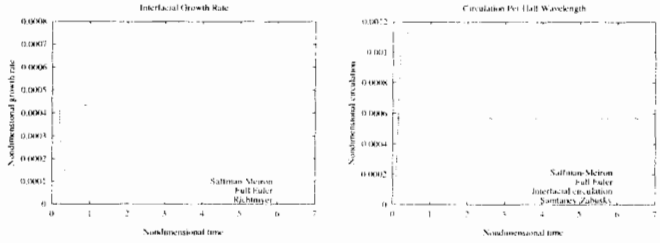

Figure 7. Results for $M = 4.0$, At $= 0.2$, $L = 0.1$, $a = 0.01$. Shown on the left is the growth rate vs. time. On the right is the circulation.

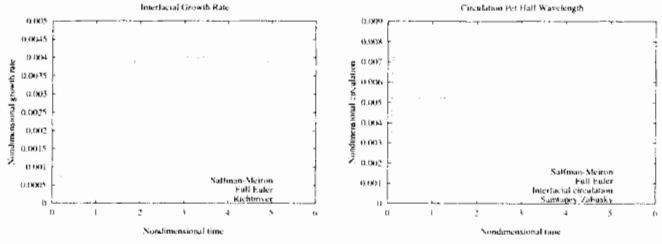

Figure 8. Results for $M = 4.0$, At $= 0.8$, $L = 0.1$, $a = 0.01$. Shown on the left is the growth rate vs. time. On the right is the circulation.

4. Conclusions

From these preliminary calculations we can conclude that the impulsive theory is accurate for weak shocks even when the amplitude of the perturbation is large and the layers have thickness. The classical Richtmyer impulsive model can be modified so as to account for these effects. It is also apparent that the impulsive theory is not adequate for strong shocks. This is particularly true when the density contrast is low. The modifications of the Saffman theory do

not improve the classical results. This leads one to conclude that the shock cannot be modeled as a pressure impulse in these cases and that the complex shock refraction which occurs here is crucial in setting up the initial vorticity. However at later times the flow near the mixing layer is incompressible even in the strong shock limit. In Fig. 9 we show a plot of the divergence of the flow for a strong shock case with two different density contrasts. It can be seen that the flow is predominantly incompressible. This indicates that an improved theory can be obtained by properly modeling the generation of the vorticity in the strong shock case and using this initial condition to determine the subsequent development via incompressible or weakly compressible dynamics. Whether such an approach can lead to an easily computed estimate for the growth rate under a wide variety of conditions is a topic for future work.

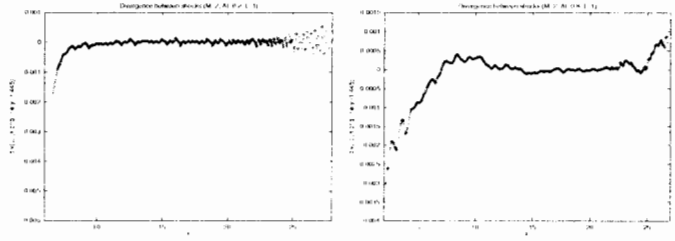

Figure 9. The flow divergence sampled along a line through the flow for a $M = 2$ shock with $L = 1$. Left At $= 0.2$, Right At $= 0.8$.

Acknowledgement. This work was supported by the Lawrence Livermore National Laboratory under the CAFDA program (Contract DOE-W-7405-ENG-48, Subcontract B295121)

References

[1] Richtmyer RD, Taylor instability in shock acceleration of compressible fluids, Communication on pure and applied mathematics, 13, 297-319, (1960).

[2] Saffman PG and Meiron DI, Kinetic energy generated by the incompressible Richtmyer-Meshkov instability in a continuously stratified fluid, Phys. Fluids A, 1, 1767, (1989).

[3] Pham T and Meiron DI, A numerical study of Richtmyer-Meshkov instability in continuously stratified fluids, Phys. Fluids A, 5, 2, 344-368, (1993).

[4] Quirk JJ and Karni S, On the dynamics of a shock-bubble interaction, J. Fluid Mech. 318, 129-163, (1996).

[5] Samtaney R and Zabusky N, On shock polar analysis and analytical expressions for vorticity deposition in shock-accelerated density-stratified interfaces Phys. Fluids. A. 5, 6, 1285-1287, (1993).

On Possibilities of Investigating Hydrodynamic Instabilities and Turbulent Mixing Development in Spherical Geometry

E.E. Meshkov, N.V. Nevmerzhitsky and V.V. Zmushko
Russian Federal Nuclear Centre - Institute of Experimental Physics
Prospect Mira 37, 607190, Sarov, Nizhny Novgorod Region, Russia

Abstract: Tentative results of a new experimental technique are discussed for investigation onto the hydrodynamic instabilities and turbulent mixing development at the interface between gas and jelly (the latter being loaded shows liquid behavior) in a spherical geometry. Some calculations and tentative experiments are described.

1. Introduction

An interface between density-different liquids being in accelerated motion will show instability when the acceleration is from lighter liquid to heavier (Rayleigh-Taylor instability) [1]. An Experimental study [2] has shown that 1D flow geometry (planar or cylindrical; implosion or explosion (expansion) case) can significantly affect the unstable interface. Therefore, it is of interest also to look at the Rayleigh-Taylor instability and turbulent mixing development in a spherical case. The boundary instability of an convergent spherical gaseous bubble in liquid is the classical illustration of limited cumulating [3] and under compression of the bubble gas [4]. Recently, numerical studies (using computational methods) have been reported, which address Rayleigh-Taylor instability for a spherical case [5, 6, 7, 8]. In view of this, it is important to develop experimental techniques to study the 1D flow instability in spherical geometry in implosion as well as explosion case. The paper describes below approaches to a jelly - based [9] experimental method to study hydrodynamic instabilities in spherical geometry both for explosion and implosion cases.

2. Flow with explosion (expansion)

Jelly technique is what offers a wide scope of opportunities to study unsteady hydrodynamic flows and, particularly, hydrodynamic instabilities of an interface (see e.g. an overview [10]). A jelly of water-solved gelatin made by a common household technology has sufficient strength to make models of various shapes. Again, this strength is not too high, so the jelly being loaded by pressures over one tenth of atmosphere shows liquid behavior . The jelly bulk layer is transparent enough to use flow visualization by optical techniques. When the jelly is mixing with the gas, its transparency gets decrease very rapidly. This would allow reliable observations of not only the mixing zone growth with respect to time but its boundary structure as well.
What may serve useful as a driver for jelly models is a gaseous explosive mixture (GEM); it has been found more suitable in practice to use acetylene mixture with oxygen ($C_2H_2+2.5O_2$). Simulation of the behavior of the GEM explosion products (while roughly estimating the flow dynamics) may be done using an ideal gas approximation with the initial pressure of 1.35 MPa and γ=1.24. Flow simulation for spherical geometry under explosion can use the following

More information - Email: otd03_2305@spd.vniief.ru

simple test configuration: a jelly-cast hemisphere is set up on the surface of a horizontal rigid plate. Its enclosed space is filled with GEM. The GEM is detonated from the hemisphere center by a high-voltage spark. The pressure of GEM detonation products causes a spherically symmetric flow to develop, and thus the shell is made to go apart in all directions. With this, there will be a turbulent mixing zone development at the inner and unstable surface of the layer. Fig.1 shows streak photos of the flows following the GEM detonation in the geometry as described. Fig.2 illustrates the penetration depth into the layer hbubble vs time; the same figure also includes the acceleration history of the unstable jelly layer surface (estimated from R-t relationship). The following specific observations should be noted: over time the h_{bubble}

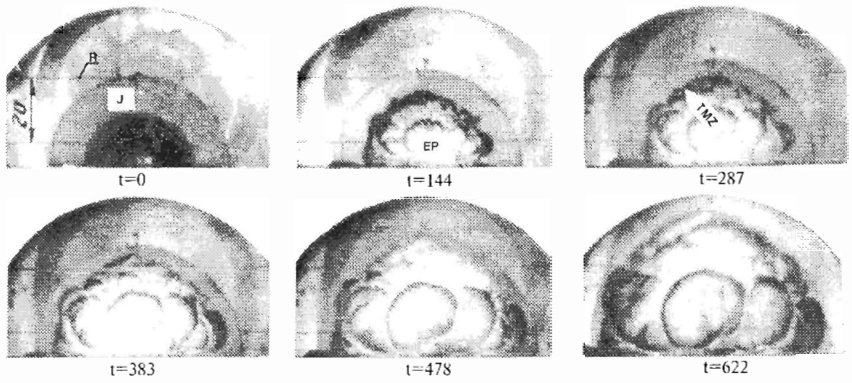

Figure 1. Turbulent mixing zone development at the inner surface of an expanded hemisphere of jelly. Notations: J - hemispherical shell (jelly); EP - GEM explosion products; TMZ - turbulent mixing zone; R - reference point; t - time count against initial shell motion (ms).

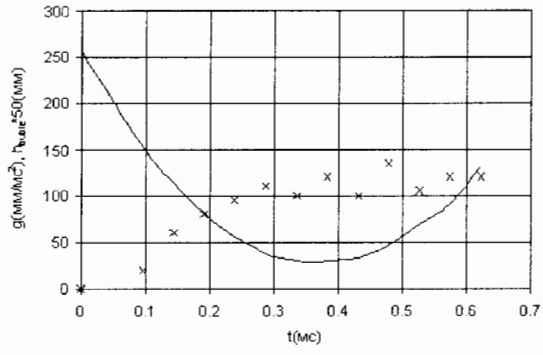

Figure 2. Turbulent mixing zone penetration into the layer, h_{bubble} , and interface acceleration, g, vs time.

growth rate goes down to zero, and then the mixing zone is no longer penetrating into the layer.

3. On the possibility to study the flow in implosion (convergence) case

The most interesting point is flow simulation in a spherical geometry for its implosion inside a spherical enclosure. The study is difficult in this case because of the consideration that although jelly technique allows a model with such inside chamber to be made, there are some conflicting problems that have to be addressed in order to generate the implosion flow. On the one hand, keeping the jelly model shape requires its rigid framing in any way, and on the other, symmetric compression of the model can be possible with the pressure uniformly applied over its entire outside surface. Finally, there is one more problem, that such a model will have a turbulent mixing zone to develop on its outer surface, that will be screening the in-model spherical chamber and so keeping from visualizing its shape change behavior with implosion. One may image the set up for symmetric gaseous bubble implosion based on the physical property that sound velocity in jelly is larger than a characteristic implosion rate, i. e., a noticeable uniformity for pressure perturbations may be possible within implosion. In a real situation, sound speed in a jelly of water-solved gelatin is virtually identical to that in water, i.e. C$\sim$1.5 km/s; and it is about 1km/s in GEM EP. Again, the jelly driven by GEM EP has its typical interface implosion velocity of about V_{typ}=50-100m/s and the ratio $\sim c/V_{typ}$ $\sim$15-30>>1. The numerical simulation to estimate the possibility of implosion inside a spherical gaseous enclosure by means of jelly technique was performed. The simulation was made in 2D geometry in hydrodynamic approximation and used the MIMOZA codes [11]. The computational model shaped as cone is given in Fig.3 Assumptions were made that - gaseous bubble radius R_2=3cm,

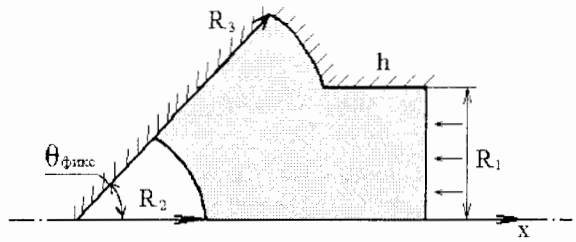

Figure 3. Flow computational model.

- jelly outer radius R_3=8cm,
- cylindrical part dimensions R_1=4.5cm h$\approx$2.4cm,
- P=13 atm - pressure maintained at the outer end.

Fig.4 below is an illustration of implosion R-t diagram of spherical air enclosure. The gaseous enclosure shape as result from the calculation for θ^0=45^0. case at instant of the highest compression, is shown in Fig.5 The enclosure is seen to be compressed quite uniformly: the radius value minimum of the gas-jelly interface, R_{min}=0.637cm, is achieved at the axis of symmetry, while its maximum R_{max}=0.687cm is observed in the neighborhood of the boundary θ=θ^*. As the angle θ^* increases, so does the volume of the calculated gas enclosure and, accordingly, the maximum compression time tmax grows. With larger θ^* angle, the difference Δ=R_{max}-R_{min} increases. Thus, the ratio (R_{max}-R_{min})/R_{min} in cases θ^*=90^o, θ^*=75^o and θ^*=45^o is $\sim$1.8 $\sim$0.255 and $\sim$0.078, respectively. Thus, θ^*=45^o is the only case where the converged spherical

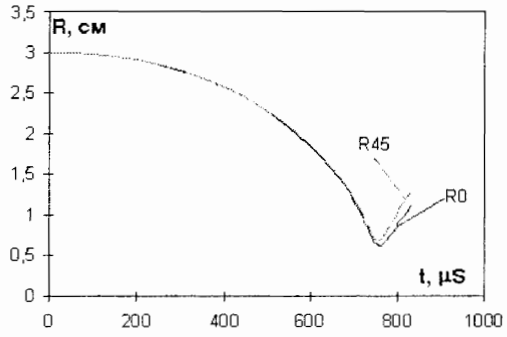

Figure 4. Implosion R-t diagram of spherical gaseous enclosure. R_0 is radius for $\theta=\theta^0$, R45 - radius for $\theta^0=45^0$.

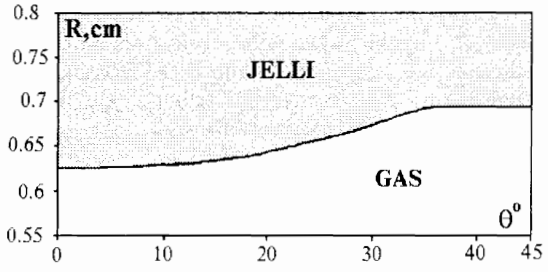

Figure 5. Gaseous enclosure shape at maximum compression (for $\theta^0=45^0$).

enclosure has its interface perturbation to radius ratio within 10%. In this way, the calculations have shown the basic possibility to implement practically symmetrical implosion of a spherical chamber in jelly when PE GEM pressure is applied on a part of outer spherical jelly layer surface. Basing on the result, one may perform tests to study the Rayleigh-Taylor instability at interface of a convergent spherical gaseous bubble.

4. Conclusions

A possibility has been shown for the jelly technique to investigate Rayleigh-Taylor instability growth at the gas-liquid interface in a spherical geometry, both in explosion and implosion. Experimental results have been described to illustrate opportunities for looking at turbulent mixing development at a spherical interface in explosion. The performed calculations have shown the basic possibility to implement the practically symmetrical implosion of a spherical chamber in jelly when PE GEM pressure is applied on a part of outer spherical jelly layer surface. The result effects the possible study of instability taking place at gas-jelly interface during implosion.

Acknowledgement. The study was performed under ISTC Project 029. The authors are thankful to E.A. Sotskov, M.V. Bliznetsov, O.Shapovalova and S.Gerasimov for their assistance in doing the

experiment and making up this paper.

References

[1] Taylor G, The Instability of Liquid Surfaces when Accelerated in a direction perpendicular to their planes. Proc.Roy.Soc., A201, 192, (1950).

[2] Kamchibekov M, Meshkov E, Nevmerzhitsky N, Sotskov E, Turbulent Mixing At The Cylindrical Gas-Liquid Interface, Preprint VNIIEF, 46-96, (1996).

[3] Zababakhin E, Zababakhin I, Unlimited Cumulating Phenomenon (in Russian) M., "Nauka", (1988).

[4] Kamchibekov M, Elementary Estimates of Losses in Compressing Gas with Convergent Shell uder Assymetrics, (in russian) VANT, ser. Teor. i pr. Ph., 3, 28, (1992).

[5] Sakagami H, Nishihara K, Three-Dimensional Rayleigh-Taylor Instability of Spherical Systems, Phys. Rev. Lett., 65, 432, (1990).

[6] Town R, Bell A, The Three Dimensional Non-Linear Evolution of the Rayleigh-Taylor Instability in Inertial Confinement Fusion Targets, Proc. of the 3rd Int. Workshop on the Physics of Compressible Turbulent Mixing, Abbey of Royaumont, France, June 17-19, 467, (1991).

[7] Klein R, Bell J, Pember R, Kelleher T, Three Dimensional Hydrodynamic Calculations with Adaptive Mesh Refinement of the Evolution of Rayleigh - Taylor and Richtmyer - Meshkov Instabilities in Converging Geometry: Multi-Mode Perturbation, Proc. of the 4th Int. Workshop on the Physics of Compressible Turbulent Mixing, 29 March-1 April, Cambridge, England, Ed. by P. Linden, D. Youngs & S. Dalziel, Cambrige Unit. Press, (1993).

[8] Ofer D, Hecht J, Shvarts D, Zinamon Z, Orszag S, McCrory R, Two and Three Dimensional Analysis of Nonlinear Raylegh-Taylor Instability, Proc. of the 4th Int. Workshop on the Physics of Compressible Turbulent Mixing, 29 March-1 April, Cambridge, England, Ed. by P. Linden, D. Youngs & S. Dalziel, Cambrige Unit. Press, (1993).

[9] Voltchenko O, Zhidov I, Klopov I, Meshkov E, Popov V, Rogachev V, Tolshmyakov A, Method of Modeling Non-Stationary Flows of Imcomressible Liquids,(in Russian) A.S. 1026154, (1983).

[10] Andronov V, Zhydov I, Meshkov E, Nevmerzhytski N, Nikiforov V, Razin A, Rogachev V, Tolshmyakov A, Yanilkin Y, Calculating-theoretical and experimental studies for gas-dynamic instabilities and turbulent mixing, An overview of papers performed in VNIIEF, LANL report LA-12896, (1994).

[11] Aphanasieva E, Vinokurov O, Voropinov A, Zmushko V, Pletnev P, Rybachenko P, Saraev V, Sokolova N, Sofronov I, Shamraev B, Codes MIMOZA for Solving 2D-3D Gasdynamic Problems, (in Russian) Proc. on Creating Algorithms and Solving Mathematical Physics Problems, at ed. G. Voskresensky, V. Zabrodin, IPM AN SSSR, 277-281, (1989).

Investigation into Turbulent Mixing Development at the Gas-Gas Interface Driven by a Convergent Cylindrical Shock Wave

E.E. Meshkov, V.V. Nikiforov and A.I. Tolshmyakov
Russian Federal Nuclear Centre - Institute of Experimental Physics
Prospect Mira 37, 607190, Sarov, Nizhny Novgorod Region, Russia

1. Introduction

Experimental data are summarized on the development of turbulent mixing zone (*TMZ*) at the cylindrical gas - gas interface accelerated by a converging shock wave at M = 3 (*in air*). The experiments were done using an electroexplosively driven shock tube. The study addressed *TMZ* development at the air - helium and air - hydrogen interfaces. The difference between the two cases is that their interface accelerations following the shock wave passage have opposite directions (from lighter to heavier gas for the air - helium case and from heavier to lighter one for air - hydrogen). Investigation has been made on the contributions to *TMZ* development by various kinds of small-scale perturbation). The experimental results are compared with calculations by *VIKHR (Vortex)* code.

2. Experimental

A modification of the technique [1] described in [2] was used in the experiments to provide a cylindrical convergent shock wave. The experimental setup is schematically presented in Fig.1. The convergent cylindrical shock wave was produced through electric detonation of 90 nichrome wires of 0.1 mm diameter each (1), arranged on the generatrices of plexiglas half-cylinder (2). The wires had been soldered on to copper bars (3) secured at the half-cylinder's ends (2). The bars had been connected to a capacitor bank through a high-voltage controllable switch K. The capacity was charged up to 32 kV voltage. The energy stored by the bank was about 3 kJ. The switch was spark-gap type, whose operation used pressurized air at 7-8 atm. It was triggered by a high-voltage pulse from the control board that operated the *SFR* camera. The switching circuit had inductance within 1.5 x 10^{-7} *Henry*.
Wire detonations would produce divergent shock waves whose interactions would eventually generate a single convergent shock wave. Areally, this wave was divided into three portions. The one went to the test section channel (20 mm wide) made up by the walls (4). The other two got into the compartments made up by the walls (4), steel half- cylinders (5) and light screens (6) and were ineffective for the flow pattern in the test channel. The walls (4) were tapered at the edge to cause no large perturbations. The test section in assembly included two mated units, the joint between them at the radius of 60 mm. Peak pressure at the convergent shock front at ~50 mm radius was about 12 atm. The front asymmetry was comparatively small. The front shape was disturbed up to ~0.5 mm, and the wave center was displaced against the geometric center of the system by ~2 mm for R=50 mm, the front radius. The film (8) was applied on the cylindrical surface of section (7) and served to separate it from the

More information - Email: otd03_2305@spd.vniief.ru

outer section. Prior to experiment, the central section had been filled with hydrogen (ρ=0.0837 kg/m^3, γ=1.401) at the atmospheric pressure. Hydrogen was loaded by the procedure that made it flow through suitable wall holes in the amount many times higher than the section volume. The outer section contained air (ρ=1.205 kg/m^3, γ=1.407). Densities are cited for atmospheric pressure and temperature 20°C. Instabilities and turbulent mixing growth were visualized by a shadowgraphy system in optical line with *SFR* camera as framing configuration.

3. Conclusion

Fig.2a illustrates streak photos for air-helium interface. Experimentally, initial perturbations are regular and represented by pressure disturbance behind the shock front due to the energy being released in discontinuous manner.

The typical perturbation amplitude and wavelength of the *TMZ* edge would be increasing gradually with time.

Initially, the perturbation wavelength is determined by the number of exploding wires (90 in a semicircle) and equal to $2\pi R/180$. Here, R is the actual radius of the *TMZ* inner edge. At times near the highest helium compression, the perturbation wavelength is typically $\sim 2\pi R/10$. How different local initial perturbations contribute to the turbulent mixing growth behavior is illustrated by streak photos of air-hydrogen experiments (Fig.2 b-d).

Fig.2b shows a streak photo of the experiment where a local perturbation was superimposed on the small-scale wire-induced perturbations. To this effect, a steel cylinder of 0.6 cm diameter was put up as stiff barrier at the radius R = 8.2 cm on the path of the convergent shock wave. The perturbed shock wave can be represented as superposition of the two waves: the primary convergent and the divergent shock wave generating two latitudinal waves that move on in opposite directions from the barrier location. There is an underpressure space between the two latitudinal waves. Where these waves are crossing the primary shock front, the front surface shows a break.

The interface portion included between the latitudinal waves moves with a lead, whereas the portions ahead of these are lagging. At later times, there would be a turbulent zone to develop at this a perturbation. At the time near the highist hydrogen compression, the initial local perturbation would be still memorized as effective. The *TMZ* thickness at this location is larger than in the areas free of perturbations.

Note, that the turbulent mixing zone in air-hydrogen experiments does not occur until the shock wave reflected from the center has reached the interface (t ¡85 μs), which is due to the flow being steady. For t ¿ 85 μs, the interface starts slowing down to become unstable. There should occur the turbulent mixing zone. development.

The experimental streak photo of Fig. 2c illustrates how *TMZ* development is related to the thickness of gas-separating film. This case is where a double film layer was provided at three points of the interface. From the earlier shots, one can notice the interface is slightly behind in these areas. With continuing *TMZ* growth, this perturbation would become not very effective. For the experiment illustrated in Fig.2d, there was no perturbation specified on purpose, but it occurred incidentally due to a secondary local breakdown between the electrodes 2 (Fig.1) following the discharge current pause. This behavior can be described as superposition of the primary convergent shock wave S_0 and divergent perturbation waves (latitudinal shock waves S_1). There is a break observed where the perturbation wave and primary wave fronts are intercrossing. It is these wave intercrossing points the largest perturbation should originate from, and their neighborhood is where small jets of substance would be subsequently generated. The jet tips would move much ahead of the remaining interface portions. These perturbations

should also remain effective with further *TMZ* growth.

Fig.3 presents *R-t* diagrams for shock-wave front and *TMZ* boundaries, that resulted from averaging the data from three identical air-hydrogen experiments. Included in the figure for comparison are *VIKHR* calculations on these experiments [3]. It is obvious from comparing between calculations and experiments, that at times t ¿ 80 μs, i.e. where the acceleration is from lighter to heavier gas, the *TMZ* growth is observed to be more violent in experiments than in calculations.

For streak image processing, the shock front and *TMZ* radii were determined by averaging the measured data over 30-50 rays originating from the center of symmetry. Root-mean-square variation in the radii is due to rough *TMZ* edges and accounts for statistical measurement error.

References

[1] Dannen R, Vilson L, Electrical excitations of converginng shock waves, in book "Electrical explosion of conductors", Mir, M., 172-184, (1964).

[2] Tolshmyakov A, Meshkov E, Perturbations growth at the interface accelerated by converging shock wave; Cylindrical geometry, FGV, 3, 109-113, (1989).

[3] Nikiforov VV, Proc. of the 4th Int. Workshop on the Physics of Compressible Turbulent Mixing, 29 March-1 April, Cambridge, England, Ed. by P. Linden, D. Youngs & S. Dalziel, Cambrige Unit. Press, 478-497,(1993).

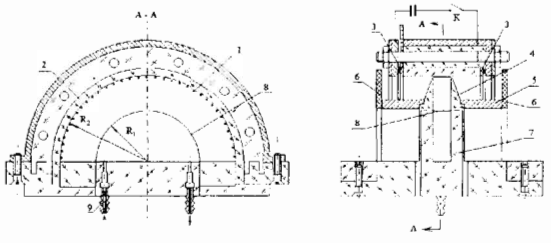

Figure 1. Schematic of the experimental setup for convergent cylindrical shock wave. 1 - exploding wires; 2 - half-cylinder of plexiglas of 100 mm inner diameter; 3 - copper bars; 4 - confinement walls; 5 - steel screen half-cylinders; 6 - light screens; 7 - test section; 8 - thin film; 9 - gas coupling to test section.

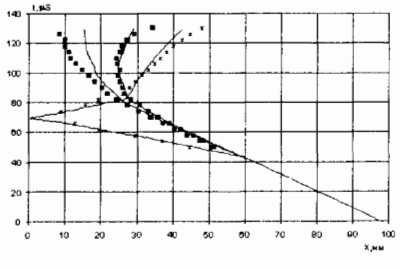

Figure 3. x - SW; □ - TMZ boundary; - - calculation.

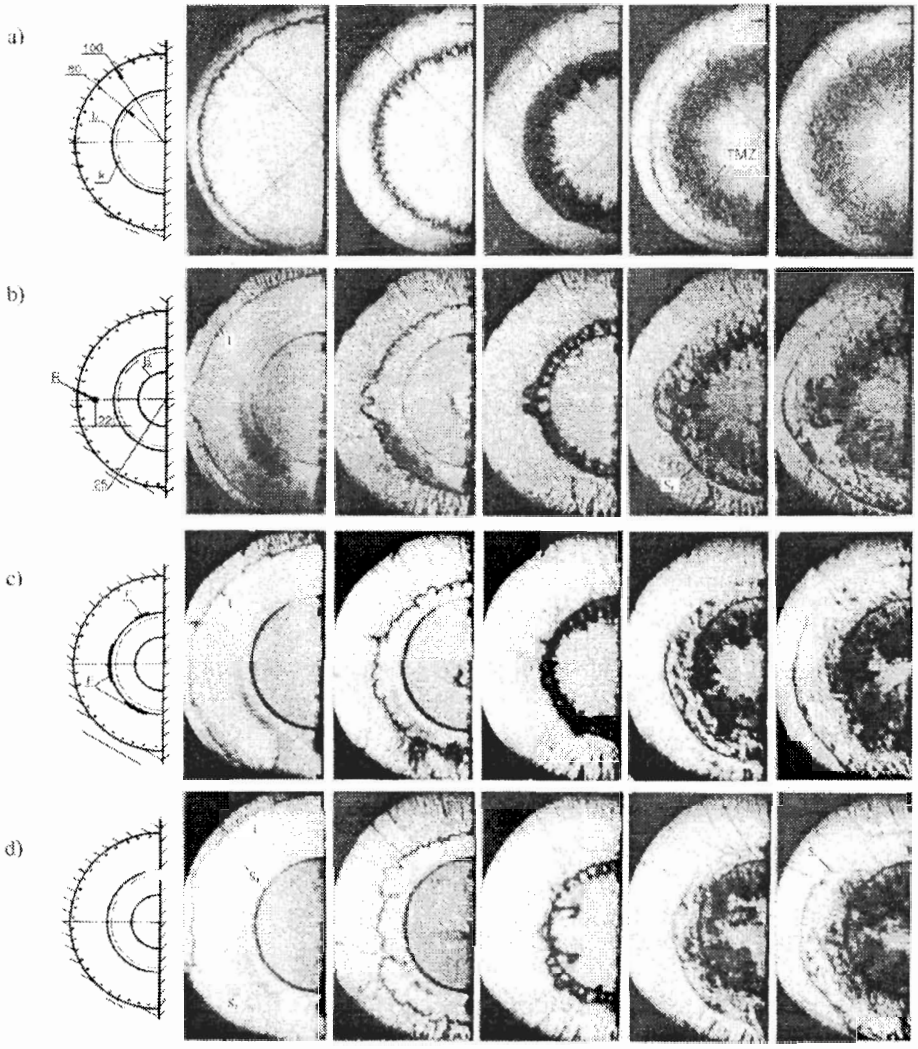

Figure 2. Turbulent mixing zone developing at the cylindrical gas-gas interface a) air-helium, b), c), d) air-hidrogen, accelerated by a convergent shock wave. a) No perturbations specifies; b)perturbation as steel rod 6 mm in diameter on the shock path in air; c) perturbation as local thickening (double film layer); d) shock-wave perturbation unexpectedly. Notation: I_0, I - initial and actual location of the gas-gas interface; k - SFR-camera limit; B - channel units joint; TMZ - turbulent mixing zone; S_0, S_1 - convergent and center-reflected shock waves; S_2 - latitudial wave; F - double film locations in the interface; R - steel rod of 6 mm diameter.

Analytic Approach to Nonlinear Rayleigh-Taylor and Richtmyer-Meshkov Instabilities

K.O. Mikaelian
Lawrence Livermore National Laboratory
P. O. Box 808, L-22, Livermore, California, 94551, USA

Abstract: We present analytic formulas for the evolution of RT and RM instabilities from the linear to the nonlinear regime, and compare our analytic formulas with direct numerical simulations.

1. Introduction

Our starting point is Layzer's theory [1] which we extend to arbitrary initial conditions and solve analytically in 2 and 3 dimensions. Details can be found in [2]. The surface of the fluid is given initially by $y_0(x_0) = \eta_0 \cos(k\, x_0)$ and $\eta_0(r_0) = \eta_0 J_0(\beta_1 r_0/R)$ for 2D and 3D respectively. Except for J_0 which is the Bessel function of order zero, the zero subscript denotes t=0 values; y and x refer to the vertical and horizontal coordinates, and similarly for z and r. Here $k = 2\pi/\lambda$ and $\beta_1 \approx 3.832$, the first zero of the Bessel function of order one.

2. Rayleigh-Taylor

We find the following nonlinear differential equation:

$$\theta(2\theta^3 + 1 - 3\eta_0 k)\ddot{\theta} + (\theta^3 - 1 + 3\eta_0 k)\dot{\theta}^2 - gk\theta^2(\theta^3 - 1 + 3\eta_0 k) = 0\,, \tag{1}$$

$$\theta(\theta^2 + 1 - 2\eta_0\beta_1/R)\ddot{\theta} - (1 - 2\eta_0\beta_1/R)\dot{\theta}^2 - (g\beta_1/R)\theta^2(\theta^2 - 1 + 2\eta_0\beta_1/R) = 0 \tag{2}$$

for 2D and 3D respectively. The function $\theta(t)$ is defined as $\theta = e^{(\eta-\eta_0)k}$ and $\theta = e^{(\eta-\eta_0)\beta_1/R}$ and is related to Layzer's T(t) via $\theta = 1 + (T-1)e^{-\eta_0 k}$ and $\theta = 1 + T - 1)e^{\eta_0\beta_1/R}$ for 2D and 3D respectively. As a check, for $\eta_0 = 0$ we have $\theta = T$ and Eqs. (1a) and (1b) reduce to Layzer's Eqs. (55) and (32) respectively.

Despite their nonlinear nature Eqs. (1, 2) can be integrated to reveal the existence of a conserved quantity which we denote by E. We find

$$\dot{\theta}^2[\theta + (1 - 3\eta_0 k)/2\theta^2] - gk[\theta^3/3 - (1 - 3\eta_0 k)\ln\theta] = E\,, \tag{3}$$

$$\dot{\theta}^2[1 + (1 - 2\eta_0\beta_1/R)\theta^2] - (g\beta_1/R)[\theta^2 - 2(1 - 2\eta_0\beta_1/R)\ln\theta] = E \tag{4}$$

Eqs. (1, 2) follows from conservation of E (dE/dt=0). Being a constant E is determined by the initial data:

$$E/gk = 3(\dot{\eta_0})^2(1 - \eta_0 k)k/2g - 1/3\,, \tag{5}$$

$$ER/g\beta_1 = 2(\dot{\eta_0})^2(1 - \eta_0\beta_1/R)\beta_1/gR - 1. \tag{6}$$

We have achieved our first purpose - how the asymptotic bubble velocity, which we denote by $\dot{\eta_\infty}$, is approached starting from arbitrary initial conditions η_0 and $\dot{\eta_0}$: Using the definitions for

More information - Email: mikaelian1@llnl.gov

θ Eqs.(3, 4) read:

$$\dot{\eta} = (g/3k)^{1/2} \left\{ \frac{e^{3(\eta-\eta_0)k} - 3(1-3\eta_0 k)(\eta-\eta_0)k + 3E/gk}{e^{3(\eta-\eta_0)k} + 1/2 - 3\eta_0 k/2} \right\}^{1/2} , \tag{7}$$

$$\dot{\eta} = (gR/\beta_1)^{1/2} \left\{ \frac{e^{2(\eta-\eta_0)\beta_1/R} - 2(1-2\eta_0\beta_1/R)(\eta-\eta_0)\beta_1/R + ER/g\beta_1}{e^{2(\eta-\eta_0)\beta_1/R} + 1 - 2\eta_0\beta_1/R} \right\}^{1/2} , \tag{8}$$

As η grows $\dot{\eta} \to \dot{\eta_\infty}$ given by

$$\dot{\eta_\infty} = (g/3k)^{1/2} , \tag{9}$$

$$\dot{\eta_\infty} = (gR/\beta_1)^{1/2} . \tag{10}$$

To find $\eta(t)$ for any time t one must integrate Eqs. (7, 8). For the cases when $\eta_0 = 1/3k$ or $R/2\beta_1$ for 2D or 3D flow the equations simplify so much that a completely analytic answer is obtained:

$$\eta k = \eta_0 k + (2/3)\ln\{\cosh[(3gk)^{1/2}t/2] + (\dot{\eta_0}/\dot{\eta_\infty})\sinh[(3gk)^{1/2}t/2]\} , \tag{11}$$

$$\eta\beta_1/R = \eta_0\beta_1/R + \ln\{\cosh[(g\beta_1/R)^{1/2}t] + (\dot{\eta_0}/\dot{\eta_\infty})\sinh[(g\beta_1/R)^{1/2}t]\} , \tag{12}$$

where $\eta_0 k = 1/3$ and $\eta_0\beta_1/R = 1/2$, with asymptotic velocities $\dot{\eta_\infty}$ as defined in Eqs. (9) and (10) for 2D and 3D flow respectively.

3. Richtmyer-Meshkov

Taking t=0 as the shock arrival time and Δv as the jump velocity induced by the shock we let $g \to \Delta v\delta(t)$ in the Bernoulli equations and find $\dot{\eta_0} = \Delta v k\eta_0$ and $\dot{\eta_0} = \Delta v\beta_1\eta_0/R$ for 2D and 3D respectively. After the passage of the shock the evolution equations are the same as in the RT case with g=0. Eqs. (7, 8) can be solved analytically and, for the 2D case, we find

$$\eta k = \eta_0 k + (2/3)\ln(1 + 3\dot{\eta_0} k t/2) , \quad \eta_0 k = 1/3 , \tag{13}$$

$$3Y_0\dot{\eta_0} k t/2 = Y - Y_0 + (b^{1/2}/2)\ln\left\{ \frac{(\{Y - b^{1/2})(Y_0 + b^{1/2})}{(Y + b^{1/2})(Y_0 - b^{1/2})} \right\} , \quad \eta_0 k < 1/3 , \tag{14}$$

$$3Y_0\dot{\eta_0} k t/2 = Y - Y_0 + \sqrt{-b}[\mathrm{atan}(Y_0/\sqrt{-b}) - \mathrm{atan}(Y/\sqrt{-b})] , \quad \eta_0 k > 1/3 . \tag{15}$$

Here $Y_0 = \sqrt{3(1-\eta_0 k)/2}$, $b = (1-3\eta_0 k)/2$, and Y is defined by $Y^2 = \theta^3 + b = e^{3(\eta-\eta_0)k} + 1/2 - 3\dot{\eta_0} k/2$.

For 3D flow we find

$$\eta\beta_1/R = \eta_0\beta_1/R + \ln(1 + \beta_1\dot{\eta_0} t/R) , \quad \eta_0\beta_1/R = 1/2 , \tag{16}$$

$$Y_0\dot{\eta_0}\beta_1 t/R = Y - Y_0 + b^{1/2}\ln\left\{ \frac{\theta(Y_0 + b^{1/2})}{Y + b^{1/2}} \right\} , \quad \eta_0\beta_1/R < 1/2, \tag{17}$$

$$Y_0\dot{\eta_0}\beta_1 t/R = Y - Y_0 + \sqrt{-b}[\mathrm{acos}(\sqrt{-b}) - \mathrm{acos}(\sqrt{-b}/\theta)] , \quad \eta_0\beta_1/R > 1/2 . \tag{18}$$

Here $Y_0 = \sqrt{2(1-\eta_0\beta_1/R)}$, $b = 1 - 2\eta_0\beta_1/R$, and Y is defined by $Y^2 = \theta^2 + b = e^{2(\eta-\eta_0)\beta_1/R} + 1 - 2\eta_0\beta_1/R$. The asymptotic velocities can be obtained directly from Eqs. (3, 4):

$$\dot{\eta_\infty} = 2/3kt , \tag{19}$$

$$\dot{\eta_\infty} = R/\beta_1 t , \tag{20}$$

for 2D and 3D respectively, and are independent of η_0 and $\dot{\eta_0}$.

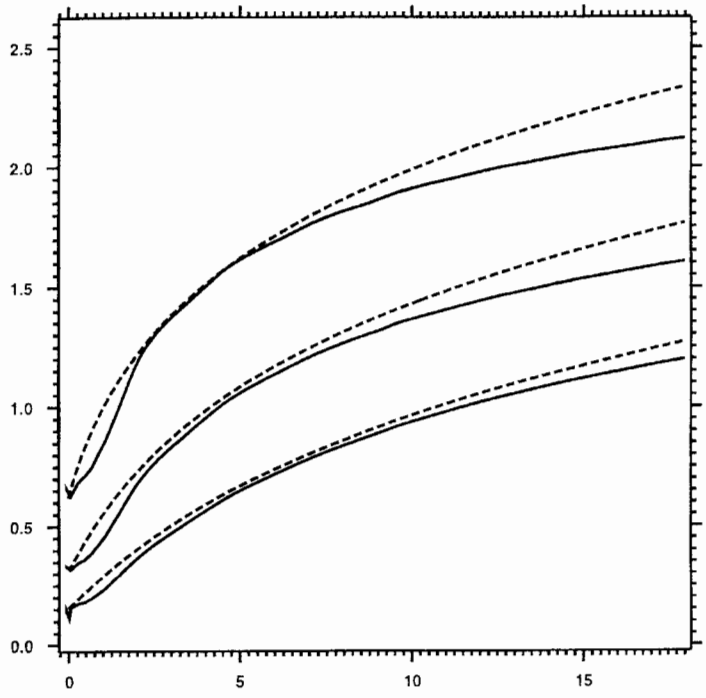

Figure 1. ηk as a function of Δvk$t$ for η_0k = 1/6, 1/3, and 2/3. The continuous curves are from direct numerical simulations with η_0 = 0.35, 0.70, and 1.40 cm, k=$2\pi/13$ cm^{-1}. A Mach 1.2 shock travelling at $W_i \approx 121$ cm/ms in Helium strikes a He/Xe interface (an example is shown in Fig. 2) giving $\Delta v \approx 8.25$ cm/ms. The dashed curves are from Eqs. (13)-(15).

4. Discussion

Comparing 2D and 3D geometries we find $\dot{\eta_\infty}(3D)/\dot{\eta_\infty}(2D) = (3kR/\beta_1)^{1/2}$ and $3kR/2\beta_1$ for RT and RM respectively. If we identify kR with π we get $\sqrt{3\pi/\beta_1} \approx 1.6$ and $3\pi/2\beta_1 \approx 1.2$ respectively. If we identify kR with β_1 we get $\sqrt{3} \approx 1.7$ and 1.5 respectively. The first identification, adopted by Layzer, is perhaps more physical (the radius of the tube is half the distance between the parallel walls), while the second identification yields equal initial growth rates. In either case the ratio is larger for RT than for RM.

Eqs. (13)-(15) are plotted in Fig. 1 for η_0k = 1/6, 1/3, and 2/3. Eq. (13) is an equally good representation for all three curves, differing by no more than 10% from the exact results. Note that Eq. (13) implies

$$\dot{\eta}(t) = \frac{\dot{\eta_0}}{1 + 3\dot{\eta_0} k t/2} \tag{21}$$

which automatically gives the correct $\dot{\eta_0}$ and $\dot{\eta_\infty}(= 2/3kt)$. For each value of k we also plot the results of direct numerical simulations with the fully compressible hydrocode CALE. We chose perturbations of λ = 13 cm and η_0 = 0.35, 0.7, and 1.4 cm at the interface between Helium (ρ = 0.17mg/cm^3, γ=5/3) and Xenon (ρ=5.4 mg/cm^3, γ=5/3) which have an Atwood

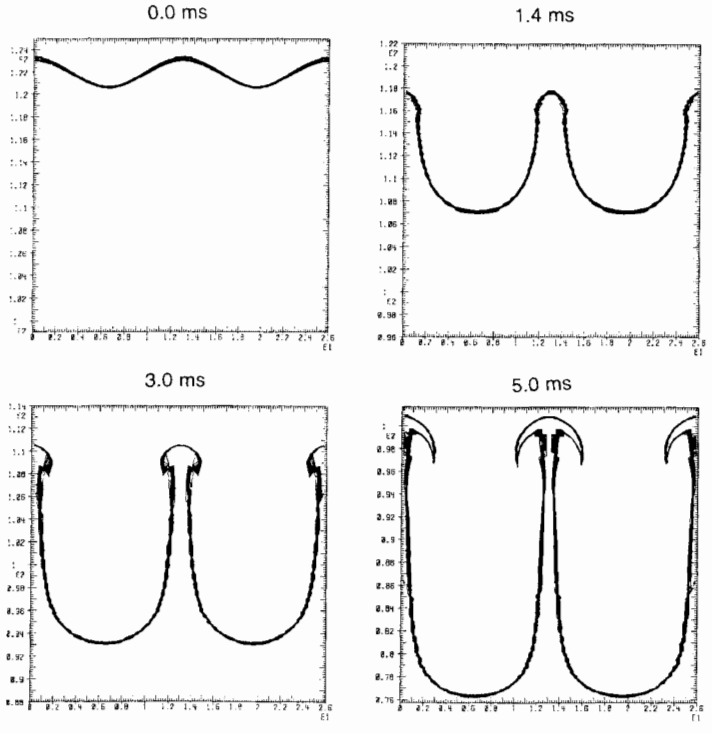

Figure 2. Isodensity contours from a Mach 1.2 He/Xe simulation with perturbations of $\eta_0 = 1.40$ cm and $\lambda = 13$ cm.

number of 0.94. A Mach 1.2 shock directed from He to Xe induces a $\Delta v \approx 8.25$ cm/ms. These parameters were chosen from CalTech's 17 inch shock tube with a 122 cm long test section.

Fig. 1 shows good agreement between Eqs. (13) through (15) and the direct numerical simulations. Snapshots of the large-amplitude run, η_0=1.4 cm, are shown in Fig. 2. Many features of the interface, particularly the mushrooming spikes, are beyond the scope of Layzer's theory. What we have shown is that his theory, generalized to $\eta_0 \neq 0$ and applied to the RM instability, can be solved analytically and captures well the motion of the bubble vertex from the linear to the nonlinear regime.

Acknowledgement. The author would like to thank P. Miller for help with the formatting of this paper.
This work was performed under the auspices of the U.S. Department of Energy by the Lawrence Livermore National Laboratory under Contract No. W-7405-ENG-48.

References

[1] Layzer D, Astrophys. J., 122, 1, (1955).
[2] Mikaelian KO, UCRL-JC-125113, (1996).

2D Navier-Stokes Simulations of Richtmyer-Meshkov Instability in Shock Tube

C. Mügler and S. Gauthier
CEA/Centre de Limeil-Valenton
94195 Villeneuve-Saint-Georges Cedex, France

Abstract: 2-D numerical simulations of the fluid instability of shock-accelerated interfaces between a light fluid and an heavy one are compared with experimental measurements. Numerical and experimental amplitude growth rates are in good agreement. In the experiments performed at C.E.A./Vaujours, the laser Doppler anemometry technique gives measurements of the fluctuating velocity. In these experiments, turbulent boundary layers strongly perturb the basic flow. This behaviour has been reproduced by two-dimensional simulations which take the turbulent boundary layers into account.

1. Introduction

When two different fluids are impulsively accelerated into each other by a shock wave, small perturbations at the interface grow first linearly and then evolve into nonlinear structures having the form of "bubbles" and "spikes". This instability was theoretically discovered and described by Richtmyer [1], and confirmed experimentally by Meshkov [2]. This phenomenon, known as the Richtmyer-Meshkov (RM) instability is a typical mechanism for turbulent mixing of layered fluids. It is closely related to Rayleigh-Taylor (RT) instability [3], which is the instability of a planar interface undergoing constant acceleration, such as caused by the suspension of a heavy fluid over a lighter one in the earth's gravitational field. RT and RM instabilities are of critical importance to inertial confinement fusion.

RM instability is often studied in shock tubes, where measurements are easier to carry out than in small pellets [4, 5, 6].

A number of numerical studies have been performed on the RM instability [7, 8, 9]. The initial growth rate of the perturbation (that is between the first and second shocks across the interface) was predicted in the two-dimensional calculations to be approximately a factor of two too large, as compared with the experimental results. More recently, front-tracking numerical simulations produced growth rates in much closer agreement to the experimental values [10]. In this paper, we present numerical simulations of single-mode and multimode Richtmyer-Meshkov instabilities. In first, we briefly describe the code used. Afterwards, numerical simulations are compared with experimental measurements in the linear and turbulent regimes.

2. Motivation and description of the numerical choices

In order to carry out two-dimensional simulations of compressible mixing, as those occuring in shock tubes, we have developed the code CADMEE [11]. This code, derived from the code CFDLIB [12], takes all molecular transport effects into account: it solves the 2D unsteady Navier-Stokes equations and mixing is described by a concentration governed by an advection-diffusion equation. A Godunov method is used to accurately describe strong discontinuities

More information - Email: gauthier@limeil.cea.fr

such as shock waves. The computation is performed in two phases: a lagrangian phase and a remapping phase in which conservative variables are transfered from the lagrangian mesh to an arbitrary specified mesh. This approach is the so-called Arbitrary Lagrangian-Eulerian (ALE) formulation. As the accuracy of the numerical method is very important, second order differencing techniques in space and time are used. A turbulent algebraic model, the Baldwin-Lomax model, has been implemented in order to modelize turbulent boundary layers which usually develop along shock tube walls.
This code has been validated against numerous configurations of compressible viscous flows [11].

3. Richtmyer-Meshkov instability with a single-mode interface

The present study uses the experimental conditions of Zaytsev *et al.* [13], performed in a $72 \times 72\,mm^2$ square cross section shock tube. In these experiments, a very thin membrane separates two inert gases, a light one (Krypton) and an heavy one (Xenon) and provides a known two-dimensional (2D) sinusoidal initial interface perturbation. The experimental images show well-resolved flow patterns. A detailed description of the set-up can be found in [13].
In these experiments, the initial perturbation at the Kr/Xe interface is well defined: its wavelength is equal to $36\,mm$ and its amplitude a_0^- is equal to $5\,mm$. The pressure ahead of the shock is $5.0 \times 10^4\,Pa$. The Kr/Xe interface is accelerated by a strong shock of Mach number 3.5 moving from Kr to Xe, i.e. from the light gas to the heavy one. To observe the evolution of the instability on a sufficiently long time, three experimental shots have been necessary. The Mach number is not exactly the same for the three experiments but does not differ too much from 3.5. The instant $t = 0$ corresponds to the moment the shock strikes the interface.
In numerical simulations, the region where the instability develops is covered with $0.1875 \times 0.18\,mm^2$ zones.

Experimental schlieren pictures and numerical concentration isovalues of the RM instability at the times $t = 0$ and $t = 464\,\mu s$ are presented in Figure 1. As the incident shock wave

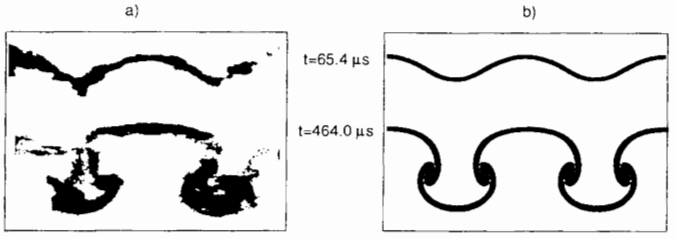

Figure 1. Experimental schlieren pictures and numerical patterns of the mixing zone at $t = 0$ and $t = 464\,\mu s$.

travels from the light gas to the heavy one, there is no inversion of concavity after the shock passage. The dimensionless initial perturbation amplitude $a_0^- k$ is equal to 0.87. As a result, the perturbation rapidly evolves into nonlinear structures called "bubbles" and "spikes": the heavy fluid penetrates into the light fluid. As the Atwood number is small ($A = 0.22$ and $A = 0.184$ before and after the passage of the incident shock wave) the difference of structure between bubbles and spikes is not important and the Kelvin-Helmholtz instability is well developed. In the above, the Atwood number is defined as $(\rho_2 - \rho_1)/(\rho_2 + \rho_1)$ where ρ_1 is the density of the

first shocked fluid. As one can see in Fig.1, the visual agreement between the data and the simulation is good.

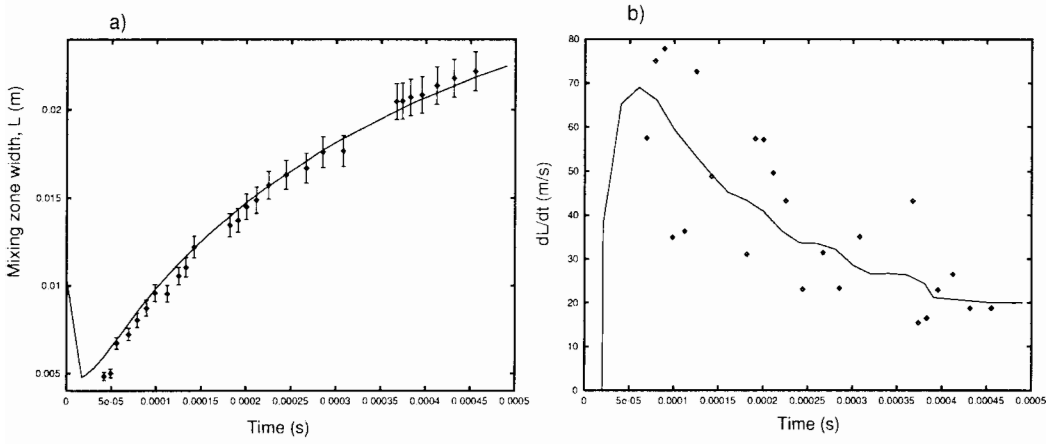

Figure 2. Evolution of the mixing zone width and mixing zone growth rate versus time. Plots correspond to experimental results. The errorbars are equal to 10%. Full lines correspond to numerical results obtained from code CADMEE.

From schlieren pictures, the interface and refracted shock locations and the perturbation amplitude are measured at various times. In order to compare experiments with calculations on a quantitative way, we have plotted the mixing zone width versus time (see Fig.2.(a)). The numerical width is defined as the largest distance between the isovalues of the concentration $c = 5\%$ and $c = 95\%$. The errorbars of the experimental results are equal to 10%. As one can see, the mixing zone width in the simulation is approximately the same as in the experimental pictures. We also plotted in Figure 2.(b) the amplitude growth rate of the perturbation as obtained from experiments and numerical simulations. Here again, numerical simulation results are in agreement with experimental results even in the nonlinear regime.

4. Richtmyer-Meshkov instability with a multimode interface

In the experiments performed in the $80 \times 80\,mm^2$ shock tube at C.E.A./Vaujours [14], a multimode interface is accelerated by a shock wave moving from SF6 to air. The Mach number of the incident shock wave ranges between 1.445 and 1.455. The discontinuous interface is made of a plastic membrane $0.3\,\mu m$ thick, which is placed directly below a thin wire mesh (wire spacing and diameter: $1.01\,mm$ and $0.08\,mm$). The membrane is broken into small pieces by the passing incident shock wave through the grid. A schlieren visualization allows us to measure the time-dependent location and thickness of the mixing zone.

In numerical simulations, the initial perturbation of the interface is multimode and composed of eight wavelengths λ with $0.5\,mm \leq \lambda \leq 2.5\,mm$. All amplitudes are equal to $0.2\,mm$. The initial shock Mach number is equal to 1.453. The eulerian formulation of the code CADMEE is used. As a consequence, the grid is fixed. The region where the instability initially develops is covered with $0.05 \times 0.08\,mm^2$ zones. At last time, the mixing zone moves in a region covered with $0.7 \times 0.08\,mm^2$ zones.

Figure 3 displays the evolution versus time of the experimental and numerical mixing zone widths. The experimental width is measured from optical pictures and the numerical one is defined from numerical density profiles in the mixing zone. In Fig.3, compressions due to the interaction of the reflected shock waves with the mixing zone clearly appear. Before the first reflected shock/mixing zone interaction, microdensitometry of schlieren photographs (crosses in Fig.3) gives mixing zone width greater than direct measurement from optical pictures. Numerical simulation results are between these two experimental results. After the first interaction and before the second one, experimental and numerical widths are very similar.

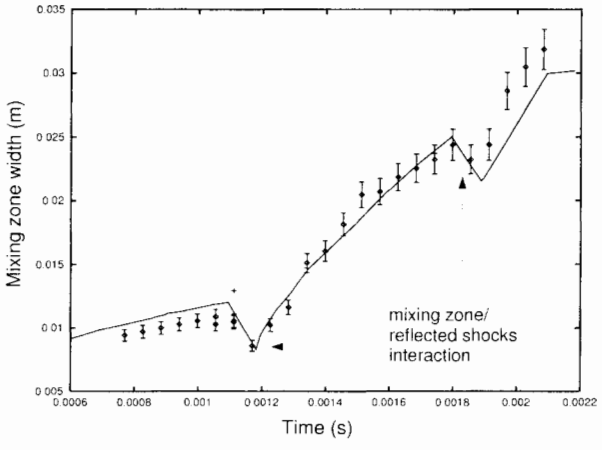

Figure 3. Evolution of the mixing zone width versus time. Plots correspond to experimental results. The errorbars are equal to 10%. Crosses correspond to microdensitometry of schlieren photographs. Full line corresponds to numerical simulation with code CADMEE.

Another diagnostic, the Laser Doppler Anemometry (LDA), gives measurements of the fluctuating flow velocity. This quantitative experimental measurement may be directly compared with results of numerical simulations. In the experiments [14], the position of the LDA probe is successively at $125.5\,mm$, $161\,mm$ and $178.5\,mm$ downstream the initial interface abscissa. Here, we will only consider the first location at $125.5\,mm$, in order to study boundary layer effects. Figure 4 shows velocity measurements at this abscissa. The instant $t = 0$ corresponds the moment the shock arrives at the probe. In Fig.4, the first velocity plateau at $131\,m/s$ firstly corresponds to air accelerated by the incident shock (for $t \leq 0.6\,ms$) and afterwards to SF6. The second plateau at $57\,m/s$ corresponds to SF6 decelerated by the first reflected shock on the end wall. This second plateau ends with the arrival of the second reflected shock wave.

Two simulations of this experiment have been performed. They principally differ by the boundary conditions used. In the first simulation, the four shock tube walls are considered as reflective walls and the SF6/air interface is planar. In the second simulation, no slip and isotherm ($T_w = 293\,K$) boundary conditions are assumed and turbulent boundary layers are modelled by using the Baldwin-Lomax model. Furthermore, the interface is multimode. As one can see in Fig.4, one effect of the turbulent boundary layers is to accelerate the SF6. The first simulation, whose results in pure gases are similar to the Rankine-Hugoniot solutions, gives a theoretical mean velocity of $47\,m/s$ in the second plateau, while experimental measurements give a value of $57\,m/s$. When two turbulent boundary layers are simulated, the mean velocity

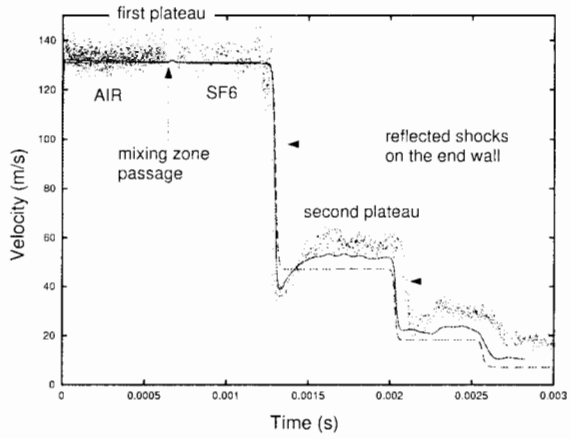

Figure 4. Velocity measurements at $125\,mm$. Dots correspond to experimental results. Full and dashed lines correspond to numerical simulations respectively with and without turbulent boundary layers.

equals $52\,m/s$. By simulating with a 3D code the four turbulent boundary layers which develop in the shock tube, we should find the experimental value.

Another effect of the turbulent boundary layers is the undershoot of the velocity just after

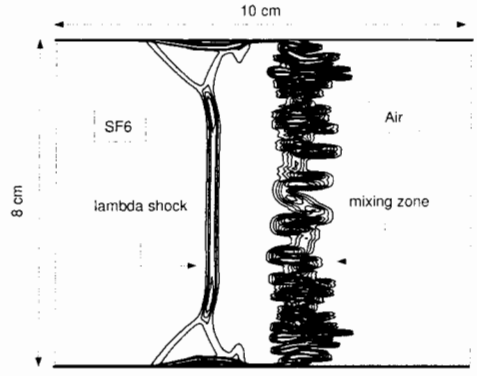

Figure 5. Numerical schlieren picture at a time t just after the first reflected shock wave/mixing zone interaction. Because of its interaction with the boundary layer, the transmitted shock in the SF6 bifurcates.

the passage of the first reflected shock. As this shock interacts with the mixing zone, a 0.42 Mach number shock is transmitted in the SF6. Because of its interaction with the boundary layer in the SF6 and according to the hydrodynamical conditions (Mach number and adiabatic coefficient values), this transmitted shock bifurcates. In Fig.5, one clearly sees the lambda shock structure. The bifurcation height increases as the shock moves in the SF6. Other simulations of the interaction of a shock wave with side wall boundaries in a shock tube have already been carried out. Good agreement between numerical results and experimental measurements

available in the literature has been observed [11].

We also calculated velocity versus time at $161\,mm$ and $178.5\,mm$ downstream the initial interface abscissa. Experimental LDA measurements clearly show the turbulent stage of the mixing zone at these abscissas. Unfortunatly, these 2D numerical simulations did not allow us to observe turbulent fluctuating velocity. It is probably due to the restriction to the bidimensional geometry.

5. Conclusion

2-D numerical simulation of the fluid instability of a shock-accelerated single-mode interface between a light fluid and an heavy one shows flow pattern very similar to experimental pictures. Furthermore, numerical and experimental amplitude growth rates are in good agreement and are decaying in time in a similar way. On one hand, this comparison shows that when the experimental initial conditions (amplitude and wavenumber of the 2-D perturbation) are well known, it is possible to simulate it accurately. On the other hand, this result allows to conclude that front tracking is not necessary to obtain good agreement with experiments. Indeed, in the code used, mixing is described by a concentration. These conclusions are still valid for multimode RM experiments performed in a $80 \times 80\,mm^2$ square cross section shock tube. Numerical simulations of these experiments also show the influence of turbulent boundary layers on mean flow velocity measured in the middle of the tube. Turbulent boundary layers confine the flow and accelerate it. In 3-D simulations, these effects could be compared with experiments on a quantitative way. Furthermore, 3-D simulations should permit to observe turbulent fluctuating velocity.

References

[1] Richtmyer RD, Comm. Pure Appl. Math., 13, 297, (1960).
[2] Meshkov EE, Izv. Acad. Sci. USSR Fluid Dyn., 4, 101, (1969).
[3] Taylor GI, Proc. Soc. London, 201, 192, (1950).
[4] Galametz I, Delouis G, Thorembey MH, Rayer C, Rodriguez G and Haas JF, Proc. of the 5th Int. Workshop on the Physics of Compressible Turbulent Mixing, Stony Brook, NY, edited by R. Young, J. Glimm and B. Boston, (1996).
[5] Jourdan G, Houas L and Billiotte M, Phys. Rev Lett., 78, 452, (1997).
[6] Bonazza R, Sturtevant B, Phys. Fluids, 8, 9, 2496, (1996).
[7] Meyer KA and Blewett PJ, Phys. Fluids, 15, 753, (1972).
[8] Cloutman LD, Wehner MF, Phys. Fluids A, 4, 8, 1821, (1992).
[9] Baltrusaitis RM, Gittings ML, Weaver RP, Benjamin RF and Budzinski JM, Phys. Fluids, 8, 9, 2471, (1996).
[10] Grove JW, Holmes R, Sharp DH, Yang Y, Zhang Q, Phys. Rev. Lett., 71, 3473, (1993).
[11] Mügler C, Gauthier S, Hallo L, Aubert S, AIAA Paper, 96-2068, New Orleans, (1996).
[12] Addesio FL, Baumgardner JR, Dukowicz JK, Johnson NL, Kashiva BA, Rauenzhan RM, Zemach C, Los Alamos Report, LA-10613-MS, (1990).
[13] Zaytsev S, Aleshin A, Lazareva E, Titov S, Chebotareva E, Rozanov V, Lebo I, Demchenko V, Proc. of the 3rd Int. Workshop on the Physics of Compressible Turbulent Mixing, Royaumont, France, the experimental study of a two-dimensional RMI has to be published, (1991).
[14] Poggi F, communication in this workshop and Poggi F, Thorembey MH, Rodriguez G and Haas JF, IUTAM Symp. on Variable Density Low Speed Turbulent Flows, Marseille, (1996).

Turbulent Mixing of Two Fluids Moving in Gravitational Field

V.E. Neuvazhayev
Institute of Technical Physics
456770, P.O.245, Snezhinsk, Chelyabinsk region, Russia

Abstract: Two fluids of different density move in gravitation field with different velocities relatively one another. Reynolds number is large enough, therefore the interface collapses and turbulent mixing takes place. Analytical formula was derived for width of mixing zone depending on distance and initial parameters of a problem. Comparison with known experiments of G.L. Brown and A. Rozhko [2] and O.V. Yakovlevsky [1]. In these experiments the influence of gravity acceleration can be neglected. The consent of the theory with experiments is received not always, as well as the consent of experiments among themselves.

1. Introduction

The work is dedicated to theoretical study of turbulent mixing resulting from combined influence of shear and gravitational (convective) instabilities (Fig.1). The theory is based on semiempirical model using equation of balance for kinetic energy of turbulence. Source giving birth to turbulent mixing is specified through increment obtained as a result of studying resistance to small perturbations of initial flow. Separately the both phenomena have been studied

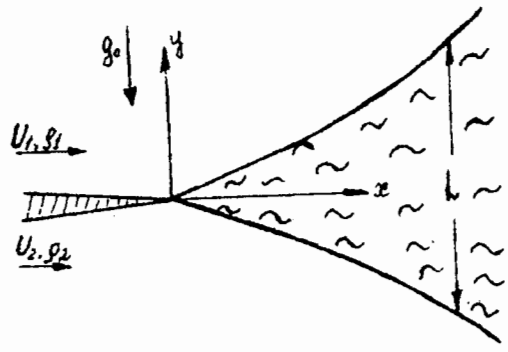

Figure 1.

in detail. In the simplest case when there are two incompressible flows moving along axis x with different velocities U_1 and U_2 the interface between these flows is gets turbulent, and the mixing zone width increase linearly according to the law

$$L = \alpha_u A_u x, \tag{1}$$

where x - is a distance from point $x = 0$ in which the flows adjoin, α_u is some constant determined from experiment, $A_u = \frac{U_1 - U_2}{U_1 + U_2}$. If two incompressible liquids are in gravitational

More information - Email: nio3@eco.ch70.chel.su

field g_0 in unstable position, when the heavy liquid ρ_1 is above the light one, then the interface is destroyed and subsequently evolves according to quadratic law:

$$L = \alpha_g A g_o \left(\frac{x}{U_o}\right)^2, \tag{2}$$

where $= \alpha_g$ is some constant determined from experiment; $A = \frac{\rho_1 - \rho_2}{\rho_1 + \rho_2}$ is Atwood number, $U_o = \frac{\rho_1 U_1 + \rho_2 U_2}{\rho_1 + \rho_2}$, $x = U_o t$.

The laws (1) and (2) can be obtained from general deliberations proceeding from analysis of dimensional constants which leads to establishment of the fact that the both motions if considered separately are of self-similar nature. Here a general case is considered when two flows with different densities are moving with respect to each other in gravitational field g_0 perpendicular to their interface.

In the paper a formula for general case of flows moving in gravitational field is obtained. It is constructed for the case when there is initial non-zero roughness L_0:

$$L = L_o + \alpha_g g_o A \left(\frac{x}{U_o}\right)^2 + \frac{x}{U_o}\sqrt{4\alpha_g g_o A L_o + \alpha_u^2 (1 - A^2)\frac{(U_1 - U_2)^2}{4}}. \tag{3}$$

The formula presentation (3) obtained leads to the law of evolution of shear mixing of flows with different densities. In a particular case of zero acceleration the formula (3) has the form:

$$L = L_o + \alpha_u \sqrt{1 - A^2}\ \frac{A_u}{1 + A A_u} x \tag{4}$$

This case was investigated in experiments by O.V.Yakovlevsky [1] and A.Roshko [2]. The theoretical dependence obtained agrees well with experimental results at $A < 0$ where results by different authors agree. Unfortunately, at $A > 0$ the experimental results disagree. Therefore, additional experimentation is needed to verify validity of formula (4).

2. Conditions of instability and balance equation for kinetic energy of turbulence

Instability conditions are known in the case under study increment ω, characterizing evolution of small perturbations in time is

$$\omega = k U_o \pm \sqrt{g_o A k - \frac{(1 - A^2) A_u^2}{(1 + A A_u)^2} k^2 U_o^2}. \tag{5}$$

Balance equation for kinetic energy of turbulence is taken in the form proposed by Prandtle and Kolmogorov:

$$\frac{\partial \overline{\rho} V_t^2}{2\partial t} + \frac{\partial(\overline{\rho}\tilde{u}_k V_t^2)}{\partial x_k} = \frac{\overline{\acute{u}_k \acute{\rho}_k}}{\overline{\rho}} \frac{\partial \overline{P}}{\partial x_k} - \overline{\rho \acute{u}_k \acute{u}_i} \frac{\partial \tilde{u}_k}{\partial x_i} - \overline{\acute{u}_k \frac{\partial \acute{P}}{\partial x_k}}, \tag{6}$$

$$V_t^2 = \overline{\acute{u}_k \acute{u}_i}, \tag{7}$$

$$\tilde{u}_k = \overline{u}_k + \frac{\overline{\acute{\rho}\acute{u}_k}}{\overline{\rho}}, \tag{8}$$

$u_k = \bar{u}_k + \acute{u}_k, \quad \rho = \bar{\rho} + \acute{\rho}$. The balance equation is supplemented by averaged equations of hydrodynamics. Closute conditions are determined according to Prandle hypothesis:

$$\overline{\acute{u}_k \acute{\rho}} = -D \frac{\partial \bar{\rho}}{\partial x_k}, \tag{9}$$

$$\overline{\acute{u}_k \acute{E}} = -D \frac{\partial \tilde{E}}{\partial x_k}, \tag{10}$$

$$\overline{\acute{u}_k \acute{u}_i} = \frac{1}{3} V_t^2 \delta_{ki} - D_u \left[\left(\frac{\partial \tilde{u}_k}{\partial x_i} + \frac{\partial \tilde{u}_i}{\partial x_k} \right) + \frac{2}{3} \frac{d \ln \bar{\rho}}{dt} \delta_{ki} \right] \tag{11}$$

where $D = lV_t$ and $D_u = l_u V_t$ - are coefficients of turbulent diffusion and velocity, respectively, $l = \alpha L, \quad l_u = \alpha_u L$. For incompressible liquids the final system of equations has the form:

$$\frac{\partial}{\partial x} \rho u + \frac{\partial}{\partial y} \rho V = 0, \tag{12}$$

$$u \frac{\partial \ln \rho}{\partial x} + V \frac{\partial \ln \rho}{\partial y} = \frac{\partial}{\partial y} \left(D \frac{\partial \ln \rho}{\partial y} \right), \tag{13}$$

$$u \frac{\partial u}{\partial x} + V \frac{\partial u}{\partial y} = \frac{1}{\rho} \frac{\partial}{\partial y} \left(D_y \rho \frac{\partial u}{\partial y} \right), \tag{14}$$

$$\frac{u}{2} \frac{\partial}{\partial x} \left(\rho V_t^2 \right) + \frac{V}{2} \frac{\partial (\rho V_t^2)}{\partial y} = \underline{D \frac{\partial P}{\partial y} g + \rho D_u \left(\frac{\partial u}{\partial y} \right)^2} - \frac{\nu V_t^2 \rho}{l} + \text{diffusion and additional terms},$$

ν is a new empirical constant. Hereinafter the averaging simbol is dropped. In turbulent mixing theory the underlined terms in the right part of balance equation play a decisive role as source terms. Their value is specified using:

$$\frac{u}{2} \frac{\partial (\rho V_t^2)}{\partial x} + \frac{V}{2} \frac{\partial (\rho V_t^2)}{\partial y} = \rho D [Im \omega] - \frac{\nu V_t^2 \rho}{l} + \ldots. \tag{15}$$

3. Approximate integration

Assume that turbulent velocity in direction x does not depend on y: $\frac{\partial V_t}{\partial y} = 0$. Then for coefficients: $D = D(x)$; $D_u = D_u(x)$. Making another assumptions obtain finally two equations:

$$\frac{dL}{dx} = 8 \eta_1^2 \frac{\alpha}{U_o} V_t, \tag{16}$$

$$\frac{dV_t^2}{dL} = \frac{g_o A}{2 \eta_1^2} + B_o (1 - A^2) \frac{(U_1 - U_2)^2}{L} - \left[1 + \frac{\nu}{4 \eta_1^2 \alpha^2} \right] \frac{V_t^2}{L}, \tag{17}$$

$\eta_1^2 = \frac{4}{\pi}$. Solution of equations (16), (17) is

$$V_t^2 = V_t^2(0) + \frac{g_o A L}{2 \eta_1^2 (2 + \frac{\nu}{4 \eta_1^2 \alpha^2})}. \tag{18}$$

If initial data lie on the straight line, then the general solution will be relationship (3).

4. Comparison with experiments $g = 0$

In [2] and [1] the effect of flow different densities on mixing intensity determined by derivative $\frac{dL}{dx}$ was studied. In [2] flows of nitrogen, helium, and air were considered for different velocities and for different combinations. Three cases were provided: $1)\rho_1 = \rho_2 (A = 0)$; $A_u = 0.75$; $2)\rho_1/\rho_2 = 7$; $(A = 0.75)$; $A_u = 0.75$; $3)\rho_1/\rho_2 = 1/7$; $(A = 0.75)$; $A_u = 0.75$. The experiments of O.V.Yakovlevsky [1] were carried out for Atwood numbers $A = -0.18$; 0; 0.515 and for different A_u within the range $0.25 < A_u < 1$. It was found that at $A < 0$ mixing is more intensive than at $A = 0$ (identical densities) and at $A > 0$ it is less intensive. Experimental results are presented in Fig 2. and Fig.3. It is seen that agreement with the experiments takes

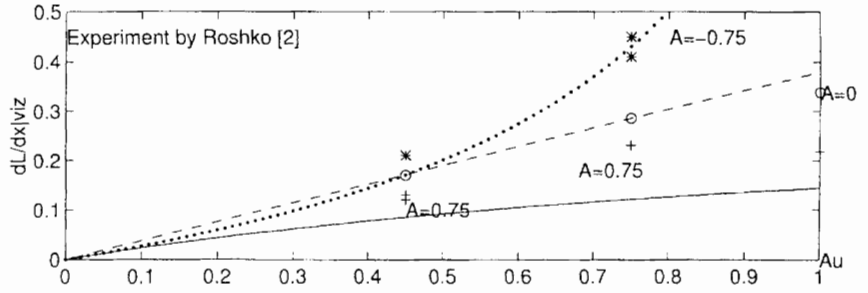

Figure 2. Dependence of jet inclination $\left.\frac{dL}{dx}\right|_{viz}$ on A_u for various Atwood numbers A, $g_0 = 0$ experiments from [2], $\odot$ for $A = 0$; $+$ for $A = 0.75$; $*$ for $A = -0.75$; - - - for $A = -0.75$; — formula (4) for $A = 0.75$.

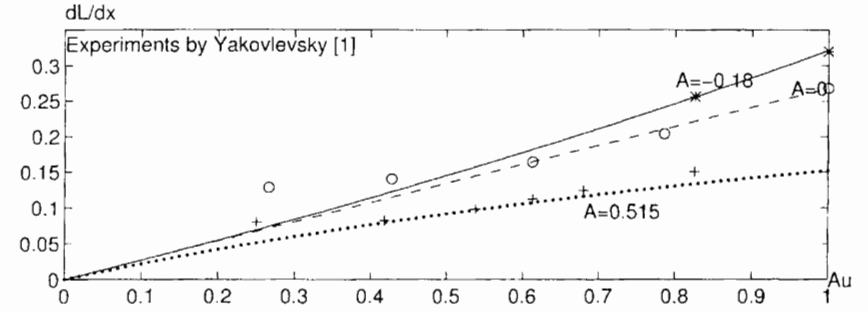

Figure 3. Dependence of jet inclination $\frac{dL}{dx}$ on A_u for various Atwood numbers A. $g_0 = 0$; experiments from [1], $\odot$ for $A = 0$; $*$ for $A = -0.18$; $+$ for $A = 0.515$; - - - formula (4) for $A = -0.18$; $\cdots$ formula (4) for $A = 0.515$.

place when intensity increases, i.e. at $A < 0$. Let us consider the analytical dependence determined by formula (4). Unlike known dependencies ([1], [2]), the key feature of the dependence proposed is that maximum width of a jet (at fixed $A_u > 0$) is achieved at certain negative value

of Atwood number which is equal to $A_m = -\frac{A_u}{\sqrt{1+\frac{A_u^2}{3}}}$. Here $\frac{dL}{dx}(A_m)$:

$$\frac{dL}{dx}\Big|_{max} = \alpha_u \frac{A_u}{\sqrt{1-\frac{2}{3}A_u^2}}.$$

This feature seems to be natural. In extreme cases, when Atwood number $A = \pm 1$, i.e. incompressible fluid moves in parallel with a fluid of null density, flow is stable according to formula (5). Therefore, there are no turbulent mixing and mixing intensity $\frac{dL}{dx}$ is equal to zero. This follows from formula (4). Unfortunately, the theoretical inference on existence of maximum inclination was not verified experimentally because of lack of sufficient information.

Fig. 2 and 3 illustrate the comparison between theory and experiments. Fig 2 presents the experiments from [2] and Fig.3 - those from [1]. The experiments of O.V.Yakovlevsky [1] well agree with theory. As to the experiments of Roshko [2], one can say about the agreement only in the region where $A \leq 0$. When $A = 0.75$, there is a significant discrepancy which remains non clear. Maybe, in the experiments [2] the influence of the initial conditions took place (initial turbulence, initial roughness, etc.) resulted in overestimated inclination of turbulent mixing. One more note should be made. If in (4) we turn from x to $\bar{x}$:

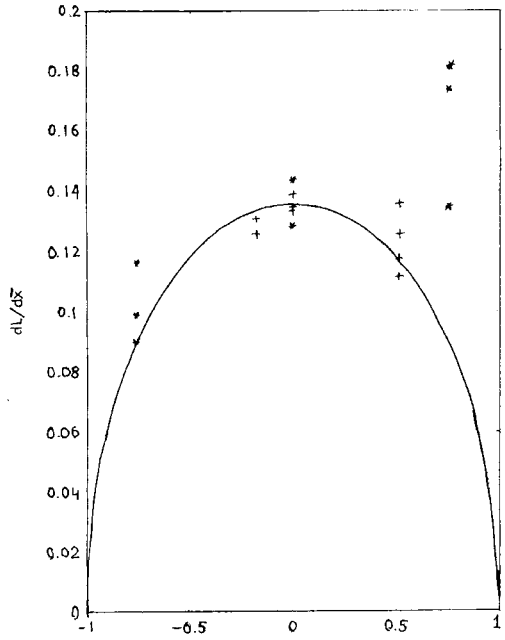

Figure 4. Dependence of jet inclination $\frac{dL}{d\bar{x}}$ on Atwood number A; $*$ Roshko's experiments [2]; $+$ Yakovlevsky's experiments [1]; — formula (20).

$$\bar{x} = \frac{(\rho_1+\rho_2)(U_1-U_2)}{\rho_1 U_1 + \rho_2 U_2} x, \tag{19}$$

then we obtain:

$$\frac{dL}{d\tilde{x}} = \frac{\alpha_u}{\alpha}\sqrt{1 - A^2}. \tag{20}$$

Thus, intensity $\frac{dL}{d\tilde{x}}$ depends only on Atwood number and achieves its maximum value at $A = 0$, when flows are identical density. Fig.4 demonstrates the comparison with the experiment on dependence of intensity $\frac{dL}{d\tilde{x}}$ on A for different Atwood numbers. When $A > 0$, results of the experiments [1] and [2] disagree. Like Fig.2, Fig.4 shows the essential difference between theory and results of the experiments [2], when $A > 0$.

References

[1] Yakovlevsky OV, On Issue of Turbulent Mixing Zone Width at Interface of Two Gas Flows of Different Velocities and Densities, Izvestiya AN SSSR, Technical Sciences, 0, 153-155, (1958).

[2] Brown GL, Roshko A, On density effects and large structure in turbulent mixing layers, Fluid Mech, 64, 4, 775-815,(1974).

Non-Linear Stage in the Development of Perturbations at a Shocked Interface

V.E. Neuvazhayev and I.E. Parshukov
Institute of Technical Physics
456770, P.O.245, Snezhinsk, Chelyabinsk region, Russia

Abstract: The problem concerning the development of the perturbations at the shocked interface is considered in approximation of the action of impulsive acceleration on the interface between two ideal incompressible fluids. For numerical study vortex method is used. The regularities of interface evolution during the linear and nonlinear stages are obtained. A quantitative estimation of linear theory applicability is given. The approach is described which allows to obtain the estimation of compressible fluids interface development, describing both initial and nonlinear stages. Comparison with some experimental and numerical results is given.

1. Introduction

When a shock wave passes through interface between two media any small interface perturbations begin to grow (Richtmyer-Meshkov instability) [1,2]. In this paper the problem is considered in approximation of the action of impulsive acceleration on the interface between two ideal incompressible liquids. An effective numerical method based on the representation of fluids interface by a vortex sheet [3-5] is used. Some general regularities of the interface evolution in nonlinear stage, determined by the Atwood number A and initial interface amplitude a_0, are obtained.

Previously [6] the applicability of vortex technique for approximate description of the development of single-mode perturbation of interface between compressible gases after the propagation of a plane stationary shock wave was shown.

Vortex method being used provides correct description of the nonlinear stage of the Richtmyer-Meshkov instability for the case of compressible fluids, but it does not describe an initial stage, when the shock wave is still in the vicinity of the interface and the compressibility influence is still essential. An approach is described that allows for the specific initial conditions of the problem for compressible media on the basis of computations of corresponding incompressible case and linearized gas-dynamic equations to obtain the estimation of interface development and thus describing both initial and nonlinear stages. The idea of such approach was prompted in [7], however its implementation in [7] had in our opinion some shortcomings, that we tried to eliminate. This approach was applied to describe the experiments [8].

2. Incompressible fluids: Impulsive acceleration

Consider a two-dimensional problem on the behavior of interface between two infinitely deep ideal incompressible liquids, when the affecting acceleration has the form $g(t) = U\delta(t)$, where $\delta(t)$ is the Dirac delta function. $U > 0$ corresponds to the case when the shock wave passes from lower half-plane into upper one in the direction of axis y. The initial interface perturbation is $y = a_0 cos(kx)$. The densities of fluids occupying the half-spaces $y < 0$ and $y > 0$ are ρ_1 and ρ_2, respectively. The linear theory [1] ($ak << 1$) gives following dependence of amplitude growth

More information - Email: nio3@eco.ch70.chel.su

upon time

$$a(t) = a_0(1 - Uakt), \tag{1}$$

where $A = (\rho_1 - \rho_2)/(\rho_1 + \rho_2)$ is the Atwood number.
However, since some moment condition $ak << 1$ is always being violated, and the linear theory becomes inapplicable. It is necessary to solve the system of nonlinear equations describing the initial problem. The problem is studied numerically using vortex method [3,4]. The opportunity and peculiarities of technique application for the case of impulsive acceleration were shown in [5].
Some general interface development regularities in the nonlinear stage are obtained. For $|A| = 1$ tendencies of the spike velocity to constant value and bubble velocity to zero are discovered. For equal initial conditions, the spike velocity for $A = +1$ (when change of interface phase takes place) is more than for $A = -1$. The quantitative dependence of perturbation growth rate (especially noticeable for spike) on initial perturbation amplitude is observed. When $a_0k \to 0$ the nonlinear spike velocity $v_s \to 1.92a_0kU$. It is obvious that if one considers interface development not separately for light and heavy substances but for total amplitude ($a = 0.5(a_s + a_b)$, where a_s and a_b are the coordinates of spike and bubble, respectively), the law of amplitude growth is obtained similar to (1), and the difference of obtained for advanced nonlinear stage amplitude growth rate from Richtmyer's formula is dependent on a_0k value.
The problem about the border of the linear stage of interface evolution is considered. For the small values of a_0 deviation of spike and bubble development from linear law (1) takes place almost simultaneously, but as the initial amplitude increases, one can observe faster deviation of bubble (in comparison with spike) from the linear theory. It is important to consider spike and bubble development separately, especially for absolute values of the Atwood number close to 1. On the basis of computations one can infer that the linear theory is applicable (within the error of 10the moment, when the ratio of bubble amplitude to wavelength becomes equal to 0.05-0.1.
For $|A| < 1$ spike and bubble growth rates are approaching zero. For this case the dependence of the law of spike velocity change on initial perturbation amplitude was discovered (there exists a critical value of initial perturbation amplitude a_0^{cr} and when $a_0 < a_0^{cr}$ spike velocity grows only within a finite time interval). In all cases the reduction of interface growth rate at nonlinear stage follows the law close to $1/t$.

3. Account of compressibility

Richtmyer [1] showed that after small transition stage, growth rate of total amplitude is approximately constant in time. For sinusoidal perturbation $y = a_0cos(kx)$ linear theory [1] gives approximate growth rate of amplitude

$$da/dt = v_o = kAUa(0+), \tag{2}$$

where U is the increment of interface velocity, imparted by the shock, A and $a(0+)$ are the Atwood number and the perturbation amplitude after the shock, respectively. Some time after the shock wave has passed through the interface, the gases can be approximately considered as incompressible fluids. Compressibility is essential in some vicinity of the shock wave and is taken into account only as change of initial perturbation amplitude which for the case of the shock wave propagation from light substance into heavy one is given by the approximate formula from [1]

$$a(0+) = a_o(1 - U/D), \tag{3}$$

where D is the velocity of incident shock wave.
The condition of the linear theory applicability ($ak << 1$) is not met frequently in real experiments for large times, where nonlinearity plays an essential role. Using approximation of gases interface as the interface of ideal incompressible liquids allows additionally, remaining within the framework of impulsive Richtmyer's model, to take into account nonlinearity of the process under investigation.
In approximation of incompressibility we compute the problem with initial data $a(0+)$, k, A, U, where A, U are obtained as the result of solving one-dimensional problem for ideal polytropic gases, $a(0+)$ is found from (3). As it was shown in [5], such approach gives correct description of interface growth rate at the nonlinear stage, but the initial stage is described incorrectly, since in incompressible case growth rate changes instantly and spasmodically as the result of impulsive acceleration, while in compressible case there exists the finite transition period of getting a specified velocity value. It was verified in [6,9] by the example of computations of a series of test problems, where qualitative and quantitative agreement was observed between computational vortex results and results obtained according to the gas-dynamic techniques.

4. Comparison with experiment

In [8] the behavior of air-SF_6 interface is considered. A plane stationary shock wave with Mach number $M = 1.2$ propagates from air to SF_6 (i.e. from light substance into heavy one). Incident shock wave velocity $D = 408$ m/s, the interface velocity increment $U = 66.6$ m/s, and postshocked Atwood number is $A = -0.7$. The initial amplitude and the wavelength of the interface perturbation are $a_0 = 2.4$ mm, $\lambda = 37.5$ mm ($a/\lambda = 0.064$).
Approximation of incompressible fluids in similar cases is quite applicable, since the growth rates of interface perturbations are small in comparison with the speed of sound ($v/c \approx 0.1$, where c is a minimum value from the values of speed of sound obtained on both sides of interface after the shock). For the case of the shock wave propagation from light substance into heavy one, according to the computational results [5,6], the formula of Richtmyer gives the upper limit for the value of the initial growth rate of total amplitude, then the rate decreases in time. Results of computations of experiment [8] are presented in Figure 1. Also for comparison, the numerical results [10] are given, where it is stated that for the first time the quantitative agreement with experiment is achieved in terms of coincidence of the growth rates of interface total amplitude. The value of velocity obtained in the experiment is $v \approx 9.2$ m/s. However, the computations show considerable decrease of velocity in time. At a final moment $t = 800$ mcs growth rate is less than maximum initial value by a factor of 2. The coincidence in [10] is obtained for the velocity averaged over the period of supervision from 300 up to 700 mcs, that takes place also in our calculations. Such coincidence of average velocities is, apparently, accidental since it depends both on the processing method and on the time interval of averaging. We have good agreement between the results for the total amplitude obtained with different numerical techniques. For total amplitude significant shift is observed between the experimental and computational curves, which is explained in [10] by the possible effects of the membrane.

5. The nonlinear theory

The most of theoretical works, studying the Richtmyer-Meshkov instability, are focused on solving the linearized Euler's equations and can not describe the nonlinear stage of the interface development, though in some cases they allow to improve the formula of Richtmyer (2) for the linear stage.
In [7] analytical expression for the growth rate of unstable interface in the case of compressible

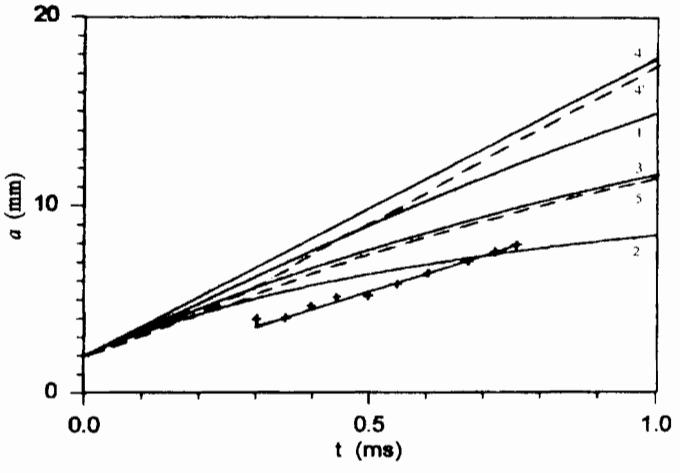

Figure 1. Simulations of experiments [8]: 1 - spike, 2- bubble, 3 - total amplitude, 4,4' - linear theory (for incompressible and compressible cases, respectively), - - - - result [8], 5 - result [10].

fluids is presented and agreement with computations [10] is obtained. The result has the form

$$v = F(v_{lin}) = \frac{v_{lin}}{1 + v_{lin}a_0k^2t + max[0, a_0^2k^2 - A^2 + 0.5]v_{lin}^2k^2t^2}, \tag{4}$$

where for incompressible case $v_{lin} = a_0kAU$, and for compressible case v_{lin} is taken from the appropriate computations of the linearized gas-dynamic equations like [1]. The form of functional F is derived from the theory of incompressible liquids, since at the nonlinear stage (when the shock wave has already retreated far enough from the interface) the fluids may be approximately considered as incompressible (compressibility is essential only at the initial stage). The numerical simulations of experiments [8] using this formula are presented in [7] and agreement with numerical results [10] is obtained.

In our opinion in [7] there are several controversial issues in derivation of (4). To build F authors of [7] use their theory of perturbations in the form of Taylor series with respect to the amplitude of the initial perturbation and Pade approximation of this series. It is known from computations and theoretical reasons that the interface growth rate tends to zero when $t \to \infty$. Knowing the behavior of required function near $t = 0$ (taking the finite part of the series) and at infinity, authors of [7] build an approximating function as a rational fraction with respect to t. But its form essentially depends both on a number of the series terms taken into account and on the character of approaching zero at infinity. It is obvious, that available data are not sufficient to construct such function reliably, since there are many functions (not only rational fractions) which meet the specified conditions in zero and in infinity and give essentially different results for the finite values of t interesting to us.

In the case of incompressible liquids the vortex method allows to obtain rather precise results, which, however, show essential disagreement with the formula (4). As it was mentioned above, our computations show that for large times tendency of velocity to zero has the form $1/t$, while (4), for example for experiments [8], gives $1/t^2$, that actually means that interface amplitude becomes constant that does not agree with numerical simulations and experiments.

Our approach consists in finding the functional F from vortex computations of incompressible case with initial data A, U, a_0k. And we obtain three functionals $F_i, i = 1, 2, 3$, describing the development of spike, bubble and total amplitude respectively.

For the case of ideal incompressible liquids the development of interface may be written down in the following general form $a = a(a_0k, U, A, t)$. Taking into account the invariant properties of hydrodynamics equations it is possible to write down for fixed values a_0,A
$a = \tilde{F}(v_0kt)$ (where $v_0 = a_0kAU$), and respectively $v = \partial a/\partial t = v_0F(v_0kt)$.

Thus, construction of estimate of the Richtmyer-Meshkov instability development for the interface between compressible fluids involves the following stages: 1) computing linearized gas-dynamic equations (for example as it is in [1]) we obtain v_{lin}; 2) for values $A, k, U, a(0+)$ appropriate to the initial problem we calculate (using vortex method) incompressible case and obtain the required dependencies for spike, bubble and total amplitude $v_i/v_0 = F_i(v_0kt)$, where $v_0 = a(0+)kAU$; 3) as the result we obtain the estimates in the form $v_i = v_{lin}F_i(v_{lin}kt)$, $i = 1, 2, 3$.

This approach is used to describe experiments [8]. The result is presented in Figure 2. For small time values F_i are close to 1 and the behavior of interface is specified by v_{lin}. And when v_{lin} gets the constant value, the development goes as in the incompressible case. For large times one can observe distinction in the character of change of growth rate of the total amplitude if compared with results of [7,10], where the decrease of growth rate in time is faster.

In May 1996 at the Joint Conference of Computational Mathematics held in Snezhinsk

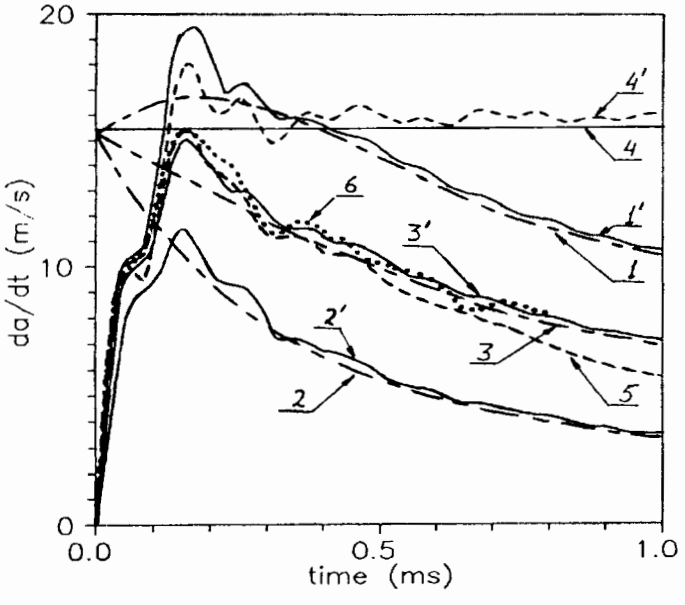

Figure 2. Simulations of experiments [8] (interface growth rate versus time). Incompressible case: 1 - spike, 2 - bubble, 3 - total amplitude, 4 - linear theory; 1'-4' the same for compressible case, 5 - result [7,10], 6 - RAGE.

the results of computations (code RAGE) of the mentioned experiments were presented by

Dr. T. Adams from Los Alamos and they are also given in Figure 2. They are in good agreement with our results.

6. Conclusions

The problem of the perturbation development at the interface between two ideal incompressible liquids under the effect of impulsive acceleration describes approximately the development of the shocked gas-gas interface. The results obtained are confirmed qualitatively and quantitatively by numerical simulations using other techniques and experiments.

Numerical simulations using vortex method allowed to obtain regularities of interface development within nonlinear stage in relation to the initial conditions of the problem.

It is shown that in studies of the nonlinear stage of the Richtmyer-Meshkov instability one should follow the development of spikes and bubbles separately, especially for the cases with Atwood numbers close to 1. It is possible to make the conclusion that the linear theory is applicable up to the moment when the ratio of amplitude of bubble to the wavelength becomes equal to 0.05-0.1.

The offered method of the estimation of the interface development based on the appropriate computations of the incompressible case and linearized gas-dynamic equations allows to describe both initial linear and nonlinear stages rather precisely.

References

[1] Richtmyer RD, Taylor instability in shock acceleration of compressible fluids, Communication on pure and applied mathematics, 13, 297-319, (1960).

[2] Meshkov EE, Instability of a shock wave accelerated interface between two gases, Izvestiya AN SSSR, Mekh.Zhidk.Gaza, 5, 151-157, (1969).

[3] Baker GR, Meiron DI, Orszag SA, Vortex simulation of the Rayleigh-Taylor instability, Phys.Fluids, 23, 1485-1490, (1980).

[4] Kerr RM, Simulations of the Rayleigh-Taylor instability using vortex blobs, J.Comp.Phys., 76, 48-84, (1988).

[5] Neuvazhayev VE, Parshukov IE, Investigation of Richtmyer-Meshkov instability by vortex method, Modeling in Mechanics, 5, 22, 81-100, (1991).

[6] Neuvazhaev VE, Parshukov IE, Study of fluids interface stability under joint action of impulsive and constant accelerations, Mathematical Modeling, 5, 16-24, (1993).

[7] Zhang Q, Sohn SI, An analitical nonlinear theory of Richtmyer-Meshkov instability, Physics Letters A, 212, 149-155, (1996).

[8] Benjamin R, Besnard D, Haas J, Shock and reshock of on unstable interface, LANL Report No. LA-UR 92-1185, Los Alamos National Laboratory, (1993).

[9] Kuz'min AY, Neuvazhaev VE, Parshukov IE, Frolov VD, Numerical investigation of the Richtmyer-Meshkov instability in problems V.Rupert for technique TIGR and vortex method, Preprint, 17, VNIITF, Chelyabinsk-70, (1993).

[10] Grove JV, Holmes R, Sharp DH, Yang Y, Zhang Q, Quantitative theory of Richtmyer-Meshkov instability, Phys. Rev. Lett., 71, 21, 3473-3476, (1993).

Numerical Simulation of Turbulent Mixing in Two-Dimensional Flows

V.V. Nikiforov, Y.V. Yanilkin, Y.A. Yudin, G.V. Zharova and V.A. Andronov
Russian Federal Nuclear Centre - Institute of Experimental Physics
Prospect Mira 37, 607190, Sarov, Nizhny Novgorod Region, Russia

1. Introduction

Numerical results for turbulent mixing in various one-dimensional and two-dimensional flows are presented in this presentation. Computations were carried out using the one-dimensional VIKHR code and the two-dimensional EGAK-V numerical method. The multi-parameter turbulent mixing model of Nikiforov, which was previously realized within the VIKHR code, now is numerically implemented within the EGAK-V code. Computational results were compared with available experimental data.

2. EGAK-V method for numerical simulation of turbulent mixing with multi-parameter turbulence model

The general from of the EGAK-V equation system is presented below in cylindrical coordinates. Equation for averaged quantities are as lollows:

* Equation of motion

$$\frac{\partial}{\partial t}(\rho\vec{u}) + div\,(\rho\vec{u}\vec{u}) = -\nabla P - div\sigma_T,$$

* Equation of continuity for components

$$\frac{\partial}{\partial t}(\alpha_i\,\rho) + div\,(\alpha_i\rho\vec{u}) = div\,(\rho D\nabla\alpha_i)\,,$$

* Equation of conservation of volume for components

$$\frac{\partial}{\partial t}\beta_i + div\,(\beta_i\vec{u}) = \beta_i div\vec{u}_i + DIF(\beta_i),$$

* Equation of energy for components

$$\frac{\partial}{\partial t}(\alpha_i\rho e_i) + div\,(\alpha_i\rho\epsilon_i\vec{u}) = div\,(\rho D\nabla\alpha_i e_i) - \beta_i P_i div\,(\vec{u}-\vec{w}) + \alpha_i\rho\varepsilon\frac{\Phi}{e^T}.$$

Viscous stress tensor σ_T has four components in two-dimensional case

$$\begin{vmatrix} \sigma_{11} & \sigma_{12} & 0 \\ \sigma_{21} & \sigma_{22} & 0 \\ 0 & 0 & \sigma_{33} \end{vmatrix} \quad \text{where } \sigma_{ik} = 2\rho\sigma'_{ik}, \quad \sigma'_{ik} = 2\rho\frac{e^T_{ik}}{e^T}\Phi\ ,$$

More information - Email: otd03_2305@spd.vniief.ru

$\Phi = \left\langle u'_j u'_j \right\rangle + \frac{1}{\rho} \left\langle \rho' u'_j u'_j \right\rangle$ - full kinetic turbulence energy.

Equations for turbulent quantities:

$$\frac{de_1^T}{dt} = \Pi_{11} - e_1^T div\vec{w} - 2e_1^T V_{11} - 2e_{12}^T V_{12} + \left(1 - \frac{2}{10}k\right) f_1 w_1 g_1 + \frac{1}{10} k f_1 w_2 g_2 - -\gamma\omega \left(e_1^T - \frac{1}{3}e^T\right) - k_1 \omega e_1^T;$$

$$\frac{de_2^T}{dt} = \Pi_{22} - e_2^T div\vec{w} - 2e_2^T V_{22} - 2e_{12}^T V_{21} + \left(1 - \frac{2}{10}k\right) f_1 w_2 g_2 + \frac{1}{10} k f_1 w_1 g_1 - -\gamma\omega \left(e_2^T - \frac{1}{3}e^T\right) - k_2 \omega e_2^T;$$

$$\frac{de_3^T}{dt} = \Pi_{33} - e_3^T div\vec{w} - 2e_3^T V_{33} + \frac{1}{10} k f_1 (w_1 g_1 + w_2 g_2) - \gamma\omega \left(e_3^T - \frac{1}{3}e^T\right) - k_3 \omega e_3^T;$$

$$\frac{de_{12}^T}{dt} = \Pi_{12} - e_{12}^T div\vec{w} - e_1^T V_{21} - e_2^T V_{12} - e_{12}^T (V_{11} + V_{22}) + +\frac{1}{2}\left(1 - \frac{3}{20}k\right)(w_1 g_2 + w_2 g_1) f_1 - \gamma\omega e_{12}^T;$$

$$\frac{dw_1}{dt} = \Pi_1^w - w_1 V_{11} - w_2 V_{12} + 2e_1^T A_1 + 2e_{12}^T A_2 + f_1 R g_1 - k_w \omega w_1;$$

$$\frac{dw_2}{dt} = \Pi_2^w - w_2 V_{22} - w_1 V_{21} + 2e_2^T A_2 + 2e_{12}^T A_1 + f_1 R g_2 - k_w \omega w_2;$$

$$\frac{dR}{dt} = \Pi^R + R div\vec{w} + 2(w_1 A_1 + w_2 A_2) - k_R \omega R;$$

$$\frac{d\Phi}{dt} = \Pi^\Phi - 2\sigma t_{ij} V_{ij} - \vec{w}\frac{d\vec{u}}{dt} - \omega\Phi;$$

$$\frac{d\varepsilon}{dt} = \Pi^\varepsilon - \varepsilon div\vec{w} - \frac{4}{3}\varepsilon div(\vec{u} - \vec{w}) - 2\frac{\varepsilon^2}{ke^T} - -c_{\varepsilon 1}\gamma\frac{\varepsilon}{e^T}\left\{\left(e_1^T - \frac{1}{3}e^T\right)V_{11} + \left(e_2^T - \frac{1}{3}e^T\right)V_{22} + \left(e_3^T - \frac{1}{3}e^T\right)V_{33} + e_{12}^T (V_{12} + V_{21})\right\} + +c_{\varepsilon 2} f_1 \frac{\varepsilon}{3e^T}(w_1 g_1 + w_2 g_2) + +c_{\varepsilon 3}\varphi(R)\left\{k f_1 \left(\frac{2}{10}w_1 g_1 - \frac{1}{10}w_2 g_2\right) + \gamma\omega\left(e_1^T - \frac{1}{3}e^T\right)\right\} w_1 A_1 + +c_{\varepsilon 3}\varphi(R)\left\{k f_1 \left(\frac{2}{10}w_2 g_2 - \frac{1}{10}w_1 g_1\right) + \gamma\omega\left(e_2^T - \frac{1}{3}e^T\right)\right\} w_2 A_2 + +c_{\varepsilon 3}\varphi(R)\left\{\frac{3}{20}k f_1 (w_1 - w_2)(g_2 - g_1) + \gamma\omega e_{12}^T\right\}(w_1 A_2 + w_2 A_1).$$

Here we introduce the following additional notifications:

$$e_{ii}^T \equiv e_i^T = \frac{1}{2}\langle u_i' u_i' \rangle, \quad i = 1,2,3; \quad e^T = \sum_i e_i^T; \quad e_{12}^T = \frac{1}{2}\langle u_1' u_2' \rangle;$$

$$w_i = \frac{1}{\rho}\langle \rho' u_i' \rangle, \quad i = 1,2; \quad R = \frac{1}{\rho^2}\left\langle \rho'^2 \right\rangle; \quad \vec{g} = \frac{1}{\rho}\nabla P;$$

$$\varphi(R) = \frac{1+R}{R}.$$

$$V_{11} = \frac{\partial(u_1 - w_1)}{\partial x}, \quad V_{22} = \frac{\partial(u_2 - w_2)}{\partial r}, \quad V_{33} = \frac{(u_2 - w_2)}{r},$$

$$V_{12} = \frac{1}{2}\left(\frac{\partial(u_1 - w_1)}{\partial r} + \frac{\partial(u_2 - w_2)}{\partial x}\right)$$

where $\vec{u}(u_1, u_2)$- velocity vector; ρ - average density of medium; ρ_i - density of the i-th component of medium; e_i - specific internal energy of the i-th component of medium; P - average pressure of medium; P_i - pressure of the i-th component of medium; β_i -volume concentration of the i-th component ($\beta_i = V_i/V$); α_i - mass concentration of the i-th component ($\alpha_i = M_i/M$); ε - viscous dissipation rate for turbulent energy; e_{ij}^T- components of velocity component fluctuation tensor (e_{ii}^T are denoted as e_i^T); V_{ij} - components of deformation rate tensor; $\vec{w}(w_1, w_2)$- velocity vector for turbulent mass flow; R - relative mean square for density fluctuations; V_{11}, V_{22}, V_{33} - components of deformation rate tensor; ε - rate of viscous dissipation of turbulence energy, $\omega = \varepsilon/e^T$. Here and below indexes 1, 2 indicate longitudinal and radial components, respectively. Transport terms Π, being divergences of third order tensors, have a quite bulky form. Therefore, in the original version of the numerical method we use a diffusion approximation for them in the following form:

$$\Pi_{ik} = div\left(D_T^e \nabla e_{ik}^T - \vec{w} e_{ik}^T\right), \qquad \Pi^\Phi = div\left(D_T^\Phi \nabla \Phi - \vec{w}\Phi\right),$$

$$\Pi_1^w = \frac{1}{\rho} div\rho\left(D_T^w \nabla w_1 - \vec{w} w_1\right), \qquad \Pi_2^w = \frac{1}{\rho} div\rho\left(D_T^w \nabla w_2 - \vec{w} w_2\right),$$

$$\Pi^R = \frac{1}{\rho^2} div\rho^2\left(D_T^R \nabla R - \vec{w} R\right), \qquad \Pi^\varepsilon = div\left(D_T^\varepsilon \nabla \varepsilon - \vec{w}\varepsilon\right).$$

We have adopted the following expressions for coefficients:

$$k_i = \frac{e^T}{3e_i^T}, \qquad k_R = 1.5, \qquad k = 3\sqrt{3}\sqrt{\frac{e_1^T e_2^T e_3^T}{(e^T)^3}},$$

$$k_W = \frac{e^T}{6\tilde{e}^T} + \frac{1}{10} c_{e^T}\, k f_1 \frac{\vec{w}\cdot\nabla P}{\tilde{e}^T} \frac{c^T}{\varepsilon}\frac{1}{\rho} + \frac{\gamma}{2} + \frac{k_R}{2},$$

$$where \qquad |w| = \sqrt{w_1^2 + w_2^2},$$

$$f_1 = \frac{1}{1 + R - \frac{D_T}{|w|}\frac{dR}{dl}},$$

$$where \qquad \frac{dR}{dl} = \frac{dR}{dx}\frac{w_1}{|w|} + \frac{dR}{dy}\frac{w_2}{|w|}.$$

$$\tilde{e}^T = e_1^T \cos^2\varphi + 2e_{12}^T \cos\varphi \sin\varphi + e_2^T \sin^2\varphi, \qquad \cos\varphi = \frac{w_1}{|w|}, \qquad \sin\varphi = \frac{w_2}{|w|}.$$

$\tilde{e}^T$ is a component of the tensor e_{ik} in a local coordinate system where one of the axes coincides with the direction of the turbulent mass flow.

$$\gamma = 1 + \frac{\varphi_2}{2} + \frac{\varphi_3}{2} + \sqrt{\left(\frac{\gamma_1 - 1}{2}\right)^2 + \frac{\varphi_2^2}{4}} + \sqrt{\left(\frac{\gamma_1 - 1}{2}\right)^2 + \frac{\varphi_3^2}{4}},$$

$$\varphi_2 = \gamma_2 \frac{w_1 A_1 + w_2 A_2}{R\omega},$$

$$\varphi_3 = -\gamma_3 \frac{e_1^T V_{11} + e_2^T V_{22} + e_3^T V_{33} + e_{12}^T (V_{12} + V_{21})}{\epsilon},$$

$$\vec{A} = A_S + \left(\vec{A}_T - \vec{A}_S\right)[1 - y(\varphi)],$$

$$\vec{A}_S = \frac{1}{\rho}\left.\frac{\partial\rho}{\partial P}\right|_S \nabla P - \frac{\nabla\rho}{\rho}, \qquad \vec{A}_T = \frac{1}{\rho}\left.\frac{\partial\rho}{\partial P}\right|_T \nabla P + \frac{1}{\rho}\left.\frac{\partial\rho}{\partial T}\right|_P \nabla T - \frac{\nabla\rho}{\rho},$$

where $y(\varphi) = \frac{1}{\varphi}(1 - e^{-\varphi})$, $\varphi = \chi/(\rho c_P l_t \sqrt{2e^T})$, χ - heat conductivity, $l_t \approx \frac{\sqrt{2e^T}}{\omega}$ - scale of turbulence. Diffusion coefficients are:

$$D_T^{(e_1^T)} = D_T^{(e_2^T)} = D_T^{(e_3^T)} = D_T^{(e_{12}^T)} = D_T^{\Phi} = 3D_T,$$

$$D_T^w = 2D_T, \quad D_T^R = D_T, \quad D_T^\varepsilon = \frac{5}{3}D_T, \quad D_T = 2\,c_{D_T}\frac{\tilde{e}^T e^T}{k_\gamma \varepsilon}\frac{1}{1+b},$$

$$b = \frac{1}{4}\frac{k_R}{k_\gamma}\left(\psi + |\psi|\right), \qquad \psi = \frac{2(w_1 A_1 + w_2 A_2)e^T}{k_R \varepsilon R} - 1, \qquad k_\gamma = \frac{3}{2} + \frac{e^T}{6e_1^T} + \frac{\gamma}{2}.$$

Diffusion coefficient D in equation of continuity for components and in equation of energy is assumed to be equal $D = DT$ in two-dimensional case instead of $D = |\vec{w}| / \left|\vec{A}\right|$ in one-dimensional case. Such assumption seems to be more accurate for a *2D* computational method because turbulent mixing may take place even in the case when both $|\vec{w}|$ and $\left|\vec{A}\right|$ are equal to zero (for example, tangential discontinuity of the velocity on the interface between two fluids with equal densities).

3. Numerical results

Numerical results for simulation of turbulent mixing in various one-dimensional and two-dimensional flows are presented below. These computations were carried out using the one-dimensional VIKHR code and the two-dimensional EGAK-V code that is a two-dimensional simplified version of the multi-parameter model implemented within the VIKHR code. Computations with the EGAK-V code were carried out on a fixed computational grid. One-dimensional computations were used to test the two-dimensional code itself. Numerical simulation of gravity- and shear-driven turbulent mixing in plane geometry and Richtmyer-Meshkov instability in cylindrical geometry was carried out with the EGAK-V method. Obtained results are in good agreement with results obtained earlier with the VIKHR and EGAK-T (the $k - \varepsilon$ model) codes [1]. For two-dimensional computations obtained results are shown in form of isolines of volume concentrations. Computational results are compared with experiments where such data are available. For all computations, if not otherwise stated, boundaries of the turbulent mixing zone were determined from the volume concentration levels $\beta = 0.01$ and $\beta = 0.99$.

3.1. Gravity and shear driven turbulent mixing

Two incompressible fluids were separated by a plane interface. The gravity acceleration g was directed normally to the interface. Tangential discontinuity of the velocity Δu was set on the interface. Normal component of the velocity was assumed to be zero. Note that g can have either positive or negative sign so that the flow can be either stable or unstable regarding the Rayleigh-Taylor instability. The *TMZ* growth with time for different signs of g is illustrated by Figure 1. It can be shown that for $g > 0$ the mixing zone grows faster that for a merely gravity- or shear-driven mixing case. For $g < 0$ the *TMZ* growth slows down and finally stops with time. For the latter case the *TMZ* width should be proportional to $\Delta u^2/g$:

$$L = A\frac{\Delta u^2}{g}.$$

Coefficient A can be determined from computations. Three EGAK-V computations of gravity- and shear-driven turbulent mixing case were conducted for $g = +10; 0; -10$ and $\Delta u = 6$. These computations fully confirm theoretical concepts regarding the character of the *TMZ* spreading (see Figure 1). All flows with $g < 0$ became stable with time. Coefficient A determined by the EGAK-V method turned out to be $A \approx 5/6$.

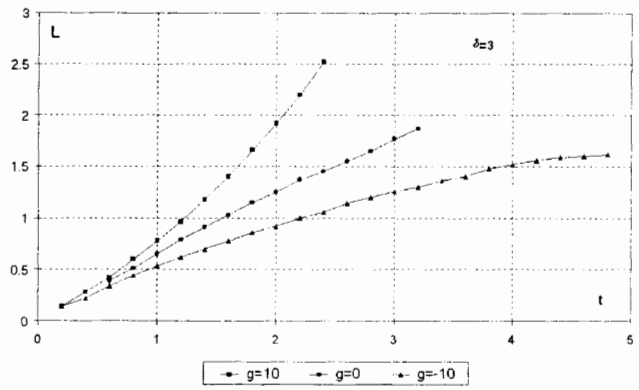

Figure 1. Dependence of *TMZ* width L on time t for gravity- and shear-driven turbulent mixing (EGAK-V).

3.2. Slanting interface

The computed configuration is shown in Figure 2. The slanting interface between air and helium was located on 20 cm from the right rigid wall and it had the amplitude $\Delta x/2 = 1.2$ cm and the wave length 24 cm. The Mach number of the incident shock wave was $M = 1.3$. For helium the equation of state for perfect gas was used with adiabatic index $\gamma = 1.63$. Air parameters corresponded to normal conditions. For the considered problem experiments with

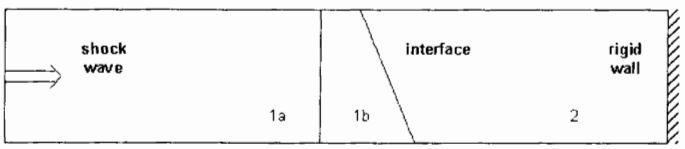

Figure 2. Initial geometry for *2D* computations with slanting interface.

the slanting interface between air and helium were conducted on a shock tube by Meshkov's team [2]. The experimental data obtained in these experiments allow to use this problem as a reliable test for numerical techniques. Earlier the MIMOZA and VKL computations of the problem were carried out [2]. Figure 3 shows isolines of volume concentration $\beta = 0.01$ and $\beta = 0.99$ plotted on the frame photographs of the flow obtained in the experiments. In this Figure contours of volume concentrations obtained in the EGAK-T computation (the $k - \varepsilon$ model of turbulent mixing) is plotted by black line, and contours of volume concentrations obtained in the EGAK-V computation - by white line. The obtained numerical results are consistent for all numerical techniques (including the MIMOZA and VKL codes). Moreover, their comparison with the experimental data also shows satisfactory agreement. However it should be noted that all above-mentioned numerical techniques (including the EGAK-V code) failed to describe properly the progression of a "bell" in the lower part of the flow. In the upper part of the flow some differences can also be seen as more rapid movement along the wall obtained in the computations in comparison with the experiment. At present there is no justified explanation for these differences. It is possible that presence of the boundary layer in

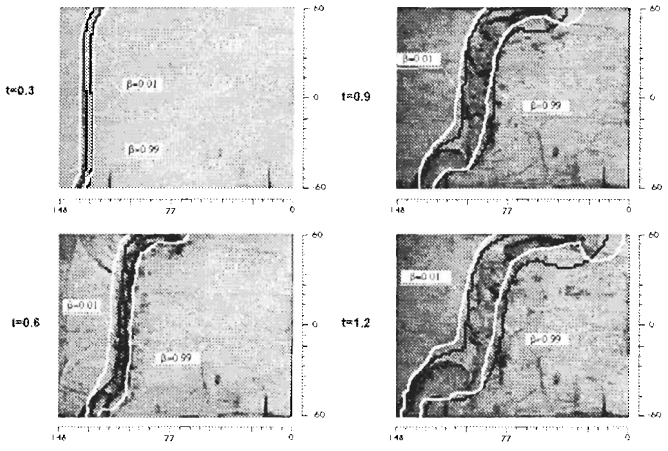

Figure 3. Experimental frame photographs of slanting interface evolution with calculated isolines of volume concentrations (EGAK-T and EGAK-V computations).

the experiments affected the flow near the walls. Note that the computations were carried out in assumption of ideal sliding.

4. Conclusion

Numerical investigations of turbulent mixing in various one-dimensional and two-dimensional hydrodynamics flows were carried. Computations were conducted with the one-dimensional VIKHR code and the two-dimensional EGAK-V code. The multi-parameter turbulent mixing model of Nikiforov, which was previously realized within the VIKHR code, now is numerically implemented within the EGAK-V code. Numerical results were presented and discussed in this presentation. They were compared with available experimental data. Good agreement between the VIKHR code and the EGAK-V code was observed for one-dimensional flows (gravity-driven turbulent mixing and computations in cylindrical geometry). For two-dimensional modeling of shock tube experiments the EGAK-V method gave results that are consistent with the experimental data. In conclusion, it can be summarized that developed computational techniques allow to carry out numerical simulation of turbulent mixing in the wide range of one- and two-dimensional hydrodynamics flows with reasonably good accuracy.

References

[1] Andronov VA, Zhidov IG, Meshkov EE, Nevmerzhitskii NV, Nikiforov VV, Razin AN, Rogachev VG, Tolshmyakov AI, Yanilkin YV, Computational and Experimental Studies of Hydrodynamic Instabilities and Turbulent Mixing (Review of VNIIEF Efforts), Los Alamos National Laboratory report LA-12896, UC-700, (1995).

[2] Bashurov VV, Bondarenko YA, Gubkov EV, Dudin VI, Zmushko VV, Meshkov EE, Shanin AA, Stenin AM, Tilkunov VA, Tolshmyakov AI, Trofimova LY, Yanilkin YV, Experimental and Numerical Studies of *2D* Perturbations Growth at the Interface Accelerated by Sequential Shock Waves, Proc. of 5^{th} Int. Workshop on the Physics of Compressible Turbulent Mixing, Stony Brook, USA, (1995).

Numerical Simulations of Nonlinear and Transitional Stages of Richtmyer-Meshkov and Rayleigh-Taylor Instabilities

V.V. Nikishin[1], V.F. Tishkin[1], N.V. Zmitrenko[1], I.G. Lebo[2], V.B. Rozanov[2] and A.P. Favorsky[3]
[1]The Institute for Mathematical Modeling, 4a Miusskaya sq., 125047, Moscow, Russia
[2]Lebedev Physics Institute, 53 Leninsky Pr., 117924, Moscow, Russia
[3]Moscow State University, Vorobiovy Gory, 117234, Moscow, Russia

Abstract: The report presents the results from studying the nonlinear stage of the development of Richtmyer-Meshkov and Rayleigh-Taylor instabilities. The simulations have been made with the help of 2D and 3D code "NUT" [1]. The criteria for the transition to the turbulence in accordance with different values of the Atwood and Mach numbers and the initial parameters of the perturbations (amplitude and shape) have been found basing on the performed simulations. We have also found the temporal dependences of the amplitude and mass growth and the perturbation circulation.

1. Modeling of the Richtmyer-Meshkov instability. Comparison with the shock tube experiment

The NUT code was been used in numerical modeling of the RM instabilities at the gas boundary for the cases: 1) $Kr - Xe$ (Atwood number 0.188); 2) $Ar - Xe$ (Atwood number 0.535); 3) $He - Xe$ (Atwood number 0.94). The initial pressure in both gases was 0.5 bar. At the contact boundary the sinusoidal perturbations were produced. The perturbations had the form $Z(x) = a_0 * cos(k * x) + Z_a$, where $k = 2\pi/\lambda$. We varied the perturbation initial amplitudes and wavelengths as well as the Mach number in the shockwave. The gas parameters were taken in accordance with the experiments made at Krzhizhanovsky Power Institute. The perturbation development strongly depends on the listed parameters. Below are given the examples of such calculations. Fig. 1 illustrates the development of perturbation with the wavelength of $\lambda = 3.6cm$ and the initial amplitude (the distance from the "bottom" to the "top" of the perturbation) of $a_0 = 1cm$. To the left one can see the temporal dependence of the perturbation amplitude for the gas pair $Kr - Xe$; to the right - for $Ar - Xe$. The dots show the experimental data [1]. The left figure also shows the results obtained for such perturbations at Courant Institute, Univ. of New York (dotted line). One can see good agreement between the calculated and experimental data. The dotted line in the right figure shows the amplitude temporal dependence for a "solitary" perturbation (the side boundaries were shifted by half of the wavelength). The solid line illustrates the "sinusoidal" perturbation. Fig 1 also shows the density isolines for $Ar - Xe$ at $400\mu s$. Figure 2 illustrates the temporal dependences of amplitude of contact boundary for gas pair $He - Xe$ and different wavelengths such as $\lambda = 3.6cm$, $\lambda = 2.4cm$, and $\lambda = 1.2cm$. The initial amplitudes were supposed to be equal $a_0 = 1cm$. In this case an "unregular" regime of perturbation growth is observed. We can see that the growth rate is the same for the different wavelengths. The dotted line in fig. 2 shows the experimental data obtained by S.G.Zaitsev's group from Krzhizhanovsky Power

More information - Email: nikishin#4@imamod.msk.su

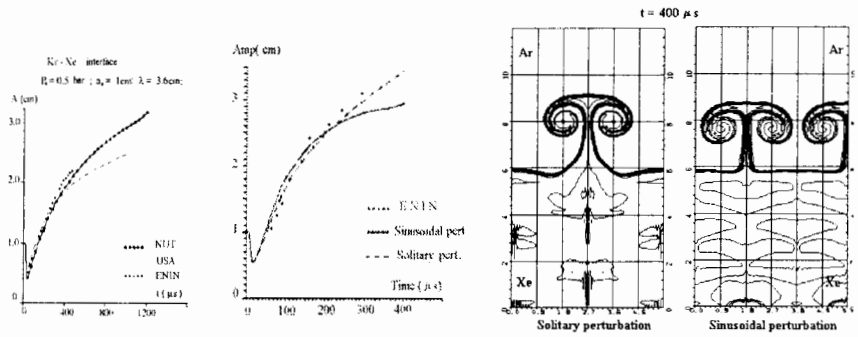

Figure 1. Comparison 2D results: a) $Kr - Xe$ b), c) $Ar - Xe$.

Institute [2]. To the left side of the figure one can see the comparison of the results obtained by "NUT" code with experimental data and with results of the group of scientists from Moscow Institute of Physics and Technology [3] for "unregular" case ($\lambda = 0.8cm, a_0 = 1cm$). Fig. 2 also shows the density isolines for one case from the set of the describing problems. It is seen the similar amplitude for different wavelengths is observed at the same time. Numerical simulations

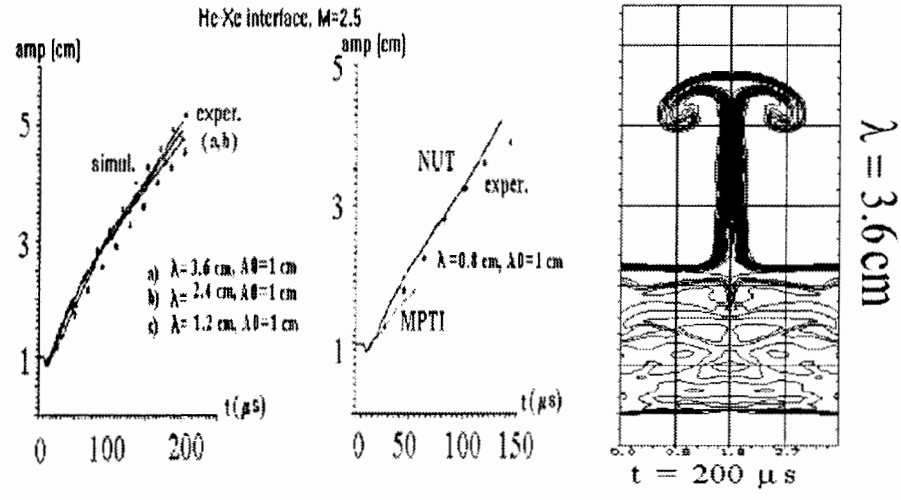

Figure 2. $He - Xe$ 2D interface; "unregular" case.

with different initial forms of the perturbation such as sinusoidal, triangle and parabolic was made. All perturbation had the same initial mass. left Fig. 3 shows density isolines for these cases at the time moment $400\mu s$. Fig. 3b,c illustrate the temporal dependences of amplitude and perturbation mass. We have carried out the series of numerical simulations of multimode

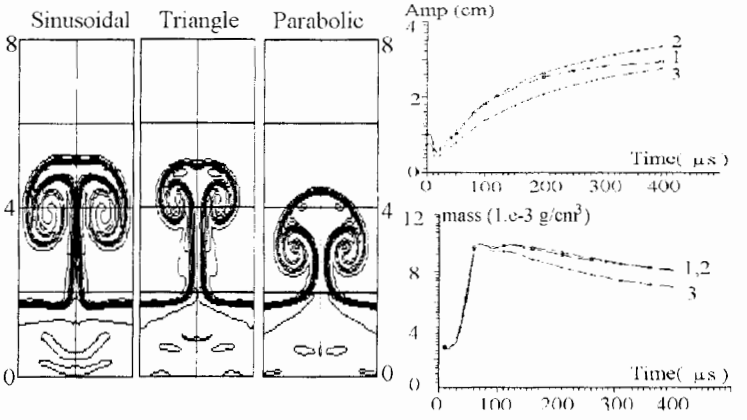

Figure 3. Different forms of initial perturbation.

initial perturbations in 2D geometry for different gas pairs. Fig. 4 presents such numerical results for $He - Xe$ interface. In the first case perturbation modes are in the same phases ($a_1 = +0.5cm, \lambda_1 = 1.8cm$; $a_2 = 1cm, \lambda_2 = 3.6cm$) and in the second case modes are in the opposite phases. ($a_1 = -0.5cm, \lambda_1 = 1.8cm$; $a_2 = 1cm, \lambda_2 = 3.6cm$). The distance between spikes was equal $2.7cm$. The growth rate of the contact boundaries was the same for these cases (see fig. 4). Below the results of 3D simulations of $He - Xe$ gas pair perturbations are

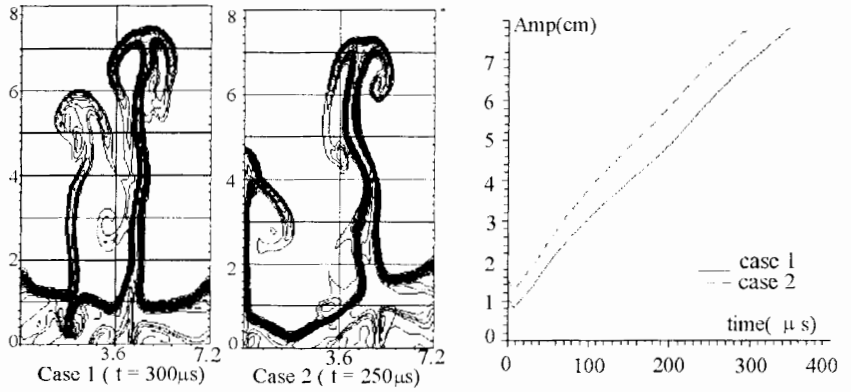

Figure 4. $He - Xe$ 2D multimode perturbations.

presented. Contact boundary between interacting gases has the harmonic form: $Z(x,y) = a_1 * cos(\frac{\pi}{\lambda_x}x)cos(\frac{\pi}{\lambda_y}y) + Z_c$, where We took into account three cases of initial perturbation: 1) $a_1 = 1cm$, $\lambda_x = \lambda_y = 7.2cm$. The Mach number of incident shock wave was equal to 2.5. 2) $a_1 = 0.91cm$, $\lambda_x = \lambda_y = 3.6cm$ and $M = 3.11$. 3) $a_1 = -0.91cm$, $\lambda_x = \lambda_y = 3.6cm$ and $M = 3.11$. We have compared our results with numerical solutions obtained by Prof.D.Youngs (AWE Aldermaston, UK) and experimental data. Figure 5a shows time dependences of amplitude for 1), 2) and 3) cases. Solid line corresponds to the "NUT" solution and the "crosses" present

the results of Prof. D.Youngs. At the middle of this figure the experimental data obtained by Zaitsev's group are presented [2]. Right figure 5 exhibits the isolines of average concentration alone OY axe at the $100\mu s$. One can see a good agreement between these results. Besides

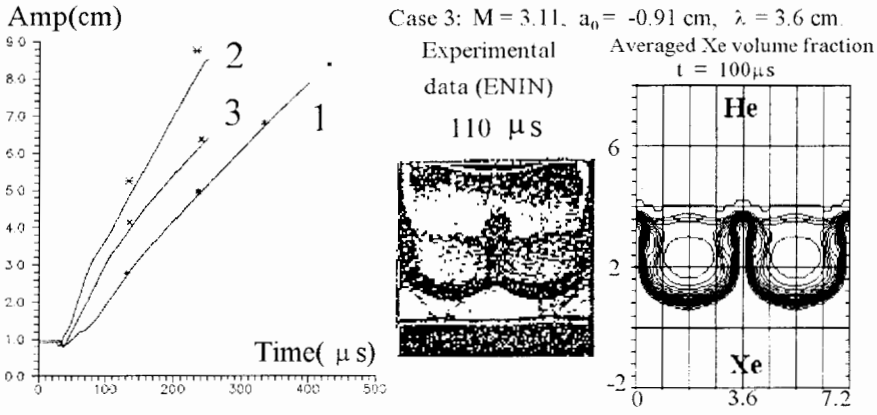

Figure 5. Comparison $He - Xe$ 3D results (ENIN,IMM,AWE).

we have started the numerical simulations of multimode three dimensional perturbations. We divided all region (area parameters: $7.2 \times 7.2cm$) on six subregions. We assumed that these subregions were formed with the help of thin wires. Two wires were put alone OY axis (at $x = 1.2cm$ and $x = 3.6cm$) and another one alone OX axis (at $y = 2.4cm$). We supposed sinusoidal initial perturbation in all subregions. Initial amplitude in each subregion is chosen according to the law: $Z(x,y) = A_{ij} * sin(\frac{\pi}{W_{xi}}x)sin(\frac{\pi}{W_{yj}}y)$, where $A_{ij} = 0.91\sqrt{W_{xi}W_{yj}}/3.6$. Using subregions parameters was next: $W_{x1} = 1.2cm$, $W_{x2} = 2.4cm$, $W_{x3} = 3.6cm$ and $W_{y1} = 2.4cm$, $W_{y2} = 4.8cm$. Fig. 6a show averaged concentration at $200\mu s$, obtained by "NUT" code. The right illustration presents temporal dependences of amplitude "NUT" results (solid line) and AWE results (points).

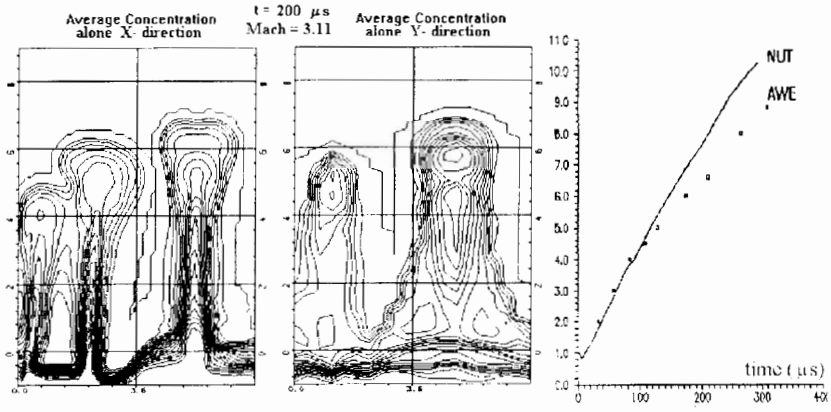

Figure 6. Multimode $He - Xe$ 3D results.

2. Rayleigh-Taylor instability modeling

In this section we consider the contact boundary between gases in the field of constant acceleration g. We assume the heavy gas (with density ρ_2) to be disposed at the top of the region. Below the light gas (with density ρ_1) is placed. Atwood number is equal $A = \frac{\rho_2 - \rho_1}{\rho_2 + \rho_1}$ (for incompressible case).

Let the initial perturbation contact boundary have the form $Z_{cr} = Z_0 + \frac{a_0}{2}\sin(kx)$. Where a_0 is the full amplitude from the "bottom" to the "spike" of boundary, $k = \frac{2\pi}{\lambda}$ is the wave number. We suppose that the value $ka(t)$ to be the "current age" of the structure. Hence ka_0 is the initial age of structure. In the case of zero initial velocity the amplitude growth rate in linear stage is changed with accordance the law: $a(t) = a_0 ch(\gamma_0 t)$, where $\gamma_0 = \sqrt{gkA}$ is classical increment of the Rayleigh - Taylor instability (RTI) under condition $ka_0 << 1$.

Gases is submitted the isoentropic state equation $P_\alpha = B_\alpha \rho_\alpha^\gamma, \quad (\alpha = 1, 2)$. We take pressure p and density ρ near interactive area from simulations of RMI. Using stationary Euler equation with the constant acceleration along OZ axis we can obtain that $\rho_\alpha(z) = [\rho_\alpha^{\gamma-1}(0) - \frac{gz(\gamma-1)}{\gamma B_\alpha}]^{\frac{1}{\gamma-1}}$, and $P_\alpha(z) = [P_\alpha^{\frac{\gamma-1}{\gamma}}(0) - \frac{gz(\gamma-1)}{\gamma B_\alpha^{\frac{1}{\gamma}}}]^{\frac{\gamma}{\gamma-1}}$. In numerical simulations we set the initial parameters with accordance to these formulae.

We consider next problems setup for gas pair $Ar - Xe$: case a) $g = 0.02mm/\mu s^2, P_0^{0.4} = 0.18(GPa)^{0.4}$ and case b) $g = 0.2mm/\mu s^2, P_0^{0.4} = 1.8(GPa)^{0.4}$. Wave length and initial amplitude are the same for both cases ($\lambda = 24mm, a_0 = 3mm$). At linear stage the formula $a(t) = a_0 ch(\gamma_0 t)$ is true. It allows to compute the value of effective increment RTI γ_e as function of relation $a(t)/a_0$: $\gamma_e = \frac{1}{t} ln[\frac{a(t)}{a_0} + \sqrt{(\frac{a(t)}{a_0})^2 - 1}]$. We obtain a good agreement between numerical effective γ_e and theoretical RTI increment $\gamma_0 = \sqrt{kgA}$ in these cases. Also numerical

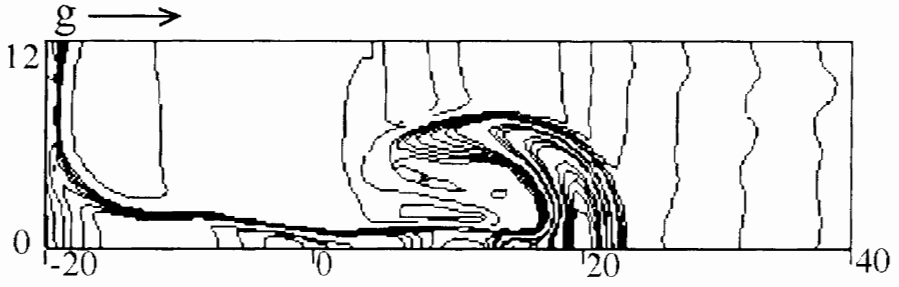

Figure 7. RTI; density isolines at 30 μs.

simulations was carried out for the compressible gases (like case "b" which density isolines is shown at the top of fig. 7).

In next section we made more detailed computations, for example, in compressible gases variants. Easy to understand, the influence of compressibility is characterized by the scale : $L_{c\alpha} = c_\alpha^2(0)/(\gamma - 1)g$, where c_α is adiabatic sound velocity. Initial pressure distribution may be rewritten in the follow form: $p_\alpha(z) = p_\alpha(0)\left[1 - \frac{z}{L_{c\alpha}}\right]^{\gamma/(\gamma-1)}$. For less entropy heavy gas like Xe gas in early described computations have $L_{c1} \approx 20mm$ and at the time the amplitude grew up to value $40mm$. It is advisable to start exploration of weakly compressible gas for detail

analisys the dependences of RTI characteristics which depended from the structure age and including for the checking of analytic theory formula ($ka << 1$). We carried out computation with $B_1 = 1.35$, $P^{0.4}(0) = 2.5$ and $g = 0.05$ (system units see above). The value L_{c1} was equal to $150mm$ for this case. We took into account the traditional gas pairs $Ar - Xe$ and $He - Xe$ with Atwood numbers 0.535 and 0.941 corresponding. Wave length was $36mm$. The amplitude of perturbation on developed stage was reached $\approx 50mm$. We obtain the formula for evolution the periodic structure on linear stage. The expressions for the momentum P and velocity circulation C on "halflength" area are equal to : $P = -\frac{\pi\rho_{heavy}\gamma_0 a}{2k^2}th(\gamma_0 t)I_1(ka/2)$, $C = \frac{2a\gamma_0}{k}th(\gamma_0 t)ch(ka/2)$. Fig. 8 shows the computational results for impulse P (subfigure a)

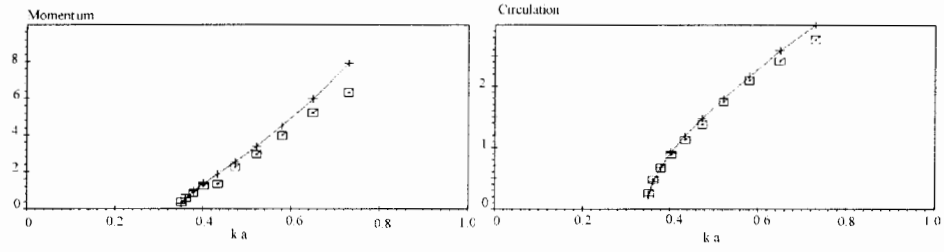

Figure 8. Momentum and circulation versus ka for linear stage.

and circulation C (subfigure b). The solid line is theoretical results and squares is the numerical data. One can see the perturbation growth follows the linear theory for $ka \leq 1$ and afterwards it rejects from this theory. Magnitude of circulation is the important thing to describe sliding velocity and it may be predicted up to non linear stage. Indeed, like theory says $\frac{dC}{dt} = 2Aga$, where $a = a_0 ch(\gamma t.)$ Obtained from numerical simulations value $\frac{dC}{dt}$ has a marked difference from expression $2Aga_0 ch(\gamma_0 t)$, but it is practically equals expression $2Aga$, where $a = a(t)$ is amplitude value getting from this computation. This fact we can see at figure 9. Some distinguish for case "b" connect with "falling" the spike of the heavy fluid on the bottom of the computational region. We may compute circulation C with the help obtained characteristic

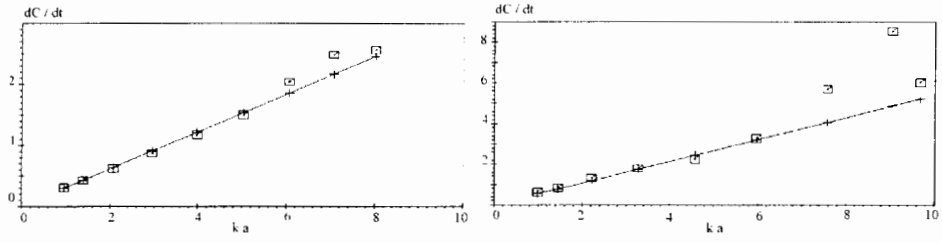

Figure 9. Comparison of the theoretical and numerical results for dC/dt versus ka for different Atwood numbers a) $A = 0.535$ and b) $A = 0.941$.

velocity $\frac{da}{at}$ and corresponding curve length from "bottom" to "spike" of the perturbation. If

the vorticity structure in the "mushroomlike" region developed not so strong We may take the chord length Λ instead of value L. Results of these tests is shown on figure 10"a", "b" for different Atwood numbers. Here by square is marked numerical results for expression C, by crosses we mark expression Lda/dt and by stars we mark another one for $\Lambda da/dt$. One can see

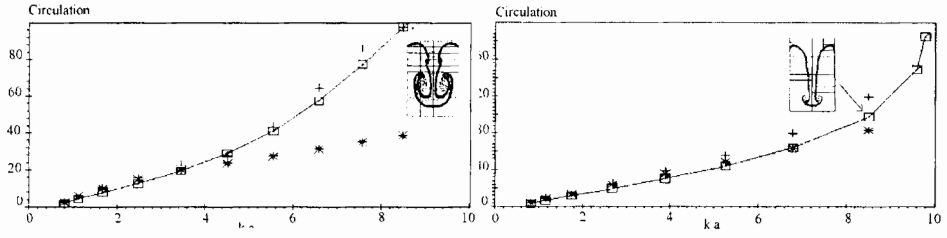

Figure 10. Comparison different formulae for circulation C versus ka for a) $A = 0.535$ and b) $A = 0.941$.

for case "b" the "mushroom" don't presented and both approximated expression was the same as numerical results. For case lower Atwood number (case "a") the perturbation has a great "mushroom" structure and only the value Lda/dt is fitted to numerical results.

Acknowledgement. Autors gratitude D. Youngs (AWE, Aldermaston,UK), R. Holmes (New-York University, USA) and S.G. Zaitsev (ENIN) for cooperation. Study was supported by ISTC (Grant N° 94-039).

References

[1] Tishkin VF, Nikishin VV, Popov IV, Favorsky AP, Math. Modeling, 7, 5, 15, (1995).
[2] Aleshin AN, Lazareva EV, Zaitsev SG, Rozanov VB, Gamaly EG, Lebo IG, Dokladi Akademii Nauk SSSR, Fizika, 310, 5, (1990).
[3] Belotcherkovsky 0M, Demchenko VV, Oparin AM, DAN, 39, 2, 118, (1994).

Propagation of Gasdynamic Perturbations Via Light Gaseous Layer in Plane Stratus Cumulating Systems Numerical Study

P.N. Nizovtsev, V.A. Rayevsky and V.P. Soloviov
Russian Federal Nuclear Centre - Institute of Experimental Physics
Prospect Mira 37, 607190, Sarov, Nizhny Novgorod Region, Russia

1. Introduction

Gasdynamic systems assigned for energy concentration increase (cumulating systems) oftenly use alternating layers of light and heavy materials. When compression wave is propagated towards decreasing layer thicknesses, the front wave pressure and specific layer energy are increasing. These systems are used either for gasdynamic thermonuclear inertial fusion [1], laser fusion or for the devices accelerating plane liners to high velocities used for high energy density physics [2]. Gasdynamic energy transfer from layer to layer is accompanied by growth of perturbations initially presented in any system. Perturbations grow intensively when heavy layer is accelerated by light gas or when layer is decelerated at lighter layers, that is when Rayleigh-Taylor instability is realized. Perturbations growth in hydrodynamic instability conditions is the main reason of cumulating devices effectiveness drop. Perturbations propagating intensiveness depends on initial conditions-layer surface bending and density difference. In many cases of practical value the main source of perturbation growth is heterogeneous pressure in compression wave accelerating the layer. Under these conditions acceleration of initially "ideal" smooth layer is accompanied by perturbation growth. Perturbations transfer from layer to layer depends on many factors such as: initial system geometry, perturbation wavelength, layer substance density gradient, layer material strength. Perturbation propagation from layer to layer may be completely supressed at specific combination of system parameters. This phenomenon was registered by A.D. Sakharov, A.I. Davydov, V.P. Pheodoritov. We have studied numerically perturbations propagation from cascade to cascade in plane geometry.

2. Results of calculations

The simpliest case of interaction between substance layer and bended rigid wall via light gaseous layer was dealt with. Initial geometry of system under investigation is shown on Fig. 1. At the initial time period substance (titanium) layer of 0.05 cm thickness and gaseous layer move towards rigid wall with $U_0 = 8$ km/s velocity. Perturbation of $a = a_0 cos(2\pi y/\lambda)$ is specified at rigid wall surface. The calculation simulates the position where titanium layer is accelerated by significantly heavier and more dense substance layer. Fig. 2 shows the diagram of layer motion without perturbations (one-dimensional calculation) and dependence of pressure a velocity on titanium boundary on time.
Maximum gas compression is $x_0/x_m \sim 27.8$ (x_0, x_m - initial and min gas layer thicknesses), provided that sound density and velocity in it are $p_m \sim 0.136$ g/cm^3, $C_m \sim 12.6$ km/s. Fig.3 shows perturbations amplitude at titanium layer surface contacting gaseous layer, for different

More information - Email: otd03_2305@spd.vniief.ru

λ values, vs time.

At great wavelength ($\lambda/x_m >> 1$) simple perturbation reflection occurs. When wavelength

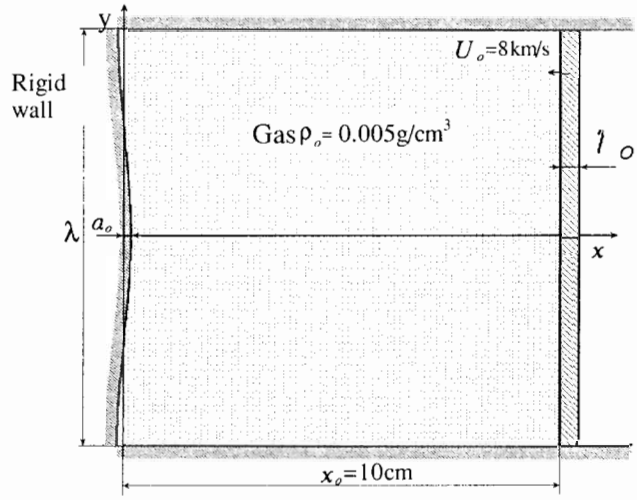

Figure 1. Initial system configuration.

is shortened, one or more pressure perturbation waves happen to travel towards OY, provided that pressure perturbation value at titanium layer surface changes the sign. As a result, perturbation of titanium threshold position changes the sign to the opposite one. Titanium strength in this area vaguely effects perturbations propagation. In shorter wavelength area ($\lambda/x_m \sim 2-5$) pressure perturbation at layer surface changes the phase several times as titanium layer is reflected.

As a result, instability propagation for several wavelengths ($\lambda \sim 0.7 - 1.8$ cm) in titanium layer is noticeably decelerated. Strength effect in this area becomes more evident. (Fig. 4a, b, c). Fig. 4 shows the amplitude of perturbations on titanium layer surface in time at different strength: continuous line corresponds to $Y = 0.1$ GPa, broken line - to $Y = 2$ GPa.

One of the peculiarities of this wavelength area is change of sign of perturbations at plate surface, wavelength being slightly changed. It should be noted that perturbations sign changes as well when the initial amplitude is changed. At the first sight it could be viewed as a paradox that for several l values (Fig. 4c), when strength is increased, perturbations amplitude value grows. This is a result of complex interference of waves in gaseous matter.

In the area of $\lambda/x_m \sim 1$ and shorter wavelengths pressure pulsation period $\tau_p \sim \lambda/c_m$ is significantly shorter than specific reflection time. Above all, perturbations growth time at the expense of Rayleigh-Taylor instability becomes substantially low.

In this wavelength area strength has the most evident stabilizing effect. Propagation of perturbations emerging from the rigid wall at the area of very short wavelengths ($\lambda \to 0$) for ideal liquid layer is out of question as soon as turbulent mixture occurs in it, which leads to complete destruction of the layer.

Actually, turbulent mixture layer width for specific reflection time will be $\alpha \sim 0.4\ g\ \tau_0^2/2 \sim 3.18\ (\gamma - 1)x_m \sim 0.7$ cm, which significantly exceeds titanium layer thickness.

3. Discussion of results

The most characteristic of perturbations propagation through lightgas layer is multiple change of perturbation phase depending on wavelength. Fig. 5 shows relative perturbation amplitude $(a(t)/a_0)$ vs wavelength rated to min gasdynamic thickness (λ/x_m) for the time momentum $t = 20$ ns.

It can be seen that for determined wavelength values $(\lambda/x_m \sim 40; 3; 2)$ perturbation amplitude converts to zero. This can be explained by interaction of several waves in gas with accelerated layer. At short wavelength area perturbations depression can be due to layer strength. For ideal liquid medium the nature of perturbation propagation from cascade to cascade via lightgas layer is determined by relationship of three characteristic time values:

- reflection time $\tau_0 \sim 4x_m/c_m$;
- time of compression wave circulation over the gas layer perpendicularly to motion $\tau_s \sim \lambda/c_m$;
- perturbation growth time due to Rayleigh-Taylor instability $\tau_i \sim \frac{1}{U_0}\sqrt{\frac{x_m\lambda}{\gamma-1}}$.

In case of $\tau_s << \tau_i$ perturbation amplitude is doubled when reflection occurs. When $\tau_0 \sim \tau_s$ and $\tau_s \leq \tau_i$ substantial perturbation depression is possible due to interaction of compression waves with rarefaction waves in gas having thick layer. When $\tau_0 >> \tau_i$, perturbations grow rapidly thanks to Rayleigh-Taylor instability. In this case perturbation depression is possible only due to thick layer strength or viscosity. Substantial strength effect in the above case manifests itself at $\lambda/x_m < 2.78$ ($\lambda < 1$ cm). Practical significance of the above results is as follows. If the most "dangerous" perturbations wavelength is known, optimum light gas layer thickness (or density) selection is possible only at precise gas parameters selection. The results are to some extent true for spherical cumulating systems as well.

References

[1] Kosyrev AS, Aleksandrov VA, Popov NA, Fusion first for USSR, Nature, 275, 5680, 476, (1978).

[2] Chabildas *et al.*, Shock compression of condensed matter, Proc. of the American Physical Society Topical Conference, 1025, (1991).

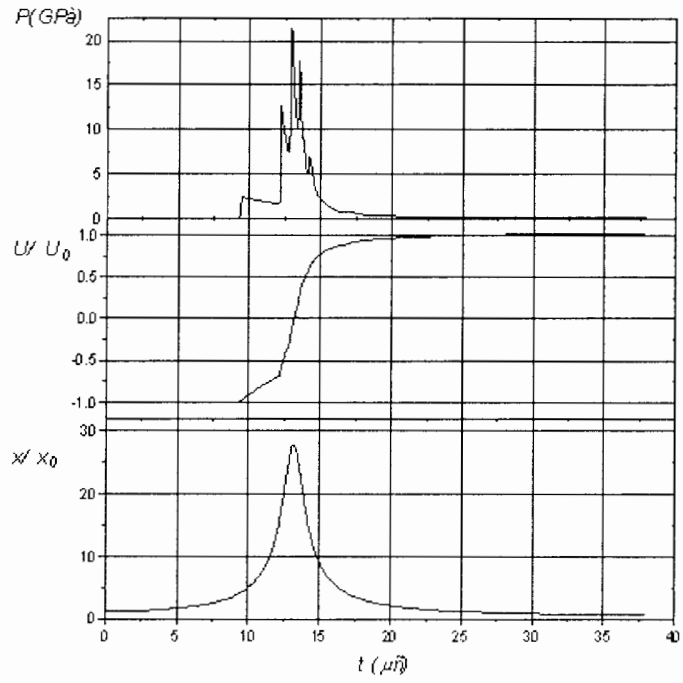

Figure 2. Characteristics of Ti layer motion.

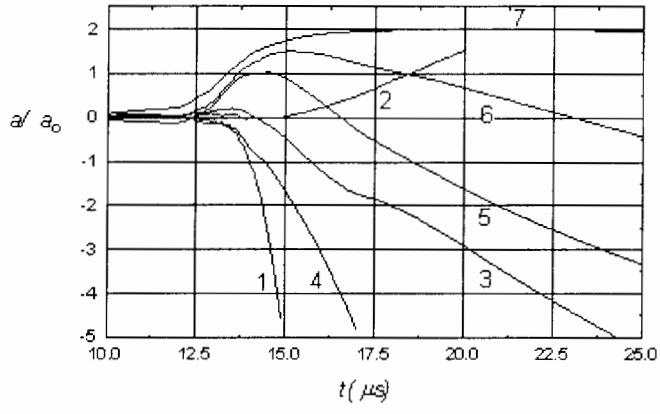

Figure 3. Perturbations amplitude vs time for different λ. 1) 0.5 cm; 2) 1 cm; 3) 2 cm; 4) 5 cm; 5) 10 cm; 6) 20 cm; 7) 100 cm.

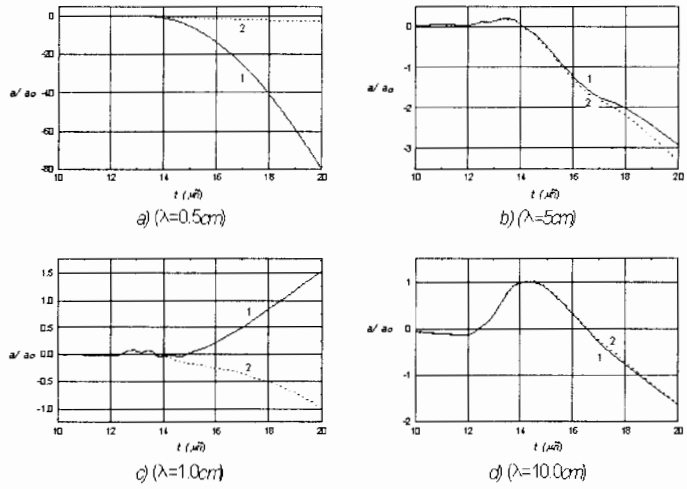

Figure 4. Perturbations amplitude on Ti layer surface in time at different strengths. 1) $Y = 0.1$ GPa; 2) $Y = 2$ GPa.

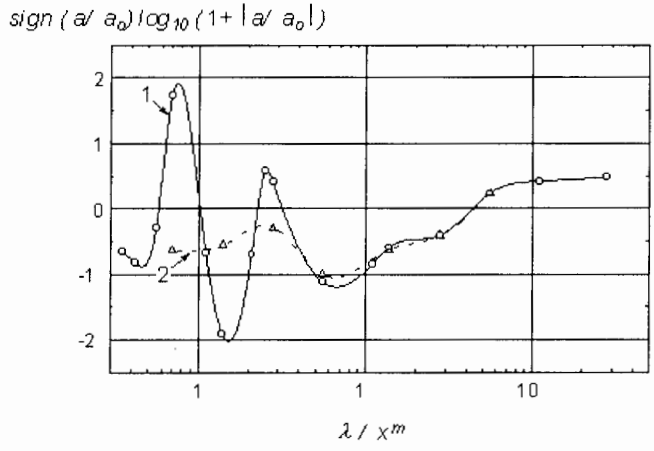

Figure 5. Relative perturbation amplitude on Ti layer surface facing gas layer vs wavelength for time momentum $t = 20$ ms. 1) $Y = 0.1$ GPa; 2) $Y = 2$ GPa.

Measurements of Turbulent Richtmyer-Meshkov Mixing on the AWE HELEN Laser

K. Oades
AWE(A), Building C15, READING, Berkshire, RG7 4PR, England

Abstract: The growth of the turbulent mixing zone at a Richtmyer-Meshkov unstable interface is being investigated in a series of experiments on the HELEN laser. In the experiment, two beams of the laser, delivering a total of 900 J in a 900 ps Gaussian pulse, are used to heat a gold hohlraum target. This produces a radiation drive which causes a shock to be driven down a thin-walled tube, mounted on the end wall of the hohlraum, which contains two plastic foams, of densities 0.2 g cm^{-3} and 0.04 g cm^{-3} respectively; the shock being driven from the high density to the low density material. A random three-dimensional perturbation is added to the interface between the two foams by forming the foams against a pre-characterised surface. Measurements of the width of the turbulent mixing zone are made via X-radiography, by seeding the interface with a highly opaque tracer layer with a mass negligible compared to that of the foams. Information on the distributions of the materials within the mixing zone can be obtained by using spectroscopically distinct materials for the foams and the tracer layer

1. Introduction

The growth of Richtmyer-Meshkov instability [1, 2] in the non-linear and fully turbulent regimes is currently the subject of widespread investigation, both experimental [3, 4] and theoretical [5, 6]. An experiment has been designed for the AWE HELEN laser, in which we aim to measure the growth of a turbulent mixing zone initiated by Richtmyer-Meshkov instability at the interface between two low-density foams. The ultimate aim of the experiment is to use spectroscopic methods to measure the individual material distributions within this turbulent mix region for comparison with model calculations. In this way it should also be possible to address issues such as the relative growth rates of bubbles and spikes. Foams, not full-density material, are used to give acceptable X-ray transmission through the relatively wide target, which is necessary to reduce problems due to two-dimensional effects. The target design is shown in Figure 1. The target consists of a 1mm long two-section tube with an internal diameter of 400 microns. The first section of tube contains the higher density foam, triacrylate at 0.20 g cm^{-3}, which is contained within 25 micron thick gold walls to reduce lateral energy losses and maintain the planarity of the shock. The second section of tube contains lower density foam, triacrylate at 0.04 g cm^{-3}, contained within a plastic-walled tube, with a wall thickness of less than 10 microns, to allow X-ray diagnosis at photon energies of around 3 keV. The length of the first tube section is 200 microns, and that of the second section is 800 microns. A random three-dimensional perturbation with an rms amplitude in the range 3 - 5 microns is formed on the interface by creating a suitable surface on a thin plastic barrier, characterising this on a Laser Scanning Microscope, and forming the two foams against it in situ. A typical power spectrum obtained from the measurement of the interface barrier is shown in Figure 2; destructive characterisation of sample foam surfaces created in this way has shown good replication of the original surface. For the preliminary measurements reported here the

More information - Email: koades@awe.co.uk

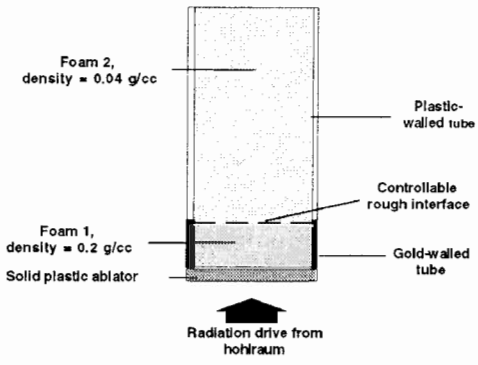

Figure 1. Schematic of the Richtmyer-Meshkov experiment target design.

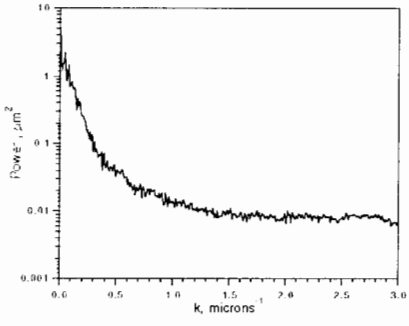

Figure 2. Power spectrum obtained from Laser Scanning Microscope measurement of interface.

barrier consisted of 1 micron of Parylene-N, and this was coated with a 0.1 micron thick disc of gold, with a diameter of 300 microns, to act as an opaque tracer to identify the width of the mix region. Future targets will either use a lower opacity tracer material with spectroscopic absorption features matched to those of a foam dopant material or two doped foams with no tracer layer.

2. Experimental

In the experiment, two 900ps, 450J laser pulses are used to heat a gold hohlraum target. This hohlraum produces a radiation drive, with a peak Planckian-equivalent temperature of approximately 132 eV, which drives a shock wave from the solid plastic ablator into the foam-filled tube. The shock passes through the foam-foam interface from the dense to the less dense foam after approximately 7 ns, resulting in a post-shock Atwood number of -0.6 and an instantaneous acceleration which gives the interface a velocity of 35 microns/ns. Previous experimental work [7] and two-dimensional hydrocode simulations confirm that the shock and

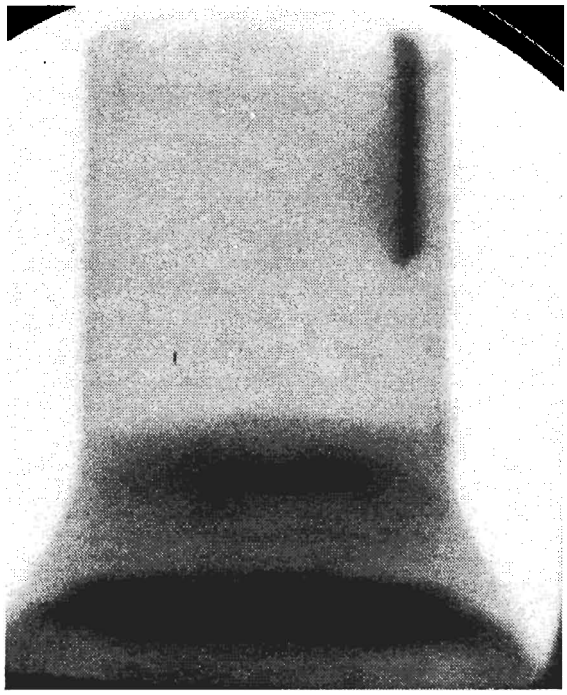

Figure 3. Experimental data - transmission image from HELEN shot 9049, t = 17 ns.

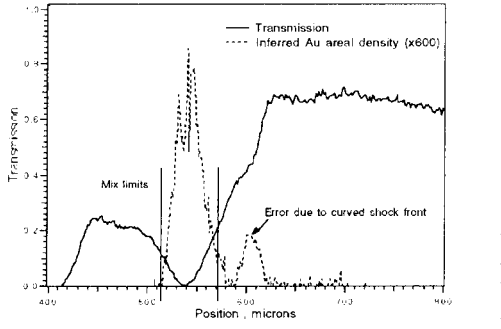

Figure 4. Transmission along axis, and areal density profile - HELEN shot 9049, t = 17 ns.

interface remain sufficiently planar for a reliable measurement to be made on the growth of the turbulent mix region. Later in time, two further laser pulses, with pulse durations of only 100ps, are focused onto 5 micron diameter silver-coated carbon fibres to provide the sources for point-projection radiography of the foam target. Typically these radiographs are taken 5ns apart to give a clear indication of the development of the mix region. Spatial resolution, due to the finite size of the emitting region, is about 10 microns, and motion blurring due to the 100 ps pulselength is less than 5 microns. On each shot the carbon fibres are carefully positioned to the calculated position of the interface for each backlighting time to minimise the effect of parallax on the measurement.

3. Results

Typical radiographs from this experiment are shown in Figures 3 and 5, with the shock being driven from the bottom to the top of the figure in each case. These images have been processed to take into account the response of the detector, and then converted to show the target transmission by dividing by the unattenuated backlighter signal. The images show the unshocked foam towards the top of the tube, the position of the shock front (clearly visible due to the lower transmission of the compressed foam behind the shock) and the extent of the opaque region due to the gold tracer disc on the interface (limited to the central section of the tube). The opaque region in the lower part of each figure is that part of the plastic ablator which is driven up the tube. A tungsten wire visible on the tube wall is used as a spatial fiducial. The width of the mixing zone can be determined by taking linescans along the axis of the tube and identifying the changes in transmission due to the gold layer. A more detailed analysis is performed by using the information on the foam density profile in the annular region away from the gold layer to infer the areal density of the gold in the axial region. These linescans and the associated areal density profiles are shown in Figure 4 for the backlighting time of 17 ns, and in Figure 6 for 22 ns. For the target shown here the width of the turbulent mixing zone is 55 microns at 17ns (10ns after shock passage) and 80 microns at 22ns. These data are compared with the results of a one-dimensional hydrocode calculation including a turbulent mix model due to Youngs [6]. Figures 7 and 8 show the calculated mass fractions through the mixing zone at the measurement times; comparing the overall widths of the mix region at the two times shows good agreement between the experiment and this calculation.

4. Conclusions

Experiments have been conducted using the AWE HELEN laser to investigate the growth of the turbulent mixing zone at a Richtmyer-Meshkov unstable interface. A strong shock is driven through a foam column in which there is an interface between high density and low density foam. A random three-dimensional perturbation with an rms amplitude of 3 - 5 microns is formed on this interface. Measurements of the width of the turbulent mixing zone, made via X-radiography of the opaque tracer layer, are shown to be in good agreement with calculations performed with a one-dimensional hydrocode containing a turbulent mixing model. Further experiments are planned to extend the range of these measurements, and ultimately information on the distributions of the materials within the mixing zone will be obtained using spectroscopic methods.

Acknowledgement. Acknowledgements are due to all those people without whom this work would not have been possible, notably the Laser Operations and Target Fabrication groups, and in particular Colin Horsfield and Wigan Nazarov (Dundee University) for their work on the development of the foam

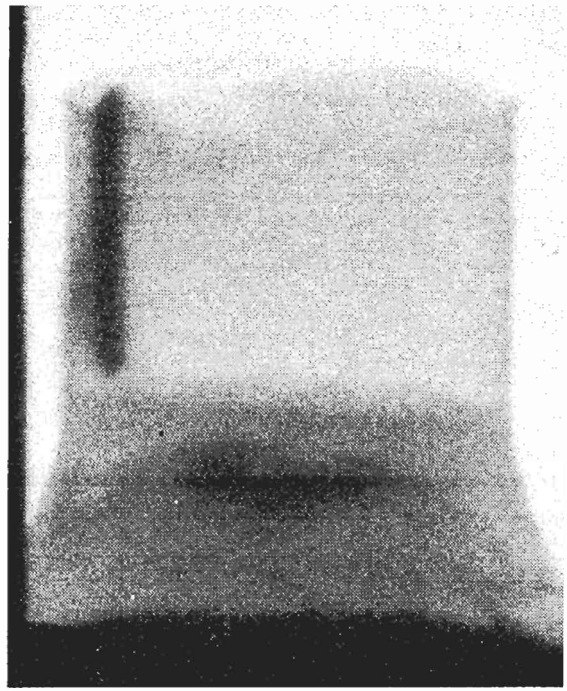

Figure 5. Experimental data - transmission image from HELEN shot 9049, t = 22 ns.

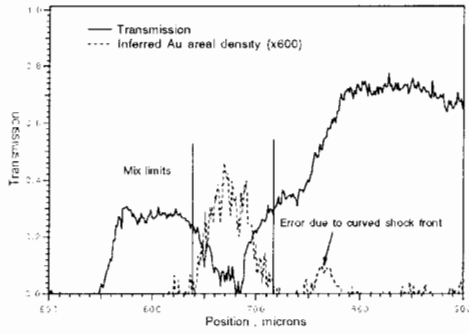

Figure 6. Transmission along axis, and areal density profile - HELEN shot 9049, t = 22 ns.

targets.

(c) British Crown Copyright 1997/MOD Published with the permission of the controller of Her Britannic Majesty's Stationery Office.

References

[1] Richtmyer RD, Communication on pure and applied mathematics, 13, 297-319, (1960).
[2] Meshkov EE, NASA TT F-13, 074, (1970).
[3] Dimonte G *et al.*, Phys. Rev. Lett., 74, 4855, (1995).
[4] Peyser T *et al.*, Phys. Rev. Lett., 75, 2332, (1995)
[5] Alon U *et al.*, Phys. Rev. Lett., 74, 534, (1995)
[6] Youngs DL, Laser Particle Beams, 12, (1994)
[7] Oades K *et al.*, Proc. of the 5th International Workshop on the Physics of Compressible Turbulent Mixing, Stony Brook, NY, USA, (1995)

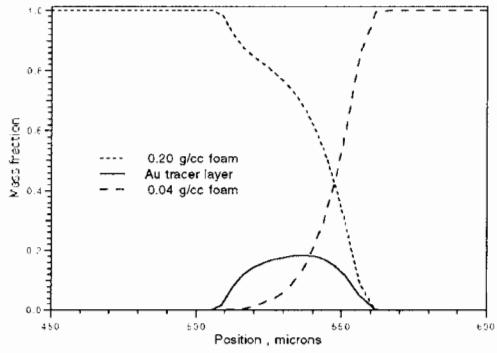

Figure 7. Calculated mass fractions at t = 17 ns.

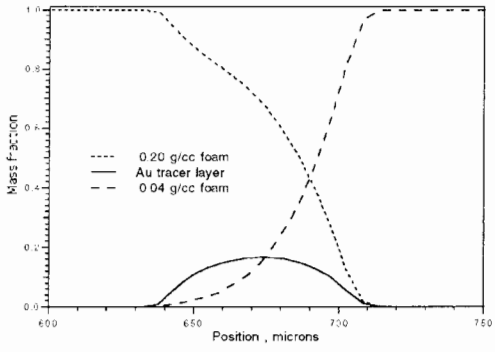

Figure 8. Calculated mass fractions at t = 22 ns.

Scaling of the Rayleigh-Taylor Nonlinear Evolution in Ablatively Driven ICF

D. Oron[1,2], U. Alon[1,3] and D. Shvarts[1,4]
[1]Dept. of Physics, Nuclear Research Center Negev, Israel
[2]Dept. of Physics, Ben Gurion University, Beer-Sheva, Israel
[3]Dept. of Physics, Princeton University, Princeton, NJ, USA
[4]Dept. of Mechanical Engineering, Ben Gurion University, Beer-Sheva, Israel

Abstract: A theoretical model for the ablatively driven Rayleigh-Taylor (RT) instability single-mode and multimode mixing fronts is presented. The effect of ablation is approximately included in a Layzer-type potential flow model, yielding the description of both the single-mode evolution and the two-bubble nonlinear competition. The ablative stabilization of the linear growth rate obtained by the model is similar to the Takabe formula. The single-bubble terminal velocity is found to be reduced by ablation, in good agreement with numerical simulations. Two-bubble competition is then calculated, and a statistical mechanics model for multi-bubble fronts is presented. The asymptotic ablation correction to the classical RT $\alpha g t^2$ law is derived. The effect of this correction to the ablation front mixing zone evolution in an ICF target is discussed.

1. Introduction

The understanding of hydrodynamic instability growth at an ablation front is crucial for the achievement of energy gain in inertial confinement fusion (ICF). RT instabilities may break up the imploding shell and prevent the formation of a hot spot. Thus, RT instabilities limit the radius of the imploding shell to several times its thickness. The stabilizing effects due to the ablative flow, that reduce the instability growth rate as compared with "classical" RT instability, may enable the design of fusion pellets with higher aspect ratios, thus requiring less driver energy to achieve energy gain [1].

The initial perturbation, due to both surface roughness and laser imprint, is of a multimode nature, with wave numbers spanning over 3 orders of magnitude. A full numerical simulation of the problem is practically impossible. As a result, the bubble front evolution has to be described by a simple model. Two main classes of models of this kind exist [11].

Modal models (Haan [2], Ofer [3]) describe the front evolution in k-space, taking into account the single-mode behavior, multimode saturation, and mode coupling effects. Bubble competition models (Glimm and Sharp [4], Alon *et al.*[5]) describe the instability front in real space, taking into account single "particle" (bubble) behavior and two-particle interaction (bubble merger). These models deal with classical RT instability in the incompressible limit.

Simpler models, such as those by Takabe [6] and Neuvuzayev [7], include the nonlinear effects in an effective diffusion equation for the evolution of the mixing zone thickness.

In the present work, the bubble competition model of Alon *et al.*[5] is extended to include, albeit approximately, the main effects of ablative stabilization, in order to estimate the effects of ablative stabilization on the bubble front evolution. Since spherical effects are relatively

More information - Email: danor@bgumail.bgu.ac.il or schwartz@bgumail.bgu.ac.il

unimportant during the acceleration stage, the present mode is planar. In the absence of a satisfactory 3D bubble merger model, and since much of the physics in 2D and 3D appears to be similar [12], the present model is 2D.

In section 2, the potential flow model, describing the single- and the two-bubble behavior, is discussed in detail. In section 3, the statistical mechanics model for multimode perturbations is developed.

2. The potential flow model

In this section an incompressible potential flow model, which is a generalization of Layzer's single-bubble model [8] and the Hecht *et al.*[9] two-bubble competition model, is described. The model considers the simple case of an incompressible inviscid fluid accelerated by a much lighter fluid (A=1), represented by a free boundary with constant supporting pressure.

The fluid velocity is derived from a potential, $\vec{u} = \nabla\Phi$. The time dependence of all flow variables is found by expanding the flow equations and the Bernoulli equation to second order at the bubble tips [9].

2.1. Single-mode RT bubble with ablation

The effect of the ablative flow is included in the model through the addition of an ablative term $\Delta\Phi = -cV_a z$ to the potential, resulting in a net flow of the fluid perpendicular to the fluid interface, where c is a constant of order 1 to be determined later, and V_a is the ablation velocity. The definition of the constant c includes the ambiguity of the definition of the ablation velocity $V_a = \overset{o}{M}/\rho_{\max}$ (where $\overset{o}{M}$ is the mass ablation rate per unit area) using a sharp boundary density profile. c ¿ 1 since the density at the instability front is lower then the maximum density. We, therefore, choose the potential:

$$\Phi(x,z,t) = a(t)\cos(kx)\,e^{-kz} - cV_a z \tag{1}$$

where $k = 2\pi/\lambda$ and c is a constant of order unity.

The bubble tip has to satisfy two equations: the Bernoulli equation for a constant supporting pressure, and a kinematic equation, requiring that the fluid move with the ablation velocity relative to the interface. Expanding the interface to second order near the bubble tip results in three ODE's in the bubble height, bubble curvature and the potential parameter a(t) [9].

For small initial perturbations we get the linear growth rate:

$$\gamma = \frac{-ckV_a + \sqrt{(ckV_a)^2 + 4kg}}{2} = \gamma_{cl}\cdot\left[-\frac{c}{2}\overline{V_a} + \sqrt{1+\left(\frac{c}{2}\overline{V_a}\right)^2}\right] \tag{2}$$

where $\overline{V_a}$ is the non-dimensional ablation velocity: $\overline{V_a} = \frac{kV_a}{\sqrt{kg}}$, and $\gamma_{cl} = \sqrt{kg}$.

The Takabe formula for laser accelerated targets [6], $\gamma = \sqrt{kg} - 3kV_a = \gamma_{cl}\left(1 - 3\overline{V_a}\right)$ is recovered for small values of V_a using c=6.

Nevertheless, it should be noticed that the present potential flow model result exhibits no cutoff in the linear growth rate, and thus deviates from the Takabe result at high values of the

non-dimensional ablation velocity. A comparison of the model results for the reduction of γ with the Takabe formula is presented in fig. 1(a).

Using the constant c=6 derived earlier, the asymptotic bubble velocity is:

$$u_{asy} = -2V_a + \sqrt{4V_a^2 + \frac{g}{3k}} = u_{cl} \cdot \left[-2\sqrt{3}\overline{V_a} + \sqrt{1 + 12\overline{V_a}^2}\right] \tag{3}$$

where $u_{cl} = \sqrt{g/3k}$ is the classical asymptotic bubble velocity.

A comparison of the model results for the reduction of u_{asy} with simulation results is presented in fig. 1(b). Also plotted is the value $0.09\gamma\lambda$, which is the asymptotic velocity assuming that the transition to nonlinearity occurs at an amplitude of 0.09λ (dotted). The agreement between the model, the simulation and the $0.09\gamma\lambda$ prediction is good.

The simulations were performed on LEEOR-3D, an ALE hydrodynamic code [3] including laser energy deposition, 2-group radiation diffusion, and two temperatures (ions and electrons). The equation of state was taken as that of an ideal gas. The foil was a 90μm CH2 foil, irradiated by a 350nm laser, with an intensity $I \approx 5 \cdot 10^{14} W/cm^2$. The acceleration is approximately $4 \cdot 10^{15} cm/\sec^2$, and the initial perturbation was seeded only after the ablation front had reached a steady profile.

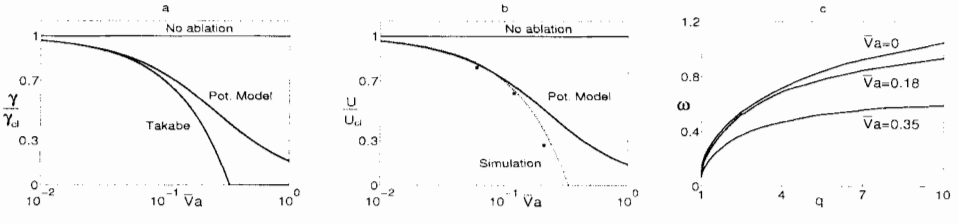

Figure 1. a) The reduction of γ due to ablation: Takabe formula vs. model. b) The reduction of u_{asy} due to ablation: simulation, model, prediction of $0.09\gamma\lambda$. c) The merger rate ω(q) at several values of $\overline{V_a}$, where $q = \lambda_1/\lambda_2$.

2.2. Two-bubble competition with ablation

Following Hecht *et al.*[9] we use the potential:

$$\Phi = \sum_{n=1}^{3} a_n(t) \cos(nkx)\, e^{-nkz} - 6V_a z \tag{4}$$

and solve seven ODE's in the potential parameters $a_i, i = 1,2,3$ and the bubble heights Za_0, Zb_0 and curvatures Za_1, Zb_1. The initial condition is a velocity perturbation creating two slightly asymmetric bubbles. A typical merger process goes through several stages: a linear growth stage, in which both bubbles grow independently, a coexistence stage, where both bubbles enter the nonlinear stage almost independently and the larger one begins to outgrow the smaller one, and the merger stage, where the smaller bubble is washed downstream [9].

The time scale for a merger of two bubbles of radii λ_1, λ_2 under the conditions g, V_a can be obtained from these calculations. Defining the time of the merger process as the time between

t_1, the peak velocity of the small bubble, and t_2, when the small bubble has reached $u = 0$, and the ratio $q = \lambda_1/\lambda_2$ from the velocity ratios at t_1, the function $\Delta\tau_{merger}(\lambda_1, \lambda_2, g, V_a) = t_2 - t_1$ is defined. The fit between model and simulation is good if neither bubble is near the cutoff.

We define the merger rate $\omega = 1/\Delta t$. Changing variables to $k = (\lambda_1 + \lambda_2)^{-1}$, $q = \lambda_1/\lambda_2$, the function ω obeys two symmetry rules in which the non-dimensional variable $\overline{V_a} = kV_a/\sqrt{kg}$ is conserved, since the merger process time evolution is scalable on both the length scale and the time scale.

Thus, the function ω is actually a function of the two non-dimensional variables $q, \overline{V_a}$:

$$\omega(k, q, V_a, g) = \sqrt{kg} \cdot \omega\left(q, \overline{V_a}\right) \tag{5}$$

The value of $\omega(q)$ in several values of $\overline{V_a}$ is plotted in fig. 1(c). The merger rate $\omega(\lambda_1, \lambda_2, V_a, g)$ and the asymptotic bubble velocities $u_{asy}(\lambda, V_a, g)$ serve as input for the statistical mechanics bubble front calculation described in the following section.

3. The statistical mechanics bubble merger model

In the classical RT case, where after a sufficiently long time only the time scale associated with the acceleration is left, the bubble front reaches a scale invariant regime (Glimm and Sharp [4], Zhang [10], Alon *et al.*[5]). The addition of ablative flow adds a second time scale to the problem. A true scale invariant regime would be attained either when $kV_a << \sqrt{kg}$, which is the classical limit, or when $\overline{V_a} = kV_a/\sqrt{kg} = const.$

We first consider the case of a constant $\overline{V_a}$ where the bubble front reaches a scale invariant distribution, from which we may calculate the acceleration of the bubble ensemble. Following Alon *et al.*[5] we use the mean field approximation. The scale invariant distribution is calculated for each value of $\overline{V_a}$.

For each distribution the bubble front velocity is given by:

$$\frac{\partial h_{front}}{\partial t} = \langle u \rangle = \sqrt{g \langle \lambda \rangle} \cdot \langle \overline{u} \rangle \tag{6}$$

where $\langle f \rangle = N^{-1} \int f(\lambda) N(\lambda) d\lambda$ denotes the ensemble average, and barred values are averages over the scale invariant distribution (where the length is scaled out). Using:

$$\frac{\partial \langle \lambda \rangle}{\partial t} = \langle \omega \rangle \cdot \langle \lambda(t) \rangle = \sqrt{\frac{g}{\langle \lambda(t) \rangle}} \cdot \langle \overline{\omega} \rangle \cdot \langle \lambda(t) \rangle \tag{7}$$

we may calculate the bubble front acceleration:

$$\frac{\partial^2 h_{front}}{\partial t^2} = \frac{\partial \langle u \rangle}{\partial t} = \frac{g}{2} \cdot \langle \overline{u} \rangle \cdot \langle \overline{\omega} \rangle \tag{8}$$

Thus, assuming a constant $\overline{V_a}$, the bubble front height scales, after reaching the scale invariant regime, as:

$$h = \alpha\left(\overline{V_a}\right) \cdot gt^2, \ \alpha\left(\overline{V_a}\right) = \frac{1}{4} \langle \overline{u} \rangle \cdot \langle \overline{\omega} \rangle \tag{9}$$

For small values of $\overline{V_a}$, typical of ICF applications, the model predicts
$\alpha\left(\overline{V_a}\right) = \alpha_{cl} \cdot \left(1 - 2\overline{V_a}\right)$, where $\alpha_{cl} \approx 0.05$.

In realistic problems, $\overline{V_a}$ decreases as longer wavelengths are generated. We may now use the adiabatic assumption, that the non-dimensional ablation velocity changes slowly enough that the bubble size distribution may adjust itself to the distribution of the changing value of $\overline{V_a}$ and remain the scale-invariant one. The adiabatic approximation is found to be accurate numerically [13].

We may now write two ordinary differential equations for the time evolution of the bubble front height, assuming the scale invariant distribution for the initial value of $\overline{V_a}$ as the initial bubble spectrum:

$$\frac{d\langle\lambda\rangle}{dt} = \langle\omega\rangle \cdot \langle\lambda\rangle \tag{10}$$

$$\frac{d^2h}{dt^2} = 2 \cdot \alpha\left(\overline{V_a}\right) \cdot g \tag{11}$$

where the ensemble averages are calculated using the scale invariant spectrum of the current value of $\overline{V_a}$.

The model has been compared to a full multimode numerical simulation. The target and laser parameters were as those quoted above, except that the initial condition is a wide spectrum multimode one, using the asymptotic bubble size distribution corresponding to the initial value of $\overline{V_a}$. The initial condition included fifty bubbles with an average size of $4\mu m$, totaling an area of slightly over $200\mu m$. The acceleration is $g \approx 4 \cdot 10^{15} cm/\sec^2$, and the ablation velocity $V_a \approx 1.2 \cdot 10^5 cm/\sec$, thus $\overline{V_a}(t=0) \approx 0.21$. In fig. 2(a) the temporal evolution of the bubble front is shown, with the rising bubbles (those which dominate the flow) denoted by a '*'. In fig. 2(b) the temporal evolution of the bubble front "envelope", resulting from a bubble merger model is shown. It should be noted that the full merger model shown is slightly different from the mean-field model shown above, taking into account the finite number of bubbles, the exact initial conditions, and the correlations both in size and in temporal evolution between neighboring bubbles [13].

In fig. 3 the average penetration of the rising bubbles is shown, comparing the simulation, the mean-field model, the full model, and the mean-field model without the ablative stabilization correction, starting with the same initial velocity. There is very good agreement between the simulation and both the full and the mean-field models. The model predicts that the allowed value of $R/\Delta R$ for typical conditions of laser-driven shells is approximately 25, while the classical allowed value is $\approx$10.

References

[1] Kilkenny JD, Glendenning SG, Haan SW, Hammel BA, Lindl JD, Munro D, Remington BA, Weber SV, Phys. Plasmas, 1, 1379 and references therein, (1994) .
[2] Haan SW, Phys. Rev. A, 39, 5812, (1989); Haan SW, Phys. Fluids B, 3, 2349, (1991).
[3] Ofer D, Alon U, Shvarts D, McCrory RL, Verdon CP, Phys. Plasmas, 3, 3073, (1996).
[4] Glimm J, Sharp DH, Phys. Rev. Lett., 64, 2137, (1990).
[5] Alon U, Shvarts D, Mukamel D, Phys. Rev. E, 48, 1008, (1993).
[6] Takabe H, Yamamoto A, Phys. Rev. A, 44, 5142, (1991).

[7] Neuvazhayev VE, Phys. Rev. E, 50, 1394, (1994).
[8] Layzer D, Astrophys. J., 122, 1, (1955).
[9] Hecht J, Alon U, Shvarts D, Phys. Fluids, 6, 4019, (1994).
[10] Zhang Q, Phys. Lett. A, 151, 18, (1990).
[11] Shvarts D, Alon U, Ofer D, McCrory RL, Verdon CP, Phys. Plasmas, 2, 2465, (1995).
[12] Hecht J, Ofer D, Alon U, Shvarts D, Orszag SA, McCrory RL, Laser and Particle Beams, 13, 423, (1995); Youngs DL, Phys. Fluids A, 3, 1312, (1991)
[13] Oron D, Alon U, Shvarts D, to be submitted.

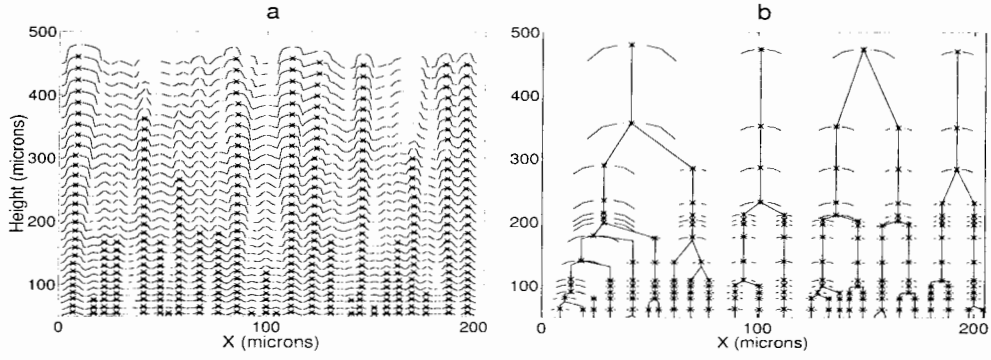

Figure 2. a) Simulation bubble front (contour of maximal light fluid penetration) evolution, rising bubbles denoted by '*'. b) Model bubble front evolution and merger history.

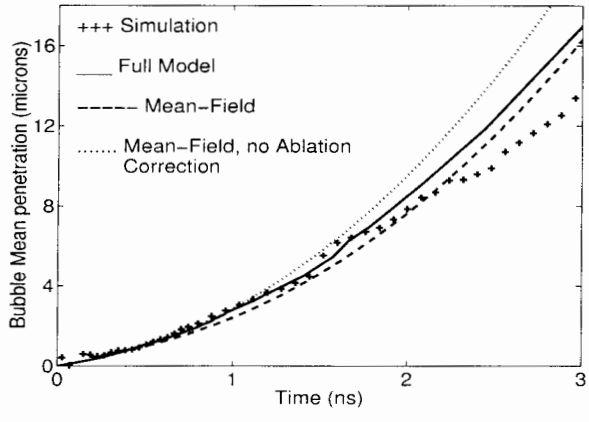

Figure 3. Mean bubble front penetration in: Simulation, Full model, Mean-field model, Mean-field model without ablation correction.

Review of Experiments and Calculations of the Compressible Richtmyer-Meshkov Instability from a Single-Mode, Nonlinear Initial Perturbation

T.A. Peyser, S.D. Murray, P.L. Miller, D.R. Farley, L.M. Logory, P.E. Stry, K.S. Budil and E.W. Burke
Lawrence Livermore National Laboratory
P. O. Box 808, L-22, Livermore, California, 94551, USA

Abstract: We review experiments and calculations of the compressible Richtmyer-Meshkov instability from a single-mode, nonlinear initial perturbation. These experiments were performed using the Nova laser. Measurements of the time-evolution of the mixing region were reported previously. We compared the experimental measurements with numerical simulations [1,2]. We found both experiment and simulation to be in good agreement with recent theories for the nonlinear evolution of the instability [3,4].

Experimental results beyond those previously presented provide additional support for the use of two phase flow models to describe the flow in the nonlinear regime. These experiments include measurement of the mixing region at additional times, including times earlier in the evolution of the instability than previously reported. We have also carried out experiments to examine the difference in the evolution of the instability from initial perturbations consisting of circular sawtooth grooves as well as rectilinear sawteeth. Our previous two-dimensional numerical simulations approximated the experimental linear grooves as circular grooves. We reasoned that the difference between the two cases would be small, based on scaling arguments, and limited to a very small region near the centerline. New experimental and numerical results confirm this. Finally, we discuss some additional issues in the derivation of the two-phase flow model used previously in describing the growth of the Richtmyer-Meshkov instability in the nonlinear phase relevant to other work presented at this meeting [5,6].

1. Review of the experiment

The experiments used a miniature beryllium shock tube mounted over a 700 μm diameter hole made at the center of the side of a 3 mm-long, 1.5 mm-diameter cylindrical gold Nova Hohlraum [7]. The shock tube was 2200 μm long, 700 μm in diameter with a 100 μm wall thickness. The working material of the shock tube consisted of a 500 μm -diameter, 300 μm -long section of a high-density (1.22 g/cm^3) brominated polystyrene ablator and a 500 μm diameter, 1900 μm long low-density (0.1 g/cm^3) carbon resorcinol foam payload. A schematic of the Hohlraum and the attached shock tube can be obtained elsewhere in these proceedings and in the literature [1,2,5,6]. Thermal x-ray radiation from the interior Hohlraum walls incident onto the exposed brominated polystyrene results in a rapid ablation of material and the generation of a strong shock (85 Mbar) which travels down the shock tube towards the perturbed plastic-foam interface. A rectilinear sawtooth pattern was machined into the high density plastic with a high initial amplitude ($a_0 = 10\,\mu$m) relative to the dominant wavelength ($\lambda = 23\,\mu$m). The large amplitude-to-wavelength ($a_0/\lambda = 0.43$) initial perturbation was chosen so that the instability would make an early transition into the nonlinear stage. The mixing region width was measured

More information - Email: peyser1@llnl.gov

with high-speed gated x-ray framing camera diagnostics using radiography side-on to the shock tube cylinder axis [1,2,5,6].

2. Effect of Mach number on the spike and bubble amplitude

High-power laser-driven experiments make it possible to achieve extremely high Mach number shocks. At the time the shock is incident on the interface, the Mach number is greater than or equal to 20. This is important since experiments at high Mach number exhibit the effects of compressibility more strongly than low Mach number experiments.

The experiments were simulated using CALE, a two-dimensional arbitrary Lagrangian-Eulerian (ALE) hydrodynamics code [8]. In ALE-type codes, the mesh moves with the flow, giving added resolution in regions of high compression. Unlike purely Lagrangian codes, however, advection is allowed so as to avoid mesh tangling. For the simulations presented here, we use an initially rectilinear grid (unless otherwise noted) with 1 micron square resolution near the material boundary. The resolution decreases away from the boundary. Because the grid moves with the flow, however, high resolution of the mix region is maintained. The numerical simulations include the cylindrical region containing the plastic, the foam, the beryllium sleeve and a portion of the gold support ring. The effects of the laser drive are simulated by applying a temperature source to the edges of the plastic which extend into the hohlraum.

Previously, we found excellent agreement on the time evolution of the mixing region between the 2D CALE simulations and the measured results of the experiment. Fig. 1 shows the time evolution of the material interface during the growth of the instability. The calculations suggest, in contrast with incompressible or weakly compressible flows, that the Mach numbers of the present flows result in spike and bubble amplitudes of roughly comparable magnitudes [9]. As shown in Fig. 1a, the instability is well within the nonlinear regime by 4 ns (approximately 0.5 ns after the shock was incident on the interface). The similarity in the morphology of the spikes (heavy material) and bubbles (light material) is readily apparent at this time. The spikes and bubbles shapes and amplitudes in subsequent material plots at 5, 6 and 7 ns continue to appear highly symmetric as shown in Figs. 1b, 1c, and 1d.

A detailed comparison of the instability with a simulation of a smooth, unperturbed interface allows us to obtain quantitative estimates of the spike and bubble amplitudes as shown in Fig. 2a. The spike and bubble amplitudes in the perturbed calculation are determined by analysis of the material plots as in Fig. 1 above and comparison with the location of the unperturbed interface at the same time in the problem. We have followed the same procedure as in our earlier work and removed the effect of the axial target decompression to facilitate comparison between experiment and calculation on the one hand and nonlinear theory on the other hand [1,2]. Fig. 2b shows the growth of the overall mix region represented by the sum of the spike and bubble amplitudes (see below). The initial interface location for the unperturbed calculation was chosen to be 290 μm, i.e., at the centerline of the 20 μm peak-to-valley saw-tooth perturbation, so as to conserve the total mass of the high-density brominated polystyrene in the calculation. We assume that the presence of the instability does not significantly alter the overall hydrodynamic trajectory of the interface. This is consistent with estimates from the numerical simulations suggesting that the kinetic energy in the mix region is much less than 0.05 of the kinetic energy in the axial flow. We find that the spike and bubble amplitudes are roughly comparable (although not identical) for the duration of the calculation and the experiment.

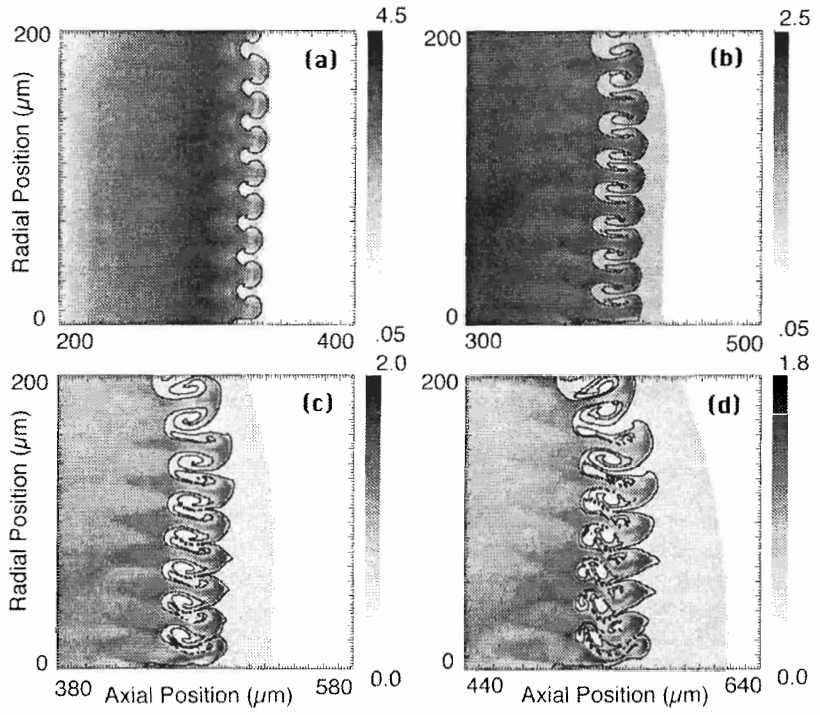

Figure 1. Density plots showing the time evolution of the material interface, from 2D CALE simulations, at (a) 4 ns, (b) 5 ns, (c) 6 ns, and (d) 7 ns

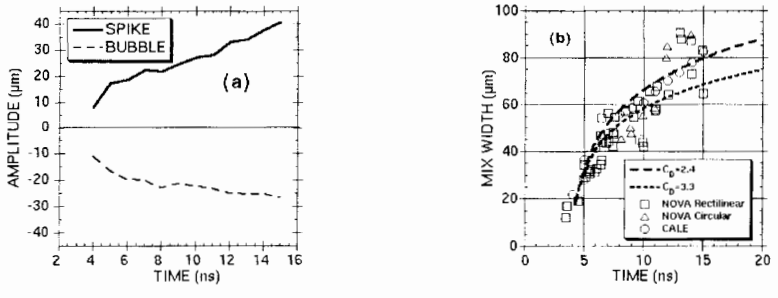

Figure 2. (a) Approximate spike and bubble amplitudes (corrected for axial target decompression), as a function of time, from comparison of perturbed and unperturbed 2D CALE simulations of the experiment; (b) Comparison of experimental data, 2D CALE simulations and results of a simple two-phase flow model for the nonlinear evolution of the instability using two values for the coefficient of drag

3. A simple two-phase flow model for nonlinear Richtmyer-Meshkov growth in the high Mach number regime

There are now numerous models for growth of the Richtmyer-Meshkov bubbles in the nonlinear regime which suggest that the evolution of the bubble velocity goes inversely with time for a single-mode perturbation. It follows accordingly that the bubble amplitudes in these models have a logarithmic time dependence [10-13]. As shown above, for conditions in the present experiment, the spike and bubble penetrations are roughly equal. The spikes are remarkably bubble-like in their appearance and time evolution, hence the total mix width for the single mode problem under these conditions can be approximated by a single, simple logarithmic time dependence [1,2].

We repeat here our derivation of a simple two-phase flow model with a clearer statement of the assumptions and the parameters in the model than provided earlier [1,2]. The equation of motion for a bubble of low density ρ_p displacing a heavier fluid of density ρ_c can be written as

$$V\left(\rho_c \frac{\Delta_A}{2} + \rho_p\right)\frac{dU}{dt} = F_a - A\,C_d\,\rho_c\,U^2 \tag{1}$$

where V is the volume of the bubble, $\Delta_A/2$ is the added mass coefficient, A is the frontal area ($A = \pi d^2/4$ for bubble of diameter d) and C_d is the coefficient of drag. Numerous experiments on bubble rise beginning with the work of Davies *et al.*in the early 1950s have shown that the bubble front retains its spherical character during its rise [14]. This is consistent with more recent compilations of bubble geometry at high Reynolds numbers applicable to this problem [15]. Since we are invoking nonlinear theory only when the amplitude and wavelength are comparable, it is permissible from the assumption of sphericity as well as from general dimensional analysis to treat the ratio of area to volume in Eq. 1 as a characteristic scalelength given by the wavelength λ of the single mode perturbation. In the high velocity limit, the added mass coefficient $\Delta_A/2$ is equal to one. Finally we assume further that there are no additional forces (gravity, pressure gradient terms etc.) acting on the system. Eq. 1 then becomes

$$\frac{dU}{dt} = -\frac{C_d}{\lambda}\left(\frac{\rho_c}{\rho_c + \rho_p}\right)U^2 \tag{2}$$

Eq. 2 can be rearranged and integrated to give the following expression for the bubble velocity

$$U = \frac{U_0}{1 + U_0\,m\,t} \tag{3}$$

where

$$m = \frac{C_d}{\lambda}\left(\frac{\rho_c}{\rho_c + \rho_p}\right) \tag{4}$$

Finally, a further integration of Eq. 3 gives

$$a = a_0 + \frac{1}{m}\ln[1 + m\,U_0\,(t - t_0)] \tag{5}$$

where a_0 is the initial nonlinear amplitude, m is given by Eq. 5 above and depends on the coefficient of drag, the densities of the material and the wavelength of the perturbation, U_0 is the initial relative velocity of the bubbles (compared to the nominal interface location) after the passage of the shock and is the time at which the nonlinear phase of the instability begins. Given

the similarity between spike and bubble amplitude growth in the high Mach numbers of the present problem, Eq. 5 can be rewritten as an equation for the total mix width evolution w where w_0 is equal to two times the instantaneous nonlinear amplitude and $U_0 = \frac{1}{2}(U_z^{spike} - U_z^{bubble})$ at the time of onset of nonlinearity.

$$w = w_0 + \frac{2}{m} \ln[1 + m\,U_0\,(t - t_0)] \tag{6}$$

This is motivated, in part, by the fact that the experimental observable from the experiment was the total mix width, not separate spike and bubble amplitudes. Since we do not know the values of the initial nonlinear amplitudes, relative velocities or time of onset of nonlinearity either a priori or directly from the experimental data, we make use of the 2D numerical simulation to obtain estimates of these quantities. An examination of the calculations suggests that the instability begins to exhibit nonlinearity at approximately 3.8 ns to 4.3 ns. Fig. 3 shows the density and velocity plots at 3.8 ns from the 2D CALE simulations. At this time, we find from

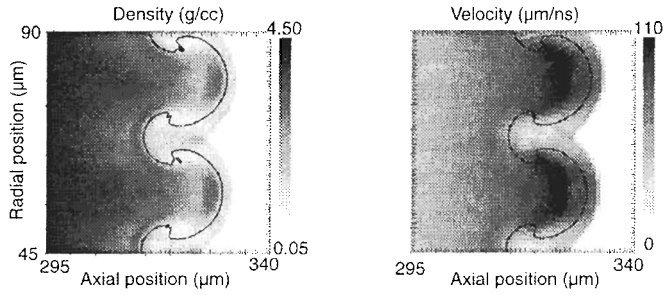

Figure 3. Density and velocity plots at 3.8 ns showing onset of nonlinear amplitudes from 2D CALE simulation

the simulations that the total mix width $w_0 = 18\,\mu m$ and one-half the relative velocity of the spike and bubble $U_0 = 14\,\mu m$ /ns. A least squares fit of the data shows further that the behavior of the measured mixing region admits a logarithmic time dependence with $m = 0.096\,\mu m^{-1}$. Assuming densities in Eq. 4 of $\rho_c = 0.4\,g/cm^3$ and $\rho_p = 1.6\,g/cm^3$ consistent with the numerical simulation, we find a value for the apparent coefficient of drag $C_d \approx 2.8 \pm 0.4$ where the uncertainty is due to the scatter in the data as well as the simplifying assumption used in the model. Predictions from the nonlinear theory for two values of the coefficient of drag are shown above in Fig. 2b. Interestingly, the coefficient of drag thus inferred from this experiment is consistent with published values for an air bubble in water at high Reynolds numbers [15].

4. Additional experimental data on the nonlinear mix width

Measurements from additional experiments carried out subsequent to the results reported previously are shown in Fig. 2b above. As with the previous results, the total mix width is inferred from a detailed analysis of the $5 - 95\%$ transmission of x-rays across the nominal mix region. The experimental data (squares) are in good agreement with both the numerical simulation (circles) and Eq. 6 above using the quoted parameters. These data points were all obtained with initial perturbations that were rectilinear in nature as shown in a high-resolution scanning electron microscope image in Fig. 4a. We have also plotted the measured mix width (triangles

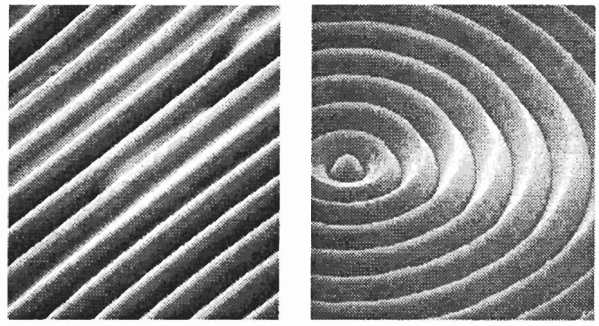

Figure 4. High-resolution scanning electron microscope image of (a) the original rectilinear sawtooth perturbations and (b) the curvilinear perturbations

in Fig. 2b) from experiments in which the initial perturbations were circular in nature as shown in Fig. 4b. There appears to be little difference between the two perturbation types which affirms the use of a two-dimensional axisymmetric code to simulate the instability growth from the non-axisymmetric perturbations used in the experiment. We have also found little difference in the growth of the mix region between numerical simulations having cylindrical and Cartesian geometries. This is not surprising from simple dimensional considerations since the radius of curvature in the calculations is large compared with the amplitude and wavelength of the perturbation.

Acknowledgement. The authors wish to thank the operations staff at the Nova laser facility for their expert technical assistance. In addition, we wish to thank H. Louis, T. Demiris and their colleagues for their assistance with the target fabrication and characterization. This work was performed under the auspices of the U.S. Department of Energy by the Lawrence Livermore National Laboratory under Contract No. W-7405-ENG-48.

References

[1] Peyser TA *et al.*, in: Proc. of the Fifth IWCTM, 257, (1996).
[2] Miller PL *et al.*, in: Proc. of the Twentieth ISSW, 581, (1996).
[3] Peyser TA, *et al.*, Phys. Rev. Lett., 75, 2332, (1995).
[4] Alon U *et al.*, Phys. Rev. Lett., 72, 2867, (1994); J. Hecht *et al.*, Phys. Fluids, 6, 4019, (1994).
[5] Farley DR *et al.*, these proceedings.
[6] Logory LM *et al.*, these proceedings.
[7] Campbell EM, Lasers and Particle Beams, 9, 209-231, (1991).
[8] Barton RT, Numerical Astrophysics, 482, (1985).
[9] Shvarts D, Oron D, personal communication, (1997).
[10] Hecht J, Alon U, Shvarts D, Phys. Fluids, 6, 4019-4030, (1994).
[11] Haan SW, Phys. Rev. A, 39, 5812-5825, (1989).
[12] Jacobs JW and Shelley JM, Phys. Fluids, 8, 405, (1996).
[13] Zhang Q and Sohn S, Phys. Fluids, 9, 1106, (1997).
[14] Davies RM and Taylor G, Proc. Roy. Soc of London A, 200, 375, (1950).
[15] Clift R, Grace JR and Weber ME, Bubbles, Drops and Particles, Academic Press, NY, (1978).

Software for TMZ Image Processing

A. Poduvalov
Russian Federal Nuclear Centre - Institute of Experimental Physics
Prospect Mira 37, 607190, Sarov, Nizhny Novgorod Region, Russia

Abstract: The paper describes software capabilities for processing images obtained by experiments looking into the turbulent mixing zone (*TMZ*) structure used shock tubes (*ST*) and convergent jelly cylinders. The software is applied to image processing based on multi-shot imaging. Each scanned image is using as a background for marker definition of the location of interface or wave front. Specific processing algorithms for these coordinates are to develop a protocol with relationships to account for *TMZ* behavior with time. With "laser sheet" application, the software also incorporates functions to visualize the flow images produced by both numerical simulation and experimention in superposition way.

1. Introduction

From the multiple-shot *TMZ* imaging, there may be up to 32 images provided for processing in each experiment. Every image contains information on the behavior of interface or wave front at a certain point in time. Every interface or wave front is accounted by a certain group of points, their coordinates relative. Processing the coordinates of grouped points can result in relationships that define the *TMZ* behavior in time. Shock-tube experiments have up to 7 the groups per image, each containing about 80 points.

It had been the author's task to develop software that would cover the entire processing run for scanned *TMZ* images. What motivated the softwave development for *TMZ* coordinates entry to PC is that the market had no inexpensive and easy-to-operate codes operating in *OS* Windows environment and capable of reading the digital coordinates of an outline from the image and then storing these coordinates as charts into the text file. For example, such code as Corel Photo Paint [1] can only allow the user to highlight in the status line the current template coordinates of the cursor moving around the image, but it is unable to keep them accessibly formatted in the file. The system is required to store as many as 32 images and allow their ready interswitching. Given the total number of points up to about 2000, the marking becomes a long procedure, therefore the software must involve the exit possibility with the current status saved. With a repeat entry, a states file can be opened to go back throng the previous digitization history. Moreover, the software should provide for a specialized algorithm for the data from a set of images to be processed and integrated into a resulting protocol. The same software incorporating bath coordinates identification and final data processing functions helps improve performance and efficiency of the whole system. All processing procedures are consistently implemented in the same application.

2. Software elements

The software incorporates two Windows applications:

More information - Email: otd03_2305@spd.vniief.ru

- **Autoview** (intended for *TMZ* image processing in ST and convergent jelly cylinder experiments);
- **Profi** (*TMZ* image processing in "laser sheet" experiments).

2.1. TMZ image processing for ST experiments

The **Autoview**-based data processing technology in ST experiments includes the following steps:

- *scanning and saving the TMZ images from photonegatives or prints;*
- *reading digital coordinates of the interface or wave front.* This process must be followed carefully, because of the application exit being possible with the current status saved. With repeat application loading, the file can be opened to scan back the previous digitization history. The image in the application window can be highlighted in shades of gray, while digitized point coordinates can be indicated at user's will with color markers variable in size. This feature is useful to discriminate one group of points from another. The image is scrollable. A status line has been incorporated which is to display the cursor coordinates, shape and color, the point darkening code, and the grouped number of points. Switching from one image to another is provided by switches in the non-modal dialog window. There is a service to delete and move the marked points.
- *systematization and integration of data from a set of images, output protocol generation.* Every image has an average value to be set for each digitized interface or wave front, with the independent variable being the time point, and the average mentioned as dependent variable (i.e. interface or wave front displacement in relative units at a certain time). Eventually, there should be a family of curves generated, each curve shoving the *TMZ* or wave front behavior at a specified point in time.

2.2. TMZ image processing in convergent jelly cylinder experiments

Figure 1 shows a scanned flow image from multiple-shot imaging of the experiments with jelly cylinder convergence.

The following data are digitized interactively for each image:

- point coordinates of the inner shell boundary (the points are needed to define the center for each image);
- coordinates of the points defining protruded shapes (as "bubbles") on the *TMZ* inner boundary;
- coordinates of points for the *TMZ* outer boundary shape;
- coordinates of points for jelly penetrating into explosion products (EP) on the outer boundary.

The following quantities are obtained as interim (i.e. at a specified time) for each image:

- front radius of *TMZ* inner boundary as the arithmetic mean;
- front radius of *TMZ* inner boundary with the allowance for "bubble" magnitudes;
- front radius of *TMZ* outer boundary;
- front radius of jelly penetrations into EP.

The software run results in a protocol containing relationships such as interface displacement versus time, interface acceleration versus time, total *TMZ* thickness versus time and other derivative data.

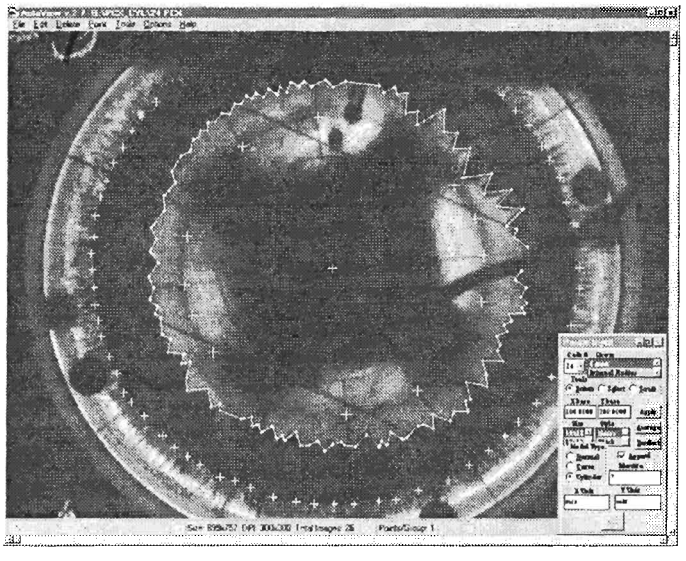

Figure 1. Flow image from jelly cylinder convergence experiments.

2.3. Image processing in "laser sheet" experiments

The "laser sheet" experiments [2] were required to evaluate qualitatively the agreement (in geometry and time history) between the flow images obtained by numerical simulation and experiment. This check for agreement is done by superposing the volume concentration isolines of the experimental images on those of the images produced by simulation.

Profi performs the flows image processing in steps as follows:

- enters the experimental *TMZ* flow images into the system memory;
- converts the entered images into a volume concentrations matrix through the optical wedge (OW) while adjusting for nonuniform backlighting across the channel where volume concentrations are non-zero;
- builds isolines; superimposes the simulated and experimental isolines;

- superimposes the images of volume concentration matrices obtained experimentally and the calculated isolines.

As a second step, darkening intensities are converted to volume concentrations using optical wedge technique. The *OW* pattern (individual for each experiment) is represented by several rectangles varying in darkening intensity. The light intensity is decreasing from grade to grade in *OW* by a constant factor of $\sqrt{2}$. The darkening intensity for each point of the image is converted to the air volume concentration in a line-by-line manner via *OW* pattern. The *OW* reference points are used to generate a tabulated transfer function to translate from one unit of measurement to another. The points in between the *OW* reference points are found by linear interpolation.

Figure 2 shows a scanned image of "step"-shaped flow. It is apparent from the figure, that the image darkening intensity in the arrow-pointed direction (100% air volume concentration) is not constant, but it has the maximum in the middle and is decreased towards the edges. For line-by-line image processing, a darkening code is set in each line of 100% air volume concentration, which is taken from the vertical dashed line in white, whose location is predetermined to be in the air region. The transfer function for each line is updated based on this code.

When a volume concentrations matrix has been developed from the flow image, isolines are to be built at 0.15 and 0.9 levels, respectively, and then superimposed on the respective isolines as obtained by numerical simulation (Fig.3a). Also, superposition is performed for calculated isolines on the experimental volume concentrations matrix (Fig.3b).

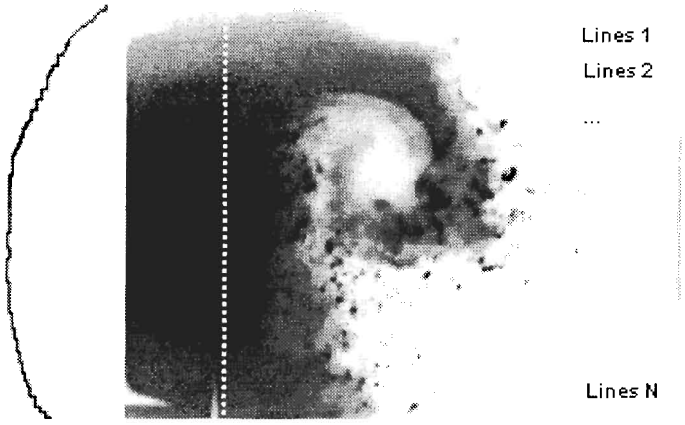

Figure 2. Scanned flow image Left-darkening intensity variation over the image area (arrow-pointed along white line).

3. Conclusions

The software package **Autoview** v.2.7 for Windows 95 has been developed and is successfully used for *TMZ* image processing in shock-tube and jelly cylinder convergence experiments. With this software, all the *TMZ* image data can be digitized interactively and then obtain a protocol with relationships describing the *TMZ* behavior. Using this software allows higher speed of

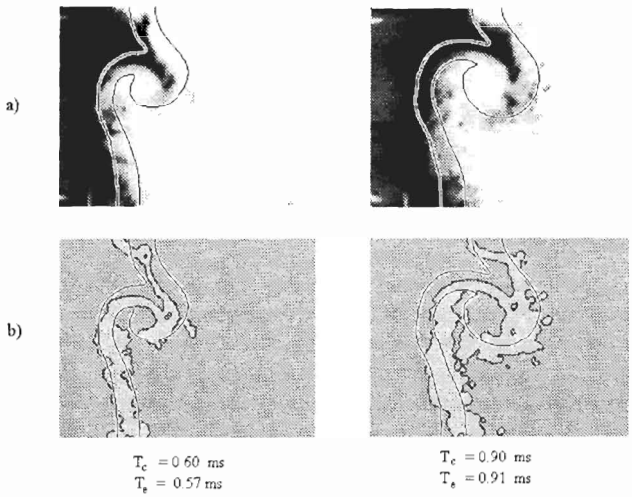

Figure 3. "Step"-shaped initial perturbation. Volume concentration isolines taken at the levels β_{lower} = 0.15 and β_{higher} = 0.9 T_c-time point in calculations, T_e-time point in experiment.

TMZ image processing, as well as unbiased and accurate output data resulting from more numerous input points.

Comparative analysis has been done for image processing manually and using this software. The analysis has found a good agreement to be between the manually obtained data and those resulting from software processing. There have been no significant inconsistencies in terms of basic relationships (inner shall radius, interface displacement length) for jelly cylinder convergence experiments.

The above-described software has been successfully applied in selected experiments to study *TMZ* interface and wave front behavior, the cases with spherical shape (reproducibility experiments).

References

[1] CorelDRAW User's Manual, Version 4.0., COREL CORPORATION, (1993).

[2] Dudin VI, Kholkin SA, Meshkov EE, Poduvalov AN, Til'kunov VA, Tolshmyakov AI, Yanilkin YB, Studying for evolution of perturbations and turbulent mixing at the gas-gas interface by "laser knife" method, Preprint, RFNC-VNIIEF, 49-96, Sarov, VNIIEF, 8, (1996).

Velocity Measurements in Turbulent Gaseous Mixtures Induced by Richtmyer-Meshkov Instability

F. Poggi, M.H. Thorembey, G. Rodriguez and J.F. Haas
Commissariat à l'Energie Atomique / Vaujours-Moronvilliers
B.P. 7, 77181 Courtry, France

Abstract: Instantaneous velocity measurements in a gaseous mixture arising from the shock wave-induced Richtmyer-Meshkov instability are conducted for the first time in a shock tube. Laser Doppler anemometry gives us the turbulent kinetic energy evolution of the mixing zone at several locations. In particular, we study the gaseous mixture interaction with reflected shock waves from the shock tube end wall. Experimental results quantify the turbulence level before and after the amplification by shock interaction and the decrease of that level between two shock arrivals.

1. Introduction

The Richtmyer-Meshkov instability (RMI) occurs when a shock wave accelerates a perturbed interface between two fluids of different densities. The RMI is a baroclinic phenomenon: the production of vorticity is proportional to the vector product of pressure gradient of the shock and density gradient at the interface. It leads to an amplification of the interface perturbations and possibly to the formation of a turbulent mixing zone (TMZ). This instability appears in technological applications such as the inertial confinement fusion capsules [1]. Thus this subject is widely investigated from experimental, theoretical and numerical points of view [2]. However the available experiments are essentially schlieren visualizations of the flow. Only some diagnostics (X-rays, infra-red absorption or emission and differential interferometry) provide, in addition to the thickness, average density profiles of the gaseous mixture [3, 4]. These quantities (thickness and density distribution) result of the turbulence diffusion of the mixing zone. They give an insufficient information about it.

The purpose of the present experimental investigation is to directly characterize the turbulence intensity in a gaseous mixture arising from a plane discontinuous heavy-light interface between sulphur hexafluoride (SF_6) and air. Kinetic energy profiles are obtained from velocity measurements when the TMZ sweeps by the fixed measurement abscissa. We measure instantaneous velocities by Laser Doppler Anemometry (LDA). The few investigators who study turbulent air flows in shock tubes generally use hot wires [5, 6]. The hot wire output is a function of the turbulent mass flux and the temperature. In our case, the unknown distribution of density through the mixing zone thickness incited us to choose LDA, which is a non intrusive diagnostics. We adapted this to our specific study.

2. Experimental configuration

In a vertical shock tube, the two gases are impulsively accelerated by an incident upward propagating shock wave (Mach number 1.45) and decelerated by several reshocks of decreasing strength (Fig. 1). The tube has a square cross section (8 x $8cm^2$) and the distance between the initial interface position and the end wall is set to $30cm$. Plane discontinuous interfaces

More information - Email: haas@vaujours.cea.fr

are usually materialized by a flat membrane separating the gases. The initial perturbation wavelengths influence the instability development. They strongly depend on the membrane behaviour at shock crossing. In order to fix these initial scales, we place a thin wire mesh (wire spacing $1010\mu m$ and diameter $80\mu m$) directly above a plastic membrane $0.3\mu m$ thick. This mesh does not induce any measurable turbulence by itself. The membrane is torn by the propagation of the incident shock wave through the grid. Thus, the initial perturbation scales are essentially imposed by the mesh size. As a result, the mixing zone is more uniform across the tube.

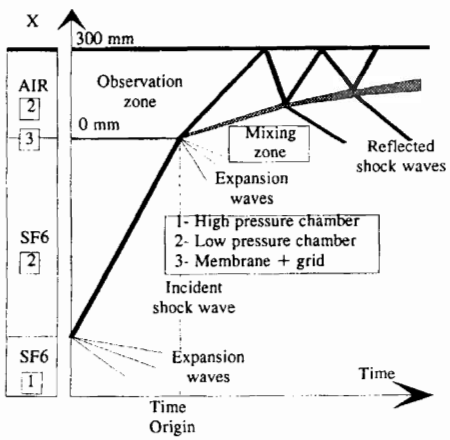

Figure 1. Schematic shock tube and (x,t) diagram.

3. Measurements

3.1. Schlieren measurements

We first performed a schlieren visualization to measure the time-dependent location and thickness of the mixing zone. In these experiments, we used a high speed camera (CORDIN 350 DYNAFAX - $35000 frames/s$ maximum). The recorded images include the interactions of the mixing zone with the first and the second reflected shock waves. In Fig. 2, the shock waves and the mixing zone edge positions versus time are drawn. The abscissa origin is the initial position of the interface and the time origin corresponds to the incident shock wave crossing at this location. We also performed a schlieren visualization of the mixing zone when it crosses the abscissa of $51mm$. We measure a mixing thickness of about $5mm$.

3.2. Choice of the LDA abscissas

First of all, we can try to estimate the beginning of the mixing zone turbulent period. The linear period occurs as long as $\left|\eta 2\pi\sqrt{2}/\lambda\right| < 1$, where λ and η are the perturbation wavelength (equal to the mesh size: $930\mu m$) and the amplitude respectively and where $\sqrt{2}$ takes into account the 3D perturbation. We can estimate an upper bound $t_{n.l.}$ of the non-linear regime beginning by taking $\eta = -\lambda$ in the Richtmyer formula [7]:

$$\eta(t) = \left(2\pi\sqrt{2}/\lambda\right) UA\eta_0' t + \eta_0' \tag{1}$$

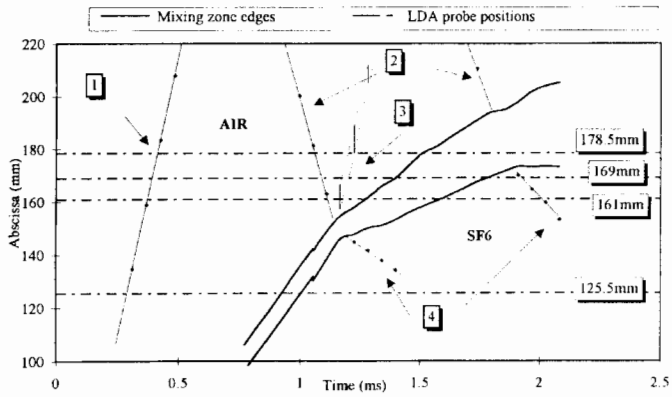

Figure 2. Time evolution of the mixing zone edges and of the shock wave locations. Positions of the LDA abscissas. The numbered squares mean: 1, transmitted shock in air; 2, first and second reflected shocks from the end wall; 3, compression waves reflected from the mixing zone and coalescing into a shock wave; 4, transmitted shocks in SF6.

with $A = (\rho_{air} - \rho_{SF6}) / (\rho_{air} + \rho_{SF6})$ the Atwood number with post shock densities, and U the gas velocity. We need to know the post shock amplitude of the perturbation η'_0. In this aim, we placed a membrane alone in the tube cross section. We deformed this membrane by an over-pressure of $1.44mbar$. Over this critical value, the membrane was torn. By an optical technique, we measured an amplitude of $7mm$. We suppose that the maximal amplitude of an inflated membrane in a square section is proportional to the side of the square. In the grid cell, the membrane has then an amplitude $\eta'_0 = 0.093 \cdot 7/80 = 0.08mm$ caused by the overpressure at shock crossing. Thus, the Richtmyer formula gives $t_{n.l.} = 13.5\mu s$. As the mixing zone crosses the abscissa of $51mm$ at $t \approx 390\mu s$, it is already in a turbulent stage. Then, we choose to locate the LDA probe successively at $51mm$ and $125.5mm$ downstream the initial interface abscissa (Fig. 2). This allows us to measure the decrease of turbulence level before the first reshock arrival. We also choose to realize velocity measurements at $161mm$ in order to quantify the enhancement of turbulence level in the mixing zone at shock crossing. Finally, we choose to perform velocity measurements at $178.5mm$. Indeed, the comparison of the measurements performed at 161 and $178.5mm$ allow to quantify the turbulence decrease between two interactions with shock waves.

3.3. LDA method

For our velocity measurements, we use an argon laser of $300mW$ maximal power and a Dantec burst spectrum analyser (BSA). LDA is a non intrusive diagnostics based on the Doppler effect. It requires to seed particles in the studied gases. Unfortunately, compared with stationary flows, the studied phenomenon is very brief: the mixing zone crossing at a fixed abscissa lasts no more than a few hundred microseconds. Thus we have to seed particles in gases at rest, before shock acceleration. The concentration of particles is higher than in stationary flows, so is the data rate acquisition. In the mixture, we obtain generally about $400kHz$ before the first reshock arrival and about $100kHz$ between the first and the second reshock passages. In air, we use carbon particles from the combustion of incense cones and in SF6, where there is no possible

combustion, we use olive oil droplets produced by a diffuser. In terms of turbulence rate[1], our global measurement noise is a little higher with olive oil than with incense: 2% versus 1.5%. This can be explained by a higher dispersion of olive oil droplet sizes. Consequently, we prefer using incense in air instead of olive oil. Such a level of noise is comparable to the one found in wind-tunnel tests, although our data rate is much higher. Moreover, the presence of the wire mesh above the membrane perturbs a little the transmitted shock wave in air and increases the dispersion of the velocity points from 1.5-2% to 2.5-3%. This measurement noise corresponds to a $\overline{u'^2}$ level of about $16(m/s)^2$.

Once the LDA was tested in simplified flows, we started velocity measurements in SF6/air mixing zones. We only measured the axial velocity component. According to our data rate and the values of the interface thickness in our flow, about 40 shock tube runs need to be done, at the same location, to get statistically convergent measurements. This requires to reproduce identical initial conditions: plane membrane and grid, a 1.45 incident Mach number M_i (in fact, M_i ranges from 1.445 to 1.455), purity of gases. After each shot, we superpose the pressure measurements to the ones stored during previous experiments. If there is no good agreement, the velocity measurements are rejected.

3.4. Velocity measurements

We first set the probe at $51mm$ on the tube axis. We performed about 10 experiments at this abscissa. At this location, we should observe the mixing zone passage between $390\mu s$ and $428\mu s$ after the incident shock interaction with the initial interface. In this time interval, we measure a level of velocity fluctuations above the level of the measurement noise. This clearly means that the mixing zone has already reached a turbulent phase.

Then, we realized velocity measurements at $125.5mm$. According to the schlieren images, we should observe the mixing zone crossing before the first reflected shock arrival (Fig. 2). Actually, we do not observe any increased level of turbulence during that period. The turbulent kinetic energy level is under the limit of the measurement noise.

The third position investigated is $161mm$. At this location, the TMZ crossing is observed just after its interaction with the first reshock. About 40 experiments were necessary to describe the turbulence level during the gaseous mixture crossing (Fig. 3). The first velocity plateau at $130m/s$ corresponds to air accelerated by the incident shock. Then, a brief plateau at $0m/s$ corresponds to air decelerated by the first reflected shock on the end wall. This latter shock reflects gradually on the density gradient in the TMZ. Consequently, it accelerates one more time the gases. Then, we observe a second, perturbed plateau which includes the crossing of the turbulent mixture. With the Rankine-Hugoniot relations, we calculate a theoretical mean velocity of $47m/s$ in this plateau. But we measure a mean velocity of $59m/s$. This acceleration is due to the boundary layer reversal effect in the SF6 at shock crossing [8]. This second plateau ends with the arrival of the second reflected shock wave on the end wall.

At the fourth location investigated, $178.5mm$, we obtain the same behaviour except the TMZ crossing is not quite entirely observed before the second reshock arrival. At this location, we also performed about 40 experiments.

[1] We call u the instantaneous axial velocity component. The Reynolds decomposition gives the instantaneous velocity as a sum of a mean velocity and a fluctuation: $u = \overline{u} + u'$ with $\overline{u} = \frac{1}{N}\sum_{i=1}^{N} u_i$. N is equal to the number of realizations. The turbulence rate τ is defined as: $\tau = \sqrt{\overline{u'^2}}/\overline{u}$, with a variance defined as $\overline{u'^2}$.

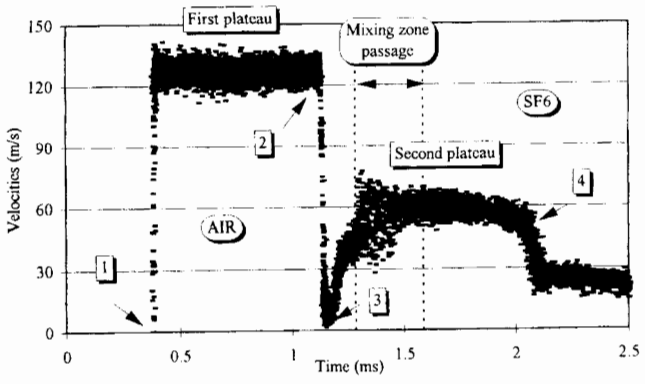

Figure 3. Cumulated measurements of the axial velocity component at 161 mm, from the superposition of 39 experiments with a plane interface of SF6/air submitted to an incident shock of Mach number 1.45. The numbered squares mean : 1, transmitted shock in air; 2, first reshock on the end wall; 3, compression waves reflected from the mixing zone and coalescing into a shock wave; 4, second reshock on the end wall transmitted in SF6.

3.5. Profiles of the Reynolds stress component $\overline{u'^2}$

At 161 and 178.5mm, we sample the mixing zone passage duration in time intervals of 23μs in order to quantify the profile of the Reynolds stress component $\overline{u'^2}$. The characteristic time scale of turbulence can be estimated, in an isotropic hypothesis, with the ratio of the TMZ width to the level of $\sqrt{\frac{3}{2}\overline{u'^2}}$: we find about 1 ms. Therefore, during the sampling period, we can neglect variations of $\overline{u'^2}$ due to dissipation. Moreover, the relative variation of thickness in the mixing zone during 23μs is only about 4% : we also neglect the variation of $\overline{u'^2}$ due to diffusion. Only the variation of $\overline{u'^2}$ due to convection could influence the results. Actually, there is an instantaneous spatial distribution of $\overline{u'^2}$ in the TMZ width. This profile is unknown, then the sampling period must be as short as possible. On the other hand, this period must contain a sufficient number of velocity points to get a statistically convergent description of turbulence. According to statistical laws, we estimate an error bar of $\pm 15\%$ on $\overline{u'^2}$ in a 23μs long sample at 161 and 178.5mm.

At 51mm, we observe the TMZ passage during 38μs. We could give a mean level of $\overline{u'^2}$ calculated from all the velocity points obtained during this period. But, if we want to estimate the shape of the $\overline{u'^2}$ profile, we have to divide the passage period in 3 samples at least. In that latter case, we estimate an error bar of $\pm 23\%$ in each sample. If we increase the number of samples, the error bar will be higher. As a result, we choose to calculate the $\overline{u'^2}$ profile with only 3 samples.

At 125.5mm, it is not necessary to sample the TMZ passage because we do not measure any turbulence above the measurement noise.

With these precautions, we obtain a convolution of time and spatial profile of $\overline{u'^2}$ during the mixing zone crossing at all the measurement abscissas (Fig. 4). At 51mm, $\overline{u'^2}$ reaches a maximum value of about $60(m/s)^2$. At 125.5mm, the turbulence level has decreased to less than $16(m/s)^2$ by both dissipation and diffusion effects. At 161mm, with a peak at $117(m/s)^2$,

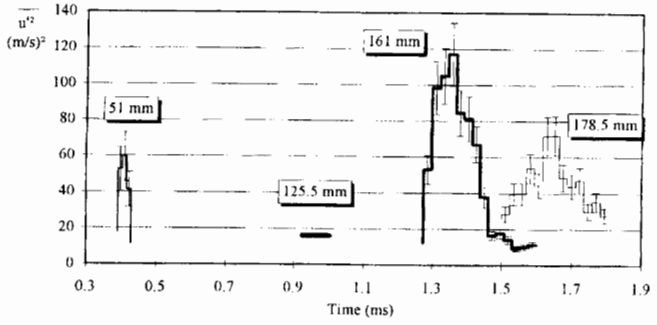

Figure 4. Profiles of the axial component of the Reynolds stress $\overline{u'^2}$ in the mixing zone crossing at 51, 125.5, 161 and 178.5 mm. These profiles are obtained by averaging the measurements on time intervals.

we observe a strong increase of $\overline{u'^2}$ compared to the level measured at $125.5mm$, (about 7 times more). The turbulence in the gaseous mixture has been excited by the reflected shock because of the baroclinic vorticity source term. Then, we notice a global decrease of the variance levels between 161 and $178.5mm$. Indeed, between these abscissas, there is no turbulence production by shock, whereas there is diffusion and dissipation.

4. Conclusion

To summarize, for the first time, velocity measurements have been performed to directly characterize the turbulence level in a mixing zone generated by the Richtmyer-Meshkov instability. In our shock tube, the first reflected shock wave from the end wall interacts with a pre-existing turbulent mixture induced by the RMI. Although this turbulence level is weak (about our measurement noise level), we measure an amplification of the axial velocity variance in the mixture by a reflected shock wave crossing. We interpretate this phenomenon as a baroclinic effect. Furthermore, we measure a decrease of the turbulence level between two successive shock arrivals, which is explained both by dissipation and diffusion effects.

Acknowledgement. We thank S. Barre, S. Gauthier, L. Jacquin, C. Mügler, and D. Souffland for useful discussions.

References

[1] Sharp DH, Physica D12, 3, (1984).
[2] Rupert V, in Shock Waves, Proc. of the 18th ISSW, Sendai (Japan), edited by K. Takayama, (1991).
[3] Rodriguez G, Galametz I, Thorembey MH, Rayer C and Haas JF., Proc. of the 20th ISSW, Pasadena (USA), Sturtevant, Shepherd and Hornung editors, World Scientific, (1997).
[4] Jourdan G, Houas L and Billiotte M, Phys. Rev. Lett., 78, 452, (1997).
[5] Trolier JW and Duffy RE, AIAA Journal, 23, 8, 1172-1178, (1985).
[6] Honkan and Andreopoulos J, AIAA, paper 90-1647, (1990).
[7] Richtmyer RD, Commun. Pure Appl. Math., 13, 297-319, (1960).
[8] Mark H, J. Aero. Sciences, 24, 304, (1957).

Fractal Characteristics of Reactive Fronts and Shock Tube Mixing Layers

J.M. Redondo
Dept. Fisica Aplicada, Univ. Politecnica de Catalunya
Campus Nord B5, Barcelona 08034 - Spain

Abstract: We investigate the geometrical complex structure of the instability due to plane shocks in different geometries by means of fractal analysis. An important point in the understanding of the complex structures that produce mixing across density interfaces with or without chemical reactions is the combination and comparison between numerical calculations and selected experiments performed using either shock tubes or explosives which produce shocks that traverse sharp density interfaces between different layers. Two experimental configurations are analysed, one is the growth of a reactive unstable density interface at low Atwood number produced by placing a layer of brine over a fresh water layer and removing the barrier that separates them initially [1], the other one is the mixing zone produced by the passage of a high Mach number shock across a density interface [4]. Changes in the fractal structure, which is related to the relative space fillingness of the large and small eddies, is used to identify areas where boundary effects may disturbe the basic RT and RM instabilities

1. Introduction

A very important problem regarding the mixing of strongly accelerated interfaces is the effect of geometry on the development of Richtmyer-Meshkov and Rayleigh-Taylor instabilities. These instabilities produce often undesired mixing at compressive interfaces which reduce the yield of inertial confinement fussion. Simple experiments where detailled measurements of the growth of the mixing front have been done have confirmed numerical calculations [1, 2], these effects are also important in the application of shock-induced mixing zone to supersonic impulses, in the context of combustion, chemical reactions or in astrophysics. Molecular mixing takes place at the smalest scales generated in the flow, which are supposed to be independent on the most energetic or large scales in turn produced as coherent structures by the dominant instabilities, In this paper we investigate, using fractal analysis the effect of different instabilities on the self-similarity of the turbulent mixing and reactive fronts.

Many shock-tube investigations on shock-induced turbulent mixing zone studies have used visualization techniques [3, 4] measuring only gross features of the flow, fractal analysis coupled with spectral methods allows to use the selfsimilarity of the turbulence at high Reynolds number to investigate for example boundary effects or membrane effects in shocks.

2. Description of the fractal analysis

From dimensional arguments Kolmogorov's spectral relations for the density of energy,

$$E(k) = c\epsilon^{2/3}k^{-\frac{5}{3}} \tag{1}$$

More information - Email: redondo@etseccpb.upc.es

where ϵ is the mean dissipation $\epsilon = \nu\overline{\frac{\partial u_i'}{\partial x_i}\frac{\partial u_i'}{\partial x_i}}$. this is equivalent to state that the second order moment of the structure function scales like $< \delta v(\ell) >^2 = c(\epsilon\ell)^{2/3}$, also valid for higher moments. Detailed experiments show that agreement is not as good as initially expected by the earlier succesess of the theory. Obukov and Kolmogorov introduced a correction by taking into account the intermittency of the distribution, by adding a factor $(\ell k)^{\mathcal{N}}$ where $\mathcal{N}$ is called the intermittency, and represents the average number of vortices which are formed when a larger vortex decays. $E(k) = c\epsilon^{2/3}k^{-\beta}\,(\ell k)^N$.

This intermittency of the turbulence is reflected in the Fractal dimension which is related to the percentage of space occupied by the remnants of a decayed vortex at a smaller scale. The spectrum of turbulence often has an inertial subrange, or range of scales where the energy coming from the larger eddies is the same as the energy transfered towards the smaller ones. If ϵ and ν are the only relevant parameters, the smallest possible turbulent eddy size, before viscosity acts, is Kolmogorov's lengthscale $\eta = (\nu^3/\epsilon)^{1/4}$ and similar lentghscales may be defined if a scalar, such as temperature or concentration is involved. Then depending on the Prandtl number, the microstructure is diffused either faster $Pr < 1$ or slower $Pr > 1$ than the velocity, and we have the Batchelor $\eta_b = Pr^{-1/2}\eta$ or the Corrsin $\eta_c = Pr^{-3/4}\eta$ scales. These diffusive lengthscales dominate when a chemical reaction takes place.

The range of time and length scales involved in compressible turbulence is large due to the high speeds which reduce the Kolmogorov, Batchelor or Corsin lenghtscales. The analysis of convoluted surfaces and its application to turbulence has witnessed a rapid expansion due mostly to Mandelbrot who gave practical definitions of fractal dimensions of real objects. Fractal objects, as they are called, display self-similarity over a range of scales. Mathematical fractal objects may display self-similarity over an infinite range and the Hausdorff dimension can be used to describe them; for physical objects, there is a limited range where self-similarity applies. In turbulence this range may be between the largest scale and the Kolmogorov scale. A practical definition of the fractal dimension,D can be given as

$$D = \frac{logN}{log(1/\sigma)} \tag{2}$$

where N is the number of self-similar parts or covering boxes at size σ. An extension of the fractal dimension to a set where different isolines have different fractal dimensions may be done using multifractals. For a fractal curve, its measured length L will have a power law dependence on the measuring yardstick σ as $L \propto \sigma^{1-D_i}$ The exponent D_i is called the fractal dimension of the curve and is a measure of the roughness of fragmentation of the curve. The subindex i indicates the imbedded Euclidean space,(1 for a line, 2 for a plane, 3 for a volume, etc) from which the fractal dimension is derived as a projection. Many experiments have calculated the fractal dimension for several flows, both for velocity and for marked scalar regions in the flow, and found slightly different values for different classical turbulent flows; 1.38 for a boundary layer, 1.35 for an axisymmetric jet, 1.33 for a mixing layer, for D_2 and 0.40 for D_1.

The fractal convolutions of turbulent interfaces will increase the area between different marked regions of the flow, In a similar way as for a line we can express the area determined by the fractal set as $A \propto \sigma^{2-D_2}$. If the range of scales where self-similarity is exhibited is limited by, say, a large scale ℓ and a small scale, say the Kolmogorov lenthscale η, then the fractal nature of turbulence will increase the area of any turbulent interface marked by a scalar. If the area of a surface, filtered by the measurement at scales comparable to ℓ measures A_ℓ, then due to the additional fractal scales the fractal (real) area is $A_D = A_\ell \left(\frac{\ell}{\eta}\right)^{2-D_2}$. This increase in

contact area needs to be taken into account when discussing mixing through density interface, the real fluxes will be greater that the euclidean calculated ones.

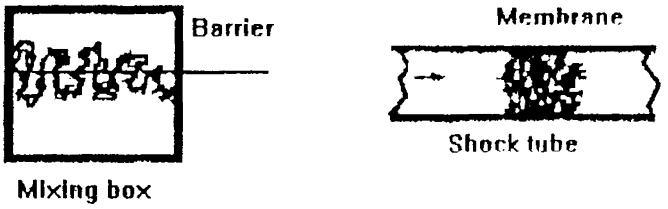

Figure 1. Experimental apparatus used in the reactive mixing.

3. Experimental method

Fig. 1 presents the two experimental configurations analysed. A reactive Rayleigh-Taylor mixing front generated by placing dense fluid (brine) with (NaOH) basic pH plus phenolphthalein on top of fresh water with (ClH) acid. The other configuration is a shock tube experiment of which only selected shliering images have been analysed, here Richmayer-Meshkov instability is produced. More details may be found in [1, 4, 5].

In both experiments the Atwood number, defined as:

$$A = \frac{\rho_2 - \rho_1}{\rho_2 + \rho_1} \tag{3}$$

where the acceleration or shock wave goes from fluid 1 to fluid 2, was used.

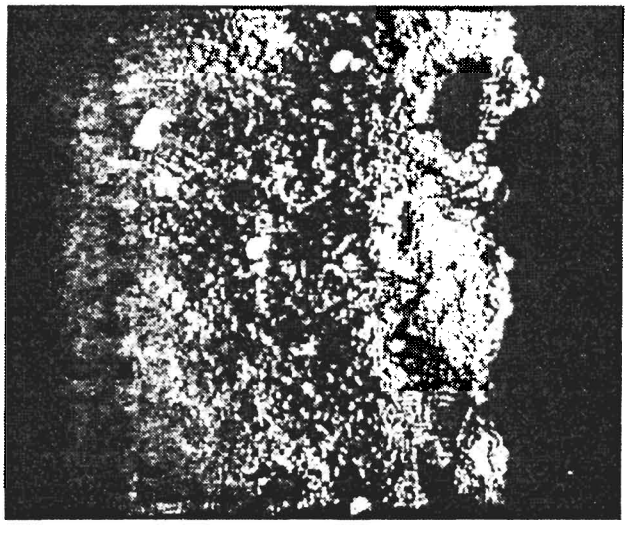

Figure 2. Shadowgraph of an Air/CO_2 mixing zone experiment.

4. Results

For the shock experiment shown in Fig 2. measurements of the fractal dimension were made for different intensity levels and diferent positions and the resulting values are given in Table 1. This experiment was performed at $M = 1.28$ with a membrane of 0.5 microns separating the two layers Air/CO_2 at a position of 250 mm. The different regions of the turbulent flow visualized by shliering show different self-similar structure as indicated in the table. The position X/X_0= 0.9 corresponds with the turbulent mixing zone and there is a similar fractal behaviour for all intensities, the center region has more convolutions at the darker areas while earlier there is no developed turbulence. The effect of adding smaller scales at the initial conditions, with

X/X_0 at I/I_0	0.2	0.4	0.6	0.8
0.3	1.22	1.27	1.31	1.12
0.6	1.33	1.43	1.10	1.07
0.9	1.37	1.35	1.38	1.34

Table 1. Fractal dimension for different positions and levels.

an increment in the complexity of the instability patterns, produces higher fractal dimensions and thus a mixing enhancement. The overall prediction seems to be that the more complex the initial perturbations the greater the ensuing instability. It is clear that only in fully developed turbulent flows the fractal dimension aproaches $D_n = n - 2/3$ where n is the Euclidean dimension of the embedding space. The effect of membrane pieces may be detected by a large decrease of the local fractal dimension in their wake.

For the reactive mixing experiment, the time evolution of the fractal dimension of a low Atwood number, $10^{-4} < A < 5 \times 10^{-2}$, mixed layer shows an increase while the R-T instability developes. A decrease in D_2 is observed after a non dimensional time described below of 2.5. This is due to the large scale flow induced by the sides of the experimental tank, but also to the restoring effect of the stratification, once the whole tank overturns. The numerical calculations do not show this behaviour, and the value of D_2 continues near 1.4.

The effect of stratification, specially at high Richardson numbers, produces a marked reduction in the vertical velocities, and of the thickness of stable interfaces this is taken into account using the results of Redondo (1987) [6]. and of Redondo and Linden (1996) [2].

$$w_3' \propto w_1' Ri^{-1/6} \tag{4}$$

where the local Richardson number is defined as $Ri = \frac{g\Delta\rho\ell}{\rho w'^2}$ and the non-dimensional time scale used is scaled on A as $\tau = (\frac{Ag}{\ell})^{-1/2}t$

In the same way as stratification reduces vertical scales the wall boundary layer becomes the dominant feature and the large density fluctuations observed by shiliering or other techniques have two different sources, the baroclinic vorticity production and the shear from the boundary layer, which seem to have different scaling laws and might be detected geometrically.

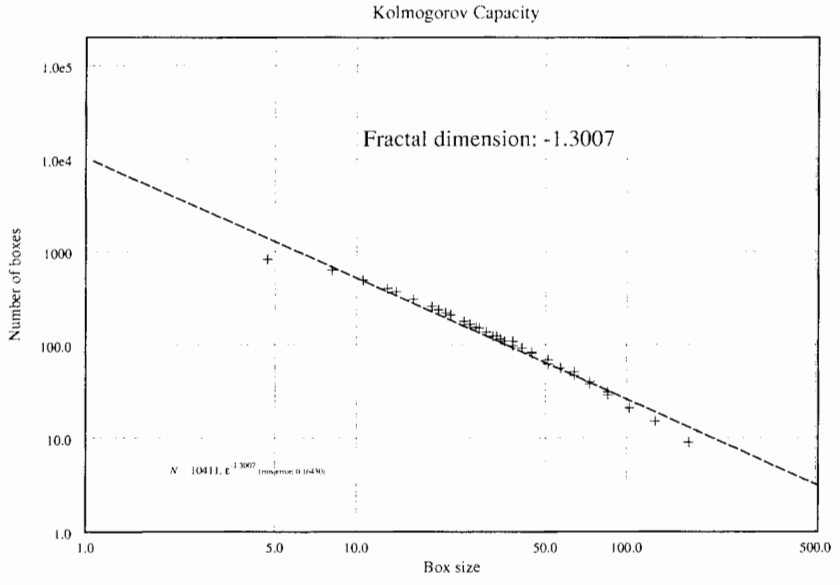

Figure 3. Relationship between the number of boxes needed to cover a fractal intensity contour at a shock induced turbulent mixing zone.

5. Conclusions and discussion

An introduction of the basic Richtmyer-Meshkov (RM) and Rayleigh-Taylor (RT) instabilities and the effect of these on the geometrical (Fractal) structure might lead in the future to a wide clasification of different types of turbulent instabilities acording to the measured fractal and multifractal dimensions.

The information obtained by the visualization of the interface mixing zone by several methods, such as shadowgraph, shliering and reactive colour change may be used to clasify the growth and characteristics of the interfaces, in particular changes in the fractal structure, which is related to the relative *space fillingness* of the large and small eddies, is used to identify areas where boundary effects disturbe the basic RT and RM instabilities. These instabilities are seen to be dependent on the complexities of the initial conditiondifferentnd combinations of random and well controled superpositions of azimutal wavenumbers show this dependence very clearly as seen by Toque(1996) [7] in implosions for plane and cilindrical shocks with different azimutal waveforms. The variation of the fractal dimension with time together with a comparison of the different geometrical characteristics as a function of Atwood number provides a better understanding of the evolution of the turbulent instability.

Acknowledgement. This work is supported by the European Union and DGES, Contracts N° IC15-CT96-0111 and EU-960014, I thank N. Toque, J.F. Haas and L. Houas for providing some of the images used here and for helpfull discussions.

References

[1] Linden PF, Redondo JM and Youngs D, Molecular mixing in RT instability, J. Fluid Mech., 265, 97-124, (1994).

[2] Redondo JM and Linden PF, Geometrical observations of turbulent density interfaces in The physics of deforming surfaces, IMA series, 56, 221-248, (1996).

[3] Rodriguez G, Galametz I, Croso H and Haas JF, Richtmyer-Meshkov instability in a vertical shock tube, Proc. of the 19th International Symposium on Shock Waves, Marseille, France, IV, 275, (1993).

[4] Houas L, Chemouni I, Touat A and Brun R, 3rd. Int. Workshop on the physics of Compressible Turbulent Mixing, Rouyamont, 127-136, (1991).

[5] Fortes J, Ramdani A and Houas L, CO_2 laser absorption measurements of temperature and density in shock induced Richtmyer-Meshkov mixing zone, Phys. Rev. E, 50, 4, 3041-3049, (1994).

[6] Redondo JM, Effects of ground proximity on dense gas entrainment, J. Haz. Mat., 16, 381-393, (1987).

[7] Toque N, Ph D. Thesis, Univ. Paris IV, (1996).

Indirect Drive Ablation Front Instability Experiments on Phébus

A. Richard, H. Croso, M. Valadon , F. Mucchielli, P. Salvatore, C. Reverdin, O. Lamontagne, F. Zielinski and B. Meyer
CEA-DRIF Limeil-Valenton
Villeneuve Saint Georges, 94195 Cedex - France

Abstract: Experiments devoted to the measurement of the growth rate of the ablation front instability have been performed with the Phebus laser facility at CEA-DRIF. We used X-rays converted from 3ω laser light (1.3 ns FWHM square pulse, 2.8 kJ) in a gold hohlraum to accelerate modulated foils and we studied the Rayleigh-Taylor instability at the ablation front. The accelerated samples were 18 μm and 24 μm thick brominated plastic. The wavelength of the perturbations was 50 μm and their amplitudes 0.9 μm and 1.8 μm. Face-on radiography was used to measure the growth of the perturbations. We used a laser beam to create a radiography source on a copper disk (1.5 keV). Good contrast pictures were recorded with a framing camera. Time resolution is 80 ps and spatial resolution was obtained with pinholes of 10 μm diameter. The experimental results and their analysis are presented. 2D simulations were carried out and their results are compared to the measurements.

1. Introduction

Big laser facilities for ICF are planned in the next decades in the United States (National Ignition Facility) [1] and in France (Laser MégaJoules) [2]. They are devoted to reach DT ignition with direct or indirect drive. Hydrodynamics instabilities impose limits on the definition of these facilities and to control the physics of the implosion we have to understand it.

The experiments we performed with the Phébus laser facility at CEA-DRIF focused onto the Rayleigh-Taylor [3] instability at the ablation front in indirect drive.

Indirect drive [4] consists in converting the laser light into X-rays onto the walls of high-Z hohlraums. In the implosion process, matter is ablated by X-rays from the outer surface and by reaction implodes the microballoon. The ablated plasma (lighter) accelerates the shell (heavier) which is a Rayleigh-Taylor unstable situation. Irradiation non-uniformities and surface roughness are seeks for the development of the abalation front instability. Then the perturbations are transmitted to inner interfaces, where they grow again at the stagnation phase, when the lighter fuel decelerates the heavier shell.

Finally hydrodynamics instabilities growth perturbs the fuel and degrades the performance of the implosion.

Compared to classical Rayleigh-Taylor instability, the growth rate of the ablation front instability, in its linear phase, is reduced due to the density gradient at the ablation front and due to the ablation process itself. The growth rate of the instability can be modelized by a Bodner-Takabe [5] like formula :

$$\gamma = \alpha\sqrt{kg} - \beta k V_a$$

More information - Email: richarda@limeil.cea.fr

The parameters α (depending on the density gradient length) and β have to be determined through the comparison between simulations and experiments.

A number of experiments addressing these issues have already been performed on other laser facilities [6].

2. Experimental configuration

Phébus is a Neodynium glass laser facility at 1.06 μm wavelength. It consists of two beams delivering about two times 3 kJ after conversion to 0.35 μm wavelength. We used square laser pulses about 1.3 ns FWHM.

3. Growth measurement

The experimental arrangement for this experiment is shown in figure 1.

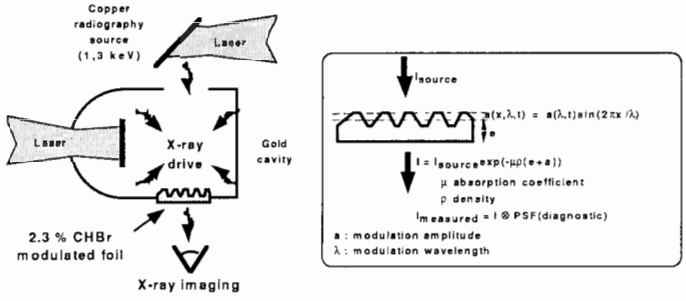

Figure 1. Experimental setup.

As in many previous experiments in other laboratories, we measured the growth of the perturbation by face-on radiography. We used one of the laser beams to create the X-ray drive in the 1 mm diameter gold hohlraum onto a gold converter. The other beam was used to create a source around 1.3 keV onto a copper disk. It was smoothed with a RPP. The modulated 2.3 % CHBr sample was placed on the wall of the cylindrical part of the hohlraum. The wavelength of the perturbation was 50 μm.

We imaged the transmission of the X-ray source light through the sample (figure 1). The measured intensity is related to the thickness of the CHBr and is convolved with the diagnostic Point Spread Function. X-ray imaging of the foil was realized with a twelve pinholes gated imager. Its magnification was 10 and the pinholes diameters were 10 μm. The exposure time was 80 ps. An example of recorded radiographs is shown in figure 2.

4. Drive characterization

We characterized the X-ray flux in the hohlraum and checked the opacity of the brominated plastic samples with burnthrough measurements.

The hohlraum geometry was the same (dimensions and apertures) as for the growth rate measurements.

A gold foil and a CHBr foil were set over a window in the wall. We observed with a 140 eV to 280 eV energy range soft X-ray streak camera and measured the delay between the light

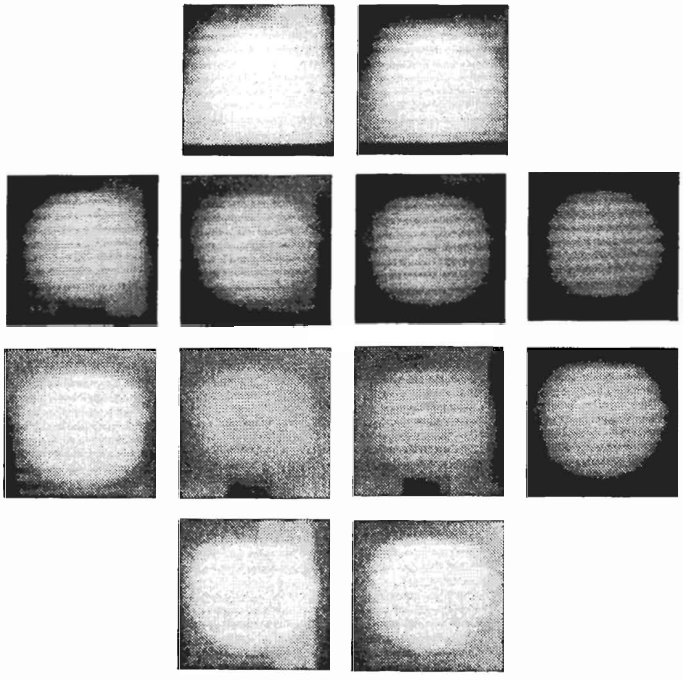

Figure 2. Radiographs of the modulated foil.

appearing after burnthrough of the samples and the light coming out of a reference hole. We got a maximum radiation temperature around 140 eV.

5. Data analysis

The initial perturbations were measured and analysed. In figure 3 we show the modulations for the 18 μm thick / 1.7 μm peak to valley CHBr sample and its Fourier decomposition. We notice that it presents a strong initial second harmonic, about 25 % of the fundamental amplitude.

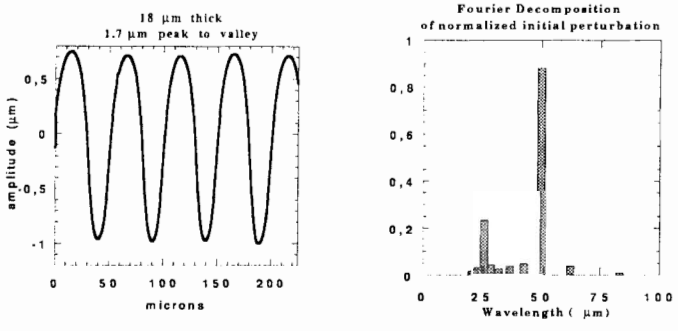

Figure 3. Initial modulation.

The datas were analyzed as follows [7] (figure 4) :

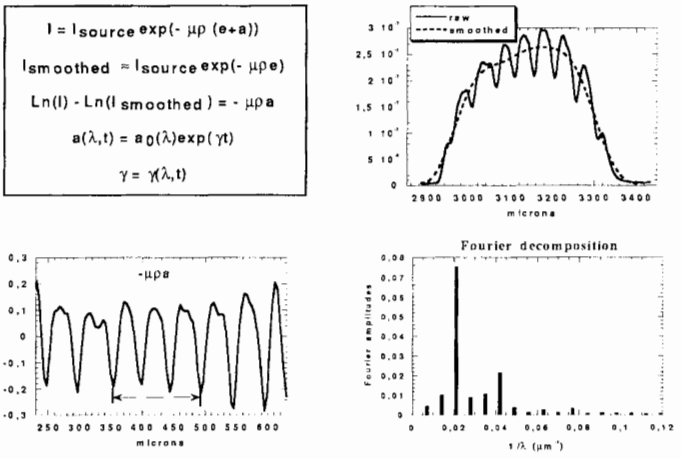

Figure 4. Data analysis principle.

- the transmitted intensity is related to the source intensity,
- we get profiles across the measured signals modulations. Then we smooth it, we divide the measured signal by the smoothed one and we take the natural logarithm of it. Doing so we remove the effect of the source non-uniformity and we get the optical depth amplitude,
- from this flattened signal, we took a finite number of periods on which we applied a Fourier decomposition to derive the amplitudes of the perturbation for each wavelength present in it.

In this case, we have contributions at 50 μm and 25 μm wavelengths.

6. Results and comparison with 2D simulations

In figure 5, we give the Fourier amplitudes that we derived for two different shots with similar CHBr samples : 24 μm thick, initial peak to valley amplitude 0.9 μm. These values were not

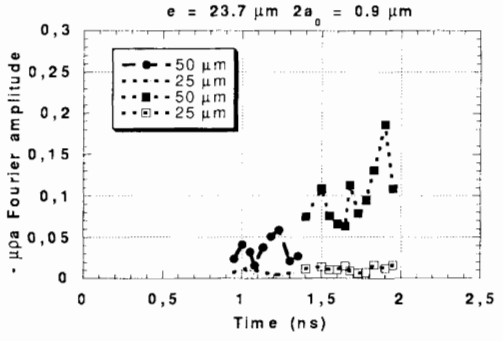

Figure 5. Example of experimental results.

corrected from the diagnostic Modulation Transfer Function.

We observe that the perturbation's fundamental grows. The second harmonic does not grow much on these shots at the times of the measurements.

Two dimensional simulations were carried out for these experiments. In figure 6, we give the values of some important parameters given by the simulation. The foil is set in motion after

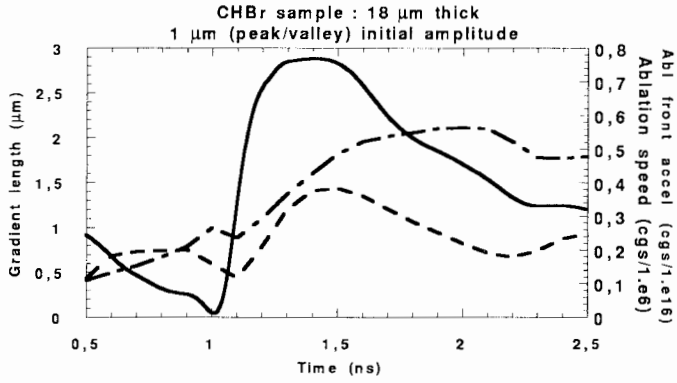

Figure 6. Fundamental parameters given by the simulations.

the shock break out at 1 ns. The ablation front acceleration, continuous line, is about 7e15 $cm.s^{-2}$. The ablation speed, dashed plot, varies from 1 to 4e5 $cm.s^{-1}$. The density gradient length, dot-dashed plot, used to calculate α, goes from 0.5 μm to about 2 μm.

On the plots in figure 7 we compare the experimental datas, corrected from the MTF, with a mean growth factor given by the simulations. We scaled the data to the simulations values

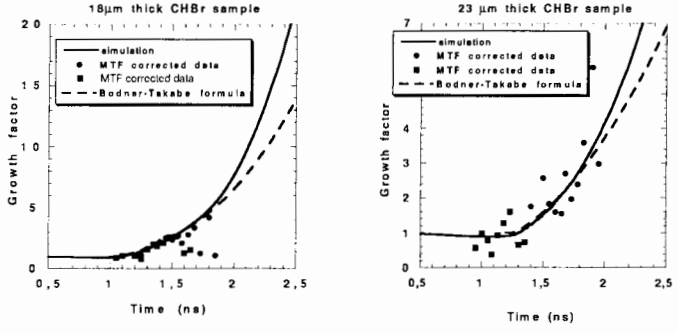

Figure 7. Comparison of experimental results with simulations and with Bodner-Takabe formula.

at the time of shock break-out. Doing so, we get a reasonable agreement between experimental data and simulation for both thicknesses samples used (18 μm and 24 μm).

A post-processing of the diagnostic is in progress and will allow a more precise and more rigorous comparison.

We also compared datas and simulations with a fit by the Bodner-Takabe formula. We calculated it with the values of α, g_a and V_a given by the simulation, taking a β of 1.5 (from LLNL experiments). The agreement at the times of the measurements is good but after 1.8 ns begins to deteriorate. This could be due to the decompression of the foils that is not taken into account in the formula.

7. Conclusion

We measured, by face-on radiography, the growth rate of the Rayleigh-Taylor instability at the ablation front of planar geometry samples accelerated by indirect drive.

We observed growth of the perturbations for both thicknesses used : 18 μm and 24 μm.

2D simulations were carried out and agree reasonably with experiments.

The diagnostic post-processing is in progress and will allow more rigorous comparison.

We plan to perform experiments in the near future with smaller wavelengths to validate the Bodner-Takabe formula.

Acknowledgement. We would like to thank the staff of Phébus and the target laboratory for their essential participation to these experiments, J.L. Bourgade and D. Gontier for the diagnostic development, C. Cherfils-Clerouin and D. Galmiche for our fruitful discussions.
We would like also to thank Nicolas Dague and Jean-Paul Jadaud for their help in having this text formatted under LaTeX.

References

[1] The National Ignition Facility, Energy & Technology Review, December 1994.
[2] Chocs, 13, April 1995
[3] Lindl J., Phys. Plasmas 2 (11) (1995)
[4] Lord Rayleigh, Scientific Papers (Cambridge University Press, Cambridge, 2, 200, (1900) ; Taylor GI, Proc. R. Soc. London Ser., A 201, 192, (1950); Chandrasekhar S, Hydrodynamic and Hydromagnetic Stability (Oxford University Press, London), 10,(1968).
[5] Bodner S, Phys. Rev. Lett., 33, 761, (1974); Takabe H, Mima K, Montierth L, Morse RL, Phys. Fluids, 28, 3676, (1985); Munro DH, Phys. Rev. A, 38, 1433, (1988); Tabak M, Munro DH and Lindl JD, Phys. Fluids B, 2, 1007, (1990).
[6] Nishimura H *et al.*, Phys. Fluids, 31, 2875, (1988); Kilkenny JD, Phys. Fluids B, 2, 1400, (1990); Katayama M *et al.*, 34th Annual Meeting of the Division of Plasma Physics, American Physical Society, Seattle, Wa, USA November 16-20, (1992); Remington BA, Haan SW, Glendinning SG, Kilkenny JD, Munro DH and Wallace RJ, Phys. Fluids B, 4, 4, 967, (1992); Remington BA, Weber SV, Marinak MM, Haan SW, Kilkenny JD, Wallace RJ and Dimonte G, Phys. Plasmas, 2, 1, 241, (1995).
[7] Glendinning SG, Remington BA, Haan SW, Munro DH and Weber SV, Rev. Sci. Instrum., 63, 10, 5108, (1992)

Vortex Model for the Richtmyer-Meshkov Instability at Low Atwood Numbers

A. Rikanati[1,3], U. Alon[1,2] and D. Shvarts[1,4]
[1]Dept. of Physics, Nuclear Research Center Negev, Israel
[2]Dept. of Physics, Princeton University, Princeton NJ, USA
[3]Dept. of Physics, Ben Gurion University, Beer Sheva, Israel
[4]Dept. of Mechanical Engineering, Ben Gurion University, Beer Sheva, Israel

Abstract: The nonlinear growth of the multi-mode RM instability in the limit of two fluids of similar densities (A $\rightarrow$ 0) is treated by the motion of point potential vortices. Two-bubble merger is demonstrated and bubble competition rates are calculated. Using a statistical bubble merger model, similar to that used in the limit of A=1 [6], the front evolution scaling law is derived. A power law of $t^{0.4}$ for the mixing zone growth rate is obtained, similar to that derived for the A=1 case, in good agreement with simulations and experiments.

1. Introduction

The Richtmyer-Meshkov [1] (RM) instability occurs when a shock wave passes through an interface between two fluids. Under this instability, small perturbations on the interface grow into a formation of bubbles and spikes. Recently, Alon *et al.*[2] applied a bubble competition model to study the time evolution of bubble fronts of the RM and RT (Rayleigh-Taylor) instabilities in the limit of infinite density ratio (Atwood number of A=1). The model is based on modeling the front by an array of 2D bubbles, each rising with its single-mode asymptotic velocity obtained from Layzer's potential flow model [3, 4]: $V = C \cdot \lambda/t$, with $C = 1/3\pi$ for the case of A=1. Bubbles overtake smaller neighboring ones to form larger bubbles ("bubble merger") [2, 4] at a rate ω calculated using an extension of the potential flow model to describe two-bubble competition. The results from the model were that asymptotically the bubble front evolution is dominated by a self-similar growth. The bubble size spectrum, normalized to the average bubble size, reaches a fixed distribution. The turbulent mixing zone (TMZ) growth rate was found to grow according to the power law: $h_b = a_0 \cdot t^{\theta_b}$ with $\theta_b = 0.4$ and a_0 depending on the initial perturbation. This result was confirmed by full 2D numerical simulations [2] and recently by experiments done by Dimonte *et al.*[5].

For Atwood numbers smaller than one, numerical results [6] show that the single bubble velocity will remain as $V = C\lambda/t$ but with C having a weak dependence on A (varying from about 0.11 for A=1 to about 0.16 as A$\rightarrow$0), and that the multi-mode bubble front still obeys the power law of $t^{0.4}$ for all Atwood numbers.

The RM instability evolution can be considered as a shock-imposed velocity perturbation followed by a TMZ evolution. When A is exactly zero a shock wave leaves no velocity perturbation, but since the TMZ evolves from the initial perturbation in the velocity, regardless of the source of the perturbation, one can study it also for A=0. This serves as a model for the RM at low Atwood numbers. The purpose of the present work is to study this limit of A=0 (two fluids having the same density) by constructing a vortex model for the single bubble evolution and two-bubble interaction and applying it to a statistical model in order to derive the

More information - Email: rkavi@bgumail.bgu.ac.il or schwartz@bgumail.bgu.ac.il

asymptotic behavior of the multi-mode perturbation. Our vortex model is based on extending the single-mode vortex models of Jacobs *et al.*[7] and Zabusky *et al.*[10].

2. The vortex model

2.1. Rotational flow

From theory, numerical simulation [10] and experiments [7] of the RM instability at low Atwood numbers, one can clearly see the early formation of vortices in the flow patterns, formed by the strong attractive effective potential between vorticity points in the vorticity field. This observation implies that the flow is rotational rather than potential, which is the case for Atwood number A=1. In a rotational flow field the vorticity ω is defined as: $\vec{\omega} = \nabla \times V$

The vortex strength can be calculated from Kelvin's theorem of circulation:

$$\Gamma = \int^{Surface} \vec{\omega} \cdot ds = \oint^{Contour} V \cdot dl = Const \tag{1}$$

where the surface integral is taken over the area containing the vorticity from which the vortex is generated, and the contour integral is taken over a contour limiting this area. The integrals are taken for the initial velocity distribution. Kelvin's theorem of circulation also states that the vortex strength remains constant in time as long there is no viscous loss of turbulent energy.

In our problem we are dealing with arrays of bubbles, each consisting of two vortices in opposite directions. We model this array by a set of infinite vortex lines each contributing the complex potential [7, 8]:

$$w(z) = \sum_{n=-\infty}^{\infty} (i \cdot \frac{\Gamma}{2\pi}) \ln (z - na) = \frac{i \cdot \Gamma}{2\pi} \ln \sin(\pi \cdot z/a). \tag{2}$$

where a is the distance between neighboring vortices along the line, Γ is the vortex strength and z is the complex location coordinate, $z = x + i \cdot y$.

2.2. Single-bubble perturbation

In this work we examine the case of a perturbation given by a combination of sines and cosines, rather than localized vortices. In the case of Atwood number A=0, an initial cosine perturbation transforms, early in time, into a localized vortex array. This enables us to model the problem, as suggested by Jacobs *et al.*[7] and Zabusky *et al.*[10] as an infinite vortex line with alternating directions, as can be seen in Fig.1.

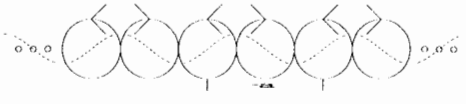

Figure 1. Schematic drawing of two vortex lines, with a distance a between the vortices in each line and with a vortex strength $\pm\Gamma$, representing a single-bubble array perturbation. The interface perturbation is represented by a dashed line.

For a given cosine velocity perturbation the strength of each vortex in the vortex line, using Eq(1), is: $\Gamma = 4v_0/k$ where v_0 and k are the perturbation amplitude and wave number. In

the case of a single-bubble array there is a full symmetry between the vortices and therefore the velocities of their centers are zero. This allows us to solve the equations for the bubble tip analytically, as was done by Jacobs *et al.*[7] and Zabusky *et al.*[10] to give: $h(t) = 1/k \cdot \sin h^{-1}(\Gamma k^2/2\pi \cdot t)$, where the asymptotic velocity for that solution is:

$$V_{asy} = \frac{1}{2\pi} \cdot \frac{\lambda}{t} \tag{3}$$

This result should be compared to the result at A=1 where $V_{asy} = 1/3\pi \cdot \lambda/t$, as was derived from a potential flow model by Hecht *et al.*[4]. The difference in the coefficient should be attributed to the added mass in the A=0 case. The result of Eq(3) is compared, in Fig.2, with a full 2D simulation of a single-mode cosine perturbation evolution, and the agreement is very good. Previous numerical work by Alon *et al.*[6] showed that for the case of A=0 the velocity behaves as: $V_{asy} \cong 0.15 \cdot \lambda/t$, very close to the model prediction.

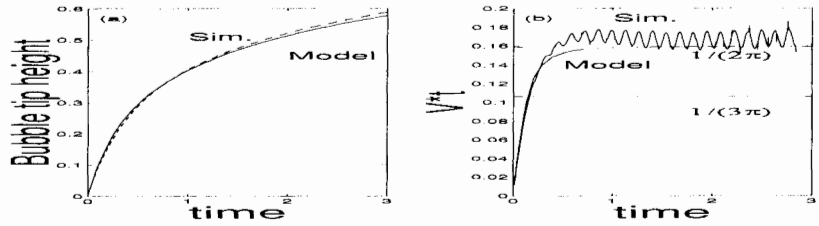

Figure 2. Comparison between the model and a full 2D simulation for the case of $\lambda = 1$: (a) bubble tip height, (b) bubble tip velocity multiplied by the time. Marked in the figure is $1/(3 \cdot \pi)$ and $1/(2 \cdot \pi)$, the asymptotic behavior for A=0 and A=1 respectively.

Since we know, due to symmetry, that the vortex locations remain constant with time, we know that the complex flow potential will be the sum of two vortex lines(Eq(1)) with a distance $a = \lambda$ between each vortex in the line and an opposite strength of $\pm\Gamma$ as seen in Fig.1 This enables us to numerically find the evolution of the whole interface. The agreement between the model and the full numerical 2D simulation is very good, as will be demonstrated for the case of two bubbles.

2.3. Two-bubble interaction

In order to model the random perturbation case with a statistical model, as was done for A=1 by Alon *et al.*[2, 6], we constructed a model for the interaction between two neighboring bubbles. The single-bubble model was extended to the case of two-bubble interaction by setting an array of four periodic infinite vortex lines creating an array of alternating large and small bubbles, as described in Fig.3.

In this case the symmetry of the problem prevents relative motion between the vortices of a given line, but enables relative motion between the lines themselves. Thus, we followed the line motion in time, where each line moves in the complex potential field induced by the other three. In this case, of an initial perturbation of the sun of two cosines, there are two different vortex strengths (each appearing twice, $\pm\Gamma_1$ and $\pm\Gamma_2$)as is shown in Fig.3:

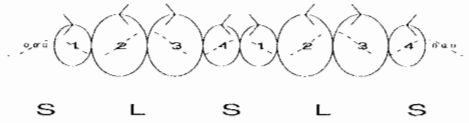

Figure 3. Schematic drawing of 4 vortex lines representing a two-bubble perturbation. The perturbation is represented by the dashed line which is a sum of two cosines, L stands for a large bubble ,S for a small one and the 4 vortex lines are numbered 1-4. Notice that lines 1 and 3 represent vortices with a clockwise direction where line 1 is of small vortices of strength Γ_2 and line 3 is of large vortices of strength Γ_1. Lines 2 and 4 are directed counter-clockwise of strength Γ_1 and Γ_2 respectively.

$$\Gamma_1 = 2\left(\frac{v_L\left(1+Cos\left(k_1\cdot x_m\right)\right)}{k_1}+\frac{v_s\left(1+Cos\left(k_2\cdot x_m\right)\right)}{k_2}\right) \tag{4}$$

$$\Gamma_2 = 2\left(\frac{v_L\left(1+Cos\left(k_1\cdot x_m\right)\right)}{k_1}+\frac{v_s\left(-1+Cos\left(k_2\cdot x_m\right)\right)}{k_2}\right) \tag{5}$$

Where v_L and v_S are the two bubbles' initial velocities, k_1 and k_2 are the wave numbers from which the initial perturbation is formed and x_m is a reference point between the two bubbles(the point where the initial flow velocity is zero).

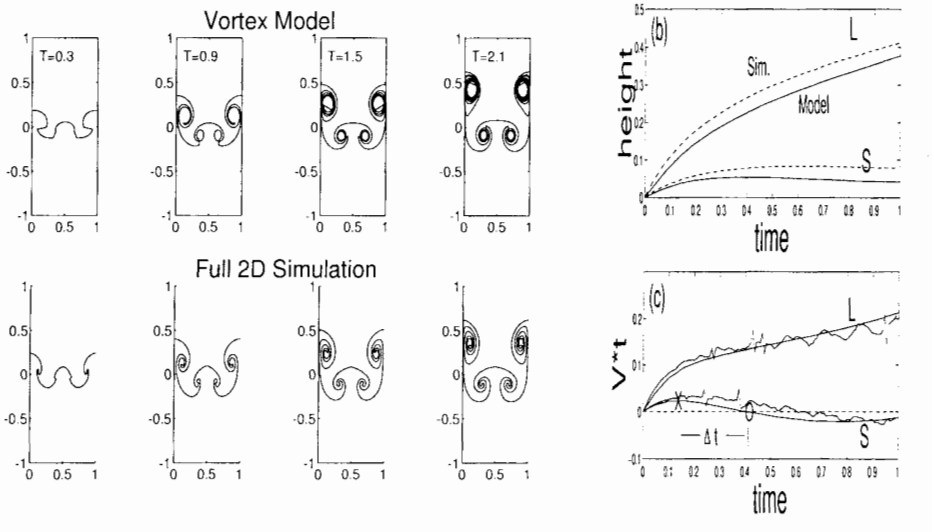

Figure 4. Comaprison between the model and a full 2D simulation, using an ALE code with interface tracking [6] for $v_L = 1$ and $v_S = 0.5$: (a) bubble interface. (b) bubble tip heights. (c) bubble tip velocity multiplied by time.

From the complex potential induced by the vortex lines, two equations, for the location $x_1(t)$ and $y_1(t)$ of one of the lines of the large vortices and two equations for the location $x_2(t)$ and $y_2(t)$ of the lines of the small vortices are obtained, where the locations of the other two

are mirror images of the previous ones. After numerically solving the equations one gets the motion of the vortex lines, from which one can derive the complex potential dependence on time in all of the domain. The comparison of the model to full 2D simulations is very good, as can be seen in Fig.4.

From the model we can define the merger rate ω to be:

$$\omega(q) = \frac{1}{\Delta t_{merger}} \tag{6}$$

where q is the wavelength ratio λ_1/λ_2 and Δt_{merger} is the merging time. The merging time is the time interval between the time at which the small bubble's velocity multiplied by the time (which is asymptotically constant for a single bubble) starts to decrease (point x in Fig.4c, marking the coexistence stage) and the time at which the small bubble reaches negative velocity (point O in Fig.4c, marking the end of the merger stage). The merger rate $\omega(q)$ is plotted in Fig.5a and compared to the merger rate $\omega(q)$ obtained by Alon *et al.*[6] for A=1, using the potential flow model.

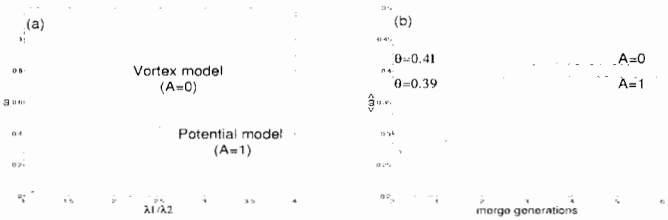

Figure 5. (a) Calculated merger rate ω for A=0 compared to the A=1 case. (b) TMZ power exponent θ for A=0 and A=1 as a function of the number of merger generations.

3. The statistical model

The next stage is to apply the single-bubble evolution and two-bubble interaction to a statistical model in order to get the turbulent mixing zone growth rate for an initial random perturbation. The statistical model is described by Alon *et al.*[2, 9] for the A=1 case, resulting in a power law of t^{θ}, where $\theta = 0.4$.

In the statistical model, for the case of the Richtmyer-Meshkov instability: $\theta =< \omega(q) >$ where the average is taken over the bubble spectrum derived from the calculated merger rate. From Fig.5b one can see that asymptotically, when a self similar regime is reached, θ approaches the value $\theta_{asy} = 0.41$ for A=0 as compared to $\theta_{asy} = 0.39$ for A=1. The result for A=0 was compared to a full 2D simulation resulting in good agreement for the power law exponent, as can be seen in Fig.6b.

The TMZ growth is similar for A=1 and A=0 despite somewhat different physics. The reason for this is that θ is determined by $\omega(q)$, which is similar in both cases for $\lambda_1/\lambda_2 < 2.5$ (the dominant regime of the self-similar bubble spectrum.) and since while in the Rayleigh-Taylor (RT) case the buoyancy, which strongly depends on A, leads to a linear dependence on A, in the RM case the drag, which is weakly dependent on A, dominates. This result was previously suggested by Alon *et al.*[6] based on a set of a full 2D numerical simulations.

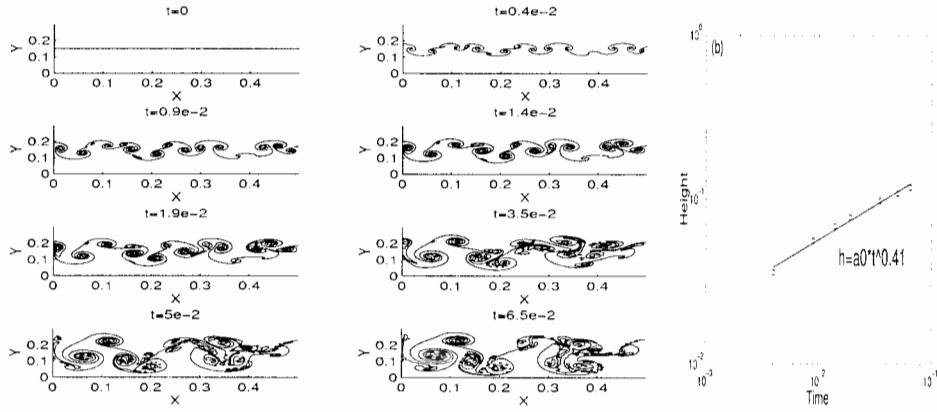

Figure 6. Comaprison between the model and a full 2D simulation for A=0. (a) a full 2D simulation, (b) the simulation TMZ height.

4. Conclusion

Using a vortex model for the Richtmyer-Meshkov instability for Atwood number A=0, we model the single-bubble velocity to get the asymptotic value $v_{asy} = 1/2\pi \cdot \lambda/t$ and the complex interaction between two neighboring bubbles. Furthermore, using a statistical model we describe the development of random perturbations. The mechanism of bubble merger, modeled by the vortex model, leads to the power law of $t^{0.4}$, supporting the conclusion that the power law exponent for the RM instability for the bubble front is independent of the Atwood number. Note that for the spike front, an Atwood number dependent power law was found [2]. At A$\rightarrow$ 0 bubbles and spikes become symmetric and the entire TMZ grows as $t^{0.4}$.

Presently we are using a similar vortex model to model the Kelvin-Helmholtz instability in the limit of A=0.

References

[1] Richtmyer RD, Commun. Pure. Appl. Math., 13, 297, (1960); Meshkov EE, Fluid Dyn., 4, 101, (1969).
[2] Alon U, Hecht J, Mukamel D and Shvarts D, Phys. Rev. Lett., 72, 2867, (1994).
[3] Layzer D, Astrophys. J., 122, 1, (1955).
[4] Hecht J, Alon U, Shvarts D, Phys. Fluids, 6, 4019, (1994).
[5] Dimonte G and Schneider M, Phys. Rev. E, 54, 3740, (1996).
[6] Alon U, Hecht J, Ofer D, Shvarts D, Phys. Rev. Lett., 73, 534, (1995).
[7] Jacobs JW and Sheeley JM, Phys. Fluids, 8, 405, (1996).
[8] Paterson AR, "A First Course in Fluid Dynamics", Cambridge University Press, (1983).
[9] Alon U, Shvarts D and Mukamel D, Phys. Rev. E, 48, 1008, (1993).
[10] Zabusky N, Ray J, Samtaney RS, Proc. of the 5th international workshop on Compressible Turbulent Mixing, R. Young, J. Glimm, B. Boyton editors, World Scientific, (1995).

Experimental and Theoretical Study of Nonlinear Evolution of Single-mode and Two-Bubble Interaction under Richtmyer-Meshkov Instability

O. Sadot[1], L. Erez[1], U. Alon[3,4], D. Oron[1,3], L.A. Levin[3], G. Erez[1], G. Ben-Dor[2] and D. Shvarts[2,3]
[1]Physics Dept., Ben Gurion University of the Negev, Beer Sheva 84105, Israel
[2]Mechanical Eng. Dept., Ben Gurion University of the Negev, Beer Sheva 84105, Israel
[3]Physics Dept., Nuclear Research Center-Negev, Beer Sheva 84190, Israel
[4]Physics Dept., Princeton University, Princeton NJ 08540, USA

Abstract: Experiments have been performed measuring the time development of shock-wave induced turbulent mixing between two gases initially separated by a thin membrane. For the single-mode experiments bubble and spike were measured separately in both linear and non-linear growth regimes. The experimental results were found to be in very good agreement with the results of a potential flow model which describes the linear, early non-linear and late asymptotic behavior of the bubble. In addition to the single-mode experiment, two-bubble experiments were performed and analyzed. Bubble competition was identified. The experimental results of the bubble competition, which determines the front evolution, were found to be in good agreement with both full numerical simulations and the potential flow model.

1. Introduction

The instability mechanism which appears at an interface between two fluids of different densities accelerated by a shock wave, known as the Richtmyer-Meshkov(RM) instability, can give rise to turbulent mixing. The turbulent mixing caused by the RM instability is of great interest in inertial confinement fusion and astrophysics. Recent theoretical work [1, 2] has predicted the evolution of the instability through the late nonlinear stage. After the shock passage the interface can be described by an incompressible evolution of the flow field [1, 2, 3]. For a single mode perturbation the instability can be described by a linear stage, during which the growth is characterized by a constant velocity, followed by a nonlinear stage during which the growth velocity reaches an asymptotic 1/t behavior [2].

An expansion of the flow equation to second order [1, 3] yields $U(t) = U_0(1 \pm AkU_0t)$ (the minus sign is for the bubble, the plus for the spike), showing that the bubble velocity begins to decrease. At late time, the A=1 bubble attains an asymptotic velocity of $U_b = 1/3\pi \cdot \lambda/t$ [2]. For $A < 1$ all bubble velocities approach the same asymptotic form, $U_b = C \cdot \lambda/t$, where $C = 1/3\pi$ for $A \geq 0.5$ and rises to about $C = 1/2\pi$ at low A's [4]. The difference in the value of the coefficient C is attributed to the added mass effect. The spikes at A=1 initially accelerate, in accordance with the second-order expansion, and then saturate to a constant velocity. At $A < 1$ the spike velocity also initially rises and then begins to decreases, asymptotically going as $U_s = (1 + A)/(1 - A) \cdot C \cdot \lambda/t$ [1]. The difference between the spike and the bubble velocity is attributed to the difference in the drag forces.

We find that the whole evolution can be fitted by a simple formula which captures the

More information - Email: sorens@bgumail.bgu.ac.il or schwartz@bgumail.bgu.ac.il

linear, early nonlinear and asymptotic behavior of the bubble and spike evolution :

$$U(t) = U_0 \frac{1 + Bt}{1 + Dt + Et^2} \tag{1}$$

with $B = U_0 k$ for the bubble and for the spike, $D = (1 + A) \cdot U_0 k$ for the bubble and $D = (1 - A) \cdot U_0 k$ for the spike, and $E = \pi/2C \cdot U_0^2 k^2$ for the bubble and $E = \pi/2C \cdot (1 - A))/(1 + A) \cdot U_0^2 k^2$ for the spike. This formula captures the linear and early nonlinear stages, up to 2^{nd} order, with the correct A dependence (except for $A \geq 0.9$ for the spike) and converges to the correct asymptotic limit with C=$1/3\pi$ for $A \geq 0.5$ and $1/2\pi$ for $A \rightarrow 0$. Note that a similar Pade expansion has been suggested by Zhang [3]. The present expression extends the Pade approach by capturing not only the early stages but also the correct asymptotic form.

For the case of an initial multi-mode perturbation, Alon *et al.*[1]. have employed a statistical-mechanics bubble-merger model for the bubble front evolution. The model, which is an extension of the Sharp-Wheeler model [5] describes the behavior of an ensemble of rising bubbles, with overtake or merger interactions that lead to a continual increase of the typical bubble size. In the model the 2D front is treated as an ensemble of bubbles arranged along a line , characterized by their wavelengths, λ_i. Each of the bubbles rises with a velocity $U_i(\lambda_i)$, equal to the asymptotic velocity of a periodic array of bubbles with wavelength λ_i. The nonlinear interaction of bubbles of different wavelengths is described by a bubble-merger rate [1]. In this model, two adjacent bubbles of wavelength λ_i and λ_{i+1} merge at a rate $w(\lambda_i, \lambda_{i+1})$, forming a new bubble of wavelength $\lambda_i + \lambda_{i+1}$. This represents expansion of the surviving bubble to fill the space vacated by the bubble swept away from the front. The model was applied to derive the scaling laws for multi-mode classical RT and RM cases, resulting in new scaling laws for the bubble front evolution. From the bubble front evolution and the single-mode spike-to-bubble asymmetry it was possible to infer also the scaling laws for the spike front. It is therefore essential to provide the model with the three basic physical elements: the single-mode bubble evolution, the single-mode spike evolution, and the two-bubble interaction. These elements were provided in Ref. [1] using an A=1 incompressible potential flow model [2] numerical simulation and simple buoyancy and drag arguments.

The present paper describes the first direct experimental test of these elements under a real shock acceleration and with real fluids. We describe shock tube experiments with a shock of $M \simeq 1.3$ crossing an Air/SF_6 ($A = 0.67$) interface with an initial perturbation. The initial perturbations that are reported include a single-mode perturbation, for studying the single-mode bubble and single-mode spike evolution, and an initial two-bubble shape perturbation, for studying the bubble-competition process. The experimental results are compared with full numerical simulations as well as the simple potential-flow model [2].

The experiments are performed in a 7.5 meter-long horizontal double-diaphragm shock tube with an 8×8 cm^2 cross section. A thin membrane separates the two gases. To produce the initial perturbation, we mount thin copper wires at different positions across the shock tube and stretch over them a 0.1μm nitrocelluloid membrane. The development of the mixing region induced by the shock wave is measured by photographing a series of Schlieren pictures using a copper-vapor laser pulsed at a rate of about 10000 pulses per second and a shutterless rotating prism camera. More detail on the experimental apparatus can be found in Ref. [6].

2. Experimental results-single mode

Single-mode experiments were carried out with initial perturbation wavelengths of 80, 40, 26 and 16mm, corresponding to wave numbers 1,2,3 and 5 respectively. Fig.1(a) shows a time evolution sequence of the λ=80mm case. During most of the experiment the perturbation amplitude is small enough so it can be expected to stay at the linear regime. However, for the $\lambda = 26mm$ case, Fig.1(b), the perturbation has entered deep into the nonlinear stage from early times.

In the first few frames of each case one can see the shock advancing ahead of the perturbed interface. Since we would like to infer the location of the bubble and spike front relative to the unperturbed interface, one has to measure the location of the unperturbed interface. The interface velocity is obtained from the measured shock velocity using the Rankine-Hugoniot equation. Fig.2 shows the evolution of the bubble and spike tips relative to the unperturbed interface. In order to put all the single-mode experiments on one unified graph, we have plotted in Fig.2 the bubble and spike tip heights, $H(t)$, in dimensionless units, $(H(t) - H(0)) \cdot k$, as a function of dimensionless time, $U_0 \cdot k \cdot t$, with U_0 the Richtmyer initial velocity. Also plotted in Fig.2 are the heights obtained from the analytical formula of Eq.1 using $C = 1/3\pi$ and $C = 1/2\pi$. It can be seen that the C=$1/3\pi$ coefficient fits better the experimental results, as is expected for A=0.67. The agreement is very good for the bubble front and reasonably good for the spike front, where the experimental error in determining the tip location is larger.

A similar experiment was conducted by Aleshin *et al.*[7] using Xe and Ar as gases (A = 0.53) at much higher Mach number, $M = 3.5$, where compressible effects are much more pronounced. The agreement between our model, Eq.1, and the experiment results of Ref. [7] is good (data not shown). It should be noted that the theory which underlines the simple analytical formula, Eq.1, is an incompressible theory. The fact that the same formula fits well both the weakly compressible case (M=1.3) and the strongly compressible case ($M = 3.5$) suggests that the evolution of the RM instability after passage of the shock is determined mainly by incompressible effects.

3. Experimental results-bubble competition

We now turn to the two-bubble interaction experiments. We chose an array of alternating large (about 25mm) and small (10-15mm) bubbles for comparison with similar simulations and modeling of Hecht *et al.*[2] The central part of the membrane always consisted of a small bubble flanked by two large bubbles, and the two sides were completed by partial small bubbles. The initial amplitudes of the large and small bubbles were chosen such that the initial velocities of both bubbles according to Richtmyer formula are similar (i.e., $a_l/a_s = \lambda_s/\lambda_l$ where s and l are the small and large bubble respectively). Fig.3 shows the time evolution of the interface in the 27mm/17mm experiment. Superimposed on the experimental pictures is the interface structure from the full simulation results. The agreement between the experimental results and the numerical simulation is very good, including the change in the small bubble location and size relative to the two large neighboring bubbles. The bubble merger process can be seen from the shape of the small and large bubbles and especially from the orientation of the spikes between the larger and smaller bubbles, which skew toward the large bubble as the small bubble disappear.

The competition process is most dramatically demonstrated by plotting the bubble tip locations relative to those measured and calculated for the single-mode case. In Fig.4(a) we

have plotted the two bubble heights, relative to the unperturbed interface. The figure shows the experimental results, the full numerical simulation and the potential flow model of Hecht *et al.*[2]. For the model we use the A=1 description but with the initial bubble velocity taken from the Richtmyer formula, which includes the A dependence. As is explained by Alon *et al.*[1], this is the main A dependence of the process. Also plotted are the two individual non-interacting bubble evolution lines, derived from Eq.1, which was shown above to fit the single-mode bubble evolution very well (Fig.2). As can be seen, the bubble competition process is very evident and pronounced. Initially the two bubbles evolve according to the non-interacting lines, but in the nonlinear stage a strong interaction takes place, the result of which is the faster growth of the larger bubble and the shrinking of the smaller bubble downstream. The agreement between the full simulation and the experimental results is very good. Similar agreement is also found when comparing the experimental results with the simple potential flow model, especially in the prediction of the merger time. The bubble competition is even more pronounced when one looks at the height difference between the tips of the two bubbles. This provides an accurate experimental measurement since it is independent of the interface location. Fig 4(b) shows the time evolution of the difference in the heights of the two bubbles. The rapid increase in the height difference compared to that of two non-interacting bubbles is clearly seen, demonstrating the bubble-merger process, in which the larger bubble overtakes the smaller one.

4. Summary

We have performed the first experiments that clearly demonstrate the key elements of the bubble-merger model: the single-mode bubble and spike evolution and the two-bubble interaction process in which the larger bubble overtakes the smaller bubble. The experimental results were found to be in very good agreement with both full numerical simulations and the theoretical model, which was used to infer the evolution of a multi-mode initial perturbation.

References

[1] Alon U, Hecht J, Ofer D and Shvarts D, Phys. Rev. Lett., 74, 534, (1995).

[2] Hecht J, Alon U and Shvarts D, Phys. Fluids, 6, 4019, (1994).

[3] Zhang Q and Sohn SI, Phys. Fluids, 9, 1106, (1997).

[4] Jacobs JW and Sheeley JM, Phys. Fluids, 8, 405, (1996); Zabusky N, Ray J and Samtany RS, in the Proc. of the 5^{th} International Workshop on Compressible Turbulent Mixing, Stony Brook 1995, Ed. R. Young, J. Glimm and B. Boston, 89, (1996); Rikanati A, Alon U and Shvarts D, the present proceedings.

[5] Sharp DH, Physica 12D, 3, (1984); Gardner CL, Glimm J, McBryan O, Menikoff R, Sharp DH and Zhang Q, Phys. Fluids, 31, 447, (1988); Glimm J, Li XR, Menikoff R, Sharp DH and Zhang Q, Phys. Fluids A, 2, 2046, (1990).

[6] Erez L, Sadot O, Erez G and Levin LA, in the Proc. of the 5^{th} International Workshop on Compressible Turbulent Mixing, Stony Brook 1995, Ed. R. Young, J. Glimm and B. Boston, 169, (1996).

[7] Aleshin AN, Lazareva EV, Zaitsev SG, Rozanov VB, Gamali EG and Lebo IB, Sov.Phys. Dokl., 35, 159, (1990).

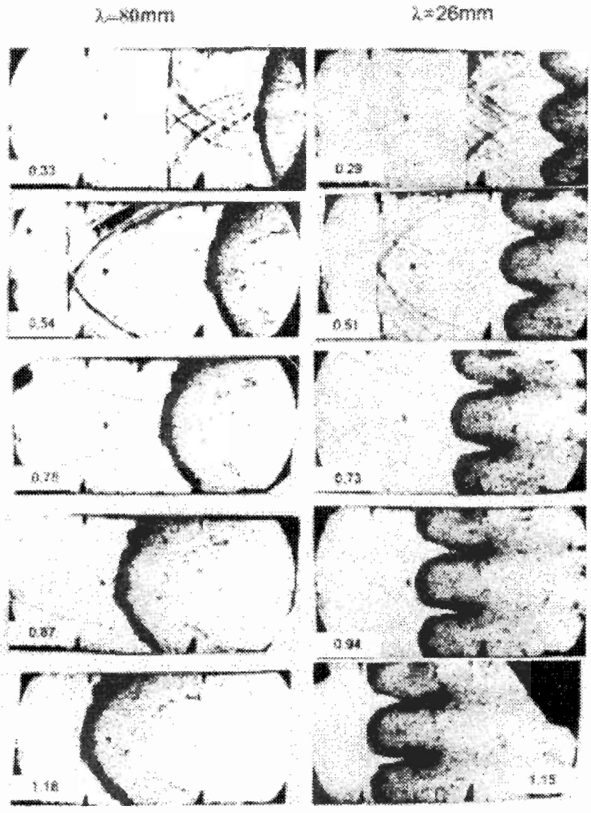

Figure 1. Series of Schlieren photographs from single experiment (a) Air to SF_6, λ=80mm. (b) Air to SF_6, λ=26mm, numbers indicate time after shock passage in msec.

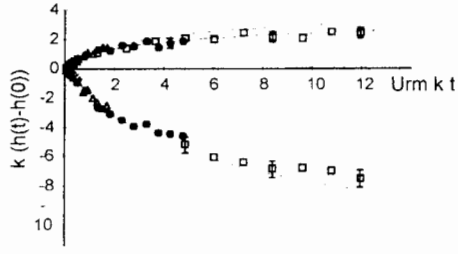

Figure 2. Bubble and spike height in normalized coordinates.

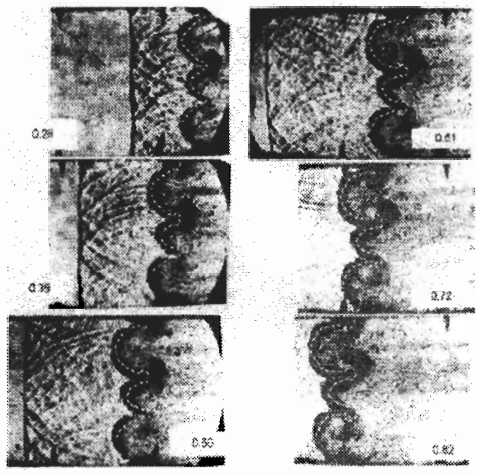

Figure 3. The evolution of the interface for M=1.25, $\lambda_1 = 27mm$, $\lambda_2 = 17mm$. sinulation results -dashed line.

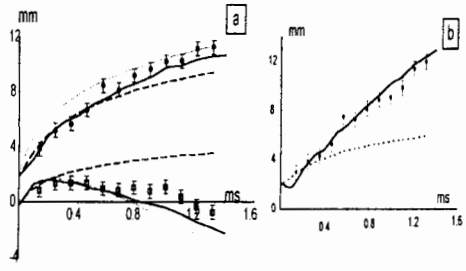

Figure 4. (a) Bubble height in the bubble-competition experiment: experiment -dots; potential flow model -light line; full-scale simulation -full line; and independent bubble front growth -dashed line. (b) Bubble height difference.

Baroclinic Circulation Generation on Shock Accelerated Slow/Fast Gas Interfaces

R. Samtaney[1], J. Ray[2] and N.J. Zabusky[2]
[1]Sarnoff Corporation, CN 5300, Princeton, NJ 08543-5300, USA
[2]Dept. of Mech. & Aero Engg., P.O. Box 909
Rutgers University, Piscataway, NJ-08855-0909, USA

Abstract: Vorticity is deposited baroclinically by shock waves on density inhomogeneities. We present 2D analytical results for σ, the circulation deposition per unit unshocked interface length, within the regular refraction regime. We also derive scalings for strong and weak shocks. Our results are validated by quantifications of numerical simulations of the compressible Euler equations using a second-order Godunov code. The results derived for the planar interface are generalized to calculate the total circulation deposition on sinusoidal interfaces.

1. Introduction

The interactions of shock waves with density inhomogeneities are of fundamental importance in compressible turbulence and occur in a myriad of practical and natural situations [1, 2]. This interaction is often referred to as the *Richtmyer-Meshkov Instability* environment after Richtmyer (linear stability analysis [3]) and Meshkov (experimental confirmation [4]).

Circulation deposition is the dominant fluid dynamical process in early time Richtmyer-Meshkov instability environment. In this paper we employ local analysis [5, 6], to quantify the circulation on simple 2-dimensional (oblique-planar and sinusoidal) interfaces.

The physical problem may be characterized by a shock wave of Mach number M propagating in a rectangular shock-tube through a gas of density ρ_0 (and ratio of specific heats γ_0), and an interface separating a gas of density ρ_b (and ratio of specific heats γ_b). We consider two possible physical situations : a sinusoidal interface with amplitude A and wavelength λ or an oblique interface inclined at angle α. The parameter space is four dimensional: the shock strength $(\xi(M) = (p_1 - p_0)/p_1 = [\frac{2\gamma}{\gamma+1}(M^2 - 1)]/[1 + \frac{2\gamma}{\gamma+1}(M^2 - 1)])$, the stratification $(\eta = \rho_b/\rho_0)$, the geometry of the interface (α or A/λ) and γ_b/γ_0. There are two generic classes of interaction: "slow-fast" (s/f) and "fast/slow" (f/s) [8]. We will focus on s/f interactions where the density ratio η is less than unity and where the reflected wave is a rarefaction. For details of shock refractions at slow-fast interfaces, see [7].

As the shock traverses the interface, the misalignment of $\nabla\rho$ and ∇p leads to rapid vorticity deposition on the interface. The baroclinic vorticity drives the the slower evolution of the interface later. We will assume that the gas interface is initially vorticity free. Samtaney and Zabusky [6] developed exact and approximate expressions for circulation deposition for fast/slow (f/s) interfaces using shock polar analysis. In this paper we apply their approach to s/f interfaces with *regular* shock refractions. These refractions consist of a transmitted shock and a reflected centered expansion (RRE) which meet the incident shock at a *node*.

More information - Email: jaray@caip.rutgers.edu

2. Circulation at a planar slow-fast interface

2.1. Local analysis equations

Fig. 1 is a schematic of a planar shock refracting at a planar interface inclined at an angle α to the vertical. For $\alpha < \alpha_{cr}$, a critical angle, the refraction is RRE. The density ratio of the gases separated by the interface is η ($\eta < 1$). In Fig. 1 mm is the interface; i, r, t are the incident, reflected and transmitted waves respectively; $s1$ and $s2$ are the streamlines in the incident and transmitted media [1]; δ_0 and δ_1 are the deflections of $s1$ due to i and r, respectively and δ_b is the deflection of $s2$ due to t. p_0 and p_b are the initial pressures in the incident and transmitted gases respectively; p_1, p_2 and p_t are respectively the pressures behind the incident, reflected and transmitted waves. The freestream Mach number in front (behind) the incident, reflected and transmitted waves are $M_0(M_1)$, $M_1(M_2)$ and $M_b(M_t)$ respectively.

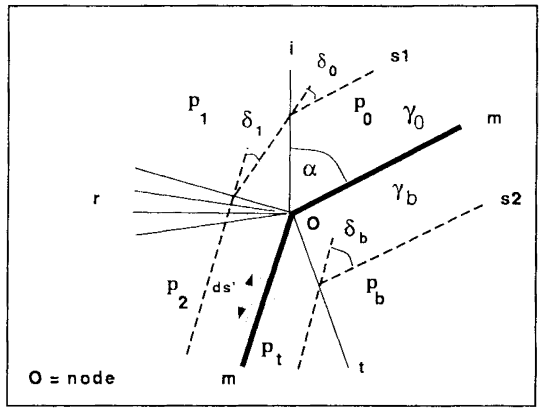

Figure 1. Schematic diagram of RRE refraction at an interface.

Following Henderson [5] we write equations of shock polars as

$$\tan\delta_i(p) = -\frac{(p/p_i)-1}{(p/p_i)-1-\gamma_i M_i^2}\left[\frac{(1+\mu_i^2)M_i^2-\mu_i^2-(p/p_i)}{\mu_i^2+(p/p_i)}\right]^{\frac{1}{2}}, \tag{1}$$

where $i = 0, b$ for the incident and transmitted shocks and $\mu_i^2 = \frac{\gamma_i-1}{\gamma_i+1}$. In the shock polar plane (δ, p) δ is the streamline deflection, p is the pressure ratio across the shock and the origin of the reflected polar is $(\delta_0(p_1), p_1)$. The deflection of the streamline through the rarefaction is given by the Prandtl-Meyer expansion expression, $\delta_1 = \nu(M_2) - \nu(M_1)$. Since the velocity of the node in the two media is the same, $M_b = M_0\sqrt{\eta}(\gamma_0/\gamma_b)^{\frac{1}{2}}$.

The fact that the streamlines in the shocked incident and transmitted gases have to be parallel as well as the continuity of pressure across the shocked contact discontinuity leads to the following two compatibility conditions: (a) $\delta_0(p_1) + \delta_1(p_2) = \delta_b(p_t)$ and (b) $p_t/p_b = p_2/p_0 = (p_2/p_1) \times (p_1/p_0)$. The compatibility conditions hold only for regular refractions. For $\alpha \geq \alpha_{cr}$, the refraction may include a reflected shock instead of an expansion or may become irregular. Details of the transition criterion are in [10].

[1] The gas in which the incident shock is initialized is loosely defined as the "incident" gas. The gas on the other side of the interface is loosely defined as the "transmitted" gas.

For simplicity, we assume $p_b = p_0 = \rho_0 = 1$ and $\rho_b = \eta$. All results will have units of circulation per unit length i.e. units of velocity. In order to convert to physical units, our normalized circulation must be multiplied by $c_0/\sqrt{\gamma_0}$, the ratio of the sound speed (in physical units) in the incident gas to $\gamma_0^{\frac{1}{2}}$.

2.2. Exact circulation

Consider *regular refraction* of a shock at a slow-fast gas interface (see Fig. 1). Let σ' be the circulation per unit *shocked* length of the interface i.e. σ' is the jump in the tangential velocity across the interface. Then σ' is given by $\sigma' = v_t - v_2$, where $v_t = M_t c_t$ and $v_2 = M_2 c_2$. The difference $v_t - v_2$ multiplied by the geometric factor $ds'/ds = (\cos\alpha/\cos(\alpha - \delta_b))$ gives the circulation per unit *unshocked* length σ. Omitting the algebra, we obtain

$$\sigma = \frac{\gamma_0^{\frac{1}{2}}\cot\alpha}{\cos(\alpha-\delta_b)} \left(\left[M^2 + \frac{2}{\gamma_b - 1}\left(\frac{1-\psi(p_2,\mu_b)}{\eta\gamma_0/\gamma_b} \right) \sin^2\alpha \right]^{\frac{1}{2}} - \left[M^2 + \frac{2}{\gamma_0 - 1}(1 - \phi(p_2/p_1,\gamma_0)\psi(p_1,\mu_0))\sin^2\alpha \right]^{\frac{1}{2}} \right). \quad (2)$$

Here ds and ds' are the lengths of an infinitesmal element of the interface before and after being shocked. The only unknown quantity in Eq.(2) is the pressure behind the transmitted shock (p_t) or the reflected rarefaction p_2, which is obtained by solving the compatibility conditions along with the equations of polar analysis.

2.3. Approximate circulation

For $\alpha > \alpha_{cr}$, σ does not exist and consequently an "approximate" expression needs to be derived. As in the analysis for fast-slow interfaces [6], we express σ as an asymptotic series in $\sin\alpha$. This gives

$$\sigma = \sigma_1 \sin\alpha + \sigma_3 \sin^3\alpha + O(\sin^5\alpha), \quad (3)$$

where σ_1 is given by

$$\sigma_1 = \frac{1}{\gamma_0^{\frac{1}{2}} M}\left(\frac{\gamma_b}{\gamma_b - 1}\frac{1-\psi(p_{20},\mu_b)}{\eta} - \frac{\gamma_0}{\gamma_0 - 1}(1 - \phi(p_{20}/p_1,\gamma_0)\psi(p_1,\mu_0)) \right), \quad (4)$$

where the limiting pressure $p_{20} = \lim_{\alpha\to 0} p_2$ is obtained from a one dimensional slow-fast interaction. The derivation of σ_3 is omitted here. Note that the numerical values of the coefficients σ_1 and σ_3 are actually negative because of the derivation.

The series expansion (Eq.(3)) is terminated after one or two terms to yield the "approximate" local analysis result for circulation. Thus, the approximate result to the first order is $\tilde{\sigma}_1 = \sigma_1 \sin\alpha$ and to the third order is $\tilde{\sigma}_3 = \sigma_1 \sin\alpha + \sigma_3 \sin^3\alpha$.

3. Numerical simulation and quantifications

Our numerical method is a second-order accurate Godunov scheme to solve the 2D compressible Euler equation and includes interface tracking. The boundary conditions are reflecting in the y-direction and inflow-outflow in the x-direction. Details of this method and the resolution convergence study can be obtained from [9] and [10].

We ran the code until the shock traverses the interface completely. At any instant the total interfacial vorticity is computed as $\tilde{\Gamma}(t) = \sum_D \omega(i,j,t)\Delta x\Delta y$, where $D = (i,j,t)\forall|\zeta(\mathbf{x},t)| < 1$.

$\omega(i,j,t)$ is computed using a second–order central difference. The total interfacial circulation ($\hat{\Gamma}$) divided by l, the unshocked length of the interface, to get the numerical value of the circulation per unit length of the original interface ($\hat{\sigma}$). In Fig. 2 we plot the exact result (σ), the third order approximate result ($\tilde{\sigma}_3$) and the numerical result ($\hat{\sigma}$) normalized by the first order approximate circulation ($\tilde{\sigma}_1$) as a function of $\xi(M)$ for an $\alpha = 15^0$ CO2-Air and R22-Air interfaces. We see a good agreement between the numerical, exact and approximate results.

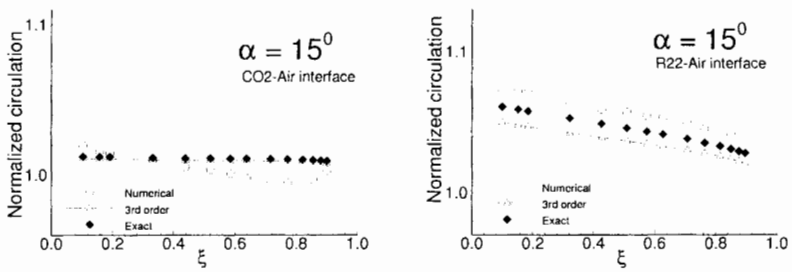

Figure 2. Normalized circulation per unit original length at different ξ for a CO2-Air (η=0.65) and R22 - Air (η=0.33) interface. α=15^0. 'o' = $\hat{\sigma}/\tilde{\sigma}_1$, '$\triangle$' = $\tilde{\sigma}_3/\tilde{\sigma}_1$, and filled '$\diamond$' = $\sigma/\tilde{\sigma}_1$.

4. Circulation for sinusoidal interfaces

Eq.(3) can be integrated for interfaces where α varies over the length of the interface. Consider a sinusoidal interface defined by $x = x_0 - A\cos ky$. Here $k = 2\pi/\lambda$ is the wavenumber. $\tilde{\Gamma}_3$, the total third-order accurate circulation on one half-wavelength sinusoidal interface ($0 \le y \le \lambda/2$) is given by

$$\frac{\tilde{\Gamma}_3}{2A} = \sigma_1 + \sigma_3 - \sigma_3 \frac{1}{2kA(1+k^2A^2)^{\frac{1}{2}}} \log\left[\frac{(1+k^2A^2)^{\frac{1}{2}} + kA}{(1+k^2A^2)^{\frac{1}{2}} - kA}\right]. \tag{5}$$

The largest angle between the shock and the interface occurs at $(0, \lambda/4)$ and is given by $\tan\alpha_{max} = kA$. For $A/\lambda = 0.05, \alpha_{max} = 17.4^o$.

We quantified the total circulation on CO2-Air and R22-Air interfaces in numerical experiments, $\hat{\Gamma}$ and compare this with $\tilde{\Gamma}_3$ in Fig. 3. We also plot the third order accurate circulation for a $A/\lambda = 0.01$ interface in each of the figures to show the effect of A in the third order term in Eq. 5.

We see that the discrepancy between $\tilde{\Gamma}_3$ and $\hat{\Gamma}$ increases with decreasing η and decreases with increasing ξ. Higher values of A/λ show a bigger discrepancy because they contain larger areas of irregular refraction. Higher ξ increases α_{cr}, rendering a larger part of the sinusoidal interface amenable to RRE refraction, and thus increasing the agreement between the analytical and numerical results.

5. Scaling laws

Since the exact expression for circulation deposition is coupled to the expression derived by local analysis (by the term p_2), it is desirable that scaling laws be derived to understand the phenomenon in a certain region of the parameter space of $(\xi(M), \eta, \alpha)$. In a previous section we derived an asymptotic series in $\sin\alpha$ for the circulation deposition per unit length (Eq.(3)).

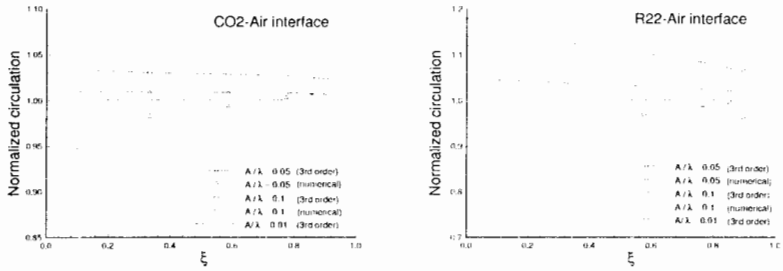

Figure 3. Total circulation deposition normalized by $\tilde{\Gamma}_1 = 2A\sigma_1$ for a sinusoidal CO2-Air interface (η=0.65) and a R22-Air interface (η=0.33) . '$\circ$' is for an interface with $A/\lambda = 0.01$, '$\triangle$' is for an interface with $A/\lambda = 0.05$ and '$\circ$' is for an interface with $A/\lambda = 0.1$. The lines denote the analytic 3^{rd} order circulation ($\tilde{\Gamma}_3$) and the unconnected points are the numerical results ($\hat{\Gamma}$).

Thus clearly, the scaling in α goes as $\sin\alpha$. Next, we try to determine the scaling of σ_1 with respect to ξ and η, in the limit of $M \to \infty$ ($\xi \to 1$) and $M \to 1$ ($\xi \to 0$). For simplicity we assume $\gamma_0 = \gamma_b = \gamma$. Omitting the algebra, we get $\sigma_s = \frac{2}{\gamma^{1/2}}(1 - \frac{1}{\sqrt{\eta}})\xi(M)\sin\alpha$ for weak shocks and $\sigma_s = \frac{K(\eta,\alpha)}{\sqrt{(1-\xi(M))}}$ where

$$K(\eta,\alpha) = \frac{\sqrt{\gamma+1}\cot\alpha}{\sqrt{2}\cos(\alpha-\delta_b)} \left[\left(1 - \frac{1}{\eta}\frac{4\gamma\bar{p}^{\frac{\gamma-1}{\gamma}}\sin^2\alpha}{(1+\mu^2)^{\frac{\gamma-1}{\gamma}}(\gamma+1)^2}\right)^{\frac{1}{2}} - \left(1 - \frac{4\gamma\bar{p}^{\frac{\gamma-1}{\gamma}}\sin^2\alpha}{(1+\mu^2)^{\frac{\gamma-1}{\gamma}}((\gamma+1)^2 - 4\gamma\sin^2\alpha)}\right)^{\frac{1}{2}}\right],$$

$\bar{p} = \lim_{\xi\to 1}\frac{2\gamma}{\gamma+1}p_2(1-\xi)$ and δ_b is the streamline deflection caused by the transmitted shock, for strong shocks.

In Fig. 4 we compare the weak and strong shock scaling for a planar 15° CO2-Air interface with the exact solution. We see that as $\xi \to 1$, the exact and strong shock scaling results for circulation deposition overlap.

6. Conclusions

An analytical model to estimate the circulation deposition on a slow-fast gas interface by a regular shock refraction system with a reflected rarefaction was developed. An approximate expression for the same was developed by expanding the analytical expression in terms of $\sin\alpha$. This model was derived for two dimensional interfaces only. For regular refractions and for weak stratifications ($\eta \to 1$) and strong shocks ($\xi(M) \to 1$), the exact and approximate circulations from local analysis agree well with quantifications from numerical simulations. Furthermore, we derived the scaling laws for baroclinic circulation generation at a slow-fast gas interface.

We believe that the quantification of baroclinic circulation will find application in building models of compressible turbulent mixing in the future.

Acknowledgement. This work was supported by the U. S. Department of Energy (Grant No. DE-

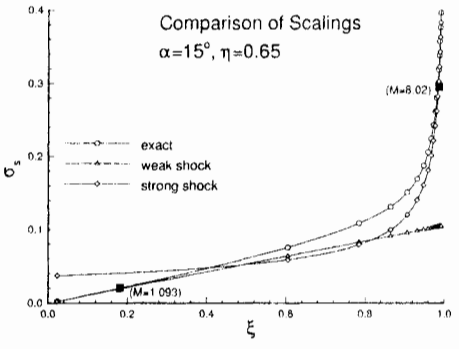

Figure 4. Circulation scaling for strong and weak shocks compared with the exact circulation for a 15° CO2-Air interface. $\gamma_0 = \gamma_b = 1.4$. 'o' denotes exact circulation per unit unshocked interface, 'Δ' denotes the weak shock circulation scaling and '$\diamond$' the strong shock circulation scaling. The filled rectangles denote the weak and strong shock limits for 5% error between the scaling and exact results. The figures in the parenthesis are the corresponding Mach numbers.

FG02-93ER25179.A00) monitored by Dr. Daniel Hitchcock. R. Samtaney acknowledges the support of Drs. Sam Uselton and Michael Gerald-Yamasaki during his stay at NASA Ames where part of this work was accomplished. We thank the National Center for Supercomputer Applications at Urbana, Il. for computer time on the Connection Machine, CM-5.

References

[1] Yang J, Kubota T and Zukoski EE, Applications of shock induced-mixing to supersonic combustion, AIAA J., 31, 5, 854-862, (1993).

[2] Lindl JD, McCrory RL and Campbell EM, Progress towards ignition and burn propagation in inertial confinement fusion, Physics Today, 32-40, September (1992).

[3] Richtmyer RD, Taylor instability in shock acceleration of compressible fluids, Comm. Pure and Appld. Math., XIII, 297-319, (1960).

[4] Meshkov EE, Instability of a shock wave accelerated interface between two gases, NASA Tech. Trans., NASA TT F-13, 074, (1970).

[5] Henderson LF, The refraction of a plane shock at a gas interface, J. Fluid Mech., 26, 607-637.

[6] Samtaney R and Zabusky NJ, Circulation deposition on shock-accelerated planar and curved density stratified interfaces : Models and scaling laws, J. Fluid Mech., 269, 45-85, (1994).

[7] Henderson LF, Colella P and Puckett EG, On the refraction of shock waves at a slow-fast gas interface, J. Fluid Mech., 224, 1-27, (1991).

[8] Henderson LF, On the refraction of shock waves, J. Fluid Mech., 198, 365, (1989).

[9] Yang X, Chern IL, Zabusky NJ, Samtaney R and Hawley JF, Vorticity generation and evolution in shock-accelerated density-stratified interfaces, Phys. Fluids A., 4, 1531-1540, (1992).

[10] Samtaney R, Ray J and Zabusky NJ, Baroclinic circulation generation on shock-accelerated slow/fast gas interfaces, Submitted Phys. Fluids.

Three-Dimensional High-Resolution Simulations of Compressible Rayleigh-Taylor Instability and Turbulent Mixing

O. Schilling[1], R.H. Cohen[1], W.P. Dannevik[1], A.M. Dimits[1], D.E. Eliason[1], A.A. Mirin[1], D.H. Porter[2], and P.R. Woodward[2]
[1]University of California, Lawrence Livermore National Laboratory, CA 94551, USA
[2]Department of Astronomy, University of Minnesota, Minneapolis, MN 55415, USA

Abstract: Preliminary results of three-dimensional simulations of compressible Rayleigh-Taylor instability and turbulent mixing in an ideal gas using the piecewise-parabolic method (PPM) (with and without molecular dissipation terms) are presented. Simulations with spatial resolutions up to 512^3 were performed. Two types of convergence studies are presented. Statistical analyses of the data are discussed, including: 1) spectra, and; 2) horizontally-averaged terms in the kinetic energy and enstrophy density evolution equations. The application of this statistical data to the development and testing of subgrid-scale models appropriate for compressible Rayleigh-Taylor instability-induced turbulent mixing is discussed.

1. Introduction

The classical Rayleigh-Taylor instability [1, 2] of a fluid layer with density ρ_1 superposed upon a fluid layer with density $\rho_2 < \rho_1$ subject to a downward acceleration exists in a variety of flows, ranging from the overturn of the outer portion of the collapsed core of a massive star to the laser implosion of deuterium-tritium fusion targets. The three-dimensional incompressible and nearly-incompressible forms of this instability—in which the densities are uniform in each layer and compressibility effects are minimized, respectively—have been extensively studied theoretically [3], numerically (*e.g.*, [4, 5]), and experimentally (*e.g.*, [6-8]). However, the fully-compressible form of this instability has been studied less thoroughly [9-13], primarily due to the severe computational requirements for variable density flow. Presented here are preliminary results of high-resolution piecewise-parabolic method (PPM) [14] simulations of three-dimensional compressible Rayleigh-Taylor instability and turbulent mixing in two horizontally-homogeneous ideal gas layers separated by a sharp interface.

2. Numerical simulations

2.1. The equations solved

The dissipative equations solved are the continuity, Navier-Stokes, and total energy equations

$$\frac{\partial \rho}{\partial t} + \frac{\partial}{\partial x_j}(\rho v_j) = 0\,, \tag{1}$$

$$\frac{\partial}{\partial t}(\rho v_i) + \frac{\partial}{\partial x_j}(\rho v_i v_j) = -\rho g \delta_{i3} + \frac{\partial}{\partial x_j}(\sigma_{ij} - p\delta_{ij})\,, \tag{2}$$

$$\frac{\partial}{\partial t}(\rho E) + \frac{\partial}{\partial x_j}(\rho E v_j + p v_j) = -\rho g v_z + \frac{\partial}{\partial x_i}\left(\sigma_{ij} v^j + \rho c_p \kappa \frac{\partial T}{\partial x^i}\right), \tag{3}$$

More information - Email: schilling1@llnl.gov

where

$$\sigma_{ij} = \mu \left(\frac{\partial v_i}{\partial x^j} + \frac{\partial v_j}{\partial x^i} - \frac{2}{3} \delta_{ij} \frac{\partial v_k}{\partial x_k} \right) \tag{4}$$

is the viscous stress tensor, $E = v^2/2 + p/[(\gamma - 1)\rho] - \mathbf{g} \cdot \mathbf{x}$ is the total energy density per unit mass, $p = (\gamma - 1)\rho c_v T$ is the pressure, and $\gamma = 5/3$. The units are chosen such that the mean density ρ_0, initial mean sound speed c_{s0}, and gravity g are unity. The flow is assumed to be statistically-homogeneous in the xy-plane (with periodic boundary conditions) and bounded by two impenetrable planes at $z = 0$ and 1. In the Euler (PPM) calculations, $\mu = \kappa = 0$.

2.2. Initial conditions

The initial thermodynamic state is that of stably-stratified compressible hydrostatic equilibrium in each layer. Consider a sharp interface at $z = 1/2$ with limiting Atwood number $At = \lim_{z \to 1/2} [\rho_1(z) - \rho_2(z)]/[\rho_1(z) + \rho_2(z)]$, where ρ_1 and ρ_2 are the initial mean density fields in the upper and lower layers, respectively. Rather than introducing initial perturbations on the interface, the equilibrium state was initially perturbed by velocity fluctuations

$$v_x = v_y = v_z = v_0 \sin \left(\frac{2\pi n_x}{L_x} x + \frac{2\pi n_y}{L_y} y \right) \left[1 - \cos \left(\frac{2\pi n_z}{L_z} z \right) \right], \tag{5}$$

where the amplitude $v_0 = O(10^{-4})$ has a random Gaussian distribution, and L_x, L_y, and L_z are the lengths of the sides of the computational domain. The corresponding initial kinetic energy spectrum is

$$E(k_\perp, 0) \propto \left(\frac{k_\perp}{k_0} \right)^4 e^{-2[(k_\perp - k_1)/k_0]^2}, \tag{6}$$

where $k_0 = 16\pi$ and $k_1 = 32\pi$; the velocity modes are initially excited up to a horizontal wavenumber $k_\perp = \left(k_x^2 + k_y^2 \right)^{1/2} = 64\pi$. The initial rms fluctuations of density, pressure, and internal energy are zero. The initial rms Mach number is $Ma_{rms}(0) = O(10^{-3})$, the kinematic viscosity is $\nu = 4.0 \times 10^{-5}$, and the Prandtl number is $Pr = \nu/\kappa = 1.0$. The limiting Atwood numbers for the simulations reported here are $At = 1/3$ and $5/7$, corresponding to spatial resolutions of 512^3 and 256^3, respectively. In the 256^3 simulation, a passively-advected scalar with initial profile $\phi(\mathbf{x}, 0) = 2z - 1 \in [-1, 1]$ was evolved to provide a measure of fluid mixing.

2.3. Qualitative results

Both simulations were run to $\sim 5\tau_{ac}(0)$, where $\tau_{ac}(0)$ is the initial acoustic crossing time in the lower layer. The qualitative dynamics of the nonlinear development of the multi-mode Rayleigh-Taylor instability was studied by visualizing isosurfaces of the passive scalar and temperature fields. The passive scalar is advected by the velocity field, and shows the formation of bubbles of light fluid and spikes of heavy fluid, and their subsequent growth and merger. Plates 1 and 2 show the passive scalar field at $t = 3\tau_{ac}(0)$ and $4\tau_{ac}(0)$, respectively, from the 256^3 simulation. As each fluid layer is initially isothermal, the temperature field provides another view of the bubble and spike evolution, and development of turbulent mixing. Plate 3 shows the temperature field at $t = 5\tau_{ac}(0)$ from the 512^3 simulation. The horizontally-averaged thermodynamic fields (density, pressure, entropy) exhibited an asymptotic evolution towards a stably-stratified adiabatic equilibrium. The spatio-temporal development of the mixed layer is also observed by examining the enstrophy field $\omega^2/2$. A more intense and rapid growth of enstrophy was observed in the 256^3 simulations with $At = 5/7$ than in the 512^3 simulations with $At = 1/3$, as expected. Plate 4 shows the norm of the vorticity field at $t = 5\tau_{ac}(0)$ from the 512^3 simulation.

2.4. Spectra

To determine the kinematic viscosity required such that the PPM simulations with molecular dissipation (PPMNS) would be fully-resolved for a given spatial resolution, two types of convergence studies were performed. In the first, a series of 128^3 PPMNS simulations were performed for $\nu = 3.0 \times 10^{-4}$, 1.0×10^{-4}, and 4.5×10^{-5}, together with a 128^3 PPM simulation. It was found that the PPMNS spectra (*e.g.*, that of v_z^2) converged to the PPM spectra as ν was decreased. In the second, spectra from a series of PPMNS simulations with $\nu = 4.5 \times 10^{-5}$ and spatial resolutions of 128^3, 256^3, and 512^3 were compared to those from a 128^3 PPM simulation. The 256^3 and 512^3 PPMNS spectra were converged.

2.5. Statistics

A preliminary study of the statistical properties of compressible Rayleigh-Taylor instability-induced turbulent mixing was undertaken by examining horizontally-averaged terms in the evolution equations for both first-order (*e.g.*, velocity and vorticity components) and second-order (*e.g.*, kinetic energy, total energy, enstrophy) quantities as a function of height z and time t. Analysis of these terms elucidates the fundamental physical processes in buoyancy-driven compressible flows. In particular, the relative importance of these terms during the development of the instability and subsequent turbulent mixing may be determined. Furthermore, the fields can be further split into supergrid and subgrid fields using a Favre filter, and various subgrid-scale correlations that require modeling can be evaluated.

Let $\langle \cdot \rangle$ denote a horizontal average. Neglecting viscous dissipation, the horizontally-averaged kinetic energy and enstrophy density equations are

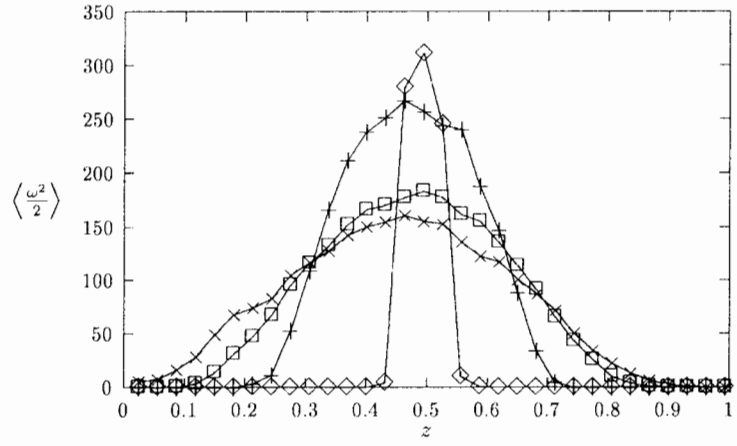

Figure 1. Time-evolution of the horizontally-averaged enstrophy density from the 256^3 simulation; $\diamond$ $t = 1$, $+$ $t = 2$, $\square$ $t = 3$, $\times$ $t = 4$.

$$\frac{\partial}{\partial t}\left\langle \frac{\rho v^2}{2} \right\rangle = \underbrace{-g\langle \rho v_z \rangle}_{\text{force production}} \quad \underbrace{+\langle \rho \epsilon \rangle}_{\text{dissipation}} \quad \underbrace{-\langle p \boldsymbol{\nabla} \cdot \mathbf{v} \rangle}_{\text{pressure dilatation}} \quad \underbrace{-\left\langle \boldsymbol{\nabla} \cdot \left(\frac{\rho v^2 \mathbf{v}}{2} \right) \right\rangle}_{\text{kinetic energy flux term}} \quad \underbrace{-\langle \boldsymbol{\nabla} \cdot (p \mathbf{v}) \rangle}_{\text{pressure flux term}}, \qquad (7)$$

$$\frac{\partial}{\partial t}\left\langle \frac{\omega^2}{2} \right\rangle = \underbrace{-\left\langle \frac{\mathbf{v}\cdot\boldsymbol{\nabla}\omega^2}{2} \right\rangle}_{\text{advection}} \underbrace{+\langle \boldsymbol{\omega}\cdot(\boldsymbol{\omega}\cdot\boldsymbol{\nabla}\mathbf{v})\rangle}_{\text{stretching}} \underbrace{-\left\langle \omega^2\,\boldsymbol{\nabla}\cdot\mathbf{v} \right\rangle}_{\text{enstrophy dilatation}} \underbrace{+\left\langle \frac{\boldsymbol{\omega}\cdot(\boldsymbol{\nabla}\rho\wedge\boldsymbol{\nabla}p)}{\rho^2} \right\rangle}_{\text{baroclinic production}}, \tag{8}$$

where $\rho\epsilon = \sigma_{ij}\partial v^i/\partial x_j$, and the viscous flux term in (7) and the dissipation terms in (8) have been neglected. Note that the force production term in (8) vanishes. Figure 1 shows the horizontally-averaged enstrophy density as a function of height z and time [in units of $\tau_{ac}(0)$] from the 256^3 simulation. At $t = 1$, $\langle\omega^2/2\rangle$ is peaked about the interface, and grows and spreads over the vertical extent of the domain in time. The enstrophy relaxes in time from its maximum value and spreads nearly symmetrically about the interface as the mixed layer develops and grows. Figures 2 and 3 show the contributions of the right sides of (7) and (8) as a function of height z at $t = 4$ from the 256^3 simulation. The pressure flux and dilatation terms in (7) contribute significantly to the kinetic energy evolution. The stretching term is the dominant term in (8), indicating strong turbulence production, while the baroclinic production term (which dominates at early times and generates the instability) dominates the advection and dilatation terms.

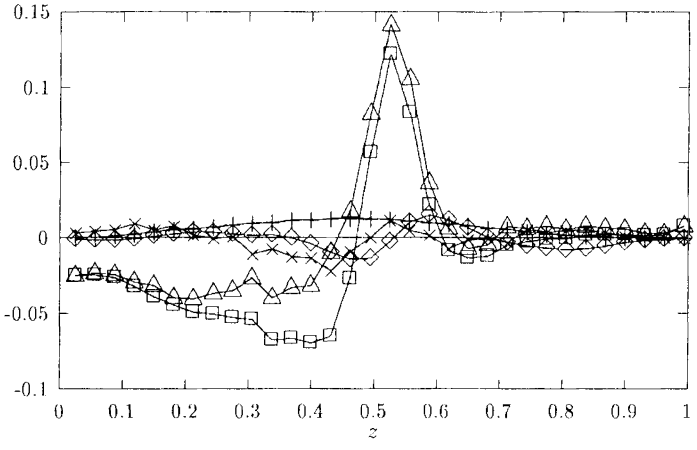

Figure 2. Terms in the horizontally-averaged kinetic energy density equation at time $4.0\tau_{ac}$ from the 256^3 simulation; $\diamond$ force production, + dissipation, $\square$ pressure-dilatation, $\times$ kinetic energy flux term, $\triangle$ pressure flux term.

3. Future work

The dependence of the mixing rates and scaling properties on the Atwood number and the degree of compressibility will be studied by diagnosing high-resolution ($\sim 10^9$ zones), longer-time simulations with aspect ratios having $L_z/L_x, L_z/L_y > 1$ to minimize vertical boundary effects. Studies of compressibility effects on the asymptotic properties of Rayleigh-Taylor instability-induced turbulent mixing will be performed. In addition, Favre decompositions will be implemented to diagnose terms in the evolution equations relevant to subgrid-scale and turbulence modeling. Several subgrid-scale models that have been proposed for compressible turbulence will be tested, and extensions of these models to *buoyancy-driven* compressible flows will be investigated.

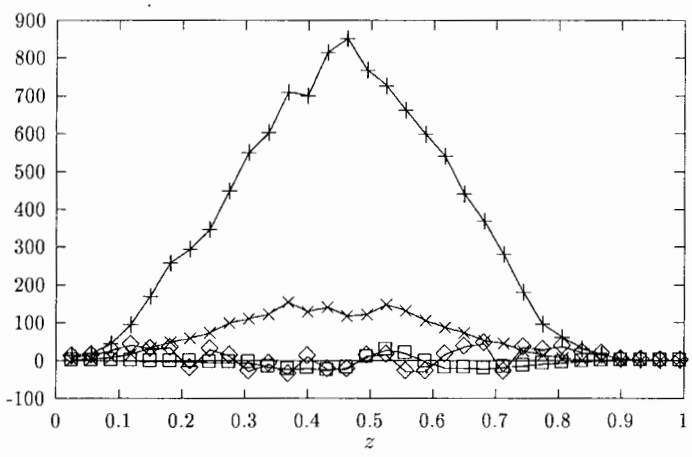

Figure 3. Terms in the horizontally-averaged enstrophy density equation at time $4.0\tau_{ac}$ from the 256^3 simulation; $\diamond$ advection term, $+$ stretching term, $\square$ enstrophy dilatation, $\times$ baroclinic production.

Acknowledgement. Work performed by LLNL and the University of Minnesota under the auspices of U.S.D.O.E. Contract W-7405-ENG-48, and by the University of Minnesota under the auspices of U.S.N.S.F. Grand Challenge Grant ASC-9217394. Computations were performed on the ASCI Blue Pacific IBM SP at LLNL.

References

[1] Lord Rayleigh, Proceedings of the London Mathematical Society, 14, 170, (1883).
[2] Taylor GI, Proceedings of the Royal Society of London A, 201, 192-196, (1950).
[3] Chandrasekhar S, Hydrodynamic and Hydromagnetic Stability, Oxford University Press, (1961).
[4] Youngs DL, Physics of Fluids A, 3, 1312-1320, (1991).
[5] Unverdi SO & Tryggvason G, Physica D60, 70-83, (1992a); Unverdi SO & Tryggvason G, Journal of Computational Physics, 100, 25-37, (1992b).
[6] Read KI, Physica D12, 45-58, (1984).
[7] Linden PF & Redondo JM, Physics of Fluids A, 3, 1269-1277, (1991); Linden PF, Redondo JM & Youngs DL, Journal of Fluid Mechanics, 265, 97-124, (1994).
[8] Dimonte G & Schneider M, Physical Review E, 54, 3740-3743, (1996).
[9] Dahlburg JP & Gardner JH, Physical Review A, 41, 5695-5698, (1990).
[10] Li XL, Physics of Fluids A, 5, 1904-1913, (1993); Li XL, Physics of Fluids, 8, 336-343, (1996); Li XL, Jin BX & Glimm J, Journal of Computational Physics, 126, 343-355, (1996).
[11] Youngs DL, Laser and Particle Beams, 12, 725-750, (1994).
[12] Town RPJ, Jones BJ, Findlay JD & Bell AR, Laser and Particle Beams, 12, 163-183, (1994).
[13] Amala PAK, Ph.D. thesis, University of California, Davis, (1994).
[14] Colella P & Woodward PR, Journal of Computational Physics, 54, 174-201, (1984); Woodward PR & Colella P, Journal of Computational Physics, 54, 115-173, (1984).

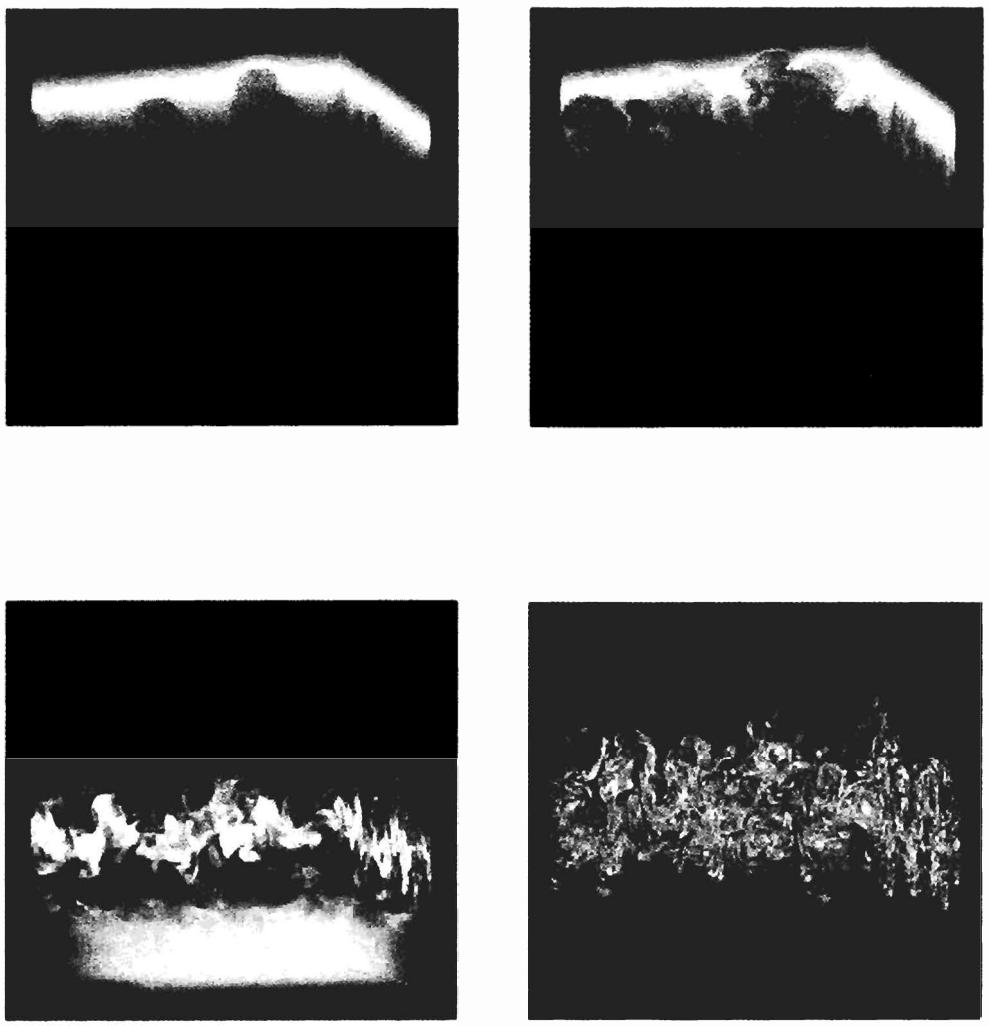

Figure 4. Plate 1. Passive scalar field at t=3 from the 256^3 simulation; Plate 2. Passive scalar field at t=4 from the 256^3 simulation. Plate 3. Temperature field at t=5 from the 512^3 simulation; Plate 4. Vorticity norm field at t=5 from the 512^3 simulation.

Structure of Mix in a Rayleigh-Taylor Unstable Fluid Cell

M.B. Schneider, G. Dimonte and B.A. Remington
Lawrence Livermore National Laboratory
P. O. Box 808, L-43, Livermore, CA 94550, USA

Abstract: Laser-induced fluorescence is used to image the central plane of the mix region of two immiscible liquids subject to the Rayleigh-Taylor instability. The familiar bubbles and spikes display a complex internal structure. This small-scale structure creates a large contact area whose density is constant in time. The size of the mixing zone, defined in a new way, grows with coefficient $\alpha_b >= 0.054$.

1. Introduction

The Rayleigh-Taylor (RT) instability [1-4], occurs during the acceleration of a heavy fluid by a light fluid. The rate of the instability is parameterized by the acceleration, g, and the Atwood number, $A=(\rho_2 - \rho_1)/(\rho_2 + \rho_1)$ where $\rho_1(\rho_2)$ is the density of the light (heavy) fluid. For small initial perturbations, there are linear [2, 6] and non-linear growth phases [5, 7, 8, 9]. Eventually a highly-disordered mixing zone (DMZ) develops, bounded by a bubble front which penetrates the heavy fluid as $\sim \alpha_b A g t^2$ and a spike front which penetrates the light fluid as $\sim \alpha_s A g t^2$. [10-15] The coefficient α_b is insensitive to A whereas α_s increases with A [13, 14].

Experiments [10, 11, 12, 15] using backlit photography obtain values of $\alpha_b \sim 0.06 - 0.07$ that are larger than those found in all 3-D [13, 16] and some 2-D [12, 16, 17] hydrodynamic simulations, but similar to those found in 2-D simulations which track the interface [18, 19]. The backlit photography experiments cannot measure the structure within the DMZ. This structure is important because it determines the constitutive properties in the DMZ such as composition (or density), energy, effective opacity, and equation of state.

This report describes RT experiments using laser-induced fluorescence (LIF) which image the DMZ of a cell containing two immiscible liquids at Reynolds number of order $\sim 10^5$. The images show a complex internal fine structure in the bubbles and spikes. While the large bubbles and spikes define the boundaries of the DMZ, their small-scale internal structures increase the mix entropy, which eventually (for miscible fluids) leads to molecular mix. This study shows that: (i) the measured α_b is consistent with recent experiments [15]; and (ii) the internal structure is responsible for the large amount of contact area between the mixing fluids.

2. Experimental configuration

The present experiments use the Linear Electric Motor (LEM) [20] at Lawrence Livermore National Laboratory to accelerate a container for 50 ms at a downward constant g ($\sim 73 g_0$ where g_0 = earth's gravity). The fluid cavity is 73mm wide, 88 mm high, and 73mm deep. For LIF, a laser sheet parallel to the acceleration illuminates the central plane of the cavity from below. Images of the fluorescence are recorded on 35mm film.

The film images are digitized, converted to intensity images, corrected for the absorption

More information - Email: schneider5@llnl.gov

of the laser light by dye molecules in the fluid, smoothed to reduce noise, and adjusted for variations in the laser beam intensity across the cell. To avoid wall effects, only the central 62 mm width of the cell is analyzed.

The fluids are decane (ρ_1 = 0.73 g/cm^3), and salt water (ρ_2 = 1.43 g/cm^3) plus a small amount of fluorescent dye (Kiton Red 620), giving an Atwood number of A = 0.34. The surfactant AOT is added to lower the interfacial tension to ultra-low values by forming a microscopically-thin microemulsion phase [21] at the interface. Glucose is added to the salt water to match its refractive index to within 0.03% of that of decane.

3. Experimental results

Corrected film density images at 27 and 45 ms are shown in the first column of Figure 1. The

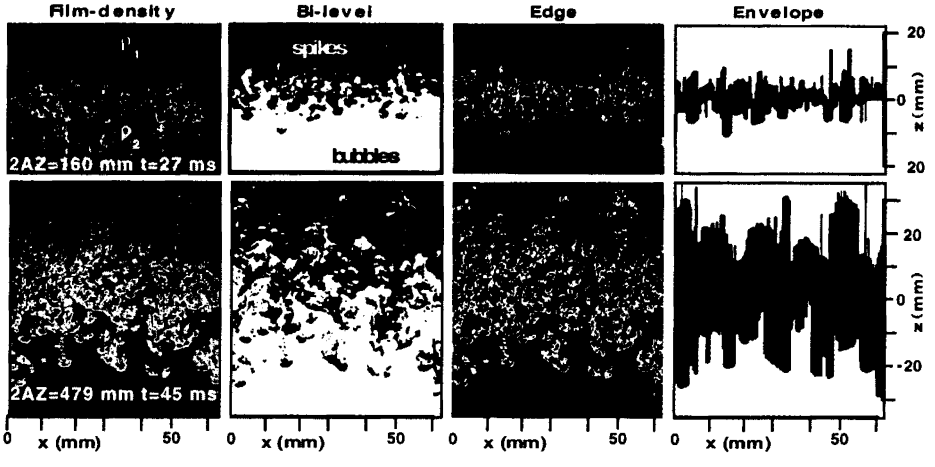

Figure 1. Images from a single run at two times illustrating the various types of processed images. The corrected film-density images are used to generate the bi-level images . The bi-level images are used to generate the edge images and the envelope images.

net displacement of the cell due to the acceleration is Z and the generalized displacement is defined as Agt^2 = 2AZ. The planar coordinate system moving with the fluid cell is x, z, with z=0 at the original interface.

The interfacial tension, σ, stabilizes the RT growth of perturbations with small wavelengths, leading to a mode of fastest growth with wavelength $2\pi\sqrt{(3/2)}L_c$ where L_c is the capillary length, $L_c^2 = 2\sigma/[(\rho_2 - \rho_1)g]$. [22] In the present experiment, L_c=0.10 mm at 73 g_0 so the fastest growing wavelength is ~0.7 mm with an e-folding time [22] ~0.9ms. When the amplitude becomes ~1/k ~ 0.1mm, the mode saturates. Thus, by 27 ms (the top image in Figure 1), the system has evolved into the DMZ regime.

The images are processed into bi-level and edge images to emphasize the internal structures, and envelope images, which display the large-scale features. This is shown in Figure 1. The bi-level image is generated from the corrected film-density image by mapping all pixels with less than ~50% intenstiy to 0, and all pixels with greater than ~50% intensity to 100. The actual cutoff level used for the mapping is adjusted to keep about the same number of pixels in each fluid (conservation of volume). The bi-level image is used to generate (i) the edge image using

the Roberts Edge method [23] and (ii) the envelope image using single-valued (in x) bubble and spike envelopes. The lower (bubble) envelope function is obtained by finding the value of z at which the maximum penetration of the top fluid into the bottom fluid occurs. The spike envelope is similar but on top. In the envelope image, the region between the two envelope functions is shown in black to mimick the backlit photographs [10, 11, 12, 15]. The resolution of the processed images is $< 1mm$ [24].

3.1. The growth of the mix region (DMZ)

The width of the DMZ is obtained from the bi-level image. Backlit photographs [10, 11, 12, 15] obtain the width by measuring the penetration of the bubble- and spike-fronts. The present data samples only one plane of the DMZ, so fewer bubbles and spikes are observed. To overcome the reduced statistics, a new penetration depth is defined from the projection of the bi-level image onto the z axis, as shown in Figure 2. The projection is plotted as a density profile and

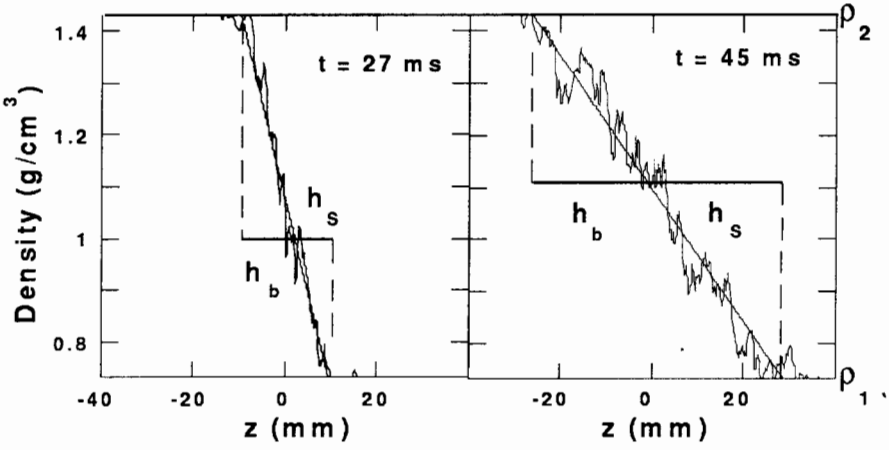

Figure 2. The projection of the bi-level images of Figure 1 onto the z axis. The projection is normalized to the density of the fluids. The definitions of bubble (h_b) and spike (h_s) penetration distances are shown.

generally has many fluctuations, so it is fit to a straight line. The bubble (spike) penetration, h_b, (h_s) is defined as the distance between the intersection of the straight line with $\rho_2(\rho_1)$ and the original location of the flat interface (z=0). The latter can be measured to within ~1mm. The present definitions of h_b and h_s are statistically robust because they depend on the entire profile. A procedure could have been employed which defines $h_b[h_s]$ by the $\rho_1 + 0.95(\rho_2 - \rho_1)[\rho_1 + 0.05(\rho_2 - \rho_1)]$ point of the profile, but the results would be too sensitive to fluctuations in the projections.

The variation of h_b and h_s with generalized displacement 2AZ appears linear, as shown in Figure 3, implying a self-similar evolution. This collection of data represents 6 separate runs, recording three images per run. The errors are the same size as the plot symbols and are due to the uncertainty in the location of the original interface. The data are fit to straight lines [10, 17], $h = h_0 + \alpha$ 2AZ. The linear fits in Figure 3 give $\alpha_b = 0.054 \pm 0.003$ and $\alpha_s = 0.062 \pm 0.003$. The value of α_b is ~10% smaller than the value obtained in backlit photography. This is expected because the laser sheet may not illuminate the most penetrating bubbles or spikes or their tips.

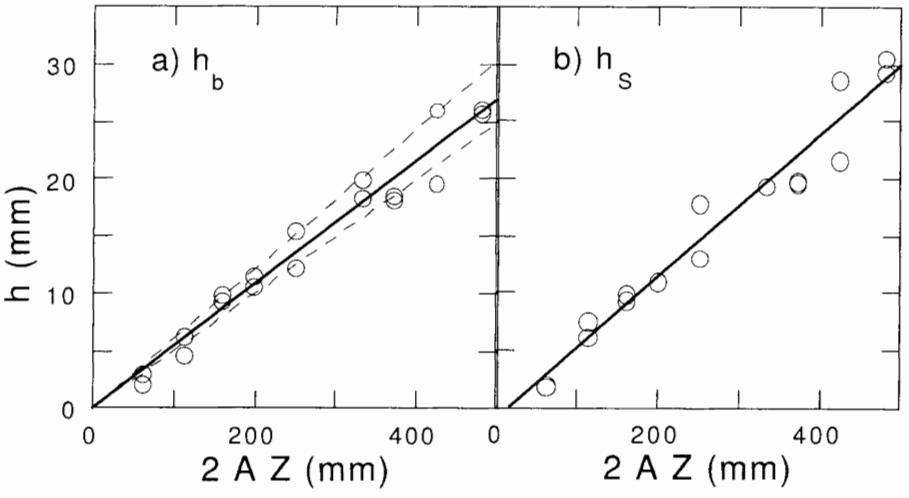

Figure 3. (a) Bubble, h_b, and (b) spike, h_s, penetrations vs. generalized displacement, 2AZ. The solid lines are (a) h_b= -0.45 + 0.054 2AZ and (b) h_s= -0.95 + 0.062 2AZ. The dashed lines in (a) show α_b= 0.061 (upper line) and 0.05 (lower line).

This effect is greater later in time when there are only a small number of bubbles (2-4) with large penetrations. The upper dashed line in Figure 3a shows the backlit photography result [15], h_b= 0.061 2AZ. This line is consistent with the early-time data ($2AZ < 200$) and with the most-penetrating late-time data. Thus, the results indicate that backlit photography is not seriously contaminated by wall effects. The measured α_b is ~5% higher than those found in 3-D hydrodynamic simulations [13, 16]. The lower dashed line in Figure 3a shows the simulation result, h_b = 0.05 2AZ. The simulations obtain h_b and h_s from the 99%, 1% [13] points of a volume-fraction profile. The simulation results may be slightly low. One difference is that the experiments use immiscible fluids whereas the fluids in the simulations are miscible.

Finally, the ratio h_s/h_b, obtained from the data in Figure 3, is $h_s/h_b = 1.1 \pm 0.05$. The error bars reflect the sensitivity of this ratio to the location of the flat interface. This ratio is in agreement with previous data (see figure 8 in Ref. [19]) and one 3-D simulation [13] but lower than the 1.3 predicted from another 3-D simulation [19] and lower than the 1.3 [19] to 1.4 [14]that models predict for A=0.34.

3.2. Structure of the DMZ

The contact area between the mixing fluids, shown in the edge images of Figure 1, determines the degree of particle and energy exchanges. In the 2-D edge image, the contact area is the length of the white pixels. The two edge images in Figure 1 display similar densities of white pixels in the centers of their respective DMZs, implying some small scale structure is always present. The edge images will be analyzed in another publication [24]. Models [9, 14, 18, 25, 26, 27] predict the evolution of the boundaries of t he DMZ to larger structure sizes. Larger structures have a smaller perimeter density than smaller structures, so processes not included in the models appear to be occuring which maintain the density of the small-scale structures.

The images in Figure 1 do suggest, however, that a large lengthscale increases with time.

This lengthscale, associated with the width and separation of the bubble and spike fronts, is seen most clearly in the envelope images. Notice the bubbles and spikes are long and skinny in these images. It will be discussed in a future publication [24].

4. Summary

In summary, images of the central plane of an RT unstable fluid cell are analyzed and give mix widths that agree with those obtained using the backlit photography technique [15], implying that the latter are not hampered by window effects. The present study uses a statistically robust definition for h_b and h_s and finds lower limits on $\alpha_b = 0.054 \pm 0.003$ and $\alpha_s = 0.062 \pm 0.003$, consistent with recent backlit photography experiments [15] (α_b= 0.061). The present results are still somewhat higher than in 3-D simulations (α_b(3D) = 0.04-0.05) [13, 16]. In addition, late in time, the bubbles and spikes are seen to maintain a complicated internal fine structure, as predicted in some numerical simulations [12, 19, 29] and models [28]. In contrast, the width of the large-scale features (bubbles and spikes) appear to grow in time [28].

Acknowledgement. We thank J. Ticehurst, S. Kiar, D. Nelson, S. Weaver, C. Allison, and T. Schwinn for their expert technical contributions. We are grateful to Drs. E. Burke, T. Clark, F. Harlow, P. L. Miller, D. Saltz, D. H. Sharp, A. Shestakov, D. Shvarts, P. Stry, D. Youngs, and Q. Zhang for invaluable discussions. We thank Dr. M. Eckart for his support. This work was performed under the auspices of the U.S. Department of Energy by the Lawrence Livermore National Laboratory under Contract No. W-7405-ENG-48.

References

[1] Lord Rayleigh, Scientific Papers, Vol. II, Cambridge Univ. Press, Cambridge, England, (1900).
[2] Taylor G, Proc. Roy. Soc. A, 201, 192, (1950).
[3] Muller E, Fryxell B and Arnett D, Astron. Astrophys., 251, 505, (1991); Herant M and Woosley SE, Astrophys. J., 425, 814, (1994).
[4] Lindl JD and Mead WC, Phys. Rev. Lett., 34, 1273, (1975); Kilkenny JD *et al.*, Phys. Plasmas; 1, 1379, (1994).
[5] Remington BA *et al.*, Phys. Plasmas, 2, 241, (1995).
[6] Lewis DJ, Proc. Roy. Soc. A, 202, 81, (1950); Jacobs JW and Catton I, J. Fluid Mech., 187, 353, (1988).
[7] Dunning MJ and Haan S, Phys. Plasmas, 2, 166, (1995).
[8] Ofer D *et al.*, Phys. Fluids B, 4, 3549, (1992).
[9] Sharp DH, Physica D9, 3, (1984).
[10] Read KI, Physica D12, 45, (1984).
[11] Kucherenko YA *et al.*, in 3rd Int Workshop on The Physics of Compressible Turbulent Mixing, Abbey of Royaumont, France, 427, (1991).
[12] Youngs DL, Physica D37, 270, (1989).
[13] Youngs DL, Phys. Fluids A, 3, 1312, (1991).
[14] Alon U *et al.*, Phys. Rev. Lett., 74, 534, (1995).
[15] Dimonte G and Schneider M, Phys. Rev. E, 54, 3740, (1996).
[16] Hecht J *et al.*, Laser and Particle Beams, 13, 423, (1995).
[17] Atzeni S and Guerrieri A, Europhysics Lett., 22, 603, (1993).
[18] Glimm J *et al.*, Phys. Fluids A, 2, 2046, (1990).
[19] Freed N *et al.*, Phys Fluids A, 3, 912, (1991).
[20] Dimonte G *et al.*, Rev. Sci. Inst., 67, 302, (1996).

[21] Aveyard R *et al.*, J. Chem Soc., Faraday Trans., 1, 82, 125, (1986).
[22] Bellman R and Pennington RH, Q. Appl. Maths, 12, 151, (1954).
[23] Russ JC, The Image Processing Handbook (CRC Press, Inc.,1995), 233-249, chapter 5.
[24] Schneider MB, Dimonte G, Remington B, (in preparation).
[25] Zufiria JA, Phys. Fluids, 31, 440, (1988); Alon U *et al.*, Phys. Rev. Lett., 72, 2867, (1994); Li XL, Phys. Fluids, 8, 336, (1996).
[26] Glimm J and Sharp DH, Phys. Rev. Lett., 64, 2137, (1990); Zhang Q, Phys. Lett. A, 151, (1990).
[27] Saltz D, private communication, (1997)
[28] Mikaelian KO, Physica D36, 343, (1989).
[29] See images at http://esd.gsfc.nasa.gov/ESS/annual.reports/ess95contents/app.inhouse.fryxell.html

Effect of Re-Shock on Richtmyer-Meshkov Mixing; an Experimental, Numerical and Theoretical Study

D. Shvarts[1,4], O. Sadot[2], L. Erez[2], D. Oron[1,2], U. Alon[1,3], G. Hanoch[1], G. Erez[2], G. Ben-Dor[4] and L.A. Levin[1]
[1] Physics Dept., Nuclear Research Center Negev, Beer Sheva, Israel
[2] Physics Dept., Ben Gurion University, Beer Sheva, Israel
[3] Physics Dept., Princeton University, Princeton NJ, USA
[4] Mechanical Eng. Dept., Ben Gurion University, Beer Sheva, Israel

Abstract: The nonlinear growth of single-mode, two-bubble and random initial pertubations were investigated in a M=1.2 Air/SF_6 shock-tube experiment. The interface evolution was studied both before and after the arrival of the reflected shock. Experimental results for the single-mode and two-bubble cases, showing distinct bubble and spike evolution, were found to be in good agreement with numerical simulations as well as with a theoretical prediction based on a recent potential-flow model. In the random pertubation case, the TMZ thickness was found to be in good agreement with numerical simulation.

1. Introduction

The Richtmyer-Meshkov (RM) instability, which appears on an interface between two fluids accelerated by a shock wave, is of great interest in inertial confinement fusion applications. Most theoretical treatments of the instability have been developed for the case of a single shock wave passing an interface with no pre-developed mixing [1, 2, 3]. The shock wave is typically assumed to pass a well-defined stationary interface with small pertubations. However, in many applications and experiments, multiple shock waves interact with the interface, often when mixing is already well developed. The present work addresses the question of the effect of a shock passing through a mixing zone generated by an earlier shock wave.

In a complementary paper in these proceedings, we described a shock tube experiment on single-mode evolution and two-bubble interaction caused by a single shock wave [4]. In the present work we extend this experiment to describe the effect of a re-shock, reflected from the end wall of the tube, on single-mode and two-bubble evolution. We also extend the experiment to study the evolution of a mixing zone generated from an initial random pertubation, which grows mainly after the re-shock passes the interface.

The shock tube apparatus used is described in Ref. [4] and [5]. A M=1.2 shock wave passed an Air/SF_6 interface (Atwood number A=0.67), where the fluids were separated by a thin membrane, on which the pertubation was imposed. In order to create a re-shock, an end wall was placed at different distances from the interface. The results in this work are from an end wall at distances of 18cm and 24cm. The 24cm configuration was designed to study single-mode and two-bubble interaction, where the wavelength is of the order of 20mm. This distance allows sufficient time for the pertubation to enter well into the nonlinear stage before the re-shock. The 18cm configuration was used for the random initial pertubation study, since the typical wavelength is much shorter (of order of a few mm) and therefore less time is needed in order to reach a well-developed mixing stage before the re-shock. The experiments are compared to full

More information - Email: schwartz@bgumail.bgu.ac.il

scale simulations using an ALE code with interface tracking and to theoretical models [1, 2].

2. Single mode experiments

In Fig. 1 the interface evolution for $\lambda = 26mm$ is shown at various times. The initial amplitude is $a_0 = 2mm$. The re-shock reaches the perturbed interface at about $t = 2.1$msec.

The pertubation is seen to develop an asymmetric bubble-spike shape before the re-shock, similar to that described in Ref. [4]. The phase reversal caused by the re-shock is clearly seen immediately after the re-shock arrives at the pertubation. Later, a very nonlinear reversed bubble-spike structure is formed.

The bubble and spike evolution, relative to the unperturbed interface, are compared in Fig. 2 to a theoretical model (Ref. [4]) which accounts for the linear, early nonlinear and asymptotic stages of the growth. In Fig. 2(a) the growth before the re-shock is shown, and in Fig. 2(b) the growth after the re-shock is shown, until t=3.2msec, when a rarefaction wave from the end wall reaches the interface. The model was initiated in Fig. 2b using the experimentally measured pertubation velocity immediately after the re-shock. Very good agreement is found between the experimental and theoretical results. The interface shape and growth is also in very good agreement with full-scale simulations (data not shown). Thus, even though the re-shock interacts with a pertubation which is highly evolved both in space and velocity, a simple incompressible model describes the evolution after re-shock well.

3. Two-bubble experiments

In order to investigate whether the bubble competition phenomenon, which is a dominant mechanism in the multi-mode evolution, is present after re-shock, we have performed two-bubble experiments with a re-shock. An array of alternating large (27mm) and small (17mm) bubbles was used, with the central part of the membrane consisting of a small bubble flanked by two large bubbles [4]. However as opposed to the structure used in Ref. [4], the initial pertubation was the inverse of that used in Ref. [4] with the bubble tip pointing toward the initial shock.

The interface evolution is shown in Fig. 3, comparing the experimental results with full numerical simulations. Immediately after the shock passage, a small spike is generated flanked by two large spikes. Since the two centered bubbles, on either side of the small spike, are identical, no bubble competition is expected at this stage. After the passage of the re-shock, at time $t = 2.1$msec, the pertubation reverses phase - the spikes become bubbles. The pertubation is thus inverted, creating a small bubble flanked by two large bubbles. As is clearly seen in both experiment and simulation, the bubble competition process begins after the re-shock passage. Very good agreement can be seen between simulation and experiment at all stages - the initial pre-reshock stage, during phase inversion, and well after phase inversion, where bubble competition takes place. In Fig. 4, the difference between the two bubble heights after the re-shock is shown, comparing the experimental and the numerical simulation results with the height difference predicted for two independent bubbles. This demonstrates the bubble competiton, similar to the single shock- experiment [4]. At early times after the re-shock the bubbles grow independently. After about 1msec after re-shock, the height difference is seen to grow faster than that expected from the growth of independent bubbles as a result of the bubble competition process. Later on, 1.4 msec after re-shock, the height difference begins to grow much faster. This is attributed to a rarefaction wave that reaches the interface from the

end wall. The agreement with the full simulation is very good at all stages.

4. Random initial pertubation experiment

In order to study the evolution of the TMZ from a random initial perturbation, a flat membrane with no specific imposed initial perturbation was used. The end wall was placed at 18cm, and thus the re-shock arrives at an earlier time than in the previous cases - at $t = 1.6$ msec. Before the re-shock passage the TMZ thickness is small and only after the re-shock hits the interface the growth is pronounced. In Fig. 5(a), three representative frames show the TMZ at three times after the re-shock passage. In Fig. 5(b) the TMZ thickness is compared with simulation results. The simulation started from an initial pertubation spectrum $\ell = 25 - 50$ and an initial amplitude of 1mm. Shown in Fig. 5(b) are the numerical simulation predictions for the 10%-90% and 1%-99% TMZ. The mixing zone grows slowly before re-shock, with a best-fit power law of roughly $t^{0.5}$. After the re-shock, the mixing zone thickness initially decreases due to shock compression, and then starts to grow at a much increased rate. This growth follows a power law of roughly $t^{0.7}$. At time $t = 2.6$msec, the rarefaction wave from the end wall arrives at the interface, causing a further increase in the growth rate, due to the density decrease and the interface deceleration. The comparison between the experimental TMZ growth rate and the simulations is seen to be good.

It is at present difficult to accurately deduce the bubble and spike front growth separately in the random front experiment. In Fig. 5(c), the numerical results for the bubble and spike fronts, defined as the 1%, 10%, 90% and 99% respectively, are shown and compared with the estimated bubble and spike front locations deduced from the experimental data. The asymmetry between the bubble and spike front power laws is clearly seen in both the numerical and experimental results. The agreement between the experimental and the numerical results is fair, considering the relative large error in defining the fronts and the unperturbed inteface in the experiment. While both fronts are predicted to evolve roughly as $t^{0.4}$ before re-shock arrival, it is seen that after the re-shock passage the bubble front grows roughly with the same power-law exponent, while the spike front grows with a larger power-law exponent, $t^{0.7}$. These power laws are roughly consistent with theoretical predictions [2].

References

[1] Hecht J, Alon U, Shvarts D, McCrory RL, Verdon CP, Phys. Plasma, 3, 8, 3073, (1996).
[2] Alon U, Hecht J, Ofer D and Shvarts D, Phys. Rev. Lett., 74, 534, (1995).
[3] Zhang Q and Sohn SI, Phys. Fluids, 9, 1106, (1997).
[4] Sadot O, Erez L, Alon U, Oron D, Levin LA, Erez G, Ben-Dor G and Shvarts D, the present proceedings.
[5] Erez L, Sadot O, Erez G and Levin LA, in the Proc. of the 5^{th} International Workshop on Compressible Turbulent Mixing, Stony Brook 1995, Ed. R. Young, J. Glimm and B. Boston, 169, (1996).

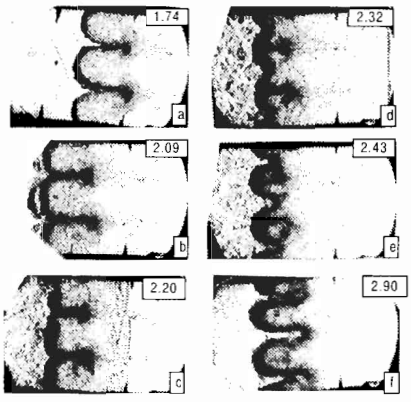

Figure 1. Experimental results of the single-mode evolution for an $M = 1.2$ Air/SF_6 case, $\lambda = 26mm$, $a_0 = 2mm$ and end wall located at 235mm.

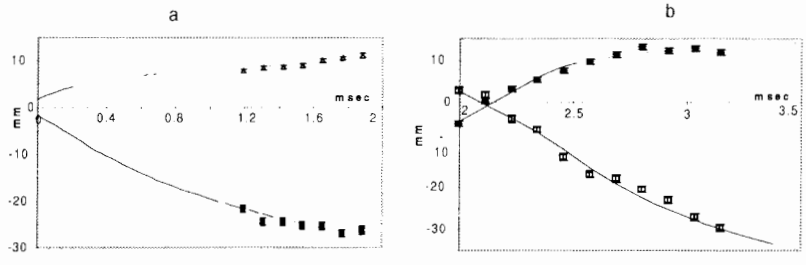

Figure 2. Experimental and potential flow model results for bubble and spike evolution in the single-mode case of Fig. 1. (a) before reshock, (b) after reshock.

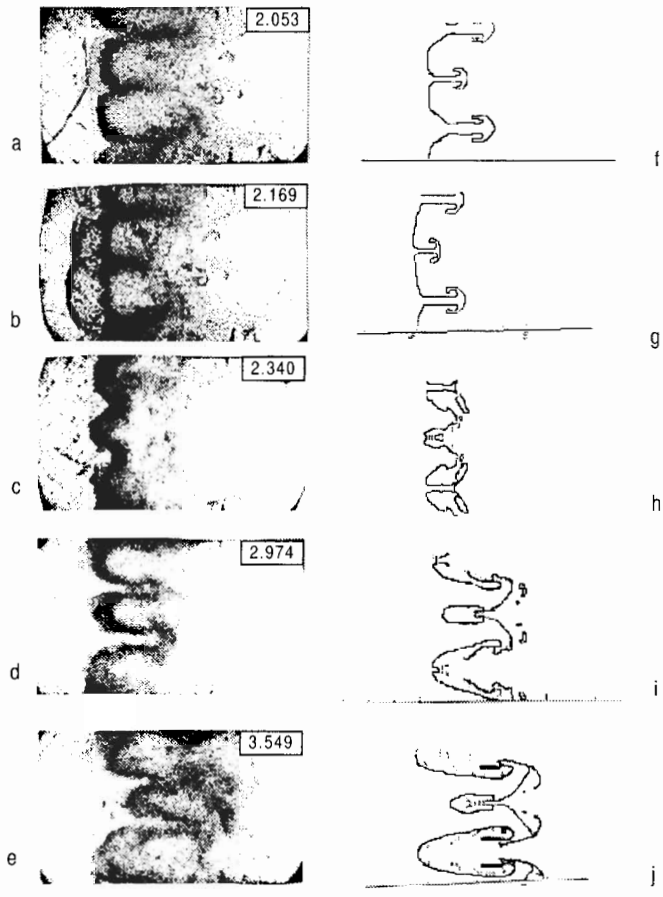

Figure 3. Experimental and numerical results for the instability evolution in the two-bubble case. $M = 1.2$ Air/SF_6, $\lambda_1 = 17mm$, $\lambda_2 = 27mm$, $a_1 = 2mm$, $a_2 = 1mm$, end wall located at 235mm.

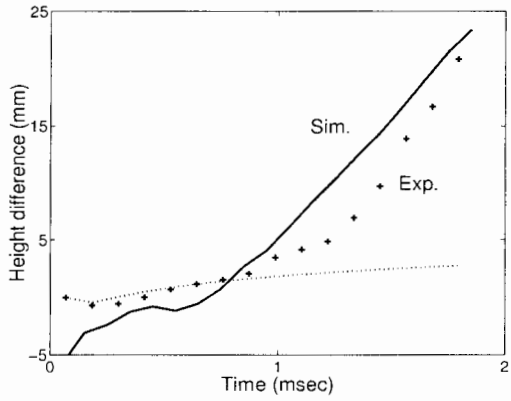

Figure 4. Bubble height difference in the two-bubble case of Fig. 3 after re-shock. Shown are the experimental and numerical results. Also shown is the difference in bubble heights when no bubble interaction takes place.

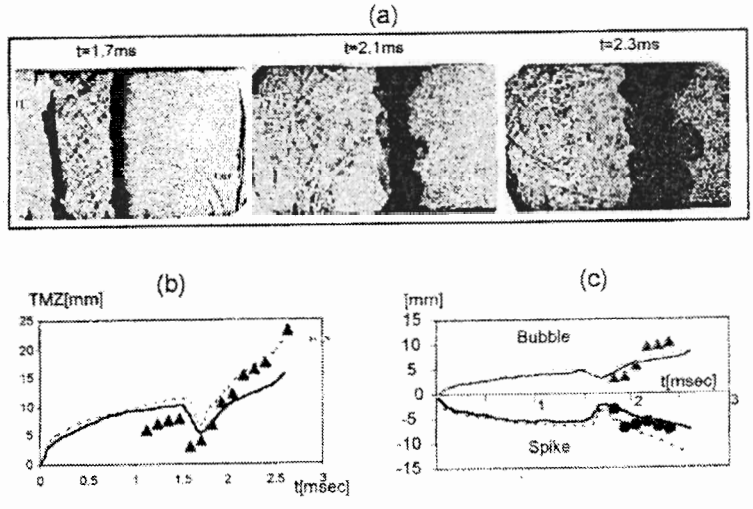

Figure 5. Evolution of a random initial perturbation. (a) Shlieren photographs after re-shock at t=1.7msec, 2.1msec, 2.3msec. (b) TMZ evolution, experiment vs. simulation. (c) Bubble and spike height evolution (relative to the unperturbed interface), experiment vs. simulation. $M = 1.2$ Air/SF_6, end wall located at 180mm.

Three-Dimensional Numerical Simulation of Gravitational Turbulent Mixing

O.G. Sin'kova, A.L. Stadnik, V.P. Statsenko, Y.V. Yanilkin and V.A. Zhmailo
Russian Federal Nuclear Centre - Institute of Experimental Physics
Prospect Mira 37, 607190, Sarov, Nizhny Novgorod Region, Russia

Abstract: The direct *3D* numerical simulation for turbulent mixing (*TM*) at the plane interface of two incompressible liquids (gases) with various density, moving at a constant acceleration was performed earlier in papers [1, 2, 3]. There are significant differences between the results of [1, 2] and [3] concerning the growth rate of turbulent mixing zone (*TMZ*) at the self-similar stage. Additional numerical investigations are desirable to expose this circumstance. In this paper we use both explicit scheme and implicit *3D* difference scheme, implemented within the TREK program complex [4], in order to make more accurate the results obtained in [3]. We have varied geometric sizes of calculation domain, as well as number of calculation cells and degree of compression. The calculation results are compared with corresponding results [1, 2, 3], and also with predictions of phenomenology turbulence models [5, 6] and known experimental data. We held the spectral analysis for both velocity pulsation and density pulsation at the mixing zone. Thus we studied the influence for approximation to Kolmogorov spectrum for these values in *3D* calculations for various setup.

1. Calculation setup

The problem setup is similar to that of [3]: at the initial moment two half-spaces separated by $z = z_c = 11$ plane are filled with perfect gases ($\gamma = 1.4$) at rest with the following densities: $\rho_1 \equiv n\rho_2 = 3$ if $z_c < z < 20$ and $\rho_2 = 1$ if $0 < z < z_c$, Atwood number $A \equiv (\rho_1 - \rho_2)/(\rho_1 + \rho_2) = 0.5$. Gravitational acceleration $g_z \equiv -g = -10$ is directed from heavier substance to lighter one. At the initial moment at the interface (in one-cell layer) we set random density perturbations (they have different spectrum for all calculations) $\delta\rho = \pm\rho_1\delta$, where $\delta = 0.05$. The calculation domain is a rectangular parallelepiped with maximal side $L_0 = 20$ - see Table 1, that presents number of calculation nodes $N_x \times N_y \times N_z$ for different calculations. In doing so the calculation grid was always uniform with equal calculation cells sizes $h_x = h_y = h_z$. At the domain outer borders, parallel to $\vec{g}$ we made a condition of periodicity with period $L_0 = 20$, for other borders - "rigid wall". Notice that pressure value ($P \approx 10^3$) is such that the condition of incompressibility was approximately fulfilled for the turbulence: $k = \xi L_t\, g \ll \gamma\rho/\rho$, where $\xi = const \ll 1$, $L_t < L_0$, L_t - width of *TMZ*, k - turbulent energy.

2. Calculation results

The flow evolution observed in these *3D* calculations is generally similar to the previous ones [3]. We can see the enlargement of vortexes by the time and exit to self-similar mode. The latter for given problem is expressed in linear dependence law for value $W(\tau) = \sqrt{L_t/L_0}$, $\tau \equiv t/t_0$, $t_0 \equiv \sqrt{L_0/Ag} \approx 2$ (Fig.1). As evident, linearity for more detailed grid is already when $\tau > 0.5$ - derivative dW/dt gives the magnitude $\sqrt{\alpha_L}$ in *TMZ* width expression: $L_t = \alpha_L A g t^2$. In our

More information - Email: otd03_2305@spd.vniief.ru

Calculation number N_0	N_x	N_y	N_z	Calculation scheme
1	46	46	46	explicit
2	100	100	100	explicit
3	25	50	50	explicit
4	23	23	49	explicit
5	75	75	75	explicit
6	75	75	75	explicit
7	75	75	75	explicit

Table 1. The initial data for calculations.

calculations it is on average close to experimental data [7, 8, 9], that is $\alpha_L \approx 0.15$, while in calculats [1, 2] it is significantly less, in particular, in [2] value of aL was approximately equal to ≈ 0.085. Noticeable deviation from linear law show itself if $\tau > 2$, when $W > 0.8 \div 0.9$, that

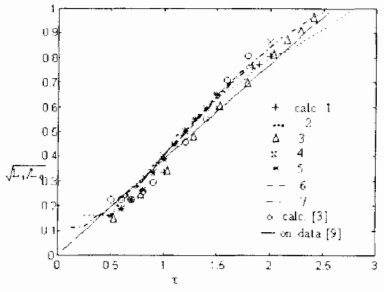

Figure 1. Mixing zone width versus time.

is *TMZ* width become comparable with vertical size of calculation domain L_0. The decrease of horizontal size in cases 3, 4 don't influence significantly to $W(\tau)$ dependence. We emphasize high reproduction ability of this law while comparing the results of the great number of very different calculations, and among them calculations [3] performed on $46 \times 46 \times 46$ grid. Higher $L_t(t)$ was determined as a width of self-similar density profile, that follows from phenomenology theory (see below), and the closest to the *3D* calculation result (Fig.2). While doing so we took from numerical calculation the profiles of value $\rho(z) \equiv \langle \rho \rangle$. Here and below we performed averaging $\langle \rangle$ at the plane $z = const$, that is parallel to the interface plane, with more detailed calculation grid in calc. $N_0 2$. It can been seen that version [5] of phenomenology theory describes better part of the profile near the heavy liquid, while version [6] (used generally in given work) describes better the profile near the light liquid. Choosing of the density profile for the pointed goal is motivated by the following circumstance: it is self-similar from the very beginning to the last moment, when *TMZ* comes into contact with calculation domain

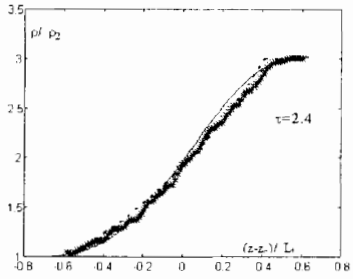

Figure 2. Density profiles: * - *3D* calculation; phenomenology theory for: — given work, - - - - work [5].

borders. By the other hand, comparison of the profiles of turbulent energy $k(z)$, obtained by phenomenology theory, and corresponding value $k \equiv < u_i' u_j' > /2$, $(u_i' \equiv u_i - \langle u_i' \rangle)$, obtained from *3D* calculation, shows (see Fig.3) that time interval with self-similarity is significantly less. Difference between these two versions of phenomenology theory is relatively small. We can observe the deviation from self-similarity to a greater extent at the initial domain ($\tau < 1$); at the last stage ($\tau \approx 2.2 \div 2.4$) borders cause non-monotony of k-profile. Phenomenology

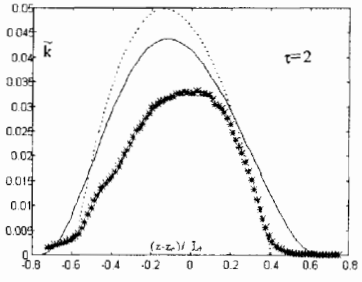

Figure 3. Profiles of turbulent energy:* - *3D* calculation; phenomenology theory for: — given work, - - - - work [5].

theory [5] (of k-ε models type) does not take into account any anisotropy of Reynolds tensor. That is why we compare (Fig. 4) value of relation of longitudinal and transverse components of Reynolds tensor

$$\frac{R_{xx}}{R_{zz}} \equiv \frac{\langle u_x' u_x' \rangle}{\langle u_z' u_z' \rangle}$$

(obtained from *3D* calculation) with version [6] of the theory (described further in this paper). We can consider self-similarity in *3D* calculation as established from $\tau \approx 1.5$, and when $\tau \approx 2.4$ we can see non-monotony in the profile. Relation of "horizontal" components R_{xx}/R_{yy} (Fig.5) is similar to the previous case. Notice that, as for [3], longitude component of Reynolds tensor is much greater than each transverse component - the transverse components are similar on the average. This corresponds to the results of semi-empirical theory, where we have to take coefficient b twice greater than in [5] (see below). Fig.6 illustrates the profiles of mean-root-

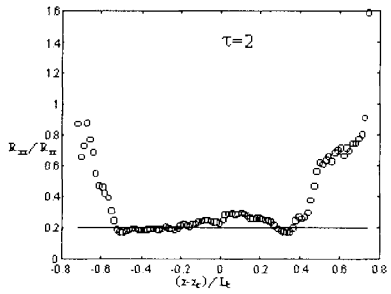

Figure 4. Profiles R_{xx}/R_{zz}: o *3D* calculation; — phenomenology model for this work.

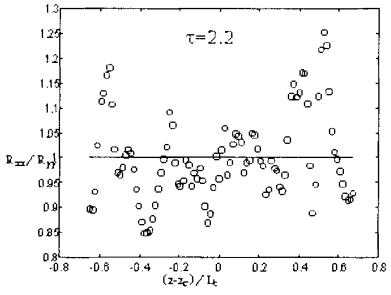

Figure 5. Profiles R_{xx}/R_{zz}: o *3D* calculation; — phenomenology model for this work.

square density pulsation value $\langle \rho'\rho' \rangle \, / \, \langle \rho \rangle^2$. Their self-similar form (as for density profiles - see Fig.2) is the same till the last moment, when *TMZ* comes into contact with calculation domain borders. It is equitable also for turbulent mass flow (Fig.7), expressed as dimension less value

$$\tilde{R}_z = \frac{\langle \rho' u_z' \rangle}{\langle \rho \rangle \sqrt{g L_t}}.$$

Linearity of the value $\sqrt{L_t(t)}$ [3] itself can not serve for the simple criteria for the self-similarity. We can take for additional criteria exit to the time-constant value $E(t) \equiv k_m/L_t g$, where $k_m \equiv max(\langle k \rangle (z))$. Fig.8 shows this value versus τ^2. As we can see in these calculations, we can consider mixing mode as self-similar for criteria $E(t) \equiv const$ only when $\tau > 2$. Notice, that it is obvious from this figure, that in calculation [3] self-similarity was not nearly achieved for the last moment, so value of E is much greater than possible self-similar value. Exit to the time-constant value of $R_m(\tau)$, where $R_m = max(R)$, $R \equiv \langle \rho'\rho' \rangle$ can serve for similar criteria. As obvious from Fig.9, in these calculations we can observe mixing mode as self-similar for criteria $R_m(\tau) = const$ already when $\tau > 1$. We can also notice high reproduction ability of $R_m(\tau)$ dependence for very different calculations. Iso-surfaces of volume concentration $\beta = 0.5$ (see Fig.10 for calculation 2) illustrates *3D* structure of this flow. While performing analyses of hydro-dynamic velocity one usually observe spectral power (obtained by Fourier-decomposition of its components) of pulsation square for these components. The result of such approach we can see from the example of calculation 2, where this *2D* Fourier-analyses was made for the points of

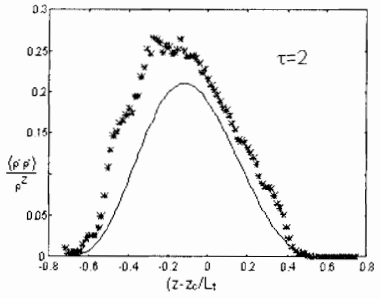

Figure 6. Profiles of relative average root square density pulsation: * *3D* calculation; — phenomenology model for this work.

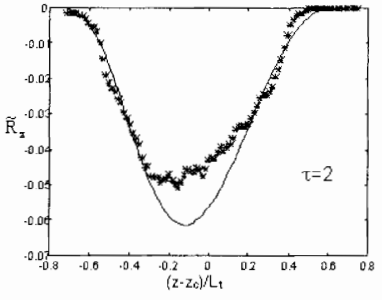

Figure 7. Profiles of relative turbulent mass flow: * *3D* calculation; — phenomenology model for this work.

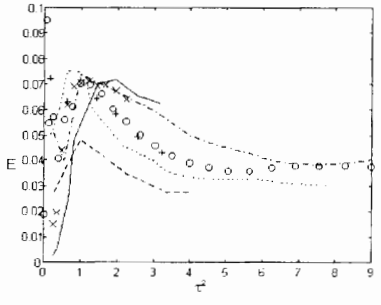

Figure 8. Time depedence of maximal value of turbulent energy: - - - calc. $N_0 1$; ... calc. $N_0 2$; + calc. $N_0 6$; o calc. $N_0 7$; x calc. $N_0 5$; -·- calc. $N_0 3$; — calc. [3] on the grid 46^3.

the plane, located in the middle of calculation domain (see Fig.11). On the average, as evident, while local non-uniformity we can see the closeness to Kolmogorov spectrum (normalized on the computation results in the range of great k) both for transversal and for longitude components of velocity on the wide interval of "wave numbers" $k_\lambda \equiv h/\lambda$ (h - calculation cell size). In doing so anisotropy preserves till the greatest values of k_λ. We also calculated the value of the spectral

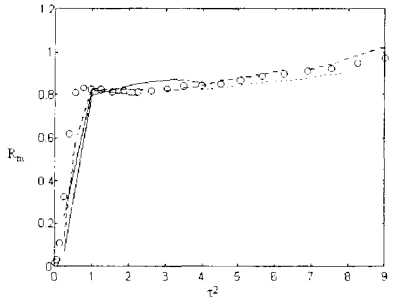

Figure 9. Time depedence of maximal value for desity pulsation square: — calc. $N_0 1$; - - - calc. $N_0 3$; ... calc. $N_0 2$; o calc. $N_0 7$; -·- calc. $N_0 4$.

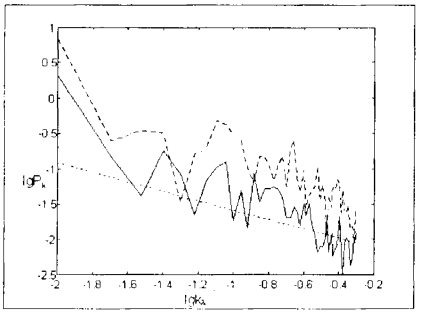

Figure 11. Spectral power of squared velocity pulsation: — E_x, - - E_z, - - - Kolmogorov spectrum.

turbulent energy (depending on averaging scale), that differ from the previous approach in more illustrative physical meaning and in more integral (and so more smooth) character (see also [3]):

$$E_{jr}^{(i)} = \left\langle \left(u_j^{(i)}\right)^2 \right\rangle |_r - \left\langle u_j^{(i)} \right\rangle^2 |_r; j = x, y, z; i = 1, 2...N; E_{jr} = \left\langle \left(E_{jr}^{(i)}\right)^2 \right\rangle |_r; r = 2, 3...N. \quad (1)$$

Here we do averaging $\langle\rangle\ |_r$ in the i-th (along the z axis) horizontal layer within the square with the side r, and then averaging ($\langle\langle\rangle\rangle$) through all squares with data r within the whole I-th layer. The results for calculation 2 are compared on Fig.12 (where $K = 2\pi/l$, $l \equiv rh$, h - size of calculation cell) with Kolmogorov spectrum for several values z when $t = 4$. We can see that in mixing zone both for full energy $E_l = E_{lx} + E_{ly} + E_{lz}$, and for separate components E_{lx}, E_{ly}, E_{lz} spectrum is very close to Kolmogorov spectrum ($\lg E_{l(K3)} = -2K/3 + const$), but in doing so, however, anisotropy takes place till the least scales. The same value for density pulsation square

$$\rho_1 \equiv \rho_r^{(i)} = \left\langle \left(\rho^{(i)}\right)^2 \right\rangle |_r - \left\langle \rho^{(i)} \right\rangle^2 |_r; i = 1, 2...N; r = 2, 3...N. \quad (2)$$

is presented on Fig.13 for calculation 2. As evident, in *TMZ* the spectrum of the full value rl at small scales tends to Kolmogorov's one. This is best shown at the edges of the zone, especially near the heavy liquid. Notice, that for all *3D* calculations we obtained (according to phenomenology model [5]) the relation of coordinates (relative to the initial location of the

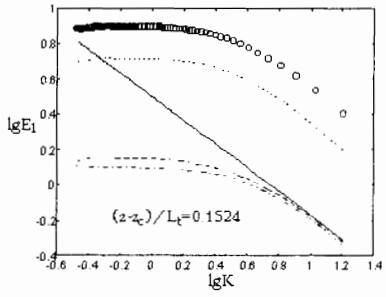

Figure 12. Spectrum of turbulent energy: *3D* calculation (calc.N$_0$2, $t = 4$): $\circ$ E_l, - - - E_{lx}, -·- E_{ly}, - - - E_{lz}; - - ρ_l, — Kolmogorov spectrum.

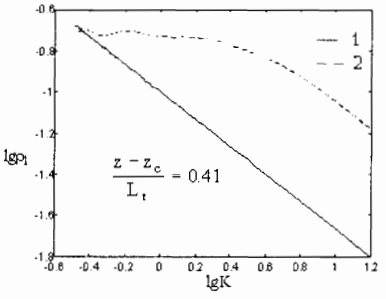

Figure 13. Spectrum of density pulsation:*3D* calculation (calc.N$_0$2, $t = 4$): $\circ$ E_l, - - - E_{lx}, -·- E_{ly}, - - - E_{lz}; - - ρ_l, — Kolmogorov spectrum.

interface) of the heavier substance in the light one and of the lighter substance in the heavy one $S_{12} \equiv L_{t2}/L_{t1} \approx 1.5$, when coordinates are determined by small value of density perturbation (see below). This is significantly larger than in [8, 9] (≈ 1.15), but much less than in calculations [2] (≈ 2.8). The described below phenomenology theory gives yet $S_{12} \approx 1.11$. However, if we get the coordinates in *3D* calculations according to [9] via density perturbation $\Delta\rho = 0.1(\rho_1 - \rho_2)$ (see Fig.2), we shall obtain the close value of $S12$ (≈ 1.15). In this case the described below phenomenology theory gives $S_{12} \approx 1.06$, that seemed to be acceptable with regard to the mistake of experiments [9].

3. Phenomenology theory

The described case ($\mathbf{u} = 0$, gravitational acceleration g) corresponds to $\mathbf{R}_i \longrightarrow -\infty$, then from version [6] of the theory like [10, 11], regarding to Reynolds tensor anisotropy, follows the equation:

$$\frac{\partial \rho}{\partial t} = -\frac{\partial R_z}{\partial z}, \tag{3}$$

where turbulent mass flow:

$$R_z = \frac{-3bc\Lambda}{a}\frac{\partial \rho}{\partial z}\sqrt{\frac{2c\Lambda^2}{a}\frac{g}{\rho}\frac{\partial \rho}{\partial z}}, \tag{4}$$

turbulent energy:

$$k = \frac{\Lambda^2}{a}\frac{g}{\rho}\frac{\partial\rho}{\partial z}, \tag{5}$$

the average square of density pulsation:

$$R \equiv \langle\rho'\rho'\rangle = -\sqrt{\frac{2}{k}}\frac{R_z\Lambda}{k}\frac{\partial\rho}{\partial z}, \tag{6}$$

relation for the Reynolds tensor components:

$$\frac{R_{xx}}{R_{zz}} = \frac{1/3-b}{1/3+2b}; R_{xx}/R_{yy} = 1. \tag{7}$$

So, directing to the results of $3D$ calculations, we can soon get exacting limit for value of b - we suppose $b = 0.19$. Here: $c \equiv 1 + \frac{1}{\zeta} + \frac{1}{k}$; $\zeta \equiv \frac{3b}{\mu}$; $\mu = \frac{1}{3} - b$. Let's take for length turbulent scale Λ:

$$\Lambda = \alpha L_t, \tag{8}$$

that is similar to using of Prandtl-Kolmogorov relation. Here $L_t = z_1 - z_2$ is TMZ width in z direction. We determine it by points z_1, z_2, in which we achieve the small enough value of perturbation for hydro-dynamic value, density, for example. Then let's consider that $\rho(z_1) = 2.95$, $\rho(z_2) = 1.05$. We determine the full TMZ width $L = z_{o1} - z_{o2}$ by points z_{o2}, z_{o1}, where perturbation of hydro-dynamic value reaches its zero value, that is $\rho(z_{o1}) = 3$, $\rho(z_{o2}) = 1$. Let's mark their relation as $k_L \equiv L/L_t$. Let's introduce self-similar variables:

$$\eta \equiv \frac{z-z_c}{gt^2c_\lambda^2\eta_L^4}; \Psi(\eta) \equiv \frac{\rho}{\rho_2}, y \equiv \sqrt{\frac{\Psi'}{\Psi}}; \Psi' \equiv \frac{\partial\Psi}{\partial\eta}, c_\lambda \equiv \frac{3\alpha^2bc}{a}\sqrt{\frac{2c}{a}}, \tag{9}$$

where z_c - the initial coordinate of interface plane for heavy and light liquids. Values η_1 and η_2, in which $\mathbf{y}$ converts into zero, correspond to the zone interface, and value $\eta_L = \eta_1 - \eta_2$ corresponds to the mixing zone width L. In our case $\partial\rho/\partial z > 0$, then we can write the equation (3):

$$2\eta + 3y' - y^3 = 0 \tag{10}$$

The stretch values of the magnitudes of interest are following: turbulent energy:

$$\tilde{k} \equiv \frac{k}{L_t g} = \frac{c}{a}\alpha^2 k_L \eta_L y^2, \tag{11}$$

turbulent mass flow:

$$\tilde{R}_z \equiv \frac{R_z}{\rho\sqrt{gL_t}} = -\frac{3bc\alpha y^3\eta_L^{3/2}}{a}\sqrt{\frac{2ck_L}{a}}, \tag{12}$$

average square of relative density pulsations:

$$\frac{\langle\rho'\rho'\rangle}{\rho^2} = -\sqrt{\frac{2}{\tilde{k}}}\frac{\tilde{R}_z y^2\alpha\eta_L}{k}. \tag{13}$$

Function $\Psi = \exp\left(\int_{\eta 2}^{\eta} y^2 d\eta\right)$, and also the values (7), (11)-(13), obtained as a result of decision of equation (9) for the parameter values $a = 2$, $b = 0.19$, $k = 0.35$, $\alpha = 0.09$ are shown on Fig.2-7. As we can see, we have significant agreement with $3D$ calculations. While doing so

TMZ growth velocity, characterized by the value $\alpha L \equiv \eta_L^5 c_\lambda^2 / A k_L \approx 0.132$, that is close to the measurements [7, 8, 9]. We have to choose the following values of phenomenology coefficients for description of given problem: $a = 2$, $b = 0.19$, $k = 0.35$. They noticeable differ from the parameters adopted in [6, 10] ($a = 0.5 \div 0.75$, $b = 0.05 \div 0.08$, $k = 0.45$), where, however, atmospheric problems were generally observed with small relative different density, or problems with $\mathbf{R}_i \geq 0$.

4. Conclusion

• High reconstruction ability of dependence $W(\tau) \equiv \sqrt{L_t / L_0}$takes place when comparing the results of the great number of much different calculations on different calculated grids, among them calculations [3], performed on the $46 \times 46 \times 46$ grid, and also calculation on the 75^3 grid, made by implicit scheme. Value of velocity of *TMZ* width growth agrees with experimental data of different authors, but differs from calculation data [1, 2].
• In a similar manner, we can observe high performance for dependence $R_m(\tau)$, where $R_m = \max(R)$, $R \equiv \langle \rho' \rho' \rangle$.
• It is shown, that exit to the constant value both of $E(t) \equiv k_m / Lg$ and $R_m(\tau)$ is proper simple criteria of exit the decision into auto-modeling mode (besides the linearity of $\sqrt{L(t)}$ value).
• Spectrum of velocity pulsation at the small scales is close to Kolmogorov spectrum - it is true for turbulent energy. Spectrum of density pulsation also tends to Kolmogorov spectrum, but in less degree.
• We have formulated version of semi-empirical model for observed flow calculation with regard of Reynolds tensor anisotropy, and obtained auto-modeling solving of equations of this model.
• Used version of semi-empirical model possess the opportunity of more representative description of corresponding experiments, than version [6] with isotropic Reynolds tensor. It also satisfactory agrees with the results of *3D* calculation.

Acknowledgement. The work was performed with the help of ISTC, contract N° 29.

References

[1] Youngs DL, Three-dimensional numerical simulation of turbulent mixing by Rayleigh-Taylor instability, Phys. Fluids A, 3, 1312, (1991).
[2] Youngs DL, Numerical simulation of mixing by Rayleigh-Taylor and Richtmyer-Meshkov instabilites, Laser and Particle Beams, 12, 4, 725-750, (1994).
[3] Stadnik AL, Statsenko VP, Yanilkin YV, Zhmailo VA, Direct numerical simulation of gravitational turbulent mixing, 5th International Workshop on the physics of compressible turbulent mixing, Stony Brook, (1995); Stadnik AL, Statsenko VP, Yanilkin YV, Zhmailo VA, The direct numerical simulation for gravitational turbulent mixing, VANT, Ser. Theoretical and applied physics, 1-2, (1996).
[4] Shanin AA, Stadnik AL, Yanilkin YV, Eulerian TREK method for 3D calculations of gasdynamic flows for multi-component mediums, VANT, Ser. Mathmatical simulation of physical processes, 4, (1994).
[5] Statsenko VP, Zherebtsov VA, Zhmailo VA, Self-similar solving for semi-empirical equations of turbulent mixing in 1D unstable flows, Numerical methods of solid mediums mechanics, Novosibirsk, 15, 1, 60-75, (1983).
[6] Statsenko VP, Testing of turbulence model with Reynolds tensor anisotropy, VANT, Ser. The-

oretical and applied physics, 3, 43-51, (1996).

[7] Read KI, Experimental investigation for turbulent mixing by Rayleigh-Taylor instability, Physica D12, 45, (1984).

[8] Youngs DL, Modeling turbulent mixing by Rayleigh-Taylor instability, Physica D37, 270, (1989).

[9] Kucherenko YA, Shibarshov LI, Chitajkin VI *et al.*, Experimental study of the gravitational turbulent mixing self-similar mode, 3rd International Workshop on the physics of compressible turbulent mixing, 345-356, (1991).

[10] Lewellen WS, Teske ME, Donaldson CP, Variable density flows computed by a second-order closure description of turbulence, AIAA Journal, 14, 3, 382-387, (1976).

[11] Backrack SM, Darova NS, Statsenko VP, Zharova GV, Zhmailo VA, Turbulent and molecular mixing in thin vortex rings, VANT, Ser. Theoretical and applied physics, 2, 14-19, (1987).

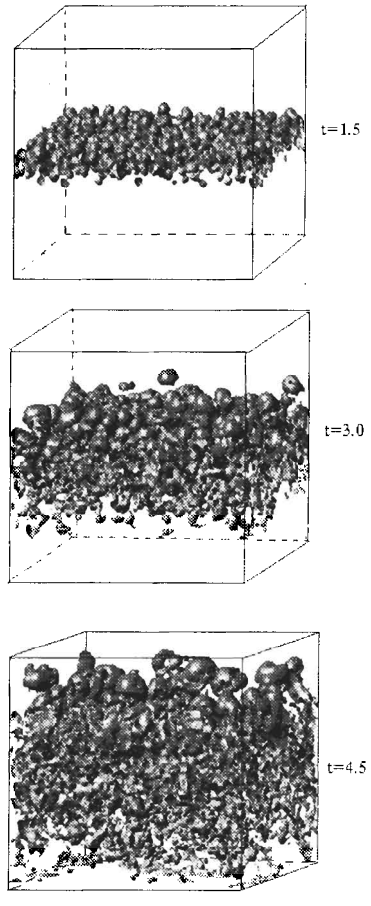

Figure 10. Iso-surface of volume concentration on 0.5 level.

Shock Tube Investigations of the Richtmyer-Meshkov Instability Due to a Single Discrete Perturbation on a Plane Gas Discontinuity

A.V. Smith, M.K. Philpott, D.B. Millar, D.A. Holder, N.W. Cowperthwaite and D.L. Youngs
AWE, Aldermaston, Readings Berkshire, RG7 4PR, England

Abstract: This paper describes an investigation of the Richtmyer-Meshkov shock-induced instability growth of a single discrete perturbation imposed on an otherwise plane interface separating two gases of different density. The experimental technique as applied to a 2D bump perturbation is described. Comparison with corresponding unperturbed membrane experiments reveals the effect of a single discrete perturbation on an essentially 1-D turbulent mixing zone. The required membrane perturbation was achieved by means of a profiled test-section and fine wire meshes that were used to support the membrane and ensure its effective fragmentation. A pulsed copper vapour laser sheet illuminated seeded particles mixed with one of the gases (sulphur hexafluoride, SF_6) which enabled a high-speed, 35mm drum camera to record, typically, forty images of the instability and mix development over a 4ms period. Direct 3-D numerical simulation was carried out using the TURMOIL 3D code with a random perturbation representative of the mesh-induced fragmentation to initiate the growth of the 1-D turbulent mixing zone. Respectable agreement was obtained with the experimental results.

1. Introduction

This study followed as an extension to the Richtmyer-Meshkov laser sheet investigations reported at the 5th IWPCTM. These new experiments were similarly performed at shock Mach N° 1.26 (shock pressure 10 psi, 69 kPa), but using a new shock tube of increased cross-section, 200 × 100mm. The test gases were air/SF_6/air at atmospheric pressure zoned as in Figure 1, below. Gas separation across each interface was achieved using a microfilm membrane (normally a single layer) supported by a wire mesh for profiling the perturbation and for fragmenting the membrane. Visualisation of the gas mixing process was by means of pulsed laser sheet illumination at 100μs intervals of a vertical plane through the seeded SF_6 gas, with recording on a synchronised 35mm rotating drum camera. From several perturbation profiles examined, a forward-facing shallow bump (circular arc, dimensions 20 × 3mm) at the downstream interface was selected for presentation together with its corresponding unperturbed (plane / plane) case, as in Figure 2. The major interest concerned the observed mixing development across both the upstream and downstream interfaces resulting from passage of the incident and the subsequent reflected shocks from the end plate of the shock tube. Comparisons are included between results from experimental and direct numerical simulation using the Turmoil 3D code. General agreement is evident conditional upon inclusion in the code of random representation of the initial mesh-generated perturbation.

More information - Fax: +44 (0) 11 89 82 48 36 or Email: dyoungs@awe.gov.uk

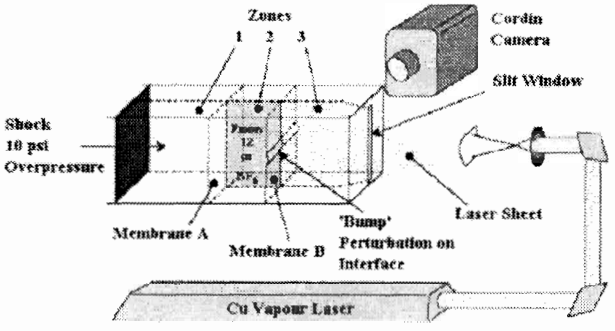

Figure 1.

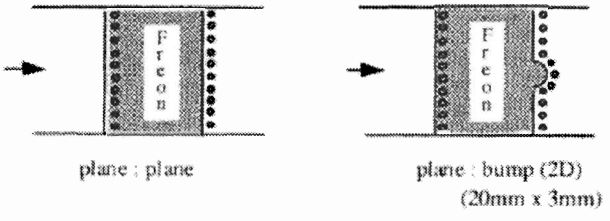

Figure 2. Schematic representation of the dense gas regions and the defining membrane and wire mesh.

2. Aim of the shock tube experiments

The aim of the shock tube experiments described was to provide data, in combination with results from 3D direct numerical simulation code calculations, for the development of a 2D turbulence mixing model. Fragmentation of the membranes induces random perturbations which lead to the growth of turbulent mixing zones which are, on average, one-dimensional. The plane - plane experiment (unperturbed "flat" membranes) served therefore to characterise such a 1D turbulent mixing zone. The plane-bump experiment served to modify this experiment with a 2D feature to give an essentially 2D turbulent mixing zone as required for 2D turbulent mix model development.

3. Profiles investigated

Figure 2 indicates the mesh/membrane configurations examined. An additional mesh was inserted at the first membrane to prevent pre-shock bulging in the upstream direction due to the SF_6 gas density. A corresponding mesh fitted in previous tests to the second membrane to preserve equivalence has been excluded. The defect on the interface as represented by the bump perturbation is equivalent to 0.17 % of the total SF_6 gas mass. The dotted outline of the mesh wires supporting the membrane is for indication only.

4. Use of wire meshes

Figure 3 illustrates the use of wire meshes individually woven from tungsten wire of 25 μm diameter and with a 4 mm square aperture. The horizontal wires were in tension; the higher tension demanded by those wires defining the perturbation normally necessitated substitution with wires of 50 μm diameter. The vertical wires were maintained in a suitably slack state to avoid interfering with the bump profile across the width of the test-section. Meshes generally remained intact after a test but are replaced as a matter of routine. Flow blockage is 1.2 % per mesh.

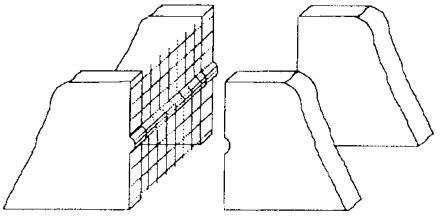

Figure 3. Detail of the wire mesh construction used to support the membranes.

5. Comparison between sample images and 3D code results

Figure 4 shows six sample photographic images selected from a sequence of forty negatives recorded during a "bump" perturbation experiment. Shown unprocessed, they provide a snapshot of the shock response of the initially perturbed SF_6 zone and its subsequent mix development. Interrogation was by a laser sheet typically 2mm thick. It was noted that, to a first approximation, the light scattered from the seeded gas in the sheet and recorded by the camera was proportional to its density. The 3D code results at the same times and on the same scale show the SF6 gas volume fraction (at contour levels 0-0.05; 0.05-0.25; 0.25-0.75; 0.75-0.95; 0.95-1) representing a slice of the calculation. The first photographic image (0.6ms after shock arrival at the first interface) shows the enhanced light intensity in the shocked SF_6 gas as the incident shock front approaches the second (perturbed) interface. The first interface is in evidence as a thin vertical line inset from the left edge of the photograph: the downstream end of the test-section is not visible but is inset a similar distance from the right edge. The second image shows a phase inversion of the perturbation and the passage of the first reflected shock through the SF_6 gas. The 50 node perturbation (200mm/4mm) originating from the downstream mesh which accounts for the predominant disturbance across both the gas boundaries cannot be seen in the reproduced photographs, but can be identified in the original negatives. Following the passage of the reflected shock though the SF_6 zone, the latter is now compressed to about 1/3 of its original volume. Memory of the wire mesh wavelength has largely disappeared along the downstream boundary by selective growth or regrouping into longer wavelength, larger amplitude structures. A second reflection is visible in the following image as is evidence of developing mixing of the gas with air across the gas boundaries. The remaining images show continuing evolution of the bubble and mix growth across both the upstream and downstream boundaries. All the images show numerous fragments from both membranes as visible confirmation of successful break-up. While comparison of gross features between experimental and code results demonstrates distinct similarities, such as the bubble size and asymmetry, the photographic

images fail to reveal the more dilute regions of SF_6 gas at later times, thereby preventing more detailed comparison. Digitisation and subsequent processing is therefore necessary for further analysis. One particular requirement is to compensate for the non-uniform spatial intensity of the laser sheet which visually precludes study of wall effects at the top and bottom of the test section (Figure 4 below).

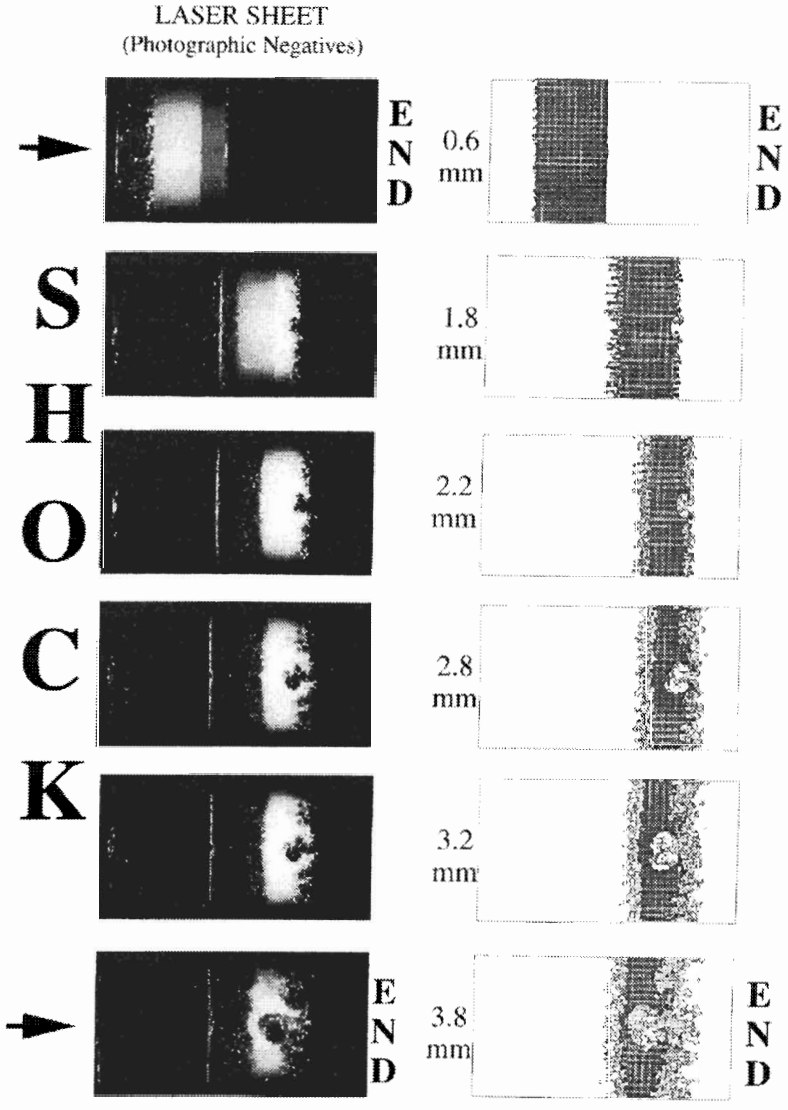

Figure 4.

6. Image processing

The first stage was digitisation of the images using a CCD camera. A basic level of processing was then performed by applying an algorithm to individually identify the membrane particles within the image. For visual enhancement purposes, the algorithm used automatically replaced each with a grey scale value representative of the immediate local environment. In the proposed densitometry technique, offering improved analysis capability, each particle will in contrast be treated on a "not a number" basis. A deficiency of the current algorithm concerned its reduced effectiveness in removing an elongated particle in the image representing a fragment of wire mesh; a necessary extension of the technique degrades the whole image quality. The problem is currently being phased out by the use of an improved technique whereby the meshes remain totally intact and in-situ.

7. Turmoil 3D code calculations

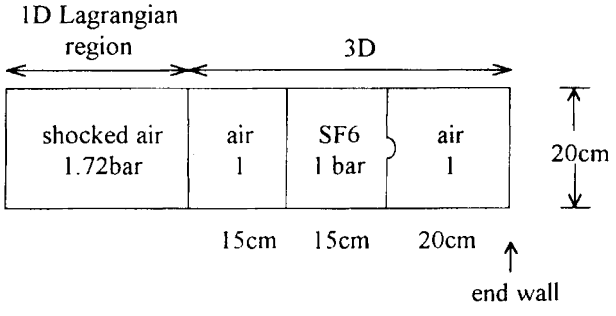

Figure 5. Zoning used in code calculations.

- Zoning used in 3D region: 400 × 320 × 160 cells
- Semi-Lagrangian calculation: x direction mesh moves with the mean fluid velocity
- Calculations were carried out with and without the "bump" perturbation
- Random initial perturbation at air/SF_6 interfaces:
  - wavelengths: 0.5cm to 5cm
  - amplitude rms: 0.01cm
- Calculations were run on a Cray C98D: ~100 CPU hours

8. Boundary/mix measurements

The location of the 0.95 mix (volume fraction) position within both the upstream and downstream boundaries was determined, by z-averaging (vertical axis) of the experimental data. On the bump experiment, it was necessary to exclude the central region and to supplement the data with that identifying the bubble base and the induced protuberance on the interface (0.95 values). Corresponding measurements were taken from the 3D code results with, in addition, the inclusion of the 0.05 level. The derived distance-time plots are shown in figure 6 below.

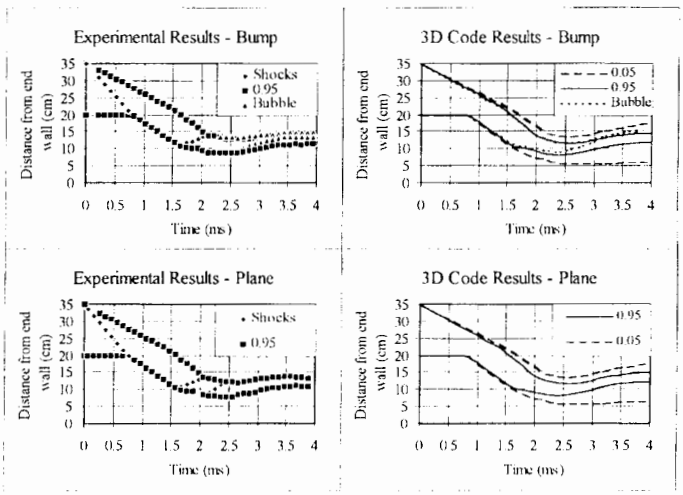

Figure 6.

9. Conclusions

Experiments similar to those reported at the 5th IWPCTM have been satisfactorily transferred to a new shock tube of larger cross-section 200 × 100mm. The results from using thin membranes supported by fine wire meshes has continued to confirm the effectiveness of such combinations in gas separation in Richtmyer-Meshkov instability experiments. Such combinations;

- guarantee fragmentation of membranes
- enable range of interface profiles to be used
- provide good agreement with 3D simulation if an initial small amplitude random perturbation of the order of the mesh spacing is used.

Only a partial analysis has been presented and a more detailed analysis is planned for the future.

10. Future studies on linear shock tube

- Improve present image analysis (film characterisation; fragment removal; non-uniform laser intensity)
- Develop densitometry techniques (providing full mix analysis of laser sheet images)
- Simultaneous recording of parallel or cross (ie both horizontal and vertical) laser sheets using a 70mm format Cordin camera
- Investigate additional perturbation profiles (eg. dual bump; step)
- Further null-type tests

Measurements and Simulation of the Turbulent Energy Levels in Mixing Zones Generated in Shock Tubes

D. Soufflan[1], O. Grégoire[1], S. Gauthier[1], F. Poggi[2] and J.M. Kœnig[2]
[1]CEA/Limeil-Valenton, F94195 Villeneuve-Saint-Georges Cedex, France
[2]CEA/Vaujours-Moronvilliers, BP7, F77181 Courtry, France

Abstract: A second order closure turbulence model is developed to simulate mixing zones generated in shock tubes. The main effort is directed towards the modelling of the production processes. Comparisons between the simulation results and the measurements of instantaneous velocities carried out at the CEA/Vaujours-Moronvilliers shock tube show satisfactory agreement. Enhancement of the turbulent kinetic energy by the shock wave crossing the mixing zone and the anisotropy of the Reynolds stress tensor are correctly reproduced.

1. Introduction

Thus far, in shock tube experiments of turbulent mixing, measurements give us global informations on the thickening of the mixing zone. Schlieren visualization, interferometry or radiography provide only evolution of the mixing zone thickness and of the concentration profiles. Direct data on turbulent energy are now available, thanks to the measurements of instantaneous velocities by laser Doppler anemometry carried out at the CEA/V-M shock tube. These informations allow one to test the capabilities of statistical turbulence models. We focus on the processes of turbulent energy production by shock waves, in particular by baroclinic effect, and on the evolution of Reynolds stress anisotropy. To this aim, we have developed a second order closure model, with evolution equations for the mass flux and the density variance. These quantities are crucial in flows with strong density gradients. After a short presentation of the experimental setup, we describe the turbulence model and present first comparisons between experimental data and simulation results.

2. Experimental configuration and diagnostics

The shock tube facility is extensively described in the contribution of Poggi *et al.*[1] in this issue. We will recall here only the features of the flow and the characteristics of the diagnostics used as a reference in this paper. A gaseous mixture between SF_6 and air is generated in a vertical shock tube. An upward propagating shock wave (M=1.45) impulsively accelerates the two gases initially separated by a $0.3\mu m$ thick flat membrane. A thin wire mesh is located directly above the membrane to break it into small pieces during the shock wave crossing. This device prevents large membrane fragments to inhibit the mixing development induced by Richtmyer- Meshkov instability. This wire mesh (wire spacing $1010\mu m$, diameter $80\mu m$) does not generate measurable turbulence by itself. To characterize the turbulent mixing zone (TMZ) we use here schlieren visualization results, which provide information on the thickness of the mixing zone, and laser Doppler anemometer (LDA), to measure instantaneous velocities. For each LDA abscissa, several experiments are needed to get enough velocity measurements and to deduce Reynolds stress values statistically converged. Five abscissas are studied, two between the setting in motion of the mixing zone by the incident shock wave and its interaction

More information - Email: soufflan@limeil.cea.fr

with the first reflected shock wave, and three between the two first reshocks (Fig. 1). The tangengial component of the velocity is measured, on top of the axial component, for the 169 mm abscissa. The set of velocity measurements obtained at this abscissa is presented in figure 2. The data from forty shots are superimposed. Statistical values, as mean velocity, axial and radial velocity variances, are calculated on intervals of $23\mu s$ (Fig. 5). By looking at figure 2, we see clearly a turbulent behaviour during the mixing zone passage.

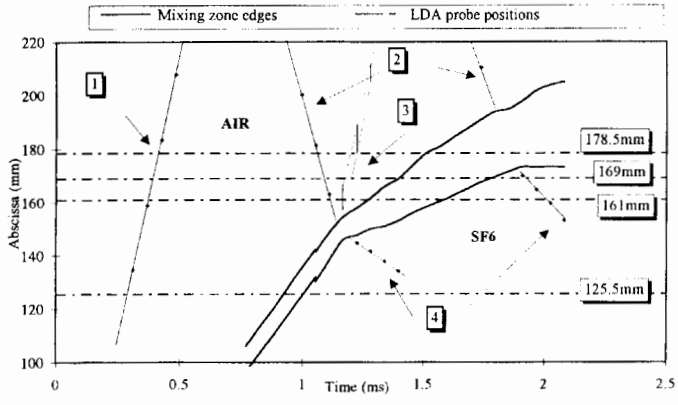

Figure 1. Evolution of the turbulent mixing zone measured by schlieren visualization and shock wave paths. The numbered squares mean: 1, transmitted shock in air; 2, first and second reflected shocks from the end wall; 3, compression waves due to the reflection on the mixing zone; 4, transmitted shocks in SF_6. Four locations of the LDA probe are also shown.

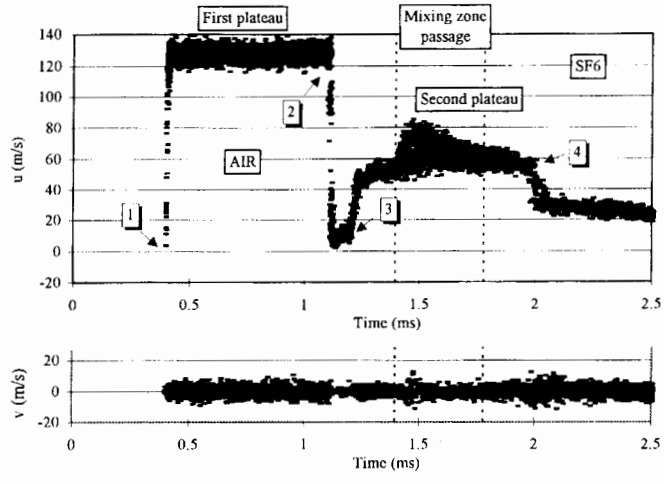

Figure 2. Measurements of the axial (u) and radial (v) components of the instantaneous velocity at 169 mm. 40 shots are superimposed.

3. The second order closure turbulence model

The flows in shock tubes are strongly compressible and turbulent mixing zones are supplied with energy by interaction with the shock waves. Therefore the generated turbulence is expected to be highly unsteady and non-isotropic. Thus, we choose to develop a second order closure turbulence model and to emphasize the correlations involved into energy production terms. Turbulent quantities are expressed within the Favre averaging framework. We have implemented the model in a 1D hydrocode, for simulation of two perfect gas mixings. Thus the model reduces to equations for five turbulent variables: two components of the Reynolds stress $\widetilde{R_{11}} = \overline{\rho u'' u''} / \overline{\rho}$ and $\widetilde{R_{22}} = \overline{\rho v'' v''} / \overline{\rho}$, the dissipation rate $\tilde{\varepsilon}$ (which is assumed to be isotropic), the mass flux $\widetilde{u''} = -\overline{\rho' u''} / \overline{\rho}$ and the density variance $\overline{\rho'^2}$. The closure relations are valid under the large Reynolds number hypothesis. If Reynolds stress models are quite common in literature, especially in incompressible flows context, there are only few second order models for compressible flows with evolution equations for $\widetilde{u''}$ and $\overline{\rho'^2}$. We can cite complete model [2] and works focused on these equations [3], [4]. The modelling adopted here, directly derived from the averaging of Navier-Stokes equations, shares some choices with the last two papers. The equations for the mean variables: density $\overline{\rho}$, velocity $\tilde{u}$, mass concentration $\tilde{c} = \overline{\rho}_{air} / (\overline{\rho}_{air} + \overline{\rho}_{SF6})$ and internal energy $\tilde{e}$, are

$$
\begin{aligned}
\frac{D\overline{\rho}}{Dt} &= -\overline{\rho}\frac{\partial \tilde{u}}{\partial x}\,, \\
\overline{\rho}\frac{D\tilde{u}}{Dt} &= -\frac{\partial \overline{P}}{\partial x} - \frac{\partial}{\partial x}\left(\overline{\rho}\widetilde{R_{11}}\right)\,, \\
\overline{\rho}\frac{D\tilde{c}}{Dt} &= \frac{\partial}{\partial x}\left(C_c\overline{\rho}\frac{\tilde{k}}{\tilde{\varepsilon}}\widetilde{R_{11}}\frac{\partial \tilde{c}}{\partial x}\right)\,, \\
\overline{\rho}\frac{D\tilde{e}}{Dt} &= -\overline{P}\frac{\partial \tilde{u}}{\partial x} + \overline{u''}\frac{\partial \overline{P}}{\partial x} + \overline{\rho}\tilde{\varepsilon} + \frac{\partial}{\partial x}\left(C_e\overline{\rho}\frac{\tilde{k}}{\tilde{\varepsilon}}\widetilde{R_{11}}\frac{\partial}{\partial x}\left(\tilde{e} + \frac{\overline{P}}{\overline{\rho}}\right)\right)\,.
\end{aligned}
\tag{1}
$$

The single fluid approximation for a binary mixture is used. The concentration and enthalpy fluxes are modelled by a classical first gradient law, with $C_c = 0.15$ and $C_e = 0.19$. In order to take into account the anisotropy of the Reynolds stress tensor we use a tensorial turbulent diffusivity. The five equations of our turbulence model read

$$
\begin{aligned}
\overline{\rho}\frac{D\widetilde{R_{11}}}{Dt} &= -2\overline{\rho}\widetilde{R_{11}}\frac{\partial \tilde{u}}{\partial x} - C_1\overline{\rho}\tilde{\varepsilon}\left(\frac{\widetilde{R_{11}}}{\tilde{k}} - \frac{2}{3}\right) + \frac{4}{3}\gamma\overline{\rho}\widetilde{R_{11}}\frac{\partial \tilde{u}}{\partial x} - 2\overline{u''}\frac{\partial \overline{P}}{\partial x} + \frac{\partial}{\partial x}\left(C_k\overline{\rho}\frac{\tilde{k}}{\tilde{\varepsilon}}\widetilde{R_{11}}\frac{\partial \widetilde{R_{11}}}{\partial x}\right) - \frac{2}{3}\overline{\rho}\tilde{\varepsilon}, \\
\overline{\rho}\frac{D\widetilde{R_{22}}}{Dt} &= -C_1\overline{\rho}\tilde{\varepsilon}\left(\frac{\widetilde{R_{22}}}{\tilde{k}} - \frac{2}{3}\right) - \frac{2}{3}\gamma\overline{\rho}\widetilde{R_{11}}\frac{\partial \tilde{u}}{\partial x} + \frac{\partial}{\partial x}\left(C_k\overline{\rho}\frac{\tilde{k}}{\tilde{\varepsilon}}\widetilde{R_{11}}\frac{\partial \widetilde{R_{22}}}{\partial x}\right) - \frac{2}{3}\overline{\rho}\tilde{\varepsilon}, \\
\overline{\rho}\frac{D\tilde{\varepsilon}}{Dt} &= -C_{\varepsilon 1}\overline{\rho}\frac{\tilde{\varepsilon}}{\tilde{k}}\widetilde{R_{11}}\frac{\partial \tilde{u}}{\partial x} - C_{\varepsilon 3}\overline{\rho}\tilde{\varepsilon}\frac{\partial \tilde{u}}{\partial x} - C_{\varepsilon 0}\frac{\tilde{\varepsilon}}{\tilde{k}}\overline{u''}\frac{\partial \overline{P}}{\partial x} + \frac{\partial}{\partial x}\left(C_\varepsilon\overline{\rho}\frac{\tilde{k}}{\tilde{\varepsilon}}\widetilde{R_{11}}\frac{\partial \tilde{\varepsilon}}{\partial x}\right) - C_{\varepsilon 2}\overline{\rho}\frac{\tilde{\varepsilon}^2}{\tilde{k}}, \\
\frac{D\widetilde{u''}}{Dt} &= -\overline{u''}\frac{\partial \tilde{u}}{\partial x} + \frac{\widetilde{R_{11}}}{\overline{\rho}}\frac{\partial \overline{\rho}}{\partial x} - C_1{}^u\frac{\tilde{\varepsilon}}{\tilde{k}}\widetilde{u''} + \gamma^u\overline{u''}\frac{\partial \tilde{u}}{\partial x} - \frac{1}{\overline{\rho}}\frac{\overline{\rho'^2}}{\overline{\rho}^2}\frac{\partial \overline{P}}{\partial x} + \frac{\partial}{\partial x}\left(2C_{u''}\frac{\tilde{k}}{\tilde{\varepsilon}}\widetilde{R_{11}}\frac{\partial \widetilde{u''}}{\partial x}\right) - C_{u2}\frac{\tilde{\varepsilon}}{\tilde{k}}\widetilde{u''}, \\
\frac{D\overline{\rho'^2}}{Dt} &= -2\overline{\rho'^2}\frac{\partial \tilde{u}}{\partial x} + 2\overline{\rho}\widetilde{u''}\frac{\partial \overline{\rho}}{\partial x} + \frac{\partial}{\partial x}\left(C_{\rho'^2}\frac{\tilde{k}}{\tilde{\varepsilon}}\widetilde{R_{11}}\frac{\partial \overline{\rho'^2}}{\partial x}\right) - C_{\rho 2}\frac{\tilde{\varepsilon}}{\tilde{k}}\overline{\rho'^2}.
\end{aligned}
\tag{2}
$$

The main choices for turbulent closures are described below. In the Reynolds stress equations, the modelling of the pressure-strain correlation follows the Launder-Reece-Rodi proposal [5].

The closure of the redistribution process in the mass flux equation is inspired by the modelling of passive scalar equations. To model the enthalpic production term in the $\overline{u''}$ equation, we only keep the first three terms of the Taylor expansion of $1/\overline{\rho}$. The destruction processes for the last three equations are gathered in dissipation like terms with a dissipation time scale equal to $\widetilde{k}/\widetilde{\varepsilon}$. The model coefficients are given in Table 1. Initialization of turbulent variables is

C_k	C_ε	$C_{u''}$	$C_{\rho'^2}$	C_1	γ	${C_1}^u$	γ^u	$C_{\varepsilon 1}$	$C_{\varepsilon 0}$	$C_{\varepsilon 3}$	$C_{\varepsilon 2}$	C_{u2}	$C_{\rho 2}$
0.22	0.15	0.15	0.15	1.8	0.6	1.0	0.5	1.47	0.75	0.4	1.9	6.0	8.0

Table 1. Model coefficients.

based on assumptions upon the development of Richt-myer-Meshkov instability at an interface. Density variance is defined from density jump through the expression $(\rho_{SF6} - \rho_{air})^2/4$. The size of the wire mesh and the elasticity of the membrane give us values for the initial perturbation wavelength and amplitude [1]. Combined with the shock strength, which supplies information about the energy transfered to the mixing, we eventually get indications upon the generated turbulence in terms of time and length scales.

4. Simulation results versus experimental data

The comparison between measured and calculated mean velocities emphasizes the 3D effects in the experiments. In particular, the interaction between the reflected shock wave and the boundary layer in SF_6 generates a λ shock wave and increases the thickness of the boundary layer [6]. As a result, the experimental mean velocity of the second plateau after the mixing zone passage (Fig. 2) is about $60m/s$, to be compared with the theoretical 1D value of $47m/s$. The chronology of the passage of TMZ at the observation (LDA) abscissas is thus slightly shifted. Figures 4 and 5 take into account this shift to facilitate the comparisons. Figure 3 presents the thicknening of the TMZ versus time. Agreement is quite good before the first reshock as well as between the two reshocks. Then, the diffusion process seems to be correctly reproduce by the model. The comparison between measured and calculated[1] Reynolds stress tensor components is shown in figures 4-5. Figure 4 demonstrates that simulated turbulent energy reproduces experimental profiles to within 30%. (The cumulate error on experimental data is estimated to $\pm 15\%$.) The results at the first two abscissas show that the Richtmyer-Meshkov instability at the interface SF_6 / air generates measurable turbulent energy, slightly underestimated by the simulations. The enhancement of the turbulent energy level by the first reshock (between the abscissas 125.5 and $161mm$) is overpredicted. The second reshock interacts with the TMZ during its passage at the $178.5mm$ abscissa. No experimental values of kinetic energies are available during this period because of the rapid variation of the mean velocity, which makes the statistical treatment of the velocity measurements meaningless considering the data acquisition rate. The shock wave passage induces the peak in the simulation profile at $1.84ms$. The

[1] As experimental data are Reynolds averages, we have to establish passage formulas from one system to another. The main quantities are velocity and Reynolds stresses. We have

$$\overline{u} = \widetilde{u} + \overline{u''}\,, \tag{3}$$

$$\overline{u'u'} = \widetilde{R_{11}} - \overline{u''}^2 - \frac{\overline{\rho' u'' u''}}{\overline{\rho}} \equiv \widetilde{R_{11}} - \overline{u''}^2 - 2C_u \frac{\widetilde{k}}{\widetilde{\varepsilon}} \widetilde{R_{11}} \frac{\partial \overline{u''}}{\partial x}\,, \quad \overline{v'v'} = \widetilde{R_{22}}\,. \tag{4}$$

The non-resolved correlation $\overline{\rho' u'' u''}/\overline{\rho}$ is modelled as in the evolution equation for $\overline{u''}$.

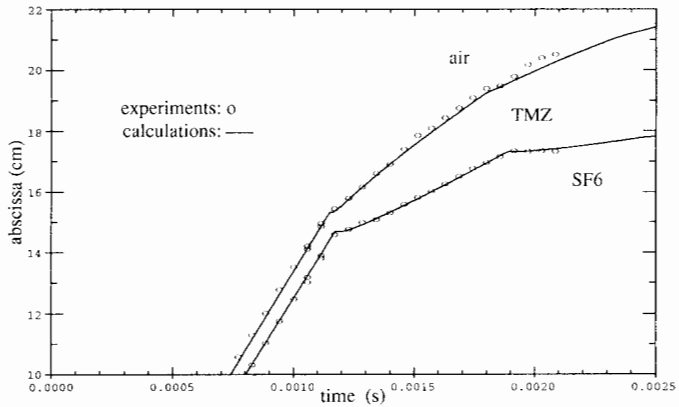

Figure 3. Evolution of the edges of the TMZ. Experimental values are obtained by schlieren visualization with an error of $\pm 10\%$. Calculated curves represent the $0.01 - 0.99\%$ limits based upon the mass concentration.

agreement after relaxation of turbulence is satisfactory. Figure 5 illustrates the anisotropy of

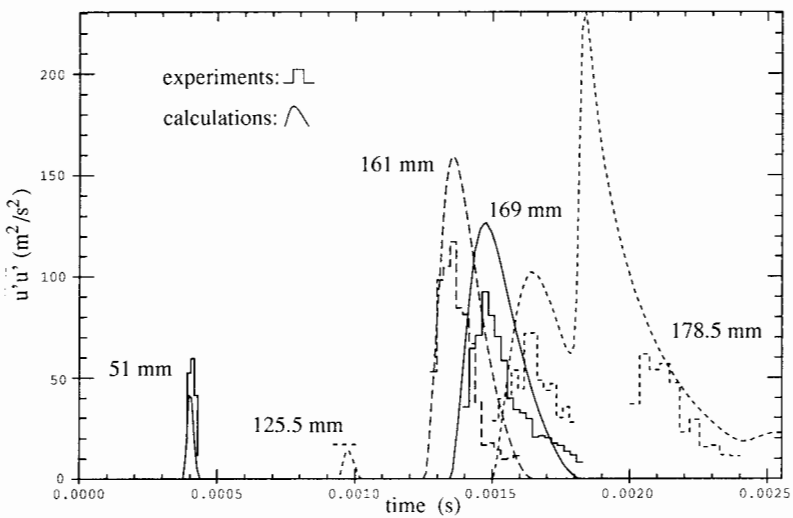

Figure 4. Evolution of the axial component of the Reynolds stress tensor, or velocity variance, at the five probe abscissas.

the Reynolds stress tensor at the $169mm$ abscissa, i.e., around $0.3ms$ after the interaction with the reflected shock wave. At the maximum of the profiles, the ratio $\overline{u'u'}/\overline{v'v'}$ reaches the value 3 in the experiments and 5 in the calculation. In the simulation, this ratio increases up to 12 during the first reshock passage. The enhancement of anisotropy has a direct influence upon the diffusivities which are proportional to $\tilde{k}R_{11}/\tilde{\varepsilon}$. Further information on experimental anisotropy at other abscissas could decide if the simulation distorts too much the tensor or if the return to isotropy is underestimated.

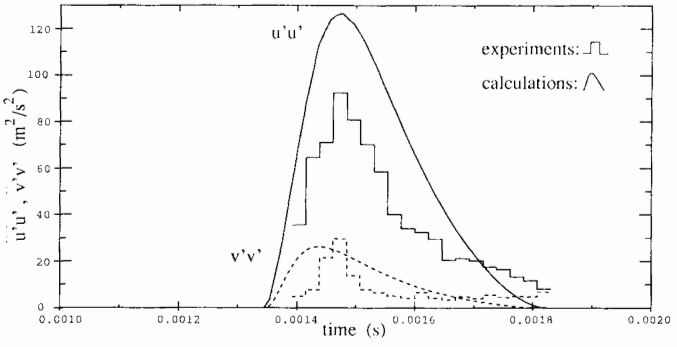

Figure 5. Evolution of the axial and radial components of the Reynolds stress tensor at the 169 mm abscissa.

5. Conclusion

The velocity measurements reported here clearly demonstrate that developed turbulence is generated in shock tube experiments even before the interaction with the reflected shock wave. This behaviour is facilitated by the wire mesh, which prevents the membrane to stay in one piece and initiates small scale perturbations. The simulation with our second order closure model is in reasonable agreement for the thickening of the TMZ as well as for the Reynolds stress tensor evolution. This agreement is achieved during the overall time interval of experimental observation. To examine the distortion of the turbulence spectrum due to the interaction with the shock wave, the two-time- scale concept, already developed for a $k - \varepsilon$ model [7], might be used. Such an approach can model the delay of the energy transfer from large scales to dissipative scales.

References

[1] Poggi F, Thorembey MH and Haas JF, Velocity measurements in turbulent gaseous mixtures induced by Richtmyer-Meshkov instability, these proceedings.

[2] Andronov VA, Bakhrakh SM, Meshkov EE, Nikiforov VV, Pevnitskii AV and Tolshmyakov AI, An experimental investigation and numerical modeling of turbulent mixing in one-dimensional flows, Sov. Phys. Dokl., 27, 5, 393-396, (1982).

[3] Taulbee D and VanOsdol J, Modeling turbulent compressible flows : The mass fluctuating velocity and squared density, 29th AIAA Aerospace Sciences Meeting, Reno, AIAA Report N° 91-0524, (1991).

[4] Ristorcelli JR, A representation for the turbulent mass flux contribution to Reynolds-stress and two-equation closures for compressible turbulence, ICASE Report N° 93-88, november (1993).

[5] Launder BE, Reece GJ and Rodi W, Progress in the development of a Reynolds-stress turbulence closure, J. Fluid Mech., 68, 3, 537-566, (1975).

[6] Mügler C and Gauthier S, 2D Navier-Stokes of Richtmyer-Meshkov instability in shock tube, these proceedings.

[7] Souffland D, Grgoire O, Gauthier S and Schiestel R, A multi-scale turbulence model for compressible mixing flows, in Proc. of the 5th International Workshop on Compressible Turbulent Mixing, 78-82, R. Young, J. Glimm and B. Boston editors, (1995).

Numerical Studies of Hydrodynamic Instability Effects on Spherical Implosion Performance

H. Takabe, A. Sunahara, S. Naruo, Y. Ochi, H. Nishimura, H. Shiraga, H. Azechi, N. Ohnishi, H. Nagatomo and K. Mima
Institute of Laser Engineering, Osaka University
2-6 Yamada-oka, Suita, Osaka, 565, Japan

Abstract: Numerical analysis of spherical implosion experiments done with Gekko XII laser system is described by mainly focusing on a nonuniform implosion with relatively long-wavelength perturbations. By use of a two-dimensional code, it is shown that all the available experimental data such as neutron yield, ion temperature by time-of-flight, and doped argon emission dynamics are well reproduced, when we assume that the velocity nonuniformity of 20% for ℓ=6 the most dominant mode in Gekko XII irradiation configuration, at the time when the stagnation phase starts.

1. Introduction

In the inertial confinement fusion research, the most critical issue is an accomplishment of spherically symmetric implosion and a variety of efforts have been devoted to study the physics of hydrodynamic instability and analyze the implosion performance with multi-dimensional implosion codes [1]. At ILE, Osaka University, beam smoothing and power balance of Gekko XII laser system (12 beams) have been achieved as a project "P-project" [2]. After the improvement of optical system of Gekko XII, a series of implosion experiments have been carried out to demonstrate the technical accomplishment for improving implosion performance. Data of the implosion experiments have been at first compared to one-dimensional (1-D) code ILESTA-1D [3] and a good agreement of implosion dynamics has been obtained. However, such as neutron yield is still below the 1-D yield and two-dimensional (2-D) simulation has been carried out to know the physics mechanism reducing the neutron yield. By focusing on the detail dynamics in the stagnation phase, we clarify the physics of degradation of implosion performance due to nonuniform hydrodynamics characterized by the spherical wavenumber ℓ=1-12, relatively long wavelength perturbations. It is concluded that all experimental data available at the present time can be explained self-consistently if we assume 20% velocity nonuniformity of ℓ=6 at the time of start of the stagnation phase.

In Sec.2, the implosion dynamics is compared between experiments and 1-D simulations and the discrepancy in neutron yield is discussed. In Sec.3, two-dimensional simulations are carried out to explain the discrepancy by focusing on relatively long wavelength perturbation effect. In Sec.4, time evolution and spatial profile of argon line emissions are compared with the two dimensional simulations. In Sec.5, brief summary and conclusion are described.

2. Implosion experiment and 1-D simulations

In the P-project campaign experiment, plastic targets filled with deuterium gas are irradiated by the laser with 12 beams of 0.53μm in wavelength. The diameter of the targets are about 500μm and the irradiated laser energy is roughly 1.5-2kJ on target.

More information - Email: takabe@ile.osaka-u.ac.jp

In Fig.1, the experimental neutron yields are plotted with 1-D simulation yields obtained with three different models. The irradiated laser pulse shape is of a single pulse or double pulses consisting of square picket pulse of 0.2 ns pulse width and a main square pulse of 1.6 ns width. The gap between the two pulses is chosen as a parameter to control the density at the ablation front in the acceleration phase. That is, we expect an increase of ablation flow velocity by reducing the ablation front density with increase of the gap interval. Since the ablative stabilization is enhanced by increasing the ablation flow velocity [1], we expect stable implosion at larger pulse gap.

In Fig.1, the experimental neutron yields with the irradiation (shot) numbers are plotted. The neutron yields obtained with 1-D code are also plotted with square masks. It is seen that the experimental yield is an order of magnitudes less compared to 1-D for the case of no gap, while it approaches slightly to 1-D with longer gap. For reference, the 1-D yields obtained by turning off the radiation transport and modifying the equation of state for ions according to the Cowan's model [4] are plotted with + and × marks, respectively. It is clear that with such modifications of physics included in 1-D code, we can not explain the substantial reduction of the yields seen in Fig.1.

It is instructive to study the details of a typical shot (♯16623). In this shot, total energy of 1.63kJ is irradiated on a target of 244μm outer radius with plastic layer of 8.2μm thickness and D_2 gas of 30 atm. The ion temperature in 1-D is almost 1keV at the peak neutron emission time and the radius convergence ratio C_R=7.5. By taking account of the fact that the core temperature is low by roughly an order of magnitude compared to the old experiments of LHART [5], the difference of a factor 4 in neutron yield indicates much better uniformity compared to the case of LHART.

There are also another experimental data such as neutron time-of-flight ion temperature and time history of line emissions of argons slightly doped in the fuel gas, indicating discrepancy against those predicted by 1-D simulations. In what follows, we try to explain these experimental data consistently by carrying out 2-D model simulation for nonuniform implosion dynamics near the maximum compression.

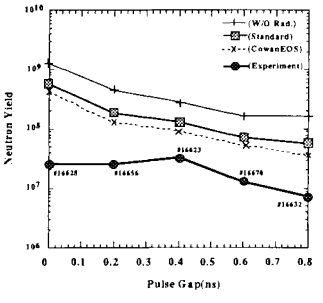

Figure 1. The experimental and numerical (1-D) neutron yields as a function of the pulse gap of laser pulse shape.

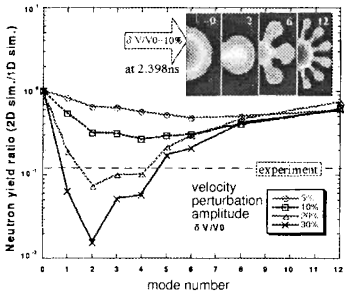

Figure 2. The 2-D neutron yields normalized by 1-D ones as a function of spherical wave number (mode number) ℓ. The velocity perturbation amplitude is a parameter.

3. Two dimensional simulations

In order to explain the experimental results, we have carried out 2-D hydrodynamic simulation in axially symmetric geometry with an Eulerian code based on the 2-nd order Godunov scheme [6]. The flux limited Spitzer-Härm electron heat transport and multi-group radiation transport are solved by time-splitting method after solving hydrodynamics at each time step. The equation of state is assumed to be of ideal plasmas in fully ionized state. The contact surface between the fuel and the plastic (CH) capsule is tracked by a surface-tracking method which is modeled after modifying the basic idea given in Ref. [7].

We have studied the effect of single mode nonuniformity in the stagnation phase. For this purposed, we at first store numerical data at the time of the beginning of the stagnation phase (in what follows, we devote this time as $t=t_s$) obtained by 1-D simulation. Then, the numerical data are absorbed in the 2-D code as the initial condition after modification by imposing velocity perturbation so that a surface-mode-like structure is localized around the contact surface.

We have carried out a parameter study for the case of ♯16623. The stagnation phase is defined so that it starts when the shock wave arrives at the center of the target and t_s=1.9 ns in this shot. We have varied two parameters : one is the spherical mode number ℓ and the other is the amplitude of the velocity perturbation.

In Fig.2, the normalized neutron yield [=(2-D yield)/(1-D yield)] is plotted as a function of the mode number of ℓ=1-12 for four different amplitudes of the velocity perturbations ($\delta v/v_0$=5, 10, 20 and 30%). It is seen in Fig.2 that the decrease of the neutron yield is enhanced around ℓ=2, while no substantial reduction is seen for the modes $\ell \geq 8$. The temperature profiles near the time of peak neutron emission rate are shown for the case of ℓ=2, 6 and 12 with $\delta v/v_0$=10%.

The reason why the reduction of neutron yield is not so enhanced for ℓ roughly larger than 5 is as follows. In these cases, the spikes penetrating into the central region confine and heat the central part of the fuel. As the result, a small fraction of fuel becomes higher temperature than 1-D case and enhancement of neutron production is observed. As the result of compensation between this enhancement and less heating of the fuel in outer region, the total neutron yield does not change substantialy. For the case of the perturbation of relatively long wavelength such as ℓ=2, on the other hand, the fuel is not confined in the central region and the yield reduces drastically as seen in Fig.2.

In the irradiation configuration of Gekko XII laser system, the dominant nonuniformity of intensity distribution is ℓ=6. As far as we limit our discussion to the contribution from ℓ=6 nonuniformity, it is concluded that the experimental neutron yield can be reproduced by assuming that the velocity perturbation of 20% is generated through the acceleration phase.

Regarding not only the neutron yield, but also the ion temperature observed with time-of-flight method by use of the multi-channel neutron detector, we have compared experimental data to those from the 2-D simulation. In Fig.3, the time and space integrated ion temperature weighted by neutron emission rate is plotted as a function of the mode number for the cases of $\delta v/v_0$=10, 20 and 30%. The ion temperature decreases for ℓ=2 mode, while it effectively increases for $\ell \geq 6$ because of the confinement effect by spikes. In this shot (♯19714), the observed ion temperature is plotted with the shaded region which covers an error bar of the data point. It is clear that by assuming about 20% nonuniformity we can reproduce this experimental data. It should be noted that in general the observed ion temperature is higher than the 1-D ion temperature although the neutron yield is lower in the experiment.

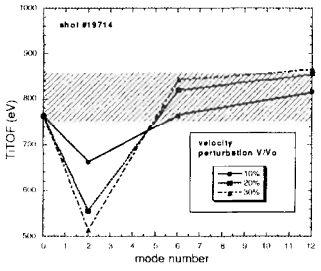

Figure 3. The time and space integrated ion temperature weighted by neutron emission rate as a function of the mode number. The data are calculated with 2-D code and experimental data is shown with the shaded area.

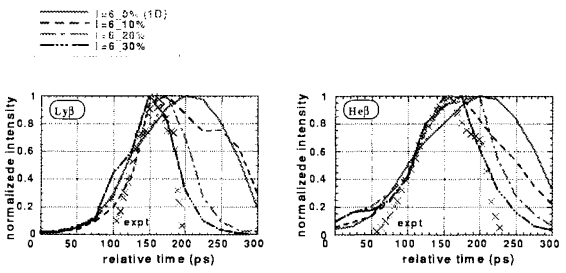

Figure 4. The time evolution of the normalized line intensity of Ly^{β} and He^{β} of argon atoms. The lines are obtained with 2-D code, while the $\times$ marks are experimental data.

This fact indicates that a part of the fuel which predominantly heated by spikes due to instability growth plays impotent role in producing neutrons as seen in the 2-D simulations.

4. Line emission from argon doped in fuel

In order to study the time evolution of implosion dynamics near the maximum compression, line emissions from argon doped in the fuel gas have been observed with space-and-time resolved X-ray spectroscopic method. We have focused on Ly^{β} line [Ar^{17+} ($1s$-$3p$)] from H-like and He^{β} line [Ar^{16+} ($1s^2$-$1s3p$)] from He-like argon plasmas [8]. The line emission history has been calculated as post process for the 2-D simulation explained in the previous section. In the post-process package, line radiation transport is calculated with spectral emissivity and opacity given by RATION code [9]. In the process, we have prepared data table for T_e=100eV-2keV with 10 data points and n_e=10^{21}-10^{25} cm^{-3} with 10 data points. Each line profile is divided roughly into 100 groups for 20eV energy range around the line peak.

At first, emission intensity profiles as a function of time is compared with an experiment of ♯19714 in which a plastic capsule of diameter of 500μm (thickness 7.2μm) over-coated by palylene (0.5μm) and Al (0.03μm) filled with 9.5 atm fuel gas is irradiated by 2ω laser with 1.85kJ on target. In this shot, the laser pulse shape is same as ♯16623 discussed above. In this shot, the fuel consists of H_2 , D_2 and T_2 gases in ratio of 6 : 4 : 0.02 and Ar of 0.025 atm is doped for diagnostic purpose.

In Fig.4, the time evolutions of normalized line intensity are plotted by lines for the case of 2-D simulation. On the other hand, the profile observed in the experiment is plotted with $\times$ marks. It is clear that in 1-D simulation, which is indicated by the solid line, relatively long confinement time in the stagnation phase provides a long emission time of highly ionized Ar plasma. This tendency can be seen in both of Ly^{β} and He^{β} emission profiles. By increasing nonuniformity of ℓ=6 mode in 2-D simulation, effective confinement time reduces and, roughly saying, a good agreement is obtained when we assume 20-30% velocity perturbation at t=t_s. This conclusion is consistent with that described in the previous section regarding the neutron yield and ion temperature. At the present time, no absolute values of the emission intensity are available. It should be, however, noted that in 2-D simulation the intensities of both line

emissions drop by about a factor of 5 in case of 20% nonuniformity compared to 1-D case.

In the experiment of ♯19714, the time-integrated spatial profiles of these line emissions have also been observed. In Fig.5, the line emission profile of Ar He^{β} obtained in the experiment is compared with three numerical profiles obtained from 1-D simulation and 2-D with 10% and 20% nonuniformities. It is clear that the observed emission zone shrinks compared to 1-D and the profile of the emission is well reproduced by assuming 10-20% nonuniformity, being consistent with the above discussion.

The line intensity ratio of Ly^{β}/He^{β} has been used to derive electron temperature of the compressed fuel. Then, the experimental line intensity ratio is compared to that calculated, for example, with collision-radiative equilibrium (CRE) atomic model like RATION. Regarding the line intensity ratio, the numerical value increases from 0.2 (1-D) to about 0.4 (2-D, 20%), while this value does not coincide with the observed value of 0.75. Within the present model based on RATION code, it seems to be impossible to reproduce such intensity ratio. If we dare to increase the line ratio, higher temperature of the compressed fuel is required. Then, however, the other data such as neutron yield can not be explained with 2-D code. It is, therefore, concluded that the most ambiguous point is the assumption of CRE and the rate equation for argon atomic state should be solved. This work is on going with the code FLY [10].

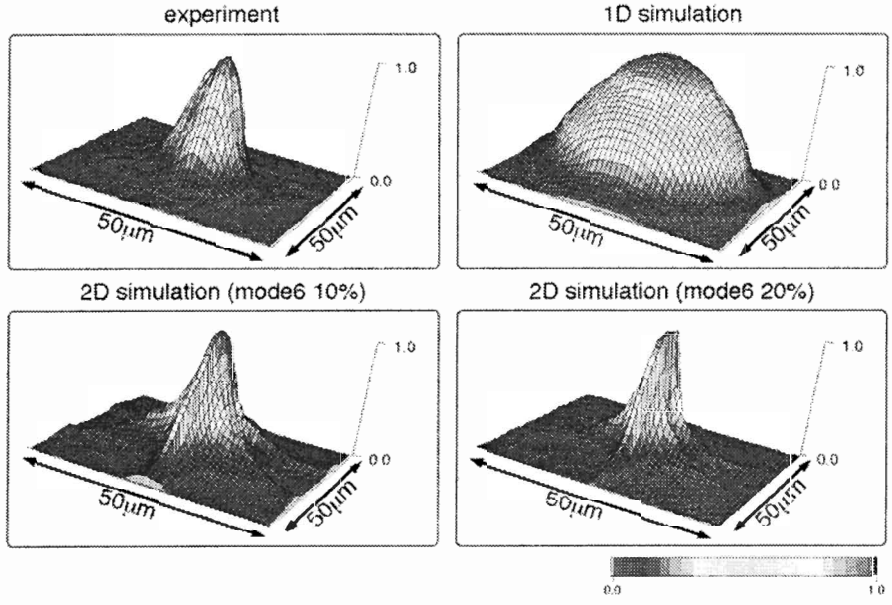

Figure 5. The time-integrated He^{β} emission profiles obtained in the experimental and 2-D simulations.

5. Conclusion

A Series of Implosion experiments have been carried out with Gekko XII laser system after improving beam intensity uniformity and beam power balance. At first, the experimental data have been compared to simulations with 1-D implosion code ILESTA-1D. Regarding implosion dynamics it is confirmed that 1-D simulation well reproduces the experimental data by com-

paring x-ray streak image. However, the other data such as neutron yield and ion temperature have not been reproduced.

In order to study the physical mechanism resulting in such discrepancy, we have carried out 2-D simulation by focusing on a single-mode nonuniformity of ℓ=6, which is the dominant intensity nonuniformity in Gekko XII irradiation configuration. It is shown that most of the experimental data are well reproduced as the result of instability growth at the contact surface between fuel and plastic capsule. Higher ion temperature while less neutron yield in the experiment can be explained so that a small fraction of the fuel near the target center is confined and heated by the spikes of capsule as seen in 2-D simulation. About 20% nonuniformity in the velocity field is concluded to be generated by the time when the stagnation phase starts.

Spectroscopic measurement of doped Ar line emission has also been compared to the simulations. The time history of $Ar^{+17}Ly^{\beta}$ and $Ar^{+16}He^{\beta}$ line emissions and their time-integrated spatial profiles are found to be well reproduced in 2-D simulation, which is consistent with the ion temperature and neutron yield. There remains, however, a discrepancy in the line ratio and further improvement of atomic model is left as a subject to be done next.

References

[1] Takabe H, Hydrodynamic Instability and Inertial Confinement Fusion, J. Plasma and Fusion Res., 73, in Japanese, in the process of translation to English, (1997).
[2] Mima K *et al.*, Phys. Plasmas, 3, 2077, (1996).
[3] Takabe H, Hydrodynamic Simulation Code ILESTA for Laser Driven Implosion, unpublished.
[4] More RL *et al.*, Phys. Fluids, 31, 3059, (1988).
[5] Takabe H *et al.*, Phys. Fluids, 31, 2884, (1988).
[6] Colella P and Glaz HM, J. Comp. Phys., 59, 264, (1985).
[7] Youngs DL, Physica D37, 270, (1989).
[8] Ochi Y *et al.*, Observation of implosion dynamics by line emissions from direct-drive fusion capsule, to appear.
[9] Lee RW, User Manual for RATION, LLNL Report, January (1990).
[10] Lee RW, The How to for FLY, November (1995).

Comparison Between Numerical and Experimental Results for Turbulent Mixing Induced by Richtmyer-Meshkov Instability

E. Valerio[1], D. Zeitoun[1], G. Jourdan[1], L. Houas[1] and D. Besnard[2]
[1]IUSTI, Umr CNRS, Université de Provence, Technopôle de Château Gombert
5 rue Enrico Fermi 13453 Marseille Cedex 13, France
[2]C.E.A. Grenoble, Departement Thermohydraulique et Physique
17 rue des Martyrs 38054 Grenoble cedex 9, France

Abstract: Results given by the 1D version BHR turbulence transport model are compared with shock tube experimental data. Different couples of gases with both various Atwood and incident shock wave Mach numbers are considered. Mixing zone thickness time evoltions are presented and directly compared with experimental results to test and analyse the second order turbulence model. Using two different initializations, to better describe the first phases of the phenomenon under study, i.e. taking into account the presence of an initial membrane in a horizontal shock tube configuration, we have found that agreement between calculations and experiments are satisfactory.

1. Introduction

Over the last decade, a large effort has been devoted to the understanding of the problem of the stability of an interface between two fluids of different densities submitted to a pressure gradient and inducing turbulent mixing, problem often referred to as Richtmyer-Meshkov [1, 2] instability. Among possible experimental tools for studying these processes, shock tubes are very convenient ones, since they allow for easier diagnostics than any other experimental facility. However, a specific difficulty is related to the presence of the membrane that generally separates the two gases to be mixed under the shock passage. In this paper, we compare BHR simulations with an update of experiments performed at IUSTI [3], using a spectroscopic method to investigate different experimental configurations, in which the two gases are initially separated by a thin plastic membrane (1.5 μm). The cases where the shock wave passes from the heavy gas to the light one (CO_2/He), from one gas to an other of close density (CO_2/Ar) and from the light gas to the heavy one (CO_2/Kr) have been studied in a square cross section horizontal shock tube.

1.1. Equations for 1D flow

For 1D flow, the BHR model [4] can be written as follows:

$$\frac{d\rho}{dt} = -\rho\frac{\partial u_x}{\partial x} \tag{1}$$

$$\frac{du_x}{dt} = -\frac{1}{\rho}\frac{\partial p}{\partial x} - \frac{1}{\rho}\frac{\partial}{\partial x}\left(\rho(k - k_\perp)\right) \tag{2}$$

$$\frac{dI}{dt} = -\frac{p}{\rho}\frac{\partial(u_x - a_x)}{\partial x} + C_k k\sqrt{D} + \frac{1}{\rho}\frac{\partial}{\partial x}(4C_\epsilon c(1-c)\rho a_x I + C_\epsilon C_\mu \mu_t \frac{\partial I}{\partial x}) \tag{3}$$

More information - Email: houas@iusti.univ-mrs.fr

$$\frac{dc}{dt} = \frac{1}{\rho}\frac{\partial}{\partial x}(-4C_e c(1-c)\rho a_x + C_e C_\mu \mu_t \frac{\partial c}{\partial x}) \quad (4)$$

$$\frac{dk}{dt} = -2(k-k_\perp)\frac{\partial u_x}{\partial x} + \frac{2a_x}{\rho}\frac{\partial p}{\partial x} - C_k k\sqrt{D} + \frac{1}{\rho}\frac{\partial}{\partial x}(\alpha_k \mu_t \frac{\partial k}{\partial x}) \quad (5)$$

$$\frac{dk_\perp}{dt} = C_{k_1}\sqrt{D}(\frac{2}{3}k - k_\perp) - C_k k_\perp \sqrt{D} + \frac{1}{\rho}\frac{\partial}{\partial x}(\alpha_k \mu_t \frac{\partial k_\perp}{\partial x}) \quad (6)$$

$$\frac{da_x}{dt} = -\frac{1}{\rho}(k-k_\perp)\frac{\partial \rho}{\partial x} + \frac{\partial {a_x}^2}{\partial x} - a_x\frac{\partial(u_x - a_x)}{\partial x} + \frac{B}{\rho^2}\frac{\partial p}{\partial x} + \frac{1}{\rho}\frac{\partial}{\partial x}(\alpha_a \mu_t \frac{\partial a_x}{\partial x}) \quad (7)$$

$$- C_a a_x \sqrt{D} \quad (8)$$

$$\frac{dB}{dt} = -2a_x\frac{\partial \rho}{\partial x} + \frac{\partial(\rho a_x B)}{\partial x} - B\frac{\partial(u_x - a_x)}{\partial x} + \frac{1}{\rho}\frac{\partial}{\partial x}(\alpha_B \mu_t \frac{\partial B}{\partial x}) - C_B B\sqrt{D} \quad (9)$$

$$\frac{dD}{dt} = -2(D - D_\perp)\frac{\partial u_x}{\partial x} + 2D_{ax}\frac{1}{\rho}\frac{\partial P}{\partial x} + \frac{1}{\rho}\frac{\partial}{\partial x}(\alpha_D \mu_t \frac{\partial D}{\partial x}) - C_D D\sqrt{D} \quad (10)$$

$$\frac{dD_\perp}{dt} = C_{k_1}\sqrt{D}(\frac{2}{3}D - D_\perp) - C_D D_\perp \sqrt{D} + \frac{1}{\rho}\frac{\partial}{\partial x}(\alpha_D \mu_t \frac{\partial D_\perp}{\partial x}) \quad (11)$$

$$\frac{dD_{ax}}{dt} = -\frac{1}{\rho}C_{Da_1}(D - D_\perp)\frac{\partial \rho}{\partial x} - D_{ax}\frac{\partial(u_x)}{\partial x} + C_{Da_2}\frac{D_B}{\rho^2}\frac{\partial p}{\partial x} + \frac{1}{\rho}\frac{\partial}{\partial x}(\alpha_{D_a}\mu_t \frac{\partial D_{ax}}{\partial x}) \quad (12)$$

$$- C_{Da} D_{ax}\sqrt{D} \quad (13)$$

$$\frac{dD_B}{dt} = -2D_{ax}\frac{\partial \rho}{\partial x} + \frac{\partial(\rho a_x D_B)}{\partial x} - D_B\frac{\partial(u_x - a_x)}{\partial x} + \frac{1}{\rho}\frac{\partial}{\partial x}(\alpha_{D_B}\mu_t \frac{\partial D_B}{\partial x}) \quad (14)$$

$$- C_{D_B} D_B \sqrt{D} \quad (15)$$

where $\mu_t = \rho\frac{k}{\sqrt{D}}$ corresponds to the coefficient of turbulent dynamic viscosity and p, I, u_x, ρ and c represent the pressure, the internal energy, the mean flow velocity, the density and the concentration, respectively.

1.2. Correlations

The full BHR model equations which are reported use different correlations such as the turbulent kinetic energy $k = (\overline{\rho u_x u_x} - \rho u_x u_x)/\rho$, its orthogonal component $k_\perp = (\overline{\rho u_k u_k} - \rho u_x u_x)/\rho$, the turbulent mass flux $a_x = \overline{\rho' u'_x}/\rho$, the self correlation of the density fluctuation $B = \overline{\rho'\rho'}/\rho$, the dissipation correlation for k, $D = \overline{\frac{\partial u'_i}{\partial x_k}\frac{\partial u'_i}{\partial x_k}}$, the dissipation correlation for $k_\perp$, $D_\perp = D - \overline{\frac{\partial u'_x}{\partial x_k}\frac{\partial u'_x}{\partial x_k}}$, the dissipation correlation for a_x, $D_{ax} = \overline{\frac{\partial \rho'}{\partial x_k}\frac{\partial u'_x}{\partial x_k}}$ and the dissipation correlation for B, $D_B = \overline{\frac{\partial \rho'}{\partial x_k}\frac{\partial \rho'}{\partial x_k}}$.

1.3. Model constants

As with all transport models, BHR contains modeling constants of order 1, determined either by numerical optimization or by comparison with some key published experiments performed with incompressible and compressible fluids [5], as well as from theoretical results [6], using a spectral turbulence model [7]. Note that for the present study, all the simulations have been conducted with the same coefficient set, which is given in Table 1.

C_k	C_e	C_μ	α_k	C_{k_1}	α_a	C_a	α_b	C_B
0.16	0.5	0.09	0.09	0.25	0.09	1.02	0.09	0.9
C_D	C_{Da_1}	C_{Da_2}	α_{D_a}	C_{D_a}	α_{D_B}	C_{D_B}	α_D	
1.0	1.0	1.0	0.09	1.0	0.09	0.9	0.06	

Table 1. Model coefficient set.

2. Resolution

2.1. Numerical method

BHR is implanted in one-dimensional Lagrangian hydro-code, which uses a finite difference scheme. The time step is splitted in three phases: the first one solves the hydrodynamic with a Richtmyer and Morton explicit scheme and the second explicitly solves turbulent part in averaged equations and the non convective terms in turbulent equations. Diffusion terms are implicitly calculated in an third additional phase.

2.2. Initialization

The rupture of the membrane initially separating the test gases is not considered in detail in the present work, but rather modeled. A turbulent mixing layer X_{IMZT} was considered, in which the volume fractions were linearly distributed between $[0; 1]$. For example:

$$\alpha_1 = \frac{x}{X_{IMZT}} + cst \qquad \text{and} \qquad \alpha_2 = 1 - \alpha_1 \tag{16}$$

From that, the 1D BHR code can initialize the computation by two different ways. The first (type A) considers the pre-mixing X_{IMZT}, over which the density variance B is defined by:

$$B = \alpha_1 \alpha_2 \rho \frac{(\rho_1 - \rho_2)^2}{\rho_1 \rho_2} \tag{17}$$

where α_i and ρ_i represent the volume fraction and the density of each constituent of the mixing zone, respectively. Calculations starte with no mean velocity u_x and therefore initialize the turbulent kinetic energy k and its dissipation D to zero. The density gradient constitutes the turbulent source production. The second (type B) corresponds to a "$k - \epsilon$" initialization type where the pre-mixing layer X_{IMZT} is initialized with a triangular turbulent kinetic energy profile and a dissipation rate ϵ in the form of $f(k^{\frac{3}{2}})$. The velocity, the density variance B and the turbulent mass flux a_x were put to zero.

3. Results

3.1. Description of the numerical applications

In order to prove the ability of the BHR model to simulate several configurations, with different Atwood numbers, defined by $A = \frac{\rho_1 - \rho_2}{\rho_1 + \rho_2}$, and Mach numbers, we have directly compared the BHR calculated evolution of the mixing zone thickness with some experimental points, obtained in the double diaphragm 8 meters horizontal shock tube of IUSTI [3, 8]. The cross section of the test chamber is $8.5 \times 8.5\ cm^2$, and its length was of about 115 cm downstream of the second diaphragm. Table 2 gives the initial conditions of the different considered tests, where P_i, M_{isw}, A', ρ_1, ρ_2 and ΔU correspond to the initial pressure, the incident Mach number, the post-shock Atwood number, the initial density of the gases 1 and 2 at rest and the velocity jump of the interface through the impulsive acceleration, respectively.

Gas combinations	P_i $[Pa]$	M_{isw}	ρ_1 $[kg/m^3]$	ρ_2 $[kg/m^3]$	A'	ΔU $[m/s]$
CO_2/He	2000	2.4	3.6E-2	5.4E-3	-0.74	605
CO_2/Kr	2000	2.4	3.6E-2	6.9E-2	+0.06	370
CO_2/Ar	2000	2.4	3.6E-2	3.3E-2	-0.24	450
CO_2/He	2000	4.5	3.6E-2	3.3E-2	-0.4	1020

Table 2. Initial conditions of the different simulated configurations.

4. Comments

Both the mixing zone thickness and the profiles of the space integral of the turbulent kinetic energy $\int k dx$ time evoltions, are presented on Figs. 1, 2 and 3 for the CO_2/He, CO_2/Kr and CO_2/Ar cases, respectively, initiated by a 2.4 shock wave Mach number. First, the code correctly reacts to the Atwood number variations, since the higher the density ratio is, the thicker the mixing zone is [9]. For the CO_2/He and CO_2/Kr cases (Figs. 1 and 2), where the initial Atwood number A is positively or negatively far from zero ($A_{CO_2/He} = -0.73$ and $A_{CO_2/Kr} = +0.33$), experiments with calculations are in good agreement. For the CO_2/Ar case (Fig. 3), where the initial Atwood number is close to zero ($A_{CO_2/Ar} = -0.05$), we can observe that calculations and experimental data are in disagreement. The present restitution of the CO_2/Ar turbulent mixing zone thickness is not satisfactory when using the same initialization principles as above. This relatively small thicknening of the calculated CO_2/Ar mixing zone is logical, given that the density gradient is the production source of turbulence. This discrepancy between calculations and experiments is probably related to the very complex phenomena which occur during the initial interaction (membrane rupture process) and which generate additional turbulent kinetic energy.

In this way, for the CO_2/Ar case, in order to take into account this membrane induced energy, we have initialized the mixing zone with a triangular profile of kinetic energy as shown in the Figs. 4 and 5. The CO_2/Ar illustrations represent the results of BHR calculations with two different initializations (A and B) for an incident shock wave Mach number of about 2.4 (Fig. 4) and 4.5 (Fig.5). One can see that, the mixing zone thickness and the created kinetic energy level increases with the incident shock wave Mach number. Moreover, it appears that the "$k-\epsilon$" initialization better describes the mixing growth with an adequate additional initial kinetic energy (k_{INI}). However, up to this day we have not yet found rigorous arguments to calculate k_{INI}.

5. Conclusion

BHR code describes correctly the mixing zone growth for different couples of gases. Even for low Atwood number experiments (as CO_2/Ar) which are usually very difficult to simulate, we found an initialization state which gives correct results. One of our principal center of interest for the moment is to find an analytic method to rigorously calculate the initial turbulent kinetic energy level used in the initialization B.

References

[1] Richtmyer RD, Taylor instability in shock acceleration of compressible fluids, Commun. Pure Applied Math., 13, 297-319, (1960).

[2] Meshkov EE, Instability of a shock wave accelerated interface between two gases, Sov. Fluid

Dyn., 4, 107-108, (1969).

[3] Jourdan G, Houas L, Haas JF and Ben-Dor G, Thickness and volume measurements of a Richtmyer-Meshkov instability induced mixing zone in a square shock tube, J. Fluid. Mech., 349, 67-94, (1997).

[4] Besnard DC, Haas JF, Rauenzahn RM, Statistical modeling of shock-interface interaction, Physica D37, 227-247, (1989).

[5] Besnard DC, Harlow FH and Rauenzahn RM, Conservation and transport properties of turbulence with large density variations, Los Alamos Report, LA-10911-MS, (1987); Besnard DC, Haas JF, Bonnet M, Froger A, Gauthier S and Sitt B, Comparison of two model models of Rayleigh-Taylor induced turbulent mixing, Proceedings of the Los Alamos - CEA Limeil conference on numerical methods, (1987); Besnard DC and Harlow FH, CEA notes, 2525-2526, (1987).

[6] Leith CE, Acceleration-induced turbulent mixing, Lawrence Livermore Report, (1985).

[7] Besnard DC *et al.*, Spectral transport for turbulence, Theo. & Comp. Physics, (1995).

[8] Houas L and Chemouni I, Experimental investigation of Richtmyer-Meshkov instability in shock tube, Phys. Fluids, 8, 2, 614-627, (1996).

[9] Besnard D, Jourdan G, Valerio E and Zeitoun D, Shock wave induced mixing: Experimental results and numerical modeling, Proc. of the 21^{st} Int. Symposium on Shock Wave, Great Keppel, Australia, to appear, (1997).

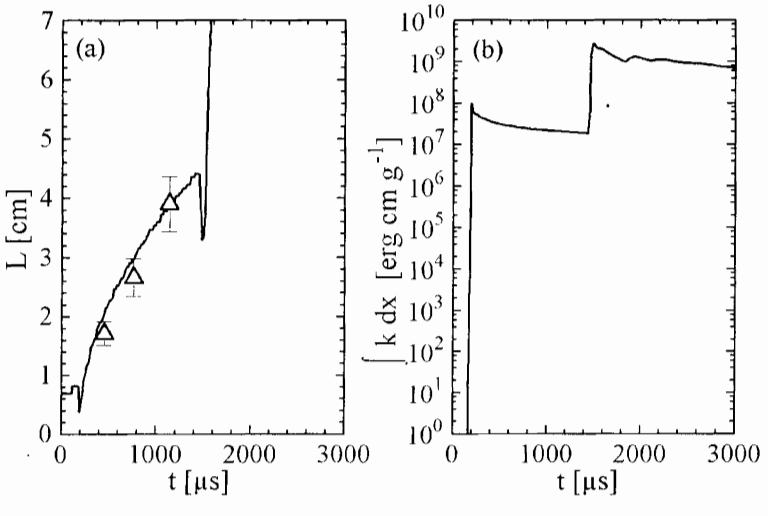

Figure 1. (a) Mixing zone thickness (△ experimental points, — calculations) and (b) space integral turbulent kinetic energy evolutions versus the time, for the CO_2/He mixing zone induced by 2.4 incident shock wave Mach number; BHR calculations were initialized with the type A for $X_{IMZT} = 0.6$ and 7 nodes $/cm$.

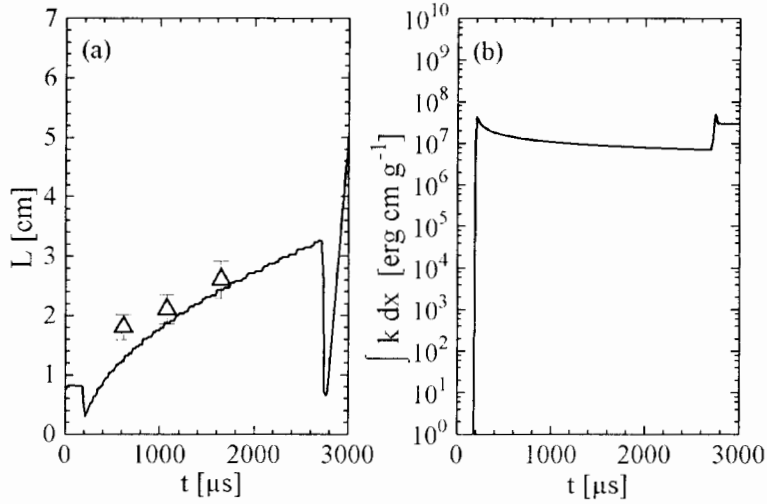

Figure 2. (a) Mixing zone thickness (△ experimental points, — calculations) and (b) space integral turbulent kinetic energy evolutions versus the time, for the CO_2/Kr mixing zone induced by 2.4 incident shock wave Mach number; BHR calculations were initialized with the type A for $X_{IMZT} = 0.6$ and 7 nodes $/cm$.

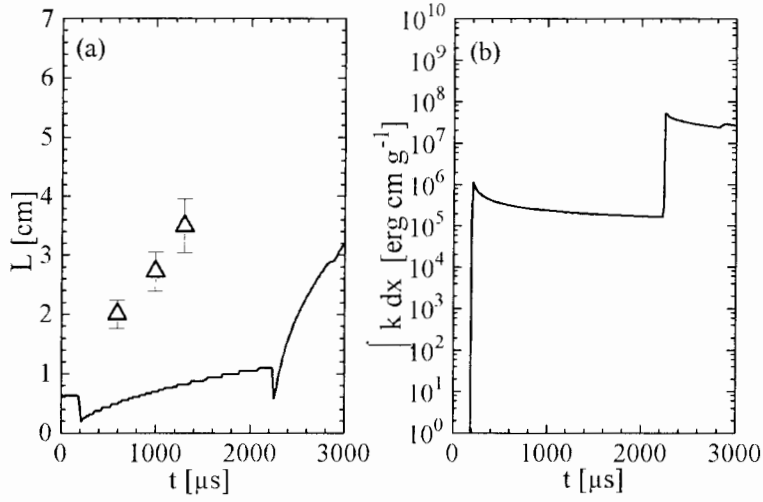

Figure 3. (a) Mixing zone thickness (△ experimental points, — calculations) and (b) space integral turbulent kinetic energy evolutions versus the time, for the CO_2/Ar mixing zone induced by 2.4 incident shock wave Mach number; BHR calculations were initialized with the type A for $X_{IMZT} = 0.6$ and 11 nodes $/cm$.

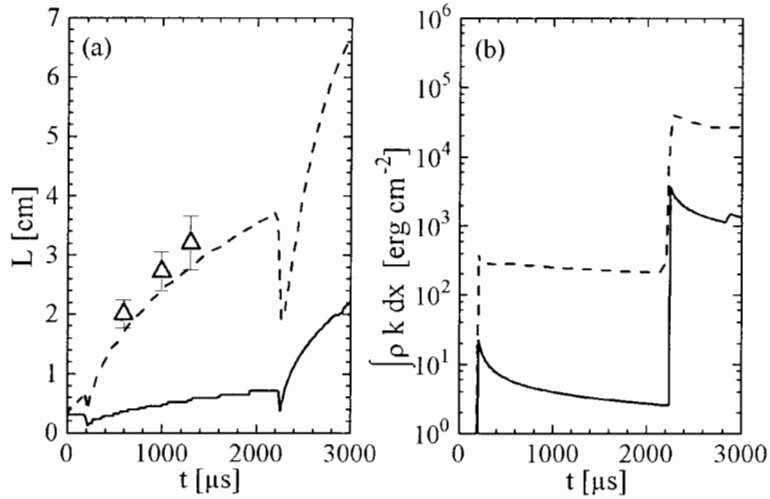

Figure 4. (a) Mixing zone thickness and (b) space integral turbulent kinetic energy evolutions versus the time, for the CO_2/Ar mixing zone induced by 2.4 incident shock wave Mach number; Comparison between results given by the initialization type A — and type B − − − (X_{IMZT}=0.3 and $k_{INI} = 5.10^7$).

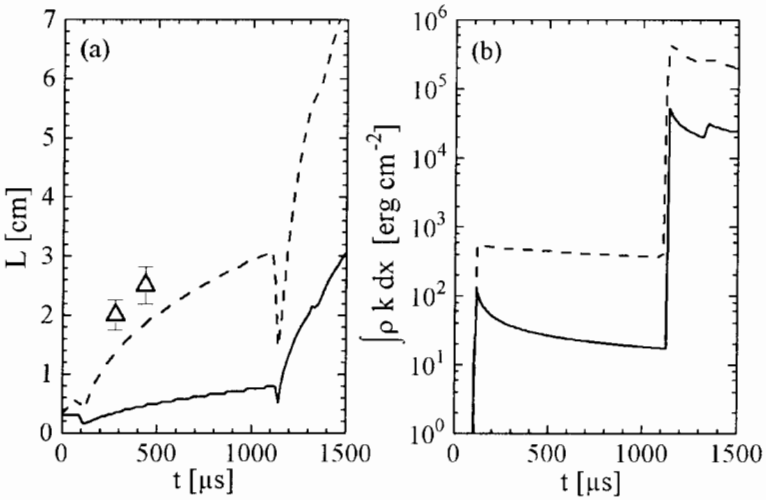

Figure 5. (a) Mixing zone thickness and (b) space integral turbulent kinetic energy evolutions versus the time, for the CO_2/Ar mixing zone induced by 4.5 incident shock wave Mach number; Comparison between results given by the initialization type A — and type B − − − (X_{IMZT}=0.3 and $k_{INI} = 6.10^7$).

Richtmyer-Meshkov Instability: The Impulsive Model Revisited

M. Vandenboomgaerde, C. Mügler and S. Gauthier
CEA/Limeil-Valenton, 94195 Villeneuve St Georges CEDEX, France

Abstract: In a previous communication [8], a new general formula for the growth rate of the Richtmyer-Meshkov instability was derived within the framework of the impulsive model. It was only tested against a few cases. This formula is now validated over more than one hundred cases available in the literature. It allows us to predict the growth rate in both heavy-light and light-heavy configurations. The range of validity of the impulsive model is also specified: the shock strength must be smaller than 0.4 and the ratio of the adiabatic exponents smaller than 1.5.

1. Introduction

When two different materials are impulsively accelerated into each other by a shock wave, small perturbations of the interface are first compressed, then grow linearly and finally evolve into non-linear structures. This instability was theoretically discovered and described by Richtmyer [1], and experimentally confirmed by Meshkov [2]. The Richtmyer-Meshkov (RM) instability occurs, in particular, in inertial confinement fusion. In the framework of the impulsive model, Richtmyer [1] proposed the following expression for the linear growth rate of the instability

$$\frac{da}{dt} = k\Delta u A^+ a_0^+, \tag{1}$$

where a is the amplitude of the perturbation, k its wave number, Δu the velocity jump across the shock wave, a_0^+ the amplitude immediately after the shock passage and A^+ the Atwood number after the interaction. In the above, the Atwood number is defined as $(\rho_2 - \rho_1)/(\rho_2 + \rho_1)$ where ρ_1 is the density of the first shocked fluid. It is usually admitted that expression (1) gives relatively good results for light to heavy accelerations although several exceptions to Richtmyer's formula have been found [3, 4]. For heavy to light accelerations, Meyer & Blewett [5], hereafter noted MB, recommend to use the following expression, where a_0^- is the preshocked amplitude

$$\frac{da}{dt} = \frac{1}{2} k\Delta u A^+ \left(a_0^+ + a_0^-\right). \tag{2}$$

These two formulas are just prescriptions.
Various theoretical results are available in the literature: Fraley [6] solved the perturbation equations for the case of a reflected shock wave. The results obtained from this approach were compared with Richtmyer's prescription by Mikaelian [3]. Yang *et al.* [4] have numerically solved the linear theory of the RM instability. Velikovich, using the same kind of techniques as Fraley, proposed an analytic theory of RM instability for the case of a reflected rarefaction wave [7].
However, in the context of inertial confinement fusion, simple formulas are very welcome and this explains the success of both Richtmyer's and Meyer & Blewett's prescriptions.

More information - Email: gauthier@limeil.cea.fr

In this paper, a new simple formula [8] based on the impulsive model is proposed. It is first postulated and validated [9] against configurations taken in Refs. [3, 4, 7]. This formula has been heuristically derived by using the equation of evolution of a perturbation subjected to a Rayleigh-Taylor instability for incompressible fluids [9]. An expression of this new formula is

$$\frac{da}{dt} = \frac{1}{2} k \Delta u \left(A^+ a_0^+ + A^- a_0^- \right). \tag{3}$$

Specific limit cases lead Eq.(3) to either Richtmyer's or Meyer & Blewett's prescriptions.
In the next section, the formula (3) is validated on the reflected shock wave cases. In Section 3, the reflected rarefaction wave case is studied. In Section 4, we shall discuss the validity of our proposal and consequently the range of applicability of the impulsive model.

2. Case of a reflected shock wave

Formula (3) is now validated for the case of a reflected shock wave. Mikaelian [3] compares the growth rate obtained from the work of Fraley [6], hereafter noted FM, with classical Richtmyer's growth rate for several initial Atwood numbers A^- and various pairs of adiabatic exponents (γ_1, γ_2). The normalized growth rate is defined as $NGR = \dot{a}/(a_0^- \Delta u k)$, the shock strength ϵ as $\epsilon = 1 - P_0/P_3$ where P_0 is the initial pressure and P_3 the pressure behind the incident shock wave. The evolutions of NGR are computed versus ϵ. We present here one of the configurations of Ref. [3]: $(\gamma_1, \gamma_2) = (1.667, 1.667)$ and $A^- = (0.25, 0.5, 0.75, 0.95)$. Fig.1(a) presents FM's results (dashed lines) and Richtmyer's prescription (continous lines). For the same values of parameters, Fig.1(b) presents FM's results and those of Eq.(3). It appears clearly that, in

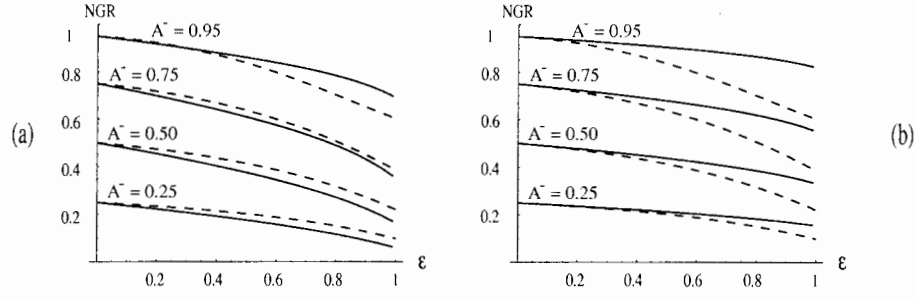

Figure 1. Part (a): Normalized Growth Rate (NGR) according to Richtmyer's prescription (continuous lines) and according to Fraley's analysis (dashed lines). Part (b): NGR according to formula (3) (continuous lines) and according to Fraley's analysis (dashed lined). A^-=0.25, 0.50, 0.75 and 0.95; γ_1=1.667 and γ_2=1.667.

the weak shock limit, all growth rates obtained from formula (3) are tangential to Mikaelian's curves. On the contrary, the NGR obtained from Richtmyer's prescription deviates from FM values even for very small ϵ. The relative errors defined as $E = \dot{a}_{Impulsive}/\dot{a}_{Theory} - 1$ for the two considered impulsive models can be computed versus ϵ. For ϵ smaller than 0.4, the relative error for Eq.(3) is less than 10% and is tangential to zero when ϵ decreases. This is not true for Richtmyer's prescription (1). These conclusions are still valid for other configurations of Ref. [3].
In Ref.[4], Yang *et al.*, hereafter noted YZS, compare the results of Richtmyer's impulsive model to those obtained with small amplitude theory. The relative error between the terminal growth

rate of the linear theory and the one of Richtmyer's impulsive model is plotted, for various combinations of gases, versus ϵ in Fig. 16 of Ref. [4] and reproduced in Fig. 2(a). The relative error for the model presented in this paper is plotted in Fig. 2(b). The conclusions previously

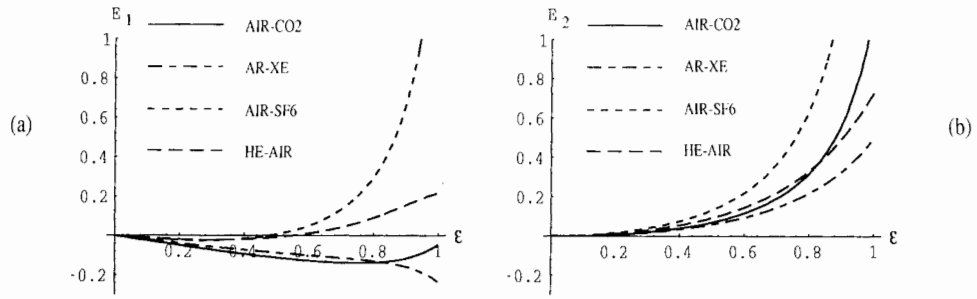

Figure 2. Part (a): The relative error $E_1 = \dot{a}_{Richtmyer}/\dot{a}_{YZS}$-1 versus the incident shock strength parameter ϵ for various combinations of gases. The parameters used are $\gamma_{He} = \gamma_{Ar} = \gamma_{Xe} = 1.667$, $\gamma_{Air} = 1.4$, $\gamma_{CO_2} = 1.3$, $\gamma_{SF_6} = 1.0935$, $\rho_{CO_2}/\rho_{Air} = 1.53$, $\rho_{Xe}/\rho_{Ar} = 3.29$, $\rho_{SF_6}/\rho_{Air} = 5.1$, $\rho_{Air}/\rho_{He} = 7.25$. Part (b): Same as in Part (a) for the relative error $E_2 = \dot{a}_{Eq.(3)}/\dot{a}_{YZS} - 1$. The slope at the origin of E_2 is clearly zero. This is not true for E_1.

drawn from Fig. 1 still hold in these cases. The results of the linear theory [4] and the impulsive model defined by Eq.(3) tend to each other as the incident shock strength decreases. In the weak incident shock limit, they are in better agreement than the linear theory and Richtmyer's impulsive model are.

To confirm this conclusion, as it was presented in the 45 test case Table I of Ref. [4], we have carried out a comparison of the predictions of the linear theory with those of impulsive models. Varying parameters are the adiabatic exponents γ_1 and γ_2, the incident shock strength ϵ and the preshocked density ratio ρ_2/ρ_1. For small ϵ, the NGR calculated with formula (3) are closer to the linear theory than Richtmyer's results. But, as one could expect from an incompressible model, the discrepancy between formula (3) and the linear theory increases with the shock strength parameter ϵ and the difference between the adiabatic exponents.

3. Case of a reflected rarefaction wave

Same kind of comparisons between the linear theory solved in Ref. [4] and the impulsive model can be carried out for the case of a reflected rarefaction wave. Let us remark that, in Ref. [4], the authors use MB's prescription (2) for the case of a reflected rarefaction wave. We emphasize that in this paper the same formula (3) is used in both cases (ligth/heavy and heavy/light). In Fig. 3(a), the relative error between the terminal growth rates of the impulsive model with MB's prescription and the linear theory is plotted for various combinaisons of gases. The relative error for the formula (3) is presented in Fig. 3(b). For the considered parameter values, the errors remain smaller than 10% for values of ϵ as large as 0.5.

We also carried out the same comparisons about growth rates as in Table II of Ref. [4]. Formula (3) gives again good results in the weak shock limit, for γ_1/γ_2 not too different from 1.

This formula can also be tested in configurations defined by Velikovich [7] who uses failure of both Richtmyer's and MB's prescriptions to deny the relevance of the impulsive model. Parameter values are: $\gamma_1 = 1.8$, $\gamma_2 = 1.45$, $\epsilon = 0.213$ and the preshocked Atwood number varies from -0.02 to 0. As shown in Fig. 4, formula (3) gives NGR almost equal to the one obtained

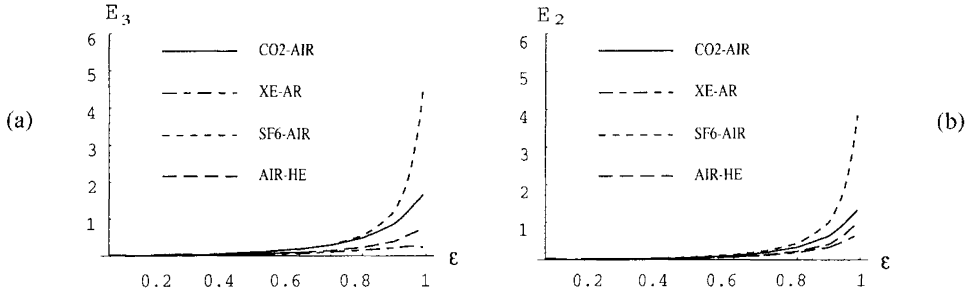

Figure 3. Part (a): The relative error $E_3 = \dot{a}_{MB}/\dot{a}_{YZS}$-1 between the terminal growth rate of the linear theory [4] and the one of the prescription of Meyer & Blewett versus ϵ for the same combinations of gases as in Fig.2. Part (b): Same as in Part (a) for the relative error $E_2 = \dot{a}_{Eq.(3)}/\dot{a}_{YZS}$-1.

from Velikovich's analytic theory whereas Richtmyer and MB's prescriptions are far from the theoretical result. For example, for A^- equal to 0, the relative error for the NGR is about 9%

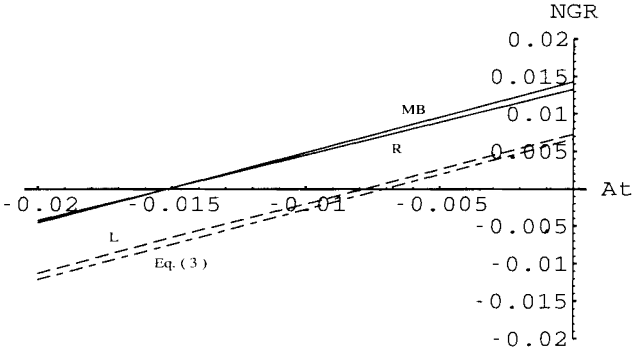

Figure 4. Normalized Growth Rates given by Velikovich's linear theory (curve L), the impulsive model with the prescription of Richtmyer (curve R), the prescription of Meyer & Blewett (curve MB) and the formula (3) (curve Eq.(3)) versus initial Atwood number. $\gamma_1 = 1.8$, $\gamma_2 = 1.45$, ϵ=0.213.

for our model whereas it is about 97% for MB's prescription.

4. Concluding remarks

From the results presented in Sections 2 and 3, it appears that the maximum relative errors between the various theoretical results [4, 6, 7] and Eq. (3) is about 10% for ϵ-parameter values smaller than 0.4 and ratios of adiabatic exponents $\gamma_{max}/\gamma_{min}$ smaller than 1.5, where γ_{max} (resp. γ_{min}) is the maximum (resp. minimum) of the two adiabatic exponents. No counter-example, for both reflected shock and reflected rarefaction cases, has been found in the range of validity. On the contrary, Richtmyer's prescription is only used for reflected shock wave case whereas MB's prescription has been introduced to handle reflected rarefaction wave case, and nobody was able to establish a reliable range of validity for these two prescriptions: for example, Richtmyer applied his incompressible prescription to a very compressible configuration ($\epsilon = 1$) with fortunate good results [1]. But, on the other hand, for quasi-incompressible configurations

Richtmyer's prescription can fail. For example, in the case of a reflected shock wave, we consider two gases with $\gamma_1 = 1.667$ and $\gamma_2 = 1.9$ ($\gamma_{max}/\gamma_{min} = 1.14$), molar masses $\mathcal{M}_1 = 40\,g/mol$, $\mathcal{M}_2 = 44\,g/mol$ and $\epsilon = 0.4$. Eq.(3) produces a quite good result: the relative error with respect to Fraley's theory is less than 2%. However, Richtmyer's prescription is inaccurate: the relative error is about 40%. For the reflected rarefaction case, we borrowed from Velikovich [7] the following configuration: $A^- = -0.02$, $\epsilon = 0.213$, $\gamma_1 = 1.8$ and $\gamma_2 = 1.45$. Here again, even in these quasi-incompressible conditions ($\epsilon = 0.213$ and $\gamma_1/\gamma_2 = 1.24$) MB's prescription fails to give a reasonable value. The relative error is about 60%. However, Eq.(3) provides a rather good result with a 7% error.

The new formula Eq.(3) has been heuristically established from the Rayleigh-Taylor growth rate. The only compressibility effect that we consider are variations of both the perturbation amplitude and the Atwood number during the interaction. All previous comparisons have shown that this formula produces a good estimate of the growth rate of the Richtmyer-Meshkov instability provided it is used within its range of validity, i.e., the shock strength parameter $\epsilon \leq 0.4$ and the ratio of the adiabatic exponents $\gamma_{max}/\gamma_{min} \leq 1.5$. It allows us to predict the growth rate in both heavy-light, light-heavy configurations. In this respect, systematic condemnation of the impulsive model appears to be unjustifiable.

References

[1] Richtmyer RD, Comm. Pure Appl. Math., 13, 297, (1960).
[2] Meshkov EE, Izv. Acad. Sci. USSR Fluid Dyn., 4, 101, (1969).
[3] Mikaelian KO, Phys. Fluids, 6, 356, (1994).
[4] Yang Y, Zhang Q and Sharp DH, Phys. Fluids, 6, 1856, (1994).
[5] Meyer KA and Blewett PJ, Phys. Fluids, 15, 753, (1972).
[6] Fraley G, Phys. Fluids, 29, 376, (1986).
[7] Velikovich AL, Phys. Fluids, 8, 1666, (1996).
[8] Mügler C, Vandenboomgaerde M and Gauthier S, Proc. of the Fifth International Workshop on the Physics of Compressible Turbulent Mixing, edited by R. Young, J. Glimm & B. Boston, Stony Brook, NY, (1996).
[9] Vandenboomgaerde M, Mügler C and Gauthier S, On the impulsive model for the Richtmyer-Meshkov instability, submitted to publication, (1997).

Growth Rate and Transition to Turbulence of a Gas Curtain

P. Vorobieff, P. Rightley and R. Benjamin
Los Alamos National Laboratory, group DX-3 Hydrodynamics
Los Alamos, NM 87545, USA

Abstract: We conduct shock-tube experiments to investigate Richtmyer-Meshkov (RM) instability of a narrow curtain of heavy gas (SF_6) embedded in lighter gas (air). Initial perturbations of the curtain can be varied, producing different flow patterns in the subsequent evolution of the curtain. Multiple-exposure flow visualization provides images of the growth of the instability and its transition to turbulence, making it possible to extract quantitative information such as the width of the perturbed curtain. We demonstrate that the width of the curtain with initial perturbation primarily on the downstream interface is non-monotonic. As the initial perturbation undergoes phase inversion, the width of the curtain actually decreases before beginning to grow as the RM instability evolves.

1. Introduction

Richtmyer-Meshkov instability [1, 2] is the impulsively-driven analog of the well-known Rayleigh-Taylor instability. Understanding and quantification of the evolution of RM instability is important in many fields ranging from astrophysics [3, 4] to high-speed combustion [5] and inertial confinement fusion [6]. There also has been a significant interest in numerical simulations of RM instability [7]. The present study provides both the qualitative information on the flow morphology during the instability growth and the measurements of the thickness of the mixing layer associated with the instability. The latter also serve as a benchmark for CFD codes.

Earlier experimental studies [8, 9, 10] revealed the existence of three basic flow patterns in the evolution of a shock-accelerated heavy gas curtain embedded in a lighter gas. Both the upstream and the downstream interfaces of the curtain are Richtmyer-Meshkov unstable. At the upstream interface the shock front moves across a positive density gradient, and an initial sinusoidal perturbation of this interface begins to grow immediately after shock compression, producing the flow pattern known as the upstream mushrooms. If similar perturbations are initially present at the downstream interface, where the shock front traverses a negative density gradient, the perturbations must first reverse phase and then grow, evolving into the pattern known as the downstream mushrooms. If both sides of the curtain are perturbed and its initial cross-section is approximately varicose, the downstream perturbation reverses phase while the phase of the upstream perturbation does not reverse, leading to formation of the sinuous flow pattern. Earlier studies did not possess the temporal resolution to detect the narrowing of the gas curtain corresponding to phase reversal of the downstream interface. Initially only one or two successive exposures per one-millisecond event were captured, and our more recent investigation [11] provided 8–10 images per event. The present study increases the temporal resolution to 30–32 images per event. With this resolution, it becomes possible to observe non-monotonic growth of the mixing layer for the case of the gas curtain with the initially perturbed downstream side.

More information - Email: kalmoth@lanl.gov; WWW: http://cnls-www.lanl.gov/~azathoth/dx3.html

2. Experimental setup and techniques

Our experiments employed a 5.5 m horizontal shock tube with internal dimensions of 75 mm square producing a Mach 1.2 planar shock wave. The driver section and the driven section (which is kept at ambient pressure) are separated by a membrane of three thin sheets of polypropylene which are punctured by a solenoid-actuated spike. Two flush-mounted pressure transducers mounted near the downstream end of the driven section monitored shock quality and speed. One final transducer just upstream of the test section triggers the diagnostics.

A curtain of heavy gas (sulfur hexafluoride SF_6, nominal density at ambient pressure about 5 times that of air) flows vertically through the test section. The curtain enters the test section through a contoured nozzle. Microscopic water/glycol droplets are produced with a modified theatrical fog generator and mixed with SF_6. The mean size of the droplets is estimated to be 0.5 μm; the cloud of droplets does not contribute any significant mass loading. After flowing vertically downward through the test section, the gas curtain is removed from the shock tube by a vacuum system. The contoured nozzle through which the gas curtain enters the shock tube provides the desired initial conditions. The vertical motion of the gas curtain does not provide a significant perturbation to the motion of the flow on the timescales of interest. Also, the slow temporal evolution of the gas curtain provides a rich variety of initial conditions, but also eliminates shot-to-shot reproducibility. This requires that a s ignificant amount of data be obtained for each event if the time evolution of the flow is to be characterized. The experimental apparatus and diagnostics are discussed in greater detail elsewhere [11].

Laser-sheet flow visualization employed a 1 W Ar+ (Lexel Model 94) laser. We recorded the evolution of the flow in the plane of the laser sheet (parallel to the direction of shock propagation and perpendicular to the gas curtain) with a Hadland Photonics 468 video camera. This camera is composed of eight individual MCP-intensified CCD cameras arranged to use a single optical axis. The gas curtain is thin and its mean downstream motion after shock acceleration makes it possible to acquire up to four exposures on each CCD by pulsing the optical intensifier. Thus the total number of successive exposures of the curtain that can be acquired in one experiment is 32. Each of the CCD cameras internal to the 468 is independently programmable, and the camera as a whole is triggered by the third pressure transducer just upstream of the test section.

3. Observations

Figure 1 shows the typical evolutionary sequence of the downstream mushroom flow pattern. The leftmost exposure (1 in the figure) shows the initial condition with the prevailing 6-mm wavelength perturbation on the downstream side. The following exposures are acquired starting with the beginning of the interaction of the shock wave with the curtain. Time intervals between exposures 2 to 14 are 20 μs, and 40 μs for later exposures. The duration of each exposure is 10 μs. The initial compression and phase inversion of the downstream interface lead to noticeable thinning of the curtain in exposures 2–4 and flattening of the downstream boundary. Subsequent exposures show the growth of the perturbation and formation of mushroom-like shapes formed by the curtain material rolling up around the vortices deposited by the interaction of the shock with the curtain [11] (exposures 12–15). Until exposure 15, there is little or no evidence of interaction between the individual wavelengths of the curtain; however, later mode-coupling becomes evident, as well as emergence of small-scale spatial structures. Figure 2 shows the evolution of upstream mushrooms from initial conditions with upstream-side perturbation prevailing. In this image sequence, there were two wavelengths initially present, 6

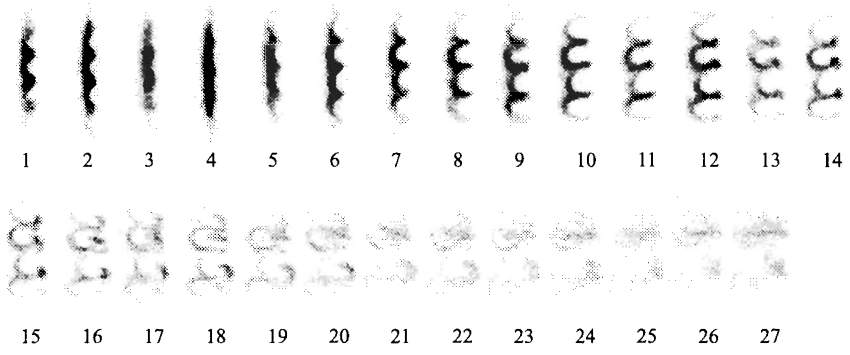

Figure 1. Evolution of downstream mushroom flow pattern. One wavelength (6 mm) was present in initial perturbation.

mm and 12 mm. Time intervals between exposures 1–13 are 20 μs, and 40 μs for subsequent exposures. Unlike the downstream mushrooms in Figure 1, upstream mushrooms begin growing immediately after the shock compresses the curtain (exposure 2), and smaller spatial structures indicative of transition to turbulence are more prominent than in the previous data set, likely due to the presence of two wavelengths in the initial conditions that creates a broader spectrum of scales.

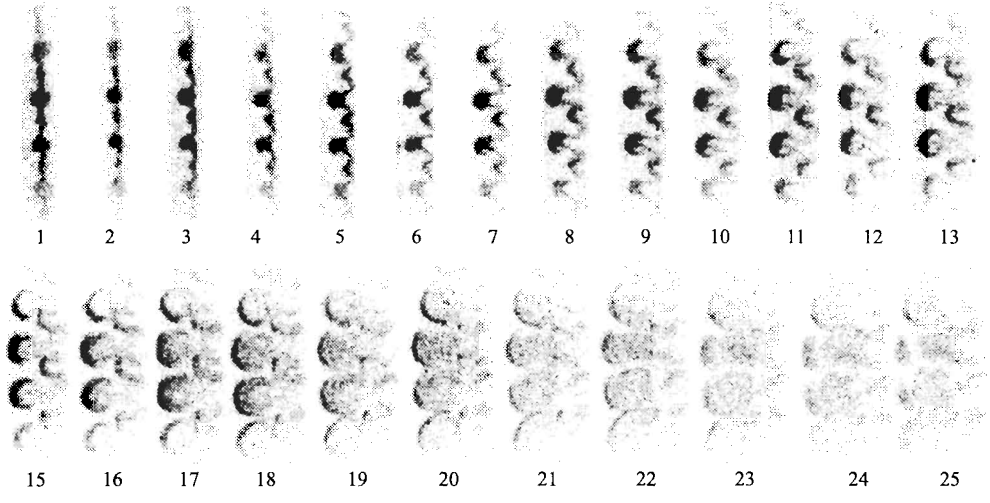

Figure 2. Evolution of upstream mushroom flow pattern with two wavelengths (6 and 12 mm) present in initial perturbation.

4. Analysis

The image sequence in Figure 1 shows that at the early stages of the evolution of the downstream mushroom flow pattern the width of the gas curtain decreases. In Figure 3, time history of

the widths of the individual wavelengths of the curtain is plotted for this image sequence. The picture in the bottom right corner of the graph shows the image of the gas curtain with a schematic depicting how the width per wavelength is measured. The measurement procedure is described in detail elsewhere [11]. Widths of all three wavelengths measured have a local minimum at the time approximately 40 μs after the shock hits the curtain.

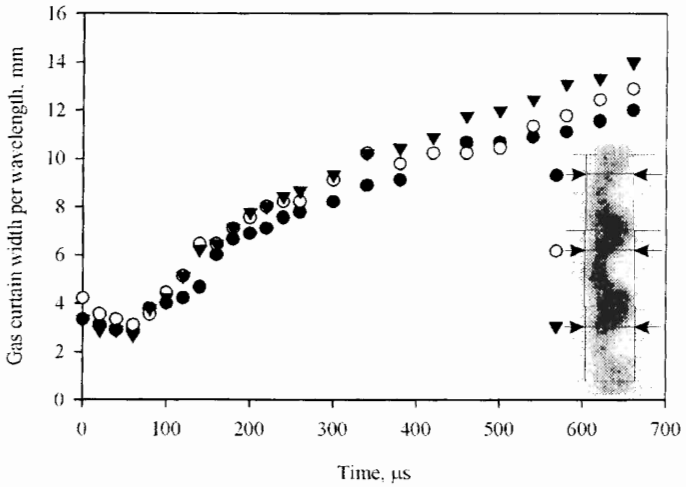

Figure 3. Width of the perturbed gas curtain per wavelength vs. time, downstream mushrooms. Schematic shows measurement of curtain width for individual wavelengths.

Some previous studies [10, 11] used a simple model that approximates vorticity deposited by the shock interaction with the curtain as an infinite row of point vortices and assumes initial symmetry of the layer and vorticity distribution. This model is clearly not adequate for the description of the evolution of downstream mushrooms, because it predicts monotonic growth. However, qualitatively the graphs closely resemble those produced with a simplified vortex-blob numerical simulation that neglects density gradients or compressibility but uses finite Gaussian vortex cores and takes into account the asymmetric initial conditions and resulting asymmetry in the deposition of vorticity [11].

Another interesting feature of the graph is that at times earlier than 400 μs perturbation in the first wavelength (•) grows faster than that in the second wavelength (○), while at later times the amplitude of the second wavelength exceeds that of the first wavelength. This may be the effect of wavelength interaction and mode coupling.

5. Conclusion

With the recent refinements of the gas-curtain experimental technique, now it is possible to acquire more than thirty images of the evolution of the gas curtain during and after the shock interaction. The temporal resolution of 20 μs between subsequent exposures is sufficient to resolve the phase inversion on the downstream interface of the curtain resulting, in the case of the downstream mushroom flow morphology, in delay in the growth of the perturbations in the curtain. There is also more evidence of both mode-coupling and emergence of smaller spatial scales at later stages of evolution, eventually leading to turbulence.

Acknowledgement. This work is supported by DOE contract N° W–7405–ENG–36. One of the authors is partially supported by the Center for Nonlinear Studies (CNLS) at Los Alamos National Laboratory.

References

[1] Richtmyer RD, Taylor instability in shock acceleration of compressible fluids, Commun. Pure Appl. Maths., 23, 297-319, (1960).

[2] Meshkov EE, Instability of a shock wave accelerated interface between two gases, NASA TT F-13, 074, (1970).

[3] Burrows A, Hayes J and Fryxell BA, On the nature of core-collapse supernova explosions, Astrophys. J., 450, 830, (1995).

[4] Stone JM, Xu J and Mundy LG, Formation of "bullets" by hydrodynamical instabilities in stellar outflows, Nature (London), 377, 315-317, (1995).

[5] Markstein GH, A shock tube study of flame front-pressure wave interaction, 6th International Symposium on Combustion, Reinhold, 387-398, (1957).

[6] Sunahara A, Takeuchi H, Takabe H, and Mima K, Effects of multiple shock and thermal conduction on mixing layer evolution in a stagnating high-gain inertial confinement fusion TA, Jap. Journ. App. Phys., Part 1, 35, 6265-6272, (1996).

[7] Baltrusaitis RM, Gittings ML, Weaver RP, Benjamin RF and Budzinski JM, Simulation of shock-generated instabilities, Phys. Fluids, 8, 2471-2483, (1996).

[8] Jacobs JW, Klein DL, Jenkins DG and Benjamin RF, Instability growth patterns of a shock-accelerated thin fluid layer, Phys. Rev. Lett., 70, 583-586, (1993).

[9] Budzinski JM, Benjamin RF and Jacobs JW, Influence of initial conditions on the flow patterns of a shock-accelerated thin fluid layer, Phys. Fluids, 6, 3510-3512, (1994).

[10] Jacobs JW, Jenkins DG, Klein DL and Benjamin RF, Nonlinear growth of the shock-accelerated instability of a thin fluid layer, J. Fluid Mech., 295, 23-42, (1995).

[11] Rightley PM, Vorobieff P, and Benjamin RF, Evolution of a shock-accelerated thin fluid layer, Phys. Fluids, 9, 1770-1782, (1997).

Rayleigh-Taylor Instability Growth Experiments in a Cylindrically Convergent Geometry

S.T. Weir, E.A. Chandler and B.T. Goodwin
Lawrence Livermore National Laboratory
University of California, P.O. Box 808, Livermore, CA 94550, USA

Abstract: Convergent geometry Rayleigh-Taylor experiments have been performed with a 122-point detonation initiation system on cylinders having sinusoidal perturbations on the outer surface ranging from mode-6 to mode-36. Experiments were performed with various perturbation mode numbers, perturbation amplitudes, and ring accelerations. Feedthrough perturbation growth on the inner surface was observed in several experiments, and in one experiment the feedthrough perturbation underwent a phase inversion. These experimental results were found to be in good agreement with linear, small-amplitude analysis of feedthrough growth in an incompressible, cylindrically convergent geometry.

1. Introduction

The gelatin cylinder technique [1] has many features which make it a very attractive method for studying Rayleigh-Taylor instabilities. Precise control can be exercised over the gelatin strength, the driving pressure, and the initial perturbations. In addition, by using high-speed framing cameras, it is possible to obtain high-resolution images of the entire implosion history and to examine in detail all stages of the instability growth and cylinder collapse.

A number of interesting topics can be studied with this technique, including the rate of turbulent mix development in a convergent geometry, the mode-mode coupling of RT unstable modes in the weakly non-linear regime, and the feedthrough growth of perturbations on the inner surface of the cylinder. This last topic is of special interest to members of the intertial confinement fusion (ICF) community, since the feedthrough growth of instabilities is an important ICF capsule design concern [2]. In our most recent experiments, we have chosen to focus on the observation and analysis of feedthrough growth in a cylindrically convergent geometry.

2. Experimental

In the previous set of experiments, we utilized up to 12 exploding bridge wires (EBW_s) to initiate the detonation of the oxygen-acetylene driving gas. However, with this small number of initiation points, detonation front interactions between adjacent EBW_s were significant, and this seeded large localized perturbations on the cylinder. In our latest series of experiments, we eliminated these large pressure-induced perturbations by using a 122-point EBW system. With this new initiation system, we are able to systematically study the RT and feedthrough growth rates for various initial perturbation wavelengths and amplitudes.

Our apparatus is essentially the same as that used in our previous experiments [3], except for the introduction of the 122-point EBW system. The gelatin rings were formed using water with a 6% concentration of gelatin (Kind and Knox Company, 225 Bloom gelatin). The rings were fabricated by an in-place casting technique. Judging by the surface finish of the Plexiglas

More information - Email: Samuel.Weir@quickmail.llnl.gov

parts used to cast the gelatin, we estimate that the surface roughness of the gelatin ring is <12 μm, which is much less than typical imposed perturbation amplitudes of about 1 mm. Gelation was performed at a temperature of 7 °C for at least 12 hours.

Optical diagnostics included two high-speed framing cameras (Cordin, Model 6 and Model 121). Illumination was provided by back-lighting the gelatin ring with a high-intensity xenon flashbulb, and control electronics were programmed so that the high-speed cameras were properly synchronized to the xenon flash and the firing of the EBW$_s$.

3. Experiments performed

In our experiments we fabricated small sinusoidal perturbations in the azimuthal direction in order to seed Rayleigh-Taylor instability growth. These sinusoidal perturbations are characterized by two parameters: the initial amplitude A and the mode number m_θ (Figure 1). In addition, we varied the ring thickness ΔR, which has the effect of varying the acceleration history as well as varying the amplitude of the perturbations which feed through to the inner surface of the ring. No perturbations were fabricated in the axial (z) direction on either the outer or inner interfaces. A summary of the experiments performed is listed in Table I. We

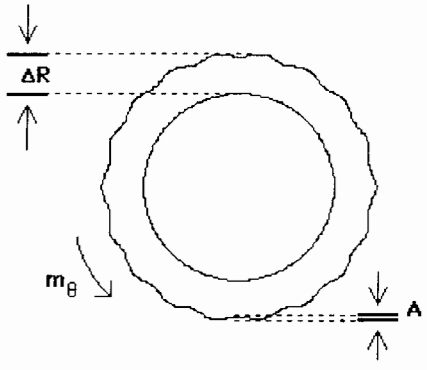

Figure 1. Gelatin Ring Geometry.

analyzed the growth of the fundamental mode and of the first four harmonics for both the Rayleigh-Taylor growth on the outer surface of each ring and, for those experiments which showed measureable feedthrough growth, the perturbation growth on the inner surface. The growth rates were determined by digitizing the framing image records, tracing the gas-gelatin interface boundaries for the inner and outer ring surfaces, and then Fourier analyzing these boundaries.

In a planar, thin-wall geometry, the amplitude of a feedthrough perturbation is related to the amplitude of the associated RT perturbation by an attenuation factor of exp(-kΔR). In our experiments, kΔR_o ranges from 1.1 to 9.8. We observe measurable feedthrough amplitudes only in the three experiments where kΔR_o is less than 1.7 (GELB-4, GELB-7, and GELB-11). In the other experiments, the inner surfaces of the rings showed no feedthrough perturbations to within the resolution of our system ($\approx$0.1 mm).

A mode number 6 experiment (GELB-11) is shown in Figure 2. In this experiment the Rayleigh-Taylor instability growth on the outer surface of the ring is clearly seen to feed

Experiment	Mode Number	Initial Amplitude (mm)	Initial ΔR (cm)
GELB-1	36	0.5	0.5
GELB-4	18	0.5	0.5
GELB-5	36	0.5	1.0
GELB-7	6	1.0	1.0
GELB-10	36	1.0	1.5
GELB-11	6	1.0	1.5
GELB-14	18	0.5	1.0
GELB-15	12	1.0	1.5
GELB-16	36	0.2	1.0
GELB-17	18	0.5	1.5
GELB-18	36	0.1	1.0

Table 1. Summary of Gelatin Ring Experiments.

through to the inner surface, imprinting a mode number 6 perturbation. At 540 μsec, the feedthrough perturbation is in-phase with the outer perturbation, i.e., the peaks of the inner feedthrough perturbation correspond to peaks in the outer perturbation. The development of the feedthrough perturbation is interesting. At a later time of 675 μsec, the feedthrough perturbation has reduced to nearly zero amplitude. Finally, at 729 μsec, the feedthrough perturbation is seen to be present again, but with an opposite phase.

Feedthrough growth was also observed in two other experiments (GELB-4, GELB-7), but in these experiments the feedthrough growth remained in-phase with the RT perturbation within the time period of observation.

4. Analysis

For the long wavelength mode-6 experiments, both the RT and the feedthrough perturbations remain in the linear growth stage throughout the experiment, and so it is possible to apply small amplitude analysis to compute both the RT and feedthrough growth rates. First, we determined the acceleration history of the cylinder using Lagrangian analysis and taking into account the potential energies due to the expanding gas outside the cylinder, the gas inside the cylinder, and the elastic energy of the cylinder itself. Gamma-law equations-of-state were used to describe the detonation product gases outside the cylinder and the air inside the cylinder. Good agreement between experimental and calculated ring motions was obtained for an initial pressure of P_o=16.5 atm. Figure 3 shows the normalized accelerations at the outer cylinder surface plotted versus the instantaneous outer surface radius. Note that the accelerations decrease very rapidly as the cylinder collapses due to the convergent geometry of the ring. In other words, there is a significant "funneling" effect which affects the acceleration even at very early times. This is an important fact to note when analyzing convergent ring experiments for instability and turbulent mix growth. Simulations based on a P_o=16.5 atm were also performed for rings with initial radial thicknesses of 0.5 cm and 1.0 cm. These simulations were also found to be in excellent agreement with experimental data. Initial t=0 accelerations were 8.85×10^6 cm/sec^2 for a ΔR=1.5 cm ring, 1.40×10^7 cm/sec^2 for a 1.0 cm ring, and 2.96×10^7 cm/sec^2 for a 0.5 cm ring.

We also derived the linear-stage perturbation evolution equations for an incompressible

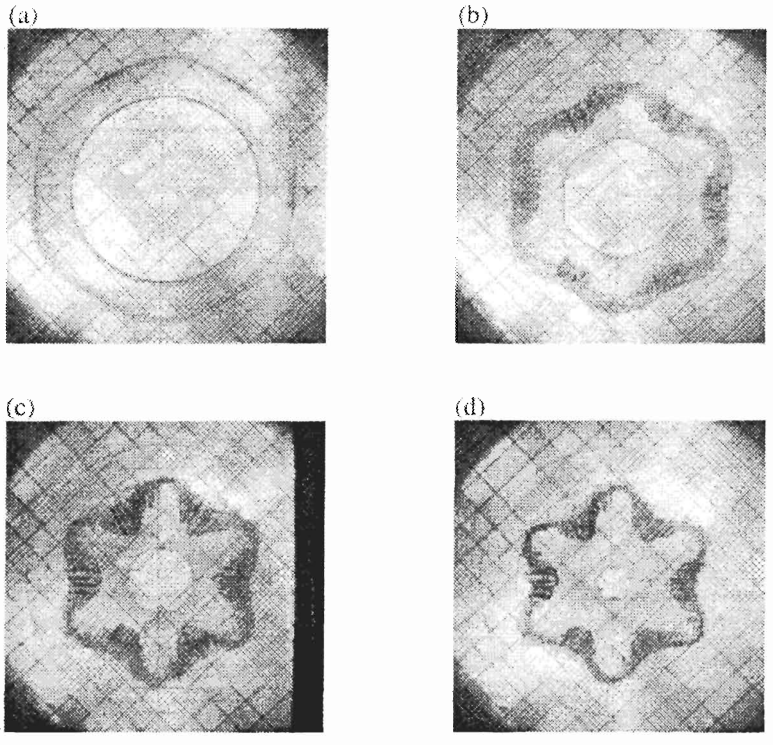

Figure 2. Framing Images from the GELB-11 Experiment (perturbation amplitude = 1 mm, m_θ= 6, and ΔR=1.5 cm). (a) 90 μsec. (b) 540 μsec. (c) 675 μsec. (d) 729 μsec.

cylinder undergoing a radial implosion. This cylindrical geometry derivation proceeds along essentially the same path used by Plesset [4] and Mikaelian [5] to study spherically imploding shells. The small amplitude analysis resulted in two, coupled, 2^{nd} order differential equations in a(t) and b(t), the amplitudes of the outer and inner perturbations, respectively. The equations can be presented in the form

$$G_{11}(t)\cdot a''(t) + G_{12}(t)\cdot a'(t) + G_{13}(t)\cdot a(t) + G_{14}(t)\cdot b''(t) + G_{15}(t)\cdot b'(t) + G_{16}(t)\cdot b(t) = 0 \quad (1)$$

$$G_{21}(t)\cdot a''(t) + G_{22}(t)\cdot a'(t) + G_{23}(t)\cdot a(t) + G_{24}(t)\cdot b''(t) + G_{25}(t)\cdot b'(t) + G_{26}(t)\cdot b(t) = 0 \quad (2)$$

where the G_{ij} are functions of the outer cylinder radius r_o(t) and the mode number m_θ. By numerically solving these coupled differential equations, we were able to accurately predict the growth of both the outer perturbations as well as the inner, feedthrough perturbations for our mode-6 experiments. In particular, these equations predict the development of the feedthrough phase inversion at about the time actually observed in the GELB-11 experiment [6].

5. Conclusion

The latest set of experiments shows that we can eliminate the effect of shock perturbations on the gelatin cylinder with a 122-point initiation system. Furthermore, by using an in-place

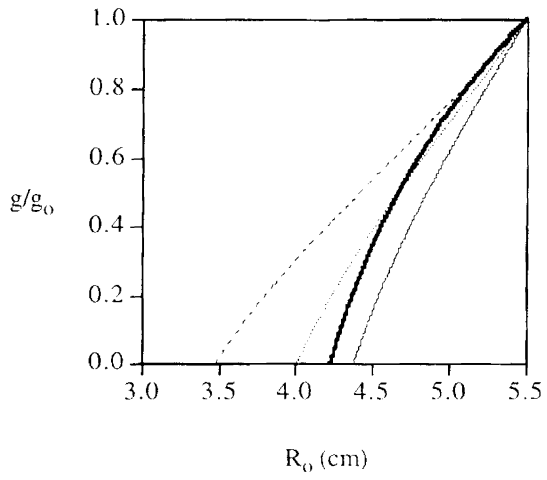

Figure 3. Normalized accelerations of the outer cylinder surface vs. outer radius. Thin solid line: 1.5 cm thick ring. Thin dotted line: 1.0 cm thick ring. Thin dashed line: 0.5 cm thick ring. Thick solid line: 1.5 cm thick ring with outer gas pressure fixed at 15.5 atm and inner gas pressure fixed at 0 atm.

casting technique, we can fabricate precise initial cylinder surface perturbations. Recent experiments have focused on studying feedthrough growth, and interesting behavior such as a feedthrough phase inversion has been observed. Although this phase inversion behavior cannot be explained by the standard, first-order Exp(-kΔR) attenuation factor, we can accurately predict this and other feedthrough behavior using linear, small amplitude analysis. Future experiments will focus on the issues of mode-mode coupling and turbulent mix development.

Acknowledgement. We would like to acknowledge the efforts and contributions of the experimental team of D. Anderson, B. Gray, D. Burns, A. Hernandez, and K. Moua. Also, we thank K. Mikaelian, B. Remington, and P. Urtiew for valuable discussions. This work was performed under the auspices of the U.S. Department of Energy under Contract No. W-7405-ENG-48.

References

[1] Meshkov EE, Nevmershitsky NV, Rogachev VG and Zhidov IG, Proc. 4^{th} Int. Workshop on the Phys. of Comp. Turb. Mixing, Cambridge, England, 578, (1993).

[2] Dittrich TR, Hammel BA, Keane CJ, McEachern R, Turner RE, Haan SW and Suter LJ, Diagnosis of Pusher-Fuel Mix in Indirectly Driven Nova Implosions, Phys. Rev. Lett, 73, 2324, (1994).

[3] Goodwin B and Weir S, Proc. 5^{th} Int. Workshop on the Phys. of Comp. Turb. Mixing, Stony Brook, NY, 185, (1995).

[4] Plesset MS, On the Stability of Fluid Flows with Spherical Symmetry J. Appl. Phys., 25, 96, (1954).

[5] Mikaelian KO, Rayleigh-Taylor and Richtmyer-Meshkov Instabilities and Mixing in Stratified Spherical Shells, Phys. Rev. A, 42, 3400, (1990).

[6] Weir ST, Chandler EA and Goodwin B, to be published.

Numerical Simulation of Turbulent Mixing Zone Evolution at the Gas-Liquid Interface

Y.V. Yanilkin, V.I. Tarasov, E.E. Meshkov, N.V. Nevmergitsky, E.A. Sotskov and V.P. Statsenko
Russian Federal Nuclear Centre - Institute of Experimental Physics
Prospect Mira 37, 607190, Sarov, Nizhny Novgorod Region, Russia

Abstract: This paper presents turbulent mixing (*TM*) at the plane gas-liquid interface, and also at the convergent and divergent interfaces within cylindrical flows. The paper adduces the results of 2D and 3D direct numerical simulation (with gas-dynamic approximation) of experiments, performed by jelly method. Two-dimensional calculations were performed by *EGAK* complex programs, and three-dimensional calculations - by Lagrangian-Eulerian gas-dynamic method of TREK complex. The results of calculations are compared with the data of phenomenology theory and with experimental data. The calculation data satisfactorily agree with the theory and with experimental data for *R-t* charts of stable interfaces and of turbulent mixing zone (*TMZ*) width.

1. Introduction

Investigations of *TM* evolution at the interface of two substances grow essentially for the last time in connection with increasing of experimental, and especially calculation opportunities. Nevertheless, this problem is far removed from termination, in part, dynamics of *TMZ* evolution for accelerated non-plane interfaces was not studied practically. Difficulties of experimental investigations of such flows are connected both with the problem of initial setting of these interfaces, and also with opportunities of implementation of accelerated motion of these interfaces. In terms of numerical simulation the difficulties are those, that these problems, as a rule, are three-dimensional and need the great memory and computer performance. The jelly method [1, 2] is better developed now for experimental studying of described process. It gives the opportunity to set the complicated forms of gas-liquid interfaces. This paper presents the results of numerical studying of *TMZ* evolution both at the plane interface and at the convergent and divergent interfaces within cylindrical geometry of experiments, described in [3].

2. Experiment setup

Acceleration of the plane jelly layers by compressed gas was performed as follows: two compartments on each side of the jelly, located in hermetic acceleration channel, filled by compressed gas (helium) with equal pressure. The initial gas pressure P=17 atm. Then fast dehermetization of one compartment was performed by destruction of diaphragm on one side of the channel: gas flows from beneath the jelly layer to atmospheric medium, and the layer accelerated vertically down by the upper gas pressure. In the acceleration process the downer interface of the layer was stable, and the upper one - unstable. Compressing of cylindrical jelly shells was performed by compressed gas in the special experimental environment. Inner and outer (relative to the shell) volumes of experimental environment were filled by gas with equal pressure. Then gas was quickly trampled down into atmospheric medium, and the shell converges to the center

More information - Email: otd03_2305@spd.vniief.ru

rapidly by the gas pressure in the outer volume. In the shell convergence process its outer surface was unstable. Shell geometry: outer radius $R_H \cong 70$ mm; inner radius $r \cong 58$ mm; shell height b=16 mm; initial pressure of compressed gas (helium) $P \cong 18$ atm. Divergence of cylindrical shell was performed within the same experimental environment, but by the action of the explosion products of gas explosive stechiometric acetylene-oxygen mixture. (This mixture filled the inner compartment of the shell and was blasted in one point in a center.) The shell scattered into the atmospheric medium, its inner surface was unstable. Shell geometry: $R_H \cong$ 39 mm; $r \cong 18$ mm; b=30 mm. The shells were made from the jellies of the water solution of gelatin with concentration C=3.6%. The initial periodical 3D perturbations with amplitude $a_o \cong 0.15$ mm and wave length $\lambda_o \cong 0.5$ mm were set at the shell surfaces known to be unstable. The arrangement of experiments was presented in details in [3].

3. Calculation setup

Numerical simulation of experiments described was performed in 2D and 3D approximation by the methods of *EGAK* program complex [4] and *TREK* program complex [5]. We would not enlarge on the features of the methods, implemented in the complex, because they are described in details in [6, 7]. Notice only, that calculations were performed in Eulerian and Lagrangian-Eulerian settings in gas-dynamic and elastic-plastic approximations. The calculations with using $k-\varepsilon$ [8] and multi-parameter [9] *TM* models were also performed, but the results obtained are not satisfactory and demand further investigations. The initial geometry for calculations corresponded to above presented sizes of experimental environments. The state equation for jelly was got in Mi-Grunaisen form with the following parameters: density $\rho_o = 1$ g/sm^3, sound velocity $c_o = 1.48$ km/s, compression index $n = 7.15$, Grunaisen coefficient $\Gamma = 0.105$. Air ($\rho_o =$ 0.0013 g/sm^3), and explosion products of inflammable explosive mixture (*IEM*) were described by perfect gas state equation with $\gamma = 1.4$ and γ =1.136, correspondingly. Detonation of *IEM* respected to be perfect with detonation velocity $D = 3.09$ km/s and calorie content $Q = 12.3 \cdot 10^{10}$ erg/g. For all 2D and 3D calculations at the unstable jelly interface there were set randomly distributed perturbations with the form of the interface and with amplitude equal to 1 mm. Border conditions: pressure 1 atm was supported on the border, corresponding to the damaged diaphragm in the experiments, on the other borders there was set non-flow condition (rigid wall). Before discussing the results, notice some circumstances, that prevent from identical 2D and 3D simulation of the flows presented. First of all notice, that we can not fully simulate the border conditions on the borders, where the pressure is trampled down. It takes place due to both 3D flow character in this region (in 2D calculations) and using of motionless calculation grid (in all calculations). In principle, we can take the fully identical setting of calculations in 3D calculations, however, computer opportunities don't permit to do so. The second difficulty is connected with the fact, that in *TM* dynamics there are significant differences in an extent of flow chaotization for different density relations. In the experiments considered perturbations for the extended period have regular character in agreement with given 3D initial perturbations and without noticeable flow chaotization (see [3]). Unfortunately, there was observed only 2D flow pattern in these experiments, that is 2D sample of 3D perturbations. Moreover in the experiment the flow pattern is get from the pavement of cylinder, but in 2D calculations perturbations are axis-symmetrical. The third circumstance connects with the fact, that in experiments jelly has some viscosity and firmness, that can influence on the results. The fourth circumstance connects with the fact, that precise state equation for *GEM* is unknown, and *GEM* can have different mixture content for different experiments. And finally, these problems needs for high precision of mathematician methods for describing of mixed cells, containing two

or more substances, because of the great difference in densities of substances and in their state equations. This circumstance also prevents from using of semi-empirical *TM* models. Studying of all above mentioned items needs in performing the great number of calculations and falls outside the scope of this paper. We adduce below the results of some calculations (see Table 1). In these calculations we used calculation grid with cell size h=1 mm for 2D calculations and $h = 2$ mm for 3D calculations. Calculation 6 was repeated also on the grid with $h = 1.5$ mm and $h = 1$ mm.

calculation number	geometry	flow type
1	2D(axis-symmetrical)	divergence
2	2D(axis-symmetrical)	convergence
3	2D	plane
4	3D	plane
5	3D	divergence
6	3D	convergence

Table 1. Calculation setup.

4. Calculation results

In the experiments performed full *TMZ* width $H = R_2 - R_1$ and average depth of penetration front for light substance (*EP*, helium) into jelly $H_L = R_L - R_1$ were determined by motion pictures. Here R_1 - location of *TMZ* border on jelly side, R_2 - location of *TMZ* border on light substance side, R_L - location of jelly border, calculated from its condition of non-compression, that is from condition of volume constancy of jelly. Motion pictures for experiments adduced are presented in [3]. The pattern, typical for all 2D calculations presented on Fig.1 as raster patterns of volume concentrations for calculation 3, and the pattern, typical for 3D calculations - as iso-surface of jelly volume concentration on 0.5 level for calculation 4 - see Fig.2. These figures give illustrative pattern of evolution of unstability and *TM*. As evident from comparing, evolution of perturbations in 3D calculations significantly differs from experimental data. While evolution of perturbations goes in accordance with given initial perturbations at the interface (for observing time prevailing harmonics have little changed visually), number of cogs (jets) at the gas interface in calculations is significantly less. In doing so spectrum of harmonics is essentially wider because of random initial perturbations. That is why there take place significantly greater flow chaotization. Fig.3 presents dependencies of the track passed for the jelly stable border SR versus time square t^2 for 2D calculations (they are similar in both 2D and 3D calculations) and for experiments for three flows being observed. As evident from Fig.3, calculated $S_R(t^2)$ charts is somewhat different than experimental one, because of non-adequate setting of the calculations. In part, detonation model being used and state equation for *GEM* explosive products lead finally to some increasing of $S_R(t^2)$. However, we can notice that these dependencies are close to linear ones with exception of initial interval both in calculations and experiments. Thus, motion of the border is evenly accelerated, magnitudes in the experiments

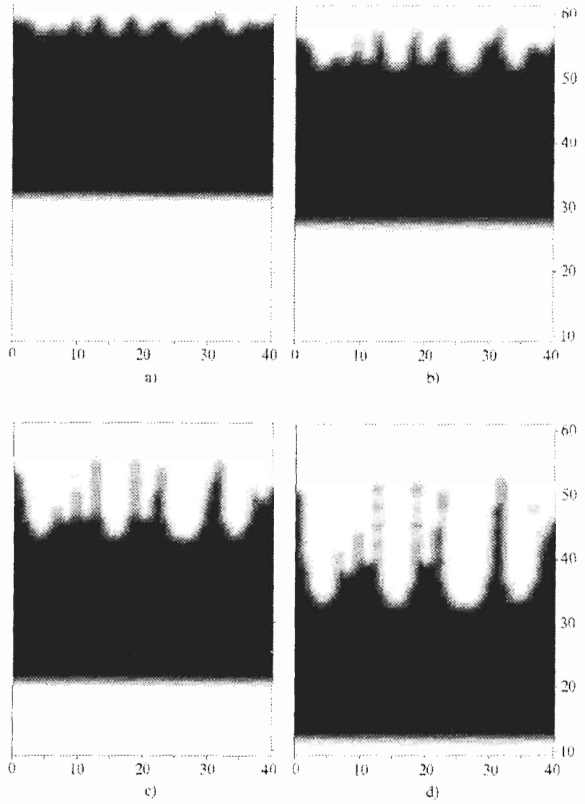

Figure 1. Raster patterns of volume concentrations for calculation of plane task: - t=0.3, b) - t=0.5, c) - t=0.7, d) - t=0.9msec.

and in 3D calculations have the following values: for divergent flow $gR(exp) \cong 58.6$, $gR(calc) \cong 63.8$; for convergent one - $gR(exp) \cong 82.8$, $gR(calc) \cong 80.8$; for plane flow $gR(exp) \cong 77.6$ and $gR(calc) \cong 53.8$. The significant differences between calculation and experimental data at the initial interval are result from different initial perturbations of the interface. However, the differences presented are not deciding for the problems observed, since we are firstly interested in *TM* evolution laws in self-similar variables. That is why information about *TMZ* width versus the distance passed presents the most interest. *TMZ* borders were determined in calculations by averaged profiles (in their cross-section) of the jelly volume concentrations for level 0.01 and 0.99. We consider dependence $\sqrt{H_L}$ versus value $J = \int_0^t \sqrt{g}dt$, where H_L - width of penetrating of the light substance into the heavier one, g - acceleration of the interface, t - time. Both in the experiment and in all calculations performed (see Fig.4,5,6) $\sqrt{H_L}(J)$ are close to the linear ones for every geometry, except of the initial dependence interval. But we must notice that in calculations with scattering shell it is difficult to isolate precisely intervals with linear law of the growth. Notice that penetration velocities in calculations agree with the experiment, and therewith value velocity in 2D calculations is less than in 3D calculations. This fact agrees with

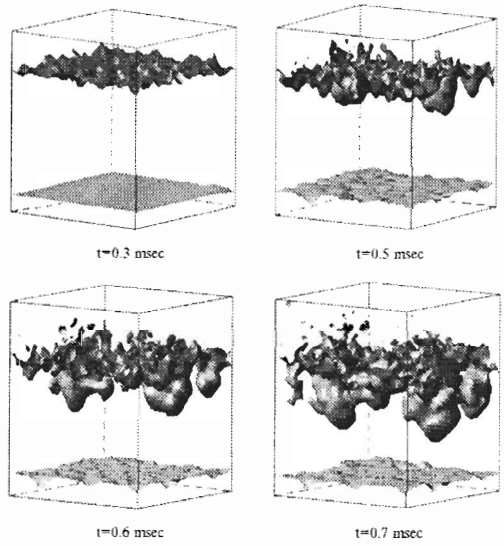

Figure 2. Iso-surface of jelly volume concentration on 0.5 level a) - t=0.3, b) - t=0.5, c) - t=0.6, d) - t=0.7msec.

the data obtained in the work [10] for gravitational TM in the case of relation of substances densities n=3. Table 2 adduces calculation and experimental values of self-similar constant a, obtained by the formula $H_L = \alpha S$, where $S = J^2$ (for the plane case the average value for three calculations presented). The table also shows the phenomenology theory data, obtained under the assumption of the light substance small density. Generally, one can get the greater (comparing with the experiment) value of α in 3D calculations. It is properly with regard to the fact that we don't observe viscosity and surface tension of jelly in the calculations. As a rule, coefficient α for 2D calculations is significantly less than in 3D calculations. Analysis show that there is linear law of growth for common TMZ width in calculations, with regard to the distance passed. Comparing with calculations for the common TMZ width were performed for two experiments (see Fig.7). As evident, there is a good agreement for the convergent shell, and significant difference for the plane one.

Interest is in the relation of width of zone of penetration of light substance into the heavier one and of the heavy substance into the lighter one. Table 2 adduces the coefficients $\chi = H_T/H_L$ on the self-similar interval, where H_T - width of zone of penetration of the heavy liquid into the gas. Phenomenology theory solving [10] is presented for the plane case. The agreement may be thought to be satisfactory.

From analysis of the results of 3D calculations follows that in the case of compression the faster penetration of the light substance into the heavier one takes place, and that in the case of divergence there is more decelerated front evolution comparing with the plane case. This agrees with experimental data. Notice, however, that this effect doesn't present for 2D calculations. Further investigations with wide varying settings of calculations (especially for divergent shell) are necessary for quantitative estimation of the effect obtained. At the same time, mentioned above effect of geometry takes place for full width of TMZ in 2D calculations also.

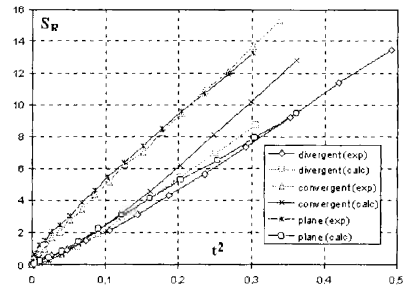

Figure 3. Dependence S_R versus t^2.

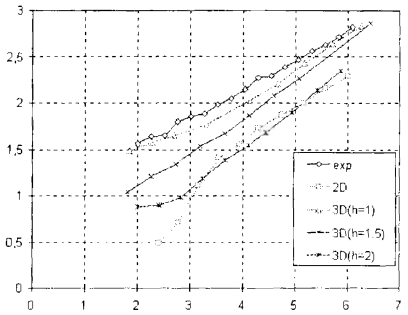

Figure 4. Dependencies $\sqrt{H_L}$ versus J (plane geometry).

5. Conclusion

Thus, in spite of the above mentioned difficulties, concerning with simulation of observed flows, we get the satisfactory agreement of calculation and experimental data both for R-t charts for interfaces, and for $H(S)$ and $H_L(S)$ dependencies. Thereby, studies performed show that *EGAK* and *TREK* program complexes can be successfully used for numerical simulation of the flows presented. We have numerically confirm the conclusion of [3] that character of behavior of *TMZ* fronts depends on the flow geometry. It follows from the analysis of the results that faster penetration of light substance into the heavy one takes place in the case of convergence, and also more decelerated (comparing with the plane case) front evolution in the case of divergence. This study is the first numerical investigation of the flows observed, so the results obtained have unfinished character. There are some questions, having significantly unproved answers:

- discount of viscosity and surface tension of the jelly,
- influence of real *GEM* state equation,
- the wider variation of calculation grid,
- discount of *TM* by mixing models, evolution of determined 2D and 3D perturbations.

Authors hope to get the answers for set questions in their further work.

References

[1] Volchenko OI, Klopov BA, Meshkov EE *et al.*, Simulation method for non-stationary flows of uncompressed liquid, A.C.1026154, invention bull., 24, (1983).

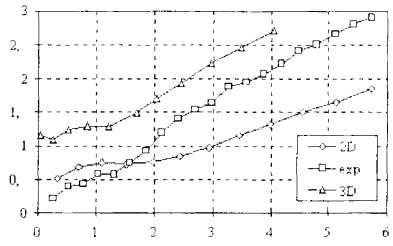

Figure 5. Dependencies $\sqrt{H_L}$ versus J (convergence).

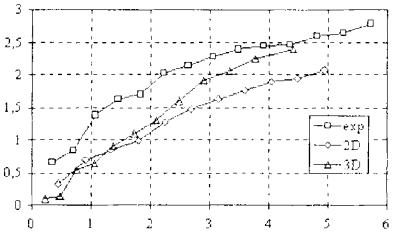

Figure 6. Dependencies $\sqrt{H_L}$ versus J (divergence).

[2] Meshkov EE, Nevmerzhitsky N *et al.*, Turbulent Mixing Devolepment Investigation with Converging jelly Rings, Proc. of the 4 IWPCTM, Cambridge, England, Edited by Linden P.F., Youngs D.L. & Dalziel S.B., 578, (1993).

[3] Kamchibekov M, Meshkov EE *et al.*, Turbulent Mixing at the Cilindrical Gas-Liquid interface, VNIIEF preprint, 46, 42, (1996).

[4] Yanilkin YV, Shanin AA *et al.*, EGAK program complex for calculation of 2D flows in multi-component medium, VANT, Ser. MSPP, 4, (1993).

[5] Gavrilova ES, Dibirov OA *et al.*, TREK program complex for numerical simulation of 3D flows in multi-component medium, Thesises for reports to 11th All-Russian conference, "Theoretical basis and construction of numerical algorithms for solving the problems of mathematical physics", Pushchino, October 5-9, 24, (1996).

[6] Darova NS, Dibirov OA *et al.*, EGAK program complex. Lagrangian-Eulerian method for 2D calculation of gas-dynamic flows in multi-component medium, VANT, Ser. MSPP, 2, (1994).

[7] Shanin AA, Stadnik AL, Yanilkin YV, Eulerian TREK method for calculation of 3D gas-dynamic flows in multi-component medium, VANT, Ser. MSPP, 4, 71-78, (1994).

[8] Bondarenko Y, Gubkov E *et al.*, Two-Parameter Model and Method for Computations of Turbulent Mixing in 2D Compressible Flows, Proc. of the 5-th IWPCTM, New York, USA, Edited by R.Young, J.Glimm & B.Boston, 402-413, (1995).

[9] Nikiforov VV, Yanilkin YV *et al.*, Numerical simulation of turbulent mixing in 2D flows, these proceedings.

[10] Sin'kova OG, Stadnik AL *et al.*, Three-Dimensional Numerical Simulation of Gravitational Turbulent Mixing, these proceedings.

	Exp.	3D	2D	theory
α	0.09±0.02	0.14	0.09	0.083
χ	1	1.22	1.31	1.49

Table 2. Values of coefficient α, Plane shell.

	Exp.	3D	2D
α	0.25±0.05	0.25	0.10
χ	1.35	1.17	2.3

Table 3. Values of coefficient α, Convergent shell.

	Exp.	3D	2D
α	0.05±0.02	0.06-0.19	0.09

Table 4. Values of coefficient α, Divergent shell.

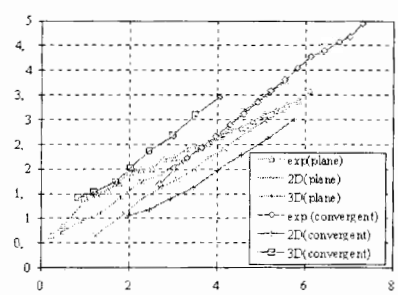

Figure 7. Dependencies $\sqrt{H_L}$ versus J.

Single and Multi-Mode Rayleigh-Taylor Instability In Cylindrical Systems

Y. Yedvab[1,2], U. Alon[1,3], D. Oron[1,2] and D. Shvarts[1,4]
[1]Physics Dept., Nuclear Research Center Negev, Beer Sheva, Israel
[2]Physics Dept., Ben Gurion University, Beer Sheva, Israel
[3]Physics Dept., Princeton University, Princeton, NJ, USA
[4]Mechanical Engineering Dept., Ben Gurion University, Beer Sheva, Israel

Abstract: The Rayleigh-Taylor bubble evolution in cylindrical geometry is described using a new potential flow model which incorporates Bell's flow potential into a Layzer-type model. The correct cylindrical linear growth rate is obtained. The late time bubble evolution is shown to display different behavior from the planar case. In a cylindrically expanding geometry, the bubble reaches a constant acceleration, while in a converging geometry it reaches the origin in a finite time. A treatment of the multi-mode front using a bubble-merger approach is described and applied to the cylindrical case. The growth rate of the mixing zone in converging and expanding geometries are shown to be larger and smaller respectively than the planar growth, in agreement with recent experimental results.

1. Introduction

Understanding the evolution of the Rayleigh-Taylor (RT) instability is crucial for achieving Inertial Confinement Fusion (ICF). Most theoretical investigations of the RT instability have been in a planar geometry. In ICF as well as astrophysical applications, the instability typically develops in a non-planar geometry. It is of interest, therefore, to study the effects of non-planar geometry, such as cylindrical or spherical geometry, on the mixing zone growth.

Theoretical approaches have so far mainly been concerned with the linear growth regime. Bell [1] and later Plesset [2] derived an expression for the linear growth in cylindrical and spherical geometry. There is, to our knowledge, no theoretical analysis of the late nonlinear stages of the evolution. Several groups have recently studied single and multi-mode evolution in cylindrical geometry experimentally [3, 4] and numerically [5]. In particular, Meshkov *et al.*[4] found that the multi-mode front evolution is affected by cylindrical geometry - the growth rate is greater than the classical planar growth in a converging cylindrical geometry, and smaller than the planar growth rate in an expanding cylindrical geometry.

In the present study we consider the RT evolution in cylindrical geometry using a potential flow model [6, 7]. This allows us to describe the single-mode bubble motion in the linear, early nonlinear and late stages of the flow. In order to study the multi-mode front evolution, we use these results in a statistical-mechanics model [8], and uncover the main physical effects that determine the front evolution.

2. Potential flow model for a bubble in cylindrical geometry

We consider an interface between an incompressible fluid and a much lighter fluid (Atwood number $A = 1$). Two geometries are defined: an expanding geometry where the bubbles grow

More information - Email: schwartz@bgumail.bgu.ac.il

on the inner interface of a radially expanding fluid layer, and a converging geometry where the bubbles grow on the outer interface of a radially converging layer. The layer is assumed to be much thicker than the perturbation wavelength. The radial position of the interface is $R(t)$, the radial position of the bubble tip is $R_0(t)$ and the bubble amplitude is $h(t) = |R_0(t) - R(t)|$. The interface acceleration is given by $\ddot{R}$, and is positive (outgoing) in the expanding case and negative (ingoing) in the converging case. The same model has been also applied to these cases where the velocity is directed in the opposite direction to the acceleration and will be discussed in a future publication [9].

We extend the models of Layzer [6] and Hecht *et al.*[7] to the cylindrical case. The essential idea is to expand the flow equations and flow potential near the bubble tip, assuming a simple time-dependent flow potential. This model is known to accurately describe all stages of the bubble flow in various planar geometries [7]. We use the flow potential first proposed by Bell [1]:

$$\Phi(r,\theta,t) = R\dot{R}\ln(r) + a(t)[R_0/r]^{\mp\ell}\cos(\ell\theta) \tag{1}$$

where ℓ is the mode number, the plus sign in the power law corresponds to the expanding geometry and the minus sign corresponds to the converging geometry. The first term on the right-hand side corresponds to a radially symmetric potential flow of a cylindrical fluid layer, and the second term represents the perturbation. The interface is assumed to move with the fluid as specified by the kinematic equation, $V_r = \frac{Dr}{Dt}|_{interface}$, and the flow dynamics is described by the Bernoulli equation, $\dot{\Phi} + \frac{1}{2}V^2 = \text{const}$. The interface is then expanded to second order in θ: $r(\theta) = R_0 + R_1\theta^2$, and the flow equations are solved to the same order [7], yielding three ODE'S in the three unknowns $R_0(t), R_1(t), a(t)$:

$$\dot{R}_0 = R\dot{R}/R_0 \pm \ell \cdot a/R_0 \tag{2}$$

$$\dot{R}_1 = (\ell \cdot a/R_0)\cdot\left[(3\ell \mp 1)\cdot R_1/R_0 \mp \ell^2/2\right] - \left(R\dot{R}/R_0^2\right)\cdot R_1 \tag{3}$$

$$\dot{a} = \frac{\left(R\dot{R}\right)^2\cdot R_1 \pm 2\ell\cdot aR\dot{R}R_1 - \left(\dot{R}^2 + R\,\ddot{R}\right)\cdot R_1R_0^2 - \ell^2a^2\left(\ell^2R_0/2 - R_1\right)}{(\pm\ell R_1/R_0 - \ell^2/2)\cdot R_0^3} \tag{4}$$

The upper signs in Eq's 2-4 correspond to a converging geometry and the lower signs to an expanding geometry. Thus, given the interface position as a function of time, $R(t)$, one can solve for and get the bubble amplitude, curvature and the potential amplitude near the tip.

3. Results for single mode bubbles

3.1. Linear regime

The model equations yield the expression for the linear growth rate derived by Bell [1] in the regime when $h/\lambda \ll 1$, where λ is the effective wavelength $\lambda = 2\pi R/\ell$.

The linear growth rate equation is:

$$R\frac{d^2}{dt^2}(R\cdot h) \pm \ell\cdot\ddot{R}\cdot(R\cdot h) = 0 \tag{5}$$

In the case where $\ell >> 1$ the result of the linearized equations yields a simple and useful solution [5, 10]:

$$h(t) = h\,(t=0) \cdot \left[(R(t=0)/R(t)) \cdot \exp\left(\int_0^t dt' \sqrt{\mp \ell \ \ddot{R}\,/R} \right) \right] \tag{6}$$

Note that the effective growth rate $\gamma = \sqrt{\left| \ell \ \ddot{R}\,/R \right|}$ is analogous to the classical planar result $\gamma = \sqrt{k \cdot g}$, where $k = \ell/R$.

We now describe the late time behavior for the expanding and converging cases.

3.2. Expanding geometry

In Fig 1, the bubble velocity is plotted for an expanding geometry. After the linear stage, the growth is slowed and approaches an asymptotic growth rate at late times. The model allows an analytic solution for the asymptotic velocity. For wavenumbers $\ell > 6$, the asymptotic velocity grows linearly in time:

$$V_{cyl}(t) = \left[\left(1/\sqrt{\left(1 + \frac{13}{12\ell} - \sqrt{(24\ell + 25)\,/\,(144\ell^2)} \right)} \right) - 1 \right] \cdot \ddot{R} \cdot t \tag{7}$$

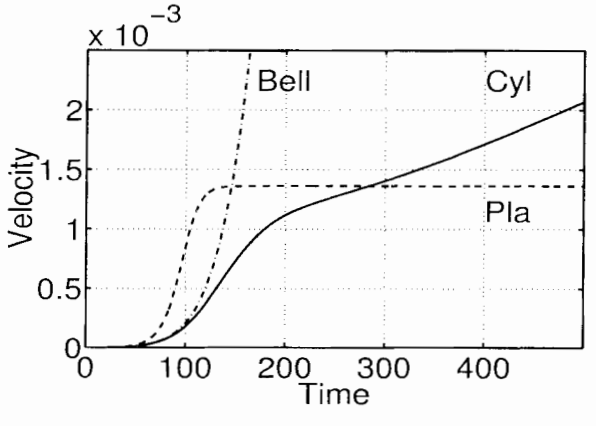

Figure 1. Single-mode bubble velocity in an expanding geometry, compared with Bell's expression, and with planar bubble velocity. In this case $R(t=0) = 1$, $g = \ddot{R} = 2e - 4$, and $\ell = 36$.

Notice that this result is in contrast with the planar case, where the bubble reaches a constant asymptotic velocity $V_{planar} = \sqrt{(g \cdot \lambda)\,/\,(6\pi)}$. To understand this result, we note that the effective bubble wavelength, $\lambda = 2\pi R/\ell$, increases with time in the expanding geometry, and thus increases the buoyant force on the bubble, causing the velocity to increase with time.

We can describe the asymptotic bubble behavior using an adiabatic approximation. Substituting the effective wavelength into the expression for V_{planar}, and taking into account the effect of the thinning of the perturbation due to the cylindrical flow (the fluid layer, and the perturbation, become thinner as the radius increases) leads to:

$$V_{adiabatic} = \sqrt{(g \cdot \lambda)/(6\pi)} + \left(R\dot{R}/R_0 - \dot{R}\right) = \left(1/\sqrt{24\ell}\right) \cdot \ddot{R} \cdot t \tag{8}$$

This adiabatic approximation agrees with the full potential flow model result (Eq. 7) in the limit $\ell >> 1$.

At very low ℓ, $\ell < 6$, the thinning effect becomes dominant and a different asymptotic growth is found,

$$V_{cyl}(t) = C_0 \cdot t^{\beta} \tag{9}$$

with $\beta = \left(\sqrt{8\ell + 1} - 5\right)/2$, and C_0 depends on the initial amplitude. In this regime, the thinning effect keeps the perturbation small, and in fact, Eq. 9 is the solution of Bell's equation (Eq. 5) at late times.

3.3. Converging geometry

In Fig 2, the bubble velocity in a converging geometry is shown. After the linear growth, the bubble accelerates and reaches the origin in a finite time t_f. The physical reason for this is that in the converging geometry the dominant effect at late times for any ℓ is the thickening of the fluid layer due to the converging radial flow. The perturbation flows in the sink potential and the contribution of the pure RT growth is small. Thus, as the bubble approaches the center it grows as $V = \dot{R} - R\dot{R}/R_0$. The analytical form of the perturbation growth is in this case

$$h = R - \sqrt{R^2 - R_f^2} \tag{10}$$

where R_f is the radial position of the interface at time t_f.

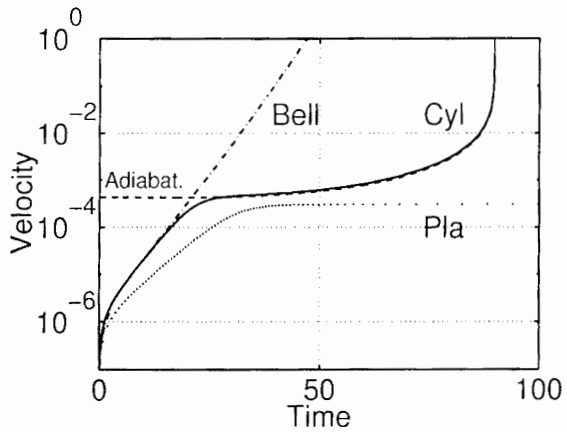

Figure 2. Single-mode bubble velocity in a converging geometry, compared with the adiabatic approximation (Eq. 11), Bell's expression, and with planar bubble velocity. In this case $R(t = 0) = 1$, $g = -\ddot{R} = 2e - 4$, and $\ell = 360$.

4. Multi-mode bubble front

Recent theoretical studies [8] have shown that the planar RT multi-mode evolution can be described in terms of a statistical mechanics model. The main ingredients are the single mode bubble evolution and the two-bubble overtake interactions (mergers), which can be viewed as effective single particle and two-particle interactions in the flow.

In the planar case, the bubble merger rate was calculated using a potential flow two-bubble model [8]. This merger rate is the rate at which bubble pairs merge into larger, and faster, bubbles. The bubble size distribution flows to a self-similar distribution, in which the only length scale is gt^2. The bubble front growth rate was found to be $h = \alpha g t^2$ where $\alpha = 0.05$, in agreement with simulations and experiments.

In order to assess the effect of cylindrical geometry on the multi-mode front evolution, we employ the statistical mechanics model used for the planar case. However, instead of the planar asymptotic bubble velocity we use the asymptotic bubble velocity from the present cylindrical potential flow model in the limit $\ell >> 1$,

$$V_{bubble} = \sqrt{(g \cdot \lambda)/(6\pi)} + \left(R\dot{R}/R_0 - \dot{R}\right) \tag{11}$$

where $\lambda = 2\pi R/\ell$.

In the present work, the merger rates are assumed to be equal to the planar merger rate. This is assumed to be justified when the bubble wavelengths are much smaller than the interface radius. When the wavelengths and R are comparable, cylindrical effects are expected to influence the merger rate. In future work these effects will be investigated more rigorously.

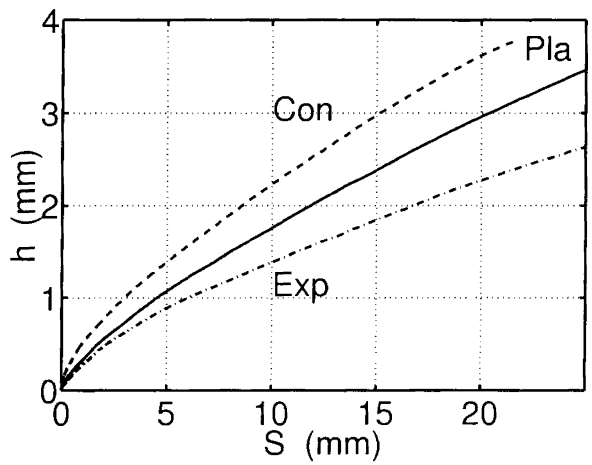

Figure 3. Multi-mode bubble front growth rates vs. the distance covered by the unstable interface, for planar, converging and expanding geometries. The cases are taken from ref. [4].

The model results for the growth rate are shown in Fig. 3 for planar, converging and expanding geometries. The interface position, acceleration and initial perturbation are taken as roughly similar to the experiment of Meshkov *et al.*[4] It is seen that in the converging case,

the growth rate is larger than the corresponding planar case, while in the expanding case the growth rate is smaller than the planar growth rate. This is in agreement with the results obtained by Meshkov *et al.*[4] Quantitatively, the growth rates predicted by our hybrid model are in fair agreement with those obtained in the experiment.

The basic physics responsible for these differences, according to our model, is based on the competition between two effects which are inherently non-planar in nature: 1) The change of the effective wavelength due to the change in interface radius. 2) The effect of dilation or compression of the fluid due to the cylindrical flow - the shell thickness changes and the perturbations are accordingly distorted. These effects enter the model through the asymptotic bubble velocity (the two terms in the right hand side of Eq. 11). We note that the second effect (thickness changes) is dominant and qualitatively determines the differences in growth rate between the various cases. Thus, in the converging geometry the perturbation is dilated as the shell approaches the origin, while in the expanding geometry, the asymptotic velocity is reduced in comparison to the planar case due to the shell compression.

In the planar case, it was found by Alon *et al.*[8], that in the self-similar regime $h\backslash\lambda = const.$ It seems that also in cylindrical geometries h/λ reaches a constant at late times, but the value of the constant is different in different geometries:

$$(h\backslash\lambda)_{con} > (h\backslash\lambda)_{pla} > (h\backslash\lambda)_{\exp} \tag{12}$$

This result is consistent with the different bubble shapes that were observed by Meshkov *et al.*[4] for the different geometries. These differences can also be explained in terms of the two non-planar effects discussed above, as will be done in more detail in a future publication [9].

References

[1] Bell GI, Los Alamos Scientific Laboratory Report N° LA-1321, (1951).

[2] Plesset MS, J. Appl. Phys., 25, 96, (1954).

[3] Hsing WW, Barnes CW, Beck JB, Hoffman NM, Galmiche D, Richard A, Edwards J, Graham P, Rothman S and Thomas B, Phys. Plasmas, 4, 1832, (1997); Hsing WW, Hoffman NM, Phys. Rev. Lett., 78, 3876, (1997).

[4] Kamchibekov MD, Meshkov EE, Nevmerzhitsky NV, Sotskov EA, Turbulent mixing at the cylindrical gas-liquid interface, presented in this workshop.

[5] Beck JB, Hoffman NM, Choi CK, Los Alamos Scientific Laboratory Report N° LA-UR-94-1879, (1994).

[6] Layzer D, Astrophys. J., 122, 1, (1955).

[7] Hecht J, Alon U, Shvarts D, Phys. Fluids, 6, 4019, (1994).

[8] Alon U, Shvarts D, Mukamel D, Phys. Rev. E, 48, 1008, (1993); Alon U, Hecht J, Mukamel D, Shvarts D, Phys. Rev. Lett., 72, 2867, (1994); Alon U, Hecht J, Ofer D, Shvarts D, Phys. Rev. Lett., 74, 534, (1995).

[9] Yedvab Y, Alon U, Oron D, Shvarts D, to be published.

[10] Hattori F, Takabe H, Mima K, Phys. Fluids, 29, 1719, (1986).

Variable Acceleration Rayleigh-Taylor Mixing

D.L. Youngs
AWE, Aldermaston, Reading RG7 4PR, England

Abstract: High resolution direct numerical simulation using the TURMOIL3D code with mesh sizes up to $420 \times 320 \times 320$ has been used to investigate Rayleigh-Taylor mixing in which the acceleration g varies with time (changes sign). The main purpose of this study is to see if a 1D turbulence model for Rayleigh-Taylor mixing gives reasonable results in this situation. The turbulence model includes an explicit treatment for the dissipation of density fluctuations (molecular mixing) which plays a key role in this problem. The paper demonstrates how 3D direct numerical simulations in simple situations may be used to aid the development of the turbulence models which are needed to represent mixing in more complex practical applications.

1. Introduction

In the problem considered, fluid of density ρ_1 initially rests above fluid of density ρ_2 ($< \rho_1$) in a gravitational field g which varies with time. Initially, g is positive (unstable). Then g is negative for a period (stable). Finally, g is positive again.
High resolution 3D direct numerical simulation using the TURMOIL3D code [2], is used to investigate the mixing process. TURMOIL3D is a simple finite-volume compressible code without interface tracking. The monatonic advection method of van Leer is used for all fluid variables. This provides the required dissipation at high wavenumbers. Low Mach number calculations are used to represent incompressible mixing. The effect of mesh size in the 3D calculations is considered. The difference between 2D and 3D calculations is shown.
Results from the 3D simulations are compared with those obtained by using a 1D turbulence model [3]. The main objective of the study is to see if the 1D turbulence model gives reasonable results.

2. Calculations performed

The initial density distribution is given by $\rho = \rho_1 = 3$ for $x < 0$, $\rho = \rho_2 = 1$ for $x > 0$. For the gravitational field g three cases are considered:

$$constant\ g: \qquad g = g_1 \tag{1}$$

$$unstable/stable/unstable: \qquad g = \begin{cases} {}^{+}g_1 & 0 < t < 1.5 \\ {}^{-}g_1 & 1.5 < t < 3.0 \\ {}^{+}g_1 & 3.0 < t \end{cases} \tag{2}$$

$$extended\ stable\ phase: \qquad g = \begin{cases} {}^{+}g_1 & 0 < t < 1.5 \\ {}^{-}g_1 & 1.5 < t < 4.5 \\ {}^{+}g_1 & 4.5 < t \end{cases} \tag{3}$$

where

$$\frac{\rho_1 - \rho_2}{\rho_1 + \rho_2} g_1 = 1 \tag{4}$$

More information - Email: dyoungs@awe.gov.uk or dyoungs@awe.co.uk

The cross-section for the computational domain is $0.0 \leq y, z \leq 1.0$. Three choices for the zoning are used:
Coarse 3D mesh : $210 \times 160 \times 160$
Fine 3D mesh : $420 \times 320 \times 320$
Fine 2D mesh : $420 \times 320 \times 1$
An initial random perturbation is applied to the interface with wavelengths of order 6 Δx and amplitude $\sim 0.2\ \Delta x$, where Δx is the mesh size.
As TURMOIL3D is a compressible code, varying g continuously is impractical. This would require continually adjusting the pressure gradient in order to maintain hydrostatic equilibrium outside the mixing zone. However, the discrete changes in g referred to above are feasible. In order to change g from g^- to g^+ at time t_0 , the calculation is first run to time to using $g = g^-$. At time t_0 , the density (ρ), fluid 1 mass fraction (m_1) and velocity (u) distributions are left unaltered but the pressure gradient is adjusted to allow for the change in g. It is assumed that the rate of change of $div\ u$ (which should be close to zero) is the same before and after the change in g. This gives a Poisson equation for the pressure distribution (p^+) immediately after the change in g:

$$div\left(\frac{1}{\rho}\nabla p^+\right) = div\left(\frac{1}{\rho}\nabla p^+\right) \tag{5}$$

with boundary conditions

$$\frac{\partial p^+}{\partial x} = \rho g^+ \tag{6}$$

at $x = x_{min}$ and $x = x_{max}$ The Poisson equation for p^+ is solved by the conjugate gradient method. Internal energies are then adjusted to give the required pressure distribution and the calculation continues with the new value of $g = g^+$.

3. Overall behaviour of the mixing zone

Figure 1 shows a sequence of 2D sections from the 3D calculation for the problem with the extended stable phase (case (iii)) using $420 \times 320 \times 320$ zones.
At the end of the first unstable phase, $t = 1.5$ (Figure 1a), approximate self-similar mixing is achieved with mixing zone width growing in proportion to gt^2. There has, however, been significant dissipation of density fluctuations. When the stable phase starts (Figure 1b) dissipation of density fluctuations continues and as a result little de-mixing occurs. By the end of the stable phase (Figure 1c) a smooth density gradient is established. This reduces the growth rate in the early part of the second unstable phase. By $t = 6.5$ (Figure 1d) mixing is well underway again.

4. Quantitative results

The time variation of two quantitative measures of the amount of mixing is shown in Figure 2. The integral width of the mixing zone is calculated from:

$$W = \int \overline{f_1}.\overline{f_2}\ dx \tag{7}$$

where $\overline{f_r}$ is the plane average of the volume fraction for fluid r. As $W \sim gt^2$ for the unstable case, $\sqrt{W}$ is plotted against t for all the cases considered. A measure of the concentration fluctuations is given by

$$I = \frac{\int \sigma^2\ dx}{\int \overline{f_1}.\overline{f_2}\ dx} \tag{8}$$

where $\sigma^2 = \overline{(f_1 - \overline{f_1})^2}$. The quantity I lies in the range 0 to 1. If there were no dissipation of density (concentration) fluctuations, σ^2 would equal $\overline{f_1}.\overline{f_2}$ and I would be unity. The paper by Dalziel *et al.*[1] shows that TURMOIL3D gives $k^{-5/3}$ (Kolmogorov-like) power spectra for concentration fluctuations similar to those measured in a Rayleigh-Taylor experiment. This gives some confidence in the ability to calculate the fine-scale structure. As the power spectra decay at high wave numbers, the values of σ^2 should be dominated by contributions from the lower part of wave number spectrum which is resolved in the simulations. Hence it should be possible to estimate I from the numerical simulations with some degree of reliability.

For the 3D calculations the effect of mesh size is not large (Figures 2a, 2b). For the constant g case, the slope of the $\sqrt{W}$ vs t curve and the values of I are initially higher than the late-time (self-similar) values. This is attributed to the inability to resolve the small-scale features until the mixing zone is of order 50 meshes wide. During the stable phases, the absence of de-mixing and the decay of concentration fluctuations is very similar for the two mesh sizes. At the start of the second unstable phase there is a slight delay in the growth of the mixing zone, due to the smooth density gradient established during the stable phase. However, when mixing does get underway again the rate (as given by the slope of the $\sqrt{W}$ versus t curve) overshoots that for the constant g case. Moreover, values of I also overshoot the limiting value for the constant g case and then diminish by the end of the calculation. This is attributed to the fact that when mixing begins for the second time, the smooth density gradient suppresses the growth of the short wavelength perturbations which generate the fine-scale turbulence needed to dissipate concentration fluctuations.

For the 2D calculations (Figure 2c), the behaviour of the mixing zone width (W) is similar to that seen for the 3D calculations. However, concentration fluctuations are significantly higher in the 2D calculations which are not able to model the fine-scale mixing correctly.

5. Turbulence model calculations

A 1D turbulence model for Rayleigh-Taylor mixing was described by Youngs [3]. The model is based on the equations of two-phase flow with turbulent diffusion terms added. Mass exchange between the phases is used to represent the dissipation of concentration fluctuations. This makes the model very suitable for the problems considered here in which the magnitude of the concentration fluctuations varies significantly with time. Results for the three cases are shown in Figure 2d. The behaviour is similar to that seen in the 3D simulations. There is little de-mixing in the stable phases. Concentration fluctuations decay during the stable phase and then grow again in the second unstable phase.

6. Conclusions

Rayleigh-Taylor mixing for the case when the acceleration varies with time (changes sign) shows some interesting behaviour. 3D numerical simulation has given results which are insensitive to the mesh size. The results obtained have been used to check the validity of a one-dimensional turbulence model.

References

[1] Dalziel SB, Linden PF and Youngs DL, these proceedings.
[2] Youngs DL, Phys. Fluids A, 3, 1312-1320, (1991).
[3] Youngs DL, Proc. of the 5th International Workshop on the Physics of Compressible Turbulent Mixing, Ed. Young, Glimm & Boston; World Scientific, Singapore, (1996).

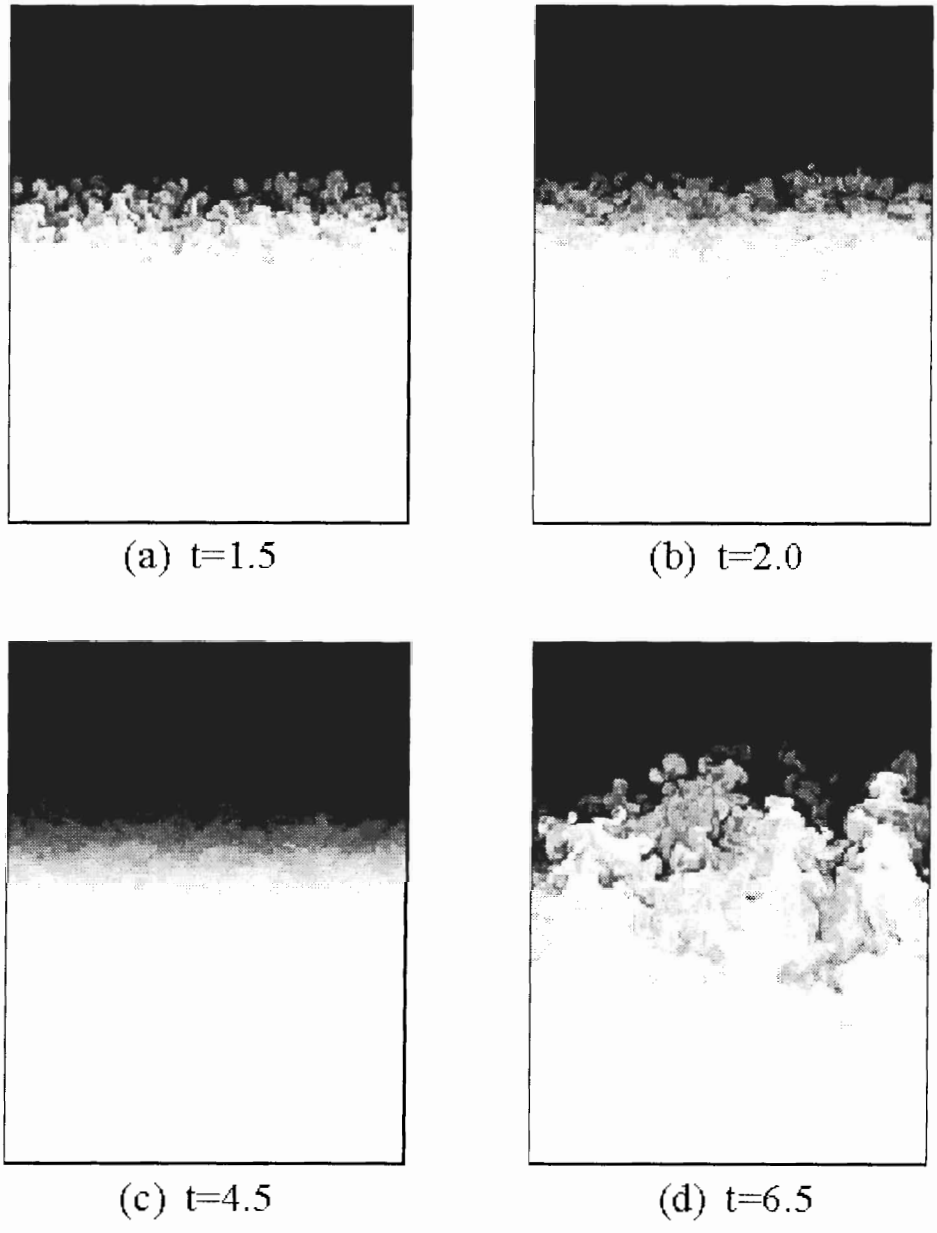

Figure 1. Volume fraction distributions. 2D sections from a 3D calculation. (a) t = 1.5, end of first unstable phase (b) t = 2.0, early part of stable phase. (c) t = 4.5, end of stable phase (d) t = 6.5, second unstable phase.

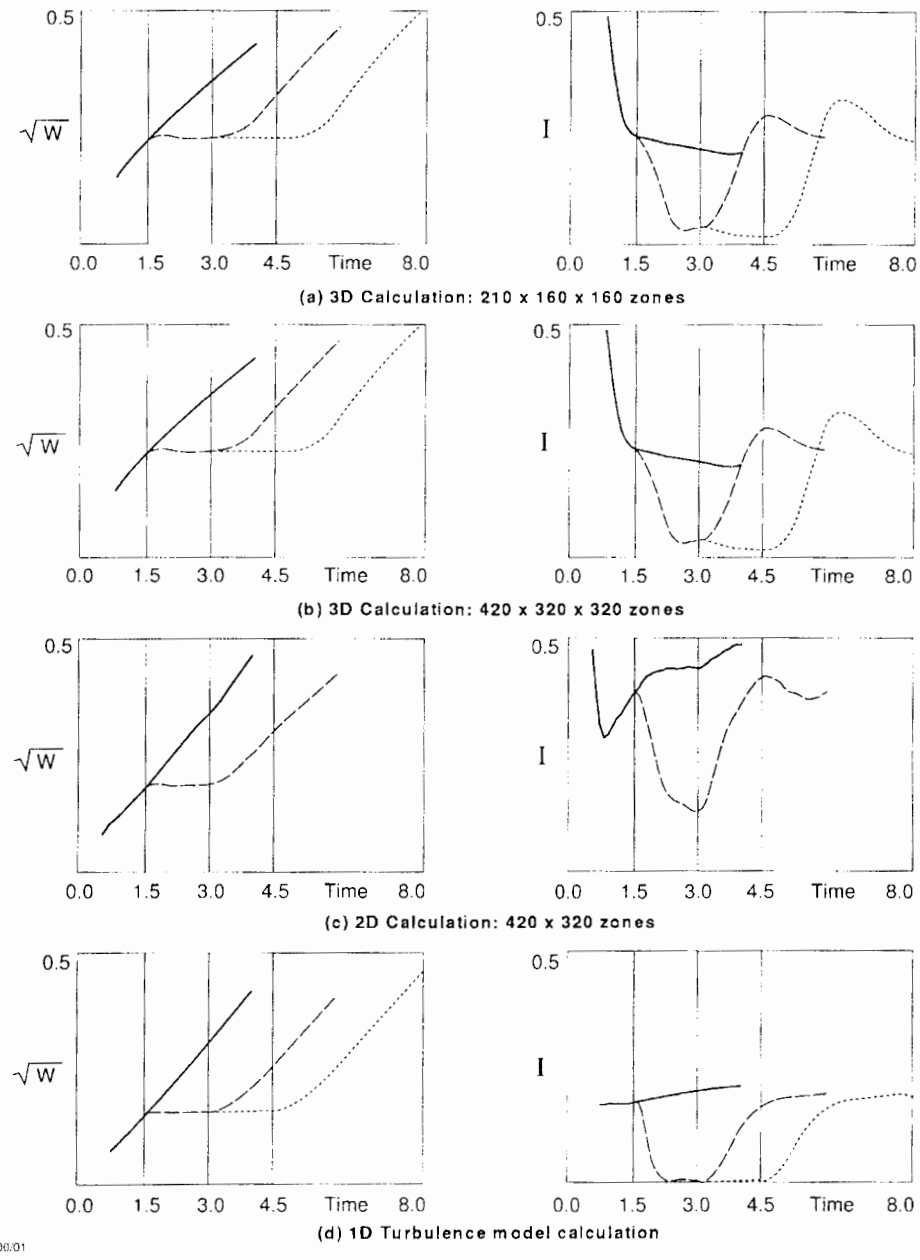

Figure 2. Variation with time of mixing zone width (W) and the measure of concentration fluctuations (I). Solid line: constant g, case (i). Dashed line: unstable/stable/unstable, case (iii). Dotted line: extended stable phase, case (iii).

Vortical Projectiles from Shock-Bubble Interactions

N.J. Zabusky[1], S. Zeng[1], J. Ray[1] and R. Samtaney[2]
[1]Dept. of Mech. & Aero Engg., P.O. Box 909
Rutgers University, Piscataway, NJ-08855-0909, USA
[2] Sarnoff Corporation, CN 5300, Princeton, NJ 08543-5300, USA

Abstract: We introduce the concept of a moving "vortical projectile" (VP) to synthesize a new understanding of vortex dynamics in the vicinity of interacting nearby layers or structures of *opposite-signed* vorticity. In particular those layers deposited at contact surfaces when a shock or blast wave interacts with a spherical or elliptical bubble, heavier than ambient. This concept is generic to complex shapes in two and three dimensions. We conjecture that recent observations of "explosion fragments" in the vicinity of supernova remnants(SNR) could be VPs.

1. Introduction

We use the generic term, "vortical projectile" or (VP) to identify coherent vortex structures (CVS) of positive and negative circulation in 2D or oppositely-directed nearby tube-like regions (e.g. a vortex "ring") in 3D. These VPs move under their own self induction, i.e. they have a dominant translational motion in a frame of reference in which the mean flow is nearly zero. The simplest examples include: (2D) the rectilinear pair of point vortices, $(\Gamma, -\Gamma)$ separated by d, which translates with speed $\Gamma/(2\pi d)$ or the ideal small core circular ring vortex of circulation, Γ, radius, R, and core size δ, $(\delta/R << 1)$ which translates with velocity $\approx \frac{\Gamma}{4\pi R}[log\frac{8R}{\delta} - \frac{1}{4}]$. The "V-states" [1], stationary configurations of the Euler equations in two dimensions are CVS of *piecewise-constant* vorticity domains which may translate. Hills vortex is another finite domain axisymmetric translating CVS.

These 2d and 3d VPs may arise thru instability of some stationary or slowly evolving configurations of positive and negative circulation. Couder and colleagues [2, 3] in pioneering experiments and simulations on 2d cylinder wakes showed that perturbations will induce strain fields that cause nearby opposite-signed vortices to link-up or "bind"and move together as a single dipolar VP [4, 2] which are frequently manifest as "mushroom" or "tadpole" structures. Note, in *compressible* media isolated dipoles move with variable speeds which depend upon their Mach number and aspect ratio [5].

In 3 dimensions, VPs may arise from vortex collisions, as seen by Lim and Nickels [6]. They collided oppositely directed coaxial equal radii rings at Re= 1,450, and found that the rings reconnect and disassemble into about nineteen *small rings*. The authors note. "As the Reynolds number is increased from $\sim$ 1,500 to 3,000 (Fig 4b), the flow goes through a transition in which the small rings appear to have fine structure superimposed on them".

2. Recent simulations at $M > 2$

Winkler *et al.*[7, 8] were first to observe and carefully visualize the simple coaxial vortex rings that arise in axisymmetry on the downstream (aft) side of a heavy spherical bubble when the Mach number and density ratio are sufficiently large. Zabusky and Samtaney [9] observed (in

More information - Email: nzabusky@caip.rutgers.edu

their Fig. 9) a complex configuration of two dipolar vortices aft of a 2d cylinder when $M = 4.0$ and density ratio $\eta = 3.0$. Klein *et al.*[10] did the first systematic study of the parameter space for a fast/slow spherical bubble. In their canonical case ($M = 10$ and $\eta = 10$) they presented evidence of new "swirling motions" (see their Fig. 6), but did not provide any discussion of creation mechanisms or long-time consequences.

VPs have been seen in other compressible simulations. D. Youngs [11] simulated a randomly perturbed interface and observed "... vortex pairs that propagate away from the mixing zone". Müller *et al.*[13] simulated SN 1987a in axisymmetry and observed the formation of elongated "fingers and mushroom caps". Maclow *et al.*[14] presented very high resolution shock bubble runs with structures similar to ours. In all cases only density structures were shown and no causal interpretation of their evolution was given.

Recently, Zeng and Zabusky [15] have quantified the vortex deposition phenomena at $M \leq 5$ and demonstrated that the coaxial ring arises from the roll up of the Mach stem shear layer which results from the collision of the curved incident shock on the downstream side of the bubble, as sketched in Fig. 1, where three phases of the interaction of a planar shock with a heavy bubble are shown. In the last phase the upward going shock wave, reflected from the axis on the aft side of the bubble, deposits opposite-signed (positive) vorticity on the interface and will account for the off-axis VPs found as shown below.

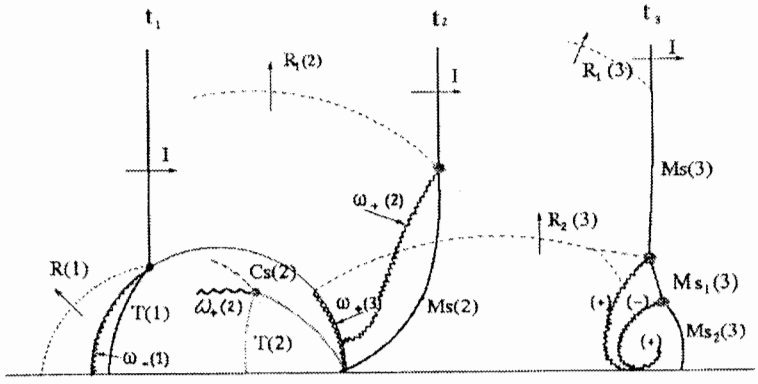

Figure 1. Three phases during the interaction of a shock wave with an axisymmetric spherical bubble. 1) The incoming shock (I) is in contact at a node with the upstream side of the bubble . Shown are the reflected (R) and transmitted (T) shocks and the negative vorticity layer. 2) The incoming shock (I) is in contact via a curved Mach stem with the downstream side of the bubble . Shown are the reflected (R) and transmitted (T) shocks and the positive vorticity layer arising at the triple point. The transmitted shock has created a cavity (dotted) with a shocklet, Cs(2), (dashed) at its point of highest curvature. Also a shear layer is produced at this point 3) The incoming shock (I) is in contact with Mach stem (Ms) at a triple point. Shown are two reflected waves, the original R_1 and a new one, R_2 reflected from the axis. The latter is travelling upward and thus deposits a positive vorticity $\omega_+(3)$ layer on the perturbed downstream bubble face. This is adjacent to the negative vorticity layer the continuation of $\omega_+(1)$ (not shown for clarity) deposited by the passage of the Mach stem. The strong vortex produced at the triple point between Ms and Ms_1 produces a bulge in the shock and hence an additional triple point at which a negative vortex layer arises.

Type of Run	Strength	Density ratio	Geometry	Resolution	Num. Method
Blast Wave - Bubble	$E/e_0 = 40{,}000$	10	Sphere	R= 120 Δx R_b=40 Δx	2^{nd} Order, Harten-Yee TVD code
Shock-Ellipse	$M = 10.0$	10	Ellipse $AR = 1.5$ $\alpha = -30$	b = 60 Δx a = 90 Δx	2^{nd} Order, EFM code

Table 1. Parameters of the runs. M is the Mach number of the shock, R_b is the initial radius of the blast wave, E is the energy inside the blast wave, $e_0 = C_p T/\gamma$ is the energy in the ambient flow, T is the temperature of the flow, C_p is the specific heat at constant pressure, a is the semi-major axis of the ellipse, b is the semi-minor axis, $AR = a/b$ is the aspect ratio of the ellipse and α is the deviation in degrees of the major axis of the ellipse from the vertical.

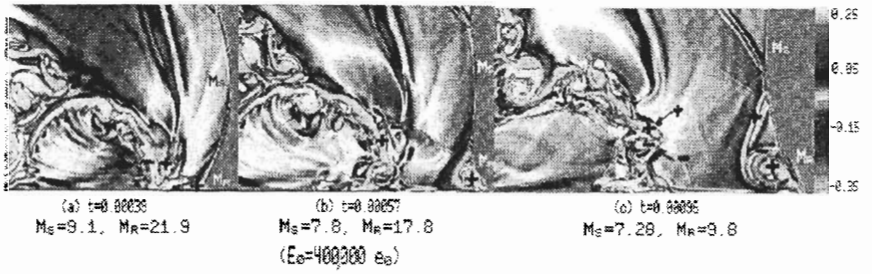

Figure 2. Vorticity patterns resulting from an axisymmetric blast wave impacting from the left with an $\eta = 10$ bubble. The blast wave was initiated by raising the internal energy of a small domain of radius 20 zones to the left of the bubble of radius 80 zones (The time required for the blast wave to cross a bubble diameter is 0.0017. The energy enhancement factor was 40,000 over the ambient internal energy, $e_0 = p_0/[\rho_0(\gamma - 1)]$. This simulation was done with our Harten-Yee second-order accurate code.

3. New results

Below we show in 2d or 2d-axisymmetry that these dipolar and near dipolar VPs arise in shock and blast wave bubble interactions. Because the physical environment is similar, it is reasonable to conjecture that these structures may belong to the population of of objects ("interstellar bullets", " explosion fragments" or "cometary knots") seen in the vicinity of SNR and astrophysical jets.

In Table 1 we present the parameters for the runs illustrated briefly in Figs. 2- 3.

In Fig. 2 we see the vorticity patterns resulting from an axisymmetric blast wave interacting with an $\eta = 10$ bubble. The blast wave was initiated by raising the internal energy of a small domain of radius 20 zones to the left of the bubble of radius 80 zones. The time required for the blast wave to cross a bubble diameter is 0.0017. The energy enhancement factor was 400,000 over the ambient internal energy, $e_0 = p_0/[\rho_0(\gamma - 1)]$. In Fig. 2a the curved blast M_s has a Mach number of 9.1 whereas the coaxial VP has a Mach number of 21.9. The speed of the VP is also decreasing, e.g. to $M = 9.8$ in Fig. 2c (by a self-similar effect). Note the circulation continues to flow into the VP as its centroid departs from the axis. In Fig. 2b we see a new

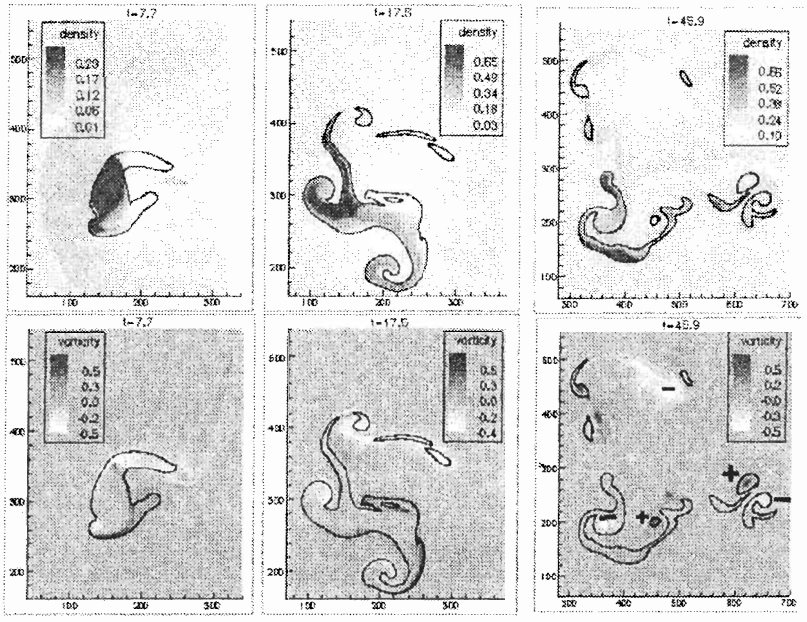

Figure 3. Density and vorticity at three times for $M = 10$ shock impacting an elliptical bubble of aspect ratio 1.5 and major axis 180 grid points and tilted by 30 degrees. The density ratio $\eta = 10$ and $\gamma = 7/5$ for both media. The bubble interface (obtained from our interface tracker) is shown as the black line on the density (above) and vorticity (below). This simulation was done on a uniform mesh with our second-order accurate EFM code.

VP forming off axis as a consequence of the interaction of the two layers. We believe that in a run at higher resolution, this protruding double structure would continue to escape from the bubble. It should be emphasized, that in a realistic 3-dimensional study, perturbations to axisymmetry will cause the nearby opposite signed rings to reconnect and yield an outgoing array of VPs, e.g. as seen by Lim and Nickell.

Finally in Fig. 3 we see a $M = 10$ shock striking an $\eta = 10$ and 1.5:1 *elliptical* bubble with its semi-major axis tilted by 30 degrees from the horizontal. The bubble interface (obtained from our interface tracker) is shown as the black line on the density (above) and vorticity (below).

In Fig. 3 (t=7.7), the incoming shock has passed the bubble and at its "kink" has a Mach shock which produces a (-/+) VP separating from the interface into regions of very low density on the downstream side of the bubble.

In the last frame (t= 45.9) the bubble is "shredded" or destroyed by the differential strains produced by the vorticity and in the lower region we see two VPs forming, the largest (-,+) at left moving downward and the smaller (+,-) moving to the upper right. Note that the mass within the lower two regions is much larger than the mass associated with the dominant negative vorticity. We conclude that symmetry breaking enhances VP formation. In all cases, the codes are too dissipative to carry our calculations to longer times.

4. Conclusions and discussion

We are familiar with laboratory experiments at $M \leq 2.5$ (Haas and Sturtevant [16] for Freon and He bubbles in air; Bourne and Field [17] for air in gelatin; Yamada, Kodama and Takayama [12] for a He bubble in HOH; and Zerf and Hornung for [18] for HOH bubbles in air) and so our results amount to predictions. Bryson and Gross [19] captured many aspects of the early-time flows with *rigid* cylinders ($M = 2.84$) and spheres ($M = 2.89$). However, although the schlieren and shadowgraphs in these experiments exhibit vortical manifestations, the new phenomena and mechanisms described in this paper have not been previously been advanced. This is due to the difficulty of visualizing vorticity.

We conclude that the intermediate and late time manifestations of jets or strong pressure gradient flows (e.g. shock or blast waves) over inhomogeneities or fluctuations of density are the appearance of coherent vortex structures which we have named "vortical projectiles" or VPs. These projectiles are ring like regions of vorticity and are manifest as "mushroom" structures which could be used to explain "bullets", "explosion fragments" or " cometary knots" observed in the vicinity of supernova remnants [20, 21]. The quantification of the temporal variation of the translational speed, radius and *internal rotational* motion associated with VPs, will allow us to substantiate the conjecture made here as well as provide information about the inner (and remote) state of their sources.

Acknowledgement. The author received helpful advice and comments from J. Hawley, J. P. Hughes and C. R. O'Dell.This work was supported by DOE Grant No. DE-FG0293ER25179 under Dr. Daniel Hitchcock. Computations were done on the CM5 at NCSA and the IBM SP2 at the Cornell Theory Center (CTC), two of the four high performance computing and communication centers supported by the National Science Foundation. Activities of CTC center are also funded by New York State, the Advanced Research Projects Agency, the National Center for Research Resources at the National Institutes of Health, IBM, and other members of CTC's Corporate Partnership Program."

References

[1] Deem GS and Zabusky NJ, Vortex waves: stationary 'V-states,' Interactions, recurrence and breaking, Phys. Rev. Lett., 40:859, (1978).

[2] Couder Y and Basdevant C, Experimental and numerical study of vortex dipoles in two-dimensional flows, J. Fluid Mech., 173, 225-251, (1986).

[3] Chomaz JM, Couder Y and Rabaud M, Physica D37, 384-405, (1989).

[4] Deem GS and Zabusky NJ, Stationary 'V-state,' Interactions, Recurrence and Breaking, Solitons in Action, Proceedings of the Soliton Workshop, Huntsville, Alabama, Academic Press, New York, (1978).

[5] Zabusky NJ and Scheidegger T, Effect of compressibility on vortex dipoles, Phys. Fluids, to be submitted, (1997).

[6] Lim TT and Nickels TB, Instability and reconnection in the head-on collision of two vortex rings, Nature, 357, 225-227, (1992).

[7] Winkler KH, Chalmers JW, Hodson SW, Woodward PR and Zabusky NJ, A Numerical Laboratory, Physics Today, 40, 10, 28-37, October (1987).

[8] Chalmers JW, Hodson SW, Winkler KH, Woodward PR and Zabusky NJ, Shock-bubble interactions: Generation and evolution of vorticity in two-dimensional supersonic flows, Fluid Dynamics Research, 3, 392-394, (1988).

[9] Zabusky NJ, Samtaney R, Yang X, Chern IL and Hawley JR, Vorticity deposition, evolution

and mixing in shocked-density stratified interfaces and bubbles, Proceedings of 18th Int'l Symposium on Shock Waves, (1992).

[10] Klein RI, McKee CF and Colella P, On the hydrodynamic interaction of shock waves with interstellar clouds. I Nonradiative shocks in small clouds, Astrophysical J., 420, 213-236, (1994).

[11] Youngs DL, Numerical simulation of mixing by Rayleigh-Taylor and Richtmyer-Meshkov instabilities, Laser and Particle Beams, 12, 725-750, (1994).

[12] Yamada K, Kodama T and Takayama K, Mechanisms of shock wave generation resulting from the interaction between a shock wave and a gas bubble in a liquid, Proceedings of 20th Int. Symposium on Shock Waves, Pasadena, CA, 1, 569-574, Editors B. Sturtevant,J. E. Shepherd and H. Hornung, World Scientific, Singapore, (1996).

[13] Muller E, Fryxell B and Arnett D, Instability and clumping in SN 1987a, Astronomy and Astrophysics, 251, 505-514, (1991).

[14] Klein RI, Stone JM, Mac Low M, McKee CF and Norman ML, Shock interactions with magnetized interstellar clouds. 1/ Steady shocks hitting nonradiative clouds, Astrophysical J., 433, 757-777, (1994).

[15] Zeng S and Zabusky NJ, Shock implosion morphologies and vorticity ring generation in shock-spherical axisymmetric bubble F/S interactions, J. Fluid. Mech., in press, (1998).

[16] Haas JF and Sturtevant B, Interaction of weak shock waves with cylindrical and spherical gas inhomogeneities, J.Fluid Mech., 181, 41-76, (1987).

[17] Bourne NK and Field JE, Shock-induced collapse of single cavities in liquids, J. Fluid. Mech., 244, 225-240, (1992).

[18] Zerf G and Hornung K, Complex droplet deformation-and breakup-modes at intermediate Weber numbers from laser holography, Proceedings of 20th Int. Symposium on Shock Waves, (1996).

[19] Bryson AE and Gross RWF, Diffraction of strong shocks by cones, cylinders and spheres, J. Fluid Mech., 19, 1-16, (1961).

[20] Egger R, Aschenbach B and Trumper J, Discovery of explosion fragments outside the Vela supernova remnant shock-wave boundary, Nature, 373, 587-590, (1995).

[21] Strom R, Johnston HM, Verbunt F and Aschenbach B, A radio-emitting X-ray bullet ejected by the Vela supernonva, Nature, 373, 590-592, (1995).

[22] Pullin DI. Direct simulation methods for compressible ideal gas flow, J. Comp.Phys., 34, 231, (1980).

[23] Samtaney R, Computational methods for self–similar solutions of the compressible Euler equations, J. Comp Phys., 132, 327-345, (1997).

Investigation of Rayleigh-Taylor Instability on an Interface Between Two Gases

S.G. Zaytsev, E.I. Chebotareva, S.N. Titov and V.V. Krivets
Krzhizhanovsky Power Engineering Institute (ENIN)
Leninsky pr. 19, Moscow, 117071, Russia

Abstract: In the present study, we performed an experimental investigation of parameters around the continuous interface during the accelerated motion (up to $g \simeq 10^7$ cm·s^{-1}). The represented data include the continuation of the studies of linear stage of RTI started in [1], and also the investigations of nonlinear, transitional and early turbulent stages.

1. Experimental set-up and wave diagram of the process

The experimental set-up is a vertical channel of 72×72 mm^2 cross-section connected to the test-section of the same cross-section. The side walls of the test-section have optical glasses to visualize the process under investigation. The test-section is equipped with a 2 mm metal plate P, inserted to separate the top and bottom parts of the channel prior to experiment. Both top and bottom parts of the channel are closed with flanges. The top part of the channel is filled with oxygen-hydrogen mixture (molecular weight 18.5), and the bottom part is filled with one of inert gases (He, Ne, Ar, Kr, Xe) or SF_6. Prior to experiment, both parts of the channel are simultaneously pumped out to 10^{-2} torr. Then, these spaces are filled with the gases indicated above. Prior to experiment, the pressures p_0 in both spaces are set strictly the same and equal to 0.5 at. The plate P is removed from the channel by a spring mechanism. The total time of plate removal is varied within 40-150 ms. During the removal of the plate P, the initial interface K_0 between oxygen-hydrogen mixture A_0 and gas B_0 is formed. After the plate P is completely removed from the channel, the mixture A_0 is ignited in the top part. Ahead of the flame front F, the compression wave C_{0a} is generated which imparts the acceleration to the interface K_0. The process was recorded by Mach-Zehnder interferometer. The plate P was removed from the channel towards y axis. Figure 1 gives an x,t-diagram for the motions of the flame front F,

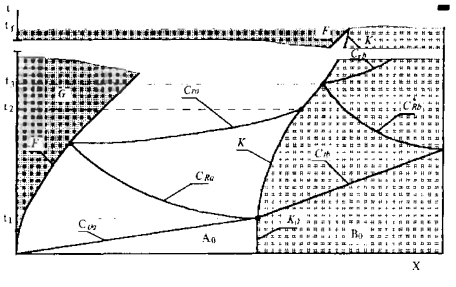

Figure 1. x, t - diagram. F - the front of flame; C_{0a} - the head front of compression wave; K_0 - initial interface; C_{Ra}, C_{tb} - the reflected and refracted compression waves; C_{ra} and C_{rb} - rarefaction waves; C_{Rb}^* - the compression wave reflected from the bottom flange; K - interface; G - the region filled with the products of burning; A_0 - initial oxygen-hydrogen mixture; B_0 - inert gas or SF_6.

nonstationary compression waves C_{0a}, C_{tb}, the interface , etc. Here, x = 0 is matched with the point of the flame initiation. The head front of the compression wave C_{0a} is generated by the flame front F. C_{0a}, reaching K_0 at the time t = t_1, generates the refracted (C_{tb}) and reflected

More information - Email: sgz@mazilin.msk.ru

(C_{Ra}) compression waves and entraps the interface K into accelerated motion. Parameters of the "pure" gases around K are dependent of the characteristics of nonstationary compression waves C_{Ra} and C_{tb}. The interaction of compression wave C_{Ra} with the flame front F results in generation of the reflected rarefaction wave C_{ra} traveling in gas A_0. Interaction of this wave with K at t=t_2 decelerates the latter. The strongest deceleration of K is observed when K interacts with the compression wave reflected from the bottom flange, C_{Rb}^* at t = t_3. The deceleration of K must be accompanied by stratification of the interface. The interaction of the flow A with K is ended at t = t_f.

The experimental set-up and the properties of initial continuous interface were discussed in [1]. The scheme of interface, denotations of its characteristic points and measured parameters are given in Fig. 2 and in relations (1) and (2). Here λ is the wavelength; a_{K_i} is the perturbation amplitude; L_{K_i} is the depth of penetration of one gas into the other for the considered perturbation; S_i is the distance passed by the median of perturbation; $\delta_i(y)$ is the thickness of interface:

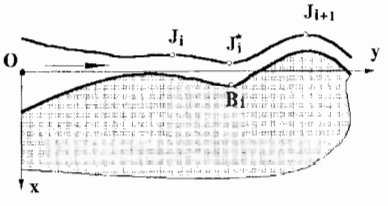

Figure 2. A sketch of initial interface. J_i, J_i^*, J_{i+1}, B_i are positions of characteristic points on the fronts separating the mixing zone from gases A_0 and B_0.

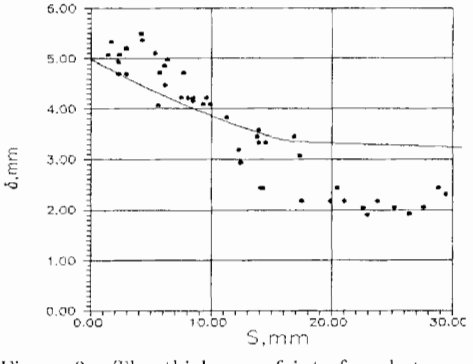

Figure 3. The thickness of interface between oxygen-hydrogen mixture and Xe plotted against the distance passed. Solid line represents the data of one-dimensional calculation.

$$\lambda_i = y(J_{i+1}) - y(J_i); a_{K_i} = x(J_i^*) - x(J_i); L_{K_i} = x(B_i) - x(J_i); \quad (1)$$

$$S_i = 0.5 \cdot x(B_i) + 0.25 \cdot [x(J_{i+1}) + x(J_i)]; \delta_i(y) = x(B_i) - x(J_i^*). \quad (2)$$

Let us note the following properties of the resulting interfaces: the density distribution inside the interface coincides with that calculated using the model of molecular diffusion; the wavelengths of observed perturbations increase with decreasing gas density in bottom part of the channel. Table 1 gives the values of $\bar{\lambda} = \frac{\sum_i^N \lambda_i}{N}$ for gases B_0, used in the present study (p_0 = 0.5 at, the time of plate removal $\sim$ 100 ms).

Table 1. Values of $\bar{\lambda}$ (mm) for the perturbations on the front of continuous interface measured on the side of gas A_0.

B_0	He	Ne	Ar	Kr	Xe	SF_6
$\bar{\lambda}$	20±2	-	15±2	12±2	9±2	6±2

The absolute error for the measurements of the amplitude a_{K_i}, the depth of penetration L_{K_i}, and the wavelength is ± 0.3 mm.

2. Results of experiment

2.1. Compressibility

We have measured the change in thickness δ of the interface during its motion along the visualization field. The measurements were performed in a specified cross-section y_i. Fig. 3 gives the values of δ measured in xenon. In the section $x < 20$ mm, the value of $\delta(y_i)$ decreases by 50%. Solid line in Fig. 3 corresponds to the data calculated by 1D model of the process, on the assumption that initial interface is a layer with diffuse density distribution.

2.2. Linear stage of RTI

To obtain the quantitative information on the evolution of RTI at linear stage, we chose the perturbations with the smallest amplitudes. This allowed us to make enough measurements before we observed the signs of distortions in the shape of perturbation indicating to the start of spike formation. Two sections corresponding to the different change rates of perturbation amplitude may be distinguished. In the first section, $a_{K_i} < \lambda/2$, the experimentally measured values of $a_{K_i}(\sqrt{2S})$ are satisfactorily approximated by the relation

$$a_{K_i}(\sqrt{2S}) = a_{K_i}^{(0)} \exp(W\sqrt{2S}).$$

In the second section, the growth rate of a_{K_i} is markedly decreased. The values of perturbation amplitude growth rates W measured on the border between the mixing zone and the light gas (a_{K_i}), are given in Table 2. The experimental data are compared to the data calculated by the relation suggested by Taylor [2]:

$$a_{K_i} = a_{K_0} \exp(W_T\sqrt{2S}), \text{ where } W_T = \sqrt{At \cdot k}, k = \frac{2\pi}{\lambda}.$$

This relation assumes the discontinuous change in density on the interface and the noncompressibility of media. The area of applicability of the relation is restricted to $a_{K_i} < 0.4\lambda$ [3]. Table 2 represents the data calculated by the relation suggested in [4]. Here,

$$a_{K_i} = a_{K_0} \exp(W_D\sqrt{2S}), \text{ where } W_D = \sqrt{\frac{At \cdot k}{\Psi(\delta, At)}}.$$

The function $\Psi(\delta, At)$ is calculated numerically. This relation allows us to estimate the effect of replacement of the discontinuous interface, for which Ψ=1, for the continuous interface of thickness δ. The density distribution on continuous interface depends on molecular diffusion. The theory suggested in [4] assumes that the media under consideration are noncompressible.

Table 2. The values of perturbation amplitude growth rates W, W_T, W_D for the linear stage of RTI.

Run No.	$\mathbf{B_0}$	λ, mm	δ_0, mm	$\mathbf{W}_T$	$\mathbf{W}_D$	**W**
400A	Ar	14	8	.407	.206	.183
402A	Ar	15	6	.391	.225	.172
585A	Kr	14	3	.540	.381	.120
584A	Xe	8.3	5	.755	.401	.278
584A	Xe	6.5	1.5	.879	.646	.370

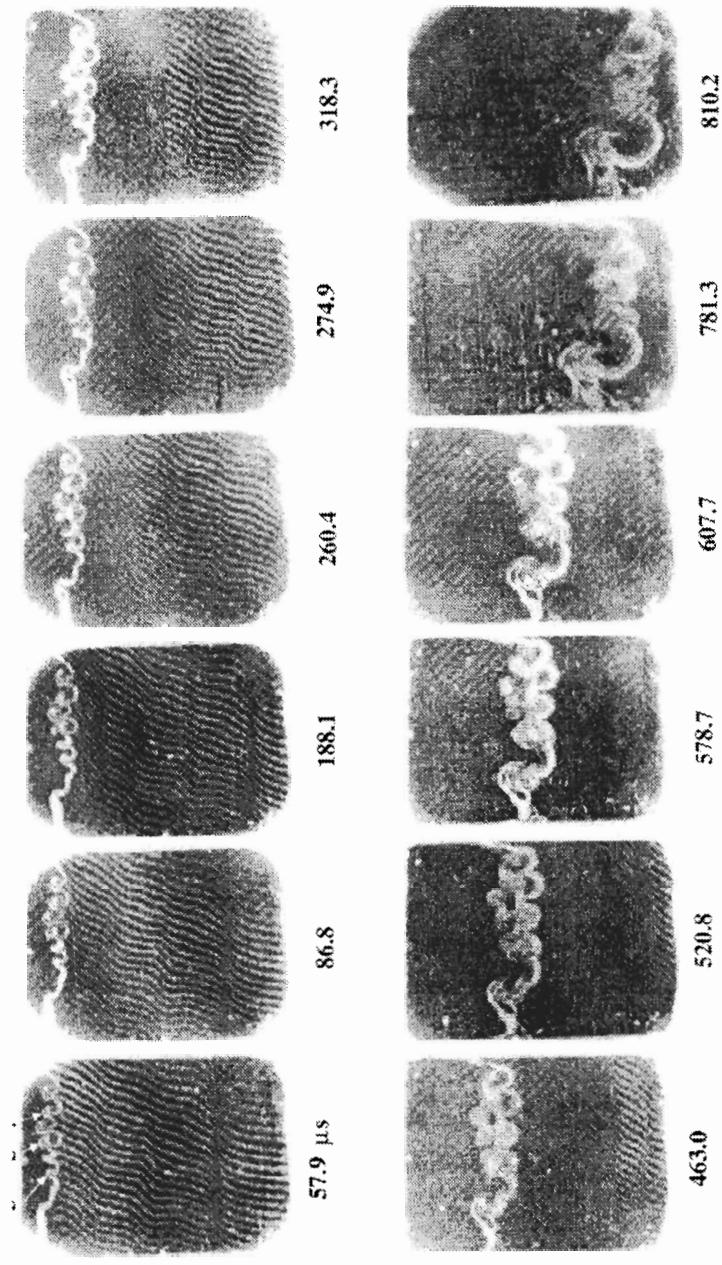

Figure 4. Evolution of Rayleigh-Taylor instability on the continuous interface between oxygen-hydrogen mixture and SF_6.

2.3. Nonlinear and transitional stages of RTI

Figure 4 gives a series of interferograms showing the motion of continuous interface K between oxygen-hydrogen mixture and SF_6. These interferograms demonstrate the evolution of RTI at nonlinear and transitional stages. Over the frames, the values of time τ_1 are given. The τ_1 is counted off the time of recording of the first frame. A characteristic feature of the interferograms in Fig. 4 is the absence of interference bands in certain sections, due to the strong refraction in SF_6 in the sections of interferograms corresponding to large shifts of interference bands. Because we used non-monochromatic light beam, in the resulting picture the bands overlapped each other. The shift of interference bands observed in Fig. 4 below K_1 was caused by a density change in the refracted compression wave C_{tb} traveling in SF_6. As seen, C_{tb} consists of several approximately plane fronts. During the motion, the following fronts overtake the preceding ones. We measured the depth of penetration of one gas into the other for the perturbations whose evolution proceeds through nonlinear and transitional stages. Figure 5 gives the values

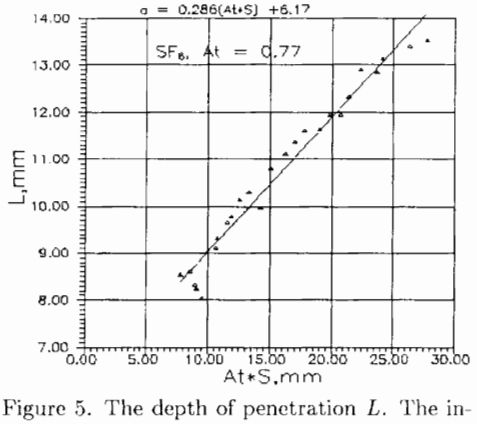

Figure 5. The depth of penetration L. The interface separates the oxygen-hydrogen mixture from SF_6. p_0=0.5 at; $g = 1.3 \cdot 10^7$ cm/s^2.

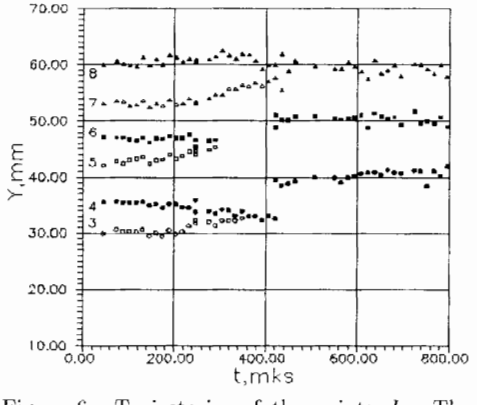

Figure 6. Trajectories of the points J_i. The numbers of configurations correspond to the numbers of points in Fig. 4.

of L_i for a selected perturbation. These values are given as the function $At \cdot S$, where $At=(\rho_2 - \rho_1)(\rho_2 + \rho_1)^{-1}$ is the Atwood number, and S is the distance passed by the median of selected perturbation.

2.4. Development of the vortex structures of second generation

Figure 6 gives the trajectories of characteristic points for several perturbations in y,t plane. The denotations for these points are given in Fig. 4. As seen, the perturbations do not shift along y axis at the initial stage of evolution. At the following stage, after vortex structures have been formed, we can observe the shifts which result in fusion of adjacent vortex structures and thus in formation of a new vortex structure. Later, a part of thus formed structure tears off to be "dissolved" in gas A. In the site of fusion of two first-generation vortex structures, a new second-generation vortex structure is formed. Significant vagueness of the boundaries of the vortex structure does not allow the reliable determination of the depth of penetration in this site. A qualitatively similar scenario of the early formation of vortex structures was observed in xenon, though here this process occurred later than in SF_6, when the interface approached the bottom border of the visualization field. Because of that, the end of the process of fusion of vortex structures was not recorded.

3. Conclusions

We have performed an experimental investigation of Rayleigh-Taylor instability in a continuous interface between accelerated gas flows of different density. The acceleration (up to $2 \cdot 10^7$ cm·s^{-2}) is imparted by the non-stationary compression wave. It has been shown that at the initial linear stage of evolution of continuous interface, the amplitude a_K, of the perturbation on the front separating the interface from light gas grows exponentially as a function of $\sqrt{2S}$, where S is the distance passed by continuous interface. At this stage, the growth of amplitude a_K is determined by the relation $a_K = a_0 \exp(W \cdot \sqrt{2S})$, for $a_K < 0.5\lambda$. The values W are 2-3-fold lower than the values obtained from the relation of Taylor [2] and by 10-70% lower than those obtained using the model suggested in [4] for the evolution of continuous interface in noncompressible media. For $a_K(t) > 0.5\lambda$, the shape of continuous interface changes. The sections corresponding to the penetration of the heavy medium into the light one, transform into spikes narrowing with time. The sections corresponding to the penetration of the light medium into the heavy one, transform into expanding bubbles. Later, the first-generation vortex structures of characteristic mushroom shape are formed on the tips of spikes. This corresponds to nonlinear and transitional stages of RTI. At these stages of RTI evolution, the depth of penetration L of one gas into the other is approximated by the relation $L \sim \alpha \cdot At \cdot S$, where S is the distance passed by the interface, At is the Atwood number, and the growth rate of the depth of penetration is approximately two-fold higher than that for the turbulent stage of mixing in accelerated noncompressible media [5, 6]. Later, we observe the vortex structures fusing in pairs and formation of the second-generation vortex structures.

Acknowledgement. We are grateful to Dr. Roger Chéret and Dr. Jean-François Haas for the useful comments made during the discussion of the work in the Centre d'Etudes de Vaujours-Moronvilliers. This study was supported by International Science and Technology Center, project No. 029-94, and Russian Foundation for Fundamental Investigations, project No. 96-01-01295.

References

[1] Zaytsev SG, Chebotareva EI, Titov SN, Rozanov VB and Lebo IG, The influence of interface on the evolution of Rayleigh-Taylor instability, Pis'ma v Zh. Eksp. i Tekh. Fiz., 15, 13, 33-36, (1989).

[2] Sir Geofrey Taylor FRS, The instability of liquid surfaces when accelerated in a direction perpendicular to their planes, Proc. of the Royal Society, Series A., 1065, 201, 192-196, (1950).

[3] Lewis DJ, The instability of liquid surfaces when accelerated in a direction perpendicular to their planes, Proc. of the Royal Society, Series A, 1068, 202, 81-96, (1950).

[4] Duff RE, Harlow FH and Hirt CW, Effects of diffusion on interface instability between gases, Phys. Fluids., 5, 4, 417-425, (1962).

[5] Youngs DL, Experimental investigation of turbulent mixing by Rayleigh-Taylor instability, Advances in compressible turbulent mixing, Eds. Dannevik WP, Buckingham AC, and Leith CE, January 1, 607-626, (1992).

[6] Kucherenko YuA, Tomashchev GG and Shibarshov LI, Experimental investigation of gravitational turbulent mixing in automodel regime, Problems of nuclear science and technology, Series: Theoretical and applied physics, 1, 13-19, (1988).

Cavity Collapse and Vortex Projectiles in Shock-Spherical Cloud at High Mach Number Interactions

S. Zeng and N.J. Zabusky
Dept. of Mech. & Aero Eng., P.O. Box 909
Rutgers University, Piscataway, NJ-08855-0909, USA

Abstract: In this paper, a comprehensive numerical study of the hydrodynamic evolution of an axisymmetric spherical cloud embedded in a less dense uniform ambient medium when struck by a strong planar shock wave is carried out. We visualize and quantify the shock implosion morphologies and the vorticity generation. We show how "double Mach reflection" generated by the downstream collision of the incident shocks evolves into a configuration of "triple Mach reflection" due to the supersonic ring generation at the Mach disk. Moreover, "vortex projectiles" arise from the binding of opposite-signed vorticity on the downstream side of the bubble.

1. Introduction

The development of supernova remnants(SNR) as a result of shock wave interactions affects galactic evolution. By a passage of strong shocks, interstellar clouds and intercloud medium may be disrupted by hydrodynamical instabilities, e.g. shock generates a Richtmyer-Meshkov(RM) instability. During the interaction, large "fingers" or coherent "mushrooms" arise which carry "fragments" away from the clouds and mix them with the interstellar medium. Our work elaborates and extends the work of [1, 2, 3].

As shown in Fig. 1, a vortex projectile is a localized region of positive and negative circulation whose centroid rotates about a point O that is remote from the configuration. For example the rectilinear pair of line vortices in 2-dimensions of circulation $\Gamma_1 > 0$ and $\Gamma_2 < 0$, separated by a distance, d, which has a velocity w about a point O with a distance of R from the centroid. If $|\Gamma_1| = |\Gamma_2|$, the centroid is midway between them and they translate with a velocity $w = \frac{\Gamma}{2\pi d}$ with $R = \infty$. The evolution of coherent ring-like vortex structures (CVS) yield a host of shock and vortex configurations. These small vortex dimples (or knots) which arise near density stratified interfaces or jets may disintegrate into small CVS, escape from the original source and become "vortex projectiles" (VP).

2. Description of the physical problem

We model multicomponent flows using the compressible Euler equations augmented by a requisite two species equations in a 2-dimensional axisymmetric representation. We use ρ, p, E, $H = \frac{(E+p)}{\rho}$, u and v to denote the density, the pressure, the total energy per unit volume, the total enthalpy per unit mass, and the velocity in both x and r directions, respectively. e denotes the internal energy per unit mass. In the case of ideal gas, $e = \frac{p}{\rho(\gamma-1)}$. In this notation, the governing equations in conservative form are

More information - Email: szeng@caip.rutgers.edu

$$\mathbf{U}_t + \mathbf{F}(\mathbf{U})_x + \mathbf{G}(\mathbf{U})_r + \frac{1}{x}\mathbf{W}(U) = 0 \tag{1}$$

The effective specific heat ratio is

$$\gamma = \frac{\frac{\gamma_a \rho_a}{m_a(\gamma_a - 1)} + \frac{\gamma_c \rho_c}{m_c(\gamma_c - 1)}}{\frac{\rho_a}{m_a(\gamma_a - 1)} + \frac{\rho_c}{m_c(\gamma_c - 1)}}. \tag{2}$$

Here m_i is the molecular weight, R_i is the gas constant and γ_i is the specific heat for both intercloud medium and cloud gases.

The computational domain considered in the present work is illustrated in Fig. 1, where the base flow field consists of a spherical cloud region and an ambient medium region. For an idea case, we assume that the ratio of specific heat, $\gamma = \frac{5}{3}$, for both cloud and ICM. The density ratio is $\eta = 10$. We drive the system with a planar shock wave of Mach numbers: 1.5, 3.0, 10 and 40. We define the time that takes for the incident shock to traverse the half of the cloud interface as a time scale $t_c = \frac{r_0}{v_a}$ where v_a is the shock speed in the the ambient intercloud medium. The mesh resolution is 903×303 zones and the radius of the bubble is 120 zones. At t=0, the shock is 40 zones to the left of the cloud. The thickness of the shock front and cloud gradient in the interface is two zones.

We solve the time-dependent two-dimensional axisymmetric two species Euler equations (1) by utilize the Harter-Yee type upwind TVD (Total Variation Diminishing) scheme. A more detail description on our numerical scheme can be found in[4, 5].

3. Visualization and results discussion

The numerical shadowgraph, $\Delta\rho$, is used to juxtapose contact discontinuities and shock fronts for numerical visualization. The numerical shadowgraph for a planar shock is shown in Fig. 3 for early time during which the shocks crosses over the cloud interface.

In Fig. 3(a), all three shock waves, the incident, I, reflected, R, and transmitted, T, meet at a node, which is the well known Regular Reflected type refraction. At the node where the incident shock meets the transmitted shock on the interface, the pressure attains its minimum value. Thereby an expansion wave occurs at the corner between incident shock and the interface, decreasing the strength of the incident shock and making it bend upstream. The phenomenon can be seen in Fig. 3(b). When the incident shock is at the apex of the cloud, the shock configuration is Mach reflection type of refraction, where a Mach stem, M_0, rises on the interface.

After crossing over the apex, the shock is diffracted and curved back to meet the interface (Fig. 3(c)). The downstream side of the cloud interface requires a deceleration of the flow which is generated by an almost normal shock on the interface. The upstream traveling expansion wave accelerates the gas around the region of the diffracting apex, and the flow behind the shock can become subsonic or supersonic depending on the strength of the incident shock.

We now study the cavity implosion phenomenon and downstream coherent shock configurations. When the fast moving incident shock (I) touches the axis on the downstream side of the cloud, two curved incoming shock waves collide on downstream side of the cloud. It generates a reflected shock (rI) from the axis. The sequence frames of divergence, div **u**, is shown in Fig. 4. In Fig. 4(a) here T and diT are the transmitted shock and its downstream component, separated by a sharp kink, from which the corner shock (cS) emanate. The corner shock interaction with the cloud interface, creates the secondary positive vorticity. The cavity collapse

cavity occurs in Fig. 4(b), where a "hexabasic point" F associate with the three shocks, T, diT, and rI, focusing inside of the cloud. The second dominating feature in Fig. 4(a, b) is the strong vortex roll-up at the downstream side of the cloud. The downstream moving shocks are generated in this region indicated by the wave front, "DS", in Fig. 4. Kelvin-Helmholtz(KH) instability develops on the backside of the clouds induced by the interaction between reflected and diffracted shock. The shock interaction results the laminar or turbulent boundary layer along the interface and a local flow separation.

Fig. 4(c) shows that the cavity implosion develops a significant "secondary shock" (sS), which propagates towards the downstream side and interacts with the perturbed vortex region near the interface. This "secondary shock" is the major effect on the evolution of the vortex mushroom (or R-T fingers) and the "escaped of vortex projectiles" as discussed below.

Due to the rapid formation of vorticity in the region of the Mach disk and the interaction between reflected shock with Mach stem, MS_1, the flow in the region of the Mach disk is accelerated. The Mach number in the the region at the vortex dipole, MS_2, may becomes greater than that on the Mach stem, MS_1. In this case, a shock interaction occurs between these two Mach shocks. The shock configuration in the Triple Mach Reflection region is illustrated in Fig. 5, which consists of : three triple-points (TP1, TP2 and TP3); Mach stems (MS_1, MS_2, andMS_3); reflected shocks(R1, R2, and R3); and slip layers(S_1, S_2, and S_3). Since the Mach shock MS_3 is generated by the axial vortex projectile, the strength of MS_3 will decrease with vorticity diffusion.

The time and the magnitude of the maximum pressure arising inside the cloud during the cavity implosion are shown in Fig. 6 for different Mach number, M=10 and M=40. If we assume that the cavity collision is an incident shock reflected at axis in the cloud; the ratio between pressure behind the reflected shock, p_3, and pressure behind the transmitted shock, p_2, can be written as follows according to the shock relationship

$$\frac{p_3}{p_2} = \frac{(3\gamma-1)M^2 - 2(\gamma-1)}{(\gamma-1)M^2+2} = \frac{(1+2\mu)(\frac{p_2}{p_1}) - \mu}{\mu(\frac{p_2}{p_1})+1} \tag{3}$$

Here $\mu = \frac{\gamma-1}{\gamma+1}$, the subscriptions 1, 2, and 3 indicate the states at in front of the shock, behind and in front of the transmitted shock in the cloud. According to (3), if the incident shock is strong enough so that we can assume that $\frac{p_2}{p_1} \to \infty$, the approximate expression for the maximum value in the cloud can be written as

$$(\frac{p_3}{p_2})_{max} = 2 + \frac{1}{\mu} = \frac{3\gamma-1}{\gamma-1} \tag{4}$$

In case $\gamma = \frac{5}{3}$, the maximum pressure is about 6 times higher than the pressure behind the transmitted shock when the shock cavity implode in the cloud (see Fig. 6).

4. Vorticity deposition and R-T instability

The vorticity deposition is the dominant fluid dynamical process during the interaction between a shock wave and a density-stratified interface, which results in the "Reyleight-Taylor" or the "Richtmyer-Meshkov" instability. The physical phenomena of the vorticity generation on the cloud can be considered as three distinct phases: the vorticity deposition phase (i) while the shock strikes the density inhomogeneity, which produces a layer of negative vorticity due to baroclinic effects; the vorticity (or positive vorticity) accelerated generation phase (ii): the

generation of the positive vorticity is associated with reflected incident shock on axis and secondary shock interaction which generated by the cavity implosion in the cloud; the vorticity evolution phase (iii): coupled with secondary baroclinic effects, which drive the flow after the primary incident shock leaves the interface.

In Fig. 3(a), a negative vorticity layer is deposited along the cloud interface. Fig. 3(c) and (d) show that, after the incident shock moves over the top of the bubble it curves back to meet the interface causing by an expansion wave to be generated around the back side of the interface. The interaction between reflected shock and diffracted shock on the downstream side of the cloud takes an very important role on the vorticity generation. It will no doubt for strong incident shock develop into vortex structures in this region, leading to turbulent mixing.

The Phase (ii) is started at time while the incident shock touches to the axis on the downstream side of the cloud. the reflected incident shock induce to positive vorticity to be accelerated generation. In Fig. 7 we show vorticity /density sequence images starting at phase(ii) for Mach shock, M=40. These positive vorticity generation can be explained by (1) the interaction between the reflected incident shock on the axis and the density inhomogeneities; (2) the secondary shock which is associated with shock cavity implosion strikes the interface from the inside of the cloud; (3) the shock interaction on the region of the Mach disk where a vortex dipole occurs.

Next to the phase (iii), we also see the vorticity evolution in Fig. 7 from (b) to (d). In Fig. 7 (a) the region of downstream vortex is developed as the incident shock passes over on the downside of the cloud. The vortex shear layer on the region of the Mach disk moves in r-direction accompany with the vorticity diffusing. In front of the interface, the vortex layer develops a weak perturbation causing strong "Kelvin-Helmholtz" instability. It rolls-up and merges with other vortex rings on the apex of the cloud with the vortex evolution. The smaller vortex ring has already developed into a mushroom on the front side of the interface which is shown in Fig. 7(c).

In Fig. 7(c) and (d) we see clearly to the phenomenon of escaped of vortex projectile. The formation of vortex projectiles is due to several effects. The dominant effect arises from the binding of parts of the original primary (-) and secondary (+) circulations near the apex of the bubble. (The latter is deposited by the downstream r-directed secondary shock (sS)). The binding is enhanced by the dominant negative circulation region which separates from the downstream bubble. Smaller projectiles arise from other binding processes.

These "vortex projectiles" (VP) may help interpret the so called "knot-like objects" seen in astrophysics that have escaped from their source of the origin.

5. Conclusions

The incident shock is diffracted after it passes the apex of the cloud. The interaction between interior transmitted shock and downstream the axial-reflected incident shock affects the collapsing cavity. An axial supersonic vortex ring emerges from the axial Mach disk which arises from collision of shocks on the downstream side of the cloud. The generation of "vortex projectiles" arises from several effects on the downstream side of the bubble. Ejected "mushroom" consist of two adjacent eddies which have opposite signs of circulation.

Acknowledgement. This work has been made possible by the continuing support of a grant from: DOE (Grant N° DE-FG0293ER25179.A000) monitored by Dr. Daniel Hitchcock.

References

[1] Winkler KH, Chalmers JW, Hodson SW, Woodward PR and Zabusky NJ, Physics Today, 40, 10, 28-37, (1987).
[2] Bedogni R and Woodward PR, A&A, 231, 481, (1990).
[3] Klein RI, McKee CF and Colella P, Astrophysical J., 420, 213-236, (1994).
[4] Roe PL, J. Comp. Phys., 43, 357-372, (1981).
[5] Zeng SM and Gralter W, Int. J. Engineering Research, 61, 11/12, 304-315, (1995).

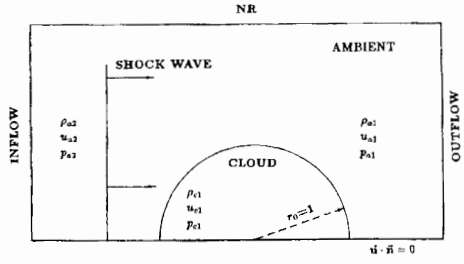

Figure 1. Initial and boundary conditions for the shocked-cloud interaction.

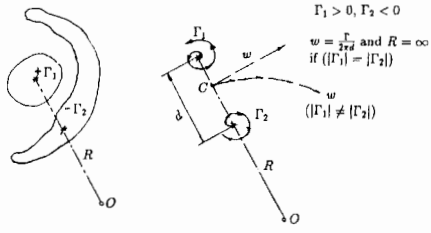

Figure 2. Schematic of vortex projectile.

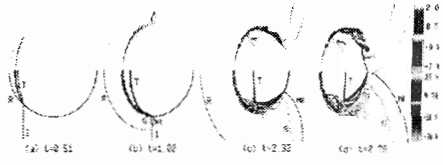

Figure 3. Vorticity/Numerical shadowgraph, $\Delta\rho$, for shock refraction on the cloud interface at initial time.

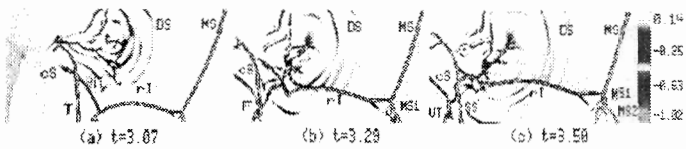

Figure 4. $\nabla \cdot \vec{u}$ patterns for shock cavity implosion.

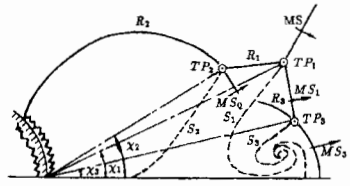

Figure 5. Configuration of "Triple Mach reflection".

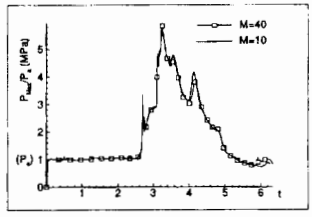

Figure 6. Maximum magnitudes of Pressures in Megapascal normalized time t/t_c.

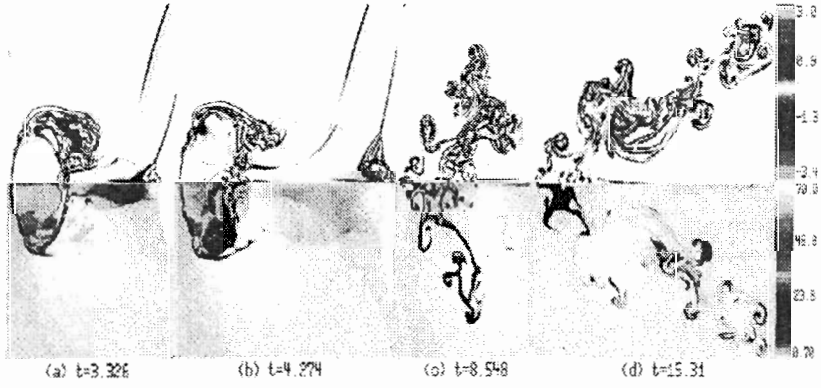

Figure 7. Vorticity/Density sequence images for Mach shock, M=40, at later time.

A Numerical Study of the Richtmyer Meshkov Instability in Cylindrical Geometry

Q. Zhang[1] **and M.J. Graham**[2]
[1]University at Stony Brook, Department of Applied Math and Statistics
Stony Brook, New York 11794–3600, USA
[2]Department of Mathematical Sciences, United States Military Academy
West Point, New York 10996-1786, USA

Abstract: Theoretical and numerical studies of the Richtmyer-Meshkov (RM) instability are mainly performed in plane geometry. In most physical applications–such as, Inertial Confinement Fusion and in Supernova–the RM instability occurs in curved geometry. We present a numerical study of the RM instability in cylindrical geometry. Unstable finger growth driven by shock waves of various Mach numbers is studied. A scaling law for material interfaces driven by strong shocks is identified.

1. Introduction

Richtmyer-Meshkov (RM) instabilities play an important role in the studies of Inertial Confinement Fusion and Supernova. In both of these applications, the instability occurs in spherical geometry. Numerical simulation of the RM instability in spherical geometry is computationally very expensive, if it is possible at all. Here we present a numerical study of the Richtmyer-Meshkov instability in cylindrical geometry. Early work on RM instabilities can be found in and traced from [1].

Curved geometry complicates the system considerably. For example, the unperturbed system does not have an analytical solution, while the unperturbed system in plane geometry does. The occurrence of re-acceleration or reshock of the material interface caused by the waves reflecting back from the origin is unavoidable in curved geometry. In plane geometry, one needs only to distinguish between the cases of the incident shock colliding with the material interace from the light and heavy fluid phase, while in curved geometry, one needs further to distinguish between the cases of an exploding shock and an imploding shock. In plane geometry, there are two classes of RM unstable systems: a shock wave collides with the material interface from the light fluid phase to the heavy fluid phase and vice versa. In curved geometry, there are four classes. The first class is a shock wave exploding from light fluid to heavy fluid (light-exploding-heavy). The second class is a shock wave imploding from light fluid to heavy fluid (light-imploding-heavy). The third class is a shock wave exploding from heavy fluid to light fluid (heavy-exploding-light). The fourth class is a shock wave imploding from heavy fluid to light fluid (heavy-imploding-light). These four classes are sketched in Figures 1(a)-(d), respectively. This classification can also be used for the RM instability in spherical geometry. In Figure 1, as well as in other figures, only the results in the first quadrant are shown. For all numerical results shown in this paper, the light fluid is Air, and the heavy fluid is SF_6.

More information - Email: zhang@ams.sunysb.edu or mjgraham@arl.mil

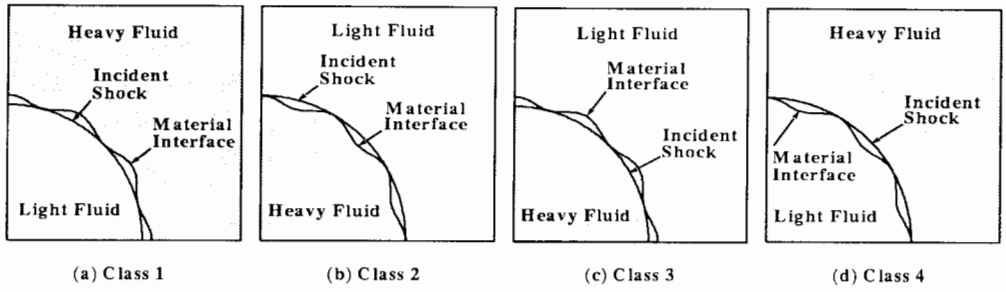

Figure 1. A classification of RM unstable systems in curved geometry. (a) Class 1: an incident shock propagates outward from the light fluid toward the heavy fluid, (light-exploding-heavy). (b) Class 2: an incident shock propagates inward from the light fluid toward the heavy fluid, (light-imploding-heavy). (c) Class 3: an incident shock propagates outward from the heavy fluid toward the light fluid, (heavy-exploding-light). (b) Class 4: an incident shock propagates inward from the heavy fluid toward the light fluid, (heavy-imploding-light).

2. General features

The general features of the development of the RM interface in cylindrical geometry are explained and shown in Figure 2 for Class 2. When an incident shock collides with the material interface, it bifurcates into a transmitted shock (TS) and a reflected wave (see the upper left frame of Figure 2). This is the bifurcation stage, or the shock–contact interaction stage. In this case the reflected wave is a shock (RS). Depending on the material properties of the fluids across the material interface and the incident shock strength, the reflected wave can be either a shock or a rarefaction wave. For the majority of real gases, the criterion is that when the shock collides with the material interface from the light fluid phase to the heavy fluid phase, the reflected wave is a shock; otherwise, it is a rarefaction wave. Here heavy and light are measured in terms of acoustic impedance, ρc, where ρ is the density of a fluid and c is the speed of sound. A more general theory on the reflected wave type can been found in [2]. At the end of the interaction stage, both the TS and the reflected wave detach from the material interface. One wave propagates away from the center (or origin); and for an open space, the outgoing wave will not interact with the material interface again. The other wave propagates toward the center (or origin). Accelerated by the incident shock, the material interface becomes unstable and fingers grow to form spikes of heavy fluid and bubbles of light fluid. In the upper right frame of Figure 2, the RS has exited the computational domain, and the TS is about to enter the origin. Later, the wave which moved toward the center reflects back from the origin. As the reflected wave propagates from the origin, it collides with the material interface again, which is known as reshock (see the lower left frame of Figure 2). A second bifurcation occurs. Thus, the occurrence of reshock is unavoidable in curved geometry. It can be seen in the lower left frame of Figure 2 that the bounced–from–the–origin TS is nestled between the peaks, and the reflected rarefaction (RR) is forming and beginning to move toward the origin. The reflected wave is a rarefaction in this case since the bounced shock was traveling through a heavy fluid to a light fluid. During the reshock, the shock wave travels from the heavy fluid to the light fluid for Class 2 shown in Figure 2. This causes a phase inversion at the material interface–namely, the portion of fluid in one region which appears in the figure as valleys (and are bubbles of light fluid) and the other portion of fluid which appears in the figure as peaks

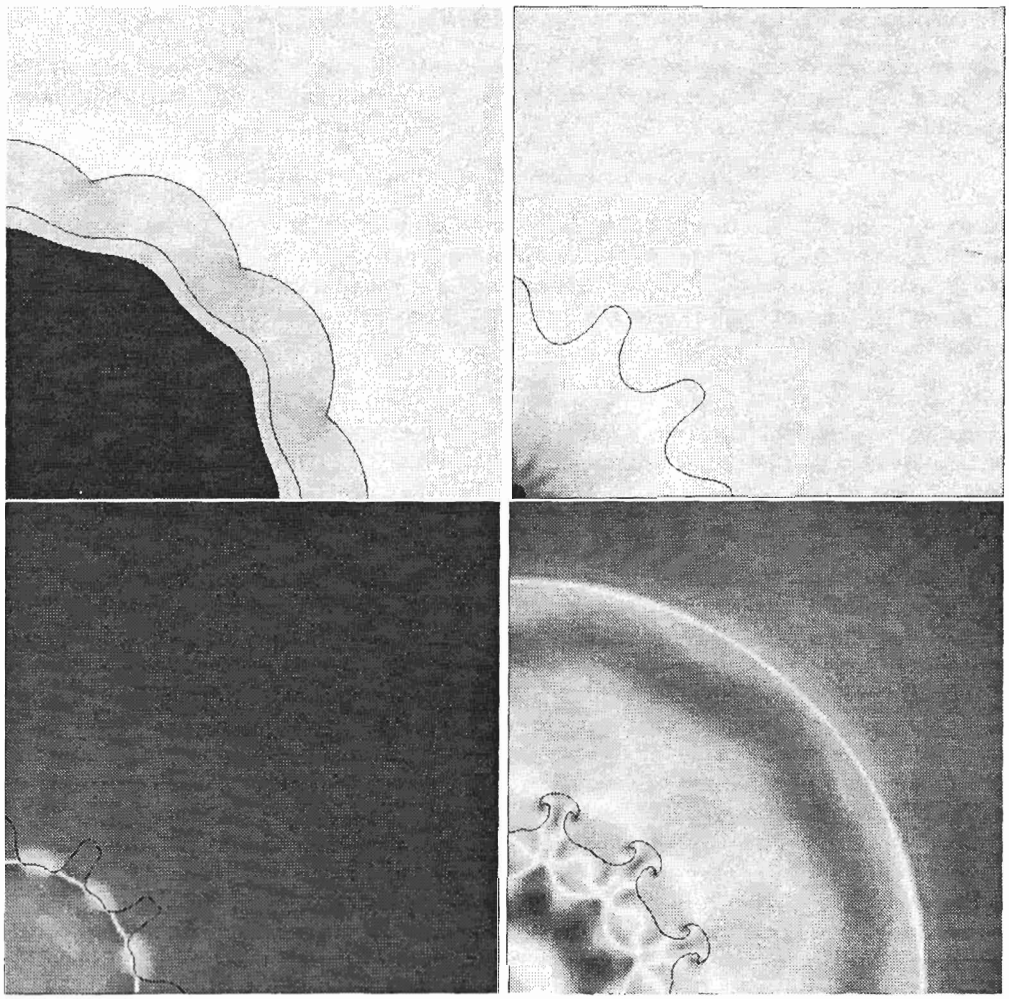

Figure 2. Evolution of material interface for Class 2 at $\tilde{t} = 0.27, 2.0, 3.9$ and 4.2. The figure shows: (upper left) interface after bifurcation, reflected shock (RS) moves radially inward, transmitted shock (TS) moves radially outward; (upper right) RS exited computational domain, TS about to enter origin; (lower left) TS bounced back from origin and reshocked the material interface, causing phase inversion; and (lower right) nonlinear finger growth at late time, with completed phase inversion.

(and are spikes of heavy fluid) prior to reshock will start to change positions after reshock and shock refraction. That is to say that the valleys (bubbles) will become peaks (spikes) and the peaks (spikes) will become valleys (bubbles). At later time, the nonlinear finger growth has formed into the full bubbles of light fluid and spikes of heavy fluid with the familiar mushroom caps at the tips of the fingers (see the lower right frame of Figure 2). By comparing the upper right frame with the lower right frame of Figure 2, one can see that the fingers at the material interfaces have been inverted.

3. Nonlinear finger growth driven by weak shocks

The growth rate of the fingers at a RM unstable material interface in the nonlinear regime is one of the most important physical quantities. The overall growth rate and perturbation amplitude are defined as

$$v = (\dot{r}_{max} - \dot{r}_{min})/2 \quad \text{and} \quad a = (r_{max} - r_{min})/2, \tag{1}$$

where r_{max} and r_{min} are the maximum radius and minimum radius of the perturbed material interface, respectively. In this section, an explanation is provided for the qualitative behavior of the growth rate for an incident shock imploding from a light fluid to a heavy fluid–namely, Class 2. We specify the units used to present the results. The dimensionless radius and dimensionless velocity are

$$\tilde{r} = \frac{r}{R_0} \qquad \text{and} \qquad \tilde{v} = \frac{v}{W_i} \tag{2}$$

respectively, where R_0 is the mean radius of the material interface (the radius of the unperturbed interface) at $t = 0$. W_i is the speed of the incident shock. These units determine dimensionless time

$$\tilde{t} = \frac{W_i t}{R_0}. \tag{3}$$

In these dimensionless units, the initial location of the material interface is given by $\tilde{r} = 1 + \tilde{a_0} cos(n\phi)$, where $\tilde{a_0} = a_0/R_0$ is a dimensionless perturbation amplitude, and a_0 is a dimensional perturbation amplitude. A typical result showing the history of the dimensionless amplitude growth rate $\dot{a}(t)$ and dimensionless perturbation amplitude $a(t)$ versus dimensionless time from numerical simulations is demonstrated in Figure 3 for a system in Class 2. In this case, a shock of Mach number 1.2 propagates from air to SF_6. The dimensionless perturbation amplitude at the initial material interface is $a_o/R_0 = 0.033$. These physical parameters are taken from the experiments performed in plane geometry [3]. We discuss several regions of the growth rate, particularly those peculiar to the effect of curvature–such as, reshock. The implosion of the incident shock causes the material interface to move toward the origin at the early stage of the development of the finger growth and continues to do so until the transmitted shock has bounced back from the origin. This can be seen in the upper right frame of Figure 2. By $\tilde{t} = 2.0$, the reflected shock has exited the computational domain, and the transmitted shock is about to converge at the origin. Since the wavelength decreases as the material interface moves inward, at early time, the growth rate in the imploding case is higher than that in the plane geometry. This can be easily understood from the fact that the linear growth rate in plane geometry is inversely proportional to the wave length. As the material interface moves closer to the origin, the velocity decreases. The slow down of the velocity field causes the slow down of the growth of the fingers at intermediate times ($1.6 \leq \tilde{t} \leq 2.85$). The reshock can be seen in the growth rate graph as the steep vertical jump down at $\tilde{t} = 3.25$ and the kink in the amplitude graph at the same time. The phase inversion process can be seen in the growth rate (Figure 3(a)) taking place from the time of reshock at $\tilde{t} = 3.25$ and continuing until approximately $\tilde{t} = 4.1$. It can also be seen in the amplitude graph Figure 3(b) at $\tilde{t} = 3.75$. Secondary shocks also form in this simulation and propagate radially outward. They hit the material interface before the reshock caused by the wave bouncing back from the origin. This is seen in the slight bump in Figure 3(a) in the time interval $2.85 < \tilde{t} < 3.1$, which is just before the reshock. There is a significant amount of wave interaction inside the region between the reshocked material interface and the reflected rarefaction. The highly nonlinear activity there accounts for the series of reshocks (or oscillations) seen in Figure 3(a) at $\tilde{t} > 4.18$.

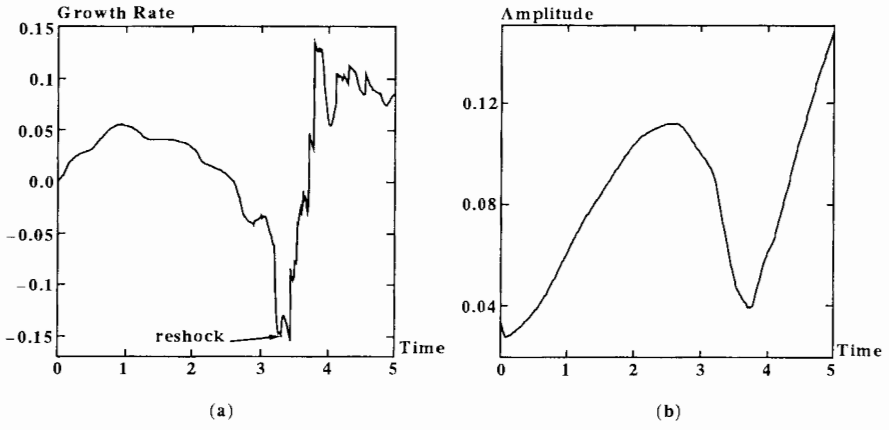

Figure 3. Scaled growth rate and scaled amplitude versus scaled time for Class 2 with an incident shock of Mach number 1.2

4. Nonlinear finger growth driven by strong shocks

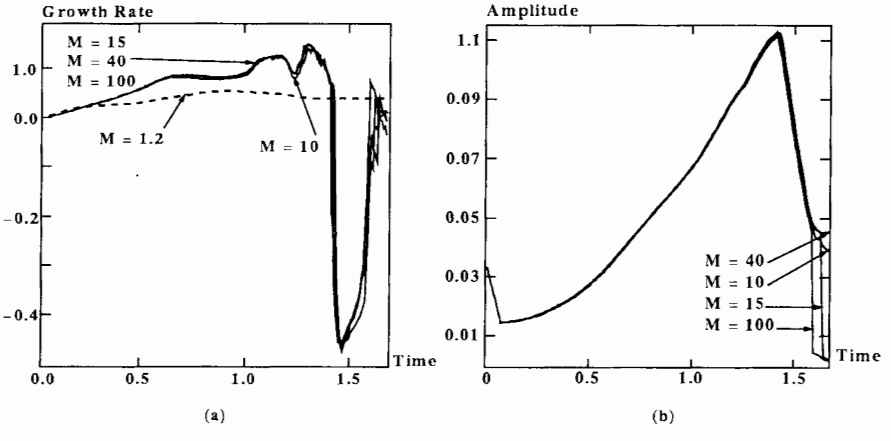

Figure 4. Scaled growth rate and scaled amplitude versus scaled time for Class 2 with various strong incident shocks.

In Figure 4, we show the growth rate and amplitude of perturbation at the material interface in Class 2 driven by shock waves of various Mach numbers. The results of growth rate for incident shocks of Mach number M =1.2, 10, 15, 40 and 100 are superimposed in Figure 4(a) and are shown in terms of dimensionless velocity and dimensionless time. The initial (preshocked) dimensionless perturbation amplitude is $a/R_0 = 0.033$. In Figure 4(b) we show the corresponding scaled dimensionless perturbation amplitude as a function of the dimensionless time. Figure 4 showed that once the Mach number of the incident shock is larger than 10, the scaled quantities are no longer sensitive to the incident shock strength. Therefore, RM unstable systems driven by strong shocks satisfy a nice scaling law. Let $v_{M_1}(t)$ be the growth

rate of a RM unstable interface driven by a strong shock of Mach number M_1, where both v and t are dimensional quantities. Then the overall growth rate, $v_{M_2}(t)$, for a RM unstable interface driven by a strong shock of Mach number M_2 can be obtained from $v_{M_1}(t)$ by the scaling relation:

$$v_{M_2}(t) = \frac{M_1}{M_2} v_{M_1}(\frac{M_1}{M_2} t).$$

Similarly, the following scaling relation holds for the amplitudes:

$$a_{M_2}(t) = a_{M_1}(\frac{M_1}{M_2} t).$$

It has been shown in [5] that the following scaling law holds for the shape of the material and wave interfaces:

$$\vec{R}_{M_2} = \vec{R}_{M_1}(\frac{M_1}{M_2} t).$$

Here $\vec{R}$ represents the locations for the material interface, the shock waves or rarefaction wave.

For further details and more computational results of RM instability in cylindrical geometry as well as the scaling laws of the RM instability driven by strong shocks, see [4] and [5].

Acknowledgement. This work was supported in part by the U.S. Department of Energy, contract DE-FG02-90ER25084, by subcontract from Oak Ridge National Laboratory (subcontract 38XSK964C) and by the National Science Foundation, contract NSF-DMS 9500568.

References

[1] PCTM Workshops, (1988-1995); Proc. First Int. Workshop on the Physics of Compressible Turbulent Mixing, Princeton, (1988); Proc. Second Int. Workshop on the Physics of Compressible Turbulent Mixing, Pleasanton CA, (1989); Proc. Third Int. Workshop on the Physics of Compressible Turbulent Mixing, Abbey of Royaumont, France, (1991); Proc. Fourth Int. Workshop on the Physics of Compressible Turbulent Mixing, Cambridge, England, (1993); Proc. Fifth Int. Workshop on the Physics of Compressible Turbulent Mixing, SUNY at Stony Brook, NY, (1995).

[2] Yang Y, Zhang Q and Sharp DH, Small Amplitude Theory of Richtmyer-Meshkov Instability, Phys. of Fluids A, 5, 1856-1873, (1994).

[3] Benjamin R, Shock and reshock of an unstable fluid interface. In *et al.*D. Besnard editor, Proc. of 3rd International Workshop on The Physics of Compressible Turbulent Mixing at Royaumont France, 325-332, CEA DAM, (1991).

[4] Zhang Q and Graham MJ, A Numerical and Theoretical Study of Richtmyer-Meshkov Instability Driven by Cylindrical Shocks, submitted to Physics of Fluids.

[5] Zhang Q and Graham MJ, Scaling Laws for Unstable Interfacial Fluid Mixing Driven by Strong Shocks, submitted to Physical Review Letters.

A Nonlinear Theory for Spike and Bubble Growth Rates in Richtmyer-Meshkov Instability

Q. Zhang[1] and S.I. Sohn[2]
[1]Department of Applied Math and Statistics, State University of New York at Stony Brook
Stony Brook, New York 11794-3600, USA
[2]School of Science, Tongmyung University of Information Technology
Pusan 608-080, Korea

Abstract: A material interface between two compressible fluids of different density is unstable under the acceleration of a shock wave. This instability plays an important role in inertial confinement fusion and supernova. The linear theory and the impulsive model provide qualitatively incorrect predictions for the growth of the fingers at the unstable material interface at intermediate and late times. We present a nonlinear theory of the growth rates of the spikes and bubble at Richtmyer-Meshkov unstable interfaces of arbitrary density ratio. It has been shown previously that our theoretical predictions are in remarkable agreement with the results from full numerical simulations and experiments for systems with no phase inversion. Here we show that the predictions of the theory are also in good agreement with the results from full numerical simulations for systems with phase inversion. Our theory is based on the methods of Padé approximation and asymptotic matching. The validity of these methods is also discussed.

1. Introduction

The study of unstable interfacial fluid mixing driven by shock waves has been carried out over three decades since the first theoretical prediction of the instability in 1960 [5] and the first experimental confirmation in 1969 [2]. Most previous theoretical studies have focused on the growth rate in the linear (small amplitude) regime. The linear impulsive model proposed by Richtmyer [5] is a widely used theoretical model. The model approximates the incident shock as an impulsive force and the postshocked fluid as incompressible. The solution of the linear impulsive model is $v^{imp} = \sigma a_0$, where $\sigma = -\triangle u Ak$. $\triangle u$ is the difference between the shocked and unshocked mean interface velocities, and $A = (\rho' - \rho)/(\rho' + \rho)$ is the Atwood number. ρ and ρ' are the fluid densities behind the reflected wave and the transmitted shock, respectively. a_0 is the postshocked perturbation amplitude at the interface. For weak shocks, the prediction of impulsive model agrees quite well with the asymptotic growth rate from the linear theory for compressible fluids. A systematic comparison between the predictions of the impulsive model and the solution of the linearized Euler equations showed, however, significant disagreement in certain physical parameter domains, including strong shocks and dissimilar materials [7]. In any case, linear theories are valid only for small amplitudes and consequently for small times. When applied to the initial amplitudes of typical weak shock experiments, the impulsive model agrees with the linear theory in the region where the linear theory is no longer valid.

Hecht *et al.*have developed a Layzer-type potential flow model for the system of infinity density ratio and determined an asymptotic bubble growth rate of $2/3kt$ [1]. Mikaelian has found an analytical solution of this model for a particular initial condition [4]. Zhang has found the analytical solution for arbitrary initial conditions and has further extended the model to

More information - Email: zhang@ams.sunysb.edu or sonsi@ams.sunysb.edu

spike [8]. The analytical solution derived by Zhang showed that for $A = 1$ the spike growth rate reaches a constant [8].

In this paper, we present a quantitative theory for the growth rates of a single bubble and spike in compressible fluids of all density ratios and for time periods and interface amplitudes from the linear into the nonlinear regimes. The results presented here are the first analytic theory with these capabilities.

The following three main steps are key to our analysis: (i) nonlinear perturbation solutions (Taylor series in the amplitude of the initial perturbation) truncated at finite order ($n = 4$ here) for incompressible fluids; (ii) Padé approximation of the finite Taylor series; (iii) Matching of the linear compressible solution at early times and the nonlinear incompressible solution at later times. The methods of Padé approximation by a finite Taylor series and of asymptotic matching were first introduced into the study of Richtmyer-Meshkov instability by the authors [9], yielding an analytic theory of the overall (combined bubble and spike) growth rates in two dimensions. A detailed presentation of our results can be found in [9, 10, 11].

2. Physical picture

Our theoretical approach is based on the following picture. The dominant effects of the compressibility occur near the shocks. Thus compressibility influences the material interface when the shocks are in the vicinity of the material interface. We assume that the initial disturbance at the interface is small. Thus at early times after the shock hits the material interface the compressibility is important and the nonlinearity is less important. As time evolves, the magnitude of the disturbance at the material interface increases significantly and the transmitted shock and reflected wave move away from the interface. The effects of compressibility are reduced and the nonlinearity associated with a large interface amplitude starts to play a dominant role in the interfacial dynamics. From this physical picture, we see that at early times the dynamics of the system are mainly governed by the Euler equations for compressible fluids linearized with respect to the interface amplitude [5, 7], while at later times the dynamics are mainly governed by the nonlinear equations for incompressible fluids. Our mathematical approach is to determine the solutions at early and later times separately. Then we match the two solutions to obtain an analytical expression which changes gradually from one to the other. These matched asymptotic solutions give quantitative predictions for the growth rates of the spike and bubble in compressible RM instability from the linear to moderately late nonlinear stages of the instability growth.

3. Perturbation expansions

At early time, small amplitude solution is given by the linear theory of the compressible Euler equations. The solutions of the compressible linear theory can found in [5] for the case of reflected shock and in [7] for the case of reflected shock and for the case of rarefaction wave.

¿From our physical picture for RM instability, the system becomes nearly incompressible at later times. Therefore, we consider incompressible, invicid and irrotational fluids to approximate the late time solution of RM instability. We have systematically derived the nonlinear perturbation solutions for such system. The detail of this derivation can be found in [11]. Conceptually, one expands a quantity f in terms of a_0, i. e. $f = \sum_{n=0}^{\infty} f_n$ where $f_n \sim (a_0)^n$.

For example, the velocity at the tip of the spike and the tip of bubble are given by

$$v_{\rm sp} = v^{(1)} + v^{(2)} + v^{(3)} + v^{(4)} + O((a_0)^5) \qquad \text{and} \qquad v_{\rm bb} = -v^{(1)} + v^{(2)} - v^{(3)} + v^{(4)} + O((a_0)^5), \quad (1)$$

respectively. Here

$$v^1 = v_0, \qquad v^{(2)} = Akv_0^2 t, \tag{2}$$

$$v^{(3)} = k^2 v_0^2[(A^2 - \frac{1}{2})v_0 t^2 - a_0 t], \tag{3}$$

$$v^{(4)} = -k^3 v_0^2[\frac{4}{3}(A^3 - A)v_0^2 t^3 - 2Aa_0 v_0 t^2]. \tag{4}$$

We have assumed that $v_0 \sim a_0$ and that only one mode has been excited at time $t = 0$. We comment only incompressibility approximation is made here. The impulsive force approximation for the incident shock is not made. For incompressible fluids driven by an impulsive force at $t = 0$, other modes can also be excited at $t = 0$. The nonlinear perturbation solutions for incompressible fluids driven an impulsive force can be found in [6] for the case of $A = 1$ and in [11] for arbitrary A.

We emphasis that the nonlinear perturbation solutions presented here are not our final results. They are only intermediate steps towards the constructions of Padé approximants.

4. Padé approximation

In general, the nonlinear solutions given by the perturbation expansion do not converge when t is large. Thus we apply the technique of Padé approximation to the perturbation solutions. From (2), $v_{\rm sp}$ and $v_{\rm bb}$ can be expressed as

$$v_{\rm sp} = v_{\rm a} + v_{\rm b} \qquad \text{and} \qquad v_{\rm bb} = -v_{\rm a} + v_{\rm b}, \tag{5}$$

where $v_{\rm a}$ represents the overall growth rate defined as $v_{\rm a} = \frac{1}{2}(v_{\rm sp} - v_{\rm bb})$ and $v_{\rm b}$ represents $\frac{1}{2}(v_{\rm sp} + v_{\rm bb})$. Then we have

$$v_{\rm a} = v_0 - a_0 v_0^2 k^2 t + (A^2 - \frac{1}{2})v_0^3 k^2 t^2 + O((a_k)^5), \tag{6}$$

$$v_{\rm b} = Akv_0^2 t - 2Ak^3 a_0 v_0^3 3t^2 2 + \frac{4}{3}k^3(A^3 - A)v_0^4 t^3 + O((a_0 k)^6). \tag{7}$$

Applying the Padé approximation to (9), we have [9, 10, 11]

$$v_{\rm a} = \frac{v_0}{1 + v_0 a_0 k^2 t + \max[0, a_0^2 k^2 - A^2 + \frac{1}{2}]v_0^2 k^2 t^2}. \tag{8}$$

Equation (9) is based on the P_2^0 Padé approximant when $A^2 - \frac{1}{2} \leq a_0^2 k^2$ and on the P_1^0 Padé approximant when $a_0^2 k^2 < A^2 - \frac{1}{2}$. The physical reason for choosing these Padé approximants is that the overall growth rate decays at large times.

Similarly, we construct the P_2^1 Padé approximant for (10), and the result is

$$v_{\rm b} = \frac{Akv_0^2 t}{1 + 2k^2 a_0 v_0 t + 4k^2 v_0^2[a_0^2 k^2 + \frac{1}{3}(1 - A^2)]t^2}. \tag{9}$$

To check the validity of Padé approximation, we consider the incompressible fluids with $A = 1$. For this system, Hecht *et al.*[1] have developed a Layzer-type potential flow model for the bubble. It has been shown that the numerical solution of the Layzer-type model for a bubble is in excellent agreement with the result of a full nonlinear numerical simulation and results from conformal mapping for systems with $A = 1$. In Figure 1, we show the comparison among the predictions of the Layzer-type potential flow model, the perturbation solutions given by (3)-(5), and the Padé approximants given by (6), (9) and (10). Here, the asymptotic bubble

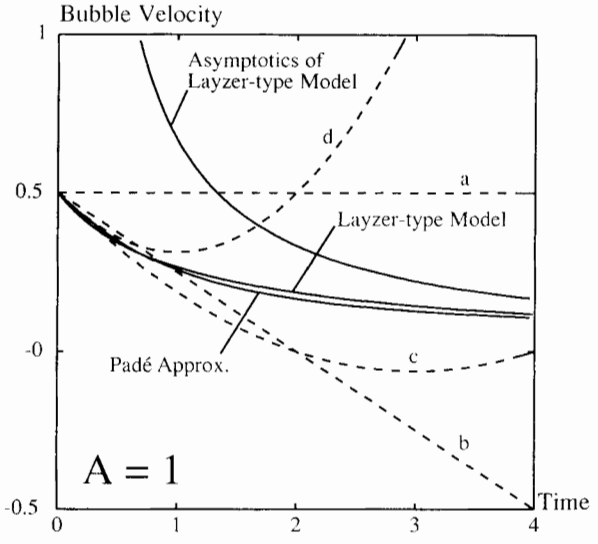

Figure 1. Comparison of the perturbation solutions given by (3)-(5), the Padé Approximation given by (6, (9) and (10), and the Layzer-type potential flow model {hecht] for $A = 1$. The asymptotic bubble growth rate of the Layzer-type model is based on the analytic expression $2/3kt$. The parameters here are $a_0k = v_0 = 1/2$. The curves labeled a, b, c and d correspond to $v^{(1)}$, $v^{(1)} - v^{(2)}$, $v^{(1)} - v^{(2)} + v^{(3)}$ and $v^{(1)} - v^{(2)} + v^{(3)} - v^{(4)}$, respectively.

growth rate of the Layzer-type model is based on the analytic expression $2/3kt$. The parameters used here are $a_0k = v_0 = 1/2$. It is clear from Figure 1, that the range of the validity of the perturbation solution is small, but the range of the validity of the Padé approximant is quite large. This is an important feature of Padé approximation.

5. Asymptotic matching

In order to obtain a nonlinear theory for compressible fluids, we apply the technique of asymptotic matching to combine the early time compressible, linear solution with the later time incompressible, nonlinear solution. The techniques of asymptotic matching were developed in boundary layer problems. In a boundary layer problem, the dynamics in a thin layer next to the boundary, called inner layer, is quite different from the dynamics in the region away from the boundary, called outer layer. One determines the solution in the inner layer, called inner solution, and the solution at the outer layer, called outer solution, separately, and match these two solutions to form matched asymptotics. Since our system is an initial value problem, rather than a boundary value problem, a boundary condition is replaced by the initial conditions and the spatial variable is replaced by the temporal variable. In our case, the inner solution is the linear compressible solution and the outer solution is the nonlinear incompressible solution given by (9). There are several ways to match asymptotics. The essence of the matched asymptotic technique is to blend the inner and outer solutions smoothly. The facts that (9) approaches v_0 at early times and that the growth rate of the linear theory for compressible fluids approaches an asymptotic constant v_{lin}^{∞} at later times show that a simply way to achieve

the matching is to replace v_0 with $v_{\rm lin}$ in (9) and (10).

6. RM interfaces with phase-inversion

In this section, we consider systems with the indirect phase inversion. Indirect phase inversion is defined as a situation for which $a_0(0+)v_{\rm lin}(t \to \infty) < 0$. For the case of reflected shock (rarefaction wave), the indirect phase inversion usually does not (does) occur [7]. During the period of indirect phase inversion, $0 < t < \tau$, the solution is given approximately by the compressible linear theory, due to the satisfaction of the assumption that $a_0 k$ is small. Here τ is the time at which the phase inversion is completed, i.e. $a(\tau) = -a_0(0+)$. Therefore, the nonlinearity is only important for $t > \tau$. Usually τ is small. These properties lead us to use $-a_0(0+)$ as the initial amplitude in (9) and (10) in the case of the indirect phase inversion. Therefore, we have

$$v = \frac{v_{\rm lin}}{1 + \epsilon v_{\rm lin} a_0 k^2 t + \max[0, a_0^2 k^2 - A^2 + \frac{1}{2}] v_{\rm lin}^2 k^2 t^2}, \tag{10}$$

$$v_{\rm bb} = -v + \frac{A k v_{\rm lin}^2 t}{1 + \epsilon 2 k^2 a_0 v_{\rm lin} t + 4 k^2 v_{\rm lin}^2 [a_0^2 k^2 + \frac{1}{3}(1 - A^2)] t^2}, \tag{11}$$

$$v_{\rm sp} = v + \frac{A k v_{\rm lin}^2 t}{1 + \epsilon 2 k^2 a_0 v_{\rm lin} t + 4 k^2 v_{\rm lin}^2 [a_0^2 k^2 + \frac{1}{3}(1 - A^2)] t^2} \tag{12}$$

for the overall growth rate, and the growth rates of spike and bubble, respectively. Here $\epsilon = 1(-1)$ for the systems with no (with) indirect phase inversion. We comment that our nonlinear theories given by (11)-(13) contain no adjustable parameter. To the author's knowledge, no comparable theories have ever been proposed for indirect phase inversion. It is easy to see that in the early time, or small amplitude limits, (11)-(13) approach $v_{\rm lin}$. Equations (12) and (13) also show that the spike grows faster than the bubble.

In Figure 2(a), a shock of Mach number 1.2 propagates from SF_6 to air. $a_0(0-)k = 0.35$ and $A(0+) = -0.69$. In Figure 2(b), a shock of Mach number 1.5 propagates from Freon-22 to air. $a_0(0-)k = 0.31$ and $A(0+) = -0.54$. In both cases, the shock waves are incident from the heavy to the light fluid, the reflected waves are rarefaction waves and the indirect phase inversions occur. Figure 2 shows that the predictions of our theory for spike and bubble growth rates are in excellent agreement with the results from full numerical simulations for systems with indirect phase inversion, while the the predictions of the linear theory and impulsive model are qualitative incorrect at later times. We use the average of the preshocked and postshocked initial amplitudes to evaluate the linear impulsive model, as proposed by Meyer and Blewett [3].

Although we have demonstrated that the range of the validity of the Padé approximant is significantly larger than that of primitive perturbation expansion, the range of the validity of the Padé approximant is still not infinity. Therefore, our theory may not applicable at asymptotic large times. In fact, at the time when $v_{\rm bb} = 0$, our theory is no longer valid. In reality, the unstable system becomes turbulent at very late times. The physics of fluid turbulence involves much more than just the nonlinearity.

Acknowledgement. This work was supported in part by the U.S. Department of Energy, contract DE-FG02-90ER25084, by subcontract from Oak Ridge National Laboratory (subcontract 38XSK964C) and by National Science Foundation, contract NSF-DMS-9500568 and contract NSF-DMS-9301200.

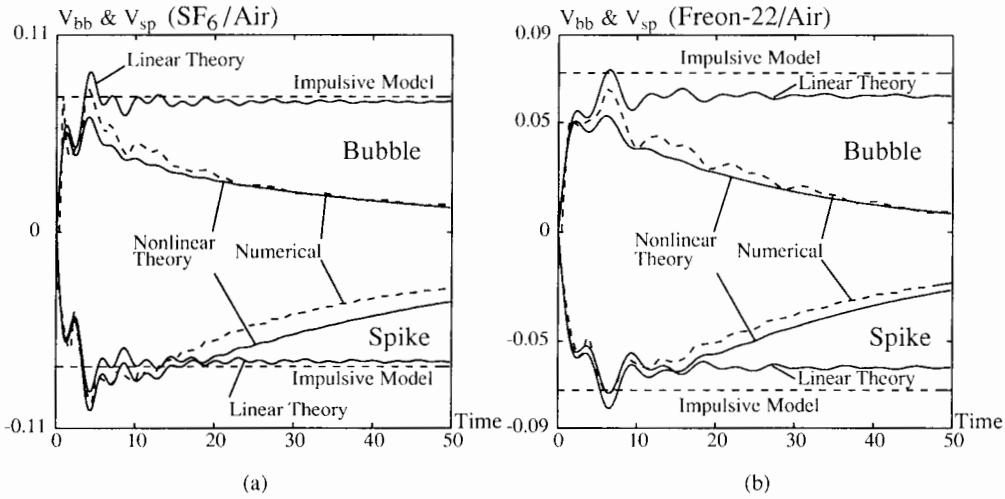

Figure 2. A comparison for the growth rates of the bubble and spike at (a) SF_6/air and (b) Freon-22/Air interface. In both cases, the shock waves are incident from the heavy fluid to the light fluid. The reflected waves are rarefaction waves and the indirect phase inversions occur.

References

[1] Hecht J, Alon U and Shvarts D, Potential flow models of Rayleigh-Taylor, and Richtmyer-Meshkov bubble fronts, Phys. Fluids, 6, 4019, (1994).

[2] Meshkov EE, Interface of two gases accelerated by a shock wave, Fluid Dyn., 4, 101, (1969).

[3] Meyer KA and Blewett PJ, Numerical investigation of the stability of a shock-accelerated interface between two fluids, Phy. Fluids, 15, 753-759, (1972).

[4] Mikaelian KO, Analytic Approach to Nonlinear Rayleigh-Taylor and Richtmyer-Meshkov Instabilities, Preprint: UCRL-JC-125113.

[5] Richtmyer RD, Taylor Instability in Shock Acceleration of Compressible Fluids, Comm. Pure Appl. Math., 13, 297, (1960).

[6] Velikovich AL and Dimonte G, Nonlinear perturbation theory of the incompressible Richtmyer-Meshkov instability, Phys. Rev. Lett., 76, 3112-3115, (1996).

[7] Yang Y, Zhang Q and Sharp DH, Small Amplitude Theory of Richtmyer-Meshkov Instability, Phys. Fluids A, 6, 1856, (1994).

[8] Zhang Q, Exact Analytical Solutions of Layzer-Type Model for Unstable Interfacial Fluid Mixing, Preprint: AMS-SUNYSB-96-28.

[9] Zhang Q and Sohn SI, An Analytical Nonlinear Theory of Richtmyer-Meshkov Instability, Phys. Lett. A, 212, 149, (1996).

[10] Zhang Q and Sohn SI, Padé Approximation for an Interfacial Fluid Mixing Problem, Applied Math. Lett., accepted, in press.

[11] Zhang Q and Sohn SI, Nonlinear Theory of Unstable Fluid Mixing Driven by Shock Waves, Phys. of Fluids, 9, 1106-1124, (1997).

Numerical Simulations of Rayleigh-Taylor Instability with the Simplified Reynolds Stress Model

Z. Zhang and J. Wang
Laboratory of Computational Physics, IAPCM, Beijing, P.R. China

Abstract: The Rayleigh-Taylor instability is investigated with 1D compressible hydrodynamic code where the simplified Reynolds-stress model is imbeded. The model is calibrated by several shock tube experiments. Here both Rodriquez's shock-tube experiments and Kucherenko's experiments are simulated. The results are basically coincident with the experiments. The turbulent mixing process under acceleration, deceleration and re-acceleration is investigated. It is found that at the first acceleration phase the turbulent mixing develops in a self-similar way as Youngs'. During deceleration phase, the turbulent mixing develops slowly and gradually stops. At re-acceleration phase it again develops as the first phase after a period of time delay. The influences of Atwood number and acceleration are also investigated. They basically agree with the existed experimental results.

1. Introduction

The Rayleigh-Taylor instability occurs on an interface separating two fluids of different densities when this two fluids are in a gravitational field whose direction is from heavy fluid towards the light one or they are accelerated in the direction of light fluid toward the heavy one [1]. Due to its great influence on inertial confinement fusion and others , it is investigated in detail by experiments, theories and numerical simulations. It is found that for random perturbation, it leads to a creation of a mixing zone between the two fluids. For some complicated physical problems, it seems difficult to directly simulate the behaviour of turbulent mixing process [2, 3]. So series of turbulent mixing models have been developed and some of them have been put into uses. Although there are some discussions on the behaviour of instability under acceleration and deceleration, no publications are found about the behaviour under re-acceleration phase [4, 5]. Besides, the turbulent statistic models are seldom used in the investigations of Rayleigh-Taylor instability. Here, the Rayleigh-Taylor instability is investigated with 1D compressible hydrodynamic code where a simplified Reynolds-stress model, calibrated by several shock tube experiments [6], is imbeded. Both Rodriquez's shock-tube experiments [7] and Kucherenko's experiments [5] are simulated. The turbulent mixing process under acceleration, deceleration and re-acceleration is investigated. The influences of Atwood number and acceleration are also studied. The model will be introduced in Sec.2. And simulated results will be presented in Sec.3, 4, and 5.

2. Simplified Reynolds stress model

Our basic hypotheses are the same as [8]. Firstly, micro-interactions of molecules are negligible. Thus the viscous can be excluded. And two fluids are immiscible. Secondly, the turbulent Mach number M_t ($M_t = \frac{\sqrt{k}}{c_s}$) is small so a local equilibrium of the pressure exists in different materials.

More information - Email: js3s@mail.iapcm.ac.cn

2.1. 1D transportation equations

From Euler equations and concentration equation, we derive the transportation equations as the Besnard *et al.*[8] and present it in [6]. As for Rayleigh-Taylor instability and Richtmyer-Meshkov instability, we can reduce them to a 1D version. The derived equations are

$$
\begin{aligned}
\frac{d\rho}{dt} &= -\rho\frac{\partial u_x}{\partial x} \\
\rho\frac{du_x}{dt} &= -\frac{\partial p}{\partial x} - \frac{\partial K_x}{\partial x} \\
\rho\frac{dI}{dt} &= -p\frac{\partial(u_x - a_x)}{\partial x} + \frac{\partial}{\partial x}\{c_1 c(1-c)\rho a_x I + c_2\rho\frac{K_x}{\sqrt{D}}\frac{\partial I}{\partial x}\} \\
\rho\frac{dc}{dt} &= \frac{\partial}{\partial x}\{c_1\mu c(1-c)\rho a_x + c_2\rho\frac{K_x}{\sqrt{D}}\frac{\partial c}{\partial x}\} \\
\rho\frac{dK}{dt} &= -2\rho K_x\frac{\partial u_x}{\partial x} + 2a_x\frac{\partial p}{\partial x} + \frac{\partial}{\partial x}(c_4\rho\frac{K_x}{\sqrt{D}}\frac{\partial K}{\partial x}) - c_3\rho\sqrt{D}K \\
\rho\frac{dK_d}{dt} &= c_5\rho\sqrt{D}(\frac{2}{3}K - K_d) + \frac{\partial}{\partial x}(c_4\rho\frac{K_x}{\sqrt{D}}\frac{\partial K_d}{\partial x}) - c_3\rho\sqrt{D}K_d \\
\rho\frac{da_x}{dt} &= -K_x\frac{\partial\rho}{\partial x} + \rho\frac{\partial a_x{}^2}{\partial x} - \rho a_x\frac{\partial(u_x - a_x)}{\partial x} + \frac{B}{\rho}\frac{\partial p}{\partial x} + \frac{\partial}{\partial x}(c_6\rho\frac{K_x}{\sqrt{D}}\frac{\partial a_x}{\partial x}) - c_7\rho\sqrt{D}a_x \\
\rho\frac{dB}{dt} &= -2\rho a_x\frac{\partial\rho}{\partial x} + \frac{\partial\rho a_x B}{\partial x} - \rho B\frac{\partial(u_x - a_x)}{\partial x} + \frac{\partial}{\partial x}(c_8\rho\frac{K_x}{\sqrt{D}}\frac{\partial B}{\partial x}) - c_9\rho\sqrt{D}B \\
\rho\frac{dD}{dt} &= -2\rho D_x\frac{\partial u_x}{\partial x} + c_{10}\frac{a_x}{L^2}\frac{\partial p}{\partial x} + \frac{\partial}{\partial x}(c_{11}\rho\frac{K_x}{\sqrt{D}}\frac{\partial D}{\partial x}) - c_{12}\rho\sqrt{D}k \\
D_d &= D\frac{K_d}{K}, \quad \mu = sign\{(c-\alpha)\}
\end{aligned}
\tag{1}
$$

Where p, ρ, c and u_x are emsemble averaged pressure and density, Favre averaged concentration and x-direction velocity; α is volume fraction; And $K = K_{ii}$, K_x, $D = D_{ii}$, D_x, B and a_x are twice turbulent fluctuating energy, x-direction Reynolds stress, the trace of dissipation correlation and its x-direction component, density fluctuating correlation and x-direction fluctuating mass flux respectively. $K_d = K - K_x$, $D_d = D - D_x$ and L is turbulent mixing thickness. First-order implicit difference scheme is used. Since we introduce the global quantity L in the equation, we have to solve the equations by iteration.

2.2. State equation of mixture

The perfect gas state equation is used for each material. The state equation of mixture is the the same as [6, 8]. All equations are listed as follow:

$$
\begin{aligned}
p_1 &= (\gamma_1 - 1)\rho_1 I_1\ ,\ \ p_2 = (\gamma_2 - 1)\rho_2 I_2\ ,\ \ p_1 = p_2 = p \\
\rho &= \alpha\rho_1 + (1-\alpha)\rho_2\ ,\ \ \rho c = \rho_1\alpha\ ,\ \ \rho(1-c) = \rho_2(1-\alpha) \\
I &= \alpha I_1 + (1-\alpha)I_2\ ,\ \ B = \alpha(1-\alpha)(\rho_1 - \rho_2)^2 \\
p &= (\gamma - 1)\rho I\ ,\ \ \frac{1}{\gamma - 1} = \frac{\alpha}{\gamma_1 - 1} + \frac{1-\alpha}{\gamma_2 - 1}
\end{aligned}
\tag{2}
$$

2.3. Model constants

The above model has been calibrated with Brouillette's shock tube experiments [9] and Houas's air/helium shock tube experiments [10]. Model constants are c_1=0.5, c_2=0.2, c_3=0.1, c_4=3.1,

c_5=2.3, c_6=0.2, c_8=1.0, c_9=0.1, c_{10}=4.0, c_{11}=0.3, c_{12}=1.67 respectively [6].

3. Simulation of R-M instability and R-T instability experiments

Here, again, the simplified Reynolds stress model is examined by the Rodriquez's shock tube experiments [7] and Kucherenko's Rayleigh-Taylor instability experiments [5].

3.1. Simulation of R-M instability experiments

SF_6/air and X_e/air shock tube experiments of Rodriquez's are simulated. The length of air is 30cm, same as the experiments'. The left boundary is a piston and the right is a rigidwall. Supposing that two fluids initially mix with the same volume fraction $\alpha = 0.5$, we get initial field of B, density, internal energy of disturbed area from Eqs.(2), which are presented in Table 1. The initial values of disturbed area in all our simulations are set in this way. Turbulent variables which are not included are set to zero at the beginning of computation. γ is 1.4, 1.09 and 1.645 for air, SF_6 and X_e respectively. Computational and experimental time evolution of

	SF_6	D. area	air	X_e	D. area	air
$\rho(g/cm^3)$	0.006	0.003645	0.00129	0.00558	0.003435	0.00129
$p(bar)$	1	1	1	1	1	1
$B(g/cm^3)$	0.	1.521×10^{-3}	0.	0.	1.339×10^{-3}	0.
$I(10^{10}cm^2/s^2)$	0.1852	0.1867	0.1938	0.02778	0.05895	0.1938

Table 1. Initial Distribution.

mixing thickness are presented in Fig.1(a,b). Both results agree with the experiments'. Here and below, the mixing thickness is defined as the width of area where c(the concentration of material 1)$\in (0.05, 0.95)$.

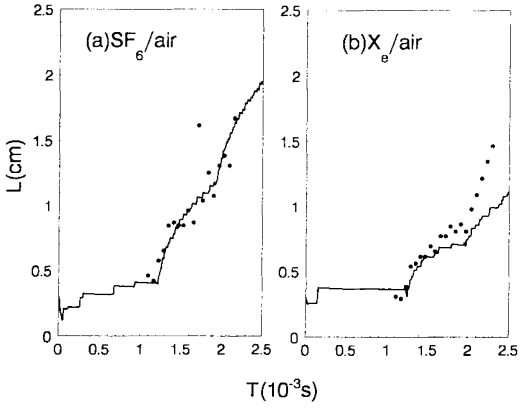

Figure 1. Evolution of turbulent mixing thickness. The real line denotes computational results. The dot denotes experimental results of Rodriquez's.

3.2. Simulations of Kucherenko's R-T experiment

Kucherenko *et al.*[5] observed that at the deceleration phase, the growth of the mixing thickness slows down and upon a time the mixing thickness begins to decrease. This experiment is

simulated with the simplified Reynolds stress model. The left and the right boundaries are pistons, moving at the same acceleration as the experiment's. The space lengths of two fluids are set to 6cm, same as the experiment's. Here the perfect gas equation of state is used and γ are set to 2000 in order to get a large sound speed. The densities of the two fluids are $0.69g/cm^3$ and $2.04g/cm^3$. The initial values of disturbed area are set in the way we mentioned in Sec.3.1. The experimental and computational results are presented in Fig.2. In the deceleration phase, the growth of mixing thickness slows down as the experiment's, but we do not observe the decrease of mixing thickness.

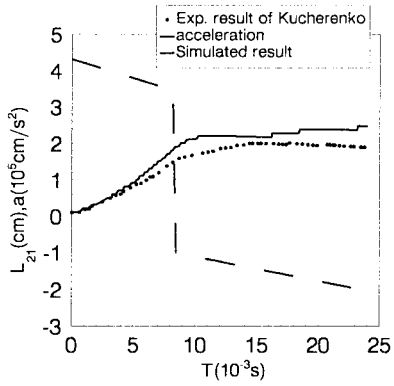

Figure 2. Evolution of turbulent mixing thickness and acceleration. L_{21} is the thickness of the heavy fluid. The dot denotes the experiment result and the real line denotes the simulated result.

4. The behaviour of turbulent mixing under acceleration, deceleration and re-acceleration

The turbulent mixing process under acceleration, deceleration and re-acceleration is investigated. The space lengths are the same as Sec.3.2, but $p_0 = 2bar$. $\rho_1 = 1$, $\rho_2 = 3g/cm^3$. It is found that at the first acceleration phase the turbulent mixing develops in a self-similar way as Youngs's [10]. During deceleration phase, the turbulent mixing develops slowly and gradually stops. At re-acceleration phase it again develops as the first phase after a period of time delay. Time evolution of turbulent mixing thickness and acceleration, are presented in Fig.3. We can see that the delayed time depends on the deceleration time.

5. Investigation of the influences of Atwood number and acceleration

5.1. The influences of Atwood numbers

Turbulent mixing induced by Rayleigh-Taylor instability with different Atwood numbers is investigated. The left and the right are piston moving under an acceleration presented in Fig.2, but without deceleration. Both space lengths of two fluids are 6cm. The initial conditions are $\rho_1 = 1g/cm^3$, $\rho_2 = 3$, 6 and $12g/cm^3$ and $p_0 = 2bar$ all other values are set in the way mentioned in Sec.3.1. The time evolutions of turbulent mixing thickness with the ratio of two materials are presented in Fig.4(a). It is obvious that as Atwood number increases, the growth rate of mixing increases slowly. It basically agrees with the existed results [11]. We fit those

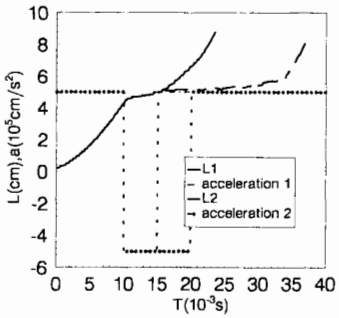

Figure 3. Evolution of turbulent mixing thickness and acceleration, real line for $\Delta t_{deceleration} = 0.005s$ and dash line for $\Delta t_{deceleration} = 0.01s$.

curves according to the following formula

$$\frac{dL}{ds} = 2\alpha' A,\ S = \frac{1}{2}(\int_0^t \sqrt{a(\tau)}d\tau)^2. \tag{3}$$

by least square method. The α' is presented in Table 2(a). The related values which are fitted from Youngs' experiment [10] are also presented in Table 2(a), denoted as α_{exp}.

ρ_2/ρ_1	3	6	12
α'	0.163	0.202	0.284
α'_{exp}	0.177	0.198	0.212

(a)

$a(10^6 cm/s^2)$	0.05	0.1	0.5	1	5
α'	0.265	0.212	0.245	0.265	0.264

(b)

Table 2. (a) The ratio of two materials and α' (b) The accelarations and α'

5.2. The influences of accelerations

The pistons move from left to right in the acceleration of 0.05, 0.1, 0.5, 1, 5 $10^6 cm/s^2$ respectively. Turbulent mixing developes between the two fluids. The initial conditions are $\rho_1 = 1g/cm^3$, $\rho_2 = 3g/cm^3$, $p_0 = 2bar$. The time evolutions of turbulent mixing thickness with the acceleration are presented in Fig.4(b). It is observed that as acceleration increases, the growth rate of mixing increases linearly. We fit those curves according to Eq.(3). The results are presented in Table 2(b). These results agree with the existed results [11].

6. Conclusion

From the above discussions, we can draw the fellowing conclusions: The first is that the simplifed Reynolds-stress model can describe both the R-T and R-M instability well. The next is that at the first acceleration phase, the turbulent mixing develops in a self-similar way as Youngs' [10], then during the deceleration phase, the turbulent mixing develops slowly and gradually stops, and at the re-acceleration phase, it again develops as the first phase after a period of time delay. And the delay time depends on the duration of the deceleration phase. The last is that the growth rate increases slowly with the density ratio of two materials and increases linearly with the acceleration. They basically agree with the existed experimental results.

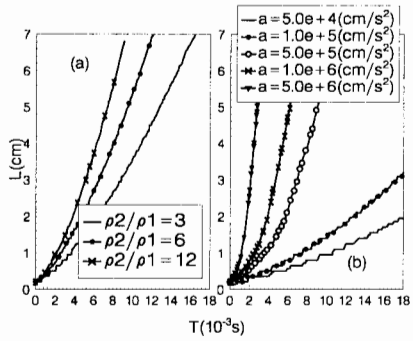

Figure 4. Evolution of turbulent mixing thickness with different Atwood numbers(a), with different accelerations(b).

Acknowledgement. The authors thank professor Sui Hongsou and Huang Yongnian for helpful discussions. This research has been financially supported by the fund of China Accademy of Engineering Physics.

References

[1] Taylor G I, The instability of liquid surfaces when accelerated in a direction perpendicular to the planes 1 , Proc. Appl. Soc., London,1950,A201:192-196.

[2] Sharp D H, An overview of Rayleigh-Taylor instability, Physica, 1984, D12:3-18.

[3] Gauthier S and Bonnet M, A k-ϵ model for turbulent mixing in shock-tube flows induced by Rayleigh-Taylor instability, Phys. Fluids, 1990, A2(9):1685-1694.

[4] Youngs D L, Numerical simulation of turbulent mixing by Rayleigh-Taylor instability, Physica, 1989, D37:45-58.

[5] Kucherenko Yu A, Neuvazayev V E and Pylaev A P. Behavior of gravitational turbulent mixing region under conditions leading separation. In proceeding of the 4th International Workshop on the Physics of Compressible Turbulent Mixing , Cambridge , England , 1995, edited by P. H. Linden, D. L. Youngs and S. B. Dalziel , P. 70-80.

[6] Zhang Zhongzheng and Wang Jihai, The simplified Reynolds stress model and numerical simulation of Richtmyer-Meshkov instability, Submitted to the 21st ISSW international conference.

[7] Rodriquez G, Galametz I, Croso H and Haas J F, Richtmyer-Meshkov instability in a vertical shock-tube, Same as Ref.5, P 260-270.

[8] Besnard D C and Hass J F , Statistical modeling of shock-interface interaction. Physica D 1989 , 37 : 227-247.

[9] Brouillette M and Sturtevant B, Experiments on Richtmyer-Meshkov instability : Small-scale perturbations on a plane interface, Phys. Fluids, 1993, A5(4): 916-930.

[10] Houas L, Brun R and Hanana M, Instability of interfaces submitted to shock acceleration and deceleration. in proceeding of the 15th ISSWST. Berkeley California : Bershader D and Hanson R.(Standford U. P., Standford. CA.1986), p415-421.

[11] Youngs D L, Numerical simulation of turbulent mixing by Rayleigh-Taylor instability, Physica, 1984, D12:3-18.

On the Nature of Differences in the Evolution Pattern of Turbulent Mixing at the Gas-Gas and Gas-Fluid Interface

V.V. Zmushko, M.D. Kamchibekov and E.E. Meshkov
Russian Federal Nuclear Centre - Institute of Experimental Physics
Prospect Mira 37, 607190, Sarov, Nizhny Novgorod Region, Russia

1. One of the problems on Rayleigh-Taylor instability that in recent years was subject to the intensive studies both experimentally and theoretically using numerical simulation is the evolution of the fronts of bubbles and jets under a complicated multimode spectrum of initial perturbations with small amplitudes [1, 2, 3, 4, 5]. As is known, (see, for example, [6]) Rayleigh -Taylor instability occurs at the interface between the heavy and light fluids (or gases) in the gravity field when the heavier fluid is up. As was shown by the experimental studies (see, e.g., [2]) and by the numerical simulation of Rayleigh-Taylor instability [4, 5] the front of the bubbles asymptotically moves with an acceleration following the law

$$h_B \sim \alpha A g t^2 \tag{1}$$

where h_B is the penetration depth of the light material with the density ρ_1 into the heavy material with the density ρ_2;

$$A = \frac{\rho_2 - \rho_1}{\rho_2 + \rho_1} \qquad \textit{Atwood number};$$

g - gravity acceleration;

t - time;

α- constant.

The $2D$ numerical calculations [4, 5] give $\alpha = 0.04...0.05$; while the experiments yielded: for fluid-fluid or fluid-gas [1, 2] $\alpha = 0.05...0.07$ and for gas-gas [3] $\alpha \geq 0.1$, i.e. approximately two times greater. The source of this discrepancy is not clear at this point. The assumption was made that this difference may be due to the different structures of the mixing zones in two cases [7]: while on the gas-fluid case the lighter gas penetrates into the fluid as bubbles, in the gas-gas case the heavier gas penetrates the turbulent mixing zone as jets. Other causes of the discrepancy between α values in (1) are also possible. In this view the following questions must be answered:

- what is the nature of the law (1); what is its versatility degree;
- what is the relation between the constant α and other known constants;

More information - Email: otd03_2305@spd.vniief.ru

- what is the role of physical characteristics such as strength, compressibility, viscosity, surface tension and others in the formulation of law (1);
- what is the role of initial spectrum of the final amplitude perturbations in the formulation of law (1) and so on.

This list can be continued. This paper proposes one of the possible ways to obtain the answers to these questions.

2. To explain the typical evolution laws at the interface experiencing the Rayleigh-Taylor instability, various models were suggested among which one can distinguish the "merging" of bubbles [6] and the modal model [8] that represents a further developed Haan model [9]. Using these models and direct numerical simulation of Rayleigh-Taylor instability with a complicated initial spectrum [4, 5, 8] it was found that with time the dynamics of the bubbles front reaches the scale-invariant (self-similar) mode where the distribution of the bubbles over size (or over the corresponding wavelengths) is determined by the only parameters: the average size of the bubbles or the average perturbation wavelength $< \lambda >$ and does not depend on the type of initial (small) perturbations. The quantity $< \lambda >$ grows with time $\sim gt^2$ which reflects the effect observed both experimentally and numerically: the formulation of ever growing structures, the so-called "inverse cascade". In this steady-state mode the linear scale of the phenomenon is determined only by the average wavelength $< \lambda >$ and the typical time in the case of Rayleigh-Taylor instability by $(g/ < \lambda >)^{-1/2}$.

Given the simple and clear dimension considerations confirmed by the numerical computations Alon, Shvarts and others [8, 10] proposed the evolution model of the bubbles fronts for Rayleigh-Taylor instability according to which the evolution of the average wavelength $< \lambda >$ is described by the equation (with $A = 1$)

$$\frac{d < \lambda >}{dt} = \beta \sqrt{\frac{g}{< \lambda >}} < \lambda >, \tag{2}$$

where the constant β was obtained from the computations using the "merging" of bubbles and was confirmed by the direct numerical computations of $\beta = 1$ [10].

The motion of the bubbles front h_b within the model [8, 10] is determined by the equation

$$\frac{dh_B}{dt} = U_B(\lambda) \mid_{\lambda = \langle \lambda \rangle}, \tag{3}$$

where $U_B(\lambda)$ is the asymptotic velocity of a single bubble with the wavelength λ.

With $A = 1$

$$U_B(\lambda) = \gamma \sqrt{g\lambda},$$

where γ is the constant depending on the bubble form, particularly, for $2D$ harmonic perturbations $\gamma = 0.23$ and for $3D$ harmonic perturbations $\gamma = 0.4$ [11].

It follows from (2, 3) that the asymptotic behavior of the bubble front is determined by the relation

$$h_B \longrightarrow \gamma\beta/4 \cdot gt^2.$$

Thus, within the model [8, 10] the constant α in (1) is related to the constants γ, β in the following way

$$\alpha = \gamma\beta/4 \tag{4}$$

The relation (4) allows to investigate basically the effect of various physical and geometric factors on α , if we know how they influence the constants γ, β.

It seems to be true that the majority of experiments [1, 2, 3] actually always implemented *3D* perturbations for which it can be expected that the parameters γ, β and hence α should be uniquely defined.

3. For the verification of this assumption the numerical computations were performed in the following formulation. The cylindrical tube with the radius $R = 1.8$ placed vertically in the gravity field with $g = 1$ contains a heavy gas having the density $\rho_2 = 0.001225\ g/cm^3$ with $z > 0$ and a light gas with the density $\rho_1 = 0.0001694\ g/cm^3$ at $z < 0$. A small perturbation was initially applied as $a = a_0 \cos \pi r/R$ at unstable interface ($z = 0$).

The computations were run for two values of a_0:

1) $a_0 = 0.018$ (central bubble);

2) $a_0 = -0.018$ (the bubble on the wall).

Figs.1, 2 show the amplitudes and the velocities of the bubble as functions of time for both types of initial conditions.

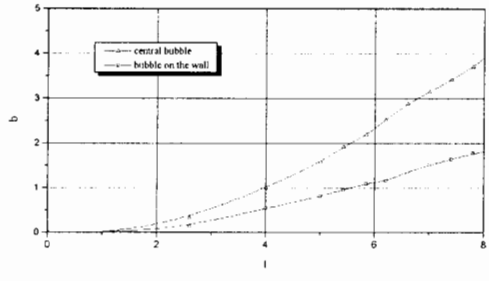

Figure 1. Bubble amplitude versus time.

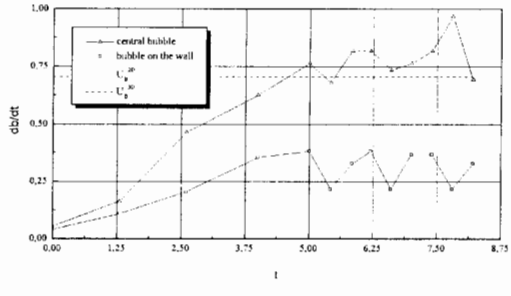

Figure 2. Bubble velocity versus time.

Fig.2 presents also the asymptotic velocities of the bubble for *2D* and *3D* geometries:

$$U_B = \gamma \sqrt{\left(\frac{\rho_2 - \rho_1}{\rho_2}\right) g\lambda},$$

where $\gamma = 0.23$ for *2D* and $\gamma \cong 0.4$ for *3D* and the wavelength corresponding to the cylindrical geometry was taken to be $\lambda = 2R$, where R is the tube radius. The data from Figs.1, 2 indicates that the central bubble rises up more rapidly than the bubble rising up on the wall and the velocity of the central bubble at later times is close to the known result for *3D* bubble while the asymptotic velocity of the bubble rising on the wall corresponds to the result for *2D* bubble.

4. The example from item 3 illustrates the effect of the geometric factor - in our case the bubble shape - on γ in *3D* geometry. If one assumes that the interaction of *3D* bubbles in the model [8, 10] does not depend on their form, i.e. $\beta = 1$, then (4) yields that the possible discrepancy in a corresponding to the discrepancy in $\gamma = 0.23...0.4$ is $\alpha = 0.06...0.1$. Returning to the above assumption about the cause of the discrepancy of the experimentally obtained a in the experiments gas-gas and gas-fluid due to the different structures of the mixing zone [7] the following can be said. The case gas-fluid corresponds to the rise-up geometry of the "central" bubble, i.e. $\gamma \approx 0.4$ while for the system gas-gas the geometry of the rising up bubbles seems to be close to the case of the bubble rising up along the wall. Then for the constant β ($\beta = 1$) within the model [8, 10] for gas-fluid we must obtain $\alpha \approx 0.1$ while for gas-gas we shall have $\alpha \approx 0.06$, i.e. the result contradicting the experimental data. Thus, if one assumes that the relation (4) resulting from the model [8, 10] is valid then the discrepancy in α does not seem to be caused by the different structures of the mixing zones for gas-gas and gas-fluid systems as was assumed in [7]. However, there is no the final comprehensive answer to the question about how the geometrical factor impacts α since we don't know how the bubbles of various forms interact in *3D* geometry. Nevertheless it seems to be promising to use the results of the models by Alon, Shvarts and others [8, 10] in the form of the relation (4) to analyze the impact of various physical and geometrical factors on α though this will require the preliminary studies of how these factors influence the constants γ and β.

References

[1] Read KI, Physica 12D, Amsterdam, 45, (1984).
[2] Youngs DL, Experimental Investigation of Turbulent Mixing by Rayleigh-Taylor Instability, Workshop on the Physics of Compressible Turbulent Plasmas, Princeton, (1988).
[3] Vasilenko AM, Olhovskaya VI, Buryakov OV, Yakovlev VG, Experimental Investigations for Turbulent Mixing of Gases at the Plane Interface under the Influence of the Decelerating Shock Wave, Proc. of the 3-rd IWPCTM, 535, (1991).
[4] Glimm J, Li XL, Menikoff R, Sharp DH and Zhang Q, Phys. Fluids A, 2, 2046, (1990).
[5] Gardner CL, Glimm J, McBryan O, Menikoff R, Sharp DH and Zhang Q, Phys. Fluids, 31, 447, (1988); Glimm J and Li XL, Phys.Fluids, 31, 2077, (1988).
[6] Sharp DH, Physica 12D, (Amsterdam), 3, (1984).
[7] Meshkov EE, Nikiforov VV, Tolshmyakov AI, FGW, 3, 71, (1990).
[8] Shvarts D, Alon U, Ofer D, McCrory RL and Verdon CP, Phys.Plasmas, 2, 6, 2465-2472, (1995).
[9] Haan SW, Phys. Rev. A, 39, 5812, (1989).
[10] Alon U, Hecht J, Ofer D, Shvarts D, Phys. Rev. Lett., 72, 18, (1994).
[11] Hecht J, Alon U, Shvarts D, Phys.Fluids, 6, 12, 4019-4030, (1994).

Index